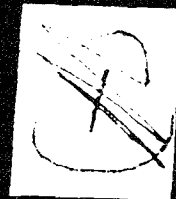


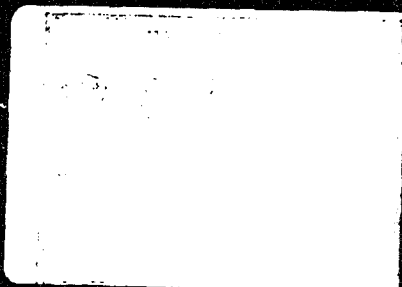
19950 111 145



Fourth Symposium :
(International)

on

DETONATION



U.S. Naval Ordnance Laboratory
White Oak

October 12-15, 1965

This document has been approved
for public release and sale; its
distribution is unlimited.

ACR-126
Office of Naval Research
Department of the Navy



PROCEEDINGS

Fourth Symposium

(International)

on

DETONATION

Sponsored by the
U.S. NAVAL ORDNANCE LABORATORY

In Cooperation with the
OFFICE OF NAVAL RESEARCH

October 12-15, 1965
U.S. Naval Ordnance Laboratory
White Oak, Maryland

Accession For	
NTIS CRA&I	<input checked="" type="checkbox"/>
DTIC TAB	<input type="checkbox"/>
Unannounced	<input type="checkbox"/>
Justification	
By	
Distribution /	
Availability Codes	
Dist	Avail and/or special
A-1	

UNANNOUNCED

19950111 145

U.S. GOVERNMENT PRINTING OFFICE

ACR-126

OFFICE OF NAVAL RESEARCH—DEPARTMENT OF THE NAVY
Washington, D.C.

For sale by the Superintendent of Documents, U.S. Government Printing Office
Washington, D.C. 20402 - Price \$5

PREVIOUS DOCUMENTS IN THIS DETONATION SERIES

"Proceedings — Conference on the Chemistry and Physics of Detonation," January 11, 12, 1951, sponsored by the Office of Naval Research, Unclassified, 110 pp.; AD 127020, printed copy - \$3.00.

"Preprints — Second ONR Symposium on Detonation," February 9, 10, 11, 1955, sponsored by the Office of Naval Research.

Unclassified Volume, 502 pp.; PB 128369, photocopy - \$81.90, microfilm - \$11.10 (available from Library of Congress, Washington, D.C. 20540).

Confidential Volume, 157 pp.; AD 52145.

"Preprints — Third Symposium on Detonation," September 26, 27, 28, 1960, cosponsored by Naval Ordnance Laboratory at White Oak and the Office of Naval Research, ONR Symposium Report ACR-52.

Volume 1 - Unclassified, 325 pp.; PB 181172, printed copy \$5.00.

Volume 2 - Unclassified, 333 pp.; PB 181173, printed copy \$5.00.

Volume 3 - Confidential, 187 pp.; AD 322061.

AVAILABILITY OF ABOVE DOCUMENTS

Persons and organizations entitled to the services of the Defense Documentation Center may apply to DDC for copies in normal manner.

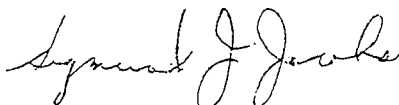
The unclassified documents (except PB 128369) are on public sale by the Clearinghouse for Federal Scientific and Technical Information, Springfield, Virginia 22151. They should be ordered by title and the identifying numbers indicated; all orders require prepayment or use of a Clearinghouse Deposit Account.

Statements and opinions contained herein are those of the authors and are not to be construed as official or reflecting the views of the Navy Department or of the naval service at large.

We wish to extend our thanks to the authors and participants who made the 1965 symposium a success. We are grateful to G. P. Cachia, W. E. Deal, R. E. Duff, and G. L. Schott for their time and effort in preparing summaries and reviews for this gathering. We wish to give thanks, as well, to their sponsoring laboratories: The Atomic Weapons Research Establishment; the University of California, Lawrence Radiation Laboratory; and the Los Alamos Scientific Laboratory for their support of the reviewers' efforts.

The existence of these proceedings is largely due to the financial support given by the Office of Naval Research. We wish to thank Dr. Ralph Roberts of ONR, past chairman of the previous U.S. Navy sponsored meetings, for his catalytic efforts in this matter. The important details of publication were ably handled by Mr. Irving Rudin of the Naval Research Laboratory. I wish to thank Andre Gleyzal, C. Dunkle, and M. Wilkins for their assistance in translating several of the French papers.

Lastly, I wish to acknowledge the tremendous effort put forth by my organizing committee; James E. Ablard, Douglas C. Hornig, Irving Kabik, John T. Oleksy, Ralph Roberts, and Donna Price. It was largely through the smooth teamwork of this group that the project moved without interruption from the time of the initial call for papers to final publication of these proceedings. I am deeply indebted to Dr. Donna Price for her able assistance in soliciting and selecting papers before the meeting and in editing them for these proceedings after it was over; to Douglas Hornig for the program and management of floor operations; to Irving Kabik for arranging the publication and delivery of preprints. We thank the management and our many associates at the Naval Ordnance Laboratory who cooperated so effectively in supplying facilities and in carrying out the details for the clock-like operation of this symposium.



Sigmund J. Jacobs, Chairman
Fourth Symposium (International) on Detonation

September 27, 1966

U.S. Naval Ordnance Laboratory, White Oak

TABLE OF CONTENTS

<u>DETONATION IN CONDENSED PHASES</u>	Page
METAL ACCELERATION BY CHEMICAL EXPLOSIVES J. W. Kury, H. C. Hornig, E. L. Lee, J. L. McDonnel, D. L. Ornellas, M. Finger, F. M. Strange, and M. L. Wilkins	3
THE MOTION OF PLATES AND CYLINDERS DRIVEN BY DETONATION WAVES AT TANGENTIAL INCIDENCE N. E. Hoskin, J. W. S. Allan, W. A. Bailey, J. W. Lethaby, and I. C. Skidmore	14
THE CHAPMAN-JOUGUET ISENTROPE AND THE UNDERWATER SHOCKWAVE PERFORMANCE OF PENTOLITE W. A. Walker and H. M. Sternberg	27
DETONATION OF A CYLINDRICAL CHARGE—STUDY OF THE FLOW OF BURNED GASES C. Fauquignon, M. Prouteau, and G. Verdès	39
THE EQUATION OF STATE OF DETONATION PRODUCTS BEHIND OVERDRIVEN DETONATION WAVES IN COMPOSITION B I. C. Skidmore and S. Hart	47
AN EQUATION OF STATE OF DETONATION PRODUCTS AT PRESSURES BELOW 30 KILOBARS J. W. S. Allan and B. D. Lambourn	52
INVITED REVIEW—STRUCTURE, CHEMISTRY, AND INSTABILITY OF DETONATION IN GASES Garry L. Schott	67
THEORETICAL CONSIDERATIONS ON THE PROPAGATION OF SHOCK AND DETONATION WAVES R. Chéret	78
FAILURE OF THE CHAPMAN-JOUGUET THEORY FOR LIQUID AND SOLID EXPLOSIVES W. C. Davis, B. G. Craig, and J. B. Ramsay	84*
RADIUS OF CURVATURE EFFECT ON DETONATION VELOCITY LeRoy G. Green and Edward James, Jr.	86
LATERAL SHOCK PRESSURE MEASUREMENTS AT AN EXPLOSIVE COLUMN . . . Lippe D. Sadwin and Norman M. Junk	92
STUDIES OF THE DIAMETER-DEPENDENCE OF DETONATION VELOCITY IN SOLID COMPOSITE PROPELLANTS—I. ATTEMPTS TO CALCULATE REACTION-ZONE THICKNESS Mary L. Pandow, K. F. Ockert, and H. M. Shuey	96
STUDIES OF THE DIAMETER-DEPENDENCE OF DETONATION VELOCITY IN SOLID COMPOSITE PROPELLANTS—II. PREDICTION OF FAILURE DIAMETERS Mary L. Pandow, K. F. Ockert, and T. H. Pratt	102
NON-IDEAL DETONATION WITH CONSTANT LATERAL EXPANSION Franz Wecken	107
DETONATIONS IN LIQUID EXPLOSIVES—THE LOW-VELOCITY REGIME R. W. Watson, C. R. Summers, F. C. Gibson, and R. W. Van Dolah	117

*Abstract Only

DETONATION OF NITROMETHANE-TETRANITROMETHANE MIXTURES: LOW AND HIGH VELOCITY WAVES	126
Adolph B. Amster, D. M. McEachern, Jr., and Z. Pressman	
OBSERVATION AND STUDY OF THE CONDITIONS FOR FORMATION OF MACH DETONATION WAVES	135
J. P. Argous, C. Peyre, and J. Thouvenin	
MACH INTERACTION OF TWO PLANE DETONATION WAVES	142
B. D. Lambourn and P. W. Wright	
INTERACTION OF OBLIQUE DETONATION WAVES WITH IRON	153*
H. M. Sternberg and D. Piacesi	
INTERACTIONS OF DETONATION WAVES IN CONDENSED EXPLOSIVES	154*
S. D. Gardner and Jerry Wackerle	
AXIAL INITIATION OF MULTI-COMPONENT EXPLOSIVES CHARGES	156
Louis Deffet and C. Fossé	
A DETONATION CALORIMETER AND THE HEAT OF PRODUCTS OF DETONATION OF PENTA-ERYTHRITOL TETRANITRATE (PETN)	167*
D. L. Ornellas, J. H. Carpenter, and S. R. Gunn	
ANOMALOUS ISENTROPE RESULTS OBTAINED WITH THE RUBY COMPUTER PROGRAM	168
Joseph Hershkowitz	
FRONT AND MASS VELOCITY AT DETONATION IN EVACUATED CHAMBERS . . .	176
N. Lundborg	
DETONATION LIMITS IN CONDENSED EXPLOSIVES	179
William E. Gordon	
INVITED REVIEW—SUMMARY OF PAPERS ON CONDENSED PHASE DETONATION	198
Russell E. Duff	

SHOCK WAVES AND RELATED FLOWS

EVALUATION OF THE GRUNEISEN PARAMETER FOR COMPRESSED SUBSTANCES—I. METALS	205
W. H. Andersen	
THE EQUATION OF STATE OF 1060 ALUMINUM FROM SHOCK WAVE MEASUREMENTS	213*
G. D. Anderson, A. L. Fahrenbruch, and G. R. Fowles	
THE COMPRESSION OF POLYMETHYL METHACRYLATE BY LOW AMPLITUDE SHOCK WAVES	214
T. P. Liddiard, Jr.	
SHOCK WAVE COMPRESSION OF PLEXIGLAS FROM 3 TO 20 KILOBARS	222
W. J. Halpin and R. A. Graham	
ANALYSIS OF SHOCK WAVE AND INITIATION DATA FOR SOLID EXPLOSIVES . .	233
J. B. Ramsay and A. Popolato	
LOW-PRESSURE HUGONIOTS OF SOLID EXPLOSIVES	239*
Richard J. Wasley and Joseph F. O'Brien	
THE UNREACTED HUGONIOT EQUATIONS-OF-STATE OF SEVERAL EXPLOSIVES	240*
N. L. Coleburn and T. P. Liddiard, Jr.	

* Abstract Only

DETERMINATION OF SHOCK HUGONIOTS FOR SEVERAL CONDENSED PHASE EXPLOSIVES	241
V. M. Boyle, R. L. Jameson, and M. Sultanoff	
SHOCK INDUCED PHASE TRANSITIONS	248
George E. Duvall and Y. Horie	
EFFECT OF A SHOCK WAVE ON A POROUS SOLID.	258
Jacques Thouvenin	
SHOCK BEHAVIOR OF SOME NON-REACTING POROUS SOLIDS	266
John R. Rempel and David N. Schmidt	
ELASTOPLASTIC EFFECTS IN THE ATTENUATION OF SHOCK WAVES.	277
John O. Erkmann	
HYDRODYNAMIC ELASTIC PLASTIC THEORY AND PLANE SHOCK WAVES IN METALS. I. THEORY.	289*
James C. Pearson	
THE ELASTO-PLASTIC RELEASE BEHAVIOUR OF MAGNESIUM AT 80 KB	290
P. J. A. Fuller and J. H. Price	
THE INFLUENCE OF MECHANICAL PROPERTIES ON WAVE PROPAGATION IN ELASTIC-PLASTIC MATERIALS	295
B. M. Butcher and D. E. Munson	
THE INSTABILITY OF AN INTERFACE BETWEEN TWO FLUIDS UNDER VARIABLE NORMAL ACCELERATION	305
I. G. Cameron and H. H. M. Pike	
CALCULATION OF THE GROWTH OF INTERFACE INSTABILITIES BY A LAGRANGIAN MESH METHOD	316
L. A. Elliott	
INVITED REVIEW—SHOCK WAVE RESEARCH ON INERT SOLIDS	321
W. E. Deal	

INITIATION, IGNITION, AND GROWTH OF REACTION

THE EFFECT OF INTERSTITIAL GAS ON THE SHOCK SENSITIVITY OF LOW DENSITY EXPLOSIVE COMPACTS.	349
Michael C. Chick	
SHOCK INITIATION OF LOW-DENSITY PRESSINGS OF AMMONIUM PERCHLORATE	359
Marjorie W. Evans, B. O. Reese, and L. B. Seely	
INITIATION OF A SOLID EXPLOSIVE BY A SHORT-DURATION SHOCK	373
Elisabeth F. Gittings	
OBLIQUE IMPACT OF A LAYER OF EXPLOSIVE BY A METAL PLATE	381
F. David, C. Fauquignon, H. Bernier, and J. Potau	
EXPERIMENTAL OBSERVATIONS OF INITIATION OF NITROMETHANE BY SHOCK INTERACTIONS AT DISCONTINUITIES	386
J. R. Travis	
INITIATION OF DETONATION BY THE INTERACTION OF SHOCK WITH DENSITY DISCONTINUITIES	394*
Charles L. Mader	
AN EQUATION OF STATE AND DERIVED SHOCK INITIATION CRITICALITY CONDITIONS FOR LIQUID EXPLOSIVES	395*
Julius W. Enig and Francis J. Petrone	

*Abstract Only

THE EFFECT OF WAX ON THE SHOCK SENSITIVITY OF EXPLOSIVE COMPACTS	399
John Eadie	
DIRECT CONTACT DETONATION SENSITIVITY	404
Jacob Savitt, Capt. Nicholas Leone, and Carl Kyselka	
THE EFFECT OF PHYSICAL AND CHEMICAL PROPERTIES ON THE SENSITIVITY OF LIQUID EXPLOSIVES	412
J. E. Hay, J. Ribovich, F. H. Scott, and F. C. Gibson	
RETONATION CAUSED BY THE REFLECTION OF DIVERGENT WAVES	426
W. R. Marlow	
COMPARISON BETWEEN SHOOTING AND BARRIER TESTS	432
N. Lundborg	
THE INITIATION PROPERTIES OF BOOSTERS IN EXPLOSIVES WITH LOW SENSITIVITY	435
C. H. Johansson and T. Sjölin	
SIZE FACTORS IN DETONATION TRANSFER	442
R. H. F. Stresau	
CONFINEMENT EFFECTS IN EXPLODING BRIDGEWIRE INITIATION OF DETONATION	449
R. H. F. Stresau, R. M. Hillyer, and J. E. Kennedy	
SURFACE RATE PROCESSES AND SENSITIVITY OF HIGH EXPLOSIVES	461*
R. F. Chaiken and F. J. Cheselske	
LOW ORDER REACTIONS IN SHOCKED EXPLOSIVES	462
Neill Griffiths and V. C. Broom	
INITIATION OF EXPLOSIVES BY LOW VELOCITY IMPACT	473
Hyla S. Napadensky	
FURTHER STUDIES ON THE IGNITION OF EXPLOSIVES	477
L. G. Green and G. D. Dorrough	
THE INITIATION OF BURNING IN HIGH EXPLOSIVES BY SHOCK WAVES	487
T. P. Liddiard, Jr.	
MECHANICAL AND DETONATION PROPERTIES OF RUBBER BONDED SHEET EXPLOSIVES	496
Werner Kegler and Rudi Schall	
EXPLICIT SOLUTIONS FOR UNSTEADY SHOCK PROPAGATION IN CHEMICALLY REACTING MEDIA	502
G. K. Adams and M. Cowperthwaite	
INVITED PAPER—SUMMARY PAPER ON INITIATION, IGNITION AND GROWTH OF REACTION	512
G. P. Cachia	
 <u>HYDRODYNAMIC COMPUTATION METHODS</u>	
THE USE OF ONE- AND TWO-DIMENSIONAL HYDRODYNAMIC MACHINE CALCULATIONS IN HIGH EXPLOSIVE RESEARCH	519
Mark L. Wilkins	
CALCULATION OF UNSTEADY 2-D FLOWS BY VARIOUS NUMERICAL METHODS	527
A. Vidart, P. Béatrix, Y. Chevalier, and H. Bouchon	

*Abstract Only

THE CALCULATION OF THE HYDRODYNAMIC BEHAVIOUR OF PLANE ONE DIMENSIONAL EXPLOSIVE/METAL SYSTEMS	538
B. D. Lambourn and J. E. Hartley	

EXPERIMENTAL METHODS

A METHOD FOR THE STUDY OF PROPERTIES OF SOLID EXPLOSIVES AND OTHER SOLID (INCLUDING POROUS) MATERIALS WHEN SUBJECTED TO SHOCK WAVES	555
W. L. Murray and J. Plant	
EXPERIMENTAL METHOD FOR ANALYSIS OF THE STRUCTURE OF A SHOCK WAVE IN A SOLID	566
C. Peyre, J. Pujol, and J. Thouvenin	
A TECHNIQUE FOR THE PRECISE MEASUREMENT OF THE MOTION OF A PLANE FREE SURFACE	573
G. Eden and P. W. Wright	
A MICROWAVE TECHNIQUE FOR STUDYING DETONATION PHENOMENA	584
Edgar G. Johnson	
ON ELECTRICAL CONDUCTIVITY IN DETONATION PRODUCTS	595
Bernard Hayes	
A TECHNIQUE FOR DETAILED TIME-RESOLVED RADIATION MEASUREMENTS IN THE REACTION ZONE OF CONDENSED EXPLOSIVES	602
Per-Anders Persson, Bertil Andersson, and Sven-Olof Ståhl	
ELECTRICAL TRANSDUCER STUDIES OF INITIATION OF LIQUID EXPLOSIVES . .	609
J. R. Travis	
ELECTRICAL PROBE TECHNIQUE FOR MEASUREMENT OF DETONATION AND DEFLAGRATION VELOCITIES	616
Locha D. Pitts	
ANOMALOUS THERMOELECTRIC EFFECT IN THE SHOCK REGIME AND APPLICATION TO A SHOCK PRESSURE TRANSDUCER	627
Jean Crosnier, Jean Jacquesson, and Andre Migault	
PERMEX APPLICATIONS TO STUDIES OF DETONATION WAVES AND SHOCK WAVES	639
Douglas Venable and T. J. Boyd, Jr.	
LIST OF ATTENDEES	649
AUTHOR INDEX	657



Accession For	
NTIS CRA&I	<input checked="" type="checkbox"/>
DTIC TAB	<input type="checkbox"/>
Unannounced	<input type="checkbox"/>
Justification	
By	
Distribution /	
Availability Codes	
Dist	Avail and/or Special
A-1	

DETONATION IN CONDENSED PHASES

Chairmen: J. E. Ablard
*U.S. Naval Ordnance Laboratory,
White Oak, Silver Spring, Maryland*

J. Berger
*Commissariat a l'Energie Atomique,
France*

METAL ACCELERATION BY CHEMICAL EXPLOSIVES

J. W. Kury, H. C. Hornig, E. L. Lee, J. L. McDonnel,
D. L. Ornellas, M. Finger, F. M. Strange, M. L. Wilkins
*Lawrence Radiation Laboratory
Livermore, California*

ABSTRACT

The ability of chemical explosives to accelerate metal has been investigated in considerable detail. An accurate hydrodynamic test has been developed to measure relative metal accelerating ability, and results have been obtained for a number of explosives.

Hydrodynamic tests have been used to generate pressure-volume-energy equations of state for detonation products. These equations of state can be used in calculations to predict the performance of an explosive in a variety of geometries. The equation of state obtained for Comp B is compared with those obtained by other investigators.

Thermochemical calculations have been shown to predict accurately the relative performance of many explosives. These calculations have also been used to correlate the effect on performance of the amount and type of binder used in explosives containing HMX.

INTRODUCTION

One of the most important uses of chemical explosives is to accelerate metal. This ability of an explosive to impart energy to metal has often been referred to as brisance, and a variety of relatively simple tests [1] have been evolved over the years to measure this property. Among them are the Trauzl block test, ballistic mortar, sand test and small scale plate push test [2]. Such tests have considerable appeal since they use small amounts of explosive and do not, in general, require expensive diagnostic equipment. Unfortunately, it has been our experience that these tests do not accurately predict the metal accelerating ability of many explosives even on a relative basis. For example, the exceptional performance of some boron-containing explosives in the sand test and small scale plate push test and of certain high density formulations in the plate dent test have not been borne out in subsequent large-scale metal acceleration tests. Moreover, information on the fundamental behavior of the detonation products of an explosive cannot be obtained from such tests because they are not amenable to accurate hydrodynamic interpretation.

The ability to measure or calculate precisely an explosive's metal accelerating

performance is of considerable importance. It permits one to determine an optimum balance between performance, sensitivity, thermal stability, and physical properties for a given explosive formulation. To do this we have developed metal acceleration tests which, not only permit a precise relative ordering of explosives, but also give sufficient information so that an accurate hydrodynamic equation of state can be generated for the detonation products. In addition, we have found that results from thermochemical-hydrodynamic calculations using a code such as RUBY [3] accurately predict the relative performance of many explosives. The details of these experimental methods and calculations are discussed in this paper, and results for a variety of explosives are presented. Also, information on the equation of state of detonation products is presented.

RELATIVE PERFORMANCE MEASUREMENT USING CYLINDER TEST

A variety of metal accelerating tests has been investigated for measuring relative performance of explosives. They include the sphere test [4], plate push test [5], flat plate test [2] and cylinder test [2]. Of these we have found the cylinder test to be the most versatile for determining relative performance.

An early variant of this test was described at the Third Detonation Symposium [2]. However, since significant changes have been made, a brief description follows.

Experimental

The standard cylinder test geometry consists of a 1-in.-diameter, 12-in.-long explosive charge fitted into a copper tube with a 0.1022-in.-thick wall. A plane wave lens and 0.5-in.-thick Comp B booster is used to initiate the explosive at one end. The radial motion of the cylinder wall is measured in a plane perpendicular to the cylinder axis 7 in. from the booster end. A streak camera records the motion, using conventional shadowgraph techniques. In addition, the detonation velocity of the explosive is measured by placing pin switches 9 in. apart on the surface of the cylinder.

The streak camera record is read on a precision comparator which punches out the data directly on IBM cards. A computer code converts film coordinates into actual radius (R) and time (t), fits the data, and calculates radial wall position and velocity at specified values of $R - R_0$. Reproducibility of radius-time data between duplicate experiments is better than 0.5 percent.

Standard 1-in.-diameter cylinder test results for Comp B, Grade A at a density of 1.717 g/cc are presented in Table 1. Results for a 2-in.-diameter scaled experiment (ratio of mass of explosive to mass of metal held constant) are also presented and show no diameter effect.

Experiments were carried out to measure wall radius-time behavior at various positions along the 12 in. long cylinder. Results, confirmed by hydrodynamic calculations, indicate that steady state conditions exist in a region ~3 in. to 9 in. from the booster end.

Interpretation of Cylinder Test

Two-dimensional hydrodynamic calculations [6] were used to investigate the behavior of the detonation products in the cylinder test. The results indicate that the detonation products expand essentially along the Chapman-Jouguet (C-J) isentrope. These calculations also showed that the relative volume (V) of the detonation products in the cylinder can be simply related to the expansion of the cylinder (see Fig. 1). Moreover, this relation is not sensitive to the explosive used. As a result, one is able to assess the relative energy delivery of explosives

TABLE 1
Radius-Time History of Copper Cylinders
Expanded by Comp B, Grade A

25.4-mm-diam. Comp B 2.606-mm Copper Wall		50.8-mm-diam. Comp B 5.21-mm Copper Wall	
$R - R_0$ (mm)	t (μ sec)	$R - R_0$ (mm)	$t/2$ (μ sec)
2	2.17	4	2.15
3	3.00	6	3.00
4	3.77	8	3.78
5	4.51	10	4.51
6	5.22	12	5.21
7	5.91	14	5.90
8	6.59	16	6.59
9	7.26	18	7.26
10	7.92	20	7.92
11	8.57	22	8.57
12	9.22	24	9.21
13	9.86	26	9.85
14	10.50	28	10.48
15	11.13	30	11.11
16	11.75	32	11.73
17	12.37	34	12.35
18	12.99	36	12.97
19	13.60	38	13.59
20	14.22	40	14.20
21	14.83	42	14.81
22	15.43	44	15.41
23	16.04	46	16.02

merely by comparing cylinder wall velocities at the same expansion. The actual expansion at which this comparison should be made depends on the geometry in which the explosives are to be used.

Hydrodynamic calculations for a variety of geometries show that, with the mass ratios of explosive to metal usually used, only two cylinder expansions need to be considered to evaluate an explosive: $R/R_0 \approx 1.3$ and $R/R_0 \approx 2$. This results from the fact that for detonations impinging head-on against metals essentially all the energy is transferred to the metal by the time the detonation products reach an expansion of $V \approx 2$. This expansion is reached in the cylinder test at $R/R_0 \approx 1.3$. In contrast, for grazing or sideways detonations the products continue to effectively transfer energy to the metal until they reach larger expansions, $V \approx 7$. These expansions are reached in the cylinder

test at $R/R_0 > 2$. One is thus able to assess the relative performance of an explosive in these two general types of metal acceleration applications by merely comparing cylinder wall velocities at early and late expansion.

Cylinder Test Results

Experimental cylinder test results at small and large expansions for a variety of explosives

are presented in Table 2. The relative ability of these explosives to deliver energy to metal in both head-on and sideways geometries is summarized in Table 3. These results were calculated from the data in Table 2 by simply squaring cylinder wall velocities and comparing them to the square of the Comp B values. Many of the values listed in Table 3 have been confirmed when the explosives were used in actual full-scale metal acceleration experiments.

TABLE 2
Cylinder Test Results

Explosive		Density (g/cc)	D (mm/ μsec)	Cylinder Wall Velocity (mm/μsec)	
Symbol	Composition ¹			at R - R ₀ = 5 mm	at R - R ₀ = 19 mm
HMX	---	1.891	9.11	1.65	1.86
PBX-9404-03	HMX, NC, CEF (94/3/3)	1.841	8.80	1.57	1.80
PETN	---	1.765	8.16	1.56	1.79
RX-09-AA	HMX, DNPA, EtDP (93.7/5.7/0.6)	1.827	8.69	1.56	1.79
RX-04-BY	HMX, FNR, (86/14)	1.894	---	1.54	1.77
LX-07-0	HMX, Viton (90/10)	1.865	8.64	1.54	1.77
Octol	HMX, TNT (78/22)	1.821	8.48	1.53	1.75
HMX-Kel F	HMX, Kel F (84/16)	1.882	---	1.52	1.73
RX-04-AT	HMX, θ_x (88/12)	1.798	8.38	1.47	1.73
X-0204	HMX, Teflon (83/17)	1.911	8.42	1.50	1.72
LX-04-1	HMX, Viton (85/15)	1.865	8.47	1.49	1.71
PBX-9010	RDX, Kel F (90/10)	1.787	8.39	1.45	1.71
Cyclotol	RDX, TNT (77/23)	1.754	8.25	1.46	1.70
PBX-9011	HMX, Estane (90/10)	1.777	8.50	1.46	1.69
RX-04-P1	HMX, Viton (80/20)	1.876	8.32	1.46	1.67
RX-04-AV	HMX (CH ₂) _n (92/8)	1.719	8.63	1.44	1.67
Comp B, Grd A	RDX, TNT (64/36)	1.717	7.99	1.39	1.63
RX-05-AA	RDX, Polstyr DOP (90/8/2)	1.675	---	1.38	1.60
TNT	---	1.630	6.94	1.18	1.40
NM	Nitromethane	1.143	6.37	1.01	1.22

¹Numerals are approximate weight percent of components.

Abbreviations:

NC = Nitrocellulose
 CEF = Tris β -chloroethylphosphate
 DNPA = 2,2-Dinitropropylacrylate
 EtDP = Ethyl 4,4-dinitropentanoate
 FNR = Tetrafluoroethylene-trifluoro
 nitroso methane copolymer
 Viton A = Trademark for vinylidene fluoride-
 hexafluoropropylene copolymer
 Kel F = Trademark for chloro-trifluoroethylene
 polymer

θ_x = Carborane-fluorocarbon
 copolymer
 Teflon = Trademark for tetrafluoro-
 ethylene polymer
 Estane = Trademark for polyester-
 urethane of adipic acid 1,4-
 butanediol, diphenylmethane
 diisocyanate
 (CH₂)_n = Polyethylene
 Polstyr = Polystyrene
 DOP = Dioctylphthalate

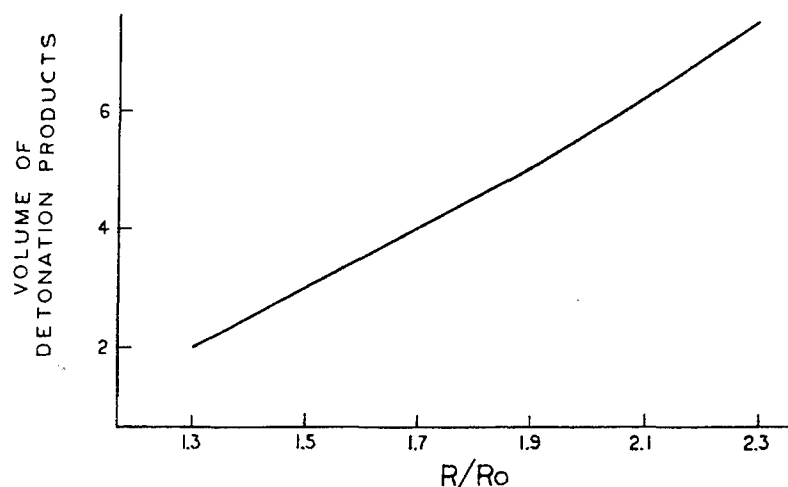


Fig. 1 - Relative volume of detonation products as a function of cylinder expansion

TABLE 3
Relative Metal Accelerating Ability

Explosive Symbol ¹	Relative Energy Delivered to Metal	
	In Geometries Characterized by Head-On Detonations	In Geometries Characterized by Sideways Detonations
HMX	1.41	1.30
PBX-9404-03	1.28	1.22
PETN	1.26	1.21
RX-09-AA	1.26	1.21
RX-04-BY	1.23	1.18
LX-07-0	1.23	1.18
Octol	1.21	1.15
HMX-Kel-F	1.20	1.13
RX-04-AT	1.12	1.13
X-0204	1.16	1.11
LX-04-1	1.14	1.10
PBX-9010	1.09	1.10
Cyclotol	1.10	1.09
PBX-9011	1.10	1.07
RX-04-P1	1.10	1.05
RX-04-AV	1.07	1.05
Comp B, Grd A	1	1
RX-05-AA	0.99	0.96
TNT	0.72	0.74
NM	0.53	0.56

¹See Table 2 for identifications.

DETONATION PRODUCT EQUATION OF STATE FOR ACCURATE PERFORMANCE CALCULATION

The ability to calculate the performance of a system containing explosive and metal has, in general, been limited to simple idealized geometries. However, the advent of high speed, large memory computers such as the IBM 7030 and the CDC 6600 has changed this. With these computers the motion of metal in fairly complex geometries can now be accurately calculated using such hydrodynamic codes as HEMP [6].

To do this however, we must have an accurate description of the pressure-volume-energy (P-V-E) behavior of an explosives' detonation products. For most metal acceleration applications only a limited region in P-V-E space is of importance (see Fig. 2). This region includes the shock Hugoniot curve and isentropic expansion curve from the C-J state (A and B in Fig. 2) and slightly higher entropy states (shaded area in Fig. 2).

A variety of equations of state, both theoretical and empirical, have been proposed for the detonation products [7]. When these are used, with appropriate constants in hydrodynamic codes, they in general do not accurately predict the metal motion of a system. It can be shown [8] that this is not the fault of the hydrodynamic codes used, but merely implies inaccuracy in the P-V-E description of the detonation products.

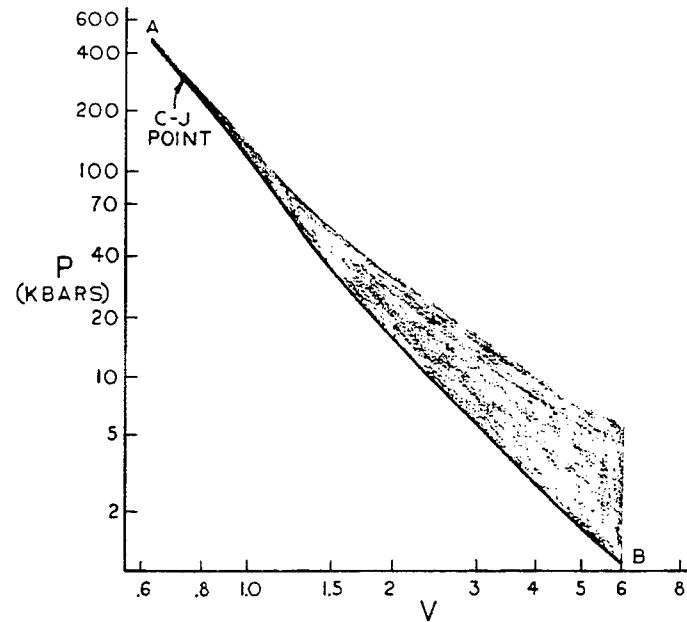


Fig. 2 - Pressure-volume region of interest in most metal acceleration applications

As a result, hydrodynamic experiments have been developed to measure more precisely the P-V-E behavior of an explosive. Wilkins [4] has found that data obtained when a sphere of explosive expands an aluminum shell can be used to determine detonation product P-V-E behavior near the C-J adiabat from ~500 to 20 kbar. Data from the cylinder test can be used to extend this pressure range down to about 1 kbar. In both these tests the P-V-E behavior for the detonation products is determined by a successive approximation procedure. Assumed P-V-E values are used in a hydrodynamic calculation and the calculated sphere or cylinder wall velocities compared with experiment. The P-V-E values are changed until agreement is reached. The sensitivity of this procedure, especially at low pressure, is considerably better than for other techniques used to measure P-V-E behavior. This sensitivity is illustrated in Table 4 by data obtained from hydrodynamic calculations on the cylinder test using two slightly different equations of state.

The P-V-E behavior deduced from expanding sphere and cylinder test data could not be described by a simple polytropic equation of state (γ -law). Neither is the behavior consistent with that calculated using the Becker-Kistiakowsky-Wilson (BKW) [9] or LJD [10] equation of state. Wilkins was able to describe P-V-E data obtained from sphere experiments by

TABLE 4
Effect of Change in Isentrope Pressure on Cylinder Test Radius-Time Behavior

Volume	Isentrope Pressure (kbar)		Cylinder R/R_0	$t - t_0$ (μ sec)	
	Case 1	Case 2		Case 1	Case 2
1.0	151.0	147.3			
1.4	47.6	43.4	1.19	2.25	2.33
2.0	16.7	14.4	1.39	3.94	4.08
4.0	5.4	4.7	1.79	6.96	7.24
5.5	3.5	3.0	2.18	9.74	10.16
7.0	2.5	2.2	2.57	12.39	12.93

$$P = A/V^Q + B \left(1 - \frac{\omega}{R_1 V} \right) e^{-R_1 V} + \frac{\omega E}{V} \quad (1)$$

This equation, however, had to be modified when the experimental data were extended to lower pressures with cylinder test results. The modified form is

$$P = A \left(1 - \frac{\omega}{R_1 V} \right) e^{-R_1 V} + B \left(1 - \frac{\omega}{R_2 V} \right) e^{-R_2 V} + \frac{\omega E}{V} \quad (2)$$

The equation for P as a function of V at constant entropy is

$$P_s = A e^{-R_1 V} + B e^{-R_2 V} + C V^{-(\omega+1)} \quad (3)$$

The constants in Eq. (2) were evaluated for Comp B, Grade A using the experimental P_{CJ} and data from cylinder and sphere tests. They are presented in Table 5. Deal's [11] and Wilkins' [12] P_{CJ} measurements were used to determine the initial slope of the C-J isentrope; sphere test data was used to determine P-V behavior at early expansions, $V \approx 1$ to 2; cylinder test data were used to determine the P-V behavior at larger expansions, $V \approx 1.5$ to 7.

TABLE 5
Equation of State Constants
for Comp B, Grade A

ρ_o	1.717	g/cc
D	0.798	cm/ μ sec
P_{CJ}	0.295	megabar
R_1	4.2	
R_2	1.1	
ω	0.34	
A	5.24229	
B	0.076783	
ϵ_o	0.085	megabar cc/cc

The P-V behavior of Eq. (2) for Comp B, Grade A can be contrasted to that predicted by other equations of state by comparing the quantity $\Gamma = -(\partial \ln P / \partial \ln V)_S$ as a function of V for the C-J isentrope. Figure 3 shows this comparison for Deal's γ -law [13]; Fig. 4 for the BKW equation [9]; and Fig. 5 for the LJD equation [10]. The new equation has a Γ behavior similar to that of the LJD equation.

The ability of Eq. (2) to describe the experimental results obtained for Comp B, Grade A has been compared to that of the other equations of state. Results for the cylinder test are summarized in Table 6. BKW, LJD and γ -law equations all deliver too much energy to the cylinder.

Results for the no-void sphere experiment are shown in Table 7. BKW and Deal's γ -law equations again deliver too much energy. The LJD equation delivers about the right amount of energy, but it predicts a low P_{CJ} (~260 kbar instead of the measured 295 kbar).

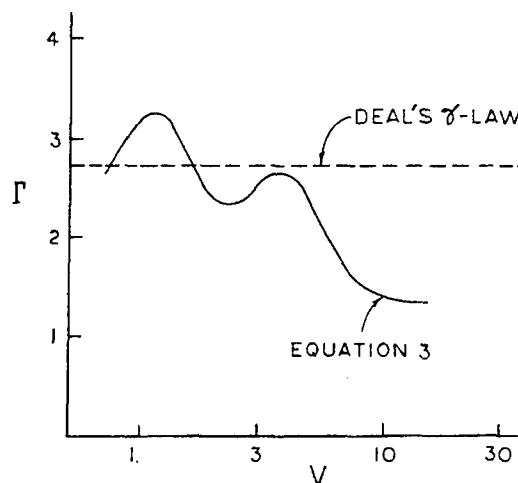


Fig. 3 - Comparison of Γ from Eq. (3) and Deal's γ -law for Comp B, Grade A

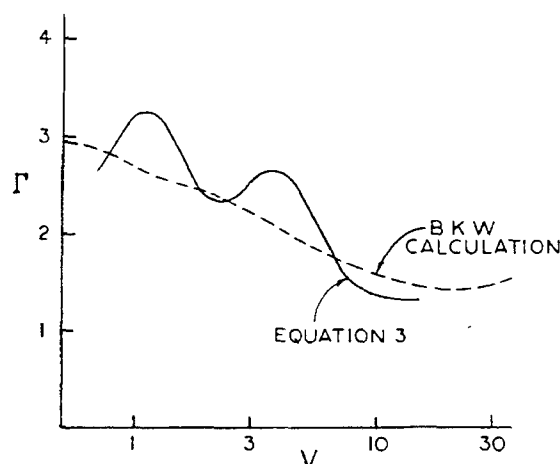


Fig. 4 - Comparison of Γ from Eq. (3) and the BKW equation for Comp B, Grade A

The Riemann integral has been calculated for Eq. (3) for Comp B, Grade A and compared to the results obtained by Deal from a series of impedance experiments [11,13] (see Figs. 6 and 7). The pressure vs particle velocity calculated from Eq. (3) agrees with the experimental data. This is also the case for pressure-particle velocity curves calculated using Deal's γ -law or the BKW equation. Results obtained using the LJD equation are, however, consistently lower.

The isentropic expansion of the detonation products of TNT, PETN, nitromethane (NM) and PBX 9404-03 has also been investigated and found to be very similar to that observed for Comp B, Grade A. Explosives with high carbon

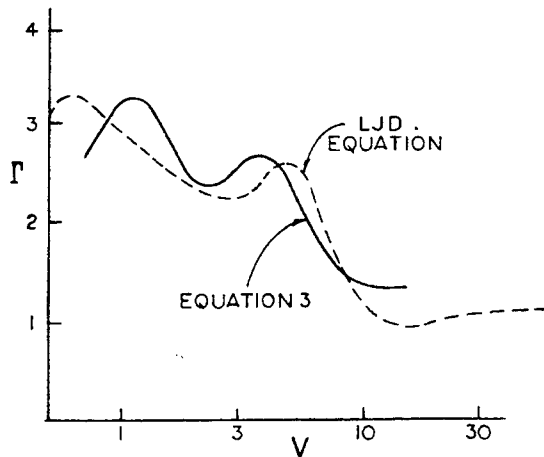


Fig. 5 - Comparison of Γ from Eq. (3) and the LJD equation for Comp B, Grade A

TABLE 7
Comparison of Calculated and Experimental
Sphere Test Results for Comp B, Grade A

R - R ₀ (mm)	t (μsec)				
	Experi- mental	Calculated Using Equation of State			
		Equa- tion (2)	Deal's γ-law	BKW	LJD
0	0	0	0	0	0
5	1.87	2.03	2.00	2.04	2.20
10	3.76	3.75	3.59	3.69	4.00
15	5.37	5.37	5.09	5.25	5.64
20	6.97	6.95	6.57	6.76	7.22
25	8.48	8.50	8.00	8.24	8.76
30	9.99	10.01	9.39	9.68	10.27
35	11.46	11.50	10.74	11.09	11.75

TABLE 6
Comparison of Calculated and Experimental
Cylinder Test Results for Comp B, Grade A

R - R ₀ (mm)	t (μsec)				
	Experi- mental	Calculated Using Equation of State			
		Equa- tion (2)	Deal's γ-law	BKW	LJD
0	0	0	0	0	0
2	2.17	2.18	2.05	2.10	2.25
4	3.77	3.76	3.50	3.62	3.84
6	5.22	5.19	4.79	4.93	5.23
8	6.59	6.56	6.03	6.20	6.56
10	7.92	7.89	7.21	7.43	7.83
12	9.22	9.19	8.38	8.62	9.09
14	10.50	10.46	9.53	9.78	10.30
16	11.75	11.72	10.67	10.93	11.50
18	12.99	12.97	11.78	12.07	12.68
20	14.22	14.20	12.91	13.19	
22	15.43	15.42	14.02		
24	16.64	16.63	15.13		
26	17.84	17.83			
28	19.04	19.04			

content (TNT), with low carbon content (PETN), with low initial density (NM) and with high initial density (PBX 9404-03) thus all seem to have a similar Γ behavior (see Figs. 8, 9, 10 and 11). Jones [14], in work on TNT, suggested solid-like behavior for the detonation products at high density. An initial increase in Γ is a consequence of this assumption.

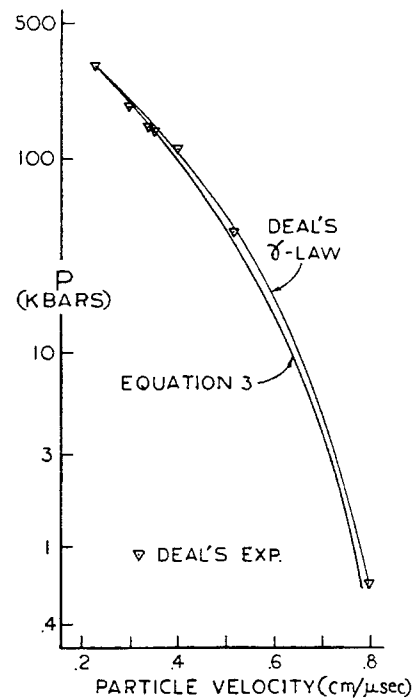


Fig. 6 - Comparison of calculated and experimental pressure vs particle velocity for Comp B, Grade A

It is important to point out that although we have used the Chapman-Jouguet hypothesis as a boundary condition for the generation of Eq. (3), the overall description of the expansion

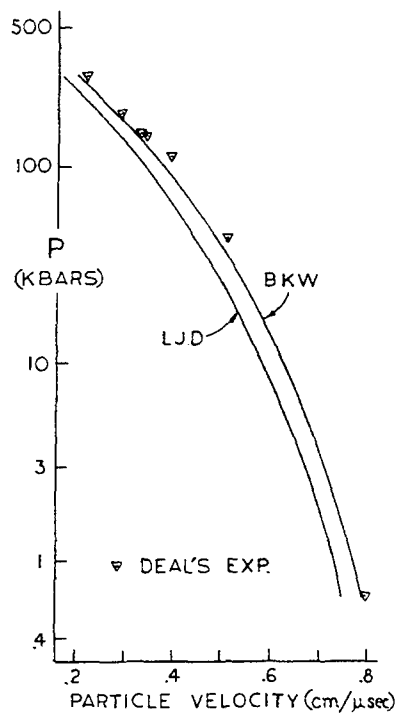


Fig. 7 - Comparison of calculated and experimental pressure vs particle velocity for Comp B, Grade A

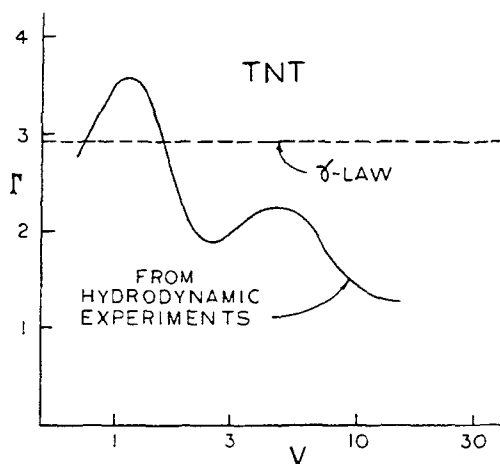


Fig. 8 - Γ vs relative volume for TNT

of the detonation products is, to an extent, independent of the hypothesis. The hypothesis specifies that if the initial pressure, P_{CJ} , is known, the slope of the isentrope through this point is determined by

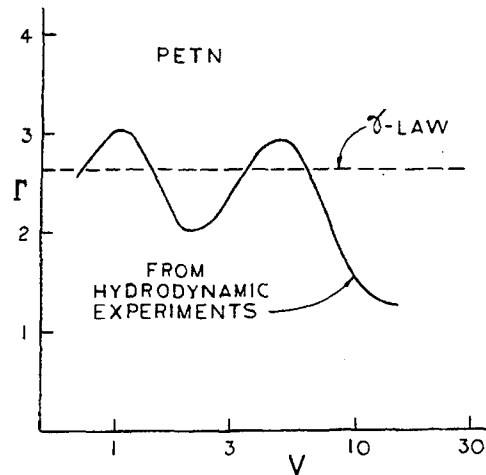


Fig. 9 - Γ vs relative volume for PETN

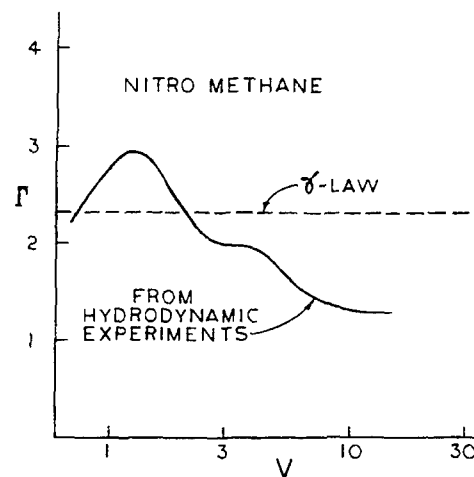


Fig. 10 - Γ vs relative volume for nitromethane

$$\Gamma = \frac{\rho_o D^2}{P_{CJ}} - 1. \quad (4)$$

Neither sphere nor cylinder tests are sensitive to the initial slope of the pressure-volume curve. This is true for any geometry in which the metal being accelerated is over a few mms thick. Data from these tests, however, do accurately determine the behavior of Γ for detonation products at specific volumes greater than 0.8.

Equation of state 2 contains the assumption that $V(\partial P/\partial E)_V = \text{constant}$. This is the same

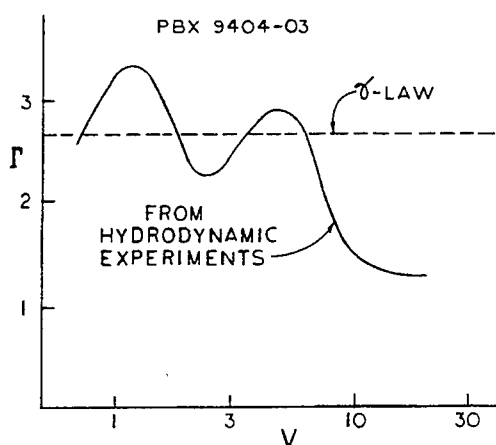


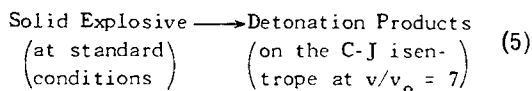
Fig. 11 - P vs relative volume for PBX 9404-03

assumption made by Fickett and Wood [15] and by Wilkins [4]. Cylinder experiments do not provide a test of this assumption. We are, therefore, using data from large-void sphere tests and detonation velocity vs loading density experiments to investigate this assumption.

In summary, it has been found that an accurate description of the P - V - E behavior of detonation products in the pressure range 500 to 1 kbar requires a rather complex equation of state (Eq. (2)). Such an equation of state, however, permits one to accurately calculate the energy an explosive delivers to metal in a variety of geometries.

DETERMINATION OF RELATIVE PERFORMANCE USING THERMOCHEMICAL CALCULATIONS

As was shown in the last section, the BKW equation of state does not accurately describe the P - V - E behavior of the detonation products. We have found, however, that it can be used in calculations to predict the relative performance of many explosives. To do this the energy release (ΔE) for the reaction



is calculated using the BKW equation in a thermodynamic-hydrodynamic code such as RUBY. In carrying out the calculation, the detonation product composition is frozen when the temperature drops below 1800°K. Comparing

this ΔE to that calculated for a reference explosive provides a relative measure of metal accelerating ability.

The relative energy release calculated in this manner for a set of standard explosives is compared to experimental data obtained in the cylinder test (see Table 8). The agreement is good.

TABLE 8
Comparison of RUBY-Calculated and Experimental Performance of Explosives Relative to Comp B, Grade A

Explosive	Relative Energy Imparted to Cylinder	RUBY-Calculated Relative Energy Release for Equation (5)
HMX	1.30	1.28
PETN	1.21	1.20
Cyclotol	1.09	1.08
Comp B, Grade A	1	1
TNT	0.74	0.72
Nitromethane	0.56	0.62

This calculation technique for evaluating performance is very useful to the chemist as a guide in the synthesis and formulation of explosives. It requires only that the composition, density and heat of formation of the explosive be known. As an example, we have found this technique useful in assessing the effect on performance of various binders and desensitizers used in HMX formulations. Figure 12 shows calculated and experimental decrease in performance as a function of volume percent HMX for some of these formulations. Again, the agreement is quite good.

CONCLUSIONS

The combination of hydrodynamic experiments and calculational techniques presented in this report provide an excellent means for assessing the metal accelerating ability of an explosive in a variety of geometries. Unfortunately, we are not aware of an easier way to accurately assess this type of performance since the results from most simple, small-scale tests are, often as not, very misleading.

REFERENCES

1. W. C. Lothrop and G. R. Handrick, Chem. Revs. 44, 419 (1949).

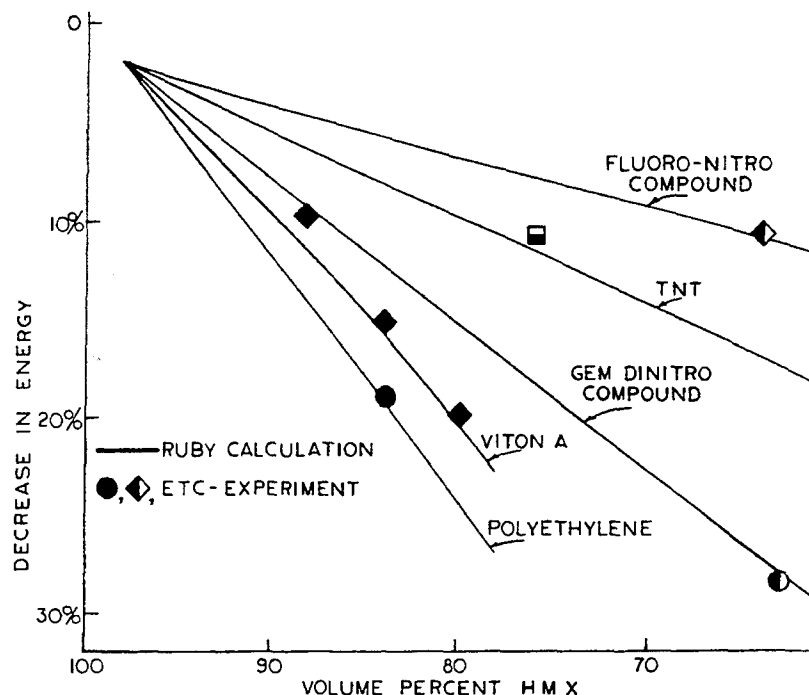


Fig. 12 - Comparison of RUBY-calculated and experimental performance of HMX-containing explosives

2. J. W. Kury, G. D. Dorrough, and R. E. Sharples, "Third Symposium on Detonation," ONR Symposium Report ACR-52, Vol. 3 (Confidential), p. 80 (1960).
3. H. B. Levine and R. E. Sharples, Univ. of Calif. Lawrence Rad. Lab., Livermore, Calif., Report UCRL-6815 (1962).
4. M. L. Wilkins, Univ. of Calif. Lawrence Rad. Lab., Livermore, Calif., Report UCRL-7797 (1964).
5. A. Solem, J. Kitchens, and J. Schneider, U.S. Naval Ordnance Lab., White Oak, Md., Report NAVORD 4006 (Confidential) (1955).
6. M. L. Wilkins, Univ. of Calif. Lawrence Rad. Lab., Livermore, Calif., Report-7322 (1963).
7. S. J. Jacobs, ARS Journal 30, 151 (1960).
8. M. L. Wilkins, "The Use of One and Two-Dimensional Machine Calculations in High Explosive Research," E-22, this Symposium.
9. C. L. Mader, Los Alamos Scientific Lab., Los Alamos, New Mex., Report LA-2900 (1963).
10. W. Fickett, Los Alamos Scientific Lab., Los Alamos, New Mex., Report LA-2712 (1962).
11. W. E. Deal, Phys. of Fluids 1, 523 (1958).
12. M. L. Wilkins, recent measurements at this Laboratory.
13. W. E. Deal, Third Symposium on Detonation, Vol. 2, p. 386, Princeton Univ. (1960).
14. H. Jones, British Repts. RC-166, RC-212 (1941) (not available). See 16, 17, 18 for results.
15. W. Fickett and W. W. Wood, Phys. of Fluids 1, 528 (1958).
16. J. Taylor, "Detonation in Condensed Explosives," Clarendon Press, Oxford, Eng. (1952).
17. R. H. Cole, "Underwater Explosions," Princeton Univ. Press, Princeton, N. J. (1948).
18. H. Jones and A. R. Miller, Proc. Roy. Soc. London, A-19, 480 (1948).

COMMENTS

G. G. DUNKLE, Applied Physics Laboratory,
Johns Hopkins University, Silver Spring,
Maryland

The suggested definition of BRISANCE may clear up some confusion. Brisance has been defined as "shattering power" and has been thought to depend on quantity of energy evolved and the speed of its liberation. Attempts have been made to correlate brisance with detonation velocity, energy, and pressure, without much more success than by the various small-scale tests noted in the first paragraph of the introduction.

Defining brisance as the ability of an explosive to accelerate metal makes it possible to measure brisance quantitatively, and clarifies the roles of both detonation energy and detonation pressure. Shattering power is an indirect effect of high values of these parameters which, as shown by various papers of this symposium, lead to generation of strong shock waves with spalling and other destructive effects on confining metals.

W. H. ANDERSEN, Shock Hydrodynamics, Inc.,
Sherman Oaks, California

During the detonation of an explosive whose charge density is about 1 gm/cc or greater, the detonation products are initially (before expansion) in a repulsive interaction potential energy state. This was pointed out many years ago by Dr. Brinkley. Because of this repulsive molecular interaction, the translational and rotational degrees of freedom of the molecules become vibrational in nature, and under this condition a Gruneisen-type of equation should be applicable in describing the state behavior of the detonation products. I have recently derived such an equation of state for the detonation products, following work initiated in 1953 by Parlin and myself. The Morse potential was used to describe the interaction energy, and the Gruneisen parameter used was that derived in my paper in this symposium. The solution of

the resulting equations show that the ideal detonation velocity is usually a linear function of the explosive charge density, as is known from experiment. Of special significance is the predicted adiabatic behavior for the expansion characteristics of the detonation products. The equations show that the pressure initially decreases more rapidly with increase in volume than is predicted by a constant gamma law gas. This behavior was found experimentally by Kury et al. and earlier by Wilkins et al. (UCRL-7797). The theoretical adiabatic exponent was found to increase with increase in volume until the volume corresponding to the minimum in the interaction potential energy was reached. It is of importance to note that the initial maxima in the adiabatic exponent versus volume plots of Kury et al. all occur at volumes which correspond roughly to that of the minimum in the potential energy.

Strictly speaking, the Gruneisen equation ceases to be valid for larger volumes but all variable covolume equations of state predict that the adiabatic exponent should thereafter decrease (essentially) monotonically with increase in volume until the low density value (about 1.3) is obtained. The Gruneisen equation reverts to a constant gamma law form under conditions that the interaction terms vanish. The initial increase in the theoretical adiabatic exponent is largely the result that the Gruneisen parameter increases with increase in volume, until the potential energy minimum is reached. This tends to rapidly reduce the thermal energy of the gas available for doing work as the volume of the detonation products is increased.

The second maxima observed in the plot of the adiabatic exponent versus volume by Kury et al. is not explained by the Gruneisen equation, but is possibly related to the nature of the chemical reactions (kinetics, equilibria shifts or heat capacity changes) which occur in the detonation products during their expansion, as suggested by Dr. Ablard. This is supported by the fact that the characteristics of the second maxima appear to be related to the composition (or oxygen balance) of the explosive.

THE MOTION OF PLATES AND CYLINDERS DRIVEN BY DETONATION WAVES AT TANGENTIAL INCIDENCE

N. E. Hoskin, J. W. S. Allan, W. A. Bailey, J. W. Lethaby and I. C. Skidmore
*Atomic Weapons Research Establishment
Aldermaston, Berkshire, England*

ABSTRACT

Flat plates and cylinders driven by detonation waves at tangential incidence provide steady two dimensional hydrodynamic systems which are theoretically tractable and experimentally simple. Such systems have been examined theoretically with the two dimensional steady state characteristic code ELA. Terminal states are found to be very similar to those assumed in the simple Gurney theory [1]. Experiments on a variety of plates with different mass loadings of Comp. B have given terminal velocities agreeing with theoretical predictions to within 2 percent. For a given copper cylinder loaded with different explosives the discrepancy between experiment and theory, assuming a polytropic gas equation of state for the detonation products, is as high as 10 percent. The effect of the compressibility of the metal is shown to be small so the effect of more sophisticated equations of state of the detonation products is being studied.

INTRODUCTION

Metal plates driven by detonation waves at normal incidence represent a one dimensional unsteady hydrodynamic problem which has received considerable theoretical and experimental attention (e.g., Aziz et al. [2]). Though computationally this is a straight-forward problem it is difficult to provide valid experimental data for comparison in the later stages of plate motion since edge effects perturb the one dimensional flow pattern of many practical systems. An equivalent stage of theoretical complexity is the two dimensional isentropic steady flow pattern which has the advantage of being experimentally attainable over all stages of plate motion. In this paper the theoretical motion of metal plates and cylinders driven by detonation waves at grazing incidence is compared with experiment. Results have been obtained from geometries where the motion is independent of end or side effects so that, with respect to the detonation front, these are truly two dimensional steady flows.

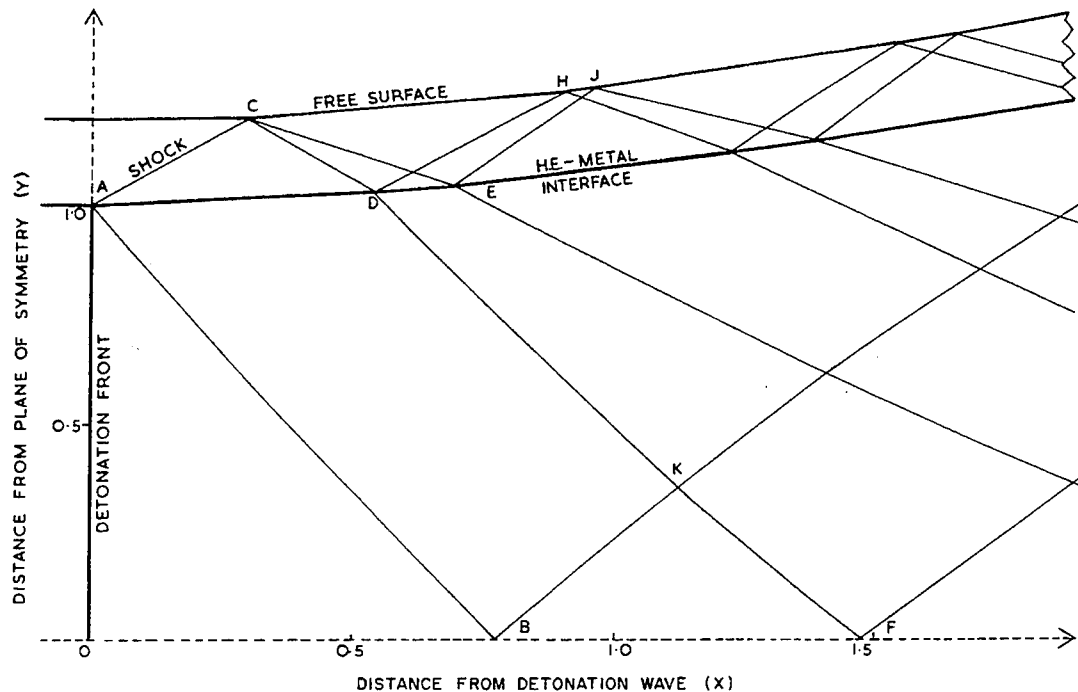
In the next section the theoretical aspects of the problem are analysed. The problem is defined, difficulties associated with the initial solution are discussed and finally the characteristic solution embodied in the computer code

ELA is derived. The numerical solution is then compared with the simple Gurney approach for predicting terminal states. The comparison with experiment is given in the subsequent sections. Experiments are described for determining the motion of explosively driven plates and cylinders. In the flat plate experiments terminal velocities have been obtained for a variety of configurations while in the cylinder experiments attention has been focussed on the details of the motion for a specific configuration.

CALCULATED RESULTS

Description of System Considered

The problem considered is shown in Fig. 1 where explosive sandwiched between two metal plates (or contained in a metal cylinder) is detonated at one end. Only one-half of the system is shown because of symmetry. A detonation wave AO (assumed to remain plane) travels along the explosive metal interface with constant velocity D while an oblique shock AC travels into the metal plate and is reflected at the free surface as a centred rarefaction DCE which gets reflected again at the explosive metal interface as a compression wave. A shock may form in this compression wave but



It will be shown that for small expansions away from the front these boundary conditions are identical for the three different conditions considered. These are a free surface, an interface with compressible material and a simple mass loading. Thus the effect of the boundary condition in the interior flow is merely to provide a scale effect to the Hill and Pack solution. The particular condition chosen then only applies at the edge of the explosive in the expansion down to a pressure determined by the conditions at the explosive surface. This will be discussed more fully in the following subsections.

The solution obtained is valid only for plane geometry. The corresponding analysis however seems intractable in cylindrical geometry but, since the radial component of velocity is extremely small in the expansion considered, it is assumed that the same initial solution holds for both plane and cylindrical geometry. The subsequent numerical solution of course deals with each geometry correctly and the results obtained support the assumption.

Hill and Pack Solution

A full discussion of this expansion is given in Ref. [4]. We introduce nondimensional variables given by

$$\begin{aligned}
 U &= u/a_{CJ}, \\
 V &= v/a_{CJ}, \\
 A &= a/a_{CJ}, \\
 M &= \rho/\rho_{CJ}, \\
 P &= p/p_{CJ}, \\
 X &= x/\ell, \\
 Y &= y/\ell
 \end{aligned} \tag{1}$$

where u, v, a, ρ, p, x, y are axial component of flow velocity, transverse component of flow velocity, sound speed, density, pressure, axial distance and transverse distance respectively. Suffices C.J. refers to Chapman-Jouguet values of the variables and 2ℓ is the width of the explosive (or diameter for cylindrical geometry). The equations governing the two dimensional steady flow are, in plane geometry

$$\frac{\partial}{\partial X} (MU) + \frac{\partial}{\partial Y} (MV) = 0 \tag{2}$$

$$Q^2 = U^2 + V^2 = \beta - \frac{2A^2}{\gamma - 1} \tag{3}$$

$$A^2 = M^{\gamma-1} \tag{4}$$

where

$$\beta = (\gamma + 1)/(\gamma - 1) \tag{5}$$

and γ is the polytropic exponent in the equation of state. Hill and Pack showed that a solution of Eqs. (2)-(4) could be found in series form viz.

$$\left. \begin{aligned}
 U &= 1 + 3G(Y) X^2 + O(X^4) \\
 V &= G'(Y) X^3 + O(X^5) \\
 M &= 1 - 3G(Y) X^2 + O(X^4)
 \end{aligned} \right\} \tag{6}$$

where $G(Y)$ satisfies the equation

$$G'' = 18(\gamma + 1) G^2 \tag{7}$$

the prime denoting differentiation w.r.t. Y .^{*} The coordinate axes are chosen so that $Y = 0$

^{*}In cylindrical geometry the equation corresponding to (7) is

$$G'' + \frac{G'}{Y} = 18(\gamma + 1) G^2,$$

i.e., a form similar to Emden's equation, but this has no known solution of the right form for subsequent analysis.

corresponds to the mid plane of the explosive or the axis of the cylinder. Here

$$V = 0 \text{ or } G'(0) = 0, \tag{8}$$

and (7) may be integrated to give

$$(G')^2 = 12(\gamma + 1) [G^3(Y) - G^3(0)]. \tag{9}$$

This equation is satisfied by the Weierstrassian elliptic function $[\wp]$ and $G(0)$ is determined when the position of the singularity is known. For a free surface Hill and Pack showed that this singularity is at the edge of the explosive. The same analysis holds for the boundary condition of a compressible plate and indeed is valid, for small expansions, for an incompressible plate (i.e., a mass loading at the edge of the explosive). Thus in all cases

$$G(Y) = \wp[\{3(\gamma + 1)\}^{1/2} (1 - Y)] \tag{10}$$

and near $Y = 1$ may be expanded as

$$\begin{aligned}
 G(Y) &= \frac{1}{3(\gamma + 1)(1 - Y)^2} \\
 &\times [1 + 0.457978(1 - Y)^6 + 0.016134(1 - Y)^{12}].
 \end{aligned} \tag{11}$$

For $X < 0.02$ then, using (11), $v < 10^{-8}$ on $Y = 0$ which is sufficiently accurate for our purposes.

Note that although $G(Y)$ is singular at $Y = 1$, $(1 - Y)^2 G(Y)$ and $(1 - Y)^3 G'(Y)$ are regular and the expressions (6) can be used right up to $Y = 1$ if $Y \rightarrow 1$ along a line through $Y = 1$ making a finite angle $\Delta\phi$ with the detonation front, i.e., with

$$\frac{X}{1 - Y} = \Delta\phi = \text{constant}. \tag{12}$$

We see in the next section that this line is a characteristic of the expansion at the boundary and the two solutions can be matched to terms in $(\Delta\phi)^2$.

Solution at the Edge of the Explosive

To evaluate the solution near A in Fig. 1 consider the explosive (and metal if present) as being semi-infinite in extent. Then expansion away from the detonation front occurs through a centred Prandtl-Meyer fan for both a compressible metal plate and a free surface, the fan being complete in the case of a free surface but terminating if a metal plate is present at a pressure such that the streamline deflection through the fan matches the pressure and deflection behind the oblique shock in the metal.

If we consider a mass loading on the surface of the explosive we must consider a generalised Prandtl-Meyer expansion where the fan is no longer centred at the edge of the explosive. However in all cases if the characteristic is defined by the angle ϕ made with the detonation front then the solution for a polytropic gas is

$$A = \cos \left(\frac{\phi}{\beta^{1/2}} \right) \quad (13)$$

and μ , the angle between the characteristic and the streamline is given by

$$\cot \mu = \beta^{1/2} \tan \left(\frac{\phi}{\beta^{1/2}} \right). \quad (14)$$

The characteristic however does not pass through A for a mass loading boundary condition. If the point of intersection of the characteristic and explosive boundary is denoted by (X_p, Y_p) it is easy to show that

$$X_p = \frac{\gamma+1}{\alpha} \int_0^\theta \frac{\cos \theta d\theta}{A^{2\gamma/(\gamma-1)}}, \quad (15)$$

$$Y_p = 1 + \frac{\gamma+1}{\alpha} \int_0^\theta \frac{\sin \theta d\theta}{A^{2\gamma/(\gamma-1)}}$$

where θ is the angle of deflection of the streamline from its original direction, i.e.,

$$\theta = \phi + \mu - \pi/2 \quad (16)$$

and

$$\alpha = \frac{\text{mass/unit area of H.E.}}{\text{mass/unit area of metal plate}}.$$

We may expand (14) and (15) for small ϕ , using (16) and find

$$X_p = \frac{2}{3\alpha} \phi^3 + \dots, \quad Y_p = 1 + \frac{2}{9(\gamma+1)\alpha} \phi^6 \dots \quad (17)$$

Thus for small enough ϕ , ($= \Delta\phi$ say) if α is not also small, the point (X_p, Y_p) coincides with A to terms in $(\Delta\phi)^2$. The velocity components U and V can also be expanded in series of powers of $\Delta\phi$ for both the Prandtl-Meyer solution and the Hill and Pack solution and it can be shown that they agree to terms in $(\Delta\phi)^2$ for U and $(\Delta\phi)^3$ for V . Thus we can fit the two solutions together smoothly in all cases considered and in this way construct an initial solution. The program ELA allows for the possibilities that in plane geometry the uppermost boundary condition may be that for a compressible metal plate of given thickness or for an incompressible plate of given mass loading. The lower boundary condition

allows for a given mass loading or a free surface, or the lower condition can be replaced by conditions of symmetry along the axis $Y=0$. This also holds in cylindrical geometry when solving the problem of a cylinder of explosive inside a metal tube (which may be assumed to be either compressible or incompressible).

Integration of the Flow Equations

As stated in previous sections, although the initial solution is obtained analytically, the general solution is obtained by solving the flow equations in characteristic form. These for two dimensional steady flow may be written

$$dU + \mu_2 dV - N dX = 0 \quad \text{along} \quad dY = \mu_1 dX \quad (18)$$

$$dU + \mu_1 dV - N dX = 0 \quad \text{along} \quad dY = \mu_2 dX \quad (19)$$

where

$$\mu_{1,2} = \frac{UV \pm A(Q^2 - A^2)^{1/2}}{U^2 - A^2} \quad (20)$$

suffixes 1 and 2 referring to the + and - sign respectively.

In plane geometry

$$N = 0 \quad (21)$$

while in cylindrical geometry

$$N = \frac{A^2}{U^2 - A^2} \frac{V}{Y} \quad \text{for } Y \neq 0 \quad (22)$$

$$= \frac{1}{2} \frac{\partial U}{\partial X} \quad \text{for } Y = 0, \quad (23)$$

i.e., on the axis. These must be solved together with Bernoulli's equation and the equation of state which we can write as a relation for the sound speed. These may in general be written as functions of density, viz.,

$$Q^2 = F_1(M), \quad A^2 = F_2(M) \quad (24)$$

and we can consider M as a parameter which we can eliminate to give Q as a function of A . In ELA we have considered forms of equations of state where this elimination must be carried out numerically, but for a polytropic gas of constant γ the elimination can be performed analytically to give Eq. (3). The solution of the Eqs. (18)-(24) in finite difference form is straightforward and no further remarks are necessary except to re-state that characteristics may cross in the metal, showing that shocks

are forming in the compression waves present. These are invariably very weak shocks so the assumption of isentropic flow will not be violated and in practice it has been found possible to ignore the shocks so formed and adjust the characteristic mesh before continuing.

Effect of Compressibility of the Metal Plate

Figure 1 shows the main rarefaction and compression waves in the upper half of the solution of a copper-explosive sandwich. It should be remembered that the centred fan OAB is matched by a similar fan from the lower plate so that the region ABKD is not uniform as it may seem from the figure. The region BKF however is uniform. If we consider conditions at a constant distance X from the detonation front the variation is quite complex because of the multiplicity of waves. For example Fig. 2 shows the pressure distribution at various distances downstream from the front and it is seen

that at $X = 1$ there is an off-axis maximum. The separate parts however can be correlated with the separate waves shown in Fig. 1. We see however that as X increases the pressure becomes much more uniform and if we compare with the broken curves on the same figure, which show the corresponding curves if the metal plate is replaced by a mass loading boundary condition of equal mass ratio, we see that by $X = 4$ (i.e., 2 explosive widths) the two curves agree quite well. The agreement improves still further as X increases. A similar situation holds for the transverse velocity component v , also shown in Fig. 2, where it is seen that at $X = 4$ the agreement between the mass loading and the compressible metal plate solutions is good. We may also consider the pressure variation at the explosive interface as a function of lateral displacement for both solutions. It is found that the compressible metal solution varies more or less uniformly about the smooth curve obtained from the mass loading condition so that the integrals under the curves may be expected to be almost equal.

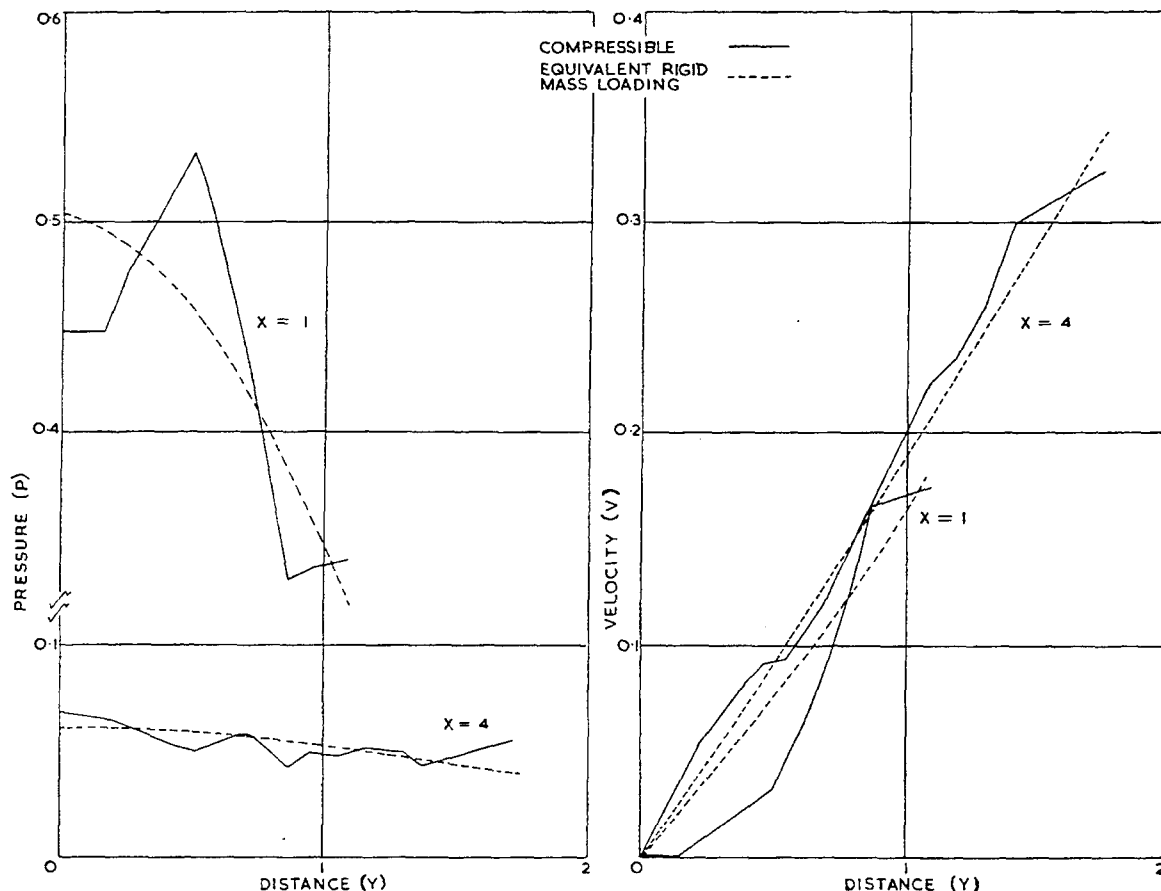


Fig. 2 - Dimensionless pressure and transverse velocity profiles at different stations X downstream

These integrals are proportional to the energy transfer from the explosive so that for consideration of energy transfer to metal plates or cylinders we can obtain very good estimates of the efficiency by replacing the metal by a mass loading condition.

Efficiency of Energy Transfer

Figure 2 shows that the pressure decreases to an almost uniform distribution and the transverse component of velocity is almost linear with distance measured parallel to the detonation front. It is easily shown that the final velocity along the axis (i.e., when pressure $\rightarrow 0$), in laboratory coordinates is

$$U_{\text{final}} = \left[\left(\frac{\gamma^2}{\gamma^2 - 1} \right)^{1/2} - 1 \right] D \quad (25)$$

where D is the detonation velocity. For $\gamma = 3$

$$U_{\text{final}} = 0.06 D \quad (26)$$

which is considerably smaller than the average value of the transverse component of velocity. Thus the approximation of complete transverse flow with a linear velocity distribution and uniform density and pressure (a model considered many years ago by Gurney [1] and others in discussing fragment velocities) is seen to fit the calculated solution quite well and it is found that it predicts efficiency of energy transfer extremely well.

If we consider the situation of two metal plates 1 and 2 of mass ratios α_1 and α_2 moving normal to themselves with velocities V_1 and V_2 and detonation products between them of uniform (but small) density and a linear velocity profile then by conservation of momentum and energy we find for plate 1

$$\frac{V_1^2}{E_0} = \frac{6\alpha_1}{3 + \alpha_1 + (\alpha_1 + 2)\{a_1(2 + z) + 6z\}/(\alpha_1 + 2z)^2} \quad (27)$$

where

$$z = \alpha_1/\alpha_2 \quad (28)$$

and

$$E_0 = D^2/2(\gamma^2 - 1). \quad (29)$$

If the mass of plate 2 tends to zero it is possible to obtain a simpler expression by imposing a limiting velocity V_0 on the free surface and equating linear momentum giving

$$\frac{V_1}{V_0} = \frac{\alpha}{2 + \alpha} \quad (30)$$

whereas (27) reduces (when $z \rightarrow 0$) to

$$\frac{V_1^2}{E_0} = \frac{6\alpha^2}{\alpha^2 + 5\alpha + 4} \quad (31)$$

showing that the difference, other than the constant, is in the coefficient of α in the denominator. The constant in (31) is not compatible with the true theoretical limiting velocity V_0 but the difference is small for the range of γ considered. Furthermore the assumption of uniform density must obviously be untrue at a free surface. The efficiency of energy transfer to plate 1 is (for the Gurney system)

$$\epsilon_G = \frac{V_1^2}{2\alpha_1 E_0} = \frac{3}{3 + \alpha_1 + (\alpha_1 + 2)\{a_1(2 + z) + 6z\}/(\alpha_1 + 2z)^2} \quad (32)$$

We may also calculate the solution by characteristics for given mass loading α_1 and α_2 and obtain the final deflections of the plates θ_1 and θ_2 . The actual particle velocities of the plates are then $2D \sin \theta_1/2$ and $2D \sin \theta_2/2$ so that the efficiency of energy transfer for plate 1 is then

$$\epsilon_C = \frac{1}{2\alpha E_0} [2D \sin (\theta_1/2)]^2. \quad (33)$$

Figure 3(a) shows the comparison of ϵ_G and ϵ_C for various values of α for the two extreme cases when the rear explosive surface is rigid or free. The numerical calculations have been performed for different values of γ (viz., 2.5, 3.0 and 3.5) and it is seen that the efficiency depends only very slightly on γ whereas in the Gurney theory ϵ_G is independent of γ . This is in agreement with the results of Aziz, et al. [2] for normal incidence systems. The agreement between calculated results and the Gurney theory is good for a rigid explosive surface but Gurney overestimates the efficiency when the rear surface is bare. This however is the situation where one expects poorest agreement for reasons already stated.

We may carry out the same analysis in cylindrical geometry and in this case

$$\epsilon_G = \frac{1}{1 + \alpha/2} \quad (34)$$

where

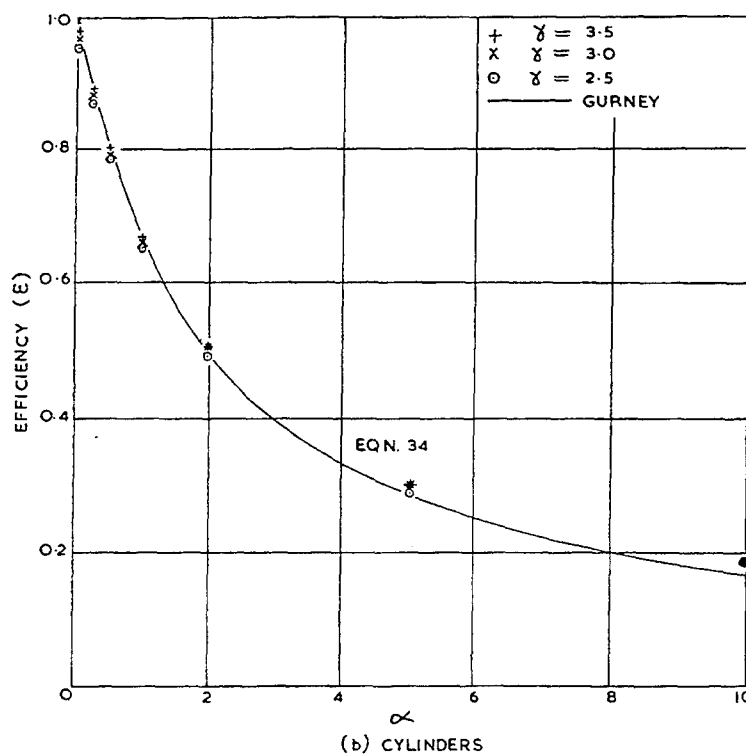
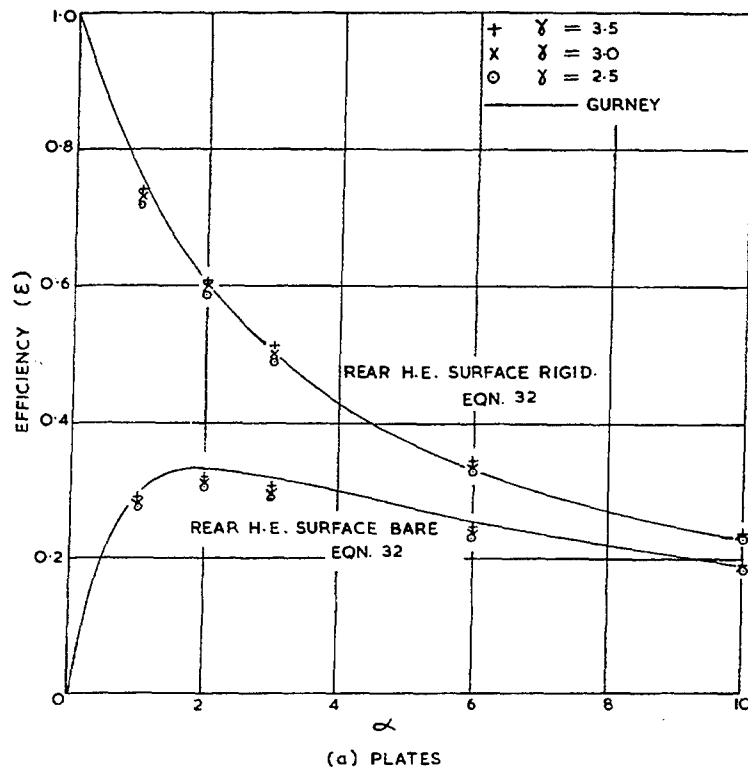


Fig. 3 - Efficiency of energy transfer

$$\alpha = \frac{\text{mass/unit length of H.E.}}{\text{mass/unit length of metal cylinder}}$$

Figure 3(b) shows the comparison which again shows efficiency to be only slightly dependent on γ and to agree well with the Gurney curve. The numerical results for $\alpha = 0$ are obtained from Taylor [5] who assumed the case to be very heavy.

TANGENTIALLY DRIVEN PLATES

Metal plates driven by a tangentially incident detonation wave are useful in plane geometry experiments where the main requirement is one dimensional conditions covering a large area. In recent years many experiments have been carried out to study fracture phenomena and metallurgical changes in specimens subjected to shocks of up to a few hundred kilobars. Here the advantage of using tangentially driven plates to provide the shock impulse is that a large flat area of driver plate can be obtained with a minimum of explosive thereby reducing destructive effects and assisting the recovery of shocked specimens. A comprehensive set of data has now been accumulated for mild steel, copper, brass and aluminum plates driven by Comp. B which offer a useful comparison with theory. For low plate velocities using thick plates and thin slabs of explosive the metal scabs. This can be avoided by introducing a gap of about 3 mm between the plate and the explosive with little effect on the resultant velocity.

Experimental Method

The experimental arrangement consisted of a large slab of explosive initiated along one edge and confined on one face by the driver plate while the opposite face was left bare. When the plate has accelerated to its terminal velocity V_n it is deflected by an angle θ from its initial position where $\sin \theta = V_n/D$. Here V_n is the velocity of the plate measured in a perpendicular direction to the deflected position and is not the true particle velocity. The actual particles move in a direction $\theta/2$ from this perpendicular and hence their velocity is $V_n \sec(\theta/2) = 2D \sin(\theta/2)$. However the component V_n is the required velocity for computing the shock strength generated in a target and is the velocity measured experimentally.

V_n was measured by placing a two dimensional probe array in the estimated position of the deflected plate so that the probe offsets were nominally perpendicular to the deflected

plate surface. The experiment was carried out in a propane atmosphere to avoid premature probe actuation due to air shock ionisation. Least squares fits to the resulting distance time data gave standard deviations in velocity of about 1 percent. Corrections were made for any small deviations in the estimated value of θ from its measured value and for tilt in the transverse direction but since these involved functions of small angles they were usually small.

Charge thicknesses varied between 0.05 and 1.0 in. while metal thicknesses were between 0.05 and 0.5 in. The plate tended to scab when the charge to metal thickness ratio was less than about 2 and this was avoided by introducing a 0.125 in. or sometimes a 0.25 in. gap between the two components.

Charge sizes were typically 9×6 in. or 9×8 in. initiated along the shorter side. Edge effects were comparable with the charge thickness. Some difficulty was experienced in getting good line initiation. A subsidiary tangentially driven plate was found to give the greatest consistency. Other methods such as a line of detonators or a line generator manufactured from sheet explosive produced unwelcome perturbations.

Results and Discussion

The measured velocities are plotted as a function of α in Fig. 4. The trend shown by velocities less than 1 mm μsec^{-1} , where gaps were used, blends quite smoothly with the higher velocities where the charge was in intimate contact with the plate.

For the arrangement where one surface of the explosive is unconfined the simple Gurney approach leads to alternative expressions for the variation of terminal velocity with α , Eqs. (30) and (31), depending on whether momentum or energy is conserved. Either expression shows a very similar variation of V_n with α though using constants consistent with other detononic data leads to velocities up to 10 percent higher than the measured values. However the form of Eqs. (30) and (31) is a good representation of the variation of the experimental data with α and the least square fit to Eq. (30) giving $V_0 = 4.46 \text{ mm } \mu\text{sec}^{-1}$ is shown by the full line in Fig. 4.

The rigorous computation using a polytropic gas equation of state with $\gamma = 2.85$, $D = 7.75 \text{ mm } \mu\text{sec}^{-1}$ appropriate to the Chapman-Jouguet state of the Comp.B used gave results shown by

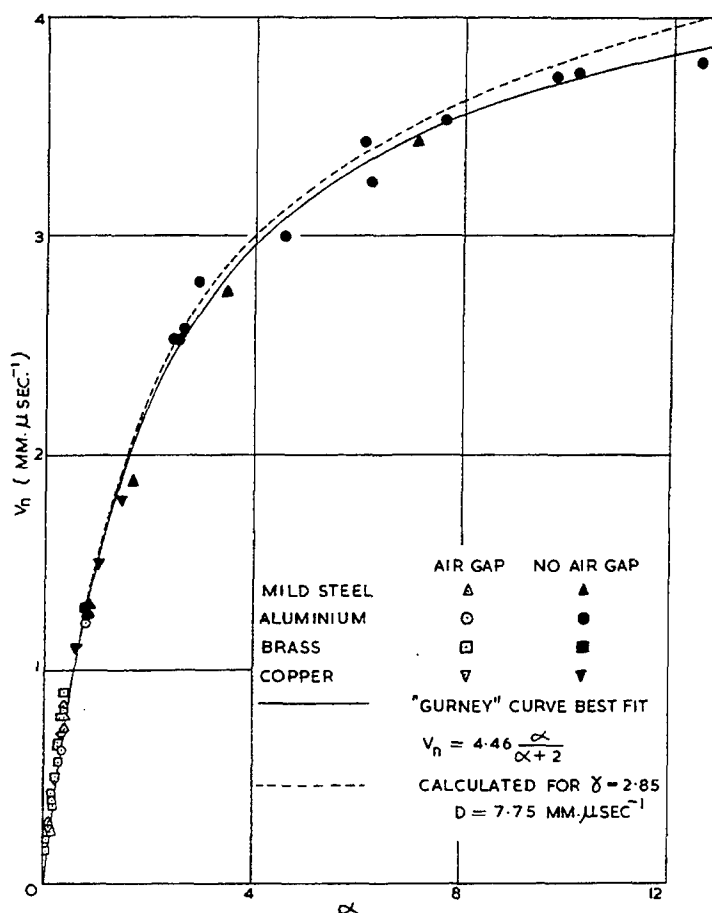


Fig. 4 - Normal component of terminal plate velocity (V_n) as a function of α

the broken curve in Fig. 4. The predicted velocities are about 2 percent higher than the experimental curve at the highest values of α but this is not much greater than the standard deviation of the experimental points. The discrepancy possibly reflects the use of an over simplified equation of state. However it is gratifying to obtain such good agreement with experiment without involving any properties of the metal other than mass.

TANGENTIALLY DRIVEN CYLINDERS

Experiments on explosively loaded cylinders have been confined to one system. Explosives of slightly different loading density have been used but, unlike the tangentially driven plate experiments, the variation in α has been quite small. The investigation has been concerned more with the detailed comparison of computations with observed motion in a given configuration rather than exploring terminal

states. Theory suggests that expansions of about two radii are required to approach the hydrodynamic terminal state. However cylinders tend to burst after some finite expansion and the motion may be perturbed before the terminal state is obtained. Early experiments were carried out using mild steel cylinders but these burst after expanding about one radius so the investigations discussed here refer to later experiments using cylinders of copper whose ductility permitted expansions of about two radii before bursting.

Experimental Technique

The explosive-metal system has consisted of an accurately machined 12 in. long copper tube, 1.000 in. internal diameter and 1.204 in. external diameter, containing an 11 in. long solid cylinder of explosive initiated from a 1 in. long plane wave generator. The clearance between explosive and metal was nominally less

than 0.001 in. For common high explosives this configuration corresponds to $\alpha \approx 0.4$.

The radial expansion r of the copper cylinder was measured as a function of time t by using either a streak camera method or contact probes. The velocity of detonation D was measured separately using probes.

The streak camera method was basically a shadowgraph technique in which the camera was aligned so that the slit, line of sight and cylinder axis were accurately orthogonal. The expanding cylinder wall cut off the back lighting provided by an argon flash and was recorded by the camera writing at about $6 \text{ mm } \mu\text{sec}^{-1}$. Some improvement in resolution was obtained by using a low quality lens to focus the argon light on the cylinder wall. Observations of cylinder wall movement were made at a point 9 in. from the initiator end where conditions were shown to be steady and free from end effects during times of interest.

In early experiments using probes these were pins mounted along eight symmetric generators of a truncated Perspex cone of semi-vertical angle $\Phi = 10.5^\circ$ mounted on the cylinder so that it made contact at one end and flared towards the detonator at the other. In later experiments the arrangement was simplified by using probes formed on printed circuit boards occupying the position of the cone generators. When conditions are steady the measured time of arrival t_x at a probe a distance x along the cone from the cylinder wall is converted to a radius time point by the transformation $r = x \sin \Phi$, $t = t_x - t_0 + x \cos \Phi / D$ where t_0 is the measured or interpolated time of arrival of the disturbance at $x = 0$ where the cone intersects the cylinder.

It is important to distinguish between the velocities derived from differentiating (r, t) data and the true velocity of the material particles of the cylinder. If the cylinder is deflected through an angle θ then, neglecting the small compressibility effects, the material particles move with a velocity $2D \sin(\theta/2)$ in a direction $\theta/2$ forward from the normal to the axis. Differentiation of the data gives a phase velocity $D \tan \theta$ normal to the cylinder axis while the phase velocity normal to the deflected cylinder wall is $D \sin \theta$. Thus for a total displacement r_1 the streak camera observes the motion of points on a length of cylinder $r_1 \sin(\theta/2)$ while the probe method records the times of arrival of points on a length $r_1 [\sin(\theta/2) + \cot \Phi]$ of cylinder. When $r_1 \approx 2 \text{ cm}$ those distances are about 2 mm and 11 cm respectively. Hence it is necessary, particularly when using the probe

method, to justify the assumption of steady state conditions over these lengths. Several experiments were carried out using the probe system with the $x = 0$ point varying between 6 and 10 in. from the detonator. No significant differences were observed in the (r, t) plots.

A comparison of results from streak camera and probe experiments, such as is made in Fig. 5, shows agreement in the later stages of cylinder expansion. The apparent high initial velocity in the optical measurement is thought to be due to spray ejected from the metal surface on the arrival of the shock wave. The spray is sufficiently dense to cut off light to the camera but not sufficiently conducting to actuate probes. The spray is eventually overtaken by the main copper surface and is not representative of the true cylinder motion.

Several experiments have been carried out on each of three explosive compositions, RDX/TNT 60/40 (Composition B), HMX/TNT/Inert 68/30/2 and HMX/Inert 95/5. For a given explosive, after correcting for systematic errors due to differences in explosive density and cylinder wall thickness, the time to reach a given radial expansion is reproducible from round to round to within 0.3 percent.

For streak camera data with $r > 5 \text{ mm}$ and probe data with $r > 1 \text{ mm}$ a suitable analytic fit to the (r, t) points has been found in the form,

$$t = t_0 + Ar + B \exp(-Cr)$$

where t_0 , A , B and C are constants. A computer programme has been written to carry out a least squares fit to this expression. Differentiation of the equation gives a velocity-radius relation showing an exponential approach to a terminal velocity $V_\infty = 1/A$ and provides a more sensitive comparison with theory than a radius-time plot.

Comparison of Theory and Experiment

In Fig. 5 the experimental radius-time curves for a copper cylinder loaded with Comp. B are compared with the theoretical prediction assuming a γ -law equation of state. The agreement appears to be quite good but differences become more apparent when the more stringent velocity-radius comparison is examined in the same figure. The theoretical velocity is derived by assuming that the computed work done on the inner surface of the cylinder is equal to the kinetic energy of the cylinder and then applying an incompressible cylindrical divergence correction to obtain the outer surface velocity.

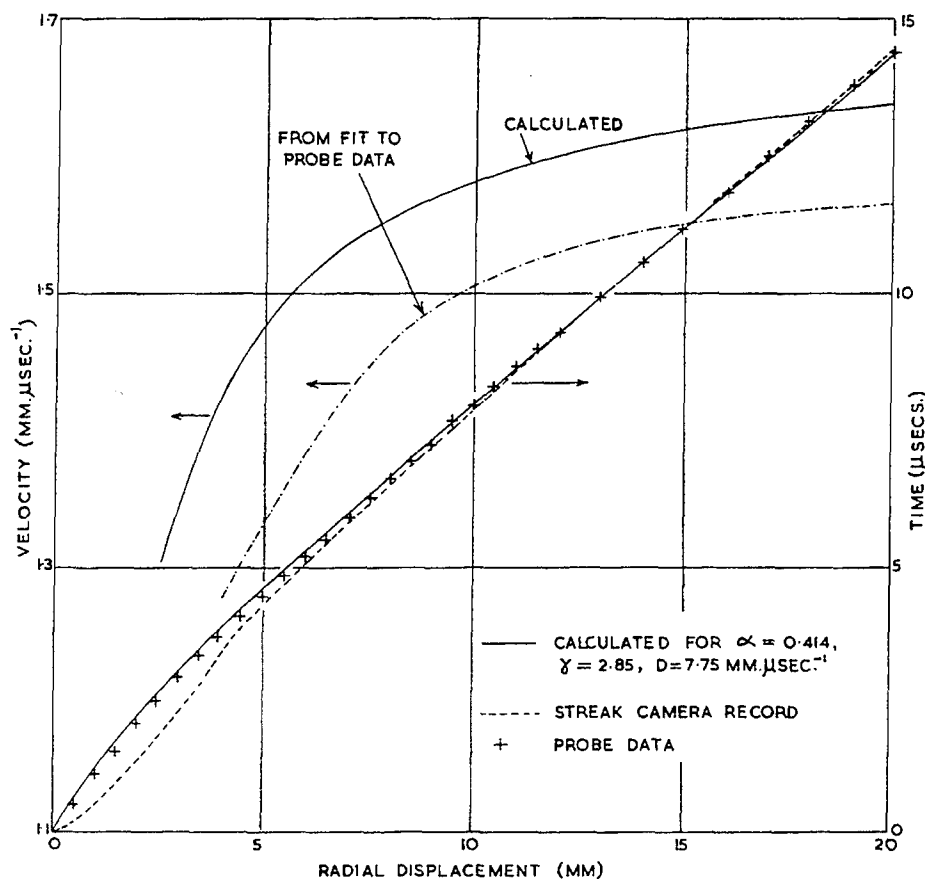


Fig. 5 - Comparison of experimental and calculated radius-time and velocity-radius curves for a copper cylinder driven by Composition B

This procedure realistically averages out the directly computed cylinder wall reverberations.

The computations show that the efficiency of energy transfer to an incompressible cylinder from detonation products following a γ -law equation of state is only about 1 percent less than the simple Gurney expression $(1 + \alpha/2)^{-1}$ for $\alpha \sim 0.4$. The empirical fit to the experimental data show that at $r = 2$ cm, just prior to bursting, the cylinder wall velocity is within 2% of the asymptotic velocity v_∞ which is the largest terminal velocity that may be reasonably extracted from the data. Converting v_∞ to a true terminal velocity $2D \sin(\theta_\infty/2)$, where $\tan \theta_\infty = V_\infty/D$, gives experimental values for RDX/TNT, HMX/TNT and HMX/Inert of 1.64, 1.66 and 1.71 mm μsec^{-1} respectively. The simple Gurney theory predicts 1.70, 1.89 and 1.90 mm μsec^{-1} respectively, a difference of about 4 percent for Comp. B and 10 percent or more for the other explosives. Possible sources of this discrepancy may lie in the effect of the compressibility of the metal or (more probably)

in the use of an inadequate equation of state for the detonation products.

The computed effect of the compressibility of the metals copper, aluminium and lead, with the same mass loading and the same equation of state of the detonation products is illustrated in Fig. 6. Here the kinetic energy of the cylinder is plotted as a function of radial expansion. It is seen that the kinetic energy transfer decreases with increasing compressibility as would be expected. For copper the decrease in velocity below that of a rigid mass loading with $\alpha \sim 0.4$ is no more than 1 percent which only accounts for a small part of the experimental discrepancy. This then suggests that the equation of state of the detonation products may require refinement.

The application of the "Wilkins" form of equation of state to these experiments is being examined. This form of equation of state has a dip in the Chapman-Jouguet adiabat at low pressure thereby reducing the potential energy

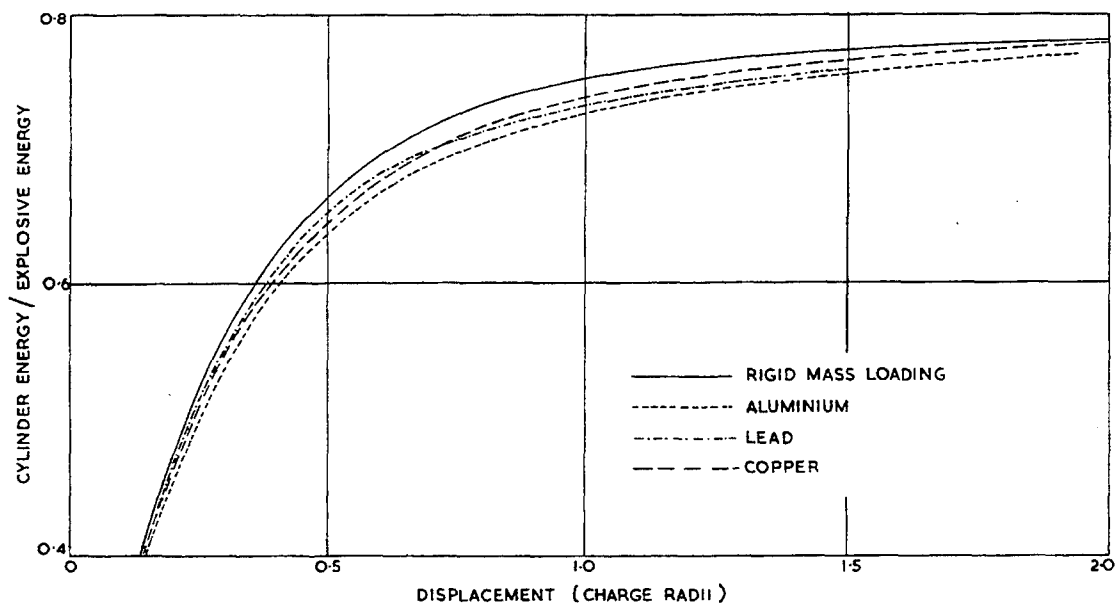


Fig. 6 - Computed energy transfer from Composition B with $\gamma = 2.85$ to cylinders of different materials with $\alpha = 0.412$

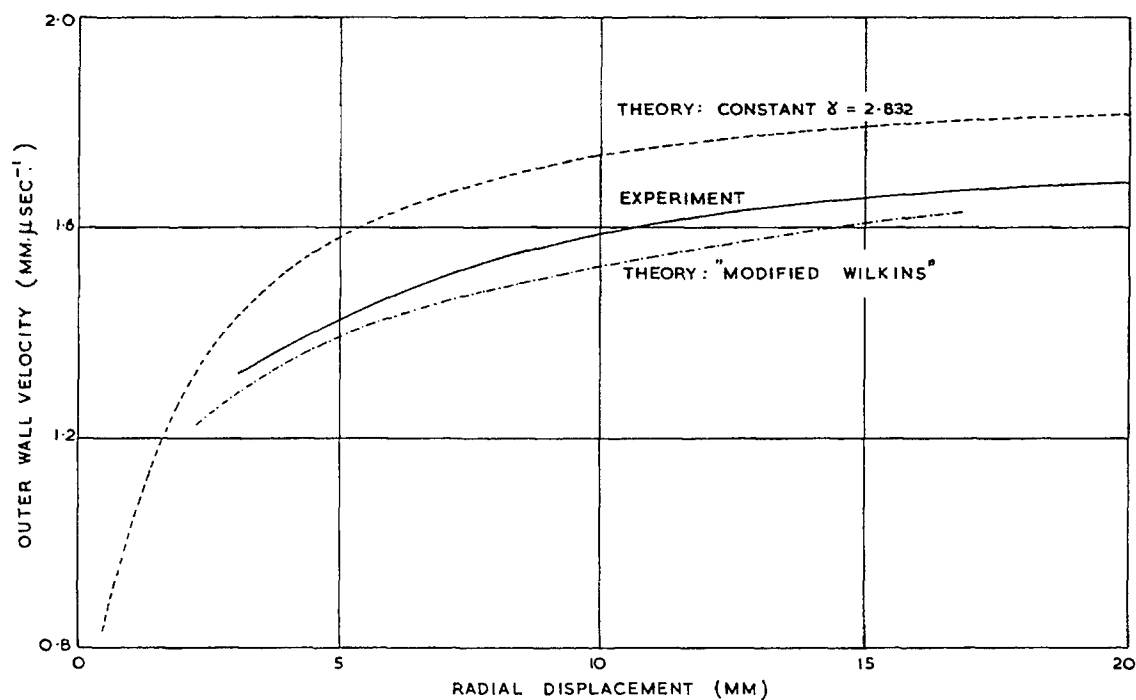


Fig. 7 - Comparison of experimental and theory for HMX/TNT/INERT loaded copper cylinder with $\alpha = 0.412$

available in the detonation products for doing work at large expansions. The comparison between the different equations of state and experiment for HMX/TNT/Inert 68/30/2 is shown in Fig. 7. The specific form of the equation of state used in this calculation is the "modified Wilkins" discussed by Allan and Lambourn [6]. While this underestimates the expansion velocity the difference between experiment and theory is now less than 4 percent and it is hoped that subsequent versions of this equation will give even better agreement.

ACKNOWLEDGMENTS

The authors wish to express their thanks for the assistance they have received from Mr. A. Choules in carrying out the computer runs, Mr. R. A. Belcher in performing the experiments, and Mrs. D. M. Brundle in analysing the data and drawing the diagrams.

REFERENCES

1. R. W. Gurney: The initial velocities of fragments from bombs, shells and grenades: B.R.L. Report 405 (1943)
2. A. K. Aziz, H. Hurwitz and H. M. Sternberg: Energy transfer to a rigid piston under detonation loading: "Third Symposium on Detonation," ONR Symposium Report ACR-52, 1960, Vol. 1, pp. 205-225
3. J. M. Walsh, M. H. Rice, R. G. McQueen and F. L. Yarger: Shock wave compression of twenty seven metals: *Phys. Rev.* **108** (1957) pp. 196-216
4. R. Hill and D. C. Pack: An investigation, by the method of characteristics, of the lateral expansion of the gases behind a detonating slab of explosive: *Proc. Roy. Soc.* **191** (1947) pp. 524-541
5. G. I. Taylor: Analysis of the explosion of a long cylindrical bomb detonated at one end: *Collected scientific papers of Sir Geoffrey Taylor*, Vol. III, pp. 277-286
6. J. W. S. Allan and B. D. Lambourn: The equation of state of detonation products at pressures below 30 kbars: Paper in present symposium

THE CHAPMAN-JOUGUET ISENTROPE AND THE UNDERWATER SHOCKWAVE PERFORMANCE OF PENTOLITE

W. A. Walker and H. M. Sternberg
U.S. Naval Ordnance Laboratory, White Oak
Silver Spring, Maryland

ABSTRACT

The underwater shockwave performance of a pentolite sphere, to 19 charge radii, is calculated with the "q" method. The detonation conditions calculated with the Kistiakowsky-Wilson equation of state are used. By comparison with experimental data it is shown that for the hydrodynamic calculations an equation of state which results in a greater energy release at low pressures is preferable to the Kistiakowsky-Wilson equation. An explicit formula for an E,p,v equation of state of water is derived for use in shock hydrodynamic calculations.

I. INTRODUCTION

In recent years thermochemical calculations with the Kistiakowsky-Wilson (K-W) equation of state

$$pv/RT = 1 + x \exp(\beta x), \quad x = k/[v(T + \theta)^a]$$

have been used with considerable success [1] to predict the Chapman-Jouguet (C-J) conditions for a variety of solid high explosives. There remains the question of how well the K-W equation describes the expansion of the detonation products. It appears from recent experiments with spherical metal shells [2] that the C-J isentrope calculated with the K-W equation is not adequate for hydrodynamic calculations involving expansions to low pressures.

In this paper, the form of the C-J isentrope of pentolite (50/50 TNT/PETN*) is investigated by comparing the results of hydrodynamic calculations of the underwater performance of spherical charges with existing experimental data. Two E,p,v (internal energy, pressure, specific volume) equations of state for the detonation products are considered. The constants in both equations are adjusted so that the C-J conditions are identical to those predicted with thermochemical calculations in which the K-W equation of state was used. One of the equations leads to a C-J isentrope duplicating the one

obtained with the K-W equation. The other equation of state, which contains an exponential term in the volume, is one proposed by Wilkins [2]. This equation leads to a C-J isentrope which is similar in form to the isentrope obtained in 1941, for TNT, by Jones [3] (see Cole [4]). The Jones TNT isentrope was calculated with a p,v,T equation which has an exponential term in the volume similar to the one in the Wilkins equation.

Aside from its use in equation of state investigations, the theoretical prediction of the underwater performance of solid high explosives, particularly the calculation of peak pressure vs distance and pressure vs time at fixed positions, is of interest in itself [4,5]. The prospects for satisfactory calculations of this type have been steadily improving. The hydrodynamic calculations can now be made, more or less routinely, with the artificial viscosity method, using modern computing machines. Sufficient equation of state data for water have become available [6-16] so that the energy dissipated through shock heating can be determined, and the shocked water can be expanded isentropically in the calculation. Also, recently obtained peak pressure vs distance data in the 1-10 charge radii range [17] provide a means of checking the calculation.

An explicit formula for the equation of state of water is derived first, for later use in the hydrodynamic calculations.

*Pentaerythritol tetranitrate.

II. THE EQUATION OF STATE OF WATER

An equation of state of water relating the pressure, specific volume and internal energy is required for the hydrodynamic calculations, the most convenient form being $p = f(v, E)$. The particular form chosen was

$$p = \frac{f_1}{v} + \frac{f_2}{v^3} + \frac{f_3}{v^5} + \frac{f_4}{v^7}, \quad (1)$$

where f_1, f_2, f_3 , and f_4 are polynomials in E , fitted to experimental data. The fits were made for use over the region in the p, v plane bounded on the left by the Hugoniot from 20°C and 1 atm, and on the right by the isentrope which intersects the Hugoniot at the 250 kilobar (kb) point. The internal energy was taken as zero at 20°C and 1 atm.

The water data were taken from several sources. Along the saturation line, the data of Keenan and Keyes [6] were used. The p, v, E values along the 300 and 1400 bar lines were those of Pistorius and Sharpe [7] who integrated p, v, T data of Kennedy et al. [8-12]. Along the Hugoniot from 20°C and 1 atm, the p, v, E values of Snay and Rosenbaum [13] were used for pressures below 25 kb. Above 25 kb, the Hugoniot p, v, E and $(\partial H/\partial v)_p$ data of Rice and Walsh [14] were used. The possibility of partial freezing at 30-35 kb on the Hugoniot was neglected. Also ignored was the phase change at 110 kb reported by Altshuler [15] et al., which would result in a small jog in the Hugoniot in the 100-120 kb range.

The functions f_1, f_2, f_3 and f_4 in Eq. (1) were found by fitting constant energy lines, as follows: For a fixed E , denoted by E_i , consider the equations

$$\frac{f_1(E_i)}{v_1} + \frac{f_2(E_i)}{v_1^3} + \frac{f_3(E_i)}{v_1^5} + \frac{f_4(E_i)}{v_1^7} = p_1, \quad (2)$$

$$\frac{f_1(E_i)}{v_2} + \frac{f_2(E_i)}{v_2^3} + \frac{f_3(E_i)}{v_2^5} + \frac{f_4(E_i)}{v_2^7} = p_2, \quad (3)$$

$$\frac{f_1(E_i)}{v_H} + \frac{f_2(E_i)}{v_H^3} + \frac{f_3(E_i)}{v_H^5} + \frac{f_4(E_i)}{v_H^7} = p_H, \quad (4)$$

$$\frac{f_1(E_i)}{v_H^2} + \frac{3f_2(E_i)}{v_H^4} + \frac{5f_3(E_i)}{v_H^6} + \frac{7f_4(E_i)}{v_H^8} = - \left(\frac{\partial p}{\partial v} \right)_{EH}. \quad (5)$$

Here, the subscript H refers to points on the Hugoniot and $(\partial p/\partial v)_{EH}$ stands for $(\partial p/\partial v)_E$ evaluated on the Hugoniot. For values of E between 0 and 0.036 mb-cc/g (the 160 kb point on the Hugoniot) the points (p_1, v_1, E_i) were taken along the saturation line up to the critical point, and along the 300 bar line for values of v_1 greater than the critical volume. The points (p_2, v_2, E_i) were taken from data on the 1400 bar line. The Hugoniot points (p_H, v_H, E_i) were taken from the Rice and Walsh data. The points $(v_H, (\partial p/\partial v)_{EH}, E_i)$ were calculated from the values given by Rice and Walsh for c_H and $(\partial H/\partial v)_{pH}$, with the thermodynamic identity

$$(\partial p/\partial v)_E = (-c^2/v^2)[1 - p/(\partial H/\partial v)_p]. \quad (6)$$

For each constant energy line the four data points were inserted in Eqs. (2)-(5) and the equations were solved for $f_3(E_i)$ and $f_4(E_i)$. After this was done for all the E_i 's, linear fits were made for the functions $f_3(E)$ and $f_4(E)$. The values of $f_1(E_i)$ and $f_2(E_i)$ were then found by solving Eqs. (2) and (4) for $E_i < 0.036$ mb-cc/g, or Eqs. (4) and (5) for $E_i > 0.036$ mb-cc/g. Least square polynomial fits were then made to $f_1(E_i)$ and $f_2(E_i)$ to get the functions $f_1(E)$ and $f_2(E)$. To improve the accuracy of the fits, the functions f_1 and f_2 were fitted in sections. The first two coefficients in the fit to each section beyond the first were chosen so that the derivatives would be continuous at the junctions. Seven significant figures were retained so that p could be calculated from v and E to within 10-20 bars, when the pressures were below 1 kb.

The following functions, found by the above process, were used in Eq. (1). The pressure is in megabars (mb) when E is in mb-cc/g and v is in cc/g.

$$\begin{aligned} 0 \leq E \leq 0.006: \quad f_1 &= 0.005722427 - 1.240522 E + 50.42535 E^2 \\ &\quad - 1.400579 \times 10^3 E^3 + 4.137950 \times 10^6 E^4 \\ &\quad - 2.726437 \times 10^8 E^5 - 1.295684 \times 10^{11} E^6 + 1.437988 \times 10^{13} E^7 \end{aligned}$$

$$\begin{aligned}
0.006 < E \leq 0.017: \quad f_1 &= 0.001015091 - 0.3270122 E' + 6.734616 E'^2 \\
(E' = E - 0.006) \quad &+ 1.552785 \times 10^4 E'^3 - 2.926440 \times 10^6 E'^4 + 2.139341 \times 10^8 E'^5 \\
&- 5.615358 \times 10^9 E'^6 \\
0.017 < E: \quad f_1 &= 5.607572 \times 10^{-4} + 0.1122840 E'' \\
(E'' = E - 0.017) \quad &+ 5.275769 E''^2 + 82.21745 E''^3 - 147.1514 E''^4 \\
&- 4.044093 \times 10^3 E''^5 - 3.130131 \times 10^4 E''^6 \\
0 \leq E \leq 0.0032: \quad f_2 &= -0.02748180 + 1.691130 E + 17.12981 E^2 \\
&+ 1.483364 \times 10^4 E^3 - 1.549072 \times 10^7 E^4 \\
&+ 3.415591 \times 10^9 E^5 - 2.357818 \times 10^{11} E^6 \\
0.0032 < E \leq 0.0245: \quad f_2 &= -0.02215430 + 1.510990 E' - 10.56299 E'^2 \\
(E' = E - 0.0032) \quad &- 5.411856 \times 10^3 E'^3 + 6.176871 \times 10^5 E'^4 \\
&- 1.810118 \times 10^7 E'^5 - 6.205700 \times 10^8 E'^6 + 4.406075 \times 10^{10} E'^7 \\
&- 6.587460 \times 10^{11} E'^8 \\
0.0245 < E: \quad f_2 &= 0.002499950 + 0.9374720 E'' \\
(E'' = E - 0.0245) \quad &- 4.624610 E''^2 - 44.52203 E''^3 + 375.1364 E''^4 \\
f_3 &= 0.0268 - 0.4148 E \\
f_4 &= -0.005 + 0.0741 E.
\end{aligned}$$

Figure 1 contains the shock Hugoniot from 20°C and 1 atm, and several isentropes, calculated with Eq. (1). Several calculated isotherms are shown in Fig. 2. The Hugoniot in Fig. 1 was found numerically by eliminating E from Eq. (1) and the Hugoniot equation

$$E - E_0 = \frac{1}{2} (p + p_0)(v_0 - v), \quad (7)$$

where $p_0 = 1$ atm, $v_0 = 1.001793$ cc/g and $E_0 = 0$. The isentropes and the temperatures along the isentropes were found by starting at the saturation line and integrating the system

$$\begin{aligned}
(\partial E / \partial v)_s &= -p, \\
(\partial T / \partial v)_s &= -T(\partial p / \partial E)_v,
\end{aligned} \quad (8)$$

using Eq. (1) for p and $(\partial p / \partial E)_v$. Some experimental data points from the Bridgman [16] and Kennedy [8,10,11] isotherms are shown in Fig. 2. On this scale, the Hugoniots of Rice and Walsh [14] and of Eq. (1) coincide.

The calculated isentropes below the saturation line, shown by the dashed lines in Fig. 1, are probably adequate to represent superheated water, i.e., they are extensions of the isentropes with partial steam formation not taken into account. Equation (1) was used in the hydrodynamic calculations as it stands for expansions to states below the saturation line and above 100°C. This occurred in the water initially between the explosive boundary and 1.3 charge radii from the center. The question of whether or not there is time for steam to form is

unimportant for the present problem, since the effect of partial steam formation on the calculated flow is negligible.

The equation of state of water fit involves interpolations over a large region in the p, v plane for which there is no experimental data, i.e., most of the region to the right of the Hugoniot and above 2.5 kb. As a partial test of the validity of the interpolation, the entropies and temperatures on the Hugoniot found by integration from the saturation line with Eqs. (1) and (8) were compared with the Rice and Walsh values [14], up to the 250 kb point. The maximum deviation of ΔS , the entropy increment from the foot of the Hugoniot, from the Rice and Walsh values is less than 2 percent. The maximum temperature deviation, about 5 percent, occurs at 50 kb. Good agreement was also found between the calculated 125°C and 175°C isotherms and the Bridgman data, although these data were not used explicitly in making the fit.

III. EQUATION OF STATE OF THE DETONATION PRODUCT GASES

When a spherical high explosive charge is detonated underwater the flow is affected by the way the energy is released as the detonation product gases expand to low pressures. This energy release is determined by the equation of state of the product gases. The process is clarified by examining the C-J isentrope, since the energy per gram available from the further expansion of a spherical shell of gas at the

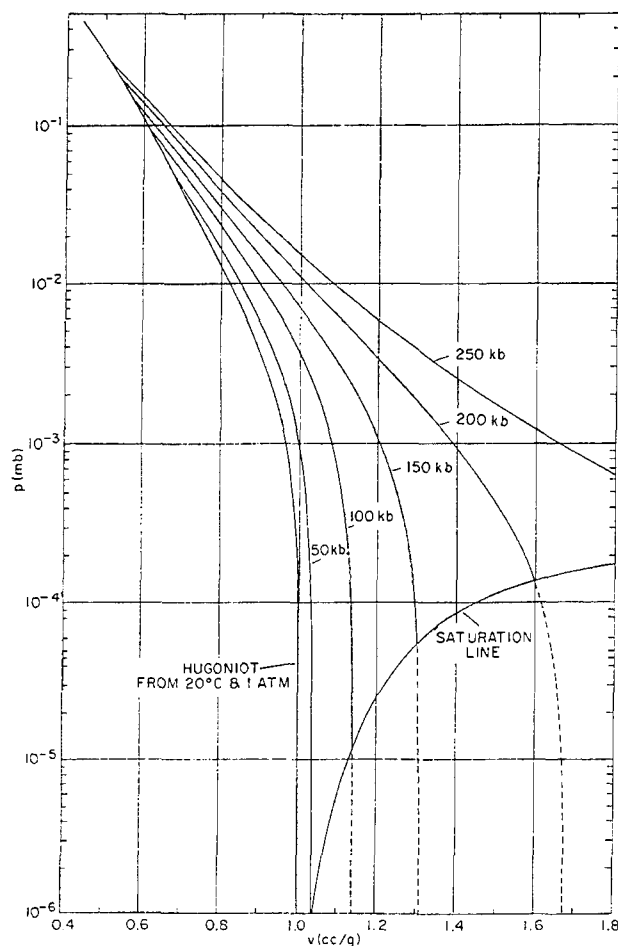


Fig. 1 - Water isentropes calculated with Eq. (1)

pressure p is equal to the area under the isentrope, i.e., to

$$\int_{v(p)}^{\infty} p \, dv.$$

Two equations of state of the product gases were tried in the hydrodynamic calculations. In both cases the constants were chosen so that the C-J pressure, density, sound speed and detonation velocity are those gotten by thermochemical calculations with the Kistiakowsky-Wilson equation of state. The RUBY computer program [18,19], with the RDX parameters of Mader [1], was used for the thermochemical calculations. The C-J detonation conditions calculated for pentolite (with the initial density $\rho_0 = 1.65$ g/cc) by the RUBY program are

$$\begin{aligned} p_j &= 0.2452 \text{ mb} & \rho_j &= 2.210 \text{ g/cc} \\ c_j &= 0.5714 \text{ cm}/\mu\text{sec} & D &= 0.7655 \text{ cm}/\mu\text{sec}. \end{aligned} \quad (9)$$

From the results of the RUBY calculation, E_j , the area under the C-J isentrope during expansion from the C-J pressure to zero pressure, was taken to be 0.0775 mb-cc/g.

The equations of state used were both of the form

$$p = a(\rho) E + b(\rho). \quad (10)$$

The chemical energy E_0 released in the detonation is specified as part of the equation of state. To duplicate a particular set of C-J conditions, the constants in Eq. (10) are chosen to satisfy the equations

$$p_j = a(\rho_j) E_j + b(\rho_j) \quad (11)$$

$$c_j^2 = \left. \frac{da}{d\rho} \right|_{\rho=\rho_j} E_j + \left. \frac{db}{d\rho} \right|_{\rho=\rho_j} + \frac{a(\rho_j) p_j}{\rho_j^2}. \quad (12)$$

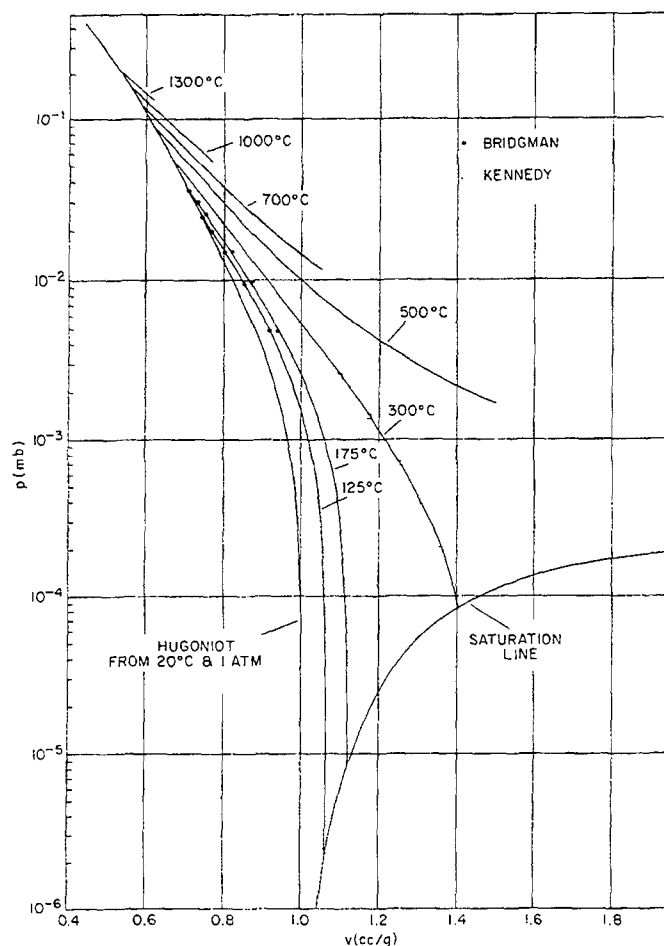


Fig. 2 - Water isotherms calculated with Eq. (1)

Here, Eq. (12) follows from Eq. (10) via the identity

$$c^2 = (\partial p / \partial \rho)_E + (\partial p / \partial E)_\rho p / \rho^2. \quad (13)$$

The first equation of state had the form

$$p = [A\rho + B\rho^2]E + C\rho^3, \quad (14)$$

where A, B, and C are constants. The value $A = 0.35$ was chosen so that the isentropes would have the correct slope as $\rho \rightarrow 0$, i.e., $A = (c_p/c_v - 1)$, where the ideal gas specific heat ratios of the calculated detonation products were averaged on a molar basis. The values of B and C found from the simultaneous solution of Eqs. (11) and (12) were

$$B = 0.1243, \quad C = 0.01279,$$

in units compatible with those in Eq. (9). The value $E_0 = 0.05866$ mb-cc/g (1402 cal/g) was

used here. This was obtained from the RUBY C-J conditions and the Hugoniot relation

$$E_j - E_0 = (p_j + p_0)(v_0 - v_j)/2. \quad (15)$$

The C-J isentrope calculated with Eq. (14), with the above values of the constants is, for practical purposes, identical to the C-J isentrope calculated with the RUBY program, where the K-W equation of state is used. The two isentropes are compared in another paper presented at this symposium but published elsewhere [25].

The second equation of state considered here, which causes more of the energy to be released at lower pressures, is the one proposed by Wilkins [2], namely

$$p = A\rho E + B\rho^4 + Ce^{-K/\rho}. \quad (16)$$

Here, as in Eq. (14), A was taken to be 0.35. Once the constant K is fixed, the constants B

and C corresponding to a given set of C-J conditions are found from the simultaneous solution of Eqs. (11) and (12). In this work $K = 6$, where ρ is in g/cc, was used with the C-J values in (9). The value $K = 6$ was chosen so that the calculated underwater peak pressure vs distance at 1.5-5 charge radii from the center of a spherical pentolite charge would be in good agreement with experimental data. The value of 0.0536 mb-cc/g (1280 cal/g) was used for E_0 . This is the average of the calorimetric values of the heats of detonation of TNT and PETN [20] with 4 percent added to allow for the energy of the gas remaining in the calorimeter. This value of E_0 was used in Eq. (15), with the p_j, v_j values from (9) to get $E_j = 0.0724$ mb-cc/g. The values of B and C found from Eqs. (11) and (12), in units compatible with those in (9), are

$$B = 0.002164, \quad C = 2.0755.$$

The C-J isentropes obtained with Eqs. (14) and (16) are plotted in Fig. 3. The locus of states behind a shock moving into the gas at the C-J state is also shown. The isentrope and reflected shock curve calculated for pentolite with the RUBY program is identical, on this scale, to the curve for Eq. (14).

Figure 4 shows the same isentropes and reflected shock loci in the pressure-particle velocity (p, u) plane. The p, u isentropes are calculated from the p, v isentropes with

$$u = u_j + \int_{p_j}^p \frac{c}{\rho} \frac{d\rho}{\rho}.$$

Note that while at low pressures the p, v isentrope gotten with Eq. (16) is above the one found with Eq. (14), the isentrope in the p, u plane lies below the one calculated with Eq. (14), which is the same as the RUBY isentrope. The p, u shock Hugoniot for water is also shown in Fig. 4.

IV. THE DETONATION WAVE

The variables p, ρ, E, u , and mass M are needed as functions of position at the time when the detonation front in the centrally initiated spherical charge impinges on the water. These functions, which are initial conditions for the "q" method hydrodynamic calculation, are found by a similarity solution [21] (referred to here as the Taylor wave) as follows: For the spherical case the continuity and momentum equations which govern the flow are

$$\partial \rho / \partial t + \rho \partial u / \partial X + u \partial \rho / \partial X + 2\rho u / X = 0 \quad (17)$$

and

$$\partial u / \partial t + u \partial u / \partial X + (1/\rho) \partial p / \partial X = 0, \quad (18)$$

where X is the distance from the center and t is the time. Also

$$dp = c^2 d\rho \quad (19)$$

since the flow behind the front is assumed isentropic. Now let the dependent variables be functions of $\beta = X/t$ only. Then, from Eqs. (17) and (18)

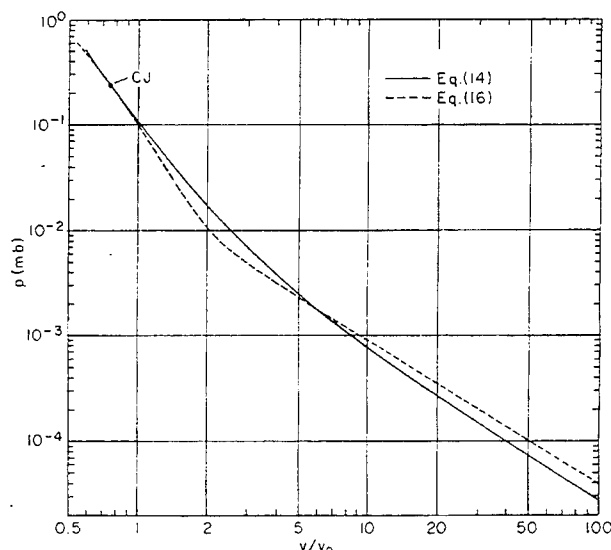


Fig. 3 - The calculated Chapman-Jouguet isentrope for pentolite in the p, v plane

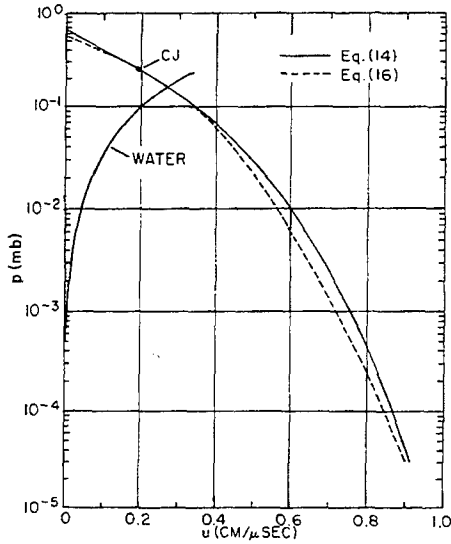


Fig. 4 - The calculated Chapman-Jouguet isentrope for pentolite in the p, u plane

$$\frac{du}{d\beta} = \frac{-2c^2 u}{\beta [c^2 - (u - \beta)^2]}, \quad (20)$$

and

$$\frac{d\rho}{d\beta} = \frac{-\rho(u - \beta)}{c^2} \frac{du}{d\beta}. \quad (21)$$

The variable c^2 is found as a function of ρ from the equation of state of the gas and Eq. (13). Let R_0 be the charge radius and let x be the distance coordinate at the time the detonation front has just reached the interface. At this time, since $x = R_0 \beta / D$ and $dM = 4\pi \rho x^2 dx$,

$$dM/d\beta \approx 4\pi \rho R_0^3 \beta^2 / D^3. \quad (22)$$

Equations (19)-(22) form the system of ordinary differential equations which is solved, numerically, for p, ρ, u and M . The energy E is then found from the equation of state. The integration is started at the detonation front, where the C-J conditions are the initial conditions. Equations (20) and (21) are singular at the detonation front since $\beta = D = u + c$ here. Hence, the first part of the integration is done with u as the independent variable, i.e., with the system

$$d\beta/du = -\beta [c^2 - (u - \beta)^2] / 2c^2 u, \quad (23)$$

$$d\rho/du = -\rho(u - \beta) / c^2, \quad (24)$$

$$\frac{dM}{du} = \frac{4\pi \rho R_0^3 \beta^2}{D^3} \frac{d\beta}{du}, \quad (25)$$

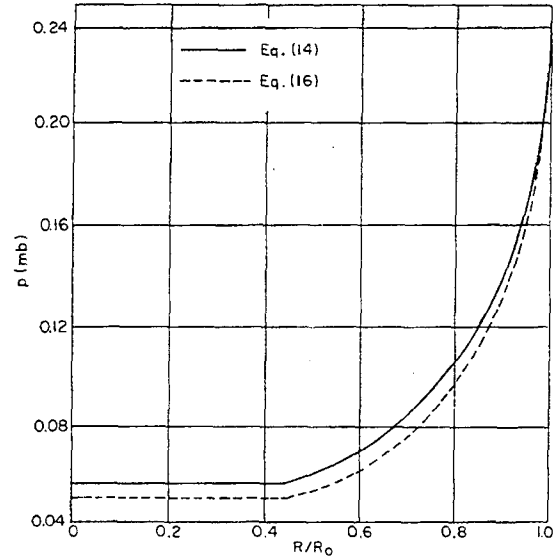


Fig. 5 - The calculated spherical Taylor wave for pentolite

$$\frac{dp}{du} = c^2 \frac{d\rho}{du}. \quad (26)$$

The spherical Taylor waves calculated with the equations of state, Eqs. (14) and (16), for use in the "q" method calculations, are shown in Fig. 5.

V. THE "q" METHOD CALCULATION

A computer program, based on the "q" method, was used to calculate the flow after the detonation front impinges on the water. To cut down the oscillations and the shock widths, 300 space points in the finite difference grid, and a linear q , were used. The factor $1/X$ was used in the q for the water in order to keep the shock from spreading at large distances from the center. The fluid flow equations and their finite difference analogues in the computer program are listed below. The superscript n refers to the time cycle and j is the Lagrangian space coordinate. The grid points are labeled with integer values of j . The equations are written for one dimensional flows in channels of varying cross sectional area $A(X)$. For the spherical flow problems treated here $A(X)$ is $4\pi X^2$.

Continuity:

$$M(j) = \int_{X(j_0, t)}^{X(j, t)} \rho(X, t) A(X) dX. \quad (27)$$

Motion:

$$\partial u / \partial t = -A(X) \partial(p+q) / \partial M \quad (28)$$

$$\partial X / \partial t = u. \quad (29)$$

Energy:

$$\partial E / \partial t = -(p+q) \partial v / \partial t. \quad (30)$$

Equation of State:

$$p = p(E, v) \quad (31)$$

$$q = \begin{cases} -(K/vX^\alpha) \partial u / \partial j, & \partial u / \partial j < 0 \\ 0, & \partial u / \partial j \geq 0. \end{cases} \quad (32)$$

Difference Equations:

$$j = 1, 2, \dots, j_{\max} \quad n = 0, 1, 2, \dots$$

$$(\Delta t)^{n+1/2} = t^{n+1} - t^n, \quad (33)$$

$$(\Delta t)^n = [(\Delta t)^{n+1/2} + (\Delta t)^{n-1/2}] / 2$$

$$P_{j+1/2}^n = P_{j+1/2}^n + q_{j+1/2}^{n-1/2} \quad (34)$$

$$(\Delta M)_{j+1/2} = M_{j+1} - M_j \quad (35)$$

$$(\partial u / \partial t)_j^n = -2(P_{j+1/2}^n - P_{j-1/2}^n) A(X_j^n) /$$

$$[(\Delta M)_{j+1/2} + (\Delta M)_{j-1/2}] \quad (36)$$

$$u_j^{n+1/2} = u_j^{n-1/2} + (\partial u / \partial t)_j^n (\Delta t)^n \quad (37)$$

$$X_j^{n+1} = X_j^n + u_j^{n+1/2} (\Delta t)^{n+1/2} \quad (38)$$

$$v_{j+1/2}^{n+1} = \frac{1}{(\Delta M)_{j+1/2}} \int_{X_j^{n+1}}^{X_{j+1}^{n+1}} A(X) dX \quad (39)$$

$$q_{j+1/2}^{n+1/2} = \begin{cases} -2K(u_{j+1}^{n+1/2} - u_j^{n+1/2}) / [(v_{j+1/2}^{n+1} + v_{j+1/2}^{n+1/2}) X^\alpha], & u_{j+1}^{n+1/2} < u_j^{n+1/2} \\ 0, & u_{j+1}^{n+1/2} \geq u_j^{n+1/2} \end{cases} \quad (40)$$

$$E_{j+1/2}^{n+1} = E_{j+1/2}^n - [q_{j+1/2}^{n+1/2} + (P_{j+1/2}^{n+1} + P_{j+1/2}^n) / 2] [v_{j+1/2}^{n+1} - v_{j+1/2}^n] \quad (41)$$

$$p_{j+1/2}^{n+1} = p(E_{j+1/2}^{n+1}, v_{j+1/2}^{n+1}). \quad (42)$$

For each computation cycle, Eqs. (36)-(42) were solved in the listed order. Equations (41) and (42) were solved simultaneously, by iteration. In Eq. (40), α was taken to be zero in the gas and one in the water. Conventional stability criteria were used to calculate the time steps [22]. The computation grid was chosen so that

the masses of the two zones at the interface, the last zone in the gas and the first zone in the water, would be equal.

The calculation to 19 charge radii was started with 300 zones (301 space grid points) in the first 10 charge radii from the center, 50 zones in the gas and 250 zones in the water. When the calculated position of the shock in the water was close to 10 charge radii, the computation grid was rezoned by deleting alternate grid points up to 10 charge radii and adding 150 zones between 10 and 20 charge radii. The total energy was conserved in the consolidation process.

VI. CALCULATED RESULTS

Two calculations were made of the flow following the central detonation of a spherical pentolite charge in fresh water at 20°C and 1 atm, one with Eq. (14) and one with Eq. (16) for the detonation products. Equation (1) with the functions listed in Sec. II was used for the water in both cases. The calculated detonation wave (Sec. IV and Fig. 5) was inserted as part of the initial conditions and the "q" method computation was begun when the detonation front first impinges on the water. At this time, since p and u must be continuous across the interface, there is an instantaneous adjustment at the boundary (see Fig. 4) which results in an initial transmitted pressure into the water of 162 kb and an initial interface velocity of 0.27 cm/ μ sec. The subsequent spherical flow contains the second shock [5,23], which appears automatically when the "q" method is used. This shock is formed at the gas-water interface and moves back into the gas, following the rarefaction.

Figure 6 contains plots of the calculated pressure at the gas-water interface vs the position of the interface (all distances are shown in charge radii R/R_0 from the center). Note that when Eq. (14) (for which the C-J isentrope is identical with the one from the RUBY thermochemical calculation) is used the pressures acting on the water are higher than those calculated with Eq. (16) until the boundary is at 2 charge radii, after which they are lower. The position of the shock front in the water is noted at several points on the plots, e.g., when Eq. (16) is used the main shock front in the water is at 7 charge radii when the interface is at about 2.6 charge radii. The pressure jump when the gas-water boundary is at about 3 charge radii is due to the impact of the second (Wecken) shock, which, after reflection at the center, has now reached the interface.

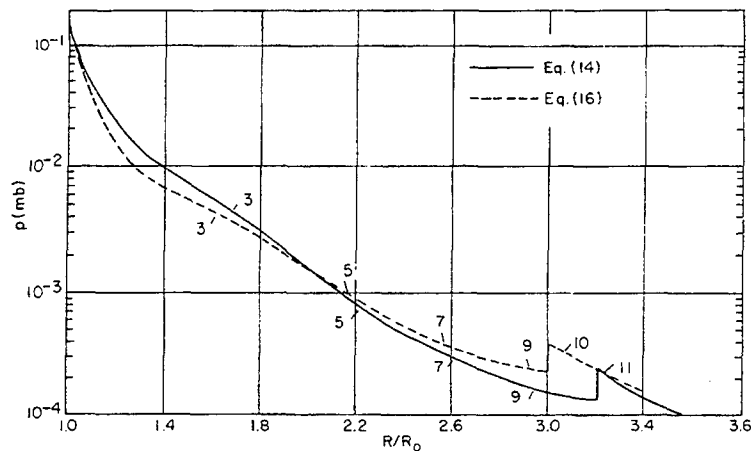


Fig. 6 - Calculated pressure at the gas-water interface vs interface position for a spherical pentolite explosion in water; the positions of the shock front are noted in the figure

The calculated peak shock pressures p_m vs distance are shown in Fig. 7, where they are compared with a plot made from experimental data. The dashed curve between 1 and 6.5 charge radii was obtained recently by N. L. Coleburn [17], who measured x vs t , differentiated to get the shock velocity, and then used the known Hugoniot for water to find the pressure. These data are closely reproducible in the 1.5-6.5 charge radii range. The dashed line extending beyond 10 charge radii in Fig. 7 is a plot of a relation for pentolite found by fitting piezoelectric gage data from a large number of firings made over a 15-year period [24], namely,

$$p_m = 2.35 \times 10^4 (W^{1/3}/R)^{1.14}$$

where W is in lb, R is in ft and p_m is in psi. The pressure scale in Fig. 7 is in megabars.

It should be noted that the peak pressures calculated with Eq. (14) are higher than the experimental values over the range of the calculation (to 19 charge radii). The peak pressure at 10 charge radii calculated with Eq. (14) is 1.40 kb (20,300 psi), compared with the experimental value of 1.18 kb (17,100). It appears in Fig. 7 that at larger distances the peak pressures calculated with Eq. (14) may become lower than the experimental values despite the fact that 1402 cal/g, which is near the maximum possible chemical energy, was used for E_0 .

The peak pressure vs distance calculated with Eq. (16) for the detonation products is also shown in Fig. 7. The values are in good agreement

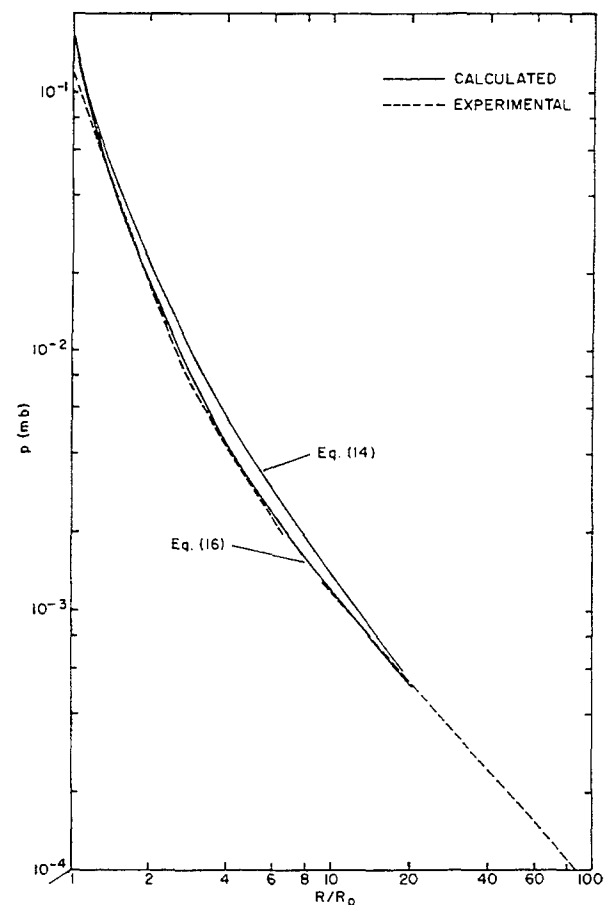


Fig. 7 - Calculated and experimental shock pressures vs distance for a spherical pentolite charge in water

with the piezoelectric gage data to 20 charge radii, where the computation ended. Good agreement with the piezoelectric gage data (with slightly lower close in values) is also gotten by taking $K = 6.6$ and using the same procedure to get B and C . With $K = 6.6$, the exponential term in the equation of state corresponds exactly to the term $\exp [4/(\rho/\rho_0)]$ used by Wilkins [2] in the equations of state for the explosives PBX 9404 and LX 04-01.

Figure 8 contains calculated pressure vs time curves for several fixed positions in the water (4, 10 and 17 charge radii). Note that the initial pressure decay is exponential, in agreement with the decays observed experimentally. The pressures calculated with Eq. (14), which are initially higher, decay more rapidly than those calculated with Eq. (16).

The time constant θ , the time for the pressure to fall from p_m to p_m/e , is plotted (in terms of θ/R_0) vs distance in charge radii, in Fig. 9. Also shown in Fig. 9 are experimental values found from the firing of 50 and 80 lb spherical charges [26]. The lack of data at closer ranges than 13 charge radii, and the scatter in the data at distances of 13 charge radii and over, seems to preclude the use of θ to test the validity of the equation of state of the detonation product gases.

VII. CONCLUSIONS

Calculations of the underwater shockwave performance of pentolite which are in good agreement with experimental data can be made within the general framework of the hydrodynamic

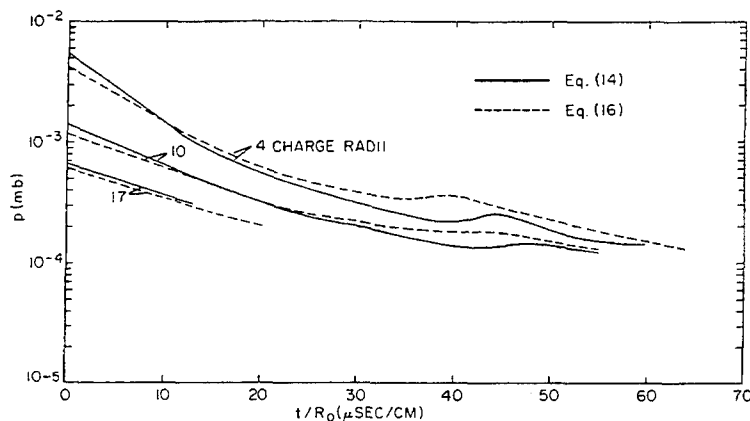


Fig. 8 - Calculated pressure vs time at 4, 10, and 17 charge radii, for a spherical pentolite explosion in water

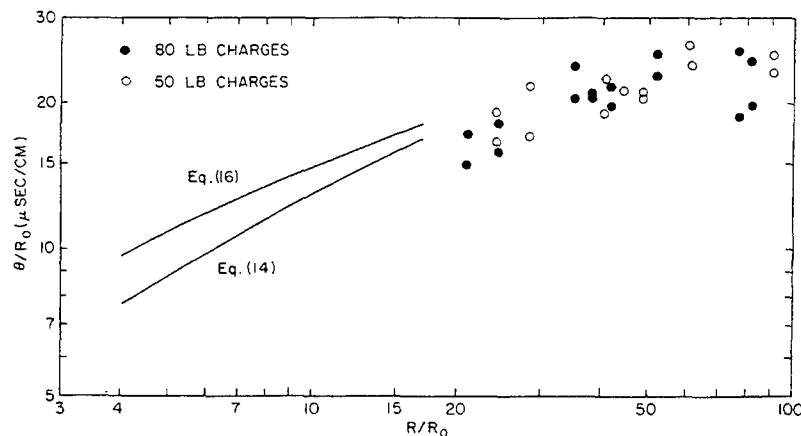


Fig. 9 - Calculated and experimental time constants for a spherical pentolite explosion in water

theory of detonation, with the finite reaction zone neglected, using an equation of state of water developed from shock wave measurements and the detonation conditions calculated with the Kistiakowsky-Wilson equation of state. It is necessary, however, to use an equation of state for the detonation product gases which treats the expansion to low pressures differently than the Kistiakowsky-Wilson equation. The product gas equation of state form proposed by Wilkins [2], which contains an exponential term in the volume similar to the one in the Jones equation [3], is satisfactory for use in hydrodynamic calculations of underwater pentolite explosions.

It should be possible with the equations of state Eqs. (1) and (16) to calculate the underwater shockwave performance of pentolite for situations where there is little or no data, e.g., plane and cylindrical flows and explosions at great depths.

One would like, of course, to have a single equation of state of the detonation product gases for which both the thermochemical calculation of the detonation conditions and the subsequent hydrodynamic calculations would match the experimental results. It would then be possible to predict the underwater performance of a hypothetical explosive.

ACKNOWLEDGMENT

The authors thank H. Hurwitz for the RUBY thermochemical calculations. The work was supported by the Mines and Explosives Division of the Bureau of Naval Weapons.

REFERENCES

1. C. L. Mader, "Detonation Properties of Condensed Explosives Computed Using the Becker-Kistiakowsky-Wilson Equation of States," Los Alamos Scientific Laboratory Report LA 2900 (1963).
2. M. L. Wilkins, B. Squier, and B. Halperin, "The Equation of State of PBX 9404 and LX04-01," Tenth Symposium (International) on Combustion, The Combustion Institute (1964), pp. 769-778.
3. H. Jones and A. R. Miller, Proc. Roy. Soc. (London) v. A194, 480 (1948).
4. R. H. Cole, "Underwater Explosions," Princeton University Press, Princeton, New Jersey (1948).
5. (a) S. A. Berger and M. Holt, "Implosive Phase of a Spherical Explosion in Sea Water," Phys. Fluids v5, 426 (1962).
(b) H. Snay, "Unterwasser Explosionen, Hydromechanische Vorgänge und Wirkungen," Jahrbuch der Schiffbautechnischen Gesellschaft, 51. Band 1957.
6. J. H. Keenan and F. G. Keyes, "Thermodynamic Properties of Steam," John Wiley and Sons, New York (1936).
7. C. Pistorius and W. E. Sharp, "Properties of Water. Part VI. Entropy and Gibbs Free Energy of Water in the Range 10-1000 C and 1-250,000 Bars," Am. Jour. Sci. v. 258, 757-768 (1960).
8. G. C. Kennedy, "Pressure-Volume-Temperature Relations in Water at Elevated Temperatures and Pressures," Am. Jour. Sci. v. 248, 540-564 (1950).
9. G. C. Kennedy, "Properties of Water, Part I. Pressure-Volume-Temperature Relations in Steam to 1000 C and 100 Bars Pressure," Am. Jour. Sci. v. 255, 724-730 (1957).
10. G. C. Kennedy, W. L. Knight and W. T. Holser, "Properties of Water. Part III. Specific Volume of Liquid Water to 100 C and 1400 Bars," Am. Jour. Sci. v. 256, 590-595 (1958).
11. W. T. Holser and G. C. Kennedy, "Properties of Water. Part IV. Pressure-Volume-Temperature Relations of Water in the Range 100-400 C and 100-1400 Bars," Am. Jour. Sci. v. 256, 744-754 (1958).
12. W. T. Holser and G. C. Kennedy, "Properties of Water. Part V. Pressure-Volume-Temperature Relations of Water in the Range 400-1000 C and 100-1400 Bars," Am. Jour. Sci. v. 257, 71-77 (1959).
13. H. G. Snay and J. H. Rosenbaum, "Shock Wave Parameters in Fresh Water for Pressures up to 95 Kilobars," Naval Ordnance Laboratory, White Oak, Md., Report NavOrd 2383 (1952).
14. M. H. Rice and J. M. Walsh, "Equation of State of Water to 250 Kilobars," J. Chem. Phys. v. 256, 824 (1957).
15. L. V. Al'tshuler, A. A. Bakanova and R. F. Trunin, "Phase Transformations of Water Compressed by Strong Shock Waves," Soviet Physics-Doklady v. 3, 761 (1958).

16. P. W. Bridgman, *Proc. Am. Acad. Arts. Sci.* v. 74, 419 (1942).
17. N. L. Coleburn, *Bull. Am. Phys. Soc.* v. 7, 20 (1962).
18. H. B. Levine and R. E. Sharples, "Operator's Manual for RUBY," Lawrence Radiation Laboratory (Livermore, California), Report UCRL-6815 (1962).
19. H. Hurwitz, "Calculation of Detonation Parameters with the RUBY Code," Naval Ordnance Laboratory (White Oak, Md.), Technical Report NOLTR 63-205 (1965).
20. D. Price, "Dependence of Damage Effects Upon Detonation Parameters of Organic High Explosives," *Chem. Revs.* v. 59, 801 (1959).
21. G. I. Taylor, "The Dynamics of the Combustion Products Behind Plane and Spherical Detonation Fronts in Explosives," *Proc. Roy. Soc.* v. A200, 235 (1950).
22. R. D. Richtmyer, "Difference Methods for Initial-Value Problems," Interscience, New York (1957).
23. F. Wecken and L. Muecke, "Detonation of a Spherical Charge," Saint-Louis Technical Research Laboratory (Saint-Louis, France), Report No. 8/50 (1950).
24. M. A. Thiel, "Revised Similitude Equations for the Underwater Shockwave Performance of Pentolite and HBX-1," Naval Ordnance Laboratory (White Oak, Md.), NAVWEPS Report 7380 (1961).
25. H. M. Sternberg and D. Piacesi, "Interaction of Oblique Detonation Waves with Iron," *Phys. Fluids*, v. 9, 1307 (1966).
26. Division 2 Interim Report on "Underwater Explosives and Explosions," UE-32 OSRD 4874, 15 March 1945-15 April 1945.

DETONATION OF A CYLINDRICAL CHARGE

* * *

STUDY OF THE FLOW OF BURNED GASES

C. Fauquignon, M. Prouteau, G. Verdes
*Commissariat à l'Energie Atomique
France*

ABSTRACT

The detonation of a cylindrical charge may be considered as a steady phenomenon if the ratio length/diameter is large enough. The radiographic observation of the motion of very thin gold foils, carried along by the burned gases, allows the former hypothesis to be verified, the measurement of the particle velocity of the gases along the axis, and the measurement of zero-velocity points given as a function of their distance to the shock front.

A confrontation between the experimental results and a theoretical model based upon a Meyer rarefaction allows the determination of the burned gases isentrope.

1. INTRODUCTION

In regard to detonation studies most of the interest of the workers is based upon what happens in front and behind the Chapman-Jouguet plane, that is upon the reaction zone structure and the burned gases flow; however, the experimental conditions are so difficult that in spite of the quantity and quality of the reports a lot of questions remain unanswered.

Most of the experimental methods concern velocity measurements in an inert medium close to the explosive, e.g.:

- free surface velocity imparted to metallic plates of increasing thicknesses [1-5];
- water or plexiglas induced shock wave velocity [6,7].

Another method based on the metallic transition of sulfur has been used for the same purpose [8].

One of the most interesting features of the previous methods is to give an enlarged picture of the reaction zone; however distortions, particularly those due to explosive reflected waves, may be expected.

Actually, it seems that a direct visualisation of the explosive flow must appeal to the flash radiography techniques. The method which is presented here, similar to an earlier one [9], consists in following the displacement of one or more very thin gold foils; initially drowned in the explosive, they are drawn, at the same velocity, by the burned gases; it will be verified that no perturbation will be caused in the flow by the foils presence.

This technique was not precise enough for the reaction zone examination, but was particularly fitted for the study of the rarefaction in reacted products until rather low pressures are reached (~10 Kbars), allowing, in accordance with the chosen theoretical flow model, the determination of the gases isentrope.

The explosive under study (Explosive D [10]), was cast in cylindrical charges of 20- and 30-mm diameter and of different lengths: the geometry and dimensions of the charge were determined by the X-ray penetration capability, the necessity of a good optical definition and the need of attaining a permanent flow with a reasonable charge length.

The experiment-theory correlation only concerned the 30-mm diameter charges for

which the flatness of the shock front was sufficient to assume a simple flow scheme.

2. EXPERIMENTS

2.1. Explosive Assembly

The charge was mounted by gluing elementary cylinders (Fig. 1); the first one is used to establish a permanent flow; between the 6-mm thick cylinders are placed the gold foils (1/100 mm thick), having the same diameter as the explosive cylinders.

Gold was chosen by reason of its chemical neutrality, of its high X-ray absorption and of its good malleability. It was verified that the foils had no influence upon the flow by changing the interval between two foils (3 mm instead of 6 mm); no difference in the results was observed. On the other hand, it was calculated that the equilibrium in the pressures on both sides of a 1/100-mm-thick gold foil was reached in about 10 nanoseconds.

The density of each cylinder was measured, the average value being $1.64 \pm 0.02 \text{ g/cm}^3$; the homogeneity of the density inside the explosive was controlled while making shock front curvature measurements by observing local irregularities.

The curvature measurements, using a streak camera, showed that, in the case of the 30-mm diameter charge, the flatness of the front was better than 0.5 mm for a radius of 13.5 mm; the calculations presented in the rest of this paper neglect the rarefaction related to the 1.5-mm-thick curved zone.

The 20-mm diameter charges showed a more pronounced curvature; it would have been necessary to introduce additional hypotheses to take account of this and no calculation has yet been undertaken.

2.2. Observations and Measurements

The experimental process is illustrated in Fig. 1. After the passage of the shock front the

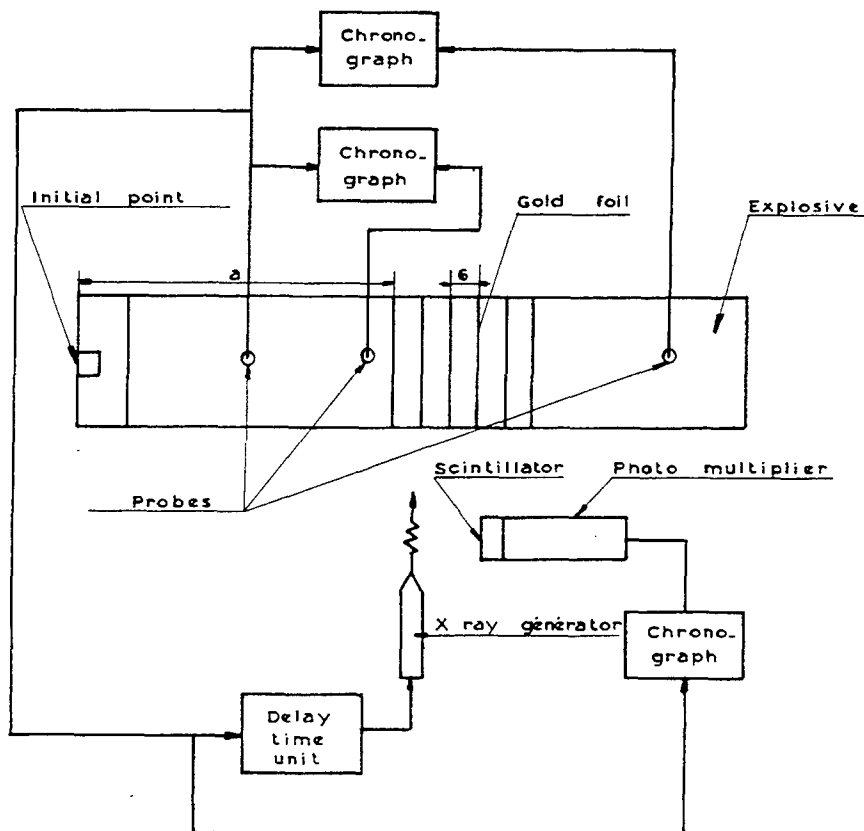


Fig. 1 - Experimental arrangement

foils are carried along by the products; the radiographic observation of their position at different known instants allows the construction of their path versus time diagram. As this diagram will be graphically derived later, the pictures must be of good quality.

A 300-Kvolt X-ray FEXITRON unit was used, the flash duration being $0.12 \mu s$ and the optical magnification 1.1; the observation field was limited to about 30 mm.

Ionization probes placed on the axis of the charge were used for time measurements and X-ray flash synchronization. A first probe located between the initiation-point and the observation area is used as a time origin; it triggers three 40-MHz ROCHAR chronographs and, through a delay time unit, the X-ray flash.

Two of the chronographs are used for detonation velocity measurement, the third one is stopped by the impulse coming from the scintillator-photomultiplier and establishes the correlation between the picture time and the instant of passage of the shock front at a known point (first ionization probe).

The displacements of the foils are referred either to their initial positions by double exposing the dynamic and static pictures or to the position of another foil which has not yet been reached by the shock at the time of the radiography. Figure 2 reproduces a typical record.

2.3. Results

Time measurements and X-ray pictures are used to construct the path versus time diagram of the foils; this construction was done for points along the axis and points located at various radii. In fact, it is impossible to characterize the motion of the different points of a foil; consequently valid information for off-axis points is the radial distribution of the zero-velocity points with respect to the shock front.

Figure 3 represents the path versus time diagram (x, t) for the points along the axis in the case of the 30-mm diameter charge.

The (x, t) curves were graphically derived to give the material velocity versus time (u, t), the time origin being the same for the different foils.

The variation of the material velocity with respect to the distance to the shock front was then established by using the $x(t)$ and $u(t)$

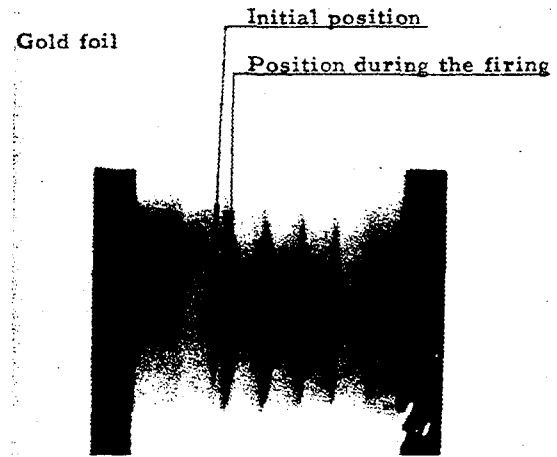


Fig. 2 - Radiography

curves, at different initiation point-to-shock front distances; u is given for the different foils, for a given t and for given space coordinate $Z = X_D - X$; where X_D is the position of the shock front at that instant. By varying t , within the regions of densest beam of the curves $u(t)$ in order to obtain the maximum number of points, $u(Z)$ is calculated.

Figure 4, gives $u(Z)$ in the region within which steady conditions develop and Figs 5 and 6 give $u(Z)$ when steady conditions are complete (30- and 20-mm-diameter charges).

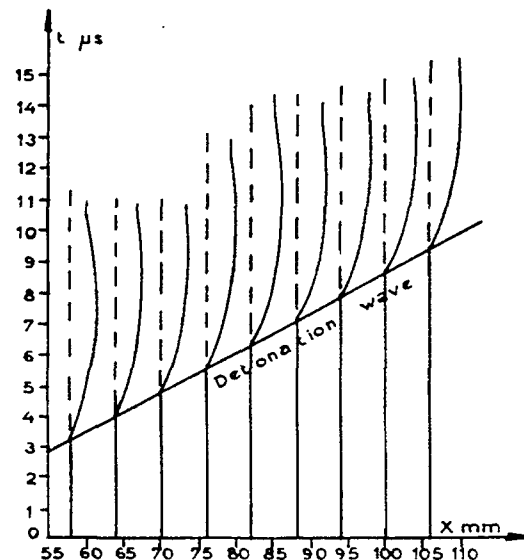


Fig. 3 - (x, t) diagram -- cylindrical charge 30-mm diameter

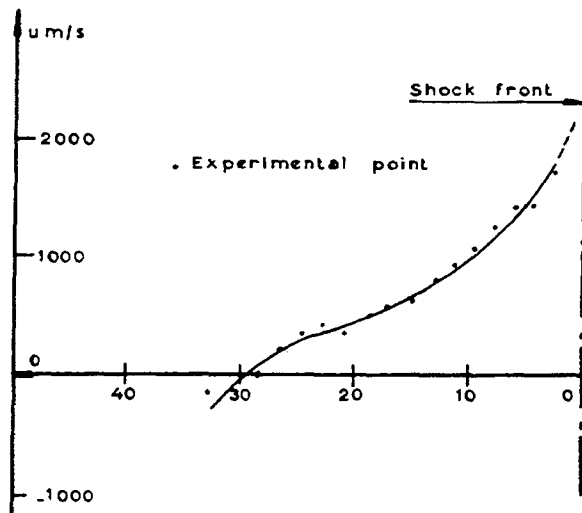


Fig. 4 - $u(Z)$ diagram -- cylindrical charge 30-mm diameter, initiation point -- shock front distance = 95 mm

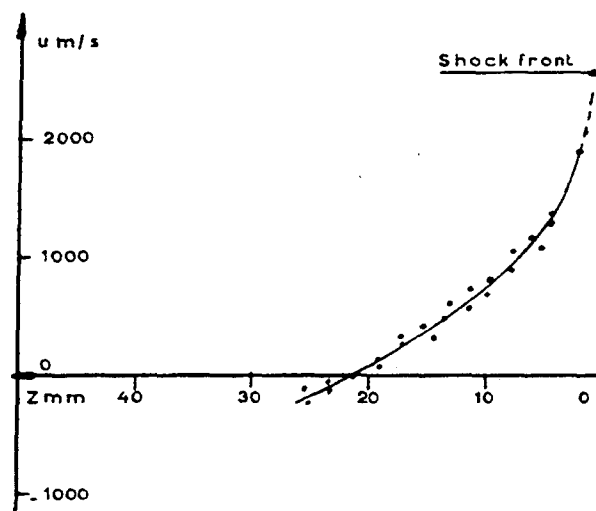


Fig. 6 - $u(Z)$ diagram -- cylindrical charge 20-mm diameter, initiation point -- shock front distance > 90 mm

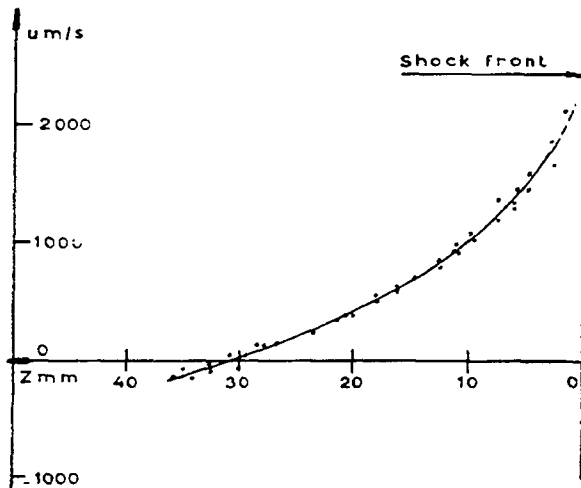


Fig. 5 - $u(Z)$ diagram -- cylindrical charge 30-mm diameter, initiation point -- shock front distance > 100 mm

The steady aspect of the flow is shown by tracing the variation of the distance of the zero-velocity point to the shock front, as a function of the initiation point-shock front distance (Fig. 7).

Once steady conditions are established the radial distribution of zero-velocity points are obtained in a similar manner (Fig. 8).

2.4. Remarks

- The small number of measurements within the neighbourhood of the shock front and their poor quality do not enable us to detect the reaction zone.
- There is an uncertainty as to the physical origin of the ionization probes triggering and hence on the exact position of the shock front with respect to the distribution of the measured velocity.

Subsequently, experimental results have been limited to the burned gases rarefaction study.

3. THEORY AND CALCULATIONS

3.1. Flow is Assumed to be Described by a Meyer Rarefaction; This Rarefaction is Centered on the Edge of the Cylinder; and the Characteristic Equations are Solved in this Scheme

The basic assumptions are:

- permanent flow;
- plane detonation front and CJ conditions existing just behind the front;

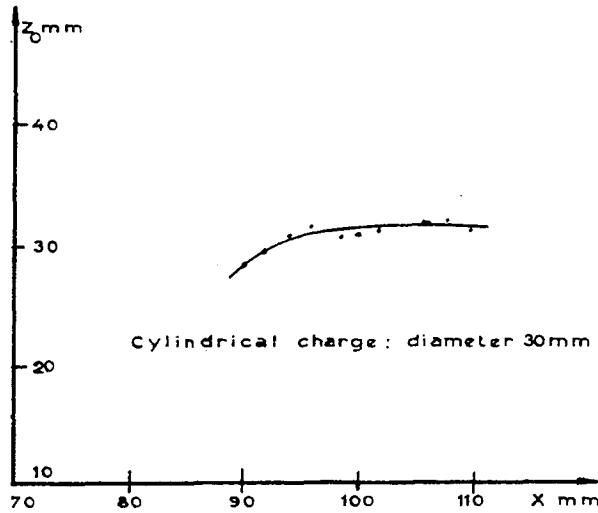


Fig. 7 - Position of the zero material velocity Z_0 (along the axis) in function of the distance shock front -- initiation point X

• constant entropy flow: $p = f(\rho)$ with Γ defined by

$$\Gamma = \left| \frac{d \log p}{d \log \rho} \right|_{\text{adiab.}}$$

Notations:

- p = pressure,
- ρ = local density,
- H = enthalpy,
- a = sound speed, and
- V = relative material velocity.

3.2. Introducing the Theory of the Characteristic Equations and Calculation of the Current Point [11]

For two-dimensional cylindrical flow there are three families of characteristic curves (Fig. 9a):

- stream lines of constant entropy - M_x ;
- Mach lines (C_{+a} and C_{-a}).

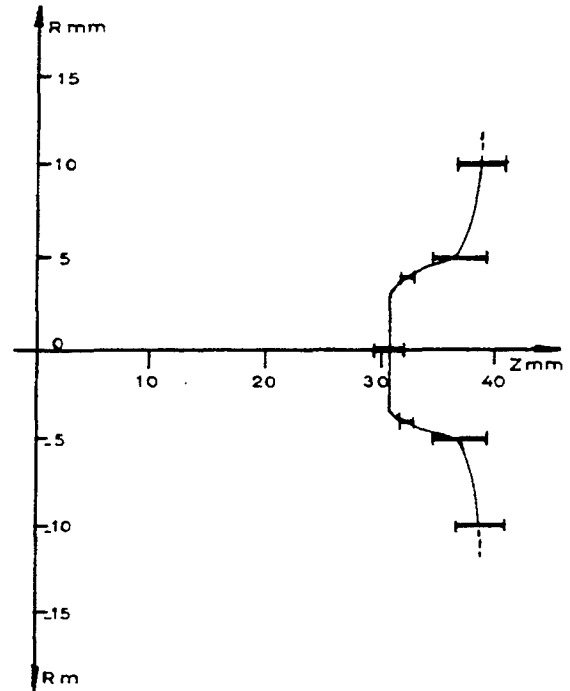


Fig. 8 - Radial repartition of the zero-velocity points with respect to the shock front position

Following the Mach lines, the equations are as follows:

$$\left. \begin{aligned} \text{On } C_{+a} \dots & \frac{\sin \alpha \cos \alpha}{\Gamma p} \left(\frac{\partial p}{\partial \eta} \right)_{+a} + \left(\frac{\partial \varphi}{\partial \eta} \right)_{+a} \\ & = - \frac{\sin \alpha \sin \varphi}{y} \\ \text{On } C_{-a} \dots & \frac{\sin \alpha \cos \alpha}{p} \left(\frac{\partial p}{\partial \xi} \right)_{-a} - \left(\frac{\partial \varphi}{\partial \xi} \right)_{-a} \\ & = - \frac{\sin \alpha \sin \varphi}{y} \end{aligned} \right\} \quad (1)$$

Calculation of the current point (Fig. 9b):

Assuming that the functions are known at two neighbouring points i and k , it is possible to calculate functions at n , given by the intersection C_{+a} and C_{-a} .

At point n which is common to C_{+a} and C_{-a} , Eqs. (1) are written as:

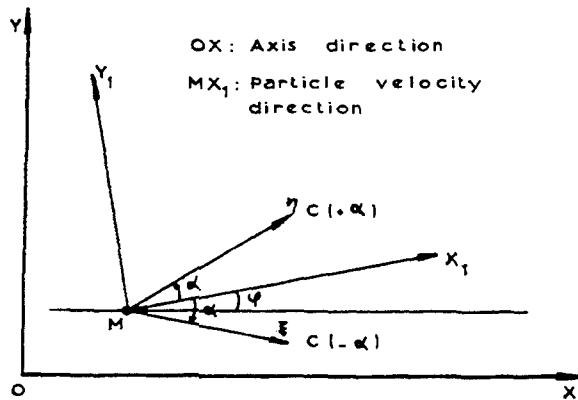


Fig. 9a - Characteristic curves

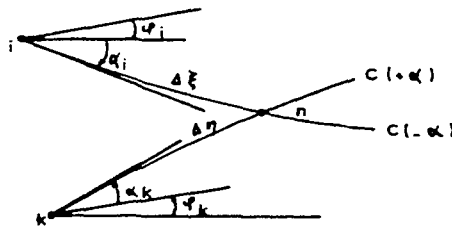


Fig. 9b - Calculation of the current point

$$\left. \begin{aligned} & \left(\frac{\sin \alpha \cos \alpha}{\Gamma_p} \right)_{kn} (p_n - p_k) + (\varphi_n - \varphi_k) \\ & = - \left(\frac{\sin \alpha \sin \varphi}{y} \right)_{kn} \Delta \eta \\ & \left(\frac{\sin \alpha \cos \alpha}{\Gamma_p} \right)_{in} (p_n - p_i) - (\varphi_n - \varphi_i) \\ & = - \left(\frac{\sin \alpha \sin \varphi}{y} \right)_{in} \Delta \xi \end{aligned} \right\} \quad (2)$$

Putting

$$dP = \frac{\sin \alpha \cos \alpha}{\Gamma_p} dp$$

and

$$A = - \frac{1}{2} \frac{\sin \alpha \sin \varphi}{y}$$

$$\left. \begin{aligned} \mu &= \frac{P + \varphi}{2}, \quad \lambda = \frac{P - \varphi}{2}; \\ \mu_n - \mu_k &= A_{nk} \Delta \eta, \\ \lambda_n - \lambda_i &= A_{ik} \Delta \xi. \end{aligned} \right\} \quad (3)$$

Moreover the assumption of constant entropy implies that $dP = \sin \alpha \cos \alpha (d\rho/\rho)$.

The origin of P and therefore of μ and λ is arbitrary. α_n and φ_n are first of all calculated by

$$\alpha_n = \frac{(\alpha_i + \alpha_k) - (\varphi_i + \varphi_k)}{2}, \quad \varphi_n = \frac{(\alpha_k - \alpha_i) + (\varphi_i - \varphi_k)}{2}.$$

If the arcs in and kn are approximated by straight lines with slopes:

$$\tan \frac{(\varphi_i - \alpha_i) + (\varphi_n + \alpha_n)}{2}$$

and

$$\tan \frac{(\varphi_k + \alpha_k) + (\varphi_n + \alpha_n)}{2}$$

it is then possible to calculate x_n and y_n ; hence also $\Delta \eta$, $\Delta \xi$, μ_n and λ_n .

It follows that:

$$P_n = \lambda_n + \mu_n, \quad \varphi_n = \mu_n - \lambda_n,$$

$$\rho_n = \rho_i \left[\frac{1 + \frac{P_n - p_i}{2(\sin \alpha \cos \alpha)_{in}}}{1 - \frac{P_n - p_i}{2(\sin \alpha \cos \alpha)_{in}}} \right],$$

$$a_n^2 = f'(\rho_n) H_n = H_{CJ} + \int_{\rho_{CJ}}^{\rho_n} \frac{f'(\rho)}{\rho} d\rho,$$

$$V_n^2 = V_{CJ}^2 - 2 [H_n - H_{CJ}],$$

$$\alpha_n = \arcsin \sqrt{\frac{a_n^2}{V_n^2}}.$$

The calculation is begun anew with improved values of α_n and φ_n , the iterations ending after α_n has converged.

Finally,

$$p_n = f(\rho_n).$$

3.3. The Particular Case of Cylindrical Flow with Meyer Rarefaction

The rarefaction centered on the edge of the charge can be taken as a particular upwards characteristic curve for which $\mu_n = \text{constant}$.

In order to calculate it, α is incremented so that at each point $\alpha_n = \alpha_i - \Delta\alpha$. Knowing α_n , ρ_n is obtained by solving:

$$\sqrt{\frac{f'(\rho_n)}{V_{CJ}^2 - 2 \int_{\rho_{CJ}}^{\rho_n} \frac{f'(\rho)}{\rho} d\rho}} - a \sin \alpha_n = 0.$$

All other quantities (p_n , Γ_n , ...) are then found easily.

Calculation of the axial point: The method is the same as for the general case with $\varphi_n = 0$ and $\lambda_n = \mu_n$. The first approximation of α_n is $\alpha_i - \varphi_i$.

4. CONSTRUCTION OF THE ISENTROPE

The preceding calculated were based with isentropic equation $p = f(\rho)$ formulated as

$$p = K \rho^{\Gamma_{CJ}} + \Delta p$$

$$K = \left[\frac{p}{\rho^{\Gamma}} \right]_{CJ}$$

where Δp is a correction factor chosen as

$$\Delta p = M(\rho_{CJ} - \rho)^2 \rho^N (R \rho_{CJ} - \rho).$$

The values of the different quantities on the CJ plane are known for the D-explosive [10]:

$$p_{CJ} = 259 \text{ Kbars},$$

$$\rho_{CJ} = 2.186 \text{ g/cm}^3,$$

$$\Gamma_{CJ} = 3.00.$$

The unknown parameters M, N, R are obtained by trying all possible values until a good coincidence is reached between experimental and theoretical $u(Z)$ curves.

Figure 10 shows the isentrope in the $p, \rho/\rho_{CJ}$ plane.

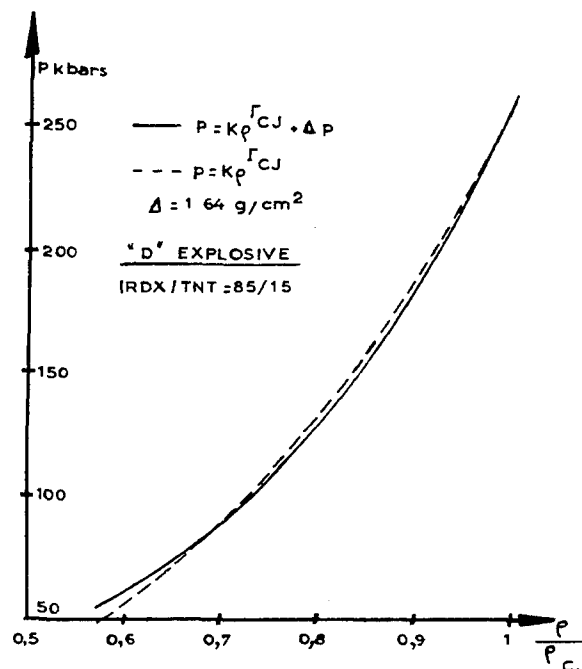


Fig. 10 - Isentrope curve of burned gases $p = K \rho^{\Gamma_{CJ}} + \Delta p$

REFERENCES

1. R. E. Duff and E. Houston, J. Chem. Phys. **23**, 1268 (1955).
2. W. E. Deal, J. Chem. Phys. **27**, 796 (1957).
3. A. N. Dremin and P. F. Pokhil, Dokl. Akad. Nauk, SSSR - **128**, 889 (1959).
4. M. L. Wilkins, B. Squier, and B. Halperin, UCRL Report 7797 (1964).
5. B. G. Craig, 10th International Symposium on Combustion, Cambridge (1964).
6. M. A. Cook, R. T. Keyes, and W. O. Ursenbach, J. Appl. Phys. **33**, 3413 (1962).
7. C. Fauquignon, C. R. Acad. Sc. Paris - **251**, 38 (1960).
8. G. E. Hauver, "Third Symposium on Detonation," ONR Symposium Report ACR-52, Vol. 1, p. 120, 1960.

9. J. C. Clark, J. Appl. Phys. 20, 363 (1949)
and J. Viard, C. R. Acad. Sc. Paris 244,
1619 (1957).
10. J. Berger, J. Favier, and Y. Nault, Annales
de Physique 13, t.5, 51 (1960).
11. P. Carriere, Publications Scientifiques et
Techniques de Ministère de l'Air n° 339 -
1957.

THE EQUATION OF STATE OF DETONATION PRODUCTS BEHIND OVERDRIVEN DETONATION WAVES IN COMPOSITION B

I. C. Skidmore and S. Hart*
*Atomic Weapons Research Establishment
Aldermaston, Berkshire, England*

ABSTRACT

Overdriven detonation waves in Composition B carrying pressures up to twice the Chapman-Jouguet pressure have been generated by an explosive driven plate impact technique. The hydrodynamic properties of these waves have been determined by an impedance match method. In addition the pressure-particle velocity locus for reflected waves in the detonation products from a given overdriven state has been obtained in a similar way. The results agree with predictions using a simple polytropic gas equation of state with a constant adiabatic exponent appropriate to the Chapman-Jouguet state. The measurements are confined to pressures greater than 300 kb except for some experiments matching with air at about 1 kb which show that the simple equation of state is not valid down to this pressure.

1. INTRODUCTION

Experiments [1,2] show that in many high explosives shock compressions and adiabatic expansions of the detonation products from the Chapman-Jouguet (C-J) state are consistent with a polytropic gas equation of state having an adiabatic exponent of about three, applicable for pressures above about 100 kb. This equation of state cannot account for the variation of detonation velocity with loading density but for an explosive of prescribed loading density this simple description seems adequate when the gaseous product densities are near the condensed state density.

In some applications of explosives detonation waves are overdriven to pressures considerably higher than the C-J pressure. The object of the present investigation was to test whether the simple equation of state could successfully predict overdriven detonation wave properties, and shock compressions and adiabatic expansions from a given overdriven state. The relevant theoretical expressions are derived in section 2, the experiments are described in section 3 and the comparison of the results with theory is discussed in section 4.

2. THEORY

With the notation, pressure P , specific volume V , specific internal energy E , detonation velocity D , particle velocity U , sound velocity C , adiabatic exponent γ and specific detonation energy Q , the velocity of propagation and particle velocity immediately behind any plane detonation wave in explosive defined by initial conditions, P_0 , V_0 , E_0 , and U_0 are given by the first two Rankine-Hugoniot relations,

$$D = U_0 + V_0 \left[(P - P_0) / (V_0 - V) \right]^{1/2} \quad (1)$$

$$U = U_0 + \left[(P - P_0)(V_0 - V) \right]^{1/2} \quad (2)$$

The pressure and volume of the detonation products immediately behind the detonation front are related by the third Rankine-Hugoniot equation which defines the Hugoniot curve,

$$E - E_0 = Q + \frac{1}{2} (P + P_0)(V_0 - V) \quad (3)$$

If the detonation products obey a polytropic gas equation of state,

*Present address of S. Hart: Department of Natural Philosophy, University of Aberdeen, Scotland.

$$E = PV/(\gamma - 1) \quad (4)$$

and

$$C^2 = \gamma PV. \quad (5)$$

For a steady unsupported detonation wave with properties designated by suffix 1, the C-J condition is

$$C_1 = D_1 - U_1. \quad (6)$$

In solid explosive initially at atmospheric pressure P_0 is negligible compared with P_1 so that substituting Eqs. (1), (2) and (5) in (6) gives,

$$V_1/V_0 = C_1/D_1 = \gamma/(\gamma + 1). \quad (7)$$

Then when $U_0 = 0$, Eqs. (1) - (4) with the simplification provided by Eq. (7) give the familiar expressions

$$\begin{aligned} D_1^2 &= (\gamma + 1)^2 U_1^2 \\ &= (\gamma + 1) P_1 V_0 \\ &= 2(\gamma^2 - 1)(Q + E_0). \end{aligned} \quad (8)$$

For an overdriven detonation wave, with properties designated by suffix 2, Eq. (6) and hence Eq. (8) no longer hold so that Eqs. (1) - (4), simplified using Eq. (8), now give

$$\frac{D_1}{D_2} = \left[\frac{P_1}{P_2} \left(2 - \frac{P_1}{P_2} \right) \right]^{1/2} = \frac{2U_1/U_2}{1 + (U_1/U_2)^2} \quad (9)$$

which is independent of the actual value of γ .

The P-U locus for reflected shocks in the detonation products is given by Eq. (2) with suffix 2 replacing suffix 0 and the sign of the last term changed. The same transformation in Eq. (3) with $Q = 0$ gives the Hugoniot curve for reflected shocks so that eliminating v gives

$$U = U_2 - C_2 \left(\frac{P}{P_2} - 1 \right) \left[\frac{2/\gamma}{(\gamma + 1)P/P_2 + (\gamma - 1)} \right]^{1/2}. \quad (10)$$

For reflected rarefaction waves the adiabatic relation $PV^\gamma = P_2V_2^\gamma$ holds and the P-U locus is given by

$$\begin{aligned} U &= U_2 + \int_P^{P_2} (-dP/dV)^{1/2} \\ &= U_2 + \frac{2C_2}{\gamma - 1} \left[1 - \left(\frac{P}{P_2} \right)^{\frac{\gamma - 1}{2\gamma}} \right]. \end{aligned} \quad (11)$$

3. EXPERIMENTS

The explosive investigated was Composition B (RDX/TNT 60/40) at a loading density of 1.65 gm cm^{-3} , with C-J properties $D_1 = 7.74 \text{ mm } \mu\text{sec}^{-1}$, $U_1 = 2.01 \text{ mm } \mu\text{sec}^{-1}$, $P_1 = 257 \text{ kb}$ corresponding to $\gamma = 2.85$.

The basis of the technique is to explosively propel a metal driver plate at a similar target plate on which rests a sample layer of explosive backed by a further layer of inert solid. When the driver plate velocity is sufficiently high this process generates a steady overdriven detonation wave in the explosive unless or until it is overtaken by the rarefaction from the rear of the driver plate. The shock transit times through each layer of the system are measured to determine the transmitted shock or detonation velocities. The measured driver plate impact velocity or the shock velocity in the target plate, whose shock properties are known, defines the incident shock strength. An impedance match at the target plate-explosive interface using the measured overdriven detonation velocity then defines the corresponding detonation pressure and particle velocity. The properties of reflected waves in the detonation products are determined by a similar impedance match at the explosive-backing plate interface using the measured transmitted shock velocity in the backing plate whose Hugoniot curve is known. This technique has been described by Al'tshuler [3] for determining the shock properties of inert solids. McQueen and Marsh [4] used the same technique and discuss the geometrical limitations necessary to retain uniform flows. The particular variation of the technique with practical aspects applicable to the present experiments is given by Skidmore and Morris [5]. In particular this paper describes the pin probe method used to record transit times, the treatment of the time data to remove errors due to gross driver plate curvature and local nonplanarities, and the corrections of systematic errors arising from density differences in nominally identical samples and impact velocity differences in nominally identical experiments.

In a first series of experiments detonation velocity was determined as a function of particle velocity at three detonation pressures of about 350, 420 and 520 kb. These pressures were generated by using a plane wave initiated 5 in. diameter 5 in. long cylindrical charge of HMX/TNT 75/25 to propel driver plates of mild steel 4.8-mm thick, brass 3.2-mm thick and mild steel 1.6-mm thick against a target plate of the same material. The target plate supported three 30-mm-diameter cylindrical

explosive specimens in a four fold symmetric array with centres on a 25-mm radius circle. The target plate free surface velocity was measured in the fourth location. Pin probes were used to record various transit times giving the driver plate impact velocity, together with the target plate shock and free surface velocity as a consistency check, and the detonation velocity in the explosive samples. The explosive samples were of two thicknesses, 3.2 and 6.4 mm, to detect possible shock attenuation effects which could invalidate the analysis. No such effects were observed. The mean results for each pressure are given in Table 1.

TABLE 1

Mean Results for Overdriven Detonation Waves in Composition B. Errors Refer to One Standard Deviation. N is the number of experiments.

N	Detonation Velocity (mm μsec^{-1})	Detonation Pressure (kb)	Particle Velocity (mm μsec^{-1})
(C-J)	7.74	257	2.01
4	$8.00 \pm .13$	346 ± 4	$2.62 \pm .01$
4	$8.28 \pm .11$	412 ± 4	$3.02 \pm .01$
4	$8.93 \pm .06$	520 ± 3	$3.53 \pm .01$

In a second series of experiments shock compressions and adiabatic expansions from a detonation pressure of 420 kb were examined using the brass driver plate and measuring the transmitted shock velocity in 3.2-mm thick explosive samples. The matching materials were tungsten alloy, nickel, brass, titanium, Dural, magnesium, Perspex and air at 1 atmosphere. In some of the later experiments the geometry was changed from discs to quadrants to obtain an improved probe coverage over a larger surface area. In some duplicate experiments the

explosive and matching disc thickness was increased to 4 mm to test for possible attenuation effects but none was observed. The mean results from this series of experiments are given in Table 2.

To enable the impedance matches to be carried out the shock wave data for the various materials used in these experiments were obtained from the following sources. Nickel, brass and titanium data were obtained from Ref. 4. Mild steel, magnesium and Perspex data are contained in Ref. 5. The shock tables in Ref. 6 were used for air. The tungsten alloy data is given graphically in Ref. 7. Dural was assumed to have the same shock velocity - particle velocity relation as that for pure aluminium given in Ref. 5.

4. DISCUSSION OF RESULTS

In Table 1 the data from each set of nominally identical experiments have been normalised to the mean target plate shock pressure by correcting for the deviations from this mean. Since each experiment defines a measured overdriven state this procedure is not strictly necessary. It is adopted for consistency of presentation with the data in Table 2 where reflected wave data are referred to a given overdriven state and here it is desirable to eliminate systematic errors by correcting for experimental deviations from this mean state.

In Fig. 1 the overdriven detonation velocities are plotted as a function of detonation pressure and compared with the predictions of Eq. (9). In Fig. 2 the corresponding comparison is made in the pressure-particle velocity plane. Also in Fig. 2 the reflected wave data are compared with Eqs. (10) and (11) using the value

TABLE 2

Mean Results for Reflected Waves in Overdriven Composition B. Errors Refer to One Standard Deviation. N is the Number of Experiments.

Matching Material	N	Density (gm cm^{-3})	Shock Velocity (mm μsec^{-1})	Pressure (kb)	Particle Velocity (mm μsec^{-1})
W Alloy	2	16.8	$5.02 \pm .09$	818 ± 62	$0.97 \pm .06$
Ni	2	8.86	$6.46 \pm .21$	716 ± 110	$1.25 \pm .15$
Brass	2	8.44	$5.79 \pm .03$	689 ± 13	$1.41 \pm .02$
Ti	2	4.51	$6.87 \pm .04$	604 ± 16	$1.95 \pm .04$
Dural	2	2.65	$8.52 \pm .08$	522 ± 10	$2.31 \pm .04$
Mg	2	1.74	$8.12 \pm .16$	407 ± 26	$2.88 \pm .13$
Perspex	2	1.18	$7.77 \pm .06$	332 ± 6	$3.62 \pm .04$
Air	2	1.29×10^{-3}	$10.27 \pm .18$	1.26 ± 0.05	$9.50 \pm .17$
Comp. B	16	1.65	$8.40 \pm .14$	420 ± 10	$3.03 \pm .06$

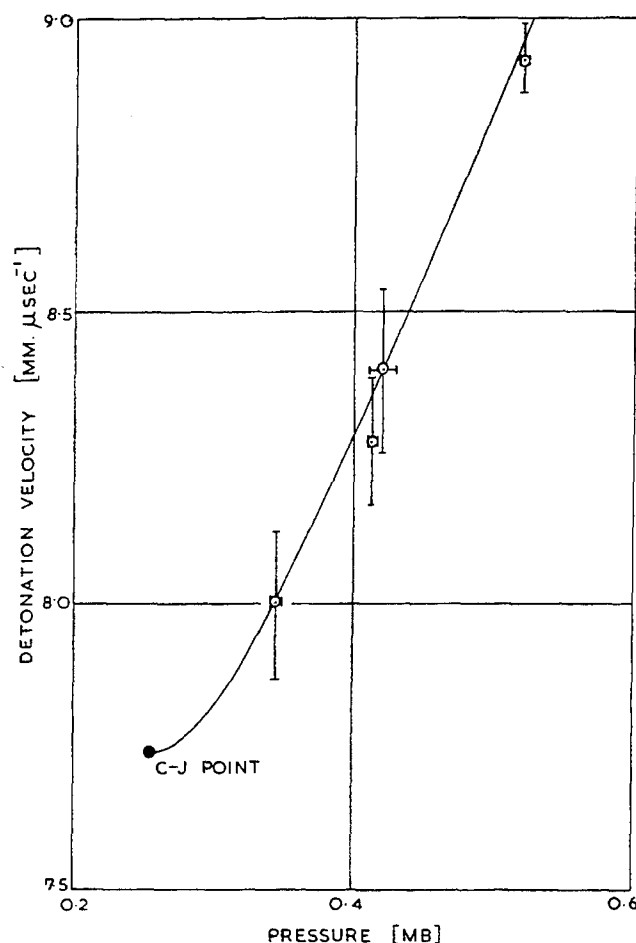


Fig. 1 - Comparison of theory and experiment for overdriven detonation velocities as a function of detonation pressure in Composition B

of γ appropriate to the C-J state. It is seen that agreement is within one standard deviation for all experimental points. These represent relative errors of rather less than 3 percent for the overdriven states and generally rather more for the reflected wave data. The error in any one velocity measurement is of the order of 5 percent. The air point corresponds to a pressure of about 1.3 kb and the measured particle velocity is about 8 percent less than the predicted value which is the same relative difference observed at the foot of the C-J adiabat.

The comparison in the P-U plane does not represent a stringent test of the equation of state since P-U curves for reflected waves are not sensitive to small variations in γ . At a given particle velocity an increase in γ of $\Delta\gamma$ gives a relative increase in reflected shock pressure of about $\Delta\gamma/2\gamma$ so that a 2 percent

error in reflected wave pressure represents a possible variation in γ of about 0.1. However in uniform flow situations this simple representation appears adequate for the prediction of transmitted shock strengths into solids within the accuracy of current experimentation. The deviation from this simple equation of state at low pressures is consistent with current views on the behaviour of detonation products at large expansions [8,9].

REFERENCES

1. H. Lawton and I. C. Skidmore, Faraday Soc. Discussions, No. 22, 188 (1956).
2. W. E. Deal, Phys. Fluids, 1, 523 (1958).
3. L. V. Al'tshuler, et al., Soviet Phys., J.E.T.P., 34, 606 (1958).

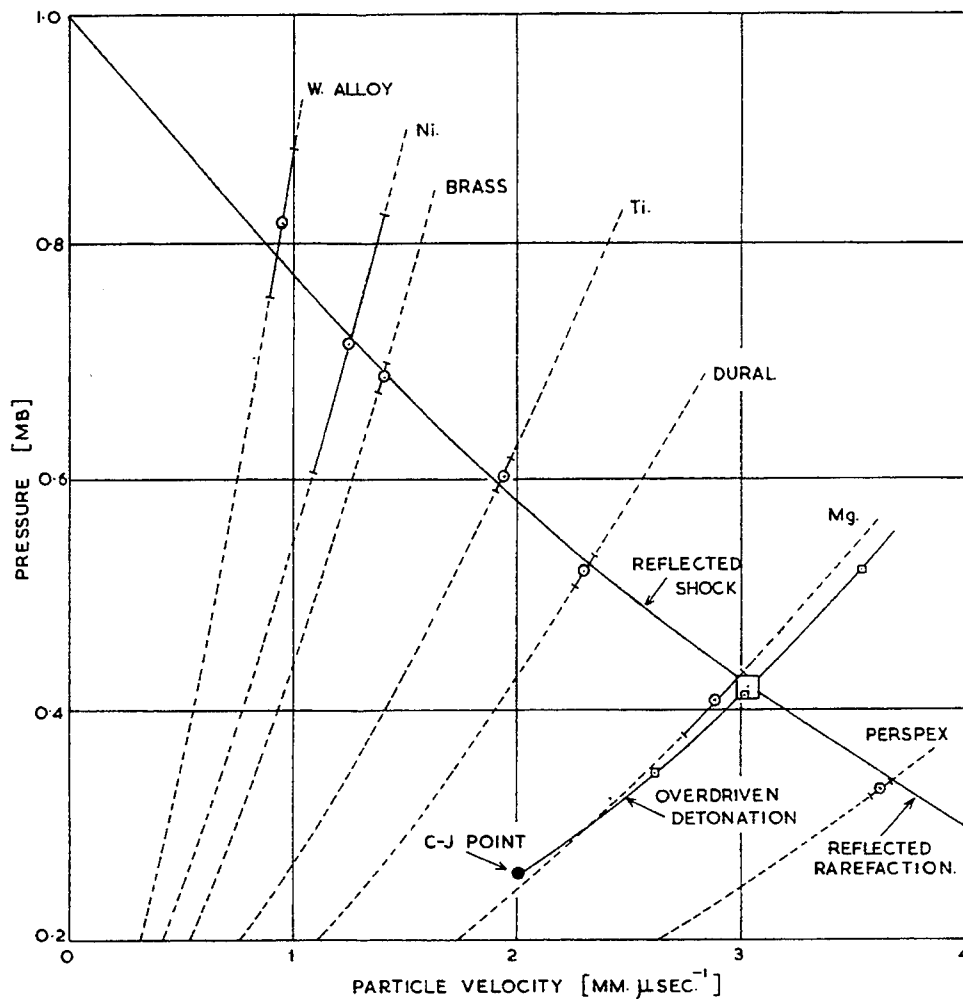


Fig. 2 - Pressure-particle velocity points for overdriven detonation waves and reflected waves in Composition B compared with theory for $\gamma = 2.85$

4. R. G. McQueen and S. P. Marsh, J. App. Phys., 31, 1253 (1960).
5. I. C. Skidmore and E. Morris, "Thermodynamics of Nuclear Materials," p. 173 (I.A.E.A., Vienna, 1962).
6. S. R. Brinkley, J. G. Kirkwood, and J. M. Richardson, O.S.R.D. Report 3550 (1944).
7. I. C. Skidmore, Applied Materials Research, 4, 131 (1965).
8. M. L. Wilkins, B. Squier, and B. Halperin, University of California, L.R.L. Report, U.C.R.L. - 7797 (1964).
9. J. W. S. Allan and B. D. Lambourn, this Symposium.

AN EQUATION OF STATE OF DETONATION PRODUCTS AT PRESSURES BELOW 30 KILOBARS

J. W. S. Allan and B. D. Lambourn
*Atomic Weapons Research Establishment
Aldermaston, Berkshire, England*

ABSTRACT

Wilkins has suggested that the observed details of explosive driven plate motion indicate that at pressures below about 150 kb the Chapman-Jouguet adiabat may dip well below the constant adiabatic exponent form. This paper describes a more direct approach to the determination of the form of the adiabat in the relevant portion of the pressure-particle velocity plane by extending the impedance matching method to include matching with compressed gases. A streak camera technique has been used to measure the velocities of luminous shocks transmitted from the end of cylindrical charges into air, argon and krypton initially at pressures between 0.2 and 30 bars. These measurements have allowed pressure-particle velocity points to be obtained in the pressure range 0.2 to 30 kb for two explosive compositions. The data have been used in conjunction with other hydrodynamic properties to determine the coefficients in a form of equation of state similar to one proposed by Wilkins.

1. INTRODUCTION

When using high explosives to drive metal plates the energy transfer process depends in detail on the shape of the adiabatic pressure-specific volume (p - v) relation for the detonation products. The pressure range of practical interest is from a few hundred kilobars down to about one kilobar. Until recently it has been assumed for simplicity of calculation and on the basis of Deal's work [1,2] that the Chapman-Jouguet (CJ) adiabat has constant exponent γ of order 3 for the whole of the pressure range. Thus the adiabat is a straight line in the $\log p - \log v$ plane. However, in 1964, Wilkins [3] found in calculations of the motion of a spherical shell driven by a sphere of explosive detonated at the centre, that a straight line adiabat equation of state gave too high an energy transfer when compared with experiment. To account for the measured motion he found it necessary to introduce a different form of adiabat which dipped below the constant γ form at around 150 kb and recrossed it at around 3 kb. This implies that less energy is available for transfer to plates and shells in the pressure range 150 to 3 kb. A further plausible consequence of the Wilkins form is that at pressures below a few kilobars the products are behaving

like a normal gas with γ about 1.5. It is interesting to note that in 1948, Jones and Miller [4] published a form of the CJ adiabat for TNT with a similar dip.

In this paper we present a modified form of Wilkins equation of state fitted to more direct experimental measurements on the CJ adiabats of two explosive compositions HMX/TNT/Inert (68/30/2) and HMX/Inert (95/5). Section 2 contains a formulation of the equation of state. Section 3 describes the experiments and lists the results. Section 4 describes the method of fitting the experimental data to obtain the constants in the equation of state.

2. FORMULATION OF THE EQUATION OF STATE

Fickett and Wood [5] have pointed out that because the region of interest for an equation of state of detonation products is a narrow band above the CJ adiabat on a $\log p - \log v$ diagram, a Gruneisen form can be used. The relation between specific internal energy e , pressure p and specific volume v is then

$$e(p, v) = e_r(v) + [p - p_r(v)] v/w(v) \quad (1)$$

where $e_r(v)$ and $p_r(v)$ define internal energy and pressure on the reference curve as functions of v ; $w(v)$ is Gruneisen's ratio, which on Fickett and Wood's evidence is sensibly constant.

For detonation products the reference curve is taken to be the CJ adiabat so that

$$e_r(v) = \int_v^{\infty} p_r(v) dv, \quad (2)$$

i.e., we take the origin of internal energy to be zero at infinite expansion.

In this section we first write down some Hugoniot and adiabatic relations for the Gruneisen equation in the general form, then give the forms of adiabatic relations chosen by various authors and finally develop the modified Wilkins equation.

Adiabatic and Hugoniot Relations for Gruneisen Equation of State

The p - v relation for a shock reflected into detonation products initially in their CJ state is found by solving the Rankine-Hugoniot relation,

$$e - e_{cj} = \frac{1}{2} (p + p_{cj})(v_{cj} - v) \quad (3)$$

with the equation of state (1) written in the form

$$e = pv/w + f(v) \quad (4)$$

where

$$f(v) = e_r(v) - vp_r(v)/w. \quad (5)$$

The reflected shock Hugoniot curve is therefore

$$p = 2w \left[e_{cj} - f(v) + \frac{1}{2} p_{cj}(v_{cj} - v) \right] / [(w+2)v - wv_{cj}] \quad (6)$$

and the particle velocity behind a reflected shock is given by

$$u = u_{cj} - \sqrt{(p - p_{cj})(v_{cj} - v)}. \quad (7)$$

For the p - u relation in a reflected rarefaction, it is necessary to integrate the Riemann characteristic relation, which it is convenient to write as

$$du/d(\ln v) = c \quad (8)$$

where c is the velocity of sound. On the CJ adiabat c is given by

$$c = c_r(v) = v \sqrt{-p'_r(v)} \quad (9)$$

where the prime denotes differentiation with respect to v along the adiabat. In general, Eq. (8) needs to be integrated numerically.

The detonation Hugoniot for an explosive of initial specific volume v_e is found by substituting the equation of state (4) into the Rankine-Hugoniot relation across a detonation front

$$e = e_o + \frac{1}{2} p(v_e - v) \quad (10)$$

giving

$$p = 2w [e_o - f(v)] / [(w+2)v - wv_e] \quad (11)$$

where e_o is the sum of the energy released in the detonation and the difference in internal energy between undetonated explosive and the products at infinite expansion. A value of e_o can be found from any known (e_{cj}, p_{cj}, v_{cj}) state via (10).

The locus of CJ states is obtained by finding the point of tangency of the Rayleigh line

$$D^2/v_e^2 = p/(v_e - v) \quad (12)$$

to the detonation Hugoniot, D being the detonation velocity. The equation relating the variation of v_{cj} with v_e is then

$$\frac{2\{e_o - f(v_{cj})\}}{(w+2)v_{cj} - wv_e} = \frac{(v_e - v_{cj}) f'(v_{cj})}{(w+2)v_{cj} - (w+1)v_e} \quad (13)$$

which in general needs to be solved by iteration.

The Fickett and Wood Equation of State

Deal's [1] experiments on Grade A, Composition B showed that the adiabatic exponent γ was sensibly constant over the pressure range 1 to 500 kb. Fickett and Wood [5] therefore used a straight line CJ adiabat as reference curve

$$p_r(v) = A v^{-\delta} \quad (14)$$

where A and δ are constants; δ in this case being γ_{cj} .

The Pike Equation

Pike of AWRE has generalised Fickett and Wood's adiabatic relation to

$$P_r(v) = A v^{-\delta} + w G v^{-(1+w)} \quad (15)$$

where G is a constant, to allow for those explosives which have an air-match point above the straight line adiabat. The adiabat (15) is curved concave upwards and has an adiabatic exponent which tends to $1+w$ at very low pressures.

The Wilkins Equation

In order to obtain the dip in the adiabat below the constant γ form, Wilkins [3] added an exponential term to the Pike form, giving

$$p_r(v) = A v^{-\delta} + B \exp(-kv) + w G v^{-(1+w)} \quad (16)$$

where B and k are constants. The three terms are dominant in three different regions of a $\log p - \log v$ diagram (Fig. 1). With $\delta \sim 4$ the first term $A v^{-\delta}$ is dominant for small v , say up to $(1/2)v_{cj}$. Between $(1/2)v_{cj}$ and $2v_{cj}$ the exponential term dominates but falls off rapidly. This falling off causes the dip in the adiabat below the constant γ form between 150 kb and 3 kb. Finally for large v , the third term dominates and since for most explosives $w \sim 0.5$, the final slope of the adiabat is ~ 1.5 .

The Proposed Form of Equation of State

Wilkins has given sets of constants A, δ, B, k, G, w for two explosives. One significant fact about the values is that A is small and

negative. Since it is negative, there must be some value of v for which the adiabat turns over and has an unreal slope, though this value of v is at very high pressure and out of the region of interest. The fact that A is small suggests that the whole term $A v^{-\delta}$ may be neglected, leaving what may be called an exponential equation of state

$$p_v(v) = B \exp(-kv) + w G v^{-(1+w)} \quad (17)$$

This adiabat has all the properties of the Wilkins equation of state for $p < p_{cj}$, i.e., it has the dip below the constant γ adiabat and it has a γ tending to $1+w$ at low pressures. It has the advantage over the Wilkins equation that there are now only four constants to determine instead of six. However there are also two disadvantages to the exponential equation:

1. When the exponential term dominates, the adiabatic exponent is $\gamma = kv$ which means that γ decreases with decreasing volume. The behaviour at high pressures is therefore poor.
2. The $p-u$ relation for the adiabat (17) tends to fall away too rapidly from the constant γ adiabat.

To overcome these difficulties, the equations of state proposed for the two explosives HMX/TNT/Inert and HMX/Inert have been chosen by using a Pike equation of state for volumes v less than some critical volume v_c and an exponential equation for volumes greater than v_c . Hence

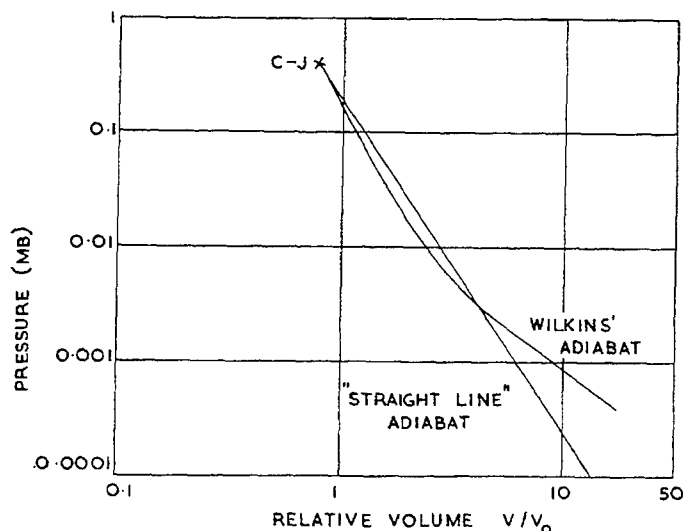


Fig. 1 - Form of Wilkins' adiabat

$$p_r(v) = \begin{cases} A v^{-\delta} + w G_1 v^{-(1+w)}, & v \leq v_c \\ B \exp(-kv) + w G_2 v^{-(1+w)}, & v > v_c \end{cases} \quad (18)$$

We have called this the modified Wilkins equation. It is shown in the Appendix that the values of $e_r(v_c)$, $p_r(v_c)$, and $p'_r(v_c)$ can be matched for the two relations, giving three equations relating A, δ, G_1 to B, k, G_2 . It is also shown that the Gruneisen constant w must be the same in both regions.

A p - v relation cannot be obtained by direct measurement but a p - u curve can be outlined by measuring the shock or particle velocities transmitted into various materials of known equation of state by a normally incident detonation wave. In principle a p - v relation can be deduced from the measured p - u curve but in practice it is simpler to assume the form of the p - v relation (for example, the proposed adiabat (18)) and then adjust the constants until a best fit is made to the p - u data.

In order to fix a sufficient number of constants in the proposed equation of state, measurements are required of (1) detonation velocity and its variation with charge density, (2) the CJ constants and (3) p - u points in the lower pressure range of the CJ adiabat.

3. EXPERIMENTAL METHODS AND RESULTS

All solid explosive charges used were 5-in. diameter by 5-in.-long pressed cylinders, each being initiated by a 5-in.-diameter Comp. B/Baratol plane wave generator.

Measurements of Detonation Velocity

Detonation velocity in each solid charge was measured by 0.052-in.-diameter coaxial ionization probes inserted in 1-in.-deep holes drilled radially at 1-cm intervals up the side of the cylinder. Pulses resulting from actuation of these probes by the passage of the detonation wave were recorded on calibrated oscillograph tubes.

Similar measurements of detonation velocity were also carried out on powdered charges, the densities of which lay in the range 0.7 to 0.8 gm cm⁻³. Each charge was contained in a 6-in. long, 4-in. OD, 2-in. ID mild steel barrel and was initiated by a 2-in.-diameter plane wave generator. Additional measurements on

5-in.-diameter powdered charges contained in 1-in.-thick steel barrels showed that this confinement was sufficient to eliminate diameter effects.

A linear regression analysis, minimising errors in detonation velocity, was carried out on detonation velocity, D , and charge density, ρ , values obtained from the measurements on solid and powdered charges. These analyses gave

$$\text{HMX/TNT/Inert: } D = 2.093 (\pm 0.045) + 3.446 (\pm 0.028) \rho \quad (19)$$

$$\text{HMX/Inert: } D = 2.568 (\pm 0.053) + 3.456 (\pm 0.035) \rho \quad (20)$$

with D in mm μsec^{-1} , ρ in gm cm⁻³.

In all the experiments subsequently described there were variations in charge density from round to round and it was necessary to normalise the results to suitable standard values of ρ and D . From the D, ρ relations (19) and (20), were obtained the standard charge density and detonation velocity values given in Tables 3 and 4.

Determination of Chapman-Jouguet Point

The experimental arrangement used to obtain impedance match data from solids and liquids placed in contact with the explosive is shown in Fig. 2. The mean free surface velocity of a disc of each metal was measured over a given flight distance, using forty 0.052-in.-diameter coaxial probes placed at known distances from the surface of the metal; each disc was 5-mm thick, sufficient to avoid reaction zone effects. The velocity measurement was in all cases made within the disc's shock reverberation time. The probe assembly was enclosed in propane gas to prevent premature triggering of the probes by air shock. In the cases of Perspex and water, the mean shock velocity over a thickness of 4.4 mm was measured by 0.018-in. probes set at known depths in the material. All free surface and shock velocity measurements were confined to the 2-in.-diameter axial region of the assembly.

Results of these mean velocity measurements are presented in Table 1. Each measured velocity value was normalised to its standard explosive density by taking an approximate modified Wilkins equation of state for the detonation products and finding the points of

TABLE 1
Velocity Measurements for Determination of CJ Point

H.E.	Contacting Material	Charge Density (gm cm ⁻³)	Detonation Velocity (mm/μsec)	Flight Distance (mm)	Measured Mean Free-Surface (FS) and Shock (S) Velocities (mm/μsec)	Velocities Corrected to Zero Disc Thickness (mm/μsec)
HMX/TNT/Inert: 68/30/2	Nickel	1.772	8.213 (±0.038)	2.8	1.782 (±0.014) (FS)	1.948 (±0.014) (FS)
		1.775	8.144 (±0.055)	2.9	1.800 (±0.032) (FS)	1.970 (±0.032) (FS)
	Brass (ρ = 8.44)	1.773	8.227 (±0.016)	3.0	1.991 (±0.019) (FS)	2.155 (±0.019) (FS)
		1.774	8.178 (±0.026)	2.8	2.088 (±0.020) (FS)	2.244 (±0.020) (FS)
	Titanium	1.773	8.123 (±0.013)	2.9	2.722 (±0.036) (FS)	2.877 (±0.036) (FS)
		1.773	8.165 (±0.023)	2.7	2.742 (±0.043) (FS)	2.889 (±0.043) (FS)
	Aluminium	1.775	8.273 (±0.024)	2.8	3.460 (±0.034) (FS)	3.600 (±0.034) (FS)
	NE6 Dural (ρ = 2.65)	1.782	8.250 (±0.050)	3.0	3.509 (±0.041) (FS)	3.609 (±0.041) (FS)
	Magnesium	1.774	8.242 (±0.029)	5.0	4.544 (±0.040) (FS)	4.745 (±0.040) (FS)
		1.777	8.252 (±0.032)	4.5	4.579 (±0.061) (FS)	4.763 (±0.061) (FS)
HMX/Inert: 95/5	Nickel	1.782	8.239 (±0.017)	-	6.598 (±0.098) (S)	6.622 (±0.098) (S)
		1.779	8.242 (±0.030)	-	6.662 (±0.047) (S)	6.686 (±0.047) (S)
	Water	1.774	8.226 (±0.035)	-	6.839 (±0.082) (S)	6.871 (±0.082) (S)
	Nickel	1.782	8.661 (±0.036)	3.0	1.884 (±0.021) (FS)	2.074 (±0.021) (FS)
		1.780	8.745 (±0.044)	3.2	1.894 (±0.041) (FS)	2.094 (±0.041) (FS)
	Titanium	1.782	8.693 (±0.035)	2.9	2.735 (±0.037) (FS)	2.901 (±0.037) (FS)
		1.783	8.686 (±0.031)	3.0	2.837 (±0.028) (FS)	3.007 (±0.028) (FS)
	NE6 Dural (ρ = 2.65)	1.775	8.685 (±0.040)	4.1	3.566 (±0.079) (FS)	3.760 (±0.079) (FS)
	Magnesium	1.783	8.749 (±0.075)	5.2	4.547 (±0.053) (FS)	4.763 (±0.053) (FS)
		1.784	8.772 (±0.034)	5.1	4.602 (±0.086) (FS)*	4.809 (±0.086) (FS)

*Disc thickness 4.5 mm.

TABLE 2
Gas Shock Velocity Measurements

H.E.	Gas	Charge Density (gm cm ⁻³)	Initial Pressure (bars)	Ambient T (°K)	Gas Shock Velocity U (mm/μsec)	Calculated U/u	Normalised	
							P (kb)	U (mm/μsec)
HMX/TNT/Inert: 68/30/2	Air	1.783	0.256 (±0.001)	285.4 (±0.3)	9.142 (±0.048)	1.084	0.241 (±0.004)	8.428 (±0.045)
		1.784	0.260 (±0.001)	279.1 (±0.3)	9.087 (±0.063)	1.084	0.247 (±0.005)	8.376 (±0.058)
		1.789	0.990 (±0.002)	285.8 (±0.3)	8.387 (±0.042)	1.090	0.777 (±0.010)	7.679 (±0.038)
		1.790	0.990 (±0.002)	285.9 (±0.3)	8.331 (±0.025)	1.090	0.765 (±0.007)	7.627 (±0.023)
		1.780	1.001 (±0.002)	287.2 (±0.3)	8.477 (±0.031)	1.090	0.800 (±0.008)	7.772 (±0.029)
		1.783	2.98 (±0.01)	294.6 (±0.3)	7.678 (±0.021)	1.098	1.89 (±0.02)	6.983 (±0.020)
		1.778	3.15 (±0.01)	290.0 (±0.3)	7.836 (±0.031)	1.098	2.12 (±0.03)	7.134 (±0.030)
		1.787	8.91 (±0.05)	284.4 (±0.3)	7.149 (±0.048)	1.115	4.99 (±0.10)	6.390 (±0.041)
		1.790	9.05 (±0.05)	290.0 (±0.3)	7.422 (±0.024)	1.114	5.36 (±0.08)	6.635 (±0.021)
		1.789	9.08 (±0.05)	293.5 (±0.3)	7.275 (±0.033)	1.115	5.10 (±0.08)	6.500 (±0.030)
	Argon	1.781	6.46 (±0.04)	279.0 (±0.3)	7.579 (±0.036)	1.115	5.75 (±0.10)	6.787 (±0.034)
		1.786	30.7 (±0.3)	281.2 (±0.3)	6.862 (±0.055)	1.152	21.8 (±0.6)	5.933 (±0.048)
		1.783	31.0 (±0.3)	294.6 (±0.3)	6.700 (±0.054)	1.156	20.0 (±0.5)	5.779 (±0.046)
HMX/Inert: 95/5	Air	1.784	0.240 (±0.001)	278.6 (±0.3)	8.903 (±0.057)	1.084	0.220 (±0.004)	8.212 (±0.053)
		1.784	0.243 (±0.001)	280.9 (±0.3)	8.855 (±0.045)	1.084	0.218 (±0.004)	8.169 (±0.042)
		1.774	0.998 (±0.002)	290.8 (±0.3)	8.236 (±0.030)	1.090	0.746 (±0.007)	7.563 (±0.027)
		1.775	0.999 (±0.002)	292.1 (±0.3)	8.236 (±0.023)	1.090	0.743 (±0.007)	7.562 (±0.022)
		1.781	9.05 (±0.05)	295.4 (±0.3)	7.421 (±0.037)	1.114	5.30 (±0.10)	6.529 (±0.033)
		1.781	9.22 (±0.05)	298.6 (±0.3)	7.276 (±0.024)	1.115	5.13 (±0.08)	6.664 (±0.023)
	Argon	1.781	6.39 (±0.19)	290.3 (±0.3)	7.723 (±0.062)	1.112	5.71 (±0.27)	6.947 (±0.056)
		1.784	14.04 (±0.04)	282.2 (±0.3)	7.009 (±0.053)	1.134	10.5 (±0.2)	6.179 (±0.049)
		1.781	31.1 (±0.3)	301.5 (±0.3)	6.604 (±0.016)	1.159	19.0 (±0.3)	5.702 (±0.014)
		1.782	32.0 (±0.3)	292.7 (±0.3)	6.759 (±0.095)	1.155	21.3 (±0.8)	5.854 (±0.083)
	Krypton	1.780	19.3 (±0.2)	293.1 (±0.3)	6.381 (±0.051)	1.103	25.6 (±0.7)	5.791 (±0.046)

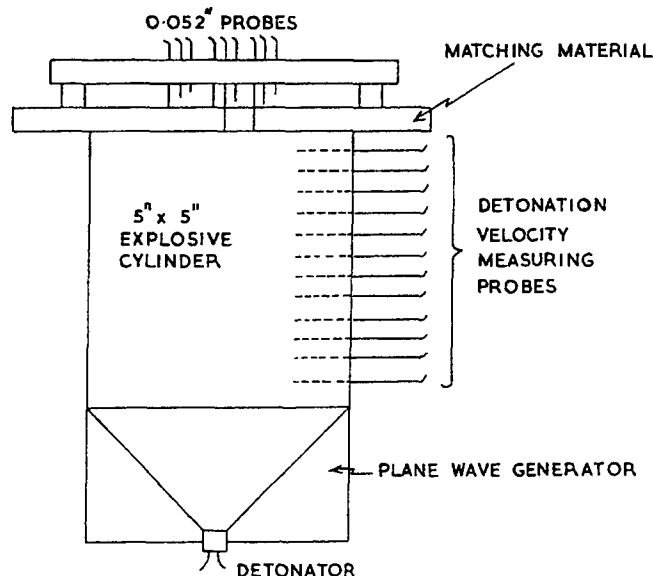


Fig. 2 - Measurement of C-J point

intersection with the Hugoniot of the matching material of the adiabats for two different charge densities ρ and $\rho + \Delta\rho$ where the CJ conditions for this latter density are found by using Eq. (13). In this way values of $\Delta p/\Delta\rho$ and $\Delta u/\Delta\rho$, and consequently $\Delta u_{fs}/\Delta\rho$ and $\Delta U/\Delta\rho$, were found, u_{fs} being the free surface velocity and U the shock velocity. The normalised mean velocity for a given thickness of material had now to be converted to a velocity corresponding to zero disc thickness, in order to correct for velocity attenuation which had occurred during the passage of the shock through the disc and the movement of the disc over its flight distance. This was done by inserting a plausible value of γ in the one-D characteristic code, NIP [6], and computing the decay of the shock and free surface velocities for each matching material. γ was varied until agreement was obtained between experiment and the appropriate mean velocity derived from NIP. The value of velocity corresponding to zero disc thickness was extracted from the successful NIP run and from this a p - u point on the Hugoniot of the matching material was derived. A constant γ CJ adiabat passing through this p - u point was then found by trial and the relevant value of γ_{CJ} noted. After repetition of this procedure for each experimental velocity measurement, a weighted mean was taken of the γ_{CJ} values thus obtained. The CJ point was defined by this mean γ_{CJ} and the standard values of charge density and detonation velocity. The CJ constants thereby obtained are given in Tables 3 and 4.

Determination of Lower Portion of CJ Adiat

Owing to a lack of suitable matching materials, no CJ adiabat appears to have been directly determined in the range between 100 kb and 1 kb, excepting a foam matching point at 44 kb in Grade A, Comp. B, obtained by Deal [1]. By using different gases compressed to various initial densities, a range of matches may be made within the unexplored pressure range.

The experimental arrangement used is shown in Fig. 3. An explosive charge was enclosed in an expendable pressure vessel, which was capable of withstanding 32 bars. This vessel was fitted with front and back Perspex windows, which were plane and parallel and carried accurately machined sighting lines.

The vessel was filled with compressed gas to the desired pressure, or was partially evacuated in some cases. Pressure was measured and cross-checked by means of two calibrated Bourdon gauges connected as in Fig. 3. The estimated accuracy of this static pressure measurement improved with increasing pressure from 0.5 percent at 0.25 bars to 0.1 percent at 1 bar (measured by a mercury barometer) and then deteriorated to 1 percent at 30 bars. A mercury thermometer measured the ambient temperature to an accuracy of 0.1 percent.

TABLE 3
Values of Modified Wilkins Constants for HMX/TNT/Inert

$\rho = 1.776 (\pm 0.003) \text{ gm cm}^{-3}$ $D = 8.213 (\pm 0.047) \text{ mm } \mu\text{sec}^{-1}$					
$\gamma_{cj} = 2.85 (\pm 0.03)$ $P_{cj} = 311.5 (\pm 4.0) \text{ kb}$					
$w = 0.4780$					
v_c	0.4	0.5	0.6	0.7	$\text{cm}^3 \text{ gm}^{-1}$
P_c			110.5	71.4	Kbars
A		0.02536	0.02521	0.02517	Mbars $(\text{cm}^3 \text{ gm}^{-1})^\delta$
δ		2.856	2.860	2.861	
B	5.683	3.391	2.014	1.296	Mbars
k	7.273	6.085	5.077	4.353	gm cm^{-3}
e_o	0.04722	0.04863	0.04905	0.04916	Mbars $\text{cm}^3 \text{ gm}^{-1}$
Δ^2_u	0.254	0.216	0.255	0.364	$(\text{mm } \mu\text{sec}^{-1})^2$
ΔD	-0.81	-0.49	-0.19	0.028	$\text{mm } \mu\text{sec}^{-1}$

TABLE 4
Values of Modified Wilkins Constants for HMX/Inert

$\rho = 1.783 (\pm 0.002) \text{ gm cm}^{-3}$ $D = 8.730 (\pm 0.037) \text{ mm } \mu\text{sec}^{-1}$				
$\gamma_{cj} = 3.05 (\pm 0.03)$ $P_{cj} = 335 (\pm 4) \text{ kb}$				
$w = 0.8323$				
v_c	0.4	0.5	0.6	$\text{cm}^3 \text{ gm}^{-1}$
P_c		200.3	140.8	Kbars
A	0.03368	0.02695	0.02635	Mbars $(\text{cm}^3 \text{ gm}^{-1})^\delta$
δ	2.763	2.988	3.001	
B	7.556	4.597	3.362	Mbars
k	7.814	6.645	5.944	gm cm^{-3}
e_o	0.04133	0.04262	0.04329	Mbars $\text{cm}^3 \text{ gm}^{-1}$
Δ^2_u	0.084	0.109	0.177	$(\text{mm } \mu\text{sec}^{-1})^2$
ΔD	-0.49	-0.20	-0.02	$\text{mm } \mu\text{sec}^{-1}$

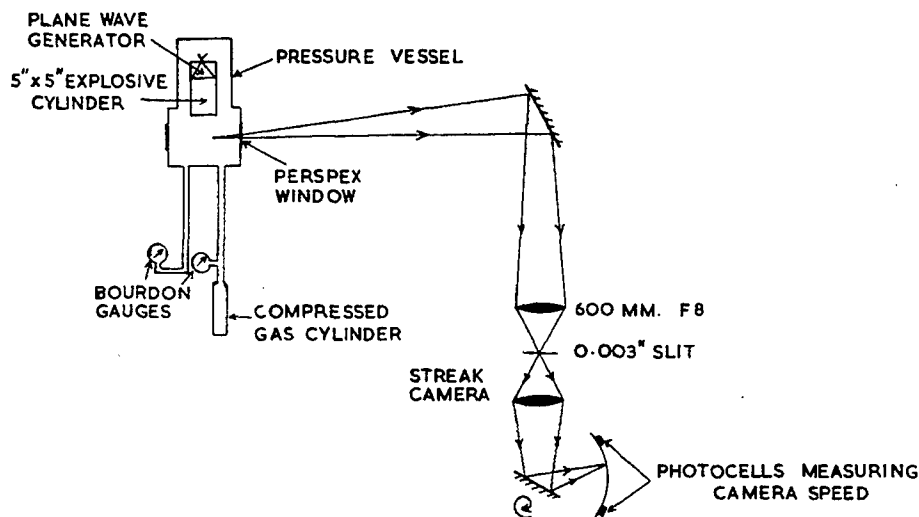


Fig. 3 - Measurement of gas shock velocity

The passage of the self-luminous shock front transmitted from the front face of the detonated charge into the ambient gas was observed by a streak camera. The optical magnification of ~ 0.5 was measured to 0.1 percent from a still photograph of a 2-in.-diameter ball bearing placed on the charge axis. The image sweep speed, measured to 0.2 percent by oscillographic timing of the exposures of two photocells placed on the film track, was $\sim 6 \text{ mm } \mu\text{sec}^{-1}$, giving a streak trace angle of $\sim 45^\circ$.

Measurement of the streak record on a digitalised reader showed that the gradient of the trace was virtually constant over a distance 6-60 mm from the front face of the static charge; except for the rounds fired at 0.25 bars initial pressure, where spray from the charge surface confused the first 25 mm of shock travel. A linear regression was fitted to the coordinates of the straight portion of a record, giving a gradient which combined with the measurements of optical magnification and image sweep speed to give the gas shock velocity.

In order to obtain pressure and particle velocity values in a shocked gas from measurements of the gas shock velocity and the pressure and temperature of the unshocked state, a knowledge is required of the equations of state of both the shocked and unshocked gas.

The equation of state used for the shocked argon and krypton has been developed by E. Morris of AWRE, following Rowlinson [7]. This equation has the form

$$pv/RT = (1 + x + x^2)/(1 - x)^3 \quad (21)$$

where R is the gas constant, T the temperature of the shocked gas and $x = B(T)/4V$, $B(T)$ being the second virial coefficient. Fickett [8] has quoted a private communication by Wackerle and Hughes giving measured shock and particle velocities in argon initially at a pressure of 1 kb. Relation (21) is in good agreement with these experimental results and others from the same source.

Data for shocked air, unshocked air and unshocked inert gas are to be found in Refs. 9, 10, and 11, respectively.

To obtain p and u , we write the Rankine-Hugoniot energy equation in the form

$$v_1/v = 1 + 2e/pv \\ - p_1 v_1 / pv (1 + 2e_1/p_1 v_1 - v/v_1) \quad (22)$$

where subscript 1 refers to the unshocked state. Choosing successive values for the slowly varying ratio of shock velocity to particle velocity allows p and u to be found by iteration. An error analysis of Eq. (22) shows that, for a given measured shock velocity, the calculated value of u is not closely dependent on the equation of state data used; for example, a 10 percent error in e/pv results in less than 1 percent error in u .

The measured and calculated quantities obtained from the gas matching rounds are listed in Table 2. Each pair of calculated p, u values was normalised to the standard explosive density. These normalised results, also listed

in Table 2, are plotted in Figs. 5 and 6. It is apparent from these graphs that there is some disagreement between the equations of state used for air and for argon in the region of 5 kb. This discrepancy has still to be resolved.

If the particle velocity of the detonation products could have been measured from the same record as the gas shock velocity, no knowledge of the equation of state of the shocked gas would have been required. Superficial consideration would suggest that the particle velocity could be determined by recording the motion of the boundary between the intensely luminous shocked gas and the comparatively nonluminous detonation products. In fact, the quality of the record of this apparent particle velocity was improved, by placing a 0.001-in.-thick aluminium foil on the front face of the charge, to the extent of making a measurement within an accuracy of 1 percent. However, further consideration of the effect of the refraction of light passing out through the shock front indicated that such a particle velocity measurement

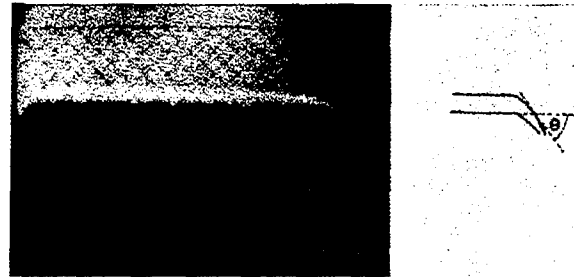


Fig. 4 - Framing camera record of detonating charge

was spurious. A framing camera examination of the detonating charge (Fig. 4) showed that the angle, θ , which the optical axis from the front of the detonation products made with the gas shock front, varied with time. Hence a correction for refraction would have been unreliable, since it depended on θ , which was difficult to measure accurately in any case.

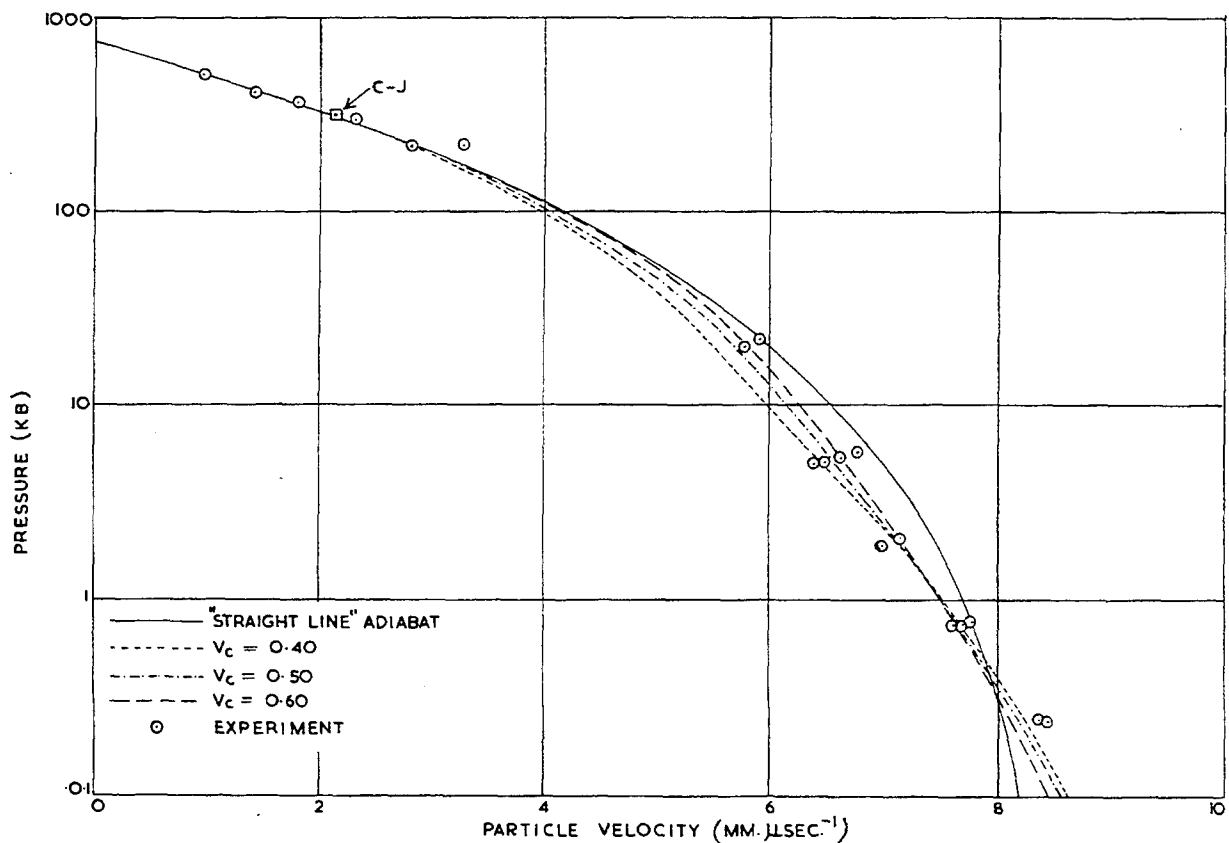


Fig. 5 - Various v_{crit} fits to experimental $p-u$ points for HMX/TNT/Inert

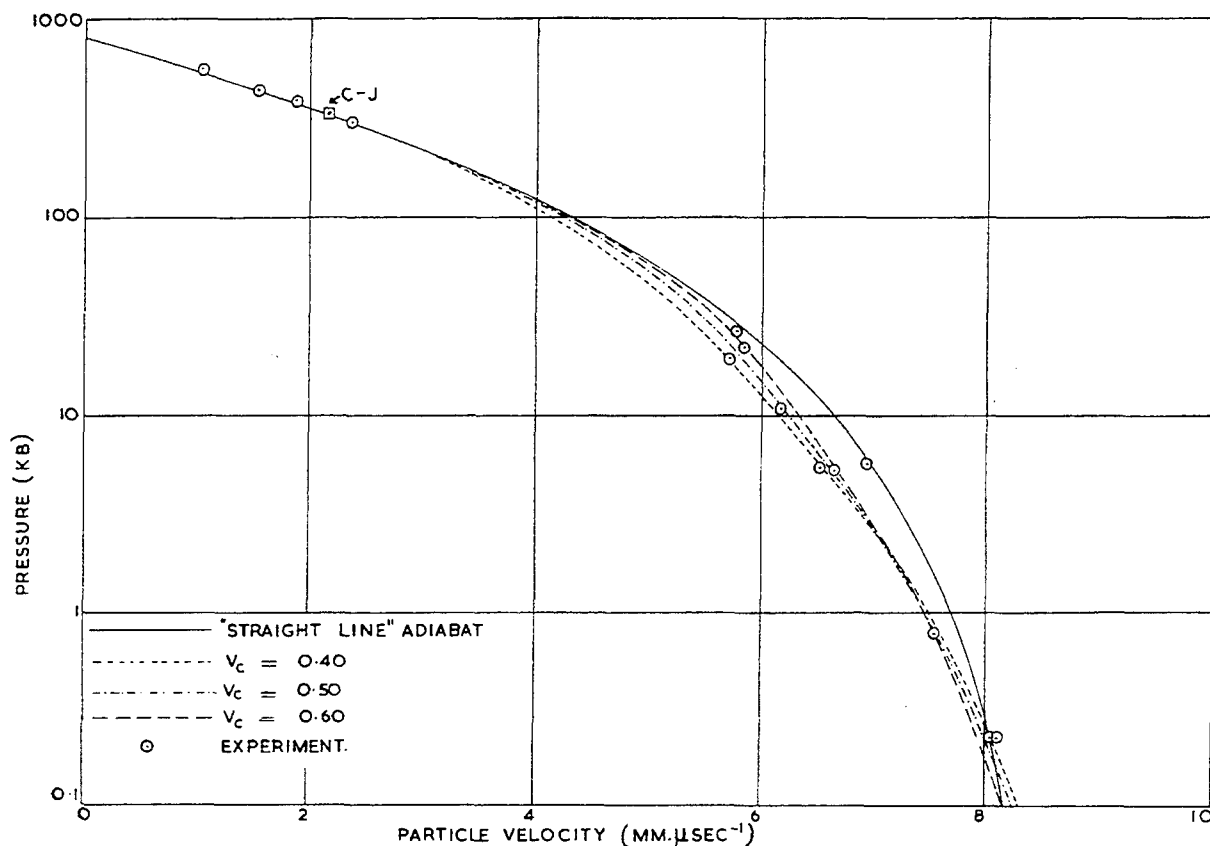


Fig. 6 - Various v_{crit} fits to experimental p - u points for HMX/Inert

4. FITTING THE EQUATION OF STATE TO THE DATA

The p - u points for the compressed gas experiments are plotted in Figs. 5 and 6 for the two explosives, together with the constant γ CJ adiabats. It will be seen that the compressed gas points lie below the constant γ adiabat with the exception of the two reduced air pressure points. This confirms Wilkins idea, at least for these two explosives, that the true CJ adiabat dips away from the constant γ form. We therefore feel justified in using the data to choose the parameters of the modified Wilkins form proposed in Eq. (18).

Method of Choosing the Constants

In the proposed adiabatic relation (18) there were eight parameters $A, \delta, G_1, w, B, k, G_2, v_c$, which needed to be determined. Taking the usual case where $v_{cj} < v_c$, four steps were made in choosing the constants, a process which begins by selecting a value of v_c .

1. The quite general relation derived by Jones [12] was used to find w from

$$w = \alpha \gamma_{cj} / (\alpha + 1) \quad (23)$$

where in this case

$$\alpha = \left[(\gamma_{cj} + 1) / (1 + d \ln D / d \ln \rho) \right] - 2. \quad (24)$$

2. An estimate was made of δ . Then the experimentally determined values of p_{cj}, γ_{cj} gave two independent relations between A, G_1, w and δ , for p_{cj}, v_{cj} defines a point on $p_r(v)$, and γ_{cj} is related to $p_r'(v)$ at the CJ point. These relations were:

$$A = p_{cj} v_{cj}^{\delta} (\gamma_{cj} - 1 - w) / (\delta - 1 - w) \quad (25)$$

$$G_1 = p_{cj} v_{cj}^{(1+w)} (\delta - \gamma_{cj}) / w (\delta - 1 - w). \quad (26)$$

3. The equations expressing continuity of c_r, p_r and p_r' at v_c , given in the Appendix, then gave B, k and G_2 .

4. At this stage of the calculation, w had been determined from the experimental values, v_c had been selected and the other coefficients all depended on the estimate of δ . Hence the shape of the adiabat depended on this value of δ which was therefore adjusted until a best fit was made to the compressed gas p - v points. The p - v relation for the adiabat was determined from Eq. (8), and $p_r(v)$.

In the course of choosing the parameters it was necessary to correct the p - v data both at high and low pressures to the standard charge density. The method used has been described in Section 3 above and depended on using an approximate set of constants. The process described above was therefore iterative. We assumed CJ conditions and fitted the parameters by using an uncorrected gas p - v point. All p - v points were then corrected and a new set of parameters evaluated which fitted the adjusted CJ point and compressed gas data. The process converged rapidly.

Results

The variation of the parameters with v_c for the two explosives is recorded in Tables 3 and 4. $\Delta^2 u$ is the minimum value of the sum of the squares of the deviations of the experimental compressed gas particle velocities about the chosen curve for given v_c . On this basis the best value of v_c is 0.50 cc/gm for HMX/TNT/Inert and 0.45 for HMX/Inert. The corresponding best p - v curves for $v_c = 0.4$, 0.5 and 0.6 are plotted in Figs. 5 and 6, together with the normalised experimental p - v points and a p - v curve for the constant γ adiabat. The corresponding p - v curves are plotted in Figs. 7 and 8 for the best v_c values.

The value of $dD/d\rho$ and hence w has been determined by fitting a straight line to D - ρ values obtained at normal density and powder density (0.7 to 0.8 gm/cc). The ΔD in Tables 3 and 4 represents the difference between the detonation velocity calculated from the equation of state at $\rho = 0.75$ gm/cc and the experimental value. If we had chosen v_c on the basis of making ΔD zero it would have been 0.68 for HMX/TNT/Inert and 0.60 for HMX/Inert.

5. DISCUSSION

We have shown experimentally that, for the two explosives examined, the CJ adiabat dips below the constant γ form and recrosses it at a low pressure, as suggested by Jones and by Wilkins. Because of this tendency of the two

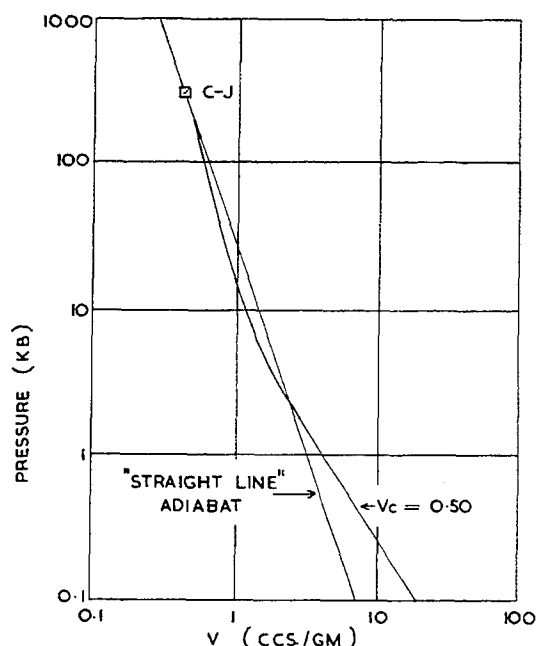


Fig. 7 - Pressure-volume adiabatic relation for HMX/TNT/Inert

types of adiabat to cross at a low pressure, Deal's [2] air-match points on four explosives are not inconsistent with a Wilkins form. However, Deal's [1] foam-match results at 113 kb

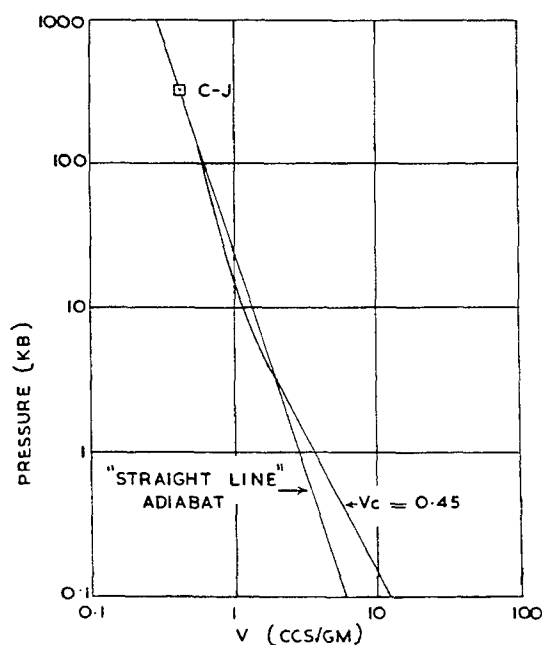


Fig. 8 - Pressure-volume adiabatic relation for HMX/Inert

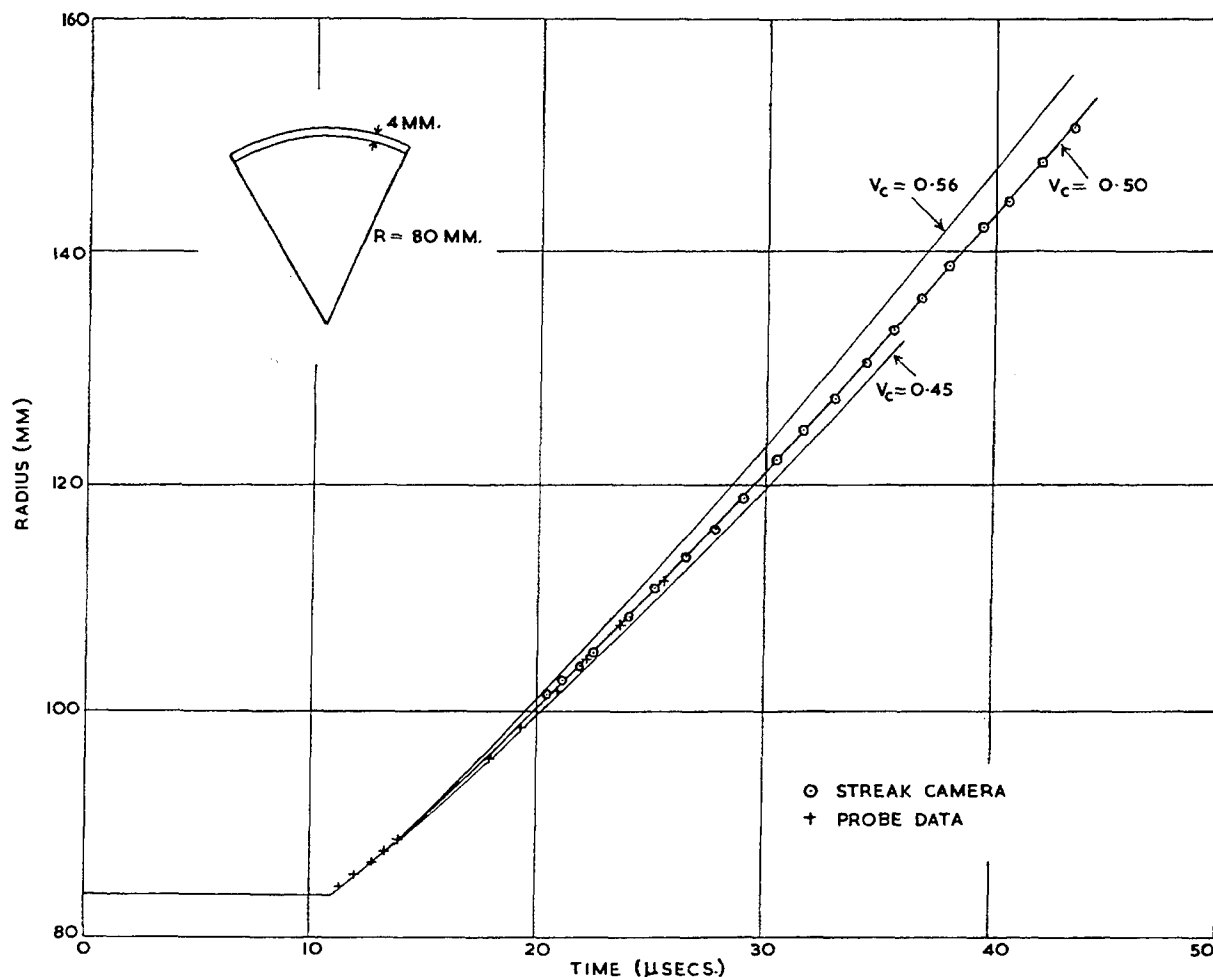


Fig. 9 - Comparison of experiment and calculation on HMX/TNT/Inert -- copper spherical assemblies

and 44 kb in Grade A, Comp. B suggest that this composition may not have a dip in its CJ adiabat.

Having established by comparatively direct measurement the coefficients to be used in the modified Wilkins equation, the next step was the important one of testing the equation's ability to predict the results of an integrated experiment, such as the Wilkins sphere test [3]. Billings of AWRE has measured the expansion of a 4-mm-thick copper shell driven by a centrally initiated 80-mm-radius sphere of the HMX/TNT/Inert composition. Figure 9 presents the results obtained with the copper shell and explosive sphere in contact and compares them with one-dimensional unsteady hydrodynamic mesh code runs using the modified Wilkins equation with various values of v_c . Good agreement between theory and experiment is

obtained with $v_c = 0.50$. Results are also available on a sphere test in which an 8-mm air gap was left between the copper and the explosive. With $v_c = 0.45$, the modified Wilkins fits this motion equally well. Both these values of v_c are near the minimum of the $\Delta^2 u$ values in Table 3.

It is slightly disturbing that two different values of v_c are required to fit the two experiments. A possible source of error is the assumption that a value of $dD/d\rho$ obtained by fitting two widely differing explosive densities holds accurately in the region close to the upper of the two densities. Such an assumption has certainly been shown to be invalid in the case of TNT [13]. In fact if $dD/d\rho$ is slightly increased and a new set of constants evaluated for the explosive, both sets of sphere test results can be fitted with the same value of v_c .

It follows that the accuracy of the equation of state should be improved by a closer examination of $dD/d\rho$ in the higher density range, together with the extension of the gas matching measurements up to ~80 kb, using stronger pressure vessels currently being manufactured.

REFERENCES

1. W. E. Deal, "Measurement of the Reflected Shock Hugoniot and Isentrope for Explosive Reaction Products," *Physics of Fluids*, 1, 523 (1958).
2. W. E. Deal, "Low Pressure Points on the Isentropes of Several High Explosives," Third O.N.R. Symposium on Detonation, 386 (1960).
3. M. Wilkins, B. Squier, and B. Halperin, "The Equation of State of PBX.9404 and LX04-01," University of California Report UCRL-7797 (April, 1964).
4. H. Jones and A. R. Miller, "The Detonation of Solid Explosives, the Equilibrium Conditions in the Detonation Wave-Front and the Adiabatic Expansion of the Products of Detonation," *Proc. Roy. Soc. A* 194, 480 (1948).
5. W. Fickett and W. W. Wood, "A Detonation-Product Equation of State Obtained from Hydrodynamic Data," *Physics of Fluids* 1, 528 (1958).
6. B. D. Lambourn and J. E. Hartley, "The Calculation of the Hydrodynamic Behaviour of Plane One-Dimensional Explosive/Metal Systems," Fourth O.N.R. Symposium on Detonation (1965).
7. J. S. Rowlinson, "An Equation of State of Gases at High Temperatures and Densities," *Molecular Physics*, 7, 349 (1964).
8. W. Fickett, "Intermolecular Potential Functions for some Simple Molecules from Available Experimental Data," LA-2665 (July 1962).
9. J. Hilsenrath and M. Klein, "Tables of Thermodynamic Properties of Air in Chemical Equilibrium including Second Virial Corrections from 1500°K to 15,000°K," AEDC-TDR-63-161 (August 1963).
10. J. Hilsenrath et al., "Tables of Thermal Properties of Gases," Natl. Bur. Standards Circ. 564, Washington (1955).
11. G. A. Cook et al., "Argon, Helium and the Rare Gases," Vol. 1 New York/London, 1961.
12. H. Jones, "The Properties of Gases at High Pressures which can be Deduced from Explosion Experiments," Third Symposium on Combustion, Flame and Explosion Phenomena (1949).
13. M. J. Urizar, E. James, and L. C. Smith, "The Detonation Velocity of Pressed TNT," in Third Symposium on Detonation, ONR Symposium Report ACR-52 (1960).

APPENDIX A

Continuity Conditions in a Modified Wilkins Equation of State

Let the two equations of state be of the general Gruneisen form

$$e = \begin{cases} e_{r1}(v) + v [p - p_{r1}(v)]/w_1, & v < v_c \\ e_{r2}(v) + v [p - p_{r2}(v)]/w_2, & v > v_c \end{cases} \quad (A1)$$

Then if the two linear $e-p$ relations are to have the same slope and intercept and we are to have continuity of the reference adiabat, we require

$$w_1 = w_2 = w \quad (A2)$$

$$p_{r1}(v_c) = p_{r2}(v_c) \quad (A3)$$

$$e_{r1}(v_c) = e_{r2}(v_c) \quad (A4)$$

In both the exponential and Pike equations of state used for the modified Wilkins Eq. (18) there are four constants. Hence in addition we can require continuity of p'_r , i.e.,

$$p'_{r1}(v_c) = p'_{r2}(v_c) \quad (A5)$$

For the two equations this leads to

$$\begin{aligned} e_r(v_c) &= A v_c^{1-\varepsilon}/(\varepsilon-1) + G_1 v_c^{-w} \\ &= B \exp(-kv_c)/k + G_2 v_c^{-w} \end{aligned} \quad (A6)$$

$$p_r(v_c) = A v_c^{-\delta} + w G_1 v_c^{-(1+w)} \quad (A7)$$

$$= B \exp(-k v_c) + w G_2 v_c^{-(1+w)}$$

$$-p'_r(v_c) = \delta A v_c^{-(\delta+1)} + w(1+w) G_1 v_c^{-(2+w)} \quad (A8)$$

$$= k B \exp(-k v_c) + w(1+w) G_2 v_c^{-(2+w)}$$

This in turn leads to

$$\delta = k v_c - w / (k v_c - w) \quad (A9)$$

or

$$k v_c = \frac{1}{2} \left[\delta + w - \sqrt{(\delta - w)^2 + 4w} \right] \quad (A10)$$

$$(\delta - 1 - w) A v_c^{-\delta} = (k v_c - 1 - w) B \exp(-k v_c). \quad (A11)$$

Then $p_c = p_r(v_c)$ can be found from one of (A7) and G_1 or G_2 from the other. Hence given one set of constants we can find the other set.

Conditions (A2) to (A5) also guarantee continuity of e , p and p' at v_c for any other adiabat.

Invited Review

**STRUCTURE, CHEMISTRY, AND INSTABILITY
OF DETONATION IN GASES**

Garry L. Schott
*University of California, Los Alamos Scientific Laboratory
Los Alamos, New Mexico*

ABSTRACT

The lesson from gas detonation research in the last ten years is that the Chapman-Jouguet description of the detonation process, with its many refinements, is inadequate. The equilibrium properties of the reaction products of detonable gases can be calculated reliably, and the predictions of Chapman-Jouguet theory have been tested directly against experimental observations. Several kinds of experiments have revealed manifestations of the principal area of failure of the steady, one dimensional theory, namely the occurrence of significant transverse motions which, like the detonation itself, are sustained by energy from the exothermic chemical reaction. The characteristic form of the laterally propagating perturbations which accompany this motion is analogous to the Mach stem interaction of two dimensional flow. This particular structural form is seen to be developed most strikingly by fuel-oxygen systems which exhibit branching chain chemical kinetics, and relationships between the reaction course and the Mach stem structure and between the structure and propagation failure limits in gases are indicated. The nonsteady process of initiation of detonation by a plane shock wave has also received attention, and one dimensional gas-dynamic computations are able to account for this process fairly well. Nevertheless there are unmistakable indications of the appearance and growth of transverse perturbations in this process as well. Finally, the results of theoretical treatment of the question of stability of steady, one dimensional shock wave flow in the presence of exothermic reaction have indicated certain regimes of instability, and current computational explorations of possible manifestations of such instability include examinations of fluctuations of intensity of plane waves with time and of the kinematics of laterally propagating high frequency sonic disturbances in reactive one dimensional flows.

INTRODUCTION

In discussing gaseous detonations in this Symposium which commemorates the twenty-fifth anniversary of a historic advance in the scientific study of condensed explosives, it may be appropriate to recall briefly the state of understanding of detonations in gases that existed twenty-five years ago. When we do this, we observe that a renaissance in thinking was signaled by the appearance, in the May 1940 issue of the Russian Journal of Experimental and Theoretical Physics, of a paper, "On the

Theory of Detonation in Gaseous Systems," by Ya. B. Zeldovich [1].

In that paper, Zeldovich studied "the conditions of one dimensional steady detonation, effect of heat transfer and resistance, and distribution of temperature, pressure, and so forth, in a strictly steady regime." We recognize this, of course, as the basis of the very familiar Zeldovich-von Neumann-Döring model of detonation and the "von Neumann spike." Zeldovich continued, however, with a very prophetic statement in the sentence following the

Note: This work was performed under the auspices of the U.S. Atomic Energy Commission.

one quoted above, "Such computations are required as a starting point of the whole more complicated theory of the propagation of detonation in three dimensions, the theory of periodic states, and so forth."

Elsewhere in the paper, Zeldovich summarized the gas detonation research of the preceding half century, more or less, and foretold that of the past quarter century by the observations, "Up to the most recent times, the hydrodynamic (Chapman-Jouguet) theory of the velocity of detonation, excellently confirmed by test, did not arouse a need for seeking the mechanism of the chemical reaction and an investigation of the conditions at the detonation wave front. If the present work gives rise to new experimental investigations, which penetrate more deeply into the nature of the phenomenon, the object will have been attained."

The present survey does not review all the historical developments comprehensively. Rather it attempts to outline current thinking about the detonation process, and its development from observations and considerations of gaseous detonations. This current picture has emerged largely from the recognition of the important role of nonlaminar flow processes in gaseous detonation, which has occupied a position of prominence since about 1960. In the proceedings of the Discussion on Detonation at the Ninth International Combustion Symposium [2] at Ithaca in 1962, and in two review articles which appeared in late 1963 [3,4], the reader may find much of the material included in the present survey, as well as other related material, presented from other authors' points of view. In various monographs [5-8] and in selected recent journal articles, one may find expositions of the more classic topics of gaseous detonations, such as the Chapman-Jouguet-Zeldovich-von Neumann-Döring theoretical model [9], and the phenomenology of limits of detonability, spinning detonations, spherical detonation, the transition from subsonic flame to detonation [10], diameter effects [11], and the rarefaction zone behind the detonation.

TESTS OF STEADY, ONE DIMENSIONAL THEORY

Chemically, the detonable gases most studied are mixtures of carbon and/or hydrogen containing fuels with an oxidizer, usually O_2 . Nitrogenous compounds are of lesser prominence, and metals (save boron in B_2H_6) [12] are substantially absent from consideration. The density and the composition of the mixtures, which often include inert diluents, are favorite

experimental variables whose effects are determined over wide ranges. Except in carbonaceous systems containing insufficient oxygen [13], the reaction products of the more familiar gaseous detonations are also exclusively gaseous molecules whose thermodynamic properties are well known at the low densities normally studied. This means that the Hugoniot equations can be solved numerically for the pertinent states of no reaction and of equilibrium as well as for arbitrary states of intermediate composition, and the predictions of the steady, one dimensional theory can be tested directly.

Of course the detonation velocity is one of the quantities which can be tested, but there are many others as well. Since the mid-1950's, there have been reported a large variety of experimental observations of detonation waves aimed at determining the condition of the detonation products at the "Chapman-Jouguet plane" and the extent and structure of the reaction zone near the shock front. Some of the quantities which are available for experimental study are indicated in Fig. 1. This pressure vs specific volume diagram shows computed conditions for selected hypothetical states in the steady, one dimensional detonation of a particular detonable gas, pure ozone. This example, rather than a fuel oxygen mixture, has been chosen for simplicity and to emphasize the fact that the properties represented by this familiar diagram are determined by thermochemistry, not by reaction mechanism.

For the Chapman-Jouguet velocity wave considered in Fig. 1 there are, between the no-reaction and equilibrium states, substantial changes in pressure, density, temperature, and mass flow velocity, and complete replacement of the initial O_3 by the products O_2 and O . Many possibilities are offered for measurement of the course of the reaction provided the requisite time and space resolution can be achieved. Extensive measurements to dissect the wave front structure have been made by x-ray densitometry [14], spectroscopic temperature determination [15], photoelectric schlieren densitometry [16], optical interferometric densitometry [17], absorption [18] and emission [17] spectrophotometry of individual species concentrations, and pressure profile measurements [19]. While all of these approaches did yield some observations of wave front structure in detonations at low pressures, real quantitative confirmation of the von Neumann spike was never abundantly evident.

The terminal state of the detonation products prior to their gradual expansion in the

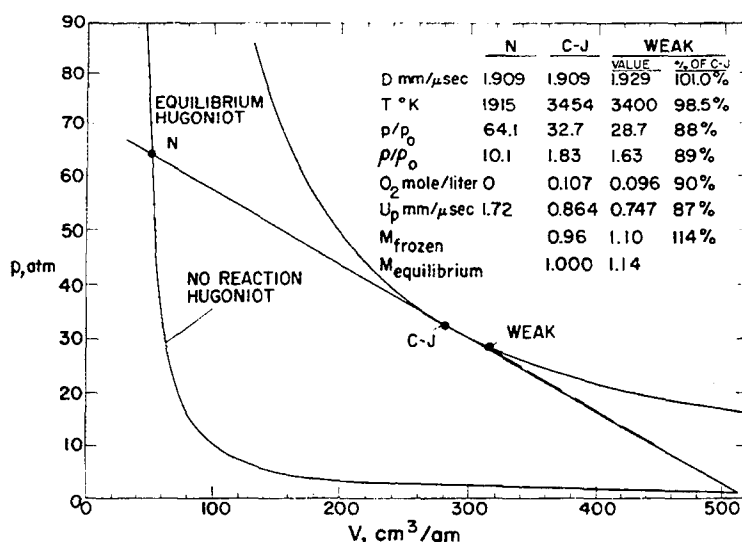


Fig. 1 - Computed pressure - volume diagram for steady, one dimensional detonation of pure ozone at 1 atm initial pressure, with chart comparing experimentally observable properties at no reaction, equilibrium Chapman-Jouguet, and weak equilibrium detonation conditions. D, detonation velocity; T, temperature; p, pressure; ρ , density; U_p , particle velocity; M, Mach number of equilibrium flow, with respect to shock front.

rarefaction wave is also examinable quantitatively, with less stringent space/time resolution requirements. Figure 1 includes a comparison of several potentially observable quantities between the equilibrium Chapman-Jouguet state and a neighboring state on the weak detonation branch of the equilibrium Hugoniot curve. This comparison illustrates the futility of distinguishing equilibrium states near the minimum velocity Chapman-Jouguet solution on the basis of measured detonation velocity or post-detonation temperature, particularly in the face of the finite perturbation in velocity that arises from wall proximity effects.

The most convincing observations of the conditions reached immediately behind the reaction zone have been quantitative measurements of density (averaged across the width of the tube) by means of x-ray absorption [20] and interferometry [17] and the deduction of the flow velocity from the angle of weak disturbances in the flow field detected in schlieren photographs [21,22]. The densities are found to be significantly (ca. 10%) lower than the computed Chapman-Jouguet density, and the flow velocities are also lower, i.e., the gas is receding from the detonation front at Mach numbers

of 1.1 or greater. Also, pressure measurements made at the tube walls [17,19] and chemical concentrations measured quantitatively by photometry of visible light emission [17] are in agreement with the conclusion that the condition of the detonation products lies in the vicinity of the weak detonation branch of the equilibrium Hugoniot curve. The effects of the occurrence of such "weak" detonations upon the performance of explosives have not been explored by the investigators working with gases, but they may be important in condensed phase systems.

The weak detonation solution of the steady, one dimensional equations predicts a velocity slightly greater than the minimum, or Chapman-Jouguet velocity. This prediction is apparently confirmed [23,24] by precise experiments, although the small uncertainties in thermodynamic data and in assessing the finite diameter effects cloud the interpretation. In fact, the approximate attainment of the computed Chapman-Jouguet velocity in gaseous detonations can be used as evidence for the substantially complete release of the available chemical energy [25] and can even be used successfully to establish thermochemical parameters of major constituents [26].

NONLAMINAR FLOW EFFECTS

The most productive explanation of the failure of gaseous detonations to exhibit the predicted steady, one dimensional structure has been given by White [17] primarily on the basis of his own two dimensional interferometric observations of nonlaminar structure involving significant transverse motions at the wave front. Qualitatively, it can be appreciated that departure from one dimensional motion obscures the detonation front structure to observations which depend for their interpretation upon constancy of properties across a one dimensional wave, and negates the validity of computations which constrain the detonating system to pressure-volume states along a Rayleigh line or on partial reaction Hugoniot curves.

The consequences of the additional motions have been considered quantitatively in terms of an isotropic turbulence model. The resulting first order contributions to the momentum and energy conservation equations lead, with generalization of the minimum velocity Chapman-Jouguet condition, to solutions with detonation velocities somewhat greater than the one dimensional value. Experimentally, the weak detonation branch of the one dimensional Hugoniot is apparently approached by unsupported detonations whenever the nonlaminar behavior in the detonation front becomes dissipated before appreciable rarefaction of the products has occurred behind the wave. The "strong" branch solutions are of course also accessible for wave velocities greater than the minimum, and densitometric observations indicate that adequately supported or overtly overdriven [17,20] waves approach these solutions when the nonlaminar motions subside.

TRANSVERSE STRUCTURE

In the preceding sections we examined the evidence related to the axial structure of detonation in gases, and saw that nonaxial motions play a significant role. We now turn to investigations of the irregularities in the detonation front, that is the transverse structure. Such investigations are, in a sense, an outgrowth of the phenomenological studies of spinning detonation published thirty to forty years ago. Finely resolved observations of detonation fronts using streak [27] or even still [28] photography of the luminous reaction zone, or streak schlieren photography of transverse density gradients [29-31] have revealed the presence of high frequency disturbances. The spatial distribution of these disturbances, and the nature of their motions, including their

mutual refraction, have been studied very profitably by means of the inscriptions made in a soot coating on the interior surface of the detonation vessel [32,33]. The shape of the detonation front is indicated by soot inscription records of the interaction of detonations with plane waves, and also by those instantaneous schlieren [34] or interferometric photographs [17] which view an area of the wave simultaneously. The shock front is found to consist of convex segments whose boundaries are not stationary but move across the detonation front as it advances. At the boundaries of these segments, the shock front is broken discontinuously, and additional gasdynamic processes extend from the intersection loci into the reaction zone region behind the primary shock front.

The structure of these shock wave interactions which occur in detonations has been adduced largely by analogy with the familiar behavior of shock waves reflected from an oblique obstacle. This structure is the Mach stem, an unsymmetrical configuration in which the stronger of the two shock wave segments advances across the weaker one, and a third shock wave emanates from the intersection locus and compresses and deflects the flow behind the weaker initial shock to match the pressure and flow direction behind the stronger one, thereby establishing the contact discontinuity between the fluids passing on either side of the intersection locus.

The identification of this two dimensional, triple shock wave interaction at the intersections of the convex segments of gaseous detonation fronts has been made most positively by means of a clever variation of streak schlieren photography in which combinations of slit angles and sweep speeds and directions are arranged to compensate the major wave motions [35].

The Mach stem has recently been subjected to direct interferometric examination in isolated form in a detonable gas by a technique introduced by D. R. White [36]. This technique generates a temporarily laminar detonation wave by the passage of an ordinary, nonlaminar detonation through a narrow rectangular slot at the throat of a nozzle formed by placing entrance and exit ramps in a square channel. The detonation emerging from this nozzle is overdriven and attenuating as it expands cylindrically, and transverse structure is not detectable interferometrically. When the nozzle is terminated abruptly at the end of the exit ramp, the wave is reflected obliquely from the main channel wall, and a Mach stem is formed which can be observed on its initial traversal across the channel. The structure so generated is

shown in the interferogram in Fig. 2, which shows the shock fronts and also the zones of exothermic reaction.

Strehlow [37] has applied the Rankine-Hugoniot equations to the oblique plane shock fronts in this interaction and demonstrated their consistency with the flow matching conditions across the initial portion of the contact discontinuity which separates unreacted gas behind the Mach stem from the unreacted gas behind the reflected shock. The general behavior of Mach stems in reactive media, for such cases as that in which there is no macroscopic region of unreacted material surrounding the three shock intersection locus, has not yet been examined at all thoroughly, either experimentally or theoretically.

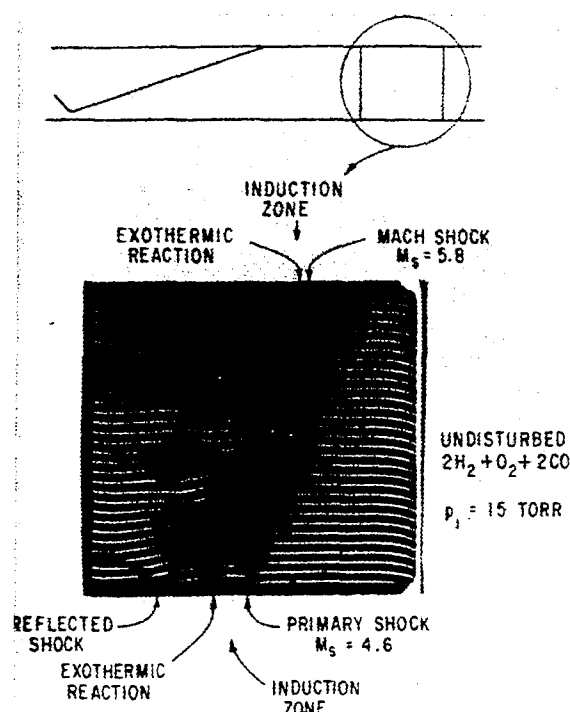


Fig. 2 - Instantaneous interferogram of reactive Mach stem generated in otherwise laminar wave in detonable gas by nozzle technique. (Fig. 1 of Ref. 36.)

PLANE WAVE INITIATION

We have seen that by suitably constraining the system one can realize detonations which are temporarily free of detectable transverse perturbations. Another instance of such a constrained system is the initiation of detonation by a plane shock front transmitted from an inert

material. In gases, this is done by reflection of a plane, unreactive shock wave at the flat closed end of a shock tube. Strehlow and co-workers [38] have studied the nonsteady wave motions of such detonation initiation by streak schlieren and combined streak schlieren interferometric techniques. An example of the record produced by the combined technique is shown in the top part of Fig. 3. Just as in the case of plane shock initiation of liquid nitromethane [39], the shocked explosive reacts first at the piston face, after some delay, and this explosive reaction generates compression waves which coalesce to a shock closely followed by reaction. This wave overtakes the original, externally supplied shock, momentarily overdriving it, establishing a contact surface, and ultimately producing a conventional detonation. Depending upon conditions, the nonsteady wave which overtakes the external shock may have the Chapman-Jouguet velocity for the gas mixture heated and compressed by the external shock, or it may be an accelerating, nonsteady wave whose velocity is only about half of the Chapman-Jouguet velocity. The behavior of this nonsteady wave development can be accounted for quite well by one dimensional, time dependent computations using the method of characteristics [40], and the optical observations failed to indicate any departure from plane, one dimensional behavior in this initiation process.

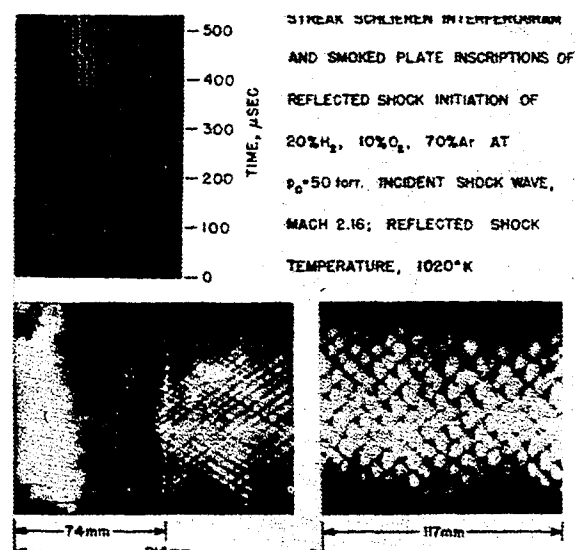


Fig. 3 - Streak schlieren interferogram and smoked plate inscription record of reflected shock initiation event in rectangular shock tube. (Similar experiment to that represented in Fig. 1 of Ref. 55 or Figs. 1 and 2 of Ref. 41.)

Nevertheless, when smoke inscription plates were made in the same apparatus, finely structured patterns qualitatively like those seen in gaseous detonations after long, unsupported runs were observed [41]. This structure was not evident right at the end wall of the tube, but developed some distance away. In the case shown in Fig. 3, the structure developed between the end wall and the position at which the nonsteady detonation overtook the external shock, and a boundary with a discontinuous change in the slope of the diagonal structure pattern occurred where the two waves met. The size of the structure pattern then changed gradually as the overdriven detonation attenuated to a steady, unsupported velocity.

STRUCTURE IN OTHER DETONATION SITUATIONS

Overdriven detonations are conveniently achieved in gases by shock tube methods. Such detonations have been found to exhibit final state properties described satisfactorily by the strong detonation branch solution of the Rankine-Hugoniot equations. Examination of overdriven detonations for transverse structure [17,33] has shown that the structure is present in a form qualitatively similar to that found in supported, lower (Chapman-Jouguet) velocity waves. The scale of the structure is found to be progressively finer in more and more overdriven waves, and the finer structure is correspondingly more difficult to resolve, but there is no evidence of a limit for the occurrence of transverse structure, at least within the regime of shock strengths in which the reaction remains exothermic.

Gaseous detonations have also been studied in spherical and cylindrical geometries, by soot inscription [42,43] and visible light emission [44] techniques, and regularly space transverse structure has been found.

Another observation which is relevant to the generality of transverse structure in detonation is a hitherto unpublished one made in our laboratory on the occurrence of transverse structure in dilute gas mixtures which are outside the limits of detonability. When a 1% acetylene, 1.5% oxygen, 97.5% argon mixture at about 50 torr initial pressure in a 10 cm diameter shock tube was shocked weakly at a velocity near its computed Chapman-Jouguet velocity (ca 0.9 mm/ μ sec) no evidence of transverse structure was obtained. But at a threshold velocity of about 1.2 mm/ μ sec, single spin was evident in photographic and smoked foil records, and at higher velocities, up to ca 1.5 mm/ μ sec, progressively higher modes of transverse structure were observed by the smoked foil technique.

Thus spin and its higher mode transverse wave analogs are seen to be widely occurring finite amplitude manifestations of structural instability of plane, exothermically reacting shock waves in gases, and not to be characteristic of proximity to a Chapman-Jouguet, sonic flow condition or of the waves being externally supported or unsupported.

THEORETICAL EXAMINATION OF STABILITY

The observation of the widespread occurrence of transverse perturbations in the detonation front has led to theoretical examination of the stability, or the lack of it, of the classical plane detonation wave. From Rayleigh's writings about the enhancement of sound by heat addition [45] we have the very simple principle that sonic disturbances in an exothermically reacting medium are amplified when the reaction rate is enhanced, relative to the rate in the undisturbed medium, in phase with the pressure crests and retarded, relatively, in phase with the troughs.

In discussing problems in the development of the steady, one dimensional wave theory twenty-five years ago, Zeldovich [1] noted, "On the other hand, when small disturbances are imposed the velocity of the chemical reaction is likewise subject to variation. It is, at present, impossible to predict the result of the computation of the stability with respect to small disturbances, which may depend upon the special properties of the chemical kinetics (autocatalysis, heat of activation)."

Shchelkin [46] has proposed a basis for assessing the stability of the plane, one dimensional detonation wave model which involves the difference in properties between the shock front and the equilibrium condition and the activation energy for the reaction. His semiquantitative argument has not actually been usable as a neutral stability criterion, but rather has served only to indicate the expectation of instability in substantially all detonating gas systems of interest. Shchelkin and co-workers [47] have also proposed a quantitative relationship between the frequency of finite amplitude transverse perturbations in detonations and the induction period for the exothermic reaction, again emphasizing the dependence of these quantities on the temperature through the activation energy.

The detailed consideration of the stability of the plane, steady detonation front to sonic perturbations has been carried out by Erpenbeck [48]. The formalism which he developed

from a complicated linearization of the full flow equations permits one to consider the exponential rate of growth of harmonic displacements of the shock front position of any particular transverse wavelength. Stability is recognized by the absence of positive growth rates for any transverse wavelength. Thus the complete question of stability for any particular chemical reaction system and shock strength requires examination of the entire spectrum from zero to infinite transverse wavelength. The necessary computation for each point is quite formidable and requires high speed computing machinery even for an ideal gas chemical system described by many simplifying assumptions.

Nevertheless, stability of overdriven detonations in such a system has been examined [49,50] for a range of interesting values of the exothermicity and the activation energy. Shock waves without exothermic reaction are found to be stable [51]. With an exothermic reaction present, analysis for wavelengths greater than a few tenths of the unperturbed reaction zone half-thickness indicates that waves approaching the Chapman-Jouguet velocity are unstable with respect to all wavelengths when the exothermicity and activation energy are sizable. For sufficiently overdriven waves, the very long wavelengths and the very short ones do not grow, but there appears to remain a range of wavelengths near one reaction zone half-length to which the detonation is unstable for arbitrarily large overdrive. With lower activation energy, and thus reduced dependence of the chemical energy release rate upon the state of the gas, the Chapman-Jouguet wave may be stable to very long or very short wavelengths, but the wavelengths in a broad band near the reaction zone half-thickness remain unstable. Reducing the exothermicity to very low levels, which are somewhat dependent upon the activation energy but are not large even for zero activation energy [50], does cause disappearance of the instability for wavelengths near the reaction zone half-length. On the other hand, even arbitrarily small amounts of exothermicity are not free of instability at some range of shock strength, provided the activation energy exceeds some modest minimum.

This last finding has come from a consideration of the limiting form of the stability criterion for very short wavelengths [52]. This asymptotic stability analysis yields a form which is computationally much more tractable to apply to a specific chemical system than the general finite wavelength criterion. Thus the determination of the existence of instability, in the short wavelength regime, is now practical for any detonation system for which the steady wave properties can be specified.

Of course, the above stability analysis only applies to infinitesimal perturbations, and does not determine the ultimate form or spectrum of finite amplitude disturbances. It does, however, cover the limiting case of infinitely long wavelength, i.e., the case of one dimensional unsteadiness in time [49]. This class of instabilities is subject to numerical examination by already developed methods for treating one dimensional time dependent flows. Two types of computational procedures have recently been applied to cases in which the detonation is predicted to be stable to infinitesimal one dimensional perturbations at one shock strength and unstable at another. One of these computational investigations has considered the detonating fluid as an inviscid, ideal gas, containing discontinuous shock fronts, by the method of characteristics [53]. The other has treated a viscous fluid with shocks of finite thickness by direct numerical integration of the Navier-Stokes equations in Lagrangian finite difference form [54]. The results of computations by these two methods for an ideal gas system with substantial exothermicity and activation energy are in agreement with each other and with the infinitesimal amplitude stability predictions. For a strong enough piston supported shock wave, the wave structure approached the steady structure of classical theory after some numerically unavoidable initial transients. However, for a less strongly driven wave, one for which longitudinal instability is predicted by the formal analysis, quasi-periodic fluctuations in the properties of the detonation front developed after a short time. These occurred, for the particular case tested, at intervals of about nine times the unperturbed half-reaction time, and the amplitude of the fluctuations, as measured by the shock front pressure, was a substantial fraction of the steady wave amplitude.

It has also been possible to make some progress in considering the growth of transverse instabilities in idealized computational systems. Strehlow and Fernandes [55] have explored the propagation of transverse acoustic waves in exothermically reactive shocks in the short wavelength limit by means of the equations for ray propagation in a variable flow velocity, variable sound velocity medium. They have focused attention on the position in the one dimensional reaction zone at which the propagation ray is parallel to the shock front, such that the disturbance will propagate large lateral distances, and have considered the amplification of such a disturbance. In subsequent work, Barthel and Strehlow [56] have examined the kinematics of disturbances in the region between the shock front and the lateral propagation position in the reaction zone. They find that, for an idealized but reasonable model,

sound waves are trapped in this region and become convoluted, in time contacting the shock front repeatedly with regular periodicity. The qualitative correspondence of this periodicity with that exhibited by the finite amplitude, Mach stem disturbances observed in real gaseous detonations is encouraging in indicating the utility of further consideration of this aspect of the general problem of the manifestations of instability.

MARGINALLY PROPAGATING DETONATIONS

As we have seen, the structure of detonation waves has two aspects, one being the sequence of physico-chemical states experienced by the detonating medium and the other the geometric configuration of boundaries or transition zones between these states. Likewise, stability has two somewhat different aspects, one having to do with the failure of detonations to exhibit steady, laminar flow and the other with the ability or inability of detonation to propagate indefinitely long times or distances under particular experimental circumstances. It is in this area of limits of propagation that perhaps the least quantitative progress has been achieved in recent gaseous detonation research. Zeldovich approached propagation limits theoretically by considering heat and momentum losses to confining walls within the steady, laminar flow model [1], and has since concluded [5] that this is not an adequate approach to the problem.

Progress has been made, however, in characterizing the behavior of marginally propagating detonations. This progress has served to make evident the considerable complexity of the question of propagation failure. There does not appear to be any clearly definable boundary between stable and unstable detonation propagation, but rather there are ranges of conditions in which transitional behavior can be recognized.

The best recognized characteristic feature of marginally propagating detonation waves in gases is the occurrence of spin, which is now identified simply as the coarsest mode of transverse shock wave disturbance compatible with the geometry of the detonating system. In a round tube this is, to a good approximation, the fundamental circumferential mode of acoustic vibration of the column of burned gas [57,58]. The geometric structure of the front of spinning detonations has recently been elucidated [59,60], and the major features are indicated in Fig. 4.

Other studies [61,62] of marginally propagating detonation over quite long runs have revealed the occurrence of periodic large separations of the shock front and the chemical reaction zone, with accompanying changes in the shock front strength and velocity. This behavior has not been strictly analogous to the computationally investigated behavior of one dimensional, time dependent detonation flow because the observed "galloping" behavior in gases has invariably been accompanied by transverse perturbations as well. In fact, the

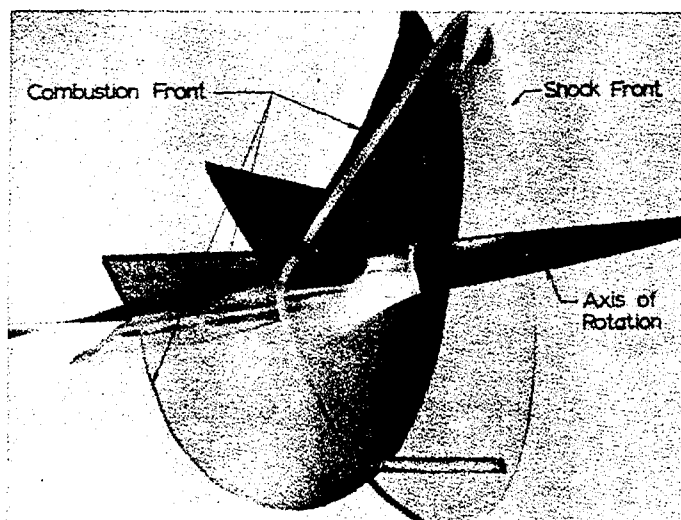


Fig. 4 - Annotated photograph of three dimensional, colored model of spinning detonation wave front

analogy between the behavior of such unsteadily propagating detonations in their re-initiation cycle and the much studied initial transition from deflagration to detonation in gases is striking [63].

CHEMICAL KINETICS IN DETONATION

The final area to be considered in this survey is the chemical kinetics of exothermic reactions under detonation wave conditions. As was indicated earlier, the detonable gases with which the most experience exists are mixtures of fuels, mostly hydrogenous, with oxygen. The outstanding characteristic of the kinetics of combustion of such mixtures is the acceleration of the reaction during its early stages by a branching chain mechanism. In such a process, the reaction rate is proportional to the amount of one of the reaction products that has accumulated. Mathematically, the reaction rate increases as $e^{\alpha t}$, where t is time and α is a positive proportionality coefficient which is a function of the temperature, density, and composition of the system. Thus a very minute initial rate of reaction may be increased by a very large factor, while α remains constant, before macroscopic reaction with appreciable temperature rise and consumption of reactants is evident. The finite period of time required for the appearance of macroscopic reaction, the so-called induction time, is a very well developed feature of the reaction zone structure of the familiar gas detonations.

Condensed explosives, on the other hand, are generally supposed, on the basis of low temperature thermal decomposition and thermal explosion limit experiments, to exhibit first order decomposition kinetics with a rate coefficient related to the temperature by an Arrhenius factor, $e^{-E_{act}/RT}$. Such a reaction accelerates during its course only as the temperature rises due to macroscopic reaction. While long induction periods do occur in low temperature experiments on a time scale determined by conductive heat losses, realistic activation energies are such that at the high temperatures encountered in the shock fronts of detonation, reaction is initially quite rapid and acceleration factors greater than about 10^2 are not possible between shock front and equilibrium conditions. Thus sharply terminated induction zones are not characteristic of thermally accelerating reaction under detonation conditions.

The distinction is drawn because much emphasis has been given by some authors [43] to the role of the induction period in determining the form and periodicity of the transverse

structure of gaseous detonations. It should not be overlooked, however, that Erpenbeck's [50] analysis for thermally accelerating reaction mechanisms has shown that for reasonable exothermicity, acceleration is not necessary for transverse instability. Moreover, the decomposition of ozone, which is known to occur by a thermally accelerated mechanism and not by a branching chain, also exhibits instabilities, both in unsupported [64] and overdriven detonations [65,66].

The finite amplitude form of the instabilities in the ozone decomposition detonation or other detonations without branching chain kinetics has not been well characterized, however, and this area of incomplete knowledge of gaseous detonations may harbor important clues to two questions. The first is the possibility that gaseous explosives without branching chain kinetics may exhibit recognizably different detailed forms of transverse instability and propagation limit behavior. The second, related question concerns the possibility that condensed explosives, if they do react by thermally accelerating mechanisms, might be more closely akin to gaseous detonation systems with thermal acceleration than to the branching chain systems.

ACKNOWLEDGMENTS

The author is grateful to Dr. D. R. White, Professor R. A. Strehlow, and Professor A. K. Oppenheim for having provided photographs used in Figs. 2, 3, and 4.

REFERENCES

1. Quotations from the paper of Ya. B. Zeldovich, *Zh. Eksperim. Teor. Fiz.* **10** 542 (1940), are taken from the English translation by S. Reiss published as Technical Memorandum 1261 by the National Advisory Committee for Aeronautics.
2. D. R. White, and others, Discussion on Detonations, *Symp. Combust. Ninth*, Ithaca, New York, 1962, 415 ff. (1963).
3. R. I. Soloukhin, *Usp. Fiz. Nauk* **80**, 525 (1963), English Translation: *Soviet Phys.-Usp.* **6**, 523 (1964).
4. A. K. Oppenheim, N. Manson, and H. Gg. Wagner, *Am. Inst. Aeron. Astronaut. J.* **1**, 2243 (1963).
5. Ya. B. Zeldovich and A. S. Kompaneets, *Theory of Detonation* (Academic Press, Inc., New York, 1960; original edition in Russian, Gostekhteorizdat, Moscow, 1955).

6. H. Gg. Wagner, in Fundamental Data Obtained from Shock-Tube Experiments, A. Ferri, Editor (Pergamon Press, New York, 1961), Chapter IX.
7. A. S. Sokolik, Self-Ignition, Flame, and Detonation in Gases, translated into English by N. Kaner (Israel Program for Scientific Translations, Ltd., Jerusalem, 1963). (Original Russian edition published by Izdatelstvo Akad. Nauk SSSR, Moscow, 1960), Chapter VI.
8. B. Lewis and G. vonElbe, Combustion, Flames, and Explosions in Gases, 2nd Edition (Academic Press, Inc., New York, 1961), Chapter VIII.
9. W. W. Wood and Z. W. Salsburg, Phys. Fluids **3**, 549 (1960).
10. A. K. Oppenheim, A. J. Laderman, and P. A. Urtiew, Combust. Flame **6**, 193 (1962).
11. J. A. Fay, Phys. Fluids **2**, 283 (1959).
12. F. J. Martin, P. H. Kydd and W. G. Browne, Symp. Combust. Eighth, Pasadena, Calif., 1960, 633 (1962).
13. R. E. Duff and S. H. Bauer, J. Chem. Phys. **36**, 1754 (1962).
14. J. P. Chesick and G. B. Kistiakowsky, J. Chem. Phys. **28**, 956 (1958); G. B. Kistiakowsky and P. H. Kydd, ibid. **25**, 824 (1956).
15. G. B. Kistiakowsky and R. K. Lyon, J. Chem. Phys. **35**, 995 (1961).
16. Th. Just and H. Gg. Wagner, Z. Physik. Chem. (Frankfurt) **19**, 250 (1959). W. Jost, Th. Just, and H. Gg. Wagner, Symp. Combust. Eighth, Pasadena, Calif., 1960, 582 (1962).
17. D. R. White, Phys. Fluids **4**, 465 (1961).
18. Th. Just and H. Gg. Wagner, Z. Elektrochem. **64**, 501 (1960); Th. Just and H. Gg. Wagner, Z. Physik. Chem. (Frankfurt) **13**, 241 (1957).
19. D. H. Edwards, G. T. Williams, and B. Price, Les Ondes de Detonation (CNRS, Paris, 1962), p. 249; D. H. Edwards, G. T. Williams, and J. C. Breeze, J. Fluid Mech. **6**, 497 (1959).
20. R. E. Duff, H. T. Knight, and J. P. Rink, Phys. Fluids **1**, 393 (1958).
21. J. A. Fay and G. Opel, J. Chem. Phys. **29**, 955 (1958).
22. D. H. Edwards, T. G. Jones, and B. Price, J. Fluid Mech. **17**, 21 (1963).
23. C. Brochet, N. Manson, M. Rouze, and W. Struck, Compt. Rend. **247**, 2412 (1963).
24. H. M. Peek and R. G. Thrap, J. Chem. Phys. **26**, 740 (1957).
25. R. W. Getzinger, J. R. Bowen, A. K. Oppenheim, and M. Boudart, Symp. Combust. Tenth, Cambridge, England, 1964, 779 (1965).
26. G. B. Kistiakowsky, H. T. Knight, and M. E. Malin, J. Chem. Phys. **20**, 876 (1952).
27. Yu. N. Denisov and Ya. K. Troshin, Zh. Tekn. Fiz. **30**, 450 (1960). English Translation: Soviet Phys.-Tech. Phys. **5**, 419 (1960).
28. B. V. Voitsekhovskii, B. E. Kotov, V. V. Mitrofanov, and M. E. Topchian, Izv. Akad. Nauk SSSR, Sibirsk. Otd. **1958**, No. 9, 44 (English Translation: J.P.R.S. 7465, OTS6121118, Office of Technical Services, Washington (1961)).
29. B. Greifer, J. C. Cooper, F. C. Gibson, and C. M. Mason, J. Appl. Phys. **28**, 289 (1957).
30. D. H. Edwards and T. G. Jones, Brit. J. Appl. Phys. **11**, 190 (1960).
31. N. Manson, C. Brochet, J. Brossard, and Y. Pujol, Symp. Combust. Ninth, Ithaca, New York, 1962, 461 (1963).
32. Yu. N. Denisov and Ya. K. Troshin, Dokl. Akad. Nauk SSSR **125**, 110 (1959). (English Translation: Soviet Phys.-Dokl., Phys. Chem. Sect. **125**, 217 (1960).)
33. R. E. Duff, Phys. Fluids **4**, 1427 (1961).
34. J. A. Fay, Symp. Combust. Eighth, Pasadena, Calif., 1960, 30 (1962).
35. B. V. Voitsekhovskii, V. V. Mitrofanov, and M. E. Topchian, Structure of the Front of Detonations in Gases (Izd-vo Sibirsk. Otdel. Akad. Nauk SSSR, Novosibirsk, 1963), pp. 108-111.
36. D. R. White and K. H. Cary, Phys. Fluids **6**, 749 (1963); D. R. White, ibid. **6**, 1011 (1963).
37. R. A. Strehlow, Phys. Fluids **7**, 908 (1964).

38. R. A. Strehlow and A. Cohen, Phys. Fluids **5**, 97 (1962); R. A. Strehlow and H. B. Dyner, Am. Inst. Aeron. Astronaut. J. **1**, 591 (1963).
39. A. W. Campbell, W. C. Davis, and J. R. Travis, Phys. Fluids **4**, 498 (1961).
40. R. A. Strehlow and H. B. Dyner, loc. cit.; R. B. Gilbert, Master of Science thesis, Department of Aeronautical and Astronautical Engineering, Univ. of Illinois, 1964.
41. R. A. Strehlow, Am. Inst. Aeron. Astronaut. J. **2**, 783 (1964).
42. R. E. Duff and M. Finger, Phys. Fluids **8**, 764 (1965).
43. K. I. Shchelkin and Ya. K. Troshin, Gasdynamics of Combustion, Chapter I, Sect. 5. (Izdatel'stvo Akad. Nauk SSSR, Moscow, 1963.) (English Translation: NASA TT F-231, National Aeronautics and Space Administration, Washington, D.C., 1964.)
44. R. I. Soloukhin, Izv. Akad. Nauk. SSSR, Otd. Tekn. Nauk, Mekhan. i Mashinostr. 1959, No. 6, 145; R. I. Soloukhin, Symp. Combust. Tenth, Cambridge, England, 1964, 814 (1965).
45. Lord Rayleigh, Theory of Sound (Macmillan, London, 1894), Vol. II, sect. 322.
46. K. I. Shchelkin, Zh. Eksperim. Teor. Fiz. **36**, 600 (1959). (Soviet Phys. - JETP **9**, 416 (1959).)
47. B. P. Volin, Ya. K. Troshin, G. I. Filatov, and K. I. Shchelkin, Zh. Prikl. Mekhan. Tekn. Fiz., 1960, No. 2, 78.
48. J. J. Erpenbeck, Phys. Fluids **5**, 604 (1962).
49. J. J. Erpenbeck, Phys. Fluids **7**, 684 (1964).
50. J. J. Erpenbeck, Phys. Fluids **8**, 1192 (1965).
51. J. J. Erpenbeck, Phys. Fluids **5**, 1181 (1962).
52. J. J. Erpenbeck, Los Alamos Scientific Laboratory Report LA-3306 (1965), and manuscript submitted to Phys. Fluids.
53. W. Fickett and W. W. Wood, "Flow Calculations for Pulsating One-Dimensional Detonations." Manuscript submitted to Physics of Fluids, 1965.
54. C. L. Mader, Los Alamos Scientific Laboratory Report LA-3297 (1965).
55. R. A. Strehlow and F. D. Fernandes, Combust. Flame **9**, 109 (1965).
56. R. A. Strehlow, University of Illinois, Private Communication, April, 1965, and 1965 Progress Reports for Contract No. DA-11-022-AMC-329(R).
57. N. Manson, Compt. Rend. **222**, 46 (1946); N. Manson, Propagation des Detonations et des Deflagrations dans les Melanges Gazeux (L'office National d'Etudes et de Recherches Aeronautiques et L'Institute Francais des Petroles, Paris, 1947).
58. J. A. Fay, J. Chem. Phys. **20**, 942 (1952).
59. G. L. Schott, Phys. Fluids **8**, 850 (1965).
60. B. V. Voitsekhovskii, V. V. Mitrofanov, and M. E. Topchian, Zh. Prikl. Mekhan. Tekn. Fiz., 1962, No. 3, 27; M. E. Topchian, ibid., 1962, No. 4, 94; V. V. Mitrofanov, V. A. Subbotin, and M. E. Topchian, ibid., 1963, No. 3, 45.
61. R. E. Duff, H. T. Knight, and H. R. Wright, J. Chem. Phys. **22**, 1618 (1954).
62. C. Brochet and N. Manson, Les Ondes de Detonation (CNRS, Paris, 1962), p. 209.
63. A. K. Oppenheim, Symp. Combust. Ninth, Ithaca, New York, 1962, 469 (1963).
64. S. A. Harper and W. E. Gordon, in Ozone Chemistry and Technology (American Chemical Society, Washington, D.C., 1959), p. 28.
65. W. M. Jones and N. Davidson, J. Am. Chem. Soc. **84**, 2868 (1962).
66. J. H. Kiefer and R. W. Lutz, J. Chem. Phys. **42**, 1709 (1965).

THEORETICAL CONSIDERATIONS ON THE PROPAGATION OF SHOCK AND DETONATION WAVES

R. Chéret
*Commissariat à l'Energie Atomique
France*

ABSTRACT

The propagation of the boundary surface Σ of a three-dimensional isentropic unsteady fluid flow is examined: when Σ is assumed to be normal to the stream-lines at every moment, two remarkable relations are available between thermodynamic, cinematic and geometric parameters on Σ . Then the consequences of these relations are investigated when Σ is the hot boundary of (i) a shock wave, (ii) a one-dimensional detonation wave, and (iii) a cylindrically symmetric steady detonation wave moving through a still uniform medium. Since it is almost impossible to summarize our theoretical discussion, we shall only quote the most striking results as far as detonation phenomena are concerned: a way of estimating the Von Neumann spike density is set up -- it is shown that the Rankine-Hugoniot equations and the C-J condition are not appropriate to the description of a "steady" diverging cylindrical or spherical detonation wave -- it is evidenced that the hot boundary of a steady cylindrically symmetric curved detonation wave cannot be considered as a "Chapman-Jouguet surface."

1. RESULTS AS TO THE PROPAGATION OF THE BOUNDARY SURFACE OF A THREE-DIMENSIONAL ISENTROPIC UNSTEADY FLUID FLOW

1.1

Let us consider a medium moving in a frame $oxyz$. The position of a small part M of this medium is described, at time t , by its three coordinates $x(M, t)$, $y(M, t)$, $z(M, t)$. The components on $oxyz$ of the velocity vector $V(M, t)$ with respect to the frame $oxyz$ are: $u(M, t)$, $v(M, t)$, $w(M, t)$.

Let us consider a surface Σ , the equation of which is at time t : $t = \tau(x, y, z)$. τ is a given function, the three partial derivatives of which are supposed to be neither simultaneously zero nor infinity. This assumption only means that Σ is rather smooth, and involves that

$$D = (\tau_x'^2 + \tau_y'^2 + \tau_z'^2)^{-1/2}$$

is finite and strictly positive.

On the normal to Σ , let us consider the unit vector N directed towards the increasing times

t . The components of N on $oxyz$ are:

$$\lambda = \frac{\tau_x'}{D} \quad \mu = \frac{\tau_y'}{D} \quad \nu = \frac{\tau_z'}{D} \quad (1.1)$$

The normal velocity of Σ , along N , which is defined by

$$\lim_{dn \rightarrow 0} \frac{dn}{\tau(x + \lambda dn, y + \mu dn, z + \nu dn) - \tau(x, y, z)} \quad (1.2)$$

is easily seen to be equal to D .

Let the coordinates of M be ξ, η, ζ when it crosses Σ , i.e., at time $\tau(\xi, \eta, \zeta)$. ξ, η, ζ make up a system of Lagrange coordinates (although different from the usual ones). Let θ be a new variable, independent of ξ, η, ζ . The position (x, y, z) of $M(\xi, \eta, \zeta)$ at time $t = \tau(\xi, \eta, \zeta) + \theta$ is specified by the three functions:

$$\begin{aligned} x &= X(\xi, \eta, \zeta, \theta) \\ y &= Y(\xi, \eta, \zeta, \theta) \\ z &= Z(\xi, \eta, \zeta, \theta). \end{aligned} \quad (1.3)$$

Otherwise speaking, these functions give the position of element $M(\xi, \eta, \zeta)$ when time interval

θ has elapsed since the instant $\tau(\xi, \eta, \zeta)$ when it crossed Σ . We know nothing about them, except that

$$\begin{aligned} X(\xi, \eta, \zeta, 0) &= \xi \\ Y(\xi, \eta, \zeta, 0) &= \eta \\ Z(\xi, \eta, \zeta, 0) &= \zeta \end{aligned} \quad (1.4)$$

and that

$$\left(\frac{\partial X}{\partial \xi} \right)_{\theta=0} = 1, \quad \left(\frac{\partial Y}{\partial \eta} \right)_{\theta=0} = 1, \quad \left(\frac{\partial Z}{\partial \zeta} \right)_{\theta=0} = 1. \quad (1.5)$$

Besides, one may notice that

$$\frac{\partial}{\partial \theta} t(M, \theta) = 1 \quad (1.6)$$

and therefore,

$$\begin{aligned} \frac{\partial}{\partial \theta} X(M, \theta) &= u(M, \theta) \\ \frac{\partial}{\partial \theta} Y(M, \theta) &= v(M, \theta) \\ \frac{\partial}{\partial \theta} Z(M, \theta) &= w(M, \theta) \end{aligned} \quad (1.7)$$

1.2

Let us assume now that the movement of M can be considered as a nonviscous fluid flow when $\theta \geq 0$. The Eulerian equations of continuity and motion are:

$$\left. \begin{aligned} \frac{\partial \rho}{\partial t} + \operatorname{div}(\rho \mathbf{V}) &= 0 \\ \frac{d\mathbf{V}}{dt} + \frac{1}{\rho} \operatorname{grad} p &= 0 \end{aligned} \right\} \quad (1.8)$$

where ρ and p are respectively the overall density and the pressure. In Lagrangian coordinates $(\xi, \eta, \zeta, \theta)$, (1.8) becomes a system of four linear equations in the partial derivatives of p, ρ, u, v, w with respect to the variables ξ, η, ζ, θ . We shall only consider the four peculiar relations which link these twenty partial derivatives when $\theta = 0$. In order to simplify the writing, we shall use the following notations:

$$\left. \begin{aligned} p(M, 0) &= \hat{p} & p'_{\theta}(M, 0) &= P \\ \rho(M, 0) &= \hat{\rho} & \rho'_{\theta}(M, 0) &= R \\ u(M, 0) &= \hat{u} & u'_{\theta}(M, 0) &= U \\ v(M, 0) &= \hat{v} & v'_{\theta}(M, 0) &= V \\ w(M, 0) &= \hat{w} & w'_{\theta}(M, 0) &= W \\ \mathbf{V}(M, 0) &= \hat{\mathbf{V}} & \mathbf{N}(M) &= \hat{\mathbf{N}} \end{aligned} \right\} \quad (1.9)$$

One might insist upon the fact that $\hat{p}, \hat{\rho}, \hat{u}, \hat{v}, \hat{w}, V, P, R, U, V, W$ are functions of $M(\xi, \eta, \zeta)$.

Relations (1.3) to (1.7) enable us to infer Eqs. (1.10) from system (1.8):

$$\left. \begin{aligned} \frac{1}{\hat{\rho}} \left(1 - \frac{\hat{V}}{D} \right) R - \frac{\lambda}{D} U - \frac{\mu}{D} V - \frac{\nu}{D} W + A &= 0 \\ - \frac{\lambda}{D} P + \hat{\rho} \left(1 - \frac{\hat{V}}{D} \right) U + B_1 &= 0 \\ - \frac{\mu}{D} P + \hat{\rho} \left(1 - \frac{\hat{V}}{D} \right) V + B_2 &= 0 \\ - \frac{\nu}{D} P + \hat{\rho} \left(1 - \frac{\hat{V}}{D} \right) W + B_3 &= 0 \end{aligned} \right\} \quad (1.10)$$

where A, B_1, B_2, B_3 are quantities linear as to the partial derivatives of $\hat{p}, \hat{\rho}, \hat{u}, \hat{v}, \hat{w}$ with respect to ξ, η, ζ .

1.3

Let us assume now that the movement of M is isentropic when $\theta \geq 0$. Then we may write:

$$\frac{\partial \rho}{\partial \theta}(M, \theta) = \frac{1}{a^2} \frac{\partial p}{\partial \theta}(M, \theta) \quad (1.11)$$

where $a(M, \theta)$ is the equilibrium or a frozen sound speed according as the medium is assumed to be in the equilibrium or a frozen chemical state when $\theta \geq 0$. When $\theta = 0$, (1.11) yields:

$$R = \frac{1}{\hat{a}^2} P. \quad (1.12)$$

By use of (1.12), Eqs. (1.10) become a system of four equations linear with respect to P, U, V, W .

$$\left. \begin{aligned} \frac{1}{\hat{\rho} \hat{a}^2} \left(1 - \frac{\hat{V}}{D} \right) P - \frac{\lambda}{D} U - \frac{\mu}{D} V - \frac{\nu}{D} W + A &= 0 \\ - \frac{\lambda}{D} P + \hat{\rho} \left(1 - \frac{\hat{V}}{D} \right) U + B_1 &= 0 \\ - \frac{\mu}{D} P + \hat{\rho} \left(1 - \frac{\hat{V}}{D} \right) V + B_2 &= 0 \\ - \frac{\nu}{D} P + \hat{\rho} \left(1 - \frac{\hat{V}}{D} \right) W + B_3 &= 0 \end{aligned} \right\} \quad (1.13)$$

The determinant Δ of (1.13) is easily found to be given by

$$\Delta = \frac{\hat{\rho}^2}{D^2} \left(1 - \frac{\hat{V}}{D} \right)^2 \left[\left(\frac{D - \hat{V}}{\hat{a}} \right)^2 - 1 \right]. \quad (1.14)$$

The presence of factor $(D - \hat{V})^2 - \hat{a}^2$ is consistent with the well-known solution of Cauchy's

problem for a n -dimensional isentropic fluid flow [1].

Cramer's method, used in (1.13) for variable P , leads us on the peculiar equation:

$$\Delta P = -\frac{\hat{p}^2}{D} \left(1 - \frac{\hat{V}}{D}\right)^2 \left[\lambda B_1 + \mu B_2 + \nu B_3 + A \hat{p}(D - \hat{V}) \right]. \quad (1.15)$$

1.4

The complexity of quantities A, B_1, B_2, B_3 prevents us from getting any interesting result when the surface Σ behaves arbitrarily with respect to the flow. However, we are led to strikingly simple conclusions when are set up the two following assumptions:

(i) Σ is not a weak tangential discontinuity and consequently

$$D - \hat{V} \neq 0. \quad (1.16)$$

(ii) The velocity vector \hat{V} is nonvanishing and parallel to N at every time at every point of Σ , i.e.,

$$\frac{\hat{u}}{\lambda} = \frac{\hat{v}}{\mu} = \frac{\hat{w}}{\nu} = \hat{V} \neq 0. \quad (1.17)$$

Then, one finds out that

$$\lambda B_1 + \mu B_2 + \nu B_3 = \frac{d\hat{p}}{dn} \quad (1.18)$$

where d/dn is the normal derivative in the point (ξ, η, ζ) of Σ . One also finds out that

$$\frac{A}{\hat{V}} = \frac{1}{\hat{V}} \frac{d\hat{V}}{dn} - \left(1 - \frac{\hat{V}}{D}\right) \frac{1}{r} \quad (1.19)$$

where $1/r$ is twice the mean curvature of Σ at point (ξ, η, ζ) . We should remember that, if $C_1(\xi, \eta, \zeta)$ and $C_2(\xi, \eta, \zeta)$ are the principal curvature centers at point $M(\xi, \eta, \zeta)$ of Σ , $1/r$ is the algebraic number defined by

$$\frac{1}{r} = \frac{1}{N \cdot MC_1} + \frac{1}{N \cdot MC_2}. \quad (1.20)$$

According to (1.16), (1.18) and (1.19) Eqs. (1.14) and (1.15) yield the remarkable following result:

$$\frac{1}{D} \frac{P}{\hat{p}} \left[1 - \left(\frac{D - \hat{V}}{\hat{a}}\right)^2\right] = \frac{1}{\hat{p}} \frac{d\hat{p}}{dn} + \frac{1}{\hat{V}} \frac{d\hat{V}}{dn} - \frac{D - \hat{V}}{D} \frac{1}{r} \quad (1.21)$$

where \hat{p} is given by

$$\hat{p} = \hat{p}(D - \hat{V}). \quad (1.22)$$

Let G be the component with respect to N of the acceleration vector of element $M(\xi, \eta, \zeta)$ at the time $\tau(\xi, \eta, \zeta)$ when he passes through Σ ; i.e.,

$$G = \lambda U + \mu V + \nu W. \quad (1.23)$$

Taking (1.18) and (1.21) into account, the linear combination by λ, μ, ν of the three last equations of (1.13) gives

$$\frac{1}{D} \frac{G}{\hat{V}} \left[1 - \left(\frac{D - \hat{V}}{\hat{a}}\right)^2\right] = \left(\frac{D - \hat{V}}{\hat{a}}\right)^2 \frac{1}{\hat{p}} \frac{d\hat{p}}{dn} + \frac{1}{\hat{V}} \frac{d\hat{V}}{dn} - \frac{D - \hat{V}}{D} \frac{1}{r}. \quad (1.24)$$

Thus, owing to assumptions (1.16) and (1.17) we succeeded in setting up two equations (1.21) and (1.24) which connect the values of pressure and medium velocity on $\Sigma(\hat{p}, \hat{V})$ and their normal derivatives with respect to $\Sigma(d\hat{p}/dn, d\hat{V}/dn)$, the movement of the medium immediately behind $\Sigma(P, G)$, and the movement of the surface (D) and its mean local curvature ($1/r$).

In the three following paragraphs, we discuss the consequences of Eqs. (1.21) and (1.24) when Σ is supposed to be the hot boundary of a shock wave or of peculiar detonation waves propagating through a still uniform medium the density and pressure of which are respectively ρ_0 and p_0 .

2. Σ IS THE HOT BOUNDARY OF A SHOCK WAVE

If one refers to the Hugoniot equation of motion

$$(\hat{p} - p_0) N = \hat{p}(D - \hat{V}) \hat{V} \quad (2.1)$$

one easily sees that the assumptions (1.16) and (1.17) are satisfied by the hot boundary of a shock wave. Taking into account the orientation of the normal to Σ which has been defined in Section 1.1, Hugoniot's theory leads also to the following inequalities:

$$\hat{V} > 0, \quad D - \hat{V} > 0, \quad \hat{p} = \hat{p} - p_0 > 0 \quad (2.2)$$

$$\frac{d\hat{p}}{dn} \times \frac{d\hat{V}}{dn} > 0 \quad \text{or} \quad \frac{d\hat{p}}{dn} = \frac{d\hat{V}}{dn} = 0 \quad (2.3)$$

$$1 - \left(\frac{D - \hat{V}}{\hat{a}}\right)^2 > 0. \quad (2.4)$$

From Eqs. (1.21) and (1.24) and in Eqs. (2.2) to (2.4), can be drawn Table 1 which sums up the signs of P and G when $1/r$ and $d\hat{p}/dn$ are taken to be independently positive, equal to zero or negative.

Table 1

$\frac{d\hat{p}}{dn} \backslash \frac{1}{r}$	+	0	-
+	$P > 0$ $G > 0$	$P < 0$	$G < 0$
0	$P > 0$	$P = 0$ $G = 0$	$G < 0$
-	$P > 0$	$G > 0$	$P > 0$ $G > 0$

Table 1 enables us to draw conclusions as for the local modalities of the propagation of shock waves. A strikingly clear view of these modalities is obtained through the consideration of uniform mean-curvature shock waves, i.e., plane, cylindrical or spherical.

1. A diverging ($1/r < 0$) cylindrical or spherical shock wave does not decrease ($d\hat{p}/dn \geq 0$) only if the medium undergoes compression ($P > 0$) and acceleration ($G > 0$) behind the shock wave.
2. A converging ($1/r > 0$) cylindrical or spherical shock wave does not increase ($d\hat{p}/dn \leq 0$) only if the medium undergoes rarefaction ($P < 0$) and deceleration ($G < 0$) behind the shock wave.
3. A plane shock wave ($1/r = 0$) is steady ($d\hat{p}/dn = 0$) only if the pressure and the velocity of the medium are stationary behind the shock wave ($P = G = 0$).
4. A plane shock wave increases ($d\hat{p}/dn > 0$) only if the medium undergoes compression ($P > 0$) and acceleration ($G > 0$) behind the shock wave.
5. A plane shock wave decreases ($d\hat{p}/dn < 0$) only if the medium undergoes rarefaction ($P < 0$) and deceleration ($G < 0$) behind the shock wave.

It is worth emphasizing that a converging cylindrical or spherical shock wave may increase whatever be the signs of P and G . The case $P = 0$, and consequently $G < 0$ as results from Eqs. (1.21) and (1.24), is yet of remarkable

interest for it corresponds with the propagation of the Von Neumann spike of a converging cylindrical or spherical detonation wave.*

The differential equation describing this propagation is easily deduced from (1.21):

$$\frac{1}{\hat{p} - p_0} \frac{d\hat{p}}{dR} + \frac{1}{\hat{V}} \frac{d\hat{V}}{dR} + \frac{D - \hat{V}}{D} \frac{\alpha}{R} = 0. \quad (2.5)$$

R is the arithmetic distance from the center (or the axis) to the wave; integer α equals 1 or 2 according to the wave being cylindrical or spherical. In order to fix up the ideas, one may reasonably assume that:

$$\frac{\rho_0}{\hat{\rho}} = \beta \quad (2.6)$$

$$\hat{p} - p_0 = (1 - \beta) \times \rho_0 \times D^2 \quad (2.7)$$

where β is constant with respect to R . Then (2.5) becomes:

$$3 \frac{dD}{D} + \alpha \beta \frac{dR}{R} = 0 \quad (2.8)$$

the solution of which is $R^{\alpha\beta} \cdot D^3 = \text{cte.}$

We shall now consider an arbitrary position of the wave with which corresponds a speed D_0 , and compute the time interval $t(\varphi)$ it takes the wave to go from position R_0 to position φR_0 ($0 \leq \varphi \leq 1$):

$$t(\varphi) = \frac{R_0}{D_0} \left(1 + \frac{\alpha\beta}{3}\right)^{-1} \left(1 - \varphi^{1+\frac{\alpha\beta}{3}}\right). \quad (2.9)$$

The quantity

$$1 - \frac{D_0}{R_0} t(0) = \left(1 + \frac{\alpha\beta}{3}\right)^{-1}$$

may be chosen as a measure of the effect of curvature of the wave. One notices that this effect is larger for a spherical wave ($\alpha = 2$) than for a cylindrical wave ($\alpha = 1$); this result was to be expected for. An experimental value of

$$1 - \frac{D_0}{R_0} t(0),$$

*Of course the flow behind the Von Neumann spike is not isentropic; but it is consistent with the Von Neumann-Döring-Zeldovich theory to assume that the entropy of element M is stationary when undergoing the Von Neumann spike; therefore Eq. (1.12) and its consequences remain valid.

obtained in a way similar (but more accurate) to that used in Ref. 2, would lead to a value of β .

3. Σ IS THE HOT BOUNDARY OF A ONE-DIMENSIONAL DETONATION WAVE

The hot boundary of a one-dimensional (i.e., plane, cylindrical or spherical) detonation wave obviously satisfy the assumptions (1.16) and (1.17). We are thus permitted to use Eqs. (1.21) and (1.24).

We shall not specify the conservation laws through the detonation wave. Our present purpose needs only the following assumptions which are reasonable as far as ordinary experiments are concerned:

$$\hat{V} > 0, \quad D - \hat{V} > 0 \quad \text{and consequently} \quad \hat{p} > 0 \quad (3.1)$$

$$\frac{d\hat{p}}{dn} \times \frac{d\hat{V}}{dn} > 0 \quad \text{or} \quad \frac{d\hat{p}}{dn} = \frac{d\hat{V}}{dn} = 0 \quad (3.2)$$

$$P < 0, \quad G < 0. \quad (3.3)$$

From Eqs. (1.21) and (1.24) and in Eqs. (3.1) to (3.3) can be drawn Table 2 which sums up the sign of $J = 1 - (D - \hat{V}/\hat{a})^2$ when $1/r$ and $d\hat{p}/dn$ are taken to be independently positive, equal to zero or negative.

Table 2

$d\hat{p}/dn$ \ $1/r$	+	0	-
+	$J > 0$		
0		$J = 0$	$J > 0$
-	$J < 0$		$J < 0$

Table 2 enables us to state the following theorem, which will be referred to as T.1 "For a one-dimensional steady detonation wave, Chapman-Jouguet condition and vanishing mean curvature of the hot boundary are equivalent properties." It is worth emphasizing that T.1 contains more than the ordinary so-called Chapman-Jouguet condition. It shows that the sonic character of the relative flow behind a steady one-dimensional detonation wave is an "accident" specific of the plane wave as the Riemann's formulae are specific of the isentropic plane flow. Theorem T.1 may even be enhanced with the following ones:

T.2 - A converging cylindrical or spherical detonation wave is steady only if it is subsonic with respect to the rear.

T.3 - A diverging cylindrical or spherical detonation wave is steady only if it is supersonic with respect to the rear.

The latter need a few comments, since Zeldovich [3] thinks of having established the C-J condition for a steady diverging spherical wave. One should therefore notice

a) that Zeldovich's argument is based on the property of the Rayleigh line which is not valid in the case of a curved wave;

b) that the C-J condition involves, according to (1.24), an infinite value of G , which is inadmissible for two reasons at least:

o at the rear of the wave, the flow was supposed to be isentropic, therefore the normal Eulerian velocity gradient ($\partial\hat{V}/\partial n$) is essentially finite, and the same conclusion is valid for G since

$$G = D \frac{d\hat{V}}{dn} - (D - \hat{V}) \frac{\partial\hat{V}}{\partial n} = - (D - \hat{V}) \frac{\partial\hat{V}}{\partial n};$$

o for sufficiently high values of r , the flow of the detonation products is not much different from the one behind a plane wave initiated at the surface of a rigid wall. Now, in the latter case, one obviously has

$$\lim_{r \rightarrow \infty} G = 0.$$

Equation (1.21) will also be useful for the interpretation of the steady-velocity diverging spherical wave* which has been experimentally evidenced [4,5]. One may reasonably assume that the characteristics $\hat{p}, \hat{V}, \hat{\rho}, \hat{a}$ of such a wave tend towards those of a steady plane wave when r goes to infinity. This assumption has three consequences:

1. The "steady" DSDW cannot be actually steady since, according to T.2, that would involve a constant (with respect to r) negative value of J .

2. The "steady" DSDW cannot satisfy the Rankine-Hugoniot equations since the representative point in the $(p, 1/\rho)$ plane would move along the (R-H) adiabat towards the C-J point

*Abbreviated: "steady" DSDW.

when $r \rightarrow \infty$ and would thus involve a varying velocity D , which is contradictory.

3. The "steady" DSDW cannot satisfy the C-J condition since, according to Eq. (1.21), that would involve $\hat{p}(r)$ and $\hat{v}(r)$ behaving like $\log r$ in the neighbourhood of $r \infty$, which is absurd.

4. Σ IS THE HOT BOUNDARY OF A CYLINDRICALLY SYMMETRIC STEADY DETONATION WAVE

Let us consider a cylindrically symmetric steady detonation wave, with ox as the axis of symmetry. Let A be the point of intersection between ox and the hot boundary. Assumptions (1.16) and (1.17) are obviously satisfied at point A where we are therefore permitted to use Eqs. (1.21) and (1.24).

The symmetry and steadiness of the wave clearly involve:

$$\lambda(A) = 1, \quad \mu(A) = \nu(A) = 0 \quad (4.1)$$

$$\frac{d\hat{p}}{d\xi}(A) = \frac{d\hat{v}}{d\xi}(A) = 0 \quad (4.2)$$

$$\frac{1}{r}(A) = \frac{2}{R(A)} \quad (4.3)$$

where $R(A)$ is the algebraic radius of curvature at point A of Σ . Then, at point A , (1.21) becomes

$$\frac{1}{D} \frac{P}{\hat{p}} J + \frac{D - \hat{v}}{D} \frac{2}{R} = 0. \quad (4.4)$$

If we take into account the inequalities (3.1) to (3.3) assumed in the previous paragraph, (4.4) enables us to state the following theorem, which will be referred to as T.4: "On the axis of a cylindrically symmetric steady detonation wave, C-J condition and vanishing curvature of the hot boundary are equivalent properties."

T. 4 is of particular interest since it extends T.1 to a detonation wave which is a good

description of the steady phenomenon which appears in the explosion of a cylindrical cartridge, initiated on its axis. T.4 also shows that the C-J condition is inconsistent with the meridian of the wave in a cylindrical cartridge being fitted by a circle or an ellipse. Otherwise speaking, T.4 shows that a curved hot boundary should never be referred to as a "Chapman-Jouguet surface."

5. CONCLUSION

It is well known that Rankine-Hugoniot equations and Chapman-Jouguet condition are rigorously true for a steady plane detonation wave. On the other hand they have never been seriously established in any other case. In fact our discussion showed that they would lead to absurdities when applied for instance to the "steady" diverging spherical detonation wave. Now the problem remains to find out what is to be substituted for them in the experimental cases which all more or less differ from the ideal steady plane detonation wave.

REFERENCES

1. R. Courant, "Partial Differential Equations," Interscience Publishers, 1962.
2. A. Cachin and J. Lutfalla, "Détermination Expérimentale des Diagrammes de Marche d'ondes de Detonation Cylindriques Convergentes," C.N.R.S., Paris, 1962.
3. I. B. Zeldovich and A. S. Kompaneets, "Theory of Detonation," Academic Press, New York and London, 1960.
4. N. Manson, "Formation et Célérité des Ondes Explosives Sphériques Dans les Mélanges Gazeux," Revue I.F.P. IX, No. 4, Avril 1954.
5. J. W. Plickebaum, W. A. Strauss, and R. Edse, "Propagation of Spherical Combustion Waves," Aeronautical Research Laboratories, Columbus University, Ohio, June 1963.

FAILURE OF THE CHAPMAN-JOUGUET THEORY FOR LIQUID AND SOLID EXPLOSIVES

W. C. Davis, B. G. Craig, and J. B. Ramsay
*Los Alamos Scientific Laboratory
Los Alamos, New Mexico*

ABSTRACT

The usual treatment of unsupported detonation, often called the Chapman-Jouguet theory, is based on four assumptions: (1) the detonation approaches a steady state, (2) the flow is laminar and one-dimensional, (3) the detonation products approach a state of chemical equilibrium some distance behind the detonation front, and (4) the detonation velocity is the minimum permitted by the conservation conditions. In a recent paper Wood and Fickett (Phys. Fluids 6, 648 (1963)) proposed experiments to test the validity of the Chapman-Jouguet "theory," not requiring knowledge or assumptions about the nature of the equation of state of the detonation products, by making variations of the initial state of the explosive. In this paper we report the results of experiments in which (1) the initial state was varied by using mixtures of nitromethane and another liquid made of equal molar parts of nitric acid, acetonitrile, and water, which has the same atomic composition as nitromethane, and (2) the initial state was varied by using TNT as liquid and as solid. These results show that the Chapman-Jouguet theory is violated. The calculated pressures are 15 to 20 percent below the measured pressures. Results of measurements using other explosives are also presented to support the conclusion that the theory fails. No explanation or alternative theory is offered.

Note: This paper has been published in Phys. Fluids 8, 2169 (1965).

COMMENTS

G. P. CACHIA, Atomic Weapons Research Establishment, England

If the theory does not hold for real explosives it must be that one or more of the basic assumptions is not correct. It is suggested that one possibility is that the flow never becomes steady, one dimensional, and laminar, and that rapid oscillations may occur and persist. This suggestion is not sound, since in an infinite diameter charge all relative motion between particles must eventually be damped out by viscous effects and temperature variations by conduction. Thus it is only necessary to take a large enough charge and let the detonation run long enough to fulfil this assumption.

I would suggest that the conclusion from the experiments is that the Chapman-Jouguet

theory does not hold for charges of the dimensions of those tested.

F. J. WARNER, Strathclyde University, Glasgow

It would seem that a proof (or otherwise) of the Chapman-Jouguet hypothesis should be attainable by consideration of a generalized form of the basic differential equations governing one dimensional explosions. A typical set in Lagrangian form [1] is

$$\left. \begin{aligned} \frac{\partial v}{\partial t} &= \frac{\partial u}{\partial m} \\ \frac{\partial u}{\partial t} &= -\frac{\partial p}{\partial m} \\ C_v \frac{\partial T}{\partial t} &= Q \frac{\partial f}{\partial t} - p \frac{\partial u}{\partial m} \end{aligned} \right\} \text{(conservation laws)}$$

$$Q \frac{\partial f}{\partial t} = F(t, p, t) \quad (\text{a law of burning})$$

$$p = p(f, v, t) \quad (\text{a generalized equation of state})$$

$$\frac{\partial r}{\partial t} = u \quad (\text{the defining quadrature for Eulerian distance}).$$

The authors seem to imply the use of a single equation of state to represent both solid explosive and gaseous detonation products, but this is not necessary. We may assume the co-existence of two phases, gas and solid, each with its own temperature [1], and even with its own pressure [2], provided that the pressure is a computable function in the sense of Turing.

This set of equations can be expressed in matrix form as $w_t = A w_m + b$, where suffixes denote differentiation, and can be rearranged and partitioned as

$$\begin{pmatrix} v \\ u \\ T - Qf \\ f \end{pmatrix}_t = \begin{pmatrix} A_1 & 0 \\ 0 & 0 \end{pmatrix} \begin{pmatrix} v \\ u \\ T \\ f \end{pmatrix}_m + \begin{pmatrix} 0 \\ 0 \\ 0 \\ b_1 \end{pmatrix}$$

where A_1 is hyperbolic, that is it has real and distinct latent roots, and b_1 is positive for all values of its variables and is monotonic decreasing in f . The zeros are believed to be sufficient, and may also be necessary, in order to obtain a stable steady-state solution, certainly with unsupported or mildly supported flow. It is known that spherical geometry, with a non-zero constant term in the equations for v and T , leads to a non-steady solution, as was pointed out by Mader [3]. The proof of stability would seem to be a long and difficult one; a proof of the stability of the generalized solution of the corresponding homogeneous set of equations

$$w_t = A w_m$$

has only recently been attained [4], and that only for a single conservation law. Part, at least, of the difficulty lies in the multiplicity of eigenvalues, and hence of wave speeds, of the

matrix A_1 . In passing, it does not seem intuitively obvious that Chapman's hypothesis [5] is identical to Jouguet's hypothesis [6] for all equations of state.

If a steady state detonation is assumed, then the basic partial differential equations integrate up to

$$\left. \begin{aligned} u &= (p-1)/s \\ v &= v_0 - u/s \\ C_v(T - T_0) &= (p^2 - 1)/2s^2 + Qf \\ p &= p(f, v, t) \end{aligned} \right\} \quad (\text{algebraic relations})$$

$$sQ \frac{df}{dt} = -F(f, p, T) \quad (\text{one differential equation})$$

$$s \frac{dx}{dm} = -u \quad (\text{one quadrature}),$$

for a shock of s cm/ μ sec traveling into still undetonated explosive at unit pressure. The single differential equation implies that the interpretation of the authors' Fig. 2 requires some knowledge of the law of burning, as well as knowledge of the differentials of the equation of state.

REFERENCES

1. F. J. Warner, 9th Symposium (International on Combustion, Academic Press, 1963, p. 536.
2. H. Bernier, A. Vidart, and F. Prouteau, International Conference on Sensitivity and Hazards of Explosive, ERDE, London, 1963.
3. C. L. Mader, Remarks (this Symposium).
4. A. Schlissel, J. Math. Analysis and Applications, 9, p. 356 (1964).
5. D. L. Chapman, Phil. Mag., Series 5, 47, p. 90 (1899).
6. E. Jouguet, Comptes Rendus, 142, p. 831 (1907).

RADIUS OF CURVATURE EFFECT ON DETONATION VELOCITY

LeRoy G. Green and Edward James, Jr.

*Lawrence Radiation Laboratory
University of California
Livermore, California*

ABSTRACT

The effect of the radius of curvature of the detonation front on the detonation velocity of certain explosives has been measured. The technique employed is to determine the transit time of a divergent detonation wave of known initial radius of curvature through various thicknesses of acceptor explosive. The results of the measurements are then used to calculate a reaction zone thickness based upon an approximate solution to the Wood-Kirkwood equations relating detonation velocity and radius of curvature of the detonation wave. The average reaction zone thickness so obtained for an 85/15 HMX/Viton made with Holston HMX was found to be 0.064 mm, whereas for the same type plastic-bonded explosive made from UK Bridgwater HMX it was 0.182 mm. This reaction zone thickness is compared with shock sensitivity. Other explosives, including PBX-9404, are discussed.

INTRODUCTION

At the Lawrence Radiation Laboratory we have been making precise transit time measurements of detonation waves which initially have a rather small radius of curvature. One purpose of this study is to see if the experimental observations are consistent with the model proposed by Wood and Kirkwood [1]. Another reason is to see if there is a plausible explanation for the so-called booster/acceptor interface delay.

Within our experimental error, the form of Wood and Kirkwood's approximate equation

$$D = D_{\infty} (1 - 3.5 a^*/S) \quad (1)$$

does fit the observed data nicely. Thus, we can derive a value for the quantity a^* for a given explosive. In Eq. (1) S is the radius of curvature of the detonation front. The parameter a^* is defined as the reaction zone thickness. (This reaction zone thickness is a factor of 7 smaller than the value obtained from the relationship suggested by Eyring et al. [2]).

If the transit time of an initially divergent detonation wave through some thickness of explosive is calculated from the infinite diameter

detonation velocity, this time will invariably be shorter than the measured transit time. Such a time difference, or excess transit time, is observed when a small detonator is used to initiate a larger acceptor explosive. This has often been called an interface delay. It is our contention that, unless there is a gap or barrier between the detonator and the acceptor, the so-called delay is not a delay at all. We believe it is simply a consequence of the fact that highly divergent detonation waves travel at lower velocities than plane waves. As a divergent wave passes through an explosive, its radius of curvature becomes larger and so it should accelerate to the limiting plane wave velocity in an infinitely large charge. Our experimental observation that excess transit time increases (but at a decreasing rate) with distance of travel in the acceptor explosive is, we think, a good argument against there being a real interface delay. If there were a delay, we would expect it to be constant and not dependent upon the distance the wave has traveled.

We calculate from our data thicker reaction zones in the compositions made from the more perfectly formed HMX crystals made by the UK Bridgwater process than we do for those made with Holston's HMX. These results suggest that to a great extent the "reaction zone

thickness" of a heterogeneous explosive is determined by the density of imperfections which become initiation sites, and is not just dependent upon the chemical kinetics of the explosive. This is in agreement with the model proposed by Campbell et al. [3,4].

EXPERIMENTAL

Test Method

In the experiments reported here, the initiating explosive in the small detonator is a 23-mg pellet 3.8 mm in diameter and 1.3 mm long. The pellet is PBX-9407 pressed to a density of 1.60 g/cc. This high energy booster explosive has an infinite diameter detonation velocity of 7.91 mm/ μ sec at this density and so matches fairly closely the explosive properties of the acceptor explosives we have worked with [5]. The perturbations due to refraction effects are therefore minimal.

flash that is recorded on the film occurs when the emerging shock from the detonating explosive crosses the 3-mil air gap between the explosive and the Plexiglas cover on the bottom face.

Time measurements are obtained from the writing speed of the camera for the particular experiment, and distance measurements are made on the film record with a comparator capable of reading to 1 micron. The limiting time resolution of the Mark II camera is between 0.2 and 0.3 shakes. The explosive thickness under each detonator is measured to the nearest 0.1 mil. The true thickness of the explosive is probably not known to closer than ± 0.15 mil.

The initiating wave front entering the acceptor explosive from the detonator is approximately spherical. The radius of curvature was established by converting the x, t film record of the reference detonators to a set of

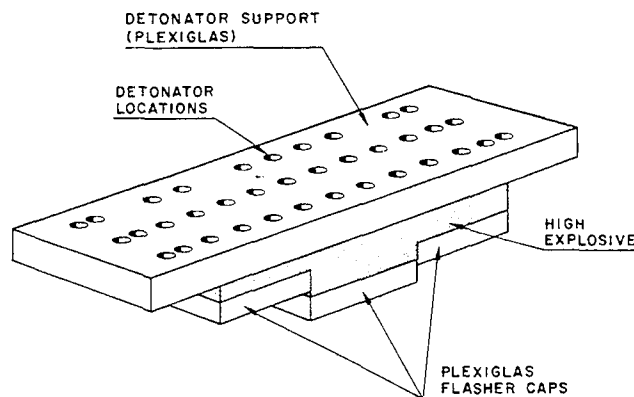


Fig. 1 - Test configuration

A set of detonators simultaneously initiates the stepped slab of acceptor explosive such as the one illustrated in Fig. 1. Time measurements are obtained with a Mark II high speed camera designed by Group GMX-8 of the Los Alamos Scientific Laboratory (LASL) and equipped with a Beckman-Whitley beryllium rotor. The breakout face of the explosive is imaged on the slit plane of the camera in such a way that the images of the points on the explosive directly under the detonators are on one of three slits at the slit plane, as shown in Fig. 2. The images of the breakout faces of the twelve reference detonators are also centered on one of the three slits. A typical trace is illustrated in Fig. 3. The short duration light

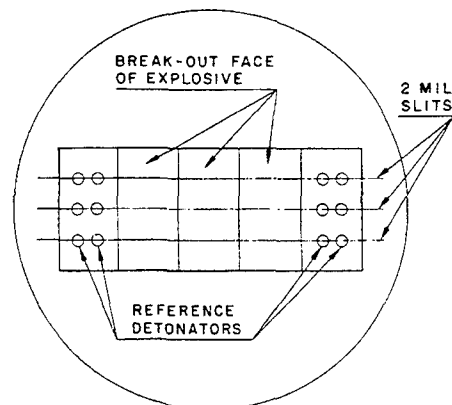


Fig. 2 - Slit plane image

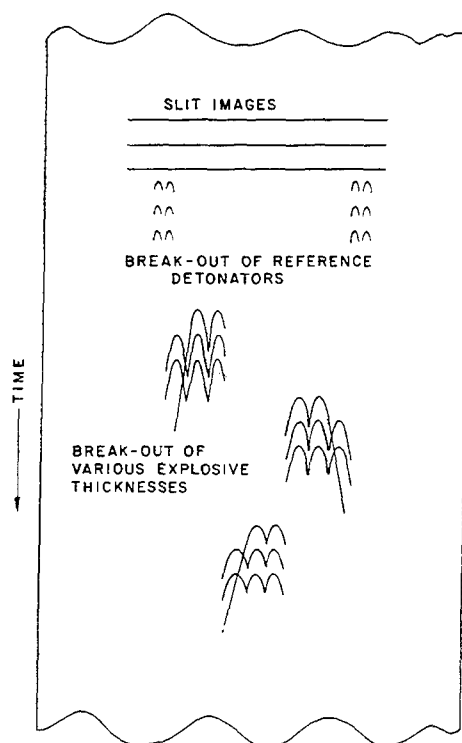


Fig. 3 - Smear camera record

x, y coordinates. In our experiments the curvature averaged 4.2 mm. The value so obtained is the one characteristic of the detonation front passing from the booster explosive to an identical acceptor explosive. In the actual experimental data reduction, a correction is made for the refraction between the nonidentical explosives.

For a particular experiment, the average breakout time of the twelve reference detonators

was taken as the average time zero for the group of eight detonators used to initiate the acceptor explosive at each of the three thicknesses. The average breakout time of the eight points on the explosive directly under the detonators at each particular explosive thickness minus the average time zero was taken as the measured transit time for the detonation through that particular thickness of explosive. Duplicate experiments were run on each explosive and the results were statistically combined. The experimental data are given in Tables 1 and 2.

Explosives

The test explosives Nos. 1 through 8, described in Table 1, are variants of the class of plastic bonded explosives made from HMX and DuPont's Viton. The Viton used in all of these explosives was their Viton A which is a copolymer of perfluoropropylene and vinylidene fluoride. In experiment No. 9, because of fabrication problems, a simple slab of solvent pressed HMX was used, rather than the stepped slabs used in all the others [6]. The PBX-9404 of experiment No. 10 was taken from a production lot meeting the requirements of the LASL specification 13Y-103159 A-2.

The HMX came from two sources. The Holston HMX used in the Viton formulations was Grade II, Class B, meeting the requirements of the U.S. Military Specification MIL-H-45444A (Ord), 24 April 1961. The purity was better than 99.5%. Less than 0.2% RDX was present. This same HMX was used to produce the solvent pressed HMX for experiment No. 9. The Bridgwater HMX used in the Viton formulations, No. 6 and No. 7, was obtained from the AWRE at Aldermaston, England. The purity of

TABLE 1
Description of Explosives

Expt. No.	Explosive	HMX Source	Composition (wt %)		Density (g/cc)	D_x (mm μ sec)
			HMX	Viton-A		
1	RX-04-P-1	Holston	81.1	18.9	1.878	8.363
2	LX-04-1	Holston	84.7	15.3	1.835	8.358
3	LX-04-1	Holston	84.7	15.3	1.852	8.416
4	LX-04-1	Holston	84.7	15.3	1.864	8.454
5	LX-04-1	Holston	85.2	14.8	1.860	8.458
6	LX-04-1	Bridgwater	85.2	14.8	1.870	8.491
7	LX-07-0	Bridgwater	90.1	9.9	1.870	8.677
8	LX-07-0	Holston	90.7	9.3	1.864	8.682
9	HMX	Holston	100.0	—	1.895	9.118
10	PBX-9404	Holston	94.0	—	1.842	8.808

TABLE 2
Transit Time Data

Expt. No.	Thickness (mm)	Measured Transit Time (μ sec)	Transit Time at D_∞ (μ sec)	Excess Transit Time (μ sec)
1	9.52	1.169	1.139	0.030
	15.88	1.934	1.898	0.036
	25.40	3.084	3.037	0.047
2	9.52	1.171	1.140	0.031
	15.88	1.956	1.899	0.057
	25.40	3.101	3.039	0.062
3	9.52	1.171	1.132	0.039
	15.88	1.936	1.886	0.050
	25.40	3.074	3.018	0.056
4	9.52	1.156	1.127	0.029
	15.88	1.908	1.878	0.030
	25.40	3.050	3.004	0.046
5	9.52	1.159	1.126	0.033
	15.88	1.919	1.877	0.042
	25.40	3.065	3.003	0.062
6	9.52	1.229	1.122	0.107
	15.88	1.989	1.870	0.119
	25.40	3.144	2.991	0.153
7	9.52	1.168	1.098	0.070
	15.88	1.929	1.830	0.099
	25.40	3.026	2.927	0.099
8	9.52	1.114	1.097	0.017
	15.88	1.862	1.829	0.033
	25.40	2.965	2.926	0.039
9	12.70	1.428	1.393	0.035
10	9.52	1.115	1.081	0.034
	15.88	1.857	1.802	0.055
	25.40	2.933	2.884	0.049

this HMX was essentially the same as the Holston material.

CALCULATIONS

If the detonation front is assumed to expand spherically in the acceptor explosive, then the radius of curvature at a distance X will be

$$S = X + S_0 \quad (2)$$

where S_0 is the radius of curvature of the entering detonation front. The time derivative of Eq. (2) is

$$\frac{dS}{dt} = \frac{dX}{dt} = D \quad (3)$$

If we combine the Wood-Kirkwood equation, Eq. (1), with Eq. (3) above and integrate, we obtain, with some rearrangement, the equation

$$(t_2 - t_1) - \frac{S_2 - S_1}{D_{\infty(\rho)}} = \frac{3.5a^*}{D_{\infty(\rho)}} \ln \frac{S_2 - 3.5a^*}{S_1 - 3.5a^*} \quad (4)$$

The term $(t_2 - t_1)$ on the left-hand side of the equation is the detonation wave transit time. The right-hand side of the equation, which contains the reaction zone term a^* , is the expression for the excess transit time. S_1 is obtained from the radius of curvature S_0 of the detonator breakout by correcting for the refraction of the wave as it passes from the PBX-9407 into the acceptor. The velocity assumed for the initiating wave at $S_0 = 4.2$ mm was 7.4 mm/ μ sec, and an iterative process was used to calculate

an S_1 , since S_1 is somewhat dependent on the value of a^* . S_2 is simply S_1 plus the sample thickness. $D_{\infty(\rho)}$, the infinite diameter detonation velocity as a function of density for the HMX/Viton compositions, is calculated for each experiment from the equation

$$D_{\infty} = 2.727 + 3.384\rho - 0.038 (\% \text{ Viton}). \quad (5)$$

This equation is obtained by applying the method of least squares to a large number of detonation velocity measurements of HMX/Viton systems in which both the density and composition are widely varied. Data on pure HMX are also included. The 95% confidence limits on the velocities predicted by Eq. (5) over the range of composition and densities covered in cases No. 1 through 9 are $\pm 0.008 \text{ mm}/\mu\text{sec}$, or about 0.1%. The reaction zone thickness a^* is then calculated at each explosive thickness by a trial and error iteration. The a^* values reported in Table 3 are weighted averages, the least weight being given to the transit times measured through the thinnest section. As a check on the equation used to calculate a^* , the fitted a^* values are used to calculate the excess transit times for the various explosive thicknesses, and the results are compared with the measured values in Table 3. The agreement is quite good.

DISCUSSION

The set of experiments represents variations in composition, density, actual lots of HMX, HMX particle size, and HMX source. The reaction zone thicknesses range from 0.043 mm to 0.182 mm. Since the 95% confidence limits for the measured excess transit times is about $\pm 0.008 \mu\text{sec}$, the 95% confidence limit for the calculated a^* 's is about $\pm 0.010 \text{ mm}$. This uncertainty in a^* is enough to obscure the effects due to density, HMX lot, HMX particle size, and composition variations (with Holston HMX). What is left is the effect due to HMX source. This effect is large enough so that the two compositions made with Bridgwater HMX are clearly distinguished from the Holston HMX compositions. The Bridgwater formulations also show a definite trend in reaction zone thickness with composition. Explosives fabricated with Bridgwater process HMX have also been shown to be less shock sensitive than the equivalent explosives made with Holston process HMX. This is illustrated in Table 4, which shows the small-scale gap test results obtained on 85/15 HMX/Viton formulations made with Bridgwater and Holston process HMX's. Differences between Holston and Bridgwater HMX's can be seen by microscopic examination. The

TABLE 3
Reaction Zone Thickness Data

Expt. No.	a^* (mm)	Excess Transit Time for Each Thickness Calculated from a^* (μsec)			Measures Excess Transit Time Minus Excess Transit Transit Time Calculated from a^* (μsec)		
		9.52 mm	15.88 mm	25.40 mm	9.52 mm	15.88 mm	25.40 mm
1	0.054	0.029	0.038	0.047	+0.001	-0.002	± 0.000
2	0.071	0.038	0.050	0.062	-0.007	+0.007	± 0.000
3	0.070	0.037	0.048	0.060	+0.002	+0.002	-0.004
4	0.050	0.027	0.035	0.043	+0.002	-0.005	+0.003
5	0.066	0.035	0.046	0.057	-0.002	-0.004	+0.005
6	0.182	0.096	0.126	0.156	+0.011	-0.007	-0.003
7	0.130	0.068	0.089	0.110	+0.002	+0.010	-0.011
8	0.043	0.022	0.029	0.036	-0.005	+0.004	+0.003
9	0.058						
10	0.067	0.035	0.046	0.056	-0.001	+0.009	-0.007

TABLE 4
Small-Scale Gap Test Results
85/15 HMX/Viton Formulations

HMX Crystallization Process	Brass Spacer Thickness $\pm L_{95}$ (mils)
Holston	78 ± 7
Bridgwater	44 ± 6

Holston HMX crystals appear much more imperfect. The crystal surface is quite irregular and a large number of internal flaws are visible. The Bridgwater crystals generally show well formed faces and are virtually free of visible internal imperfections.

One obvious conclusion to be drawn from the data is that the "reaction zone thickness" of a heterogeneous explosive is not the same as the "reaction zone thickness" of a homogeneous explosive. Even though a^* as measured here may be an average distance from the shock front to the C-J state, the fact that this distance can be varied by a factor of 3 in chemically identical systems (see Table 3) is proof that the physical structuring of the system plays an important role in establishing the reaction zone. For heterogeneous explosives, it seems quite probable that the runaway reaction originates at discrete sites behind the shock front. The density of initiation sites, then, becomes an important factor in determining the reaction zone thickness of a heterogeneous explosive. It is to be emphasized that in this study we are dealing only with dense explosives with very little void space. The initiation sites we hypothesize therefore are not void type imperfections, but rather structural discontinuities in the crystals of HMX. Both the HMX types studied had very nearly the same particle size distribution, so the grain structure of the PBXs made from the two types of HMX was not greatly different. The principal difference appears therefore to be in the HMX crystal form.

Future experiments are planned with much more highly divergent wave systems, which should allow a much more precise determination of a^* .

ACKNOWLEDGMENT

The authors are indebted to Mr. John Cast for his assistance in perfecting the techniques used in measuring the short transit times. They also wish to express their appreciation to the personnel of the Development Group of the Pantex AEC Plant, Amarillo, Texas, for their help in obtaining the detonation velocity measurements used to predict infinite diameter velocities as well as the gap test data quoted.

REFERENCES

1. W. W. Wood, and J. G. Kirkwood, "Diameter Effect in Condensed Explosives. The Relation Velocity and Radius of Curvature of the Detonation Wave," *J. Chem. Phys.* 22, 1920-24 (1954).
2. H. Eyring, R. E. Powell, G. H. Duffey, and R. B. Parlin, *Chem. Revs.* 45, 69 (1949).
3. A. W. Campbell, W. C. Davis, and J. R. Travis, "Shock Initiation of Detonation in Liquid Explosives," *Phys. Fluids* 4, 498-510 (1961).
4. A. W. Campbell, W. C. Davis, and J. R. Travis, "Shock Initiation of Solid Explosives," *Phys. Fluids* 4, 511-21 (1961).
5. L. C. Smith, Los Alamos Scientific Laboratory, private communication.
6. P. Archibald, "Isostatic Solvent Pressing," *Industrial and Engineering Chem.* 53, 737 (1961).

Work performed under the auspices of the U.S. Atomic Energy Commission.

LATERAL SHOCK PRESSURE MEASUREMENTS AT AN EXPLOSIVE COLUMN*

Lippe D. Sadwin†
*U.S. Naval Ordnance Laboratory, White Oak
Silver Spring, Maryland*

and

Norman M. Junk
*Atlas Chemical Industries, Inc.
Tamaqua, Pennsylvania*

ABSTRACT

A high speed streak camera technique for measuring the lateral shock pressure generated from an end initiated, cylindrical explosive charge is described. Observations made in a water medium show that for several explosives at various diameters, the lateral pressure is 38 to 73 percent of the shock pressure generated at the terminal end of the explosive column.

INTRODUCTION

Detonation pressure observations are frequently made by a high speed streak camera method commonly called the "aquarium" technique [3,6]. In the "aquarium" technique the slit of a streak camera is oriented along the axis of the explosive; displacement of the detonation wave and of the shock wave generated from the terminal end is recorded photographically as a continuous function of time.

Usually, a medium such as water is selected for "aquarium" type measurements as its equation of state properties are well known in the pressure range of interest [3] and both its transparency and change of refractive index with pressure [2] aid in high speed photographic observation of shock wave propagation.

For the numerous applications involving long explosive columns which are detonated from one end, observations of the shock wave generated from the terminal end are less meaningful than lateral shock pressure measurements, as shock loading phenomena in a

lateral direction are experienced along the entire length of such charges.

The purpose of this paper is to describe the use of a high speed, rotating mirror, streak camera in making lateral shock pressure measurements. In addition, data comparing the lateral and end shock pressures generated from a number of commercial and military explosives are presented.

EXPERIMENTAL METHOD

The method of making lateral shock pressure measurements described herein is a unique variation of the "aquarium" technique. The slit of the streak camera is oriented at an acute angle β with respect to the axis of detonation (see Figs. 1 and 2) rather than along the axis, as in "aquarium" type detonation pressure measurements.

In an earlier method of making lateral shock pressure measurements [7] the slit of the streak camera was oriented at a 90-degree angle with respect to the axis of detonation. Since

*This work was performed under a cooperative agreement between the U.S. Bureau of Mines and the Atlas Chemical Industries, Inc.

†Formerly employed at the Applied Physics Laboratory, U.S. Department of Interior, College Park, Maryland.

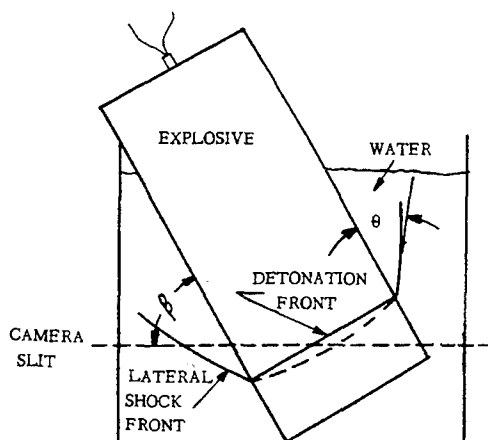


Fig. 1 - Schematic diagram illustrating orientation of explosive and streak camera slit

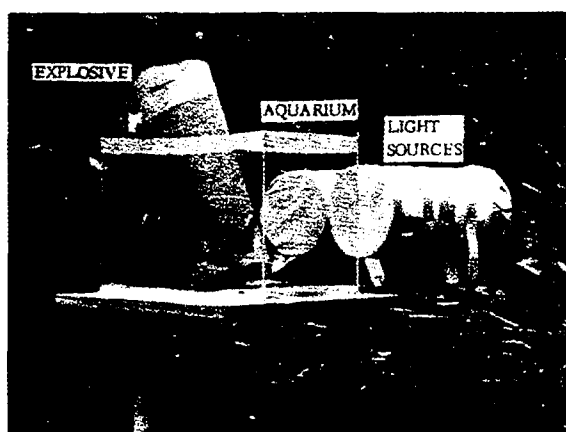


Fig. 2 - View of experimental arrangement used in making lateral shock pressure measurements

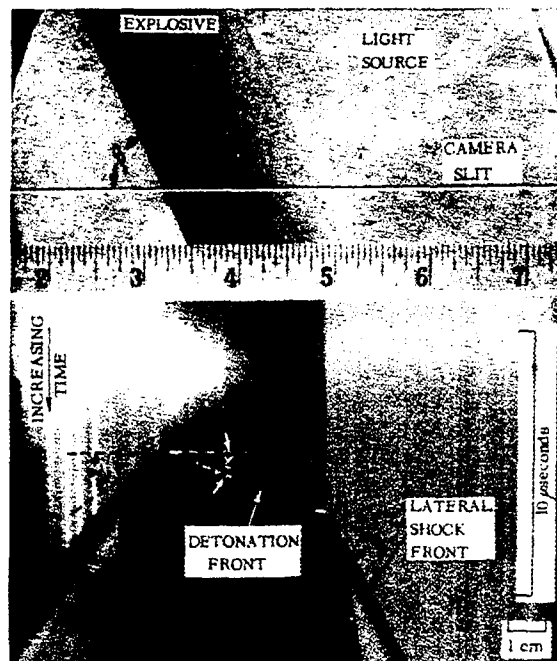


Fig. 3 - Typical streak camera record

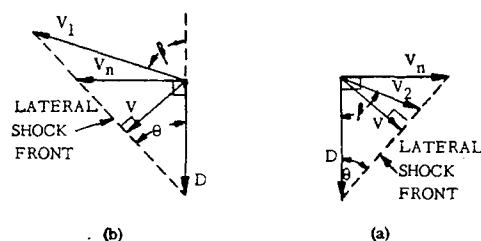


Fig. 4 - Vector diagrams for right (a) and left (b) sides

the detonation velocity D must be known in order to calculate the shock velocity V in a direction normal to the lateral shock front, an independent measurement of D was needed in the earlier experiments. In the present technique the detonation velocity and shock velocity normal to the lateral shock front are both determined from a single streak camera record; simultaneous observations being made of detonation and lateral shock wave propagation.

Since the camera slit is oriented at an angle both with respect to the axis of detonation and the normals to the laterally generated shock waves on each side of the charge, the

trigonometric analysis which follows must be used.

Referring to Figs. 1, 3, and 4:

$$D = \cot \gamma \cos \beta \left[\frac{S}{T} \right], \quad (1)$$

$$V_1 = \cot \alpha_1 \left[\frac{S}{T} \right] \quad (2)$$

and

$$V_2 = \cot \alpha_2 \left[\frac{S}{T} \right], \quad (3)$$

where V_1 and V_2 are the velocities of the lateral shock fronts in the direction of the camera

slit for left and right side lateral shocks respectively, S and T are the camera record scale factors for displacement and time respectively, and α_1 , α_2 and γ are the angles formed on the camera record between the displacement axis and the wave front displacement versus time information for the left and right lateral shocks and the detonation wave, respectively.

The values of γ , α_1 , α_2 , β , S and T are obtained directly from measurements made on the streak camera record (Fig. 3).

Considering Fig. 4a,

$$V_n = V_2 \sin \beta + V_2 \cos \beta \tan \theta, \quad (4a)$$

where V_n is the shock velocity in a direction normal to the charge axis.

Since $\tan \theta = V_n/D$, where θ is the acute angle formed by the lateral shock front and the charge axis, we may write Eq. (4a) as

$$V_n = \frac{DV_2 \sin \beta}{D - V_2 \cos \beta}. \quad (4b)$$

Combining Eqs. (1), (3) and (4b) we obtain

$$V_n = \frac{\cot \gamma \cot \alpha_2 \sin \beta}{\cot \gamma - \cot \alpha_2} \left[\frac{S}{T} \right]. \quad (4c)$$

Finally, since $V = V_n \cos \theta$ (Fig. 4a),

$$V = \frac{\cot \gamma \cot \alpha_2 \sin \beta \cos \theta}{\cot \gamma - \cot \alpha_2} \left[\frac{S}{T} \right]. \quad (5a)$$

Following a similar procedure for the left side (Fig. 4b)

$$V = \frac{\cot \gamma \cot \alpha_1 \sin \beta \cos \theta}{\cot \gamma + \cot \alpha_1} \left[\frac{S}{T} \right]. \quad (5b)$$

The values of V obtained through the use of Eqs. (5a) and (5b) are now used to determine the lateral shock pressure by use of equation of state data for water [3].

EXPERIMENTAL OBSERVATIONS AND DISCUSSION OF RESULTS

Table 1 lists the observations made on several explosives*; the method of Ref. 7,

where the streak camera slit is normal to the explosive axis, was used in addition to the method described above.

Several investigators have studied the lateral shock pressure generated from an explosive. Clay, et al. [1] reported a framing camera observation for Composition B where the lateral shock pressure in plexiglas was approximately 50 percent of the end generated pressure. Direct comparisons between this work and that reported by Eyring, et al. [5] and Erkman [4] are not feasible as a water medium was not described in the former and flat explosive slabs were studied in the latter. However, from Refs. 4 and 5, the general observation can be made that the magnitude of the lateral shock pressure increases with respect to the end pressure as the condition of oblique incidence created by the detonation front at the side of the explosive varies from a 90-degree angle of incidence to smaller values. This concept may be used to interpret the results obtained for the 45 percent semigelatin dynamite.

The 45 percent semigelatin dynamite experiences a pronounced "diameter effect." The radius of curvature of the detonation front decreases as the diameter of the explosive decreases. Thus, for the smaller diameters the angle of lateral incidence will be smaller, and the ratio of the lateral shock pressure to end pressure should be higher. However, this concept, which should be applicable to all nonideal explosives, appears to lose strength in the case of ammonium nitrate-fuel oil, which has become one of the best known, nonideal, commercial explosives [8]. This apparent anomaly is also observed in the data for 40 percent extra dynamite which is also considered a nonideal explosive. It is hoped that an explanation of this behavior will be possible from future measurements.

SUMMARY

Lateral shock pressure measurements by a high speed streak camera technique have been described and the results for several explosives in a water medium have been presented. Comparing the lateral pressure with that generated from the end of identical explosive charges gives some insight into the importance of these measurements for various applications where long explosive columns are used extensively.

REFERENCES

1. R. B. Clay, M. A. Cook, and R. T. Keyes, "Shock Waves in Solids and Rock

*The streak camera was operated by William L. Frantz of the Atlas Chemical Industries, Reynolds Experimental Laboratory, Tamaqua, Pennsylvania.

TABLE 1
Comparison of Shock Pressures Generated in Water Laterally
and From End of Cylindrical Explosive Columns

Explosive	Density (g/cm ³)	Diam- eter (cm)	Detonation Velocity* (m/sec)	Peak Pressure Generated		Lateral to End, Pressure Ratio
				From End* (kbars)	Laterally* (kbars)	
50/50 Pentolite	1.65	13	7960	135	71.7 [†]	0.531
50/50 Pentolite	1.65	6.2	7720	119	72.0 [‡]	0.605
50/50 Pentolite	1.65	3.7	7480	135	59.5 [‡]	0.441
45% Semigelatin Dynamite	1.27	13	4980	83.0	36.5 [‡]	0.440
	1.27	6.2	4340	39.5	29.3 ^{†,‡}	0.734
	1.27	3.7	3770	28.0	20.5 [‡]	0.732
94/6 Ammonium Nitrate-Fuel Oil	0.93	13	3130	28.0	13.3 [‡]	0.475
	0.83	10	2640	23.0	9.0 [†]	0.391
75% Ammonia Gelatin Dynamite	1.50	10	5980	82.5	45.1 [†]	0.546
40% Extra Dynamite	1.36	10	4100	41.0	15.5 [†]	0.378
175 Grains per Foot Primacord	1.5	0.8	7530	78.0	38.0 [†]	0.487

*Where possible, average values are presented.

[†]Using method of Ref. 7.

[‡]Using method of this paper.

- Mechanics," International Symposium on Mining Research, ed. by G. B. Clark, Pergamon Press, Vol. 2, p. 694, 1962.
- R. H. Cole, "Underwater Explosions," Princeton University Press, Princeton, New Jersey, 1948.
- M. A. Cook, R. T. Keyes, and W. O. Ursenbach, "Measurements of Detonation Pressure," Journal of Applied Physics, Vol. 33, No. 12, pp. 3413-3421, Dec. 1962.
- J. O. Erkman, "Explosively Induced Non-Uniform Oblique Shocks," Stanford Research Institute, Poulter Laboratories Technical Report 023-57, Dec. 1957.
- H. Eyring, R. E. Powell, G. H. Duffey, and R. B. Parlin, Chemical Reviews, Vol. 45, pp. 69-181, 1949.
- W. C. Holton, "The Detonation Pressures in Explosives as Measured by Transmitted Shocks in Water," NavOrd 3968, U.S. Naval Ordnance Laboratory, White Oak, Maryland, Dec. 1954.
- L. D. Sadwin and N. M. Junk, "Measurement of Lateral Pressure Generated from Cylindrical Explosive Charges," U.S. Bureau of Mines, Report of Investigations 6701, 1965.
- L. D. Sadwin, R. H. Stresau, S. J. Porter, and J. Savitt, "Nonideal Detonation of Ammonium Nitrate-Fuel Mixtures," Third Symposium on Detonation, ONR Symposium Report ACR-52, Vol. 1, pp. 309-325, 1960.

STUDIES OF THE DIAMETER-DEPENDENCE OF DETONATION VELOCITY IN SOLID COMPOSITE PROPELLANTS

I. Attempts to Calculate Reaction-Zone Thickness

Mary L. Pandow, K. F. Ockert, and H. M. Shuey
Rohm and Haas Company
Redstone Research Laboratories
Huntsville, Alabama 35807

INTRODUCTION

Many solid propellants, although much less sensitive to initiation by shock or other stimuli than most high explosives, are detonable in charge sizes which are small enough to make storage and handling of such compositions extremely hazardous. In a study of the sensitivity of a material, knowledge of the factors which influence the detonation propagation in a system are desired. There exists, for a given composition at a specific density, a diameter below which detonation cannot be propagated in a cylindrical charge. This critical or failure diameter, D_f , appears to be related to the kinetics of the reacting system.

Because of the rapidity of the detonation reaction, kinetic measurements cannot readily be made, and any knowledge of the kinetics must involve extrapolations from data obtained at lower temperatures and pressures. No kinetic data are available for systems as complex as a multicomponent propellant. However, relationships exist which relate detonation velocity to the reaction-zone length or the reaction time of a detonation reaction. The detonation velocity can be measured with relative ease and good precision.

In general, with cylindrical charges of porous high explosives, the detonation velocity, U , increases with charge diameter. The increase is rapid near the failure diameter and then levels off, approaching the "ideal" value, U° , at large diameters. (U° is the value given by hydrodynamic-thermodynamic theory for a one-dimensional, steady-state detonation wave.) Detonation velocities of high explosives at or near failure diameter are often as much as 30 to 40 percent below the "ideal" value [1,2]. It has been reported that there is no change of velocity in gun powder with charge diameter [3],

but the accuracy of these measurements is in doubt.

Several theories have been developed to explain the variation of detonation velocity with diameter. These theories relate the velocity, U , at a particular diameter, D , to the "ideal" velocity, U° , and the reaction zone length, ξ_1 , or the reaction time, t_1 .

The "curved front" theory of Eyring and coworkers [1] expresses the relationship by the equation

$$\frac{U}{U^\circ} = 1 - \frac{\xi_1}{D} \quad (1)$$

The reaction-zone length is related to the reaction time by the expression

$$\xi_1 = \frac{\rho_0}{\rho_2} U t_1 \approx 0.75 U t_1 \quad (2)$$

where ρ_0 and ρ_2 are the initial and final density, respectively.

The "nozzle" theory of H. Jones [1,4] can be expressed by the equation

$$\left(\frac{U^\circ}{U}\right)^2 = 1 + 3.2 \left(\frac{t_1 U^\circ}{D}\right)^2 \quad (3)$$

This is an empirical relationship given by Taylor to express Jones' results. Taylor [4] used $t_1 = \xi_1/U$, so that

$$\left(\frac{U}{U^\circ}\right)^2 = 1 - 3.2 \left(\frac{\xi_1}{D}\right)^2 \quad (4)$$

Wood and Kirkwood [5] have described the velocity dependence in terms of the radius of

curvature of the detonation front rather than in terms of the charge diameter. Their equation is

$$\frac{U^0 - U}{U^0} = 3.5 \frac{\xi}{s} \quad (5)$$

where s is the radius of curvature of the detonation front.

These three theories are the most commonly used. In the present work, failure diameters and detonation velocities as functions of diameter have been measured for several plastisol-nitrocellulose composite propellants, and for ammonium perchlorate and C-4 for comparison purposes. The reaction times and reaction-zone lengths have been calculated using the "curved front" and "nozzle" theories. Since the radius of curvature of the detonation front as a function of diameter was not known, correlation with the Wood and Kirkwood equation was not attempted.

MEASUREMENT OF THE DIAMETER-DEPENDENCE OF DETONATION VELOCITY

Detonation velocities were measured by ion probes inserted at five positions along the axis of 40-inch-long, unconfined, cylindrical propellant charges varying in diameter from 1-1/4 to 7-1/2 inches. In addition to propellant formulations (Table 1), granular ammonium perchlorate and C-4 (91 percent RDX, 9 percent wax) were studied. Formulation A was examined in both confined and unconfined states and for two different particle sizes of ammonium perchlorate (55-60 μ and 10-18 μ weight median diameters). The ammonium perchlorate particle size in the other compositions was 55-60 μ . The aluminum in A and F was 6-8 μ weight median diameter.

TABLE 1
Compositions Used in Detonation Studies

Formulation	Weight % ^a			
	NH ₄ ClO ₄	KCl	RDX	Al
A	30.00 ^b	0	0	15.00
B	35.29	0	0	0
C	29.41	0	5.88	0
D	20.29	0	15.00	0
E	0	0	35.29	0
F	0	30.40	0	14.90

^aBinder by difference.

^bTwo particle sizes used: 55-60 μ (A-1) and 10-18 μ (A-2).

Each round was initiated at one end by means of a C-4 explosive booster having a bulk density of 1.59 gm/cc and a diameter equal to that of the charge. The boosters had length-to-diameter ratios of 3; they were cylindrical in shape through 2-1/2-inch diameters and conical at the larger sizes. Initiation of the boosters was by No. 8 electric detonators.

The ion probes were fabricated at these Laboratories from 19-gage stainless-steel tubing normally used in the manufacture of hypodermic needles. Within these, in lengths varying from 1 to 9 inches, depending upon the charge size with which they were to be used, were inserted 24-gage enameled magnet wire, secured in place by Duco cement. The steel sheath was partially cut away from the sensing end to expose the inner conductor; the tip of the assembly was beveled to permit easy insertion into the propellant charge (Fig. 1). After initial development, these probes proved to have excellent reliability and loss of information at a station was rare.

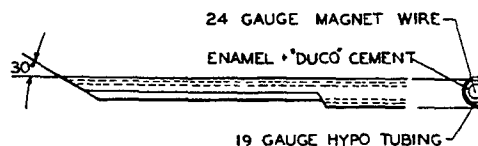


Fig. 1 - Ion-probe assembly

One probe, serving as a trigger, was placed between the booster and charge. Five additional probes were located at various stations down the charge, the first at 3 inches from the interface and the others in 8-inch increments. Each downstream probe led to an 8-megacycle counter chronograph (Potter); circuitry was so arranged that the counter would be stopped upon the probe's becoming conductive (Fig. 2). The chronographs were started in common by the trigger so a malfunction at one station would not affect readings from subsequent stations. The incremental times were obtained by difference. This arrangement gave as many as four replicate measurements for each round (excluding the first 3-inch measurement); two or three rounds were fired at each diameter.

Efforts were made to learn something of the transition phenomena by means of a continuous-wire resistance probe, in the manner of that developed by the Bureau of Mines [6], located at the initial part of the charge. Owing to

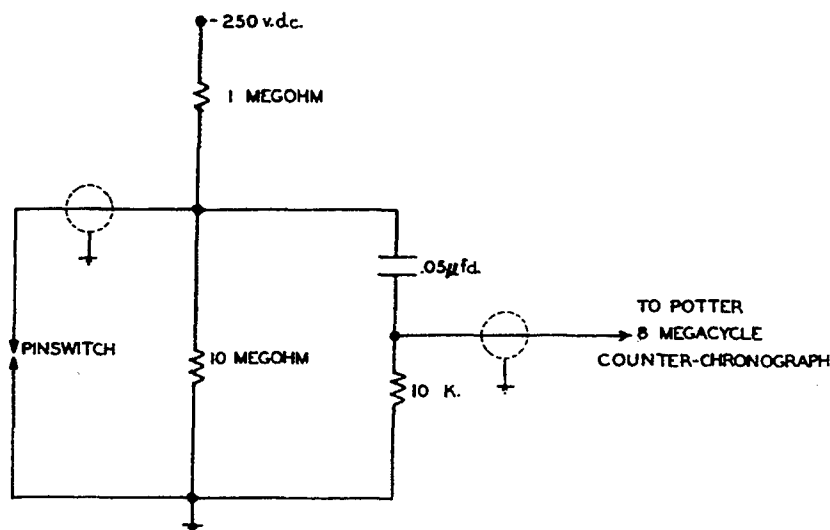


Fig. 2 - Ion-probe circuitry

the difficulty in casting the propellant with the probe in the center, the probe was attached to the exterior of the charge. These attempts failed to produce records of sufficient continuity and resolution to permit intelligent inferences to be made.

The failure diameter, D_f , was established, within limits, with charges of various diameters ($L/D \geq 4$) initiated by C-4 boosters of matching diameters; the occurrence of detonation was determined by perforation of a 1/2-inch-thick mild steel witness plate located at the downstream end of the charge.

CALCULATION OF REACTION-ZONE LENGTH AND EFFECTS OF CONSTITUTIVE VARIATIONS

The velocity data for formulations A through F and for Composition C-4 are given in Table 2. The data for the non-aluminized formulations, B, C, D, and E, are plotted in Fig. 3 and for the aluminized formulations A-1, A-2, and F in Fig. 4. The straight lines drawn in the figures were obtained by a least-squares fit of the data to Eq. (1).

The reaction-zone lengths and ideal detonation velocities were calculated using both "curved front" and "nozzle" theories (Table 3). Owing to the small change in velocity as a function of diameter and the scatter of the data, the two theories appear to fit the data equally well. However, the "curved front" theory gives a slightly better overall fit. In several cases, the ideal velocity given by the "nozzle" theory is lower than the measured velocity at the large-

est diameter measured. Because of this, a straight-line fit of velocity vs $1/D$ has been used to describe the data.

Comparison of A-1 and B shows that the aluminized propellant has a lower velocity and, by implication, a shorter reaction zone than its aluminum-free counterpart. The non-aluminized formulation, B, has the same ratio of ammonium perchlorate to binder as the aluminized formulation, A-1. Thus, if aluminum did not play a role in the detonation reaction, the stoichiometry of the two compositions would be the same. The difference in velocity and

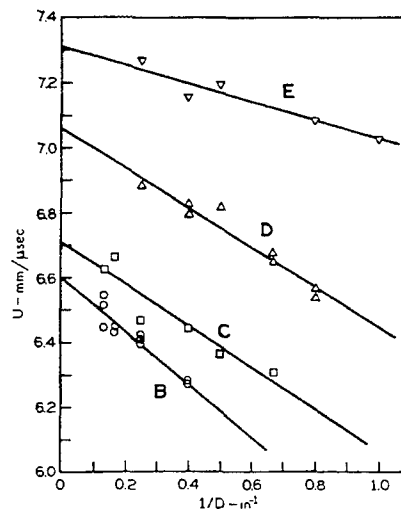


Fig. 3 - Diameter-dependence of detonation velocity of non-aluminized plastisol-nitrocellulose composite propellants

TABLE 2
Detonation Velocity as a Function of Charge Diameter in
Plastisol-Nitrocellulose Propellants and in Composition C-4

Charge Diameter (in.)	Detonation Velocity (mm/ μ sec)							
	A-1	A-2	B	C	D	E	F	C-4
1/2	-	-	-	-	-	-	-	7.825
3/4	-	-	-	-	-	-	-	8.026
1	-	6.105	-	-	-	7.027	-	7.924
	-	6.094	-	-	-	-	-	-
1-1/4	5.970	6.200	-	-	6.535	7.097	-	-
	5.931	6.154	-	-	6.564	-	-	-
1-1/2	6.074	6.337	-	6.301	6.649	7.082	-	8.019
	6.050	-	-	-	6.676	-	-	-
	6.072	-	-	-	-	-	-	-
1-3/4	-	-	-	-	-	-	5.596	-
	-	-	-	-	-	-	5.552	-
2	6.074	6.345	-	6.369	6.816	7.194	5.627	8.039
	6.050	-	-	-	-	-	5.654	-
	6.072	-	-	-	-	-	-	-
2-1/2	6.086	6.325	6.272	6.443	6.826	7.153	5.666	-
	6.150	-	6.274	-	6.795	-	5.736	-
	6.173	-	-	-	-	-	-	-
4	6.277	-	6.418	6.468	6.887	7.262	5.787	-
	6.313	-	6.393	-	-	-	-	-
	-	-	6.414	-	-	-	-	-
6	6.305	-	6.443	6.662	-	-	-	-
	6.281	-	6.439	-	-	-	-	-
	-	-	6.443	-	-	-	-	-
7-1/2	6.353	-	6.515	-	-	-	-	-
	6.361	-	6.545	-	-	-	-	-
	-	-	6.443	-	-	-	-	-

reaction-zone length indicate that aluminum does react in the detonation reaction zone.

Figure 4 shows the influence of ammonium perchlorate particle size. The reaction-zone length is shorter for the formulation containing the smaller particles. This is to be expected if the mechanism of the detonation reaction is a grain-burning type. It is somewhat surprising that the ideal velocity is not the same, since this should depend on the final products and not the rate of reaction. This may indicate that more material reacts between the detonation front and the C-J plane when the particle size of the reacting material is smaller. The data

for propellant F show the effect of replacing ammonium perchlorate with an inert material.

The small change in detonation velocity with charge diameter is not peculiar to propellants; Composition C-4 high explosive exhibits similar behavior (Table 2).

Comparison between granular materials and composite substances, that is, between porous and nonporous (consolidated) media, is given by the data for 55-60 μ ammonium perchlorate and the corresponding propellant, A-1. Because of the inconveniently high failure diameter of unconfined ammonium perchlorate,

TABLE 3
Reaction-Zone Lengths and Ideal Detonation Velocities

Formulation	D_f (in.)	"Curved Front" Theory		"Nozzle" Theory	
		U^0 (mm/ μ sec)	ξ_1 (in.)	U^0 (mm/ μ sec)	ξ_1 (in.)
A-1	1.05-1.15	6.407	0.089	6.301	0.235
A-2	0.75-0.82	6.522	0.060	6.406	0.122
B	1.82-1.92	6.598	0.124	6.503	0.377
C	1.25-1.50	6.702	0.095	6.601	0.267
D	1.00-1.05	7.060	0.087	6.918	0.224
E	0.36-0.50	7.309	0.039	7.228	0.136
F	1.50-1.61	5.951	0.109	5.833	0.206

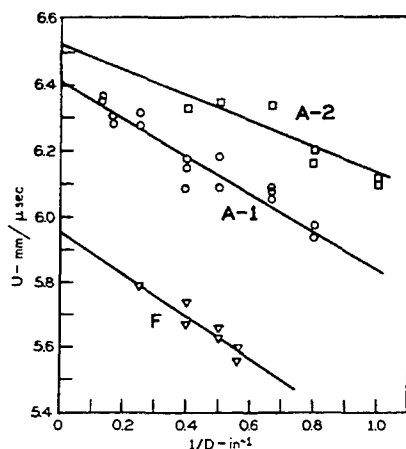


Fig. 4 - Diameter-dependence of detonation velocity of aluminized plastisol-nitrocellulose composite propellants

both substances were studied in steel water pipe (Table 4). The behavior of the granular material is quite different from that for consolidated materials. In the former case, the velocity increases by almost 50 percent when the diameter is increased from 1 to 2-1/2 inches. In the same confinement and for the same increase in diameter, A-1 increases only by about 1 percent.

Since C-4 is "granular" on a microscopic scale, it is not strictly pore-free. At first glance it would seem that C-4 should more closely resemble ammonium perchlorate in its diameter-dependence of detonation velocity than it does propellant. However, it must be borne in mind that, in these experiments, the bulk density of the C-4 is much closer to its limiting value than is the

TABLE 4
Detonation Velocities as a Function of Diameter of Propellant A-1 and Ammonium Perchlorate (1.24 gm/cc) in Steel Water Pipe

Charge Diameter (in.)	Velocity (mm/ μ sec)	
	A-1	AP
3/4	6.020	-
1	6.086	2.654
	-	2.650
	-	2.647
1-1/4	6.139	-
1-1/2	6.192	-
2	6.196	-
2-1/2	6.161	3.804
	-	3.882

perchlorate density. The amount of interstitial space is therefore much smaller. Moreover, the RDX crystals of the C-4 are wetted by plasticizer and have no exposed free surfaces.

SUMMARY OF CONCLUSIONS

1. The change in detonation velocity with charge diameter in consolidated propellants is much smaller than the velocity change in porous explosives.

2. A nonporous high explosive, C-4, even though granular, also shows only a small change in velocity with charge diameter.

3. Because of the scatter of the data and the small change in velocity as a function of diameter, no distinct applicability of either the "curved front" or the "nozzle" theory over the other can be shown as regards the relation between detonation velocity and reaction-zone length.

4. Regardless of the implications as to reaction-zone length, the data give a good fit to a linear plot of detonation velocity versus inverse charge diameter.

5. The presence of aluminum in propellant lowers the detonation velocity and the failure diameter, indicating that aluminum plays a role in the kinetics of the detonating system.

6. A decrease in the ammonium perchlorate particle size decreases the failure diameter and gives a slight increase in "ideal" velocity, implying that smaller particles react more rapidly, as would be expected in a grain-burning reaction.

ACKNOWLEDGMENT

This work was sponsored by the Advanced Research Projects Agency of the Department of Defense under Contract DA-01-021

ORD-11909(Z), administered by the U.S. Army Missile Command.

The authors would like to thank Messrs. J. F. Foster and R. T. Smith of these Laboratories for formulating and casting the charges and Messrs. J. F. Hester and W. H. Evans for the design and fabrication of the probes and other special instrumentation.

REFERENCES

1. H. Eyring, R. E. Powell, G. H. Duffey, and R. B. Parlin, *Chem. Rev.* 45, 69 (1949).
2. M. A. Cook, "The Science of High Explosives," Reinhold Publishing Corp., New York (1958), Chapter 6.
3. A. Ya. Apin, I. D. Kostin, and L. N. Stesik, *Dokl. Akad. Nauk SSSR* 137, 652 (1961).
4. J. Taylor, "Detonation in Condensed Explosives," Oxford University Press, London (1952), pp. 148-155.
5. W. W. Wood and J. G. Kirkwood, *J. Chem. Phys.* 22, 1920 (1954).
6. F. C. Gibson, *Rev. Sci. Instr.* 25, 226 (1954).

STUDIES OF THE DIAMETER-DEPENDENCE OF DETONATION VELOCITY IN SOLID COMPOSITE PROPELLANTS

II. Prediction of Failure Diameters

Mary L. Pandow, K. F. Ockert, and T. H. Pratt
Rohm and Haas Company
Redstone Research Laboratories
Huntsville, Alabama 35807

INTRODUCTION

In an attempt to find a method of determining the failure diameter of propellants which detonate in charge sizes too large to be handled conveniently, a means of extrapolating from results on RDX-adulterated propellants has been derived. The method has been tested on plastisol-nitrocellulose-type propellants and then applied to PBAA-binder propellants.

A general method for calculating failure diameter has been given by Evans [1]. The reaction time, defined in terms of a single first-order rate process is

$$t = \frac{c_v RT^2}{\nu E_a Q} \exp \left(\frac{E_a}{RT} \right) \quad (1)$$

where

t = reaction time,

c_v = specific heat at constant volume,

R = gas constant per mole,

ν = frequency factor,

E_a = activation energy,

Q = energy released in detonation reaction zone, and

T = temperature produced in unreacted propellant by the detonation front.

The reaction time can also be related to the charge diameter through one of the many theories dealing with detonation velocity -- diameter relations. The relation used in this paper is that given by Eyring's "curved front" theory

$$\frac{U^0 - U}{U^0} = \frac{\xi}{D} \quad (2)$$

where

U = detonation velocity,

U^0 = detonation velocity calculated from one-dimensional hydrodynamic theory,

ξ = reaction-zone length, and

D = charge diameter.

Eyring et al. [2] also use the relation

$$\xi = 0.75 tU. \quad (3)$$

Combination of Eqs. (1), (2), and (3) gives

$$\frac{D}{0.75 U} \left(\frac{U^0 - U}{U^0} \right) = \frac{c_v RT^2}{\nu E_a Q} \exp \left(\frac{E_a}{RT} \right). \quad (4)$$

At the failure diameter this becomes

$$\frac{D_f}{0.75 U_f} \left(\frac{U^0 - U_f}{U^0} \right) = \frac{c_v RT^2}{\nu E_a Q} \exp \left(\frac{E_a}{RT} \right). \quad (5)$$

If a high explosive which releases a large amount of energy (e.g., RDX) is added to a relatively inert propellant formulation, the reaction time and, consequently, the failure diameter will be smaller in the formulation containing the explosive than in the unadulterated formulation. If it is assumed that the rate-determining step is not changed by the high explosive, the temperature T necessary for detonation, the activation energy E_a , and the frequency ν are unchanged. If, at the same time, the physical properties of the explosive are not significantly

altered, c_v is also constant. Equation (5) can then be reduced to

$$D_f \left(\frac{U^\circ - U_f}{U^\circ} \right) = \frac{AU_f}{Q} \quad (6)$$

where

$$A = \frac{0.75 c_v RT^2}{\nu E_a} \exp \left(\frac{E_a}{RT} \right) \quad (7)$$

A is a constant for any given base propellant.

In this equation, Q is the total heat of detonation for the base propellant and the added explosive, or

$$Q = n_1 Q_1 + n_2 Q_2$$

where

n_1 = weight fraction of explosive,

n_2 = weight fraction of base propellant,

Q_1 = heat of detonation of explosive per gram, and

Q_2 = heat of detonation of base propellant per gram.

The velocities U° and U_f in Eq. (6) can be obtained from measurements of velocity as a function of diameter. The velocity data are plotted as a function of $1/D$ and an extrapolation is made to give the velocity values at infinite diameter and at failure diameter. Measurements of velocity as a function of diameter at two RDX concentrations give values of A and Q_2

for the base propellant. Q_1 is assumed to be the heat of explosion of RDX.

Thus, the quantities U° and U_f are the only quantities in Eq. (6) which must be determined for the calculation of the failure diameter of the base propellant. The "ideal" velocity U° can be determined from hydrodynamic theory. However, U_f is still unknown and, since the quantity $(U^\circ - U_f)/U^\circ$ involves a small difference of two large numbers, an approximation of U_f would not give sufficient accuracy. A relationship between $(U^\circ - U_f)/U^\circ$ and some property of the propellant is needed.

FAILURE-DIAMETER CALCULATIONS FOR PLASTISOL-NITROCELLULOSE PROPELLANTS

Measurements of velocity vs diameter on plastisol-nitrocellulose composite propellants* were used to develop a relation between the quantity $(U^\circ - U_f)/U^\circ$ and D_f (Table 1 and Fig. 1). Formulation A-1 is an aluminized, ammonium perchlorate-containing propellant. Formulation B has the same oxidizer-to-binder ratio as A-1, but contains no aluminum. Formulations C, D, and E resemble B but with the specified amount of RDX replacing an equal weight of ammonium perchlorate. Fig. 1 shows that $\log [(U^\circ - U_f)/U^\circ]$ vs D_f gives a straight line:

$$-\log \left(\frac{U^\circ - U_f}{U^\circ} \right) = 0.0415 D_f + 0.990 [D_f \text{ in cm}]. \quad (8)$$

*See Part I: Attempts to Calculate Reaction-Zone Thickness.

Fig. 1 - Empirical relation between D_f and $(U^\circ - U_f)/U^\circ$ for plastisol-nitrocellulose composite propellants (Eq. (8))

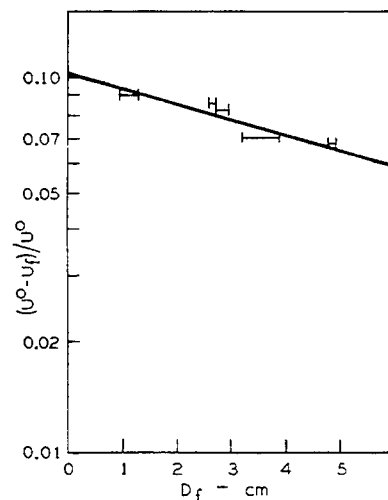


TABLE 1
Detonation Parameters for Plastisol-Nitrocellulose Propellants

Formulation	% RDX	D_f (in.)	U^o (mm/ μ sec)	$(U^o - U_f)/U^o$
A-1	0	1.05-1.15	6.407	0.081
B	0	1.82-1.92	6.598	0.066
C	5.88	1.25-1.50	6.702	0.069
D	15.00	1.00-1.05	7.060	0.085
E	35.29	0.36-0.50	7.309	0.090

Equations (6) and (8) were applied to Formulations C, D, and E to back-calculate the failure diameter of Formulation B. The calculated value was $D_f = 1.96$ in. compared with a measured value of 1.82 in. $< D_f < 1.92$ in., giving a satisfactory check on the calculation.

Another series of failure-diameter measurements [3] had been made on a different plastisol propellant composition with varying amounts of RDX. The base composition contained 20 percent aluminum, 30 percent ammonium perchlorate and 50 percent binder. The RDX added replaced an equal weight of ammonium perchlorate. The failure diameters measured for the RDX-containing formulations are given in Table 2. These data were used to calculate the failure diameter of the propellant with no RDX. Values of U^o were assumed from the data on other similar formulations. The calculated value of D_f was 1.26 in.; the measured value was 1.05 in. $< D_f < 1.38$ in.

TABLE 2
Failure Diameters for Aluminized, Plastisol-Nitrocellulose Composite Propellant, with RDX Replacing a Portion of the Ammonium Perchlorate (Ref. 3)

% RDX	D_f (in.)	% RDX	D_f (in.)
2	0.82-1.05	10	0.36-0.62
5	0.65-0.82	20	< 0.36

Inspection of Eqs. (6) and (8) shows that, depending on the value of AU_f/Q , the number of possible solutions is two, one, or none. The two curves are tangent (single solution) when $AU_f/Q \approx 0.4$ and $D_f = 11$ cm or 4 in. For $AU_f/Q < 0.4$ there are two solutions and for $AU_f/Q > 0.4$, none. Thus any material to which Eq. (8) applies must have a failure diameter under 4 in. or it will not detonate. Since A/Q is

proportional to the reaction time, this sets an upper limit on the possible reaction time for detonation.

APPLICATION OF METHOD TO INERT-BINDER PROPELLANTS

The propellants to which the failure-diameter method was applied have failure diameters which are easily measured. The real value of this technique would be for the prediction of failure diameters in relatively inert materials, which have failure diameters too large to measure directly. If Eq. (8) were valid, it would indicate that no material with a failure diameter over 4 inches would be detonable. This was tested for a polybutadiene-acrylic acid composite.

Two PBAA formulations containing RDX were selected for velocity determinations. The base formulation was composed of 62.5 weight percent of a bimodal blend, 70 percent 180μ and 30 percent 105μ weight-median-diameter ammonium perchlorate, 12.5 weight percent 3-5 μ aluminum in a PBAA binder. To this base Type B, Class E RDX was added to make formulations which contained 25 and 18 percent RDX. The failure diameters and velocities as a function of diameter were measured as described in Part I.* Rather than substitute RDX for ammonium perchlorate and maintain a constant solids loading, RDX, which is stoichiometrically balanced, was added to the fixed-composition base propellant so that the stoichiometry of the final propellant would be constant.

Failure-diameter measurements were also made on formulations containing 20 and 16 percent RDX.

The detonation velocities as a function of charge diameter are given in Table 3 for the formulations containing 18 and 25 percent RDX. The velocities are plotted as a function of $1/D$ in Fig. 2. The straight lines shown in the figure are

$$\frac{U}{5.738} = 1 - \frac{0.0448}{D} \quad (9)$$

for 25 percent RDX and

$$\frac{U}{5.358} = 1 - \frac{0.117}{D} \quad (10)$$

for 18 percent RDX.

*See Part I: Attempts to Calculate Reaction-Zone Thickness.

TABLE 3
Diameter-Dependence of Detonation
Velocity of PBAA-Binder Propellants
Containing RDX

% RDX	D_f (in.)	Charge Diam- eter (in.)	Velocity (mm/ μ sec)
25	1.00-1.15	1-1/4	5.519
		1-1/4	5.531
		2	5.594
		2	5.644
		2-1/2	5.633
		2-1/2	5.622
		4	5.666
18	2.25-2.50	2-1/2	5.116
		3	5.144
		3	5.137
		4	5.222
		4	5.188
		6	5.252

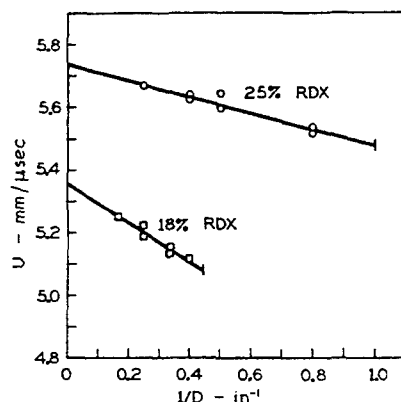


Fig. 2 - Diameter-dependence
of detonation velocity of PBAA
composite propellants contain-
ing RDX

Table 4 gives the detonation parameters calculated with Eqs. (9) and (10). An average value of 1.08 in. was used for D_f of the 25-percent-RDX formulation. Since there was one "no go" obtained for the 18-percent-RDX formulation at 2.5 in. in five determinations, 2.5 in. was used for the failure diameter of this formulation.

If a relation of the form of Eq. (8) is assumed, the following relation is obtained from the detonation parameters of these two formulations (Table 4):

$$-\log \left(\frac{U^0 - U_f}{U^0} \right) = 1.4178 - 0.0352 D_f [D_f \text{ in in.}] \quad (11)$$

TABLE 4
Detonation Parameters for PBAA
Propellant Containing RDX

% RDX	D_f (in.)	U^0 (mm/ μ sec)	U_f (mm/ μ sec)	$(U^0 - U_f)/U^0$
25	1.00-1.15	5.735	5.496	0.0417
18	2.25-2.50	5.358	5.107	0.0468

Solving for the constants in Eq. (6) gives
 $Q_2 = -210$ cal/gm and $A = 1.325$ or

$$D_f \left(\frac{U^0 - U_f}{U^0} \right) = \frac{1.325 U_f}{1280 n_1 - 210 n_2} \quad (12)$$

This equation was used to plot curves of $(U^0 - U_f)/U^0$ vs D_f for formulations containing 25, 20, 18, and 16 percent RDX (Fig. 3). The failure diameter of a particular formulation is given by the intersection of the curve of Eq. (12) for that formulation with the curve given by Eq. (11). Comparison of the calculated and measured failure diameter shows good agreement for all formulations except that containing 16 percent RDX (Table 5).

TABLE 5
Calculated and Measured Failure Diameters
for PBAA Propellants Containing RDX

% RDX	D_f Measured (in.)	D_f Calculated (in.)
25	1.00-1.15	1.12
20	1.61-1.75	1.81
18	2.25-2.50	2.52
16	2.75-3.00	4.63

The large discrepancy between the measured and calculated failure diameter for the 16-percent-RDX formulation indicates that Eq. (11) does not adequately describe this propellant system. Before the method described above can be applied to inert-binder systems, a relation between D_f and $(U^0 - U_f)/U^0$ must be determined by velocity-versus-diameter measurements at several RDX concentrations.

Because $(U^0 - U_f)/U^0$ appears to increase with increasing failure diameter, there is no

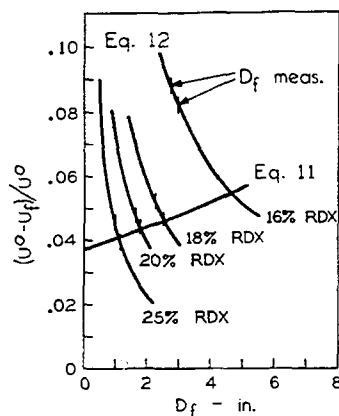


Fig. 3 - Calculated relation between D_f and $(U^o - U_f)/U^o$ for PBAA composite propellants containing RDX

limiting failure diameter as there was in the case of plastisol-nitrocellulose propellants. However, in this case the negative value of Q_2 would be limiting. When $n_1Q_1 + n_2Q_2 = 0$, detonation is no longer possible. The significance of a negative value of Q_2 can be seen by considering this as an effective heat of reaction for this particular detonation reaction. If the ammonium perchlorate does not react in the detonation reaction zone, but instead reacts beyond the C-J plane and some of the energy released by the RDX is used to start reaction in the ammonium perchlorate, Q_2 would appear as a negative quantity. This, in effect, would mean that the base propellant is not detonable.

CONCLUSION

A method of obtaining the failure diameter of a propellant by measurements on RDX-containing formulations has been developed. The method works well for plastisol-nitrocellulose composite formulations, with the use of an empirical relation between D_f and $(U^o - U_f)/U^o$ obtained for these formulations.

An attempt to apply the same empirical relation to PBAA-binder propellants was unsuccessful. Further work must be done to develop a relation for this system. Indications from the experiments which have been done are

that the base propellant is not detonable in this case.

ACKNOWLEDGMENT

This work was sponsored by the Advanced Research Projects Agency of the Department of Defense and by the U.S. Air Force under Contracts DA-01-021 ORD-11909(Z) and DA-01-021 506 ORD-785(Z), respectively, both administered through the U.S. Army Missile Command.

The authors would like to thank Dr. Henry M. Shuey of these Laboratories under whose direction this investigation was initiated. We would also like to thank Messrs. J. F. Foster and R. T. Smith for formulating and casting the charges.

REFERENCES

1. M. W. Evans, *J. Chem. Phys.* **36**, 193 (1962).
2. H. Eyring, R. E. Powell, G. H. Duffey, and R. B. Parlin, *Chem. Rev.* **45**, 69 (1949).
3. W. W. Brandon, Rohm & Haas Company Quarterly Progress Report on Interior Ballistics, P-61-7, October 3, 1961 (Confidential), p. 10.

NON-IDEAL DETONATION WITH CONSTANT LATERAL EXPANSION

Franz Wecken

*Deutsch-Französisches Forschungsinstitut Saint-Louis
France*

ABSTRACT

Based on simple assumptions for the equation of state, reaction rate and increase of cross section behind the shock front, ordinary differential equations are established which determine the structure of the reaction zone of a steady non-ideal detonation in a perfect gas. Starting the numerical integration at the C-J point, profiles of the reaction zone for $\gamma = 1.4$ and $\gamma = 3$ are obtained, and examples are presented in the form of graphs. The range and limit of detonation for a given initial state are discussed, and for $\gamma = 1.4$ some limit curves are plotted. Some concluding remarks concern nonsteady detonations.

1. INTRODUCTION

A nearly steady, non-ideal detonation, i.e., one with a convex curved shock front and with a detonation velocity inferior to its normal value, occurs with a detonating gas column or an explosive rod of a moderate diameter, with or without confinement. The preference given to steady cases in theoretical studies is justified, the exact definition of "detonation" under unsteady conditions being rather problematic. In numerous papers [1-6] non-ideal detonations have been studied theoretically, always with strongly simplifying approximative assumptions.

In the plane and axisymmetric cases there is a two-dimensional flow with a subsonic and a supersonic range. Mathematical difficulties are caused by the mixed (elliptic and hyperbolic) behavior, by the shock wave shape and detonation velocity both unknown a priori, and by the simultaneous chemical reaction. An isolated investigation of the velocity deficit without determining the flow pattern and reaction profile is not satisfactory. Further complications, such as three-dimensional geometry, unsteady processes, mechanical behavior of the surroundings, transport properties and instabilities may be disregarded in a first approximation.

But the interaction of flow and reaction may even be studied in case of a single stream filament by making appropriate assumptions on the variation of cross section $A = A(z)$ along the

stream line, replacing thereby the interdependence of the different stream filaments.

Once $A(z)$ has been fixed the problem is similar to the case of the ideal detonation ($A = \text{const}$). According to shock strength or oncoming flow velocity the integration of the relevant differential equations will in general give a zone pattern either totally subsonic or terminated by thermal choking at the sonic limit, therefore not resulting in a steady solution. The desired solution represents the limiting case of these two domains — corresponding to the experimental fact that the stable, self-propagating detonation forms the limiting case between shocks running too fast and decelerating (overdriven detonations) and those running too slowly and self-accelerating.

To fix $A(z)$ we use the quantity

$$\frac{1}{A} \frac{dA}{dz} = \epsilon, \quad (1)$$

occurring in the basic equations, as a local measure of the lateral expansion, and we assume it to be a constant for simplicity and for want of detailed information. So we can calculate reaction profiles; further by variation of shock intensity (or shock Mach number M_0) and expansion coefficient (ϵ) we can find the conditions for the development of a detonation. The limiting curve in the $M_0 - \epsilon$ plane is in general not monotonic; the descending branch represents

the dependence of the detonation velocity on the confining conditions; the ascending branch is interpreted as a sensitivity curve.

The numerical calculations have been carried out on a Bull Gamma ET Computer.

2. ESTABLISHMENT OF THE DIFFERENTIAL EQUATIONS

The fundamental equations of one-dimensional steady flow in the usual notation, with (1), $v = 1/\rho$ and with a single reaction progress variable λ read

$$\begin{aligned} dz &= u dt, & u du + v dp &= 0, & dH - v dp &= 0, \\ \frac{dv}{v} - \frac{du}{u} &= \epsilon dz, & d\lambda &= r dt. \end{aligned} \quad (2)$$

It follows immediately

$$H + \frac{u^2}{2} = \text{const} = H_r. \quad (3)$$

Concerning state equation, reaction rate and expansion we make the special assumptions

$$H = H(p, v, \lambda) = h(p, v) + q(\lambda), \quad q \geq 0, \quad (4)$$

$$h = \frac{\gamma}{\gamma-1} p v, \quad q = \lambda H_r, \quad \gamma = \text{const};$$

$$r = r(p, v, \lambda) = -\frac{\lambda}{t_c} e^{-h_c/h}, \quad (5)$$

$$\begin{aligned} t_c &= \text{const}, & h_c &= \text{const}; \\ \epsilon &= \text{const}. \end{aligned} \quad (6)$$

The expression (5), derived from Eq. (30) in Ref. 3, has been so chosen that in near-equilibrium the reaction rate is proportional to the distance from the equilibrium. Equation (4) implies $0 \leq \lambda \leq 1$. The stagnation enthalpy H_r only apparently enters into the rate function.

We need further the (frozen) sound velocity a , the coefficient σ serving as a measure of the mechanical effect of the reaction [7]

$$a = v \sqrt{\frac{\partial H / \partial v}{\partial H / \partial p - v}}, \quad \sigma = -\frac{\partial H / \partial \lambda}{v \partial H / \partial v}$$

and the flow Mach number $M = u/a$.

From (4) results

$$a^2 = \gamma p v = (\gamma-1)h, \quad \sigma = -H_r/h, \quad (7)$$

from (2) and (6)

$$\frac{u}{v} e^{\epsilon z} = \text{const}. \quad (8)$$

Using the integrals (3), (8) and dropping the time t Eq. (2) is reduced to a system of second order that may be written

$$\frac{du}{dz} = \frac{\epsilon u - \sigma r}{M^2 - 1}, \quad \frac{d\lambda}{dz} = \frac{r}{u}. \quad (9)$$

The flow starting with $M < 1$ behind the normal shock and later on proceeding to $M > 1$, according to Eq. (9) a point with*

$$\epsilon u = \sigma r \quad \text{at } M = 1 \quad (10)$$

(C-J point) has to be passed (generalized C-J condition).

One might suppose that in the general case the integration starting at the shock either ends at $M = 1$, $\epsilon u \neq \sigma r$ (choking, no steady solution, self-acceleration) or remains totally subsonic (can only be steady with energy supply; otherwise decelerating), and that transonic integration paths satisfying Eq. (10) (steady and self-propagating; not necessarily stable) are realized only as limiting cases between these two types. But this conception will be corrected later on.

By introducing dimensionless quantities and using Eq. (7) we obtain from (9) a differential equation

$$\begin{aligned} \frac{dM}{d\lambda} &= \left(1 + \frac{\gamma-1}{2} M^2\right) \frac{M}{1-\lambda} \\ &\times \left[\left(1 + \frac{\gamma-1}{2} M^2\right) (M^2 - 1)^{-1} \left(1 - \frac{\epsilon u}{\sigma r}\right) + \frac{1}{2} \right] \end{aligned} \quad (11)$$

with

$$\frac{\epsilon u}{\sigma r} = \frac{\epsilon'}{H_r} \frac{M}{\lambda} h'^{3/2} e^{1/h'},$$

$$h' = \frac{h}{h_c} = H_r'(1-\lambda) / \left(1 + \frac{\gamma-1}{2} M^2\right),$$

$$\epsilon' = \epsilon t_c \sqrt{(\gamma-1)h_c}, \quad H_r' = H_r/h_c. \quad (12)$$

Integration of Eq. (11) yields $M = M(\lambda)$ and h ; then H is found from (4), u from (3), z by quadrature according to (9), v from (8), p from (4).

*Since $\sigma r > 0$ and $u > 0$ we must have $\epsilon > 0$.

3. INITIAL VALUES AND SINGULAR POINTS

We suppose the original substance (index 0) to impinge normally on a convex shock front with a velocity u_0 . The state behind the vertex of the shock (index 1) uniquely results by application of the shock conditions. If the flow is plane or axisymmetric we get $\epsilon = 1/R[(v_0/v_1) - 1]$ in the first and $\epsilon = 2/R[(v_0/v_1) - 1]$ in the second case, R being the vertex curvature radius (cf. Ref. 3, Eq. (19*)). Therefore we can replace R by ϵ and characterize the shock by the dimensionless parameters

$$\{h'_0 = h_0/h_c, \quad q'_0 = q_0/h_c, \quad M_0, \epsilon'\}. \quad (13)$$

Corresponding to the ω^4 possible initial conditions (13) there are, for a fixed γ, ω^4 integral paths which have to be classified as choking, subsonic and transonic. The first type is separated within the parameter space from the second type by the third; therefore we have only to look for the transonic paths. We begin the integration of (11) at the C-J point P_* ; afterwards we shall determine the corresponding initial values (13).

So we choose λ_* and h'_* with

$$0 < \lambda_* < 1, \quad 0 < h'_* < \infty; \quad (14)$$

the quantities (12) determining the direction field for (11) are functions of these values:

$$\epsilon' = \lambda_* h'_*{}^{-3/2} e^{-1/h'_*} H'_r, \quad H'_r = \frac{\gamma+1}{2} \frac{h'_*}{1-\lambda_*}. \quad (15)$$

The direction field (Fig. 1) has two singular points, P_1 and P_2 ; detailed discussion [8,9] shows that P_1 (with smaller value λ) is always

a saddle point whereas P_2 is either a nodal or a focal (spiral) point. The range (14) is divided into three zones (Fig. 2):

$$h'_*{}^{-1} < \lambda_*^{-1} + \frac{1}{2}: \quad P_* = P_1 \text{ (saddle)} \quad (16)$$

$$\lambda_* > \tilde{\lambda}(h'_*): \quad P_* = P_2 \text{ (focus)}$$

$$\tilde{\lambda} = \left[\frac{f^2 + 1}{2} - \frac{(h'_*{}^{-1} - f^2 - 1)^2}{2f^2} \right]^{-1}, \quad f = \frac{2}{\gamma - 1} \quad (17)$$

$$h'_*{}^{-1} - \frac{1}{2} > \lambda_*^{-1} > \tilde{\lambda}^{-1}: \quad P_* = P_2 \text{ (node)}. \quad (18)$$

The boundary

$$\Lambda_1: \quad h'_*{}^{-1} = \lambda_*^{-1} + \frac{1}{2},$$

on which $P_1 = P_2$, is independent of γ . The second boundary

$$\Lambda_2: \quad \lambda_* = \tilde{\lambda}(h'_*)$$

merges for $\gamma \rightarrow 1$ in the lines Λ_1 and $h'_* = 0$, so that the nodal zone disappears. At $\gamma = 3$ it follows $\tilde{\lambda} \geq 1$, so the focal zone vanishes.

The transonic paths must, besides Eq. (10), fulfill at P_* the condition $dM/d\lambda < 0$. In the saddle case there is at P_* exactly one characteristic direction with negative slope:

$$\left(\frac{dM}{d\lambda} \right)_* = \frac{1}{2} \frac{H'_r}{h'_*} \left[f^{-1}(1 - h'_*{}^{-1}) - \sqrt{f^{-2}(1 - h'_*{}^{-1})^2 + 2\lambda_*^{-1} + 1 - 2h'_*{}^{-1}} \right]. \quad (19)$$

The separatrix passing through $P_* = P_1$ in this direction (heavy continuous line in Fig. 1a,b)

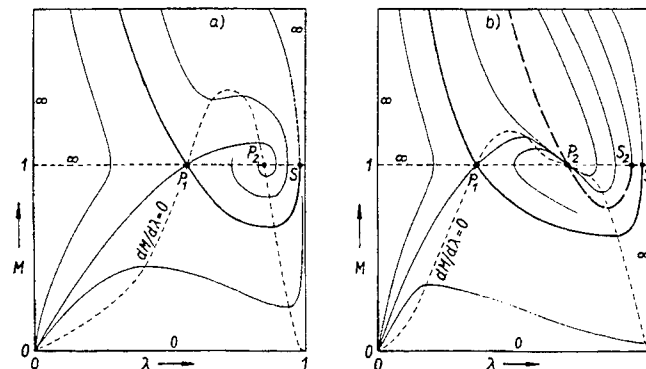


Fig. 1 - Direction field, singular points and integral curves (schematic); lines of horizontal (0) and vertical direction (∞); (a) saddle and focal points, (b) saddle and nodal points

has the desired properties and separates choking paths from subsonic paths, forming an element of the detonation limit we are looking for. The paths satisfying (16) and (19) are shortly called " ℓ paths."

In the nodal case (18) there are at P_* two negative characteristic slopes: (19) with a uniquely determined quasi-separatrix (heavy dashed line in Fig. 1b), the other with ∞^1 integral paths in each of two directions (subsonic and supersonic). These are separated from choking paths by the quasi-separatrix.

Hence the transonic paths through P_2 do not border on subsonic paths but are situated within the detonation range, this being characterized by paths attaining $M = 1$. We shall not further investigate the physical meaning of the paths through P_2 , but refer to some papers [10-12] on ideal detonation with two reactions, which seem to be concerned with quite similar problems.

The focal case (17) yields no transonic paths.

The physically meaningful part of each ℓ path (Figs. 1, 3) extends in the supersonic range to a point P_∞ with $M = \infty$, $z = \infty$, $0 < \lambda_\infty < \lambda_*$; the chemical equilibrium ($\lambda = 0$) is not attained, the reaction freezing previously owing to strong expansion. In the subsonic range the ℓ path ends at a second sonic point S with $(dM/d\lambda)_S = \infty$, $\lambda_* < \lambda_S < 1$. Between P_* and S , M has a minimum value on the ℓ path:

$$M = M_{\min} \text{ at } \lambda = \lambda_m.$$

Now, in order to coordinate an initial state (13) with the C-J state $P_* = P_1$, we choose a

value $\lambda = \lambda_1 = \lambda_0$ with $\lambda_* < \lambda_1 < \lambda_S$ and with corresponding values M_1, u_1, v_1, p_1 given by the integration. From Eq. (15), (4) and the jump conditions

$$\frac{p_1}{p_0} = \frac{\gamma + 1}{2\gamma M_1^2 - \gamma + 1}, \quad M_0^2 = \frac{\gamma + 1}{2\gamma} \frac{p_1}{p_0} + \frac{\gamma - 1}{2\gamma}, \quad (20)$$

$$\frac{u_0}{u_1} = \frac{v_0}{v_1} = \frac{(\gamma + 1)p_1 + (\gamma - 1)p_0}{(\gamma - 1)p_1 + (\gamma + 1)p_0}$$

the initial parameters (13) result uniquely as far as

$$M_1^2 > \frac{\gamma - 1}{2\gamma}. \quad (21)$$

Hence for $M_{\min}^2 > (\gamma - 1)/2\gamma$ (cf. Fig. 5) all values λ_1 between λ_* and λ_S are permitted; in case of

$$M_{\min}^2 < (\gamma - 1)/2\gamma \quad (22)$$

there is between λ_* and λ_S a smaller interval, the points of which do not represent shock states, (21) being invalid.

Thus the ∞^2 saddle states (Fig. 2) give ∞^3 initial states which in the parameter space (13) form the hypersurface referred to as detonation limit. The nodal states on the other hand yield ∞^3 transonic paths and ∞^4 initial states.

4. MARGINAL CASES

Of the four margins of the saddle zone (Fig. 2) the line $\lambda_* = 0$ is the most important, as it corresponds to the ideal detonation ($\epsilon = 0$) because of Eq. (15). The supersonic part of

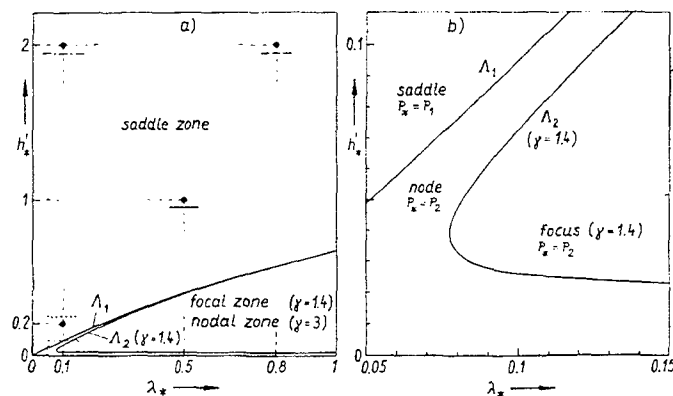


Fig. 2 - Ranges and limits for P_* ; (a) position of and key to the examples in Figs. 3-10, (b) detail from (a)

the λ - M curve (Fig. 3) for $\lambda_* \rightarrow 0$ degenerates into a straight line $\lambda \approx \text{const} \approx 0$ and disappears at $\lambda_* = 0$. For the subsonic part

$$\lim_{\lambda_* \rightarrow 0} M_{\min} = 0,$$

$\lim_{M \rightarrow 1} \lambda_m = 1$ holds; the ascending branch merges into the segment $\lambda = 1$, $0 < M < 1$ and is finally omitted. The descending branch for $\lambda_* = 0$ is represented by algebraic formulae [13] not depending on h_*

$$M^2 = (1 - \sqrt{\lambda}) / (1 + \gamma \sqrt{\lambda}),$$

$$u/a_* = v/v_* = 1 - \sqrt{\lambda}, \quad p/p_* = 1 + \gamma \sqrt{\lambda}.$$

z has to be calculated by quadrature; it transpires that $z_* = \infty$. Because of Eq. (21) the condition $\lambda < \gamma^{-2}$ is to be imposed, and the dashed parts of the curves in Fig. 3c become insignificant. On the border $\epsilon' = 0$ of the parameter space (13) the detonation limit is represented by

$$2(\gamma + 1) q'_0 = h'_0 (M_0 - M_0^{-1})^2. \quad (23)$$

On the border curve Λ_1 there is $P_1 = P_2$; the ℓ path (separatrix) becomes a quasi-separatrix without degenerating. It is only when P_* traverses Λ_1 and approaches Λ_2 that the subsonic part shrinks to a point, whereby $M_{\min} \rightarrow 1$. So Eq. (22) is violated near Λ_2 but fulfilled for $\lambda_* \approx 0$. The earlier mentioned dependence of the position of Λ_2 on γ explains the fact that (22) holds in the whole saddle zone for $\gamma = 3$ but not for $\gamma = 1.4$ (see Fig. 5).

At the margins $h'_* = \infty$ and $\lambda_* = 1$ some degeneration of the ℓ paths occurs which can be overcome by using other variables.

5. CALCULATED REACTION ZONE STRUCTURES

By numerical integration following the Runge-Kutta method about 100 ℓ paths have

been calculated for $\gamma = 1.4$ and 60 for $\gamma = 3$. For graphs to be presented eight cases (four for each γ) have been chosen and distinguished by different lines according to Fig. 2a and Table 1. Each of the Figs. 3-10 (zone structures of eight ℓ paths) shows separately the examples for $\gamma = 1.4$ (part a) and $\gamma = 3$ (part b). Table 1 gives some characteristic numerical values.

Figure 3 shows the direct result of the integration of Eq. (11). In many cases the curvature near $M = M_{\min}$ was very strong, making a careful choice of the step size necessary. The freezing for $M \rightarrow \infty$ is more pronounced for $\gamma = 3$ than for $\gamma = 1.4$; further it is favoured by a low C-J temperature (low h'_*). The limit values

$$\lambda_\infty = \lim_{M \rightarrow \infty} \lambda$$

are listed in Table 1.

Figures 4-7 illustrate the reaction zone structure by plotting λ , M , h/h_c , p/p_* as functions of a dimensionless space coordinate $z' = \epsilon z h'_*^{-1/2}$ which was chosen so that $z'_* - z'_s$ shows a small variation. It was convenient to assume $z'_* = 0$, so $M \geq 1$ for $z' \geq 0$.

The examples largely behave in a similar manner showing clear differences from the ideal detonation (Fig. 3c) which are essential for subsequent considerations (sect. 6).

At high h'_* there is in Figs. 4-7 a well defined induction time after which the reaction starts abruptly. Depending on the value of λ_* a considerable part of the reaction may still occur in the supersonic range (Fig. 4), discernible from the difference $\lambda_* - \lambda_\infty$ (Table 1) or quotient $(\lambda_* - \lambda_\infty) / (\lambda_s - \lambda_*)$.

One of the examples (Fig. 6a) shows a remarkable temperature rise due to the reaction even in the supersonic range, whereas all

TABLE 1
Numerical Values Belonging to Figs. 3-10

γ	h'_*	λ_*	ϵ'	H'_r	M_{\min}	λ_∞	
1.4	0.2	0.1	0.0020	0.267	0.64	0.010	-----
1.4	1	0.5	0.441	2.40	0.43	0.109	=====
1.4	2	0.1	0.0572	2.67	0.13	3.8×10^{-5}	-----
1.4	2	0.8	2.06	12.0	0.27	0.388	-----
3	0.2	0.1	0.0033	0.444	0.27	0.082	-----
3	1	0.5	0.736	4.00	0.22	0.369	=====
3	2	0.1	0.0953	4.44	0.075	0.015	-----
3	2	0.8	3.43	20.0	0.15	0.635	-----

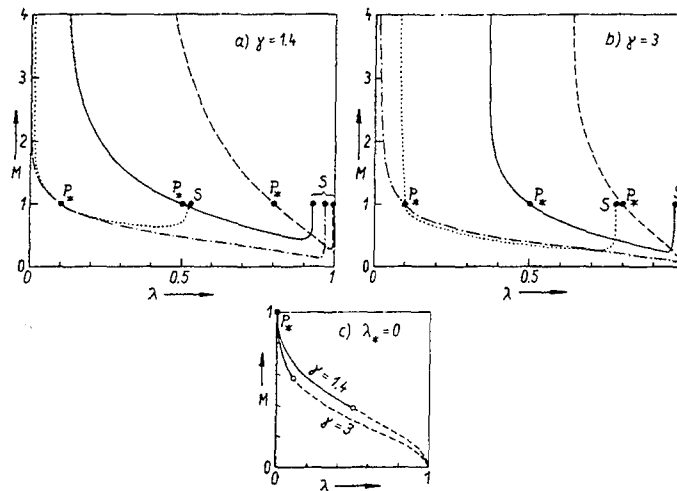


Fig. 3 - Integral curves to Eq. (11); (a) (b) four examples in each case according to Fig. 2a, (c) ideal detonations for comparison

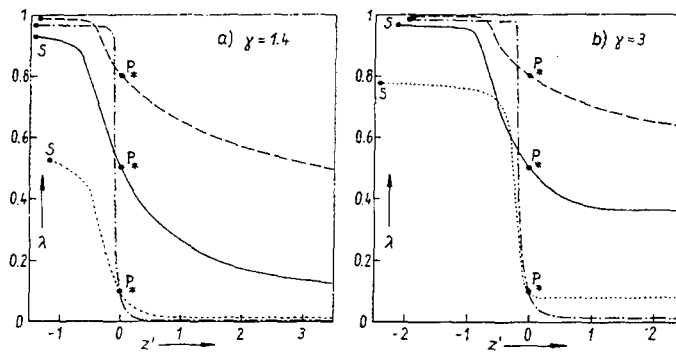


Fig. 4 - Spatial variation of the reaction progress variable

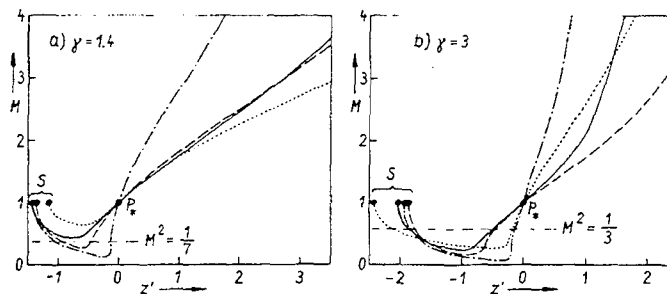


Fig. 5 - Spatial variation of the flow Mach number $M = u/a$ for eight ℓ paths; cf (22)

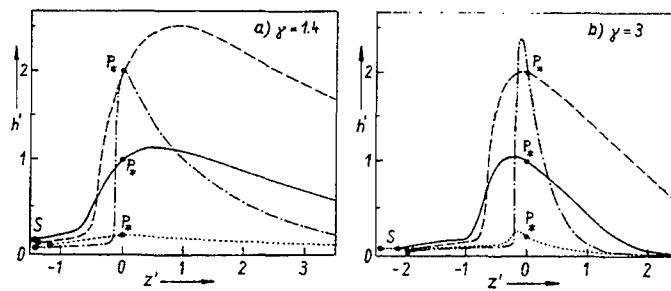
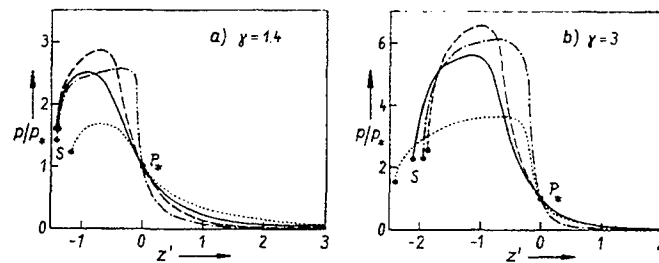
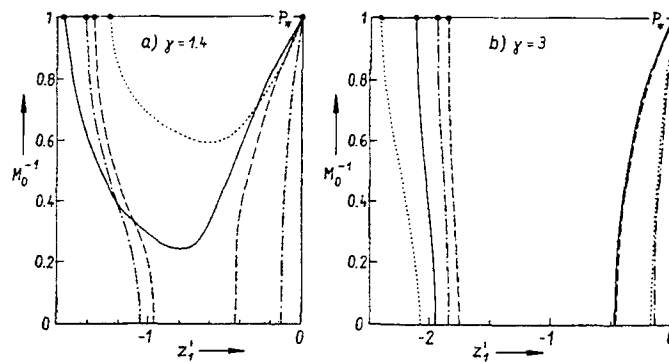
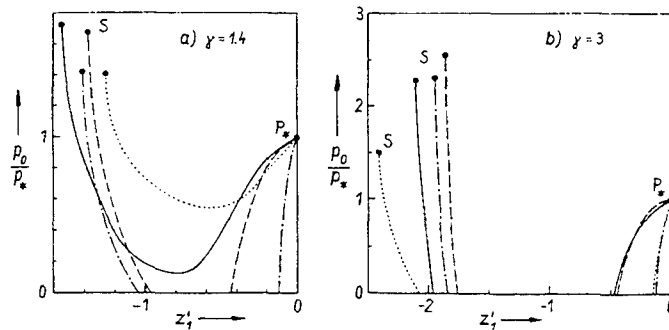

 Fig. 6 - Spatial variation of the enthalpy, $h' = h/h_c$


Fig. 7 - Spatial variation of pressure


 Fig. 8 - Reciprocal initial flow or shock Mach number $M_0^{-1} = a_0/u_0$ as a function of the space coordinate or negative zone depth z'_1

 Fig. 9 - Reciprocal detonation pressure ratio as a function of the space coordinate or negative zone depth z'_1

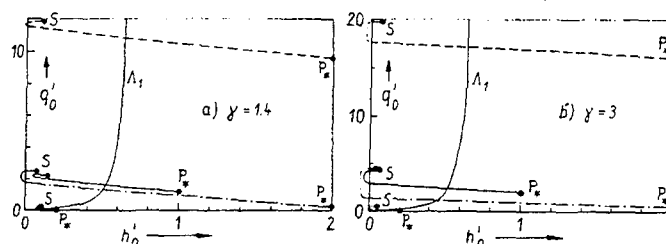


Fig. 10 - Chemical-thermodynamical initial states $Q = \{h'_0, q'_0\}$ along Γ paths, parts of discontinuous curves have been connected by light lines, curve Λ_1 as in Fig. 2

2 paths calculated with $\gamma = 3$ had their maximum of enthalpy in the subsonic range. The pressure maximum found in all cases in the subsonic range (Fig. 7) may amount to a multiple of the C-J pressure at high values of γ and ϵ' .

Figures 8-10 have to do with the state of the oncoming flow which is related by (20) to the subsonic state interpreted as a shock state insofar as (21) is valid. The 6 examples with (22), therefore, show curves with an interruption. Figure 8 shows the shock Mach number, Fig. 9 the detonation pressure ratio as a function of the space coordinate z'_j , that is of the distance between shock and C-J plane.

6. DETERMINATION OF DETONATION LIMITS

Figure 10 shows for the chosen examples the image curves in the $h'_0 - q'_0$ plane, i.e., the manifold of the chemical-thermodynamic initial states $Q = \{h'_0, q'_0\}$ belonging to P_* . P_* and S are among them, and the relations

$$h'_0 = h'_*, \quad q'_0 = \frac{\gamma+1}{2} \frac{h'_* \lambda_*}{1-\lambda_*}$$

valid in case of $\lambda_1 = \lambda_*$ bring about a one-to-one correspondence between the domains $0 < \lambda_* < 1$, $h'_* > 0$ (Fig. 2) and $q'_0 > 0$, $h'_0 > 0$. Curve Λ_1 has the equation

$$q'_0 = (\gamma+1) h_0'^2 / (2 - 3h'_0)$$

(Fig. 10). P_* is situated in the saddle zone, to the right of Λ_1 ; S was always found to the left of Λ_1 . Through every point Q run ∞^1 integral curves, and the corresponding ∞^1 pairs of values $\{M_0, \epsilon'\}$ form the detonation limit for the state Q . By evaluating the calculated paths, redrawing and interpolation we obtained such limiting curves for $\gamma = 1.4$ (Fig. 11a-c).

From (5) it results that $r \neq 0$ for $h > 0$, $\lambda > 0$; the reaction takes place however weak the shock wave, the detonation range extending to $\epsilon' = 0$, $M_0 = 1$. Accordingly limit curves of type I or II (Fig. 11d) were found, ending at $M_0 = 1$ with $\epsilon' > 0$.

A more realistic curve, such as III in Fig. 11d, would result if we set $r = 0$ beneath a temperature limit (ignition temperature). Our assumption should, with a sufficiently small h'_0 (and possibly small q'_0), also yield curves approaching the form III. Studies in this sense have not yet been possible because of the necessary accuracy or the amount of computation work.

On Λ_1 being always $h'_0 \leq 2/3$ the Q with $h'_0 = 0.7$ (Fig. 11a) are all situated in the saddle zone. The manifold of the ∞^1 C-J states P_* corresponding to Q then has one of its ends at the ideal detonation, cf. (23):

$$\epsilon' = \lambda_* = 0, \quad M_0 = \sqrt{\frac{\gamma+1}{2} \frac{q'_0}{h'_0}} + \sqrt{1 + \frac{\gamma+1}{2} \frac{q'_0}{h'_0}},$$

the other at $P_* = Q$ with

$$M_0 = 1, \quad h'_* = h'_0, \quad H'_r = q'_0 + \frac{\gamma+1}{2} h'_0, \quad \lambda_* = \frac{q'_0}{H'_r}, \quad \epsilon' =$$

from (15). Both end points of the limiting curve are given explicitly without integration. In case of Fig. 11b,c this is only valid for the first mentioned end point: Q lies to the left of Λ_1 , $P_* = Q$ is not possible. The end point $M_0 = 1$ is realized by $S = Q$; determination requires the integration of (11).

7. DISCUSSION

Detonation Limit Curves

The monotonic curve type I (Fig. 11d) cannot occur in real cases for this would mean that

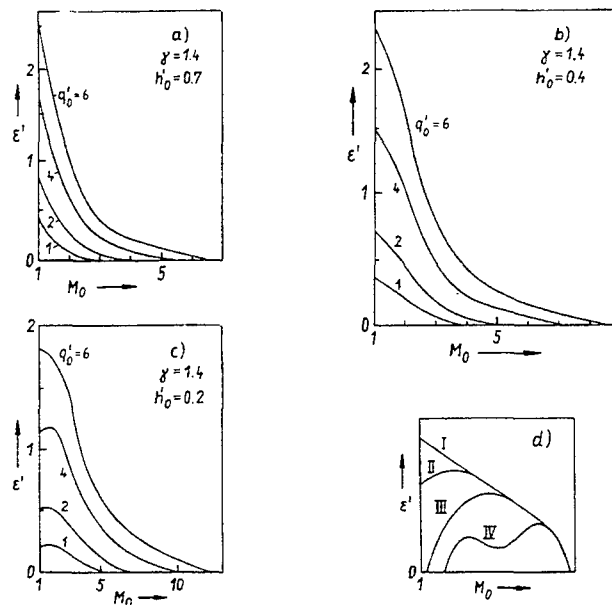


Fig. 11 - Detonation limits for fixed initial states; (a) (b) (c) calculated limit curves, (d) possible curve shapes for ideal and real substances

even a shock of vanishing strength would initiate a vigorous reaction, in other words that the initial state cannot exist. A stable substance, insensitive even with a strong confinement (small ϵ) against shocks of moderate intensity may have a limiting curve of type III.

Whereas the descending branch of the limiting curve describes the dependence of the stable detonation velocity on the confinement conditions, the ascending branch expresses the sensitivity of the explosive to shocks — more precisely: to nearly steady shock waves with a constant expansion behind their front. One should coordinate effective values M_0 and ϵ with an arbitrary shock load in order to localize the process with respect to the detonation limit.

Two detonation speeds at a given charge diameter also resulted formally in Ref. 6, Fig. 6. However, the discussion in this reference concerning the second branch appears somewhat unsatisfactory. From our considerations it clearly follows that no stable detonations exist here, because a shock only a little weaker would decelerate and a stronger one would accelerate.

The failure point, the end point of the stable branch, should lie at $\epsilon = \max$ as far as the experimental conditions, e.g., a given charge diameter, are equivalent to $\epsilon \approx \text{const}$. As from experience the detonation speed until failure

falls not more than 10 percent below its normal value, the curves of Fig. 11 c are unrealistic in this respect.

Two stable detonation speeds for the same initial state Q and the same ϵ will exist, if ϵ has two maxima on the limit curve (type IV in Fig. 11 d). If the energy-yielding reactions proceed in two steps with very different rates, after the first step a pseudo-equilibrium will be established. Nevertheless, only a single ideal detonation speed can exist, a true chemical equilibrium being required at the C-J point. But above a certain threshold expansion (corresponding to the minimum of ϵ' in curve IV) suddenly the lower speed may be observed. It is felt that the phenomenon of a twofold detonation speed can be really understood only in the framework of a theory of non-ideal detonation.

While the physical situation is somewhat obscure in the detonation range enclosed by the limiting curve, the remaining range in the $M_0 - \epsilon$ quadrant is uniformly characterized by subsonic paths. It is not possible here logically to separate strong shocks with nearly complete reaction as overdriven detonations from weak shocks with negligible reaction. Therefore, only in the case of processes proceeding at constant area should one speak of "overdriven detonation," otherwise of "shock-induced combustion."

A strong convex steady shock is induced as a detached bow wave by a not too large blunt body fired into an explosive gas with a velocity superior to the normal detonation velocity of the gas (see e.g., Fig. 4a in Ref. 14). The combustion front which, near the vertex, adheres to the shock, further on separates from the shock which eventually degenerates to a Mach line. Decreasing the flight velocity does not produce a self-propagating detonation but the flame is gradually extinguished. So the above stated continuous transition may be demonstrated experimentally.

Unsteady Processes

In spite of being concerned essentially with steady processes, we assigned a corresponding tendency of acceleration or deceleration to a reactive shock of definite strength and front curvature. This is only justified in cases which approach steady behavior.

An important case of a curved unsteady detonation front is the spherical symmetric detonation self-propagating outwards. The theory of Zeldovich (1942), Döring (1944) and Taylor (1950) neglecting the reaction zone length gives as a result a self-similar flow process with constant shock front velocity.

In a non-ideal, quasi-steady treatment, one will assume a reduced detonation velocity, which approaches the normal value with increasing shock front radius R . So it is also found in Ref. 15. Contrary to this, there is the reliable observation that in a big charge a running detonation initiated at the center may decay if an insufficient booster charge is applied [16].

Now there is, according to the above mentioned theory, an infinitely steep pressure decay just behind the front in the spherical and cylindrical case which is impossible for a (nearly) steady detonation in these cases [17]. This may call in question the stability of the expanding detonation (also according to Ref. 18, p. 21). The additional energy released by the booster will at first prevent the steep pressure decay; however, with increasing R , the self-similar solution will establish itself asymptotically, apparently with a far higher effective expansion than corresponding to

$$\epsilon = \frac{2}{R} \left(\frac{v_0}{v_1} - 1 \right)$$

Our method does not apply to detonations running spherically or cylindrically inwards or to other concave detonation waves; for in these cases $\epsilon < 0$ which was to be excluded (see footnote before (10)).

The author is much obliged to Dr. R. Schall for valuable suggestions and discussions.

REFERENCES

1. H. Jones, Proc. Roy. Soc. A 189, 415-426 (1947).
2. H. Eyring, R. E. Powell, G. H. Duffey, and R. B. Parlin, Chem. Review 45, 69-181 (1949).
3. W. W. Wood, and J. G. Kirkwood, J. Chem. Phys. 22, 1920-1924 (1954).
4. J. A. Fay, Phys. Fluids 2, 283-289 (1959).
5. J. Berger, R. Blanchard, and A. Roux, Les ondes de détonation, Symposium, 147-156, Paris, 1962, Centre Nat. de la Rech. Sci.
6. M. W. Evans, J. Chem. Phys. 36, 193-200 (1962).
7. J. G. Kirkwood, and W. W. Wood, J. Chem. Phys. 22, 1915-1919 (1954).
8. C. W. Jones, Proc. Roy. Soc. A 217, 327-343 (1953).
9. J. Kestin, and S. K. Zaremba, Appl. Sci. Res. B 3, 149-189 (1954).
10. W. W. Wood, and Z. W. Salsburg, Phys. Fluids 3, 549-566 (1960).
11. J. J. Erpenbeck, Phys. Fluids 4, 481-492 (1961).
12. J. J. Erpenbeck, Phys. Fluids 7, 1424-1432 (1964).
13. V. V. Pukhnachev, Soviet Phys. - Doklady 8, 338-340 (1963).
14. W. Struth, Proc. 6th Int. Congr. High-Speed Photography, Scheveningen, 443-449. Willink en Zoon, Haarlem, 1963.
15. L. Rudlin, NAVWEPS-Rep. 7364 - DASA 1228 (1961).
16. C. L. Mader, Los Alamos Rep. LA-3297 (1965).
17. R. Chéret, "Theoretical Considerations on the propagation of Shock and Detonation Waves." This symposium.
18. J. H. Lee, "Inviscid Hypersonic Flow of a Detonating Gas." Preprint for CASI Astronautical Symposium, Toronto, 1965.

DETONATIONS IN LIQUID EXPLOSIVES— THE LOW-VELOCITY REGIME

R. W. Watson, C. R. Summers, F. C. Gibson, and R. W. Van Dolah
*Explosives Research Center, Bureau of Mines
U.S. Department of the Interior
Pittsburgh, Pennsylvania*

ABSTRACT

It is well known that some liquid explosives can detonate at either high or low rates depending primarily on the strength of the initiating stimulus. Earlier experimental and theoretical work conducted at the Bureau and elsewhere suggests that inhomogeneities in the form of cavities play an important role in the initiation of both high- and low-velocity detonations. A recent experimental program has been carried out in an effort to define more clearly features that are characteristic of low-velocity detonation in liquids. Photographic studies of the growth, propagation, and stability of low-velocity detonations in 50/50 nitroglycerin-ethylene glycol dinitrate (NG-EGDN) have yielded a simple physical model describing the qualitative features of the phenomena. This model suggests that precursor wall waves with associated rarefactions generate fluid cavitation ahead of the chemical reaction zone. These cavities then serve as incipient reaction centers with initiation occurring when they are overtaken by the high-pressure field associated with the reaction zone. Correlating experiments using air-filled hemispherical cavities located on the free surface of fluids as well as air-filled bubbles in a bulk of the liquid explosive indicate that liquid microjetting may be responsible for the initiation of reaction within the cavities.

INTRODUCTION

It has long been known that most liquid explosives can detonate at either high or low velocities depending on the strength of the initiating stimulus [1], but the basis for the existence of the two regimes has never been satisfactorily elucidated. Experience has shown that strong initiation tended to give high-velocity detonation, and weaker initiation low-velocity detonation. High-velocity detonations (HVD) in homogeneous liquids, for example, require shock initiating pressures of 50 to 100 kilobars [2,3] and progress at rates ranging from 6 to 8 mm/ μ sec depending on the system. These detonation rates, and the associated detonation pressures and temperatures, are in reasonable agreement with values predicted by the hydrodynamic theory of detonation. Low-velocity detonations (LVD), on the other hand, can be initiated by pressures one to two orders of magnitude less than that required for the HVD and have rates of about 2.0 mm/ μ sec. It is generally thought that for the LVD only a fraction of the total available energy serves to

support the detonation wave directly, but various attempts to treat the LVD theoretically have met with only limited success.

In 1919, Stettbacher [4] suggested that low- and high-velocity detonation in nitroglycerin should be associated with the liquid derived from two crystalline modifications recognized for this material. This suggestion was later supported by Dserhkovich and Andreev [5]. This theory was not consistent with observations that both high- and low-velocity detonations could be initiated in the same system with primers of different strength. Bowden and Gurton [6] attempted to define a minimum possible detonation velocity in thin films on the basis of hydrodynamic theory without making a detailed assumption as to the nature of the reaction zone except that reaction took place at reduced pressures because of the absence of confinement. Their theory was not consistent with the observation that the LVD could take place in heavily confined thin films without appreciable lateral expansion. Eyring and associates [7] in a treatment of the diameter-effect derived a double

valued rate-diameter curve and suggested that the LVD may be associated with the lower branch of the curve. This theory predicts that the low-velocity detonation would be impossible below the critical charge diameter. Again, this has not been confirmed experimentally. Schall [8] has treated the stable LVD on the basis of incomplete reaction and the assumption that reaction takes place at specific centers located in the fluid. Support for his theory, as well as the others, suffers from a lack of detailed information concerning the structure of the low-velocity detonation wave and details of the reaction mechanism. Recent experimental work has indicated that inhomogeneities in the form of bubbles play an important role in the initiation of high-velocity detonations [3] and in the initiation and propagation of LVD's [9-13]. Precursor shocks, propagated along container walls ahead of the reaction zone, have also been observed to accompany low-velocity reactions [13,14].

Recently, interest in the low-velocity phenomenon has developed following recognition that these abnormal detonations play an important part in characterizing the hazards of liquid explosive systems, as demonstrated by the too frequent accidents that have occurred in nitroglycerin and liquid monopropellant facilities from relatively mild stimuli. It is the purpose of this paper to describe some experiments carried out at the Explosives Research Center in an effort to define the nature of the low-velocity detonation regime in liquid explosives more clearly.

EXPERIMENTAL STUDIES

Taylor [1] quotes low-velocity detonation rates for nitroglycerin ranging from roughly 1.0 mm/ μ sec to 2.5 mm/ μ sec depending on the diameter of the explosive column and the strength of the initiating source. However, since these values represent rates averaged over the entire length of the column, it cannot be concluded that the rates are constant. Since the question of stability is an essential one in gaining a more thorough understanding of low-velocity detonations (LVD), a series of experiments were conducted to determine the effect of the kind and thickness of confining wall material on the stability of the LVD in 50/50 nitroglycerin-ethylene glycol dinitrate (NG-EGDN).

The basic charge arrangement used in these studies is shown in Fig. 1. It consisted of a cylindrical tube 16 inches long, having a nominal 1-inch inside diameter; a 1-inch long \times 1-5/8-inch diameter tetryl charge coupled to a

4.0-inch long Plexiglas* shock attenuator of the same diameter served as an initiation source. The explosive-attenuator combination delivers a peak pressure of about 2.4 kilobars to the NG-EGDN and has proven adequate for the initiation of a low-velocity reaction under most circumstances. The tube materials investigated were lead, Plexiglas, aluminum, and steel with wall thicknesses of 1/16 inch, 1/8 inch, and 1/4 inch.

Detonation stability was determined from streak camera records of the progress of the luminous reaction front along the entire length of the charge. In the case of transparent Plexiglas containers, the LVD could be viewed directly. The progress of the reaction in opaque containers was viewed through 1/4-inch diameter ports spaced at 1-inch intervals along the length of the tube as indicated in Fig. 1. The ports were sealed by a strip of transparent tape cemented to the interior of the tube.

Typical streak camera records illustrating both stable and unstable low-order detonations in Plexiglas containers are presented in Fig. 2. Figure 2(a) shows the results obtained with a 1/4-inch wall container; after the first 10 to 15 cm of travel the detonation stabilizes and traverses the remainder of the column at a uniform rate of 1.9 mm/ μ sec. While the initial phase of the reaction in the 1/16-inch wall tube, shown in Fig. 2(b), resembles that obtained with the 1/4-inch wall container, the reaction in the 1/16-inch wall progresses in a pulsating fashion and appears to be dying out as it approaches the downstream end of the tube.

Both stable and unstable reactions were also observed in charges contained in the metal tubes. The combined results are presented in Table 1 in terms of the type of reaction observed. Detonation rates are also included for the cases where stable detonations took place. Independent measurements of the low-velocity detonation pressures using a resistive gage being developed at this Center yielded values ranging from 5 to 20 kilobars depending on conditions of confinement.

The results in Table 1 indicate that both the sonic velocity of the wall material, relative to that of the NG-EGDN, and the tube wall thickness appear to be the factors in determining the stability of the detonations. In particular, for

*Trade names are used for information only and endorsement by the Bureau of Mines is not implied.

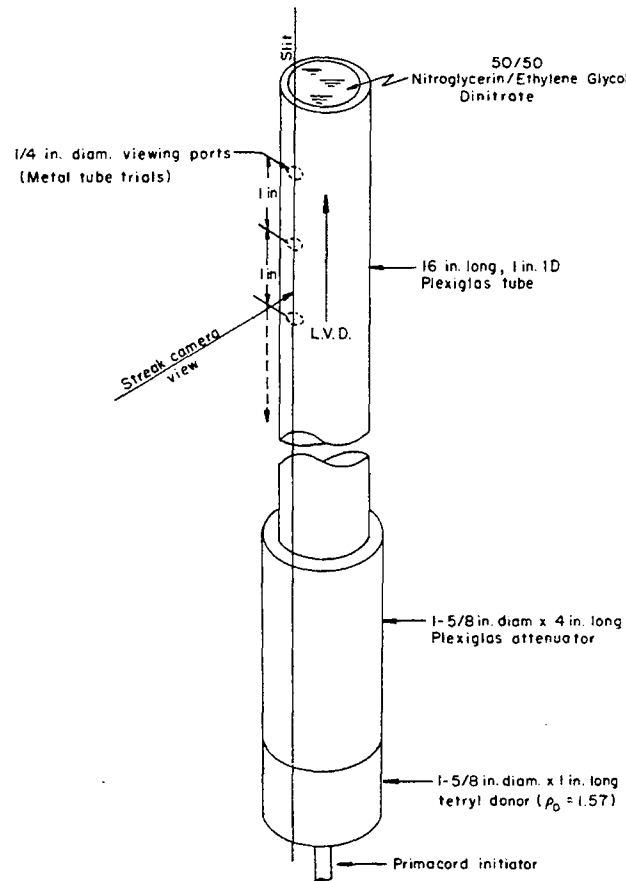


Fig. 1 - Basic charge geometry used in studies of the stability of the low-velocity detonations

the case of lead tubes where the sound velocity is less than that of the liquid, unstable reactions were observed for all wall thicknesses studied. With Plexiglas, which has a sound velocity slightly greater than that of NG-EGDN, unstable reactions were observed in the 1/16-inch wall tubes whereas stable detonations occurred in the 1/8-inch and 1/4-inch wall containers. Essentially the same results were obtained for trials using 1/16-inch and 1/4-inch thick wall aluminum. On the other hand, stable detonations were observed for all three wall thicknesses of the steel containers. It will also be noted that for the stable low-velocity detonations the rates are invariably in excess of the sonic velocity of the explosive, suggesting that the subsonic detonation rates reported in the literature may represent unstable reactions. A consideration of inertial and strength effects associated with the various confinement materials used in these studies does not, in itself, lead to a satisfactory explanation of the observed results. From this it may be concluded that perturbations of the liquid, resulting from precursor wall waves,

exert a strong influence on the subsequent reactions. The results of stability studies reported here together with conclusions concerning the importance of the precursor wall wave are in excellent agreement with the results of similar studies recently reported by Sosnova et al. [14].

In view of these results, two additional sets of experiments were performed in an effort to define reaction zone structure more clearly. The first set of experiments was designed to locate the position of the precursor wall shock relative to the reaction zone for stable low-order detonations in NG-EGDN. The experimental geometry used for this purpose is indicated in Fig. 3. It is essentially the same as that described above with the exception that a transparent water-filled chamber was positioned around the downstream end of the tube. A framing camera, together with a simple schlieren optical system employing an exploding wire background light source, was then used to observe shocks generated by the wall waves

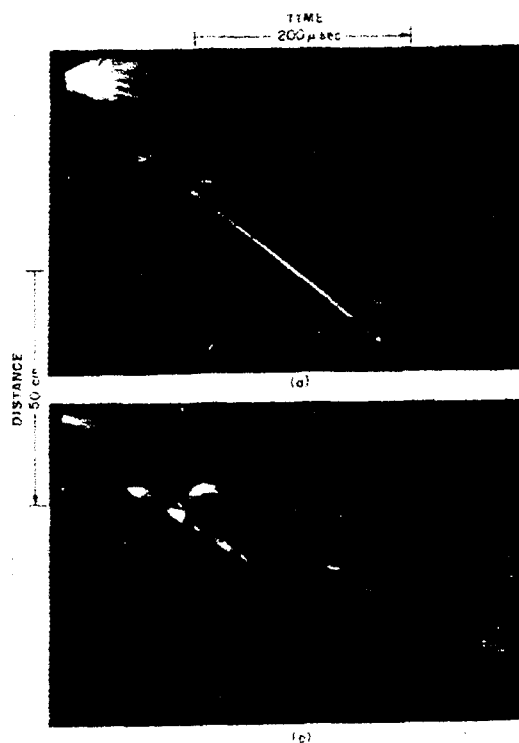


Fig. 2 - Typical streak camera records illustrating: (a) stable low-velocity detonation in a 1/4-inch wall Plexiglas tube; (b) unstable reaction in a 1/16-inch wall Plexiglas tube

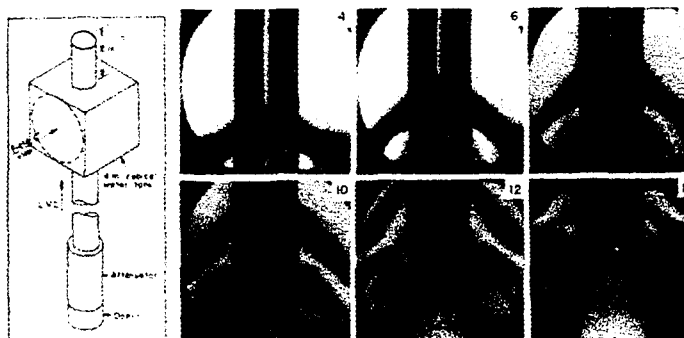


Fig. 3 - Experimental setup and selected frames showing the precursor wall shock relative to the reaction zone

TABLE 1
Results of Low-Velocity Stability Studies with NG-EGDN
($c_o = 1.48 \text{ mm}/\mu\text{sec}$; $\rho_o = 1.55 \text{ g}/\text{cm}^3$)

Wall Thickness (in.)	Result	Detonation Rate (mm/ μsec)
Lead Tubes; $c_o = 1.21 \text{ mm}/\mu\text{sec}$		
1/16	Unstable L.V.D.	-
1/8	Unstable L.V.D.	-
1/4	Unstable L.V.D.	-
Plexiglas Tubes; $c_o = 1.84 \text{ mm}/\mu\text{sec}$		
1/16	Unstable L.V.D.	-
1/8	Stable L.V.D.	2.14
1/4	Stable L.V.D.	1.87
Steel Tubes; $c_o = 5.20 \text{ mm}/\mu\text{sec}$		
1/16	Stable L.V.D.	1.96
1/8	Stable L.V.D.	1.88
1/4	Stable L.V.D.	2.11
Aluminum Tubes; $c_o = 5.00 \text{ mm}/\mu\text{sec}$		
1/16	Unstable L.V.D.	-
1/4	Stable L.V.D.	2.04

Note: Sound velocities (c_o) listed for the solids are thin rod velocities taken from the American Institute of Physics Handbook.

as the reaction front moved through the charge surrounded by the water chamber. Other optical and electronic methods had been used in an attempt to detect the precursor wave, but the system described here proved to be the most useful. Selected frames from a trial made with a 1/4-inch wall Plexiglas tube are also shown in Fig. 3; the interframe time in this case was 4 μsec and the exposure time for each frame was 0.66 μsec . This corresponds to 8 μsec between the alternate frames shown in Fig. 3. The "V" shaped water shock associated with the precursor wall wave can be seen in the first frame (No. 4) of the series. (It should be noted that as a consequence of the schlieren optical system and the cylindrical test geometry the back light is only visible along the charge axis.) Considerable more detail of the wave structure is seen in Frame No. 8. The precursor shock appears to be followed immediately by a rarefaction as suggested by the reappearance of transmitted background light on the tube axis behind the precursor shock. In turn, the rarefaction is followed by a region in the fluid that is intensely cavitated. Six frames later (24 μsec) the luminous reaction zone can be seen

entering the field of view (Frame No. 14). A careful analysis of the entire framing camera sequence showed that for this location the precursor wall wave was 4 inches ahead of the luminous reaction zone while the visibly cavitated region lagged the precursor wave by about 1 inch. The detonation rate in this case was 1.9 mm/ μsec .

A second set of framing camera studies illustrates more clearly the relationship of the reaction zone to the cavitated region. Again, the charge geometry was the same as shown in Fig. 1. For the selected frames shown in Fig. 4 the NG-EGDN was contained in a 1/4-inch wall Plexiglas tube, 16 inches long with an inside diameter of 1.0 inch. In order to define the liquid surface, the tube was only partially filled. In addition, a 45° mirror was positioned over the open end of the tube so that events occurring along the tube axis, ahead of the reaction zone, could be observed. An opaque paper disk, as a light shield, was inserted in the interior of the tube to prevent early obscuration of the cavitation field by light from the reaction zone. These details can be seen in Frame No. 5 of

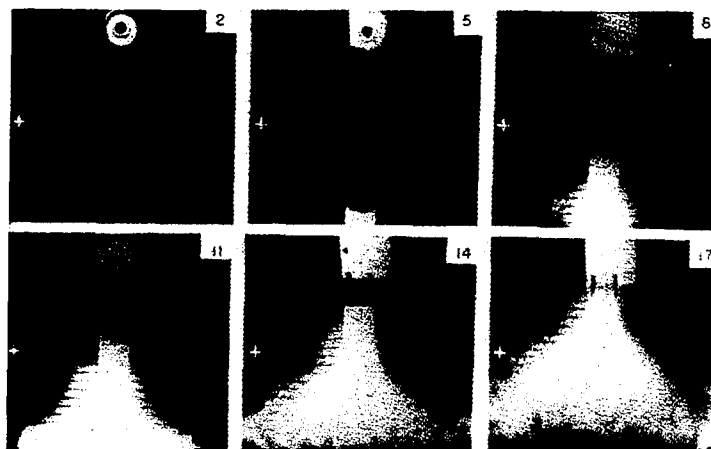


Fig. 4 - Selected frames of a sequence illustrating the cavitation field which precedes the reaction zone in a system undergoing stable low-velocity detonation; the interframe time was $10.0 \mu\text{sec}$.

Fig. 4. The event was photographed in its own light with an interframe time of $10 \mu\text{sec}$; the lines on the ruled background screen were spaced 1 cm apart. The synchronization of the framing camera with the event was adjusted so that reaction was well underway by Frame No. 2 as is evidenced by the light transmitted through the tube wall, as seen in the end-on view, and by the illuminated meniscus. In Frame No. 5 the cavitated region of the fluid has progressed beyond the light shield and can be seen in the end-on view. The bubbles appearing beyond the light shield are not self-luminous at this time. They are illuminated from internally reflected and refracted light from the reaction zone some distance behind in the same manner as is the meniscus of the liquid. This is deduced from the fact that the bubble illumination is preferentially directed toward the tube walls, a detail that is discernible only on the original negative. A more convincing argument in favor of this point lies in the consideration that an intensely self-luminous bubble would imply some appreciable degree of chemical reaction resulting in high internal pressures. Yet an examination of Frames 11 and 14 of the sequence shows that the bubbles remain under the surface of the liquid for an appreciable time ($\sim 50 \mu\text{sec}$) without disturbing it. The highly luminous reaction zone accompanied by rapidly expanding tube walls can be seen in Frames No. 8 through 14 while highly luminous reaction, and perhaps still reacting, products are expelled from the surface of the liquid in Frame No. 17. Close examination of the photograph from this and other similar shots shows that the bubbles serve as reaction centers that rapidly expand and coalesce to form the luminous reaction zone.

Taken together, the evidence presented here suggests the model for low-velocity detonations illustrated in Fig. 5. With the usual change of coordinates such that the observer moves with the reaction, the sequence of events can be visualized as: (a) the undisturbed liquid moving along particle paths uu is first compressed by the bow waves derived from the precursor wave in the wall; (b) the compressed fluid moves into an expanded region beginning at cc where the wall begins to move outward due to pressures generated in the reaction zone which supports the precursor wave; (c) the liquid continues to expand and cavitates in the region of dd ; and (d) the cavities grow until they encounter shocks in the liquid near the reaction zone. At this point the cavities collapse, generating high pressures and associated temperatures that are adequate to initiate chemical reaction. This model suggests that a low-velocity detonation will be stable if the shock velocity in the wall exceeds that in the liquid, and conversely, unstable if it is equal to or less than the shock velocity in the liquid. The model also suggests that the reaction is a deflagration induced by a shock wave, the shock wave causing the liquid to break up and provide sufficient surface area for a reaction capable of supporting the precursor shock. The mechanism for the low-velocity mode thus bears a close relationship to the surface-burning mechanism usually postulated for porous beds of condensed phase explosives. It explains as well the reason for the ready initiation of some liquid explosives by weak shocks through run-up to detonation such as typically occurs in solid explosives when initiated by shocks of marginal amplitude. The concept of a reaction made

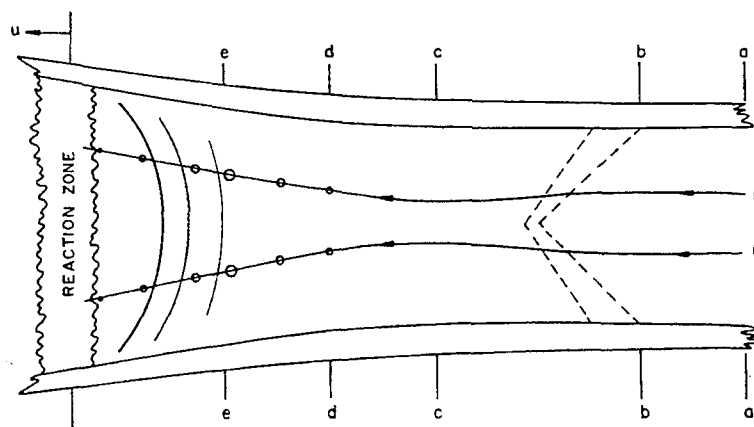


Fig. 5 - A simple physical model illustrating the mechanics of a stable low-velocity detonation

possible by a precursor shock which is in turn supported by the reaction was offered by Bowden [15] in the case of single crystals of silver azide immersed in water. Here the shock in the crystal caused sufficient heterogeneities to form, such that the following shock in the water was able to initiate a deflagration.

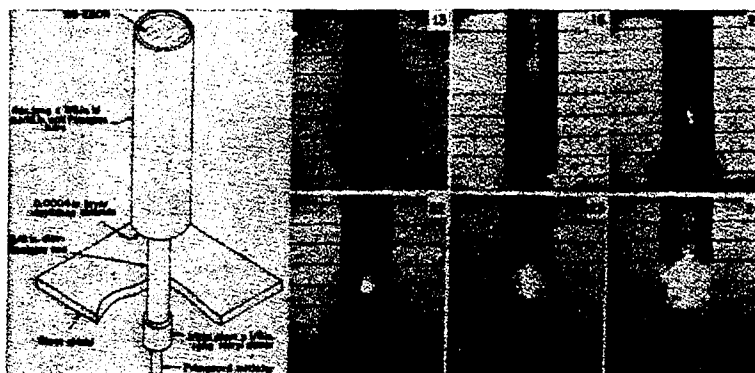
INITIATION MECHANISMS

While the foregoing model serves to define the gross features of the low-velocity detonation process, the details of the initiation of reaction at the cavity sites are not suggested. A variety of mechanisms have been proposed for the initiation of reaction in bubbles. Local heating arising from the adiabatic compression of bubble content has been suggested by several investigators [9,11]. Heat generated by shock-wave interaction or by viscous flow during the bubble collapse must also be considered. For example, Evans and co-workers [16] and Mader [17] have computed the temperature distribution in a shocked fluid containing cavities. Mader suggests that hydrodynamic hot spots, generated in the vicinity of the collapsing cavity, are responsible for the initiation of nitromethane when subjected to a plane shock wave having an amplitude of 95 kilobars. Since the pressures generated by low-velocity detonations are an order of magnitude less than this, the direct applicability of Mader's hypothesis is questionable. The possible role of micro-Munro jets has been suggested by Bowden [15], and the generation and impact explosion of microjets of NG-EGDN was described in a recent note by two of the authors [18].

In an effort to concentrate attention on the behavior of a single reaction center, the growth

phases of detonation have been studied with various charge arrangements, including that sketched in Fig. 6. In this case the explosive is confined in a 4-inch long Plexiglas tube having an inside diameter of 7/8 inch and a wall thickness of 1/16 inch. The liquid is then subjected to a weak shock derived from a 1/2-inch long \times 1/2-inch diameter tetryl donor used in conjunction with a 3/8-inch diameter Plexiglas rod. The rod and liquid charge are coaxially aligned with a 0.0004-inch thick layer of vinylidene chloride separating the two.

Selected frames from a sequence obtained using a 1-inch long attenuator are also shown in Fig. 6. The interframe time for this trial was 5 μ sec; the background was ruled with lines spaced at 1 cm. In Frame No. 13 the donor shock has traversed approximately 1 inch of the column as can be seen from the obscuration of the two background lines at the donor end of the charge. In addition, a cavitated region can be seen forming behind the input shock. In Frame No. 16 the initial shock has progressed approximately half-way down the column and the cavitated region has considerably enlarged. The earliest evidence of luminous reaction was observed to take place in Frame No. 21, 50 μ sec after the shock entered the system. In this case, the reaction was first observed in two separate regions near the axis of the tube. In other similar trials the first reaction was observed to take place at single sites. However, in all cases the first appearance of luminosity was confined to locations near the charge axis indicating that the pressure increases due to shock wave convergence probably play an important role in the initiation phases of low-velocity detonations. In Frames 22 through 24 the reaction spreads through the body of the fluid and an interesting fracture pattern in the wall material is observed



to accompany the growing detonation. While these observations do not establish the above initiation mechanism, they do add considerable insight relative to the growth phases of low-velocity detonation. Additional experiments, including thin films of NG-EGDN that also undergo LVD, are underway.

Some of the aspects of the initiation and propagation of low-velocity detonations in liquid explosives have been explored. The experimental evidence leads to the conclusion that an essential feature of the steady low-velocity detonation is fluid cavitation by precursor waves propagated in the container walls ahead of the reaction zone. The cavities thus created serve as reaction centers which in turn supply energy for the support of the precursor wall wave. Related experiments show that fluid cavitation plays an equally important role during the initiation phases of low-velocity detonations. The mechanism(s) for initiation at the cavity sites is not known at present; additional studies in this area are being carried out in an effort to resolve this question.

This work was formerly supported by the Advanced Research Projects Agency, Department of Defense, Order No. 44 and, currently, by the Bureau of Naval Weapons, Department of the Navy, under Contract No. 19-65-8023-WEPS.

1. J. Taylor, "Detonation in Condensed Explosives," Oxford at the Clarendon Press, London, 156-168 (1952).
2. B. S. Ilyukhin, P. F. Pokhill, O. K. Rozanov, and N. S. Shvedova, "Measurement of the Shock Adiabatic Curves for Cast TNT, Crystalline RDX and Nitromethane," Dokl. Akad. Nauk, 131, 4, 793-796 (1960) USSR.
3. A. W. Campbell, W. C. Davis, and J. R. Travis, "Shock Initiation of Detonation in Liquid Explosives," Phys. Fluids, 4, 4, 498-510 (1961).
4. A. Stettbacher, "Schiess-und Sprengstoffe," p. 125 (1919).
5. A. A. Dserhkovich, and K. K. Andreev, "Z. ges. Schiess-Sprengstoffe," 25, 353-356 (1930).
6. F. P. Bowden and O. A. Gurton, Proc. Roy. Soc., A198, 1054, 337-349 (1949).
7. H. Eyring, R. E. Powell, G. H. Duffey, and R. B. Parlin, Chem. Rev., 45, 69 (1949).
8. R. Schall, "The Stability of Slow Detonations," ZEITSCHRIFT fur angewandte PHYSIK, 6, 10, 470-475 (1954).
9. F. P. Bowden, M. F. R. Mulcahy, R. G. Vines, and A. Yoffe, "The Detonation of Liquid Explosives by Gentle Impact: The Effect of Minute Gas Spaces," Proc. Roy. Soc., A188, 291-311 (1947).

10. M. Zippermayr, *Explosivstoffe* 3/4, 25-40 (1955).
11. C. H. Johansson and H. L. Selberg, "The Ignition Mechanism of High Explosives," *Appl. Sci. Res.*, A5, 439-449 (1956).
12. C. H. Winning, "Initiation of Nitroglycerin," *Explosivstoffe* 11, 2 (1963).
13. F. C. Gibson, C. R. Summers, C. M. Mason, and R. W. Van Dolah, "Third Symposium on Detonation," Princeton University, Vol. 2, 436-454 (1960).
14. G. S. Sosnova, I. M. Voskoboinikov, and A. V. Dubovik, "Light Emitted by a Detonation Front of Low Velocity in Nitroglycerin," *Dokl. Akad. Nauk*, 149, 3, 642-643 (1963) USSR.
15. F. P. Bowden, "The Initiation and Growth of Explosion in the Condensed Phase," Ninth International Symposium on Combustion, Academic Press, Inc., New York (1963).
16. M. W. Evans, F. H. Harlow, and B. D. Meixner, "Interaction of Shock or Rarefaction with a Bubble," *Phys. Fluids*, 5, 6, 651-656 (1962).
17. C. L. Mader, "Shock and Hot Spot Initiation of Homogeneous Explosives," *Phys. Fluids*, 6, 3, 375-381 (1963).
18. R. W. Watson and F. C. Gibson, "Jets from Imploding Bubbles," *Nature*, 204, 4965, 1296-1297 (1964).

DETONATION OF NITROMETHANE-TETRANITROMETHANE MIXTURES: LOW AND HIGH VELOCITY WAVES

Adolph B. Amster, D. M. McEachern, Jr., and Z. Pressman
*Stanford Research Institute
Menlo Park, California*

ABSTRACT

Shock wave propagation has been studied in nitromethane and in nitromethane-tetranitromethane mixtures. Both sustain a high velocity detonation; only the latter exhibits weakly initiated low velocity detonation and only when in cylindrical confinement of a material of high sonic velocity. Convergence of shock waves in this geometry causes a high pressure axial Mach disc which could initiate rapid chemical reaction. In planar geometry the Mach region is probably at a much lower pressure, which accounts for failure to observe low velocity detonations in cells having this configuration.

INTRODUCTION

Detonation studies have generally been restricted to regimes predicted by the von Neumann-Zeldovich model and including the Chapman-Jouget conditions [1]. Typically, these processes propagate at a linear velocity of the order of 6-8mm/ μ sec; the supporting theory assumes that (a) all of the energy of chemical reaction contributes to sustaining the shock wave, and (b) the effects of lateral material confinement are negligible.

There have been reliable reports, however, of detonation-like processes characterized by velocities of the order of 2mm/ μ sec (Ref. 1, Ch. X). These waves propagate stably and have been termed low velocity detonations (LVD) to distinguish them from their more "normal" counterparts, the high velocity detonations (HVD). The two may be of comparable destructiveness.

Recent, careful studies by the group at the Bureau of Mines [2] have confirmed, beyond any reasonable doubt, that LVD do occur. Propagation characteristics are strongly dependent upon the nature of confinement and the initiating shock strength. In addition, it appears the LVD occur most readily, but not exclusively, in mixed liquids. We have studied some of the phenomena associated with the LVD of nitromethane-tetranitromethane (NM-TNM)

mixtures. This is a report of our investigations. Briefly we conclude that NM-TNM does sustain LVD but, though some of the proposed mechanisms may offer sufficient explanation, many unanswered questions still remain.

EXPERIMENTAL

Van Dolah and co-workers have reported that a number of liquid mixtures sustain LVD. Most contain nitroglycerine and, largely for safety reasons, were not suitable for our use. One of these mixtures, NM:TNM (90:10 by weight), was selected for our study. Purity and availability of the ingredients were important in the selection, and also the detonation of the principal ingredient had been well characterized [3].

We have studied the selected system in two geometries. In instrumented metal tubes we have been able to observe LVD; in windowed sample cells — rectangular in cross section — those processes presumably precursor to LVD have been studied.

The nitromethane employed was Commercial Solvents commercial grade, 95% purity. Impurities included nitroethane and nitropropane. The tetranitromethane, from K & K Labs (Plainview, New Jersey) was of similar grade, the impurities were other nitromethanes.

Instrumented Steel Tubes

Detonation sensitivity testing is conducted in steel tubes and much is known about the behavior of liquids in this confinement. For this reason our initial tests were conducted using the apparatus shown in Fig. 1 which is conventional except for the instrumentation. Prior to testing, the steel tube was filled to the brim with the test liquid. Initiation was by a train consisting of an exploding bridgewire detonator (EBW), 18-inch Primacord,* a 2-inch diameter plane wave generator, and a pressed tetryl pellet. Measurements were made with a high resistance wire along the longitudinal axis of the tube [4] — hopefully to measure detonation velocity — and with a manganin wire gauge [5] to measure shock pressure. When possible the steel tube fragments were recovered after each experiment.

The use of different thicknesses of Plexiglas attenuator enabled us to control the shock

pressure entering the liquid [6]. Furthermore, the shock Hugoniot of the mixture appears to be close to that of the plastic and pressures could be assumed to be continuous across the attenuator-liquid interface. Values for pressure quoted below were obtained in a conventional fashion.

In a number of experiments with the NM:TNM mixture it was established that the initiation of HVD required pressures of the order of 100 kbar. Velocities of 6.1 to 6.4 mm/ μ sec were reliably measured with the wire and high pressures recorded with the gauge. Entering pressures of 60 kbar or less initiated a sequence of events which can properly be called an LVD. When tests were conducted with water as the subject, damage was minimal (see Fig. 2); with the NM:TNM mixture the confining tubes were shattered into large pieces (see Fig. 3). (For HVD the resultant fragments are many and small.) Some of the larger fragments penetrated a 2-inch plywood sheet 200 ft from the explosion; others were recovered as far away as 1000 ft. Pressures of the order of

*Trademark, Registered U.S. Patent Office.

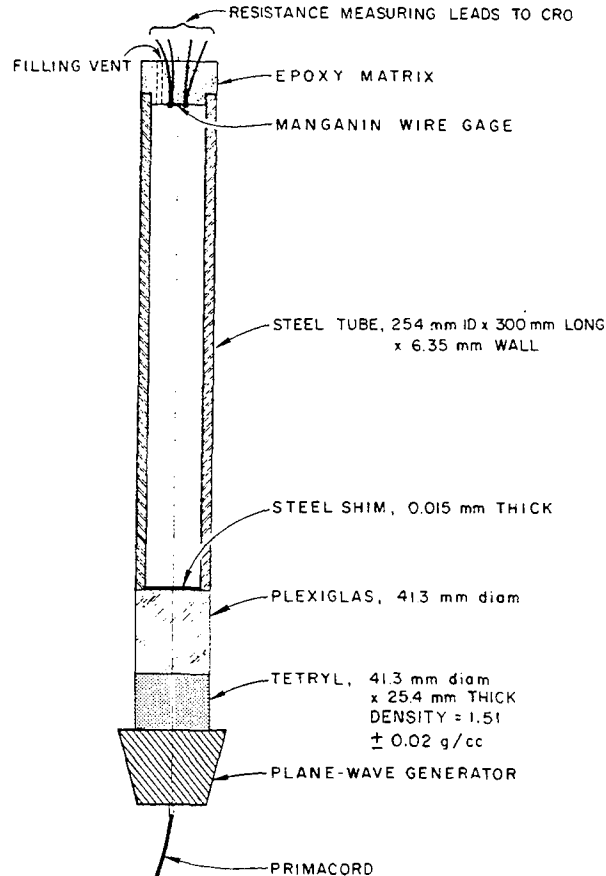


Fig. 1 - Apparatus for studies in steel tubes

Fig. 2 - Steel tube damage due to booster only



5-15 kbar were recorded by the high frequency expendable pressure gauge (vs ≈ 100 kbar in HVD). On the other hand, ionization of any reaction wave within the tube was insufficient to permit normal functioning of the velocity sensor. Irregularities in the oscilloscope trace — found to correspond to the entry and exit of the shock wave — indicated average velocities within the liquid of $\approx 1.7 \text{ mm}/\mu\text{sec}$. This is consistent with values estimated from the arrival time of the low pressure wave.

These observations, resulting from the analysis of several experiments, justify the conclusion that for strong initiating shocks, weaker than those required for HVD, the 10% TNM:90% NM mixture sustains an apparently stable, very energetic, low velocity detonation when the sample is confined in steel.

We have conducted many analogous experiments with neat nitromethane. Although stable HVD can be reliably initiated for entering pressures of ≈ 100 kbar, we have been unable to initiate anything resembling LVD for lesser pressures. This is consistent with results reported by others.

Photographic Observation with Windowed Metal Cells

The mechanism proposed by van Dolah [2] for the initiation and propagation of LVD requires that (a) the speed of sound in the confinement be greater than that in the explosive, (b) a precursor bow wave and subsequent rarefactions cause bubble formation, and (c)



Fig. 3 - Steel tube damage due to low velocity waves

recompression of the bubbles initiates the rapid chemical reaction which sustains wave propagation. That shocks impinging upon bubbles can initiate reaction has been shown by Campbell [3d] and, for the situation at hand by van Dolah [7] and, especially by Bowden [8]. Using a special photographic technique we have observed shock propagation and the events precursor to bubble formation in the TNM:NM mixture.

The optical apparatus we have used is shown schematically in Fig. 4. In early experiments an EBW light source was used as shown. Later, with long sample containers and, therefore, relatively long observation times, we used an a.c. powdered electronic flash gun of the type normally used for amateur photography (the Spiralite — available from Spiratone, Inc., New York, N.Y.). The light from this source was of more than adequate intensity, duration, and uniformity. (Its low cost, reliability, and ease of use recommend it for additional use in similar experiments.) An expendable cast plastic Fresnel lens between the light source and the sample was chosen to focus the source image upon a diamond stop on the Beckman and Whitley framing camera. A sample container (Fig. 5) was aligned with the windows normal to the optical axis. Refraction gradients in the liquid were readily apparent in the shadowgraph recorded by the camera. The same shock donor was used as in the experiments with the steel tubes and dimensions were chosen so that (a) the sample thickness would be above the known failure diameter of NM, and (b) the length of the optical path would be great compared to the metal wall separation. The latter was to eliminate interference by spurious effects of CR-39 plastic windows. As will be seen, we may not have succeeded in this goal.

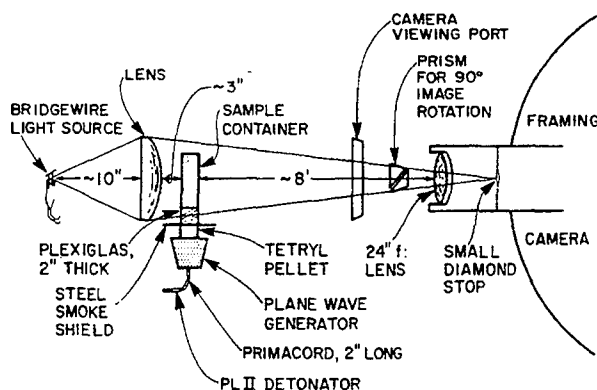
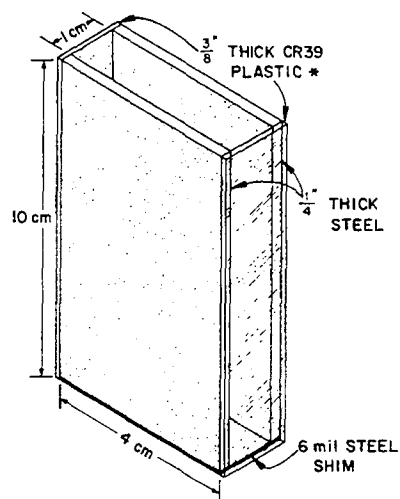


Fig. 4 - Apparatus for obtaining shadowgraphs with high-speed framing camera



* POLY DIETHYLENEGLYCOL-BIS-ALLYL CARBONATE

Fig. 5 - Windowed sample container

In one type of experiment stable HVD was initiated in a cell with steel walls. The results of this experiment are shown in Fig. 6. Here the advancing shock wave is clearly seen and also the material expansion behind it. Note, that the detonation light emitted by the sample was not recorded.

A number of tests were conducted using shocks of a magnitude appropriate to initiating LVD. Also walls of different metals were used to observe the effect of confinement on sonic velocity. The following describes results typical of a much larger number of experiments.

Experiments were conducted under the following conditions:

Type	Wall Material (1/4-inch)	Liquid	Shock Strength (kbar)
I	Steel	10% TNM:90% NM	≈ 10
II	Lead	10% TNM:90% NM	≈ 55
III	Steel	Neat NM	≈ 10
IV	Steel	H ₂ O	≈ 10

The photographs of a typical Type I experiment are shown in Figs. 7 and 8* in which zero time is taken to be when the shock wave enters the liquid. The first picture in Fig. 7 shows the undisturbed charge. The next frame — 5.6 μ sec later — shows the precursor or "bow" waves in the liquid. The forward velocity of the bow wave quickly drops to the sonic velocity of the steel, 5.0mm/ μ sec, and the angle of the bow wave with the wall is consistent with a liquid sonic velocity of ≈ 1.4 mm/ μ sec. In this second frame we also see a relatively planar dark zone behind the bow wave which, with information from later frames, is determined to travel at ≈ 2 mm/ μ sec. It is not until 12-14 μ sec after the stage shown in the first frame that bubbles become detectable. In this and similar shots we have made careful measurements to detect lateral movement of the metal walls. So far none has been detected until after appearance of the bubbles. The later frames show multiple

*These are pictures of identical experiments except that the film of Fig. 8 was given a greater exposure to record more details in the dark zone.

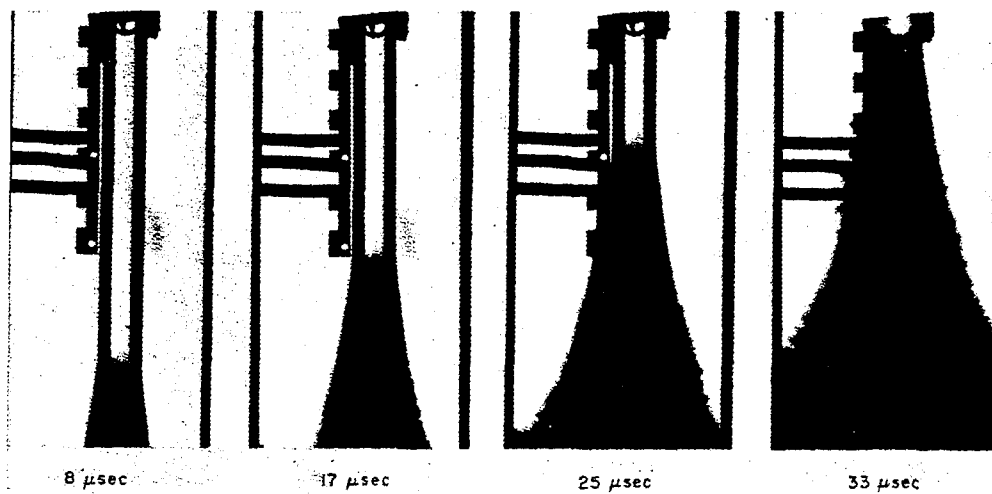


Fig. 6 - Framing camera photographs of high velocity detonation in 10% TNM:90% NM

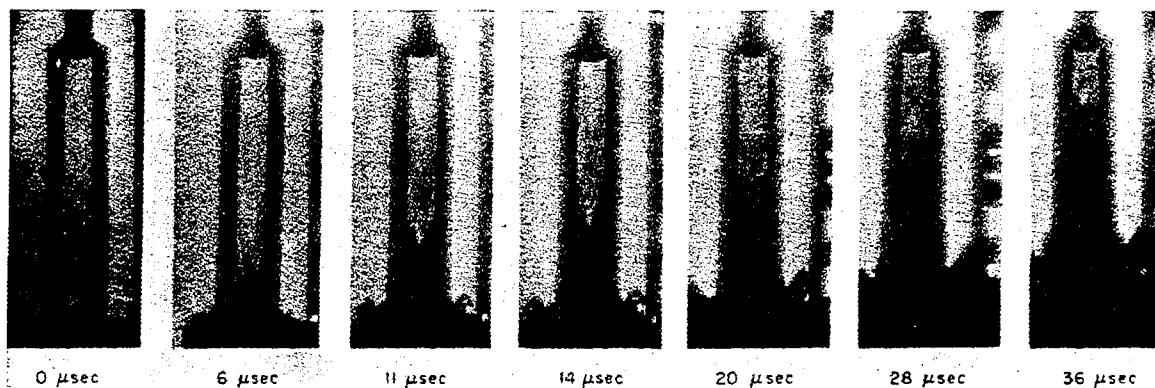


Fig. 7 - Framing camera photographs of shock propagation in 10% TNM:90% NM contained in 1/4-inch steel walls

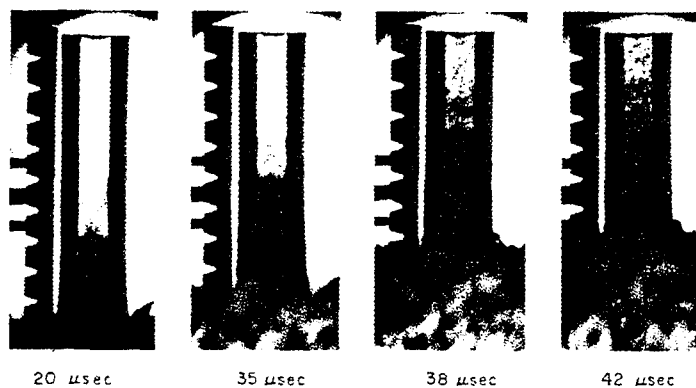


Fig. 8 - Framing camera photographs of shock propagation in 10% TNM:90% NM contained in 1/4-inch steel walls (dark zone study)

reflections of the bow wave from the opposite walls. The gradually increasing angle of the wave with the wall may be due to shock heating of the liquid. The alternating dark and light zones seen in Fig. 8 may be apparent rather than real phenomena. One should be careful not to attach too much significance to them. Figures 9 and 10 are graphical representations of the velocity-distance behavior of the leading dark waves in Figs. 7 and 8, respectively.

Figure 11 shows a Type II shot (lead wall). Because of the low sonic speed of the lead ($1.2\text{mm}/\mu\text{sec}$) no bow wave is seen. Yet similar dark zones which progress at $\approx 2\text{mm}/\mu\text{sec}$ are evident. Figure 12 is a graph of the velocity-position behavior.

Using neat nitromethane in steel (Type III) the photographic evidence appears to be essentially the same as for the Type I experiments. Most surprisingly, Type IV shots with water in steel appear to differ in no significant way from the Type I and II shots, whether the criterion is the photographic record or damage to the metal walls.

Additional tests with 300mm long cells were made under the following conditions:

Type	Wall Material (1/4-inch)	Liquid	Shock Strength (kbar)
V	Steel	NM	≈ 55
VI	Steel	H ₂ O	≈ 55
VII	Pb	NM	≈ 55
VIII	Pb	H ₂ O	≈ 55
IX	Pb	90% NM:10% TNM	≈ 55

With the Type V and VI shots the precursor bow wave degenerated so much that it became invisible over the terminal 200mm. In the same region the slower dark zones were not seen but some diffuse bubble formation was detected in shots of Type V-IX. At the same time cracks were seen in the plastic windows.

DISCUSSION

Conventional sensitivity testing assumes that for each explosive there exists both a critical shock pressure and failure diameter

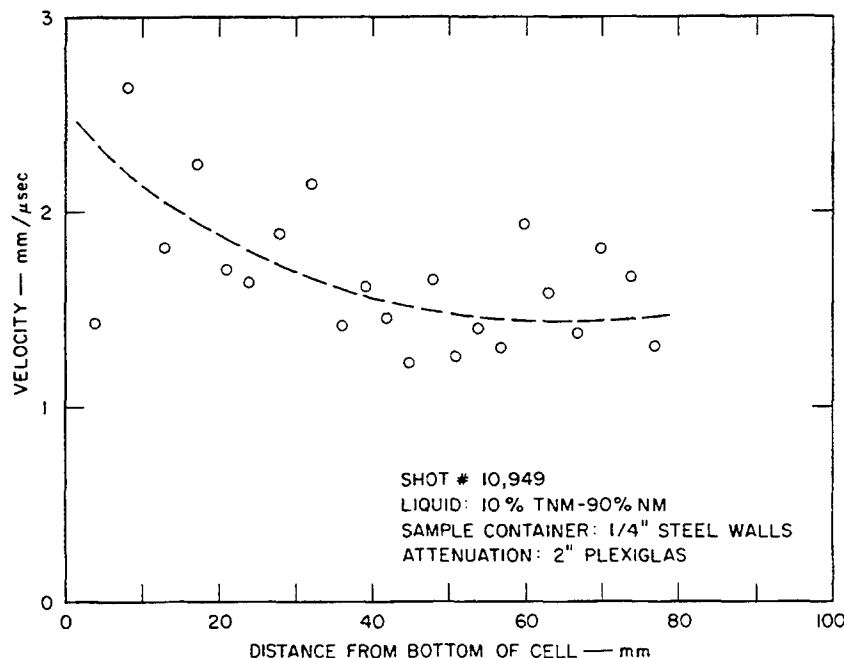


Fig. 9 - Shock velocity in 10% TNM:90% NM in windowed sample container: 1/4-inch steel walls, 2-inch Plexiglas attenuation

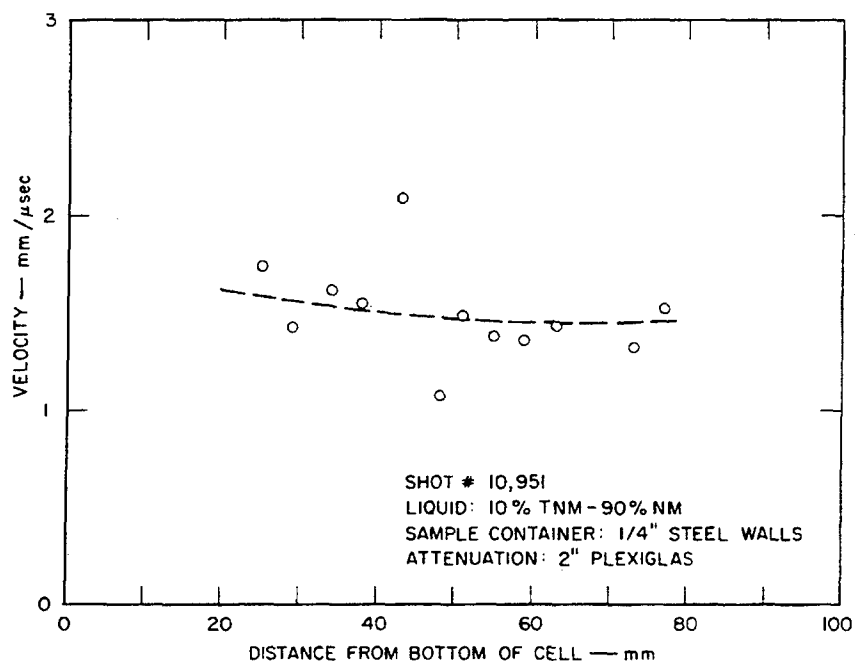


Fig. 10 - Shock velocity in 10% TNM:90% NM in windowed sample container: 1/4-inch steel walls, 2-inch Plexiglas attenuation (dark zone study)

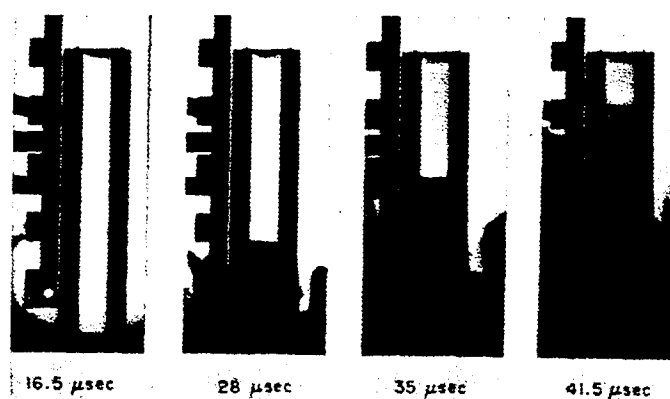


Fig. 11 - Framing camera photographs of shock propagation in 10% TNM:90% NM contained in 1/4-inch lead walls

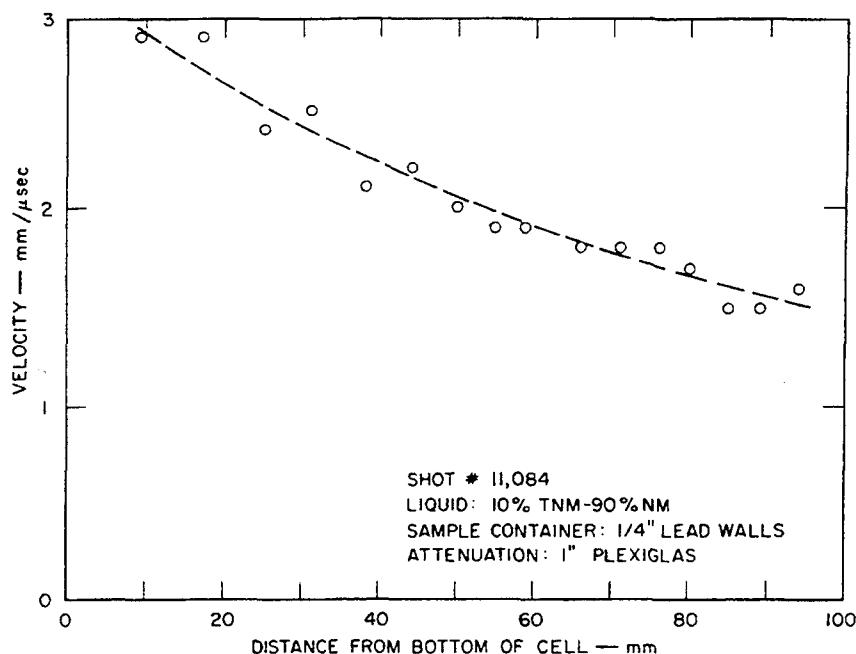


Fig. 12 - Shock velocity in windowed sample container: 1/4-inch lead walls, 1-inch Plexiglas attenuation

below which initiation to stable detonation does not occur. These characteristics are also assumed to be relatively independent of the material confinement. Acceptance of this model permits design of processes and of explosive handling systems in order to preclude accidents.

The reliably reported occurrence of low velocity detonations alters this picture considerably. For example, present sensitivity testing methods do not detect LVD. Furthermore, initiation of LVD seems to require relatively low pressures; it is very much a function of the material confinement; and the consequences may be even more damaging than those of a stable HVD because of the larger resulting fragments. It is, therefore, most important that the mechanism of LVD initiation and propagation be understood.

As noted previously, it is a sufficient (though, perhaps, not necessary) condition that bubbles in the liquid be shocked, for this can lead to reaction propagation. There remains, however, the question as to the origin and necessity of the bubbles. Van Dolah has described experiments in which cavitation occurs subsequent to case expansion. In our photographic experiments we have observed bubble formation prior to detectable movement of the metal walls. It is possible that movement of the plastic

windows — which would not be recorded — accounts for the bubbles.

We would like to direct attention to another hypothesis. Fowles and Isbell [9] have described a method for producing high pressure shock waves which is, in most respects, identical to that used to initiate LVD. The bow waves observed in the windowed cells are, of course, convergent shock waves. Birkhoff and Walsh [10] have shown that irregular reflection must always occur in such conically convergent flow of a material with a "normal" equation of state. This reflection produces a Mach disc traveling with the forward velocity of the converging waves. For an NM:TNM mixture confined in steel, this velocity ($\approx 5 \text{ mm}/\mu\text{sec}$) corresponds to a pressure in the liquid of $\approx 85 \text{ kbar}$. Though this condition exists within a very small region the accompanying temperatures are obviously high enough to initiate significant chemical reaction. In fact, this pressure is only marginally below and may not differ significantly from that required to initiate stable detonation. The accompanying exotherm may be enough to sustain the continuing process, though at less than C-J detonation velocity — because the bulk of the material reacts more slowly at a lower temperature. Bubbles accompanying this sequence would, of course, serve as foci for further propagation but would not be necessary for the process to occur.

With planar convergent waves a much more complicated situation prevails. At some critical convergence angle ($\approx 90^\circ$) the pressure is approximately that in the cylindrical case. However, the pressure is a very sensitive function which falls off rapidly with changes in the angle. This would explain lack of LVD in the windowed cells.

CONCLUSIONS

The occurrence of low velocity detonations has been established. One reasonable model entails the formation and shocking of bubbles within the liquid. This is a sufficient but may not be a necessary condition. We propose an alternative model which depends upon the occurrence of a Mach disc formed by converging shock waves. Within these discs temperatures are sufficiently high to initiate considerable chemical reaction. The latter may or may not cause bubbles which, therefore, become important but not essential contributors to the process.

Additional experiments are being performed to examine this hypothesis further.

ACKNOWLEDGMENT

We are grateful for the opportunity to discuss some aspects of this research with Professor George Duvall of Washington State University and Stanford Research Institute. This program has been supported by the Office of Naval Research and the Advanced Research Projects Agency of the Department of Defense.

REFERENCES

1. J. Taylor, "Detonation in Condensed Explosives," Oxford, 1952.
2. R. W. van Dolah, R. W. Watson, F. C. Gibson, C. M. Mason, and J. Ribovich, "Low Velocity Detonations in Liquid Explosives," International Conference on Sensitivity and Hazards of Explosives, London, October 1963.
- 3a. M. P. Murgai, J. Appl. Phys. 28, 745 (1957).
- 3b. A. N. Dremine, O. K. Rozanov, and V. S. Trofimov, Combustion and Flame 7, 153 (1963).
- 3c. G. Nahmani and Y. Manheimer, J. Chem. Phys. 24, 1074 (1956).
- 3d. A. W. Campbell, W. C. Davis, and J. R. Travis, Phys. Fluids, 4, 498 (1961).
4. A. B. Amster, P. A. Kendall, L. J. Veillette, and B. Harrell, Rev. Sci. Instr., 31, 188 (1960).
5. D. Keough, D. Bernstein, and R. F. Williams, ASME Publication 64-WA/PT-5.
6. I. Jaffe, R. Beauregard, and A. Amster, ARS Journal, 32, 22 (1962).
7. R. W. van Dolah, private communication.
8. F. P. Bowden and M. P. McOnie, Nature, 206, 380 (1965).
9. J. R. Fowles and W. M. Isbell, J. Appl. Phys., 36, 1377 (1965).
10. G. Birkhoff and J. Walsh, Publ. Sci. Tech. Min. Air (France) (1954).

OBSERVATION AND STUDY OF THE CONDITIONS FOR FORMATION OF MACH DETONATION WAVES

J. P. Argous, C. Peyre, and J. Thouvenin
*Commissariat à l'Energie Atomique
Paris, France*

ABSTRACT

Formation of Mach detonation waves in a given explosive is observed and studied. Mach detonation velocities as high as 10-14 mm/ μ sec have been measured. Shock pressures two or three times higher than for normal detonations are induced by this wave in a metal such as copper.

The history of the Mach detonation wave is analyzed after it is formed. The possibility that a stationary state can be reached under the condition that the incident waves are stationary is shown.

1. INTRODUCTION

It is generally agreed that a detonation wave consists of a shock wave which propagates in the explosive, followed by a zone of finite dimension in which the chemical reaction initiated by the shock front provides the necessary energy to maintain the shock wave. If the initiating shock front possesses a vertex point of suitable angle, a Mach wave will be created in the interior of the explosive and chemical reactions will develop in a region that is more compressed than would be the case for a normal shock front: there is reason to believe that the hydrodynamic detonation parameters, velocity, D , and pressure, p , will therefore be of greater magnitude in the zone covered by the Mach wave than in a region of a normal detonation wave. This particular and localized detonation wave constitutes a Mach detonation wave.

In the present article we describe three experimental cases where we have observed the formation of a Mach detonation wave and have analyzed some of its properties — its high velocity, and the evolution or build-up of this velocity; the shock pressures induced in an inert medium, the conditions for a stationary Mach detonation wave, investigating the maximum velocity.

The explosive used was near Composition B. Its normal detonation velocity is 8.1 mm/ μ sec.

It should be noted that the first and third cases described below lead to axially symmetric Mach waves, while case 2 is for plane waves interaction. The conditions for formation of axially symmetric Mach waves would differ from plane Mach waves, and the properties in these waves would also be different. But the present paper is rather a summary of experimental descriptions and observations, than an exhaustive discussion about the Mach phenomenon.

2. FIRST CASE OBSERVED: CISSEOIDAL DETONATION WAVE

The creation of a vertex point in a detonation wave may be obtained by mismatching the constituents of a plane wave explosive lens, that is, by causing a delay, Δt_0 , on the axis of the lens in relation to its edge. The detonation wave transmitted by such a lens to the main explosive charge has the form of a cissoid, and for a suitable value of Δt_0 , the Mach phenomenon appears.

We have observed this for charges having a diameter of 100 mm, beginning with $\Delta t_0 = 3 \mu$ sec [2].

The following measurements were made under the initiation conditions described.

(a) Diagram of the Progress of the
Mach Detonation Wave

The explosive charge has a length, L , which we vary (Fig. 1). The arrival of the detonation wave on the terminal surface is marked by the strong luminosity of the air trapped between the charge and a plexiglas disc placed in contact with it. The luminous trace, recorded by a streak camera, shows a plane center portion of width Δx delayed by Δt from the periphery of the detonation wave: this plane portion constitutes the action zone of the Mach wave (Photo 1). Knowing that the detonation wave has a velocity of $D_0 = 8.1 \text{ mm}/\mu\text{sec}$ on the edges of the charge, we can make a distance-time plot of the plane central portion in plotting the delay, Δt , for each length, L , above the straight line having the slope D_0 (Graph 1). Differentiating, we obtain a curve which gives approximately the variation of the velocity, D , of the Mach detonation wave as a function of the length, L , of the explosive (Graph 2). When the Mach phenomenon appears, that is at L of approximately 30 mm, the velocity, D , is high, higher than $11 \text{ mm}/\mu\text{sec}$; then it decreases and approaches the value of D_0 .

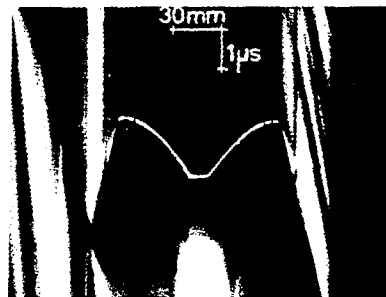
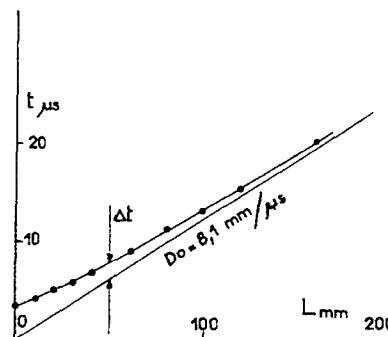


Photo 1



Graph 1 - Time-distance plot of the Mach detonation wave

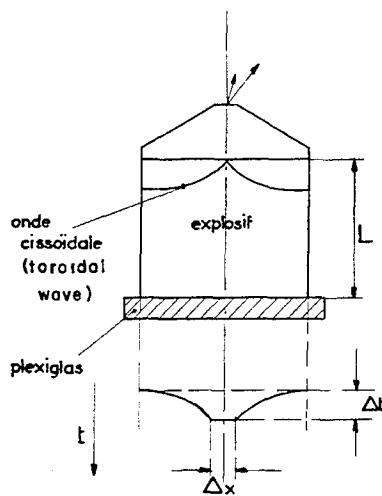
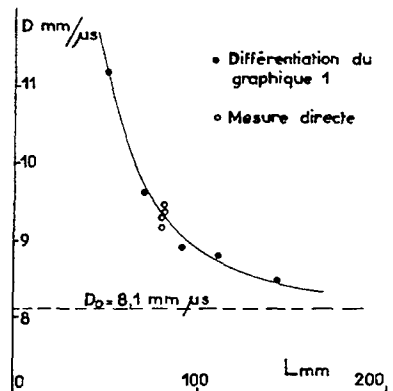


Figure 1

As the length, L , of the charge increases, the width, Δx , of the Mach zone increases quasilinearly. We have observed that this increase of Δx was independent of the diameter of the charge: for $L = 160 \text{ mm}$, for example, the width of the Mach zone for charges from 100-200 mm in diameter is 27 mm.



Graph 2 - Mach detonation velocity as a function of distance

(b) Precise Measurements of the
Mach Detonation Velocity

This measurement was made with the aid of a plexiglas cylinder 20 mm long imbedded in

the explosive (Fig. 2). The luminous traces observed by the streak camera (Photo 2) give the time required for the detonation to travel the length of the cylinder. This cylinder was placed in the Mach zone, in the neighbourhood of the axis of the charge. Values of D thus obtained directly are shown on Graph 2, and are in good agreement with those obtained by differentiating the distance-time plot.

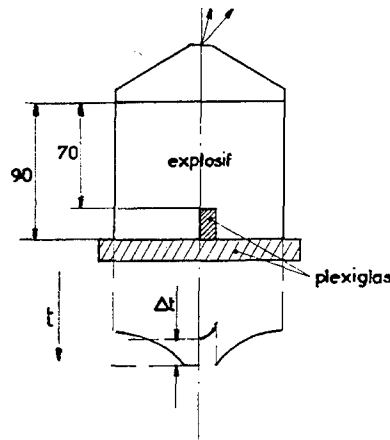


Figure 2

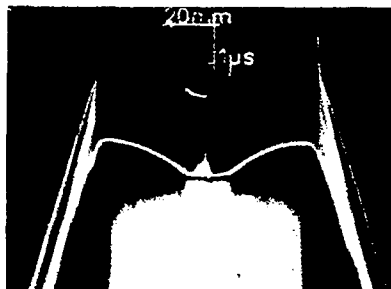


Photo 2

(c) Shock Pressures Induced in an Inert Medium

A copper disc 3 mm thick is placed on the terminal surface of the charge (Fig. 3). The free surface of this disc is polished and lighted by a flash during the experiment. The arrival of a shock wave on the free surface of the copper causes a rotation of this disc, hence a decrease in light reflected towards the camera. The shape of the shock wave is thus faithfully recorded (Photo 3). We can clearly distinguish the arrival of the incident shocks, the Mach

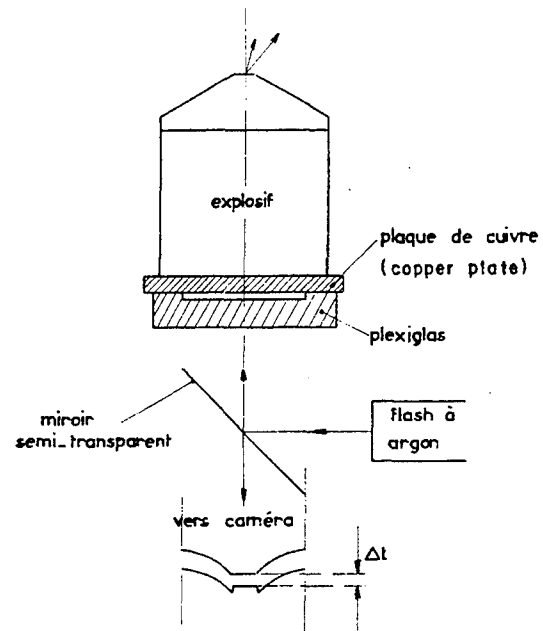


Figure 3

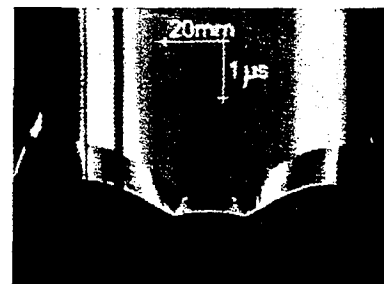


Photo 3

wave, and the triple points. We also are able to distinguish reflected shock waves issuing from the triple points, for these cause an opposite rotation of the free surface, redirecting light from the flash back toward the camera.

In addition, a plexiglas plate was placed parallel to and 1 mm away from the copper to record the arrival of each element of the free surface by means of the luminous flash produced on arrival by the ionisation of the air.

This experiment enables one to measure the velocity of the free surface of the copper disc in and out of the Mach zone, hence to ascertain the shock pressures induced at different points.

These experiments were carried out with charges 80 mm long, for which we know (Graph 2) that the Mach detonation velocities are in order $9.3 \text{ mm}/\mu\text{sec}$. Outside of the Mach zone the shock pressures in the copper disc are in order 450 kbars. In the Mach zone, the pressures measured in seven experiments were 1.06 ± 0.03 megabars. There is thus a net, clearly shown, contrast between the action of a Mach detonation wave and a normal detonation wave.

3. SECOND CASE OBSERVED: THE COLLISION OF TWO PLANE DETONATION WAVES

The experiments described above make obvious the existence of the Mach phenomenon in the detonation and its property of inducing high shock pressures. In order to analyze in a more precise fashion the conditions for their formation, experiments were made with the following set-up (Fig. 4).

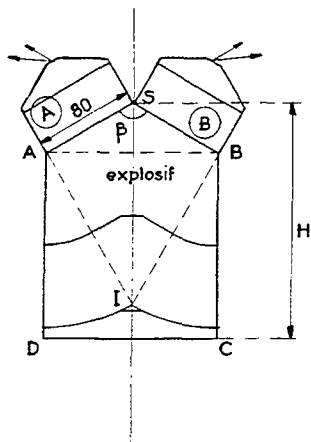


Figure 4

Two plane detonation waves are initiated in two parallelepipeds, charges A and B. These reach, simultaneously, the two surfaces SA and SB of a prism made of the explosive to be studied ($SA = SB = 80 \text{ mm}$). This prism is extended by a charge in the shape of a parallelepiped ABCD.

The incident waves form an angle, β , which by construction, remains constant until it reaches the point, I, the length SI being equal to SA divided by $\cos \beta/2$. In the region beyond the point I the interaction takes place between cylindrical waves which emanate from the

corners A and B, and the angle of incidence increases. We can thus observe the conditions of formation and the buildup of a Mach wave by varying the angle, β , and the height, H.

(a) Formation of the Mach Wave as a Function of the Angle of Incidence β

We observe the arrival of the detonation wave on the terminal surface, CD, by the same procedure as described above. The angles $\beta = 60^\circ, 90^\circ, 95^\circ, 100^\circ, 110^\circ, 120^\circ$, and 150° were used, and for each several values of H.

The Mach phenomenon appears, from the base of the prism, AB, for all angles equal to or greater than 100° . For $\beta = 90^\circ$ it does not appear. For $\beta = 95^\circ$ it appears in one out of two cases. Photos 4, 5 and 6 represent records obtained for $\beta = 90^\circ, \beta = 100^\circ$ and $\beta = 120^\circ$. Therefore the critical angle for the explosive studied and in the initiation conditions described is between 95° and 100° .

(b) The Development of the Mach Wave

With the aid of the records obtained by observing the arrival of the wave on the terminal

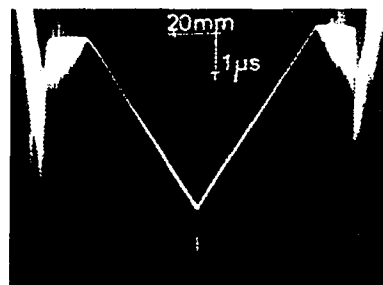


Photo 4

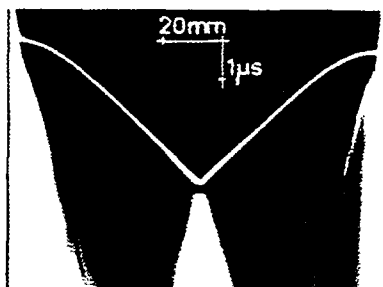


Photo 5

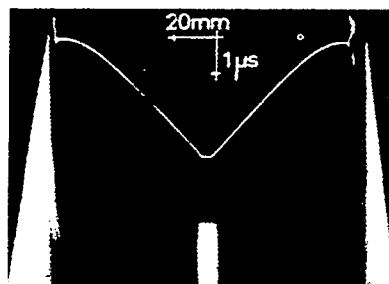


Photo 6

surface, it is possible to reconstruct the form of this wave at the instant when the Mach zone reaches the abscissa H. The quantity H was varied from 80 to 315 mm for $\beta = 120^\circ$. In this case the distance, CI, was 160 mm.

We have observed, therefore, that as long as the incident waves have not reached the point, I, that is to say, as long as H is smaller than or equal to 160 mm, the velocity of the Mach wave remains constant and equal to the value deduced by a simple kinematic calculation

$$D_{\text{Mach}} = \frac{D_0}{\sin \beta/2} \quad (1)$$

In the case where $\beta = 120^\circ$ this velocity had a value of 9.35 mm/ μsec .

Moreover, the length of the central plane portion, Δx , remains constant and equal to 4.5 mm as long as the point, I, is not reached. Beyond the point, I, the angle of incidence between the two lateral waves increases continually. We have observed that the velocity of the Mach wave decreases from this point and that its width, Δx , increases linearly with H, and reaches a value of 14 mm at H = 315 mm.

These experiments demonstrate an interesting property of the Mach detonation wave: the property of remaining stationary when it is formed by two detonation waves which are themselves stationary, i.e., plane and jointly forming a constant angle. This is an important difference opposite to the Mach waves which are obtained in inert media by means of two intersecting shock waves. The stability of the Mach detonation wave is connected to the stability of the simple detonation wave and may be brought about by the same cause: the reactive nature of the medium and the localization of the interaction phenomenon at the chemical reaction region.

(c) The Measurement of the Detonation Pressures in a Mach Wave

An attempt to measure the detonation pressure was made by utilizing a method described by Duff and Houston [1]: variation of the velocity of the free surface of a metallic plate as a function of its thickness. The Mach wave is formed by the prism shown in Fig. 4, where $\beta = 100^\circ$ and H = 90 mm. It is in the stationary regime. A copper plate of thickness, e, is placed on the terminal surface, CD. The measurement of its free surface velocity is made by the method described in 2(c), and we obtain records of the type shown in Photo 7. The distance which separates the plexiglas plate and the copper surface is chosen small enough to prevent the shock accumulation phenomenon. The values obtained are shown in Table 1 and on Graph 3; they represent the mean of 4 to 8 measurements.

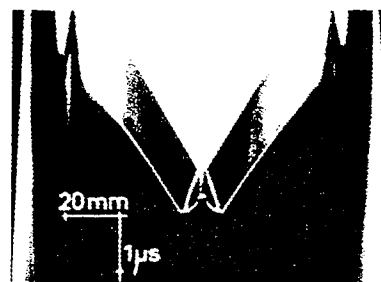
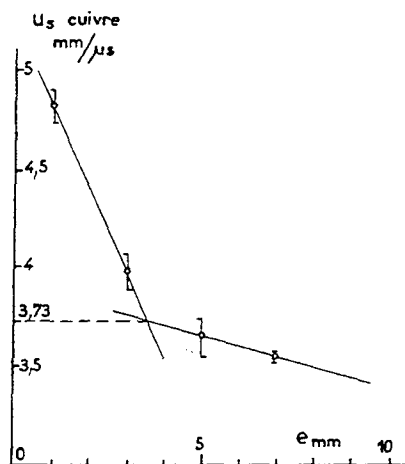


Photo 7

TABLE 1
Velocity of the Free Surface u_s of Copper as a Function of Thickness e

e (mm)	u_s (mm/ μsec)	e (mm)	u_s (mm/ μsec)
1	4.82 ± 0.08	5	3.65 ± 0.10
3	3.98 ± 0.10	7	3.54 ± 0.02

On Graph 3 we note a rapid decrease of u_s followed by a slower decrease. According to the method described by Duff and Houston, we are tempted to conclude that a "CJ point" defined as the point of completed reaction, exists in the Mach detonation wave, and to determine its characteristics from the intersection of two straight lines which one can draw on Graph 3.



Graph 3 - Free surface velocity of copper as a function of thickness

This point has a value of $u_s = 3.73 \text{ mm}/\mu\text{sec}$, and corresponds to a shock pressure of 1.09 megabars in the copper. On assuming that the value of the polytropic coefficient, Γ , of the detonation gases are the same behind the Mach wave and behind a plane wave, we obtain for the Mach detonation wave, having a velocity $D = 10.6 \text{ mm}/\mu\text{sec}$, detonation pressures in order 700 kilobars (instead of 280 kilobars for the normal detonation wave).

4. THIRD CASE OBSERVED: RESEARCH OF A MAXIMUM VELOCITY

We have shown in 2(a) that the detonation velocity, D , may have a very high value at the time of the appearance of the Mach phenomenon. A simple experiment, using a small quantity of explosive, was prepared to study the Mach wave in the time region near the instant when it is formed (Fig. 5). A copper plate was projected with a velocity, V , on an explosive block in which we had bored a conical cavity. On the exterior of this hollow cone the detonation wave initiated by the impact is plane, and at the instant, t , it is at C (Fig. 6). In the interior of the cavity the projected plate successively strikes the points of the surface of the cone, and at the time, t , the point of impact is at A.

If the velocity, V , is small, the detonation wave which started at O will arrive at A before the impact of the copper plate, and the component of the wave CA would be circular. However, if the V is greater than $D_0 \sin \alpha$, we easily see that this wave component involves a

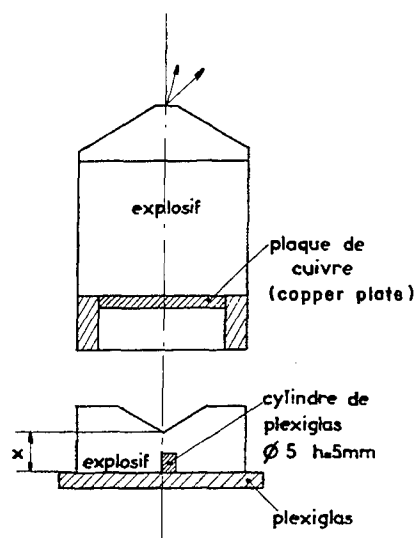


Figure 5

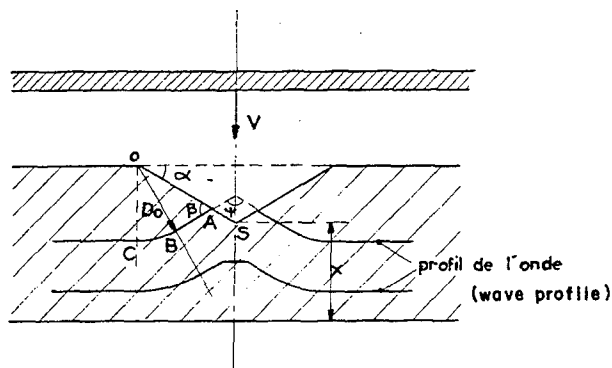


Figure 6

straight portion, AB, having an angle β with respect to the cone generators given by

$$\sin \beta = \frac{D_0}{V} \sin \alpha.$$

We have thus formed in the explosive target a truncated conical detonation wave whose angle ψ at the summit is defined by

$$\psi = \pi - 2(\beta - \alpha).$$

If the angle ψ has a value equal to or greater than 100° this wave gives rise, beginning with the vertex S, to the formation of a Mach detonation wave.

By varying the distance X which separates the vertex S from the terminal surface, we may observe the initial phase of the phenomenon. The detonation velocity is measured, on a 5 mm base, by the plexiglas cylinder method described in 2. Photo 8 shows a record obtained for the case where $X = 30$ mm.

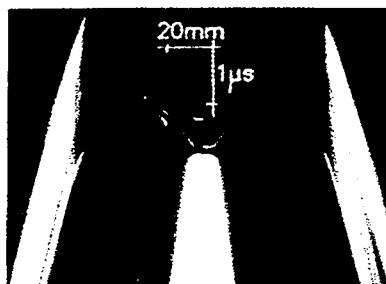


Photo 8

In our experiments the impact velocity, V , was approximately $3.5 \text{ mm}/\mu\text{sec}$. The angle, α , has a value of $(21.8)^\circ$. From this the angle, β , has the value $(59.4)^\circ$ and the angle, ψ , will be about 105° . Table 2 shows the values of D which were measured. They represent the mean value of D between the abscissas x and $(x - 5)$ mm. If there were no Mach phenomenon in the axis of the explosive block, the vertex of the conical detonation wave would propagate with the velocity given by relation 1, here about $10.2 \text{ mm}/\mu\text{sec}$. In addition to the existence of a plane central zone, we measured velocities which are somewhat larger. This proves that the Mach detonation has appeared, and that, during its formation, it possesses a high initial velocity which permits it to become rapidly larger.

NOTE: The apparatus of Fig. 5 were also used to induce Mach waves in copper, the explosive block with the conical bore being replaced by an identical block, made of copper. We thus measured shock pressures of magnitude 4 megabars, the explosive charge which was used being only 1.5 kilograms. This confirms that the description given above of the phenomena was correct.

TABLE 2
Detonation Velocities of Mach D Between
Abcissa x and $(x - 5)$ mm

x (mm)	D (mm/ μsec)	x (mm)	D (mm/ μsec)
10	14.31	50	9.31
20	11.84	60	8.79
30	10.29	70	8.25
40	9.85		

5. CONCLUSIONS

Comparing the results of paragraphs 3 and 4, we may describe the development of the Mach detonation wave as follows:

- A formation phase where the velocity, initially very high, decreases rapidly. At the same time the Mach zone becomes larger.
- A stationary phase, wherein the detonation velocity remains constant as does also the thickness of the zone. It should be understood that this phase exists only if the incident conditions are stationary.
- A return to normal detonation phase, which develops as soon as the incident conditions are no longer stationary.

In addition, the Mach detonation wave is of particular interest in obtaining high shock pressures in inert media having a small volume.

REFERENCES

1. R. E. Duff and E. Houston, J. Chem. Phys. **23**, 1268 (1955).
2. J. Thouvenin and J. P. Argous, C. R. Acad. Sc. Paris, **258**, 1725 (1964).

MACH INTERACTION OF TWO PLANE DETONATION WAVES

B. D. Lambourn and P. W. Wright
Atomic Weapons Research Establishment
Aldermaston, Berkshire, England

ABSTRACT

Streak camera and probe techniques have been used to determine the rate of growth of the Mach Bridge formed between two plane intersecting detonation waves in Composition B charges, at angles of incidence beyond the critical for regular interaction. The results expressed by Mach bridge growth angle as a function of angle of incidence, are compared with simplified theoretical solutions of the problem. The standard triple shock solution predicts growth angles about four times larger than those observed. An alternative approach due to Whitham, which represents the Mach bridge as a speeding up of the detonation wave due to the reduction in area available for transmission, predicts growth angles about double those observed. Finally a modification to Whitham's method, which makes some allowance for rarefactions following the detonation waves, gives good but probably fortuitous agreement with observed growth angles.

1. INTRODUCTION

The problem of the oblique interaction of two identical gas shocks has received a good deal of attention in the last twenty years [1-3]. The situation prevailing is by symmetry the same as a single shock reflection at a rigid wall. Briefly, the experiments show that for angles of incidence α less than some critical angle α_c a regime of regular reflection exists. In this case a reflected shock moves with the point of intersection of the incident wave and the wall such that the flow behind it is parallel to the wall. For angles greater than α_c , the position of intersection of the reflected and incident shocks moves away from the wall, and a third shock, the Mach stem, joins the triple point to the wall. A slip stream emanates from the triple point between the reflected shock and Mach stem. The situation is illustrated in Fig. 1. Experiments show that the Mach stem is curved and grows at constant rate so that the trajectory of the triple points makes angle χ with the wall.

The oblique interaction of detonation waves in condensed explosives has only recently been discussed in the open literature. Dunne [4], has given experimental results on the interaction of divergent detonation waves, and more recently [5], the solution for the regular interaction of plane detonation waves. He shows that the critical angle of incidence α_c defining the limit of

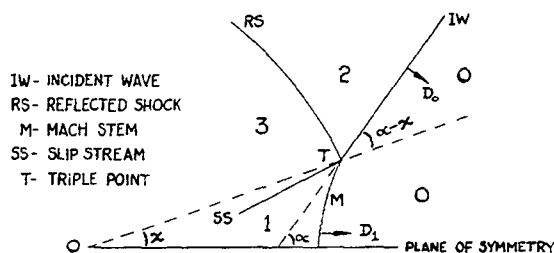


Figure 1

regular reflection is theoretically close to 45° . Feoktistova [6] has carried out experiments on the interaction of plane detonation waves in a triangular prism of unspecified explosive and has quoted the critical angle as 49° .

In this paper we report a series of experiments similar to Feoktistova's to observe Mach interaction in Composition B prisms, using both streak camera and probe techniques. The results are compared with three simplified theoretical approaches.

1. Simple three shock theory in which the Mach stem is assumed to be plane and conditions behind it are taken to be constant.

2. An alternative approximate approach due to Whitham [7] in which the interaction of

detonation waves with the wall is represented by a reduction in the area of transmission space available to the detonation wave.

3. A modification to Whitham's method to make some approximate allowance for the rarefaction following the incident detonation wave.

2. THE EXPERIMENTS

2.1 Experimental Method

The experimental assembly consisted basically of an accurately machined explosive prism of apex angle 2α in either triangular or pentagonal form, which was simultaneously initiated on the adjacent slant faces by two Comp. B/Baratol plane wave lenses (Fig. 2). Observations were made on the base surface of the H.E. prism by "streak" and/or small diameter ionisation probes. The plane wave lenses were of square external cross section, in the main 4-in. x 4-in., and were synchronously initiated.

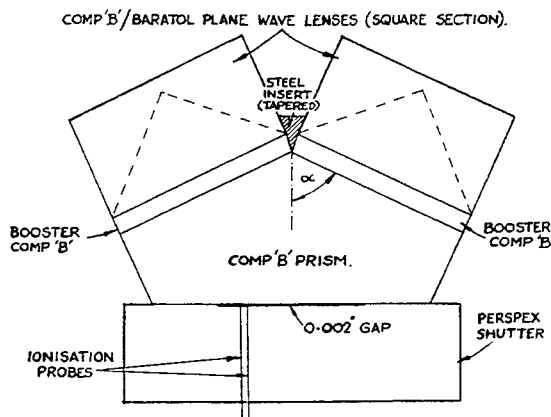


Fig. 2 - Schematic diagram of a typical experiment

In the cases where ionisation probes were used they were arranged on a close spaced diagonal array which extended well beyond the expected limits of the Mach region. The results obtained from these probes were subjected to least squares analysis to obtain cusp degeneration (Δt) and Mach Bridge width ($2s$). These quantities are defined in the inset diagram in Fig. 4.

Some early (1957/58) photographic shots used a streak camera with a $2 \text{ mm}/\mu\text{sec}$ writing speed. To facilitate differentiation between the Mach and adjacent regions the bare charge

surface was viewed in air, in which circumstances the higher pressure Mach region gives an appreciably higher luminosity to the resultant gas shock and the extent of the Mach region is easily discernible, (c.f. Fig. 14 which shows this phenomenon in the case of a toroidal cusp). In later shots a $20 \text{ mm}/\mu\text{sec}$ writing speed camera was used. With this increased resolution it was sufficient to observe only the time of arrival of the detonation front at the base of the explosive prism by using a "perspex shutter" spaced off 0.002 inch from the explosive surface. The mechanism by which a "shutter" of this type operates has been discussed by Mallory & McEwan [8] and Plauson & Mallory [9]. The application of this technique with several parallel slits on the charge, enabled several sections of the wave-front to be viewed simultaneously and a record such as shown in Fig. 3 to be obtained. From such a record an estimate can be made of the valid field of view, which is defined as the region unaffected by lateral rarefactions. These lateral rarefactions have the effect of decreasing the width of the Mach Bridge, as is shown in Fig. 4.

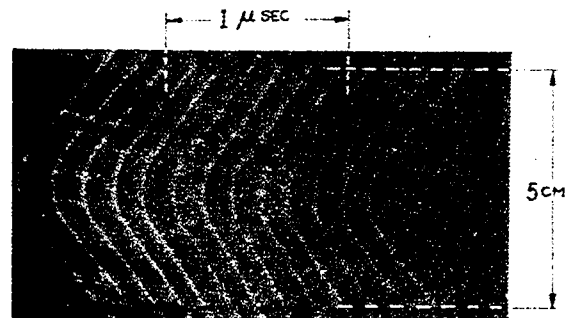


Fig. 3 - Typical multi-slit "streak" camera record ($\alpha = 81^\circ$)

In the majority of shots there was a thin slab of Comp. B interposed between the baratol surface of each plane wave lens and the slant surface of the prism. This was to ensure that at the slant faces detonation had built up to normal, since Baratol will initially underdrive Comp. B. Where the apex angle of the prism permitted these booster charges were tapered and at the apex were confined by a steel wedge, as shown in Fig. 2. The angle of taper was chosen to approximate to the critical configuration where the interaction of the detonation wave with the steel gives (theoretically) no reflected wave in the detonation products. Some of the earlier charges were encased in steel in an attempt to reduce the effect of lateral rarefactions.

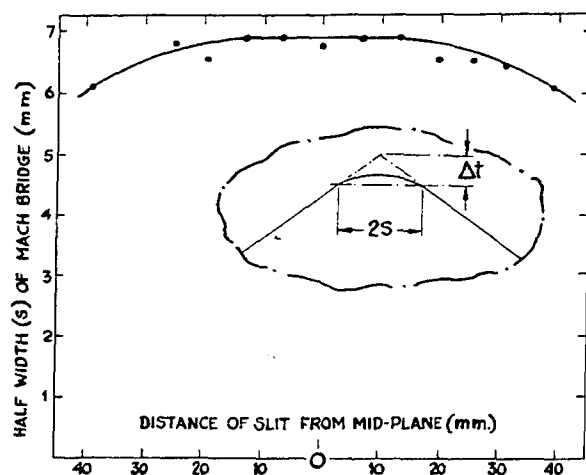


Fig. 4 - Effect of lateral rarefaction on Mach bridge width (analysis of multi-slit record shown in Fig. 3)

2.2 Results

The results are summarised in Table 1.

TABLE 1
Widths of Mach Bridges Formed Between
Colliding Detonation Waves in Comp. B

α	Height of Prism (cms)	χ
60°	8.57	2.4°
65°	3.22 ~ 8.015	2.5° ~ 3.0°
70°	2.78 ~ 7.29	3.0° ~ 3.2°
75°	6.44	4.15°
80°	5.59	4.4°
81°	7.67	5.1°

In the above table α is the semi-angle of collision and χ is the semi-angle defining the locus of the triple-point (c.f. Fig. 1).

For collision semi-angles of 65° and 70° the growth of the Mach Bridge with height of prism was studied to determine the constancy of the angle χ and the location of its origin. The results for prisms of $\alpha = 70^\circ$ are shown in Fig. 5. It is reasonably inferred that (in regions unaffected by lateral rarefactions) χ is constant and that the Mach Bridge is first formed within 1 cm of the apex of the prism.

An additional study was undertaken where the thickness of booster charge and degree of confinement were varied. The relatively large scatter of results prevented any significant trend being seen.

It is clearly seen from Fig. 3 that the Mach Bridge is curved. The values of Mach Bridge width ($2s$) given in Table 1 were based on the limits of the Mach region being given by the departure from linearity of the shock arrival plot, (c.f. inset diagram Fig. 4). This criterion is borne out by the direct observations of the bare surface of the charge in air where the extent of the high luminosity region corresponds to the Mach stem (as in Fig. 14).

3. THEORY

No complete analysis has been reported on the flow behind a Mach stem and its rate of growth. In this section are recorded three simplified theoretical approaches. The first two assume that conditions are constant behind the incident detonation wave, and the third shows how the second approach can be modified to allow approximately for the effect of the Taylor wave. All three methods assume that the incident detonation wave is a shock discontinuity with C-J conditions behind it.

3.1 Simple Three-Wave Theory

In the configuration shown in Fig. 6 it is assumed that the Mach stem (an overdriven detonation wave) is plane and has constant conditions between it, the slipstream, and the wall. In the neighbourhood of the triple point it is assumed that the reflected shock is also plane and has constant conditions behind it. The Mach stem grows uniformly with time so that the triple point moves along a trajectory at an angle χ to the plane of symmetry.

To solve the problem it is convenient to bring the flow to rest by considering an observer moving with the triple point. A velocity $D \cos(\alpha - \chi)$ is therefore added to the particle motion, where D is the detonation velocity. It then appears to the observer that particles are flowing into the incident detonation wave and Mach stem at this velocity and at angle χ to the plane of symmetry. Consider two such streamlines ABC and DE (Fig. 6). The boundary conditions to be satisfied are that the two streamlines must have the same total deflection, (i.e., $\theta_3 = \theta_1$), and the same pressure ($p_3 = p_1$). The upper streamline ABC which meets the incident

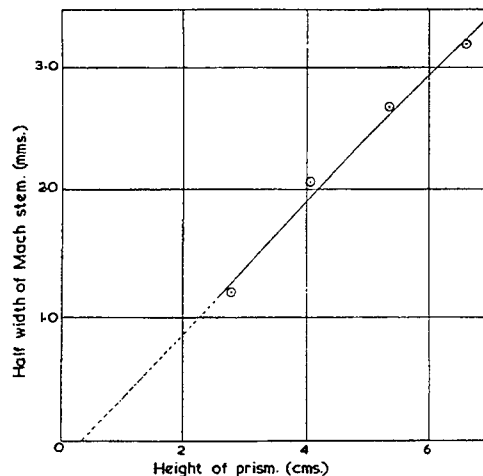


Fig. 5 - Variation of half width of Mach stem with height of prism ($\alpha = 70^\circ$)

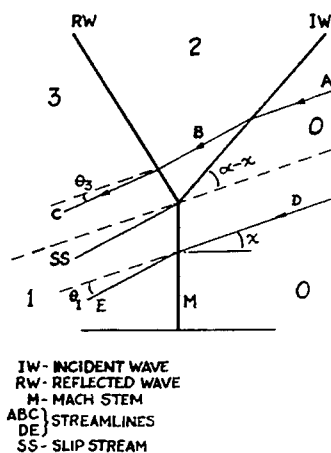


Fig. 6 - Streamlines and deflection angles in simple three shock theory

detonation wave at an angle $\alpha - \chi$ is deflected downwards in passing through the incident wave and upwards again by the reflected wave. The lower streamline DE is deflected downwards by the Mach stem.

The equations used for solving the triple shock problem are well known (see for example Ref. 1). To solve the equations an estimate is made of pressure p_3 equal to p_1 , from which are calculated the total deflections θ_3 and θ_1 of the two streamlines. The pressure is then adjusted to meet the boundary condition $\theta_3 = \theta_1$ across the contact discontinuity. The angle χ

is determined in calculating the deflection of the flow across the Mach stem.

3.2 Whitham's Method

Whitham's approximation [7] is mainly concerned with the propagation and change of shape of curved shock waves. The complete solution of such a problem requires the solution of the equations of motion for the shock and the flow behind it. Whitham simplifies the problem by drawing the orthogonal trajectories or rays to the successive shock positions, and then assumes that two adjacent rays form a tube through which an element of the shock is passing. For example in Fig. 7, the full lines represent the successive shapes, and the dotted lines the orthogonal trajectories, of a shock as it moves from left to right. The area of the tube varies as the shock progresses, so that a convergent region in a shock can become a divergent region and vice versa. Simple geometrical considerations lead Whitham to a partial differential equation with dependent variables shock speed and tube area. One of these variables can be eliminated if the variation of shock strength is known in terms of tube area. The solution of the differential equation then represents compression or rarefaction waves moving in each direction on the surface of the shock, and problems are solved by similar methods to those used for 1D unsteady flow. The problems where Whitham's method can give approximate solutions are those in which disturbances are created at the shock front and propagate along the shock.

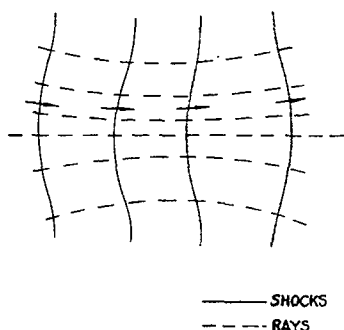


Fig. 7 - Shocks and rays for shock moving from left to right

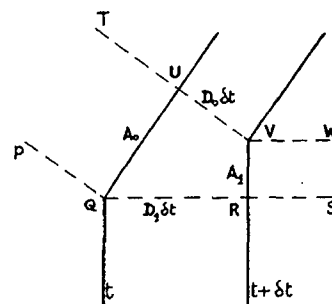


Fig. 8 - Shocks and rays in neighbourhood of triple point

We can apply Whitham's method to the interaction of two constant strength detonation waves. The plane of symmetry forms a ray in Whitham's terminology since the Mach stem is perpendicular to the wall. In Fig. 8 consider two detonation wave - Mach stem shapes near the triple point at times t and $t + \delta t$. Let PQRS and TUVW be two rays such that Q is the triple point at time t and V is the triple point at $t + \delta t$. These two rays form a tube which narrows in cross sectional area so that the detonation wave accelerates and becomes part of the Mach stem. The area of the tube is A_0 at QU and A_1 at RV. QR is parallel to the plane of symmetry, so that angle VQR is χ the growth angle of the Mach stem, and angle UQR is α , the angle of incidence. Then from Fig. 8,

$$\tan \alpha = \left(\frac{A_1}{D_1 \delta t} + \frac{D_0 \delta t}{A_0} \right) / \left(1 - \frac{A_1}{A_0} \frac{D_0}{D_1} \right) \quad (1)$$

and

$$\tan \chi = \frac{A_1}{D_1 \delta t} \quad (2)$$

We can eliminate δt by expressing $(QV)^2$ as

$$QV^2 = A_0^2 + (D_0 \delta t)^2 = A_1^2 + (D_1 \delta t)^2 \quad (3)$$

Then

$$\tan \alpha = \left(\frac{D_0}{D_1} + \frac{A_1}{A_0} \right) \left\{ \left[1 - \left(\frac{D_0}{D_1} \right)^2 \right] \left[1 - \left(\frac{A_1}{A_0} \right)^2 \right] \right\}^{-1/2} \quad (4)$$

$$\tan \chi = \frac{A_1}{A_0} \times \left[\frac{1 - (D_0/D_1)^2}{1 - (A_1/A_0)^2} \right]^{1/2} \quad (5)$$

Following Whitham it is assumed that the relation between D and A for an infinitesimal change of tube area, can be carried over into a finite change of area in a Mach interaction. The relation $A(M)$ for a shock wave was derived by Chester [10] and Chisnell [11], by considering the interaction of a shock with a small discontinuity in a tube area, such that there is an infinitesimal reflected wave (Fig. 9). The corresponding differential relation for an overdriven detonation wave can be derived by following the procedure used by Chisnell [11]. Assuming the detonation products obey a perfect gas equation of state with adiabatic exponent γ , it is: -

$$-\frac{1}{A} \frac{dA}{dZ} = \frac{1}{\gamma Z} + \frac{1}{2Z-1} + \frac{\gamma Z + 1}{\sqrt{\gamma Z^2 (2Z-1) [(\gamma-1)Z+1]}} \quad (6)$$

where dA is the change in area of the tube, Z is the ratio of overdriven wave pressure to C-J pressure and dZ is the corresponding change in detonation wave strength. Assuming that it is valid to integrate this expression, the $A(Z)$ relation is of the form:

$$A \cdot f(Z) = \text{constant} = A_0 f(1) \quad (7)$$

where

$$f(Z) = Z^{1/\gamma} \times (2Z-1)^{1/2} \times B(Z) \times C(Z) \quad (8)$$

$$B(Z) = \left\{ [2(\gamma-1)(2Z-1)]^{1/2} + 2[(\gamma-1)Z+1]^{1/2} \right\} \sqrt{\frac{2\gamma}{\gamma-1}} \quad (9a)$$

$$C(Z) = \exp \left\{ -1/2 \sin^{-1} \left[\frac{(3-\gamma)Z-2}{(\gamma+1)Z} \right] \right\} \quad (9b)$$

The pressure ratio Z is related to D_1/D_0 , the ratio of the overdriven detonation velocity to C-J velocity by

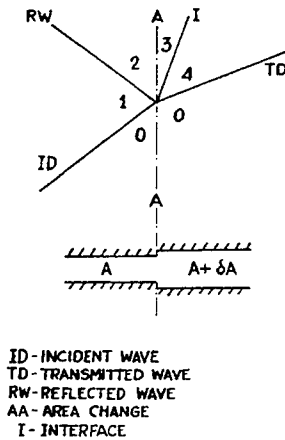


Fig. 9 - Interaction diagram for detonation wave meeting small change of tube area δA

$$\frac{D_1^2}{D_0^2} = \frac{Z^2}{2Z-1} \quad (10)$$

The validity of Eq. (7) has been checked for the case where a detonation wave converges in a sphere of explosive which has been initiated by a spherical piston driving the outer boundary in at C-J particle velocity (Fig. 10a). This has been calculated by a 1D code which treats the detonation wave as a shock discontinuity, and the results are in good agreement with Eq. (7).

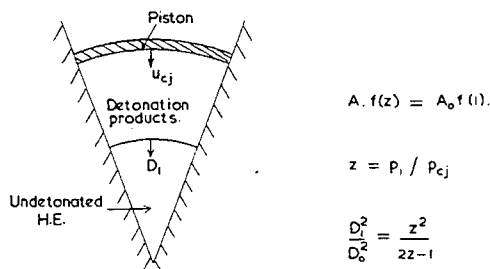


Fig. 10a - Confirmation of $A(D)$ relation, no following rarefaction

Equations (7) and (10) give the required $A(D)$ relation to be substituted into Eqs. (4) and (5). The final result is a relation between χ and α .

3.3 Modification to Whitham's Theory to Allow for Following Rarefactions

In the two theoretical approaches described above, it has been assumed that the detonation wave has uniform conditions behind it, whereas in the experiments described in para. 2, the incident detonation wave in the main explosive is initiated from an explosive lens, and will therefore be followed by a partial Taylor wave. The interaction of the Taylor waves following the incident detonation waves will introduce a rarefaction behind the Mach stem. Since the flow behind the Mach stem is subsonic, this rarefaction will interact with the Mach stem and reduce the rate of growth.

In Whitham's method the effect of a following rarefaction is equivalent to saying that the increase in wave strength is smaller for given change of tube area than it would be without the following rarefaction. Strictly Whitham's method is only applicable to a disturbance originating at the incident wave front, so the insertion of a following rarefaction can only be done to give some order of magnitude to the effect of a Taylor wave. In addition with a following rarefaction there is no unique relation between wave strength and area of a tube. The relation depends on the origin of the rarefaction and the initial wave strength.

To find the effect on the wave strength/tube area relation of the rarefaction behind the Mach stem, it seems reasonable to take another situation in which the overdriven detonation wave is followed by a Taylor wave starting at the point of initiation. Such a situation is the increase in strength of a spherical detonation wave converging in a sphere of explosive which has been initiated at its bare outer surface (Fig. 10b). From calculation on this configuration, a numerical relation between tube area and detonation wave strength has been determined. Approximately it can be written in the form,

$$A(2Z-1)^{1/2k(Z)} = A_0 \quad (11)$$

where $k(Z)$ varies slowly from ~ 0.21 for $Z = 1$ to ~ 0.29 for $Z \sim 50$. To test whether $k(Z)$ is roughly the same in another situation, the calculation was repeated in cylindrical geometry. In this case $k(Z)$ varies from 0.19 to 0.3.

The calculation in this case for determining the growth of Mach stems is exactly the same as for normal Whitham theory except that Eq. (11) replaces (7). As may be expected for

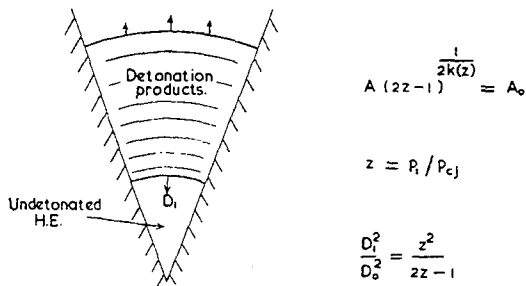


Fig. 10b - Determination of $A(D)$ relation, with following rarefaction

any α , the rate of growth of the stem χ is smaller than with the full Whitham method.

4. COMPARISON BETWEEN THEORY AND EXPERIMENT

The experimental values of χ are plotted against α in Fig. 11 together with curves for the three theoretical methods. It will be seen that the three shock theory gives values of χ about three to four times the experimental values, Whitham's theory for constant conditions behind the detonation wave gives χ values about twice the experimental results, but Whitham's theory modified to allow approximately for the following rarefactions seems to agree well with experiment.

Taking the three shock theory first, two points emerge:

(1) The value of χ starts from zero at $\alpha \sim 41^\circ$ at an angle less than the critical angle α_c for regular reflection. Hence for some angles either regular or Mach interactions are theoretically permissible.

(2) χ decreases to zero again at $\alpha = 90^\circ$. This is unlike the behaviour for the interaction of shocks which have a finite limiting value of χ for $\alpha = 90^\circ$. The zero limiting value of χ for detonation waves is a consequence of the C-J condition where the flow immediately behind a detonation wave is just sonic. This suggests that an experimental investigation of the behaviour of χ near $\alpha = 90^\circ$ might well indicate whether the C-J condition really holds.

Whitham's method with constant conditions behind the detonation wave ought to agree with three shock theory since it is based on the same premise of a straight Mach stem with constant conditions behind it. The disagreement is worse than Whitham obtained between the two theories for very strong gas shocks.

Whitham's method requires the wave to be normal to the plane of symmetry for all angles of incidence. Hence there is a Mach stem for all values of α . However χ values are small for $\alpha < 45^\circ$.

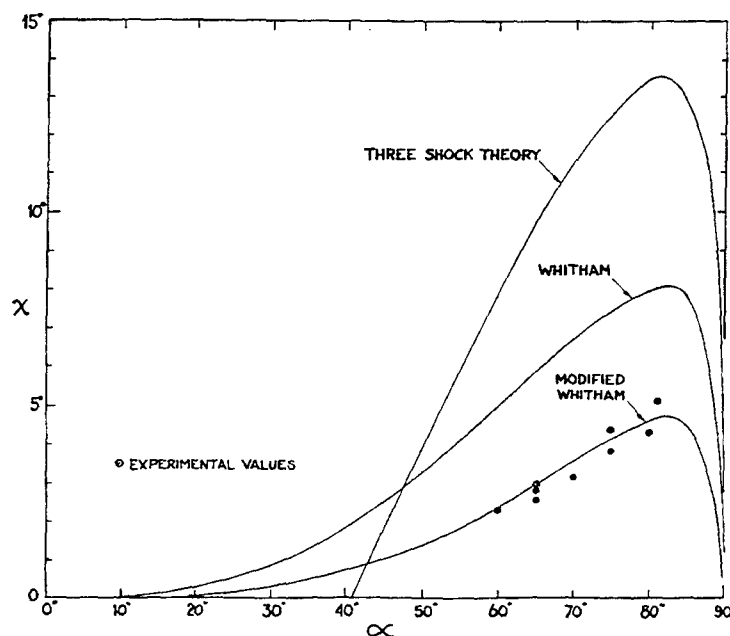


Fig. 11 - Rate of growth of Mach stem

It is also of interest to plot the pressure ratio Z behind the Mach stem as a function of angle of incidence. This is done in Fig. 12 for the three theories. Since all three theories assume constant conditions behind the Mach stem, this pressure is appropriate to the plane of symmetry. Also plotted is the curve for regular reflections.

The velocity of the Mach Bridge along the plane of symmetry (D_1) can be determined from the cusp degeneration Δt , i.e., the time interval between the arrival of the Mach Bridge and that of the theoretical cusp; the plane wave detonation velocity, and the height of the prism. Alternatively for a plane Mach Bridge:

$$D_1 = \frac{D_0 \cos \chi}{\sin(\alpha - \chi)} \quad (12)$$

Table 2 gives the values D_1/D_0 derived from the experimental results and the values of pressure ratio Z obtained from them using Eq. (10).

TABLE 2
Pressure Ratio Behind Mach Bridge
Calculated from Experimental Values

α	χ (Experimental)	D_1/D_0	Z
60°	2.4°	1.17	2.08
65°	2.75°	1.128	1.86
70°	3.2°	1.086	1.64
75°	4.15°	1.056	1.475
80°-81°	4.8°	1.026	1.285

The results are plotted in Fig. 12 together with values given by Feoktistova which were obtained from the interaction of divergent detonation waves. Again the modified Whitham theory gives the best agreement with experimental results.

5. DISCUSSION

The experimental results have established that the Mach stem probably starts growing from where the two incident waves first intersect. Values of χ have been determined for α values in the range 60-81°. In every case the Mach stem is curved.

Of the simple theories, all assuming that conditions are uniform behind a straight Mach stem, only the modified Whitham theory gives agreement with experimental values of χ and the pressure on the plane of symmetry. Since this is an approximate modification, allowing for following rarefactions, to an inexact theory, the agreement may be very largely regarded as fortuitous. One would be more confident if the unmodified Whitham theory agreed with three shock theory. The reasons for the disagreement are twofold.

(1) Although pressure behind the reflected wave in Whitham's method has been equated to the pressure behind the Mach stem, no attempt has been made to equalise flow deflections; the necessity to do so having been removed by the simplifying assumptions.

(2) The formula for variation of wave strength with tube area used in Whitham's method has been derived for infinitesimal area changes, but is used for finite changes.

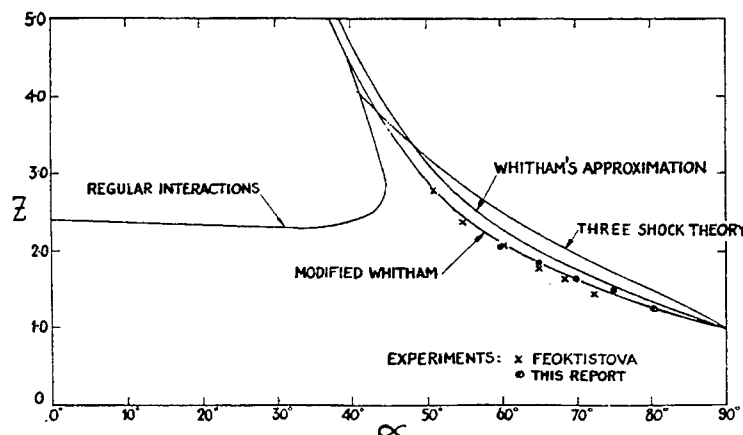


Fig. 12 - Variation of z = (pressure behind reflected wave/pressure behind incident wave) against angle of incidence α

However the importance of the difference between the two Whitham theories is that it indicates the strong effect which a following rarefaction has on the rate of growth of a Mach stem. In addition the fact that the modified Whitham theory does agree with experiment indicates that the $A(Z)$ function (11) might be used for the transmission of detonation waves in other experimental geometries, just as Bryson and Gross [12] have successfully used Whitham's theory to predict the diffraction of a gas shock around a sphere.

Apart from rarefactions following the incident wave affecting the rate of growth of the Mach stem, Sternberg [3] has suggested that the interaction of the structures of gas shocks at the

triple point could affect the flow there. The effect must be more true of detonation waves for which the reaction zone is a few tenths of a mm thick. This has been illustrated by one experiment, of the type described in section 2, that has been carried out in Baratol which has a reaction zone of approximately 1 mm. At an α of 65° , χ was 11.1° assuming it commenced at the apex, i.e., much closer in agreement with three shock theory. The Mach stem was very curved. It should be noted however, that in this experiment the Taylor wave was much less important since it started at the back of the plane wave lens.

To tackle interaction of detonation waves, theory needs therefore to include the effects of

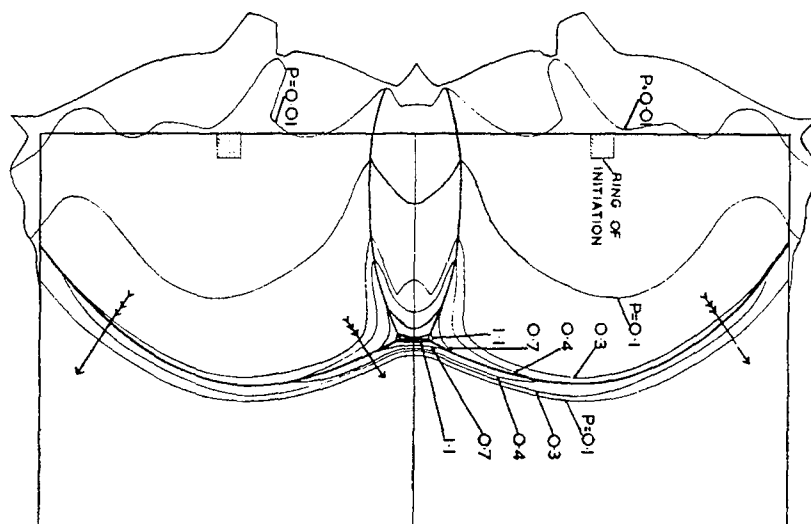


Fig. 13 - Pressure distribution (ring initiation) at $T = 6.1 \mu\text{secs}$

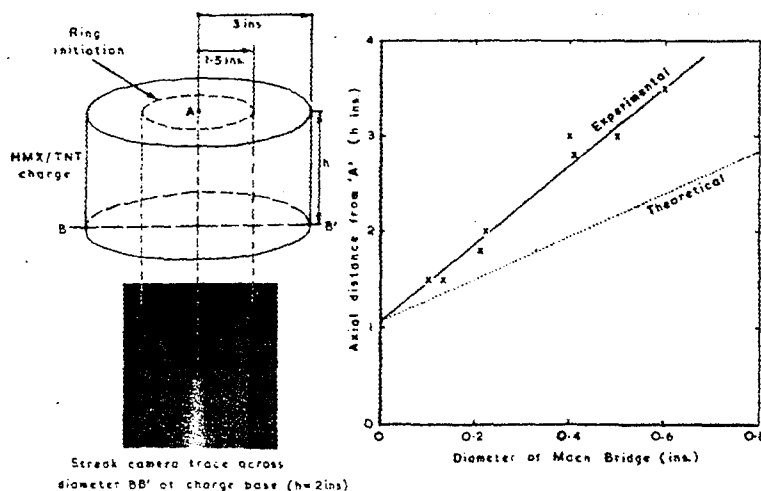


Fig. 14 - Growth of Mach bridge in toroidal interaction

the reaction zone, the Taylor wave and the corner signal emanating from where the waves first intersect. The most likely approach seems to be to use a 2D unsteady hydrodynamics code. One such calculation has been done at AWRE on the problem of the growth of Mach stem on the axis of a cylindrical HMX/TNT charge which was initiated at one plane face on a concentric ring. A typical set of pressure contours at one time is shown in Fig. 13. A typical streak record of the bare charge in air for a particular charge thickness is shown in Fig. 14. The Mach stem is again curved. Also in Fig. 14, the observed and calculated Mach stem diameters are plotted against distance travelled by the stem along the axis. It will be seen that the calculation gives the Mach stem growing at about twice the rate of experiment though the critical angle for the start of the Mach stem is about the same ($\sim 35^\circ$). This angle is less than for plane C-J detonation waves probably because the detonation wave in ring initiation is overdriven when it converges on to the axis. The divergence between calculation and experiment is probably because the mesh used in the calculation was too coarse. The whole explosive was represented by 30 meshes in each direction (1 mesh = 0.1 in.) the Mach stem was 4 meshes at its maximum radius and the calculation requires of order 1 to 2 meshes for the "reaction zone." It is clear that a much finer mesh is needed to provide computational resolution comparable with experiment.

ACKNOWLEDGMENTS

The authors wish to acknowledge the valuable experimental assistance given by Messrs. B. L. Asher and M. G. Young, and the computational assistance given by Mr. M. P. Tuck.

REFERENCES

1. R. Courant and K. O. Friedrichs, "Supersonic Flow and Shock Waves," Interscience, 1948.
2. W. Bleakney and A. H. Taub, "Interaction of Shock Waves," *Revs. Modern Physics* **21** (4), 584-605 (Oct. 1949).
3. J. Sternberg, "Triple Shock Intersections," *The Physics of Fluids* **2** (2), 179-206 (Mar.-Apr. 1959).
4. B. B. Dunne, "Mach Reflection of Detonation Waves in Condensed High Explosives I," *Physics Fluids* **4** (7), 918-924 (July 1961).
5. B. B. Dunne, "Mach Reflection of Detonation Waves in Condensed High Explosives II," *Physics Fluids* **7** (10), 1707-1712 (Oct. 1964).
6. E. A. Feoktistova, "Experimental Observation of Mach Reflection of Detonation Waves in a Solid Explosive," *Sov. Phys.-Doklady* **6** (2), 162-163 (Aug. 1961).
7. G. B. Whitham, "A New Approach to Problems of Shock Dynamics, Part I—Two Dimensional Problems," *Jrnl. Fluid Mechanics* **2**, 145-171, (1957).
8. H. D. Mallory and W. S. McEwan, "Transparency of Glass and Certain Plastics under Shock Attack," *Jrnl. Appld. Phys.* **32** (11), 2421-2424 (Nov. 1961).
9. R. A. Plauson and H. D. Mallory, "Extinction of Gas-Shock Luminosity Against Transparent Surfaces," *Jrnl. Appld. Phys.* **35** (3, 1), 502-507 (March 1964).
10. W. Chester, "The Quasi-Cylindrical Shock Tube," *Phil. Mag.* (7) **45**, 1293-1301 (1954).
11. R. F. Chisnell, "The Motion of a Shock Wave in a Channel with Applications to Cylindrical and Spherical Shock Waves," *Jrnl. Fluid Mechanics* **2**, 286-298 (1957).
12. A. E. Bryson and R. W. F. Gross, "Diffraction of Strong Shocks by Cones, Cylinders and Spheres," *Jrnl. Fluid Mechanics* **10**, 1-16 (1961).

NOTE ADDED IN PROOF

Subsequent experiments at values of α in the range 81° to 87.5° have shown that the value of χ continues to increase with α and not decrease as predicted by the approximate theories. Unless a sudden drop to zero occurred between $87\frac{1}{2}^\circ$ and 90° , an apparent hydrodynamic paradox would seem to exist since a finite value of χ at $\alpha = 90^\circ$ would be inconsistent with the C.J. hypothesis for plane detonation waves.

COMMENTS

S. JOIGNEAU (Commissariat a l'Energie Atomique, France): There are two approximations to calculate the angle χ .

(1) The plane Mach stem.

(2) The rays, or paths orthogonal to the successive shock positions, which are assumed to lie along the particle paths.

Do the two corresponding errors balance each other? If so, could it account for the very good agreement between theory and experiment?

B. D. LAMBOURN (Atomic Weapons Research Establishment, Aldermaston, England): The two assumptions mentioned are discussed by Whitham in his paper when he applies his approximations to gas shock interactions. It would appear that as the results of the Modified Whitham method do give agreement with the experiments reported in our paper, then in some way all the errors in the approximation must have fortuitously cancelled out.

INTERACTION OF OBLIQUE DETONATION WAVES WITH IRON

H. M. Sternberg and D. Piacesi
*U.S. Naval Ordnance Laboratory, White Oak
Silver Spring, Maryland*

ABSTRACT

Impacts of oblique detonations in pentolite on iron are treated by the methods of plane, steady, compressible flow. Regular reflection, three shock Mach reflection, and expansion are discussed. The maximum transmitted pressure, 452 kb, is shown to occur at an impact angle of 63.4° , at the onset of Mach reflection. The steady double plastic wave structure in iron, which appears at impact angles between 71.3° and 90° , is calculated. Results for two colliding detonation waves are obtained as a special case.

This paper, with some changes and additions, has been published in the *Phys. Fluids* 9, 1307 (1966).

INTERACTIONS OF DETONATION WAVES IN CONDENSED EXPLOSIVES

S. D. Gardner and Jerry Wackerle
*University of California, Los Alamos Scientific Laboratory
Los Alamos, New Mexico*

ABSTRACT

Flow patterns similar to regular and Mach reflection resulting from the interaction of detonation waves in condensed explosives have been observed with rotating mirror cameras and flash radiography. The principal emphasis of the study has been with the oblique collision of plane detonation waves. In this configuration the assumptions of steady flow, infinitesimal reaction zone thicknesses, the Chapman-Jouguet hypothesis and simple reaction-product equations of state permit an analytic solution for the detonation parameters for regular reflection and the computation of the critical angle for the onset of Mach reflection. These critical angles have been measured for Composition B, 9404-03 PBX, Baratol, and nitromethane. Additional data obtained on Composition B include a measurement of Mach stem pressure and stem shape. In inhomogeneous explosives Mach stems and reflected shocks have displayed substantial curvatures and flash x-ray studies have revealed anomalous density regions in the symmetry planes in both regular and Mach reflection experiments. These observations, along with deviations in computed and measured critical angle values, have indicated a degree of failure of the simplified theory to provide an exact, detailed description of the interaction phenomena; this failure is currently believed to result primarily from the nonuniform structure of the detonation wave.

COMMENTS

S. JOIGNEAU (Commissariat à l'Energie Atomique, France): The sonic angle of critical reflection calculated with a "polytropic" equation of state is in better agreement with experiment than the limiting angle of regular reflection calculated with the same equation. Can one conclude that the critical angle is the sonic angle, rather than the limiting angle of regular reflection?

S. D. GARDNER and J. WACKERLE (Los Alamos Scientific Laboratory, Los Alamos, New Mexico): The sonic angles for both Composition B and nitromethane are calculated to be about 1° less than the calculated critical angles for regular reflection and therefore are in better

agreement with the experimental transition angles to Mach reflection. However, in view of the rather large variation of α_{cr} (as well as the sonic angle) with the several equation-of-state representations, and without an independent means for choosing which of these is most appropriate, it is impossible for us to infer to which of the three limiting angles the experimental transition angle corresponds, i.e., to the critical angle for regular reflection, the sonic angle, or the critical angle for Mach reflection.

A. RAUCH (Commissariat à l'Energie Atomique, France): We have used an experimental arrangement which was nearly the same as those

used by Gardner and Wackerle. The colliding angle was 60° and the explosive was equivalent to Composition B.

We have found that the Mach stem width grows from 0 to 4.5 mm for a stem run of about 80 mm. For runs between 80 mm and 160 mm the stem width remains constant. It seems the Mach detonation wave is stationary between these two limits.

We don't know why the stem width remains constant; we think the release waves lower the Mach detonation speed. I want to ask Mr. Gardner and Mr. Wackerle if they have done experiments for stem runs greater than 100 mm and if they have made the same observations.

S. D. GARDNER and J. WACKERLE: In our measurements of stem growth rates there was no indication of a decreasing growth rate for stem runs up to 100 mm, so measurements for

longer runs were not considered necessary. Without knowing the details of your experiment, we would like to point out that considerable care must be taken to protect the interacting waves from side rarefactions in an experiment with a long stem run. The effect of these rarefactions will be to eventually lower the pressure of the colliding waves, which in turn will result in a lower growth rate. Assuming that such a mechanism was not responsible for your observed zero growth rate, it is conceivable that the rarefaction centered behind the interaction attenuates the stem over a very long run, causing a gradual change in the orientation of its intersection with the triple point, which in turn might result in a decreasing or vanishing growth rate. A preliminary calculation of a Mach reflection at this angle of incidence (60°) shows that a solution exists for a zero-growth-rate stationary flow-pattern in the immediate vicinity of the triple point, provided the stem is sufficiently curved for it to intersect the triple point at the necessary angle.

AXIAL INITIATION OF MULTI-COMPONENT EXPLOSIVES CHARGES

Louis Deffet and C. Fossé
*Centre de Recherches pour l'Industrie des Produits Explosifs
Belgium*

ABSTRACT

The effect of axial initiation with a detonating fuse is compared with the normal booster initiation. The propagation of detonation is observed in the explosive by means of flash-radiography; the properties of shock waves emerging in surrounding Perspex are used to evaluate the pressure effects on the walls of the charge. Two explosive mixtures containing ammonium nitrate (AN-FO and AN-TNT-Al), an ion-exchanged explosive (EIE) and RDX were tested. For RDX and AN-TNT-Al, no significant difference was observed between axial and normal initiation. The discussion of results obtained with AN-FO and EIE shows some details of axial initiation with detonating fuse.

INTRODUCTION

The industrial explosives containing mainly ammonium nitrate can be primed either by a detonator or by a high explosive booster, placed at one end of the charge or by one or several detonating fuses, placed along the same. The point of determining, which of both methods is most adequate for improving the detonation efficiency has been often raised and was raised once more when the ammonium nitrate-fuel oil mixtures made their appearance.

Numerous priming laboratory tests were conducted by Cook [1] and coworkers who came to the conclusion that the charge was less completely detonated by the detonating fuse than by a booster such as dynamite or high explosives. The high energy detonating fuses continued however to be successfully used in quarry blasting, and AN-FO mixtures have given rise to an abundant and varied technical literature. More recently Sadwin and Stresau [2] studied this problem again by applying a photographic method for observing the detonation wave, obtained in the ammonium nitrate-fuel oil explosive, centrally primed. By measuring the expansion speed, they concluded to a non-ideal detonation. As a contribution to such studies,

we have examined cylindrical charges, primed by means of axial detonating fuses; these charges are of such a length and diameter that they are capable of reproducing the real phenomenon completely. Moreover we have compared the results obtained by testing ammonium nitrate-fuel oil explosive in this way, with other results obtained in a similar way for RDX and other explosive mixtures. We used flash-radiography for observing and analysing the propagation of the detonation wave in the explosive. It was possible, in some cases, to compare the pressure exerted on the walls, as a function of the priming of the charge, by photographing the shock wave in a Perspex block, used as a means of confining the explosive, this method being similar to this one successfully used recently by Hershkowitz [3].

EXPERIMENTAL METHODS

Observation of the Shock and Detonation Waves

The detonation wave can be observed by flash-radiography, when the charge is confined in Perspex cylinders (Fig. 1). The curvature and the thickness of the normal compression

Note: This work was sponsored by the "Association des Fabricants Belges d'Explosifs" and "I.R.S.I.A." We also thank the technicians who helped us to successfully conduct this research work and particularly M. P. Goemans, M. R. Vanden Berghe and M. G. Van Roy.

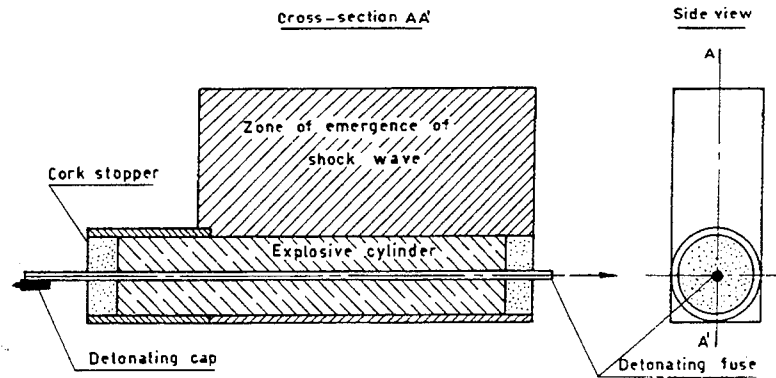


Fig. 1 - Schematic view of experimental arrangement

wave can be measured when the explosion is initiated by a booster. If the explosion is axially initiated, the detonation wave gradually developing along the axis of the detonating fuse and propagating at the velocity at which the detonation axially propagates in this fuse, laterally propagates at a velocity which can be directly deduced from the value of the angle formed by the line, tangent to the wave surface and the axis of the detonating fuse (Fig. 2). The lateral propagation velocity is obtained by the following relation:

$$v_L = v_C \sin \beta \quad (1)$$

in which v_C is the detonation velocity of the detonating fuse.

The radiographs enable us to find how the velocity and the cylinder wall attack angle, vary

in dependence with the distance to the axis and consequently the diameter of the charge. They enable us to observe the shock wave in the Perspex block, but only when the charge is capable of releasing a sufficiently high energy.

The hydrodynamic properties of translucent bodies such as water, air, glass, polymethylmethacrylate, have been largely taken advantage of, in the course of these last years for studying the shock waves generated in a dense medium by the detonation of high explosives. In 1952, Pugh [4] photographically examined the effect produced by a detonating fuse upon a glass support. Dapoigny [5] made use of the flash radiography for studying the shock wave induced in polymethylmethacrylate by an explosive detonating in a direction parallel to the wall. He deduced the relation existing between the pressure and the shock velocity in

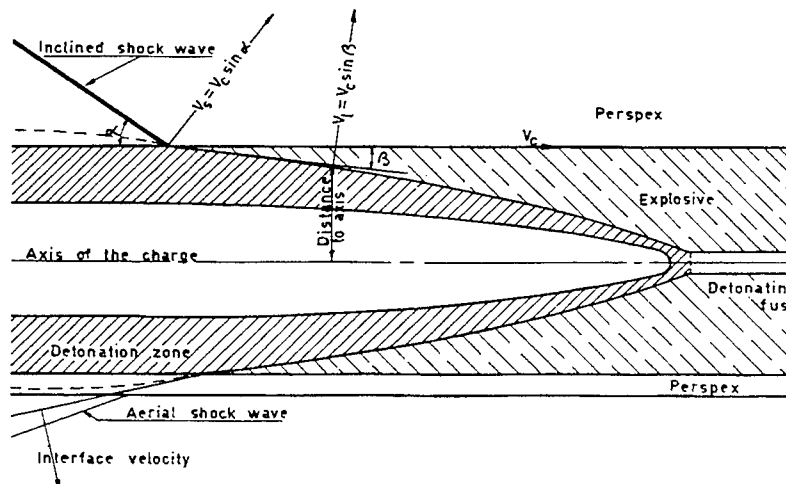


Fig. 2 - Aspect of the detonation zone in explosive and the shock wave generated in surrounding medium

this polymer. In the present work, we use the classical shock relation

$$P_s = \Delta D W \quad (2)$$

in which Δ is the density of Perspex (1.185), D , the velocity of the shock wave, and W , the particle velocity. W may, in first approximation, be related to D by the relation

$$W = \frac{1}{k} (D - C_0) \quad (2a)$$

and the numerical values obtained from a recent paper of Jaffe [6] where

$$k = 1.50, \text{ and}$$

$$C_0 = 2,590 \text{ m/s} = \text{sound velocity.}$$

The linear relation between D and W was obtained by Jaffe, with experimental results from different authors, and includes results obtained with Perspex; the lowest values ($D = 2,700$ to $3,000$ m/s) were obtained by Jaffe with Lucite. Although we are dealing with oblique incident shock waves the above relation is considered as sufficiently accurate. We wish also to note that experimental values of the $P_s - D$ relation were obtained by Cook [7] in the shock region of $D = 3,000$ to $5,000$ m/s, with Lucite; some of them disagree from the calculated values; the two figures will be given when the difference is of interest. The Lucite shock properties have been taken advantage of by Hershkowitz [3] for studying how the deflagration propagates in a granular explosive. He distinguished the supersonic waves from the elastic ones (sonic) appearing when the propagation rate is insufficiently high.

Shock waves are observed in Perspex blocks drilled through with different diameters (Fig. 1). The inner cylindrical cavity is in some cases prolonged on both ends of the block by a cylinder of which the diameter is the same as the diameter of said inner cylindrical cavity, when it is desirable to avoid any action of the initiating explosive or of the waves reflecting upon the walls. The diameters of the cylinder holes drilled and the thickness of the blocks were respectively equal to 30/40 mm, 42/52 mm and 63/76 mm; the minimum length of the charge was 200 mm. The shock wave, which develops at the top of the block as well as in the ambient air in contact with the bottom of the same have been photographed by use of high-speed photography equipment; we used the Crazz-Schardin system provided with explosive lamps of which the emission durations are about 0.1 microsecond. This equipment was developed in our

laboratories by R. Vanden Berghe [8]. The shock wave propagation or expansion velocity can be obtained by the following relation:

$$V_s = V_c \sin \alpha \quad (3)$$

in which V_c is the velocity component parallel to the axis of the charge (Fig. 2), or by superposing pictures obtained, for which the time-spacing is known with precision. The propagation velocity can be defined in this way with a precision amounting to ± 100 m/s. The pressure exerted on the walls surrounding the charge can thus be deduced using Eqs. (2) and (2a). RDX, which has been used as a standard explosive, is however the sole one which can be considered as having a characteristic impedance nearly equalled to that of the Perspex. In the other cases, the values of the shock pressure measured in the Perspex are comparable between each other when they refer to the same explosive.

Comments About the Explosives Studied

a. The ammonium nitrate-fuel oil mixture 95/5 (NA-FO mixture) was prepared with NH_4NO_3 prills of Canadian origin, encased from 0.4 to 0.7% in a mixture containing 90% clay and 10% of mono- and dimethyl-naphthalene-sulfonate. Its loading density is equal to 0.85; a No. 8 detonator detonates such a mixture in a steel cylinder. The following detonation velocities have been obtained in 3-mm-thick steel cylinder, the explosive being primed by means of 50 g of Dynamite:

inside diameter 21 mm: 1,230 m/s

inside diameter 42 mm: 3,600 m/s.

Brinkley [9] found that the detonation velocity of mixtures of this type reached 4,300 m/s on condition that the diameter of the charge be sufficiently high, the said value being near the theoretical one. In our experiments conducted in Perspex tubes, we found a detonation velocity of 1,800 m/s (inside diameter of tube: 42 mm, thickness of the tube: 52 mm, priming: 75 g Dynamite).

b. The AN-TNT-Al (80/18/2) mixture is largely used in quarries and coal mines; it is prepared with thin ammonium nitrate and TNT crystals and powdered aluminium. The No. 8 detonator initiates this mixture without need of confinement; the detonation velocity amounts to $3,680 \pm 50$ m/s, when it is loaded at density of 1.10 in a 30/40 mm Perspex tube.

c. The exchanged ion explosive (EIE) is the safety explosive which is actually the most used in Belgian coal mines. It contains 10% nitroglycerine and 90% of a $\text{NH}_4\text{Cl-KNO}_3$ stoichiometric mixture; these salts react upon each other when strongly confined and this reaction releases an energy which is equivalent to that of the well-known $\text{NH}_4\text{NO}_3\text{-NaCl}$ mixture. This explosive is detonated by a No. 8 detonator and its detonation velocity amounts to 1,350 m/s in the 30/40 mm Perspex tube; this velocity is practically unchanged, when the diameter of the charge is increased, the confinement remaining weak.

d. The following mixtures of the "Slurry" type, of which the density was nearly equal to 1.5 particularly the mixtures complying with following formulae:

AN-Tritonal- H_2O , 40/40/20

and AN-propellant powder- H_2O , 40/45/15 of which the detonation velocity in a steel cylinder (inside diameter 42 mm, thickness 3 mm) was respectively 5,400 and 5,200 m/s, led unfortunately to negative results.

e. As standard explosive we used Hexogen (RDX) in powder, of loading density equal to 1.00 and detonation velocity in Perspex tube (30/40 mm) of $5,985 \pm 50$ m/s.

f. Below are the main characteristics of the detonating fuses we made use of:

1. 12 g PETN/meter, detonation velocity 6,600 to 6,900 m/s.

2. 20 g PETN/meter, detonation velocity 7,160 m/s.

EXPERIMENTAL RESULTS

These results fall into two categories:

A. Those relating to the shock or detonation wave in the explosive.

B. Those, relating to the shock generated in the Perspex walls which surround the charge. In this group, the results relating to the poor reactive mixtures will be presented as a discussion.

Characteristics of the Wave which Propagates in the Explosive

The measurements and observation from X-ray flash pictures are mentioned in Table 1, columns (d) and (e); columns (b) and (c) of the same table show the results of measurements of the detonation velocity in the normal detonation wave and the results of calculations made in order to obtain the value of the detonation pressure. Attention is drawn to the following:

(a) The detonation wave generated by a detonating fuse propagates in the explosive at a velocity which depends upon the composition of the explosive. The wave in explosives having a high detonating velocity (RDX and AN-TNT-Al) propagates at a velocity, which remains constant.

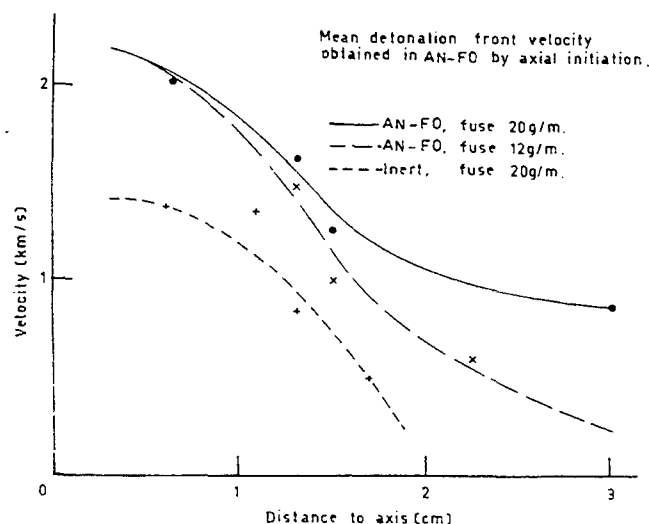


Figure 3

TABLE 1
Characteristics of the Detonation Wave

Explosive (a)	Priming by Means of a Detonator or a Booster		Priming by Means of an Axial Detonating Fuse	
	Detonation Velocity (m/s) (b)	Detonation Pressure P_D (kilobars) (c)	Propagation Velocity V_L (m/s) (d)	Angle at which the Detonation Wave Meets the Wall (β) (e)
(1) AN-TNT-Al $\Delta = 1.10$	$3,680 \pm 50$	39.4* (calculated)	$2,580 \pm 100$ (constant)	23° ϕ 30 mm ϕ 42 mm
(2) AN-FO $\Delta = 0.85$	A. I, 800 ± 50 Perspex ϕ 42 mm	7.8*	From 2,200 to 850 (Fig. 3)	12° ϕ 30 mm $(7 \pm 1)^\circ$ ϕ 42 and 63 mm
	B. $3,600 \pm 50$ Steel ϕ 42 mm	31.0*		(Detonating Fuse 20 g PETN/m)
(3) EIE $\Delta = 1.20$	$1,350 \pm 50$		2,300 (ϕ 30 mm) above this diameter decreases up to 1,700 m/s	From 19° (ϕ 30 mm) To 13° (ϕ 63 mm)
(4) RDX $\Delta = 1.00$	$5,985 \pm 50$	110 (semi-experimental)	$5,250 \pm 75$ (constant)	50° ϕ 30 mm

*Using equation formulated by Jones: $P_D = 4.157D^2\Delta(1 - 0.543\Delta + 0.193\Delta^2) 10^{-6}$.

(b) As regards the AN-FO mixtures, the form of the wave propagation velocity curve in its dependence with distance to the axis of the detonating fuse has been examined in more detail. The diagram (Fig. 3) plotted by using the results of the measurements made for this purpose shows that the 12 g/m detonating fuse generates a wave, which gradually damps down, whereas the 20 g/m detonating fuse generates a wave, for which the front progresses at a velocity which tends to stabilize in the region of 1,000 m/s. Two pictures are added (Figs. 4 and 5) as an example of radiographs obtained in this case. The wave expansion velocity, the thickness of the compressed zone, generated in the AN-FO explosive and the characteristics of the shock wave generated by the same detonating fuse in the course of an experiment, in which the AN-FO explosive was replaced by ammonium nitrate in prills, encased in chalk and consequently nonreactive, are elements, which show that a violent reaction occurs in the AN-FO explosive, the destructive effect of such a reaction upon the Perspex block being an example of its violence.

(c) The detonation wave of AN-FO and EIE looks like the ideal detonation wave, when

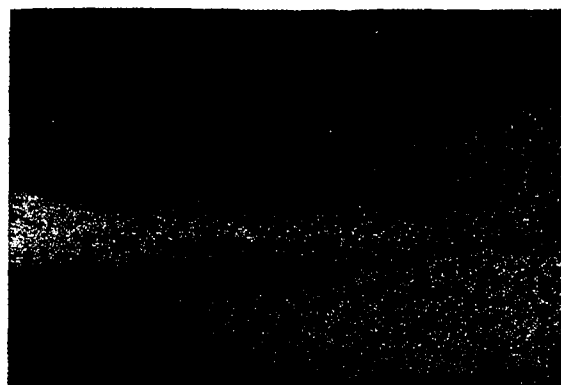


Fig. 4 - Detonation zone in AN-FO initiated by 20 g/m detonating fuse (first state), charge diameter: 42 mm

the explosion is initiated by means of a booster (slight curvature of the wave front). In RDX and AN-TNT-Al, the detonation wave curvature is more pronounced. As regards the mixtures of the "Slurry" type, it was not possible to obtain a stable detonation wave in the confinement conditions offered by Perspex, and in the severest priming conditions.

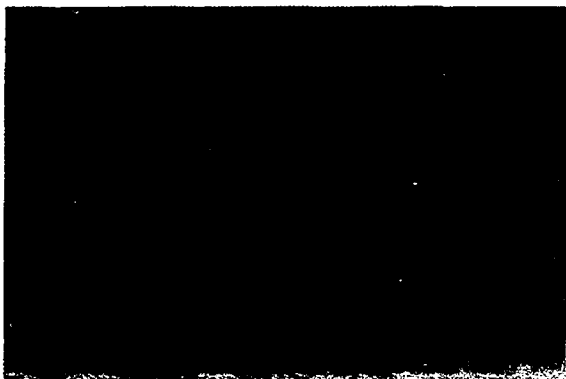


Fig. 5 - Detonation zone in AN-FO initiated by 20 g/m detonating fuse, charge diameter: 63 mm

(d) Column (e) of Table 1 mentions the angles at which the wave meets the wall, when the explosive detonation is primed by an axial detonating fuse. Note the very small value of the angle at which the AN-FO detonation wave meets the wall, when the inside diameter of the cylindrical charge is high.

(e) The explosive EIE is an exception, because the detonation wave, generated by the detonating fuse propagates at a velocity which is above the stable detonation velocity, measured on cylindrical cartridges. This is due to

the fact that NaNO_3 reacts upon NH_4Cl on the level of the detonating fuse gases. This reaction however, damps gradually down because the explosive is insufficiently confined. In fact, the EIE explosive loses its safety characteristics towards fire-damp when it is detonated by a detonating fuse of the type used.

Effects Produced on the Walls Surrounding the Charge

1. AN-TNT-Al and RDX

The results obtained by testing these two explosives have been grouped because the radiographs clearly show the detonation wave in the explosive and also the shock wave which propagates in the Perspex (see example in Fig. 7). The emergence angles determined under these conditions satisfactorily agree with those measured on the photographs. As the radiographs always show a lack of contrast, which reduces the accuracy of the measures, we have only used those measures which could be taken on photographs (Fig. 6).

Table 2 shows the characteristics of the shock wave, observed by applying both different priming methods. RDX in powder, charged with a density equal to 1.00 can be taken as standard material for making comparisons. The shock wave generated in a Perspex block placed this time opposite the detonator, propagates at an

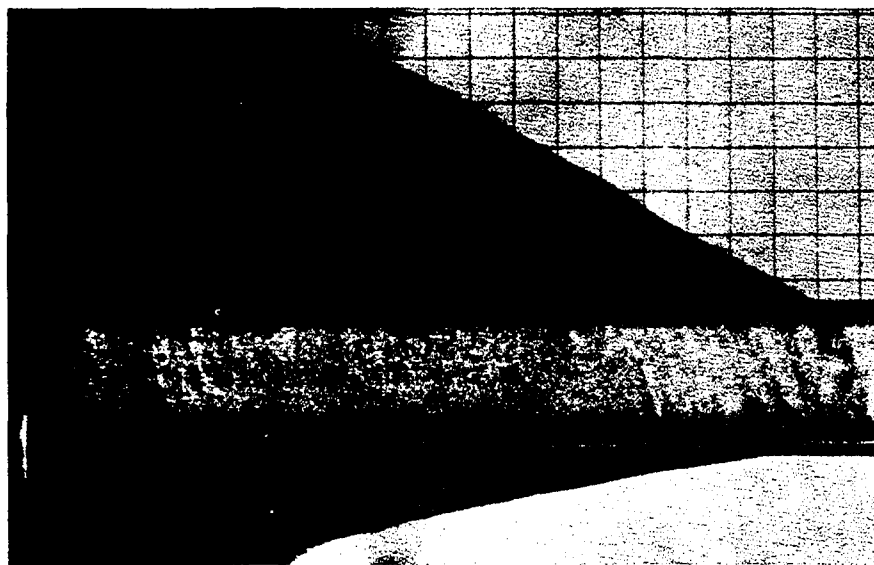


Fig. 6 - Photographic recording showing the shock wave resulting from detonation of AN-TNT-Al initiated by 12 g/m detonating fuse, charge diameter: 30 mm

TABLE 2
Comparison of the Properties of the Shock Wave Emerging in Perspex

RDX ($\Delta = 1.00$) and AN-TNT-Al; charge diameter: 30 mm; wall thickness: 40 mm; and detonating fuse 12 g/m.

	RDX ($\Delta = 1.00$)	AN-TNT-Al
(A) Priming by means of a detonator		
(1) Emergence angle (α)	$41^\circ \pm 30'$	$(63 \pm 2)^\circ$
(2) Attack angle (β)	$(78 \pm 2)^\circ$	$(65 \pm 2)^\circ$
(3) Expansion velocity ($V_c \sin \alpha$)	$(3,925 \pm 75)$ m/s	$(3,280 \pm 100)$ m/s
(4) Average pressure in Perspex (P_s)	41 kilobars*	18 kilobars
(B) Priming by means of a detonating fuse		
(1) Emergence angle (α)	$37^\circ \pm 30'$ ($V_c = 6,600$ m/s) $35^\circ \pm 30'$ ($V_c = 6,900$ m/s)	$30^\circ \pm 30'$ ($V_c = 6,600$ m/s)
(2) Attack angle (β)	$(50 \pm 2)^\circ$	$(23 \pm 1)^\circ$
(3) Expansion velocity ($V_c \sin \alpha$)	$(3,965 \pm 90)$ m/s	$(3,300 \pm 100)$ m/s
(4) Average pressure in Perspex (P_s)	43 kilobars*	19 kilobars

*According to Cook, the corresponding values are 34 and 35 kilobars.



Fig. 7 - Radiograph showing detonation zone and shock wave in Perspex; same event as Fig. 6

initial velocity which can be measured by a rotating mirror camera and is equal to 5,200 m/s, which corresponds to a pressure in the

Perspex equal to 110 kilobars.* This point of the polytropic Perspex rarefaction curve is sufficiently near the RDX straight line ("adapted impedance"), for calculating the detonation pressure by means of this method. As regards the pressure exerted on the lateral walls, this cannot be calculated with a great precision, the error made being approximately equal to 20% ($\pm 10\%$) because the shock wave propagation velocity and consequently the particle velocity W cannot be calculated with a great precision either, the error being made amounting approximately to ± 100 m/s.

As regards the AN-TNT-Al, the attention must be drawn to the fact that certain angle measurements were made with a more pronounced imprecision. As the difference between the shock velocity and the sonic one in the Perspex gets smaller, the pressure can only be known with a much lower precision (an example

*95 kbars, according to Cook.

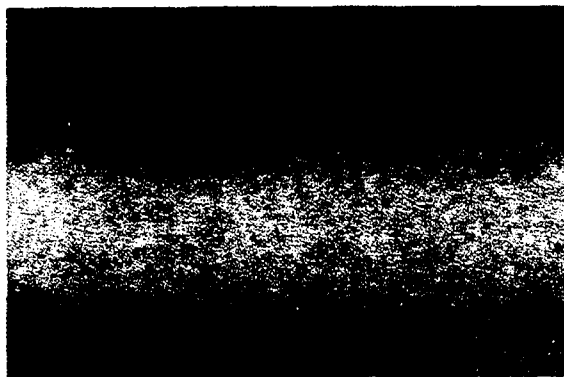


Fig. 8 - Radiograph showing final state of expansion of detonation wave in AN-FO initiated by 20 g/m detonating fuse, charge diameter: 42 mm (the deformation of the wall is visible)

of photographic recording obtained with this mixture is given in Fig. 9).

This being taken into consideration, Table 2 indicates however that the values of the pressure exerted on the walls do not depend on the priming method. Note that the wall pressure of RDX is approximately equal to 35% of its semi-experimental detonation pressure. For AN-TNT-Al, such a comparison would need a sufficiently adapted impedance with Perspex, or the use of an impedance mismatch equation.

2. AN-FO, EIE and Slurry—Discussion

As regards the low reactivity mixtures, the analysis of the compression waves propagated in the Perspex can only give qualitative results, either because the difference between the shock wave velocity and the sonic wave velocity is measured with a lower precision than the velocity which is measured, or because a sonic wave propagates ahead of an eventual shock wave and masks the effects of the latter. Shock waves of such a low amplitude do not appear on the radiographs. The movement of the explosive-Perspex interface can hardly be observed so that the particle velocity is difficult to calculate with precision (see Fig. 8). In critical cases, the particle velocity can be roughly estimated by measuring the aerial shock wave velocity and the Perspex-air interface value and by assuming that the velocity at the air-Perspex interface is roughly equal to twice the velocity at the explosive-Perspex interface.

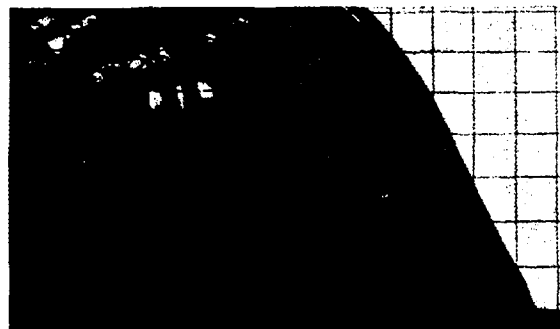


Fig. 9 - Shock wave generated in Perspex by AN-TNT-Al initiated by a No. 8 detonator

As the measurements have been made under the most favourable conditions, the values indicated must be considered as upper limit values. The stress waves propagated in the Perspex block have been qualitatively compared to each other, as regards their intensity and their shape. In the following text we will group all the results, which can be considered as sufficiently reproducible.

3. Priming of the AN-FO Explosive

a. Priming by means of a dynamite booster

Charges, placed in a cylinder of 42 mm in the diameter (thickness of the test-block 52 mm) have been tested. In the Perspex, we observe an intricate propagation of nearly sonic waves, perpendicular to the axis and masking the effects of the shock. The explosive wave propagation velocity, being equal to 1,800 m/s is below the sound velocity in the Perspex. The angle formed by the Perspex-explosive interface can be measured on the radiographs so that the particle velocity in the vicinity of the shock wave front can be calculated. It has been found equal to 215 m/s which corresponds to a pressure equal to about 7.5 kbars.

b. Priming by means of a detonating fuse 12 g/m

- Cylinder, 30/40 mm.

A compression wave propagates in the Perspex block under an angle of 23° measured from the axis of the charge. Its velocity is equal to 2,700 m/s. The velocity of the aerial shock wave, engendered around the block amounts

to 500 m/s and the particle velocity at the explosive Perspex interface, to 110 m/s. In this case, the pressure exerted on the walls would not exceed 4 kbars.

- Cylinder, 63/76 mm.

The stress wave propagates under an angle of $(16 \pm 1)^\circ$ measured from the axis. This is accounted for by the very low value of the incidence angle on the wall. This wave damps out on a 5 up to 7 cm distance.

c. Priming by means of a detonating fuse 20 g/m

- Cylinder, 42 mm, test block thickness: 52 mm.

It is not easy to explain the behaviour of waves propagating in Perspex, because the value of the incidence angle is rather low. The compression wave observed in the block shows however essential differences distinguishing it from these due to an insufficiently reactive shock (case of the "Slurry"). A supersonic velocity approximately equal to 3,300 m/s (see, for example, Fig. 10), can be observed only in a limited section of the charge. All the measurements recorded show that the expansion velocity at the interface varies from 230 to 300 m/s so that the pressure at the interface would be equal to 12 to 15 kbars and would exceed that obtained by means of a Dynamite booster. Such a value can hardly be accounted for by a simple tangential wave propagation. Wave reinforcing phenomena produced by multiple reflections are highly probable.

- Cylinder, 63 mm, test block thickness: 76 mm.

The shock in the Perspex takes on a typical character (Fig. 11). The values of the velocity determined by measuring the emergence angle would be perfectly unreliable, on account of their totality lacking in precision. A succession of thrusts and stops is in fact observed and this is due to the slight variations of the incidence angle and to emergence angles of an exaggerated value. They can be easily distinguished from the angles due to the normal propagation of the wave because their inclination very rapidly varies and reaches a much lower value. It cannot be however denied, that the charge has detonated and even violently, judging the detonating power of the explosive by its destructive effect, but the pressure develops here perpendicularly to the axis of the charge (wave near parallel to the wall), and



Fig. 10 - Aspect of stress waves generated in Perspex by AN-FO initiated by 20 g/m detonating fuse; diameter of the charge 42 mm

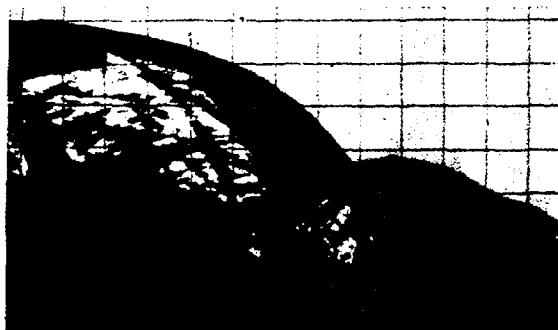


Fig. 11 - Aspect of stress waves generated in Perspex by AN-FO initiated by 20 g/m detonating fuse; diameter of the charge 63 mm

some recordings show that the axial wave moves in air around the charge at a velocity equal to ± 800 m/s, which correspond to a particle velocity amounting to ± 550 m/s. Even if this velocity is a free surface velocity, namely a velocity which can be divided by two for obtaining the value of the velocity at the explosive-Perspex interface, we will still obtain a pressure amounting to 10 up to 12 kbars. A comparison made with the nonreactive "Slurry" shows the big intensity difference existing between the waves engendered.

4. EIE Priming by Means of a Detonating Fuse 12 g/m

The intricate disposition of the waves of a typical sonic character shows however a succession of two thrusts namely a primary thrust giving a wall pressure of 4 kbars and a secondary one equal to 15 kbars (Fig. 12). This is

confirmed by analysing the aerial waves. The detonating fuse seems responsible for the couple of salts reacting upon each other (secondary reaction).

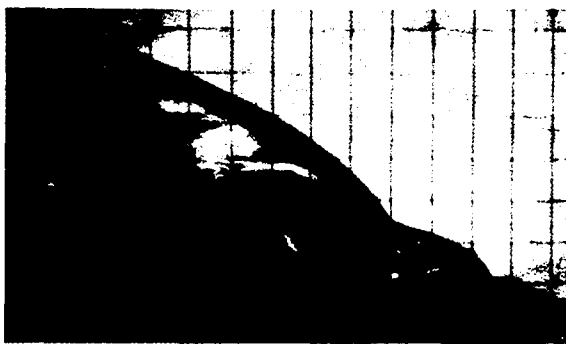


Fig. 12 - Aspect of stress waves generated in Perspex by EIE initiated by 12 g/m detonating fuse; diameter of the charge 30 mm

5. "Slurry" Priming

As the "Slurry" could not be primed even by using cylindrical blocks of a big diameter and a 20 g/m detonating fuse, the disposition of the elastic waves in the Perspex and the intensity of these waves can be used as an example of unreactive shock.

It was found that unreactive shock generates a train of waves fairly less intense than this one generated by the reactive shocks.

GENERAL DISCUSSION OF THE RESULTS AND CONCLUSIONS

The results above discussed show that the characteristics of axial initiation depends largely on the nature of the explosive involved.

With normal sensitive explosive, the detonating fuse running along the charge does not modify the wall pressure that is obtained when the charge is normally primed, at an extremity of the column, with a detonator. This has been mainly experienced with granular AN-TNT-Al (80/18/2) mixture and with RDX. The method consisting in observing the stress waves generated in Perspex can thus lead to semi-quantitative results, when used for sufficiently energetic mixtures. It is however an interesting qualitative method for studying low energy containing explosives. As an example of this, the reaction which can occur in the vicinity of

the axis of the charge of EIE explosive by the detonating fuse can clearly be distinguished from the reaction produced by normal initiation. This is also confirmed by the observation of a greater detonation velocity in the charges axially initiated.

As regards the low energy and low sensitivity explosives of the AN-FO type, the axial priming, if it can be done by making use of a high energy detonating fuse (20 g/m), generates a reaction wave which attacks the wall of the cylinder in a direction nearly perpendicular to it, particularly when the cylindrical test block has a large inside diameter. This can be considered as an advantage from the thrust point of view. Another advantage of axial initiation would result from a higher pressure exerted on the walls than with normal booster initiation. The results obtained seem to support this hypothesis, but unfortunately the pressure exerted remains in general too low to be correctly defined by the method used. A better determination would be possible by using water as a transmitting medium, but this has not been experimented with during this work. However, in our experiments, we observed by flash radiography a rather low shock propagation velocity in the explosive mixture, indicating a very partial reaction. Moreover, if we consider that in the case of a normal detonation wave the reaction can be made more complete when the explosive is strongly confined, whereas this cannot be expected when the explosion is axially initiated and when consequently the shock wave has to move along a rather long distance before the influence of the confinement can be made sensible, we are tempted not to exaggerate the importance of the pressures recorded on the walls when it is axially primed.

REFERENCES

1. M. A. Cook, 3d Symposium on Mining Research, University of Missouri, Rolla, Missouri, November 14-15, 1957, Bull. No. 95 (1958) of the School of Mines and Metallurgy, University of Missouri, p. 155
D. T. Bailey, T. R. Collins, M. A. Cook, D. H. Pack, and R. A. Schmidt, 5th Symposium on Mining Research, November 19-20, 1959, Bull. No. 98 (1960) of the School of Mines and Metallurgy, University of Missouri, p. 50.
2. L. D. Sadwin, R. H. Stresau, S. J. Porter, and J. Savitt, 3d Symposium on Detonation, September 26-28, 1960, ONR Symposium Report ACR 52, Vol. 1, p. 309.

3. J. Hershkowitz and E. W. Dalrymple, Picatinny Arsenal Technical Report No. 3185, July 1964.
4. E. M. Pugh, R. Heine-Geldern, S. Forner, and E. C. Mutschler, *J. Appl. Physics* 1952, 23, No. 1, 48.
5. J. Dapoigny, J. Kieffer, and B. Vodar, *C.R. de l'Académie des Sciences* 1957, 245, 1502.
6. I. Jaffe, R. Beauregard, and A. Amster, 3d Symposium on Detonation, September 26-28, 1960, ONR Symposium Report, ACR 52, Vol. 2, p. 584.
7. M. A. Cook, R. T. Keyes, and W. O. Ursenbach, 3d Symposium on Detonation, September 26-28, 1960, ONR Symposium Report ACR 52, Vol. 2, p. 357.
8. L. Deffet and R. Vanden Berghe, Proceedings of the 5th International Congress on High Speed Photography, Washington, 1960, p. 49.
9. S. R. Brinkley and W. E. Gordon, *C.R. XXXIe Congrès International de Chimie Industrielle*, Liège, September 1958, p. 25.

A DETONATION CALORIMETER AND THE HEAT OF PRODUCTS OF DETONATION OF PENTA-ERYTHRITOL TETRANITRATE (PETN)

D. L. Ornellas, J. H. Carpenter and S. R. Gunn
*Lawrence Radiation Laboratory, University of California
Livermore, California*

ABSTRACT

An isothermally jacketed bomb calorimeter has been developed for measurement of the heat of detonation of 25-g charges of high explosives. The stainless steel bomb has a 5.2 l internal volume and 1.25-in. walls, and weighs 115 lbs. Calibration is performed by combustion of benzoic acid; reproducibility is 0.1%. Experiments can be made in a total of one hour.

Calorimetric measurements with PETN supplemented by product analysis are described. The data are interpreted with the aid of thermodynamic and hydrodynamic calculations which show that the experiments fell into two classes, depending upon the degree of confinement used around the explosive. For unconfined or lightly confined cylindrical charges, the heat of detonation of PETN at 298°K is 1499 ± 5 cal/g, $\text{H}_2\text{O}(\ell)$; the released energy is largely retained in the products which are shocked considerably off the Chapman-Jouguet isentrope by reflections from the bomb wall. For heavily confined cylindrical charges the heat of detonation is 1487 ± 3 cal/g, $\text{H}_2\text{O}(\ell)$; the energy is largely converted to kinetic and internal energy of the confining metal, and the products expand along the Chapman-Jouguet isentrope. The reshocking of products is minimal in comparison to unconfined charges.

The product composition obtained by analysis is compared with that predicted by calculations using various equations of state for PETN detonation products. A freeze-out temperature of 1500-1800°K is found by comparing the ideal gas calculations to the experimental results obtained using unconfined charges.

This paper has been published in *The Review of Scientific Instruments*, **37**, 907 (1966).

ANOMALOUS ISENTROPE RESULTS OBTAINED WITH THE RUBY COMPUTER PROGRAM

Joseph Hershkowitz
*Engineering Sciences Laboratory
Feltman Research Laboratories, Picatinny Arsenal
Dover, New Jersey*

ABSTRACT

Points off the isentrope were erroneously provided by the RUBY computer program during a calculation of the isentrope from the Chapman-Jouguet point for a 60/40 mixture of KClO_4/Al , loading density 0.5 g/cm^3 . The error occurred at temperatures near 3120°K within a decade range of pressure centered at 5.3×10^{-5} megabars ($0.003 P_{\text{CJ}}$) where the condensed form of Al_2O_3 first appeared in the product species. The calculation involved allowed for the condensation in the products of Al and Al_2O_3 , but only $\text{Al}_2\text{O}_3(\text{C})$, or neither appeared. The computational procedure is based on determining the composition with minimum Gibbs free energy and on the existence of a single monotonically increasing curve of entropy with temperature. However, it was found that, for the region involved, the free energy vs temperature curve for a composition containing $\text{Al}_2\text{O}_3(\text{C})$ and the corresponding curve for that without $\text{Al}_2\text{O}_3(\text{C})$ are very close, while the corresponding entropy curves are far apart except at one temperature. The small differences in free energy made possible improper choices between the two compositions as the temperature was altered because the significant determination was made by the program with a two-solid matrix instead of a one-solid matrix. This led to a change (a straddle) in the sign of the difference between the calculated entropy and the isentrope value, for a temperature interval which did not contain the isentrope temperature. The exit procedure which followed only decreased the temperature width of the straddle and thus the incorrect temperature and entropy were obtained. A similar error could occur in finding a point on the Hugoniot curve if the product species behaved similarly since the same subroutine is used to minimize the energy difference from the Hugoniot. A modification of the TRANBA subprogram to try the one-solid matrix determinations before exiting with no solids, when two are anticipated, overcomes the difficulty. Other possible modifications are discussed.

INTRODUCTION

The RUBY program [1] computes, among other properties of an explosive, the isentrope from the Chapman-Jouguet point at preselected pressures. At each pressure, it starts with the stored temperature and finds the equilibrium composition by minimizing the Gibbs free energy using the method of steepest descent. It then computes the entropy of this composition and subtracts the value on the isentrope. As this difference is positive or negative, so it reduces or increases the temperature by a prescribed increment and repeats the process of finding a composition. By storing previous

values and making comparisons, two temperatures are found between which the entropy has changed from above the isentrope value to below or vice versa. This straddle region is then narrowed by successive halving until the temperature difference is below a prescribed control and a final value of entropy is computed. One would expect this final value of entropy to be a point on the isentrope and it generally is. However, it has been found that points far off the isentrope can occur for a calculation that provides for condensation of two of the product species, when in a particular pressure and temperature range only one begins to condense.

The calculations which revealed this difficulty were concerned with obtaining the isentrope to relatively low pressures for a mixture of potassium perchlorate and aluminum in a 60/40 weight ratio. The propagation of detonation of this mixture while confined in a Lucite cylinder has been observed experimentally [2]. It was found that the reaction zone contains a nonluminous region corresponding with the rupture of the Lucite and with the lateral expansion of the products. One possible explanation was that only gaseous species were present in the nonluminous region. The high luminosity behind then followed from the condensation of Al_2O_3 , providing a high emissivity. The isentrope calculation was conducted to provide information on this condensation. It was found that for a loading density of 0.5 g/cm^3 , $\text{Al}_2\text{O}_3(\text{C})$ did not appear until the pressure dropped to about 53 bars from the computed Chapman-Jouguet value of 16.7 kilobars. The temperature had correspondingly decreased from 5600°K to 3120°K . The results were achieved only after overcoming a tendency on the part of the computer program to provide results off the isentrope. The results and the reasons therefor are presented in this paper together with corrective measures.

RESULTS

Table 1 shows the many erroneous values of entropy obtained in the course of four computations. The presence or absence of $\text{Al}_2\text{O}_3(\text{C})$ in the products is also indicated. The entropy on the isentrope was $0.21583772 \text{ megabar cm}^3/\text{g ev}$.

TABLE 1
Entropy Values Obtained in Runs 89-1 to 89-4

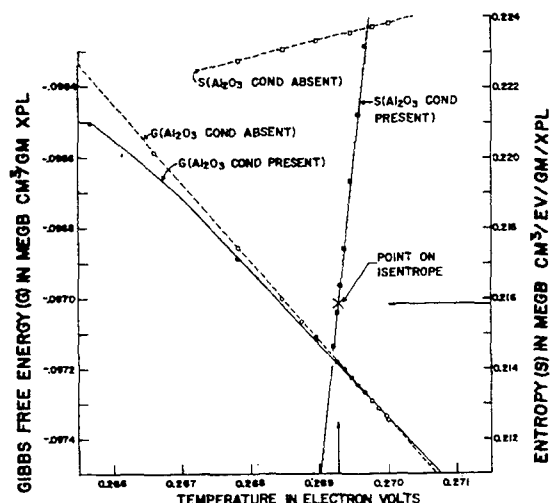
Pressure (megabars)	Entropy (megabar $\text{cm}^3/\text{g ev}$)			
	89-1	89-2	89-3	89-4
1.673-4	0.2158	0.2163	0.2163	0.2163
1.255-4			0.2158	0.2158
9.409-5		0.1467*	0.2190	0.2158
7.056-5			0.2158	0.2158
5.291-5	0.2059*	0.2166*	0.1373*	0.1375*
3.968-5			0.2240	0.2236
2.976-5		0.1242*	0.2018*	0.1276*
2.231-5			0.2156	0.2271
1.673-5	0.1533*	0.2311	0.2327	0.1188*

*Indicates that $\text{Al}_2\text{O}_3(\text{COND})$ was present in the products.

Computational parameters were $P_3 = 10^6$, $P_6, 7 = 0.0172$, $\text{EN}(1) = 0.001$, $\text{ET} = 0.002$ except for Run 89-4 where $P_6, 7$ were changed to 0.0086 and ET to 0.0002 .

The deviations, both large and small, from the isentrope value and the lack of apparent correlation with either the size of the pressure step, the presence of $\text{Al}_2\text{O}_3(\text{C})$, or the changes made in control settings suggested that the error might be more basic. The program was then modified to add a print-out of the Gibbs free energy for each composition determination and a series of runs made at a pressure of $5.291\text{-}5 \text{ megabars}$, following parts of the approach to the solution "on line." The results of all these runs were used to plot the Gibbs

Fig. 1 - Entropy and free energy of products vs temperature ($P = 5.2914 \times 10^{-5} \text{ megabars}$)



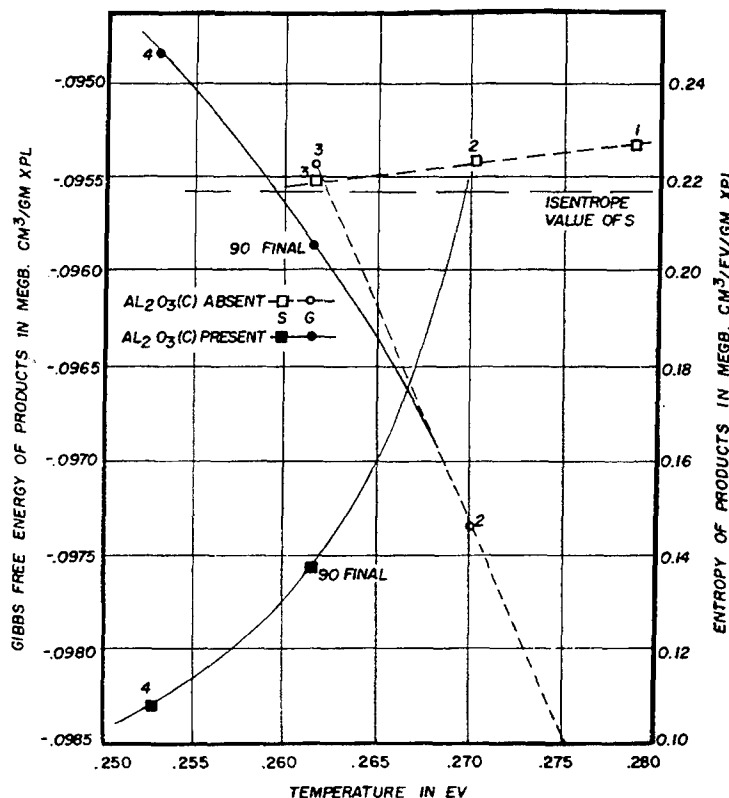


Fig. 2 - Sequence for Run 90

free energy and entropy as a function of temperature. Figure 1 shows the region in the immediate vicinity of the correct solution, that is, the point on the isentrope. Figures 2 and 3 show the course of two runs on larger scale plots.

In Fig. 1 we see that the Gibbs free energies (G) of the product compositions which contained $\text{Al}_2\text{O}_3(\text{C})$ were very close but lower than those without $\text{Al}_2\text{O}_3(\text{C})$ until the crossover at a temperature of about 0.2697 eV (3130°K). This crossover point is the boiling point of $\text{Al}_2\text{O}_3(\text{C})$ with respect to the gaseous explosive products, at the pressure of 52.9 bars. (As the temperature increased from 0.2528 eV to 0.2697 the percent of Al_2O_3 as $\text{Al}_2\text{O}_3(\text{C})$ decreased from 88% to zero, with the total Al_2O_3 remaining constant.) The exceedingly small difference between the two G curves in Fig. 1, in the region of interest, is illustrated at $T = 0.26946136$ where the free energy values for the product compositions are -0.097223556 with $\text{Al}_2\text{O}_3(\text{C})$ and -0.097223051 without $\text{Al}_2\text{O}_3(\text{C})$. The difference is in the sixth significant digit. At $T = 0.26896136$ the "with $\text{Al}_2\text{O}_3(\text{C})$ value" becomes lower only at the fifth significant digit. The entropy vs temperature curves are far apart.

Thus an improper choice of composition facilitated by the closeness of the Gibbs free energy curves can produce a large error in entropy.

TABLE 2
Run 90

Seq.	Temp.	Free Energy	Entropy Difference	Entropy
1	0.2786	-0.099288	0.012163	0.22800
2	0.2700	-0.097345	0.008003	0.22384
3	0.2614	-0.095438	0.003797	0.21963
4	0.2528	-0.094855	-0.107684	0.10815*
x5	0.2571	Print-out not obtained for this point		
x6	0.2592	Print-out not obtained for this point		
xx	-	Asymptotic approach to point below followed		
Final	0.26136	-0.095862	-0.078552	0.13729*

*Indicates that $\text{Al}_2\text{O}_3(\text{COND})$ was present in the products.

Computational parameters were $P3 = 10^6$, $P6 = 0.0172$, $\text{EN}(1) = 0.005$, $\text{EB} = 0.004$, and $\text{ET} = 0.002$, $P7 = 0.0086$.

The computational sequence leading to an erroneous result is shown in Fig. 2, with the data given in Table 2. The desired isentrope value is 0.21583772.

Note that the final value of entropy is very far from the required value. By using Fig. 2 and following the A group subroutine procedure from Ref. 1, we see that this occurred as follows. At point 1, a composition was determined with no $\text{Al}_2\text{O}_3(\text{C})$ present and with entropy greater than the required value, i.e., positive entropy difference (F4). To decrease entropy, the temperature was decreased by P7 and a new composition found, point 2. F4 was still positive, so another downward step was taken to point 3. The Gibbs free energy curves show that the correct location for point 3 should have been on the curve for $\text{Al}_2\text{O}_3(\text{C})$ present since that has lower free energy. However, since the actual point 3 still had F4 positive, the temperature was decreased by P7 to point 4. For this temperature, the free energy for $\text{Al}_2\text{O}_3(\text{C})$ present was sufficiently lower than the free energy for $\text{Al}_2\text{O}_3(\text{C})$ absent to give a result

with $\text{Al}_2\text{O}_3(\text{C})$ present. The condensed species point sharply reduced the entropy, making F4 negative. This change in sign of F4 meant the required value of entropy had been straddled, i.e., was supposed to be between points 3 and 4. The subroutine now finds the value of F4 for the average of the temperature at points 3 and 4. It then uses this midpoint and chooses either point 3 or 4 so that a straddle of the required value of entropy is retained. This process is continued until the temperature difference is less than ET. Points x5 and x6 illustrate this asymptotic process and Final shows the final point of this run. Note that the temperature is within 0.002 of point 3 (see Table 2). In effect the error at point 3 had served as an upper bound which made it impossible to reach the point on the isentrope.

Run 91 started from the end point of Run 90, and altered only the computational parameter P6, the upward temperature step, to 0.0043 ev. The relevant results are shown in Table 3 and indicated in Fig. 3 by lower case letters leading to the final result.

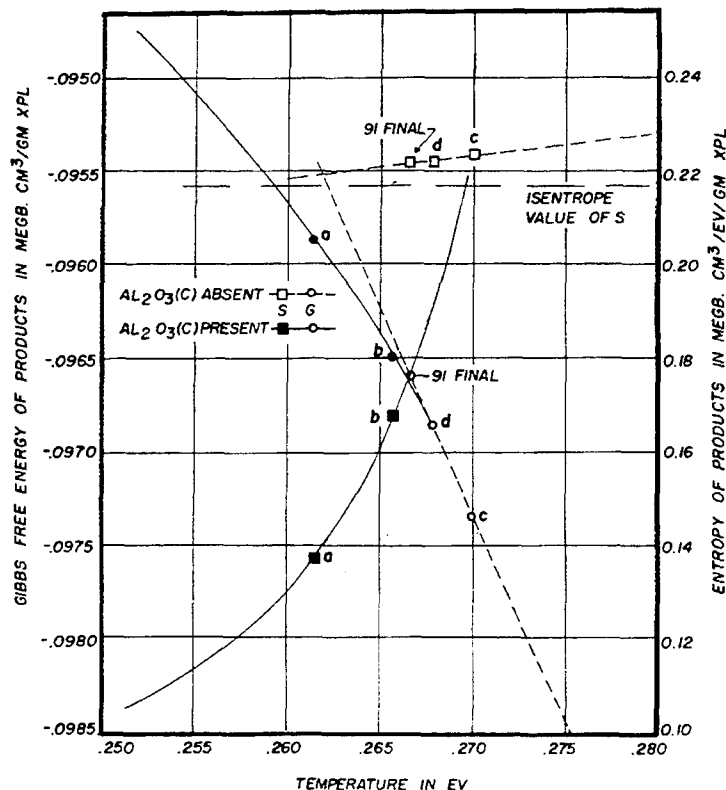


Fig. 3 - Sequence for Run 91

TABLE 3
Run 91

Seq.	Temp.	Free Energy	Entropy Difference	Entropy
a	0.2614	-0.095862	-0.078552	0.13729*
b	0.2657	-0.096503	-0.047873	0.16796*
c	0.2700	-0.097335	+0.007980	0.22382
d	0.2678	-0.096855	+0.006932	0.22770
xx	Asymptotic approach to point below followed			
Final	0.2666			0.22220

*Indicates that $\text{Al}_2\text{O}_3(\text{COND})$ was present in the products.

Computational parameters were $P_3 = 10^3$, $P_6 = 0.0043$, $P_7 = 0.0086$, $\text{EN}(1) = 0.005$, $\text{EB} = 0.004$, $\text{ET} = 0.002$.

Note that the final value of entropy is incorrect and higher than the isentrope value 0.21583722. To obtain the correct value, point d should have been on the $\text{Al}_2\text{O}_3(\text{C})$ present curve and thereafter the straddle should have kept the isentrope points within it.

Runs 90 and 91 show how erroneous values of entropy can result which are either higher or lower than the isentrope value. Other runs that were made simply reinforced the erroneous computational procedure revealed in these two runs.

PROGRAM MODIFICATION

The errors occurred because at a particular temperature (and pressure) the RUBY program did not find the composition with the lowest Gibbs free energy. The critical determination involved a choice between $\text{Al}_2\text{O}_3(\text{C})$ present or absent. By analyzing the on-line print-outs and the RUBY flow charts, which showed the steps taken to determine each composition, the difficulty was located and then overcome.

A brief description of some features of the composition determination are given in this paragraph to permit understanding the analysis that follows. Details are available in Ref. 1. In setting up the calculation one indicates the number of solids expected and their compatibility. Since both $\text{Al}_2\text{O}_3(\text{C})$ and $\text{Al}(\text{C})$ were expected as the pressure and temperature decreased along the isentrope, a "two compatible solids" indication ($U_0 = 2$, $U_2 = 0$) was incorporated. This choice starts the calculation by setting the controls U_1 and UP_1 , referring respectively to first and second solid, each equal

to 1. These controls are in the matrix which determines the direction in composition space which will most steeply reduce the Gibbs free energy. When both are set equal to 1, designated (1, 1), a calculation is done on the presumption that two solids will be present in the composition that reduces the free energy. The program provides for the possibility that at some pressures and temperatures, one or both solids may not be present. This is done by analyzing the result of the (1, 1) calculation and choosing (1, 1), (1, 0), (0, 1), or (0, 0) for the next calculation in accord with the trend shown. The results of that calculation are then analyzed and so on. Substitution of 0 for 1 eliminates that solid from the composition space considered. After a (0, 0) calculation, a new start with (1, 1) is made. A change in composition is made only when the proposed changes in the solids are in accord with the assumptions. The (0, 0), no solids, always results in a change of concentration of gaseous species. An exit occurs when the proposed changes in all species are sufficiently small as determined by assigned exit criteria ($\text{EN}(1)$ and EB).

At the pressure and temperature where erroneous values of entropy occurred, the concentration of the second solid, $\text{Al}(\text{C})$, was always zero and further reduction was called for. Thus when a (1, 1) trial calculation was made, it was rejected and a (1, 0) called for if $\text{Al}_2\text{O}_3(\text{C})$ was already present or a (0, 0) if absent, and further reduction in concentration suggested ($\text{ANS} + \text{ALAM} \times \text{DELNS} < 0$). $\text{Al}_2\text{O}_3(\text{C})$ could be absent because of descent along the isentrope or by loss during initial large steps taken to decrease the free energy. It was observed that erroneous composition decisions followed a succession of (1, 1) calculations, alternating with (0, 0) with the exit on the latter. This suggested that when sufficiently small free energy differences were involved the (1, 1) calculation did not have the sensitivity to reintroduce $\text{Al}_2\text{O}_3(\text{C})$. It was logical to redo the calculation considering only the one solid as a possibility ($U_0 = 1$, $U_2 = 0$). Under these boundary conditions correct results were obtained in all cases. It followed that the sensitivity of the (1, 0) calculation was adequate to reintroduce $\text{Al}_2\text{O}_3(\text{C})$ when the free energy was even very slightly less with $\text{Al}_2\text{O}_3(\text{C})$ present.

To provide for the general case where two solids may appear at different temperatures along the isentrope, it was necessary to modify the program to try each single solid calculation when a gases only exit was ready to occur and two solids had been anticipated. This was done by an addition to the TRANBA subroutine as shown in Fig. 4. The additional computations

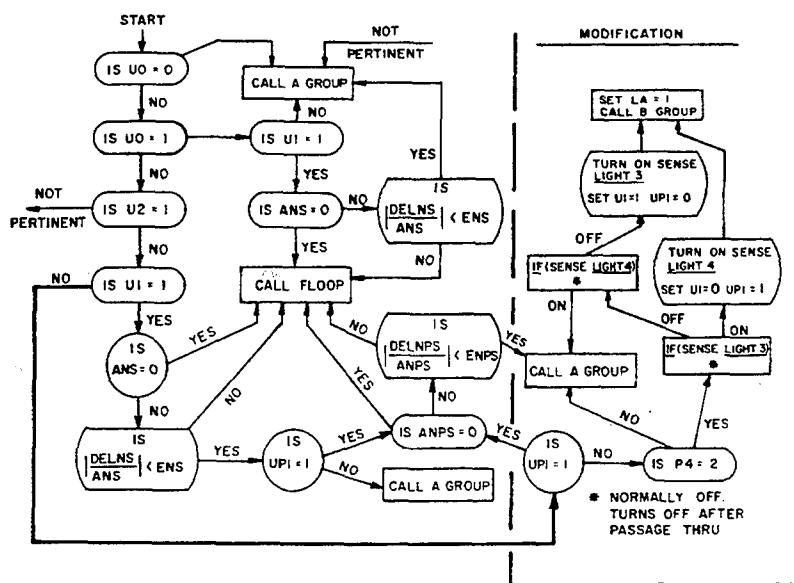


Fig. 4 - Modification to TRANBA subroutine

were done only for an isentrope determination, and the additional running time on an IBM 7090 was negligible. When the modified TRANBA subroutine was used it was found that in all cases correct values of entropy resulted. The smooth nature of the results now obtained is shown in Fig. 5 and should be compared with the inconsistencies obtained before the program modification as indicated by the asterisks in Table 1.

DISCUSSION

It is recognized that the absolute values of the results presented for this explosive depend on the input thermodynamic and equation-of-state data and on the applicability of the Kistiakowsky-Wilson equation-of-state to the product gases at the pressures involved. The inputs were most carefully chosen [3,4]. For the pressure region involved (167 to 16.7 bars) the K-W equation-of-state essentially reduces to the perfect gas equation because X is between 0.18 and 0.024. However, the absolute values of the results do not matter for the programming questions since the type of curves dealt with (free energy and entropy vs temperature) are characteristic of the vaporization as temperature increases of a condensed species in contact with gaseous products. Thus a change in the inputs would not alter either the nature of the problem or the validity of the solution presented.

To find a point on the isentrope, the program calculates, as described in the INTRODUCTION, the entropies for a succession of product temperatures and assumes monotonicity of entropy with temperature to find the desired value of entropy. However, the exit criterion is not one of entropy, but instead requires only that the temperature step between successive calculations be reduced below an assigned value. A further program change that seems worthwhile would be to make the acceptable fractional deviation from the required value of entropy, the exit criterion. The number of temperatures used in the calculation would then depend on the slope of the entropy-vs-temperature curve, but the precision of the final entropy determination would not depend on the slope. The importance of using an entropy exit criterion is emphasized when one realizes that when a condensed species is present, it must have a gaseous product with equivalent free energy (modified somewhat by mixing entropies in the gaseous phase). It is only this entropy boundary condition that can ultimately determine the quantity of the condensed species (as the volume determines the ratio of water and ice at the melting point). Thus to control the precision of the results with respect to composition, particularly that of the condensed species, one should control the tolerance on the entropy rather than on the temperature.

In finding a composition at a particular temperature the exit criterion is not directly

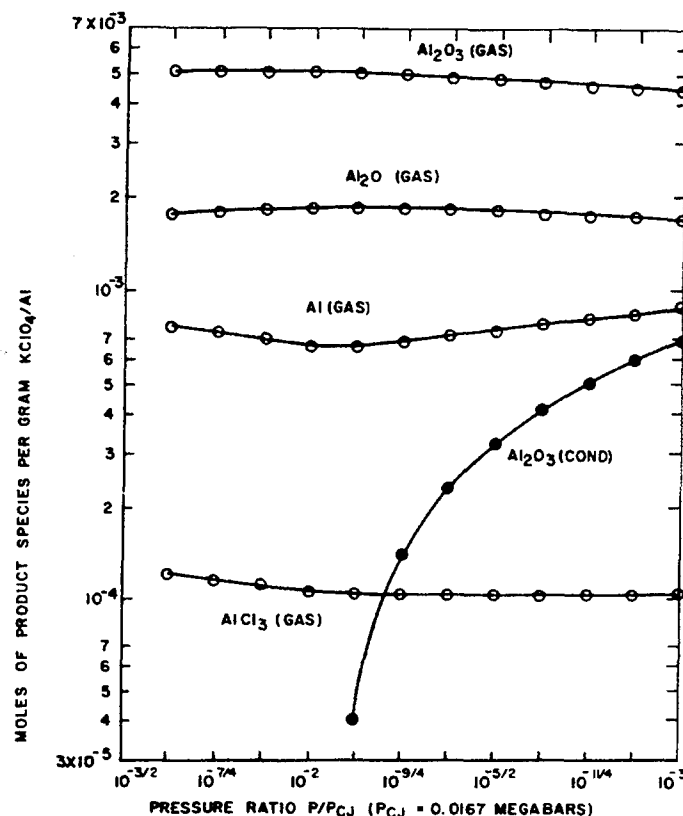


Fig. 5 - Product species in region of isentrope where $\text{Al}_2\text{O}_3(\text{COND})$ appears ($\text{AlO} \sim 10^{-6}$; $\text{Al}_2\text{O}_3 \sim 10^{-7}$) (K, K_2 , KCl , O_2 , O not pertinent)

associated with the free energy, but instead requires that the change in the fraction of each constituent in the composition be below an assigned value. Here the reliance is on the method of steepest descent [5,6] and the procedure described in the PROGRAM MODIFICATION section for successive choice of matrices and acceptance of proposed alterations in compositions. It was a flaw in the latter that was corrected by the TRANBA modification. Another approach would be to use for the entire composition calculation the procedure (see SUBROUTINE FL in Ref. 1) used in the descent until the free energy step changes from negative to positive. When this change in slope occurs, one could begin to calculate the free energy for each composition, retaining the ALAM halving technique and then add to the present exit criterion one requiring a minimum fractional change in free energy. Judicious choice of values for these criteria could meet many computing requirements. One would incorporate a free energy comparison between compositions with no, one, and two solids before the

final exit to prevent errors of the type corrected by the TRANBA modification. Also one would use separate exit criteria for the condensed species (ENS and ENPS) since they may require greater precision than the gaseous species (EN(1)) in the neighborhood of a condensation.

The presentation has been concerned solely with finding points on an isentrope. However, the Chapman-Jouguet determination requires that one find points on the Hugoniot. The procedure for finding these points is exactly the same as for the isentrope except that the Hugoniot equation is the boundary condition instead of a prescribed value of the entropy. If one of the points on the Hugoniot were in the region where one solid commences to condense and two were anticipated, it would be possible to obtain an erroneous point, just as occurred for the isentrope. At a condensation point both energy and entropy differences are large for condensed and gaseous phases of the same species. However, many pressure points are used to find

those pressures straddling that of the required slope and the error would only be significant if it occurred in the terminating calculations. This is sufficiently improbable to justify the limitation in the TRANBA modification to isentrope calculations.

ACKNOWLEDGMENT

Mr. I. Klugler, of the Computing Branch, provided guidance on incorporating the modifications required to offset the limitations in the RUBY code.

REFERENCES

1. H. B. Levine and R. E. Sharples, "Operators Manual for RUBY," University of California, Lawrence Radiation Laboratory, Livermore, California, UCRL 6815, March 20, 1962. (Available from Office of Technical Services, U.S. Dept. of Commerce, Washington 25, D.C., \$2.50.)
2. J. Hershkowitz, "The Combustion of a Granular Mixture of Potassium Perchlorate and Aluminum Considered as Either A Deflagration or a Detonation," Picatinny Arsenal Technical Report 3063, January 1963 (see Figure 1).
3. C. L. Mader, "Thermodynamic Properties of Detonation Products," Los Alamos Scientific Laboratory, University of California, Report GMX-2-R-59-3 (September 1959) and Supplement Report GMX-2-R-60-1 (April 1960).
4. R. R. V. Wiederkehr, "A General Method for Calculating the Specific Impulse of Propellant Systems," Report Nos. AR-1S-60 and AR-3S-61, Computations Research Laboratory, Dow Chemical Company (1960-1).
5. H. B. Levine, "Chemical Equilibrium in Complex Mixtures," J. Chem. Phys. 36, No. 11, pp. 3049-3050 (June 1, 1962).
6. W. B. White, S. M. Johnson, and G. B. Dantzig, "Chemical Equilibrium in Complex Mixtures," J. Chem. Phys. 28, No. 5, pp. 751-755 (May 1958).

FRONT AND MASS VELOCITY AT DETONATION IN EVACUATED CHAMBERS

N. Lundborg
*Swedish Detonic Research Foundation
Vinterviken, Stockholm SV
Sweden*

ABSTRACT

The velocity of the shock front from TNT-charges in evacuated chambers has been measured. The result shows that the velocity rises very rapidly with decreasing pressure from about 10 km/s at 1 mm Hg to about 20 km/s at 0.01 mm Hg. The high velocity is attributed to elastic impacts between light air molecules and heavy molecules of the detonation gases and the high velocity will be seen at distances shorter than the free mean path of the air molecules.

INTRODUCTION

At axial detonation of a cylindrical charge the detonation gas (here called the d-gas) expands at the end surface with super sound velocity and pushes off the surrounding atmosphere (here called the a-gas) in a compressed layer with shock front. The mass-velocity (v)* and the front velocity (w) of the a-gas is a function of the properties of the d-gas and of the initial pressure of the a-gas.

The velocities have been calculated for TNT (trinitrotoluene) with a density of 1.5 g/cm^3 [2,3,6] and measured for different explosives [1,3,4,5,7]. With cylindrical charges in tubes, velocities approximately twice as high as those calculated have been found at low pressures. This has been given different interpretations. Ericsson [5] found for TNT-balls in large containers, agreement with the theory and considered the high velocities in tubes as an effect of the slit between the charge and the tube. Petersson [2] pointed out that the conditions in the reaction zone had been neglected in the calculations. Johansson and Selberg [6] attributed the high front-velocity to elastic impacts between the light molecules of the a-gas and heavy d-molecules. The a-molecules then attain double the mass-velocity ($w = 2v$). This applies at low pressures in which the length of the free mean path is great whereas at higher pressures the front-velocity is $w = v/(1 - \rho_0/\rho)$,

the density of the a-gas being ρ_0 before and ρ after the compression. The present investigation confirms Johansson's and Selberg's hypothesis. The high velocities observed in tubes also at somewhat higher pressures may however be due to a "slit effect."

EXPERIMENTAL

An arrangement as in Fig. 1 was used in the tests. A TNT-cylinder 20 mm in diameter and 40 mm in length was placed at the bottom of a glass retort and a charge of the same kind was pasted on the outside. The retort was evacuated to a definite pressure and sealed. The specified pressure includes the vapour

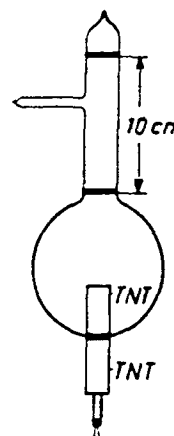


Fig. 1 - Evacuated glass retort with TNT-cylinders

*Ed. Note: Commonly called particle velocity.

pressure of the explosive. The front-velocity from the upper end of the inner TNT-cylinder was measured at detonation with a streak camera. Figures 2 and 3 reproduce the photographs for 0.1 and 0.001 mm Hg respectively. The detonation front of the TNT charge (6.6 km/s) is seen at the foot of the photographs and above this the front of the a-gas and a second bright area which may correspond to the front of the d-gas (10 km/s). The front-velocity of the a-gas has been measured for each pressure as a function of the distance (l) from the end of the charge. Table 1 and Fig. 4 show the result. At 0.5 and 1 mm Hg the velocity falls rapidly to a constant value, whereas at 0.1-0.003 mm Hg it declines more slowly and at 0.001 mm Hg is constant throughout the entire range of measurements. The initial velocity for the low pressures is ca 20 km/s.



Fig. 2 - Streak camera photograph at 0.1 mm Hg

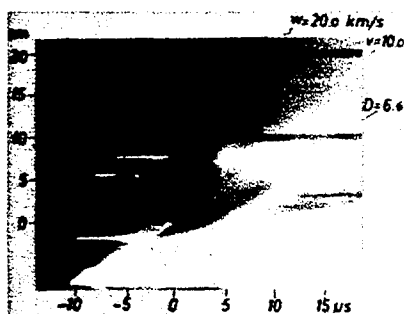


Fig. 3 - Streak camera photograph at 0.001 mm Hg

Fig. 5 gives calculated curves for the front velocity of the a-gas as a function of the pressure for $l < \lambda$ and for $l \gg \lambda$ where l is the distance from the end of the charge and λ

TABLE 1
Front-Velocities in km/s at Different Air Pressures (p) and at Different Distances (l) From the End of the Charge

l cm	p mm Hg					
	1.0	0.5	0.1	0.01	0.003	0.001
1	12.2	12.0	17.5	18.8	19.0	20.0
2	9.2	10.5	15.0	16.7	17.4	20.0
4	9.2	10.2	14.6	15.4	15.6	20.0
6	9.2	10.0	13.2	14.0	14.2	20.0
8	9.2	10.0	12.7	13.2	13.8	20.0
10	9.2	10.0	12.3	13.2	13.2	20.0
12	9.2	10.0	12.2	12.8	13.2	20.0
14	9.2	10.0	12.0	12.8	13.2	20.0
16	9.2	10.0	12.0	12.8	13.2	20.0

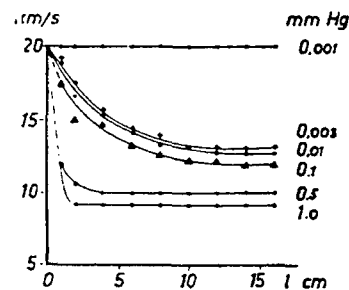


Fig. 4 - Front velocities at different air pressures as a function of the distance from the end of the charge

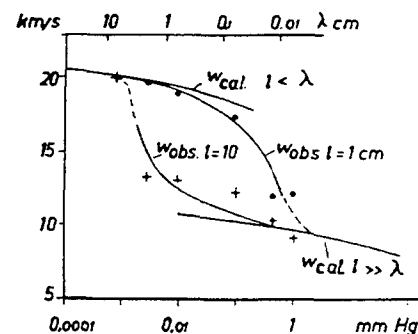


Fig. 5 - Calculated and observed front-velocities

the length of the free mean path in the a-gas. The values observed decline with the pressure from the upper curve $w = 2v$ to the lower $w = v/(1 - \rho_0/\rho)$ for l/λ between 1 and 100.

ACKNOWLEDGMENT

The author wishes to thank Prof. C. H. Johansson for useful discussions and advice.

REFERENCES

1. R. Becker, ZS Physik 8, 321 (1922).
2. S. Petersson, Report NAB 4.7.1951 (see Ref. 3).
3. C. H. Johansson and S. Ljungberg, Arkiv för Fysik 6, 369 (1952).
4. H. Ahrens, Sprengtechnik 1, 131 (1952) from 1953 Explosivstoffe.
5. U. Ericsson, Appl. Sci. Res. A5, 309 (1955).
6. C. H. Johansson and H. L. Selberg, Proc. 4th Int. Conf. Ionization Phenomena in Gases, Uppsala 17-21, Aug. 1959, IVD 1114.
7. H. Selle, Explosivstoffe 9, 195 (1960).
8. N. Lundborg, Arkiv för Fysik 25, 541 (1963).

DETONATION LIMITS IN CONDENSED EXPLOSIVES

William E. Gordon*

*Combustion and Explosives Research, Inc.
Pittsburgh, Pennsylvania*

ABSTRACT

This paper surveys published work on detonation limits in condensed explosives, correlates the data with other observable and calculated properties, reviews theories on the subject, and seeks a coherent overall view. As a working hypothesis it is assumed that at the limit the detonation shock strength becomes critical for initiation of reaction. The critical shock pressure is therefore a significant quantity to examine. The data for some dozen explosives show that charge density, per se, has the strongest influence on the critical pressure. Another important factor is the (apparent) reaction zone length, obtained from the slope of a p vs $1/d$ plot. Chemical differences between explosives have a minor effect; but dynamites containing nitroglycerin are a notable exception.

On the assumption that the Hugoniot curve for unreacted porous explosive coincides approximately with the curve for unreacted non-porous (crystal density) explosive, Gordon [9] showed from the data of Anderson and Pesante [6] for ammonium perchlorate (AP) that the critical shock energy (mechanical energy converted to heat at the shock front) is substantially constant at about 1 k joule/g over a wide density range. In contrast the critical shock pressure varies some five fold over the same region. A more refined treatment of the Hugoniot curve, given here, does not significantly alter the result. A reasonable explanation for the density effect in the cases examined (notably TNT and AP) is based on the hypothesis that a minimum energy is required for initiation. The effect of reaction zone length, which is influenced mostly by particle size, is explained qualitatively by considering the relationship between the explosion induction time and the temperature of a hot spot.

The problem of sensitivity testing is examined because detonation limit data show that the critical shock pressure decreases with increasing particle size. This seems to run counter to the results of minimum booster-type sensitivity tests. The discrepancy is resolved when shock wave initiation is viewed as a combination effect of both pressure and duration. Such a view, however, precludes any possibility of finding a satisfactory operational definition for sensitivity.

Detonation limits in truly homogeneous explosives require special treatment, because here the induction period for initiation of reaction is virtually equal to the reaction time. Evans' treatment [10] of this case is reviewed, and certain aspects of the results are critically examined.

An unusual "critical density" phenomenon is encountered with ammonium nitrate/fuel explosives. This has been attributed by Gordon [11] to diffusion-limited reaction. This case is reviewed; and the implications concerning the question of detonability in solid composite propellants are examined.

*Present address of author: 120 Ruskin Avenue, Pittsburgh, Pa. 15213.

INTRODUCTION

Many aspects of detonation are still poorly understood. This is particularly true of criteria for detonability and phenomena associated with detonation limits generally. These limits result primarily from the weakening of the shock wave as the limit is approached and the effect of this on initiation at the front. The problem is also complicated by the interaction of chemical and divergent flow effects behind the front. So little is known of any of these processes that it is not surprising the treatments we have are semi-empirical and heuristic in nature. These treatments, however, help considerably in tying together otherwise isolated observations, and they provide a basis for speculation and prediction. This paper attempts to give a coherent, but not necessarily exhaustive account of data on limits and explanations that have been forthcoming.

Since detonation depends on composition, density, charge diameter and particle size, as well as other less important factors, detonation limits should be thought of as boundaries in a many-dimensioned space. A point on a boundary may be approached along different paths. For example, the limit boundary in the density-diameter plane may be determined in a series of experiments with constant charge density, or in a series with constant charge diameter. A given point may appear, therefore, in the one case as a "critical diameter" and, in the other, as a "critical density." A general theory would describe results for any kind of experiments; but a description that refers to only one kind or another may yet retain a certain usefulness.

In experimental terms a detonation limit may be defined as the point at which the wave just fails to propagate at a steady rate, even when overdriven initially. Several experiments are required to locate a limit point with desirable accuracy. This accounts in part for the scarcity of data; but a more serious practical problem arises because of the comparative inaccessibility of the limit region for the common high explosives. The work of Stesik and Aki-mova on TNT [1], for example, gives diameter limits of the order of a few millimeters; and detonating cord containing PETN has been produced with an explosive train measuring less than 0.5 mm diameter. Less readily detonable materials like ammonium perchlorate and ammonium nitrate, and mixtures of these with organic fuels, are studied more easily, and with them more work of this nature has been done.

Limit data are usually obtained as a by-product in work on the diameter effect. For

this as well as other reasons, we give in the following section a brief description of results of this type.

THE DIAMETER EFFECT

Both in theory and practice it is known that detonation velocity D increases asymptotically when the charge diameter d is increased. This finding suggests that to determine the limiting velocity D_∞ the experimental values should be plotted against the reciprocal of the diameter and the curve extrapolated toward zero. Among the advantages of this procedure is the fact that random errors in the measurements are given approximately equal weight. On the other hand, if the velocity is plotted against diameter directly, the points for large diameter have relatively more influence in determining the asymptote than those for small. Moreover, it is a common finding that measurement errors are apt to be greater with large charges than with small. Usually a charge is either overboosted or underboosted; and the run-up distances required to reach a steady velocity vary about in proportion to the diameter. Therefore, since the charge length is usually somewhat limited, measurements at the upper end of the diameter scale are more likely to be biased (either high or low) than those at the lower end.

Besides these practical reasons for preferring a D vs $1/d$ plot to other types, one may demonstrate by a dimensional argument that, as velocity approaches a limiting value, the curve on such a plot is likely to approach a straight line. Since ΔD , the deviation from D_∞ , varies in inverse relationship with d , and since d is the only variable in a D vs d experiment, one may write a dimensional equation

$$\frac{\Delta D}{D_\infty} = f\left(\frac{a_0}{d}\right) \quad (1)$$

where a_0 is some characteristic length involved in the detonation phenomenon. The function f may be represented by a polynomial in powers of the argument. It follows, unless the coefficient of the first-order term is zero, that the function will approach linearity as ΔD vanishes. Thus, the limiting form of Eq. (1) is

$$\left(\frac{\Delta D}{D_\infty}\right)_{\Delta D \rightarrow 0} = \frac{k a_0}{d} \quad (2)$$

where k is a numerical constant.

In plotting the data available in the literature, we have almost always found that the

points on a D vs $1/d$ plot can be represented as well or better by a straight line than by any other curve. Indeed, this applies even out to quite large values of ΔD . Sometimes the points for large-diameter charges deviate from the line, but an experimental reason for this is often suggested by the authors.

Examples of various sets of data plotted in this way are shown in Fig. 1. These are quite representative of many such plots. Some authors state that their data do not conform to this pattern; but in these cases the velocity deviations are often based on a calculated value of ideal detonation velocity rather than on the empirically determined D_∞ .

In the limit of small deviations the Eyring theory [2] of the diameter effect reduces to the form of Eq. (2). In this case $k a_0$ is equated to the reaction zone length. In the following discussion we designate $k a_0$ simply by a_0 , and refer to it as the reaction zone length. However, it will be understood that in these discussions a_0 is nothing more than an empirically determined quantity.

CORRELATION OF LIMIT DATA

It is generally assumed that detonation fails at the limit because the shock wave is too weak to initiate reaction at a high enough rate to sustain detonation in a steady state. The suddenness with which detonation fails, and the sharp and reproducible appearance of the limit tends to confirm this hypothesis. This suggests, then, that there is a critical shock pressure associated with the detonation wave at the detonation limit. If the equation of state of the unreacted explosive were known, it would be possible to calculate the pressure at the shock front from the detonation velocity at the point of failure. However, since this information is generally not available, and because one is interested here only in approximate relative values of the critical shock pressure, we have chosen to use a simple formula and obtain a "nominal" value. This formula is

$$P_c \approx 0.22 \rho D_c^2 \quad (3)$$

where ρ is the bulk density of the explosive, and D_c is the steady detonation velocity just before failure. Equation (3) is derived from the continuity equation and the assumption that $(D - U)/D$ is always equal to 0.22 (U being the particle velocity behind the front). This formula underestimates the shock pressure, since the factor 0.22 is more appropriate for the

estimation of the Chapman-Jouguet pressure. But, the values calculated by Eq. (3) are correct in order of magnitude, and may be quite accurately compared with one another when differences of a factor of two or more are involved.

Table 1 summarizes the analyses of various sets of data, which were plotted as in Fig. 1. The numbers in Table 1 provide the basis for various correlations as discussed below.

Table 1, first of all, shows a remarkably strong correlation between P_c and ρ . This generally overrides the effects of chemical composition, particle size and other factors. The relationship is brought out more clearly by plotting the points as in Fig. 2. In this figure a straight line is drawn which generally indicates the trend of the points for a given explosive (of defined particle size and other characteristics). Thus, the points for TNT and AP (6μ) fall quite close to this line, and those for AN/TNT lie on a line parallel to it.

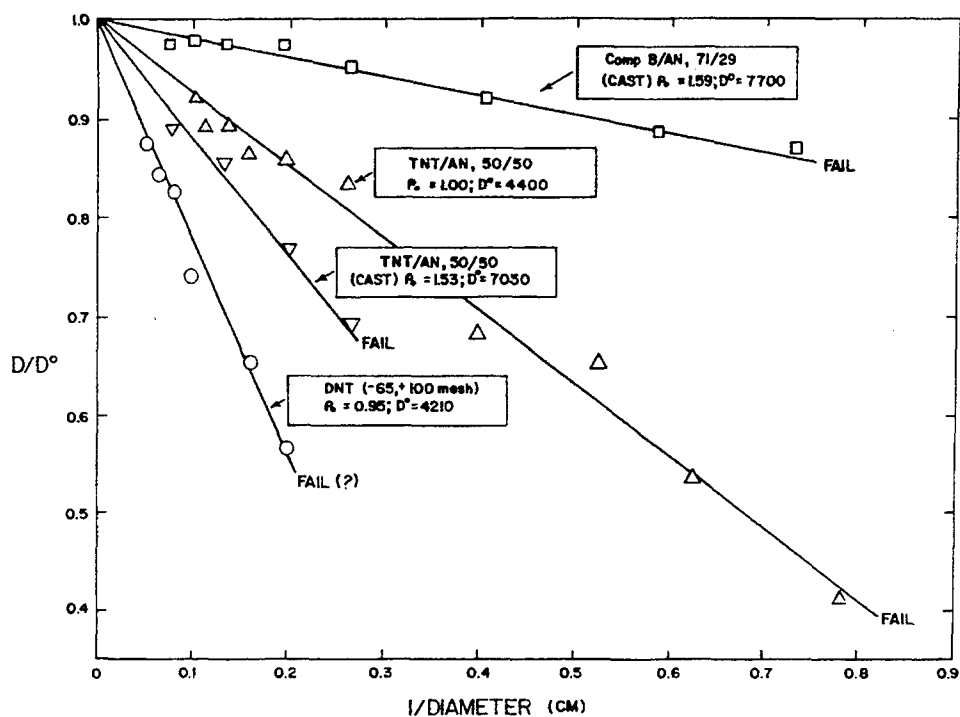
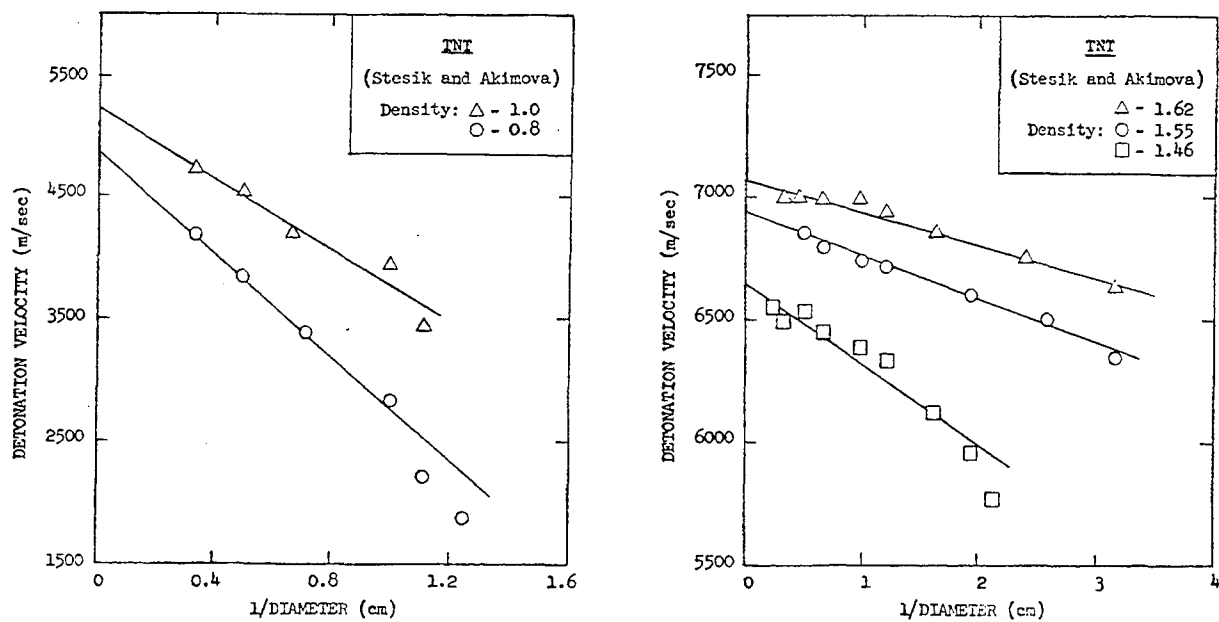
Next to the density effect, another trend becomes evident when one examines the points for various explosives at a density near 1.0 g/cm^3 . The two extreme points are for EDNA and AN at pressures of 50 and 4 kbar, respectively. These points also represent the extremes in the value of a_0 , which changes a hundredfold, from 0.1 cm for EDNA to 10 cm for AN. The points lying intermediate to these two are situated generally in conformity to this trend in a_0 , with, however, one or two notable exceptions.

The effect of particle size on P_c is consistent with its effect on a_0 and the observed effect of a_0 , in turn, on P_c . Thus the three points for AP of 6μ , 13μ and 175μ particle diameter lie at successively lower levels on the scale of P_c , falling where one would expect from the respective values of a_0 , namely, 0.8 cm, 1.2 cm and 8 cm. The particle size effect for AN/Oil is also consistent with this behavior.

The most notable exception to the foregoing generalization is found in the case of dynamite, which lies far below its expected position. Indeed, the experiments indicated that the detonation limit had not been reached for dynamite; and the point should actually be placed lower than it is in Fig. 2.

POROSITY AND IGNITION ENERGY

The correlation between P_c and ρ was considered by Gordon [9] in terms of a simplified

Fig. 1a - p vs $1/d$ plots for various data from Cook and co-workers [3,4]Fig. 1b - p vs $1/d$ plots for tetryl data taken from Stesik and Akimova [1]

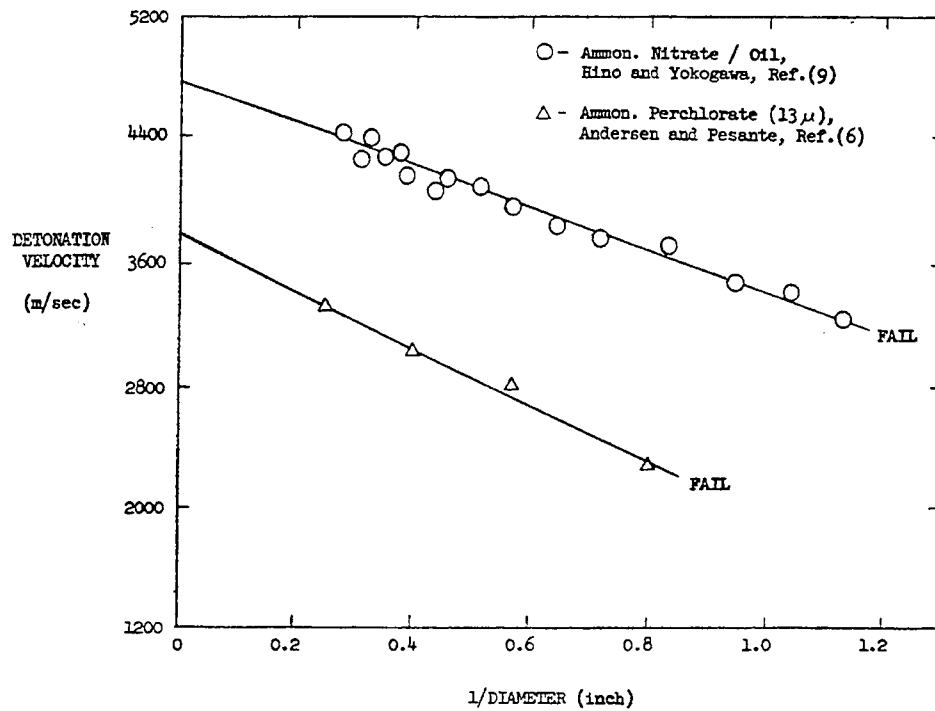


Fig. 1c - Dvs 1/d for AN/Oil⁹ and AP⁶

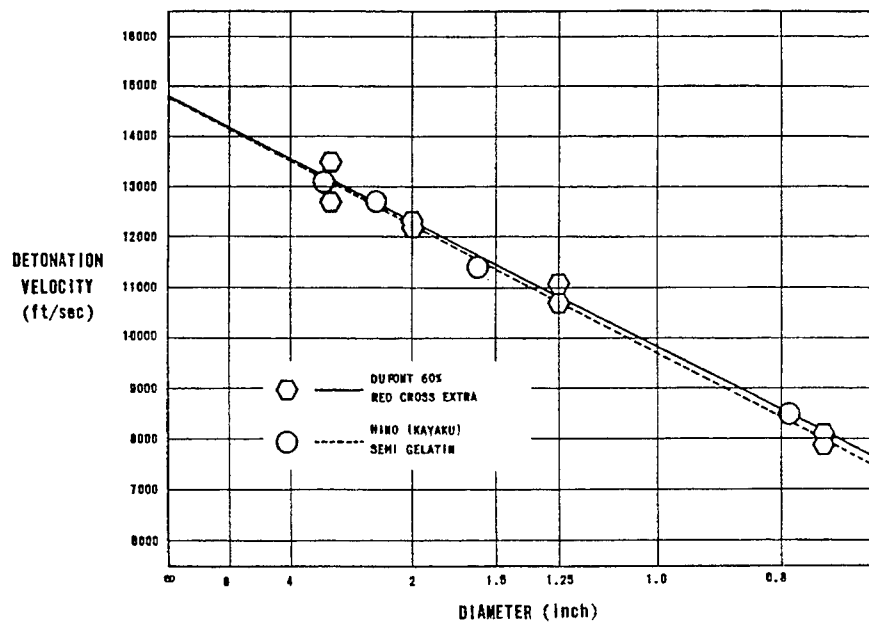


Fig. 1d - Dvs 1/d for dynamites

TABLE 1
Summary of Analyses of Limit Data

ρ - bulk density of explosive,

D_{∞} - extrapolated detonation velocity
at infinite diameter, and

a_0 - "reaction zone length" (see text),

P_c - "nominal" value of the critical
shock pressure (see text).

d_c - critical diameter,

Explosive (Average Particle Diameter)	State	ρ g (cm ³)	a_0 (cm)	d_c (cm)	D_{∞} (m/sec)	$(D/D_{\infty})_c$	P_c (kbar)	Ref.
TNT	Cast	1.62	0.09	1.3	7100	0.93	158	1
TNT	Pressed	1.62	0.021	0.3	7100	0.93	158	1
TNT	Pressed	1.55	0.023		6900			
TNT	Pressed	1.46	0.030	0.4	6600	0.88	109	1
TNT	Loose gran	1.00	0.24	0.6	5250	0.71	31	1
TNT	Loose gran	0.80	0.40	0.75	4750	0.47	9	1
AP (6 μ)	Loose gran	1.00	0.45	1.9	3850	0.76	19	6
AP (6 μ)	Loose gran	0.60	0.55	1.5	2750	0.65	4	6
AP (13 μ)	Loose gran	1.00	1.24	3.0	3850	0.59	12	6
AP (175 μ)	Loose gran	1.12	8.4	14	4150	0.41	7	7
EDNA (175 μ)	Loose gran	1.00	0.10	0.53	5910	0.81	51	5
DNT (175 μ)	Loose gran	0.95	2.25	5.0	4210	0.55	11	4
AN (200 μ)	Loose gran	1.04	10	17	3300	0.42	4	3
Ammon. Dynamite	Loose gran	1.20	0.84		4500	0.33	6	8
AN/Oil, 94/6 (50 μ)	Loose gran	0.95	0.84	2.0	4700	0.58	16	8
AN/Oil, 94/6 (500 μ)	Loose gran	0.95	2.30	4.8	4700	0.52	13	8
AN/HMTA, 91/9 (50 μ)*	Loose gran	0.95	0.58	1.0	4900	0.42	9	8
AN/TNT, 50/50	Cast	1.53	1.34	4.3	7050	0.69	80	3
AN/TNT, 50/50	Loose gran	1.00	0.75	1.2	4400	0.40	7	3
AN/Comp. B, 29/71	Cast	1.59	0.19	1.4	7700	0.86	155	3

*This explosive contains ammonium nitrate and hexamethylenetetramine in very intimate admixture. It is made by a process described in Canadian Patent No. 699,752.

model of the Hugoniot curve for a porous explosive. This is depicted in Fig. 3. Since only an insignificant quantity of energy is involved in collapsing the pores, or voids (even when they are filled with gas) the Hugoniot curve for explosive of specific volume v_0 (Fig. 3) must follow the abscissa to the point v_x , the specific volume of the voidless crystal. If S represents the terminal point on the Hugoniot for the detonation shock in explosive of this density, the area of the triangle $v_0 S v_s$ represents the internal energy imparted to unit mass of explosive by mechanical action at the front. Details of this process are obviously complex. What

happens may be simply visualized, however, if one imagines an explosive consisting of layers of intact crystal parallel to the shock front and separated by layers of void: the shock action would then consist of impacting each solid layer in succession in a perfectly inelastic collision, and thus imparting on each collision specific internal energy equal to $v_0 S v_s$. The process in a granular explosive is not essentially different from this.

The internal energy comprises thermal energy and intermolecular potential energy. The portion of the triangle represented by the shaded

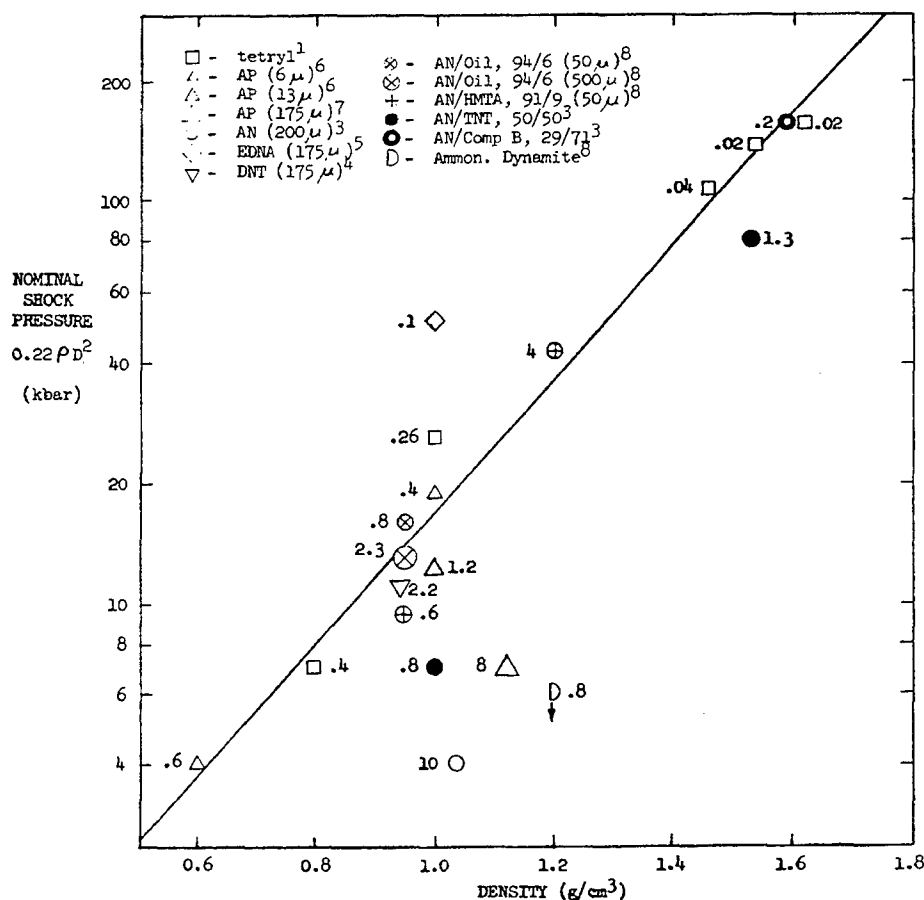


Fig. 2 - Critical shock pressure vs density for several explosives

area $v_0 S v_x$ is entirely thermal energy; and the remainder, $v_x S v_s$ —which represents the energy expended in adiabatic compression of the voidless crystal—is divided between thermal and intermolecular energy.

In first approximation the branch of the Hugoniot curve of the porous explosive that rises from v_x may be represented by the Hugoniot curve for the non-porous (voidless) explosive. Details of the argument cannot be given in the space allotted here, but it will suffice to indicate the magnitude of the error that this assumption involves. Considering a shock wave of given velocity in the porous explosive, one notes that the Rayleigh line is defined, and that the shocked state s lies somewhere on it. We assume the first approximation as stated above, and calculate by straightforward application of the Hugoniot equation the

second approximation to the point S . The change in v_s in going from the first to second approximation is given by

$$\frac{v_s^{(2)} - v_s}{v_0 - v_x} = \frac{1}{2 \left[\frac{C_p}{\alpha p_s v_s} - 1 - \frac{v_s}{\gamma (v_0 - v_s)} \right]} \quad (4)$$

where $v_s^{(2)}$ is the second approximation and v_s the first approximation to the specific volume, p_s the first approximation to the shock pressure, C_p the specific heat, α the thermal expansion coefficient and γ the Grüneisen ratio. Substitution of approximate values for the various quantities shows that the denominator on the RHS is positive, the first term being preponderant. This term is approximately inversely proportional to p_s . The displacement of the actual Hugoniot from the non-porous

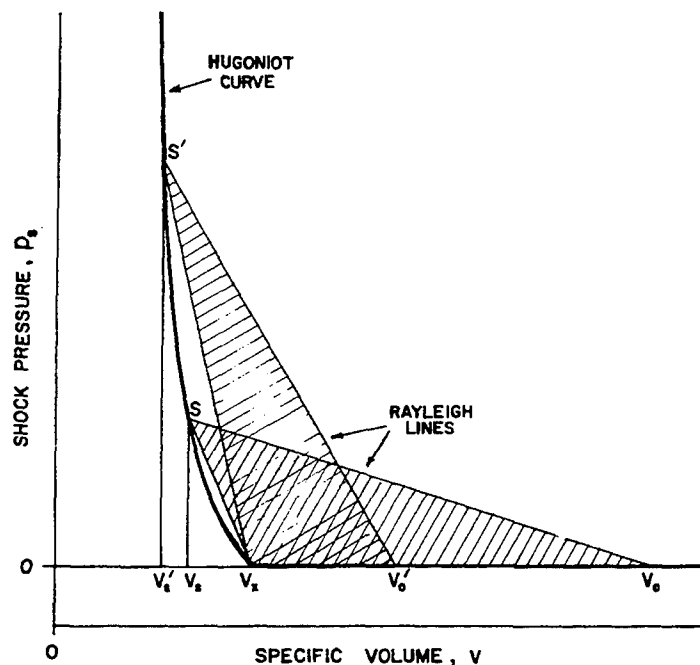


Fig. 3 - Schematic representation of the Hugoniot curve for a porous explosive

Hugoniot therefore increases (v_0 being fixed) as the shock pressure rises. This is as one would expect. At 50 kbar, however, the correction, $v_s^{(2)} - v_s$, is only about 5% of $v_0 - v_x$. For present purposes this correction can be ignored.

The initiation process in non-homogeneous explosives involves first the creation of hot spots through the action of the shock wave. In substantially porous material the hot spots are probably in large part produced by friction as a result of impacts of crystals driven together with high velocity when the voids collapse. Thus, the energy represented by the shaded triangle in Fig. 3 is largely concentrated at the impact points. One may designate this as "ignition energy" ΔE_i , although it is understood that the remainder of the shock energy represented by $v_x S v_s$ is also in part thermal. This portion of the energy, however, is distributed uniformly, since it results from homogeneous compression. Thus, one may distinguish homogeneous and heterogeneous heating, the portion designated ignition energy being the heterogeneous part.

The ignition process itself is a thermal explosion, in the one case, when the heating is uniform, being simultaneous thermal explosion of the whole mass, and in the other, when the

heating is concentrated at isolated locations, being thermal explosion of hot spots. In substantially porous explosive the hot spot mechanism predominates, and in homogeneous material the uniform thermal explosion prevails.

The two essentially different ignition mechanisms result in different reaction mechanisms, the one being grain burning, and the other homogeneous decomposition. Stesik and Akimova's data [1] for TNT seems to show a rather abrupt transition from one decomposition mode to the other. Referring to the D vs $1/d$ plots of these data in Fig. 1b, one notes that the slopes of the lines for $\rho = 1.62$ and $\rho = 1.55$ are insignificantly different, and the points in both cases adhere very closely to the Eyring formula. Moreover, the apparent reaction zone width for these two densities is very small, about 0.2 mm. The data for $\rho = 1.46$, however, begin to deviate from this pattern, and when the velocity falls below about 6000 m/sec, there is a steep falling off. Unfortunately, there is a large gap between $\rho = 1.46$ and $\rho = 1.0$; but it seems clear that at $\rho = 1.0$ and $\rho = 0.8$, grain burning predominates and the reaction zone width is an order of magnitude greater. In these two cases the data again follow closely the Eyring law. From these observations one might draw the conclusion that the transition

from hot spot to homogeneous ignition in tetryl occurs when the shock velocity is about 6000 m/sec.

With the use of the simplified model of the Hugoniot for porous explosive, the quantities associated with initiation, namely, shock pressure, ignition energy and total energy can be readily calculated. The experimental datum needed is the detonation velocity, from which the slope of the Rayleigh line can be obtained. The construction is illustrated in Fig. 3. Gordon [9] used this method to investigate conditions at the detonation limit for various loading densities in ammonium perchlorate, using as a base the data of Andersen and Pesante [6].

Figure 4 shows a D vs $1/d$ plot of the data for AP of average particle diameter 6μ . Andersen and Pesante [6] determined the critical diameter for this material at $\rho = 0.6$ and $\mu = 1.0$, and from this a line was located, as in Fig. 4, representing the approximate locus of the detonation limit. (Apparent inconsistencies in the data, especially at higher densities, make us believe that detonation velocities were recorded in some cases when the wave was failing, after being initially overdriven. We have therefore taken some liberty in handling these figures; and the analysis is admittedly rather crude.)

Figure 5 shows the model Hugoniot for AP. The Hugoniot for the non-porous material was calculated on the basis of an empirical relation between shock velocity and particle velocity described by Jacobs, Liddiard and Drimmer [12]. The Rayleigh lines were drawn with slope corresponding to the detonation velocity at the limit for each density. For explosive densities not studied by Andersen and Pesante limits were estimated by extrapolation of a smooth curve.

Figure 6 depicts the calculated shock wave characteristics in ammonium perchlorate at the limits of detonation. The pressure shows the strong dependence on density already seen in Fig. 2. In contrast, the ignition energy ΔE_i (the shaded area of Fig. 3) changes but little (1.0-1.2 k joule/g) over this density range.

These results are not really surprising when one considers the effect of density on the shock pressure and shock energy in ideal detonation. In an ideal detonation pressure varies approximately in proportion to the square of density for the common high explosives, while the shock energy (ΔE across the shock) changes only slowly. Conditions at the detonation limit necessarily reflect the ideal behavior for any given density. Therefore, before imputing special significance to the variation of conditions at the limit, one should perhaps "normalize" the pressure and energy values in terms

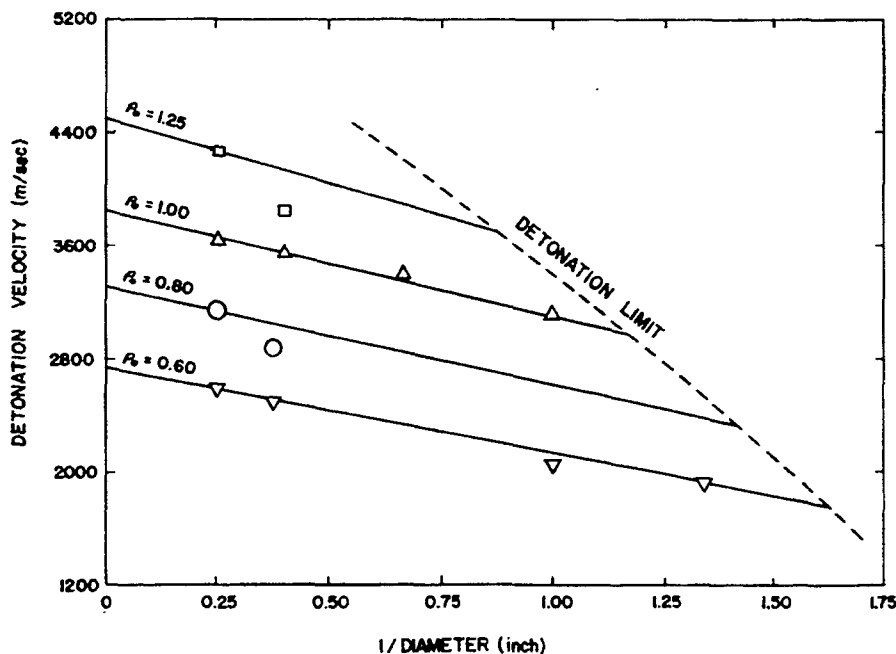


Fig. 4 - Detonation data for ammonium perchlorate of 6μ average particle diameter [6]

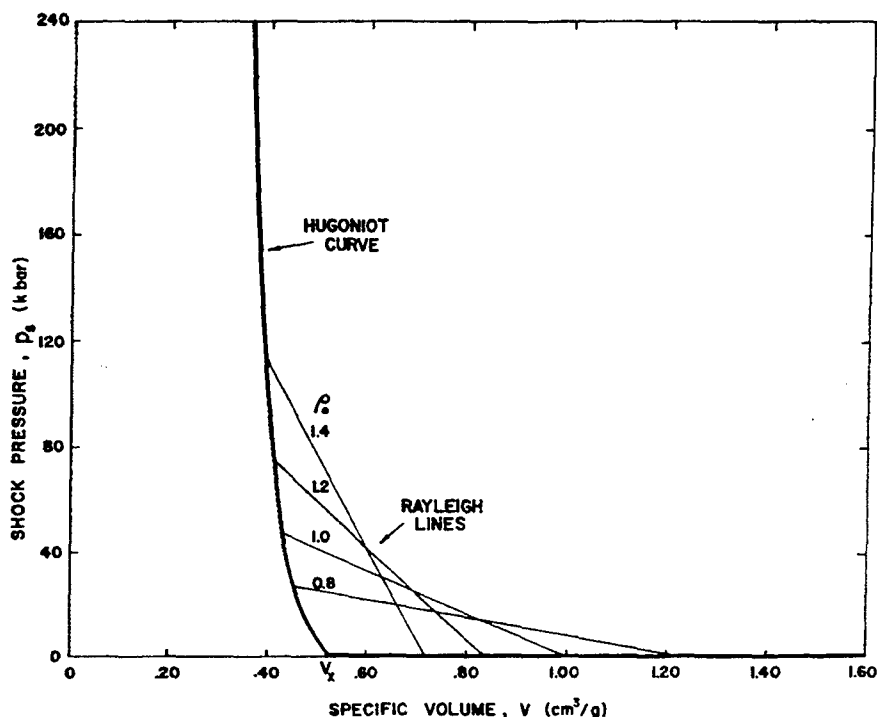


Fig. 5 - Hugoniot curve for porous AP according to simplified model, with Rayleigh line corresponding to the detonation limit data in Ref. 6

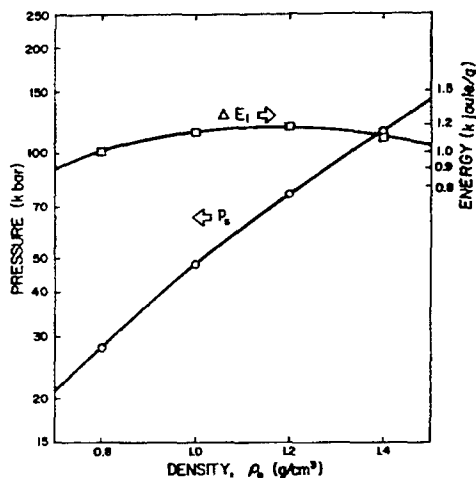


Fig. 6 - Shock pressure and "ignition energy" at the detonation limit in AP at various initial density

of the corresponding ideal detonation quantities. After making such a comparison, we conclude that the variations of pressure and energy in Fig. 6 do not differ from the variations of the corresponding quantities in ideal detonation to a degree that admits any significant conclusion to be drawn in this respect.

What this investigation clearly does show is that it is not primarily shock pressure that is important for failure of detonation at the limit, but probably the shock energy or some closely related quantity.

Another important aspect shown by the data in Fig. 2 is the effect of reaction zone width a_0 . This seems to overshadow many other factors. The fact that EDNA, a relatively "sensitive" high explosive, stands at the top of the pressure scale for explosives with $\rho \approx 1.0$, and ammonium nitrate—a material so "insensitive" it is not usually considered to be a high explosive—appears at the bottom seems to be a paradox. The explanation must be sought—if the basic assumption concerning the critical nature of the shock wave at the limit is correct—in terms of some property of the shock. It is clear, here again, that pressure is not the important factor. Nor can this phenomenon be understood in terms of shock energy, because for given bulk density energy is approximately proportional to pressure, and depends only slightly on the physical properties of the substrate.

A factor not heretofore considered is the rate at which pressure decays behind the front, or, its reciprocal, the time during which the high pressure created by the shock is sustained. This is closely linked to a_0 ; and for present

purposes duration can be considered as being proportional to a_0 , the order of magnitude being $2a_0$ (cm) μ sec. Thus, one may consider that in EDNA the shock pressure relaxes after about 0.2 μ sec, and in AN after about 20 μ sec. This wide difference must have considerable significance in the growth—or failure—of reaction.

Thermal explosion of hot spots and subsequent development of reaction in the surrounding medium has recently been studied on the computer by Mader [13]. The work applies specifically to nitromethane but the essential findings should apply to any condensed explosive in the shocked state. Mader's calculations show that whether a hot spot starts a self-propagating spherical detonation in the surrounding medium depends mainly on its size and temperature, and also on the temperature of the surrounding medium. The first stage is thermal explosion of material at the center of the hot spot; but explosion at this point does not necessarily propagate into the surroundings. The critical phenomenon determining development of detonation is usually spherical divergence of the shock wave that propagates outward from the exploding hot spot. In some cases, however, it is the spherical convergence of a rarefaction moving back toward the center of the hot spot that chokes off thermal explosion before it is fully developed. The behavior, in any case, is influenced mainly by chemical kinetics and wave motion, and not appreciably by heat conduction.

Mader's work draws as much attention, therefore, to the medium surrounding the hot spot as to the hot spot itself. When a hot spot is created by a shock wave—regardless of precisely what mechanism produces it—the surrounding medium is compressed and heated. The duration of the shock pressure in the medium determines how long it remains in the heated and compressed state. If relaxation occurs too early, the hot spot may not explode in time, and development of detonation may thus be prevented. This seems to offer a reasonable explanation for the behavior of EDNA and AN. It is precisely because EDNA burns so rapidly that detonation propagates in very narrow charges. At the detonation limit the shock pressure has a very short duration; therefore, hot spots must be produced with a sufficiently high temperature to explode in a very short time. AN burns at a rate slower by some 100 times, and the induction reaction in the hot spots need only occur, therefore, at a correspondingly slower rate. There may well be differences in kinetic factors that help account for this behavior; but the apparent overriding influence of a_0

for the several explosives examined—except for cases like nitroglycerin—suggests that this is the main effect.

SENSITIVITY TESTING

The limit data in Table 1 pose important questions about sensitivity and the nature of sensitivity testing. This is a perplexing problem even from a semantic point of view. For, one may well ask just what the term "sensitivity" is supposed to mean. A satisfactory operational definition would have to go beyond mere description of an empirical test. The observations in the previous section help to bring this problem again into focus.

At present there are perhaps three main types of sensitivity test in use: the drop-weight test, the minimum-booster type of test, and the gap test. The first two types, although quite different, are for certain practical purposes very useful. Unfortunately, they are arbitrary in the extreme, and furnish no numbers that are meaningful in terms of recognized physical quantities. It is probably for this reason that recent interest has turned to the gap test, where in principle at least, it is possible to determine at the threshold of initiation the actual value of the shock pressure. But, just how useful is this particular datum?

No matter how the sensitivity test is performed, it is abundantly clear that a figure for the critical shock pressure, unqualified in any way, has no significance whatever with regard to the chemical properties of an explosive. This is certainly demonstrated by the data in the previous section. But, if needed, further proof may be found in the growing body of literature on initiation. For example, Holland, Campbell and Malin [14] report 100 kbar as the critical shock pressure needed to initiate a single crystal of PETN, while Seay and Sealy [15] find that only about 2.5 kbar is needed to initiate granular PETN with a density of 1.0 g/cm³. (It may be incidentally noted that the latter figure is comparable with the limit pressure in AN, as given in Table 1.)

We have pointed out in the previous section that data of this sort reveal little more than the fact that detonation pressure is a strong function of density. Therefore, from what has been said in this connection, it would seem to be a minimum requirement in comparing the "sensitivity" of two explosives in a gap test to have the bulk density the same. One might then do the test in two ways, either by using the same diameter in each test and comparing the

maximum gap, or by using the same gap (i.e., the same pressure, approximately) and comparing the minimum diameter. The first procedure would fall in the category of the present gap technique, and the second more in the category of the minimum-booster test. Both are arbitrary. Which is the more informative? Unfortunately, no answer seems apparent at present to this vexing question; for the experiment inevitably retains an element of arbitrariness that no degree of precision or sophistication of technique can raise above the level of simple empiricism.

EVANS' THEORY FOR LIMITS IN HOMOGENEOUS EXPLOSIVES

A theory of detonation failure in homogeneous explosives has been advanced by Evans [10]. The premises of this theory are (1) the Zeldovich-von Neumann-Doering model of stable detonation (deflagration headed by a shock); (2) first-order Arrhenius-type reaction kinetics, with "Arrhenius temperature" T_{arr} (E/R) large compared to the temperature at the shock front T_s which initiates reaction; and (3) a theory of detonation in finite diameter charges, relating the deficit from ideal detonation velocity ($\Delta D/D^0$) to the length of the reaction zone a_0 , e.g., theories of Eyring, Jones, and Wood and Kirkwood. In essence, the critical diameter arises because the two independent conditions imposed by the theoretical restrictions in (2) and (3) can be simultaneously satisfied only if the charge diameter exceeds some minimum or critical value. To express this situation formally, the reaction time τ is related to the detonation velocity by some function, say, $f(D/D^0)$ because of condition (2), i.e.,

$$\tau = f(D/D^0); \quad (5)$$

and, τ is also related to another function involving the detonation velocity and the charge diameter d , $g(D/D^0, d)$, because of condition (3), i.e.,

$$\tau = g(D/D^0, d), \quad (6)$$

It is found that the two conditions (5) and (6) can be satisfied only if d exceeds a critical value d_c , i.e.,

$$\begin{aligned} f(D/D^0) &= g(D/D^0, d), \quad d \geq d_c \\ f(D/D^0) &\neq g(D/D^0, d), \quad d < d_c. \end{aligned} \quad (7)$$

The treatment of the steady state reaction zone in this case involves application of the

theory of thermal explosion. It may be shown that when the Arrhenius temperature is high relative to the initial temperature, which in this case is the temperature at the shock front T_s , little reaction occurs until a time t_{ind} given by

$$t_{ind} = \frac{T_s^2}{T_{arr} T_{ad}} \times \frac{1}{\nu} \times \exp(T_{arr}/T_s). \quad (8)$$

Thereafter, the reaction proceeds very rapidly until the explosive is almost completely decomposed to products. Thus, the time period for complete reaction in the detonation wave is in this case only slightly greater than the induction time, i.e.,

$$t_{ind} \approx \tau. \quad (9)$$

The shock temperature T_s depends on the shock strength, and hence on the shock velocity D . The value of D is always less than the limiting value D^0 ; thus it is convenient to express reaction time in terms of the ratio D/D^0 . The relation between T_s and D/D^0 may be obtained through the Hugoniot relations, and depends specifically on the equation of state of the intact explosive as well as on the heat of explosion and other thermal properties. Therefore no general expression can be written for the form of the function $f(D/D^0)$. It is of interest, however, to study the critical diameter analytically; and the following example for the case of unreacted explosive exhibiting an Abel equation of state, $p(v - \alpha) = RT$, with constant co-volume α , serves to illustrate important aspects of the phenomenon.

Development of the relationship between shock temperature and detonation velocity starts from a general expression which is readily derived from the Hugoniot relations

$$E_s - E_0 = 0.5[(v_0 - v_s)/v_0]D^2, \quad (10)$$

wherein the subscripts 0 and s refer respectively to conditions in front of and immediately behind the shock front. For a medium obeying the Abel equation, it is readily shown that the internal energy depends on temperature only, i.e., $(\partial E/\partial v)_T = 0$. Hence, the energy change $E_s - E_0$ in Eq. (10) can be represented by $\bar{c}_v(T_s - T_0)$ where \bar{c}_v is the average specific heat between T_0 and T_s . Also, in the case of strong shock waves associated with detonation such an equation of state means that v_s approaches closely a limiting value v_∞ which is equal to $\alpha + (v_0 - \alpha)(\bar{\gamma} - 1)/(\bar{\gamma} + 1)$, $\bar{\gamma}$ being equal to $1 + R/\bar{c}_v$. Thus, Eq. (10) for this case can be written approximately in the form

$$\bar{c}_v(T_s - T_0) \approx 0.5(1 - v_\infty/v_0)D^2. \quad (11)$$

The terms \bar{c}_v and v_∞ in Eq. (11) may be regarded as constant, at least over a narrow range of the shock velocity D . Differentiation of Eq. (11) shows that for a small departure ΔD from ideal detonation (where conditions are represented by superscript zero)

$$T_s^0 - T_s = 2(T_s^0 - T_0) \times \Delta D/D^0. \quad (12)$$

Equation (12) may be combined with Eq. (8) and (9) to give the dependence of reaction time τ on the fractional velocity deficit $\Delta D/D^0$; thus, since from Eq. (8) and (9)

$$\ln \tau^0 = \ln (T_s^{02}/T_{arr} T_{ad}^0) + T_{arr} T_s^0,$$

and

$$\ln \tau = \ln (T_s^2/T_{arr} T_{ad}^0) + T_{arr} T_s,$$

then by approximation

$$\ln (\tau/\tau^0) \approx (T_s^0 - T_s) T_{arr}/T_s^{02}. \quad (13)$$

Hence, combining Eqs. (13) and (12), one obtains the desired expression linking τ and ΔD :

$$\ln (\tau/\tau^0) \approx [2T_{arr}(T_s^0 - T_0)/T_s^{02}] \Delta D/D^0. \quad (14)$$

Equation (13), then, expresses the requirement imposed by the Arrhenius mechanism combined with an Abel equation of state. The form of the equation is obviously much more strongly influenced by the Arrhenius equation than by the equation of state; therefore, Eq. (14) may be considered approximately valid for any equation of state so long as Arrhenius kinetics apply and $T_{arr} \gg T_s^0$.

The second important condition in Evans' theory of failure in homogeneous explosives is that set by the relation between velocity deficit, charge diameter and length of the reaction zone. For small departures from ideal velocity, the theory of Eyring, Powell, Duffey and Parlin [2] gives the result,

$$\Delta D/D^0 = a_0/d \quad (15)$$

where a_0 is reaction zone length and d is charge diameter. The length of the reaction zone may be equated to $(D - \bar{u}_1)\tau$, where \bar{u}_1 is the average particle velocity in the reaction zone. Since in this case the "reaction zone" comprises essentially only the induction period,

the average particle velocity is approximately equal to u_s , the particle velocity immediately behind the shock front. From the continuity equation it follows that $(D - u_s) = D \times v_s/v_0$; and since in the case of the Abel equation of state v_s is approximately equal to v_∞ , Eq. (14) may be written for small departures from ideality

$$\Delta D/D^0 \approx (v_\infty/v_0)D^0\tau/d. \quad (16)$$

The two conditions expressed in Eq. (14) and (16) may now be combined to eliminate $\Delta D/D^0$ and give a relationship between τ and d . This relationship may be written

$$\frac{d}{a_0^0} \approx 2 \times \frac{T_{arr}(T_s^0 - T_0)}{T_s^{02}} \times \frac{\tau/\tau^0}{\ln (\tau/\tau^0)} \quad (17)$$

where a_0^0 is the reaction zone length for an ideal detonation.

The function $x/\ln x$ has a minimum value when x is equal to e , the base of natural logarithms. Hence, there is a minimum value of the charge diameter d_c , that can satisfy Eq. (16). This is given by

$$d_c \approx [2e T_{arr}(T_s^0 - T_0)/T_s^{02}] \times a_0^0 \quad (18)$$

The fractional deficit in detonation velocity at the critical diameter $(\Delta D/D^0)_c$ is obtained by combining Eq. (18) and (16); thus, noting that at the critical diameter the expression $(v_\infty/v_0)D^0\tau$ is equal to $e a_0^0$, we have

$$(\Delta D/D^0)_{cr} = T_s^{02}/2 T_{arr}(T_s^0 - T_0). \quad (19)$$

Equation (19) shows that the velocity deficit in homogeneous explosives at the point of failure is very small, of the order of a few percent. Typically, T_s^0 lies in the neighborhood of 1000°K, T_{arr} of 20,000°K and T_0 of 300°K. For these specific values $(\Delta D/D^0)_c$ has the value 0.035.

Evans calculated the critical failure properties for liquid TNT and ammonium nitrate using a more accurate and much more complicated equation of state. This was combined with experimental kinetic data for the decomposition reactions. The critical diameter was obtained graphically as illustrated in Fig. 7. Plotted in Fig. 7 are the functions f and g of Eq. (4) and (5). The points at which the curves cross represent stable detonation states according to this model. In general the f -curve cuts the d -labeled g -curve at two points, or not

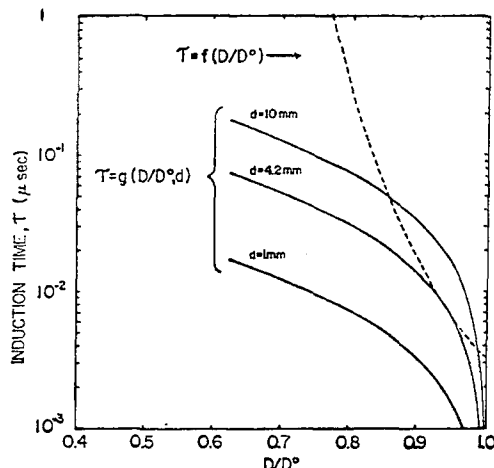


Fig. 7 - Functional relationships that determine the critical diameter in liquid TNT [10]

at all, except for the unique case where the f -curve touches a g -curve at a point of tangency. The charge diameter for which this tangency condition obtains is interpreted to be the critical diameter, being the limiting diameter for which there is a solution of the equation $f = g$. (Conditions at the point of tangency are expressed approximately by Eqs. (18) and (19).) The calculated limiting diameter for liquid TNT is therefore 4.2 mm according to Fig. 7. This may be compared with an experimental failure diameter of something less than 19 mm. Although the agreement is by no means perfect, it seems satisfactory in view of the uncertainty associated with the theoretical treatment of the charge diameter effect.

Evans' calculations show that the failure diameter in a homogeneous single crystal of ammonium nitrate is of the order of 10^7 meters. Although this result obviously cannot be verified experimentally, it is corroborated by the experimental finding that even finely pulverized ammonium nitrate at low bulk density has a critical diameter of several inches; and the critical diameter increases sharply when the material is densified.

Homogeneous induction of reaction is beautifully demonstrated in the experimental work of Campbell, Davis and Travis [16] on nitromethane. The computations of Mader [13] based on this model also give it ample support.

The contrast between homogeneous and heterogeneous ignition is clearly shown in the Los Alamos work [16,17]; and a categorical distinction may now be considered quite firmly

established. On the other hand, there are several indications that a "grey zone," where both phenomena participate, does exist. Majowicz and Jacobs [18], for example, observed a small "overshoot" in the shock wave initiation of Comp. B. This is a recognized indication of homogeneous ignition; and considerable discussion has revolved about this point because Comp. B is manifestly not a homogeneous material.

So far as Evans' theory is concerned an explosive may be considered to behave essentially like a homogeneous one if the reaction time is short compared to the induction time. Where there is hot spot ignition followed by grain burning this is usually not the case. However, when the explosive is dense, essentially voidless and chemically homogeneous, the hot spots formed by the passage of the shock wave will be but little hotter than the bulk of the material. Therefore, general homogeneous ignition will follow closely on the heels of localized ignition, and the behavior will be scarcely distinguishable from that in a truly homogeneous case.

These considerations suggest a concept that one may call a "degree of homogeneity" of ignition. This will apply especially in the case of dense explosives that are not truly homogeneous. According to Evans' theory the degree of homogeneity of ignition should bear an inverse relationship to the velocity deficit at the point of detonation failure. From Table 1, for example, one would conclude that the ignition of TNT in the cast or pressed condition at $\rho = 1.62$ is nearly homogeneous, since $(D/D_\infty)_c = 0.93$. Indeed, the very narrow reaction zone in this case also shows that decomposition must be largely homogeneous. On the other hand, in the case of cast 50/50 amatol of $\rho = 1.53$ — where the density figure itself gives evidence that there are considerable voids — the ignition appears to have a low degree of homogeneity, since $(D/D_\infty)_c = 0.69$. In this case the reaction zone is broad, showing that grain burning predominates. The case of cast AN/Comp. B, 29/71, where $(D/D_\infty)_c = 0.86$, may be considered intermediate; and the reaction zone thickness is consistent with this classification. Thus, Evans' theoretical conclusion that the velocity deficit at failure in homogeneous materials must be small seems to accord with the experimental indications in Table 1, especially if one is willing to permit a certain latitude in the use of the term "homogeneous" as applied to dense, solid explosives.

A peculiarity of Evans' theory that has not been experimentally verified, however, is the

appearance of two states of stable detonation for a charge of diameter greater than the critical diameter. Although so-called "low order" detonations are well known, they usually show a lower velocity than that given by the lower state in this theory. The reason this second state is not observed is that it actually represents not a stable condition, but a metastable one, since it is unstable with respect to either positive or negative perturbations of the velocity. Thus, by reference to Fig. 7 it is seen that an increase in shock velocity (and shock strength) from this condition leads to a shorter induction period according to the curve $\tau = f(D/D^0)$; but the increase in stable velocity for this new value of τ (at the same charge diameter, d) according to the curve $\tau = g(D/D^0, d)$ is greater than the original perturbation, meaning that the lateral energy losses have decreased disproportionately and that the wave, having achieved this new condition, will speed up even further. This process thus continues until the upper stable condition is reached. By similar reasoning a negative perturbation in velocity may be shown to lead to ultimate failure of the shock wave. According to the same type of arguments, perturbations from the upper stable state (corresponding to the upper crossing point of the f and g curves) tend to become canceled out and the original condition restored. The upper point therefore represents a truly stable condition, while the lower point is in fact metastable. It is thus not surprising that experimental verification of this aspect of the theory is lacking.

DIFFUSION EFFECT IN COMPOSITE EXPLOSIVES

The composite explosives with which this section deals are mixtures of a self-explosive oxidizer and an inert organic fuel. Although observations are available only on ammonium nitrate explosives, it is presumed that ammonium perchlorate mixtures would behave in the same way. In these materials the fuel-oxidizer reaction contributes a major fraction of the explosive energy. Most commercial explosives are of this type, although conventional dynamites contain a quantity of nitroglycerin besides the composite mixture. Solid composite propellants are also examples of this class.

Characteristically, such composite explosives behave quite differently than molecular explosives like RDX, TNT, and pure ammonium perchlorate. This is evident especially in the response to a change in the initial density ρ_0 . The difference is illustrated by the curves in Fig. 8, which show a plot of D vs ρ_0 for a proprietary AN/HMTA explosive (Table 1) and one for TNT, in both cases for a charge of fixed diameter. The increase of velocity to a maximum, followed by a steep descent as the density is further increased, is typical behavior for a composite explosive. (See, for Example, Ref. 20, p. 49.) Molecular explosives, on the other hand, show a monotonic increase in velocity right up to crystal density.

This unusual characteristic of composite explosives may be described as a limiting

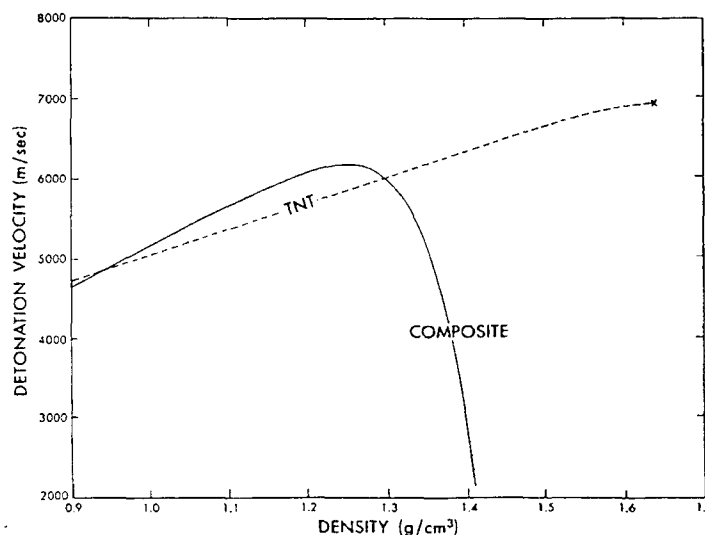


Fig. 8 - Detonation velocity vs density for a molecular explosive (TNT) and a composite explosive (AN/HMTA)

density effect, since for a given charge diameter there is an upper limit to the density at which a detonation will propagate. The limiting density rises slowly as the charge diameter is increased.

Another way in which the peculiar properties of composite explosives are manifested is in the interaction of density with the diameter effect. For pure molecular explosives the fractional velocity decrement at a given charge diameter decreases as density is increased. This, indeed, is one line of supporting argument for the grain-burning mechanism in these materials; because at higher density and consequently higher pressure the burning rate increases. The behavior is reflected, for example, in the results for TNT and for AP in Table 1. For composite materials this behavior is sharply reversed. In the AN/HMTA explosive of Fig. 8, for example, the value of a_0 increases from 0.6 cm at $\rho = 1.0$ to 4.0 cm at $\rho = 1.2$. Even in amatol, where the fuel component is TNT, there is a suggestion of this type of behavior, as may be seen from the figures in Table 1.

The unusual properties of composite materials have been noted by Cook (Ref. 21, p. 141), who suggests that they result from a slowing down of the diffusion reaction between fuel and oxidizer when the density is increased.

Gordon [11] describes a model that accounts for the effect of density on the diffusion rate in the detonation reaction zone. Under the assumption that diffusion is rate-controlling at high densities, an expression is obtained for the interdependence of detonation velocity D , density ρ_0 and diameter d that shows typical composite behavior.

Because it is so dense, the reacting medium behind the detonation shock front in a condensed explosive may be likened more to a liquid than to a gas. The diffusion constant D_0 may then be treated by the concept of "holes," which has been so fruitful for the liquid state. (See, for example, Ref. 19.) Accordingly,

$$D_0 = \lambda \bar{v} \exp(-E/RT) \quad (20)$$

where λ is a "jump" distance, comparable to the mean free path, \bar{v} is the average molecular velocity, and E is the energy required to create a hole of molecular size.

The point at which behavior in the detonation state departs most from that in ordinary liquids is in the nature of E , the activation energy. The kinetic pressure, p , which is

negligible in liquids under ordinary conditions, completely overshadows the "internal pressure" generated by intermolecular forces. In these circumstances the activation energy may be equated simply to pV , where V is the molecular volume, i.e.,

$$E = pV. \quad (21)$$

The critical effect of initial density ρ_0 on diffusion arises, therefore, simply because p is a strong function of density. Conservation of momentum in the shock front implies a relationship between ideal Chapman-Jouguet pressure p_{cj}^0 , density ρ_0 , shock velocity D^0 and particle velocity u_1^0 , namely, $p_{cj}^0 = \rho_0 D^0 u_1^0$. It is shown by Jones [20] that

$$u_1^0 = D^0 / (1 + d \log D^0 / d \log \rho_0) (2 + \alpha)$$

where α is a dimensionless thermodynamic quantity (equal to the reciprocal of $(1/p)(\partial E / \partial v)_p$) which in actual cases has a value between zero and about 0.25. The derivative $d \log D^0 / d \log \rho_0$ is the exponent m obtained empirically from the dependence of detonation velocity on density, i.e., $D^0(\rho_0)/D^{0*}(\rho_0^*) = (\rho_0/\rho_0^*)^m$, the asterisk designating a reference state, say, that with $\rho_0 = 1.0 \text{ g/cm}^3$. Using these relationships, one obtains the following expression for p_{cj}^0 in terms of ρ_0

$$p_{cj}^0 = \frac{1}{k} \rho_0^* D^{0*2} (\rho_0/\rho_0^*)^{2m+1} \quad (22)$$

where k , which replaces the expression $(1+m)(2+\alpha)$ is essentially constant and independent of density. For composite explosives m is found to be close to unity; and k therefore lies between 4.0 and 4.5. The pressure in the reaction zone p is greater than p_{cj} by the ratio of the particle velocities $u_1/u_{1(cj)}$, and since this is not much affected by ρ_0 , it is permissible for these purposes to use Eq. (22) to express approximately the relation between p and ρ_0 . Therefore, the pressure in the detonation reaction zone varies as something like the cube of density (i.e., as $2m+1$).

If diffusion is rate controlling, the reaction time τ can be equated to the time needed for a molecule such as oxygen to diffuse some average distance in the explosive δ ; thus,

$$\tau = \frac{\delta^2}{D_0} \quad (23)$$

By equating the reaction zone length a_0 to $(D - u_1)\tau$, one obtains from Eq. (20) to (23)

$$a_0 = \frac{(D - u_1) \delta^2}{\lambda v} \times \exp \left[\frac{(\rho_0^* D^{0.2} v)}{kRT} \left(\frac{\rho_0}{\rho_0^*} \right)^{2m+1} \right] \quad (24)$$

Equation (24) contains the essential explanation of the effect of density on the behavior of composite explosives, according to this treatment. The reaction zone length a_0 grows rapidly with density because of the factor $(\rho_0/\rho_0^*)^{2m+1}$ in the exponent. Compared to the effect of this factor, the relatively minor changes of the pre-exponential term $(D - u_1)\delta^2/\lambda v$ and the term $(\rho_0^* D^{0.2} v)/kRT$ have negligible influence. These terms are therefore replaced by a length parameter ℓ and a number b , respectively, which for these purposes may be regarded as constants.

Substituting the value of a_0 from Eq. (24) into the approximate Eyring expression for the diameter effect $D/D^0 = 1 - a_0/d$, and taking into account the density dependence of D^0 , one obtains

$$\frac{D}{D^0} = \left(\frac{\rho_0}{\rho_0^*} \right) \left[1 - \frac{\ell}{d} \exp b \left(\frac{\rho_0}{\rho_0^*} \right)^{2m+1} \right] \quad (25)$$

In Fig. 9 a curve of this form is fitted to experimental data for a proprietary AN/HMTA explosive. Detonation velocity data on the explosive at low density showed that the density exponent m was approximately equal to one, and this value is used for the curve in Fig. 9. A very good fit is obtained with $b = 3.0$. Substitution of values in the theoretical expression for $b (\rho_0^* D^{0.2} v/kRT)$ gives $b = 2.7$. Also, from experimental data on the same explosive a D vs $1/d$ (at constant ρ_0) plot for two different initial densities gives the value for b of 2.2. These limited observations, therefore, support this model of the diffusion effect.

The value of the diffusion distance δ consistent with the value of ℓ obtained from curve fitting (Fig. 9) is of the order of one-tenth micron. A naive view of the reaction process in a composite explosive of this nature suggests that δ should be comparable with the diameter of the oxidizer particles, which in this case was about one micron. The difference, a factor of ten, may be ascribed to fine scale turbulence or boundary-layer mixing. In this connection, however, one should bear in mind that some of the approximations made in deriving Eq. (25) can be justified only when the detonation velocity is close to the ideal value. Therefore, when

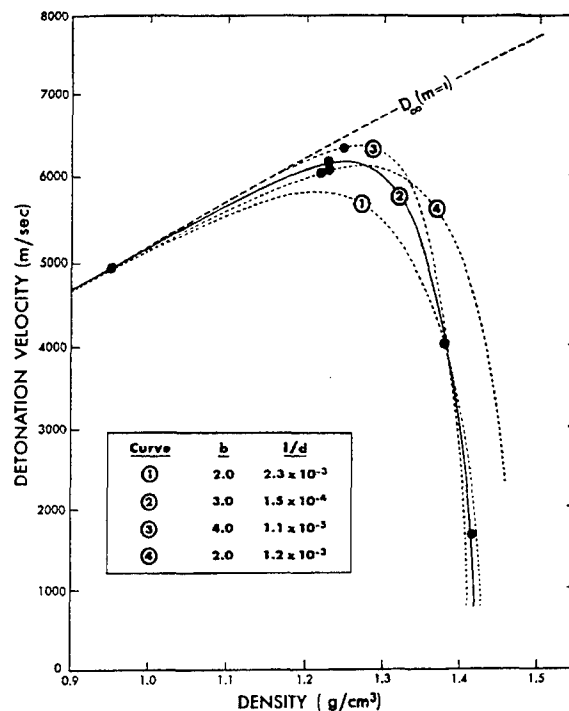


Fig. 9 - Fitting of experimental data for a composite explosive (solid circles) to theoretical curve for diffusion-controlled reaction model [11]

an equation of this form is fitted to the experimental data in which there are large departures from ideal behavior, one may be stretching too far in attempting to interpret the empirically derived constants literally in terms of the theoretical model. Certainly more data are needed to gain an insight into finer details of the reaction processes.

According to this model the critical diameter should increase exponentially with density. The dependence is expressed approximately by equating D to zero in Eq. (25), because the descent of the velocity in the failure region is so steep that actual conditions for failure differ little from those at the limiting condition $D = 0$. (See Fig. 9.) Thus,

$$\ln d_c = A + B \rho_0^{2m+1} \quad (26)$$

where $A = \ln \ell$ and $B = b/\rho_0^{*2m+1}$.

A question of considerable practical importance at present is whether solid composite propellants will detonate. Concerning the common propellants, which are based on AP with inert binder and fuel, all published evidence suggests they are not detonable, at least in

TABLE 2
Dependence of Critical Diameter on Density
for the Diffusion-Limited Model

	Critical Diameter			
	$\rho = 1.0$	$\rho = 1.25$	$\rho = 1.50$	$\rho = 1.75$
$b = 2, m = 0.67$	1 cm	3 cm	12 cm	0.6 m
$b = 3, m = 0.67$	1	5	40	5
$b = 2, m = 1.0$	1	7	120	65
$b = 3, m = 1.0$	1	17	1500	5500

diameters less than about three feet. (See, for example, the results of NOL gap tests [22], and experiments on a Seargent rocket motor [23].) This statement applies to intact propellant; but, when the propellant is shredded and tested in a porous condition with some 16-22% voids, it can become detonable [22]. This behavior suggests similarities to the AN/fuel explosives described above.

One might imagine that detonation could be "carried" in these propellants by the decomposition of AP alone, without participation of the fuel. However, the evidence suggests that AP by itself will not sustain detonation when compressed above a density of about 1.5 g/cm³. (See Andersen and Pesante [6].) When the voids in porous AP are filled with a rubbery binder, detonation is even less likely. One should therefore be able to treat a composite propellant as a diffusion-limited explosive of the type we have been considering. This has significant implications.

In the first place, it may be noted that the diffusion-limited model assumes that the substrate is intrinsically detonable. The question concerns only the critical diameter, which is a very strong function of density. The numerical results are extremely sensitive to the values of the numbers b and m . Both the empirical and theoretical value of b lies between 2 and 3; and the empirical value of m usually falls between 0.67 and 1.0. Data in Table 2 show how critical diameter depends on density for various combinations of these extreme values. As a basis for calculation we take a material that has a critical diameter of one cm when $\rho = 1.0$ g/cm³. This is typical of the figures in Table 1; and in any case, this assumption is not crucial.

The figures in Table 2 demonstrate how profound the effect of density is according to

this model. Unfortunately, with the present range of uncertainty in the values of the numerical constants, it is not possible to predict a priori from theory even the order of magnitude of the critical diameter of a composite propellant. But the behavior shown in Table 2 does suggest that a good experimental approach to this problem is to study the effect of density or porosity on the critical diameter.

One objection to this procedure is that the physical state of the propellant is seriously altered when porosity is introduced. It is certain that the nature of hot spot sites will be profoundly affected; and this will cause a radical change in sensitivity. However, according to the diffusion model, at least, sensitivity, per se is not the primary factor affecting detonability, even though it may indeed be the proximate cause of failure when it occurs. Thus, on the basis of this model, the limiting density effect illustrated in Figs. 8 and 9 would not be much affected by such factors as particle size and whether or not the grains of AP were coated with a rubbery binder.

The question whether the present model applies to composite propellants can, in any case, be tested. If the results of experiments with low-density mixtures show the typical behavior illustrated in Table 2, this in itself will determine whether confidence can be placed in an extrapolated prediction.

ACKNOWLEDGMENT

The preparation of this paper was supported in part by Contract NAS8-5229 with the National Aeronautics and Space Administration.

REFERENCES

1. L. N. Stesik and L. N. Akimova, Russian Jour. Phys. Chem., 33 (8), 148 (1959).

2. H. Eyring, R. E. Powell, G. H. Duffey, and R. B. Parlin, *Chem. Revs.*, 45, 69 (1949).
3. M. A. Cook, E. B. Mayfield, and W. S. Partridge, *J. Phys. Chem.*, 59, 675 (1955).
4. M. A. Cook and W. S. Partridge, *J. Phys. Chem.*, 59, 673 (1955).
5. M. A. Cook, R. T. Keyes, W. S. Partridge, and W. O. Ursenback, *JACS*, 79, 32 (1957).
6. W. H. Andersen and R. E. Pesante, Eighth Symposium (International) on Combustion, Williams and Wilkins Co., Baltimore, Md. (1963), p. 705.
7. M. A. Cook, L. L. Udy, P. Nance, and F. Crump, "The Explosive Properties of Ammonium Perchlorate," Intermountain Research and Engineering Co., Inc., Salt Lake City, Utah (1961).
8. W. E. Gordon, Unpublished work at Arthur D. Little, Inc. (1960-61).
9. W. E. Gordon, *Bulletin, Am. Phys. Soc.*, Ser. II, 10 (2), 269 (1965).
10. Marjorie W. Evans, *J. Chem. Phys.*, 36 193 (1962).
11. W. E. Gordon, Tenth Symposium (International) on Combustion, pp. 833-838, The Combustion Institute (1965).
12. S. J. Jacobs, T. P. Liddiard, Jr., and B. E. Drimmer, Ninth Symposium (International) on Combustion, p. 517, Academic Press, Inc., New York, N. Y. (1963).
13. C. L. Mader, *Phys. of Fluids*, 6, 375 (1963).
14. T. E. Holland, A. W. Campbell, and M. E. Malin, *J. Appl. Phys.*, 28, 1217 (1957).
15. G. E. Seay and L. B. Sealy, Jr., Third Symposium on Detonation, ONR Symposium Report ACR-52, p. 562, Office of Naval Research (1960).
16. A. W. Campbell, W. C. Davis, and J. R. Travis, *Phys. of Fluids*, 4, 498 (1961).
17. A. W. Campbell, W. C. Davis, J. B. Ramsay, and J. R. Travis, *Phys. of Fluids*, 4, 511 (1961).
18. J. M. Majowicz and S. J. Jacobs, *Bull. Am. Phys. Soc.*, 5, 293 (1958).
19. S. Glasstone, K. J. Laidler, and H. Eyring, "The Theory of Rate Processes," p. 516 ff., McGraw-Hill Book Company, Inc., New York, N. Y. (1941).
20. H. Jones, Third Symposium on Combustion, Flame and Explosion Phenomena, p. 590, Williams and Wilkins Co., Baltimore, Md. (1949).
21. M. A. Cook, "The Science of High Explosives," Reinhold Publishing Corp., New York, N. Y. (1958).
22. Donna Price and I. Jaffe, *Am. Rocket Soc. Jour.*, 31, 595 (1961).
23. F. L. Sola, *Am. Rocket Soc. Jour.*, 32, 971 (1962).

Invited Review

SUMMARY OF PAPERS ON CONDENSED PHASE DETONATION

Russell E. Duff

*Lawrence Radiation Laboratory, University of California
Livermore, California*

Our chairman, Sig Jacobs, asked me to present a summary statement on the research described in the session on detonation in condensed phases. This summary was not to be a simple restatement of the contributions of each of the authors; rather he wanted an authoritative discussion of the present status of work in this area, together with comments on where we should be going and how we should get there.

You will all agree that this is a tremendous task if one were to take those instructions literally and seriously. You will also agree it would be presumptuous of me to attempt to speak authoritatively to you, the active workers in the field.

But I'm here. It's reasonably obvious that I'm going to say something. That something is a very personal series of impressions which I hope will be provocative — which I hope will at least stimulate discussion and perhaps even controversy. These comments may be somewhat similar to those from an alumnus to the coach concerning last Saturday's game and the one coming up next week. They may be just as welcome and just as valuable.

The papers can be placed in three categories: (1) fundamental investigations of the detonation process, (2) applications of explosives to practical problems, and (3) miscellaneous investigations. Each of these areas will be considered in turn.

The first category contains only one paper, namely, "Failure of the C-J Theory for Liquid and Solid Explosives," by Davis, Craig, and Ramsey.[†] I believe this is to be a most

significant paper, one which deserves careful consideration by all of us.

It is significant because, for the first time, we see quantitative evidence of the failure of the C-J theory for condensed explosives. Evidence of the similar failure of the theory and of its elaboration in the Zeldovich, von Neumann, Doering model for gaseous systems has been with us for many years, as pointed out by Dr. Schott in his review paper.

The long-standing difficulty posed by our ignorance of the correct equation of state for a condensed system has been circumvented in this investigation by using the inverse method proposed by Manson [1], and by Wood and Fickett [2]. A C-J pressure was calculated from changes of detonation velocity with respect to initial density and initial energy. This calculated pressure was then compared with a directly measured pressure. The two pressures differ by 15 to 20%, a disagreement so large that it is unlikely that all of it can result from systematic errors in either set of measurements. However, the question of possible systematic error should be left open for the time being because details of many of the direct pressure measurements have not yet been published, and possible complications arising from tensions and spall of the metal plates used in the measurements have been discussed by Lanbourn and Wright and by Wilkins.

The quantitative evidence of the inadequacy of the current detonation theory presented in this paper should be viewed along with the qualitative evidence provided by the so-called failure waves observed by Campbell, *et al.* [3] and by Dremine and co-workers [4] in homogeneous explosives, and by the appearance of characteristic transverse waves in low velocity detonation as seen by Zimmer [5]. All of these data suggest, but certainly do not prove, that the detonation process in condensed and gaseous explosives may be quite similar. It may be

*This work was performed under the auspices of the U.S. Atomic Energy Commission.

†Whenever reference is made to a contribution in these proceedings no page listing will be noted. Usual practice will be followed in referring to other work.

that the familiar assumptions of steady, one-dimensional detonation propagation are not valid in any system if one looks at small scale details. This would mean that two of the basic assumptions of the Zeldovich, von Neumann, Doering elaboration of the C-J theory would be invalid, and the theory as a whole could no longer be accepted as a sufficient description of the detonation process. It will always be an excellent first approximation and a very useful aid in calculation, but it may not provide a reliable foundation for all aspects of detonation research.

At this point perhaps it would be illustrative to strain an analogy. The C-J theory has been with us for a long time. It has been well established. So was Newtonian mechanics in the early part of this century. Nevertheless, disturbing evidence began to accumulate which showed the inadequacy of the well-known mechanics for the explanation of atomic phenomena. A beginning toward an understanding came when the Bohr atom was proposed. This model was interesting but of limited value. In due course quantum mechanics provided the explanation for the accumulated mysteries, and the limitations of classified mechanics became clear. Perhaps the turbulent detonation theory of White [6] is our Bohr atom. Our quantum mechanics is somewhere in the future. When a more satisfactory detonation theory is developed, we will better appreciate the limitations of the present theory. Let us hope that we are intellectually better able to accept and adapt to a potential upheaval in our field than were many physicists in 1926.

The class of papers dealing with explosive applications consists of six contributions concerned with the equation of state of detonation products. This particular work arises from the primary application of explosives — namely the pushing of things. An equation of state is needed to calculate the push in particular situations.

It is important to recognize that all of these contributions are empirical. The work represents efforts to find particular analytic relations between the pressure, volume, and energy which reproduce several classes of experimental information as well as required for the intended application. In no sense is fundamental significance to be read into the form of the analytic expressions proposed.

Other equation of state work has been done which attempted a basic description of detonation products based, more or less, on first principles. These two classes of work are

different. They are motivated by different goals. They should not be confused with each other. However, of course, we expect that both approaches will lead to the same final answer.

It seems generally agreed that the characteristics of these products at pressures above approximately 150 kbar can be well described by a polytropic equation of state — one with a constant γ . The paper of Skimore and Hart demonstrates this nicely. At lower pressures it is also agreed that such a simple description is inadequate. Jones and Miller [7] on theoretical grounds and Wilkins [8] on the basis of experimental evidence have shown that the isentrope in the $\ln p - \ln v$ plane should dip below a straight line with C-J slope and then approach a value characteristic of ordinary gases at very low pressure. The qualitative features were provided by the EOS form proposed by Wilkins [8] some time ago. Apparently that particular analytic expression is unable to describe adequately the low pressure experimental observations of the motion of explosively loaded spherical and cylindrical surfaces. Workers from Aldermaston and LRL have suggested somewhat different expressions which seem to do a bit better job. It is now possible to describe very accurately the ability of several explosives to push metal systems.

It is appropriate to comment on the use of the C-J theory in this equation of state work even though other research has raised a question concerning its adequacy. In the latter case, the C-J theory was considered as a very specific set of physical and mathematical assumptions which were or were not correct. In the EOS work, the C-J theory is a convenient and well founded model through which to relate experimental observations of pressure, density, and velocity. The fact that the theory fails an essentially thermodynamic test does not destroy its usefulness as a model for correlating a related set of detonation-hydrodynamic measurements.

The rest of the papers can be loosely grouped together under the heading of miscellaneous studies, several of which will be mentioned.

Four papers deal with the interaction of detonation waves, and with Mach reflection in particular. There is no question that Mach reflection exists, but there is considerable question about its characteristics and about the appropriate theory for its description. Earlier work by Dunn [9] and Feoktistova [10] is similar to that reported here.

All experimenters except Argous, Peyre, and Thouvenin report that the width of the Mach bridge increases with time, as classical reflection theory and experiment in nonreactive gases say it should. All workers except Feoktistova observe a more-or-less curved Mach shock. The theoretical model adopted by Dunn, Gardner and Wackerle, and Labourn and Wright is the familiar three-shock, three-uniform, region model first proposed for gases many years ago. On the other hand, Sternberg and Piacesi propose a model based on a constant separation between the triple point and the plane of symmetry. Only Lanbourn and Wright even attempt to include the inevitable Taylor wave which must follow an unsupported detonation.

A useful point can now be made. There is more or less general agreement on the experimental facts of Mach reflection of detonation waves, and the phenomenon can be approximately described by theoretical analysis. Qualitatively this reflection process is understood, but a detailed, quantitative understanding will require first a detailed understanding of the detonation wave itself. Then complicating features of finite reaction zone length, Mach stem curvature, and following rarefaction waves must also be included. A great deal of careful, detailed theoretical and experimental work must be done before Mach reflection of detonation waves will be understood in detail.

The two papers on low velocity detonation by the groups at the Bureau of Mines and at Stanford Research Institute shed additional light on that interesting phenomenon. It seems clear that the low velocity propagation is observed only when the explosive has been preshocked by pressure waves moving in the confining walls. The accompanying rarefaction waves produce bubbles in the explosive which may act as reaction centers or perhaps high pressure associated with convergence of cylindrical shock waves from the walls leads to partial explosive reaction.

A further series of experiments could perhaps distinguish the influence of pressure waves and of bubbles. A bubble field artificially induced in a liquid explosive could be appropriately shocked. If the proposed mechanism were correct, low velocity propagation should be observed independent of the impedance of the confining walls. The propagation velocity would probably depend on the size and average number density of the bubbles. Perhaps the initiation work of Mader or Enig could provide the basis for the calculation of the velocity and of the critical initiation pressure to produce high velocity detonation.

The paper of Green and James dealing with reaction zone length determination illustrates an important point for detonation research. They show that the apparent initiation delay observed when a small detonator initiates a large charge is not necessarily a real delay at all. It may be a consequence of the small radius of curvature of the initiating wave. The experimental data were interpreted by using the Wood-Kirkwood [11] theory, and the coefficient of the radius of curvature term was interpreted as a reaction zone length. Since there may be real question about the applicability of classical detonation theory, it might be more appropriate to consider this coefficient as simply proportional to an effective reaction zone length. Such a change in interpretation would not influence their further conclusion that for materials of a given nominal crystal size the degree of explosive crystalline perfection strongly influences the reaction rate of the explosive. This illustrates the difficulty we will have in adequately characterizing the materials used in our research. It also suggests the futility of attempting explosive research without taking pains to assure that all material for a given series of experiments comes from a single, well-blended, carefully controlled batch of explosive.

Finally, a few words about future work. I hope that quite a few of us will try hard to design and conduct experiments which will demonstrate the microscopic nature of the detonation process. I hope that others will develop improved theories of detonation. These tasks will be hard, because the experiments must be better experiments than many done in the past fifty years, and the theory is complicated by the distressing nonlinearity of the defining equations. Nevertheless, it is important that such work be done, because out of it will come modern ideas about detonation which will have important implication for many areas of the field.

Since these experimental and theoretical tasks are so formidable, it is unlikely that any individual or laboratory will solve the problems. If this be so, overall progress can best be made by the prompt publication of more limited investigations. Such publication might serve to stimulate additional timely research at other laboratories, and it will most promptly inform other workers of the real nature of the detonation process.

The equation of state work on several explosives has reached a high degree of development. No doubt similar work will be done on other explosives. It would also be valuable to use new experimental techniques to obtain

additional information against which to test a proposed equation of state. Perhaps flash x-ray densitometry will be such a technique.

Of course, other investigators will continue to work on a wide spectrum of problems in the detonation area. All of them should be aware of the possible failure of the familiar detonation theory. I hope that they will critically examine their work so as to decide what impact, if any, such a failure might have on it.

In conclusion, I must again stress that these remarks represent only personal impressions and observations. If they provide something to think about and if they stimulate discussion and even controversy, they have fulfilled their objective.

REFERENCES

1. N. Manson, *Combust. Flame* 2, 226 (1958).
2. W. W. Wood and W. Fickett, *Phys. Fluids* 6, 648 (1963).
3. Campbell, Holland, Malin, and Cotter, *Nature* 178, 38 (1956).
4. Dremine, Rozanov and Trafinov, *Combust. Flame* 7, 153 (1964).
5. M. F. Zimmer, "Spin Detonation in Nitroglycerin," Paper 65-17, Spring Mtg. Western States Section Combustion Institute, Stanford University, Palo Alto, Calif. (April 1964).
6. D. R. White, *Phys. Fluids* 4, 465 (1961).
7. H. Jones and A. R. Miller, *Proc. Roy. Soc. A* 194, 480 (1948).
8. M. L. Wilkins, University of California, Lawrence Radiation Laboratory, Livermore, California, Report UCRL-7797 (1964).
9. B. Dunn, *Phys. Fluids* 4, 918 (1961); 4, 1565 (1961); 7, 1707 (1964).
10. Ye. A. Feoktistova, *Soviet Phys. Doklady* 6, 162 (1961).
11. W. W. Wood and J. G. Kirkwood, *J. Chem. Phys.* 22, 1920 (1954).

COMMENTS

JOSEPH HERSHKOWITZ (Picatinny Arsenal, Dover, N.J.): I would like to add to the pertinent remarks by Dr. Duff the following suggestions as to a few worthwhile areas for future effort.

a. An attempt to find a more general steady state criterion than the C-J one using the recently developed concepts in irreversible thermodynamics (Prigogine and Glansdorff, 1964). It would be hoped that the C-J condition would be then found to be either a special case for infinite reaction rates or a close approximation to the true condition. Explanations for low and high velocities of detonation as allowable phenomena might be inherent in such a theory.

b. A further experimental effort to make measurements within the detonation zone. In particular, explosives with long detonation zone should be used. A tool for this purpose is an explosive in which vaporization rates of one or more constituents limit full equilibrium of final products, but permits equilibrium of the available species. Replacement of chemical kinetics by a controlling physical rate process brings with it the possibility of control. The structure

of the detonation zone, the location of the C-J plane and the possibility of its kinetic inaccessibility should all be looked at for these media.

c. The study of explosives with two velocities of detonation needs extension to other materials and to theoretical treatments. In particular, the question raised during the meeting as to why the low velocity stable detonation does not go over to the higher mode needs quantitative treatment for the two mechanisms presented for liquid explosives and in general terms.

ROGER CHERET (Commissariat a l'Energie Atomique, France): On the one hand I would like to emphasize the point that, as Dr. Duff has said, the so-called "failure of the Chapman-Jouguet theory" might well result from an inadequate measurement of the "measured pressure." On the other hand I would like to point out that it has never been proved that the condition " $D-u=c$ " (a necessary mathematical condition for a plane steady detonation wave as evidenced in my paper) and the condition " $D=\text{minimum}$ " (which is used in the inverse method) are simultaneously achieved on the Hugoniot curve of a condensed explosive whose detonation products are not all gaseous. Nitromethane and TNT fall in this category.

SHOCK WAVES AND RELATED FLOWS

Chairmen: R. J. Eichelberger
*U.S. Army Ballistic Research Laboratories
Aberdeen Proving Ground, Maryland*

L. Lundberg
Forsvarets Forskningsanstalt, Sweden

EVALUATION OF THE GRUNEISEN PARAMETER FOR COMPRESSED SUBSTANCES - I. METALS

W. H. Andersen
Shock Hydrodynamics, Inc.
Sherman Oaks, California

ABSTRACT

An analytical expression for the Gruneisen parameter and its volume dependence is derived from the Morse potential, based on the variation of the average force constant with volume. The solid consisting of N coupled atoms is assumed to behave as a system of $3N$ independent oscillators. The derived Gruneisen parameter is shown to be identical to that obtained from the Morse potential and the Dugdale-MacDonald expression. The shock Hugoniot of several metals with different lattice structures are computed using the derived Gruneisen parameter and the Mie-Gruneisen theory. The computed Hugoniot are in reasonable agreement with experiment. It is shown that the accuracy with which certain constants in the Morse potential and the Gruneisen parameter are known apparently determines the accuracy with which the compressibility can be computed at high pressures.

INTRODUCTION

The isothermal compressibility of many substances has been investigated using static techniques [1-4]. Maximum pressures used were generally of the order of several tens of kilobars, although in some studies several hundreds of kilobars were possible. Shock compression (dynamic) techniques pioneered by the Los Alamos group [5-8] have greatly extended the measurement range of most substances, and measurements in the several megabar range are now available for some metals. Shock compression is adiabatic rather than isothermal in nature, and the compressibilities obtained by this technique (called the shock Hugoniot) thus contain the influence of the temperature increase of the substance produced by the compression.

Theoretical descriptions of compressibility are varied and range from simple empirical expressions to complex quantum mechanical treatments [1-3]. Contemporary studies have emphasized the use of the Mie-Gruneisen theory to describe the state properties of condensed matter at nominal and relatively high pressures, and the Thomas-Fermi theory at extremely high pressures. The Mie-Gruneisen theory [1-3,9-12] has had reasonable success in describing compressibility at modest pressures, and is attractive because of its relative

simplicity. Further refinement of the theory for substances and conditions not consistent with the assumptions inherent in the theory is discussed frequently in the literature [1-3, 9-16].

The Mie-Gruneisen equation of state requires a potential function to describe the interaction energy between the various molecular and/or atomic species comprising the matter, and several potential functions have been used and discussed in the past. The theory also requires the value of the so-called Gruneisen parameter at each pressure. The Gruneisen parameter is often taken to be a constant for a specified substance. However, in attempting to compute the compressibility of a substance over a wide pressure range a-priori, the variation of the Gruneisen parameter with volume must be taken into consideration.

This paper derives an expression for the Gruneisen parameter as a function of volume using the Morse potential function. This expression is used with the Mie-Gruneisen theory to compute the compressibilities of various metals to very high pressures, and the results are compared with experiment. A future paper will discuss the applicability of the equation to other substances.

MIE-GRUNEISEN THEORY

The thermodynamic properties of a condensed substance are contained in its partition function Z :

$$Z = \exp(-U/kT) \prod_{j=1}^{3N} [1 - \exp(-h\nu_j/kT)]^{-1}. \quad (1)$$

U is the cohesive lattice energy at the absolute zero of temperature, and in the present notation is the sum of the static interaction potential and the zero-point energy. It is a function of volume. k is the Boltzmann constant, h is Planck's constant, T is the absolute temperature, and ν_j is the vibrational frequency of the j th oscillator; the product is over the (essentially) $3N$ vibrations possible for the N (Avogadro's number) atoms in the crystal. The Helmholtz energy A is given by $A = -kT \ln Z$, from which the pressure P can be calculated from $P = -(\partial A / \partial V)_T$, where V is the volume. The internal energy is given by $E = kT^2 (\partial \ln Z / \partial T)$. From the preceding differentiations the Gruneisen parameter defined by

$$\gamma = -d \ln \nu / d \ln V \quad (2)$$

appears for each of the j frequencies. In the Einstein approximation the frequencies are all considered equal and the γ 's are then all equal. Alternatively, in the classical heat capacity limit, the energies of all of the oscillators are equal and γ is the average of γ_j . In either case, $P = -dU/dV + \gamma E_{th}/V$, or

$$P - P_k = \frac{\gamma}{V} E_{th} = \frac{\gamma}{V} (E - E_k). \quad (3)$$

Equation (3) is the Mie-Gruneisen equation of state, the subscript k indicating the quantity is to be evaluated as a function of volume $0^\circ K$, and E_{th} is the thermal energy, i.e., $E_{th} = C_v T$, where C_v is the constant-volume heat capacity.

GRUNEISEN PARAMETER

The Gruneisen parameter, defined by Eq. (2), essentially controls the partitioning of the compressional energy into thermal and potential energy. Its value decreases with increased compression (decreased specific volume). Differentiating Eq. (3) with respect to temperature at constant volume gives the parameter as was deduced originally by Gruneisen

$$\gamma = \alpha V_0 / \beta C_v \quad (4)$$

where α is the coefficient of thermal expansion, β is the coefficient of compressibility, and V_0 is the normal specific volume of the substance. An approximation to the volume dependence of γ appears to be to let the volume be a variable in Eq. (4). Other expressions for γ subsequently derived include those of Slater [9], Cook and Rogers [17], and Dugdale and MacDonald [18]. The Slater expression was based on the Morse potential and on a power series expression Slater developed for the equation of state of solids. An interesting expression for the volume dependence of γ given recently by Pastine [19] is also based on the Morse potential. It utilized a relationship Slater developed earlier using the Debye theory of heat capacity and the assumption that Poisson's ratio is independent of volume. In addition, the Pastine expression contains an added constant so that the relation at normal density yields the value of γ given by thermodynamic data according to the method of Zharkov and Kalinin [20]. Earlier studies by Girifalco and Weizer [21] had made use of the Morse potential to calculate the elastic constants of metals. Benedek [22] analyzed the volume dependence of the cohesive energy of several shock compressed metals, and Pastine showed that the results were in reasonable agreement with his results.

The present derivation is based on the Morse potential but does not require the assumptions inherent in the above treatments, although different assumptions are involved. The Morse interaction potential between two vibrating molecular species with internuclear distance R is:

$$U_i = U_d \exp[-2a(R-R_0)] - 2U_d \exp[-a(R-R_0)], \quad (5)$$

where U_d is the dissociation energy at zero absolute temperature of the species, R_0 is their internuclear (equilibrium) distance at the minimum of the energy potential,

$$a = \left[\frac{2\pi^2 \nu_0^2 \mu}{U_d} \right]^{1/2} \quad (6)$$

μ is the reduced mass of the oscillator, and ν_0 is the normal vibrational frequency at the potential energy minimum. In the approximation that a solid of N coupled atoms behaves as a system of $3N$ independent oscillators [9-11], Eq. (5) may be thought of as describing the interaction energy of each of these oscillators. The total interaction potential energy U is the sum of the potential energy of the $3N$ oscillators, i.e., $U = \sum U_i$; and $3U_d = D_0$, where D_0 is the $0^\circ K$ sublimation energy of the solid. The vibrational frequency of an oscillator is given by

$$\nu = \frac{1}{2\pi} \left[\frac{1}{\mu} \left(\frac{d^2U}{dR^2} \right)_{R=R_0} \right]^{1/2} \quad (7)$$

where the force constant is evaluated at the internuclear distance R , which is related to the molar volume V of the substance by

$$R = (V/NC)^{1/3}, \quad (8)$$

N is Avogadro's number, and C is the lattice constant which has the value of 1.0 for a cubic lattice, 0.707 for face-centered cubic and hexagonal close-packed lattices, and 0.77 for a body-centered cubic lattice (9). Combining Eqs. (2), (5), (7), and (8) gives the Gruneisen parameter as a function of internuclear distance and thus molar volume,

$$\gamma = \frac{aR}{6} \left[\frac{4 \exp[-a(R-R_0)] - 1}{2 \exp[-a(R-R_0)] - 1} \right]. \quad (9)$$

When $R = R_0$, $\gamma = aR_0/2$. Salter obtained $\gamma = (aR_0/2) + (1/3)$.

The value of a in Eq. (6) is estimated as follows. The frequency ν_0 is given by Eq. (7) for $R = R_0$, and hence $a^2 = (d^2U/dR^2)_{R_0}/2D_0$. At the absolute zero of temperature $(1/\beta) = V(d^2U/dV^2)$ [10-12]. Also,

$$(d^2U/dV^2) = (dR/dV)^2 (d^2U/dR^2) + (d^2R/dV^2) (dU/dR).$$

At $R = R_0$, $(dU/dR) = 0$. Utilizing Eq. (8) then gives

$$a = \frac{3(NC)^{1/3} \nu_0^{1/6}}{(2\beta D_0)^{1/2}}. \quad (10)$$

An alternative derivation leading to the same result is as follows. The compressibility of a substance is defined by

$$(1/\beta) = -V(\partial P/\partial V)_T$$

At the absolute zero of temperature the pressure is to good approximation determined by the interaction potential terms only, i.e., $P_k = -dU/dV$. Using Eq. (5) gives

$$P_k = \frac{-2D_0 a \exp[-a(R-R_0)] [1 - \exp[-a(R-R_0)]]}{3(NC)^{1/3} V^{2/3}} \quad (11)$$

Equation (11) in conjunction with the definition of compressibility gives Eq. (10).

COMPARISON WITH EXPERIMENT

Values of the parameters used in calculating P_k and γ should be zero-temperature values, but normal temperature values are used here, as is usually done, due to the lack of zero temperature values. The difference in these values is expected to be small [19]. The isothermal compressibility of a substance can be computed as a function of pressure by means of Eqs. (3), (9), and (11). In this paper we compute shock compression data in order to obtain comparisons over a larger pressure range.

It is of interest to compare the normal density values of the Gruneisen parameter computed by Eq. (9) with those obtained by other investigators, and Table 1 gives such a comparison. Values of D_0 and β used were obtained from Ref. 11, p. 99. As can be seen from the table, there are usually as many values for the Gruneisen parameter of a specified substance as there are investigators. However, the general agreement is reasonable in most cases. Actually the comparison of some of these values is not quite valid since different values of certain constants (e.g., β) may have been used in deriving the parameter. Thus, the values obtained in the present study should always be a value of 1/3 less than the value obtained by Slater if the same values of the constants were used in both cases. The most valid compressibility and cohesive energy data to be used in the computations is not known, but the data obtained from different sources often do differ, and these differences do influence the results. For example, Ref. 23 gives values of the shear modulus and the Lamé constant of various substances, from which it is possible to compute the compressibility. These computed values often differ from those given in Ref. 11. The values of γ for Al, Cu, W and Zn computed using the compressibility derived from Ref. 23 are 1.66, 1.95, 2.00 and 2.35, respectively. It should also be remembered that the experimental compressibility coefficient of a substance is often a weak function of its pretreatment.

Shock-compression obeys the Rankine-Hugoniot equation:

$$E - E_0 = (P/2)(V_0 - V), \quad (12)$$

where P and V are pressure and specific volume of the shocked substance, and E_0 is the initial energy of the uncompressed substance, i.e., $C_{v0}T_0$. Combining Eqs. (12) and (3) gives the shock Hugoniot relationship:

$$P = \frac{(2P_k V/\gamma V_0) + 2\rho_0 [C_{v0}T_0 - (U - U_0)]}{(V/V_0)[(\gamma + 2)/\gamma] - 1} \quad (13)$$

TABLE 1
Comparison of Normal-Density Gruneisen Parameter
Obtained by Different Investigators

Metal	Gruneisen ¹	Slater ¹	Benedek ²	Cook ³	Girifalco ⁴	This Study
Li	1.17	1.55	—	0.89	—	1.03
Na	1.25	1.58	—	1.78	1.22	1.21
K	1.34	1.53	—	2.35	1.93	1.21
Mg	—	2.15	—	2.69	—	1.86
W	1.62	2.39	1.70	2.48	0.00	1.74
Mn	2.42	—	—	2.40	—	1.94
Fe	1.60	2.20	1.68	1.99	0.16	1.80
Ni	1.88	2.19	2.20	1.90	3.25	1.78
Pt	2.54	2.65	3.30	3.74	—	2.31
Cu	1.96	2.13	1.90	1.92	2.11	1.79
Au	3.03	2.60	—	—	—	2.37
Zn	—	2.68	—	4.01	—	2.14
Cd	—	3.35	—	10.0	—	2.37
Al	2.17	2.05	—	1.44	1.00	1.59
Ag	2.40	2.33	2.50	2.74	2.29	1.99
Pb	2.73	—	—	3.08	0.951	2.42

¹Ref. 9; ²Ref. 22; ³Ref. 17; ⁴Ref. 21.

where ρ_0 is the density of the initial substance, and $U_0 = -D_0$ from Eq. (5).

Equation (13) was used to compute the shock Hugoniot of several metals and the results (slide-rule accuracy) are shown in Figs. 1-6. Several crystal structures are represented: face centered cubic (Al, Pb, Cu, Ag); body centered cubic (W), and hexagonal close packed (Zn). The theoretical curves were calculated using the compressibilities given in Ref. 11 to compute α (Eq. (6)), and in some cases the curves were also computed using compressibility data from Ref. 23. The agreement between experiment and theory is generally quite good and it may be concluded, as has been previously concluded several times [9,19,21], that the Morse potential is quite reasonable in describing the interaction energy between atoms in metals. Of particular significance is the fact that the compressibility at high pressures is very sensitive to the values of the parameters used in computing Eq. (6). This limits to some extent the evaluation of the potential function, the Gruneisen expression, and the assumption of a single γ by comparing theory with experiment, since in the final analysis the most valid data to be used in evaluating Eq. (6) is not known. For example, compressibility data derived from certain measurements may be more accurate than from direct compressibility measurements themselves. The fact that compressibility is temperature-dependent also poses the problem as to just what data should be used.

The general agreement between experiment and theory indicates that Eq. (9) is a useful expression for computing the Gruneisen parameter as a function of volume. Generally speaking, Eq. (9) gives a slightly weaker volume dependence on the Gruneisen parameter than does the expression of Pastine [19]. On the basis of the limited calculations summarized in Figs. 1-6 it does not appear that the general agreement of the theory with experiment is substantially best for any particular crystal structure, especially when the above remarks concerning compressibility data are considered. On the basis of theory, however, calculations for face centered cubic lattices should be most valid for a state equation using only a single Gruneisen parameter.

The temperature produced by the shock compression of a substance is determined by the thermal energy portion only of the total internal energy, as discussed previously [19]. The temperature is given by

$$T = (1/3Nk) \{ (P/2\rho_0) [1 - (V/V_0)] - (U - U_0) \} + T_0. \quad (14)$$

The temperature depends on the value of the Gruneisen parameter. Examples of the temperatures, computed for aluminum at V/V_0 ratios of 0.94, and 0.7 (using compressibility data from Ref. 23) are 310 and 1653°K, respectively.

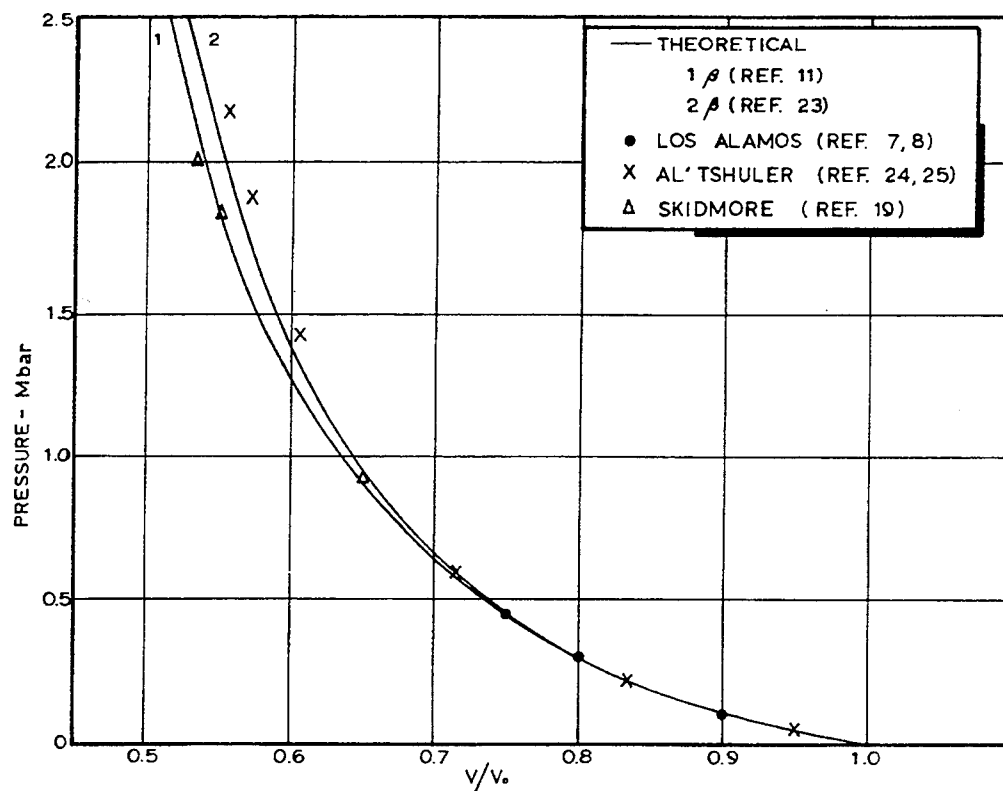


Fig. 1 - Comparison of theoretical Hugoniot of Al with experimental

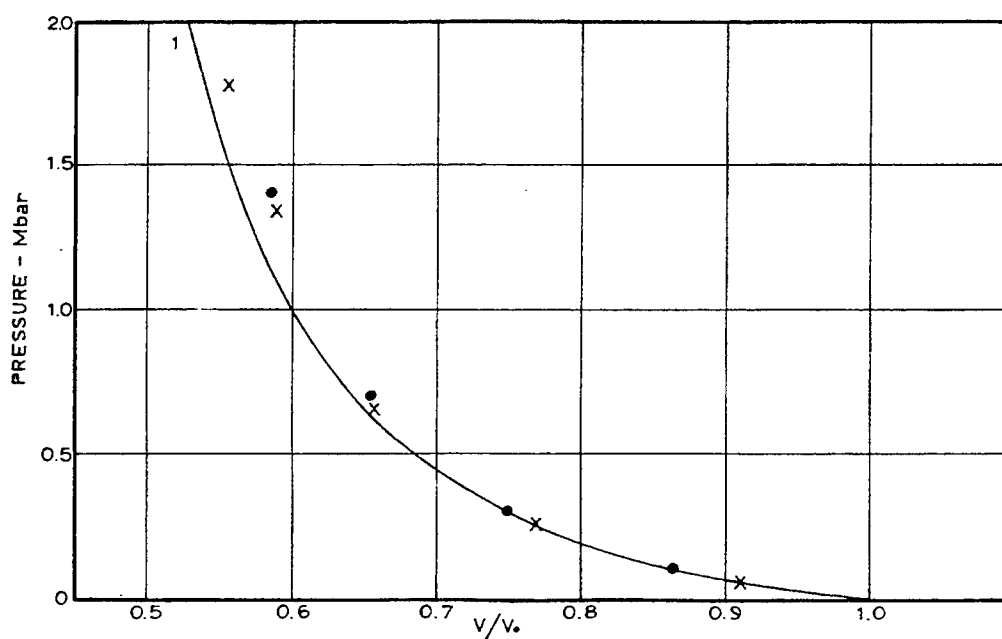


Fig. 2 - Comparison of theoretical Hugoniot of Pb with experimental

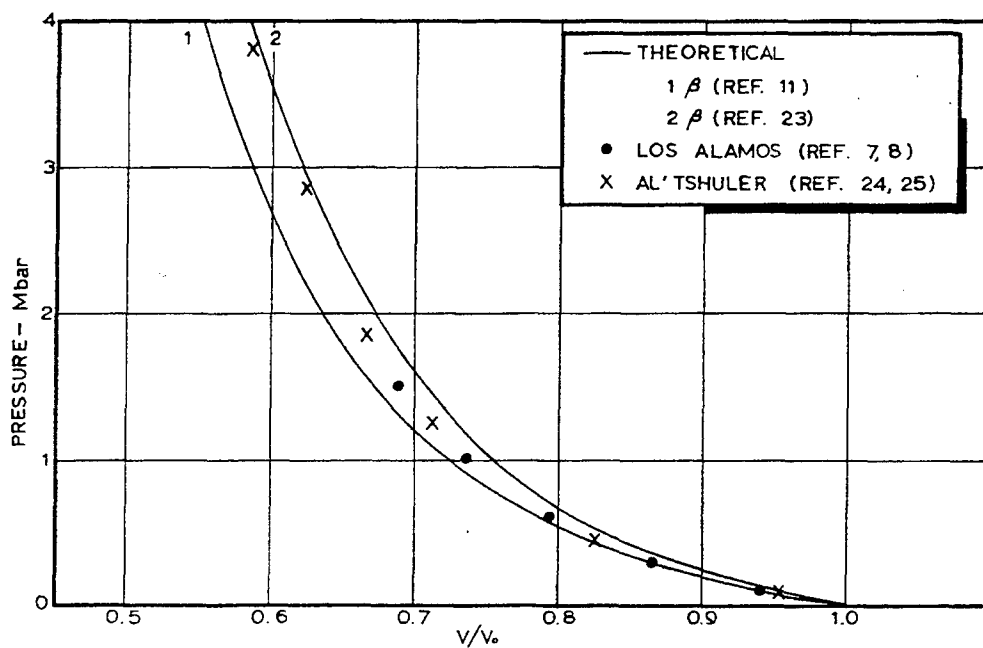


Fig. 3 - Comparison of theoretical Hugoniot of Cu with experimental

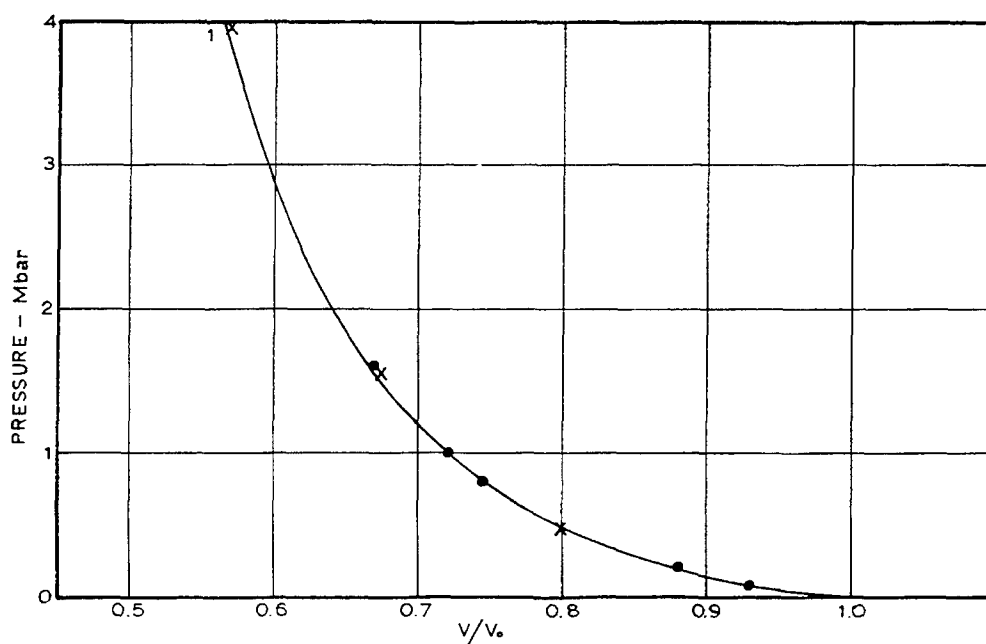


Fig. 4 - Comparison of theoretical Hugoniot of Ag with experimental

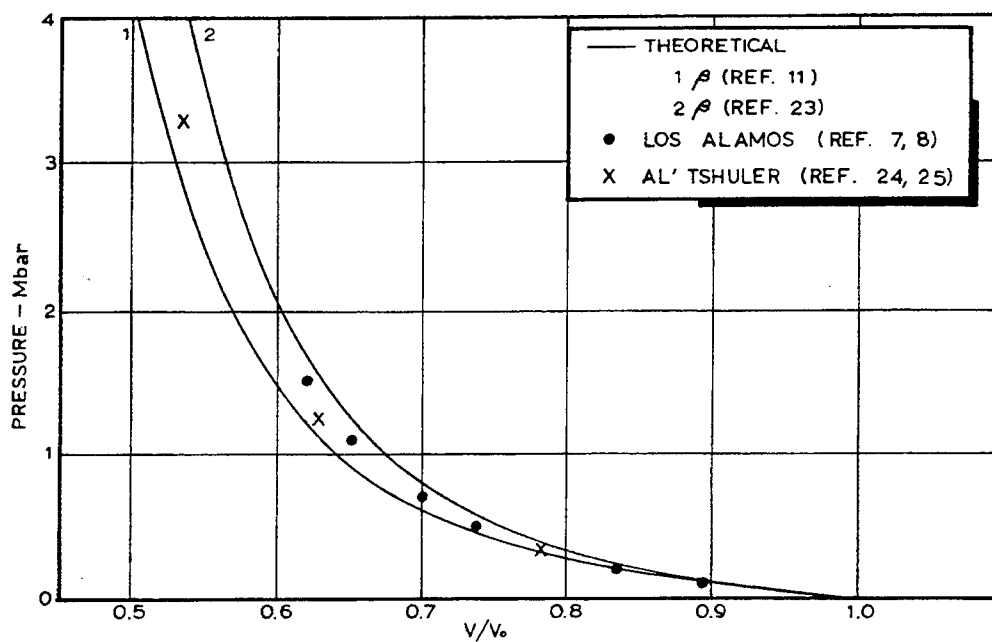


Fig. 5 - Comparison of theoretical Hugoniot of Zn with experimental

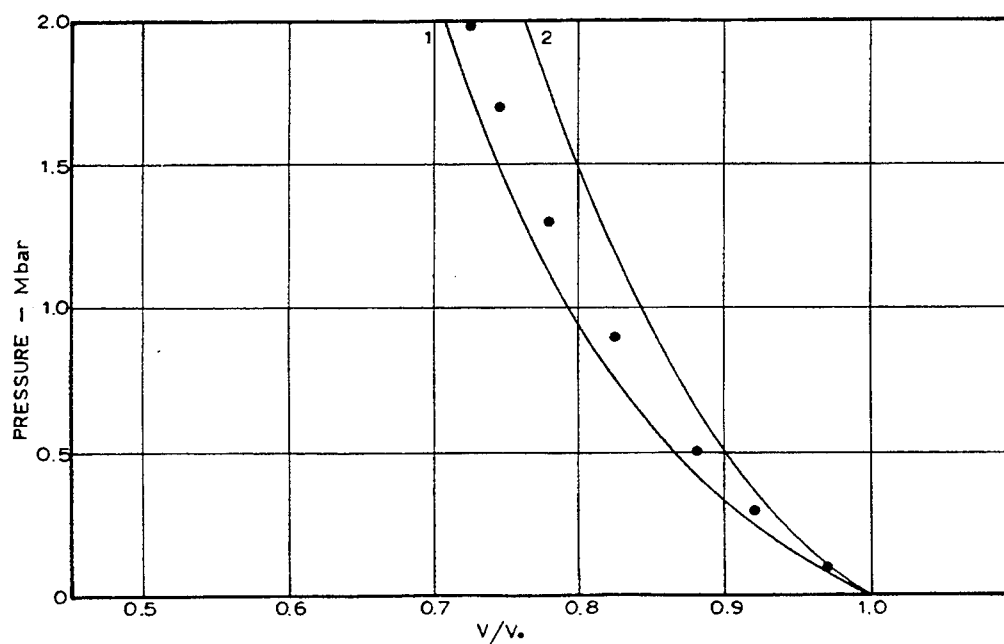


Fig. 6 - Comparison of theoretical Hugoniot of W with experimental

ACKNOWLEDGMENT

The author wishes to express his appreciation to Dr. L. Zernow for his encouragement of this work.

REFERENCES

1. P. W. Bridgman, The Physics of High Pressure, G. Bell & Sons, London, 1952.
2. High Pressure Physics and Chemistry, Edited by R. S. Bradley, Vols. 1, 2, Academic Press, New York, 1963.
3. Progress in Very High Pressure Research, Edited by F. P. Bundy, W. R. Hibbard, and H. M. Strong, John Wiley, New York, 1961.
4. High Pressure Measurement, Edited by A. A. Giardini and E. C. Lloyd, Butterworths, Washington, D.C., 1963.
5. R. W. Goranson, D. Brancroft, B. L. Burton, T. Blechar, E. E. Houston, E. F. Gittings, and S. A. Landeen, J. App. Phys., **26**, 1472 (1955).
6. J. M. Walsh and R. H. Christian, Phys. Rev., **97**, 1544 (1955).
7. J. M. Walsh, M. H. Rice, R. G. McQueen, and F. L. Yarger, Phys. Rev., **108**, 196 (1957).
8. R. G. McQueen and S. P. Marsh, J. App. Phys., **31**, 1253 (1960).
9. J. C. Slater, Introduction to Chemical Physics, McGraw-Hill, New York, 1939.
10. M. Born and K. Huang, Dynamical Theory of Crystal Lattices, Clarendon Press, Oxford (1954).
11. C. Kittel, Introduction to Solid State Physics, John Wiley, New York, 1956.
12. N. F. Mott and H. Jones, The Theory of the Properties of Metals and Alloys, Dover Publications, New York, 1958.
13. D. J. Pastine, Phys. Rev., **138**, A767 (1965).
14. E. A. Stern, Phys. Rev., **111**, 786 (1958).
15. T. H. K. Barron, Phil. Mag., **46** 720 (1955).
16. J. J. Gilvarry, Phys. Rev. **102**, 308, 317, 325, 331; **103**, 1700; **104**, 908 (1956); J. App. Phys., **28**, 1253 (1957), **33**, 3595 (1962).
17. M. A. Cook and L. A. Rogers, J. App. Phys., **34**, 2330 (1963).
18. J. S. Dugdale and D. K. MacDonald, Phys. Rev. **89**, 832 (1953).
19. D. J. Pastine, J. App. Phys., **35**, 3407 (1964).
20. V. N. Zharkov and V. A. Kalinin, Soviet Phys.-Doklady **7**, 638 (1963).
21. L. A. Girifalco and V. G. Weizer, Phys. Rev., **114**, 687 (1959).
22. G. B. Benedek, Phys. Rev., **114**, 467 (1959).
23. American Institute of Physics Handbook, McGraw-Hill Book Company, New York, 1963.
24. L. V. Al'tshuler, S. B. Kormer, A. A. Bakanova, and R. F. Trunin, Soviet Physics JETP, **11**, 473 (1960).
25. L. V. Al'tshuler, K. K. Krupnikov and M. I. Brazhnik, Soviet Physics, JETP, **34**, 614 (1958).

ADDENDUM TO PAPER

It is of interest to note that the expression obtained in the text for the Gruneisen parameter, Eq. (9), is identical to the expression that is obtained by using the Morse potential with the Dugdale-MacDonald expression for the Gruneisen parameter [18], i.e.,

$$\gamma = -\frac{v}{2} \frac{d^2(Pv^{2/3})/dv^2}{d(Pv^{2/3})/dv} - \frac{1}{3}$$

This is consistent with Gilvarry's conclusion [16, p. 331, 1956] that the Dugdale-MacDonald expression corresponds to a model of independent pairs of nearest neighbor atoms, rather than to the Debye model of coupled atomic vibrations.

THE EQUATION OF STATE OF 1060 ALUMINUM FROM SHOCK WAVE MEASUREMENTS

G. D. Anderson, A. L. Fahrenbruch, and G. R. Fowles
Poulter Laboratories
Stanford Research Institute
Menlo Park, Calif.

ABSTRACT

The internal energy along the Hugoniot curve of a thermodynamic system is given by the Rankine-Hugoniot condition

$$E - E_0 = 1/2(P + P_0)(V_0 - V).$$

To achieve pressure-volume-energy states which do not lie on a single curve, different initial states must be chosen. The initial state is varied by using porous aluminum at ambient pressure and temperature and by heating solid aluminum to initial temperatures in excess of 500°C. Explosively accelerated metal plates are used to induce strong shock waves directly into the heated samples and into 2024 aluminum targets upon which the porous samples are mounted. High-speed streak photography is used to determine shock and free-surface velocities of the samples, free-surface velocities of the 2024 aluminum targets, and flyer plate velocities from which pressure-volume-energy states of the samples may be calculated by the impedance match method. Data on porous aluminum which is singly shocked to pressures in the 300- to 600-kbar range and doubly shocked to the megabar range are presented. From these data an effective Gruneisen function defined as the ratio of the thermal pressure difference to the thermal energy density difference at a given volume can be deduced. Values of the effective Gruneisen function are found to lie in the range between 1.4 and 2.2 and tend to decrease with decreasing volume and increasing temperature. Pressure-volume-energy data obtained from shocking solid preheated aluminum to pressures in the 700-kbar region are also presented.

THE COMPRESSION OF POLYMETHYL METHACRYLATE BY LOW AMPLITUDE SHOCK WAVES

T. P. Liddiard, Jr.
U.S. Naval Ordnance Laboratory, White Oak
Silver Spring, Maryland

ABSTRACT

Results of experiments on polymethyl methacrylate (PMMA) show that the shock velocity (U) vs particle velocity (u) curve has an abrupt change of slope at a stress of 20 kbar. Above this stress the relation, $U = 2.56 + 1.69u$ (mm/ μ sec), agrees well with the data of others. Below 20 kbar the curve has a much lower slope and is also linear or perhaps slightly curved down to about 5 kbar, the limit of observation. The charge setup is essentially that used in the NOL standardized gap test. A technique is described in which small foils are used to obtain the initial PMMA motion. Without the foils a retarded motion of the PMMA is recorded since strong rarefaction waves rapidly drop the pressure behind the shock front. Several possible causes for the abrupt change in the U - u curve are given. As yet, the actual cause is not known.

INTRODUCTION

In studying the behavior of a material under compression by shock, the usual experimental procedure is to measure its shock velocity (U) and its free-surface velocity (u_{fs}), the particle velocity (u) being taken as $1/2 u_{fs}$ [1]. The parameters, U and u , are related to the shock pressure (P) by the expression, $P = \rho_0 U u$ and to the relative volume (v/v_0) by $v/v_0 = (U-u)/U$, where ρ_0 is the initial density, v_0 is the initial volume, and v is the shocked volume [2]. For liquids and most nonporous solids a plot of U vs u results in a nearly straight line, over a wide range of shock pressures, provided that no phase changes occur or elastic precursor waves are present; i.e., $U = A + B u$ [1,3].

This paper describes an experimental study of polymethyl methacrylate (Plexiglas, Lucite, or Perspex; designated PMMA hereafter). The results show that values of U and u obtained from shock-induced stresses below 20 kbar ($U \leq 3.4$, $u = 0.5$ mm/ μ sec) do not follow the same relation that holds above that stress level. This is seen as a sharp bend in the line drawn through a plot of the U vs u data in Fig. 1. Speculation is made as to possible reasons for this result.

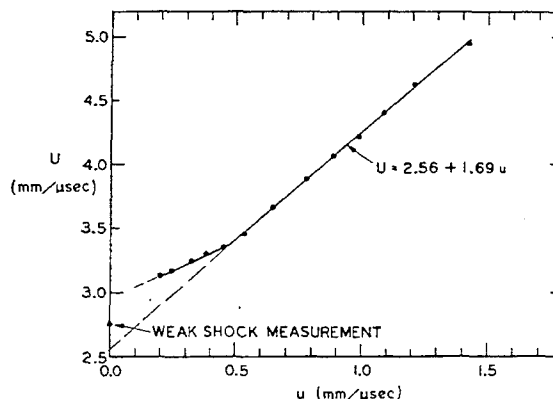


Fig. 1 - Shock velocity (U) as a function of the particle velocity (u)

EXPERIMENTS AND RESULTS

Basic Charge Assembly

In these experiments the charge assembly (donor/PMMA cylinder), Fig. 2A, essentially was that used in a standard shock sensitivity test [4]. In fact the material for this paper was obtained as a result of calibration tests (stress vs gap length) made on this donor/gap system [5]. The shock was produced by the

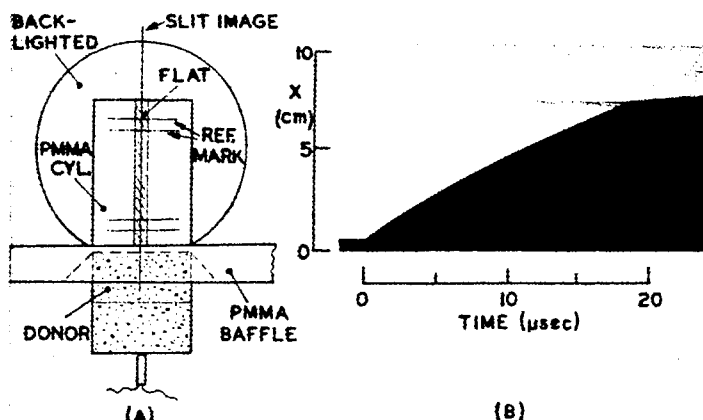


Fig. 2 - (a) Test set-up for obtaining the shock velocity with a smear camera; (b) typical smear record

detonation of a 50.8-mm diam by 50.8-mm long tetryl charge; density = 1.51 g/cm^3 . The PMMA cylinder, density = 1.185 g/cm^3 , was of the same diameter as the donor. Cast, rather than extruded, PMMA was used in these experiments. Samples of extruded rods showed considerable residual strain under polarized light examination; cast rods showed no appreciable strain. The PMMA examples in all of the experiments reported here were made from a single lot of rod castings. A baffle of wood or PMMA was used to keep the gases generated by the donor from obscuring the observation. The temperatures at which the experiments were made were in the range of $15\text{--}20^\circ\text{C}$.

PMMA Surface-Velocity Measurements; Foil Technique

The stress produced in the PMMA cylinder by the shock-generating system is rapidly relieved by rarefaction waves, both lateral and from behind. These waves quickly retard the initial surface velocity, the latter being required to determine the value of u immediately behind the shock front. To obtain the initial free-surface velocity, foils of Mylar,* Saran,† aluminum, or brass were placed on the flat, free surface of the PMMA cylinder directly over the center. When shocked the foil is forced to acquire the initial velocity of the

PMMA in contact with it, provided that: (a) the shock impedance of the foil is higher than, or equal to, the PMMA impedance; (b) the foil is sufficiently thin; and (c) it has a small enough diameter.

This is stated without mathematical proof, but it is supported by the observation that the foil velocity, at a stress of 5 kbar in the PMMA, is the same within experimental error for Mylar, Saran, aluminum, and brass. In addition, the following reasoning can be used. On the first pass of the shock through a foil of higher impedance than PMMA, the free-surface velocity of the foil will be lower than the velocity the PMMA surface would have had without the foil. However, the mass of the foil is extremely low in comparison to the mass pushing it. Thus, it will be forced to adjust to the velocity of the mass from behind after several transits of shocks and rarefactions through the foil. The foil will remain in contact with the gap material until pressure immediately behind the foil begins to fall. When this happens separation occurs since there is virtually no tensile strength between the foil and the gap surface. No cement is used to attach the foil, only a trivial amount of silicone grease to hold it in place.

For most of the tests the motion of the PMMA surface was recorded with a smear camera. In some cases the end of the cylinder was beveled 5° , as shown in Fig. 3A, leaving an 8-mm-diam platform at the center. This permitted sharp focusing of the edge of the foil and platform. Such a bevel does not affect the initial motion of the PMMA along the extended axis of the cylinder. An example of a smear-camera record using a foil is shown in Fig. 3B.

*Mylar, registered trademark for a polyester film ($\rho = 1.39 \text{ g/cm}^3$) manufactured by E. I. duPont de Nemours & Co., Wilmington, Delaware.

†Saran, registered trademark for vinylidene chloride ($\rho = 1.65 \text{ g/cm}^3$), Dow Chemical Co., Midland, Michigan.

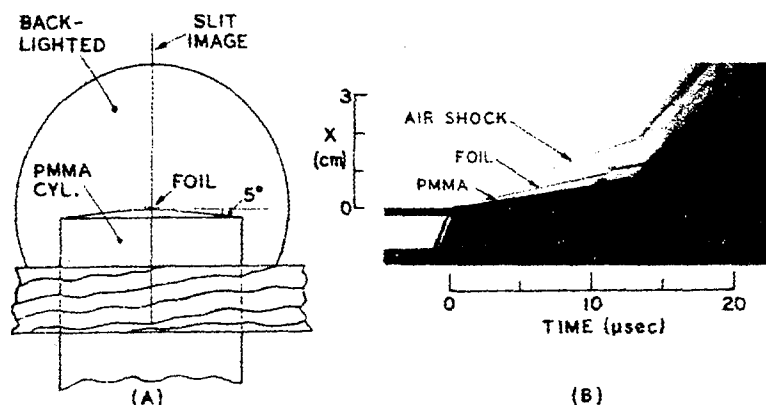


Fig. 3 - (a) Typical smear-camera set-up for measuring the free-surface velocity; (b) corresponding smear record

Backlighting was provided by an exploding wire and an expendable condenser lens to give nearly parallel light through the subject [6]. The weak air shock ahead of the foil has been retouched for reproduction. Some shots were also made with a framing camera to establish definitely what produced the traces recorded by the smear camera. In these cases diffuse light reflected from a white surface behind was used, the light being supplied by explosive flash lamps. The separation of a 0.025-mm thick, 3-mm-diam brass foil from the PMMA surface is clearly seen in Fig. 4. The foil is moving at 0.28 mm/ μ sec and the PMMA surface at 0.20 mm/ μ sec.

Note that the PMMA surface is cracking as indicated by the sharp breaks in the surface contour. The slight asymmetry in the pictures is due to the focal plane shutter, or slit, which moved from left to right to record each frame [7]. The time between corresponding points in adjacent frames in the figure is 8.2 μ sec. (Only one frame out of every six actually taken is shown here.)

Results of Surface-Velocity Measurements

The initial velocity of the foil and the retarded PMMA surface are given as functions of

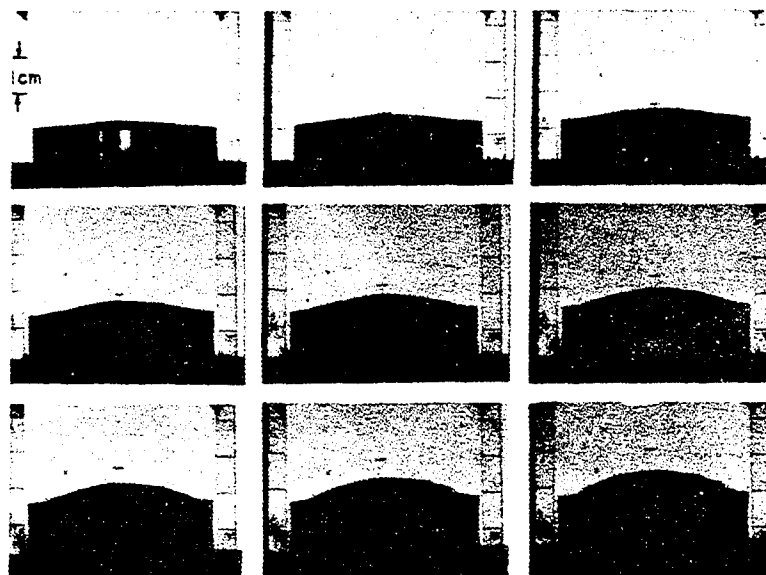


Fig. 4 - Framing camera sequence of a 0.025-mm thick brass foil separating from a shocked PMMA cylinder (inter-frame time = 8.2 μ sec)

the PMMA length (x) in Table 1. The data are grouped according to variations of foil material, foil thickness, and foil diameter. As noted in the table, Mylar foils of 49-mm diam failed to separate from the PMMA and exhibited the same retarded velocity observed for the surface without a foil. However, Mylar foils of diameters of 14 mm or less did separate from the surface and exhibited higher velocities. The lack of effect of diameter at and below 14 mm indicates that the maximum possible separation had occurred between the foil and the PMMA surface. The data also show that changing the foil material

or thickness, within limits, does not alter the foil velocity significantly. For a 100-mm long PMMA cylinder, foils of Mylar, Saran, aluminum, and brass all gave velocities within the range of 0.26 to 0.30 mm/ μ sec. At the same initial pressure the thinner (0.006 mm) plastic foil traveled no faster than the thicker (0.05 mm) foil.

The data in Table 1 are plotted in Fig. 5. The differences between the foil and retarded PMMA velocities are 0.05 to 0.08 mm/ μ sec over a stress range of 5 to 83 kbar. The

TABLE 1
The PMMA Surface Velocity and the Foil Velocity
for Various Values of x and Foil Conditions

Foil Conditions	Cylinder Length x (mm)	PMMA Velocity (mm/ μ sec)	Foil Velocity (mm/ μ sec)
A. No foil used	47.6	0.927	—
	55.2	0.699	—
	55.2	0.688	—
	65.5	0.480	—
	86.0	0.264	—
	86.0	0.278	—
B. Mylar: 0.05 mm, 49 mm diam.	10.0	*	2.742
	20.0	*	2.110
	29.4	*	1.736
	36.0	*	1.411
	36.0	*	1.419
	43.0	*	1.115
	75.0	*	0.377
	99.9	*	0.211
C. Mylar: 0.05 mm, 14 mm diam.	100.1	0.206	0.278
	100.1	0.207	0.291
D. Mylar: 0.05 mm, 3-4 mm diam.	20.0	2.086	2.174
	45.0	1.009	1.078
	100.1	0.205	0.263
	100.1	0.210	0.296
	100.0	0.208	0.290
E. Saran: 0.006 mm, 3-4 mm diam.	75.0	0.375	0.427
	100.0	0.213	0.292
	152.5	—	0.155
F. Al: 0.025 mm, 3-4 mm diam.	100.0	—	0.266
G. Brass: 0.025 mm, 3-4 mm diam.	100.0	0.199	0.276

*No apparent separation of foil and PMMA surface.

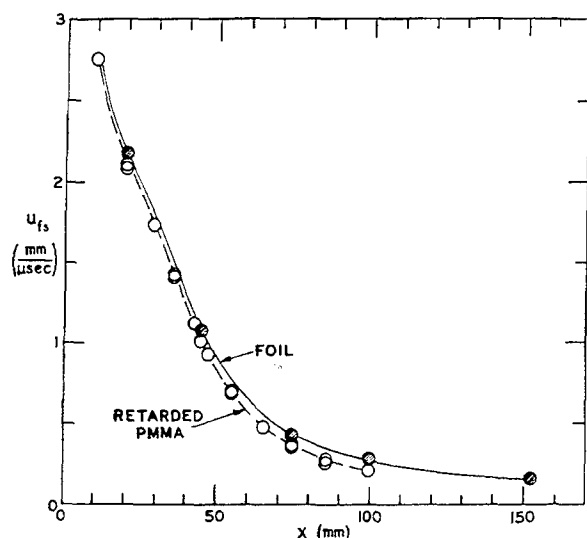


Fig. 5 - Retarded PMMA and foil velocities as functions of the distance (X) the shock has traveled in the PMMA

threshold velocity for spall reported for PMMA is $0.06 \text{ mm}/\mu\text{sec}$, corresponding to a spall tension of 1.0 to 1.5 kbar [8]. It, therefore, is reasonable to attribute the retardation in velocity to the increment of velocity produced by an internal tension which must develop before spalling will occur within the PMMA.

The foil and PMMA velocities were most difficult to measure at large values of X , i.e., in the very low stress region. This was due largely to the difficulty in measuring the low slopes obtained on the smear-camera (X -time) records. At $X = 100 \text{ mm}$ ($\sim 5 \text{ kbar}$) eight records were used to establish both the foil velocity and the PMMA surface velocity. The mean velocity of the foil is $0.282 \text{ mm}/\mu\text{sec}$ with a probable error of the mean of 0.003 or 1%, exclusive of consistent errors. The probable error of the mean is defined as

$$\epsilon_p = \pm 0.6745 [\sum \delta^2 / n(n-1)]^{1/2}$$

where $\sum \delta^2$ is the sum of the squares of the deviations of the single observations from the mean and n is the number of observations. For the retarded PMMA velocity the mean is $0.207 \text{ mm}/\mu\text{sec}$ with a probable error of the mean of 0.001 or 0.5%. Duplicate measurements of the PMMA surface velocity were made at five other values of X . In all cases the values were within $\pm 1\%$ of the mean value between each pair of measurements, except at $X = 86 \text{ mm}$ where the spread was $\pm 2.5\%$. Velocities of foils that separated from the PMMA surface were obtained at $X = 20, 45, 75, 100$, and 152.5 mm . The mean

value of the difference in foil and PMMA velocity, excluding the value determined at $X = 152.5 \text{ mm}$, is $0.07 \text{ mm}/\mu\text{sec}$. Since there are more data points for the PMMA surface velocity over the range of interest than there are for the foil velocity, the former was used as the basis in drawing the final curve. The foil velocity vs X (upper) curve was derived by adding the constant velocity difference of $0.07 \text{ mm}/\mu\text{sec}$ to the retarded PMMA velocity curve from $X = 5$ to $X = 80 \text{ mm}$.

Shock Velocity in PMMA and Results

To record the shock front motion in the PMMA, flats were ground and polished on opposing sides of the PMMA cylinder, parallel to the axis. The slit of the smear camera was aligned along the middle of these flattened surfaces, as shown in Fig. 2A. This, together with nearly parallel light passing through the cylinder, gave a relatively undistorted observation of the shock-front motion within the PMMA. Slopes were taken from seven smear-camera (X -time) records at given values of X and converted to corresponding mean shock velocities. Seven values of U for each X position were obtained from $X = 5$ to $X = 40 \text{ mm}$. Beyond $X = 40 \text{ mm}$, the number of obtainable values dropped since the length of PMMA cylinders was varied to measure simultaneously u_{fs} as a function of X . Six values were obtained from $X = 45$ to 50 mm , five from $X = 55$ to 65 mm , four at $X = 70 \text{ mm}$, and two from $X = 75$ to 80 mm .

The mean value of U as a function of X is given in Table 2 and plotted in Fig. 6. The largest and smallest velocity obtained at a particular value of X is shown by the short bars above and below each mean-value point. Ordinarily there is danger in using varying numbers of samples to determine a smooth mean-value curve. This could lead to an abrupt shift in the mean value at points where the number of samples is changed. Fortunately, the worst slope measurements occurred where the most samples were available. These were near the donor/PMMA interface, where the decay of velocity is greatest, and in the vicinity of the inflection of the curve occurring between $X = 25$ and $X = 45 \text{ mm}$. (This inflection occurs in both the U - X and u_{fs} - X curves. These will cause an increased fall-off in velocity of both U and u in the PMMA at a distance roughly equal to the radius of the cylinder; i.e., 25 mm .) At $X = 5$ and 35 mm the spread in U is 4-5%. Beyond $X = 50 \text{ mm}$, the spread is only 1-2%. The probable error of the mean value, of course, is much less than the indicated spread, excluding consistent errors. This is 0.1 to 0.4% over the entire curve.

TABLE 2
Smoothed Values of Particle Velocity (u), Shock Velocity (U), Pressure (P), and Relative Volume (v/v_0), at Various Distances (x) in the PMMA Cylinder Along the Axis

x (mm)	u (mm/ μ sec)	U (mm/ μ sec)	P (kbar)	v/v_0
5	—	5.30	—	—
10	1.420	4.95	82.4	0.715
15	1.210	4.62	66.0	0.738
20	1.088	4.40	56.6	0.753
25	0.990	4.21	49.2	0.765
30	0.890	4.06	42.6	0.781
35	0.780	3.88	35.7	0.799
40	0.650	3.66	28.1	0.822
45	0.538	3.46	22.0	0.845
50	0.455	3.35	18.0	0.864
55	0.383	3.30	14.9	0.884
60	0.325	3.24	12.4	0.900
65	0.283	3.21	10.7	0.912
70	0.245	3.17	9.2	0.923
75	0.225	3.14	8.3	0.928
80	0.200	3.13	7.4	0.936
100	0.145	(3.10)	(5.3)	(0.953)

() Extrapolated values.

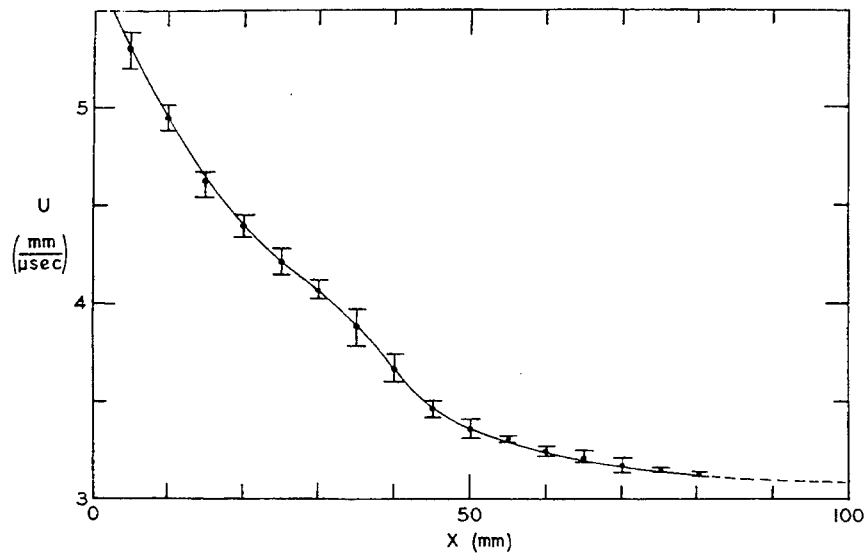


Fig. 6 - Shock velocity in the PMMA (U) as a function of x

The Shock Velocity vs Particle Velocity Curve

To derive the U vs u plot of Fig. 1, smoothed values of u were obtained at 5-mm increments of x from the foil-velocity curve of Fig. 5. These are given in Table 2 along with the mean values of U already discussed. Also given are the corresponding pressures, P , and the relative volume, v/v_0 . In Fig. 1, a fit to the U - u data, by eye, gave a straight-line relation for points corresponding to pressures above 20 kbar ($u > 0.5$ mm/ μ sec);

$$U = 2.56 + 1.69 u \quad (1)$$

These values are in fair agreement with those obtained by other workers at pressures above 20 kbar, e.g., ($A = 2.59$, $B = 1.51$) [4], (2.74, 1.35) [9], (2.68, 1.61) [10], and (2.42, 1.58) [11]. Below 20 kbar ($u < 0.5$ mm/ μ sec) another straight-line fit to the data gives

$$U = 2.95 + 0.85 u \quad (2)$$

Measurements were made at this Laboratory using very weak shocks (~ 100 bars) generated in a tank of water with transparent walls. The transit time of the shock through the submerged specimen, measured from backlighted, smear-camera records, gave a mean velocity of 2.76 mm/ μ sec [12]. This is shown on the U -axis, i.e., $u = 0$, in Fig. 1. The measurements were made on specimens machined from the same rod stock used in the other experiments described above.

SUMMARY AND DISCUSSION

1. A technique for obtaining the initial free-surface velocity of shocked PMMA by foils has been given. Data obtained in this manner enable the particle velocity in PMMA as a function of x to be derived in a cylindrically symmetrical system.

2. The difference between the foil and retarded PMMA velocities indicates a nearly constant spall tension of about 1.0 kbar over a stress range of 5 to 83 kbar.

3. Measurements of the shock velocity as a function of x has also been obtained: a plot of the shock and corresponding particle velocity shows an abrupt change of slope in the curve at about $U = 3.4$, $u = 0.5$ mm/ μ sec. Although the low-pressure portion of the curve has been drawn straight, small departures from a straight line could easily occur. The sharp break in the curve is perhaps not as important as the fact

that the shock velocity remains higher than would be expected if the linear U - u relation above 20 kbar continued on down to 5 kbar or lower. The data agree well with the work of others at 20 kbar and above. However, other workers (private communications) have found a similar behavior to that reported here for PMMA in the low-pressure region.

A satisfactory explanation for the high shock velocity at low pressure in PMMA has not been found. Several possibilities have been considered. Among these are: (a) the existence of an elastic wave which moves ahead of the plastic wave; (b) a change in phase that occurs in the PMMA; and (c) the effect of geometry of the present explosive system which may result in an experimentally determined U - u relation that is not the same as obtained with a truly plane (1-D) system in this pressure range.

In regard to (a), although attempts have been made to observe an elastic precursor wave in PMMA, no one has detected it to the author's knowledge. Because PMMA is a polymer, it should not necessarily be expected to behave like materials that resemble metals under low-amplitude shock. Metal-like materials may display an elastic precursor wave of constant amplitude. The curve of Fig. 1 suggests that an elastic wave exists in PMMA whose amplitude is stress dependent and this is what is observed here. If such a wave does exist, though, it would be the only wave; i.e., there would be no dual wave structure.

As to (b), a first-order phase transition, i.e., one involving discontinuities in volume or entropy, does not seem likely at such low pressure. The work of Bridgman [13] does not indicate any such transition up to 40 kbar under static conditions. However, the possibility of a second-order phase transition, i.e., one that involves no discontinuities in volume or entropy, has not been ruled out [14].

Regarding (c), the use of foils should establish the PMMA flow in the normal direction immediately behind the apex of the curved shock front. If the foil is thin enough, the result for a curved shock front should be the same as obtained in 1-D geometry [15]. It would be interesting to see if 1-D shock generating systems, such as the air gun, would give results comparable to those obtained with foils in these tests. The shock velocity below $u = 0.2$ mm/ μ sec may show a sharp fall-off as u approaches zero. The weak shock datum point of 2.76 mm/ μ sec should be close to the lower limit since the measurement is made in essentially the same way as the stronger shocks.

In conclusion, the designation, PMMA, implies that the results given here are for polymethyl methacrylate in general. Obviously, the degree of polymerization will not be the same for all sources of this material. Also, density variations are to be expected. As a consequence, the propagation of shock waves or sonic disturbances will not necessarily be the same in samples taken from different lots. However, we believe the differences would not be large enough to change substantially the $U-u$ results given here. In contrast, sonic measurements, such as longitudinal and shear wave velocities, might differ to a much greater extent.

The results given here and the work of others indicate that further theoretical as well as more carefully controlled experimental studies on PMMA and related materials are needed in the low-stress shock domain before the mechanism(s) of shock propagation can be explained fully.

ACKNOWLEDGMENT

The author is indebted to Drs. S. J. Jacobs and D. Price for their advice and criticism during the investigation and writing of this paper. The author acknowledges, with gratitude, the excellent way in which J. Schneider carried out the experiments.

REFERENCES

1. J. M. Walsh, R. H. Christian, "Equation of State of Metals from Shock Wave Measurements," *Phys. Rev.* **97**, 1544-56 (1955).
2. Derived in texts on shock-wave hydrodynamics.
3. W. B. Garn, "Determination of the Unreacted Hugoniot for Liquid TNT," *J. Chem. Phys.* **30**, 819-822 (1959).
4. I. Jaffe, R. Beauregard, A. Amster, "Determination of the Shock Pressure Required to Initiate Detonation of an Acceptor in the Shock Sensitivity Test," *ARS Jour.* **32**, 22-25 (1962).
5. T. P. Liddiard, Jr., D. Price, "Recalibration of the Standard Card-Gap Test," Naval Ordnance Laboratory Technical Report 65-43 (Oct. 1965).
6. T. P. Liddiard, Jr., B. E. Drimmer, "Smear-Camera Techniques," *J. SMPTE* **70**, 106-110 (1961).
7. S. J. Jacobs, J. P. McLanahan, Jr., E. C. Whitman, "A High Speed Focal Plane Shutter Framing Camera," *J. SMPTE* **72**, 923 (1963).
8. D. V. Keller, J. G. Trulio, "Mechanism of Spall in Lucite," *J. Appl. Phys.* **34**, 172-175 (1963).
9. G. E. Duvall, G. R. Fowles, "Shock Waves," *High Pressure Physics and Chemistry*, Vol. 2, 209-291, Academic Press, New York, N.Y. (1963).
10. G. E. Hauver, A. Melani, "Shock Compression of Plexiglas and Polystyrene," BRL Report 1259 (Aug. 1964).
11. W. E. Deal, work quoted by C. E. Reynolds and G. E. Seay, "Two-Wave Structure in the Ferro-Electric Ceramics Barium Titanate and Lead Zirconate Titanate," *J. Appl. Phys.* **33**, 2234-41 (1962).
12. N. L. Coleburn, T. P. Liddiard, Jr., "Hugoniot Equations of State of Several Unreacted Explosives," *J. Chem. Phys.* **44**, 1929-36 (1966).
13. P. W. Bridgman, *Proc. Am. Acad. Arts Sci.*, **76**, 71 (1948).
14. D. R. Curran, "On the Possibility of Detecting Shock-Induced Second-Order Phase Transitions in Solids. The Equation of State of Invar," *J. Appl. Phys.* **32**, 1811 (1961).
15. W. Bleakney, A. H. Taub, "Interaction of Shock Waves," *Rev. Mod. Phys.* **21**, 584-605 (1949).

SHOCK WAVE COMPRESSION OF PLEXIGLAS FROM 3 TO 20 KILOBARS*

W. J. Halpin and R. A. Graham

*Sandia Laboratory
Albuquerque, New Mexico*

ABSTRACT

Measurements on the uniaxial compression of Plexiglas specimens subjected to shock waves are reported for shock stresses ranging from 3 to 20 kilobars. The measurements were obtained from impact experiments in which a relatively new technique involving the "thick" quartz gauge was used. This technique makes possible the determination of the stress-time profile both at the impact surface of a specimen and at the opposite surface after the shock wave has propagated through the specimen thickness. Plexiglas specimen thicknesses of 5 mm and 7.5 mm were used. Data obtained for stress σ and particle velocity u_p were found to fit a quadratic relationship, $\sigma = 31.4 u_p + 23.6 u_p^2$ in the range of stress investigated (σ in kbar, u_p in mm/ μ sec). The data extrapolates into good agreement with much of the data obtained by others at higher pressure. The stress-time profiles at the impact surface were found to be step waves except for a small amount of relaxation. These profiles were essentially preserved at the opposite surface until impact stresses of about 7 kilobars were reached. Above this stress the propagated profiles were found to have undergone considerable distortion.

INTRODUCTION

Polymethylmethacrylate [2] plastics find a variety of applications in shock loading experiments. They are used, for example, in shock wave attenuator systems [3,4], in the study of the mechanics of spallation [5,6], and as impact materials when low stress at relatively high impact velocity is required [7]. Shock compression data for these plastics have been determined by a number of investigators at high pressure [8], but similar data below 20 kilobars are quite limited [9,10]. Recently the authors made an experimental investigation of the shock compression of Plexiglas in the stress range from 3 to 20 kilobars. In the experimental method employed, the shock was initiated by impact, and the required measurements were made by means of thick quartz gauges [11]. The purpose of this paper will be first to describe the experimental method, then to show how the data it produces can be analyzed, and finally to present and discuss the results that have been obtained for Plexiglas.

EXPERIMENTAL

Despite the fact that the thick quartz gauge technique used in this investigation is relatively new, it has been discussed in detail in a previous paper [12]. Consequently, only its principal features needed to understand the analysis of the data will be given here. The technique makes use of stress gauges whose principle of operation is based on the piezoelectric properties of quartz. The gauges are fashioned from circular discs of X-cut quartz. The manner in which they are used in the impact method is shown in Fig. 1. A specimen target (also a circular disc) is mounted on the end of an evacuated gun barrel and impacted by a precisely aligned flat-faced projectile, the velocity of which is accurately measured. The specimen has a gauge bonded to one of its surfaces (opposite to that being impacted) while the projectile has one embedded in its face. Upon impact, stress waves are propagated into both the projectile gauge and the specimen. The projectile gauge provides an electrical signal that

*See Ref. [1] at end of paper.

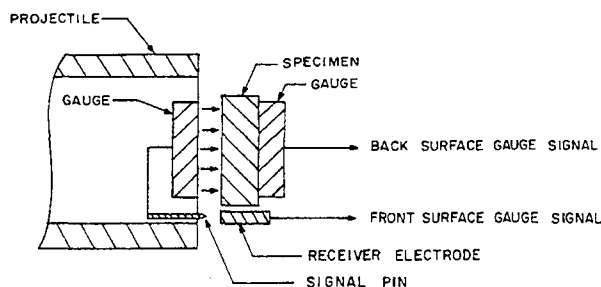


Fig. 1 - Schematic diagram of the method used for initiation and measurement of shock pressures in the specimens

measures the stress at the impact or front surface of the specimen as a function of time. Subsequently, when the wave generated in the specimen is propagated to the opposite or back surface, the back surface gauge signal measures the interface transmitted stress. These front and back surface gauge signals are cabled to oscilloscopes for recording. The two signals are referenced in time with precisely delayed fiducials so that shock wave transit time through the specimen can be measured.

DATA ANALYSIS

The front surface gauge record with projectile velocity and the back surface gauge record with transit times can be analyzed separately to provide information about the dynamic mechanical behavior of a specimen. Accordingly, each will now be considered in turn.

Front Surface Data

The front gauge records indicate that a jump in stress is impressed upon a specimen at the impact surface. The magnitude of this jump is calculated directly from the gauge signal as described in Ref. 11. In the stress range used for our experiments, the wave velocity in X-cut quartz U_{sq} is a known constant. Thus for a one-dimensional experiment (as is the case here) it follows from the conservation of momentum that:

$$u_{pq} = \frac{\sigma}{\rho_q U_{sq}} \quad (1)$$

where u_{pq} is the particle velocity imparted to the gauge (taken with respect to its unstressed portion), σ is the measured jump in stress, and ρ_q is the known density of quartz. If continuity

of mass across the impact interface is assumed, it then follows that

$$u_{ps} = U_o - u_{pq} \quad (2)$$

where u_{ps} is the particle velocity imparted to the specimen and U_o is the impact velocity of the gauge. Since U_o is measured, it is seen from Eqs. (1) and (2) that it is possible to obtain pairs of values of σ and u_{ps} which characterize the compressional behavior of the specimen under the impact shock. It should be emphasized that the analysis so far does not require any of the assumptions of the conventional free-surface methods; that is, there is no concern with whether the profile of the wave in the specimen is steady, with rate effects, or with complex wave interactions produced at a free surface. If, however, it is assumed that the stress at the impact surface is propagated into the specimen with a steady profile, then from the conservation of mass across the shock front another representation of the data follows, which is

$$\frac{V}{V_o} = 1 - \frac{\rho_s u_{ps}^2}{\sigma} \quad (3)$$

where V_o and V are, respectively, the specific volumes of the specimen before and after compression.

Back Surface Data

When the wave generated by impact is propagated to the interface between the specimen and the back surface gauge, the gauge measures the interface stress produced. If the specimen were a linear material, then a jump in stress σ_t measured by the gauge at the interface would be related to a corresponding incident stress in the specimen σ_i by the linear mismatch equation

$$\sigma_i = \frac{Z_s + Z_q}{2Z_q} \sigma_t \quad (4)$$

where Z_q is the mechanical impedance (equal to density times wave velocity) for the quartz and Z_s is that for the specimen. The latter can be computed from the measured specimen density and the velocity of the wave propagated through the specimen thickness. The wave velocity can be obtained from the experimental data simply by dividing the specimen thickness by the time difference between the start of the two signals from the front and back gauges. The incident particle velocity in the specimen u_{pi} which corresponds to σ_i is then given by

$$u_{pi} = \frac{\sigma_i}{Z_s} \quad (5)$$

A solution for the stress-particle velocity locus for a nonlinear material is possible by an iterative procedure in the stress-particle velocity plane when the locus is known to be concave upward. This is illustrated graphically in Fig. 2. The locus for the gauge material, X-cut quartz, is a solid, straight line in the plane as shown. Also shown as a solid line but with concave upward curvature is the locus for the specimen which is initially assumed to be that obtained from the front surface analysis. A reflection of this locus (dashed line) is made so that it passes through point *m* on the quartz locus, where *m* has a stress coordinate equal to the interface jump in stress σ_i , which is measured directly by the back surface gauge. The second straight (dotted) line on the plot has a slope equal to Z_s , the impedance of the specimen for the incident stress, which is obtained from the specimen density and transit time measurements as indicated above. This line will intersect the assumed locus at point *n* and the reflected locus at point *n'*. If *n* is identical with *n'* for a sufficient number of points, then the assumed locus is verified as correct. If the intersections do not coincide, then an iterative procedure, in which successively different loci are assumed for the specimen, is used until a convergence is obtained [13].

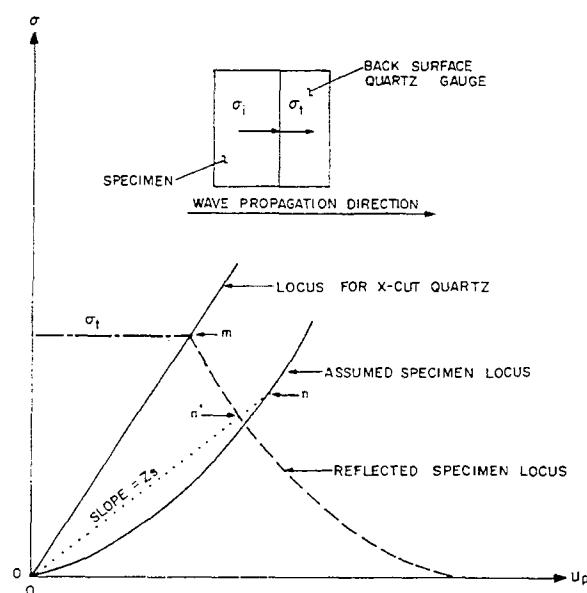


Fig. 2 - Graphical illustration of the analysis of the back surface gauge and transit time data

RESULTS FOR PLEXIGLAS

A summary of the analysis of the experimental data obtained for Plexiglas is given in Table 1. For the series of four tests designated by the letter A in the table both front and back surface gauge measurements were attempted. Front surface and transit time data were obtained on all these tests; however, only two of the tests provided propagated wave profiles of a quality acceptable for analysis. For the series of eight tests designated by the letter H, front surface gauge measurements were attempted on all of the tests, but both front and back measurements were attempted on only four. All data were obtained in the H-series tests. The estimated accuracy of the impact surface stress jump σ is 2% and of the corresponding particle velocity u_p is 1% (projectile velocity U_0 is accurate to 0.5%). The wave velocity U_s is estimated to be accurate to 1%.

The stress-particle velocity relationship obtained from the impact surface data is plotted in Fig. 3. This relationship can be closely approximated by the parabola, $\sigma = 31.4 u_p + 23.6 u_p^2$, which when extrapolated to zero stress indicates a wave velocity of 2.66 mm/ μ sec. This may be compared with the value of 2.62 listed by Hughes et al. [14]. The only other data in this stress region below 25 kbar are those of Dapoigny et al. [9], and they are in good agreement with our data [10]. Our data also extrapolates into good agreement with a point by Hearst, et al. [15], at 26 kbar, with two points by Wackerle at 30 and 36 kbar [3], and with a data fit selected by Duvall and Fowles [16].

The stress-volume relationship corresponding to the impact surface data of Fig. 3 was computed from Eq. (3) and is shown in Fig. 4. This relationship is compared with Bridgman's hydrostatic measurements on "leucite" [17] which have been corrected to adiabatic conditions [18]. The two sets of data show a roughly constant volume difference of about 1% for stresses greater than about 3 kbar. On the basis of thermodynamic models this difference is larger than would be expected between Hugoniot and adiabatic stress-volume data at these low stresses [19]. The difference might well be accounted for by an elastic stress component in the case of shock compression. However, there was no evidence of elastic wave in the back surface gauge records even for the lowest impact stress of about 3 kilobars. Although the back surface record for this test may not have shown the final stress amplitude, it was clear from the record that if any elastic wave were present, it was overdriven by the 3 kilobar input.

TABLE 1
Shock Compression Data for Plexiglas

Density $\rho = 1.178 \text{ gram/cm}^3$ ($\sigma = 0.0016$)
Specimen Thickness = 7.5 mm for tests H-232 and H-233,
= 5 mm for all other tests

Impact Surface Measurement					Propagated Profile			
Test ^a	Stress Input Time ^b	σ^c	u_p^d	V/V_0^e	Relaxation ^f (%)	U_s^g	σ_t^h	σ_i^i
A-254	100	3.25	0.0943	0.9678	2	2.96	-	-
A-253	40	5.24	0.142	0.9545	4	3.00	8.0	4.9
H-231	35	7.46	0.203	0.9348	3	3.04	11.1	6.3
H-233	60	7.50	0.203	0.9353	3	3.06	11.1	6.4
A-194	80	8.99	0.246	0.9207	-	3.04	-	-
A-199	60	9.94	0.280	0.9070	4	3.16	15.0	8.9
H-184	50	10.4	0.276	0.9138	4	-	-	-
H-230	30	10.6	0.274	0.9168	6	3.13	15.5	9.0
H-232	30	-	0.276 ^j	-	-	3.10	15.0	8.6
H-183	70	15.3	0.377	0.8920	4	-	-	-
H-182	45	19.5	0.459	0.8728	-	-	-	-
H-181	25	21.2	0.524	0.8476	-	-	-	-

^aThe "A" prefix denotes experiments done with the 10 ft air gun described in Ref. 12. The "H" prefix denotes experiments done with the 80 ft gun described in Ref. 20.

^bMeasured time for the active area of the projectile gauge to become stressed (units of 10^{-9} sec).

^cMeasured stress jump at the impact surface (units of kbar).

^dParticle velocity jump at the impact surface computed from Eqs. (1) and (2) (unit of mm/ μ sec).

^e V is stressed volume, V_0 is initial unstressed volume. V/V_0 computed from Eq. (3).

^fPercent reduction in stress in 1.1 μ sec.

^gWave velocity computed from observed transit time through specimen thickness (units of mm/ μ sec).

^hInterface stress jump recorded between the back surface gauge and the specimen (units of kbar).

ⁱStress in Plexiglas specimen at the back surface after propagation through the specimen thickness computed from the back surface interface stress and the graphical method of Fig. 2.

^jStress jump was not measured on this experiment. u_p was computed from the measured impact velocity and the specimen $\sigma - u_p$ locus of neighboring points.

The front surface gauge measurements show that the initial jump in impact stress is followed by a small but definite relaxation of stress with time. Because of the concave upward shape of the $\sigma - u_p$ locus for the Plexiglas, it is to be expected that any increment of relaxation (unloading) at the impact surface would be propagated into the material with a higher wave velocity than that of the initial jump in stress. The net result of this should be a lowering of the initial jump as it appears at the back

surface. This, in fact, was observed. The graphical procedure of Fig. 2 was applied to the propagated wave profile and transit time data with the assumed specimen $\sigma - u_p$ locus being that of Fig. 3. The stress coordinate of the point n gave the value of the incident stress jump σ_i . In every case σ_i was found to be lower than the corresponding impact stress (compare σ_i column with σ column in Table 1) by an amount that varied from about 6% at 5 kilobars to 15% at 10 kilobars. Despite this

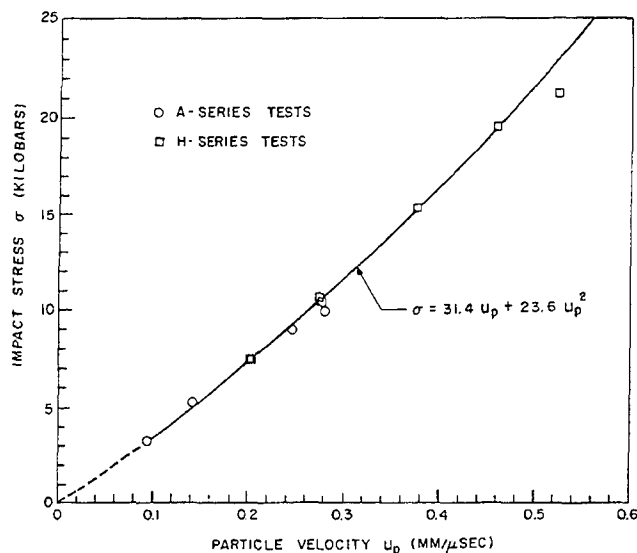


Fig. 3 - Relationship between stress and particle velocity for Plexiglas under shock loading determined from the impact (front) surface data. All data points except the highest one were used to compute the least squares fit indicated.

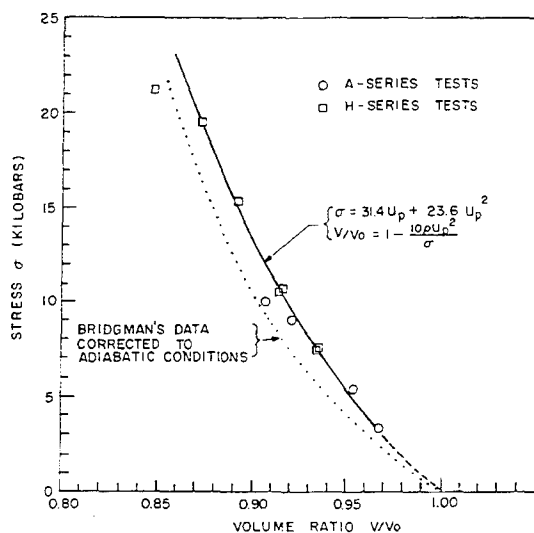


Fig. 4 - Relationship between stress and specific volume for Plexiglas under shock loading obtained by applying Eq. (3) to the data of Fig. 3. Comparison of this shock compression data with hydrostatic compression data.

difference between the impact and propagated stress jumps the $\sigma - u_p$ locus was not significantly changed from that of Fig. 3; that is, no iteration was necessary in the graphical procedure.

The propagated stress-time profiles for impact stresses greater than 7 kbar show reproducible distortion in amplitude and shape. The early parts of the profiles are noticeably "rounded off," and after about $0.6 \mu\text{sec}$ the stress begins to increase considerably in magnitude. Small amplitude, high frequency variations are also present. This behavior is shown in the typical oscilloscope record of Fig. 5 and in the summary of wave profiles of Fig. 6. It is undoubtedly a manifestation of complex time-dependent and dispersive properties of Plexiglas, which to explain would require much additional analysis that will not be attempted in this paper.

NOTES

1. This work was supported by the U.S. Atomic Energy Commission.
2. Polymethylmethacrylate plastics for which shock studies have been reported are manufactured under the following trade names by the manufacturer indicated: Lucite by E. I. DuPont de Nemours and Co., Plexiglas by Rohm and Haas Co., Perspex by Imperial Chemical Industries, Ltd.
3. Jerry Wackerle, Journal of Applied Physics 33, 922 (1962).

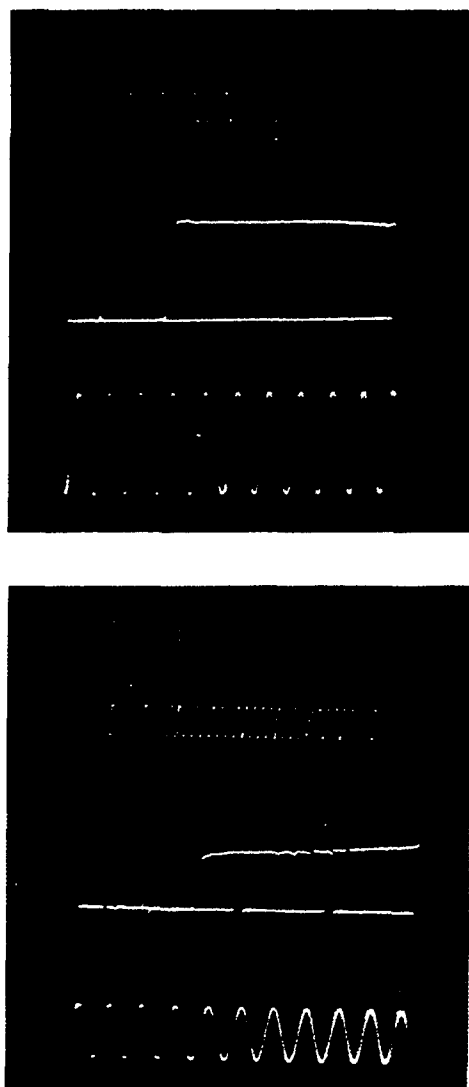


Fig. 5 - Typical oscillographic records of quartz gauge measurements of the front and back surface stress-time profiles for a Plexiglas specimen (test H-233). Time increases from left to right. Timing waves are 20 Mc (top traces).

4. G. E. Seay and L. B. Seely, Jr., *Journal of Applied Physics* 32, 1092 (1961).
5. Donald V. Keller and John G. Trulio, *Journal of Applied Physics* 34, 1962 (1963).
6. Donald W. Blincow and Donald V. Keller in *ASTM Special Technical Publication No. 336, Dynamic Behavior of Materials* (American Society for Testing and Materials, Philadelphia, 1963), p. 252.
7. One of the authors, W. J. Halpin, has utilized this technique for experiments with ferroelectric materials (paper submitted to *Journal of Applied Physics*). Higher projectile velocity reduces the "tilt" of a stress wavefront produced by impact.
8. A compilation of shock compression data for pressures greater than 20 kilobars is given in Appendix 1.
9. Jean Dapoigny, Jean Kieffer, and Boris Vodar, *Academie des Sciences, Comptes Rendus* 245, 1502 (1957).
10. Since this paper was written, considerably more data in this stress region have become available. For example, see the paper of T. P. Liddiard, Jr. and the discussion of D. E. Munson in these proceedings. Also see D. N. Schmidt and M. Evans, *Nature* 206, 1348 (1965).
11. R. A. Graham, F. W. Neilson, and W. B. Benedick, *Journal of Applied Physics* 36 (1965).
12. W. J. Halpin, O. E. Jones, and R. A. Graham in *ASTM Special Technical Publication No. 336, Dynamic Behavior of Materials* (American Society for Testing and Materials, Philadelphia, 1963), p. 208.
13. For experiments in which the impact surface data are not available a locus obtained from Eqs. (4) and (5) can be used initially. The iterative procedure will then result in a rapid convergence to a solution.
14. D. S. Hughes, E. B. Blankenship, and R. L. Mims, *Journal of Applied Physics* 21 (1950).
15. J. R. Hearst and L. B. Geesaman, *Lawrence Radiation Laboratory Report, UCRL 7877*, May 1964.
16. G. E. Duvall and G. R. Fowles in *High Pressure Physics and Chemistry* (Academic Press, New York, 1963), p. 263.
17. Bridgman did not describe this particular material other than by this apparent misnomer. The material is indexed as Lucite by the *Annotated Bibliography on High-Pressure Technology*, The American Society of Mechanical Engineers, 1964.
18. Thermodynamic constants used in the computation are: volume thermal expansion, $\beta = 2.4 \times 10^{-4} \text{ } ^\circ\text{C}^{-1}$, specific heat, $C_p = 0.35 \text{ cal gram}^{-1} \text{ } ^\circ\text{C}^{-1}$, specific volume, $v = 0.8490$

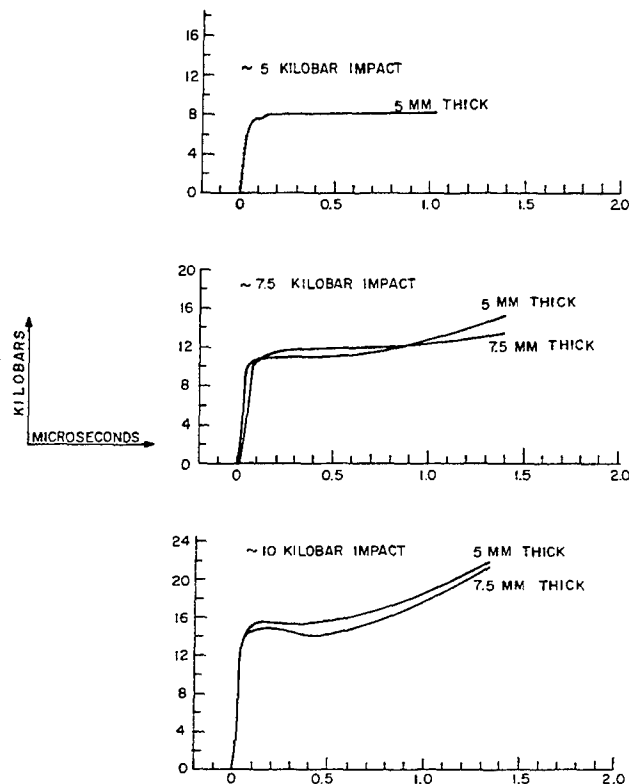


Fig. 6 - Back surface gauge stress-time profiles obtained for various impact stresses and specimen thicknesses. The profile stress is that in the gauge. High-frequency variations evident in Fig. 5 have been smoothed out in these reproductions for the 7.5 and 10 kilobar impact cases. The profile for the case of the 7.5 kilobar impact with the 7.5 mm thick specimen corresponds to the actual record shown in Fig. 5.

$\text{cm}^3 \text{ gram}^{-1}$, adiabatic compressibility,
 $k = 8.2 \times 10^{-3} \text{ kbar}^{-1}$, Grüneisen's ratio:

$$\gamma = \frac{V\beta}{C_p k} = 1.70$$

19. P. Moravek, Stanford Research Institute has calculated Hugoniot, T_H , and adiabatic, T_A , temperatures for Lucite. He finds $T_H - T_A = 4^\circ\text{K}$ at 21 kbar. This small temperature difference indicates that there should be a negligibly small volume difference between our data (Hugoniot) and Bridgman's (adiabatic) in the stress range of our data. Reference: Progress Report No. 27, SRI Project GPU-3713, December 17, 1963. DASA Contract DA-49-146-XF-096.

20. S. Thunborg, G. E. Ingram, and R. A. Graham, *The Review of Scientific Instruments* **35** (1964), p. 11.

APPENDIX 1

(References to shock compression data for polymethylmethacrylate at high pressure not cited in text.)

A summary of some of these data is given in G. E. Duvall and G. R. Fowles in *High Pressure Physics and Chemistry* (Academic Press, New York, 1963), p. 263.

References to the Literature

1. J. S. Buchanan, H. J. James and G. W. Teague, *Philosophical Magazine* 3, 1432, 1958.
2. H. Lawton and I. C. Skidmore in the *Physical Chemistry of Processes at High Pressure*. Discussions of the Faraday Society No. 22, 1956, p. 188.
3. L. V. Al'tshuler and A. P. Petrunin, *Soviet Physics - Tech. Phys.* 6, 516 (1961).

Whitcher, *On Equations of State of Solids*, The Boeing Company, Document No. D2-90472, Sept. 1964.

1. N. L. Coleburn, NAVWEPS Report 6026, 31 October 1960, U.S. Naval Ordnance Laboratory.
2. M. A. Cook, R. T. Keyes, and W. O. Ursenbach, "Third Symposium on Detonation," Vol. 2, Sept. 26-28, 1960, ONR Symposium Report ACR-52, AD242586.

References to Published Reports

A compilation of a number of equation of state determinations is given in Stanley L.

3. G. E. Hauver, A. Melani, BRL Report No. 1259, Ballistic Research Laboratories, August 1964, AD609194.

COMMENTS

D. E. MUNSON (Sandia Corporation, Albuquerque, New Mexico): A few low pressure points which augment the Plexiglas data of Halpin and Graham have been recently obtained for conditions of uniaxial strain with aluminum projectiles impacting flat Lucite targets. Shock velocities and free-surface displacements were found using a slanted resistor technique.*

These quantities were reduced to the stress-strain values given in Table 1, assuming strain-rate-independent behavior and negligible stress wave interactions at the free surface. As the stress-strain data indicates, the wave profile in Lucite does not rise as a single shock wave on the time scale of these experiments.

If strain-rate effects are small, the peak stress-strain point may be compared directly to other Hugoniot data. The Hugoniot in the pressure-particle velocity plane is given in Fig. 1; this curve is consistent with the data presented by Halpin and Graham.

*L. M. Barker and R. E. Hollenbach, "A System for Measuring the Dynamic Properties of Materials," *Rev. Sci. Instr.* 35 (1964), 742-746.

TABLE 1
Lucite Stress-Strain Points

Shot No. and Thickness t_0 (mm)	Projectile Velocity U_m (mm/ μ sec)	Stress σ_x (kbar)	Strain ϵ_x (in./in.)	Peak Stress (kbar)	Peak Strain (in./in.)	Particle Velocity $U_p \approx 1/2 U_{fs}$ U_p (mm/ μ sec)
1010 (36.974)	0.3048	6.88 7.69 8.02	0.0587 0.0671 0.0714	8.02	0.0714	0.222
1011 (23.378)	0.1927	3.32 5.11 5.36	0.0293 0.0465 0.0492	5.36	0.0492	0.151
1012 (23.571)	0.0574	0.92 1.57	0.0095 0.0166	1.57	0.0166	0.047

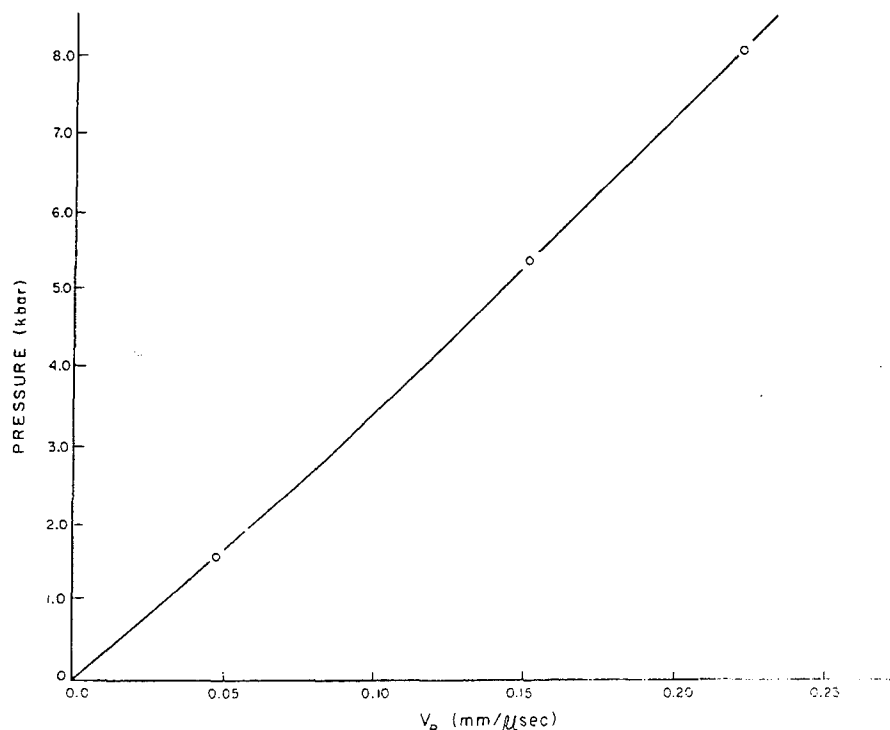


Fig. 1 - Lucite (pressure vs particle velocity)

T. P. LIDDIARD, JR. (U.S. Naval Ordnance Laboratory, White Oak, Silver Spring, Md.): Until recently there has been little available data on the shock properties of polymethylmethacrylate in the pressure range of 3 to 20 kbar. One had to extrapolate the data obtained at higher pressures down to lower stress levels. Data recently obtained at NOL show that all is not well when such an extrapolation is used. This is most easily seen in the shock velocity (U) vs particle velocity (u) plane, Fig. 1 (Fig. 1 of paper by Liddiard, this Symposium). The NOL curve, corresponding to a pressure range of 5 to 83 kbar, shows an abrupt change in slope at about 20 kbar ($U = 3.4$, $u = 0.5$ mm/ μ sec). Above 20 kbar the data are in fair agreement with most workers. Below 20 kbar the measured shock velocities, at given values of u , are higher than would be gotten by a linear (U vs u) extrapolation of the higher pressure data. In addition, the velocities are higher than would be expected by using the bulk-sound speed of 2.3-2.5 mm/ μ sec to set the lower limit ($u = 0$) of the curve. [The expression for the bulk-sound speed is $C_b^2 = C_l^2 - 4/3C_s^2$, where C_l is the longitudinal sound velocity and C_s is the shear sound velocity.]

It is gratifying to see other recent data for Plexiglas in the low stress range. These data have been obtained at the Sandia Corporation (these Proceedings) and at the Stanford Research Institute (Nature 206, 1348 (1965)). It is unfortunate, though, that both of these sets of data fail to go high enough in stress to verify the abrupt upward change of slope in the NOL curve above 20 kbar. However, these data do show higher-than-expected shock velocities below 20 kbar.

The data of Halpin and Graham are compared to the NOL curve in Fig. 2. The shock velocities used here are mean values through the Plexiglas samples. The detection of shock arrival at the front and back of the specimen was made by quartz gauges. Halpin and Graham estimate the accuracy of their measured values to be good to 1%. The values of U , which can be derived from their stress-particle velocity data, appear to have a spread of 6-8% and these values are, therefore, omitted on the comparison in Fig. 2. A straight line can be fitted to the Sandia data which would be nearly parallel to the NOL curve (under 20 kbar), but about 3% lower. Actually, the Sandia data should be

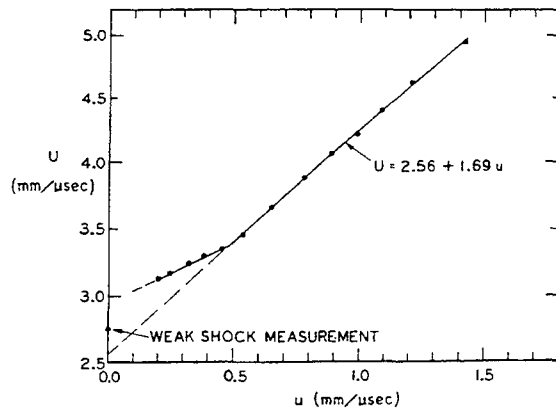


Fig. 1 - Shock velocity (U) as a function of the particle velocity (u)

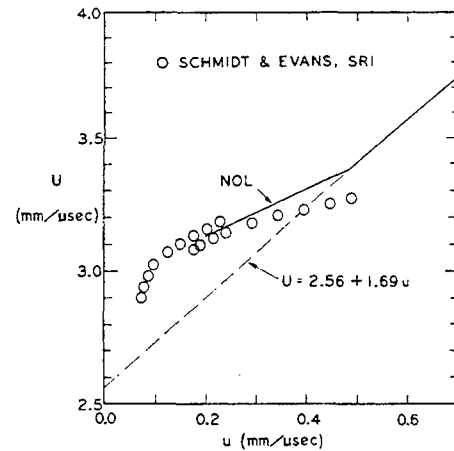


Fig. 3 - Comparison between the U vs u data obtained by SRI and the NOL curve

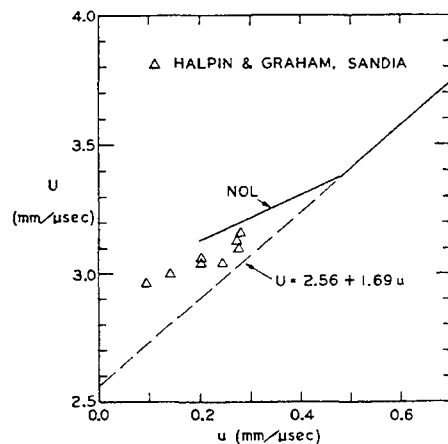


Fig. 2 - Comparison between the shock velocity (U) vs particle velocity (u) data obtained by Sandia and the NOL curve

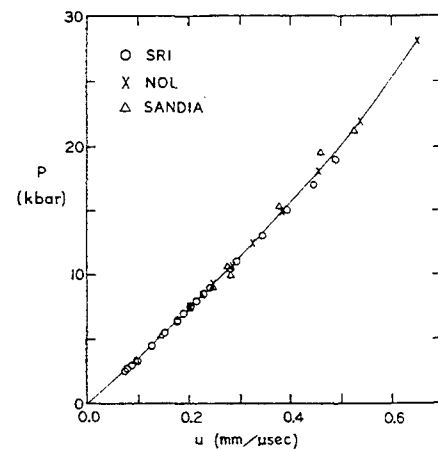


Fig. 4 - Pressure (P) vs u data plotted for Sandia, SRI, and NOL

raised slightly to compensate for the use of mean values of U . The correction probably would amount to about 1%.

In Fig. 3 are data obtained by SRI using a very different experimental approach from that used by Sandia. The low-pressure shock is generated by the detonation of a thin layer of explosive in contact with a wedge of Plexiglas. Since the shock pressure attenuates with the distance the shock travels, the pressure produced at the opposite face of the wedge varies continuously along the surface. The data points shown were determined from two experiments having different pressure ranges. The SRI data are in excellent agreement with those of NOL between $u = 0.2$ and 0.3 mm/ μ sec. It is likely

that the accuracy in the wedge method falls off toward the upper and lower pressure extremes covered by a particular wedge arrangement. This could account, at least in part, for the sharp downward bend in the SRI curve at the low end and the low slope of the curve at the high end. There is no reason, though, to expect the curve to be linear over this pressure range. On the basis of the weak-shock-velocity measurement of 2.76 mm/ μ sec made at NOL (Fig. 1), one might expect the curve to bend down toward such a value as u approaches zero.

In Fig. 4 the stress vs particle velocity curves are shown for Sandia, SRI, and NOL. Of course, displaying the data in the $P-u$ plane is not a sensitive way of making a comparison.

The Sandia stresses were obtained directly by quartz gauges and the measured shock velocities in Plexiglas were not used in the stress calculations. The stress-particle velocity data for all three sources of data appear to be in excellent agreement up to 10 kbar. Above 10 kbar, it appears that the stresses obtained with quartz

gauges are not as accurate as those calculated from both U and u measurements.

The results of the U vs u comparisons show that higher-than-expected shock velocities were obtained in Plexiglas by three widely different experimental techniques in the 3-20 kbar range. The reason for the high velocities has yet to be explained satisfactorily.

ANALYSIS OF SHOCK WAVE AND INITIATION DATA FOR SOLID EXPLOSIVES

J. B. Ramsay and A. Popolato
*Los Alamos Scientific Laboratory
Los Alamos, New Mexico*

ABSTRACT

If the usual analysis of shock-wave data is made for polycrystalline plastic-bonded HMX and pressed TNT the experimental data extrapolate to the detonation pressure point rather than to the peak spike pressure point. This is indicative of a reactive wave, which is to be expected. Limitations based on the assumptions and analysis are discussed to show that it is not possible to infer any information about the shock properties of unreacted explosive from the available shock-wave data for solid explosives.

Since no calculational model is available which will permit the computation of the details of initiation of solid explosives, empirical relationships are presented to summarize the data for engineering purposes.

INTRODUCTION

The initiation of solid explosives by shock waves has been discussed by Campbell and co-workers [1]. They have shown that shock initiation takes place in the following way. The shock wave in the polycrystalline explosive is always rough because of the small local discontinuities distributed throughout the material. Therefore, there will be small local convergences of the shock wave and the associated mass flow, with local high temperature regions. Reaction takes place in these small regions of convergence, and the energy released makes a major contribution

to initiation. The reactive wave proceeds at a slowly increasing velocity for a distance which is a function of the initial shock pressure. Then the velocity increases in a short but observable distance to the value associated with the high-order detonation. The velocity transition is not abrupt, as is the case for liquids, nor is there any strong overshoot in the detonation velocity, again in contrast to liquids. This series of events is illustrated in Fig. 1.

Gittings [2] has shown that explosive may be initiated by impacting it with very thin foils. These foils produce a very short pressure pulse

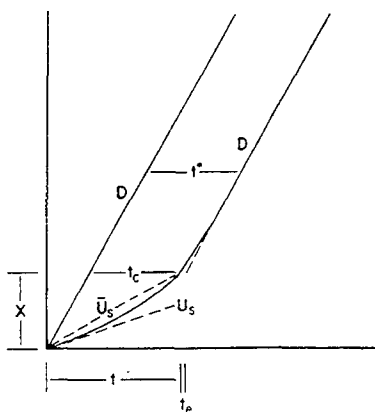


Fig. 1 - Space-Time Plot of Shock Initiation in a Solid Explosive

- D = Steady-state detonation velocity
- X = Measured distance to detonation
- t = Measured time to detonation
- t^* = Excess transit time
- t_c = Calculated excess transit time
- t_e = Error in calculated excess transit time
- \bar{U}_s = Average initiating wave velocity
- U_s = Initial shock velocity as measured

in the explosive, showing that energy which is released by the shock interactions is released very near to the shock front. This rapid release of energy will affect the shock front soon after the shock wave enters the explosive. Mader [3,4] has shown by calculational experiments how small hot spots are formed and that their energy is released a very short time after the wave has passed.

All evidence indicates that shock-waves in polycrystalline explosive are reactive waves; thus measurements of shock waves should not be thought to give information about the shock properties of unreacted explosive. In addition, the shock wave in a polycrystalline explosive is not smooth and plane, and energy added to the wave from reaction at small hot spots is not added uniformly over the wave surface.

The Hugoniot curves of solid polycrystalline explosives have been reported by several authors [1,5,6]. In two of these studies the curves have been extended to estimate the spike pressure in the unreacted explosive. In this paper we present data obtained for plastic bonded HMX (PBX-9404) and pressed TNT, and show that, if the usual assumptions and treatment are made of the data, the Hugoniot curves extrapolate to the detonation pressure (C-J pressure)* rather than to the spike* pressure. Because of the complex nature of the mechanism of shock propagation in polycrystalline materials and, in particular, in a polycrystalline explosive which is known to be reacting, it is not possible to determine whether the assumptions and treatment of the data are correct. Rather, the data are treated in an empirical manner which permits the summarization of the experimental data compactly and in a manner suitable for engineering purposes.

SHOCK MEASUREMENTS

Shock waves in solid explosives have been studied by the wedge technique in which a plane, uniform shock wave is sent into a wedge-shaped piece of explosive and the position of the intersection of the shock wave and the inclined face of the explosive recorded as a function of time with the smear camera. Solid explosives have

also been studied by the pellet technique in which the transit time of a shock wave through a thin pellet of explosive is measured either with a smear camera or with pins located at the back and front surfaces. The wedge technique gives a complete time history of the shock wave as it propagates in the explosive, while the simpler pellet technique provides only an average shock velocity. This difference is illustrated in Fig. 1 as the difference between U_s and \bar{U}_s .

The analysis of the data obtained from such studies is normally performed by assuming that the flow is one-dimensional and laminar and that the pressure at the interface where the shock enters the explosive is changing only slowly with time. These assumptions are not correct, but no practical alternative has been proposed. It is not possible to estimate the magnitude or sign of the errors which may be introduced by these assumptions.

Data from wedge-type experiments for PBX-9404 are shown in Fig. 2 and in Fig. 3 for pressed TNT. The TNT data have been supplemented by pellet-type measurements made by Garn [9]. These measurements by Garn on pressed TNT were made in 1958 and have not been reported previously. In addition, data on liquid TNT obtained by Garm [10] are shown in Fig. 3. The linear fit of the data for pressed TNT agrees within the expected experimental error with values reported by Liddiard [5] for cast TNT. Vasil'ev and co-workers [11] have reported measurements of the isothermal compressibility of TNT up to 21 kbar. These measurements have been transformed to the plane of the figure by assuming that the isotherm and the Hugoniot curve are congruent up to 21 kbar.

McQueen and Marsh [12] have shown that for a large number of solid inorganic materials the shock velocity and particle velocity are linearly related in regions where no shock-induced phase transitions occur. They also showed that the intercept for zero particle velocity is the bulk sound velocity. The bulk velocity is defined by Eq. (1)

$$C_0 = (k/\rho_0)^{1/2} \quad (1)$$

where k is the isentropic modulus of volume elasticity and ρ_0 is the density. The bulk sound speed is not measured directly for solid materials but is obtained from measurements of the longitudinal and shear sound velocities through Eq. (2)

$$C_0^2 = C_l^2 - (4/3) C_s^2 \quad (2)$$

*Because of the questions concerning the use of the term C-J pressure [7,8] we will use the term detonation pressure to refer to the abrupt change in pressure observed in reaction zone studies. This is the same point that has previously been called the C-J pressure. The term spike pressure means the pressure at the leading edge of the detonation wave.

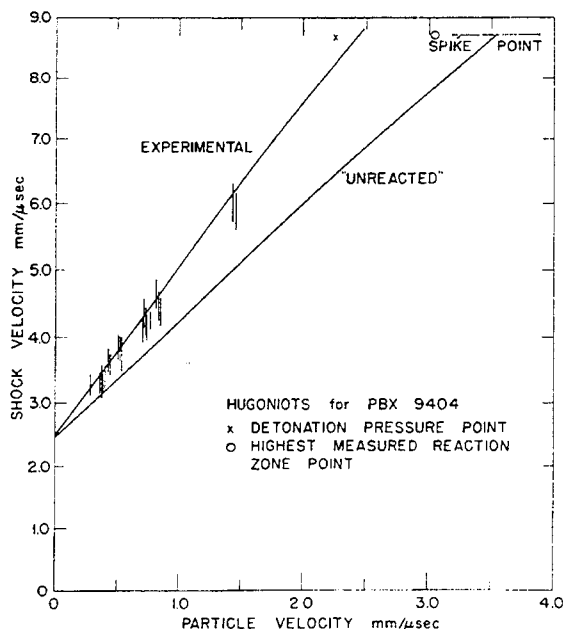


Fig. 2 - Hugoniot Curves for Plastic-Bondex HMX. The vertical lines represent the error of the measured shock velocities. The experimental line is a least-squares fit of the data including the bulk sound velocity. The line connecting the spike pressure and the bulk sound velocity is an estimate of the Hugoniot curve for the unreacted explosive.

C_l is the longitudinal sound velocity for a wave front in a specimen whose diameter is large compared to the wave length. C_s is the shear sound velocity defined in the usual manner. Table 1 gives the sound speed measured by Edwards, Finley and Grimm [13] at Los Alamos. For both TNT and PBX-9404, preliminary analysis of the experimental shock-wave data showed no significant difference existed between the intercept value and the bulk sound velocity. The lines labeled "experimental" in Figs. 2 and 3 were obtained from least-squares fit which included the measured bulk sound velocity with a weight of 4 to adjust for the difference in the expected standard deviations.

The usual model of one-dimensional, laminar detonation has a shock wave propagating in the unreacted explosive, heating the explosive, and causing reaction to take place after an induction period. The pressure and particle velocity are highest in the unreacted explosive and fall as the reaction proceeds. When the reaction is complete the rate of fall of pressure becomes small. Estimates of the particle velocity corresponding to the spike pressure and the detonation

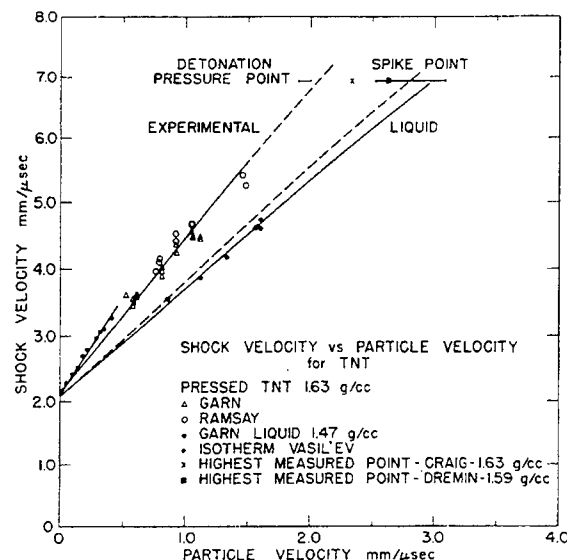


Fig. 3 - Hugoniot Curves for TNT. The dashed section of the experimentally measured curve represents an extrapolation based on the assumption that the curve is linear. The dashed line connecting the bulk sound velocity with the spike pressure is an estimate of the Hugoniot curve for the unreacted explosive.

pressure have been obtained by Craig [8,14] for PBX-9404 and pressed TNT and by Dremine [15] for pressed TNT. These points are plotted in the respective figures together with the highest measured points on the reaction zone. These data had to be analyzed on the basis that the explosive is a continuum and that the polycrystalline nature did not affect the measurement. Again this is a questionable assumption, but no other basis is available.

TABLE 1
Sound Velocities for Pressed TNT
and PBX-9404

	Pressed TNT	PBX-9404
Density, g/cc	1.635 ± 0.005	1.83 ± 0.01
Sound Velocities		
Longitudinal, mm/μsec	2.586 ± 0.080	3.060 ± 0.056
Shear, mm/μsec	1.330 ± 0.050	1.612 ± 0.056
Bulk, mm/μsec	2.08 ± 0.13	2.43 ± 0.07

It is interesting to try to interpret the curves shown in Figs. 2 and 3 with the usual treatment given shock-wave data. In the shock velocity vs particle velocity plane, the shock loci for most materials are very nearly linear, provided no shock-induced phase changes occur. It is therefore to be expected that a straight line from the bulk sound velocity to the estimated spike pressure point would approximate the shock locus of the unreacted explosive. This line has been drawn in Figs. 2 and 3 and is labeled "Unreacted" in Fig. 2 and shown as a dashed line in Fig. 3. In both cases the experimental shock points appear to lie along a line which can easily be drawn through the detonation pressure point, indicating that the experimentally measured curves represent partially reacted explosive. This behavior of the curves for solid explosives can be contrasted with that for liquid explosives. Studies of shock initiation of liquid explosives show that the shock-wave data for liquids are for the unreacted material. For liquid TNT the detonation pressure point reported by Davis, Craig, and Ramsay [7] has a particle velocity of 1.85 mm/ μ sec and a detonation velocity of 6.59 mm/ μ sec. If this point were plotted in Fig. 3, it would lie on the linear extension of the experimentally measured curve for the solid. A linear fit of the shock-wave data for the liquid cannot include this point. This conclusion, that the experimentally measured Hugoniot curves for liquids do not extrapolate in a linear manner to the detonation point, is confirmed by data for nitromethane [6,7].

It would at first appear that the isothermal compressibility data for pressed TNT indicate that the experimentally measured Hugoniot curve represents unreacted explosive. However, when a similar comparison is attempted between isothermal curves and the measured Hugoniot loci for other materials (mostly metals and inorganic compounds), the slope of the isothermal curve in the plane of shock velocity vs particle velocity is generally a factor of two higher than the slope of the Hugoniot curve. If anything, one would expect the isothermal curve to be less steep than the Hugoniot curve. Therefore, the use of the isothermal curve to determine the Hugoniot curve for the unreacted explosive must be suspect and the question remains open as to whether the true Hugoniot curve for pressed TNT can be approximated with a straight line in the shock velocity vs particle velocity plane.

It is our opinion that the measured Hugoniot curve should not be used to infer properties of the unreacted explosive until the propagation of shock waves in polycrystalline materials and the initiation of solid explosives is more completely understood. We also believe that the

very complex initiation behavior of polycrystalline explosives cannot be calculated from these data at the present time.

EMPIRICAL APPROACH TO SHOCK INITIATION

The complexity of the mechanism of shock initiation of polycrystalline explosives makes it impossible for us to calculate in detail the events leading up to the transition from a shock wave to a detonation wave. Therefore, we are forced to be less ambitious and to look for empirical relationships which make it possible to summarize experimental data compactly and to use them for engineering purposes.

While the pressure calculated from the wedge and pellet experiments is not a true measure of the conditions at the boundary, we have found it quite useful and convenient for correlating such factors as distance of run and time of run to detonation for various booster systems. It has been found that a plot of the log of the distance of run of the shock wave vs the log of the pressure of the initiating shock wave as it enters the explosive is linear over an appreciable range. This relationship is shown for several explosives in Fig. 4. The data available for PBX-9404, which cover the widest pressure range, indicate that estimates made from curves of this type will be accurate to about 25%. The low pressure points for PBX-9404 correspond to velocities only 0.1 to 0.2 mm/ μ sec faster than the longitudinal sound velocity.

Usually the easiest measurement to make on small explosive systems is a measurement of transit time. If the explosive has been under-initiated it will take longer for the wave to traverse the piece than if the wave traveled at steady-state velocity throughout. The difference between the measured transit time and the time calculated on the basis of steady-state velocity is called the excess transit time. Because of the complex relationships between shock velocity, pressure, and distance of run, it is usually not possible to relate the excess transit time to distance of run and pressure. If data from wedge-type experiments are available for a particular explosive it is possible to construct curves of the type shown in Figs. 5 and 6. The excess transit times shown were calculated from wedge-type experiments by dividing the measured distance of run by the detonation velocity and subtracting this calculated time from the measured time to detonation. In this calculation the very small excess time, which exists because the detonation does not reach steady-state velocity at the position measured

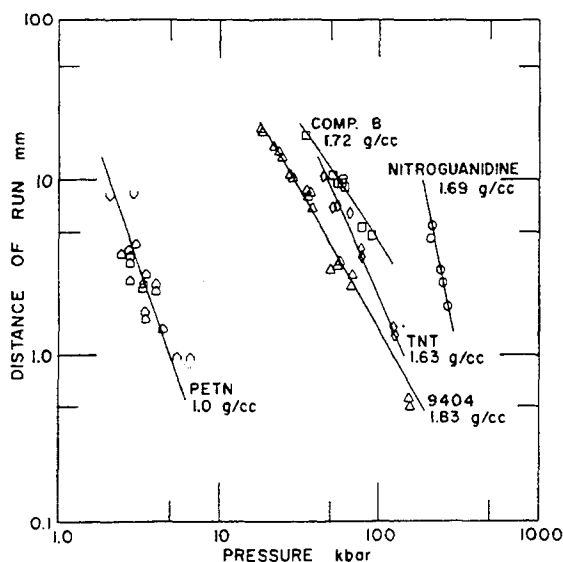


Fig. 4 - Relationship Between Distance to Detonation and Initial Shock Pressure for Various Explosives. The open symbols for PETN represent the maximum and minimum distances which could be measured. The points are located at the calculated pressures. The data for PETN are taken from Seay and Seely [16].

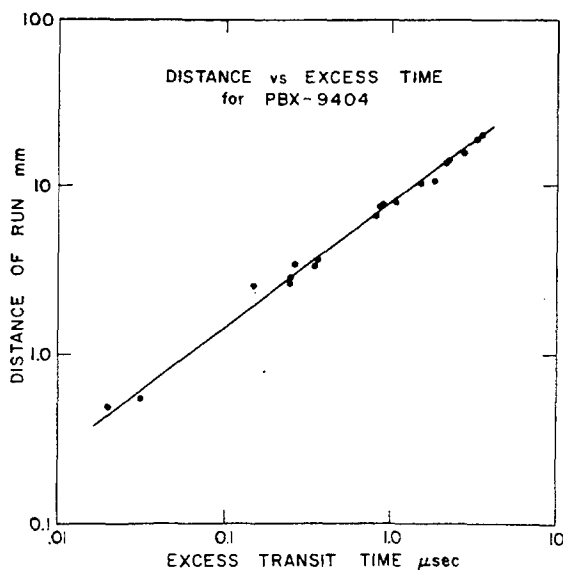


Fig. 5 - Distance of Run to Detonation vs Excess Transit Time for Plastic-Bonded HMX. $\rho_0 = 1.83 \pm 0.01$ g/cc.

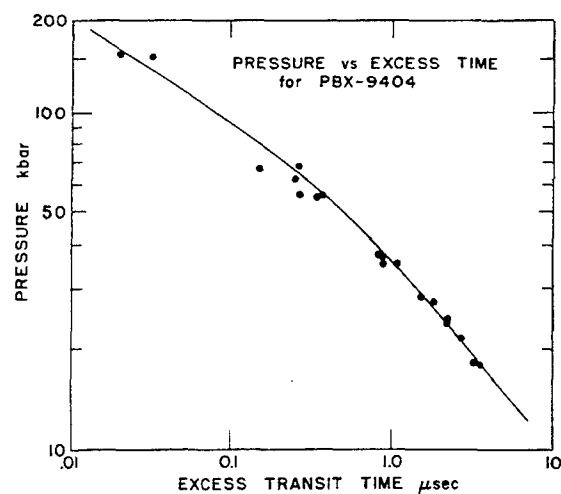


Fig. 6 - The Relationship Between the Initial Pressure and the Excess Transit Time for Plastic-Bonded HMX. $\rho_0 = 1.83 \pm 0.01$ g/cc.

as the point of onset of detonation, is neglected. This error is labeled as " t_e " in Fig. 1, and its size has been exaggerated for the purpose of illustration. In general, the increase in velocity is less than 200 m/sec. These curves have proved useful when it has been necessary to make a semiquantitative analysis of small charges.

As the initiation of solid explosives depends on such factors as particle size, density and exact composition, it seems that general curves for an explosive cannot be given, but that they must be produced for the particular lot being used.

SUMMARY

It has been shown for PBX-9404 and pressed TNT that, if the common treatment is made of the shock-wave data, the curves can be drawn through the detonation pressure point rather than the peak spike pressure point. If the usual assumptions are correct, then either the curves must be for partially reacted explosive or the curves must show a drastic change in slope above the experimentally measured range. Some of the inadequacies of the assumptions and analysis have been pointed out. It has been suggested that there is no model available now by which

one can calculate the details of the shock initiation of polycrystalline explosives.

A empirical linear relationship between the log of the shock pressure and the log of the distance of run to initiation has been presented in the hope that it may prove useful for engineering purposes. It has also been shown that the shock-wave data taken from wedge experiments may be used to relate the easily measured excess transit time to the initiating pressure and to the distance of run to detonation. These relationships have often been useful in obtaining a semiquantitative analysis of the behavior of a system.

ACKNOWLEDGMENT

The authors wish to thank the members of GMX Division who have contributed to this paper by supplying data and participating in many useful discussions. This work has been performed under the auspices of the United States Atomic Energy Commission.

REFERENCES

1. A. W. Campbell, W. C. Davis, J. B. Ramsay, and J. R. Travis, *Phys. Fluids*, **4**, 511 (1961).
2. E. F. Gittings, "Initiation by Short Duration Shocks," This Symposium.
3. C. L. Mader, LA-3077.
4. C. L. Mader, LA-3235.
5. T. P. Liddiard, "The Unreacted Shock Hugoniot for TNT and Composition B-3," International Conference on Sensitivity and Hazards of Explosives, London, 1-3 October, 1963.
6. V. S. Ilyukhin, P. F. Pokhil, O. K. Rozanov, and N. S. Shvedova, *Soviet Phys.-Doklady*, **5**, 337 (1960).
7. W. C. Davis, B. G. Craig, and J. B. Ramsay, "Failure of the Chapman-Jouguet Theory for Liquid and Solid Explosives," This Symposium.
8. B. G. Craig, 10th Symposium (International) on Combustion, pp. 863-867, The Combustion Institute, 1965.
9. W. B. Garn, private communication.
10. W. B. Garn, *J. Chem. Phys.* **30**, 819 (1959).
11. M. Ya. Vasil'ev, D. B. Balshow, and L. N. Mokrousov, *Russ. J. Phys. Chem. (English Transl.)*, **34**, 1159 (1960).
12. R. G. McQueen, and S. P. Marsh, *J. Appl. Phys.*, **31**, 1253 (1960).
13. P. D. Edwards, J. B. Finley, and D. E. Grimm, private communication.
14. B. G. Craig, private communication.
15. A. N. Dremin, and P. F. Pokhil, *Proc. Acad. Sci. USSR Phys. Chem. Sect. (English Transl.)*, **127**, 723 (1959).
16. G. E. Seay, and L. B. Seely, "Initiation of Low Density PETN Pressings by a Plane Shock Wave," 3rd Symposium on Detonation, Princeton, N. J., 1960.

COMMENTS

J. BERGER (Commissariat a l'Energie Atomique, France): I suppose your spike point as well as your detonation point are calculated for a steady detonation while your experiments refer to transient conditions. I think your experimental points are not likely to converge towards either of the steady points since the reactions are probably different in the steady and transient conditions, and the structure of the reaction zone is not the same in the two cases.

J. B. RAMSAY (Los Alamos Scientific Laboratory): The spike and detonation pressures discussed in this paper have been obtained from

experimental measurements and will lie on some locus of points representing the state variables of the explosive. They are at the present time our best estimates of these values. The transient conditions occurring during initiation must, by some mechanism, be transformed to the conditions occurring during steady-state detonation. The state points occurring during this transformation must also define some locus of points starting from the same initial state and ending at the spike point. This paper shows that for PBX-9404 and TNT either these two curves are not congruent or they must be highly curved. The conclusion reached is that low pressure shock-wave data should not be used to estimate the spike pressure.

LOW-PRESSURE HUGONIOTS OF SOLID EXPLOSIVES

Richard J. Wasley and Joseph F. O'Brien
*Lawrence Radiation Laboratory, University of California
Livermore, California*

ABSTRACT

The purpose of this work is to examine the characteristics of shock disturbances in solid explosives generated by low-velocity, one-dimensional, planar impacts. The pressure range is 3 to 25 kbar; these pressures and the time these pressures act are insufficient to initiate immediately steady-state detonations. Two materials are investigated, pressed TNT and an HMX-based plastic bonded explosive.

The principal experimental parameters of interest are shock velocity, particle velocity, and pressure in the impacted explosive. These quantities are derived from measurements with piezoelectric pins and quartz crystal pressure transducers. The latter measurements require arbitrary interpretation to obtain the desired information.

The results are expressed in terms of detailed Hugoniot data for the two explosives. The data appear to be representative of unreacted materials up to about 20 kbar. At pressures slightly above 20 kbar, both explosives exhibit evidence of chemical reaction for the sample and driver geometry given. At pressures below approximately 10 kbar, both explosives exhibit peculiarities of wave structure.

THE UNREACTED HUGONIOT EQUATIONS-OF-STATE OF SEVERAL EXPLOSIVES

N. L. Coleburn and T. P. Liddiard, Jr.
*U.S. Naval Ordnance Laboratory, White Oak
Silver Spring, Maryland*

ABSTRACT

Plane shock wave compressions and an optical method were used to obtain the unreacted equations-of-state of eleven explosives and propellants for pressures up to 90 kbar. Measurements of the transit times of weak shock waves (~100 bars) yielded approximate sound wave velocities and the initial slopes of the Hugoniot curves.

This paper has been published in J. Chem. Phys. **44**, 1929 (1966).

DETERMINATION OF SHOCK HUGONIOTS FOR SEVERAL CONDENSED PHASE EXPLOSIVES

V. M. Boyle, R. L. Jameson and M. Sultanoff
*Ballistic Research Laboratories
Aberdeen Proving Ground, Maryland*

ABSTRACT

Shock Hugoniot data for several military explosives are presented, and the experimental techniques used to obtain the data are briefly described. The shock velocity (U) is shown to be related to the particle velocity (u), behind the shock front, by the conventional linear relation, $U = c_0 + su$, where c_0 and s are experimentally determined constants.

Three different experiments are described. Two of the methods are basically refinements of techniques previously reported by others in the literature. The third experiment, designated the "split-charge experiment," is described for the first time. The latter experiment extends the range of data obtained by dynamic observations to much lower pressure ranges.

Streak rotating-mirror camera techniques were used to obtain records for shock velocity measurements. Various 'monitor' solids were placed in direct contact with the test explosive charges to obtain the experimental records. The pressure and particle velocity data were then inferred from the experimental results, using the well-known Rankine-Hugoniot conservation relations and impedance matching techniques, in conjunction with the well-defined Hugoniot relations for the 'monitor' materials.

The data, curves and equations presented, extend the range of values beyond those previously published. The range of the data reported, extends from essentially elastic 'sonic' values to the von Neumann spike pressures, and show good general agreement with the linear $U - u$ relationships and with results previously published in the literature for those cases where data is available for comparison. This data has not been previously reported for a number of these explosives. Limited experimental data indicate that agreement with the linear relation extends considerably beyond the spike pressure in the case of Baratol.

INTRODUCTION

An adequate description of strong shocks, propagating in condensed phase explosives, cannot be directly obtained because of the lack of experimental techniques for the direct determination of the hydrodynamic variable involved; i.e., shock velocity, particle velocity, pressure and density. Experiments were designed to obtain data for these hydrodynamic parameters which could be combined with the equations for conservation of mass and momentum to more fully describe strong shock waves in explosive charges.

The current state of technology in the field of instrumentation does not lend itself to the direct measurement of the dynamics of pressure, particle velocity and density. However, these parameters can be inferred, for shocked explosive charges, from the direct observations of shock velocity measured in inert monitor materials, placed in direct contact with the explosives [1-3].

The solids selected as monitors were those for which Hugoniot conditions are well established [4,5] and which readily lend themselves to accurate computational or graphical

determination of pressure and particle velocity from shock velocity measurements. The application of these well-known shock impedance matching techniques [1-3] has been used to extend the range of data for explosives tested earlier as well as to introduce data for explosives for which Hugoniot relationships have not been previously reported.

EXPERIMENTAL TECHNIQUES AND THEORETICAL DISCUSSION

Three different experiments were designed to determine values for a range of low pressure points, the von Neumann spike point, and a range of intermediate points. This program made possible a determination of the degree of confidence that could be assigned to the least square linear fit to the data obtained in these experiments. Each of these experimental techniques made use of nonexplosive 'monitor' materials for which the Hugoniot relationships were well defined [4,5].

The "split charge" experiment originally suggested by R. Vitali of these Laboratories, was used to determine the low pressure points, and is described here for the first time. This method requires a preliminary determination or calibration of the explosive-driver system to obtain the initial pressure transmitted into the test explosive. Thus, an explosive charge was used to transmit a shock through an aluminum barrier to a Plexiglas monitor. The Plexiglas was backlighted and the shock propagation velocity was recorded by the streak rotating-mirror camera. A time vs distance analysis of the streak camera record determined the shock velocity. Since the U vs u and the P vs u relationships are well defined for the aluminum [4] and Plexiglas [5], the pressure in the aluminum, at the Plexiglas interface is uniquely determined by the proper application of the interface equation [6]:

$$\frac{P_1}{P_2} = \frac{\rho_2 U_2 + \rho_1 U_1}{2\rho_2 U_2} \quad (1)$$

using values obtained from [4,5]

$$U = c_0 + su \quad (2)$$

$$P = \rho Uu \quad (3)$$

where

U = shock velocity,

u = particle velocity behind the shock,

P = pressure, and

ρ = density,

and the subscripts refer to the two different materials.

The Plexiglas was replaced by the test explosive charge, in slab form, split down the center. The slit, approximately 5 mils wide, was carefully filled with water and all precautions were taken to minimize the formation of bubbles in the slit. A backlight explosive flash bomb source was used to trans-illuminate the slit which was aligned optically with the slit of the rotating-mirror camera. Shocks of pre-determined strengths were transmitted into the explosive and their propagation was recorded by the streak camera as shock in the water layer. Typical records are shown in Figs. 1 and 2. When the shock transmitted into the explosive was reasonably strong (i.e., over 60 kilobars for Comp. B) a short run of almost constant velocity shock was followed by a build up to high order detonation (Fig. 1). With weaker shocks (i.e., down to about 20 kilobars for Comp. B) a longer run of almost constant velocity degraded to steady state sonic velocity (Fig. 2). The actual values of this build up and decay varied widely with the sensitivity of each explosive.

A time-distance analysis of the streak camera records was used to obtain the initial shock velocity U in the charge, for each previously determined pressure at the aluminum explosive interface. The standard technique of graphically reflecting the known aluminum Hugoniot in the P vs u plane around this pressure point was then employed, and a line with slope $P/u = \rho U$ for the explosive is drawn. The intersection of this straight line with the reflected aluminum Hugoniot must be at the pressure (P) in the explosive and this located a unique value for u , the particle velocity in the explosive. A series of values were determined in order to establish a Hugoniot curve for the explosive under test, and the $U = c_0 + su$ relationship for this range of pressure points was obtained.

A single U vs u curve can be determined from a series of specifically established pressures in the aluminum and a "zero point" (i.e., $u = 0$) check for the sonic velocity can be obtained from the measured slope in the low pressure tests where the reaction fades.

The higher pressure "build-up" records (Fig. 2) give, as a final velocity, normal high-order detonation. However, the von Neumann spike data cannot be obtained by this technique.

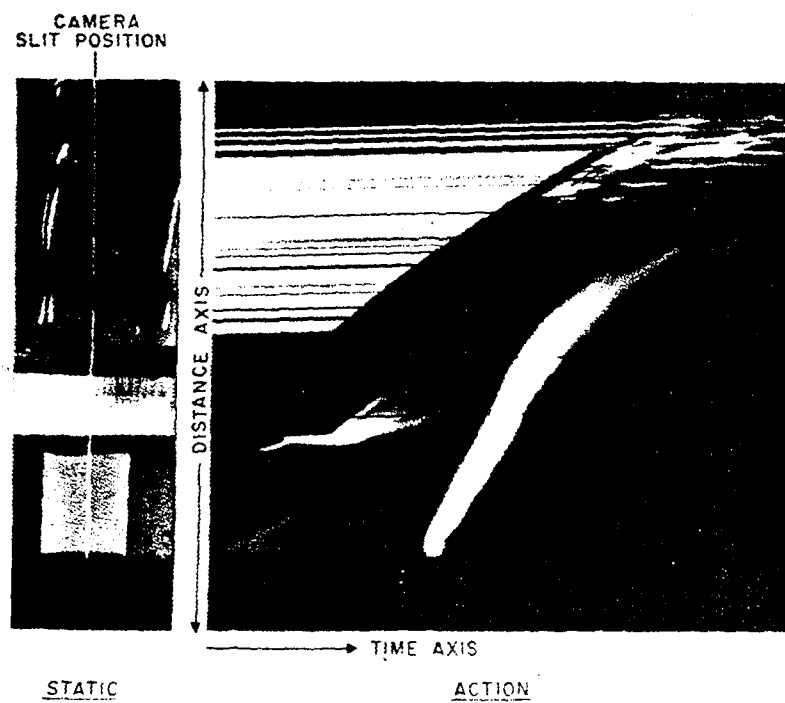


Fig. 1 - Streak rotating-mirror camera record of "split-charge" with decaying reaction

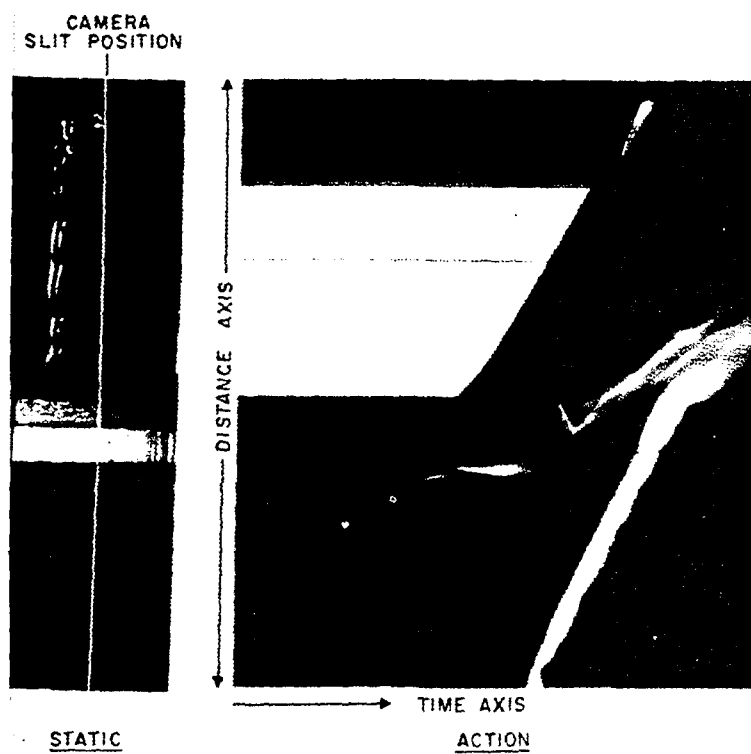


Fig. 2 - Streak rotating-mirror camera record of "split-charge" with build up to high-order detonation

The second experimental technique involves the determination of the von Neumann spike pressure for an explosive charge reacting under steady state high-order detonation conditions. A plane wave booster was placed directly in contact with the sample explosive in this experiment. Plexiglas discs of varying thickness [7] were located on the surface of the sample explosive and the streak camera was used to determine the average shock velocity through each disc (Fig. 3). The velocity at the interface was then determined by extrapolation, and since the Hugoniot for Plexiglas is well established the pressure at the interface is known. Using the interface Eq. (1), the spike pressure can be directly obtained. With this pressure known, the $P-U$ relationship can be solved for u , and the spike point is thus determined for the U vs u plane.

The split charge technique gave data in the pressure range up to about $1/3$ to $1/2$ detonation pressure and the Plexiglas disc technique gave spike pressure data. This located points for comparison with the linear relationship, $U = c_0 + sU$ curve at both extremes.

A wedge experiment was designed to obtain data to fill in this gap in the range of pressure between the high and the low points [8,9].

Briefly, a 2"x2" base by 22° wedge of test explosive was placed on a barrier of inert material, and this assembly was then placed on a plane wave booster. The plane wave lens and barrier were designed to produce pressures in the "middle region," previously noted. This design generated a plane shock of predetermined strength which moved parallel through the barrier interface and into the test explosive wedge. The wedge angle is less than the critical rarefaction angle for the explosive, preventing rarefaction from affecting the plane configuration of the shock in the critical observation region. As the shock arrived at the wedge free surface, a phase velocity can be recorded by reflected light with the streak rotating-mirror camera, Fig. 4, and a normal shock wave propagation velocity can then be obtained.

Two thin Plexiglas cover plates are overlaid on the wedge face, to extend the data to include pressure. The inner surfaces of these plastic monitors are partially silvered to give better resolution to shock arrival time illuminated by front lighting and recorded with the streak rotating-mirror camera. The simple interface equation (Eq. (1)) no longer holds with this arrangement. It must be modified to consider wave angle vs free surface and a correction for direction of propagation in the Plexiglas.

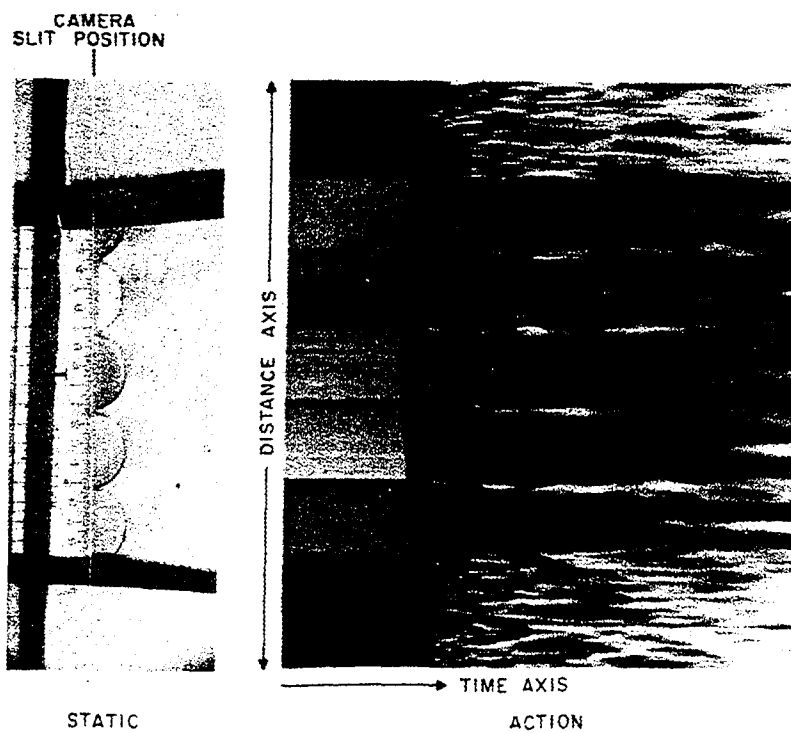


Fig. 3 - Streak rotating-mirror camera record of multithickness Plexiglas disc monitors

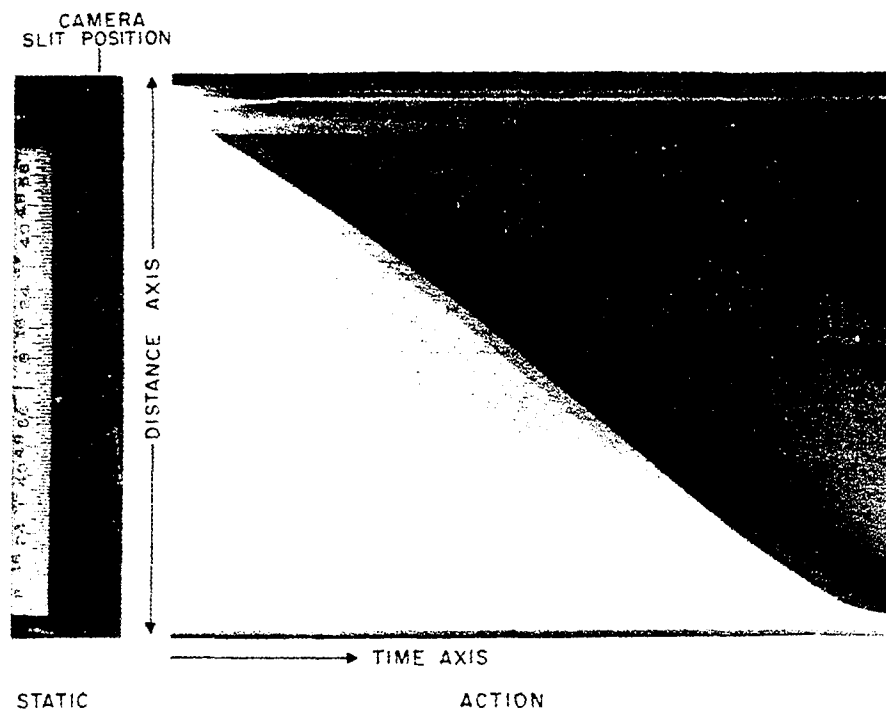


Fig. 4 - Streak rotating-mirror camera record of wedge experiment

These modifications of the interface equation are worked out in detail in Refs. 8 and 9.

RESULTS

Figure 5 is a list of the linear equations, $U = c_0 + su$, for the explosives tested having the average densities indicated with precision of $\pm 0.01 \text{ gm/cm}^3$. Figures 6a, b, c, d, e, f, and g, are the plots of these equations. A least square linear fit was made to the "split-charge" lower pressure points shown as circles; the 95% confidence limits for these fits are also plotted.

	DENSITY ($\pm 0.01 \text{ g/cm}^3$)	
PENTOLITE	(1.67 g/cm^3)	$U = 2.83 + 1.91 u$
COMP B	(1.70 g/cm^3)	$U = 2.95 + 1.58 u$
COMP B-3	(1.70 g/cm^3)	$U = 3.03 + 1.73 u$
TNT	(1.63 g/cm^3)	$U = 2.57 + 1.88 u$
75/25 OCTOL	(1.80 g/cm^3)	$U = 3.01 + 1.72 u$
76/24 BARATOL	(2.63 g/cm^3)	$U = 2.79 + 1.25 u$
NITROSOL	(1.87 g/cm^3)	$U = 2.14 + 2.36 u$

Fig. 5 - Hugoniot data for various military explosives

A cross, representing the von Neumann spike data is plotted on all of the graphs and the triangles shown on the Comp. B plot are data from the wedge experiment.

An "overdriven" high pressure point, obtained from a single flying plate experiment, is shown on the plot for Baratol [10].

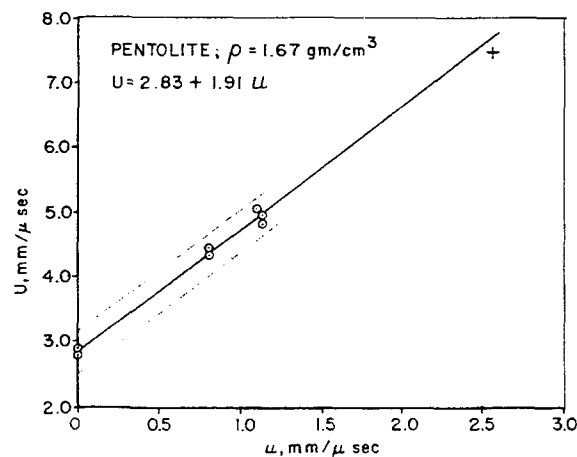


Fig. 6a - U vs u plots for Pentolite

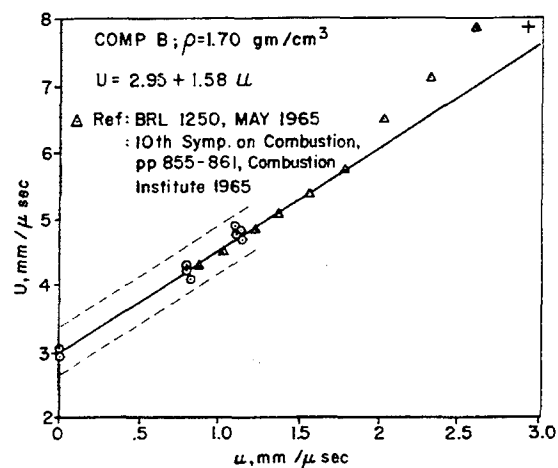


Fig. 6b - U vs u plots for Comp. B

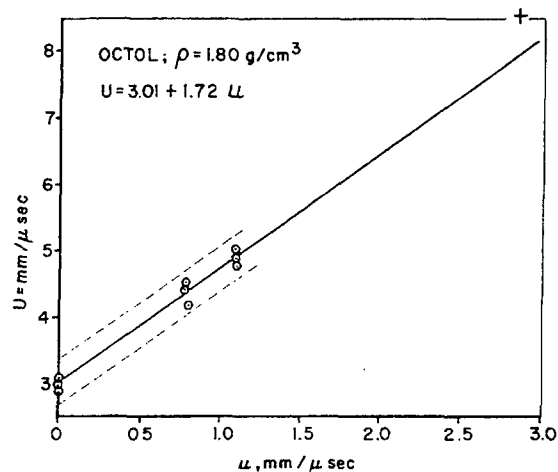


Fig. 6e - U vs u plots for Octol

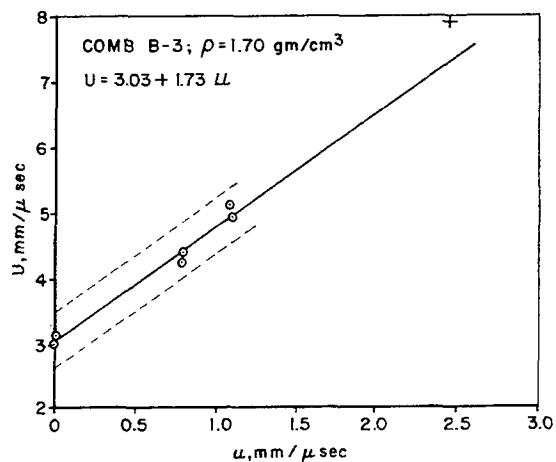


Fig. 6c - U vs u plots for Comp. B-3

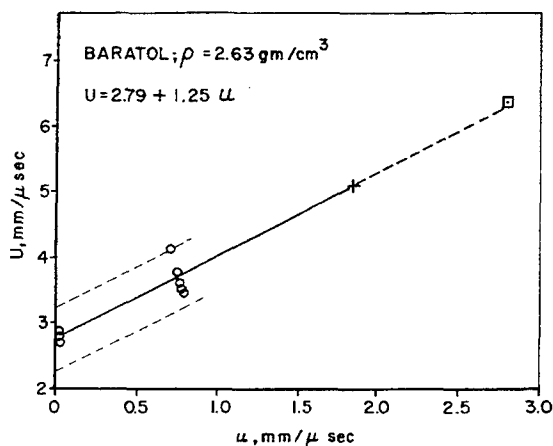


Fig. 6f - U vs u plots for Baratol

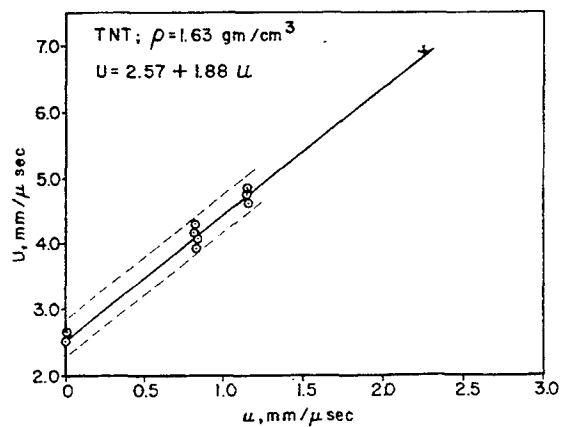


Fig. 6d - U vs u plots for TNT

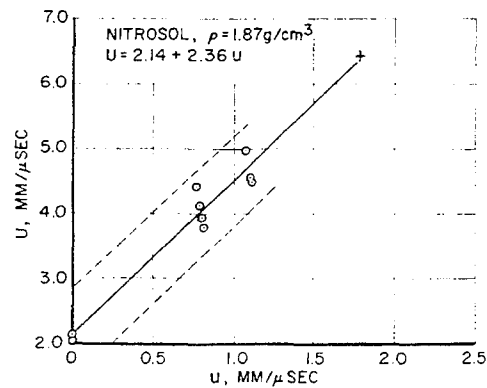


Fig. 6g - U vs u plots for Nitrosol

SUMMARY AND DISCUSSION

In general, the agreement of the spike point to the extrapolated low pressure straight line $U = c_0 + su$ fit appears to be inversely related to the reaction zone length. This deviation very probably results from the presence of appreciable chemical reaction during the time required for the shock to traverse the thin (0.53 mm) Plexiglas overlay, the thinnest specimen used in these particular experiments. Baratol, which has a very long reaction zone shows excellent agreement even at the very high overdriven pressure.

The least square U vs u line for Comp. B is in good agreement with work of other investigators [11,12]. Tests are being conducted to determine the possible contributions of chemical kinetics to these deviations.

REFERENCES

1. A. W. Campbell, W. C. Davis, and J. R. Travis, Phys. Fluids 4, 498, 1961.
2. A. W. Campbell, W. C. Davis, J. F. Ramsey, and J. R. Travis, Phys. Fluids 4, 511, 1951.
3. M. H. Rice, R. G. McQueen, and J. M. Walsh, Solid State Phys. 6, 1-63, Academic Press, 1958.
4. J. M. Walsh, M. H. Rice, R. G. McQueen, and F. L. Yarger, Phys. Rev. 108, 196, 1957.
5. G. Hauver, Ballistic Research Laboratories (Plexiglas Data, by private communication).
6. J. S. Rinehart, NOTS TP 3798, May 1965.
7. W. B. Garp, J. Chem. Phys. 30, 819 (1959).
8. V. M. Boyle, R. L. Jameson, and F. E. Allison, BRL Report No. 1250, May 1964.
9. V. M. Boyle, R. L. Jameson, and F. E. Allison, Combustion Institute (10th Symposium) 855-861, 1965.
10. J. Kineke, Ballistic Research Laboratories (private communication).
11. T. P. Liddiard, Jr., Int. Conf. on Sensitivity and Hazards of Explosives, ERDE, Ministry of Aviation, Waltham Abby, Essex, England, Oct. 63.
12. R. E. Duff and E. Huston, J. Chem. Phys. 23, 1268, 1955.

SHOCK INDUCED PHASE TRANSITIONS

George E. Duvall and Y. Horie

*Physics Department, Washington State University
Pullman, Washington*

ABSTRACT

Phase transitions for which $\Delta V < 0$ are classified into three types depending upon the signs of dP/dT and dS/dT at the phase boundary. Two for which dS/dT is positive are physically significant. The third, for which $dS/dT < 0$, is curious but unknown. This classification allows a nearly unique ordering of the slopes of adiabat and isotherm in the pure phase, the slope of the phase boundary and the slope of the adiabat in the mixed phase. Formulae for adiabatic and Hugoniot curves in the mixed phase are given and their slopes are compared. For $dP/dT > 0$ and $dS/dT > 0$, they bear the same relation as in a pure phase; for $dP/dT < 0$ the order is reversed. Shock-induced phase changes in bismuth, iron, and quartz are discussed and a comparison is made between dP/dT measured directly and that calculated from Hugoniot data. Discrepancies between the two in bismuth and quartz are in accord with other evidence that the shock does not produce equilibrium states in these materials. In iron the evidence is contradictory and suggestions are made for resolving the discrepancies.

INTRODUCTION

Both Duhem [1] and Rayleigh [2] were aware of the stability problem in the propagation of shock waves; the first for a very general equation of state and the second for gases. However, it was apparently not until Bethe's 1942 paper [3] that the importance of phase transitions in producing multiple compression shock waves and rarefaction shocks was realized. Several more years elapsed before experimentally observed instabilities were reported; the first such report was of a three wave compression shock structure in iron by Minshall in 1954 [4]. The existence of three waves was attributed to elastic failure of the material at the yield point and to transition to a new phase at 130 kb pressure. Since then there have been a number of studies of the wave structure due to elastic-plastic yield or to fracture [5] and multiple shock structures have been related to phase transitions in bismuth [6], iodine [7], quartz [8,9], carbon, silicon, and germanium [5].

The amount of shock data involving phase transitions is increasing and the pressure range of static measurements has been extended to effectively overlap the shock measurements; consequently it is appropriate at this time to reexamine the thermodynamics of phase

transitions as it applies to wave propagation. In so doing we expect to learn how to relate static measurements, shock measurements and thermodynamic calculations so as to gain the greatest knowledge of material properties in these extreme environments of high pressures rapidly applied.

CLASSIFICATION OF TRANSITIONS

Considerations are herein restricted to those first order transitions for which $\Delta V < 0$; i.e., the material starts in a pure Phase 1 and after application of sufficient pressure it is converted to a pure Phase 2 of higher density than 1. For conventional studies of transitions under quasi-static conditions it is necessary to control only the two intensive thermodynamic variables, pressure P , and temperature T ; then the change of specific volume, ΔV , can be measured as a function of either P or T . The condition that the Gibbs free energy be stationary during the transition leads to the Clausius-Clapeyron equation

$$dP/dT = \Delta S/\Delta V; \quad (1)$$

and from this the change in specific entropy, ΔS , can be determined as a function of P or T . When the transition process is described in the

P-V plane, the isotherms in the transition region satisfy the condition $(\partial P/\partial V)_{TM} = 0$.* In this way the transition process is fully described.

When a transition is occurring dynamically, as during passage of a wave of dilatation, neither P nor T remains constant. Changes in P and V are related with one another and with changes in the particle velocity through the equations of continuity and motion. They are related to changes in S and T through the equation of state. In short, it is now necessary to consider in detail and simultaneously the changes in three of the variables, P, V, S, T. If we neglect transfer of heat between adjacent mass elements, then infinitesimal changes in P or V propagate with adiabatic sound velocity. So long as dynamic effects are neglected, the transition process is reversible; therefore changes of state of a mass element are isentropic in continuous flow. In a shock transition they are described by the Rankine-Hugoniot equation. Then attention should be directed primarily to the isentropes and R-H curves in the P-V plane.

It turns out to be convenient to distinguish between types of transition according to the relative disposition of Phase 1, Phase 2 and the Mixed Phase region, or C-region, in the S-T plane. We define transitions of Types 1, 2, and 3 as shown in Table 1. The following material conditions are assumed here and throughout for pure phases:

$$(\partial V/\partial T)_P > 0 \quad (2)$$

$$(\partial V/\partial P)_S < 0. \quad (3)$$

These are similar to but somewhat more restrictive than Conditions II and III of Bethe's paper. All materials of interest in this report will satisfy them.

TABLE 1
Classification of Phase Transitions
 $\Delta V < 0$

Type of Transition	ΔS	dP/dT	dS_1/dT
1	> 0	< 0	> 0
2	< 0	> 0	> 0
3	< 0	> 0	< 0

*Here and in what follows the subscript "M" refers to quantities evaluated in the transition region or region of mixed phase; "1" refers to quantities on the phase boundary in Phase 1.

The dispositions of phases in the S-T plane for the three types are shown in Fig. 1. Under Cond. (2) this classification is exhaustive. This can be seen as follows:

$$\begin{aligned} dS_1/dT &= (\partial S/\partial T)_{P1} + (\partial S/\partial P)_{T1} dP/dT \\ &= C_{P1}/T - (\partial V/\partial T)_{P1} dP/dT. \end{aligned} \quad (4)$$

When $dP/dT < 0$, dS/dT is always positive; when $dP/dT > 0$, dS/dT may be either positive or negative. Most transitions between condensed phases are of Type 2 [10]; a substantial number are of Type 1; and those of Type 3 are very rare if they exist at all.

PHASE BOUNDARIES IN THE P-V PLANE

Consider $V = V(P, T)$, then

$$\begin{aligned} \left(\frac{\partial V}{\partial P}\right)_{S1} &= \left(\frac{\partial V}{\partial P}\right)_{T1} + \left(\frac{\partial V}{\partial T}\right)_{P1} \left(\frac{\partial T}{\partial P}\right)_{S1} \\ &= \left(\frac{\partial V}{\partial P}\right)_{T1} + \frac{T}{C_{P1}} \left(\frac{\partial V}{\partial T}\right)_{P1}^2 \end{aligned} \quad (5)$$

$$\frac{dV_1}{dP} = \left(\frac{\partial V}{\partial P}\right)_{T1} + \left(\frac{\partial V}{\partial T}\right)_{P1} \frac{dT}{dP}. \quad (6)$$

Eq. (5) implies that

$$(\partial V/\partial P)_{S1} > (\partial V/\partial P)_{T1}. \quad (7)$$

For transitions of Type 1, Cond. (2) and Eq. (6) imply that

Type 1

$$dV_1/dP < (\partial V/\partial P)_{T1}. \quad (8)$$

For transitions of Type 2, Eq. (4) implies that

$$dT/dP > (T/C_{P1})(\partial V/\partial T)_{P1}. \quad (9)$$

therefore, comparison of Eqs. (5) and (6) leads to the conclusion that

Type 2

$$dV_1/dP > (\partial V/\partial P)_{S1}. \quad (10)$$

For transitions of Type 3,

$$dV_1/dP > (\partial V/\partial P)_{T1}. \quad (11)$$

since $dT/dP > 0$; and

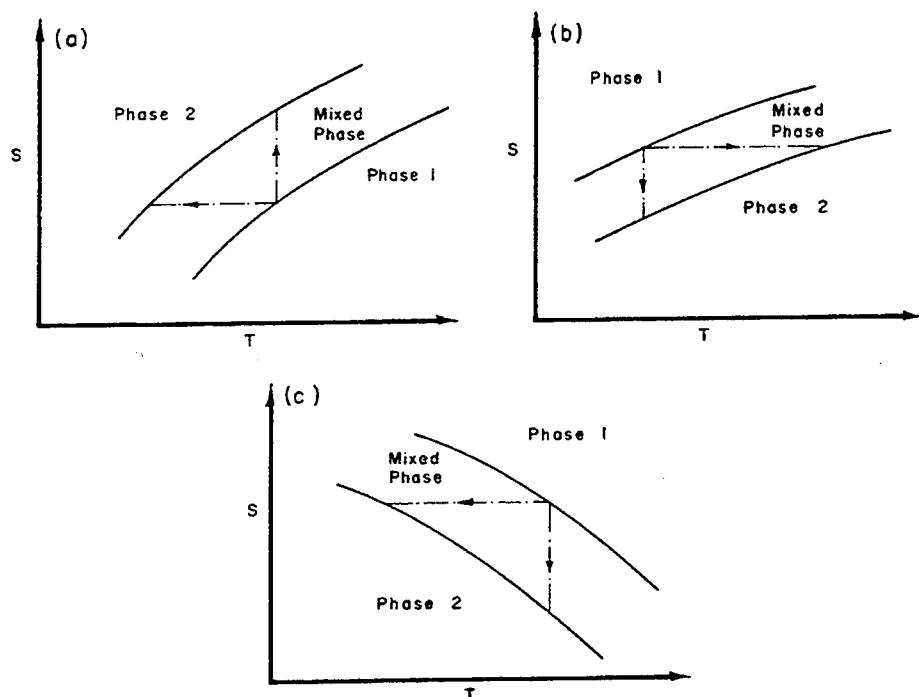


Fig. 1 - Three types of phase transition: (a) Type 1, $dP/dT < 0$, $dS/dT > 0$; (b) Type 2, $dP/dT > 0$, $dS/dT > 0$; and (c) Type 3, $dP/dT > 0$, $dS/dT < 0$

$$dV_1/dP < (\partial V/\partial P)_{S_1}, \quad (12)$$

since the inequality of Cond. (9) is now reversed.

The relative values of these derivatives are illustrated in Fig. 2. For Type 1 and 3 the slope of the phase boundary must be negative in the P-V plane; for Type 2 it may have either sign. Note also that the P-V plane is multiply-mapped by pure phase and mixed phase regions. This results from projection of the P-V-T surface onto the P-V plane. This may cause difficulty in wave computations unless proper account is taken of the history of a mass element or unless the appropriate three-dimensional equation of state is used.

ADIABATS IN MIXED PHASE

Slope Discontinuity at Phase Boundary

Let Z denote any extensive thermodynamic variable. Its value in the mixed phase region, if surface energies are neglected, is

$$Z(P, V) = Z_1 + \frac{V - V_1}{\Delta V} (Z_2 - Z_1) \quad (13)$$

where $Z_1(P)$ and $Z_2(P)$ denote values on the boundaries of the mixed phase region. For the entropy, S , Eq. (13) becomes, using Eq. (1),

$$S(P, V) = S_1(P) + (V - V_1) \frac{dP}{dT}. \quad (14)$$

In order to calculate the adiabat, we find values of P and V in the C-region for which S has the same value as the reference point (P_A, V_A) on the boundary. Then

$$S(P, V) = S(P_A, V_A) + \int_{P_A}^P \frac{dS_1}{dP} dP + (V - V_1) \frac{dP}{dT}.$$

Since $S(P, V) = S(P_A, V_A)$, this yields for the equation of the adiabat in the C-region:

$$\int_{P_A}^P \frac{dS_1}{dP} dP + (V - V_1) \frac{dP}{dT} = 0. \quad (15)$$

Differentiating this with respect to P yields an equation for the adiabatic slope:

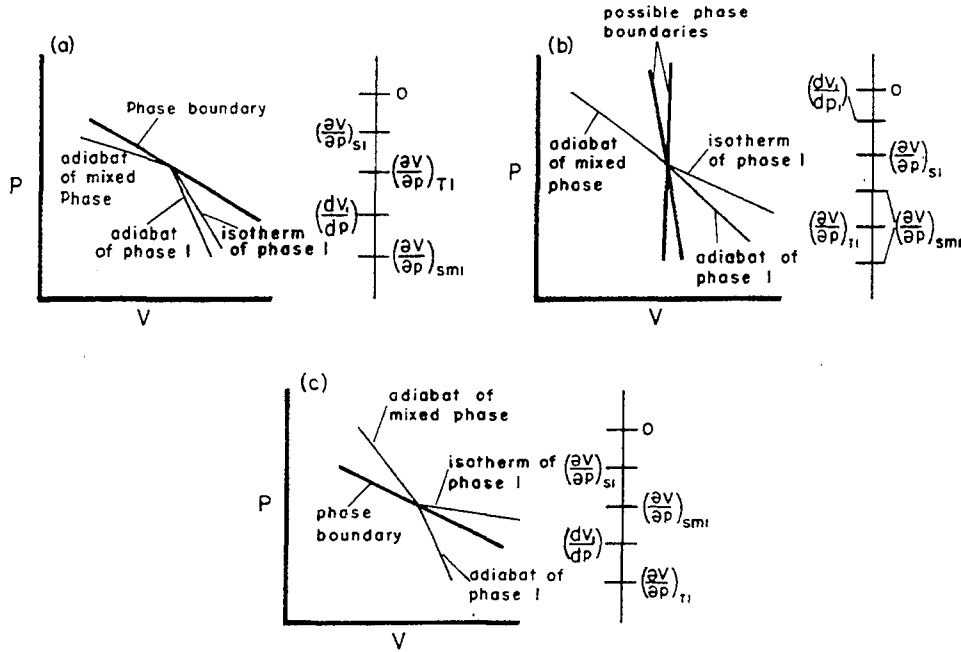


Fig. 2 - Relative slopes in the P-v plane:
(a) Type 1; (b) Type 2; and (c) Type 3

$$\left(\frac{\partial v}{\partial p}\right)_{SM} = \frac{dv_1}{dp} - \frac{dS_1}{dT} \left(\frac{dT}{dp}\right)^2 \quad \left(\frac{\partial^2 p}{\partial v^2}\right)_S > 0 \text{ for stability,} \quad (20)$$

$$- (V - V_1) \frac{d}{dp} \left(\ln \frac{dp}{dT} \right). \quad (16)$$

Setting $v = v_1$ yields the value at the phase boundary:

$$\left(\frac{\partial v}{\partial p}\right)_{SM1} = \frac{dv_1}{dp} - \frac{dS_1}{dT} \left(\frac{dT}{dp}\right)^2. \quad (17)$$

From Eqs. (4), (5) and (6),

$$\left(\frac{\partial v}{\partial p}\right)_{S1} = \frac{dv_1}{dp} - \frac{T}{C_{P1}} \left(\frac{\partial v}{\partial T}\right)_{P1} \frac{dT}{dp} \frac{dS_1}{dT}. \quad (18)$$

Subtracting Eq. (18) from Eq. (17) yields

$$\left(\frac{\partial v}{\partial p}\right)_{S1} - \left(\frac{\partial v}{\partial p}\right)_{SM1} = \frac{T}{C_{P1}} \left(\frac{dS_1}{dT}\right)^2 > 0; \quad (19)$$

i.e., the adiabat in the mixed phase region is always less steep than that in Phase 1. Since this violates Bethe's stability Condition 1, i.e.,

the phase boundary is always a point of instability in shock compression for some initial state in Phase 1.

If a single shock into the C-region from a state (P_o, v_o) in Phase 1 is to be stable, adiabatic sound velocity in the mixed phase region must exceed the shock propagation velocity relative to material in the boundary state (P_A, v_A) , i.e., it must be true that

$$\left(\frac{\partial v}{\partial p}\right)_{SM1} > \frac{v_A - v_o}{P_A - P_o}. \quad (21)$$

Violation of this condition insures that a second shock with initial state (P_A, v_A) will follow the first shock for some range of final amplitudes $P > P_A$. For transitions of Type 1, $dS_1/dT > 0$ and, from Eq. (17),

Type 1

$$\left(\frac{\partial v}{\partial p}\right)_{SM1} < dv_1/dp. \quad (22)$$

For transitions of Type 2, Eqs. (4), (6) and (17) can be combined to yield

$$\left(\frac{\partial V}{\partial P}\right)_{SM1} - \left(\frac{\partial V}{\partial P}\right)_{T1} = - \left(\frac{dT}{dP}\right)^2 \left[2 \frac{dS_1}{dT} - \frac{C_{P1}}{T} \right]. \quad (23)$$

The right-hand side of Eq. (23) is normally negative, though it may have either sign. Consequently the only positive statement that can be made about this case is that

$$(\partial V/\partial P)_{SM1} < (\partial V/\partial P)_{S1};$$

however it will be usually true that

Type 2

$$(\partial V/\partial P)_{SM1} < (\partial V/\partial P)_{T1}. \quad (24)$$

For Type 3, Eqs. (17) and (19) yield the result that

Type 3

$$(\partial V/\partial P)_{S1} > (\partial V/\partial P)_{SM1} > dV_1/dP. \quad (25)$$

These relations are illustrated in Fig. 2.

RANKINE-HUGONIOT CURVE IN MIXED PHASE

The R-H curve and adiabat in a normal material of single phase have a second-order contact at the foot of the Hugoniot [11], i.e., in the undisturbed material into which the shock is propagating; the entropy difference between Hugoniot and adiabat is then third order in the compression. If the intersection of phase boundary and Hugoniot (P_A, V_A) , is a point of instability for a single shock with final amplitude in the C-region or Phase 2, then the relation between that portion of the Hugoniot originating at (P_A, V_A) and the adiabat through (P_A, V_A) is the same as that existing between adiabat and Hugoniot in a single phase. This can be verified by direct calculation along the lines indicated below.

The locus of the R-H curve in the C-region is determined by equating the change of enthalpy given by the R-H equation to that calculated along a suitable path from the initial point (P_A, V_A) to the final point (P, V) , i.e.,

$$\begin{aligned} H(P, V) - H_A &= \frac{1}{2} (P - P_A)(V + V_A) \\ &= \int_{P_A}^P \frac{dH_1}{dP} dP + (V - V_1) \Delta H / \Delta V. \end{aligned} \quad (26)$$

Eq. (1) gives $T dP/dT = \Delta H / \Delta V$; substituting this into Eq. (26) and differentiating with respect to V yields an expression for the slope of the Hugoniot in the C-region:

$$\begin{aligned} \left(\frac{dV}{dP}\right)_{RH} \left\{ 1 - \frac{1}{2T} \frac{dT}{dP} (P - P_A) \right\} &= \frac{dV_1}{dP} - \frac{dS_1}{dT} \left(\frac{dT}{dP}\right)^2 \\ &- (V - V_1) \frac{d}{dP} \left(\ell_n \frac{dP}{dT} \right) + \frac{(V_A - V)}{2T} \frac{dT}{dP}. \end{aligned} \quad (27)$$

Here the following identity has been used:

$$dH_1/dP = V_1 + T dS_1/dP.$$

At the phase boundary,

$$(dV/dP)_{RH} = (dV/dP)_{RH1} = (\partial V/\partial P)_{SM1}.$$

At points in the C-region, removed from the boundary, a relation can be established between adiabat and R-H slopes which is analogous to that in a single phase. For a single phase, Eq. (A2) of Ref. 12 reads

$$1 - \frac{a^2}{c^2} = \frac{\Gamma}{2V} (V_o - V) \left\{ 1 - \frac{(U - u)^2}{c^2} \right\}, \quad (28)$$

where

$$c^2 = -V^2 (dP/dV)_{RH}$$

$$a^2 = -V^2 (\partial P/\partial V)_S$$

$$\Gamma = (V/C_V)(\partial P/\partial T)_V$$

$$(U - u)^2 = V^2 (P - P_o)/(V_o - V).$$

A relation identical in form can be derived for the C-region. Write Eq. (27) in the form

$$\left(\frac{dP}{dV}\right)_{RH} = \left(\frac{\partial P}{\partial V}\right)_{SM} (1 - C)/(1 + D) \quad (29)$$

where

$$C = (P - P_A)(dT/dP)/2T$$

$$D = (V_A - V)(dT/dP)(\partial P/\partial V)_{SM}/2T.$$

Define c^2 , a^2 , and $(U - u)^2$ as in Eq. (28); then Eq. (29) becomes

$$1 - \frac{a^2}{c^2} = \frac{\Gamma_M}{2V} (V_A - V) \left[1 - \frac{(U-u)^2}{c^2} \right], \quad (30)$$

where

$$\Gamma_M = \frac{V}{C_{VM}} \frac{dP}{dT} = - \frac{V}{T} \left(\frac{\partial P}{\partial V} \right)_{SM} \left(\frac{dT}{dP} \right), \quad (31)$$

$$C_{VM} = T(\partial S / \partial T)_{VM},$$

$$(\partial P / \partial T)_{VM} = (\partial P / \partial T)_{SM} = dP/dT,$$

$$(U-u)^2 = V^2(P - P_A)/(V_A - V).$$

Specific heat in the C-region can also be expressed as

$$C_{VM} = T \frac{dS_1}{dT} + T(V - V_1) \frac{d^2P}{dT^2} - T \frac{dV_1}{dP} \frac{dP}{dT}; \quad (32)$$

this is obtained by differentiating Eq. (15). In order to determine the sign of $c^2 - a^2$, note that the bracket in Eq. (30) has the sign of

$$(d^2P/dV^2)_{RH}$$

and that the sign of $(\partial P / \partial V)_{SM}$ in Eq. (31) can be obtained from the identity

$$\left(\frac{\partial V}{\partial P} \right)_{SM} = \left(\frac{\partial V}{\partial P} \right)_{SM1} - (V - V_1) \frac{d}{dP} \left(\ln \frac{dP}{dT} \right), \quad (33)$$

where $(\partial V / \partial P)_{SM1}$ is evaluated at $V_1(P)$. The second term on the right-hand side of Eq. (33) could in principle be positive and of sufficient magnitude to override the first and make the left-hand side negative. This appears to be highly unlikely, so we assume $(\partial V / \partial P)_{SM} < 0$. Then we have the following result:

$$\text{sgn}(c^2 - a^2) = \text{sgn}(d^2P/dV^2)_{RH} \text{sgn}(dT/dP). \quad (34)$$

For

$$(d^2P/dV^2)_{RH} > 0,$$

Type 1

$$c^2 - a^2 < 0;$$

Types 2 and 3

$$c^2 - a^2 > 0.$$

The relations between R-H curve, adiabats and the phase boundary are illustrated in Fig. 3 for Type 1; Type 2 is normal and Type 3 is of no interest.

For $(d^2P/dV^2)_{RH} < 0$, no compression shock will be formed.

The curvature of the adiabat in the C-region depends upon second order thermodynamic coefficients and no attempt will be made to

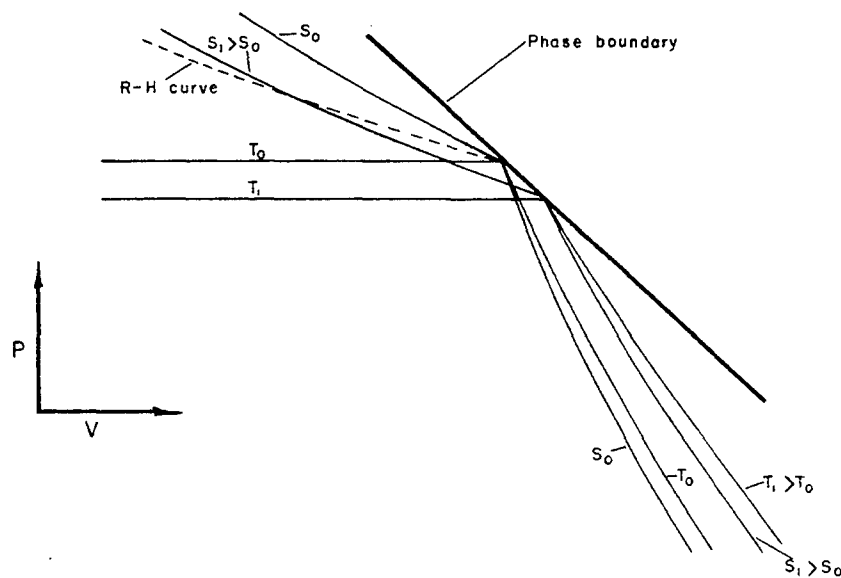


Fig. 3 - Anomalous R-H curve for Type 1 transition

estimate its sign. Bethe [3] expresses the belief that it is always positive, but does not supply a proof that this is so.

EXAMPLES

Some data pertaining to phase transitions in bismuth (Bi 1 - Bi 2), iron (α - h.c.p.), and quartz (α - stishovite) are given in Table 2. Subscript "A" refers to the intersection of the phase boundary and the Hugoniot passing through the material initially at room temperature and atmospheric pressure. Values of specific heat and thermal expansion coefficients are taken at atmospheric pressure. Values of dV_1/dP are determined from Eq. (6); values of $(dP/dT)_{calc}$ are obtained from Eq. (17), using

Eqs. (4), (5), and (6) to evaluate the total derivatives.

Bismuth

Shock measurements of first wave amplitude for different initial temperatures in the specimen yield a value for dP/dT very close to that obtained by Bridgman [14] (Table 2). Second wave amplitudes for fixed initial temperature were also measured, and these were used to obtain, by extrapolation, a value for $(dV/dP)_{RH1} = (\partial V/\partial P)_{SM1}$. This is entered as β_{RH1} in Table 2. It differs appreciably from β_{ADM1} , which is calculated from Eq. (17), using the static value for dP/dT . Substitution of β_{RH1} into Eq. (17) produced the value of $(dP/dT)_{calc}$.

TABLE 2
Physical Data on Phase Transitions

	Bismuth	Iron	Quartz (Stishovite)
V_o , cc/g	0.1020	0.128	0.3775
C_{P1} , kb cc/g °C	1.21×10^{-3} [6]	4.51×10^{-3}	9.2×10^{-3}
α_1 , °C	40.2×10^{-6} [6]	36.3×10^{-6}	38.4×10^{-6}
β_1 , kb ⁻¹	2.46×10^{-3} [6]	0.51×10^{-3} [15]	0.76×10^{-3}
P_A , kb	25.3*	132 [15]	144 [10]
V_A , cc/g	0.0929 [14]	0.1197 [15]	0.3145 [10]
T_A , °K	315 [6]	310 [15]	476 [10]
dP/dT , kb/°C	-0.0500 [14] -0.0508 [6]	-0.075 [16]	+0.0177 [9]
ΔV , cc/g	-0.0047 [14]	-0.0041 [15]	
$(-1/V) dV_1/dP$	2.86×10^{-3}	0.99×10^{-3}	-1.5×10^{-3}
β_{RH1} , kb ⁻¹	13×10^{-3} [6]	2.18×10^{-3}	1.59×10^{-3}
β_{ADM1} , kb ⁻¹	21×10^{-3}	23×10^{-3}	194×10^{-3}
$(dP/dT)_{calc}$, kb/°C	-0.067 [6]	-0.29	+0.225

*Adjusted to static value.

Numbers in brackets indicate references at end of paper. If no reference is indicated, numbers are from Smithsonian tables or calculated here.

α = isobaric volume expansion coefficient,

β_1 = isothermal compressibility of pure phase,

β_{ADM1} = adiabatic compressibility of mixed phase, and

$\beta_{RH1} = (-1/V)(dV/dP)_{RH1}$.

in the last row of Table 2. It differs considerably from the static value; the difference may result from extrapolation errors, which the authors [6] estimate at 60%, from inadequate thermodynamic data, or from physical differences between shock and static compression. Such differences include time or rate effects, shear stresses, and the possibility that the second shock data lie outside the C-region.

The R-H curve in the C-region has been constructed from Eq. (26), following a procedure described by Rice et al. [18] and assuming that C_{V1} , dP/dT , and $(\partial P/\partial T)_{V1}$ are constant. The result is shown in Fig. 4; it differs from the measured points for reasons which cannot be determined with available knowledge. This difference, coupled with the offset of the phase boundary from the static value, suggests that rate effects may be responsible for the differences, but this is pure conjecture.

Iron

This is the first material for which multiple shock structures due to a phase change

were reported [4]. An extensive set of experiments in which initial temperatures were varied was reported in 1962 [16] and from these it appeared that a new phase was present. This has since been verified in static experiments [13], and the new phase has been established as h.c.p. The data of reference [16] give $dP/dT = -0.075 \text{ kb}/^\circ\text{C}$ directly. This substituted into Eq. (17) gives β_{ADM1} , shown in Table 2. Minshall's data, as reported by Bancroft et al. [15] include measurements of the second shock amplitude. These can be extrapolated to obtain β_{RH1} as reported in Table 2. This is only 10% of β_{ADM1} ; the difference is much greater than was found for Bi. The value of $(dP/dT)_{calc}$ derived from β_{RH1} differs correspondingly from the directly measured value. Remarkably enough it is the same as dP/dT for the $\alpha - \gamma$ transition as determined by Claussen and others [16].

It is difficult to attribute such a difference to rate effects in shock, since the first-wave amplitudes agree very well with the static values. Moreover there is little evidence for decay of the 130 kb wave, which further indicates the absence of rate effects. The resolution of

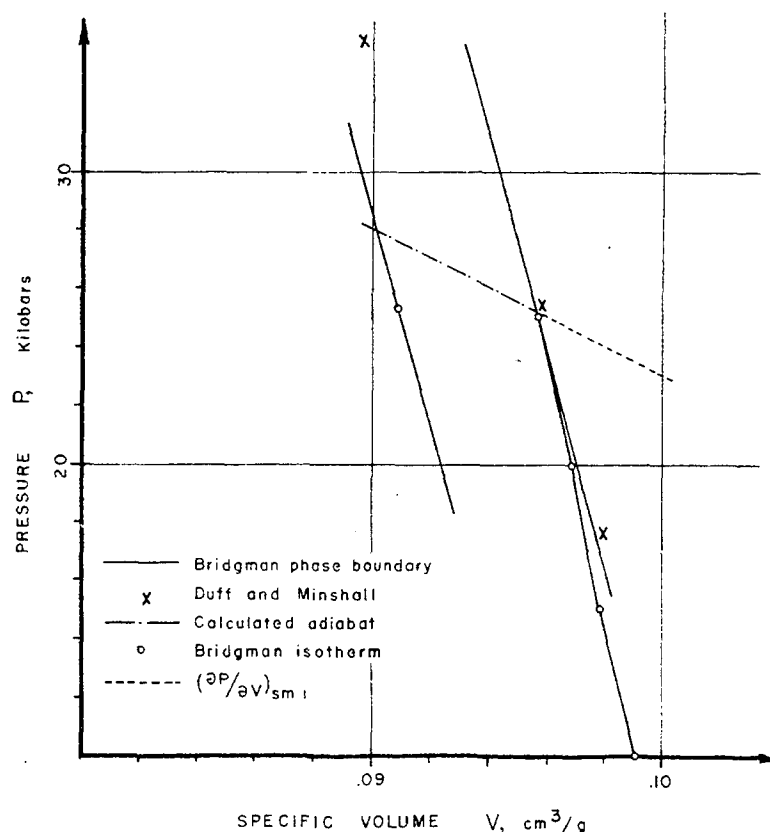


Fig. 4 - Phase diagram for bismuth

this puzzle must await additional measurements—preferably near the transition point.

Quartz

The two known high density forms of quartz are coesite and stishovite. The former is produced at relatively low pressures but is a slow transition and is believed to be produced to only a limited extent by shock compression [9]. Stishovite is believed to be produced in shock [8,9] under the conditions shown in Table 2; this is believed not to be an equilibrium point [9]. Nonetheless the Wackerle compression data have been used in Eq. (17) to determine $(dP/dT)_{calc}$. The result, shown in the last row and column of Table 2 is about twelve times greater than the static value quoted by Ahrens [9]. This can be regarded as confirmation of the nonequilibrium character of the transition. The work by Ahrens and Gregson suggests that shock recovery experiments can be used to study the kinetics of the transition, but this remains to be done.

DISCUSSION

The ordering of slopes in the P-V plane for transitions of Types 1 and 2 appears to be a useful minor tool in the evaluation of shock data. Transitions of Type 3, though curious, are of no importance. Of greater importance is the relation between adiabatic slope in the mixed phase region and dP/dT ; this allows cross comparisons to be made between different kinds of measurements. The discrepancies found between direct and inferred values of dP/dT are so large that needs for better thermodynamic data at high pressures and for more critical study of shock data and their interpretation are evidently pressing; this clearly points the way for further productive research.

The discrepancies in the iron data are particularly disturbing. The magnitude of the transition pressure agrees reasonably well with the static value. The static transition is reported to be sluggish [17]; but, on the basis of experience with stress relaxation effects [19] one would predict that incomplete transition in shock would lead to a first wave amplitude above the static transition pressure and to a decay of the first wave amplitude with time. We might assume that the shock data are equilibrium values and that the specific heat and thermal expansion coefficients are in error by a large amount. Still another possibility is that the Hugoniot points are at equilibrium and beyond the mixed phase region. The discontinuity at

the second phase boundary would then lead to differences in the observed direction between β_{RH1} and β_{ADM1} . Finally it is not inconceivable that the phase line reported by Johnson et al. is seriously in error. It was obtained by a clever but unusual technique which is not thoroughly understood; verification by more conventional measurements would not be out of order.

ACKNOWLEDGMENT

This work was supported by the U.S. Air Force through subcontract with the Stanford Research Institute. I appreciate the services of Mrs. Maxine Daniels in preparing the manuscript.

REFERENCES

1. P. Duhem, *Zeits. fur Physik. Chemie*, **69**, 169 (1909).
2. Lord Rayleigh, *Proc. Roy. Soc.*, **A84**, 247 (1910).
3. H. Bethe, "The Theory of Shock Waves, for an Arbitrary Equation of State," OSRD Report No. 545 (1942).
4. F. S. Minshall, *Bull. Am. Phys. Soc.*, **29**, 23 (12/28/54).
5. R. G. McQueen, "Metallurgy at High Pressures and High Temperatures," Gordon and Breach, 1964, K. A. Gschneidner, Jr., et al., Eds.
6. R. E. Duff and F. S. Minshall, *Phys. Rev.*, **105**, 1207 (1957).
7. B. J. Alder and R. H. Christian, *Phys. Rev.*, **104**, 550(L) (1956).
8. J. Wackerle, *J. Appl. Phys.*, **33**, 922 (1962).
9. T. Ahrens and V. Gregson, *J. Geophys. Res.*, **69**, 4839 (1964).
10. J. C. Slater, "Introduction to Chemical Physics," McGraw-Hill, 1939, pp. 220 ff.
11. R. Courant and K. O. Friedrichs, "Supersonic Flow and Shock Waves," Interscience, 1948, pp. 143 ff.
12. G. E. Duvall, *Bull. Seismol. Soc. Am.*, **52**, 869 (1962).
13. J. C. Jamieson and A. W. Lawson, *J. Appl. Phys.*, **33**, 776 (1962).

14. P. W. Bridgman, *Phys. Rev.*, **48**, 893 (1935).
15. Bancroft, et al., *J. Appl. Phys.*, **27**, 291 (1956).
16. Johnson, Stein and Davis, *J. Appl. Phys.*, **33**, 557 (1962).
17. A. S. Balchan and H. G. Drickamer, *Rev. Sci. Instr.*, **32**, 308 (1961).
18. Rice, McQueen and Walsh, *Solid State Physics*, v. 6 (1958), Seitz and Turnbull, Eds.
19. G. Duvall, *Stress Waves in Anelastic Solids*, Springer-Verlag, 1964, Prager and Kolsky, Eds.

COMMENTS

R. A. GRAHAM (Sandia Laboratory, Albuquerque, N.M.): The authors' analytical treatment of the characteristics of first order phase transitions and analysis of existing shock wave data, points to the requirement for carefully controlled shock wave experiments which yield more data concerning the thermodynamic properties of the transition. Duff and Minshall [1] showed that shock wave velocity measurements in the mixed phase region of a first order phase transition allow the slope of the pressure-temperature phase line to be computed. Atmospheric pressure values must be assumed for specific heat and thermal expansion; however, the calculation is not sensitive to uncertainties in these values. The volume change associated with the transition may also be measured with precision if close control of the stress input to the sample is achieved. Thus, it is evident from the Clausius-Clapeyron relation, $\Delta S/\Delta V = dP/dT$, that it is possible to obtain a complete thermodynamic description of the transition. The key experimental requirement is close control on the stress input to the specimen. We have previously described a compressed gas gun [2] which has that feature. Utilizing this gun we have accomplished shock velocity measurements in the mixed phase region of the bismuth I-II transition and the germanium solid-solid transition to the white tin structure. The slope of the phase line, dP/dT , for the germanium transition is found to be -3.1×10^{-2} kbar $^{\circ}\text{C}^{-1}$, while

that for the bismuth transition is -5.1×10^{-2} kbar $^{\circ}\text{C}^{-1}$. The estimated accuracy of both values is 10%. The bismuth value is in excellent agreement with Bridgman's [3] value of -5.0×10^{-2} kbar $^{\circ}\text{C}^{-1}$ and Duff and Minshall's value of -5.08×10^{-2} kbar $^{\circ}\text{C}^{-1}$. The germanium value is also in excellent agreement with the static determination of Bundy [4] and is probably more accurate than the static value. It appears that compressed gas guns with precise control for achieving a preselected impact velocity will enable more meaningful thermodynamic data to be determined from experimental measurements describing shock wave induced first order phase transitions; thus, shock data and static data may be adequately compared.

REFERENCES

1. R. E. Duff and F. S. Minshall, *Phys. Rev.* **108**, 1207 (1957).
2. S. Thunborg, Jr., G. E. Ingram and R. A. Graham, *Rev. Sci. Instr.* **35**, 11 (1964).
3. P. W. Bridgman, *Phys. Rev.* **48**, 893 (1935).
4. F. P. Bundy, *J. Chem. Phys.* **41**, 3809 (1964).

EFFECT OF A SHOCK WAVE ON A POROUS SOLID

Jacques Thouvenin
*Commissariat à l'Energie Atomique
France*

ABSTRACT

The propagation of a shock wave in a porous solid is examined from the angle of the discontinuity and of the periodicity of the phenomena associated with the granular character of the solid. Phase velocity of propagation is defined, and its values are calculated and verified experimentally for porous Cu, Al, Ni, and U. It is likewise shown that the free surface velocity of the porous solid is equal to that of the compact solid.

It is then deduced from the analysis of the waves reflected from grain to grain that the solid tends toward an equilibrium state, of which the representative point is placed, to a second order approximation, on the dynamic adiabat of the compact solid, contrary to theories published by other authors.

1. INTRODUCTION

The locus of states attained by a solid under the effect of shock compression constitutes, in the three-dimensional space (p, v, T) , a so-called dynamic adiabat curve or Hugoniot.

This curve depends on the nature of the solid and on the initial state (p_0, v_0, T_0) into which the shock propagates. For a given solid it is possible to distinguish several dynamic adiabatics on varying one of the parameters of the initial state, and to describe thereby a characteristic state surface. Making the solid porous augments appreciably its apparent specific volume, v_0 , and on measuring the shock parameters of the solid in different conditions of porosity, several authors [1,2] have published, for diverse solids, a fairly wide range of dynamic adiabatics.

The object of this paper is to analyze the phenomena linked to shock wave propagation in a porous solid, and to show that the classical measurements of the shock parameters do not have the same significance as for the homogeneous solids. Consequently the shock equations which allow calculation of the pressure and the density as functions of the measured velocities cannot be applied. It is then shown that the porous solid reaches, under the effect of the shock, an equilibrium state and that this state is situated, to a second-order approximation, on the

dynamic adiabat of the compact solid, contrary to the results of papers already published on the subject.

2. DESCRIPTION OF THE PROPAGATION SCHEME OF THE SHOCK WAVE

A porous solid is obtained industrially by frittting. It appears thence as an agglomeration of grains of compact solid, separated by air gaps. To schematize this point of view and deal with the problem, we assume in a one-dimensional model that the grains are of the same dimensions and equidistant, and that the gaps between them are equal (Fig. 1).

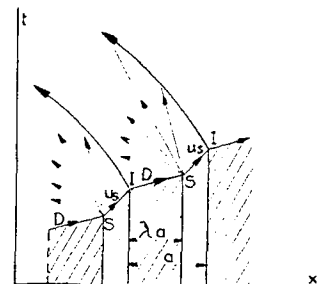


Fig. 1 - Propagation scheme

Let a shock wave propagate at velocity, D , in the first grain. Having arrived at the free surface of the grain, it places the latter in motion at speed u_s . From the point S a train of isentropic rarefaction waves reenter the grain and return it to zero pressure. The impact of the first grain on the second, at point I , induces in it a shock wave of the same velocity, D , as the first, since there exists between the shock parameters u_s and D a single-valued relationship depending only on the nature of the solid. From the point, I , a shock wave is likewise reflected into the incident grain and compresses it anew.

These processes proceed from grain to grain: there is no permanent shock wave, but a periodic series of shock waves in the grains, and of projections of matter into the gaps. The shock phenomenon is then propagated with a phase velocity which we designate D^* . This velocity, D^* , is a parameter easily accessible to experiment, but it does not have the physical significance of a shock velocity; it cannot, therefore, be introduced without precautions into the shock wave equations.

The model of Fig. 1 allows calculation of the value of D^* . We call λ the coefficient of porosity:

$$\lambda = \frac{(\text{density of the porous solid})}{(\text{density of the compact solid})}.$$

The summing of the transit times of the phase wave in the grain and in the gap leads at once to the relationship:

$$\frac{1}{D^*} = \frac{\lambda}{D} + \frac{1-\lambda}{u_s} \quad (1)$$

where D and u_s designate the shock parameters of the compact solid.

The primary result of this propagation scheme is that the speed of the free surface of the porous solid is equal to that of the compact solid: it is, in effect, equal to the speed taken by the last grain, that is, u_s . Whence the second relation

$$u_s^* = u_s, \quad (2)$$

the $*$ denoting the porous solid.

The following paragraph describes experiments made to verify these two relations.

3. EXPERIMENTAL VERIFICATION

Most of the experiments were done with copper. The Cu grains were of dendritic form. Two grain sizes were used: $20 \pm 3 \mu$ and $100 \pm 10 \mu$; however, experience has shown that the choice has no effect on the value of D^* . Pellets 20 mm in diameter and 5 mm thick were formed by sintering from these grains to two different porosities: $\lambda = 0.8$, Cu of density 7.14 g/cc and $\lambda = 0.6$, Cu of density 5.35 g/cc. The density spread of a lot of the pellets did not exceed 0.01 g/cc. Other experiments have been made with pellets of porous Al, Ni, and U.

A. Verification of Relation (1)

The pellets were submitted to the classical test for determination of the equations of state, such as described in Ref. 3. They were placed (Fig. 2) on a metallic driver plate of the same material as the porous solid studied (except Ni, for which a Cu driver plate was used). Since the materials are identical in nature one measures, during the same experiment, D^* and u_s . (Note that u_s applies to the compact solid.) The shocks are produced, either by direct contact of the driver plate with an explosive charge, or by projection of a metallic slab at great velocity (by accumulation of shock).

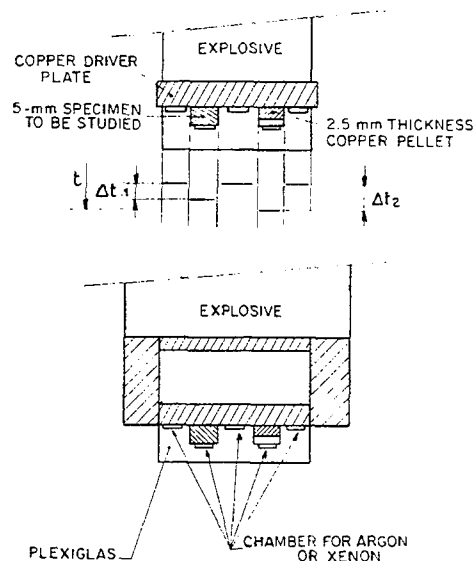
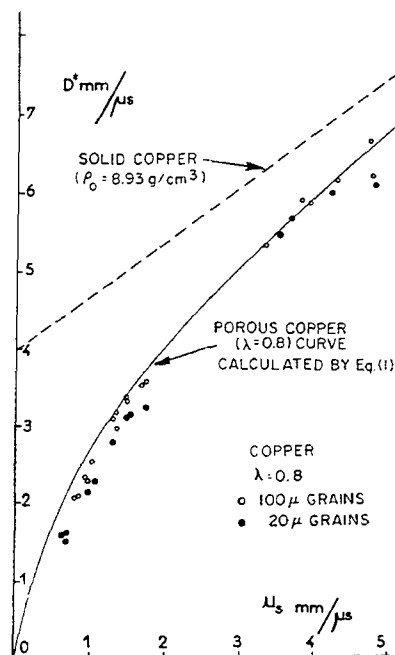


Fig. 2 - Experimental setup for measuring D^* and u_s .

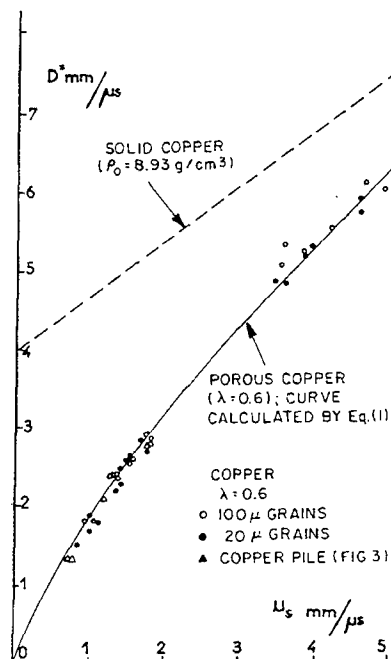
The measured values of D^* and u_s are plotted in Graphs 1 to 5. On the graphs are also traced the curves $D^* = f(u_s)$ calculated from relation (1) by use of the known relations between the shock parameters D and u_s of the compact solid; for Cu, Al, and Ni these relations were deduced from data published in Ref. 3, for U from data in Ref. 4. In the particular case of porous Ni, where the driver plate was Cu, the theoretical curve (D^* for Ni vs u_s for Cu) was displaced to the same extent toward the right at equal D^* , as that at equal D , which separates the curves $D = f(u_s)$ of compacted nickel and copper. This procedure is justified because "adjacent" metals are concerned.



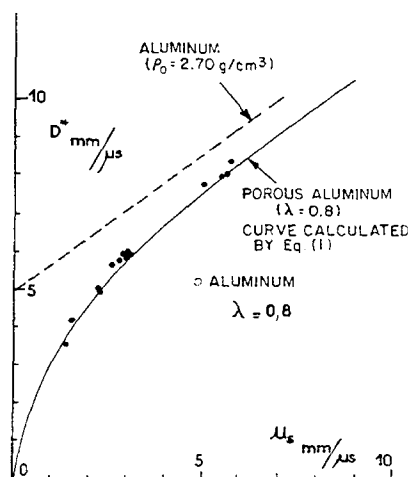
Graph 1

These graphs show that the experimental points are very close to the curves derived from relation (1). However, for the weak shocks there is noted a value of D^* slightly lower than the calculated value. This can arise from the weakening of the periodic shocks, induced from grain to grain, more evident for the weak than for the strong shocks on account of the part of the energy abstracted by the interstitial air.

In order to confirm the validity of relation (1) on a simplified model reproducing faithfully that of Fig. 1, we proceeded to the same measurements (D^* and u_s) on replacing

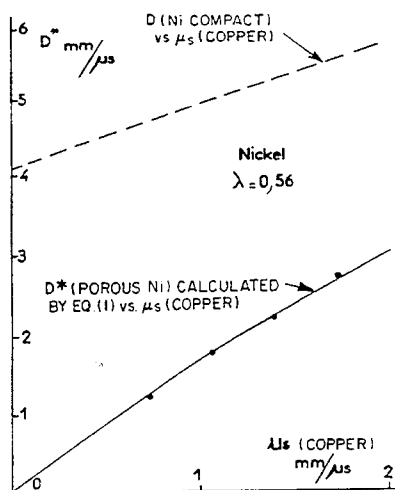


Graph 2

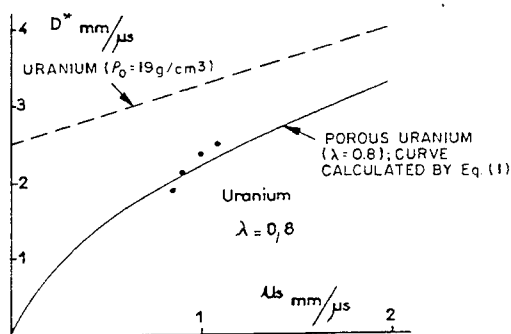


Graph 3

the porous pellet with a pile of thin plates of Cu, separated one from the other by air gaps (Fig. 3). The thickness ratio of plates and air gap is such as to make the ensemble equivalent to a porosity $\lambda = 0.6$ or mean density of 5.35 g/cc. The parameter D^* measured here represents then exactly the propagation velocity such as schematized in Fig. 1. The values are plotted on Graph 2. They place themselves nicely on the theoretical curve. This experiment



Graph 4



Graph 5

shows that the dimension and arrangement of the grains play a negligible role in the propagation phenomenon: whether there is order or disorder the velocity remains the same.

B. Limit of Validity of Relation (1)

The experiments described above used driver plates of the same material as the porous solid studied. The rarefaction waves issuing from the free surface of the grains thus propagate freely toward the rear on meeting a continuous compressed solid. One can think that it is no longer the same if the porous pellet is set on a driver of a different material: in fact in the case where the shock polar of the driver material is lower than that of the material in the grains of the porous solid, these rarefaction waves will reflect at the interface as compression waves which intensify and

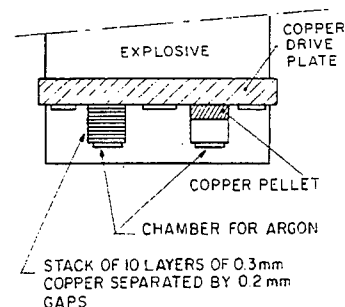


Fig. 3 - Experiment with 10 layers of 0.3-mm copper separated by 0.2-mm gaps

accelerate the incident shock, and this from the first grain. The values of D^* and u_s in each grain grow in the course of the propagation; the phenomenon is no longer linked to the periodicity of the grains, and the value of D^* can no longer be calculated by means of so simple an expression as relation (1).

We have studied this acceleration in two cases: porous Cu on an Al driver, and porous U on a Cu driver. The experimental setup is the same as that of Fig. 2, but the pellet from which u_s is measured is of the same nature as the driver plate. From this measured value of u_s one can define the intensity of the incident shock, and, in particular, calculate the state of the shock transmitted by the driver to the grains of the porous solid. It suffices to take the intersection of the shock polar of the grain material (for example that of Cu, in the first case) with the locus of reflected shocks in the driver material (e.g., the Al) by the well-known graphical method described in Ref. 3. Measurement of the speed u_s of the free surface permits calculation of the parameters D and u_s of the shock in the grains which must be introduced into relation (1). One obtains thus a calculated value of D^* .

These experiments showed that the experimental values of D^* are higher than the calculated, thus establishing that for equality of the material traversed, the shock is more intense in the grains of the porous solid than in the compact solid.

If the driver plate had a shock polar higher than the grain material, an inverse phenomenon would be produced. There would be detachment of the porous pellet, and emission of rarefaction waves forward; the shock in the porous solid would attenuate.

C. Verification of Relation (2)

Experiments were made on Cu alone. The experimental setup is shown in Fig. 4. The speed of the free surface u_s is measured in a compact Cu pellet 1-mm thick, which serves for reference. The pellets of porous Cu have a thickness of 1.25 mm ($\lambda = 0.8$) or 1.67 mm ($\lambda = 0.6$), in such manner that the shock traverses the same quantity of Cu as in the reference pellet. The speed of the free surface of the porous Cu u_s^* is measured directly from the time interval separating the traces in the argon chambers. The results are plotted in Graph 6 and verify correctly relation (2).

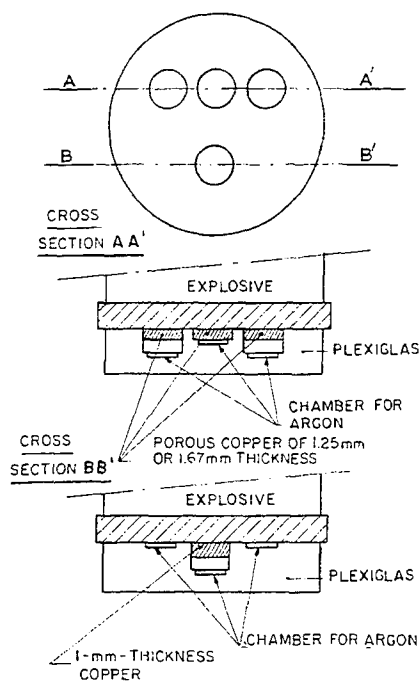
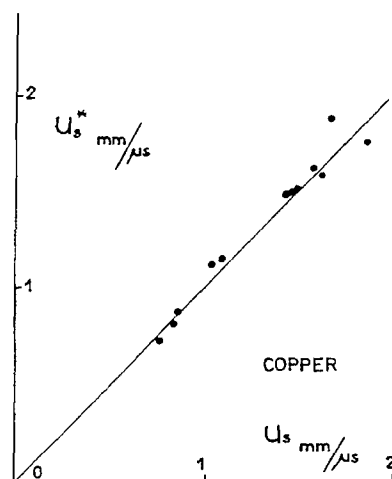


Fig. 4 - Arrangement for measuring u_s^*

NOTE: As for relation (1), the equality of the speeds of the free surface is subordinated to the existence of a driver of the same nature as the porous material (adaptation of shock impedance). As a contradictory experience, porous Cu pellets were placed in direct contact with the explosive. It was established that, for a given explosive, the velocity of the free surface grows as the coefficient of porosity diminishes: $u_s^* (\lambda = 0.4) > u_s^* (\lambda = 0.6) > u_s^* (\lambda = 0.8) > u_s$ (compact). This is explained by the accumulation of shock from grain to grain.



Graph 6 - u_s = free surface velocity of solid copper, u_s^* = free surface velocity of porous copper ($\lambda = 0.8$ and 0.6)

4. LIMITING STATE OF THE POROUS SOLID BEHIND THE SHOCK

The proposed scheme of propagation being verified by experience so far as the parameters accessible to measurement are concerned, we shall now show that the hypotheses made permit anticipation that the porous solid will attain, under the influence of the incident shock, a limiting state characterized by particular values of pressure, density, and material velocity which can be calculated entirely with the data of the equation of state of the compact solid.

A. Existence of the Limiting State

Let us follow, in the course of time, the evolution of the state of the solid element belonging to a single grain. Immediately behind the incident shock wave the state is represented by point A (p_i, u_i, ρ_i) in Fig. 5. This point, A, pertains to the shock polar, (P), and to the dynamic adiabat, (H), of the compact solid of density ρ_0 . When the first train of rarefaction waves, initiated from the free surface of the grain to which the element considered belongs, reaches this element the representative point of its state is displaced along the isentropic (S) from A up to the point S ($p = 0, u = u_s, \rho = \rho_0$). A little later the element suffers the effect of the reflected shock which issued from point I (impact of the grain on the next), and the representative point remounts abruptly toward a

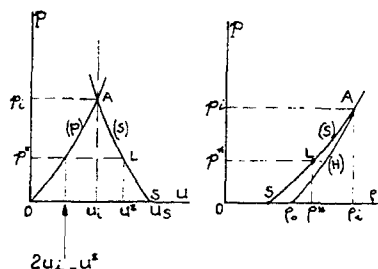


Fig. 5 - Limiting state of a porous solid under shock

point of the polar (P) situated a bit above A; this is because the shock polar issuing from S is slightly less curved than the isentropic (S). Then the second train of rarefaction waves, started back from the free surface of the following grain, leads the state anew, along an isentropic, toward a point near S.

These oscillations of the state of the medium do not continue indefinitely. They fade away in consequence of the interaction of each reflected shock wave (C) (Fig. 6), with the two trains of rarefaction waves which immediately precede and follow it. This interaction is due to the following facts:

The reflected shock wave (C) is supersonic with respect to the medium ahead; it therefore overtakes the train of rarefaction waves which precedes it. It is subsonic with respect to the medium behind, and is, therefore, overtaken by the train of rarefaction waves which follows it.

Now, in the course of this double interaction, the shock wave (C) encounters before it a medium of which the pressure increases above $p = 0$ (Fig. 1), and behind it the rarefaction waves lower the pressure from $p = p_1$. The shock wave (C) thus propagates between two states of the medium of which the difference in pressure tends toward zero, not on account of any action of the shock itself. At the limit it becomes an infinitesimal compression wave propagating at sonic velocity in the medium in equilibrium.

The limiting state of the porous solid thus exists by virtue of the transition of the shock (C) to a sonic wave. It can be described as a compressed state of the material characterized by the values p^* , ρ^* , u^* , c^* , which we shall calculate below. Taking account of the analysis of the oscillations undergone by the material element considered above, this limiting state is situated somewhere on the isentropic (S) issuing from

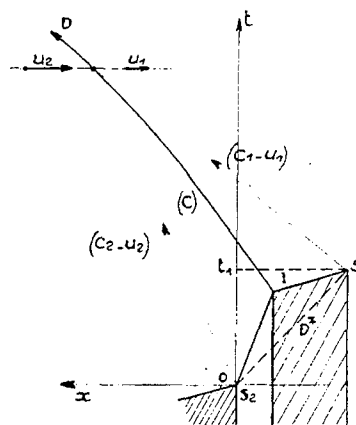


Fig. 6 - Interaction of a reflected shock wave (C) with rarefaction waves issued from S_1 and S_2

point A. For the usual shocks (up to 1 megabar in Cu), the difference between the isentropic (S) and the dynamic adiabat (H) is less than 1% above the value of ρ_0/ρ . One can therefore say that the limiting state of the porous solid (p^* , ρ^*) is a state of the compact solid, and that all the porous solids of the same chemical constitution have only, whatever their porosity, a single and identical dynamic adiabat, that of the compact solid.

B. Determination of the Limiting State

The following theorem can be demonstrated: the velocity of a shock wave is equal to the arithmetical mean of the velocities of sound of the media behind and before, both velocities being expressed with respect to the same medium.

The demonstration, purely mathematical, does not proceed from the framework of this discussion. The theorem is accurate to second order, the first order being that of u/D .

Let us consider the simultaneous interaction at point $M(x, t)$ of the shock wave (C) with two particular rarefaction waves, starting respectively from the free surfaces S_1 and S_2 of two consecutive grains (Fig. 6). The absolute material velocities, on both sides of the shock (C), are respectively u_1 and u_2 . If D is the absolute velocity of the shock (C) it measures the slope of the curve (C) at point M. Thus $D = dx/dt$.

According to the theorem noted above, we have:

$$D = \frac{1}{2} (c_1 - u_1) + (c_2 - u_2) .$$

Now

$$c_1 - u_1 = \frac{x + a}{t - t_1} ,$$

with

$$t_1 = \frac{a}{D^*}$$

and

$$c_2 - u_2 = \frac{x}{t} .$$

Whence the differential equation of the trajectory (C) of the shock wave reflected at I:

$$2 \frac{dx}{dt} = \frac{x + a}{t - t_1} + \frac{x}{t} .$$

After integration it is easy to see that this trajectory is the arc of a hyperbola centered at the mean of S_1 and S_2 . The asymptote of this hyperbolic arc has a slope equal to the desired limiting velocity of the shock wave (C), that is, equal to $(c^* - u^*)$, a parameter characteristic of the limiting state of the medium.

The interaction model of Fig. 6 represents the general case. It is preceded by a more simple scheme where the shock wave (C) interacts with only one of the two trains of waves: the trajectory (C) is provisionally a parabolic arc.

The complete calculation leads finally to the value of the desired limiting velocity of the shock wave (C), namely $(c^* - u^*)$, as a function of the intensity of the incident shock characterized, for example, by the material velocity u_1 .

To calculate, from the value of $(c^* - u^*)$ obtained, the characteristic parameters of the shock, it is assumed that the isentropic (S) is symmetric to the shock polar (F) (Fig. 5). The limiting state, L, is then equivalent, from the point of view of pressure, p^* , and density, ρ^* , to a fictitious shock producing in the compact medium a speed jump $(2u_1 - u^*)$. It is known that the relation between the velocity of sound behind a shock and the material speed jump brought about by the shock is:

$$c = A + (2B - 1) u ,$$

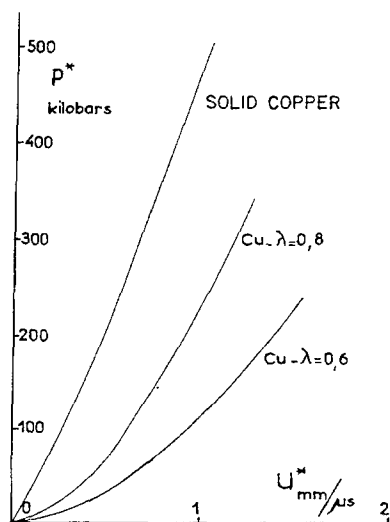
where A and B are the coefficients of the classical empirical relation of the equation of state

of the metals: $D = A + Bu$. One has here, therefore:

$$c^* - u^* = A + (2B - 1) 2u_1 - 2Bu^* ,$$

an equation permitting calculation of u^* , then p^* , and ρ^* .

The calculations have been made for Cu of two different porosities: $\lambda = 0.6$ and $\lambda = 0.8$. The values of p^* and u^* are plotted on Graph 7. The curves of this graph do not have the physical significance of a shock polar, but represent only the locus of limiting states of the porous Cu as a function of the incident shock. In the diagram (p^*, ρ^*) , the limiting states are situated on the dynamic adiabat of compact Cu, to a second order approximation. It would take very intense shocks to separate the limiting state (p^*, ρ^*) of the porous solid from the dynamic adiabat of the compact solid, and makes this difference measurable.



Graph 7 - Locus of p^* vs u^* of limiting states for porous copper

5. CONCLUSION

The shock wave propagates a discontinuity of pressure and of velocity fine enough to distinguish whether or not the medium is homogeneous. By following it in its trajectory, one can account in simple fashion for the experimental results obtained. These results cannot be interpreted as providing new information on the equation of state of the solids [5].

REFERENCES

1. K. Krupnikov, M. Brazhnick, and V. Krupnikova, Soviet Physics JETP, 15, 470 (1962).
2. T. C. Skidmore and E. Morris, Symposium on Thermodynamics of Nuclear Materials, Vienna, May 1962, p. 173.
3. M. H. Rice, R. G. McQueen, and J. M. Walsh, Solid State Physics, Academic Press, New York, Vol. 6, 1 (1958).
4. J. Viard, Colloque du C.N.R.S. sur les ondes de détonation, Gif-sur-Yvette (1961), p. 383.
5. J. Thouvenin, C. R. Acad. Sc. Paris, 258, 3461 (1964).

SHOCK BEHAVIOR OF SOME NON-REACTING POROUS SOLIDS

John R. Rempel and David N. Schmidt
*Stanford Research Institute
Menlo Park, California*

ABSTRACT

Thin layers of porous or distended materials (foams) struck by very thin flying plates may transmit pressure waves that imply the shocked foam is only partly condensed to normal density and that flow in the condensed material may be entropic over a broad band.

In our experiments aluminum flyers 0.2 to 1.0 mm thick carrying momentum densities 0.5 to 3×10^4 dyne-sec/cm² struck foam layers 4 to 13 mm thick. Target materials and distention ranges were: polyurethane (2:1 to 4:1), aluminum (2:1 to 4:1), beryllium (1.6:1), silica (2:1) and graphite (1.3:1 to 2:1). Peak pressures were in the range 0.1 to 10 kbar. Pressure histories, deduced from the motion of images of luminous points reflected in the polished surface of a steel anvil (optical lever arm) to which the foam specimens were attached, showed peak pressures to be roughly proportional to the ratio of input momentum to foam mass.

Experiments with preheated foam layers revealed a temperature dependence which may throw light on the nature of the forces acting in foams.

INTRODUCTION

Under certain conditions, an interposed layer of foamed or distended material may substantially reduce peak pressures induced in colliding solid bodies. In particular if one of the bodies is thin, rarefactions quickly reduce the stress at its interface with the foam; and it is the nature of foams that this reduction implies more drastic lowering of the peak pressure delivered to the other body than if the interposed layer were merely a solid of low shock impedance. It seems reasonable to attribute this effect to a great disparity between the speed of the shock which condenses the foam as it progresses and the speed of the relief waves reverberating behind it in the condensed material. Actually the behavior seems to be somewhat more complex than that. The initial condensing shock front does not appear to occupy the relatively narrow zone usually imagined to exist in solids; it may be more accurate to say the pressure attenuation effect is related to a broadening of the condensing front which increases as the shock advances through the foam and which is accompanied by a lessening of both the degree of condensation (within limits) and particle speed. With increasing impact speed,

decreasing layer thickness, and decreasing degree of distention,* the usual description of shock attenuation by overtaking rarefactions becomes applicable.

In many foams forerunners, similar to the elastic precursors seen in undistended materials, may appear ahead of the condensing shock, and these too contribute to pressure attenuation by carrying off momentum (which otherwise would appear behind the main front) and delivering it at low pressure.

EXPERIMENTAL METHOD

Fowles [1] has related the turning angle (positive or negative) of the surface of an elastic half-space when struck obliquely by an internal pressure front to the propagation speed of the front, angle of impact, Poisson's ratio and the pressure increment (or decrement). In Fig. 1, α is the turning angle and θ the angle of impact; O marks the point of wave break-out at

*Ratio of volume of solid plus void to volume of solid alone.

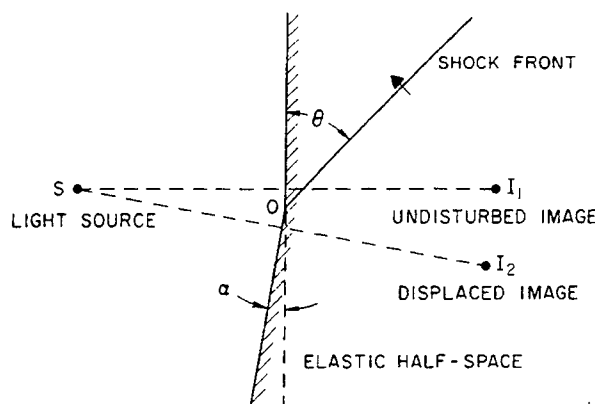


Fig. 1 - The optical lever arm

the mirror surface. Since our anvil material, 4340 steel, remains elastic for all pressures encountered, we can, from measured impact and turning angles and from the elastic properties of steel, deduce pressure as a function of time at the foam-steel interface, provided we arrange oblique impact at the anvil's free surface. Image motion from I_1 to I_2 is photographed with a high-speed streak camera.

The two basic experiments, one-dimensional (1-D) and two-dimensional (2-D), are sketched in Fig. 2. In the 1-D method (Fig. 2A), the flyer is spalled off a 1040 steel driver plate by a 130 kbar characteristic wave [2] induced by the detonation of an explosive lens and propelled across a vacuum gap to strike the foam broadside; except for slight nonplanarity of the flyer [10], there is symmetry within a certain radius from the system axis. The speed of the flyer is measured in a separate experiment; input momentum is determined by flyer thickness. In the 2-D method (Fig. 2B), the flyer is initially sandwiched between sheet explosive and the foam slab, and explosive impulse must be deduced from the thickness of the explosive. In both arrangements, impact angle at the main surface is related to the supersonic speed of the point of break-out of the wave along the mirror ("apparent speed") and to the elastic dilatational speed. The optical lever arm for measuring the turning angle is illustrated in Fig. 3 with typical distances shown.

Figure 4 is a streak camera record made with the 1-D arrangement using a 5 mm target of 0.67 g/cc polyurethane hit by a 0.50 mm aluminum flyer moving 0.80 mm/ μ sec. Points in a vertical line were exposed at the same instant of time but were reflected from successive areas along a vertical axis of the mirror.

Time increases to the right. Luminosity comes from an explosive argon light source closed on the front end by opaque glass carrying translucent horizontal lines. The technique of making a record such as Fig. 3 has been described elsewhere [1,3]. The apparent speed is related to the slope of the locus of first motion in the traces; turning angle and hence pressure, to the vertical displacement of a trace. The dotted lines in the figure mark the region of influence of side effects or relief waves stemming from the bottom and top of the anvil. The wave marked A is due to the forerunner mentioned above; the letter B indicates the disturbance due to the condensing or main wave; and the C-wave is due to a reflection of the B-wave from the flyer. The waves marked E and F have to do with the impact of the driver (see Fig. 2A). The arrival of the E-wave ends the experiment.

Streak camera records from 2-D experiments are similar except that the valid observation time is limited by the presence of reverberations within the anvil. In Fig. 5, the A-, B-, and C- waves have the same meaning as in Fig. 3; the waves A' and B' are reverberations entirely within the anvil of the A- and B-waves, respectively. Usefulness of the method depends on Gurney theory [4] and the measurements of the Gurney constant for the sheet explosive (Dupont, EL506D) by Abrahamson [5]. The existence of comparable results from both 1-D and 2-D methods provides other confirmation of the validity of the 2-D method. In interpreting our 2-D experiments, we equated 1×10^4 dyne-sec/cm² of impulse to between 0.041 and 0.056 cm of explosive thickness, depending on the surface density of the layer impacted. The wide band of light at the top of Fig. 5 is reflected in the glass mirror placed

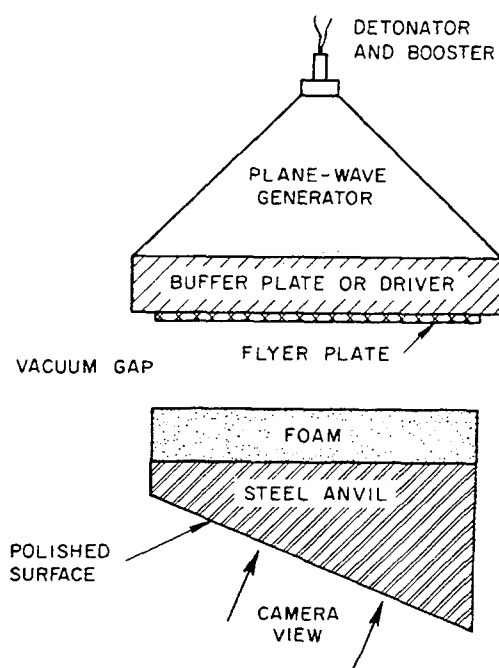


Fig. 2a - The one-dimensional (1-D) experiment

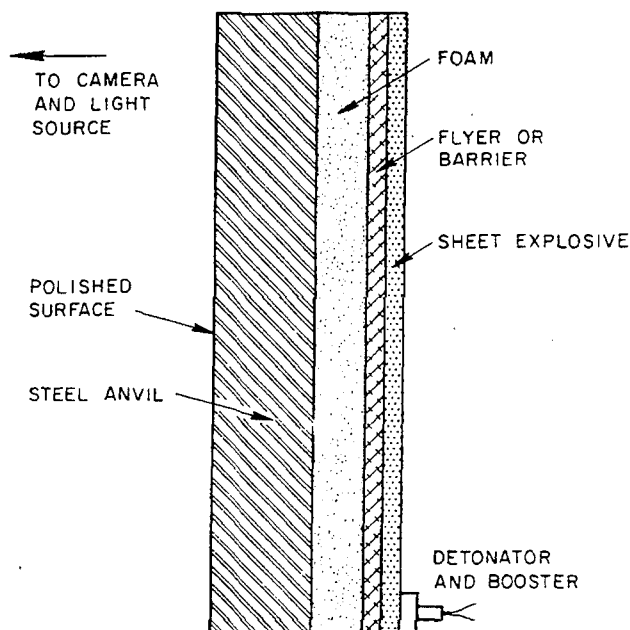


Fig. 2b - The two-dimensional (2-D) experiment

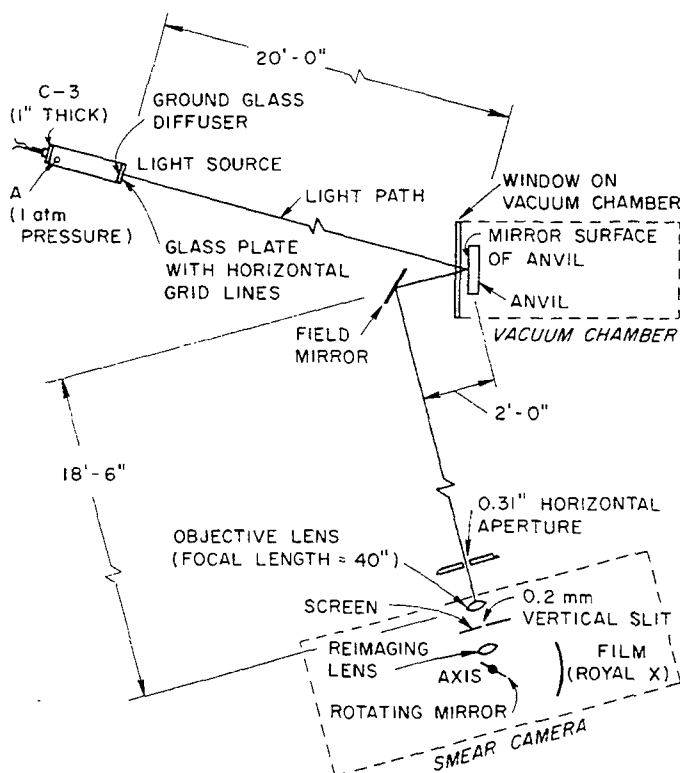


Fig. 3 - Experimental layout with typical distances

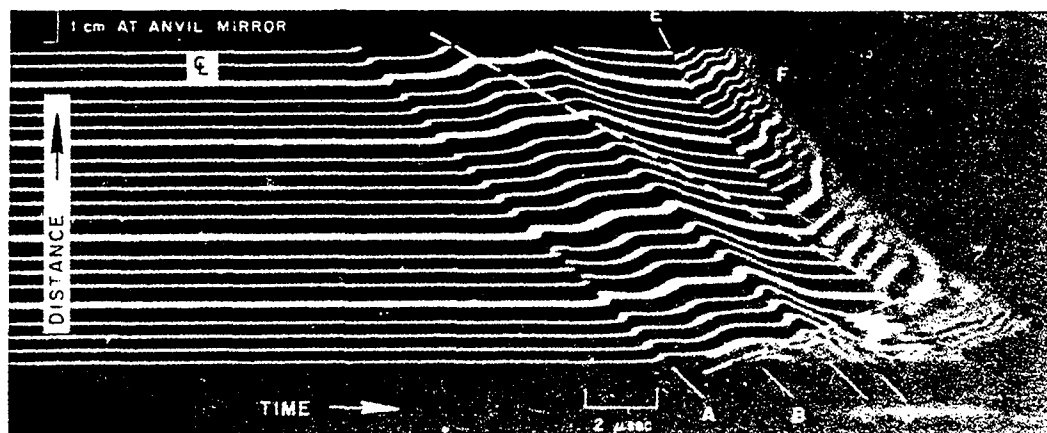


Fig. 4 - Smear camera record from 1-D experiment (shot 9155)

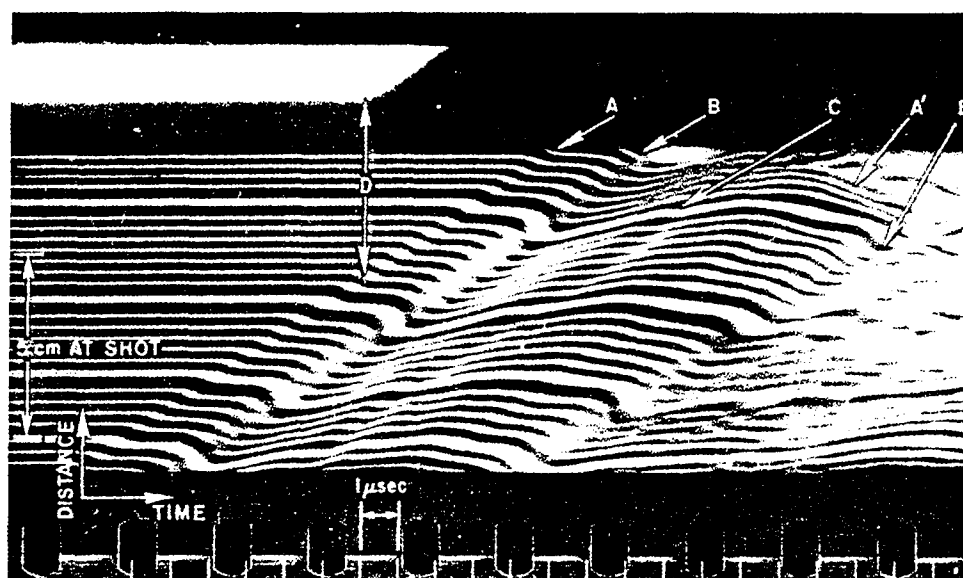


Fig. 5 - Smear camera record from 2-D experiment (shot 10,331)

at the end of the detonation run; the distance D provides an upper bound for A-wave speed through the foam.

The condensation in the foam during impact shows itself directly in flash X-ray shadowgrams of polyurethane foams made in an arrangement similar to the 2-D experiments described above [10]. Measurement of material density behind the plastic wave from these shadowgraphs has so far been inconclusive.

EXPERIMENTAL RESULTS

Observed pressure histories appear in Fig. 6; pertinent information on each experiment is listed in the figure. The arrows mark the end of the useable record and the quantity I is the total output momentum observed up to that time. I_0 is the momentum density in the flyer before impact; t is foam thickness. The identifying numbers of 1-D shots are starred. The figure shows that the presence of two waves

(A and B) is widespread. The A-wave has within experimental error a characteristic amplitude for each density and kind of material, and the A-front tends to be more sharp than the B-front. The A-front is nearly always followed by a region of uniform pressure. As input impulse per unit area I_0 is increased or foam thickness decreased, the B-wave falls in amplitude until the characteristic A-front stands alone. This is the kind of behavior predicted by Salvadori and others [6] for a type I locking medium; the A-wave appears to be the elastic forerunner* of the locking or plastic B-wave. However, the roundedness and slow relaxation from peak pressure seen in many of the B-wave forms suggest the presence of diffusive, viscous flow described by Lamb [8] and by Miles [9].†

The sometimes-seen C-wave is regarded as the first reverberation of the B-front in the foam—i.e., a double reflection of the B-wave from the anvil and the metal flyer. In Fig. 4 there is possibly a weak second reverberation between the C- and E-waves.

In Fig. 7, peak B-wave pressures in each density and kind of material are plotted against the ratio I_0/m , where m is the mass of foam per unit area. The information for aluminum is plotted separately in Fig. 7B. Taking into account the rather large uncertainties‡ in abscissae corresponding to 2-D experiments, peak pressures are linearly related to the ratio I_0/m . Forerunner strengths in each material appear as horizontal lines in the figure; the points of intersection of these lines with the summary lines for peak pressure provide the minimum values of m or maximum value of I_0 necessary to prevent the plastic wave from reaching the anvil.

These experimental results can be stated in terms of observed upper bounds to effective

shock impedances for the various foams in their condensed states behind the plastic or main front. The momentum per unit area remaining in the foam and flyer at the moment of arrival of the plastic front at the anvil is the difference between I_0 and the integrated impulse per unit area passed to the anvil by the forerunner, if any. The lower bound on maximum particle speed within the foam at this time is just the ratio of this difference to the sum of m and the surface mass density in the flyer. Thus, if P_e is the pressure induced in the anvil by the forerunner beginning at time t before main wave arrival, then

$$u_M \geq \frac{I_0 - P_e t}{m + m_0}$$

where u_M is the maximum particle speed behind the main shock just before this shock reaches the anvil, and m_0 is the surface mass density in the flyer. We presume u_M is always found just behind the main shock front and thus is associated with the peak B-wave stress in the anvil.

An upper bound on the pressure increase across the reflection of the plastic wave off the anvil is the experimentally observed peak pressure itself.§ Thus the ratio of the upper bound on pressure to the lower bound on particle speed provides an upper bound to the shock impedance of the plastically deformed foam, since we can neglect any motion of the foam-steel interface in comparison with that behind the main wave front. (Conservation of momentum through the reflection of the main front implies that the pressure jump ΔP must equal the momentum flux which is the product of density ρ , particle speed jump Δu , and propagation speed U —i.e., $\Delta P = \rho U \Delta u$. The product ρU is the impedance we seek. Our inequality then reads

$$U \geq \frac{\Delta P}{\Delta u} = \frac{P}{u_M}$$

where P is the measured pressure in the anvil corresponding to the B-wave.) These bounds, which are listed in Table 1 along with shock impedances of solid materials from the literature,¶ are, except in the case of 1.73 g/cc graphite, markedly lower than the known impedances of the corresponding solids and show a strong dependence on original distention and

*However, if this identification is true, the quasi-static yield stress is considerably enhanced by strain-rate effects, for the A-stresses are usually 2 to 4 times greater than quasi-static proportional limits under uniaxial compression. A-wave speeds are close to those predicted from the slope of the quasi-static stress-strain relation. See Ref. 7.

†The wave shapes for graphite in Fig. 6 show these features less strongly than those for other materials, suggesting that viscous forces may be less important in graphite.

‡Due to lack of precision both in I_0 and in knowledge of effective foam thickness. In contrast to the 1-D experiments, the 2-D arrangement requires waves to travel obliquely through the foam layer; knowledge of distance travelled is uncertain because the speed in foam is not known.

§Since the free-running forerunner stress is not known but only the stress behind its reflection off the anvil (which is presumably greater than the free-running value), this is the only strictly valid upper bound available.

¶The impedance of solid polyurethane has been approximated by that of lucite.

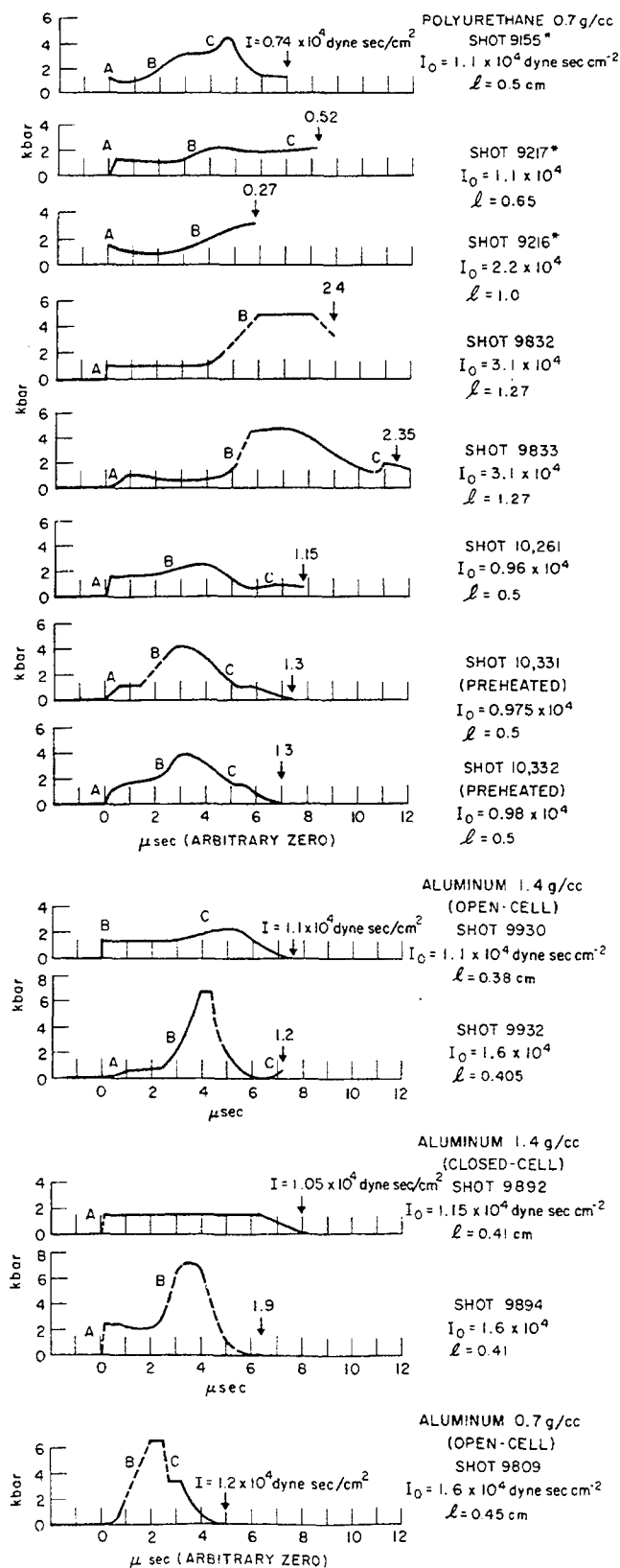


Fig. 6 - Approximate wave shapes

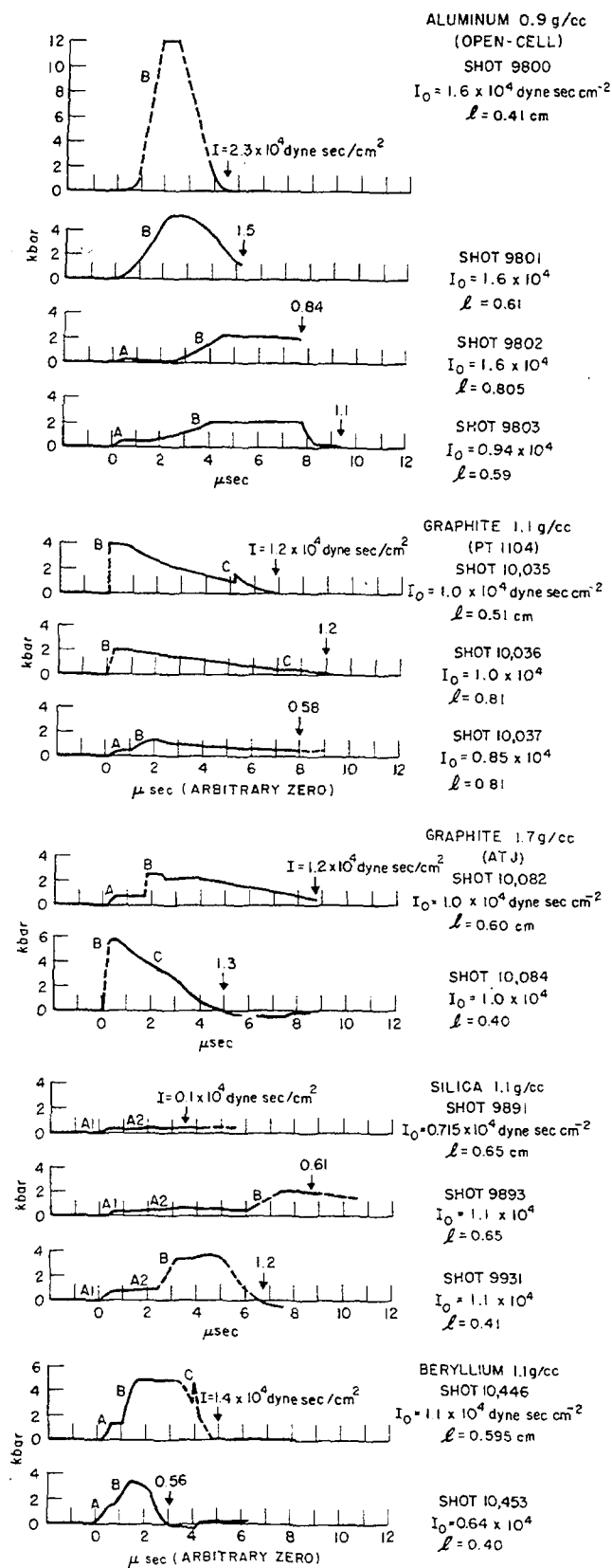


Fig. 6 - (Continued)

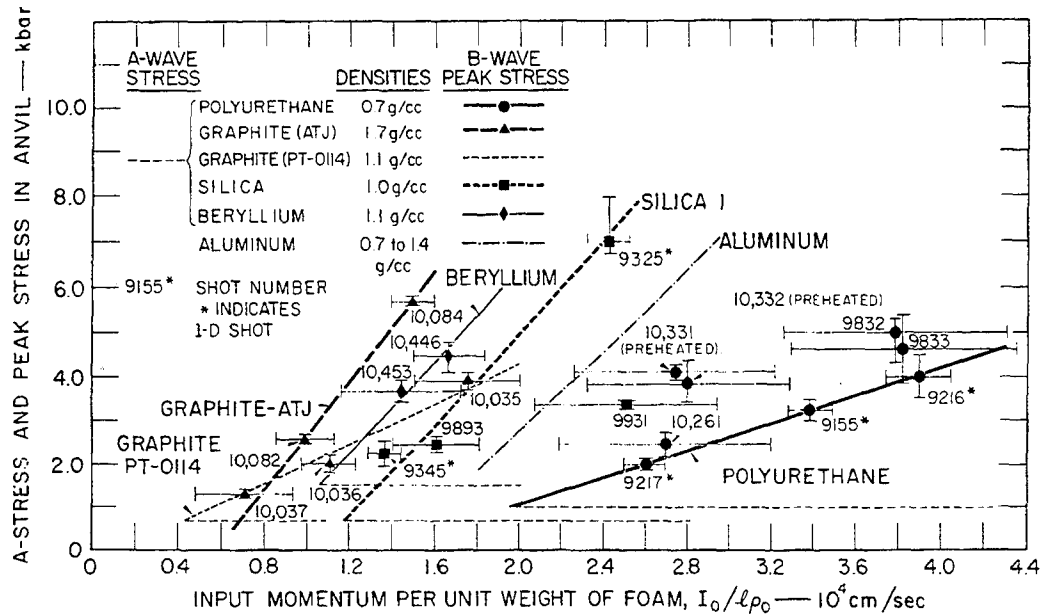


Fig. 7a - Summary of peak pressures transmitted by several foams

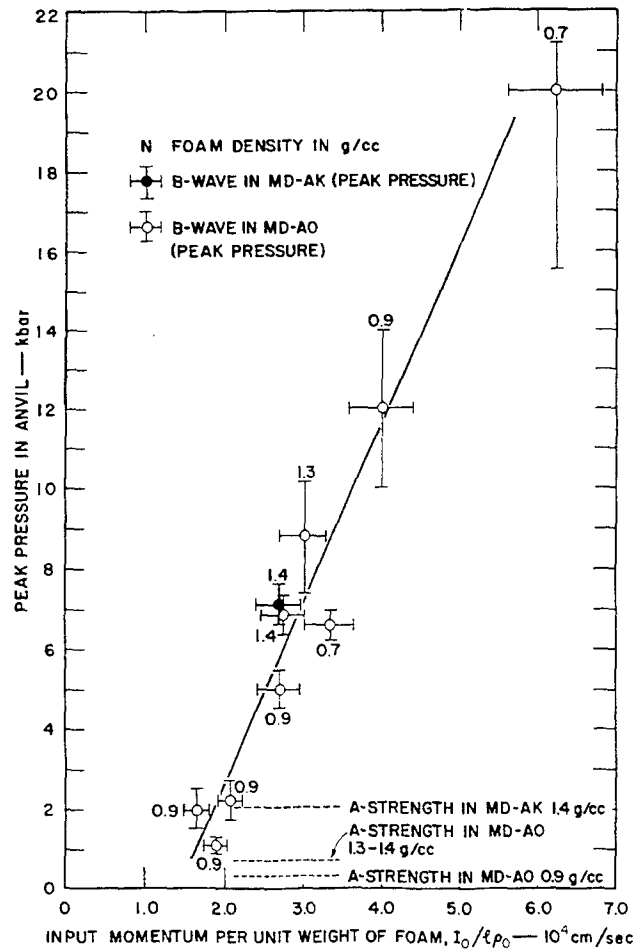


Fig. 7b - Peak pressures transmitted by several aluminum foams

TABLE 1
Sounds on Shock Impedances and Pressures

Material	Undis- tended Density (g/cc)	Foam Density (g/cc)	Foam Thick- ness (cm)	Lower Bound on the Peak Particle Speed, v_M (mm/ μ sec)	Observed Peak Pressure (kbar)	Upper Bound on Observed Impedance (10^6 gcm $^{-2}$ sec $^{-1}$)	Impedance of Undis- tended Solid † (10^6 gcm $^{-2}$ sec $^{-1}$)	Predicted Lower Bound on Peak Pressure (kbar)	Shot No.
P-C	1.1	0.67	0.50	0.21	3.25	0.17	0.40	7.0	9,155*
P-C		0.67	1.27	0.315	7.1	0.25	0.40	11.0	8,863
P-C		0.67	1.0	0.20	4.0	0.22	0.40	7.0	9,216**
P-C		0.67	0.65	0.145	2.0	0.15	0.40	5.0	9,217**
Al-O	2.7	0.7	0.45	0.26	6.6	0.29	1.6	24.0	9,809
Al-O		0.9	0.61	0.23	5.0	0.24	1.6	21.0	9,801
Al-O		0.9	0.80	0.17	2.2	0.14	1.6	16.0	9,802
Al-O		0.9	0.59	0.16	2.0	0.15	1.6	13.0	9,803
Al-O	2.6	1.4	0.40	0.19	6.9	0.43	1.6	18.0	9,932
Al-C		1.4	0.40	0.12	7.0	0.79	1.6	11.0	9,894
Be		1.1	0.595	0.13	4.5	0.405	1.6	12.0	10,446
Be		1.1	0.40	0.10	3.7	0.45	1.6	9.5	10,453
Si	2.2	1.1	0.42	0.19	7.0	0.445	1.6	18.0	9,325*
Si		1.1	0.65	0.093	2.4	0.295	1.6	8.8	9,893
Si		1.1	0.45	0.078	2.2	0.33	1.6	7.5	9,345*
C		1.1	0.51	0.15	3.9	0.29	0.55	6.7	10,035
C	1.7	1.1	0.81	0.0985	2.0	0.22	0.55	4.3	10,036
C		1.1	0.81	0.059	1.3	0.25	0.55	2.7	10,037
C		1.7	0.40	0.13	5.7	1.6	0.55	5.75	10,084
C		1.7	0.60	0.079	2.6	0.39	0.55	3.5	10,082

Legend:

P-C - Closed-cell polyurethane
 Al-O - Open-cell aluminum
 Al-C - Closed-cell aluminum
 Be - Beryllium
 Si - Silica
 C - Graphite

*1-D Shots.

† Refs. 12-15.

a lesser dependence upon peak pressure. Values of peak pressure expected from the impedances of the solids and from the calculated lower bounds on particle speed appear in the next to last column of the Table.

Shots 10332 and 10331 were carried out in polyurethane preheated 118°C before impaction. By contrast with Shot 10261, which was identical except for preheating, the peak main-wave anvil pressures in these experiments are above the values expected from unheated samples and there is some indication in the wave shapes that preheating may also lead to more rapid relaxation of pressure behind the main front. (See Fig. 6.) Heat then may weaken the viscous forces behind the main front.

Pieces of aluminum and beryllium foams recovered after these experiments show the expected permanent compaction. Surprisingly, polyurethane samples seem unchanged. Silica and graphite are not recovered. Final aftershot density of aluminum appears little affected by original density or peak pressure. Fourteen experiments in all kinds of aluminum, in which peak pressures in the anvil varied from less than 1 kbar to 20 kbar, left the foam compressed to an average density of 2.1 ± 0.3 g/cc.

DISCUSSION

The plastic (B-) waves in Fig. 6 frequently show three features which set them apart from waves of similar strengths in solid or undistended materials:* rise-times of the order of 1-2 μ sec and, as noted in Table 1, peak pressures which are lower than expected from momentum considerations, and plateaus at peak pressure lasting 1-3 μ sec. (In Fig. 6 see approximate wave shapes for Shots 9155, 9217, 9832, 9833, 9930, 9802, 9803, 9931 and 10446.) With the increase of peak pressure the tendency toward the formation of pressure plateaus becomes less strong and relaxation from the peak plastic stress becomes more rapid (cf. wave shapes in aluminum Shots 9800, 9801, 9809, 9894, and 9932 and in graphite Shot 10084 as reported in Fig. 6). (Since the speeds of relief waves in the shock-compressed materials are not well known, in a 2-D experiment precise interpretation of the wave shape behind the plastic front cannot be given, but the gross features are probably interpretable as if the experiment were 1-D.)

*As an example of the behavior of solids, see the stress distributions in solid aluminum struck by a thin flyer as observed and calculated by Fowles [11].

Salvadori and others idealized the condensed form as a region of uniform speed and density. Density was presumed to be that of the undistended solid, and particle and wave speeds were calculated from conservation laws. In the range of behavior covered by our experiments, such a procedure can furnish only upper bounds on expected pressures and time intervals. The existence of a fairly clear lower limit to the value of the ratio I_0/m needed for the transmission of a plastic wave when a forerunner is present (Fig. 7) suggest that the density of the condensed state, although possibly declining as the wave moves through the foam, cannot fall below a limit. Thus, Salvadori's approach will provide good estimates of time intervals for a given material of given distention, if a fixed, empirically chosen value of locked density less than that of the undistended solid is used in calculation [7,10]. More powerful calculational techniques require more complex consideration of the state and behavior of the locked region.

Relief waves make between 5 and 8 round trips each microsecond between the two surfaces of a flyer plate; were the flow in the locked zone isentropic, this would imply a more rapid fall in pressure behind the main wave than is actually seen in many experiments, and, because of momentum conservation, generally higher peak pressures. (Ref. 7 contains the result of calculations made on the isentropic assumption by the method of characteristics and contrasts it with the result of a corresponding experiment.)

Judging from the shapes of the waves and peak pressures transmitted, then, the shock concepts usual in the study of materials of uniform density, particularly the limitation of entropy production to a narrow zone separating two isentropic regions, do not seem realistic in thin specimens of foam at low pressures. It may be more appropriate to regard shock-condensed foam as a group of macroscopic particles frozen together to some extent (perhaps temporarily), subject to repeated flyer impacts as the flyer slows, and moving as a single mass with decreasing speed as more material is engulfed; collisions of macroscopic particles lead to continual redistribution of part of the motion to the whole mass in a way that increases random motion, rather than in the highly orderly was consistent with isentropy. The random motion may be both on a microscopic scale (heat) and on a macroscopic scale below the resolving power of the observing system. (In some of our experiments, the apparent energy loss was quite high. For example, in Shot 9802, assuming foam and flyer to be moving at a final speed equal to the entry in the fourth column of

Table 1, the final kinetic energy is 14% of the original.) Depending on the sizes of the voids, certain frequency components of the input motion probably suffer different effects than others. The elastic forerunner is not considered a feature of the characteristic foam flow but is thought to be a property of a framework which is broken as the main wave moves through the material. Locking may or may not occur, depending on the physical properties of the particles and their changing environment.

Miles' [9] description of flow in a soil subject to intense pressure shows many of the above characteristics, particularly diffusive wave shapes, loss of kinetic energy, and changing density. His solution is for a 1-D continuum and he does not consider forerunners or any features of behavior related to pore dimensions. And his closed solution for the case of a locking medium is asymptotic only. His use of accumulated gross strain as the criterion of locking is probably generally a good approximation, but it could in fact depend on other factors such as accumulated plastic deformation of individual grains, peak pressure, or temperature.

ACKNOWLEDGMENTS

The authors are indebted to G. R. Fowles for introduction to this field of study and early advice, and for the conception of the 1-D experiment; Ray Dettling, Mary Grathwol and Betty Bain for a large part of the data reduction; and Curtis Wheeler for shot assembly. The work was performed under contract with the United States Air Force Weapons Laboratory.

The authors also thank Professor George E. Duvall for helpful criticism.

REFERENCES

1. G. R. Fowles, *J. Appl. Phys.*, **32**, 1475 (1961).
2. D. Bancroft, E. L. Peterson and S. Minshall, *J. Appl. Phys.*, **27**, 291 (1956).
3. D. R. Curran, *J. Appl. Phys.*, **34**, 2677 (1963).
4. T. E. Sterne, Ballistic Research Laboratories Report No. 648, Aberdeen Proving Ground, Md., 1947.
5. G. R. Abrahamson, extension of work published in Poulter Laboratories Internal Report 009-62, Stanford Research Institute, Menlo Park, Calif., 1962.
6. M. G. Salvadori, R. Saklak, and P. Weidlinger, *J. Eng. Mech. Div. Proc. Am. Soc. Civ. Eng.*, **86**, No. EM2, 77 (1960).
7. J. R. Rempel and D. N. Schmidt, Final Report Project 4613-1, Stanford Research Institute, Menlo Park, Calif., 1964.
8. H. Lamb, *Hydrodynamics*, Dover, N. Y., 1945, p. 577.
9. J. W. Miles, *J. Appl. Mech.*, **83E**, No. 1, 21-24 (1961).
10. J. R. Rempel, Air Force Weapons Laboratory RTD TDR 63-3056, August 1, 1963.
11. G. R. Fowles, *J. Appl. Phys.*, **31**, 655 (1960).
12. C. D. Lundergan, *J. Appl. Phys.*, **34**, 7, 2046 (1963).
13. J. M. Walsh, M. H. Rice, R. G. McQueen, and F. L. Yarger, *Phys. Rev.*, **108**, 2, 196 (1957).
14. Handbook of Chem. and Phys., 42nd ed., Chemical Rubber Publishing Co., Cleveland, 1960.
15. D. N. Schmidt and M. W. Evans, *Nature*, **206**, 4991, 1348-9, 1965.

ELASTOPLASTIC EFFECTS IN THE ATTENUATION OF SHOCK WAVES*

John O. Erkman

*Poulter Laboratories, Stanford Research Institute
Menlo Park, California*

ABSTRACT

The effect of rigidity on the attenuation of shock waves in aluminum and copper has been studied. Attenuating shock waves were induced in targets by the impact of projectiles consisting of thin aluminum plates. The maximum stress induced in the aluminum targets was about 0.1 megabar and about 0.15 megabar in the copper targets. Results of the experimental study show that shock waves attenuate more rapidly than predicted by calculations based on a fluid-type equation of state. It was necessary to use an equation of state incorporating elastoplastic behavior in order to make the calculations agree reasonably well with the experimental data. In the elastoplastic model of the equation of state, Poisson's ratio is a constant and the shear modulus increases with the hydrostatic pressure in constant ratio to the bulk modulus. The variable shear modulus permits the elastic relief wave velocity in aluminum to be about 20% greater at 0.1 megabar than at ambient pressure. The critical shear stress is also permitted to increase with pressure so that the elastic relief wave in aluminum, for example, has an amplitude of about 0.032 megabar when the stress at the shock front is 0.1 megabar. This large amplitude unloading wave is consistent with the experimental data.

I. INTRODUCTION

The attenuation of shock waves in solids has been studied at Stanford Research Institute for the past four years. Among the materials studied are metals, rocks, and a plastic. Some of the earlier work with aluminum was reported by Curran [1] and Fowles [2]. Later work with aluminum, copper, rock salt, marble, basalt, and alluvium was reported by Erkman [3,4]. Some of the more recent work with aluminum, copper, and an epoxy is described in this paper.

The main reason for the study of the attenuation of shock waves in any material is to obtain information concerning the stress-strain relation of the material as the pressure is relieved. Data such as the speed of sound behind the shock front, for example, aid in determining if the material behaves as a fluid or as an elastoplastic material, or in some other manner. For materials that exhibit elastoplastic behavior, measurement of the amplitude of the initial

elastic relief wave gives information from which both the reverse yield strength and the elastic sound speed of the compressed material may be deduced.

In part of the work, attenuation of shock waves was studied by recording the response of the free surface of samples that had been impacted on the opposite surface by thin projectiles, usually aluminum plates about 0.125 inches thick. Samples were made in the shape of wedges so that the optical lever arm method of recording with the smear camera could be used [5]. In other studies, the samples were flat and the recording was accomplished by the use of Manganin wire gages placed on the surface opposite the impacted surface [6]. For aluminum, flat samples to which thin aluminum shims had been attached were also used. When the shock wave arrived at the free surface, the shims were thrown into free flight across known gaps. The last two of these techniques were used to ensure that the flow was as close

*This work was supported by the Air Force Weapons Laboratory under Contract Numbers AF 29(601)-6040 and AF 29(601)-6734.

to being one-dimensional in the strain as possible.

Results of experiments were compared with the results from calculations based on two different models for the relation between stress and strain. In one model, it was assumed that the Hugoniot curve was sufficient to relate stress to strain both in compression and in relief of stress. Hence, both rigidity and entropy changes were neglected and the method of characteristics was used to solve the flow equations. For lack of better terminology, this treatment of the problem is called hydrodynamic in the subsequent discussion.

In other calculations, stress and strain were related by elastoplastic relations so that rigidity was taken into account, but entropy changes were still neglected. Only the simple case of one-dimensional strain was treated. The yield was made to depend on the hydrostatic pressure so that the calculated results would show the early attenuation observed in the experiments. For the elastoplastic case, the flow equations were solved by use of the method devised by von Neumann and Richtmyer. This method was used because the use of the method of characteristics becomes complicated when the flow is elastoplastic.

II. EXPERIMENTAL ARRANGEMENT FOR STUDYING ATTENUATION OF SHOCKS IN SOLIDS

A. Flyer Plate Assemblies

All the attenuation experiments were performed by throwing aluminum plates with charges of high explosives. The arrangement consisted of a plane wave generator (PWG) and a charge of baratol 1 inch thick in contact with a brass plate that was 0.5 inch thick. A thermo-setting plastic cement about 0.001 inch thick affixed the aluminum plate to the brass plate. The brass plate was used partly because it held back the detonation gases so that the experiment could be viewed clearly and because it served as a base for the vacuum chamber. The impedance mismatch between the aluminum and the brass is such that the aluminum separates from the brass and travels with a considerably higher velocity than the brass.

When an 8-inch-diameter charge of baratol is initiated by an 8-inch-diameter PWG, the aluminum plate acquires a velocity of about $0.12 \text{ cm}/\mu\text{sec}$. The useful diameter of the flyer plate is about 4 inches. The flyer plates are not flat, a fault which is attributed to the plane

wave initiator. The initiators are very good in that they produce a detonation front that arrives at a surface simultaneously. However, the impulse delivered, for example, at the center of the plate is slightly different from that delivered an inch or two away from the axis of symmetry. The result is a plate that is slightly bowed, as if its center acquired slightly less momentum than did portions an inch or two from the center. Near the edge of the plate, which is originally 6 inches in diameter, edge effects tend to slow the plate. Experiments in which the shapes of several plates have been determined are reported elsewhere [4,7].

B. Methods of Recording for Attenuation Experiments

In most of the studies of attenuation, the motion of a free surface was obtained from smear camera records. In the early studies the smear camera record gave the time required for the free surface to move across a known gap. This method is not accurate for attenuating shock waves because the free surface velocity is not constant. A more reliable method makes use of the optical lever arm technique, which is capable of giving the instantaneous initial velocity of the surface [5]. This technique has the disadvantage of requiring that experimental data be differentiated, an operation that is complicated by the fact that the flyer plates are curved. Another disadvantage is that the specimen must be in the shape of a wedge so that the shock is obliquely incident on the free surface and the flow is not one-dimensional.

Some recent experiments employed a modification of the time of flight technique. Aluminum specimens were prepared as flat samples and the surface to be observed by the smear camera was covered by a thin aluminum shim (about 0.001 inch thick). The shim was held mechanically by its edges so that it was thrown off of the surface relatively easily. The smear camera recorded the time of flight of the shim across a known gap. The shim traveled in a vacuum, so its velocity was uniform and a measure of the initial shock-induced free surface velocity was obtained. These techniques gave information about the free surface velocity of the specimen when it was the shock-induced particle velocity that was desired. In this paper, it is assumed that the free surface velocity is twice the shock-induced particle velocity so that experimental and calculated results can be compared most easily.

A transducer was also used in studying the attenuation of shock waves. The device which

was developed at Stanford Research Institute [6,8] consisted of a Manganin wire cast in C-7 epoxy manufactured by Armstrong Products Company. It was calibrated to give pressure in the epoxy, so impedance mismatch solutions must be used to obtain the pressure in a material adjacent to the epoxy. The response time of the gage is adequate to record accurately the arrival of a shock wave at the Manganin wire. It also appears to respond to the variations in pressure after the passage of the shock front, and it was this possibility that was the chief attraction for using the gage to study the attenuation of shock waves. Accurate records showing pressure as a function of time would be helpful in determining the velocity of the initial relief wave behind a shock front. If the relief wave is elastic, the gage records should be useful in measuring its strength. These results would help in the formulation of models for the relation between stress and strain in the solids being studied.

III. CALCULATION OF ATTENUATING SHOCK WAVES

In some of the calculations, the material was assumed to behave hydrodynamically, i.e., material rigidity was neglected. Pressure was related to density by

$$P = A \left[\left(\frac{\rho}{\rho_0} \right)^K - 1 \right], \quad (1)$$

where P is the pressure, ρ is the density, and ρ_0 is the density at zero pressure. Values of the constants A and K were obtained by requiring the equation to fit the Hugoniot data of the medium. No adiabats were derived, it being assumed that, for the materials observed and for the pressures encountered, the adiabats were not distinguishable from the Hugoniot curves. Thus the term "hydrodynamic" is used in a restricted sense.

Table 1 gives the values of A , K , and ρ_0 for the materials for which calculations have been performed. The sources of the data used in determining the values of A and K are also given for each case. Data for the C-7 epoxy range from about 0.04 to 0.08 Mbar. For this material, the pressure encountered in the experiments was 0.046 Mbar or less.

Determinations of the constants for aluminum and copper have been reported previously [3]. For gold, the data given by Rice et al [9] were used in determining the values of constants.

TABLE 1
Values of Constants for Murnaghan
Equation of State

Material	(g/cm ³)	A ^a (Mbar)	K	Source
C-7 Epoxy	1.18	0.205	4.54	Ref. 7
Aluminum	2.785	0.196	4.10	Ref. 3
Copper	8.9	0.301	4.71	Ref. 3
Gold	19.24	0.305	5.79	Ref. 9

The computer code that employs Eq. (1) to represent the equation of state uses a finite difference scheme based on the method of characteristics. Results of this code are identified with the label "hydrodynamic solution" in the figures where results are reported. For a small distance, i.e., a small value of x/x_0 , the results amount to an impedance mismatch solution.

In order to account for the early attenuation of shock waves induced by the impact of high-speed aluminum plates, an elastoplastic relation between stress and strain was assumed [1]. This model has the notable feature that the initial attenuation in the situation described above is accomplished by an elastic relief wave. The velocity of this wave is considerably greater than the velocity of the following plastic waves. The model is described graphically in Fig. 1, where Hugoniot data are assumed to lie along the curve ac . This curve is related to the hydrostatic curve by the relation

$$p_x = \bar{p} + 2Y/3, \quad (2)$$

where p_x is the stress along the curve ac , and \bar{p} is the hydrostatic pressure. The variable Y represents what is usually called the yield stress in simple tension and is twice the maximum resolved shear stress. The curve bf is displaced from the hydrostat by $-2Y/3$.

Comparisons of theory and experiment based on this model with constant yield strength show improvement in agreement over that obtained with the fluid model; however, significant differences still remain. Good agreement can be obtained by assuming that the yield strength is a function of the hydrostatic pressure

$$Y = Y_0 + M(\bar{p} - \bar{p}_a), \quad (3)$$

where Y_0 and M are constants, \bar{p} and \bar{p}_a being defined in Fig. 1. The hydrostatic curve is represented by

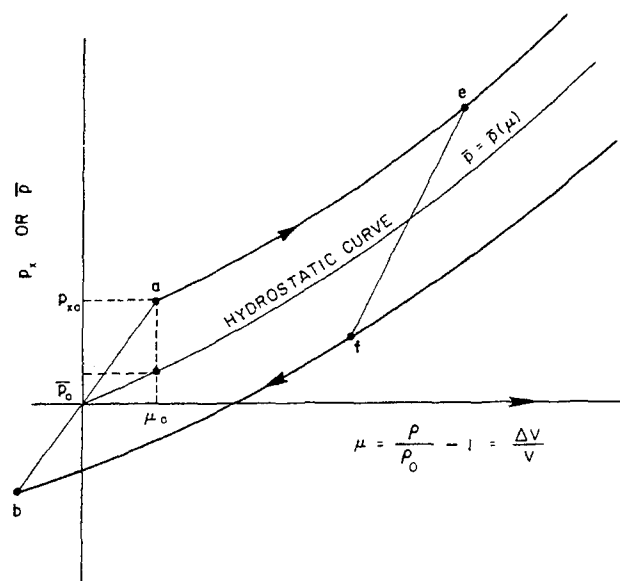


Fig. 1 - Elastoplastic equation of state

$$\bar{p} = A\mu + B\mu^2 + C\mu^3 \quad (4)$$

where $\mu = \rho/\rho_0 - 1$, ρ is the density, and ρ_0 is the density at normal pressure. Combinations of values of the constants for aluminum, copper, and C-7 are given in Table 2. Hugoniot data for aluminum and copper were taken from Rice et al. [9], while values of Y_0 and M were estimated from attenuation experiments. Data for C-7 epoxy were obtained from Keough [6]. Poisson's ratio was assumed to be 1/3 for aluminum and copper and 0.4 for the epoxy, the same as for lucite [10].

Both the bulk and shear moduli are expressed in terms of Poisson's ratio, ν , and Young's modulus, E , and do not appear explicitly in the equations describing the elastoplastic model. Poisson's ratio is assumed to be independent of pressure, and E is represented by

$$E = -3(1 - 2\nu)V \frac{d\bar{p}}{dV}, \quad (5)$$

where V is the specific volume.

TABLE 2
Values of Constants for Elastoplastic
Equations of State

Material	Y (Mbar)	M	A (Mbar)	B (Mbar)	C (Mbar)	ρ_0 (g/cc)
Aluminum	0.0025	0.055	0.755	1.29	1.197	2.785
Aluminum	0.0025	0.0	0.743	1.74	0.329	2.785
Aluminum	0.0	0.0	0.765	1.66	0.428	2.785
Copper	0.0007	0.031	1.49	0.546	11.85	8.936
C-7	0.0	0.0	0.0782	0.196	0.221	1.18
C-7	0.0006	0.0	0.0585	0.301	0.0726	1.18
C-7	0.001	0.0	0.0528	0.328	0.0379	1.18

The elastic relief wave decreases the stress from p_{xe} to p_{xf} , Fig. 1. This change in stress [11] is given by

$$p_{xe} - p_{xf} = \frac{1 - \nu}{1 - 2\nu} (Y_e + Y_f). \quad (6)$$

If Y is not strongly dependent on the pressure, and $\nu = 1/3$, the usual result is obtained,

$$p_{xe} - p_{xf} = 4Y. \quad (7)$$

The elastic longitudinal sound speed c is defined as

$$c = \sqrt{\frac{dp_x}{d\rho}}. \quad (8)$$

The derivative is evaluated by using the relation between p_x and ρ that connects points e and f in Fig. 1. The relation is

$$p_{xe} - p_x = 3(1 - \nu)(\bar{p}_e - \bar{p})/(1 + \nu), \quad (9)$$

where p_{xe} is the stress at point e , Fig. 1, and \bar{p}_e is the hydrostatic pressure at $\mu = \mu_e$. Use of Eq. (4) and the definition of μ permits Eq. (9) to be written so that p_x is a function of the density, ρ . The expression for the sound speed then becomes

$$c_1 = [-3V^2(1 - \nu)(d\bar{p}/dV)/(1 + \nu)]^{1/2} \quad (10)$$

where V is the specific volume. By use of Eqs. (2) and (3), the hydrostatic pressure \bar{p} can be replaced by the stress p_x . The result is:

$$c_1 = \{3(1 - \nu)(dp_x/d\rho)/[(1 + \nu)(1 + 2M/3)]\}^{1/2} \quad (11)$$

where $dp_x/d\rho$ is the derivative of the upper curve, Fig. 1, which represents the Hugoniot data. In the computer code where the difference scheme is based on the method of characteristics, sound speed is simply $(dp/d\rho)^{1/2}$, where p vs ρ represents the Hugoniot data and the derivative is evaluated using Eq. (1). For $\nu = 1/3$, the elastic sound speed, from Eq. (11), is

$$c = \sqrt{\frac{3}{2(1 + 2M/3)}} \times \sqrt{\frac{dp_x}{d\rho}}, \quad (12)$$

or

$$c = \sqrt{\frac{3}{2(1 + 2M/3)}} c_{\text{hydro}} \quad (13)$$

so the elastic sound speed is always greater than the hydrodynamic sound speed, c_{hydro} . The elastic sound speed is reduced a few percent when M is not zero ($M = 0.055$ for aluminum).

Any variation of ν with pressure would affect both the amplitude of the elastic wave, Eq. (6), and its velocity, Eq. (11). No calculations have been performed in which the value of ν was permitted to vary.

The computer code which uses the elastoplastic model for the equation of state employs the method of integrating the flow equations given by von Neumann and Richtmyer [12]. This method uses an artificial viscosity term which smears the shock front over a few cells or meshes. Both linear and quadratic terms are used in the expression for artificial viscosity,

$$Q = (2.9\Delta U + 0.1c) \Delta U/V, \quad (14)$$

where c is the speed of sound (the code uses the elastic sound speed), V is the specific volume, and

$$\Delta U = U_{j+1} - U_j \quad (15)$$

is the difference in particle velocities in two adjacent cells. This relation is used only when the material is being compressed, i.e., for $\Delta U < 0$. Otherwise the value of Q is taken to be zero.

Most of the calculations presented in this report were obtained by use of the artificial viscosity code (the Q -code). Each set of results is identified with the values of Y_0 and M used in the equation of state for that set. When both Y_0 and M are zero for both projectile and target, the results should agree with results obtained with the previously described characteristics code. The agreement is not exact because Eqs. (1) and (4) cannot give the same results, and because of the smearing of the shock front by the Q -code.

IV. RESULTS OF ATTENUATION STUDIES USING FREE SURFACE VELOCITY MEASUREMENTS

A. C-7 Epoxy Wedge-Shaped Specimen

Results for the C-7 epoxy wedge are given in Fig. 2, which shows the shock-induced particle velocity as a function of the distance into

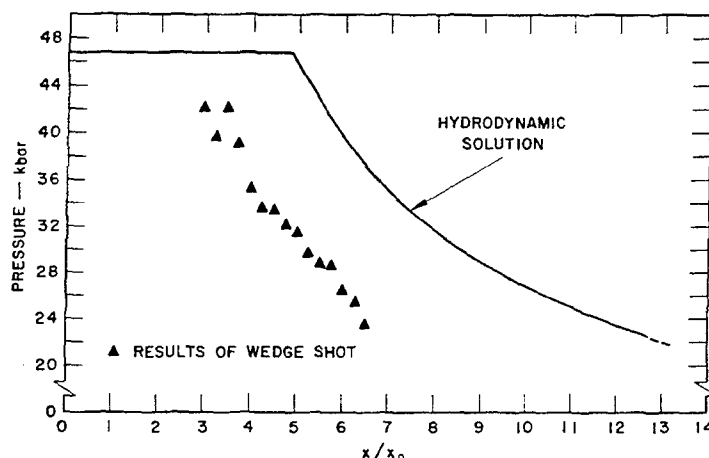


Fig. 2 - Peak pressure in C-7 epoxy vs x/x_0
(x_0 is thickness of flyer plate)

the C-7. The record was unreliable near the thin end of the wedge, so no values of the particle velocity were obtained for values of x/x_0 less than approximately 3.* An impedance "mismatch" solution gave a pressure of about 46 kbar in the absence of any attenuation. Hence attenuation of the shock commenced at a distance of about 2.5 times the thickness of the aluminum flyer plate. The hydrodynamic calculation predicted that attenuation would start at 4.9.

B. Aluminum Specimen

Specimens were fabricated from both 2024-T4 and 1060 aluminum. After being machined, the 2024 specimens were heat treated in an air atmosphere at 775°F. for three hours, and were then cooled to 500°F. at a rate of 50°F. per hour. Specimens cut from 1060 aluminum were held at a temperature of 650°F. for one-half hour.

Results for two shots, using annealed 2024 aluminum target wedges, are shown in Fig. 3. Shot 10,227 was designed to give data at a few plate thicknesses into the target by using a small wedge angle. This shot shows what can be called attenuation at about 5 plate thicknesses; at 3 plate thicknesses the results compare favorably with the hydrodynamic solution, which in this region amounts to an impedance mismatch solution using only Hugoniot data.

*It was convenient to divide the distance the shock had traveled into the specimen, x , by the thickness of the flyer plate, x_0 , which was 0.322 cm for most experiments reported here.

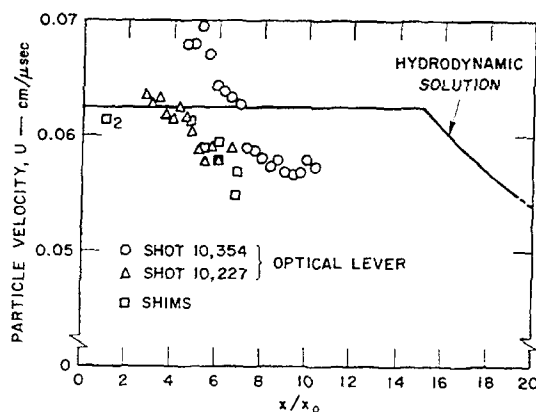


Fig. 3 - Peak particle velocity in aluminum vs x/x_0 2024 aluminum

Shot 10,354 was designed to yield data for greater values of x/x_0 . The results are given in Fig. 3; the particle velocity is surprisingly high at values of x/x_0 near 5. All shots were designed on the assumption that the explosive system gave reproducible flyer plate velocities, which were measured in separate experiments. Plate velocities have been observed in attenuation experiments at a cost of more difficulty in design of the experiment and in less satisfactory records of the motion of the free surface of the specimen. The present results show that reproducibility was not good when Baratol was used. The average of the four points near 5 plate thicknesses gives a particle velocity of close to 0.068 cm/μsec. If no attenuation at this thickness is assumed, a flyer plate velocity of 0.136 cm/μsec is implied. The unexpectedly high

values of particle velocities in Shot 10,354 may be due to the inadvertent use of a charge of Baratol that was capable of giving greater velocities.

In Shot 10,354, attenuation commenced between 5 and 6 plate thicknesses, in fair agreement with Shot 10,227. Averaging the first four points for Shot 10,354 gives a particle velocity of 0.068 cm/ μ sec, which corresponds to a stress of 120 kbar on the Hugoniot for aluminum. At approximately 8, the particle velocity is approximately 0.058, and the stress is 100 kbar. If this attenuation is entirely due to the elastic relief wave, the value of the yield strength, Y , is approximately 5 kbar, or about twice that expected for 2024 aluminum under more ordinary conditions. The relation between the yield strength and the amplitude of the elastic relief wave is given in Section III.

The most recent data have been obtained by observing the time of flight of shims across a known gap. Data for two shots, using 2024-T351 aluminum in the as-received condition, are given in Fig. 3 also. The velocity for the flyer plates for these two experiments was measured in the shots and found to be 0.127 cm/ μ sec. The two shots gave the same results for $x/x_0 = 1$, that is, a particle velocity of 0.0615 cm/ μ sec (as indicated previously, the free surface velocity is assumed to be twice the shock-induced particle velocity). The same velocity is observed at 5.8 plate thicknesses, following which attenuation definitely occurs, as was indicated by 10,227 also. The scatter in the data in the neighborhood of 6 and 7 plate thicknesses may be due to the fact that a substantial amount of attenuation was taking place and that conditions in the two shots were not identical. Further work will have to be done with this technique before the magnitude of the initial relief can be obtained.

Results of two shots using annealed 1060 aluminum are shown in Fig. 4. Attenuation in Shot 10,226 commenced at 5 or 6 plate thicknesses. The results agree well with the hydrodynamic solution for small values of x/x_0 also. Results of Shot 10,353 show unexpectedly high values of the particle velocity at about 5 plate thicknesses. As before, this must indicate that the flyer plate had a velocity greater than expected—0.125 cm/ μ sec. If this is true, attenuation in 1060 aluminum commences at about 5 or 6 plate thicknesses, just as it does in 2024 aluminum. The data are not precise enough to determine to a fractional part of a flyer plate thickness the point at which attenuation commences.

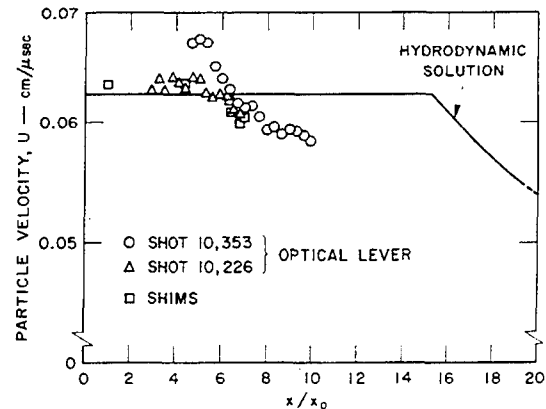


Fig. 4 - Peak particle velocity in aluminum vs x/x_0 1060 aluminum

In Shot 10,353, the particle velocity dropped from about 0.067 to 0.059 cm/ μ sec in the vicinity of x/x_0 of about 7. By using the same Hugoniot as was used above for the 2024 aluminum, the stress dropped from 118 kbar to 102 kbar, so that the value of Y is about 4 kbar. In both cases, the value of Y is approximate, and it is not certain that its value for 1060 aluminum is really smaller than it is for 2024 aluminum.

Results of two shots in which the shim technique was used on 1060 aluminum are also shown in Fig. 4. The unattenuated particle velocity for this material is 0.0635 cm/ μ sec, rather than 0.0615 as observed for the 2024 aluminum in Fig. 3. The flyer plate velocities in the two experiments with 1060 aluminum were 0.127 cm/ μ sec, so the free surface velocities for thin 1060 aluminum specimens are the same as the flyer plate velocity. This was not true for the 2024 aluminum experiments. It is not known if the discrepancy is significant, or if it is due to errors in determining the velocities of the flyer plates. These new results are in substantial agreement with the results of the 1060 aluminum wedge shots already reported in that attenuation apparently commenced at about 5 plate thicknesses in the target.

C. Copper Wedge-Shaped Specimen

Copper specimens were cut from forgings of OFHC copper having a density of 8.94 g/cc. Principal impurities in the copper were 0.001 percent silver and possibly 0.002 percent nickel (from semiquantitative analyses). After machining and polishing, the samples were heat treated at a temperature of 1100°F. for an hour in an atmosphere of dry hydrogen.

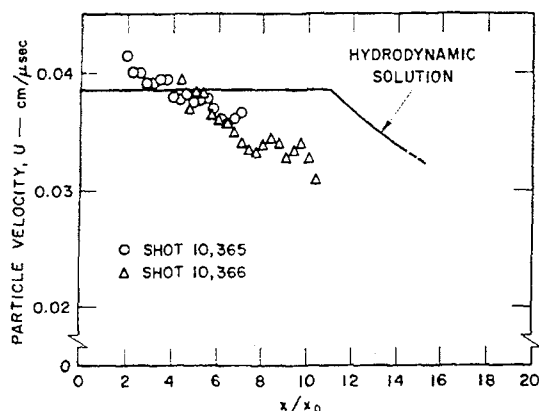


Fig. 5 - Peak particle velocity in copper vs x/x_0

Results of two experiments in which aluminum flyer plates hit copper targets are shown in Fig. 5. Results of Shot 10,366 are in reasonable agreement with the hydrodynamic solution out to 6 plate thicknesses. There is an indication that the flyer plate velocity may have been greater than 0.125 cm/μsec. Shot 10,365 indicated that some attenuation occurred at 5.5 to 6 plate thicknesses. Hence this pair of copper shots gave results that are more consistent than are the results from either pair of aluminum shots referred to above. Better reproducibility in this case, compared with the aluminum wedge shots, may be because the two copper wedge shots used Baratol that was from the same order.

The peak particle velocity for copper attenuates from approximately 0.040 to approximately 0.034 cm/μsec between 3 and 7 plate thicknesses. By using the Hugoniot for copper, the stress attenuates from 163 kbar to 136 kbar, or 27 kbar. If this is due entirely to the elastic wave in copper, the yield strength is about 7 kbar. The precision of the data may be inferred from the scatter in the results shown in Fig. 5. The scatter is about 0.002 cm/μsec near $x/x_0 = 8$, or about ± 3 percent.

D. Gold Wedge-Shaped Specimen

The gold wedge was made from 99.99 percent gold by Western Gold and Platinum Company, Belmont, California. After casting, the gold was reduced 50 percent in thickness by rolling and then was machined into the required shape. After the inclined surface was polished, the material was softened by heating to 650°C for one hour. Because of the size of the sample,

the flyer plate was also reduced to 0.040 inch in thickness. This flyer plate was observed to have a velocity of 0.133 cm/μsec, for which the probable error is less than 1 percent.

Results for the gold shot are shown in Fig. 6, along with the results of the hydrodynamic calculations. At $x/x_0 = 3.3$, the experimental results give a particle velocity of 0.028 cm/μsec, which agrees well with the predicted value, 0.0288 cm/μsec. Some attenuation took place between values of x/x_0 of 3.3 and 6.9, the particle velocity being reduced from 0.028 to 0.024 cm/μsec. These values of particle velocities correspond to Hugoniot pressures of 190 and 159 kbar, respectively. This is interpreted as being the amplitude of the elastic relief wave for gold at the pressures referred to above. As was done for aluminum and copper, a value of the yield strength, Y , is inferred. For gold, Poisson's ratio ν is 0.42, so Y is about 4 kbar. (See Section III for the method for calculating the conversion factor.)

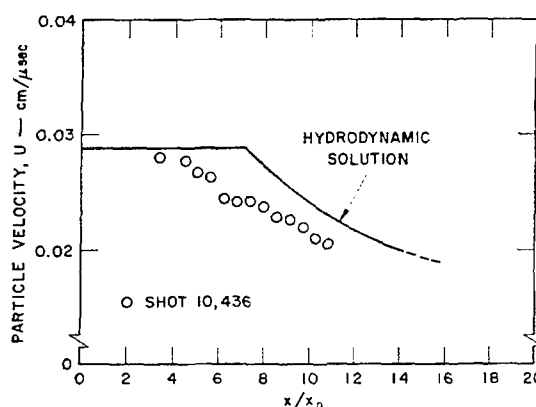


Fig. 6 - Peak particle velocity in gold vs x/x_0

V. RESULTS OF ATTENUATION STUDIES USING GAGES

A. C-7 Epoxy Specimens

Results of experiments in which "bare gages" were hit by aluminum flyer plates are given in Fig. 7. The term "bare gage" is applied to the arrangement in which no material other than epoxy separates the flyer plate from the Manganin wire after impact. Three gages were used in each shot, the wires of which were located at different depths in the epoxy so that attenuation of peak pressure could be observed. Because the oscilloscopes were triggered

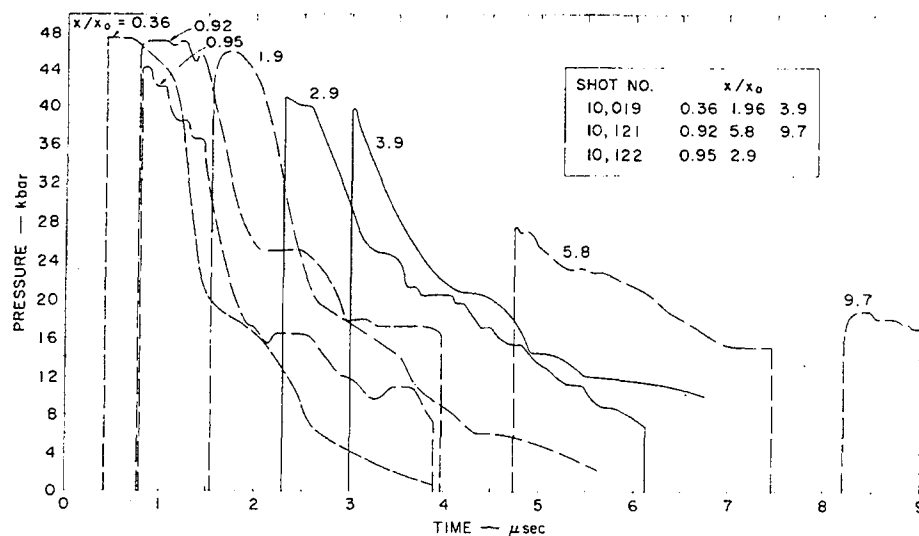


Fig. 7 - Pressure vs time from gages hit by aluminum plates

independently, the relation in time of one record to another is not known accurately even for records taken from the same shot. Placement of the records in Fig. 7 (and in subsequent figures) is therefore arbitrary, being based on calculations described earlier. Some indication of the reproducibility of results can be obtained by comparing the curves for which values of x/x_0 are 0.92 and 0.95. These differ by about 6 percent in peak pressure and have considerably different shapes. This latter disagreement is particularly distressing because it indicates that these gages may not give the shape of the pulse reliably. It may be, however, that the gage at $x/x_0 = 0.95$ was faulty.

The envelope of the curves shown in Fig. 7 shows that some attenuation takes place between $x/x_0 = 1.9$ and $x/x_0 = 2.9$, which is in fair agreement with the results of the wedge experiments shown in Fig. 2, where attenuation is observed at 3 plate thicknesses. At $x/x_0 = 6$, the wedge experiments give a pressure of about 26 kbar, which agrees well with the 27 kbar given by the gage of 5.8 plate thicknesses.

Results of calculations are given in Fig. 8 also. The method used in the calculations is described in Section III of this paper. The calculated results agree fairly well with the experimental results when both the aluminum and

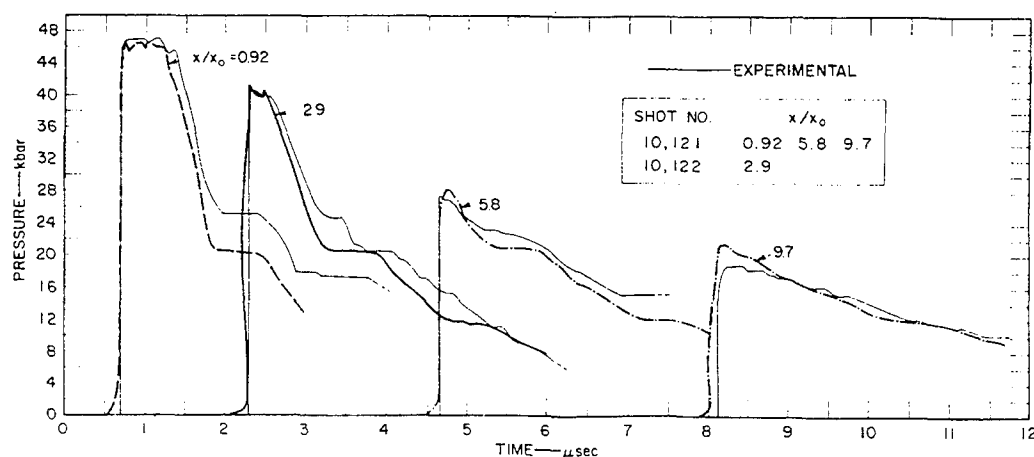


Fig. 8 - Comparison of calculated wave profiles with results of experiments for C-7 epoxy

the epoxy are treated as elastoplastic materials. As noted in the figure, the yield strength of the epoxy was taken to be 1.0 kbar in the calculations, even though no elastic precursor has been observed in the material. Obviously no final conclusion can be made about the stress-strain relation of epoxy on the basis of these observations. But it is of considerable interest that calculated results based on a simple hydrodynamic model do not agree so well with the experimental results. In other calculations, the yield, Y , of the epoxy was permitted to vary linearly from zero for stress-free material to 2 kbar when the hydrostatic pressure was 50 kbar. Results of these calculations were not significantly different from those based on a constant value of 1.0 kbar yield.

Peak pressure as a function of distance of penetration of the shock into the epoxy is shown in Fig. 9 for both gage and wedge shots. Note that changing the value of Y_0 from 0.6 kbar to 1.0 kbar makes only a small change in the calculated results. The equations of state of both the epoxy and the aluminum are given in Section III.

B. Aluminum Specimens

When gages were used on metal targets, the Manganin wire was separated from the surface of the specimen by about 0.1 cm of C-7 epoxy. Three gages were included in each shot, each gage being set on a different thickness of metal. An unexplained phenomenon occurred when a gage recorded the response of a thin target. For

a target of the same thickness as the flyer plate, 1/8 inch, the peak pressure recorded by the gage was 51 kbar. When a flyer plate hit a bare gage, the pressure was 45 kbar. If this peculiarity is overlooked, the gages give results consistent with the results reported in the previous section, that is, the attenuation of the shock wave occurs earlier than is predicted by the hydrodynamic theory.

Results from two gages on aluminum targets are given in Fig. 10 in terms of pressure as a function of time. The experimental records were reduced in amplitude by the factor 45/51 due to the peculiarity mentioned above. The impedance mismatch of aluminum and C-7 epoxy is relatively large, so a strong relief wave is reflected back into the aluminum at the interface between the two materials. This relief wave interacts with the wave from the back side of the flyer plate and puts a portion of the aluminum in a state of tension. The tension becomes great enough to cause the aluminum to fracture or spall. When this happens, compression waves are generated which propagate in both directions. One of these enters the epoxy and affects the gage response. For the gage record labeled 7.9 in Fig. 10, that portion of the record later than 5.5 μ sec may be affected by spalling. In order to calculate the pressure profile, a spall strength must be assumed. If the assumed strength is too great, the calculated gage response shows an increase in pressure, or a reloading. This happened when a strength of 10 kbars was used for the spall strength of aluminum. In order to get better agreement with the experimental results which show no

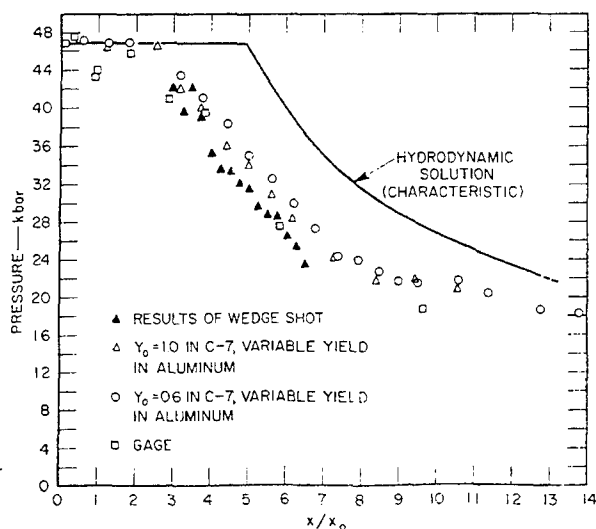


Fig. 9 - Peak pressure in C-7 epoxy vs x/x_0 from experiments and calculations

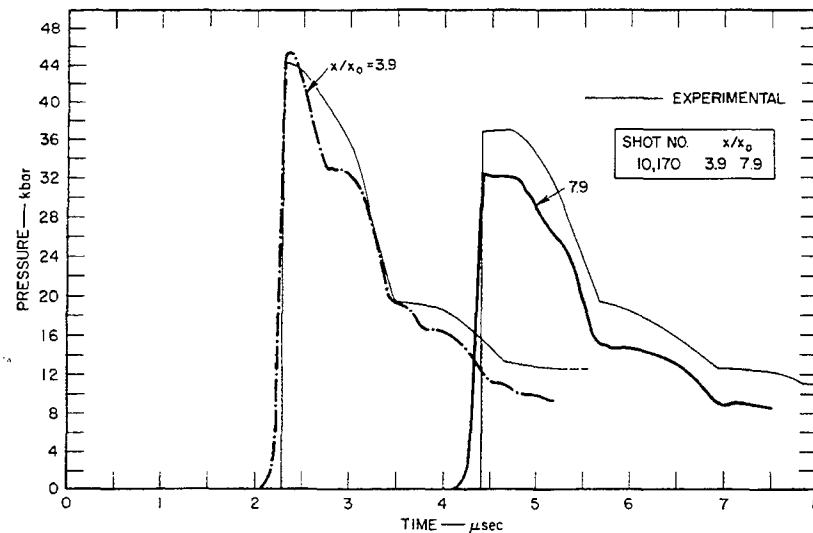


Fig. 10 - Comparison of calculated wave profiles with results of gages for aluminum targets (spall strength assumed to be 5 kbar)

reloading, the spall strength was reduced to 5 kbar, giving the results shown in Fig. 10. These results do not prove that the spall strength of aluminum is 5 kbar. One reason for this is the necessity for extrapolating the equation of state to negative pressures. The equation of state, which is discussed in Section III, was not designed to extrapolate to negative pressures in a meaningful way. Also, the method used in the calculations spreads out the relief waves as well as the shock fronts. This makes the prediction of spalling by the computer code somewhat unreliable.

C. Copper Specimens

Results from experiments in which gages were mounted on specimens of copper were in general agreement with the results from the wedge experiments reported in Section IV. That is, the attenuation occurred at a time earlier than that predicted by hydrodynamic theory. Some representative experimental results are shown in Fig. 11. These records show some evidence of the reloading mentioned above in connection with the results for gages on aluminum specimens. A spall strength of 5 kbar was used in the calculations for copper, the results of which are also shown in Fig. 11. In this case, the calculated results show some reloading, see the profile for $x/x_0 = 7.9$. It is possible that a spall strength greater than 5 kbar should have been used for copper so that more reloading would be observed in the calculated results.

VI. SUMMARY AND CONCLUSIONS

Attenuation of shock waves was studied in 1060 and 2024 aluminum, OFHC copper, gold, and Armstrong C-7 epoxy. Shock waves were induced in samples of these materials by striking them with aluminum plates with velocities of about 0.125 cm/μsec. Because the strains induced in the specimens were virtually one-dimensional, the experiments could be simulated with a computer code. Comparison of experimental and calculated results indicated that an elastoplastic relation between stress and strain should be used for aluminum, copper, and the epoxy. More data are needed before a stress-strain relation can be suggested for gold.

The amplitude of the elastic relief wave in 2024 aluminum was approximately 20 kbar when the maximum stress was 120 kbar. On the assumption that Poisson's ratio is constant, a yield strength value of 5 kbar was inferred. This is the yield in simple tension, or twice the critical resolved shear stress. For 1060 aluminum, the amplitude of the elastic relief wave was 16 kbar, so the yield was 4 kbar when the maximum stress was 120 kbar. The relief wave in copper had an amplitude of 27 kbar, so the yield was approximately 7 kbar for a stress of 106 kbar. These values of the yield strengths are all greater than those observed at engineering stress levels and imply that the yield strength is a function of the stress. All the values of the yield given above were inferred from the data obtained from experiments using wedge-shaped specimens.

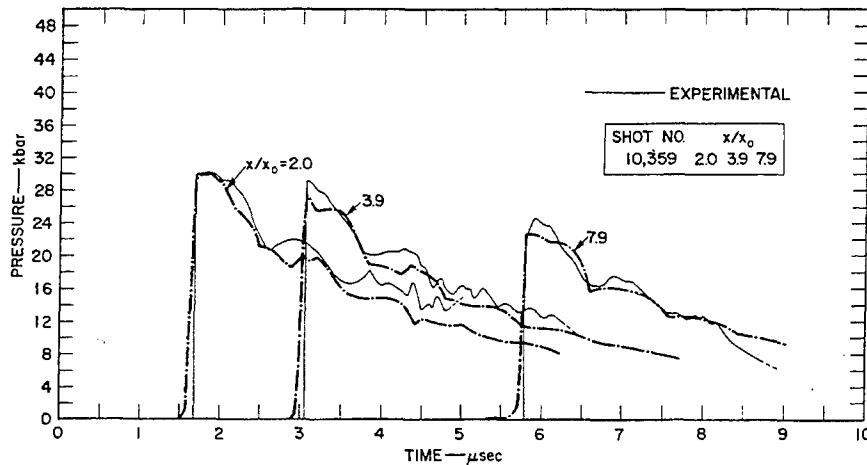


Fig. 11 - Comparison of calculated wave profiles with results of gages for copper targets (spall strength assumed to be 5 kbar in copper)

It was impossible to obtain a value of the yield strength directly from the experimental data for either gold or the epoxy. For the epoxy, the calculated attenuation matched the experimental observations fairly well when the yield was assumed to be 1.0 kbar.

The velocity of the elastic relief wave in annealed 1060 and in 2024-T351 unannealed aluminum is between 0.84 and 0.90 cm/ μ sec. Because the particle velocity in each case is about 0.062, the elastic sound velocity is between 0.78 and 0.84 cm/ μ sec. These values are about 25% greater than the hydrodynamic sound speed expected for the pressure involved (0.110 Mbar) [9]. They are also about 25% greater than the elastic compression wave speed in aluminum at ambient pressure [5]. The method of measuring the relief wave velocity has not resolved any difference in the behavior of the two types of aluminum.

REFERENCES

1. D. R. Curran, Nonhydrodynamic Attenuation of Shock Waves in Aluminum, *J. Appl. Phys.* **34**, 2677-2685 (1963).
2. G. R. Fowles and D. R. Curran, Experimental Testing of Shock-Attenuating Materials, AFSWC-TDR-62-22, 1962.
3. John O. Erkman, Hydrodynamic Theory and High Pressure Flow in Solids, Stanford Research Institute, Project No. PGU-3712, Technical Summary Report No. 2, 1962.
4. John O. Erkman, Hydrodynamic Theory and High Pressure Flow in Solids, Stanford Research Institute, Project PGU-3712, Final Report, 1963.
5. G. R. Fowles, Shock Wave Compression of Hardened and Annealed 2024 Aluminum, *J. Appl. Phys.* **32**, 1475-1487 (1961).
6. D. D. Keough, Pressure Transducer for Measuring Shock Wave Profiles, Stanford Research Institute, Project No. GPU-3713, Final Report, 1963.
7. Final Report, SRI Project No. 4613, Contract No. AF 29(601)-6040 to be published by AFWL, Albuquerque, New Mexico.
8. D. D. Keough, R. F. Williams, and D. Bernstein, Piezoresistive Pressure Transducer, paper presented at Annual Meeting of ASME, New York, Nov. 1964.
9. M. H. Rice, R. G. McQueen, and J. M. Walsh, *Solid State Physics*, F. Seitz and D. Turnbull, eds., Academic Press, Inc., New York, 1958, Vol. 6, pp. 1-63.
10. Dwight E. Gray, ed., *American Institute of Physics Handbook*, McGraw-Hill Book Co., Inc., New York, 1957.
11. G. E. Duvall, and Roy C. Alverson, Fundamental Research in Support of VELA-UNIFORM, Stanford Research Institute, Project No. PGU-3731, Semiannual Technical Summary Report No. 4, 1963.
12. J. von Neumann, and R. D. Richtmyer, A Method for the Numerical Calculation of Hydrodynamic Shocks, *J. Appl. Phys.* **21**, 232-237 (1950).

HYDRODYNAMIC ELASTIC PLASTIC THEORY AND PLANE SHOCK WAVES IN METALS. I. THEORY

James C. Pearson
U.S. Army, Picatinny Arsenal
Dover, New Jersey

ABSTRACT

In the theory of ideal isotropic plasticity the strength σ can for small strains, be given as a function of the plastic work w . Experiments performed by Bridgman have shown that the strength of a metal is a function of the pressure P . Further the strength is known to depend upon the temperature T . The question of the form and extent of the dependence of the strength upon the strain rate has not, as yet, been definitively settled. In the theory of ideal isotropic plasticity there are certain limitations to the form that a dependence $\sigma = \sigma(\dot{\epsilon}_{ij}^P, \dots)$ can take. That is, σ can depend on $\dot{\epsilon}_{ij}^P$ only through its tensor invariants J_2 and J_3 , and

$$\sigma \left[J_2(\dot{\epsilon}_{ij}^P), J_3(\dot{\epsilon}_{ij}^P), \dots \right] \xrightarrow{\dot{\epsilon}_{ij}^P \rightarrow 0} \sigma(w).$$

In this paper the equations necessary to describe hydrodynamic elastic plastic (HEP) problems, when $P = P(v, E - qw)$, $\mu = \mu(v, E - qw)$ and $\sigma = \sigma(w, T, P)$ or $\sigma = \sigma(w, T, P, J_2(\dot{\epsilon}_{ij}^P))$ will be developed.

This paper has been published as Picatinny Arsenal Technical Report 3464.

THE ELASTO-PLASTIC RELEASE BEHAVIOUR OF MAGNESIUM AT 80 Kb

P. J. A. Fuller and J. H. Price
*Atomic Weapons Research Establishment
Foulness, Essex, England*

ABSTRACT

A technique has been developed, based on the manganin wire transducer, which enables the stress-time profiles of shock and release waves produced in a block of magnesium by the impact of an explosively driven flying plate to be recorded. The profiles presented differ from those that would be predicted by hydrodynamic theory; in particular, the top of the release wave is traveling approximately 30% faster. A release stress-strain path is derived from the results and it is shown that this can be interpreted in terms of elasto-plasticity.

INTRODUCTION

There has been considerable discussion in the literature recently suggesting that the behaviour of solids under high shock stresses cannot be adequately described by hydrodynamic theory, and that the effects of yield strength are important [1]. Several experimenters have reported the initial parts of release waves behind intense shocks travelling faster than hydrodynamic theory would predict [2-5].

We have attempted to match the manganin wire transducer to a metal so that it can be used to record the stress-time profile of a plane wave inside the material, instead of observing a free surface. The advantage of this method is that, in principle, the interpretation of the results is simplified, and a complete mathematical analysis is possible, uncomplicated by lateral strain effects which have plagued much of the earlier work on plastic waves using rods and wires [6], or by the need to assume a particular theory of plasticity. Our preliminary results with magnesium show that stress-time profiles can be observed and that these can be used to calculate the stress-strain path of the release process.

TECHNIQUE

A transducer based on the linear pressure-resistance characteristic of manganin has already been used to measure stress as a function of time in electrical insulators [7]. To extend

this technique to a metal it is necessary to insulate each manganin wire and its leads from the surrounding metal without invalidating the stress-time profiles obtained. This may be attempted by using an insulator whose shock impedance approximates to that of the metal used, and by making the insulating layer so thin that any significant reverberations in it are over in a time which is short compared with that being measured.

Figures 1 and 2 show the design used. The manganin wire, of 0.005-inch diameter coated with glass to 0.008-inch overall diameter, is cast in the middle of a 0.025-inch layer of epoxy resin, loaded with powdered lead borate glass of density 6.1 gm/cc. The copper support tubes are 0.050-inch diameter, surrounded by 0.250-inch diameter soda lime glass tubing, which is a fairly good shock impedance match to magnesium. The loading of the epoxy resin was chosen so that the proportional sum of the compressed volumes of the constituents was equal to the specific volume of magnesium at the pressure of the experiment. Glass and epoxy resin were used because in previous work they have been found to be adequate insulators when shocked. The effectiveness of the insulation was shown by the agreement obtained between the measured peak pressure and that predicted from the shock and flying plate impact velocities. In addition the accuracy with which the wire resistance returned to its initial value after the passage of the stress wave indicated that the insulation remained satisfactory and that good contact with the wire was probably maintained.

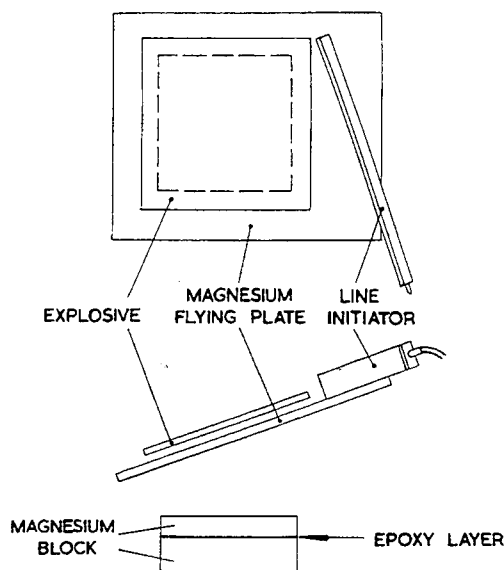


Fig. 1 - Arrangement of magnesium block and flying plate

The angle between the flying plate and the block is adjusted so as to achieve plane collision. Figure 3 shows how the shock and release waves propagate. The sides and back of the block are sufficiently remote from the transducers for reflected waves not to reach them until the measurements are completed; plane wave conditions are therefore maintained. The impact of the plate on the block is detected by capped concentric switch probes flush with the surface. In each round the square region of the flying plate striking the block is recovered in one piece and does not show any sign of scabbing.

Initially the experiments have been carried out at a comparatively low pressure of 80 Kb, a region where the strength of the metal would be expected to be important and conduction in the insulators less troublesome. The metal used was the magnesium alloy ZW 3 which has 2.9% zinc and 0.63% zirconium as its main alloying elements.

RESULTS

Figure 4a shows a typical oscillogram taken with the transducers one flying plate thickness (0.250-inch) into the block. It will be noticed that this stress-time profile is not flat-topped; there is a slight fall in stress of about 6 Kb lasting for about 0.5 microseconds after the initial rise in stress. This fall is not due

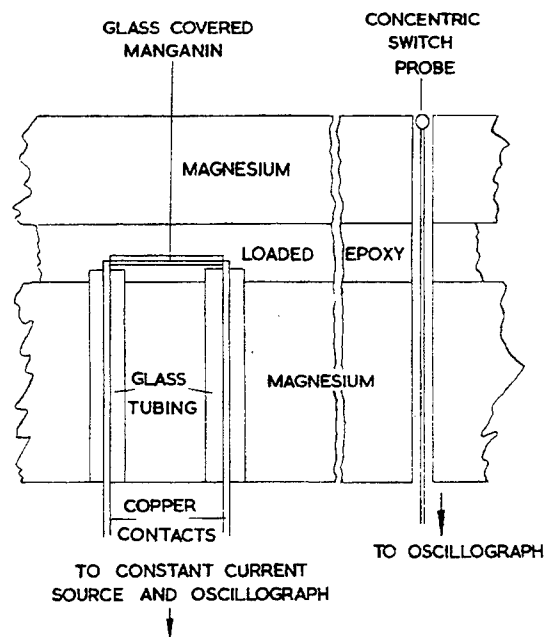


Fig. 2 - Details of transducer and insulator (not to scale)

to a release wave, which would have to travel at nearly infinite velocity, but is somehow associated with the shock front. Attempts to relate this fall in stress to features of the design of the experiment, such as the shock impedance of the insulator or its thickness for example, have not been successful. It could, therefore, be due to either some other property of the epoxy resin insulator or to the magnesium alloy. In a few experiments the glass tubing and the resin were replaced by thin PTFE sheet; the profiles from these shots tended to show a similar slope, but not when the magnesium was replaced by aluminium. A similar pressure-time profile has been reported in steel [8].

The stress drop due to the release wave begins at about 1.2 microseconds. The front of the release wave has a velocity of 7.3 ± 0.2 km/sec relative to the material, which is 30% higher than hydrodynamic theory would predict, about the same increase as has been estimated for other materials [2-5]. This higher velocity means that the top of the release wave should catch up with the shock at about five flying plate thicknesses into the block instead of fifteen as predicted by hydrodynamic theory. Figure 4b shows a typical oscillogram at five flying plate thicknesses.

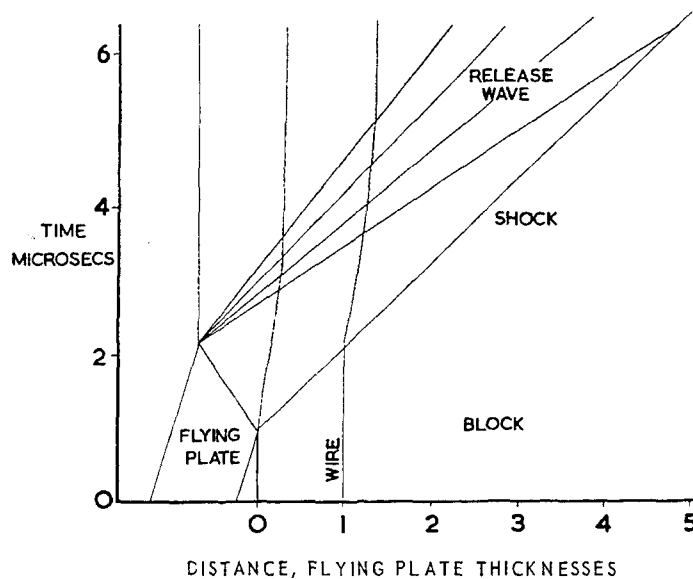


Figure 3

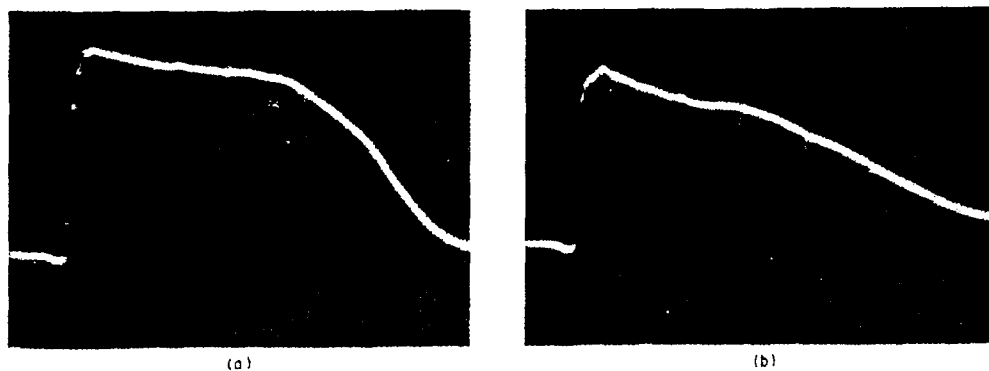


Fig. 4 - Pressure-time oscillograms at 1 and 5 flying plate thicknesses (0.5 microsecond time markers)

Interpretation

Despite the general similarity of shape shown by the profiles at one and five flying plate thicknesses it is not possible to interpret them in the same way. Following the previous interpretation and regarding the release wave at five flying plate thicknesses as beginning only after the constant stress region leads to a release velocity eight standard deviations lower

than that previously measured. Hence it is concluded that the initial fall in stress in Fig. 4b represents the front of the release wave but is possibly perturbed by the falling-stress effect seen in Fig. 4a. The initial fall followed by a constant stress region and then a further fall, is regarded as evidence of the separation of the release wave into elastic and plastic components, but is unresolved at short distances as in Fig. 4a.

Method of Calculation

From the impact time measured by the probes and the time of shock arrival at the transducers, the shock velocity can be calculated. In each round the peak stress and measured shock and impact velocities had values which were consistent with published data for magnesium. From the impact time and the shock velocity, the distance-time point is calculated where the shock in the flying plate is reflected from its back surface as a release wave. This point, together with the stress-time profile, enables the velocity of the release wave to be found as a continuous function of stress. From this, density and particle velocity are calculated using the following equations [7] based on conservation of mass and momentum:

$$\rho_1 - \rho_0 = \int_{p_0}^{p_1} \frac{dp}{c^2}$$

$$\int_{u_0}^{u_1} du = \int_{p_0}^{p_1} \frac{dp}{\rho c}$$

Here ρ represents the density, p the stress in the direction of wave propagation, c the wave velocity relative to the local material (for a continuous wave), and u the particle velocity. This calculation is done at small stress decrements down the release wave. The wave velocity is corrected for movement of the transducer and expressed relative to the local material, using the calculated particle velocity. Density and particle velocity at the top of the release wave are taken from published Hugoniot data for magnesium corresponding to the measured stress.

Stress-strain Curve

Figure 5 shows the resulting release velocities and Fig. 6 the corresponding stress-strain relation taken from experiments at one flying plate thickness. These are again markedly different from the hydrodynamic predictions. The stress-strain curve first falls steeply below the Hugoniot and then becomes shallower. This is attributed to elasto-plastic behaviour of the metal [9]. The results at five flying plate thicknesses have not been used in this type of calculation because of the possible difficulty in interpreting the initial fall in stress. However, an elasto-plastic release path would predict a discontinuity of release wave velocity at the reverse yield point, and hence a stress plateau. The period of almost constant stress shown at five flying plate

thicknesses is identified with this plateau, and the regions above and below it with the elastic and plastic parts of the release process. The size of the elastic stress release is, therefore, 16 Kb, determined by the stress difference between the plateau and the beginning of the release process as recorded by one flying plate thickness experiments. Single experiments at six and eight flying plate thicknesses support this interpretation.

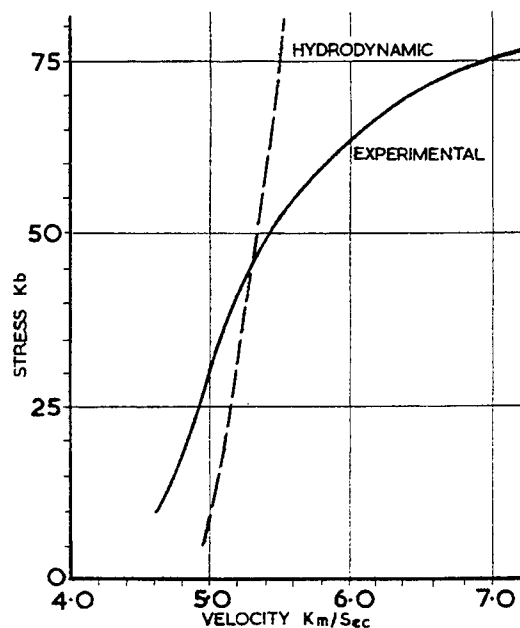


Fig. 5 - Mean velocities measured from 28 stress profiles at one flying plate thickness

Elastic Properties

Some elastic properties can now be calculated from the elastic and plastic wave velocities c_e and c_p . Bulk modulus is found in the plastic region using

$$c_p^2 = k/\rho$$

(Fig. 7); a considerable increase with stress is obtained. The curve is consistent with the small stress bulk modulus for magnesium [10].

While the initial fall in stress of the profiles at five flying plate thicknesses may be difficult to interpret, the ratio of the elastic and plastic wave velocities at the yield point nevertheless allows an estimate to be made of Poisson's ratio ν . Using

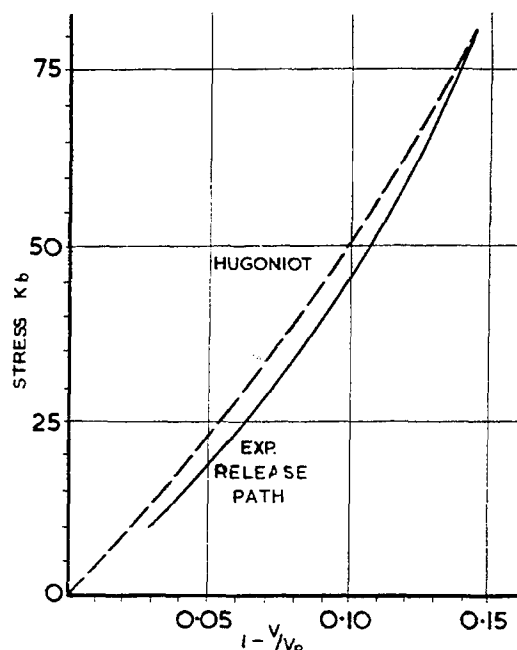


Fig. 6 - Stress-strain curve calculated from Fig. 5

$$\frac{c_e^2}{c_p^2} = 3 \frac{(1-r)}{(1+r)}$$

we obtain what may be regarded as an upper limit for Poisson's ratio of 0.42: the small stress value is 0.30 [10]. An expression for the fall in elastic stress is

$$2Y_s \frac{(1-r)}{(1-2r)}$$

where Y_s is the yield stress, assumed to be equal in tension and compression. Substitution of 16 Kbs for the elastic stress release, and the above values of Poisson's ratio gives yield strengths of 2.2 or 4.6 Kbs respectively; the results therefore suggest an increase in yield strength with stress above the static value of 1 Kb.

REFERENCES

1. G. R. Fowles, "Shock Wave Compression of Hardened and Annealed 2024 Aluminium," *J. Applied Physics*, Vol. 32, No. 8, August 1961, p. 1475.
2. L. V. Al'tshuler et al., "The Isentropic Compressibility of Aluminium, Copper, Lead and Iron at High Pressures," *Soviet Physics J.E.T.P.*, Vol. 11, No. 4, October 1960, p. 766.

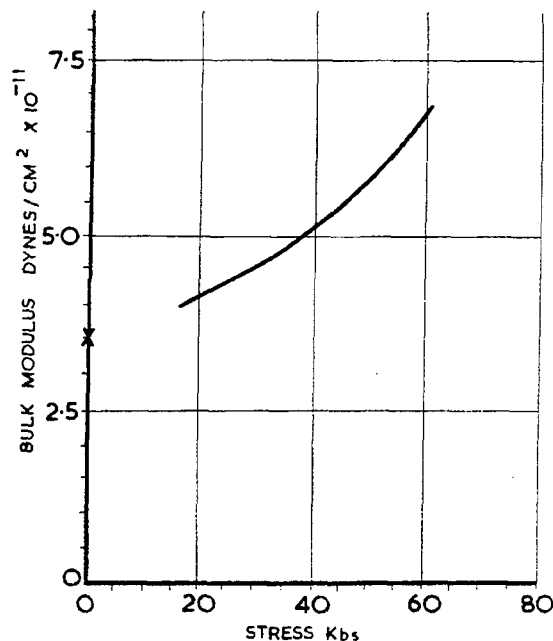


Figure 7

3. R. J. Eichelberger and G. E. Hauver, "Solid State Transducers for Recording of Intense Pressure Pulses," Paris Conference les Ondes de Detonation, September 1961.
4. U. I. Berg, "Investigations on a Very High Pressure Transducer," *Arkiv För Fysik* Band 25 nr 10.
5. D. R. Curran, "Non-hydrodynamic Attenuation of Shock Waves in Aluminium," *J. Applied Physics*, Vol. 34, No. 9, September, 1963, p. 2677.
6. J. W. Craggs, "Plastic Waves," *Progress in Solid Mechanics*, Vol. 2 (ed. by I. N. Sneddon and R. Hill), North-Holland Publishing Co., p. 141-197.
7. P. J. A. Fuller and J. H. Price, "Dynamic Pressure Measurements to 300 Kilobars with a Resistance Transducer," *Brit. J. Applied Physics*, Vol. 15, 1964, p. 751.
8. S. A. Novikov et al., "Investigations of the Structure of Compressive Shock Waves in Iron and Steel," *Soviet Physics J.E.T.P.*, Vol. 20, No. 3, March, 1965, p. 545.
9. L. W. Morland, "The Propagation of Plane Irrotational Waves through an Elasto-Plastic Medium," *Phil. Trans. Roy. Soc. London A* 251, 341 (1959), p. 341.
10. G. W. C. Kaye and T. H. Laby, "Tables of Physical and Chemical Constants," 12 ed. Longmans.

THE INFLUENCE OF MECHANICAL PROPERTIES ON WAVE PROPAGATION IN ELASTIC-PLASTIC MATERIALS*

B. M. Butcher and D. E. Munson
Sandia Corporation
Albuquerque, New Mexico

ABSTRACT

The influence of the mechanical properties of 6061T6 aluminum and 4340 steel on wave propagation in these materials at low plastic stress levels is investigated. Computer analyses of the free-surface motion of a plate-impact experiment (starting with a simple elastic, perfectly plastic, strain-rate-independent behavior) are compared with the experimentally observed result. Models which are consistent with quasistatic behavior are then used to incorporate (1) linear work hardening, and (2) general work hardening. The results are compared with the experimentally determined free surface motion. Finally, increase in flow stress with increase in strain rate is treated. While these calculations show the degree of sophistication required in the constitutive equation for accurate prediction of the free surface motion, they also indicate cases in which a considerable simplification in the constitutive equation may be made without severe misrepresentation of dynamic behavior.

INTRODUCTION

The study of dynamic behavior of materials is yielding precise constitutive equations, especially for metals. These equations, or permitted simplifications, may be of great significance to studies of explosives, if metals are used as an intermediary in determination of explosive detonation properties or if metal studies are used as an insight into possible forms of the low pressure constitutive equations for condensed explosives. In this investigation, various forms of constitutive equations which describe accurately the behavior of some typical alloys in compression will be used to predict free-surface motion of the material under impact conditions. Normally, the constitutive equation must include a resistance to shear, which increases with increasing strain and strain rate. The observed magnitude of these effects will depend upon the material, specimen geometry, and details of the impact and wave propagation. From the investigation, conclusions may be drawn concerning simple approximations to the constitutive equation, which are reasonably valid for a given metal.

DESCRIPTION OF DYNAMIC BEHAVIOR

For the description of dynamic behavior, two well defined stress conditions are experimentally amenable: uniaxial strain and uniaxial stress. Such stress states may be related analytically by assuming a yield criterion and the equivalence of plastic work. Consequently, uniaxial strain behavior under impact conditions may be linked to quasi-static tests if the strain-rate dependence is specified.

The discussion, although directed principally toward the state of one dimensional strain relevant to explosive and high pressure studies, will also involve the state of one dimensional stress. This involvement is necessary because material strength under dynamic loading is most understandable in a formulation directly comparable to quasi-static compression or Hopkinson bar experiments. However, the experimental results used for comparison have been obtained from plate impact experiments conforming to uniaxial strain.

*This work was supported by the United States Atomic Energy Commission.

General Equations

The general equations which describe dynamic material behavior are statements of both the conservation of mass and momentum and a constitutive relation which contains the material properties. Constitutive equations may be deduced in a comparatively simple manner by assuming that the Hugoniot equations for conservation of mass and momentum across a shock front apply, and that the stress pulse propagates as a series of discontinuities in stress. Each step has a unique propagation velocity. This requires a strain-rate-independent relationship, since the stress is described as a function of strain only. The Hugoniot equations [1] in uniaxial strain are:

$$\Delta\sigma = \rho_1 U_s \Delta U_p \quad (1)$$

$$\Delta\epsilon = \frac{\Delta U_p}{U_s} (1 - \epsilon_1) \quad (2)$$

where $\Delta\sigma$ and $\Delta\epsilon$ are the stress and strain increments between states 1 and 2 in the x direction, ρ_1 and ϵ_1 the density and strain ahead of the stress jump, U_s the shock velocity, and ΔU_p the change in material velocity. Experimental stress-strain values may be obtained from a knowledge of U_s and ΔU_p . An approximation that $\Delta U_p \approx 1/2 \Delta U_{fs}$ permits these quantities to be deduced crudely from free-surface motion [2].

Complete determination of the constitutive equation must be obtained from an iterative technique, since free-surface motion is not a direct result of interaction of the stress pulse with the surface [3]. Rather, it is the result of a successive series of elastic unloading waves which interact with the surface and the oncoming wave. These interactions must be taken into account. Successive modifications are made to the constitutive equation to arrive at a predicted free-surface motion consistent with the experimental curve.

For situations in which strain-rate independence is not appropriate, an alternate formulation of the conservation equations is necessary [4-6]. Using a Lagrangian coordinate system

$$\frac{\partial \sigma}{\partial x} = -\rho_0 \frac{\partial u}{\partial t} \quad (3)$$

$$\frac{\partial u}{\partial x} = -\frac{\partial \epsilon}{\partial t} \quad (4)$$

where u is the material velocity and ρ_0 is the stress free density. It is assumed that the strains are infinitesimal. The mechanical

properties of the material are introduced by separating the strain into elastic and plastic components and differentiating these with respect to time:

$$\dot{\epsilon} = \dot{\epsilon}^e + \dot{\epsilon}^p \quad (5)$$

Writing the elastic strain rate in terms of a stress rate and representing the plastic strain rate as a function of stress and strain gives

$$\dot{\epsilon} = \frac{\dot{\sigma}}{\lambda + 2\mu} + g(\sigma, \epsilon) \quad (6)$$

where λ and μ are Lamé's constants.

Equations (3), (4) and (6) may be reduced to ordinary differential equations along the characteristics,

$$\frac{dx}{dt} = +\sqrt{\frac{\lambda + 2\mu}{\rho_0}}; \quad \frac{dx}{dt} = -\sqrt{\frac{\lambda + 2\mu}{\rho_0}}; \quad dx = 0 \quad (7)$$

and integrated numerically using finite difference techniques. The detailed description of this technique may be found in references on wave propagation [1,5,7].

Constitutive Equation Models

Three distinct levels of detail are used in categorizing mechanical behavior of a metal. The first and lowest level is the simplest possible representation of material rigidity incorporating plasticity: the elastic-perfectly plastic model. This model assigns a constant flow stress, Y_0 , to all strains beyond the initial yield. Since the flow stress is not coupled to the strain except in the elastic region, this model permits a desirable simplification in computational procedures involving the flow condition. If the stress-strain pairs in uniaxial stress are denoted by (Y, α) and the corresponding pairs in uniaxial strain by (σ, ϵ) , then the connection between the two states of stress is given by:

$$\sigma = \sigma_s + \frac{2}{3} Y = K\epsilon + \frac{2}{3} Y \quad (8)$$

where $Y = Y_0$ above the yield point of the material, σ_s is the spherical or hydrostatic stress component, and K is the bulk modulus. The rigidity causes an offset of $2Y_0/3$ in stress from the hydrostat. Wave propagation in such elastic-perfectly plastic, strain-rate-independent solids may be described by the Hugoniot equations.

Unfortunately, calculations based on the elastic-perfectly plastic model do not always

yield results consistent with experiment. When this occurs, the next material property incorporated into the model is work hardening [8,9]. This addition complicates wave propagation calculations because the flow stress is a monotonically increasing function of the strain above the initial yield point:

$$Y = f(\alpha). \quad (9)$$

The one-dimensional stress state is still related to one-dimensional strain by Eq. (8). However, now the relation of the strains must also be determined. This is accomplished by relating strains through equivalent plastic work and gives.

$$\epsilon = \frac{3}{2} \alpha - \frac{Y}{6K} \quad (10)$$

where K is assumed independent of pressure. It is assumed that the flow condition may be represented by isotropic expansion of the Von Mises yield conditions. Equations (8), (9) and (10) then comprise the description of the material.

One-dimensional wave propagation in such a strain-rate-independent material depicted by this model can be described by breaking the stress-strain curve into as many straight-line segments as necessary to preserve the detail. Propagation velocity of the stress increment associated with a given line segment is

$$U_s = \frac{1}{\rho_1} \sqrt{\rho_0 \frac{\Delta \sigma}{\Delta \epsilon}}. \quad (11)$$

The change in material velocity due to the stress increment is given by Eq. (1). Using this strain-rate-independent description, a stress wave is represented by instantaneous stress steps corresponding to the distinct straight line segments used to represent the stress-strain curve. Each step will propagate at a constant velocity given by Eq. (11).

When further refinements in the constitutive relation are necessary to describe material behavior, strain rate may be included as an additional variable. In this model, the flow stress will be expressed as

$$Y = h(\alpha, \dot{\alpha}P) \quad \text{or} \quad \dot{\alpha}P = g(Y, \alpha) \quad (12)$$

where $\dot{\alpha}P$ is the plastic strain rate. Equations (8) and (10) remain valid, and the extension of the form of the yield criterion to the flow condition is retained.

The relation of plastic strain rates between uniaxial stress and uniaxial strain states can be shown from Eqs. (8) and (10) to be

$$\dot{\epsilon}P = \frac{1-2\nu}{1-\nu} \dot{\alpha}P \quad (13)$$

where ν is Poisson's ratio.

COMPARISON TO EXPERIMENT

The results of the calculations are presented in a form consistent with experimental data. Experimental observations in plate impact tests are of two kinds: (1) direct measurement of free-surface displacement with time and (2) charge or resistance changes in transducers in contact with the specimen. The changes can be related to stress.

In the first method, the free-surface motion is not the direct result of the impingement of the stress pulse at the free surface. Rather, it is the motion observed only after a complex series of subsurface interactions have occurred, as previously mentioned. The stress profile can be deduced from free-surface displacements if the subsurface interactions can be calculated; or conversely, the displacement may be predicted from a known stress profile.

In the second method, the output of the transducer is an indication of the stress history at the target-transducer interface. Only under special conditions of exact impedance matching between transducer and target does this output result directly in a stress profile. Normally, the differences in mechanical properties between the transducer and target require that the wave interactions resulting from impedance mismatch must be solved, much like those involved in the free-surface measurements. If the impedance correction can be made, then the unperturbed stress profile which existed in the target material can be deduced.

In the results of this paper, comparison between calculated and experimental data will be made using stress profiles or free-surface motion.

Two computer codes were used to obtain the results of this work. The first (SWAP) [10] assumes strain rate independence. It solves the Hugoniot Eqs. (1) and (2) for each permitted combination of shock, free surface, or interface interaction in terms of stress increments with constant velocities given by Eq. (11). Plastic unloading is usually of an inverted form identical to the compressive loading path. This simplification is allowed because the precise nature of the unloading path does not greatly influence the early free-surface motion [9]. The second computer program (SRATE) [11] permits the numerical solution of the equations

describing strain-rate sensitive behavior. Again, plastic unloading is taken to be the inversion of the loading path. In the interest of economy of computer time, the strain-rate-dependent stress profile was computed for a plane close to the free surface. This stress profile was then propagated the remaining short distance using SWAP to compute the interactions. A large number of straight-line segments were used to represent the stress profile. This device is permissible, since most of the waves propagating between the profile plane and the free surface are elastic and strain-rate effects may be neglected. As a check on the approximation, the resultant free-surface motion was found to match a complete SRATE solution.

Elastic-Perfectly Plastic, Strain-Rate Independent Model (EP-RI)

An aluminum alloy, 6061T6, and an alloy steel, 4340, were selected for examination because the experimental stress-strain behavior of these alloys is well known [3,9]. The quasi-static, compression stress-strain curve for 6061T6 aluminum is shown in Fig. 1; that for 4340 steel is shown in Fig. 2. The elastic-perfectly plastic approximations to these curves are shown as lines in the figures. For 4340 $R_c 15$, this approximation is quite close; for the aluminum, the deviation between the approximation and the actual curve is more pronounced.

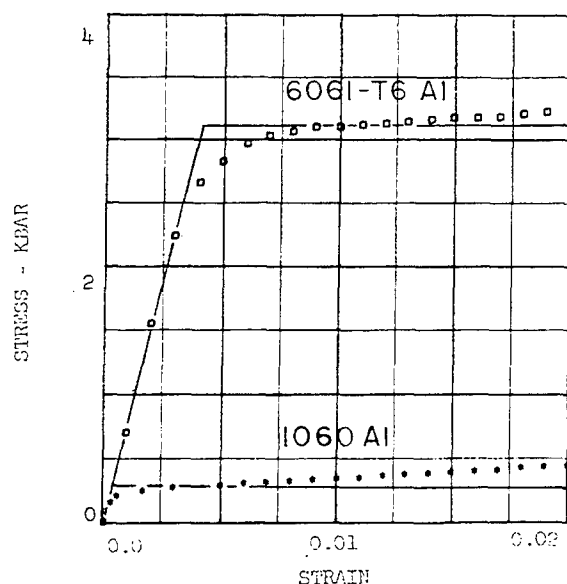


Fig. 1 - Quasi-static stress-strain curves for aluminum

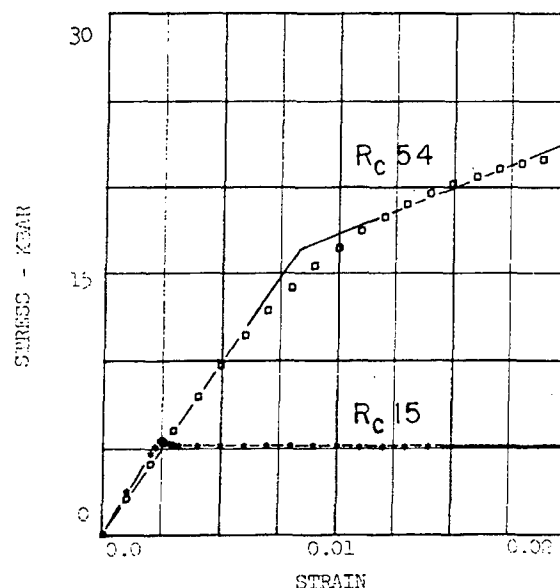


Fig. 2 - Quasi-static stress-strain curves for 4340 steel

Comparison of the free-surface motion calculated from the elastic-perfectly plastic approximation for these metals and the experimentally observed free-surface motion is made in Figs. 3 and 4. (The curves labeled EP-RI give results calculated using the elastic-perfectly plastic strain-rate independent model.) Figure 3 shows that the time difference between the approximation and actual behavior is quite small for the aluminum alloy; Fig. 4 shows the approximation is rather poorer for the steel. This difference suggests that the prediction accuracy from quasi-static measurements is related to the strain-rate sensitivity of the material. The face-centered cubic aluminum alloy is less strain-rate sensitive than the body centered cubic 4340 $R_c 15$. Often, however, the experimental or predictive requirements in a particular situation may not warrant the use of a more complex stress-strain relationship even for the steel; the elastic-perfectly plastic strain-rate-independent relation may be adequate.

Figures 5 and 6 indicate the differences between the experimentally consistent wave profile (same as the curve SR) and the elastic perfectly plastic approximation. Here it is apparent that all detail in the wave profile is lost in the approximations for both the steel and the aluminum. It should be noted that the approximation and the experimental profile of 6061T6 aluminum reach nearly the same peak stress. This would also be true for the 4340 had the calculation been carried to longer times.

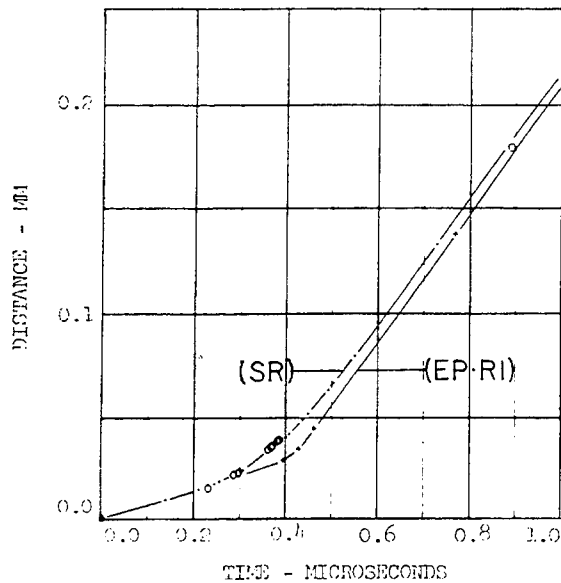


Fig. 3 - Free-surface displacement of a 12.7 mm thick target of 6061T6 aluminum; the projectile velocity is 0.32 mm/ μ sec; the circles are experimental data; SR is a strain-rate dependent solution

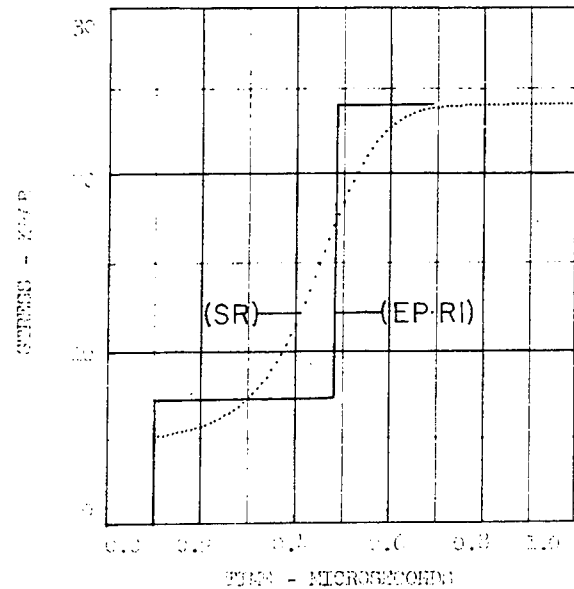


Fig. 5 - Stress histories for 6061T6 aluminum at a plane 11.2 mm from the impact surface (projectile velocity is 0.32 mm/ μ sec)

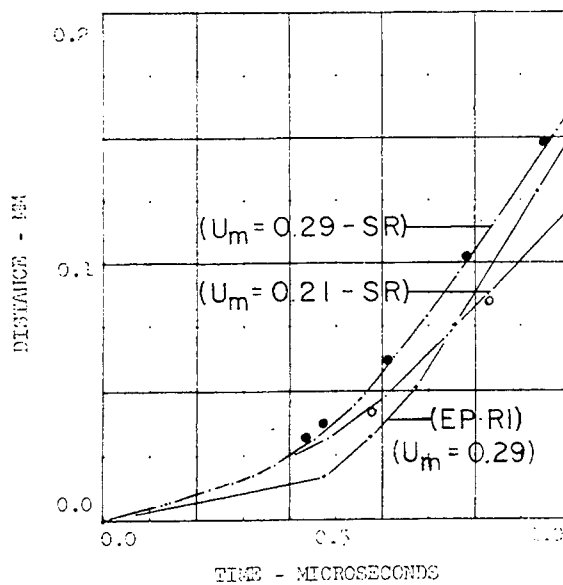


Fig. 4 - Free-surface displacement of a 12.7 mm thick 4340 R_c15 steel target (SR curves are from a strain-rate dependent solution using Eq. 15; the circles are experimental data; U_m, the projectile velocity, is in mm/ μ sec)

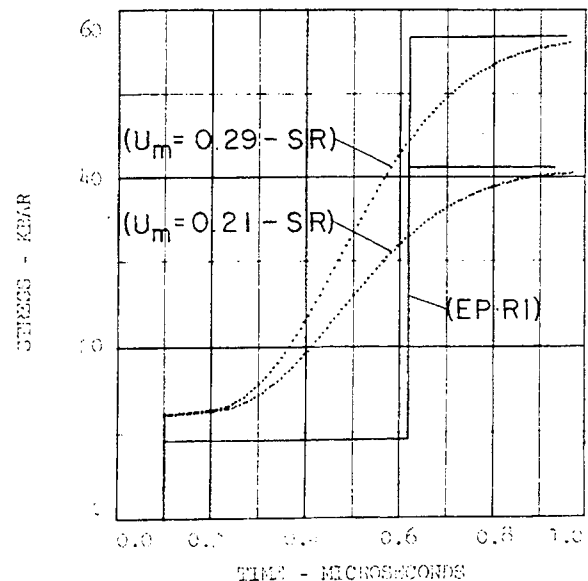


Fig. 6 - Stress histories for 4340 R_c15 steel at a plane 11.2 mm from the impact surface (Eq. 15 was used to calculate the curves SR; U_m, the projectile velocity, is in mm/ μ sec)

A physical explanation for this fact results directly from strain-rate behavior. After the rapid rise in stress has occurred, the strain rate must decay to lower values and eventually approach the quasi-static rates (this assumes work hardening is strain-rate independent).

The stress level of the elastic precursor wave sensitively reflects the approximation used for the quasi-static stress-strain curve. The yield stress given by the approximate quasi-static curve markedly overestimates the proportional limit of the 6061T6 aluminum. In the steel, the quasi-static approximation agrees closely with the actual stress-strain curve. The result of the discrepancy between proportional limit and approximate yield stress on the stress history is shown clearly in Fig. 5.

Figure 7 shows the dynamic stress-strain curves in uniaxial strain, obtained from a strain-rate-independent analysis, which duplicate the experimentally measured free-surface motion of 1/2-inch-thick 4340 R_c15 steel targets. The curves are for two different projectile velocities. Since the dynamic curves do not superimpose upon each other, one supposes that the strain-rate effects are pronounced. A similar effect will appear if the target thickness is changed while projectile velocity is held constant. A test for determining the presence of strain-rate sensitivity is to vary the experimental conditions, determine stress-strain curves assuming strain-rate independence, and check for superposition of curves in a common stress region.

Fully hardened 4340 steel (R_c 54) is an excellent example of a material with pronounced work hardening but no measurable strain-rate sensitivity [9]. The quasi-static compression curve is shown in Fig. 2. A linear work hardening approximation to the static curve is also indicated. Figure 8 clearly illustrates that the free-surface motion predicted from the linear work hardening model differs insignificantly from either the general work hardening calculation or the experimentally measured motion.

Strain-Rate Dependent Models (SR)

For metals such as 4340 R_c15 and 6061T6 aluminum, situations may arise in which the strain-rate-independent solution is inadequate. When this occurs, the formulation of the dynamic mechanical property must be modified to include the strain rate. If this modification is done properly, one expects greater fit accuracies between predicted and measured quantities. Even here, the logical starting point for

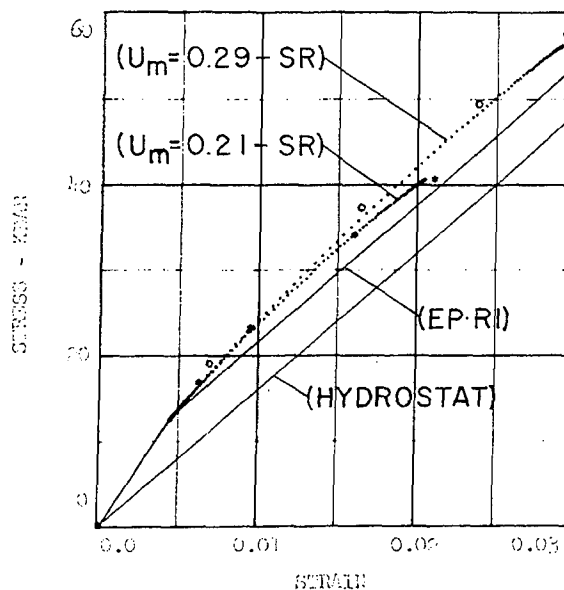


Fig. 7 - Dynamic stress-strain curves from Fig. 4 (circles and asterisks are from strain-rate-independent analysis reproducing free-surface displacement; SR calculations are "averaged" to simulate rate-independent analysis)

the material description is the quasi-static, compression stress-strain curve, which has been shown to be a good first approximation to the dynamic case. In the calculations to be described, an equation was fitted to the quasi-static curve; the strain-rate dependence was then introduced into this function. The form of the strain-rate dependence was chosen to be consistent with experimental determinations [12-14]. In the range of strain rates of 10^{-3} to 10^3 sec^{-1} , the flow stress was taken as a linear function of the logarithm of the plastic strain rate. If a similar dependence is used above 10^3 sec^{-1} , stress-wave propagation calculations are difficult or impossible to reconcile with experimental results; here, a linear function of the plastic strain rate is compatible with experimental results [15]. Further, the requirement of continuity of the plastic strain rate and the stress derivative of the plastic strain rate at the transition is used to reduce the number of parameters to two. Justification for these assumptions has been discussed by Dorn in a recent review of dislocation dynamics [15].

For 6061T6 aluminum, functions of Eq. (14) describe free-surface motion for several values of projectile velocity and target thickness: If σ is above the proportional limit in uniaxial strain of 4.07 kbar, then

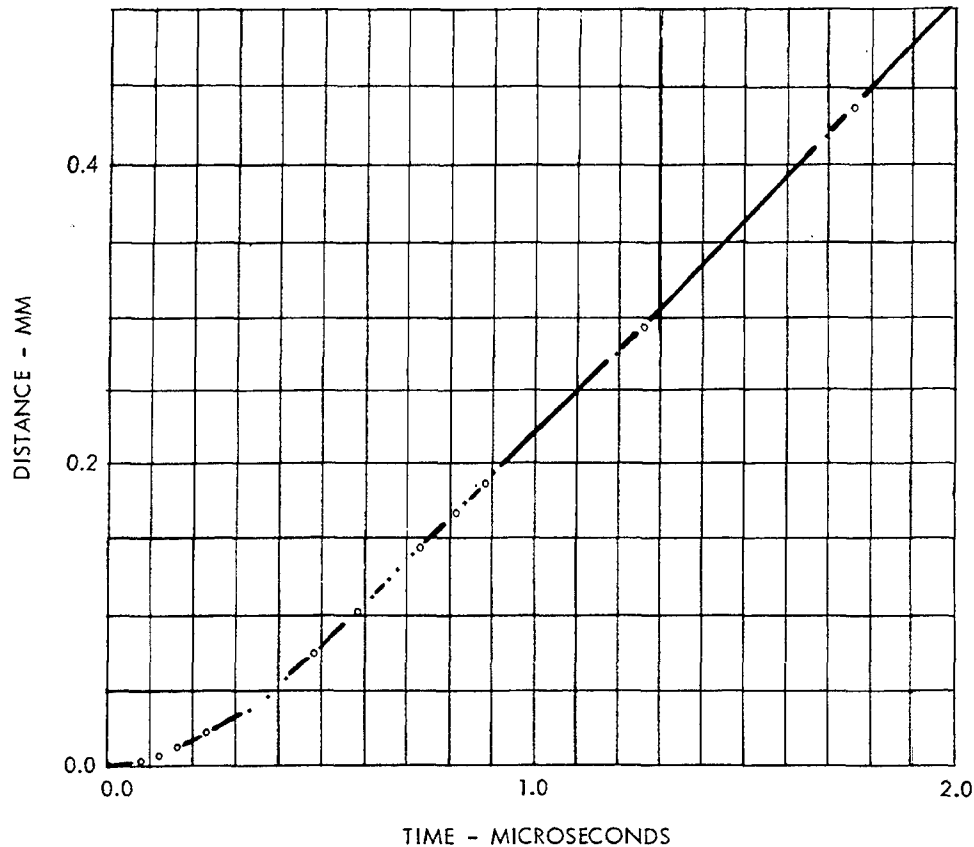


Fig. 8 - Free-surface displacement of a 12.7 mm thick target of 4340 R_c 54 steel (points + denote the linear work-hardening approximation, points o the general work-hardening approximation; the solid line reproduces experimental data)

$$\begin{aligned}
 \dot{\epsilon}^P &= 0.5 \exp \{f(\sigma, \epsilon) - 42.66\}; \\
 \dot{\epsilon}^P &\leq 1500 \text{ sec}^{-1}. \\
 \dot{\epsilon}^P &= 1500 \{f(\sigma, \epsilon) - 49.68\}; \\
 \dot{\epsilon}^P &> 1500 \text{ sec}^{-1}.
 \end{aligned}
 \quad (14)$$

$$f(\sigma, \epsilon) = \frac{1}{B} \left\{ \frac{1.497\sigma - 1139\epsilon - 1.90}{[1 - \exp(-417\epsilon - 0.184\sigma + 2.29)]} \right\};$$

$$B = 0.0233, \sigma \text{ in kbar.}$$

Curves of constant strain rate in uniaxial stress calculated from Eq. (14) are shown in Fig. 9. These functions reproduce uniaxial strain

experimental data quite accurately, as Fig. 3 shows. (The curves labeled SR give results calculated with the strain-rate dependent models.)

The sensitivity of free-surface motion to the parameters of Eq. (14) has been checked by doubling the increase in stress due to strain rate above $\dot{\epsilon}^P = 1 \text{ sec}^{-1}$. Doubling the parameter B in Eq. (14) accomplishes this nicely. The pronounced influence on the free-surface motion is shown in Fig. 10.

The function which has been constructed for the 4340 R_c 15 steel is based on elastic-perfectly plastic strain-rate-dependent behavior, Fig. 11. It has the form

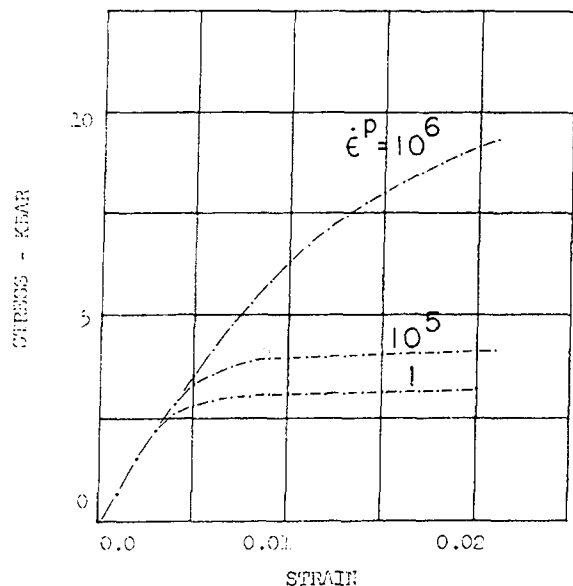


Fig. 9 - Constant strain-rate curves for uniaxial stress calculated from Eq. 14 for 6061T6 aluminum (strain rates in sec^{-1})

$$\left. \begin{aligned} \dot{\epsilon}^P &= 0.51 \exp \{9.53 Y_0 - 53.0\}; \\ \dot{\epsilon}^P &\leq 1000 \text{ sec}^{-1} \\ \dot{\epsilon}^P &= 0.51 (18700 Y_0 - 118000); \\ \dot{\epsilon}^P &> 1000 \text{ sec}^{-1}. \\ Y_0 &= 1.5 (\sigma - K\epsilon), Y_0 \text{ in kbar.} \end{aligned} \right\} \quad (15)$$

Although these functions do not permit inclusion of upper- and lower-yield point phenomenon, which is known to exist for this hardness 4340, they do approximate adequately the gross details of the free-surface motion, as shown in Fig. 4. Finally, the "average" stress-strain curves deduced from the strain-rate model are shown to be consistent with results from experiment in Fig. 7. These calculations also show that the magnitude of the elastic wave stress decreases with increasing propagation distance. The decay of the elastic wave is confirmed by experiments on Armco iron [16]. This suggests that materials which exhibit apparent changes in elastic wave amplitude with impact velocity or distance of propagation are probably strain-rate sensitive.

Hydrodynamic Model (PP)

To complete this discussion, a commercially pure aluminum (1060), often selected for its small yield stress, will be considered. The

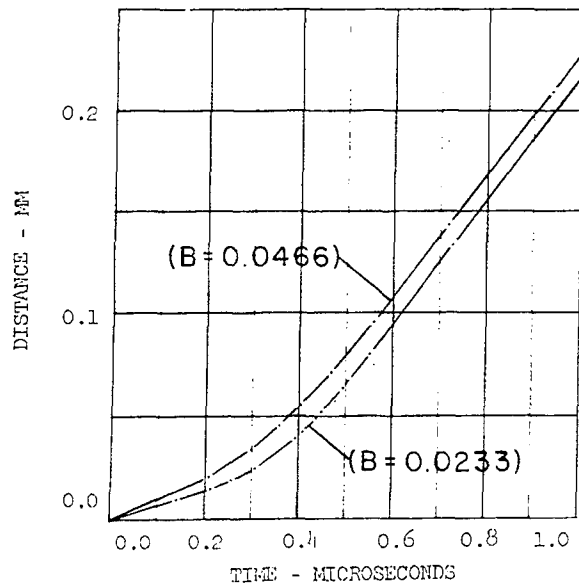


Fig. 10 - Effect of increased strain-rate sensitivity as calculated using Eq. 14 (12.7 mm thick target, projectile velocity $0.32 \text{ mm}/\mu\text{sec}$)

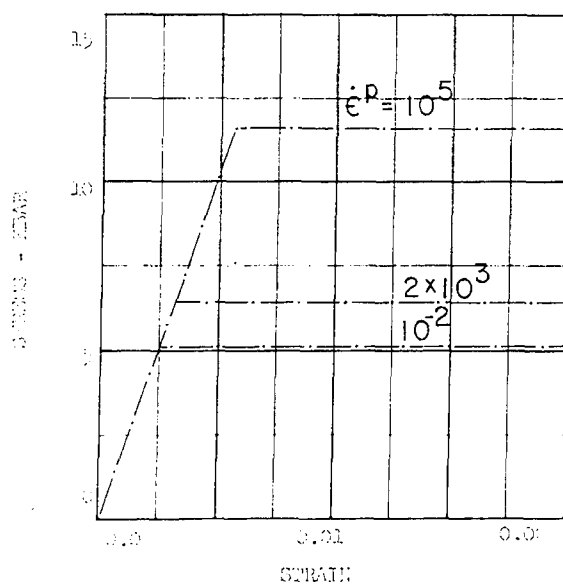


Fig. 11 - Constant strain-rate curves for uniaxial stress calculated from Eq. 15 for 4340 Rc 15 steel (strain rates in sec^{-1})

normal assumption in wave propagation problems is that a hydrodynamic model is applicable. Figure 12 shows a computation of free-surface motion of 1060 aluminum neglecting shear strength, work hardening, and strain-rate

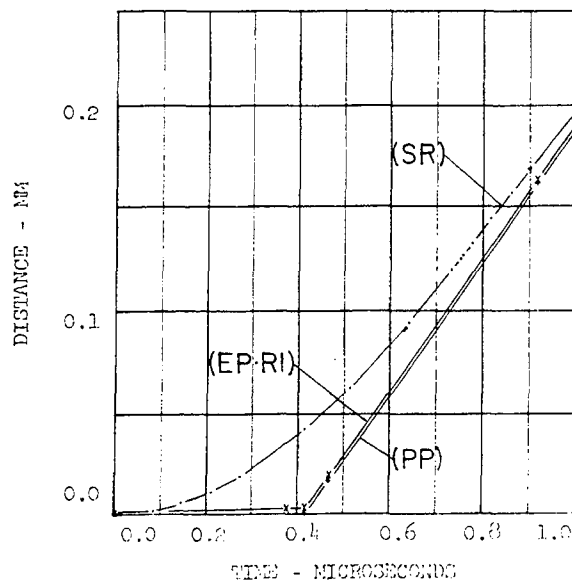


Fig. 12 - Free-surface displacement of a 12.7 mm thick target of 1060 aluminum as calculated from various models of behavior

effects; a detailed computation of the motion using a strain-rate function; and elastic-plastic results. The stress, strain, and strain-rate function was constructed in the same manner as the 6061T6 aluminum function. Increase in flow stress in the range $\dot{\epsilon}^P = 10^{-3}$ to 10^5 sec^{-1} is taken as the same order as the static yield stress, which is compatible with experimental evidence [13]. In this particular metal, the observable influence of all strength effects is demonstrated to be small.

SUMMARY

Qualitative differences have been demonstrated in the selection of constitutive equation models and rate-dependent or rate-independent analyses. For example, 4340 R_c54 is rate insensitive, but the constitutive equation should include an approximation to work hardening. On the other hand, 4340 R_c15 is rate sensitive and requires a model incorporating a rate dependence. Also, a general model must be used for 6061T6 aluminum to produce a quantitative fit to experimental data; however, this aluminum is not too rate sensitive, and other models may give adequate prediction of uniaxial-strain dynamic data. Finally, some mechanically soft materials permit a hydrodynamic model to be used, even at relatively low stresses. Normally, material descriptions must include shear strength, work hardening and strain-rate dependence to obtain quantitative agreement

between uniaxial stress and uniaxial strain data. Frequently, however, a knowledge of necessary solution accuracy of a problem may permit simplification of the constitutive model for engineering purposes or selection of a material better suited to an experiment.

ACKNOWLEDGMENT

The authors wish to thank Mrs. Emily Young for her assistance in the computer analyses.

REFERENCES

1. M. H. Rice, R. G. McQueen, and J. M. Walsh, "Compression of Solids by Strong Shock Waves," *Solid State Physics*, ed. F. Seitz and D. Turnbull (Academic Press, New York, 1958), Vol. 6, pp. 1-63.
2. J. M. Walsh and R. H. Christian, "Equation of State of Metals from Shock Wave Measurements," *Phys. Rev.*, 97 (1955), 1544-1556.
3. L. M. Barker, C. D. Lundergan, and W. Herrmann, "Dynamic Response of Aluminum," *J. Appl. Phys.*, 35 (1964), 1203-1212.
4. L. E. Malvern, "Plastic Wave Propagation in a Bar of Material Exhibiting a Strain Rate Effect," *Quart. Appl. Math.*, 7-8 (1949-1951), 405-511.
5. J. A. Simmons, F. E. Hauser, and J. E. Dorn, "Mathematical Theories of Plastic Deformation under Impulsive Loading," *University of California Publications in Engineering* (1962), Vol. 5, pp. 177-230.
6. J. Lubliner, "A Generalized Theory of Strain-Rate-Dependent Plastic Wave Propagation in Bars," *J. Mech. and Phys. Solids*, 12 (1964), 59-65.
7. R. Courant and K. O. Friedrichs, "Supersonic Flow and Shock Waves," (Interscience Publishers, Inc., New York, 1960), pp. 79-245.
8. G. R. Fowles, "Shock Wave Compression of Hardened and Annealed 2024 Aluminum," *J. Appl. Phys.*, 32 (1961), 1475-1487.
9. B. M. Butcher and J. R. Canon, "Influence of Work-Hardening on the Dynamic Stress-Strain Curves of 4340 Steel," *AIAA Jour.*, 2 (1964), 977-990.
10. L. M. Barker, "SWAP - A Computer Program for Shock Wave Analysis," Sandia

- Corporation Report, SC-RR-4796, Unclassified (1963).
11. B. M. Butcher, "A Computer Program SRATE for the Study of Strain-Rate Sensitive Stress Wave Propagation," Sandia Corporation Report, SC-RR-65-298, Unclassified (1965).
 12. F. E. Hauser, J. A. Simmons, and J. E. Dorn, "Strain-Rate Effects in Plastic Wave Propagation," Response of Metals to High Velocity Deformation, ed. P. G. Shewmon and V. F. Zackay (Interscience Publishers, Inc., New York, 1961), pp. 93-110.
 13. C. H. Karnes, "Strain Rate Effects in Cold Worked, High Purity Aluminum," University of Texas PhD Thesis (January 1964).
 14. U. S. Lindholm and L. M. Leakley, "Dynamic Deformation of Single and Polycrystalline Aluminum," J. Mech. and Phys. Solids, 13 (1964), 41-53.
 15. J. E. Dorn, J. Mitchell, and F. E. Hauser, "Dislocation Dynamics," University of California, Lawrence Radiation Laboratory Report UCRL-11977, Unclassified. (Presented 1965 Spring Meeting, Society for Experimental Stress Analysis under the title, "Plastic Response of Crystalline Materials to Dynamic Conditions of Stressing.")
 16. J. W. Taylor and M. H. Rice, "Elastic Plastic Properties of Iron," J. Appl. Phys., 34 (1963), 364-371.

THE INSTABILITY OF AN INTERFACE BETWEEN TWO FLUIDS UNDER VARIABLE NORMAL ACCELERATION

I. G. Cameron and H. H. M. Pike
*Atomic Weapons Research Establishment
Aldermaston, Berkshire, England*

ABSTRACT

Satisfactory theoretical treatments of the early (small amplitude) stages of the growth of perturbations on the interface between two incompressible fluids under variable normal acceleration already exist. For constant acceleration and one fluid of zero density, theoretical treatments of the very late (large amplitude, steady flow) stages also exist and an approximate theory given by Layzer describes both early and late stages correctly and intermediate stages in a plausible manner.

In this paper, Layzer's treatment has been extended to variable acceleration in what is thought to be a good approximation, and to the two-fluid case in a plausible manner. Further progress depends on experimental studies, particularly of the intermediate region.

Viscosity and surface tension have been omitted, i.e., the treatment is limited to high accelerations of low viscosity, incompressible fluids.

INTRODUCTION

The instability of a plane interface between two incompressible fluids under an acceleration normal to that interface was studied experimentally by Lewis (1950) [1], Davies and Taylor (1950) [2], and Emmons, Chang and Watson (1959) [3], all experiments were two-dimensional, i.e., the surface was initially perturbed by linear corrugations whose amplitude increased with time. While the amplitude of the perturbations remained small in relation to their wavelength the shape of the interface remained symmetrical about its initial position. At late times however its shape changed to a "bubble and spike" profile in which bubbles of the light fluid penetrated the heavier fluid and spikes of the latter penetrated the former. The spikes only remained connected to the parent fluid by thin curtains, hence they travelled independently of the interface and their motion could be calculated from the gravity field in which they were situated.

In the early stages the wavelength D of the perturbations remained constant but at very late times when the amplitude exceeded the wavelength, the flow became unstable, and any bubbles which had gone ahead developed bulbous

heads which swelled out over their neighbours, so effectively increasing their wavelength and accelerating their growth. We shall not treat such late times. All theoretical treatments, including our own, assume D to be constant.

The early stages of the motion, when the amplitude of the perturbation was much less than the wavelength was treated by Taylor (1950) [4] who related a , the second derivative of the amplitude of the perturbation to g , the acceleration of the interface. His treatment is valid for g varying with time or even changing sign, and although he only considered linear corrugations of the interface his treatment can readily be extended to axial symmetry by replacing trigonometric functions by Bessel functions. For linear corrugations, and constant g , Taylor's treatment can be extended to give a in the form of a power series in the initial amplitude a_0 ; the first two terms of this series have been given by Ingraham (1954) [5] and the third term, for one fluid of zero density, by Chang (1959) [6]. This series diverges as $a \rightarrow D/2\pi$ but does show the beginning of the "bubble and spike" profile. These higher order approximations include sliding of one fluid over the other, i.e., they include Helmholtz instability.

For one fluid of zero density, i.e., for one fluid, and for constant g the steady flow pattern which develops at late times has been treated by Chia-Shun Yih (1960) [7] for linear corrugations and by Davies and Taylor (1950) [2] for axial symmetry. For both geometries Layzer (1955) [8] has given approximate one-fluid treatments which can be applied at all times and which are correct at very early and very late times.

Numerous authors, e.g., Harrison (1908) [9], Chandrasekhar (1955) [10] and Reid (1961) [11] have extended Taylor's treatment of the early stages to include the effects of viscosity and surface tension. Bretherton (1961) [12] has studied the motion of long bubbles up vertical tubes for low Reynolds numbers and large surface tension effects.

The purpose of this paper is to provide an approximate treatment of the two-fluid case valid for all times for which D can be considered constant for variable g . This has been done by modifying Layzer's treatment to include the effect of inertia at late times. Only the case of axial symmetry has been considered but this is the case of practical importance since an unstable interface normally distorts in a honeycomb pattern with an arbitrary distribution of cell sizes, each cell having approximately circular symmetry. Viscosity and surface tension have been ignored in this paper.

LAYZER'S SOLUTION FOR CONSTANT g

For the rise of the bubble of constant wavelength we turn to Layzer's (1955) solution for axial symmetry, which was derived only for a bubble of negligible density. Let the perturbation be confined inside a cylinder of diameter D normal to the interface and let β be the first zero of the first order Bessel function, i.e., $J_1(\beta) = 0$. Then Layzer uses the potential function in cylindrical coordinates in separable form

$$\phi = \exp\left(-\frac{2\beta Z}{D}\right) J_0\left(\frac{2\beta R}{D}\right) F\left(gT \sqrt{\frac{2\beta}{D}}\right), \quad (1)$$

where R and Z are the usual cylindrical coordinates, and by fitting the curvature of the bubble surface near its apex he derives the differential equation

$$\left(1 + \exp\frac{4\beta a}{D}\right) \frac{d^2 a}{dT^2} + \frac{2\beta}{D} \exp\frac{4\beta a}{D} \left(\frac{da}{dT}\right)^2 + g \left(1 - \exp\frac{4\beta a}{D}\right) = 0, \quad (2)$$

for the amplitude a . This agrees with Taylor's theory for small a (and very small initial amplitude a_0), and with the steady flow theory for large a . For the intermediate range the behaviour agrees qualitatively with experiment but has not been checked numerically.

From (1) we see that g only occurs in the time function, i.e., the shape of the potential function is independent of g when g is steady. If this were still true when g was varying then (2) would still be valid. But the theory is only checked for steady flow in the late stages and hence the effective inertia in (2), i.e., the coefficient of $d^2 a/dT^2$ when a is large may be quite wrong. To correct this we must calculate the kinetic and potential energies of the fluid at late times, from the detailed structure of the flow pattern. The determination of this flow pattern is given in the next section.

THE STEADY FLOW PATTERN FOR CONSTANT g

We consider a single bubble rising in a tube of radius $D/2$ and calculate the steady flow pattern in detail. The flow near the vertex is given correctly by Layzer's solution and, if we introduce nondimensional variables t , h and r such that

$$t = \sqrt{\frac{2\beta g}{D}} \times T, \quad (3)$$

$$h = \frac{2\beta}{D} Z, \quad r = \frac{2\beta}{D} R, \quad (4)$$

then in a coordinate system moving with the bubble vertex the velocity components are

$$u_1 = J_1(r) \exp h, \quad (5)$$

$$v_1 = 1 - J_0(r) \exp h. \quad (6)$$

At large distances from the vertex the flow is steady and almost parallel to the wall of the tube; if we denote the velocity components in this region by u_2 and v_2 , then to order $h^{-3/2}$ Bernoulli's and Laplace's equations give

$$u_2 = \lambda/2h, \quad (7)$$

$$v_2 = \sqrt{(2h)} - \lambda^2/4h \sqrt{(2h)}, \quad (8)$$

where

$$\lambda = (\beta^2 - r^2)/2r. \quad (9)$$

Because the flow in these two regions is steady, the flow is steady throughout. We shall endeavour to find the velocity at any point in the flow by expressing the velocity components u and v by

$$u = au_1 + bu_2, \quad (10)$$

$$v = av_1 + bv_2, \quad (11)$$

where a and b are functions of h to be determined but such that

$$a \rightarrow 1 \quad b \rightarrow 0 \quad \text{as } h \rightarrow 0, \quad (12)$$

$$a \rightarrow 0 \quad b \rightarrow 1 \quad \text{as } h \rightarrow \infty. \quad (13)$$

We choose a and b to satisfy the three conditions (1) the flow of mass through any horizontal plane is constant, (2) Bernoulli's equation is satisfied on the bubble surface, and (3) the bubble surface is a streamline. These conditions may be written

$$\int_{\xi}^{\beta} r v dr = \beta^2/2, \quad (14)$$

$$u(\xi, h)^2 + v(\xi, h)^2 = 2h, \quad (15)$$

$$dh/d\xi = v(\xi, h)/u(\xi, h), \quad (16)$$

where $\xi = \xi(h)$ is the r coordinate of the bubble surface. Equations (14) and (15) will determine a and b as functions of h and ξ which may then be substituted into Eq. (16) to give a differential equation for the bubble surface. Near the vertex, and a long way from it, conservation of mass may be used to give the two asymptotic forms of the bubble surface. We have

$$\exp(-h) = 2J_0(\xi)/\xi \quad (17)$$

and

$$\beta^2 = (\beta^2 - \xi^2) \sqrt{2h} \quad (18)$$

in these two regions respectively.

For $h = 1.55$ the discriminant of the quadratic obtained for b from Eqs. (14) and (15) is negative for all values of ξ greater than 1.5 though a consideration of the asymptotic forms of the bubble surface shows that this is a region in which we must find real values of a and b . This difficulty arises because outside the region where they are valid u_1, v_1, u_2 and v_2 diverge rapidly. The exponential function in u_1 and v_1 , for example, will lead to very large

values of the velocities when h becomes large, whereas in fact v_1 should increase with \sqrt{h} and u_1 diminish. Again, as ξ tends to zero λ will become very large and the correction term to v_2 will dominate the main term. Because of this the velocities u_1, v_1 and u_2, v_2 must be modified in such a way that they still approximate closely to the flow in their respective regions but that outside these regions they do not take absurd values. Since Layzer's solution is only correct to first order in h , we may take

$$u_1 = (1+h) J_1(r), \quad (19)$$

$$v_1 = 1 - (1+h) J_0(r). \quad (20)$$

In addition, we modify the definition of λ in Eqs. (7) and (8) to

$$\lambda = (\beta - r)(r/\beta)^n, \quad (21)$$

where n is a positive number which has yet to be defined.

With the above definitions Eq. (14) may be written

$$a = \frac{\beta^2 - b[(\beta^2 - \xi^2) \sqrt{2h} - I/(2h)^{3/2}]}{\beta^2 - \xi^2 + 2\xi J_1(\xi)(1+h)} \quad (22)$$

where

$$I = \int_{\xi}^{\beta} r \lambda^2 dr = \frac{1}{\beta^{2n}} \int_{\xi}^{\beta} r^{2n+1} (\beta - r)^2 dr. \quad (23)$$

Figure 1 shows the regions of the h, ξ plane in which the discriminant $Y(h, \xi)$ of the quadratic for b , obtained by using the modified definitions of u_1, v_1, u_2 and v_2 , is negative for $n = 1.0$; clearly it is not now impossible to construct an integral curve satisfying Eqs. (14) to (16). If the numerical integration is started near the curve $(\beta^2 - \xi^2) \sqrt{2h} = \beta^2$ in the region where this curve and the curve $Y(h, \xi) = 0$ are close together, then the integral curves are not sensitive to small variations in the initial values provided that we integrate towards the origin. For large values of h a numerical investigation shows that in solving the quadratic for b it is the positive square root that gives values of b closest to unity; the positive sign must therefore be used for the entire solution, unless the integral curve touches the curve $Y(h, \xi) = 0$.

Figure 1 shows the integral curve representing the bubble surface for $n = 1$; it may be seen that this curve does not have the correct asymptotic form near the origin but, by taking

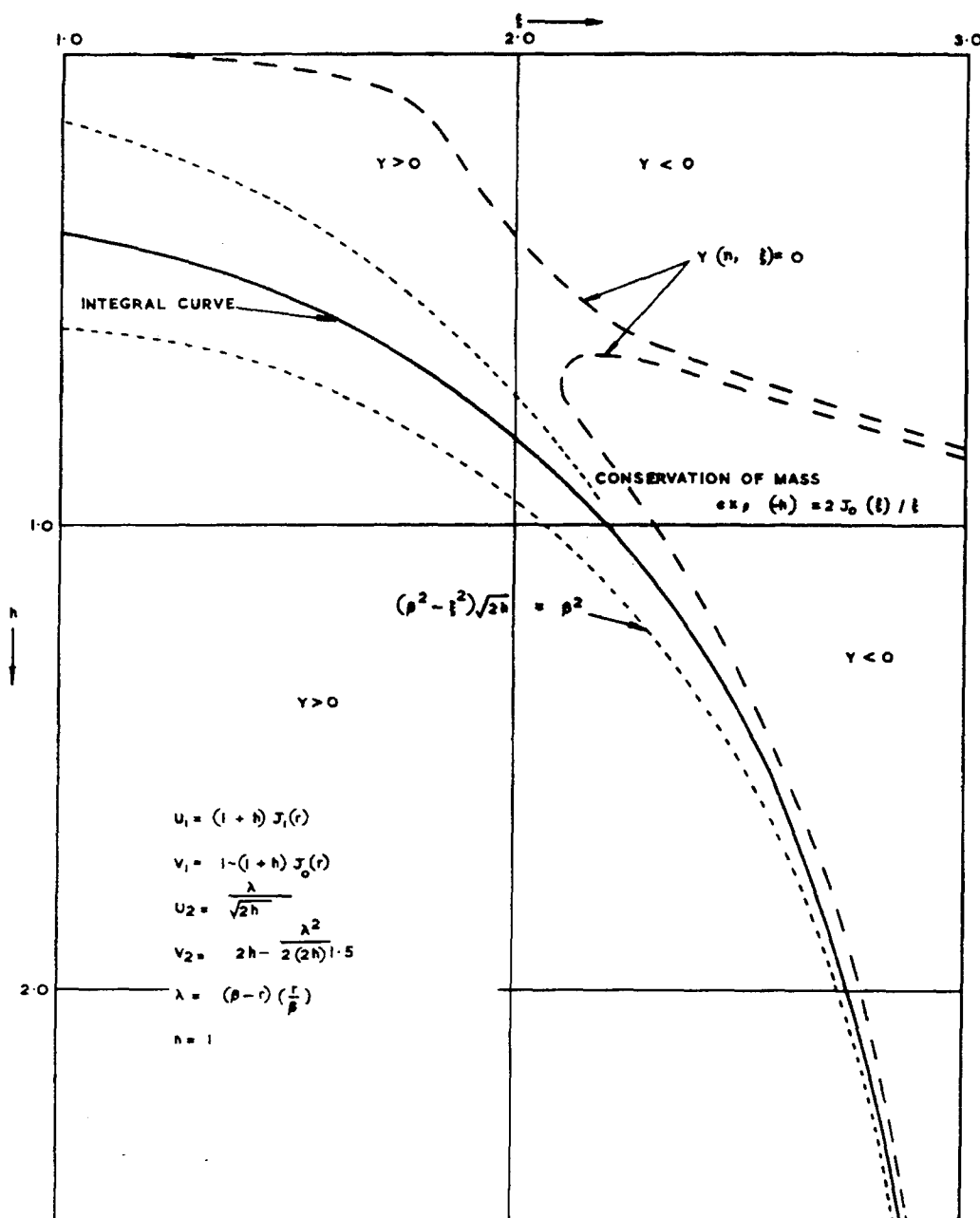
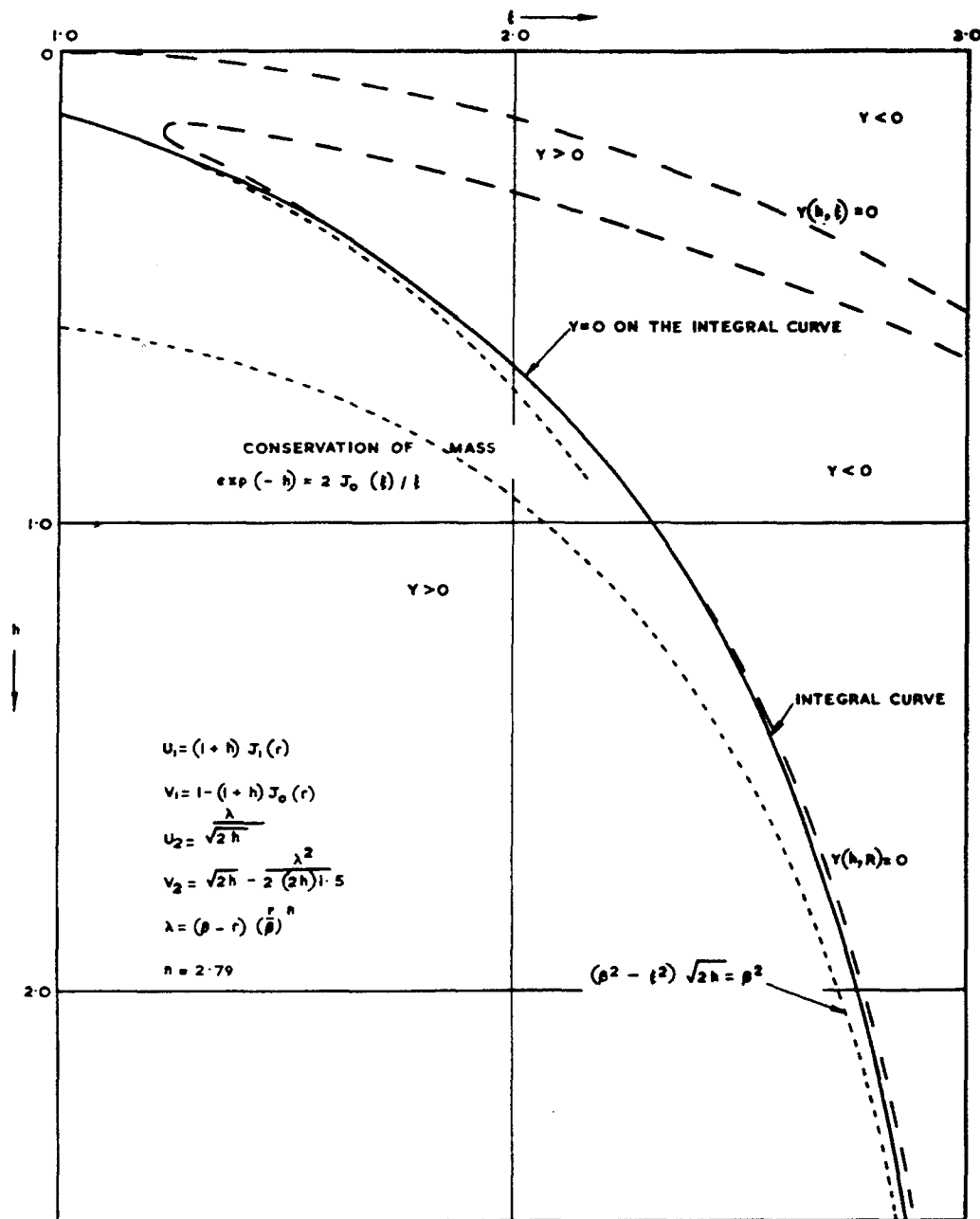


Fig. 1 - Integral curve representing the bubble surface for $n = 1$

larger values of n , when λ will converge to zero more rapidly, the integral curve approaches closer to both the curve $Y(\eta, \xi) = 0$ and to the correct form near the origin. For n greater than 2.79, however, the integral curve meets the curve $Y(\eta, \xi) = 0$ at a finite angle and thus 2.79 is the maximum value of n

possible. The integral curve for this value of n is shown in Fig. 2.

The corresponding values of a and b are shown in Fig. 3 though unfortunately as a and b do not tend to the correct limits as $h \rightarrow 0$ their definitions must be modified for small values



of h. For $\xi < \beta$ Eqs. (22) and (23) may be written

$$a = 1 + \frac{\beta^2 b}{2(n+1)(n+2)(2n+3)(2h)^{3/2}} \quad (24)$$

and thus we must choose b such that

$$b/h^{3/2} \rightarrow 0 \quad \text{as} \quad h \rightarrow 0. \quad (25)$$

We therefore take

$$b = A \exp(-p/h) \quad (26)$$

for $h \leq h_c$, where A and p are constants chosen to make b and db/dh continuous at h_c . The choice of h_c is rather arbitrary and the point at which the tangent from the origin meets the original curve is chosen, i.e., $h_c = 0.14$ where $b = 0.0275$. These final values of a and b are

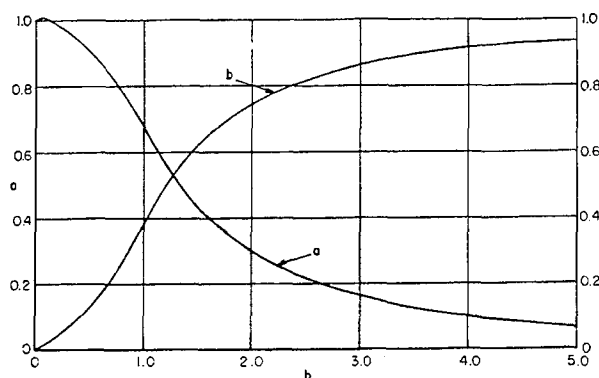


Fig. 3 - The values of a and b in Eqs. (10) and (11)

the ones shown in Fig. 3; that a rises above unity is an effect of the correction term to v_2 showing itself near the origin.

CALCULATION OF THE EFFECTIVE INERTIA IN THE LATE STAGES

Consider first a bubble of fluid of negligible density rising up a tube filled with a fluid of density ρ in a constant gravity field g_1 . We take a coordinate system in which the fluid high above the bubble vertex is at rest and the vertex is rising with velocity V_0 . Take some plane Q at a height H_1 , below the vertex and rising with it, then the total kinetic energy of the fluid above Q is finite and can be written $(1/2) M_h V_0^2$ where M_h is independent of the gravity field but not of H_1 .

Let A denote the mass of fluid that was above Q at time T , this need not be infinite but must be large enough to ensure that negligible error is introduced by assuming that its upper surface is at rest, then in a small time interval δT a mass of fluid δA will pass down through the plane Q , this small mass having a total kinetic energy which we write $-(1/2) \delta A V_1^2$. Clearly $-dA/dT$ is the integral of $\rho V dS$ over the plane Q , where V is the downward component of fluid velocity and dS is an element of area. However, the total kinetic energy above the rising plane Q is constant and hence this is the net gain in kinetic energy of the final mass of fluid A . Again by integrating ρg_1 , times the downward component of velocity over the whole volume of fluid above Q we obtain the rate at which A loses potential energy, let us denote this by $M_p g_1 V_0$.

In addition work is done on A by the fluid pressure p ; if P be the bubble pressure, then

the pressure difference $P - p$ at any point inside the fluid and on the plane Q can be obtained from Bernoulli's formula

$$\frac{2(P - p)}{\rho} = U^2 + (V_0 + V)^2 - \bar{U}^2 + (V_0 + \bar{V})^2 \quad (27)$$

where U and $(V_0 + V)$ are the horizontal and vertical components of fluid velocity measured in a steady flow coordinate system, i.e., with the bubble at rest; \bar{U} and \bar{V} are the values of U and V on the bubble surface in the plane Q . Now P does no work on A since volume is conserved and thus the net rate at which pressure does work on A is

$$\iint_Q (P - p) V dS.$$

In steady flow the rate of gain of energy must equal the work done, i.e.,

$$\begin{aligned} -\frac{1}{2} V_1^2 \frac{dA}{dT} &= \frac{1}{2} V_1^2 \iint_Q \rho V dS \\ &= M_p g_1 V_0 + \iint_Q (P - p) V dS. \end{aligned} \quad (28)$$

Suppose now that we suddenly increase the gravity field to some value $g > g_1$, then during a small time interval δT all velocities will remain unchanged to first order and in Eq. (28) only the first term on the right-hand side will be changed; also $(P - p)$ is independent of g and hence (27) is unchanged. This excess rate of loss of potential energy must be balanced by an increase in the rate of gain of kinetic energy, i.e.,

$$\frac{d}{dT} \left(\frac{1}{2} M_h V_0^2 \right) - \frac{1}{2} V_1^2 \frac{dA}{dT} = M_p g V_0 + \iint_Q (P - p) V dS, \quad (29)$$

this equation holding for any type of flow. Subtracting Eq. (29) from (28) we get

$$\frac{d}{dT} \left(\frac{1}{2} M_h V_0^2 \right) = M_p (g - g_1) V_0. \quad (30)$$

that is,

$$d^2 a / dT^2 = M_p (g - g_1) / M_h. \quad (31)$$

By definition g_1 is the value of g required to keep the flow steady, i.e.,

$$g_1 = 2\beta (da/dT)^2 / D \quad (32)$$

and hence

$$\frac{d^2 a}{dT^2} = \frac{M_p}{M_h} g - \frac{2\beta}{D} \frac{M_p}{M_h} \left(\frac{da}{dT} \right)^2. \quad (33)$$

The value of M_p/M_h in this formula can be calculated using the detailed steady flow pattern calculated in Section 3. We write m_p , m_h , v_o and h_1 for the nondimensional forms of M_p , M_h , v_o and H_1 and, as M_p/M_h is dimensionless, $M_p/M_h = m_p/m_h = \mu$. Thus, for the kinetic energy $(1/2) m_h v_o^2$ of the fluid above a plane $h = h_1$ we have

$$\frac{1}{2} m_h v_o^2 = \pi \rho \left\{ \int_{-\infty}^0 \int_0^\beta r(u^2 + v^2) dr dh + \int_0^{h_1} \int_R^\beta r(u^2 + v^2) dr dh \right\}, \quad (34)$$

where u and v are measured in a coordinate system in which the fluid high above the vertex is at rest. Using Layzer's solution for $h < 0$ we have

$$\frac{1}{2} m_h v_o^2 = \pi \rho \left\{ \frac{1}{4} (J_0^2(\beta) + J_2^2(\beta)) + \int_0^{h_1} \int_R^\beta r(u^2 + v^2) dr dh \right\}. \quad (35)$$

Since the total potential energy of the fluid above some fixed plane just above the vertex is not changing we have

$$m_p v_o = 2\pi \rho \int_0^{h_1} \int_R^\beta r v dr dh = \pi \rho \int_0^{h_1} R^2 dh. \quad (36)$$

The ratio $m_p/m_h = \mu$ may be calculated numerically using the values u and v calculated in Section 3 and Fig. 4 shows μ as a function of h_1 . When h_1 is very large μ decreases in inverse proportion to $\sqrt{h_1}$, i.e., the response to a change in g becomes increasingly sluggish as h_1 increases. It is, however, unrealistic to consider very large values of h_1 since for $h_1 > 4$ the pressure is very nearly uniform and equal to P . Hence this fluid is falling freely and has no effect on the fluid near the vertex. Again, the fluid above the vertex has finite kinetic energy but no rate of loss of potential energy, i.e., for $h_1 \leq 0$ $\mu = 0$. To obtain a realistic estimate of the response of the flow near the vertex to changes in g we should take h_1 somewhat less than the tube radius, say $h_1 = 2$. From Fig. 4 it may be seen that μ is nearly constant from $h_1 = 2$ to $h_1 = 4$, having a maximum for h_1 just less than 3.

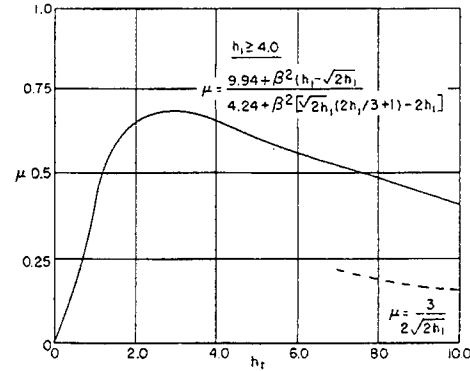


Fig. 4 - The value of μ as a function of h

Our assumption that the flow pattern is similar at all times implies that the bubble surface is rigid in shape. The fact that $\mu = 0$ as $h \rightarrow 0$ implies that the acceleration of the vertex when g increases is not due to local effects but to a pressure pulse originating from near $h_1 = 3$. Since the bubble is not rigid the flow pattern near $h_1 = 3$ will respond more quickly than that near the vertex and the bubble will be distorted as long as the acceleration lasts; this distortion increases the radius of curvature of the bubble near the vertex and so increases the equilibrium rate of rise of the vertex. We know from the principle enunciated by Garabedian (1957) [14] for the linear case that the steady form of the bubble is the stable one, and hence the vertex will accelerate in an effort to restore the original shape. Hence we should use the maximum value of μ in computing the acceleration of the vertex and ignore the changes in shape there. That μ diminishes for $h_1 > 4$ means that the thin annular column of fluid well below the vertex will become slightly distorted, but this is of no interest.

Taking the maximum value of μ we have

$$\mu = 0.68 \approx 2/3 \quad (37)$$

and substituting this into Eq. (33) gives

$$3(d^2 a/dT^2)/2 = g - 2\beta(da/dT)^2/D. \quad (38)$$

MODIFICATION TO LAYZER'S FORMULA

We have no reason to modify either the second or third terms of Layzer's equation (2) which appears to be quite satisfactory at small and large amplitudes, but at large amplitudes the coefficient of $d^2 a/dT^2$ has only 2/3 of the

value calculated in the previous section. To overcome this difficulty we modify Eq. (2) to become

$$\begin{aligned} & \frac{1}{2} \left\{ \exp(-4\beta a/D) + 3 \exp(4\beta a/D) \right\} d^2 a/dT^2 \\ & + \frac{2\beta}{D} \exp(4\beta a/D) (da/dT)^2 \\ & + g \left\{ 1 - \exp(4\beta a/D) \right\} = 0. \end{aligned} \quad (39)$$

Layzer's equation (2) gives a value for the initial acceleration

$$d^2 a/dT^2 = 2\beta g a_0/D + O(a_0^3) \quad (40)$$

that agrees with the first order theory and has no second order term. As it is not possible to find the correct second order term the

$$\exp(-4\beta a/D)$$

factor in Eq. (39) has been introduced in order to give the same zero second term.

This modification increases the effective inertia by 10, 20, 30 or 40% for $a/D = 0.052$, 0.084, 0.133, and 0.182, respectively. This is reasonable since, for constant g , the steady flow pattern is almost completely established for $a = 0.18D$ in Lewis' experiments.

THE PENETRATION OF THE HEAVY FLUID INTO THE LIGHTER FLUID

For small amplitudes the position of the interface is given by the product of its value at $r = 0$ and $J_0(r)$. Thus, in the initial stages the length of the spike is given by

$$b = a |J_0(\beta)|. \quad (41)$$

In the late stages long spikes of the heavy fluid penetrate the light one and these remain attached to their parent fluid by thin curtains. Hence their motion is independent of the motion of the interface and if we assume that the lighter fluid has zero density then

$$d^2(R-b)/dT^2 = 0$$

that is,

$$d^2 b/dT^2 = g, \quad (42)$$

where R denotes the position of the interface. In order to obtain one equation to represent the motion we modify Layzer's equation to become

$$\begin{aligned} & \left\{ \left(\frac{2\beta}{|J_0(\beta)|} - 1 \right) + \exp \left(\frac{4\beta b}{D |J_0(\beta)|} \right) \right\} d^2 b/dT^2 \\ & + \frac{2\beta}{D (J_0(\beta))^2} \left(1 + \frac{4\beta b}{D |J_0(\beta)|} + \frac{16\beta^2 b^2}{D^2 (J_0(\beta))^2} \right) (db/dT)^2 \\ & + g \left\{ 1 - \exp \left(\frac{4\beta b}{D |J_0(\beta)|} \right) \right\} = 0. \end{aligned} \quad (43)$$

COMPARISON OF RESULTS

The nondimensional forms of a , da/dT , etc., are given by

$$\begin{aligned} \eta &= 2\beta a/D, \\ \eta' &= (2\beta/Dg)^{1/2} da/dT, \\ \eta'' &= (1/g) d^2 a/dT^2, \\ \xi &= 2\beta b/D, \\ \xi' &= (2\beta/Dg)^{1/2} db/dT, \\ \xi'' &= (1/g) d^2 b/dT^2, \end{aligned} \quad (44)$$

and in Figs. 5 to 7 the values of η , η' , η'' , ξ , ξ' and ξ'' are shown obtained by using different methods to calculate the interface instability together with values of η and ξ obtained by numerical experiment. In these figures the labels A, B, C and D refer to the various ways of calculating η and the primed symbols refer to the values of ξ . The latter values were calculated by assuming that the two fluids are compressible and using the "particle in cell" finite difference method [13] to solve the appropriate hydrodynamic equations. The two materials were initially at densities of 1 and 20 gm/cc; by using fairly high sound speeds, about 14.0 for the lighter fluid in nondimensional units, we can assume that the effect of compressibility is negligible.

The initial value of η has been taken as 0.4 which corresponds to an initial amplitude of about 1/19 of the wavelength. For the curves labelled A the first order solution has been used to calculate η until $\eta' = 1.0$ when we have

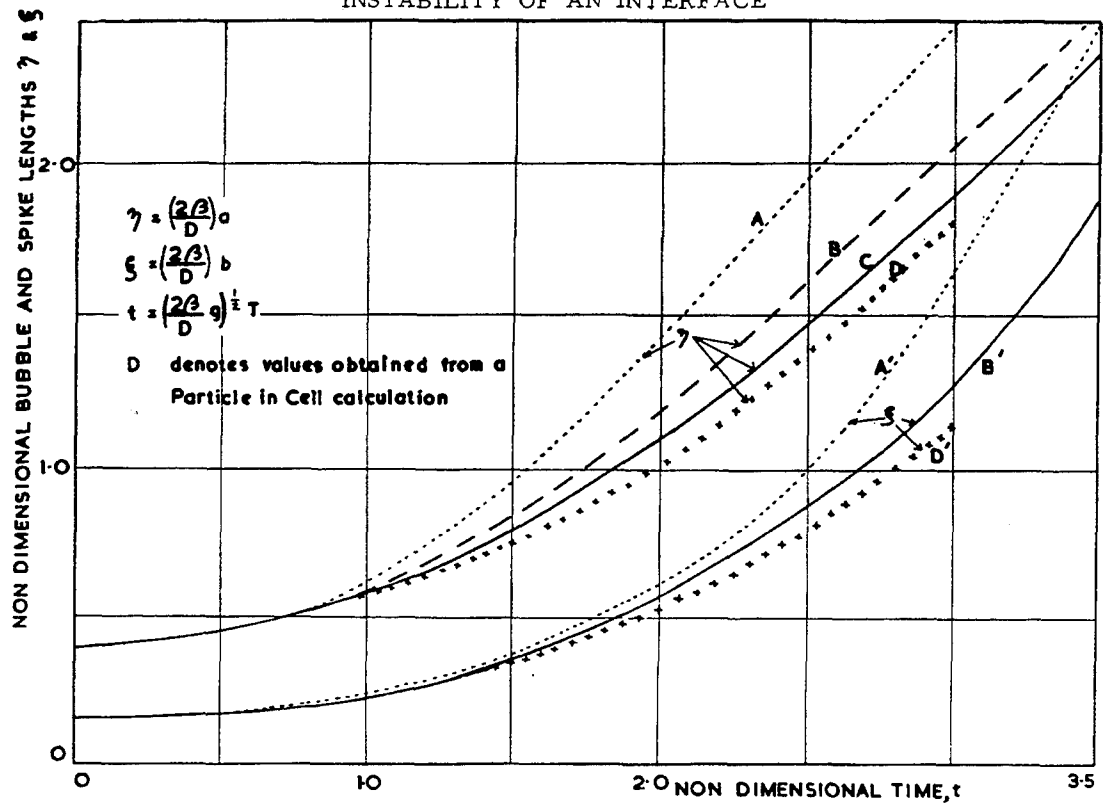


Fig. 5 - The amplitude of the bubble and length of the spike as functions of time

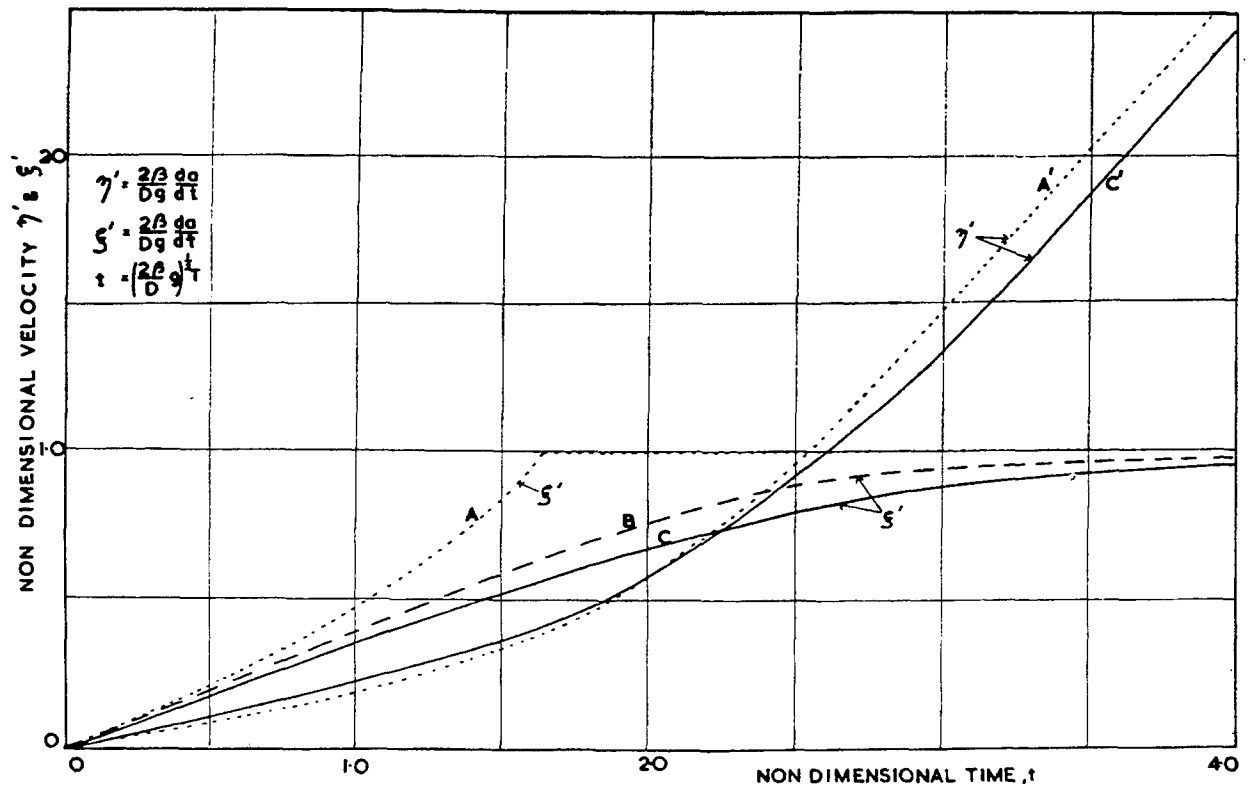


Fig. 6 - The velocities of the bubble and spike as functions of time

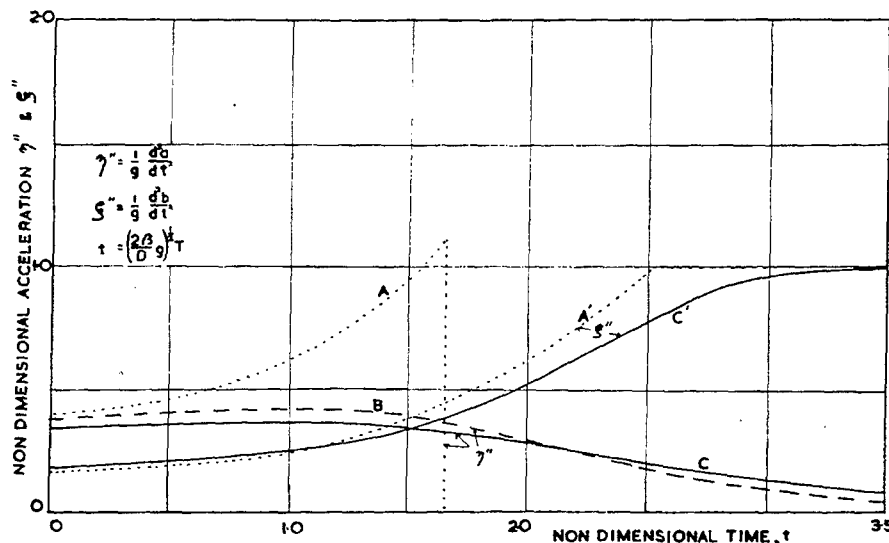


Fig. 7 - Accelerations of the bubble and spike as functions of time

changed over to the steady state. Similarly in calculating the length of the spike, the first order theory has been used until η'' equals the acceleration of the fluid, unity is the nondimensional variables, when we have changed over to the free fall theory of Eq. (42). Note that $\eta'' = 1.0$ when $\eta = 1.0$. These two changeovers take place at nondimensional times 1.648 and 1.566, respectively.

For the curves labelled B Layzer's Eq. (2) has been used to calculate the bubble amplitude at all times.

The curves labelled C have been calculated using our modifications of Layzer's equations, namely (39) and (43) for the bubbles and spikes respectively. It may be seen that the curves labelled C seem very reasonable and are closest to the numerical values which are shown as the curves D and D' in Fig. 5.

Further work is planned with the particle in cell method to obtain more values for various density ratios and initial amplitudes. Equations (39) and (43) could then be improved still further.

We have referred to the bubble and spike pattern of the interface but, because the initial amplitude of the spike is less than half the initial bubble amplitude the 'spike' length remains less than the bubble amplitude for the times shown here. At later times, however, the bubble grows at a constant rate whereas the 'spike' length grows at rate proportional to t^2 . From Figs. 5 to 7 we can see that we are about to

enter the phase when the spike grows rapidly and its length overtakes the magnitude of the bubble amplitude.

Qualitatively all the curves A, B and C agree with experiment but a direct quantitative comparison from published data is only possible in the early stages of the bubble growth and in the final steady velocity of the bubble. All the curves agree with this data. The difficulty with most experiments to date has been in trying to obtain a constant value of the acceleration. However, as Eqs. (39) and (43) should be valid for a variable acceleration, it should be possible to obtain some accurate comparisons between theory and experiment from experiments in which the acceleration was increased gradually from zero.

EXTENSION TO THE TWO FLUID CASE

The presence of a second lighter fluid of nonzero density modifies the flow in two ways — a buoyancy effect which reduces the effective value of g and an added inertia effect. When the initial amplitudes are very small the velocity distribution in the two fluids are symmetrical about the interface, and if we write g' for the effective value of g ,

$$g' = g(1 - \sigma/\rho)/(1 + \sigma/\rho), \quad (45)$$

where σ is the density of the lighter fluid.

In the late stages the interface breaks up into a honeycomb of bubbles and spikes, the

latter travelling independently of the interface in tapered cylinders of maximum cross sectional area roughly equal to cylinders of radii $A = D/2\sqrt{3}$. Thus, for the late stages, we may take the spikes to be ellipsoids travelling parallel to its axis of rotation (of length $2b$) and therefore

$$g' = g(1 - \sigma/\rho)/(1 + \alpha\sigma/\rho) \quad (46)$$

where $\alpha = A/2b$ over the limited range of values of b in which we are interested. We therefore take α to be whichever is the smaller of 1 and $D/4b\sqrt{3}$.

In the late stages of the bubble rise the lower density fluid between $h = 0$ and $h = 3$ rises with uniform velocity like a solid plug (we assume that the two fluids slide freely over each other at the interface since we ignore surface tension and viscosity). The effective value of g is now

$$g' = g(1 - \sigma/\rho)/(\sigma/\rho + \alpha), \quad (47)$$

where $\alpha = M_b/M_p = \mu$. To obtain a smooth transition from the early value of g' to the later value we take

$$\alpha = \frac{2}{3} + \frac{1}{3} \exp(-\beta a/D), \quad (48)$$

though clearly further work is required to determine more accurately the rate at which we should change from the early value to the late value.

REFERENCES

1. D. J. Lewis, Proc. Roy. Soc., A202, 81 (1950).
2. R. M. Davies and G. I. Taylor, Proc. Roy. Soc., A200, 375 (1950).
3. H. W. Emmons, C. T. Chang and B. C. Watson, J. Fl. Mech., 7, 177 (1960).
4. G. I. Taylor, Proc. Roy. Soc., A201, 192 (1950).
5. R. L. Ingraham, Proc. Phys. Soc., B67, 748 (1954).
6. C. T. Chang, Phys. of Fl., 2, 656 (1959).
7. Chia-Shun Yih, Proc. Roy. Soc., A258, 90 (1960).
8. D. Layzer, Astroph. J., 122, 1 (1955).
9. Harrison, Proc. Lond. Math. Soc., (2)Vi, 396 (1908).
10. Chandrasekhar, Proc. Camb. Phil. Soc., 51, 162 (1955).
11. W. H. Reid, Proc. Camb. Phil. Soc., 57, 415 (1961).
12. F. P. Bretherton, J. Fl. Mech., 10, 166 (1961).
13. B. Alder, A. Fernbach and M. Rotenberg, Methods in Computational Physics, Volume 3, Academic Press, p. 319 (1964).
14. P. R. Garabedian, Proc. Roy. Soc., A241, 423 (1957).

CALCULATION OF THE GROWTH OF INTERFACE INSTABILITIES BY A LAGRANGIAN MESH METHOD

L. A. Elliott
*Atomic Weapons Research Establishment
Aldermaston, Berkshire, England*

ABSTRACT

A two dimensional Lagrange mesh program has been used to calculate the growth of instabilities on a metal shell. The effects of the equation of state and shear strength of the material are investigated for the problem of a collapsing spherical shell.

INTRODUCTION

When considering explosive driven metal plates it is usual to assume that the metal behaves as a fluid, and that the surfaces display stability characteristics similar to those observed in liquids. Stability of moving fluid surfaces has been considered by a number of authors, in particular Taylor (1950). In practice all work on the subject the problem is simplified by assuming that the fluid is incompressible and that the amplitude of the perturbations is small enough to justify neglecting second order terms. By using a Lagrange mesh technique to solve numerically the hydrodynamic equations of two dimensional unsteady flow the effect of compressibility (i.e., the equation of state of the material) is included and the solution is not restricted to small perturbations.

Experiments using explosively driven plates of different materials show that for tin and lead the growth of perturbations is consistent with theoretical predictions, but for nonfusible metals such as steel the observed growth is much less, probably because of the inherent strength of solid materials. The Lagrange mesh technique is therefore extended to include the effect of material strength.

The problem considered is the stability of a collapsing spherical shell. The simplified solution for a fluid shell of constant energy is given by Hunt (1961) and has been extended to a more general rate of collapse in Ref. 3. This problem is also solved by the Lagrange hydrodynamic method using three equations of state. These are:

(a) a material with a high sound speed and low compressibility (for comparison with the simplified solution for an incompressible fluid),

(b) a highly compressible perfect fluid equation of state,

(c) a steel equation of state determined from experimental data by Walsh et al. (1957).

In case (a), when the material is comparatively incompressible, the perturbations on the inner surface of the shell grow slowly and oscillate, in agreement with the simplified theory (Ref. 3). When the perfect fluid equation of state is used, however, the perturbations grow rapidly and there is no oscillation. For a steel shell the perturbations again grow rapidly but they are different in form to case (b); also the amplitude begins to reverse in the later stages.

For all three equations of state the perturbations on the outer surface grow rapidly and have the same form. When a material strength of 20 kbar is added to steel, however, the amplitude of the perturbations is substantially reduced and only slow growth is obtained. The same is true of perturbations on the inner surface of the shell.

THE SIMPLIFIED METHOD

Perturbations on a spherical surface $r = r_o(t)$ may be expressed in terms of surface harmonics $S_n(\theta, \phi)$, i.e.,

$$r = r_o(t) + \sum_{n=1}^{\infty} b_n(t) S_n. \quad (1)$$

For axial symmetry this reduces to

$$r = r_0(t) + \sum_{n=1}^{\infty} b_n(t) P_n(\theta). \quad (2)$$

Using Hunt's technique and neglecting the effect of the shell outer surface we find for $n > 1$ that the perturbation amplitude on the inner surface is given by

$$r_0 \frac{d^2 b_n}{dt^2} + \frac{3dr_0}{dt} \frac{db_n}{dt} = (n-1) b_n \frac{d^2 r_0}{dt^2} \quad (3)$$

and similarly on the outer surface

$$r_0 \frac{d^2 b_n}{dt^2} + \frac{3dr_0}{dt} \frac{db_n}{dt} + (n+2) b_n \frac{d^2 r_0}{dt^2} = 0. \quad (4)$$

From Eq. (3) it can be shown (Ref. 3) that perturbations on the inner surface may be oscillating or nonoscillating, depending on the rate of free surface collapse and the order of the harmonic. Perturbations on the outer surface increase without oscillation if the surface is accelerating inward.

THE LAGRANGE FINITE DIFFERENCE METHOD

The equations of elastic-plastic flow in axial symmetry are

$$\begin{aligned} \frac{D\rho}{Dt} + \rho \left[\frac{\partial u}{\partial r} + \frac{\partial v}{\partial z} + \frac{u}{r} \right] &= 0 \\ \rho \frac{Du}{Dt} + \frac{\partial p_{rr}}{\partial r} + \frac{1}{r} (p_{rr} - p_{\phi\phi}) + \frac{\partial p_{rz}}{\partial z} &= 0 \\ \rho \frac{Dv}{Dt} + \frac{\partial p_{zz}}{\partial z} + \frac{\partial p_{rz}}{\partial r} + \frac{p_{rz}}{r} &= 0 \\ \frac{DE}{Dt} + p_{rr} \frac{\partial u}{\partial r} + p_{\phi\phi} \frac{u}{r} + p_{zz} \frac{\partial v}{\partial z} + p_{rz} \left(\frac{\partial v}{\partial r} + \frac{\partial u}{\partial z} \right) &= 0 \end{aligned}$$

where r and z are cylindrical coordinates, u and v are the respective velocity components, ρ is the density, and p_{rr} , $p_{\phi\phi}$, p_{zz} and p_{rz} are stress components. The internal energy E is given in terms of the mean pressure

$$p = \frac{1}{3} (p_{rr} + p_{\phi\phi} + p_{zz})$$

and ρ by the equation of state of the material. When $p_{rr} = p_{zz} = p_{\phi\phi} = p$ and $p_{rz} = 0$ the above equations reduce to the hydrodynamic equations of unsteady axial flow. When material strength is important the stresses are given by the elastic

stress-strain relations until the von Mises condition for plastic flow is satisfied, i.e.,

$$(p_{rr} - p)^2 + (p_{\phi\phi} - p)^2 + (p_{zz} - p)^2 + 2p_{rz}^2 = \frac{2}{3} Y^2$$

where Y is the yield strength.

These equations are solved by a Lagrange finite difference method. The material is divided into quadrilateral meshes which move with the fluid. Each cell has associated with it the stresses, density and internal energy, while point coordinates and velocity components are associated with the vertices of the mesh; these quantities are all recalculated at each time step. Shock waves are smoothed by the introduction of a viscous pressure term as used by von Neumann and Richtmyer (1950).

The initial mesh of the configurations to be calculated are shown in Fig. 1. These consist of a sector of a sphere of semiangle 10° , with mean inner radius 9 cm and outer radius 12 cm and an axially symmetric sinusoidal perturbation of amplitude 0.1 cm on the inner surface in Fig. 1(a) and on the outer surface in Fig. 1(b). A uniform pressure of 0.2 Mbars is applied to the outer surface of the sphere throughout the motion. This causes a shock wave to be propagated inward to set the inner surface in motion. Ambient pressures are neglected.

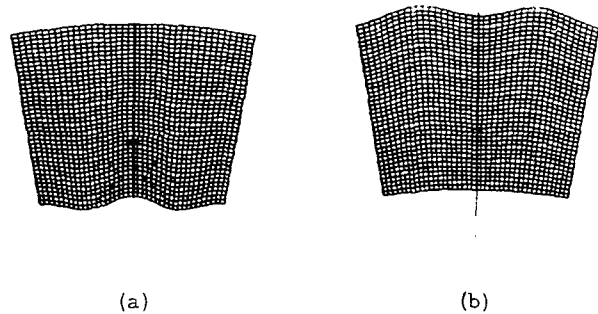


Fig. 1 Initial profiles; (a) perturbations on inner surface, (b) perturbations on outer surface

INCOMPRESSIBLE MATERIAL

When the material is incompressible the rate of collapse of the inner surface of a thick shell of constant energy is given approximately by

$$\frac{dr_0}{dt} = -kr_0^{-3/2}.$$

Under these circumstances by solving Eq. (3) we find that perturbations on the inner surface oscillate and grow as $r_o^{-1/4}$. This is confirmed by the Lagrange numerical solution which gives a slowly increasing amplitude and oscillations which agree with the simplified theory. The Lagrange calculation also shows that perturbations on the outer surface grow quickly with time and there is no oscillation. The simplified theory applies only for small perturbations but agrees qualitatively with the results of the numerical integration.

COMPRESSIBLE MATERIAL

The Lagrange calculation was carried out with a perfect fluid equation of state

$$p = (\gamma - 1) E \rho$$

with $\gamma = 3$. In this case the shock wave compresses the material to about half its original volume. When it strikes the inner perturbed surface it causes an immediate reversal of perturbation amplitude due to the uneven impact. After this stage the perturbation grows quite rapidly.

For compressible materials the rate of collapse of the free surface is slower than for incompressible materials. It has been shown by Peierls et al. (1945) that for a compressible material with adiabatic exponent $\gamma = 3$ the inner free surface motion of a thick shell of constant energy is given more exactly by

$$\frac{dr_o}{dt} = -kr_o^{-0.4}.$$

Over the range computed by the Lagrange method the fact that no reversal is observed is consistent with the simplified theory, but the rate of growth is greater. Perturbations on the outer surface of the shell grow in a very similar manner to those on the incompressible shell.

STEEL SHELL

Without Material Strength

When the numerical calculation is repeated with an equation of state derived from Walsh's data for steel the form and growth of perturbations on the inner surface are again different. As in the case of a highly compressible material the perturbations grow rapidly but the shape is different and in later stages a reversal begins to occur, similar to the oscillation on the inner surface of an incompressible shell.

Perturbations on the outer surface again grow rapidly and are similar in shape to those obtained for both the perfect fluid and the incompressible calculations.

With Material Strength

If the numerical calculation for a steel shell is repeated with a yield strength Y of 20 kbars, then perturbations on both the inner and outer surfaces of the shell are substantially less than with $Y = 0$. Perturbations on the inner surface are reversed by the impact of the shock wave and, as in the calculation with no material strength, there is evidence of another reversal in amplitude at a later stage.

Print-outs of various stages of computation for the 4 cases cited are shown in Figs. 2, 3, and 4.

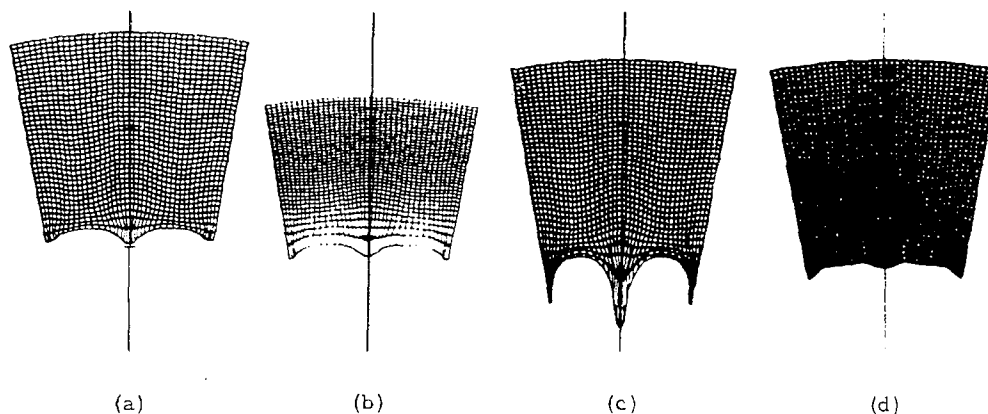


Fig. 2 - Early stage of collapse with perturbations on the inner surface: (a) incompressible material, (b) perfect fluid, (c) steel with no strength, (d) steel with 20 kbar yield strength

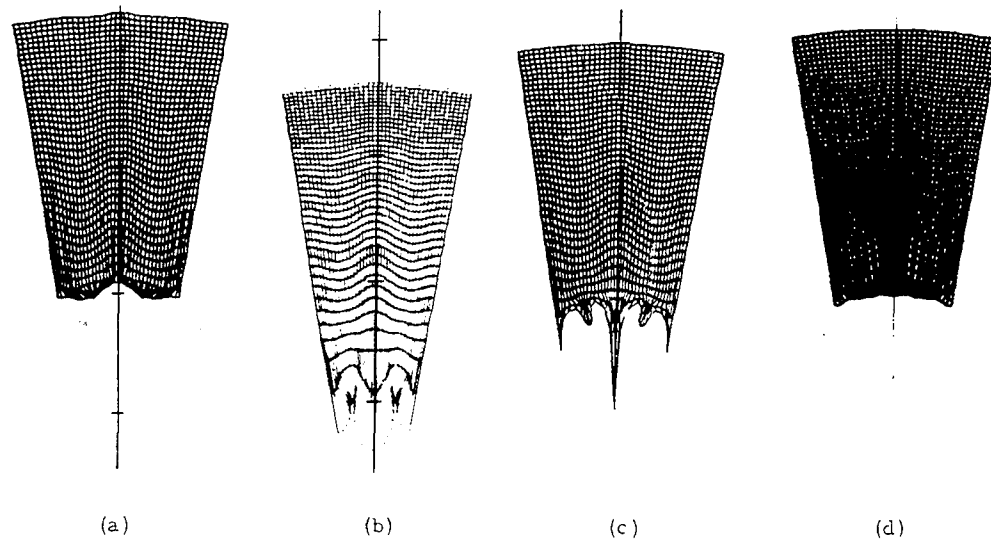


Fig. 3 - Later stage of collapse with perturbations on the inner surface; (a) incompressible material, (b) perfect fluid, (c) steel with no strength, (d) steel with 20 kbar yield strength

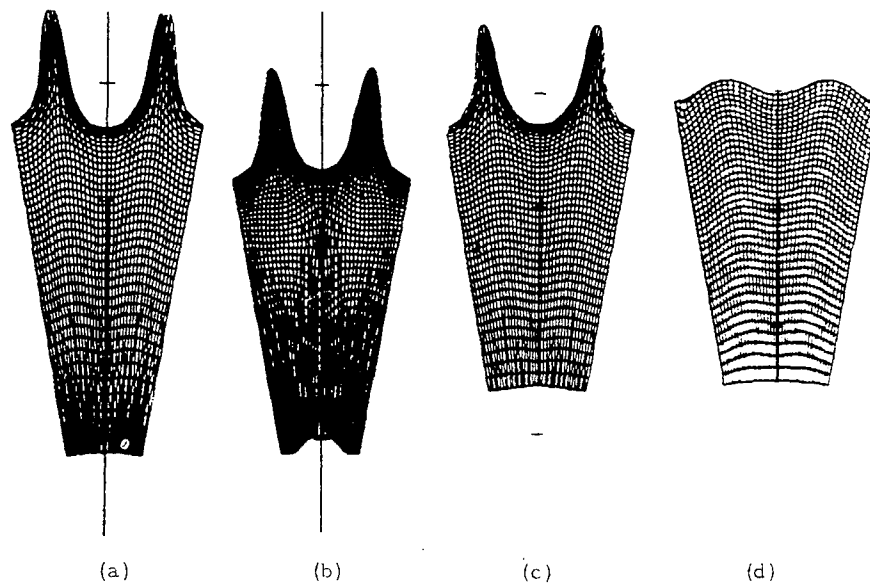


Fig. 4 - Later profiles with perturbations on the outer surface; (a) incompressible material, (b) perfect fluid, (c) steel with no strength, (d) steel with 20 kbar yield strength

CONCLUSIONS

Perturbations on the outer surface of a collapsing spherical shell grow in a similar manner for different materials, but those on

the inner surface vary substantially in rate of growth and in shape and also in amplitude reversal. The introduction of a 20 kbar yield strength in steel substantially reduces the perturbation growth on a shell with 200 kbar applied pressure.

REFERENCES

1. G. I. Taylor, Proc. Roy. Soc. A, 201, 192, 1950.
2. J. N. Hunt, Appl. Sci. Res. A. 10, 59, 1961.
3. L. A. Elliott, Proc. Roy. Soc. A, 284, 397, 1965.
4. J. von Neumann and R. D. Richtmyer, J. Appl. Phys. 21, 232, 1950.
5. R. Peierls, J. von Neumann, and J. W. Calkin, L.A.D.C. Rep. No. 2071, 1945.
6. J. Walsh, M. H. Rice, R. G. McQueen, and F. L. Yarger, Phys. Review 108, No. 2, 196, 1957.

Invited Review

SHOCK WAVE RESEARCH ON INERT SOLIDS*

W. E. Deal

*University of California, Los Alamos Scientific Laboratory
Los Alamos, New Mexico*

I have been asked to review or comment on the papers of this section, classified under the title "Shock Waves and Related Flows." Further I was requested to comment on where we have been in shock wave research, the direction in which the work appears to be heading and possibly upon the direction in which I believe the work should be headed. This is somewhat of a large order, one which I'm sure I will only partially fill.

The papers on shock wave research were seventeen in number. In classification of these papers it is convenient to use my interpretation of classifications recently adopted by several American Institute of Physics Journals; namely,

T = almost solely theoretical,

E = almost solely experimental,

T/E = mainly theoretical supported by experiments,

E/T = mainly experimental supported by theory, and

CE = computer experiments,

where the last one is a class of papers of increasing importance as attested to by the presence of an entire section of the symposium devoted to papers of this type. The seventeen papers are thus classified by me as:

T - 5 - Duvall and Horie; Pearson; Cameron and Pike; Cheret; Anderson

T/E - 1 - Butcher and Munson

E - 8 - Ramsay and Popolato; Coleburn, and Liddiard; Halpin and Graham; Liddiard; Erkman; Wasley and O'Brien; Rempel and Schmidt; Fuller and Price

E/T - 2 - Anderson, Fahrenbruch and Fowles; Thouvenin

CE - 1 - Elliot

Thus you see we had a fairly balanced section of the Symposium with reasonable numbers of both experimental and theoretical papers.

I must admit a personal prejudice in preferring to read individual papers of the E/T and T/E types which have this same type of balance internally.

There is still another way to classify and group the papers; that is, by subject matter. From this standpoint we have:

3 on unreacted Hugoniot of explosives

6 on elastic-plastic flow

2 on interface instabilities

2 on complete P - V - E equation of state

2 on shock properties of porous materials

1 on shock induced phase transitions, and

1 on general shock and detonation wave propagation.

This grouping in particular shows the definite extensive prevailing interest in elastic-plastic flow.

For the past fifteen years or so there has been interest in shock wave research on inert solids at the relatively high pressures where wave propagation was thought to be described rather accurately by hydrodynamics. In fact the pressure regime between the high static pressure work and that where the Thomas-Fermi-Dirac theoretical model describes the

*This work was supported by the U. S. Atomic Energy Commission.

equation of state well has been almost successfully bridged. In the high-pressure regime there has been a successful attainment of high precision measurements, with knowledge of pressure to 1% at a given compression being attainable. Precision dynamic measurements have, in fact, even been used for pressure calibration of static high-pressure experiments in the several hundred kilobar range.

In the pressure range above 100 kilobars the primary dynamic work has consisted in (1) experimental determination of Hugoniot of a variety of materials, (2) experimental studies of phase transitions, and (3) experimental and theoretical seeking for means of extending knowledge of the equation of state surface away from the Hugoniot locus to the surrounding $P-V-E$ space.

In the high pressure work, we have generally thought hydrodynamically, but in the last five years or so, increasing attention has been paid to the lower pressure region where elastic waves play an important role. As reflected by the number of papers at this meeting on the subject, we are still in the midst of extensive studies of elastic-plastic phenomena. We still have a way to go before we understand and explain these phenomena, though. We must change our thinking from hydrodynamic flow to include the contribution of material shear strength and resistance to various rates of deformation at all pressures. In fact neither the perfect fluid point of view nor the simple elastic solid point of view are adequate for the problems we face. However, they are useful simplifying approximations at high and low pressures respectively. We must admit the consequences of our materials behaving as nonlinear solids, having viscosity and even more complicated non-Newtonian fluid properties. Combinations of such properties must also be admitted. Most papers in the field treat the materials in question in terms of their macroscopic properties; i.e., as continuous materials. I believe the way to explaining complex elastic-plastic flow lies in consideration of the microscopic properties. We must probably, for crystalline materials in particular, consider details of dislocation dynamics. We must also be acutely aware of the exact initial state of the samples we study; that is, we must know exactly how they were prepared and know the internal structure. Our experiments will turn out to be extensions of the work of metallurgists and rheologists up to the maximum possible strain rates and to higher pressure, and we must be aware of their work and correlate it with ours. Dynamic high pressure conditions, in the past, have been considered so extreme that static and low-rate information

were often ignored. We should not continue this practice.

It has frequently been the custom to start shock wave papers with the equations of conservation of mass, momentum, and energy across a shock wave, which in their simplest form are:

$$P - P_0 = \rho_0 U_s U_p, \quad (1)$$

$$\rho/\rho_0 = V_0/V = U_s/(U_s - U_p), \quad (2)$$

and

$$E - E_0 = (P + P_0)/2(V_0 - V) \quad (3)$$

where P is pressure, ρ is density, U_s is shock velocity, U_p is particle velocity, V is specific volume, E is specific internal energy and the zero subscripts refer to the initial state ahead of the shock. For theoretical purposes, consideration is usually taken of the Hugoniot curve representation in $P-V-E$ space or the projection particularly on the $P-V$ plane. The experimentalist, on the other hand is most frequently concerned with his measured variables in the U_s-U_p plane and the representation there of the Hugoniot curve.

Here, in this U_s-U_p plane, experience has shown us that over a substantial pressure range and for a wide variety of solid materials, the Hugoniot is best represented as a straight line:

$$U_s = C_0 + S U_p. \quad (4)$$

Let us consider what the consequences are to our usual hydrodynamic representations in the $P-V$ and U_s-U_p planes by inclusion of linear elasticity.

First, we imagine the material unstrained. In the process of being deformed, the element of mass at the vector position x_j is displaced to $x_i + e_i$. The nine relative deformations $\partial e_i / \partial x_j$ are the quantities important for determining strain. Of these nine, the three combinations

$$\left(\frac{\partial e_i}{\partial x_j} - \frac{\partial e_j}{\partial x_i} \right)$$

represent rigid body rotation; thus leaving only six strain components represented by

$$\left(\frac{\partial e_i}{\partial x_j} + \frac{\partial e_j}{\partial x_i} \right)$$

The nine component stress σ_{ij} of force per unit area on the i th face of an infinitesimal cube

in the j th direction is similarly reduced to six components by recognition that for rotational balance $\sigma_{ij} = \sigma_{ji}$. For a Hooke's law solid in which each of the six stresses are linearly related to the six strains, there are thus 36 elastic constants. From the existence of an elastic potential energy, it can be shown that only 21 of these 36 are independent. Various degrees of symmetry can reduce this number further, and for an isotropic material the number of independent elastic constants reduces to only two. These are the Lamé constants λ and μ in the equation,

$$\sigma_{ij} = \lambda \delta_{ij} e_{kk} + \mu (e_{ij} + e_{ji}), \quad (5)$$

where repeated indices in the same term represent summation, δ_{ij} is the Kronecker delta, and e_{ij} represents $\partial e_i / \partial x_j$. For the force F_i on the i th face of an element of mass $\rho dx_1 dx_2 dx_3$, we have:

$$F_i = \frac{\partial \sigma_{ij}}{\partial x_j}, \quad (6)$$

so that use of Newton's Law gives for the equations of motion of an elastic body:

$$\rho \frac{\partial^2 e_i}{\partial t^2} = \frac{\partial \sigma_{ij}}{\partial x_j}, \quad (7)$$

and with Hooke's law the equations of motion become:

$$\rho \frac{\partial^2 e_i}{\partial t^2} = (\lambda + \mu) \frac{\partial e_{ji}}{\partial x_j} + \mu \frac{\partial e_{ij}}{\partial x_j}. \quad (8)$$

For plane waves where displacement is a function of the x_1 direction only as well as time, then any derivative with respect to x_2 or x_3 is zero and we have the simple equations of motion:

$$\rho \frac{\partial^2 e_1}{\partial t^2} = (\lambda + 2\mu) \frac{\partial^2 e_1}{\partial x_1^2} \quad (9)$$

$$\rho \frac{\partial^2 e_2}{\partial t^2} = \mu \frac{\partial^2 e_2}{\partial x_1^2} \quad (10)$$

$$\rho \frac{\partial^2 e_3}{\partial t^2} = \mu \frac{\partial^2 e_3}{\partial x_1^2}. \quad (11)$$

These have the form of the wave equation, the first of which represents a longitudinal wave of velocity, V_ℓ , given by:

$$V_\ell^2 = (\lambda + 2\mu) / \rho. \quad (12)$$

The other two equations represent transverse displacement waves with displacements in the x_2 and x_3 directions respectively with velocity, V_s , given by:

$$V_s^2 = \mu / \rho. \quad (13)$$

Now from the conservation equations, by elimination of U_p , we have

$$U_s^2 = V_o^2 \frac{P - P_o}{V - V_o} \quad (14)$$

so that the intercept in the $U_s - U_p$ plane is given by $\lim U_s$ as $P \rightarrow P_o$, $V \rightarrow V_o$:

$$C_o^2 = -V_o^2 \left. \frac{dP}{dV} \right|_{V=V_o}. \quad (15)$$

For an isotropic ("hydrostatic") plane wave of compression

$$e_{11} = e_{22} = e_{33} = (1/3)(\Delta V/V)$$

$$e_{ij} = 0 \quad \text{for } i \neq j \quad (16)$$

and

$$P = \sigma_{11} = \sigma_{22} = \sigma_{33} = \left(\lambda + \frac{2}{3} \mu \right) (\Delta V/V) \\ = \left(\lambda + \frac{2}{3} \mu \right) \left(\frac{V_o}{V} - 1 \right); \quad (17)$$

hence

$$C_o^2 = -V_o^2 \left. \frac{dP}{dV} \right|_{V=V_o} = \left(\lambda + \frac{2}{3} \mu \right) / \rho_o. \quad (18)$$

Note that $\lambda + (2/3)\mu$ is the bulk compressibility modulus. Thus with relations for V_ℓ , V_s , and C_o in terms of the Lamé constants, we have the relation between them of

$$C_o^2 = \frac{\lambda + \frac{2}{3} \mu}{\rho} = \frac{\lambda + 2\mu}{\rho} - \frac{4\mu}{3\rho} \\ C_o^2 = V_\ell^2 - \frac{4}{3} V_s^2. \quad (19)$$

It is unfortunate that several papers recently have failed to distinguish between the longitudinal sound speed V_ℓ and the bulk sound speed C_o .

In the $U_s - U_p$ and $P - V$ planes we have for a perfectly elastic-perfectly plastic material the simplified representations shown in Figs. 1 and 2. The situation is in truth much more

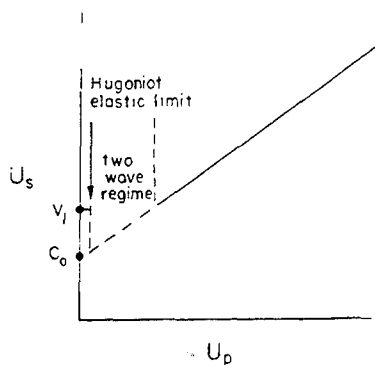


Figure 1

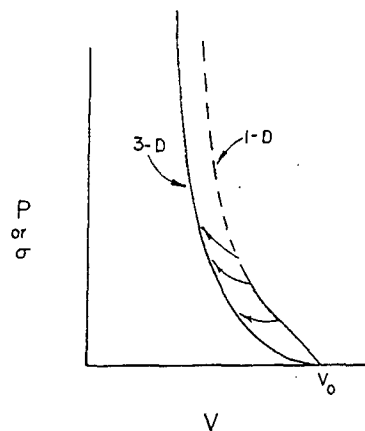


Figure 3

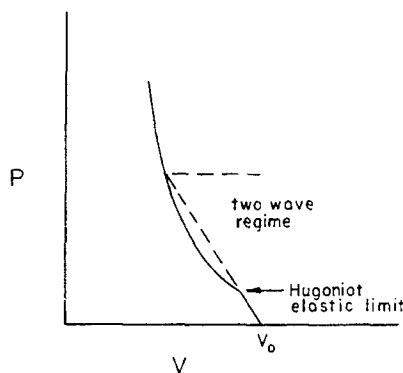


Figure 2

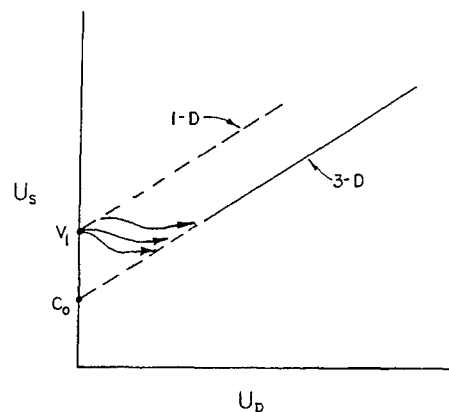


Figure 4

complicated than this. In considering the process in the $P - V$ or stress strain plane (see Fig. 3), the compression is initially one-dimensional, but nonlinear and partially relaxes at higher pressure to a more nearly three-dimensional compression by some path which is a function of the material properties (a combination of rigidity and viscosity-related properties) and the applied stress. We like to think of simple perfectly-elastic solids, or perfect fluids, we must, however, face combinations of very complex properties.

In the $U_s - U_p$ plane the one-dimensional to three-dimensional yield and relaxation processes cause the simple diagram for a single material of a completely specified initial state to appear as illustrated in Fig. 4.

Such behavior is further complicated by the fact that even behind high pressure shock waves, materials still have elastic properties and propagate elastic waves of both compression and tension.

The model is then even more highly complicated by the occurrence of phase changes behind shock waves. Here again two-wave structures are sometimes possible. Relaxation effects in phase changes are also important, mixed phase regions exist and a variety of types of phase changes occur. Some of the types of phase changes have been discussed by McQueen* and by Duvall and Horie at this symposium.† The effect of several types of phase changes on Hugoniot in our selected $U_s - U_p$ and $P - V$ planes are summarized in Figs. 5 and 6.

*R. G. McQueen, "Laboratory Techniques for Very High Pressure and the Behavior of Metals Under Dynamic Loading," *Metallurgy at High Pressures and High Temperatures* (Metallurgical Society Conferences, Dallas, Texas, Feb. 24-28, 1963, p. 44-132.

†G. E. Duvall and Y. Horie, This Symposium.

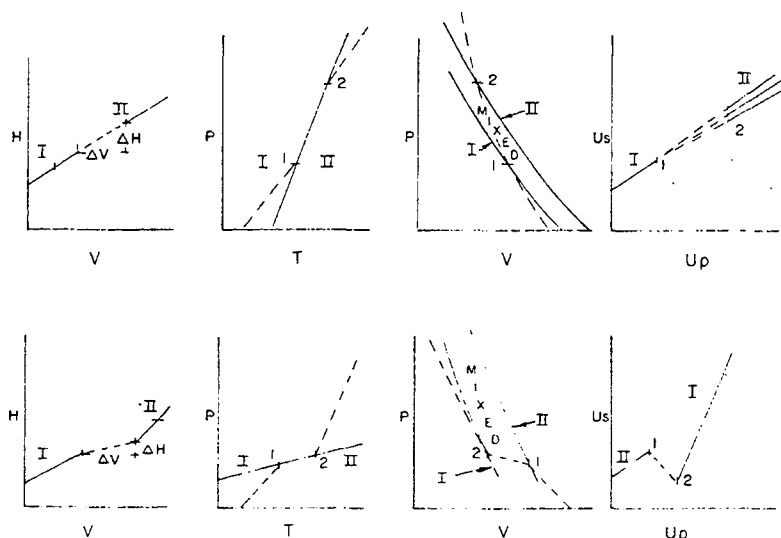


Figure 5

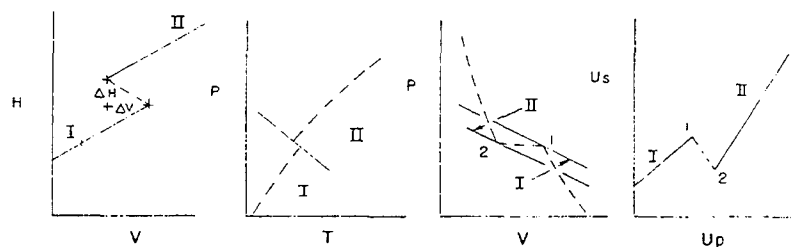


Figure 6

First, are shown two cases of phase transformation for $\Delta V/\Delta H$ positive. The diagrams on the left show enthalpy versus specific volume at constant pressure. The upper indicated behavior is typical for the melting and vaporization transition for many materials, the lower one for freezing. The ticked point in this H - V plane indicates which side of the transition is being considered as the initial state. In the second row of diagrams are shown the corresponding phase lines (solid) and Hugoniot (dashed). Where the two lines coincide, one has a mixed-phase region. The Roman numeral I refers to the low temperature phase, the II to the high temperature phase. In the third and fourth rows of diagrams are illustrated the corresponding curves in the familiar P - V and U_s - U_p planes. The only evidence from ordinary dynamic experiments for high pressure phase transformations of the upper type would thus be a bending of the U_s - U_p line. Resistivity or piezoelectric experiments might, however, be used to further

reveal the presence of such a phase transition. The lower type would be more obvious from U_s - U_p data and a two-wave system could result.

On Fig. 6 is shown a case for $\Delta V/\Delta H$ negative. The case here for a point of origin in phase II is trivial in that then the Hugoniot should never cross the phase line. A two-wave structure should arise for transitions of the kind illustrated.

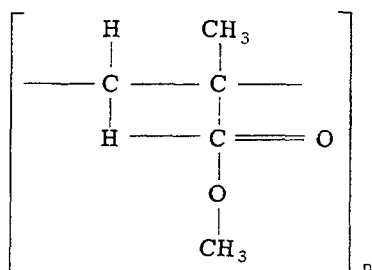
In some materials, multiple phase changes may be encountered when the Hugoniot crosses more than one phase line; e.g., near a triple point.

The motive behind the preceding discussion of various effects on the shape of the Hugoniot in the U_s - U_p plane has been to enable reasonable analysis of experimental results in terms of the quantities usually measured. Let us take for an example all of the available data for

polymethyl methacrylate and try to tie it together. Two of these sets of data are from papers in this section of this symposium.

Polymethyl methacrylate is produced* by the polymerization of the monomer by heat, light and catalysts. The polymerization may either be carried out in bulk, in which case the final polymerization is effected in molds; or it may be carried out in the presence of another fluid material, the product of this latter process being a colloid and subsequently a molding powder. In the first process, the result is the sheet or rod material from which many of us cut samples to be studied. Molding powders are used, often with a few percent of a plasticizer, to subsequently form with heat a wide variety of other shapes.

Polymethyl methacrylate polymers are usually considered to have the following formula:



Slower polymerization gives longer chain molecules and a stronger product.[†] The molding powder process yields a polymer of much lower molecular weight than that of the bulk polymerization. With variations in purity and composition of the starting monomer and a variety of polymerization conditions, a wide range of properties may result.

Polymethyl methacrylate is a major constituent in acrylic plastics manufactured in the U. S. A. largely by Cast Optics Corporation and called Evr-kleer (from a monomer made by DuPont which monomer is called Lucite), and by Rohm and Haas as Plexiglas. In the U. K., the polymer is manufactured by Imperial Chemical Industries and is called Perspex. I am not aware of the manufacturers or sources in other countries.

Substantial amounts of acrylates and other polymers forming copolymers with the methyl

methacrylate are usually present in commercial materials, some intentionally to improve the properties and others as economic levels of impurities. The variability in possible initial state for samples of polymethyl methacrylate is thus somewhat worse than that usually encountered with metallic samples for Hugoniot studies, but does point out in our example the necessity for careful definition of any material being studied by dynamic high pressure techniques.

Typical physical properties stated by American manufacturers for sheet (polymerized in bulk) polymethyl methacrylate are given in Table 1.

TABLE 1*

	Plexiglas	Evr-kleer
Refractive Index	1.489	1.496
Specific Gravity	1.18	1.18
Tensile Strength	8,000 psi	7,500 psi
Elongation at Break	min 2%	1%
Hardness, Rockwell	M-70	M-98
Compressive Strength	15,000 psi	11,000 psi
Modulus of Elasticity	$3-4 \times 10^5$ psi	---
Coeff. of Expansion	$8 \times 10^{-5}/^\circ\text{C}$	$8.8 \times 10^{-5}/^\circ\text{C}$
Specific Heat	0.35 cal/ $^\circ\text{C}$	0.35 cal/ $^\circ\text{C}$

*Since polymethyl methacrylate is a thermoplastic, the properties will vary with temperatures; values given apply to 25°C.

Most reports on the dynamic properties of polymethyl methacrylate however give little more than the trade name of the material. Only rarely is the form from which samples were made (e.g., sheet or rod and initial manufactured size) or the manufacturers type specified. Initial temperature, which is probably very important for a thermoplastic such as this, is practically never given. In a rare instance the initial state of the material has been shown to be "strain free" by photoelastic analysis. Some experimenters, however, even fail to report the initial density of their samples. Thus, you see, the set of all available shock wave data on

*J. Haslam and H. A. Willis, "Identification and Analysis of Plastics" (D. Van Nostrand Co., Princeton, N. J., 1965), p. 79.

†H. R. Simonds, A. J. Weith, and M. H. Bigelow, "Handbook of Plastics" (D. Van Nostrand, Princeton, N. J., 1949), p. 727.

polymethyl methacrylate which we are about to study probably represents data on an ensemble of polymethyl methacrylate materials of different purity, degree of polymerization, initial temperature, initial density, etc.

The reason, of course, for the widespread experimental interest in this material lies in the fact that it is an optically clear, machinable material with good electrical and thermal insulating properties and of convenient shock impedance which thus lends itself readily to experimental assembly design.

All shock wave data which the author has encountered on this material were converted to $U_s - U_p$ form and tabulated in Table 2. Twenty-four sources of data were found. These include contributions from 17 American sources, 3 British, 2 Russian, and 2 French sources. Of the 17 American ones, 13 separate laboratories appear to be represented. Not counting data for bulk and longitudinal sound speed, these 24 sources contribute 174 data points. A variety of methods of data collection are represented, including pin techniques, optical techniques of several varieties, and X-ray methods. The data are all plotted together on Fig. 7. Note that the scales on this plot and those following are in cgs units with the multiplier of a power of ten which is given at the origin for ordinate and abscissa just following the coordinates of the origin. The points represent data from 2.5 kb to 2 Mb. One is at first struck by the apparent consistency of the data. It is however only fair, not good; the wide range over which the data is plotted makes it appear deceptively consistent. In the densely populated region the data are roughly contained in a band $\pm 5\%$ wide in shock velocity and $\pm 15\%$ wide in particle velocity.

As is shown by Figs. 8-11, a linear least squares fit ($U_s = 0.288 + 1.38 U_p$) and a quadratic least squares fit ($U_s = 0.275 + 1.53 U_p - 0.22 U_p^2$) to all of the data leave substantial to be desired.

The data, however, appear in Figs. 12 and 13 to be rather well described by a linear fit ($U_s = 0.275 + 1.49 U_p$) up to a shock velocity of 0.8 cm/ μ sec and a particle velocity of 0.35 cm/ μ sec. Note that this intercept is rather close to longitudinal sound speed, not bulk sound speed as we expected. Above $U_s = 0.8$ cm/ μ sec, as shown in Figs. 14 and 15, the few data points available appear to require a slightly lesser slope ($U_s = 0.280 + 1.33 U_p$) for fitting with an offset (discontinuity) to larger U_p somewhere

in the vicinity of 0.8 cm/ μ sec. This two-line fit to the data corresponds to a phase change just above 300 kb with a volume contraction of about 5% of V_0 and resulting in a less compressible material.

This interpretation is not substantially inconsistent with the observation by Hauver and Melani (Table 2, Ref. 5) that there is a change in piezoelectric signal output quality at a shock velocity of about 0.69 cm/ μ sec. Such indications of phase change should be weighted heavily, but we must also remember there is probably a short region of mixed phase which might be better represented by two long line segments connected by a short one. The data thus allows us to conclude that there probably is a phase change somewhere in the vicinity of 300 kb.

A set of high-precision data over most of the pressure range considered on a single defined material would be required before much more could be concluded.

Let us now turn to consideration of the low pressure data. The puzzle here is why the set of data appears to extrapolate to longitudinal sound speed instead of bulk sound speed. A clue to this, though not the answer, is given by the set of data by Schmidt and Evans (Table 2, Ref. 3), taken all below 20 kb. These data are interpreted to represent a one-dimensional compressional strain at the low-stress end of the data which at the higher stresses is essentially three-dimensional. This effect, which might allow discarding data below 20 kb (0.05 cm/ μ sec particle velocity) in making a linear fit to the other data, however, still does not admit of an intercept below 0.25 cm/ μ sec. A curved fit which would allow the C_0 intercept is suggested by some of the sets of data, but the precision of the data in general precludes such elaboration. My personal prejudices are reflected in the interpretation indicated on Fig. 16.

With so much data available we should now know more about polymethyl methacrylate shock wave compression than most people would like to know; however, we must conclude that the data are generally of inadequate or unknown precision and on too wide a variety of unspecified materials to allow detailed conclusions to be drawn. One conclusion that the data do support, however, is that the behavior of commercial acrylic plastic under shock wave compression is complex. Such complexity is the rule rather than the exception in dynamic high pressure physics and leaves much for us to study and explain in the future.

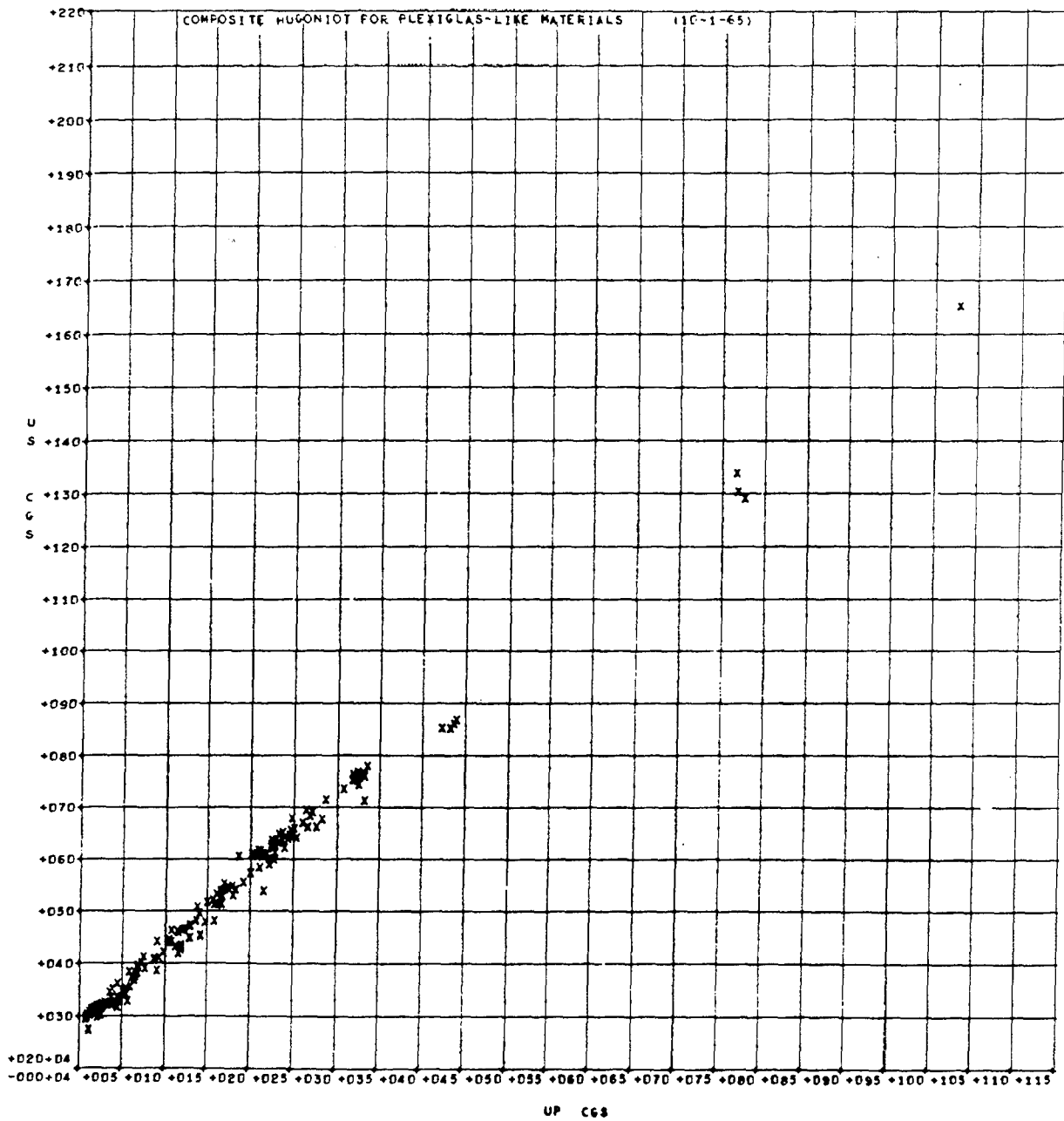


Figure 7

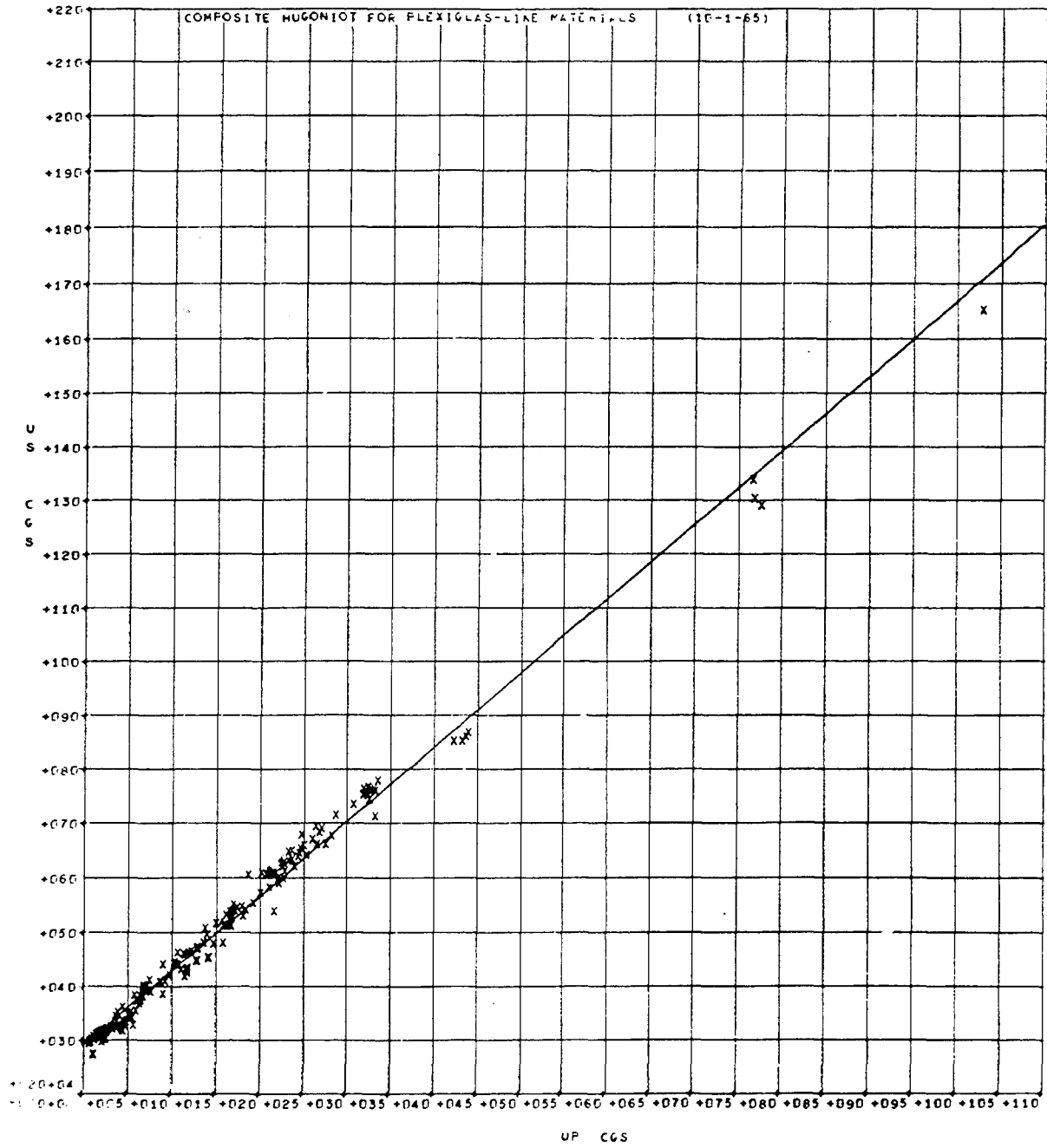


Figure 8

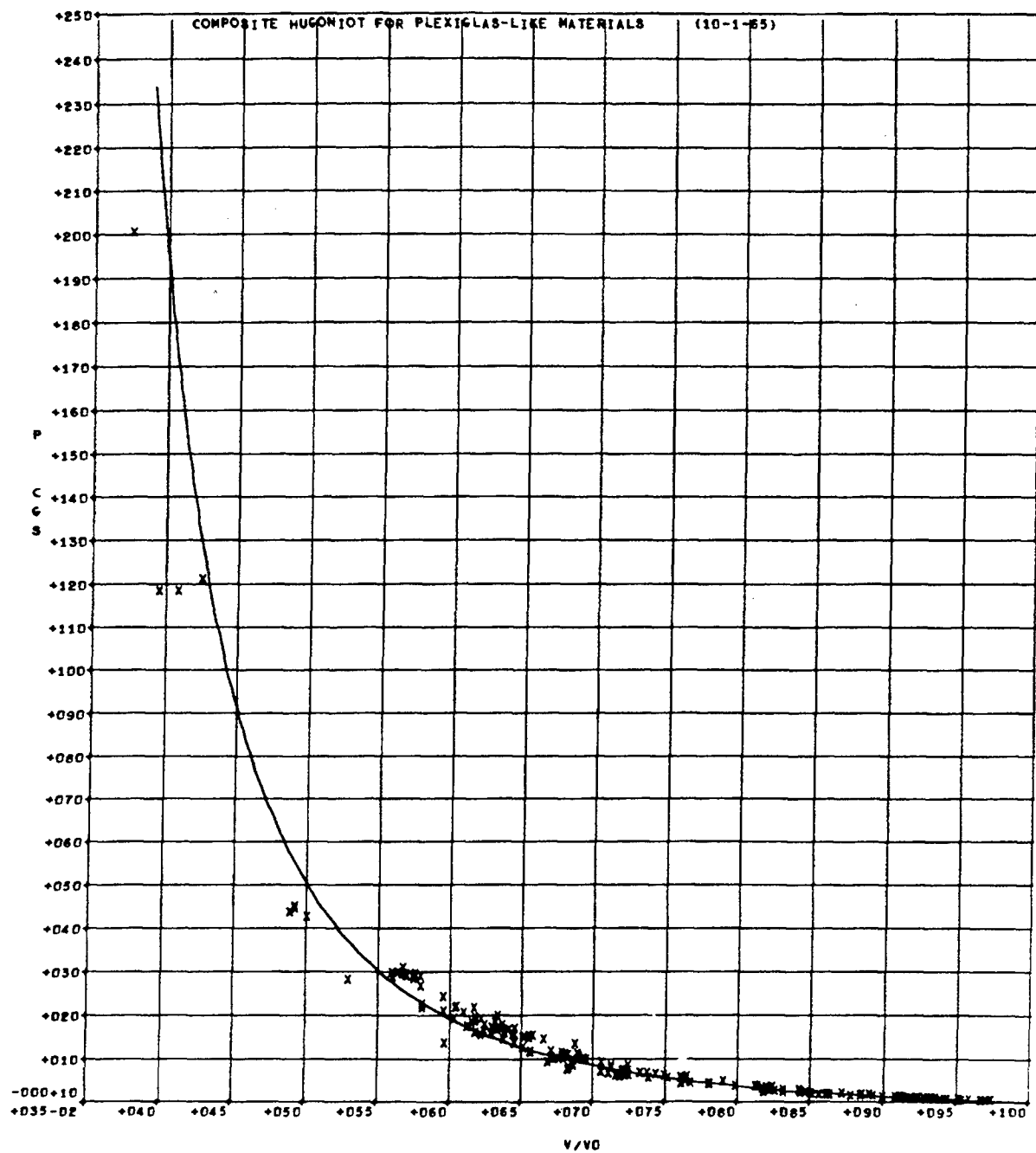


Figure 9

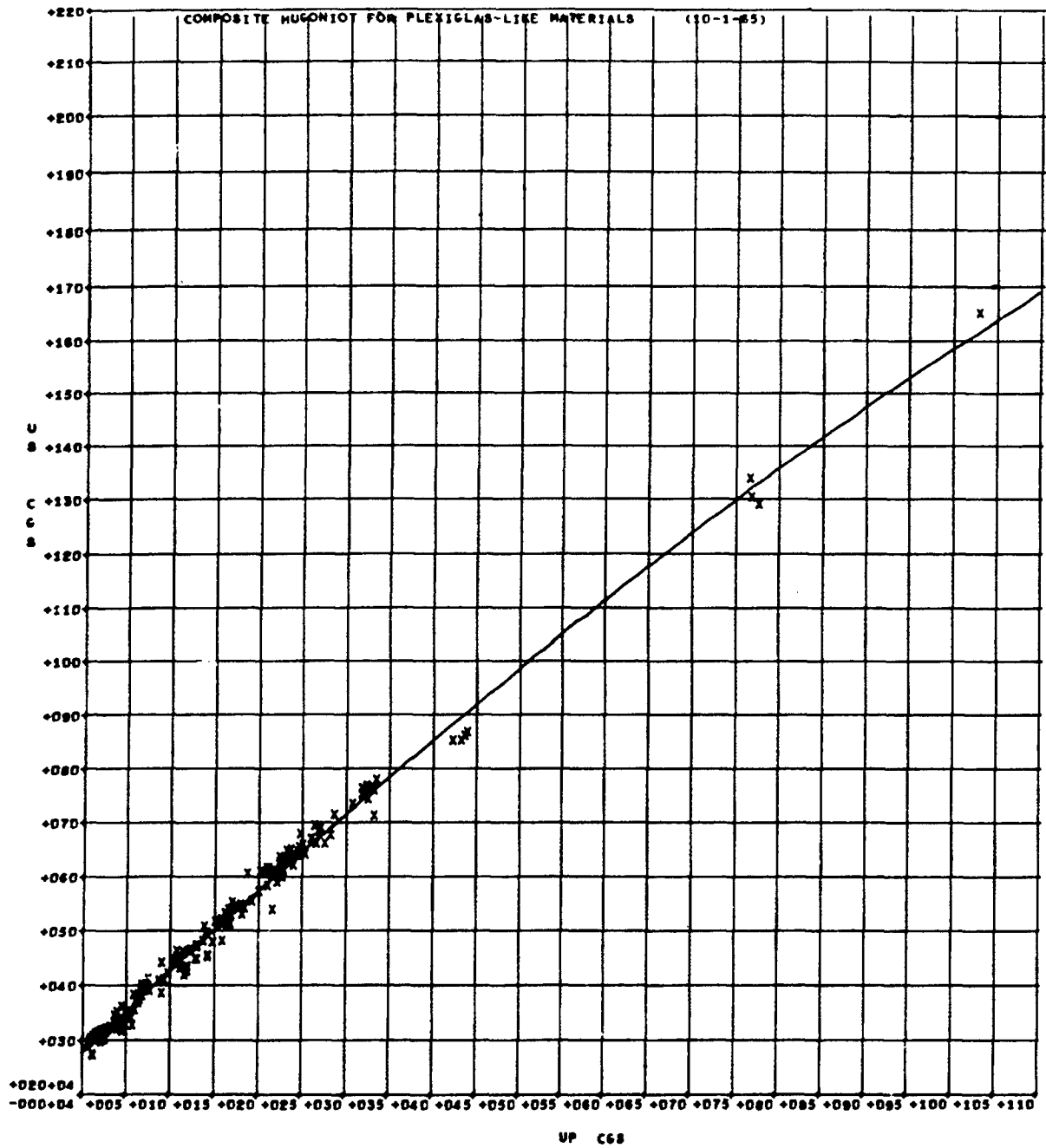


Figure 10

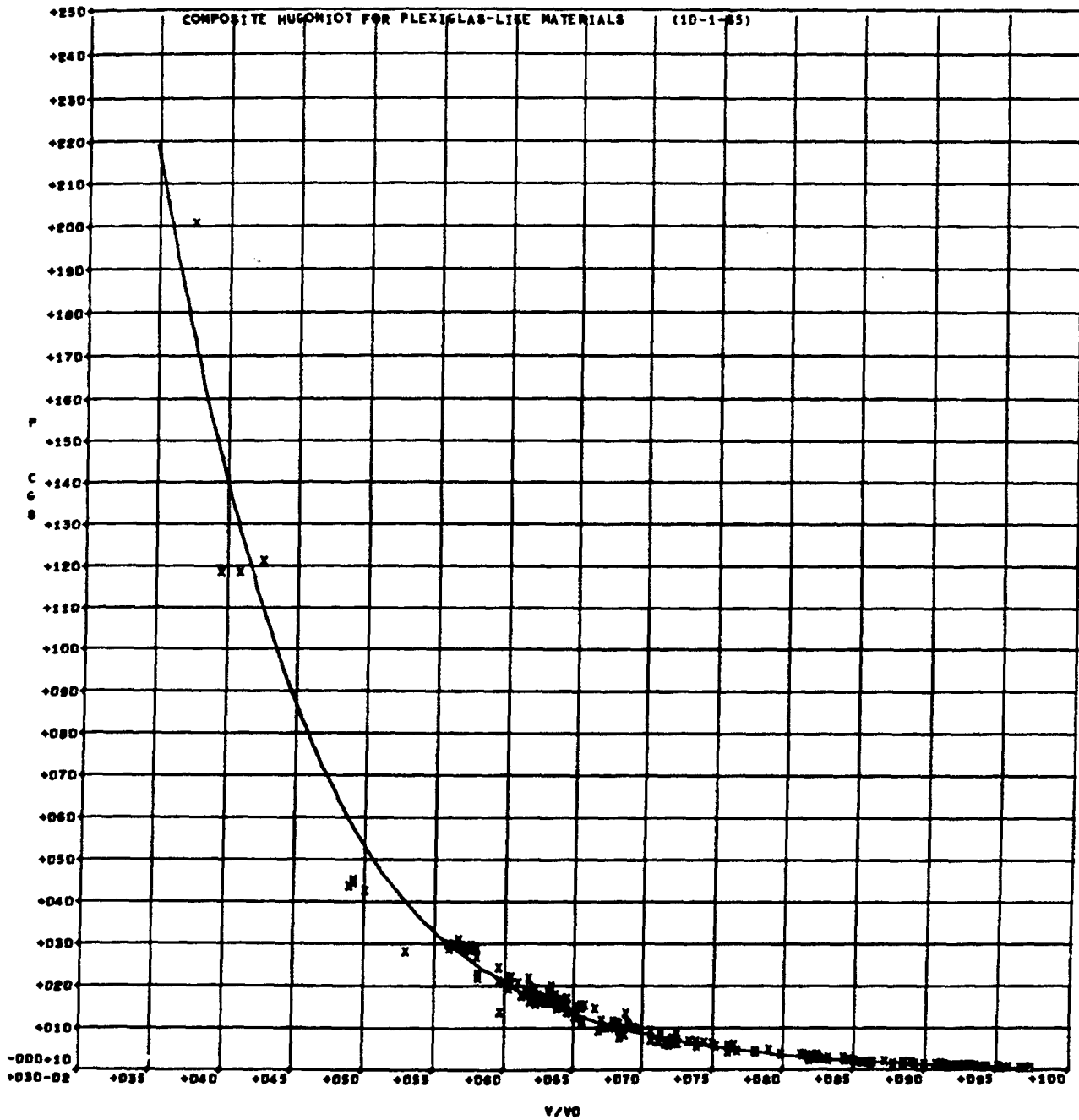


Figure 11

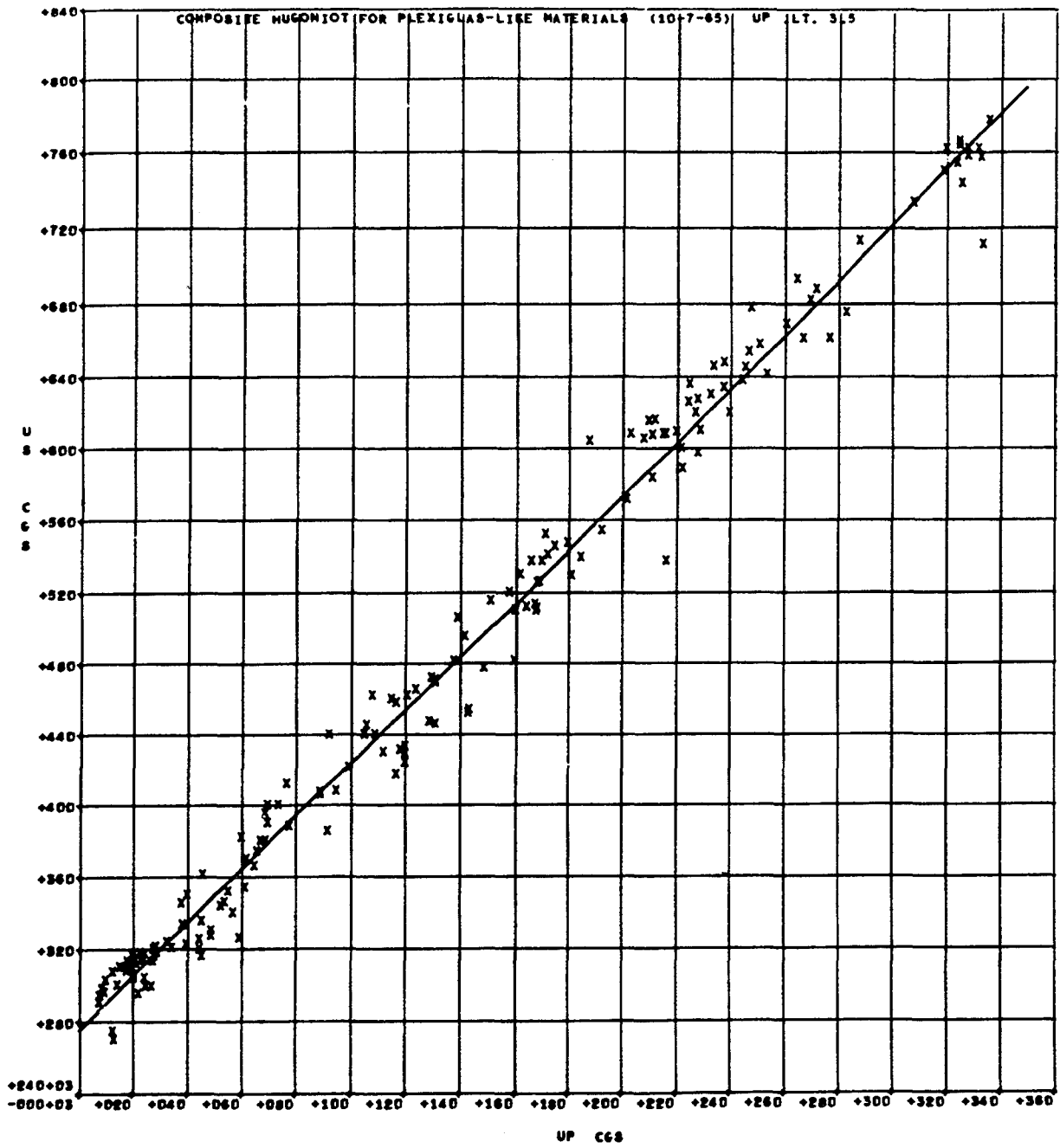


Figure 12

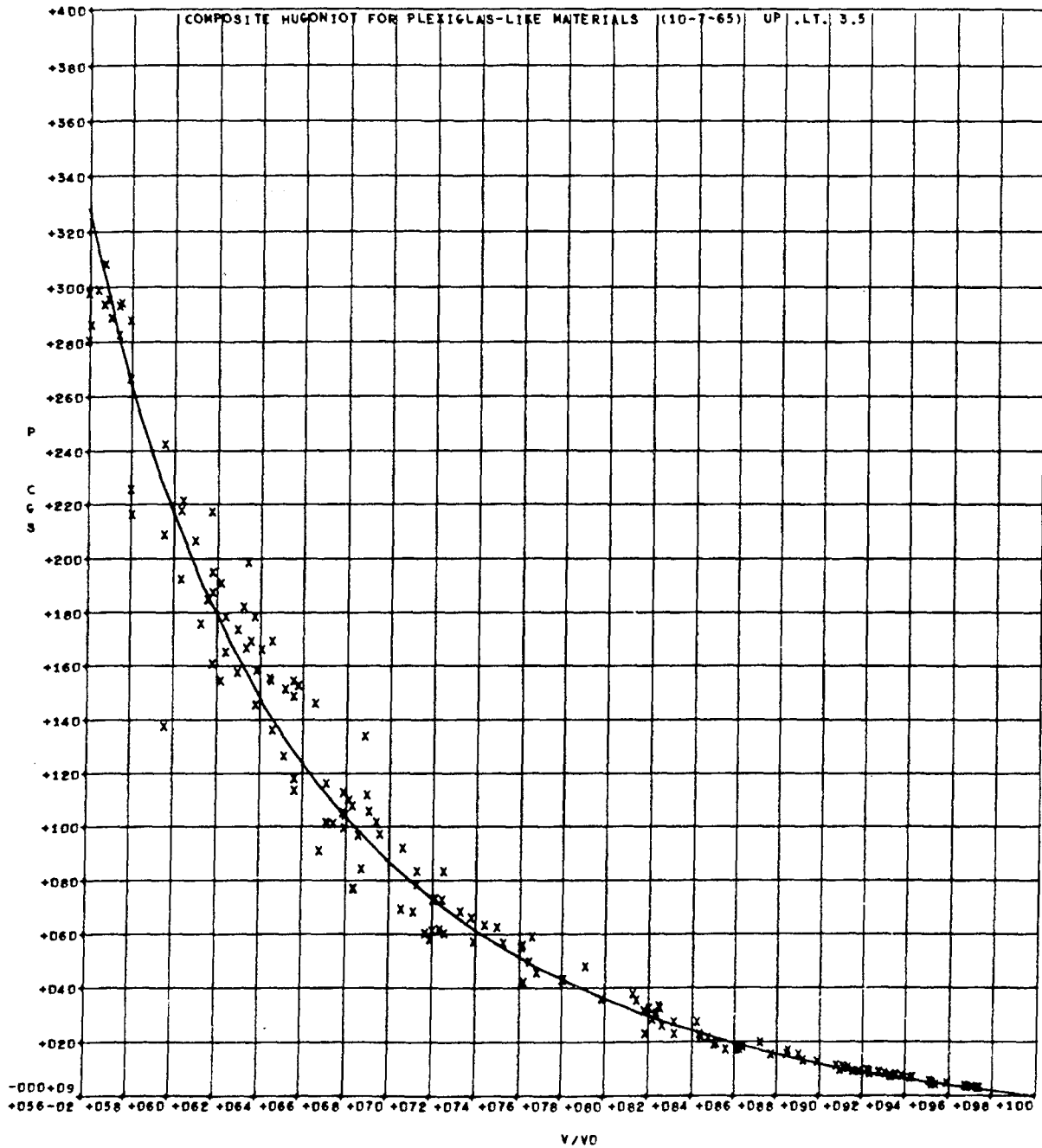


Figure 13

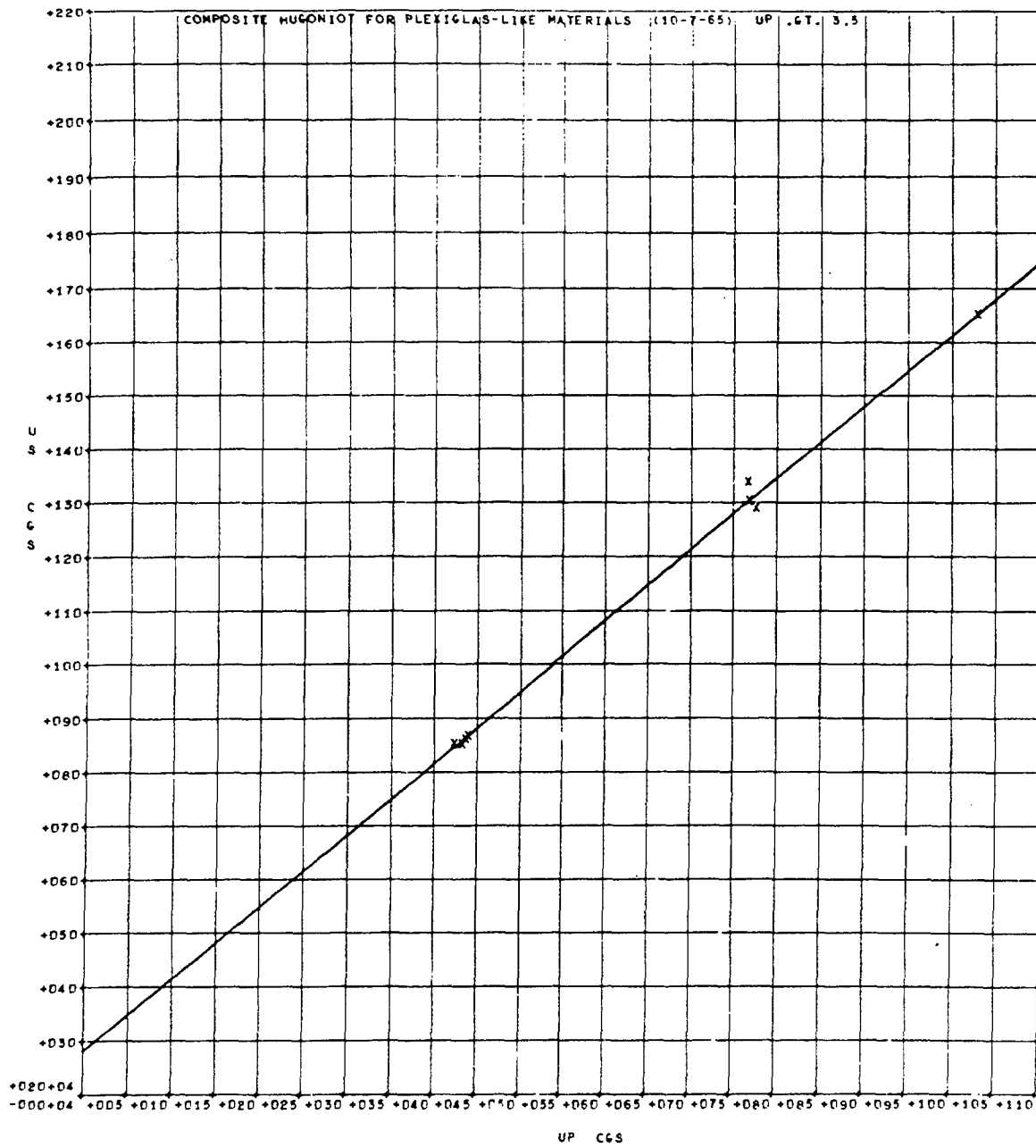


Figure 14

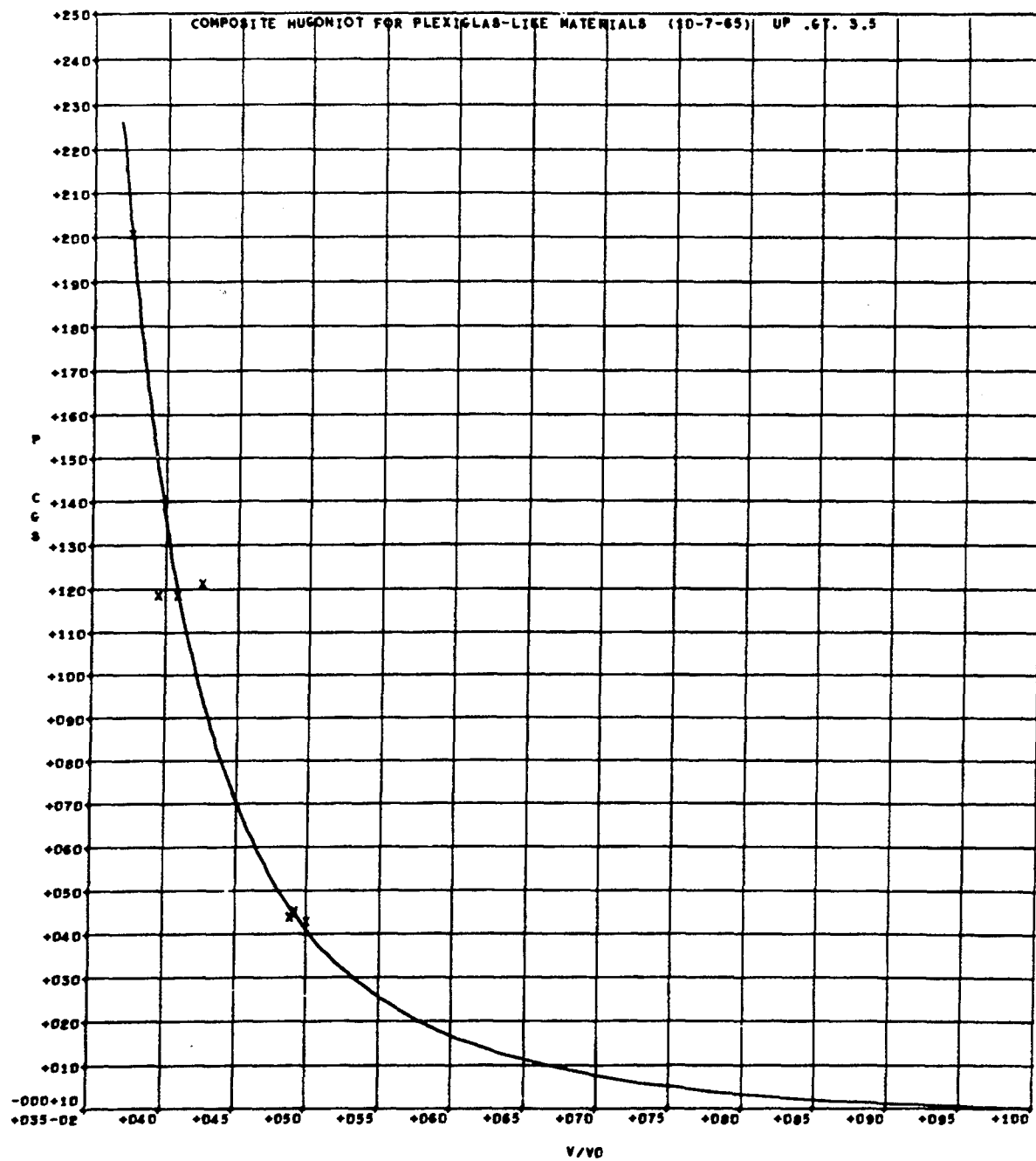


Figure 15

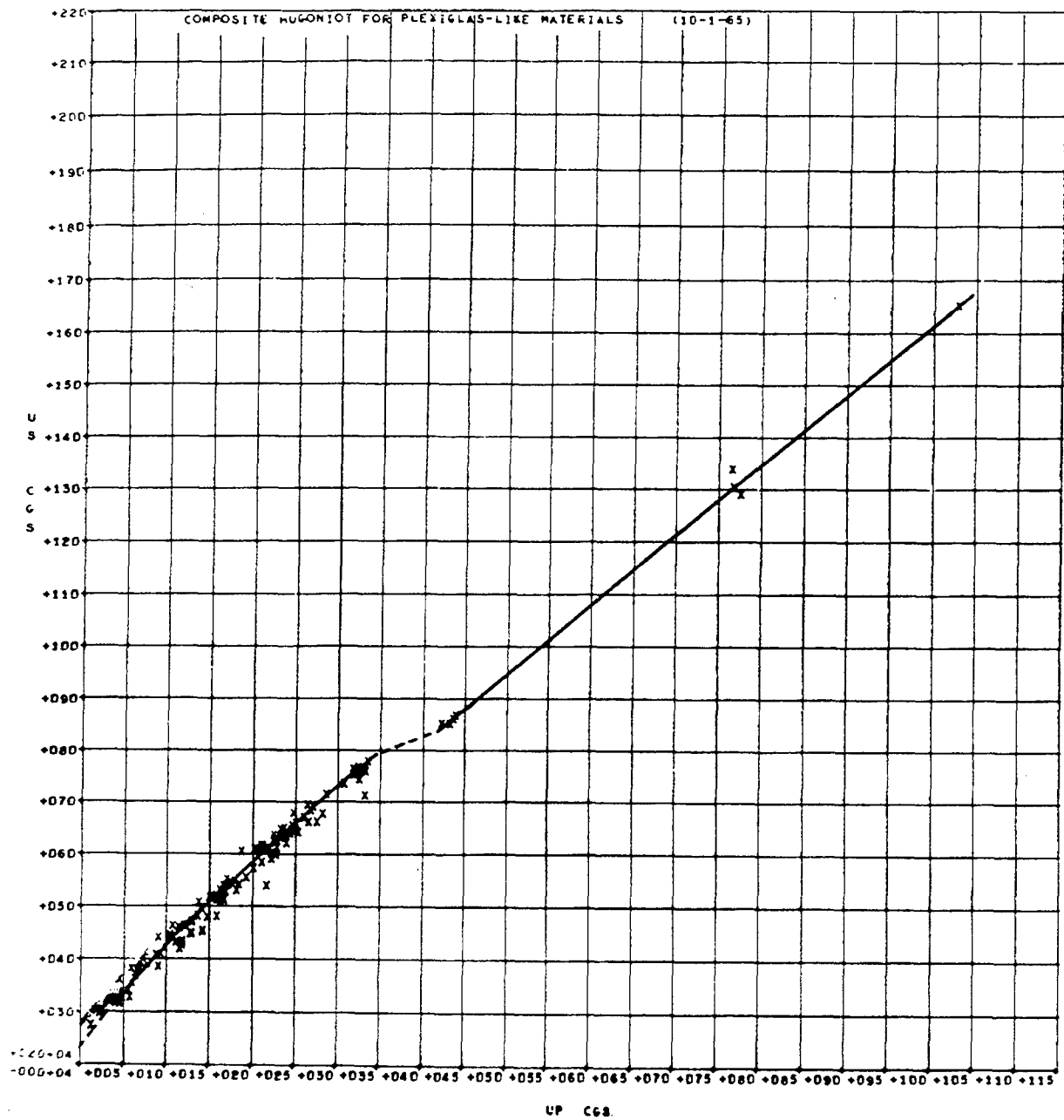


Figure 16

TABLE 2
Polymethyl Methacrylate Data

	U_s (cm/ μ sec)	U_p (cm/ μ sec)
<u>Halpin and Graham [1]</u>		
Plexiglas	0.296	0.0094
	0.300	0.0142
$\rho_o = 1.178 \pm .002$ gm/cm ³	0.304	0.0203
	0.306	0.0203
$U_s = 0.266 + 2.00 U_p$	0.304	0.0246
	0.313	0.0274
U_s are $\pm 1\%$	0.316	0.0280
	0.320	0.0276
U_p are $\pm 1\%$	0.345	0.0377
	0.361	0.0459
	0.344	0.0524
<u>Liddiard [2]</u>		
Cast polymethyl methacrylate - strain free	0.313	0.0200
	0.314	0.0225
$U_s = 0.256 + 1.69 U_p$; $U_p > 0.05$ cm/ μ sec	0.317	0.0245
	0.321	0.0283
$U_s = 0.295 + 0.85 U_p$; $U_p < 0.05$ cm/ μ sec	0.324	0.0325
	0.330	0.0383
$v_\ell = 0.271 \pm 0.003$ cm/ μ sec	0.335	0.0455
	0.346	0.0538
$v_\ell = 0.276 \pm 0.003$ cm/ μ sec	0.366	0.0650
	0.388	0.0780
U_s are $\pm 0.4\%$	0.406	0.0890
	0.421	0.0990
U_p are $\pm 1\%$	0.440	0.1088
	0.462	0.1210
	0.495	0.1420
<u>Schmidt and Evans [3]</u>		
Cast Plexiglas	0.2900	0.0073
	0.2940	0.0077
$\rho_o = 1.18$ gm/cm ³	0.2980	0.0086
	0.3025	0.0098
$v_\ell = 0.277$ cm/ μ sec	0.3070	0.0125
	0.3101	0.0150
U_s are $\pm 1\%$	0.3130	0.0176
	0.3157	0.0202
U_p are $\pm 5\%$	0.3183	0.0228
	0.3080	0.0176
	0.3097	0.0189
	0.3121	0.0215
	0.3143	0.0240
	0.3177	0.0291
	0.3204	0.0343
	0.3228	0.0394
	0.3250	0.0446
	0.3270	0.0488

(Table continues)

TABLE 2
Polymethyl Methacrylate Data (Continued)

	U_s (cm/ μ sec)	U_p (cm/ μ sec)
<u>Hauver [4] and Hauver and Melani [5]</u>		
Plexiglas II, UVA	0.407	0.089
	0.458	0.117
$\rho_o = 1.18 \text{ gm/cm}^3$	0.460	0.115
	0.545	0.175
$U_s = 0.268 + 1.61 U_p; U_p < 0.262$	0.547	0.180
	0.552	0.171
$U_s = 0.351 + 1.25 U_p; U_p > 0.262$	0.605	0.208
	0.607	0.211
	0.608	0.203
	0.608	0.216
	0.609	0.220
	0.615	0.210
	0.616	0.212
	0.646	0.234
	0.648	0.238
	0.678	0.248
	0.693	0.265
	0.688	0.272
	0.713	0.288
	0.733	0.308
	0.750	0.319
	0.754	0.324
	0.758	0.328
	0.757	0.333
	0.762	0.328
	0.762	0.332
	0.764	0.325
	0.766	0.325
	0.777	0.336
<u>Hearst and Geesaman [6]</u>		
Lucite	0.382	0.060
<u>Davenport [7]</u>		
Lucite	0.610	0.229
	0.525	0.168
	0.447	0.129
Plexiglas (in translation)	0.600	0.222
	0.513	0.167
	0.446	0.131
	0.424	0.120
<u>Keller and Penning [8]</u>		
$U_s = 0.270 + 1.76 U_p$ from 1 - 20 kb		

(Table continues)

TABLE 2
Polymethyl Methacrylate Data (Continued)

	U_s (cm/ μ sec)	U_p (cm/ μ sec)
<u>AIP Handbook [9]</u>		
Lucite	0.236	- 0 -
$v_\ell = 0.2680$ cm/ μ sec		
$v_s = 0.1100$ cm/ μ sec		
<u>Wagner, Waldorf, and Louie [10]</u>		
Plexiglas	0.316	0.0454
$\rho_o = 1.18$ gm/cm ³	0.326	0.0590
	0.385	0.0916
	0.417	0.117
	0.452	0.143
	0.597	0.228
<u>Skidmore and Morris [11]</u>		
Perspex	0.711	0.334
$\rho_o = 1.18$ gm/cm ³	0.762	0.320
$U_s = 0.307 + 1.295 U_p$	0.743	0.326
	0.850	0.424
	0.850	0.434
	0.861	0.437
	0.867	0.440
	1.288	0.778
	1.303	0.770
	1.337	0.768
<u>Al'tshuler and Petrunin [12]</u>		
Plexiglas (in translation)	0.638	0.245
$\rho_o = 1.18$ gm/cm ³		
<u>Coleburn [13]</u>		
Plexiglas	0.470	0.131
$\rho_o = 1.18$ gm/cm ³	0.481	0.138
$v_\ell = 0.271$	0.477	0.149
	0.515	0.151
	0.520	0.158
	0.530	0.162
	0.537	0.170
	0.539	0.185
	0.554	0.193
	0.571	0.202
	0.583	0.211
	0.627	0.228
	0.630	0.233
	0.634	0.238
	0.641	0.254
	0.645	0.246

(Table continues)

TABLE 2
Polymethyl Methacrylate Data (Continued)

	U_s (cm/ μ sec)	U_p (cm/ μ sec)
<u>Coleburn [13] (Cont.)</u>		
	0.654	0.247
	0.658	0.251
	0.661	0.267
	0.661	0.277
	0.669	0.261
	0.675	0.283
<u>Jaffe, Beauregard, and Amster [14]</u>		
Lucite	0.2701	0.0128
	0.2744	0.0125
	0.2952	0.0224
	0.2990	0.0250
<u>Cook, Keyes, and Ursenbach [15]</u>		
Lucite	0.330	0.049
	0.340	0.057
	0.352	0.055
	0.370	0.062
	0.374	0.066
	0.380	0.067
	0.380	0.069
	0.395	0.069
	0.400	0.070
	0.400	0.074
	0.440	0.092
	0.462	0.108
	0.537	0.166
	0.604	0.188
	0.620	0.227
	0.636	0.225
<u>Zel'dovich, Kormer, Sinitsyn, and Kuriapin [16]</u>		
Polymethyl methacrylate		
$\rho_o = 1.18 \text{ gm/cm}^3$	1.65	1.03
<u>Buchanan, James, and Teague [17]</u>		
Perspex	0.390	0.0700
	0.408	0.0945
	0.430	0.1120
	0.454	0.1435
	0.481	0.1595
	0.512	0.1640
	0.529	0.1815
	0.537	0.2165

(Table continues)

TABLE 2
Polymethyl Methacrylate Data (Continued)

	u_s (cm/ μ sec)	u_p (cm/ μ sec)
<u>Dapoigny, Kieffer, and Vodar [18]</u>		
Polymethyl methacrylate (1957)	0.299 0.350 0.412 0.445 0.465 <u>0.510</u>	0.027 0.040 0.077 0.106 0.124 <u>0.160</u>
(1958)	0.320 0.354 0.440 0.506	0.0444 0.0614 0.105 0.139
<u>Lawton and Skidmore [19]</u>		
Perspex	0.62	0.24
<u>Walsh, Yarger, and McQueen [20]</u>		
Plexiglas	0.5884 0.5110 0.5102 0.4312 0.4290 0.4336	0.2223 0.1682 0.1674 0.1181 0.1200 0.1198
Lucite	0.6257 0.6078 0.5409 0.5263 0.4705 0.4695 0.4719	0.2244 0.2153 0.1722 0.1689 0.131 0.131 0.1299
$\rho_o = 1.180$ gm/cm ³		
$\rho_o = 1.180$ gm/cm ³		
<u>Hughes, Blankenship, and Mims [21]</u>		
Lucite	0.2152	- 0 -
$\rho_o = 1.171$ gm/cm ³		
T = 33°C		
$v_\ell = 0.2621$ cm/ μ sec		
$v_s = 0.1296$ cm/ μ sec		
T = 48°C, $v_\ell = 0.2538$ cm/ μ sec		
T = 71°C, $v_\ell = 0.2468$ cm/ μ sec		
<u>Bridgman [22]</u>		
"Leucite"	0.228	- 0 -

(Table continues)

TABLE 2
Polymethyl Methacrylate Data (Continued)

	U_s (cm/ μ sec)	U_p (cm/ μ sec)
<u>Deal and Marsh [23]</u>		
1/2" Plexiglas Sheet	$0.682 \pm .002$	$0.270 \pm .001$
$\rho_o = 1.181 \pm .001$ gm/cm ³		
Plexiglas Type G Unshrunk Sheet	$0.2188 \pm .0005$	- 0 -
$\rho_o = 1.187 \pm .001$ gm/cm ³ , $T = 23 \pm 1^\circ\text{C}$		
$V_\ell = 0.2718 \pm .0004$ cm/ μ sec		
$V_s = 0.1396 \pm .0003$ cm/ μ sec		
Plexiglas Type II, UVT, sheet	$0.2186 \pm .0005$	- 0 -
$\rho_o = 1.185 \pm .001$ gm/cm ³ , $T = 23 \pm 1^\circ\text{C}$		
$V_\ell = 0.2715 \pm .0004$ cm/ μ sec		
$V_s = 0.1395 \pm .0003$ cm/ μ sec		
Evr-kleer	$0.2172 \pm .0005$	- 0 -
$\rho_o = 1.184 \pm .001$ gm/cm ³ , $T = 23 \pm 1^\circ\text{C}$		
$V_\ell = 0.2691 \pm .0004$ cm/ μ sec		
$V_s = 0.1376 \pm .0003$ cm/ μ sec		
<u>Ramsay [24]</u>		
Evr-kleer	0.2206	- 0 -
$V_\ell = 0.2713$ cm/ μ sec		
$V_s = 0.1367$ cm/ μ sec		
"Old" Evr-kleer	0.2163	- 0 -
$V_\ell = 0.2706$ cm/ μ sec		
$V_s = 0.1407$ cm/ μ sec		

REFERENCES FOR TABLE 2

1. W. J. Halpin and R. A. Graham, Paper B-38, Fourth Symposium on Detonation, Naval Ordnance Laboratory (Oct. 12-15, 1965).
2. T. P. Liddiard, Jr., Paper B-47, Fourth Symposium on Detonation, Naval Ordnance Laboratory (Oct. 12-15, 1965).
3. D. N. Schmidt and M. W. Evans, Nature 206, 1348 (1965).
4. G. E. Hauver, J. A. P. 36, 2113 (1965).

5. G. E. Hauver and A. Melani, BRL Report 1259 (1964).
6. J. R. Hearst and L. B. Geesaman, UCRL Report 7877 (1964).
7. D. A. Davenport of SRI quoted in S. L. Whitcher, Boeing Report D2-90472 (1964), p. 122.
8. D. V. Keller and J. Penning of Boeing quoted in S. L. Whitcher, Boeing Report D2-90472 (1964), p. 125.
9. AIP Handbook, 2nd ed., edited by D. E. Gray, (McGraw Hill, New York, 1963), p. 3-88.
10. M. H. Wagner, W. F. Waldorf, Jr., and N. A. Louie, SWC Report TDR-62-66, Vol. I (1962).
11. I. C. Skidmore and E. Morris, Thermodynamics of Nuclear Materials, IAEA (Vienna, 1962), p. 173.
12. L. V. Al'tshuler and A. P. Petrunin, Soviet Physics-Tech. Phys. 6, 516 (1961).
13. N. L. Coleburn, NAVWEPS Report 6026 (1960).
14. I. Jaffe, R. Beauregard, and A. Amster, Third Symposium on Detonation (Princeton, New Jersey, Sept. 26-28, 1960) Report ACR-52, Vol. 2, p. 584.
15. M. A. Cook, R. T. Keyes, and W. O. Ursenbach, Third Symposium on Detonation (Princeton, New Jersey, Sept. 26-28, 1960) Report ACR-52, Vol. 2, p. 357.
16. Ia. B. Zel'dovich, S. B. Kormer, M. V. Sinitsyn, and A. I. Kuriapin, Soviet Physics-Doklady 3, 938 (1958).
17. J. S. Buchanan, H. J. James, and G. W. Teague, Phil. Mag. 3, 1432 (1958).
18. J. Dapoigny, J. Kieffer, and B. Vodar, Comptes Rendus, Paris, 245, 1502 (1957) and 247, 269 (1958).
19. H. Lawton and I. C. Skidmore, Disc. Faraday Soc. 22, 188 (1956).
20. J. M. Walsh, F. L. Yarger, and R. G. McQueen, Los Alamos Internal Reports (1954 and 1955).
21. D. S. Hughes, E. B. Blankenship, and R. L. Mims, J. A. P. 21, 294 (1950).
22. P. W. Bridgman, Proc. Am. Acad. Arts Sci. 76, 71 (1948).
23. W. E. Deal and S. P. Marsh, New Data.
24. J. Ramsay, Private Communication.

COMMENTS

J. B. RAMSAY (Los Alamos Scientific Laboratory, Los Alamos, New Mexico): Dr. Deal has derived the relationship between the "zero pressure limit" of the Hugoniot curve and the bulk sound speed. In line with the comments on the possible nonlinear relationship between shock velocity and particle velocity observed for solid explosives, I would like to report on an observation in another area, which is not generally recognized, where the use of the linear

relationship coupled with an intercept value equal to the bulk sound velocity does not apply. Of 19 liquids for which shock wave measurements are available, only mercury and water show a "zero strength" shock velocity which is in reasonable agreement with the liquid sound velocity.

For some liquids only two or three experimental points are available; for some others,

such as C_6H_6 , CCl_4 , CH_3NO_2 , liquid TNT, and liquid argon, several points have been measured. In general (with the exception of water), linear functions represent the data within the experimental error, but the intercept values of 17 liquids lie between 0.2 and 0.85 mm/ μ sec

above the respective bulk sound velocity. This comment is not made to question the idea that a Hugoniot curve should have an intercept at zero particle velocity equal to the bulk sound speed, but is made only to show that great caution must be exercised in the use of the linear relationship.

INITIATION, IGNITION, AND GROWTH OF REACTION

Chairmen: B. Lewis
Combustion and Explosives Research, Inc.
Pittsburgh, Pennsylvania

E. G. Whitbread
Explosive Research and Development Establishment
Waltham Abbey, England

THE EFFECT OF INTERSTITIAL GAS ON THE SHOCK SENSITIVITY OF LOW DENSITY EXPLOSIVE COMPACTS

Michael C. Chick
*Atomic Weapons Research Establishment
Aldermaston, Berkshire, England*

ABSTRACT

A small scale gap test has been used to investigate the role played by the interstitial gas in the shock initiation of granular charges.

Compacts of coarse granular HMX at 1.14 g/cm^3 have been gap tested with the interstices filled with the following gases: Air, N_2 , Ar, He, H_2 , CO_2 , CH_4 , C_2H_4 , CHClF_2 , and C_3H_8 , up to pressures of 1,000 psi.

The shock sensitivity of the compacts decreased as the pressure increased but the extent of the effect varied markedly with the gas used. The effect with the methane and propane was so large that compacts filled with these gases at 1 atmosphere were detectably less sensitive than those filled with air at the same pressure.

A similar but less marked effect was observed with granular PETN at 0.9 g/cm^3 and fine HMX at 1.14 g/cm^3 both with N_2 and CH_4 as the interstitial gases.

The initial results are also reported of measurements of detonation build-up characteristics in coarse HMX compacts at 1.14 g/cm^3 in which the interstices were filled with methane.

The processes leading to the observed results are discussed and attempts made to relate their magnitude to the physical properties of the interstitial gas.

INTRODUCTION

Explosive charges of compacted powders are generally observed to be more shock sensitive than either cast charges or homogeneous explosives (liquids and single crystals) [1,3]. Also the shock sensitivities of both cast and homogeneous explosives may be enhanced by the introduction of voids [3,13]. Many mechanisms have been postulated to explain the function of voids in the shock initiation process [1,3,8] but there is little published experimental evidence to support any of these theories.

Experiments to investigate the role of the interstitial gas in granular charges during shock initiation and steady state detonation have been reported [1,2,5,6,7,9,10]. Different interstitial gases have been examined over a range of pressures but the only reported positive

effect was on the low order velocity of detonation [5,6,7].

This paper gives preliminary results from a programme whose object is to gain information on the role of the interstitial gas in the shock initiation of granular explosives with a view to identifying the processes occurring.

Some preliminary results in this programme were reported during discussion at the International Conference on Sensitivity and Hazards of Explosive held in London on 1st-3rd October, 1963 [16].

To date experiments have been confined to the measurement of the gap sensitivity and detonation build-up characteristics of low density crystalline explosive compacts. The interstices of these compacts were filled with a variety of gases at pressures up to 1,000 psi.

EXPERIMENTAL PROCEDURE

The Pressure Vessel

The pressure vessel in which the experiments were performed is shown in Fig. 1. An expendable steel liner was placed around the gap test assembly to absorb shock energy and fragments from the detonating charge, thus protecting the pressure vessel and this was found to be an important feature of the design. Additionally a bursting diaphragm was incorporated into the vessel to limit the amplitude and duration of the pressure pulse. The two conductors for the electric detonator were led into the vessel via replaceable polyethylene cone seals.

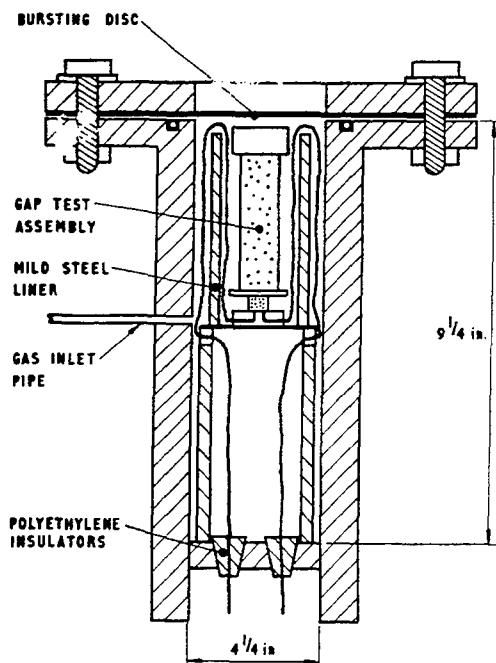


Fig. 1 - High pressure vessel with gap test assembly

The Preparation of Explosive Compacts

Compacts were prepared in brass telescope tubing 3.0 inches long, 0.74-inch O.D., and 0.719-inch I.D. One end of the tube was closed with a square brass shim 1.0 x 1.0 x 0.006 inch using a minimum of solder. Four symmetrically placed 0.020 inch diameter holes were drilled 0.0625 inch from the base of the tube to ensure that the gas entered close to the shim.

Both coarse HMX and PETN charges were prepared at their maximum bulk density by tapping the containers in a defined manner as the powders were being introduced. The coarse HMX had a surface area of 180 cm²/g with an average particle diameter of 176 microns and gave compacts with a density of 1.14 g/cm³ (40% voids). The coarse PETN had a surface area of 450 cm²/g with an average particle diameter of 75 microns and gave compacts with a density of 0.90 g/cm³ (49% voids).

Fine HMX was prepared by milling the coarse material to give a surface area of 3420 cm²/g with an average particle diameter of 8.8 microns. This was consolidated into charges of the same density as those of the coarse HMX by pressing successive 1 g increments of explosive each under a pressure of 50 psi.

Shock Sensitivity Measurements

The shock sensitivities of the compacts were measured by a gap test (1) similar to that described by Cachia and Whitbread, the experimental arrangement being shown in Fig. 2.

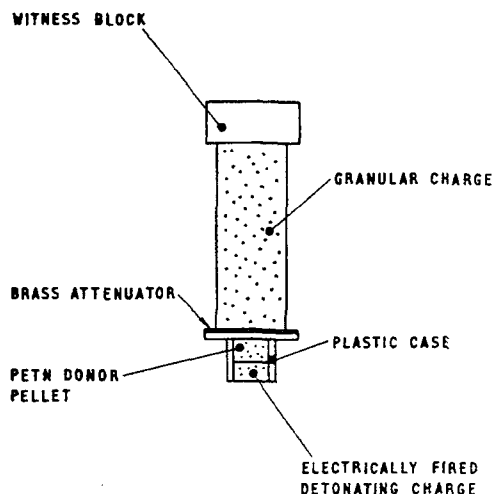


Fig. 2 - Gap test assembly

The immediate donor charge consisted of a cylindrical pellet of PETN (diam. 0.23 inch, weight 0.25 g, density 1.68 g/cm³), in a plastic case 0.435 inch O.D., the end surface of the extreme pellet being separated from the metal septum only by a disc of paper 0.006 inch thick. The donor charge was fired electrically. The

attenuating gap consisted of a stack of 0.002 inch brass shims added to the 0.006 inch closure shim of the container. A witness block was placed at the top end of the receptor charge and detonation was indicated by the characteristic impression formed on it. For each test 20 charges were fired using the Bruceton staircase procedure to determine the shim thickness required to produce detonations in 50% of the trials. Shim increments of 0.004 inch were used and the result was quoted as the critical shim thickness in thousandths of an inch.

The assembled charge was placed in the pressure vessel which was flushed with the gas being used and then sealed. The vessel was then pressurised to the required pressure, left for five minutes, exhausted, and repressurised. Pressures were measured with a calibrated Bourdon gauge accurate to 5 psi, at 1,000 psi. For experiments with gases at 1 atmosphere pressure the system was pressurised to 100 psi, left for five minutes, exhausted, pressurised, and finally depressurised to 1 atmosphere pressure.

The gases used were all obtained from commercial sources. The argon, helium, hydrogen, nitrogen and carbon dioxide were specified to be better than 99% pure; the ethylene was 98% pure (main impurity nitrogen); the methane was 94-97% pure (main impurity carbon dioxide); the propane was 90% pure (main impurities similar hydrocarbons); the monochloro-difluoromethane was 90% pure (main impurities other halogenated hydrocarbons).

Detonation Build-up Measurements

The experimental assembly is shown in Fig. 3. The brass container was similar to that used for shock sensitivity testing except that it was 4.0 inches long. The probes consisted of 31 SWG enamelled copper wire sheathed in 0.028 inch O.D. stainless steel hypodermic tubing [12]. These probes were inserted across the charge container at about 1 cm intervals, their precise positions were defined by measurement after assembly. On reaching each probe the detonation front shorted the probe wire to its sheath, this connection being recorded by means of a high speed oscillograph. The time of the emergence of the shock from the attenuator was calculated from the record produced by a flat probe placed under the donor detonator. The shock velocity through the attenuator under these conditions was deduced from previous observations [4]. A gas-tight seal through which the probe connections were led from the vessel

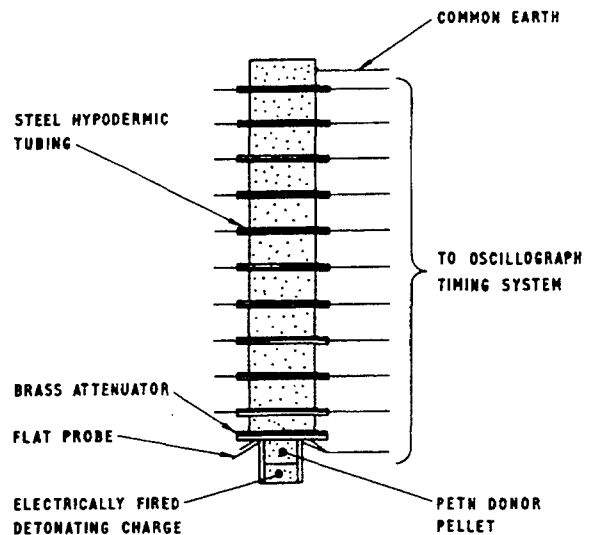


Fig. 3 - Build-up measurement assembly

was produced by squeezing the conductors between the 'O' ring sealing the lid of the vessel and a flat rubber ring placed over it.

The rounds used to study the build-up to detonation were filled by the same method as were used for the gap sensitivity experiments and to the same density of 1.14 g/cm^3 . Rounds were fired with methane at 15 and 500 psi with gaps of 0.006 inch (the thinnest possible) and with shim thicknesses of 90% of the critical thickness.

RESULTS

Gap Sensitivity Measurements

The results are summarised in Tables 1, 2 and 3 and the relationships between 50% gap thickness and interstitial gas pressure are plotted in Figs. 4, 5 and 6.

Detonation Build-up Measurements

The results from these experiments are given in Tables 4 and 5 and the space/time relationships plotted are in Fig. 7. The steady state velocity of detonation with its standard deviation was calculated by the method of least squares. The distance/time points during build-up to stable detonation were neglected and the best line computed through the remaining points. The delay time was determined by solving the equation of the line for zero distance.

TABLE 1
The Effect of Interstitial Gas Pressure on
the Shock Sensitivity of Coarse HMX (S.A.
180 cm²/g) at 1.14 g/cm³

Gas	Pressure (psi)	Shock Sensitivity	
		50% Gap Value (in. $\times 10^{-3}$)	95% Con. Lts. (in. $\times 10^{-3}$)
Ar	500	195.1	5.9
Ar	1000	121.8	6.2
He	1000	138.7	5.2
AIR	15	231.7	4.2
N ₂	15	231.2	3.7
N ₂	250	210.2	8.1
N ₂	500	196.5	2.7
N ₂	750	169.5	9.0
N ₂	1000	134.0	4.4
H ₂	500	206.7	4.2
H ₂	1000	155.2	4.2
CO ₂	250	137.0	8.7
CO ₂	500	51.2	4.2
CH ₄	15	219.3	3.3
CH ₄	250	134.9	4.0
CH ₄	500	72.5	2.7
CH ₄	600	52.4	2.8
CHClF ₂	100	187.3	8.0
C ₂ H ₄	500	48.7	2.3
C ₃ H ₈	15	214.0	4.5
C ₃ H ₈	100	124.0	4.4

DISCUSSION

The results reported in this paper form only a part of the planned experimental programme thus their interpretation is incomplete and provisional.

In view of past failures to observe changes in the shock sensitivity of explosive compacts with changes of interstitial gas and its pressure reported in the literature [1,2], care has been taken to ensure that the substantial effect observed was real. Tests were carried out to ensure that the donor shock pulse was unaffected by the nature or pressure of the gas. Firstly the donor charges were fired under a variety of conditions in contact with a steel block and the

TABLE 2
The Effect of Interstitial Gas Pressure on
the Shock Sensitivity of Coarse PETN (S.A.
450 cm²/g) at 0.90 g/cm³

Gas	Pressure (psi)	Shock Sensitivity	
		50% Gap Value (in. $\times 10^{-3}$)	95% Con. Lts. (in. $\times 10^{-3}$)
CH ₄	15	249.0	6.4
CH ₄	250	207.6	0.9
CH ₄	500	178.4	2.4
N ₂	15	248.3	5.1
N ₂	500	214.7	1.7
N ₂	1000	195.6	0.9

TABLE 3
The Effect of Interstitial Gas Pressure on
the Shock Sensitivity of Fine HMX (S.A.
3420 cm²/g) at 1.14 g/cm³

Gas	Pressure (psi)	Shock Sensitivity	
		50% Gap Value (in. $\times 10^{-3}$)	95% Con. Lts. (in. $\times 10^{-3}$)
CH ₄	15	198.4	4.8
CH ₄	250	165.6	3.0
CH ₄	500	147.2	5.2
N ₂	15	198.0	2.8
N ₂	500	196.0	0.9
N ₂	1000	177.0	5.9

depth of depression formed was measured. The results are given in Table 6 where it can be seen that there was no observable variation. Secondly the shock sensitivity of cast 60/40 RDX/TNT was measured under varying conditions. The results are given in Table 7 and again no significant effect was observed. It was thus concluded, that the observed effects were due to real variations in the shock sensitivities of the receptor charges.

Tables 1, 2 and 3 show that for a given compact at low pressures, all gases gave similar results. In all cases the shock sensitivity decreased as the pressure was raised, and the magnitude of the effect varied with the nature of the gas. In some cases the sensitivity was reduced to values comparable to those of cast explosives.

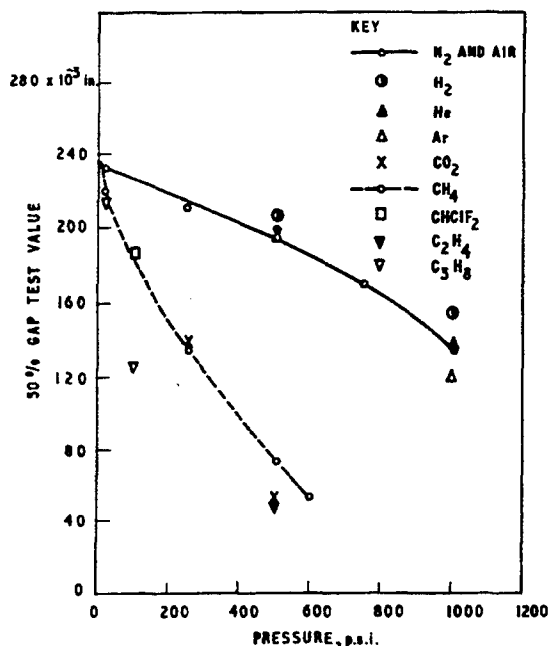


Fig. 4 - Interstitial gas pressure vs 50% gap test value for coarse HMX at 1.14 g/cc

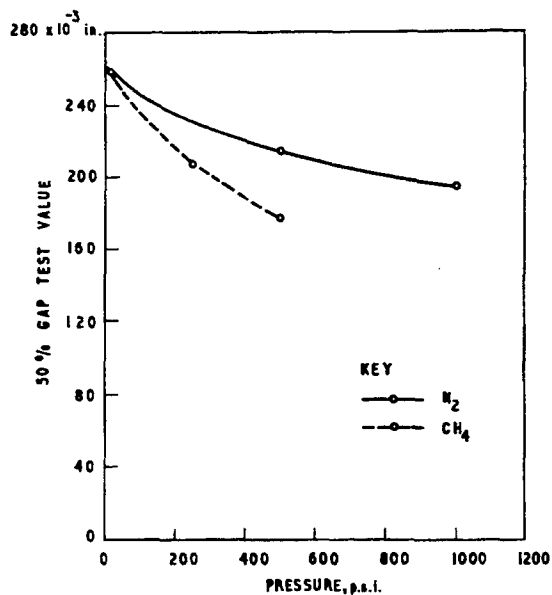


Fig. 5 - Interstitial gas pressure vs 50% gap test value for coarse PETN at 0.90 g/cc

With the coarse HMX, nitrogen was used at pressures from 15 to 1000 psi. For this gas the slope of the curve relating shock sensitivity to pressure is low at 15 psi. Thus extrapolation to zero pressure gives a value not significantly

different from that at 15 psi. With the gases with greater desensitising power such as methane and propane, the values at 15 psi are significantly lower than those for nitrogen at that pressure. However, extrapolating the curves for these gases to vacuum gives the same shock sensitivity as the extrapolated nitrogen value. There is thus strong indication that the shock sensitivity for such compacts is greatest with no gas in the interstices and decreases as the gas pressure increases, the degree of desensitisation being dependent on the gas. The high shock sensitivity of low density explosive compacts thus appears to be due to their geometrical features, the gas in the interstices merely reducing the effect. The compact is sensitive in spite of the gas and not because of it.

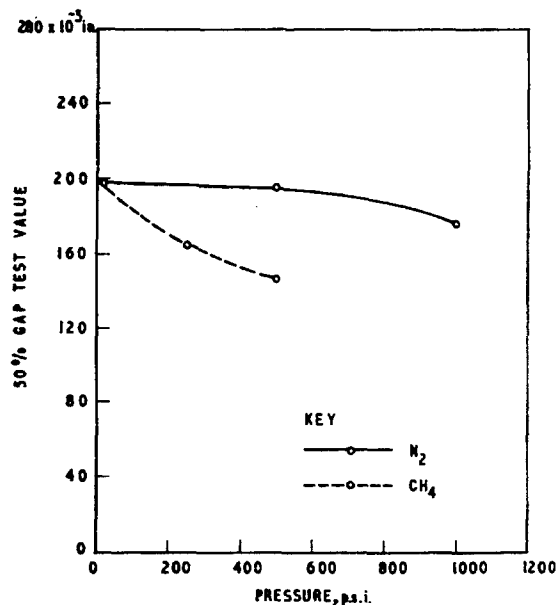


Fig. 6 - Interstitial gas pressure vs 50% gap test value for fine HMX at 1.14 g/cc

Where the interstices are filled with a reactive gas such as oxygen it is possible that reaction with the gas may sensitise the compact. An attempt was made to investigate this point by using oxygen at 1000 psi, but unfortunately the stainless steel pressure vessel was destroyed by the gas. Further attempts will, however, be made to do firings in high pressure oxygen.

The gases were chosen to cover a wide range of physical properties i.e., density, ratio of specific heats, critical temperature, molecular

TABLE 4
Build-Up to Detonation Measurements on Coarse Granular HMX at 1.14 g/cm³ in Methane Gas

Pressure	15 psi CH ₄				500 psi CH ₄			
	0.006 inch		0.197 inch		0.006 inch		0.066 inch	
Attenuator Thickness								
Time for Shock to Traverse Attenuator [4]	0.04 μ sec		1.17 μ sec		0.04 μ sec		0.38 μ sec	
Probe Position	Time from Attenuator Explosive Interface (μ sec)	Distance from Attenuator Explosive Interface (cm)	Time from Attenuator Explosive Interface (μ sec)	Distance from Attenuator Explosive Interface (cm)	Time from Attenuator Explosive Interface (μ sec)	Distance from Attenuator Explosive Interface (cm)	Time from Attenuator Explosive Interface (μ sec)	Distance from Attenuator Explosive Interface (cm)
1	0.96	0.51	26.15	0.49	1.02	0.46	2.76	0.51
2	3.10	1.50	27.87	1.45	3.00	1.44	9.34	1.47
3	4.78	2.53	29.79	2.45	4.74	2.42	13.06	2.45
4	6.44	3.51	31.31	3.44	6.36	3.42	-	3.44
5	8.04	4.50	33.17	4.42	7.96	4.41	16.32	4.42
6	9.60	5.51	34.85	5.40	-	5.40	17.92	5.40
7	11.24	6.54	36.43	6.40	11.06	6.37	19.44	6.38
8	12.74	7.55	38.01	7.39	12.68	7.37	-	7.38
9	14.38	8.50	39.61	8.37	14.24	8.36	22.60	8.37
10	15.98	9.49	41.21	9.36	15.80	9.35	24.22	9.36

- indicates that no event was recorded.

TABLE 5
Stable Detonation Velocities and Delay Times
for Coarse Granular HMX at 1.14 g/cm³
in Methane Gas

Round	Velocity of Detonation (mm/ μ sec)	Delay Time to Stable Detonation (μ sec)
15 psi CH ₄ 0.006" shim	6.24 $\sigma_v = 0.03$	0.75
15 psi CH ₄ 0.197" shim	6.03 $\sigma_v = 0.06$	25.76
500 psi CH ₄ 0.006" shim	6.21 $\sigma_v = 0.04$	0.81
500 psi CH ₄ 0.066" shim	6.22 $\sigma_v = 0.03$	9.18

TABLE 6
The Effect of Pressure on the Dent Produced
by the Donor in a Steel Block

Gas	Pressure (psi)	Dent Depth	
		Mean (10 shots) (in.)	Standard Deviation (in.)
Air	15	0.024	0.0017
N ₂	500	0.024	0.0011
N ₂	1000	0.024	0.0015
CH ₄	250	0.024	0.0014
CH ₄	500	0.025	0.0012

TABLE 7
The Effect of Pressure on the Observed
Gap Sensitivity of Cast 60/40 RDX/TNT

Gas	Pressure (psi)	Shock Sensitivity	
		50% Gap Value (in. $\times 10^{-3}$)	95% Con. Lts. (in. $\times 10^{-3}$)
Air	15	26.6	0.7
N ₂	1000	27.7	1.4
CH ₄	500	25.8	1.1

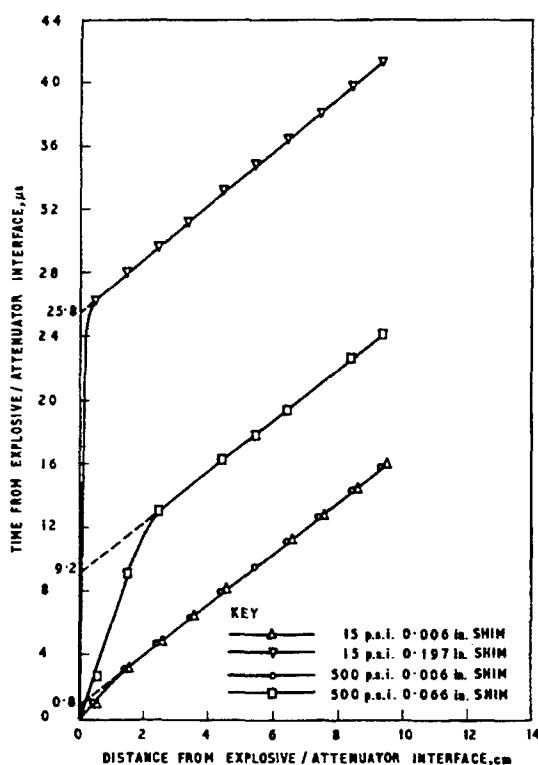


Fig. 7 - Build-up to detonation in coarse HMX compacts at 1.14 g/cc filled with CH₄

complexity, specific heat, viscosity and thermal conductivity. Although with each gas the shock sensitivity decreases smoothly with increasing pressure no single property has been found which correlates with all the observed effects.

A plausible hypothesis is that the interstitial gas slows down explosive particles being accelerated across the voids. In this case the gas density and viscosity would be important factors. The curves for H₂ and N₂ are very similar but the density and viscosity of N₂ are both greater than those of H₂. Thus this hypothesis is not supported.

Where gases were used below their critical temperature there was a possibility of condensation within micro-cracks in the crystals and heavy adsorption elsewhere on the surfaces. These deposits might be supposed to act as a desensitising barrier [14]. But CHClF₂ (critical temperature 96°C) and methane (critical temperature - 83°C) have similar desensitising characteristics at 100 psi. Also C₃H₈ (critical temperature 97°C) and CHClF₂ (critical temperature 96°C) have quite different desensitising effects at 100 psi.

Nitrogen and methane have also been tested with fine HMX compacts where the desensitising

effects were observed to be less than with the coarse HMX compacts in spite of the larger area available for adsorption. Thus adsorption does not appear to be an important factor.

It is seen that the effect increases with the molecular complexity of the gas, thus it may be that the dominant role of the gas is to act as a heat sink for reacting explosives, for reaction products or perhaps more importantly for fine spall or spray projected across voids. It is not clear which thermal properties would be involved if this process were important but the heat capacity per unit volume at elevated temperature is being considered.

Compacts of coarse and fine HMX at the same density (1.14 g/cc) were tested with nitrogen and methane to investigate the effect of particle size. The results are summarised in Fig. 8 and it is seen that although in each case the coarse HMX compacts were more sensitive at low pressures they were less sensitive at high pressures. The results at atmospheric pressure support the work of Dinegar on coarse and fine PETN [15] and the higher shock sensitivity of the coarse material may be due to its greater gas permeability [14]. Since the desensitising effect of interstitial gas is greater with the coarse HMX, it is possible that this is due to the hindering of the pressurising gas of the flow of hot reaction products through the compact. The effect would then be expected to be very much less with the fine HMX where such flow processes would be less important. The higher shock sensitivity of coarse PETN than fine PETN at atmospheric pressure has been interpreted by Dinegar [15] as indicating that the shock initiation process is not governed predominantly by surface burning reactions. However, if gas flow plays an important part in the initiation of coarse compacts only, then the initial reaction may be a surface ignition.

Failure of previous attempts to observe an effect when varying the interstitial gas at atmospheric pressure are almost certainly due to the small effect at that pressure with fine powders.

Compacts of coarse PETN were tested with nitrogen and methane, and in each case the effect was intermediate between that of coarse and fine HMX. Since the PETN particle size was also intermediate between that of the two HMX powders, the effect with PETN is similar to that with HMX. A quantitative comparison is not, however, possible with the data available.

It was observed with the coarse HMX compacts that for the rounds tested near the critical

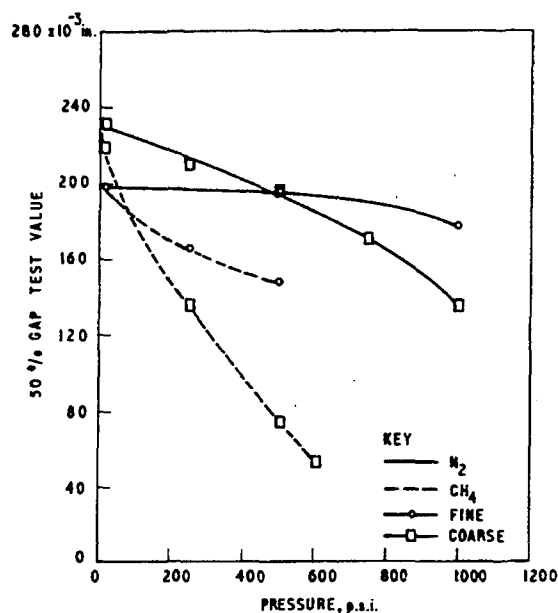


Fig. 8 - Interstitial gas pressure vs 50% gap test value for fine and coarse HMX at 1.14 g/cc in N_2 and CH_4

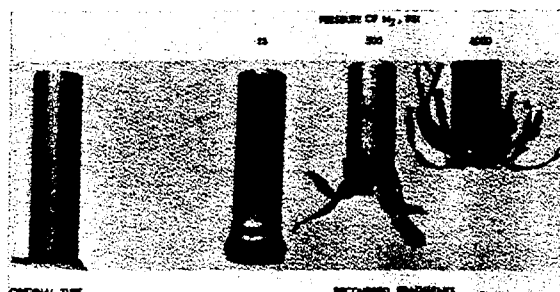


Fig. 9 - Typical fragments from nondetonating rounds during gap testing of coarse HMX

condition, but which failed, the length of container damaged increased with increasing gas pressure. This feature is illustrated in Fig. 9. The build-up to detonation experiments (Fig. 7) confirmed this observation. The methane filled round at 15 psi and 0.197 inch shim reached stable detonation in less than 0.5 cm but took 26 microseconds to do so. The corresponding round at 500 psi and 0.066 inch shim required approximately 2.5 cm and 12 microseconds to achieve stable detonation. Although it is just possible that the delay with the compact at 500 psi was due to an accelerating shock process, the 26 microsecond delay observed with the compact at 15 psi must have been due to a burning phase prior to detonation. This supports

the view that with coarse granular explosive compacts initiated by weak shocks the energy transfer mechanisms in the early stages are the relatively slow convection and conduction processes. Thus the sequence with initiation from weak shocks would be: initiating shock - burning - accelerating shock - detonation. With strong shocks on the other hand detonation would develop directly from the initiating shock.

The validity of the probe technique used appears to be demonstrated by the measured stable velocities of detonation which are in good agreement with those obtained by other methods in similar geometry. It is interesting to note that so far the pressure and nature of the interstitial gas has not been observed to affect the high order velocity of detonation.

SUMMARY OF OBSERVATIONS

1. The shock sensitivity of low density explosive compacts of HMX and PETN decrease with increasing pressure of the interstitial gas.
2. The magnitude of the effect varies with the gas but generally increases with the molecular complexity of the gas.
3. At low pressures compacts of coarse powders are more shock sensitive than corresponding compacts of fine powders.
4. The desensitising effect of interstitial gas is greater with coarse powders and at high pressures compacts of fine powders have the higher shock sensitivity.
5. Increasing the interstitial gas pressure increases the distance required to achieve high order detonation from weak initiating shocks.
6. Long initiation delays occur when coarse HMX compacts are initiated by weak shocks.
7. No significant change was observed in the velocity of the detonation of coarse HMX compacts when the interstitial methane pressure was increased from 15 to 500 psi.
8. The shock sensitivity of cast 60/40 RDX/TNT was not changed by changes of gas and pressure.

CONCLUSIONS

1. The high shock sensitivity of low density explosive compacts is due to their geometry and not to the presence of interstitial gas.

2. Interstitial gas decreases the shock sensitivity of compacts and it is suggested that possible mechanisms are the cooling of reactions by the gas and the hindering of gas convection through permeable charges.

3. Some support has been given to the suggestion that coarse compacts are more shock sensitive than fine compacts because of their higher gas permeability.

4. In the initiation of low density explosive compacts by weak shocks a burning phase must occur before a shock process leads to detonation. When initiation is achieved by strong shocks detonation appears to develop directly from the initiating shock.

ACKNOWLEDGMENTS

The author would like to thank Dr. C. M. Bean and Mr. G. P. Cachia of AWRE, Aldermaston, U.K., and Mr. W. Connick of D.S.L., Melbourne, Australia for their helpful advice and discussion. Much of the experimental work was undertaken with the assistance of Mr. E. Clinch.

REFERENCES

1. G. P. Cachia, and E. G. Whitbread, *Proc. Roy. Soc.*, **A246**, 268-273 (1958).
2. G. E. Seay, and L. B. Seely, *Jnl. Appl. Phys.* **32**, 6, 1092-1097 (1961).
3. A. W. Campbell, et al, 3rd NOL Symp. on Det. (1960).
4. W. Connick, Private communication.
5. F. P. Bowden, and H. T. Williams, *Research* **4**, 339 (1951).
6. O. A. Gurton, 2nd ONR Symp. on Det., Washington (1955).
7. T. Cottrell, and J. Gibb, *Nature*, **178**, 814 (1956).
8. J. Blackburn, and L. B. Seely, *Trans. Far. Soc.*, 537-545, (1965).
9. J. Blackburn, and L. B. Seely, *Nature* **202**, 382-383, (1964).
10. S. Patterson, *Nature*, **203**, 1057-1059, (1964).

11. W. J. Dixon, and A. M. Mood, J. Am. Stat. Ass., 43, 109, (1948).
12. J. Kirkham, Private communication.
13. G. P. Cachia, and P. Seeman, Private communication.
14. J. Eadie, This Symp.
15. R. H. Dinegar, R. H. Rochester, and M. S. Millican, Explosivestoffe, 9, 188-89 (1963).
16. Pro. Int. Con. on Sens. and Hazards of Explosives, London, 1st-3rd October, 1963, Session 2, Discussion 4.

COMMENTS

J. ROTH (Stanford Research Institute, Menlo Park, California): I would like to present some evidence in support of the view that product gas penetration into the interior of a granular explosive contributes to the initiation of steady detonation. We have been measuring the time delay in establishing steady detonation in granular lead azide as a function of the radiant energy it absorbs from an argon flashbomb (J. Chem. Phys. 41, 1929, Oct 1964). Most of this energy is absorbed in a narrow zone very near the irradiated face, and consequently rapid exothermic decomposition starts there. Even though we believe that this leads to thermal explosion, we now have good circumstantial evidence that such explosions, in the very thin regions in which they occur, do not per se

initiate steady detonation. It seems that to establish steady detonation, it is necessary to have reaction occur in a considerably thicker region. A probable mechanism of energy transfer from the reacting regions to a zone of sufficient thickness to initiate steady detonation is via inward product gas flow. This is consistent with our observations that transparent liquids placed on the irradiated face greatly increase the observed initiation delay, as does compaction of the azide. There is additional evidence which would take too long to present now.

It is also interesting to conjecture whether the well known decrease in explosive "sensitivity" as packing density is increased is, at least in part, caused by preventing inward gas flow.

SHOCK INITIATION OF LOW-DENSITY PRESSINGS OF AMMONIUM PERCHLORATE*

Marjorie W. Evans, B. O. Reese, and L. B. Seely

*Stanford Research Institute
Menlo Park, California*

and

E. L. Lee

*Lawrence Radiation Laboratory
Livermore, California*

ABSTRACT

Initiation and detonation behavior of 13-micron ammonium perchlorate was studied at loading density 1.00 g/cm^3 . Steady detonation velocities were determined experimentally at three diameters and extrapolated to $3.75 \pm 0.15 \text{ mm}/\mu\text{sec}$ at infinite diameter. Calculations with the BKW equation of state gave $4.25 \text{ mm}/\mu\text{sec}$ —as good agreement as could be expected for a low-energy chlorine-containing explosive. By introducing 24-kbar flat-topped plane shocks into pellets of various lengths, it was determined that steady full-strength detonation was reached after about 15 mm travel. The growth of pressure in the accelerating wave was followed approximately by means of free-surface measurements on thin Plexiglas at the top surfaces of the pellets, and these measurements indicated the pressure to be $55 \pm 10 \text{ kbar}$ in the full-strength wave. Reducing the air pressure in the pressings to 5 microns left the build-up to detonation unaffected. The position of the shock Hugoniot for the pressings relative to the Hugoniot of the solid crystal is discussed in terms of heat production during collapse and possible reaction processes.

INTRODUCTION

A salient feature of initiation behavior in secondary high explosives is the high sensitivity of a low-density granular pressing relative to that of a homogeneous crystal of the same compound. Thus for PETN approximately 110 kbar is required to detonate a large single crystal [1], whereas low-density pressings of small PETN crystals can be initiated with shocks of a few kilobars [2]. For a shock wave to change into a detonation wave, an energy-producing chemical reaction must proceed fast enough to support the shock ahead of it. Many workers have assumed that attaining a high reaction rate depends on attaining high temperature; in fact, most of them have assumed the Arrhenius law [3]. It has been shown [4] that the average

temperature of the material in a shocked granular explosive will barely suffice for high reaction rates in very insensitive materials, but for moderately sensitive secondary explosives it falls far short. Thus, the weak shock required to initiate granular PETN cannot raise more than a small fraction of the total mass of the pressing to the necessary temperature. Because of such instances, one is forced to postulate hot-spots, encompassing only a very small fraction of the mass in the pressing but containing the greater part of the energy.

Bowden has demonstrated that in impact processes hot-spots can be formed by (a) compression of interstitial gas, (b) intergranular friction, and (c) high-velocity flow [5]. Similarly, for shock initiation of granular explosives

*This research was supported at Stanford Research Institute by the U.S. Air Force Office of Scientific Research under Contract AF 49(638)-1124. The detonation calculations were performed at Lawrence Radiation Laboratory under the auspices of the U.S. Atomic Energy Commission.

it has been proposed that hot-spots can be formed by compression of interstitial gases [6], shock interaction within grains, intergranular friction [7], jetting [8,9], or stagnation [10,11].

Cachia and Whitbread showed that removing the interstitial gas from tetryl left the gap-test sensitivity unchanged [12]. It has also been shown [2] that distance of shock travel before detonation is unaffected by the interstitial gas in granular PETN at density 1.0 g/cm^3 . Although only a few granular explosives have thus far been investigated for interstitial gas effects, an effect of interstitial gas on initiation behavior is yet to be demonstrated. The situation with the other proposals is more equivocal and it may never be possible to eliminate any of them as possible mechanisms. Nevertheless, by studying a wide range of conditions it may be possible to establish definitely that some of them are active.

Failure diameter and variation of steady detonation velocity with charge diameter are controlled by chemical and hydrodynamic events in divergent flow behind the detonation front. Similarly, shock initiation characteristics are influenced by chemistry and flow patterns behind an initiating shock as well as by peak pressure. Presumably with adequate understanding of reactive flow, the relationships between various detonation properties could be written down and all could be derived from fundamental chemical and hydrodynamic properties of the material. Approximate theories have been developed for the effect of charge diameter on detonation velocity [13-15], and thorough experimental studies have been completed in the case of homogeneous explosives [16-18]. A relationship has been developed between failure diameter, shock sensitivity, decomposition kinetics, and flow divergence [19]. The goal seems within reach.

A quite different situation holds for low-density granular explosives. The behavior of granular pressings under shocks of less than 100 kbar peak pressure has not been investigated thoroughly, even for nonreactive systems. The hydrodynamics are much more complicated than for the homogeneous case. In a random arrangement of grains, intergranular friction, shock interaction, jetting, stagnation, and turbulence undoubtedly occur, and these details, probably not calculable, are likely to be the crucial events in starting chemical reaction. In such a complex physical situation several modes for chemical reaction may be possible.

As a contrast to PETN, on which some studies have been made, we have undertaken an

investigation of the detonation and shock initiation of ammonium perchlorate, a low-energy explosive relatively insensitive even in the granular form at low densities. Extensive information on its thermal decomposition [20] recommends it among such explosives for an investigation in which sensitivity is to be related to chemical kinetics. Results on deflagration [21] of ammonium perchlorate may be useful in explaining growth from shock to detonation, and determination of the minimum temperature for deflagration may have a bearing on shock sensitivity. So far our studies have been limited to pure ammonium perchlorate with a weight-median grain diameter of 13μ at a loading density of 1.00 g/cm^3 .

CALCULATION OF DETONATION CHARACTERISTICS

Chapman-Jouguet detonation properties were calculated for ammonium perchlorate over the loading density range from 0.55 to 1.95 g/cm^3 by means of the Ruby code developed by Levine and Sharples [22], using the method of White, Johnson, and Dantzig in the equilibrium calculations [23]. The code solves simultaneously algebraic equations given by the shock conservation equations, the chemical equations, the Becker-Kistiakowsky-Wilson (BKW) equation of state, and the Chapman-Jouguet condition applying to detonations. The BKW equation of state has been used for detonation calculations for about 25 years [24], empirically as a method for fitting well-known measurements and also for predicting properties of new explosives of a similar type. The calculation has been improved and adapted to computers by a number of workers [25,26]. Cowan and Fickett [27] obtained new values for the constants in the BKW equation by fitting their calculations to four explosives for which accurate values of detonation velocity and CJ pressure were available. The Ruby code uses the constants of Ref. 27.

The case of ammonium perchlorate is outside the range of conditions usually treated by Ruby code calculations. The energy of reaction is less than for most explosives, the calculations have been carried to lower densities than usual, the explosive contains chlorine on which there is little calculational experience involving accurately measured detonations, and carbon is absent so that the usually prominent energy-releasing components CO and CO_2 are missing from the products.

The assumed products were H_2O , H_2 , N_2 , O_2 , NO, N_2O , NO_2 , Cl_2 , and HCl. The co-volumes of the first seven components were

those used by Cowan and Fickett [27]. The co-volumes of the two chlorine-containing products were computed by the method customarily used for the other products. A van der Waals volume of the molecule was computed as a sphere with diameter equal to the largest molecular dimension. The co-volume was then obtained by multiplying this volume in \AA^3 by 10.46. The heat of formation of ammonium perchlorate was assumed to be -70.73 kcal/mole [28].

Table 1 gives the calculated hydrodynamic variables. Table 2 lists the product compositions.

TABLE 1
C-J Detonation Characteristics for
 NH_4ClO_4 Calculated by Ruby Code

ρ_0, AP	P_{CJ}	T_{CJ}	U_{CJ}
g/cm^3	kbar	$^\circ\text{K}$	$\text{mm}/\mu\text{sec}$
1.95	187	780	6.43
1.75	148	904	5.95
1.55	116	1039	5.49
1.35	88	1179	5.04
1.15	64	1322	4.59
0.95	45	1464	4.13
0.75	29	1600	3.67
0.55	17	1722	3.20

EXPERIMENTAL

All of the experiments reported here used propellant grade ammonium perchlorate specified as MPD-28A Type II. Analysis showed purity to be 99.3% ammonium perchlorate or better in each sample. The material was re-ground to the particle size shown in Fig. 1.

The booster explosive was cast Composition B-3 (64/36:RDX/TNT). Plane-wave generators made of cast Baratol [70/30: $\text{Ba}(\text{NO}_3)_2/\text{TNT}$] and Comp B were obtained in two sizes known as P-40 (10 cm diam) and P-80 (20 cm diam).

Plexiglas used in the experiments was obtained cast from the monomers. The brass was obtained as the free machining type in the form of plates. Attenuators were machined to size, lapped, and polished.

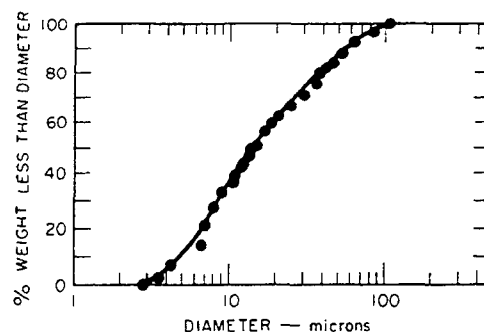


Fig. 1 - Particle size distribution of ammonium perchlorate

A 35-mm rotating-mirror smear camera writing $3.81 \text{ mm}/\mu\text{sec}$ was used for all of the initiation experiments and some of the velocity measurements. Exposures were made on Eastman Tri-X film which was developed for 6-1/2 minutes in UFG developer. Other velocity measurements were made on raster oscilloscopes, either specially manufactured by Denver Research Institute to write at $2.5 \mu\text{sec}$ per sweep or consisting of a separate Cordin Electronics $12.5\text{-}\mu\text{sec}$ raster sweep component controlling a Tektronix 535 oscilloscope.

Determination of Detonation Velocity

Detonation velocity of ammonium perchlorate was determined at three charge diameters, 3.5, 10.1, and 23.2 cm, with charge lengths ten times the diameter in each case. At 3.5 cm the charges were confined in cellulose acetate-butyrate tubing 1.5 mm thick in which elastic wave velocity was determined to be $1.9 \text{ mm}/\mu\text{sec}$, substantially below the detonation velocity of the ammonium perchlorate at this diameter. The charges were loaded in increments to $1.01 \pm 0.01 \text{ g/cm}^3$ and boosted with a 4-inch gap-test donor consisting of a P-40 plane-wave lens and solid Plexiglas attenuator. Velocity in the charge was measured by ionization probes through the wall at 25.4 mm intervals. In this way "fires" from the gap test could be used to give velocity data after initiation phenomena had disappeared.

At the two larger diameters the ammonium perchlorate was loaded in cardboard rings one-half diameter high. These rings were stacked with a copper-foil ionization switch across the diameter of each segment, so that signals from the center of the charge could be recorded on the Cordin-Tektronix oscilloscope. The 10.3-cm charge was boosted with a 10-cm-diameter, 2.5-cm-thick Comp B slab initiated by a

TABLE 2
Detonation Production Compositions for NH_4ClO_4 Calculated by Ruby Code

Moles Product Gas per Gram NH_4ClO_4	Loading Density (g/cm^3)							
	1.95	1.75	1.55	1.35	1.15	0.95	0.75	0.55
H_2O	1.71×10^{-2}	1.71×10^{-2}	1.70×10^{-2}	1.70×10^{-2}	1.70×10^{-2}	1.70×10^{-2}	1.70×10^{-2}	1.69×10^{-2}
H_2	1.68×10^{-22}	3.00×10^{-19}	1.32×10^{-16}	1.77×10^{-14}	9.33×10^{-13}	2.35×10^{-11}	3.31×10^{-10}	2.80×10^{-9}
N_2	8.17×10^{-3}	8.29×10^{-3}	8.37×10^{-3}	8.42×10^{-3}	8.45×10^{-3}	8.46×10^{-3}	8.49×10^{-3}	8.58×10^{-3}
O_2	4.08×10^{-3}	4.14×10^{-3}	4.18×10^{-3}	4.20×10^{-3}	4.22×10^{-3}	4.23×10^{-3}	4.23×10^{-3}	4.23×10^{-3}
NO_2	3.53×10^{-4}	2.33×10^{-4}	1.58×10^{-4}	1.09×10^{-4}	7.55×10^{-5}	5.26×10^{-5}	3.63×10^{-5}	2.46×10^{-5}
NO	4.01×10^{-9}	4.30×10^{-8}	2.89×10^{-7}	1.30×10^{-6}	4.30×10^{-6}	1.11×10^{-5}	2.36×10^{-5}	4.23×10^{-5}
N_2O	1.01×10^{-8}	2.57×10^{-8}	5.19×10^{-8}	8.48×10^{-8}	1.18×10^{-7}	1.43×10^{-7}	1.54×10^{-7}	1.46×10^{-7}
Cl_2	4.26×10^{-3}	4.26×10^{-3}	4.26×10^{-3}	4.26×10^{-3}	4.26×10^{-3}	4.26×10^{-3}	4.23×10^{-3}	4.06×10^{-3}
HCl	1.36×10^{-16}	3.28×10^{-13}	1.27×10^{-10}	1.21×10^{-8}	4.20×10^{-7}	6.91×10^{-6}	6.51×10^{-5}	3.95×10^{-4}

bursting-wire detonator and a 12.5 diameter by 6.3 mm RDX pellet. A velocity record was also obtained on the smear camera at this diameter through 1-cm holes punched at the center of each segment and faced on the inside with transparent tape. The 23.3-cm charge was boosted with a 20.3-cm by 5-cm Comp B charge initiated in the same way. Only oscilloscope timing was obtained on this shot.

At 3.5-cm diameter thirteen shots yielded up to nine velocity determinations each. The shot-to-shot standard deviation was $\sigma_s = 0.11$. One experiment only was performed at each of the larger two diameters, 10.1 and 23.3 cm. Standard deviations σ_i of the incremental velocities were 0.07 and 0.05 mm/ μ sec, respectively. In Fig. 2 these results are plotted with the error indicated at $2\sigma_s$ for the 0.286 cm^{-1} reciprocal diameter data and $2\sigma_i$ for the two large shots. Extrapolation to infinite diameter gave $3.75 \pm 0.15 \text{ mm}/\mu\text{sec}$, the uncertainty being estimated by extrapolation of the opposite extremes of the plotted errors.

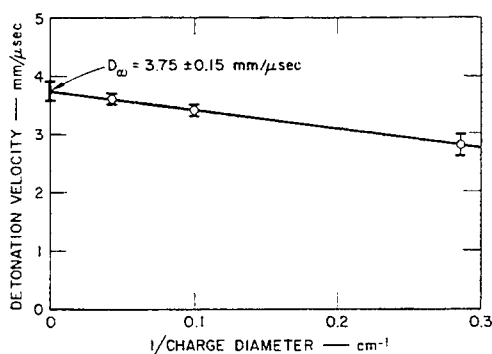


Fig. 2 - Detonation velocity of ammonium perchlorate plotted against reciprocal charge diameter

Minimum Shock for Initiation at 3.5-cm Diameter

The minimum pressure required to initiate steady detonation in long charges was qualitatively established by a variant of the gap method. The donor explosive was a P-40 plane-wave lens against which was placed an attenuator of solid Plexiglas. The ammonium perchlorate charge, 3.5 cm in diameter, packed as described in the section on velocity determination, was centered on the attenuator. The emergent wave at the attenuator-ammonium perchlorate interface was plane to $0.05 \mu\text{sec}$ over the test charge diameter. The Plexiglas free-surface velocity

for the 50% gap thickness was determined by means of the moving image camera, using a parallel mirror above the surface. Light from an argon explosive flash was reflected into the camera until the reflectivity of the mirror was destroyed by arrival of the moving surface. The resulting camera record gave the time required for the surface to traverse the distance to the bottom surface of the mirror. From this a free-surface velocity of $1.00 \pm 0.03 \text{ mm}/\mu\text{sec}$ was obtained, corresponding to a calculated shock pressure in the Plexiglas of $19.3 \pm 0.5 \text{ kbar}$. In the same experiment a Manganin resistance-wire pressure gauge [29] measured $17.0 \pm 1 \text{ kbar}$ for the Plexiglas shock pressure. The time profile of the wave at the interface was not determined.

The velocity of the wave generated in the ammonium perchlorate was first measured over the second 25.4 mm interval as $2.5 \text{ mm}/\mu\text{sec}$. It became steady after about 75 mm at $2.81 \pm 0.22 \text{ mm}/\mu\text{sec}$. Figure 3 gives a pressure-particle velocity plot measured by two groups of experimenters for Plexiglas [30,31]. We have assumed that the Plexiglas rarefaction curve is a mirror reflection of the Hugoniot. A $\rho_0 U_s$ line corresponding to the $2.5 \text{ mm}/\mu\text{sec}$ measured in the second interval intersects the rarefaction curve at about 15 kbar in the ammonium perchlorate. Thus 15 kbar is the minimum pressure which will initiate this material at this diameter with the pressure-time profile delivered by this booster-attenuator system. Data to be presented in the next section show that initiating shocks in this particle-size ammonium perchlorate at this density accelerate very little until just before rapid build-up to full detonation velocity:

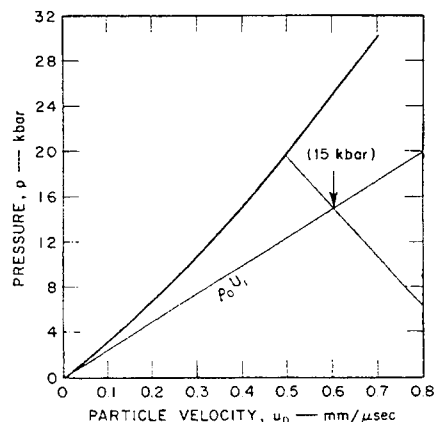


Fig. 3 - Hugoniot for Plexiglas. The $\rho_0 U_s$ line is for ammonium perchlorate at density $1.0 \text{ g}/\text{cm}^3$ and intersects the Plexiglas expansion curve at about 15 kbar.

Plane-Wave Initiation Measurements

Shock initiation of ammonium perchlorate was studied for approximately flat-topped shocks at about 24 kbar. For this pressure, transition to steady detonation occurs in times which are long enough to establish the incoming wave velocity but short enough that the transition occurs before the initial shock is influenced by reflections or rarefactions.

The driver system for the majority of the shots was a P-80 plane-wave lens detonated directly against a 1/2-inch-thick brass driver plate. The duration of the initial pulse before reflections accelerate the brass was determined by observing with a moving-image camera a reflected image of a wire on the polished driver plate [32]. For this driver system the free-surface velocity was constant for 12.5 μ sec before the first reflection arrived, as is shown in Fig. 4. The long reverberation time was not the result of spalling, as similar brass plates were recovered unspalled except at the edges. If the velocity of sound in the shocked brass is taken as the slope of the Hugoniot and the reflection from the back surface is assumed to travel at full shock velocity starting from the arrival of the head of the rarefaction (both very conservative assumptions), the reverberation time is estimated as about 6 μ sec. Our longest transit time (~ 8.5 μ sec) would be unaffected by the overtaking second shock even on this basis.

Pellets of ammonium perchlorate were formed at loading density 1.00 ± 0.005 g/cm³ by packing the powder into Plexiglas rings, whose diameters were at least three times their height. Pellets of various heights were arranged on the brass driver plate in two rows so they could be photographed through two parallel slits by a

moving-image camera. The wave was sufficiently plane over an area approximately 15 cm in diameter that as many as four pellets could be observed on one slit, depending on their diameter and the other measurements to be made.

For most of the experiments one-half of the surface of each pellet was covered with a thin sheet of Plexiglas. On small pellets a 1.6 mm thickness was adequately rigid, but for large pellets 3.2 mm was necessary. Over the covered half of the pellets an angled mirror was placed for measurement of the free-surface velocity of the Plexiglas. An explosive argon flash was reflected specularly from the mirror into the camera and also served to illuminate the uncovered surface of the pellet.

The overall array of pellets of various lengths is shown in Fig. 5. The following were directly indicated by the films: (a) arrival time of the shock at the bottom of the pellets, (b) planarity of the wave, (c) free-surface velocity of the driver, (d) arrival times at the tops of the pellets, (e) wave shapes at the tops of the pellets, and (f) free-surface velocity of the Plexiglas sheet.

A typical record showing these features is shown in Fig. 6, and for clarity a line tracing of this record is given in Fig. 7.

Signals caused by the arrival of the shock at the surface of the driver plate are indicated by the lines marked A and A' for the two slits, respectively. From these signals an indication of planarity is obtained. When there is some variation in the arrival time of the wave, individual signals at the bottoms of the Plexiglas rings can be used for their respective pellets. The free-surface velocity of the driver is obtained from the angle of the trace marked B.

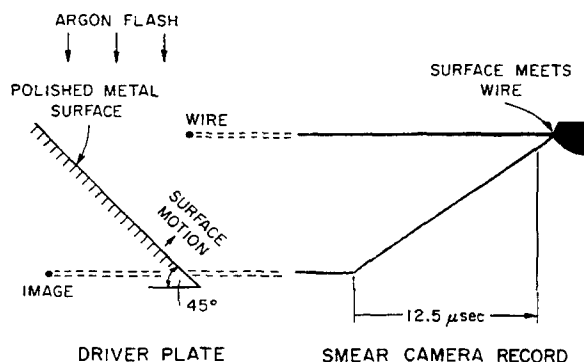


Fig. 4 - Measurement of brass driver plate free surface motion by the wire reflection technique. Experimental arrangement is shown at left and the resulting film at right.

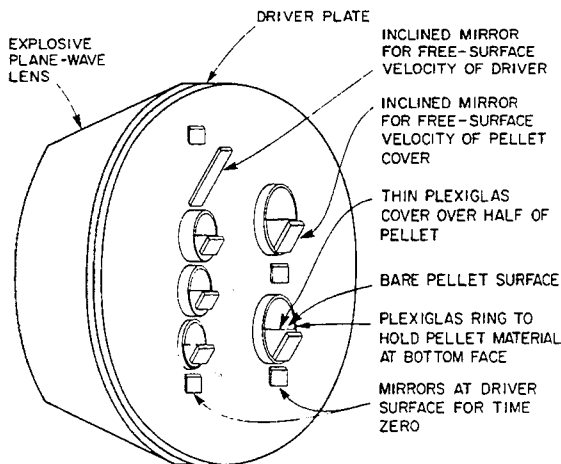


Fig. 5 - Charge arrangement for a typical shot to investigate initiation characteristics of ammonium perchlorate. Two rows of pellets are photographed simultaneously through double camera slit.

A drop in intensity of scattered light from the uncovered half of the pellet indicates the arrival of the shock at the top surface. Two such signals, one on each slit, are marked C and C'. On the covered half of the pellets the free-surface velocity of the Plexiglas is obtained from the angles of traces such as D and D'.

From these primary data the following derived quantities may be calculated: (a) driver plate pressure, (b) wave pressure at the bottom of the pellet, (c) shocked density at the bottom

of the pellet, (d) wave transit time, (e) wave pressure at the top of the pellet, (f) shocked density at the top of the pellet.

Figure 8 gives a plot of wave transit time versus pellet thickness. The error lines show two standard deviations with three to five measurements having been made at each point. The incoming wave has a velocity of $2.75 \text{ mm}/\mu\text{sec}$. After about 15 mm of travel the wave velocity increases. Establishing the precise time at which detonation is achieved is practically impossible. However, at whatever point the transition occurs the velocity will thereafter be $3.75 \pm 0.15 \text{ mm}/\mu\text{sec}$, the value determined above as D_0 , as long as the wave remains plane. A line of this slope has therefore been fitted to the points for pellet thicknesses above 15.5 mm. A thickness-time plot for an overdriven wave has also been given in Fig. 8. The wave shapes marked E and F in Figs. 6 and 7 indicate the effects of the Plexiglas retaining rings. For a short pellet 5 mm in height (at E), the wave next to the Plexiglas leads the central part of the wave because the wave velocity in the center is less than in Plexiglas. For a long pellet 15 mm in height (at F), the wave next to the Plexiglas lags behind because the wave velocity in the ammonium perchlorate is greater than in the Plexiglas. The shock velocity in Plexiglas should be $3.6 \text{ mm}/\mu\text{sec}$ near the driver plate but would fall in the long retaining rings to sound velocity, while the velocity in the ammonium perchlorate increases from 2.75 to $3.75 \text{ mm}/\mu\text{sec}$.

The pressure at the top of the pellet p_i is calculated from the pressure transmitted to the Plexiglas by use of the expression [33,34]

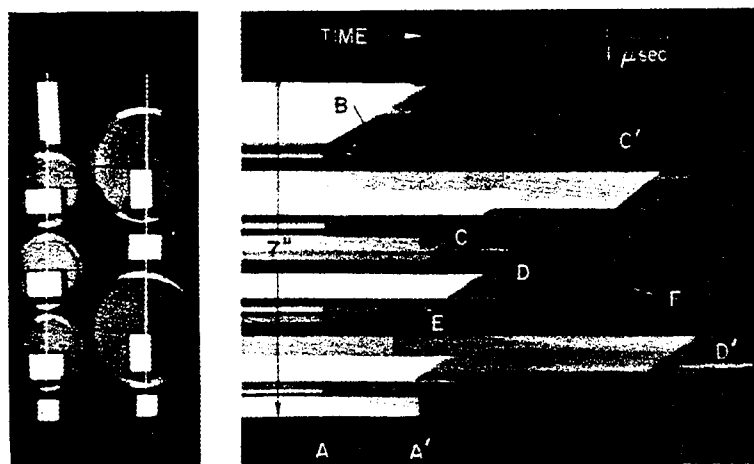


Fig. 6 - Smear camera record of pellet arrangement diagrammed in Fig. 5. At left is the still picture, at right the time record.

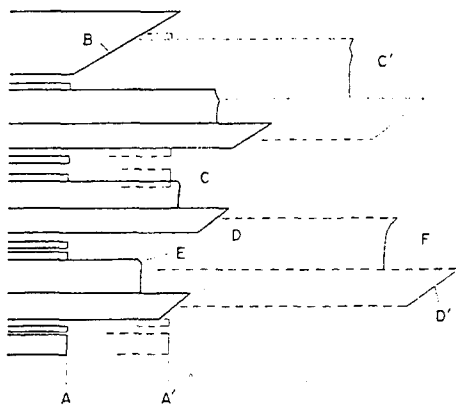


Fig. 7 - Drawing of smear camera record corresponding to film in Fig. 6

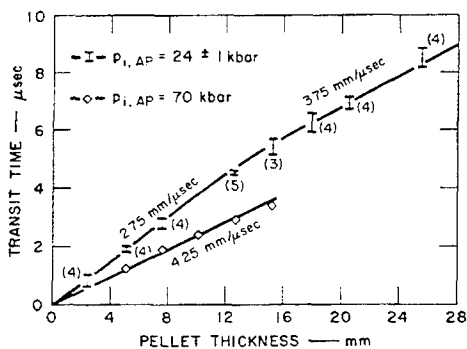


Fig. 8 - Time-distance plots of data obtained from ammonium perchlorate pellets with entering shocks at 24 kbar and 70 kbar

$$P_i = P_t \frac{\rho_{oPl} U_t + \rho_{oAP} U_i}{2\rho_{oPl} U_t}$$

where

- ρ_{oPl} is the density of the unshocked Plexiglas,
- ρ_{oAP} is the density of the unshocked ammonium perchlorate pressing,
- U_i is the velocity of the shock in the ammonium perchlorate at the given pellet height,
- U_t is the velocity of the shock transmitted to the Plexiglas, and
- P_t is the pressure in the Plexiglas calculated from the free-surface velocity of the Plexiglas.

This technique of studying a developing detonation by observing wave pressure is a variant of that first used by Fauquignon [35] who measured the shock velocity induced in Plexiglas blocks by receptor charges of various lengths and from that estimated the wave pressures.

Figure 9 gives the wave pressure at the top of the pellet as a function of pellet thickness. The value at zero thickness is the entering pressure calculated from the brass free-surface measurement. In the ammonium perchlorate the wave pressure increases over the first 15 mm and then reaches a value of about 55 ± 10 kbar. The shape of this plot depends on the slope of the curve in Fig. 8, and thus is not an independent experimental confirmation that build-up is taking place. A simpler indication is given by the trend in Plexiglas particle velocities. The average of eleven measurements made on the four shortest pellets was 1.01 mm/μsec with a standard deviation $\sigma_i = 0.09$. The average of eleven measurements made on pellets 17.8 and 20.4 mm long was 1.23 mm/μsec with $\sigma_i = 0.26$.

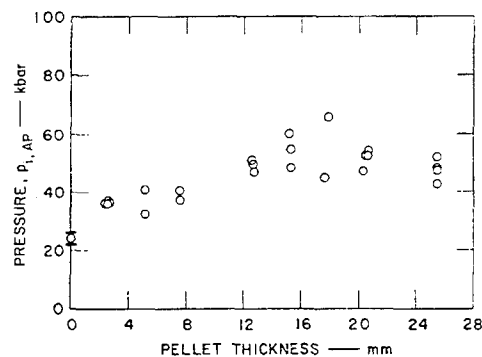


Fig. 9 - Pressures calculated from free surface velocities of Plexiglas at top of ammonium perchlorate pellets

An auxiliary experiment was carried out to confirm that the 24-kbar plane-wave initiation system would lead in a long charge to a wave that could be identified as a detonation by its steadiness and light output. An ammonium perchlorate rate stick 10.16 cm in diameter was packed in the cardboard rings described for the velocity determinations, but now provided with a narrow vertical cellulose acetate window of the same thickness as the tube wall to permit observation with a moving-image camera. Increments were stacked to a height of 30.5 cm. Initiation was by a P-80 plane-wave lens and a

1/2-inch-thick brass driver plate. The initiating system thus provided the 24-kbar input wave used in the plane-wave pellet initiation experiments.

At the start of the trace near the driver plate a low-velocity region was observed, but after about 15 mm of travel the trace became straight at 3.26 mm/ μ sec, the steady velocity for a 10-cm-diameter ammonium perchlorate charge at 1.0 g/cm³.

At the top of the charge, free-surface velocity of a 3.2-mm-thick Plexiglas cover plate was measured with the inclined mirror method. The wave was curved so that the free-surface velocity could be measured only at the axis and even there with no great accuracy. The calculated wave pressure was 59 ± 10 kbar.

Vacuum Experiments

A chamber with a glass face plate was built over the brass driver plates of four of the pellet shots so that the initiation behavior of ammonium perchlorate could be studied when most of the interstitial air had been removed. In order to permit a valid comparison without a large number of shots, similar shots were prepared from what were believed to be identical components. Construction of a vacuum shot and its control were carried forward simultaneously and the two shots were fired in succession with as little delay as possible.

The data are listed in Table 3. The differences in transit times between the vacuum shots and the corresponding one-atmosphere shots are small relative to the error limits shown in Fig. 8 and apparently of random sign.

DISCUSSION

The value 3.75 ± 0.15 mm/ μ sec for the ideal detonation velocity compares well with 3.70 mm/ μ sec found by Anderson and Pesante [36] for 12- μ ammonium perchlorate by extrapolation of data in the diameter range between 1.9 and 10.2 cm. For a low-energy insensitive explosive it is possible that velocity data collected at what might normally be considered large diameters will be in a nonlinear part of the reciprocal diameter plot. For this reason we have fired one shot at over 23 cm diameter even though it had to be fired underground. The data from this shot confirm the line established at the smaller diameters and, therefore, we believe the extrapolation is valid and that D_0 represents a true experimental estimate of the ideal detonation velocity.

TABLE 3
Comparison of x, t Data from Shots Under Vacuum and at One Atmosphere

<div style="display: inline-block; transform: rotate(-45deg);"> Pressure x mm </div>	t μ sec		
	1 atm	6 μ Hg	5 μ Hg
	Shot 10,608	Shot 10,607	
2.49		0.98	
2.53	0.96		
5.10		2.01	
5.15	2.01		
7.62		2.85	
7.62	2.82		
12.62		4.50	
12.68	4.57		
15.24	5.50		
15.25		5.49	
17.75		6.09	
17.75	6.16		
	Shot 10,899		Shot 10,960
20.40			7.02
20.45	6.98		
25.40			8.60
25.50	8.73		

The velocity computed by the Ruby Code (4.25 mm/ μ sec, Table 1) is significantly higher than the experimental determination. The calculation has been established by comparing calculated and experimental values of detonation velocity and pressure and adjusting equation-of-state constants until optimum agreement was produced. Checks have been possible on a number of CHON explosives [27] so that adequacy of the equations and the parameters is well-established for this class. Any explosives at density below 1.2 g/cm³ are not accurately calculated with this equation of state with the present constants. Calculations involving chlorine

may involve further modifications. Therefore, the agreement between experimental and calculated values of velocity is believed to be as good as expected. Any noticeable improvement would involve a considerable series of accurate measurements on ammonium perchlorate and similar compounds and perhaps shock measurements on liquid HCl and Cl₂.

Minimum Pressure for Initiation at 3.5 cm Diameter

The gap-test results were obtained with a 10-cm-diameter Plexiglas attenuator and a 10-cm plane-wave lens. The wave shape as it left the Plexiglas was plane over the 3.5-cm-diameter area occupied by the test charge. The wave speed traces of the disturbance in the ammonium perchlorate obtained at the edge of the charges became straight after about 70 mm and this indicates that initiation phenomena lasted almost this long. Since the wave shape of the shock was changing and the pressure falling, it seems reasonable that 70 mm is close to the longest initiation zone that could be observed at this diameter.

The pressure in the Plexiglas, 19.3 kbar, at the 50-percent point in these experiments is consistent with a Plexiglas pressure of 16.5 kbar obtained by Jaffe and Price [37] in their experiments on ammonium perchlorate at 0.85 g/cm³.

Plane-Wave Initiation

Ammonium perchlorate was chosen for study because it is insensitive and low-powered. The insensitivity leads directly to a relatively high velocity for the initiating shock, the low power leads directly to a low detonation velocity, and the combination of these two factors leads to a very real experimental difficulty in determining when initiation occurs. It has been impossible to establish the final detonation velocity from measurements in the pellet experiments alone because a certain amount of error in the x, t data is inevitable, and because the longest pellets may have been perturbed by edge effects. Therefore, a line with slope equal to the ideal velocity D_0 was adjusted (visually) in intercept to fit the data above 15 mm. There is some slight evidence in the x, t plot that the transit times on the pellets of greatest length have been increased by edge effects.

Pressure Measurements

Additional evidence of initiation was obtained by the pressure measurements. It is

impossible in practice to make free-surface measurements on the explosive itself when it is at low density in the granular form. Instead, the microscopically complex wave in the pressing induced a shock in Plexiglas. On this material, free-surface measurements can be made easily and converted to the pressure in the ammonium perchlorate by solving the Plexiglas-explosive interface equation. Accurate measurements of this kind would require very painstaking work and a careful study of the effect of Plexiglas thickness. We have actually accomplished only rather gross measurements in which it was assumed that effects of wave shape might lower the pressure only about 10 or 20%. The results in Fig. 9 support our interpretation of the x, t data. Note that there is an indication that the pressure is falling between the 20-mm and 25-mm pellets. This is consistent with the indication on the x, t graph in Fig. 8 that the velocity is falling off in the same interval. A further indication was the wave shape observed for the longest pellets which in most cases had only a very small plane region at the center and in some had none at all.

Effect of Vacuum on Initiation

The vacuum experiments give evidence as to whether the gas compression mechanism can be responsible for shock initiation of ammonium perchlorate. The data in Table 3 show that within the accuracy of our experiments the build-up of the wave is unaffected by the presence or absence of interstitial gas. The exact interpretation that can be placed on this statement needs some discussion.

We evacuated the pellets rather than filled them with a high specific-heat gas because the results are more definitive. When the mass of gas is reduced by a factor of 10^5 as in these vacuum experiments, the total energy for transfer to the grains is reduced by a roughly similar amount. Thus, if calculations of grain surface temperatures are in question, changes in the heat transfer coefficient are avoided. If the equilibrium temperature of small grains is being calculated, reduction of the energy available has a direct effect.

The overall shock initiation process in granular explosives should probably be considered to consist of at least two phases: (1) the primary initiation process—creation of small nuclei of decomposition, and (2) the growth process—acceleration of the shock to the point where it becomes a steady detonation. The fact that we cannot tell the difference between normal atmospheric air density and 10^{-5} of this density

in the arrival times of the shock at various positions during growth of the wave indicates at least that the interstitial gas does not affect the build-up process. This is no cause for surprise, since even for grain burning mechanisms the rate during the shock-growth period need not depend on the ambient pressure that existed before the first hot-spots were created. It is, nevertheless, a fact that the interstitial gas does not affect the rate of build-up of a 24-kbar shock in ammonium perchlorate at 1 g/cm^3 .

Our vacuum experiments also imply something about the primary initiation process. The very least that can be said is that this primary process does not depend uniquely on the presence of interstitial gas—an explosion did occur. Most theoretical calculations of the heat transfer to the solid from the gas will be very seriously altered by changing the density and total mass of the gas by a factor of 10^5 . It might be maintained that the gas compression mechanism was active at 1 atmosphere but another mechanism took over at $5 \mu\text{Hg}$. However, it is very unlikely that substitution of mechanisms would occur so precisely. The real problem is to show why the process active at $5 \mu\text{Hg}$, which clearly exists but does not involve the interstitial gas, is not adequate to explain initiation at 1 atmosphere.

Since our result was obtained at 24 kbar, considerably above the minimum pressure necessary for initiation, it might also be maintained that initiation by lower pressure shocks, 15 kbar for instance, may be controlled by the interstitial gas.

Hugoniot of Ammonium Perchlorate Pressings

In Fig. 10 are four circles, representing a p, v point from the plane-wave initiation experiments at 24 kbar, a point from the gap-test experiments at 15 kbar, and two higher pressure points which almost certainly correspond to complete reaction of the ammonium perchlorate.

Zel'dovich and Kompaneets are reported [38] to have developed the theory for Hugoniot curves of porous materials using the Mie-Grüneisen equation of state. They assumed that (1) the pressing requires negligible compaction force, (2) the specific internal energy of the crystal equals that of the granular material, (3) the shocked state can be treated as homogeneous fluid, ignoring granularity. The general form of the Hugoniot for a pressing of fairly high porosity is shown by the dashed line in Fig. 10. The exact shape and position of the curve depends

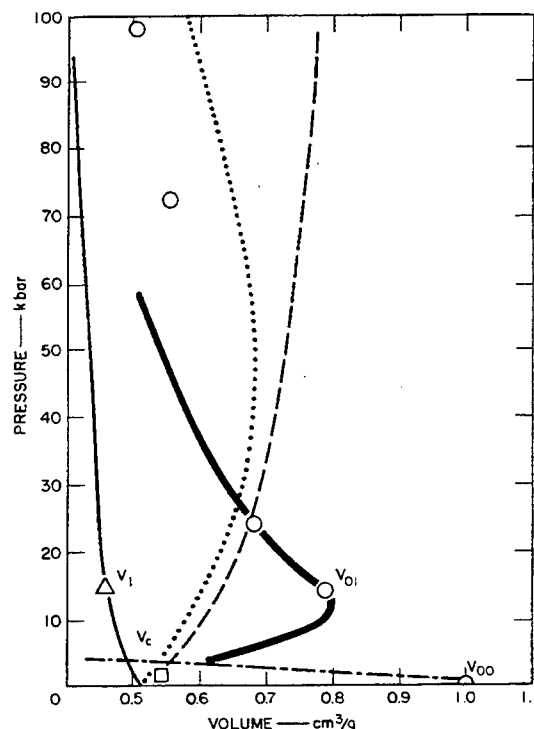


Fig. 10 - Hugoniot curves for ammonium perchlorate

- Measurements on NH_4ClO_4 pressings at four shock pressures.
- Static compression of granular pressing.
- Assumed Hugoniot of ammonium perchlorate crystal.
- △ Assumed point corresponding to experimental point at V_{01} .
- - - Typical Hugoniot of porous pressing predicted by Zel'dovich.
- Typical Hugoniot of pressing found by Russian experimenters.
- · - · Rayleigh line for low-pressure shock in ammonium perchlorate pressing.
- Hugoniot proposed for ammonium perchlorate pressing.

on the equation of state of the solid material and the porosity of the pressing.

Russian experimentalists have found that the dashed curve is not realized, but that the top part of the curve bends toward normal crystal density as illustrated by the dotted curve. In the case of powdered metals, this occurs at relatively high pressures and is ascribed to electron effects and change in the lattice specific heat. Recently data have been reported [39] on granular pressings of ionic crystals which are cases closer to that of ammonium perchlorate.

However, in all this Russian work the main interest has been extremely high pressures.

In our present data on ammonium perchlorate the experimental point at 15 kbar lies at a larger volume than that of the solid crystal, and from this we conclude that the Hugoniot is positively sloped as predicted by Zel'dovich. However, since the volume at 24 kbar is smaller than at 15 kbar, we must conclude we are in a region where pressure is double-valued. It thus becomes of some importance to determine if, in fact, the Hugoniot assumes a positive slope below 10 kbar and if the volume approaches that of the crystal under the action of very weak shocks.

Also in Fig. 10 is a square which represents the volume expected from static pressure at 2 kbar. Such a pressure is not negligible relative to weak shocks.

We have attempted two shots at very low pressure. These experiments have turned out to be more difficult than originally anticipated because of a short reverberation time in the multilayered attenuator, a poorly defined brass Hugoniot at very low pressures, poor quality optical signals from the emergence of very low intensity shocks, and difficulty in producing thin pellets of good quality. Nevertheless, it is clear that the shock velocity over the first 3 mm of travel in the pressing is in the neighborhood of 0.75 mm/ μ sec, only slightly above sound velocity, 0.54 mm/ μ sec [40]. The Rayleigh line corresponding to this velocity is drawn at the bottom of the graph in Fig. 10. A pressure between 2 and 3 kbar was obtained from the free-surface velocity of the brass by the graphical solution of the brass-perchlorate interface equation.

Taking into account the four data points that we have, the fact that 2 kbar will compress the material to 95% crystal density, and the indications of the preliminary low-pressure shock experiments, we have drawn the Hugoniot of the pressing (the heavy solid line) to resemble those used by the Russian experimenters. The main difference between this curve and the Russian Hugoniots is the low pressure at which the high-volume bulge occurs. This, at about 10 kbar, is so low that it must have an explanation in addition to the one offered for the higher pressure bulge in inert materials. In general terms, however, the explanation is the same. The material exists at the two volumes V_1 on the Hugoniot assumed for the crystal and V_{01} on the Hugoniot for the pressing not only because the specific internal energy is higher at V_{01} than at V_1 but also because the percentage of internal energy in the thermal term is higher at V_{01} .

The pressing is considered in the theory to be homogeneous; that is, the material is a fluid at the expanded state V_{00} . The positive slope of the Hugoniot arises from irreversible work during compaction. The heterogeneity itself can be expected to cause heating through jetting, turbulence, and stagnation. In this sense the shape of the Hugoniot of the pressing is an indication of the number and temperature of hot-spots.

The pressing Hugoniot has been drawn below the points at 70 and 98 kbar because they must lie on the fully reacted Hugoniot. However, some reaction may occur very rapidly in the shock at 24 and 15 kbar. A detailed comparison of the ammonium perchlorate curve with that of a mechanically similar inert may indicate the initial degree of chemical reaction at the low pressures.

ACKNOWLEDGMENTS

The authors wish to thank Dr. A. B. Amster who directed exploratory experiments on steady wave velocity and shock sensitivity, and Dr. Gordon D. Anderson and Dr. Michael Cowperthwaite for discussions of Hugoniots of porous materials.

REFERENCES

1. T. E. Holland, A. W. Campbell, and M. E. Malin, *J. Appl. Phys.* **28**, 1217 (1958).
2. G. E. Seay and L. B. Seely, *J. Appl. Phys.* **32**, 1092 (1961).
3. H. W. Hubbard and M. H. Johnson, *J. Appl. Phys.* **30**, 765 (1959).
4. Marjorie W. Evans, C. M. Ablow, B. O. Reese, and A. B. Amster, *Intl. Conf. on Sensitivity and Hazards of Explosives*, **S2**, paper 5 (Brit. Min. Aviation, 1963).
5. F. P. Bowden and A. D. Yoffe, *Initiation and Growth of Explosions in Liquids and Solids*, (Cambridge Univ. Press, 1952) p. 2.
6. J. Taylor, *Detonation in Condensed Explosives* (Clar. Press, Oxford, 1952), p. 174.
7. F. P. Bowden and A. D. Yoffe, *Fast Reactions in Solids* (Acad. Press N. Y., 1958).
8. R. W. Watson and F. C. Gibson, *Nature* **204**, 1296 (1964).

9. F. P. Bowden and M. P. McOnie, *Nature* 206, 383 (1965).
10. J. H. Blackburn and L. B. Seely, *Nature* 194, 370 (1962).
11. L. B. Seely, *Proc. Electric Initiator Symp.* (Franklin Inst., Phila.) Ch. 27.
12. G. P. Cachia and E. G. Whitbread, *Proc. Roy. Soc. (London)* A246, 268 (1958).
13. H. Jones, *Proc. Roy. Soc. (London)* A189, 415 (1947).
14. H. Eyring, R. E. Powell, G. H. Duffey, and R. B. Parlin, *Chem. Rev.* 45, 69 (1945).
15. W. W. Wood and J. G. Kirkwood, *J. Chem. Phys.* 22, 1920 (1954).
16. A. W. Campbell, W. C. Davis, and J. B. Ramsay, *Phys. Fluids* 4, 498 (1961).
17. E. A. Igel and L. B. Seely, 2nd ONR Symp. Detn. (U.S. Dept. Navy, Washington, 1955).
18. M. A. Cook, *Science of High Explosives* (Reinhold, N. Y. 1958).
19. Marjorie W. Evans, *J. Chem. Phys.* 36, 193 (1962).
20. P. W. M. Jacobs and A. R. Tariq Kureishy, 8th Comb. Symp. 1960 (Williams and Wilkins, Balt., 1962) 672, and refs. cited
21. Marjorie W. Evans, R. B. Beyer, and L. McCulley, *J. Chem. Phys.* 40, 2431 (1964), and refs. cited
22. H. B. Levine and R. E. Sharples, "Operator's Manual, Ruby," UCRL-6815, (Lawrence Radiation Lab., Mar. 1962).
23. W. B. White, S. M. Johnson, and G. B. Dantzig, *J. Chem. Phys.* 28, 751 (1958).
24. G. B. Kistiakowsky and E. B. Wilson, Jr., OSRD 114, Aug. 1941 (ASTIA, Libr. of Congress, Washington).
25. S. R. Brinkley, Jr., *J. Chem. Phys.* 15, 107 (1947).
26. C. L. Mader, *Detn. Calcs. with BKW Eqn.* LA-2900 (TID-4500) (U.S. Dept. Commerce, Washington, 1963).
27. R. D. Cowan and W. Fickett, *J. Chem. Phys.* 24, 932 (1956).
28. JANAF Interim Chemical Tables, Dow Chem. Co., Midland, Mich.
29. D. Bernstein and D. D. Keough, *J. Appl. Phys.* 35, 1471 (1964).
30. I. Jaffe, R. Beauregard, and A. Amster, "Third Symposium on Detonation," ONR Symposium Report ACR-52, p. 584, 1960.
31. D. N. Schmidt and Marjorie W. Evans, *Nature* 206, 1348 (1965).
32. W. C. Davis and G. B. Craig, *Rev. Sci. Instr.* 32, 579 (1961).
33. R. E. Duff and E. Houston, *J. Chem. Phys.* 23, 1268 (1955).
34. W. E. Deal, *2nd Detn. Symp.* (ONR, 1955) 209.
35. C. Fauquignon, *Compt. Rend.* 251, 38 (1960).
36. W. H. Andersen and R. E. Pesante, 8th Comb. Symp. (Williams and Wilkins, Baltimore, Md., 1962), p. 705.
37. Donna Price and I. Jaffe, *AIAA Jour.* 1, 394 (1963).
38. K. K. Krupnikov, M. I. Brazhnik, and V. P. Krupnikova, *JETP (USSR)* 42, 675 (1962).
39. S. B. Kormer, M. V. Sinitsyn, A. I. Funtikov, V. D. Urlin, and A. V. Blinov, *JETP (USSR)* 47, 1202 (1965).
40. R. C. Goettelman and Marjorie W. Evans, *Nature* 198, 679 (1963).

COMMENT

M. COWPERTHWAITTE (Stanford Research Institute, Menlo Park, California): In regard to the papers of Dr. William E. Gordon and Dr. Marjorie W. Evans et al., I would like to emphasize some properties of Hugoniot curves which follow directly from the simplest theory of the shocked states of granular materials.

If p , e , and v denote pressure, specific internal energy, and specific volume, and v_{oo} , v_o the initial specific volume of granular and crystalline density material at atmospheric pressure, the theory is based on the assumptions that granular material and crystal density material have initially the same specific energy e_o ,

$$e(p=0, v_{oo}) = e(p=0, v_o) = e_o \quad (1)$$

and that the shock-induced states of granular and crystal density material have the same equations of state.

In this case Properties (I) and (II) are of interest:

(I) No states on the Hugoniot curve of granular material centered at v_{oo} can lie on the Hugoniot curve of crystal density material centered at v_o .

(II) The exact shape and position of a Hugoniot curve of granular material centered at v_{oo} is determined by the $(e-p-v)$ equation of state of crystal density material and the porosity parameter $m = v_{oo}/v_o$.

Property (I) follows directly from the Hugoniot equation. A given state (e, p, v) connected to $(p=0, v_{oo})$ and $(p=0, v_o)$ by a single shock cannot satisfy the Hugoniot equations

$$e - e_o(p=0, v_{oo}) = 1/2 p(v_{oo} - v) \quad (2)$$

$$e - e_o(p=0, v_o) = 1/2 p(v_o - v) \quad (3)$$

without violating the first law of thermodynamics.

Property (II) is illustrated by the Russian work [1,2] on porous metals. For a Mie-Grüneisen equation of state the slope of the Hugoniot curve is determined by values of Grüneisen's ratio and the porosity parameter m .

REFERENCES

1. K. K. Krupnikov, M. I. Brazhnik, and V. P. Krupnikova, JETP 15, 470 (1962).
2. S. B. Kormer, A. I. Funtikov, V. D. Urlin, and A. N. Kolesnikova, JETP 15, 477 (1962).

INITIATION OF A SOLID EXPLOSIVE BY A SHORT-DURATION SHOCK

Elisabeth F. Gittings
*Los Alamos Scientific Laboratory
University of California
Los Alamos, New Mexico*

ABSTRACT

The use of the pin-contactor technique for studying the shock initiation of a solid explosive is reviewed. A form of the technique is used to determine what happens when explosive pellets are struck by free-flying aluminum foils 4-62 mils thick, and some experimental data are given. Detonation will occur in a one-quarter-inch thick pellet of HMX 9404-03 hit by a 5-mil aluminum foil moving at a velocity of 2 mm/ μ sec. As the thickness of the foil is increased, the excess transit time of the pellet quickly approaches that of a pellet hit by a thick dural plate moving at the same velocity. Some experimental difficulties are also discussed.

EXPERIMENTS WITH SUSTAINED SHOCKS

The pin contactor technique has been used to study the shock initiation of a solid explosive by having a flat projectile strike a disc-shaped pellet of explosive and making measurements of the velocity of the projectile, the time when the projectile strikes the pellet, and the time when the detonation wave emerges from the far side of the pellet. A standard experimental arrangement is shown in Fig. 1. In this investigation the projectile was dural and the pellet was HMX 9404-03. The pellet was usually one inch in diameter and one-quarter-inch thick.

In experiments with sustained shocks the projectile is always thick enough so that all measurements are completed before the

pressure is relieved at the projectile-pellet interface. By changing the driver explosive, or by inserting an attenuator between it and the projectile, the velocity of the projectile can be varied from 0.7 mm/ μ sec to more than 3 mm/ μ sec. The time interval between the signal from a pin flush with the near surface of the pellet and the signal from a pin in contact with the far surface of the pellet is measured and is called the transit time of the pellet. Since the detonation velocity of 9404-03 is known from work by other members of this laboratory the excess transit time Δt can be obtained by subtracting from the measured transit time the time which it would have taken a fully established detonation to travel the thickness of the pellet. In Fig. 2 the excess transit time of 9404-03 is shown as a function of the velocity of the dural projectile. This graph is for 9404-03 with a density range

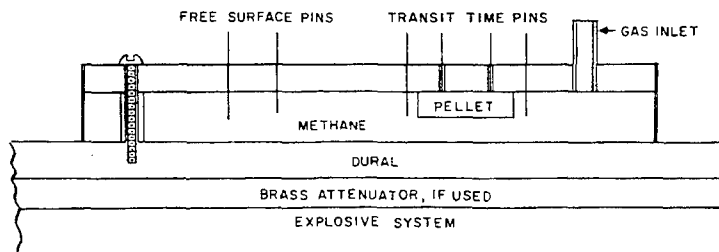


Fig. 1 - Experimental arrangement, sustained shocks

This work was supported by the U.S. Atomic Energy Commission.

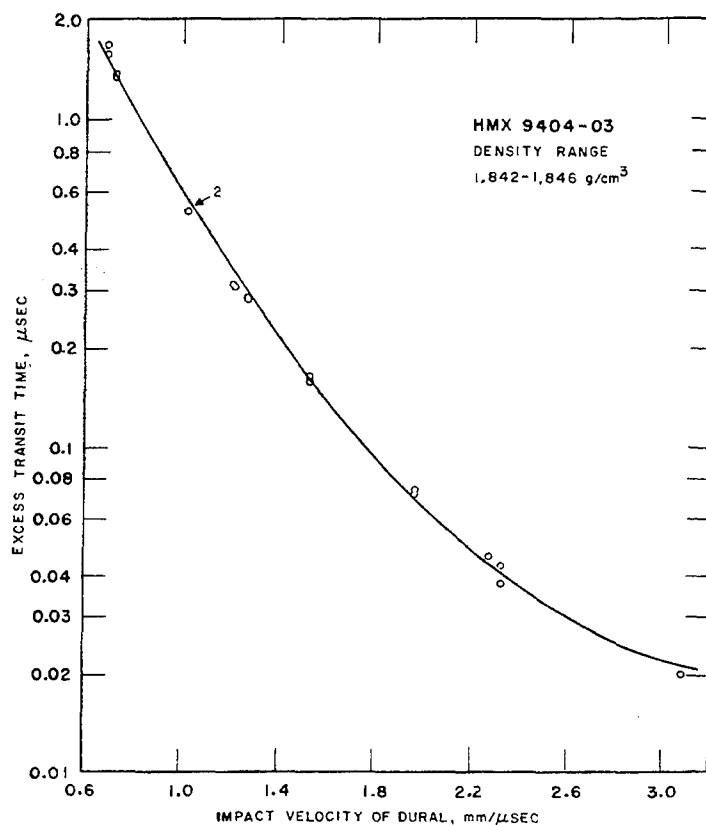


Fig. 2 - Effect of impact velocity on excess transit time

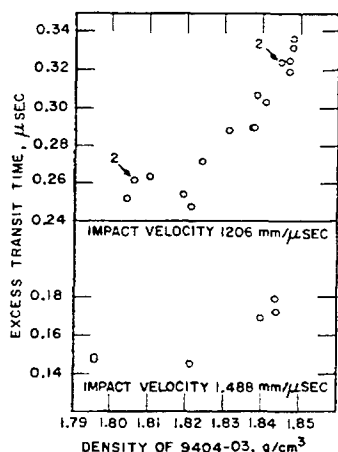


Fig. 3 - Effect of density on excess transit time

of 1.842-1.846 g/cm³. A similar graph, which is not shown, was made for material with a density range of 1.836-1.840 g/cm³. The effect at constant velocity of variations in density is

shown in Fig. 3. The scatter among these data from experiments with sustained shocks is quite small. This is not true of the data obtained from experiments with short-duration shocks.

SHORT-DURATION SHOCKS

When the experimental procedure was modified to adapt it to experiments with short-duration shocks it was necessary to ensure that the pressure pulse did a reasonably good job of dropping to zero at the required time. This was done by making the projectile plate a foil and arranging that it be unsupported for the duration of the experiment. The easiest way to provide an unsupported foil is to fly it, like an artificial spall, from the surface of a plate of material of higher ρU . Consider Fig. 4. At "A", the shock from the explosive driver enters the heavy pusher; at "B", it enters the foil; and at "C", the foil starts to move. At "D", the rarefaction from the free surface of the foil reaches the pusher-foil interface and the materials separate. If the distance between the pellet and the foil is d_x , the length of time

the earliest experiments with short-duration shocks this space was filled with methane. The reasoning which originally led to the use of a vacuum between the foil and pellet now seems dubious but the vacuum does make a difference in the Δt 's obtained in experiments with very short duration shocks.

EXPERIMENTAL RESULTS

These data were reduced to a more manageable form. The measured quantities available for each experiment were the density and thickness of the 9404-03 pellet, the thickness and velocity of the aluminum foil, and the transit time through the pellet. From this last quantity was calculated the excess transit time Δt which is identified in Tables 1 and 2 as Δt_{meas} . In addition a calculation was made of what the excess transit time would have been if the pellet had been hit by a thick dural plate instead of by a foil. This time is called Δt_{calc} . The difference between the observed and the calculated excess transit times, $\Delta t_{\text{meas}} - \Delta t_{\text{calc}}$, gives an indication of the extent to which the initiation of detonation was delayed by the short duration of the shock. This indication is rather rough: a quarter-inch pellet which barely detonates when struck by a foil with a velocity of 1.4 mm/ μ sec

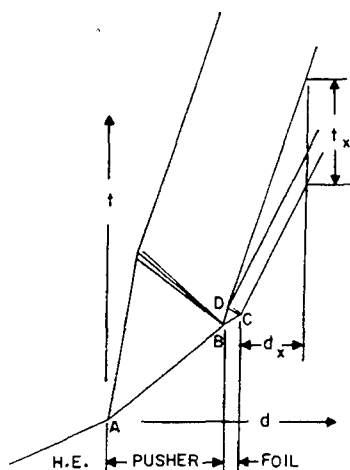


Fig. 4 - Detachment of foil from pusher

The current design for a flying foil experiment is shown in Fig. 5. This arrangement is such that two different foils; each of which strikes two pellets of explosive, can be used on a single shot. In the space between the foil and the pellet is a vacuum of about 10 microns. In the experiments with sustained shocks and in

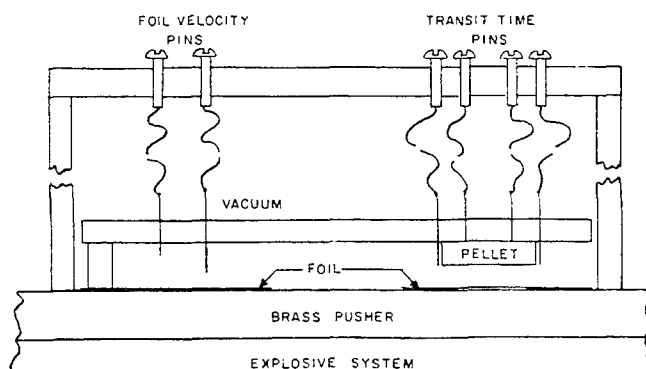


Fig. 5 - Idealized experimental arrangement, short-duration shocks

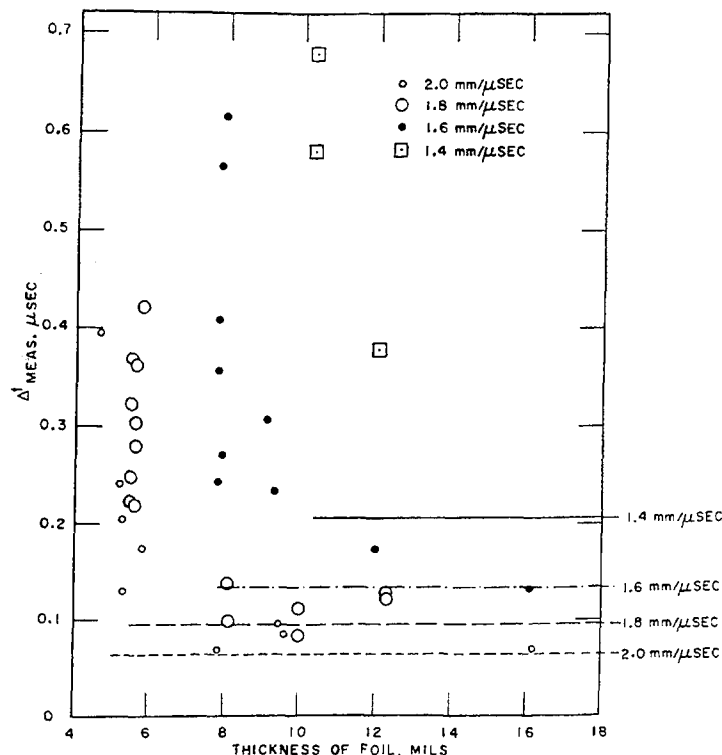


Fig. 6 - Raw data from foil experiments

has a difference in excess transit times of $0.39 \mu\text{sec}$, but one which barely detonates when struck by a foil with a velocity of $2.0 \text{ mm}/\mu\text{sec}$ has a difference in excess transit times of $0.33 \mu\text{sec}$.

A useful description of a short-duration shock is given by R which is defined as the ratio of the duration of the shock to the time to detonation of the explosive when subjected to a sustained shock of the same magnitude. This quantity can be calculated from the available data. Consider Fig. 7 which is adapted from Ramsay's Fig. 1 [1]. The time to detonation t_b can be closely approximated by

$$t_b = \frac{\Delta t_{\text{calc}} D_0}{D_0 - \bar{U}_s}$$

To obtain \bar{U}_s one uses the Hugoniot for dural [2]. Ramsay's experimentally determined Hugoniot for 9404-03 [1], and the velocity of the foil. (See Fig. 8.) An exact value for the duration of the shock is not obtainable but an approximate value t_a is the time required for a shock to travel twice the thickness of the foil. The shock velocity in the foil is also obtained by the technique shown in Fig. 8 but in this case one uses Ramsay's Hugoniot for unreacted 9404-03 [1]. The

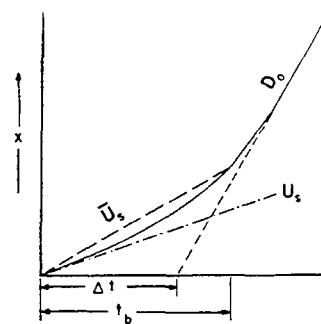


Fig. 7 - Plot of shock initiation

results of these calculations are shown in Tables 1 and 2 and in Fig. 9. They indicate that, in the range of pressures used in these experiments, 9404-03 will usually detonate if the duration of the initiating shock is about one-fifth of the time to detonation calculated for a sustained shock. For such brief shocks the excess transit time is large but as the duration of the shock approaches one-third of the time to detonation for a sustained shock the Δt_{meas} drops to a value only slightly higher than Δt_{calc} .

TABLE 1
Data From Flying Foil Experiments Conducted in a Methane Atmosphere

Shot No.	Foil Velocity (mm/ μ sec)	Foil Thickness (mils)	Δt_{meas} (μ sec)	$\sigma_{\Delta t}$ (μ sec)	Δt_{calc} (μ sec)	$\Delta t_{meas} - \Delta t_{calc}$ (μ sec)	t_a (μ sec)	t_b (μ sec)	$R = t_a/t_b$	Comments
1239	1.61	4.0			0.138		0.033	0.327	0.102	a
1242	1.61	4.2			0.137		0.035	0.325	0.108	a
1237	1.59	4.7			0.142		0.039	0.334	0.118	a
1272	1.57	5.7			0.144		0.048	0.338	0.142	a
1239	1.61	5.6			0.137		0.047	0.324	0.144	a
1233	1.61	5.7			0.137		0.048	0.325	0.147	a
1240	1.85	4.1			0.087		0.034	0.227	0.148	a
1242	1.62	5.7			0.134		0.048	0.319	0.150	a
1240	1.86	4.7			0.086		0.039	0.226	0.170	a
1235	2.02	4.3			0.066		0.035	0.185	0.188	a
1225	2.05	4.3			0.063		0.035	0.179	0.193	b
1272	1.58	7.7			0.139		0.065	0.327	0.198	b
1239	1.61	7.7			0.137		0.064	0.325	0.198	b
1226	2.09	4.3			0.059		0.034	0.171	0.202	b
1222	2.02	4.6	0.395	0.032	0.066	0.329	0.037	0.184	0.202	
1229	1.61	7.9	0.613	0.027	0.137	0.476	0.066	0.325	0.203	
1242	1.62	7.8	0.408	0.028	0.134	0.274	0.065	0.319	0.204	
1233	1.62	7.8	0.565	0.023	0.134	0.431	0.065	0.319	0.204	
1240	1.87	5.8	0.421	0.035	0.084	0.337	0.048	0.223	0.213	
1272	1.58	9.1	0.306	0.016	0.142	0.164	0.076	0.332	0.230	
1224	2.04	5.2	0.240	0.010	0.064	0.176	0.042	0.181	0.231	
1235	2.03	5.3	0.204	0.013	0.064	0.140	0.043	0.182	0.235	
1226	2.04	5.3	0.129	0.023	0.064	0.065	0.043	0.181	0.236	
1233	1.63	9.3	0.233	0.013	0.132	0.101	0.078	0.315	0.246	
1225	2.05	5.8	0.174	0.022	0.062	0.112	0.047	0.178	0.263	
1237	1.61	12.0	0.174	0.006	0.136	0.038	0.101	0.323	0.311	
1225	2.02	7.8	0.071	0.026	0.066	0.005	0.063	0.185	0.341	
1224	2.03	9.4	0.096	0.011	0.064	0.032	0.076	0.182	0.418	
1222	2.04	9.6	0.087	0.043	0.063	0.024	0.077	0.179	0.433	
1229	1.65	16.1	0.132	0.011	0.127	0.005	0.134	0.306	0.439	
1226	2.03	16.2	0.071	0.008	0.064	0.007	0.131	0.182	0.719	

$$t_a = \frac{2 \times \text{foil thickness}}{U_{\text{dural}}}$$

t_b = time to detonation for sustained shock.

a = Pellet detonated when hit by heavy metal pusher.

b = No detonation was observed.

TABLE 2
Data from Flying Foil Experiments Conducted in a Vacuum

Shot No.	Foil Velocity (mm/ μ sec)	Foil Thickness (mils)	Δt_{meas} (μ sec)	$\sigma_{\Delta t}$ (μ sec)	Δt_{calc} (μ sec)	$\Delta t_{\text{meas}} - \Delta t_{\text{calc}}$ (μ sec)	t_a (μ sec)	t_b (μ sec)	$R = t_a/t_b$	Comments
1260	1.60	4.6			0.136		0.039	0.321	0.120	A
1262	1.61	4.6			0.133		0.039	0.316	0.122	A
1262	1.61	5.7			0.133		0.048	0.316	0.151	A
1260	1.61	5.8			0.134		0.049	0.318	0.153	A
1336	1.61	5.9			0.134		0.049	0.318	0.155	A
1563*	1.79	4.8			0.097		0.040	0.248	0.160	A
1563	1.79	4.8			0.097		0.040	0.248	0.160	A
1336*	1.64	5.9			0.127		0.049	0.305	0.162	A
1565	1.78	5.5	0.369	0.047	0.100	0.269	0.045	0.253	0.179	
1565	1.78	5.5	0.248	0.065	0.100	0.148	0.045	0.253	0.179	
1563*	1.78	5.5	0.323	0.023	0.099	0.224	0.045	0.253	0.179	
1563	1.78	5.5	0.224	0.046	0.099	0.125	0.045	0.253	0.179	
1381	1.39	10.3	0.581	0.009	0.214	0.367	0.088	0.468	0.188	
1558*	1.82	5.6	0.279	0.029	0.093	0.186	0.046	0.241	0.191	
1558	1.82	5.6	0.239	0.030	0.093	0.146	0.046	0.241	0.191	
1558	1.82	5.6	0.304	0.094	0.093	0.211	0.046	0.241	0.191	
1558*	1.82	5.6	0.362	0.013	0.093	0.269	0.046	0.241	0.191	
1381	1.39	10.3	0.681	0.009	0.203	0.478	0.088	0.445	0.198	
1384	1.40	10.3			0.201		0.088	0.441	0.199	B
1583†	0.75	49.5	2.843	0.117	1.247	1.596	0.448	2.186	0.205	C
1583†	0.75	49.5	2.854	0.179	1.247	1.607	0.448	2.185	0.205	C
1260	1.61	7.9	0.271	0.023	0.133	0.138	0.066	0.316	0.209	
1262	1.64	7.8	0.244	0.031	0.126	0.118	0.065	0.303	0.215	
1336	1.66	7.8	0.355	0.024	0.122	0.233	0.065	0.296	0.220	
1381	1.38	12.0	0.378	0.024	0.212	0.166	0.102	0.461	0.221	
1562	1.80	8.1	0.100	0.012	0.096	0.004	0.067	0.246	0.271	
1562	1.80	8.1	0.139	0.024	0.096	0.043	0.067	0.246	0.271	
1574†	0.78	62.3	1.122	0.122	1.124	-0.002	0.557	1.990	0.280	
1574†	0.78	62.3	1.137	0.062	1.124	0.013	0.557	1.991	0.280	
1565	1.80	10.0	0.113	0.013	0.095	0.018	0.082	0.244	0.338	
1565	1.80	10.0	0.083	0.008	0.095	-0.012	0.082	0.244	0.338	
1562	1.76	12.3	0.122	0.047	0.102	0.020	0.102	0.258	0.394	
1562	1.76	12.3	0.130	0.017	0.102	0.028	0.102	0.258	0.394	

$$t_a = \frac{2 \times \text{foil thickness}}{U_{\text{dural}}}$$

t_b = time to detonation for sustained shock.

* = 3/8" pellet, 1" diameter.

† = 0.6" pellet, 1.8" diameter.

A = Pellet detonated when hit by pusher.

B = No detonation observed.

C = Partial detonation.

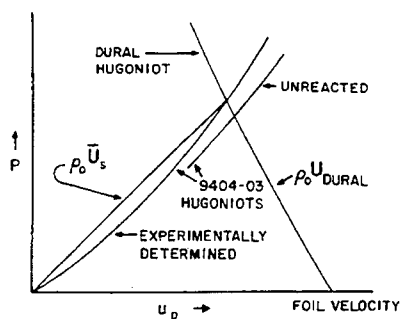


Fig. 8 - Determination of \bar{U}_s and U_{dural}

If the duration of the shock is very short the pellet of explosive is damaged so little that it later detonates, apparently when hit by the heavy metal pusher. Experiments in which this happened are identified by "a" in Tables 1 and 2. In some cases a measureable pulse never was obtained from the pins on the far side of the pellet. These experiments have been designated "b" in the tables.

DIFFICULTIES

The biggest trouble with flying foil experiments is that there is a large scatter in the

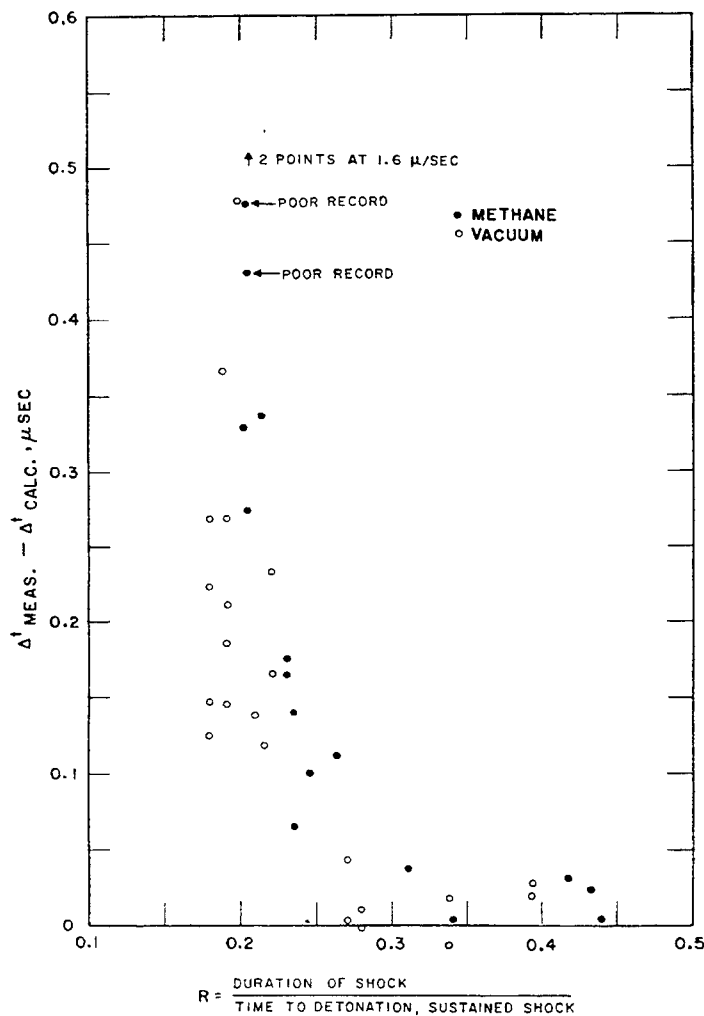


Fig. 9 - The increase in excess transit time caused by the short duration of the initiating shock

data. In pellet shots with sustained shocks it is expected that the excess transit times for different pellets of the same density will not differ by more than the standard deviation of the measurements on any one pellet even if the excess transit times are as large as one-half microsecond. This is not true for pellet shots with short-duration shocks. At first much effort was wasted in trying to track down the reasons for large differences between Δt 's from almost identical experiments. Finally enough data were accumulated to justify the assumption that, with one exception, the observed differences were random. The difference which is reproducible is that between experiments performed in a vacuum and those performed in a methane atmosphere. This can be seen on Fig. 9.

Other troubles with foil experiments are the difficulty of obtaining consistently good pulses from the velocity pins and the fact that velocity measurements on foils are usually not as accurate as those made on thick plates. The

uncertainty in the foil velocity can change the ratio $R = t_a/t_b$ by as much as 5% in an extreme case.

ACKNOWLEDGMENTS

The author wishes to thank the various people who have assisted in this project, especially Earl Faudree who assembled and fired most of the shots.

REFERENCES

1. "Analysis of Shock Wave and Initiation Data for Solid Explosives," J. B. Ramsay, A. Popolato, this symposium.
2. "Shock Wave Compressions of Twenty-Seven Metals," J. M. Walsh, M. H. Rice, R. G. McQueen, and F. L. Yarger, Phys. Rev. Vol. 108, #2, Oct. 15, 1957, pp. 196-216.

OBLIQUE IMPACT OF A LAYER OF EXPLOSIVE BY A METAL PLATE

F. David, C. Fauquignon, H. Bernier and J. Potau
*Commissariat à l'Energie Atomique
France*

ABSTRACT

It is known that the impact of a metal plate upon an explosive can initiate its detonation. When the metal plate comes in contact with the layer of explosive, not all at once but gradually, an oblique detonation wave is initiated. The possible configurations of flow are studied in the neighbourhood of the point of impact in two-dimensional plane permanent geometry. Under certain conditions it is shown theoretically, that the compatibility at the interface can be achieved only by taking into account an overdetonation wave of given characteristics. Experiments point to the existence of such a wave. By tracing graphs its characteristics may be measured.

INTRODUCTION

A metal plate, thickness ϵ , is bent through an angle ϕ by means of a detonation wave, speed D_0 , travelling through a layer of explosive. When the plate is deflected, it hits at an angle of incidence i , a block of explosive, density ρ_0 (Fig. 1). The thicknesses are sufficiently small compared to the other quantities so that the flow can be considered as plane two-dimensional and stationary. The reference system R has its origin at the point of impact I and is under uniform linear motion. Theoretical and experimental studies of the flow are carried out in the vicinity of the point of impact.

NOTATION

We define: specific mass ρ , pressure P , q relative velocity with respect to R . Indices are given to mark regions of flow: 0 for intact explosive and 0' for the metal before impact. Within the reference system the positive sense of rotation is defined as that which swings the plate away from its initial direction; $\theta = (\mathbf{q}_0, \mathbf{q})$ is the angle between the actual and initial vectors at a given point ($-\pi/2 \leq \theta \leq \pi/2$). A wave of discontinuity C_j divides the undisturbed region (k) from the disturbed region (j); ω_j is the projection of \mathbf{q}_j (or \mathbf{q}_k) on C_j and $\alpha_j = (\mathbf{q}_0, \omega_j)$ is the angle made between this projected velocity and the initial velocity \mathbf{q}_0 . ($-\pi/2 \leq \alpha_j \leq \pi/2$).

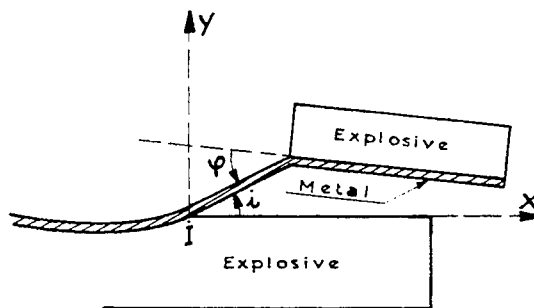


Fig. 1 - Experimental arrangement

This notation enable us to describe waves as coming from "above" or "below."

All the waves take rise in the vicinity of the point of impact so that they arrive into the explosive and its detonation products from above, and into the metal plate from below. For stability we must have $\alpha_j > 0$ and $\alpha_j < 0$ for waves coming from above and below respectively. It follows that the deflection of the velocity vector is positive for a compression wave coming from above or for a rarefaction wave coming from below, while it is negative in the opposite cases. Using the variables: ρ, P, q, θ the equations of continuity and momentum through C_j are written as: (Ref. 1):

$$\tan^2(\theta_j - \theta_k) = \frac{\rho_k \left(1 - \frac{\rho_k}{\rho_j}\right) q_k^2 (P_j - P_k) - (P_j - P_k)^2}{\left[\rho_k q_k^2 - (P_j - P_k)\right]^2}$$

$$q_j^2 = q_k^2 - \frac{P_j - P_k}{\rho_k} \left(1 + \frac{\rho_k}{\rho_j}\right).$$

Equation (1) and the Hugoniot equation $P(\rho)$ of the given substance, whose pole is (ρ_k, P_k) give us a parametric relationship for the shock polar in the θ, P coordinate system. (θ_k, P_k) is the pole of the shock polar.

CONFIGURATIONS IN THE NEIGHBOURHOOD OF THE POINT OF IMPACT

Two theoretical methods are used. The first one assumes that detonation occurs at the instant of impact (simplified method), while the second takes into account the time for the detonation to build up (method of prestressing shock).

Simplified Method

We assume that the explosive detonates by means of a wave issuing from the point of impact. If this wave is taken as discontinuous we can neglect the thickness of the reaction zone. A shock C_1 , arising from the point of impact, travels up the metal plate. In front of C_1 , the absolute velocity of the metal is given, to a good order of approximation, by the velocity of the flying plate: $D_0 \sin \phi$ so that the relative velocity q_0' of the plate makes an angle i with q_0 and has $q_0 \cos i$ for absolute value.

The deflection $\theta_1 = (\theta_0, q_1)$ through C_1 is positive, while the deflection $\theta_1' - i = (\theta_0', q_1')$ through C_1 is negative. In the (θ, P) coordinate system, the point 1' representing the state of the metal behind C_1 is to be found on the left prong of the metal shock polar π_0^m , with pole $(i, P=0)$. If π_0^m lies below the point representing the Chapman Jouguet state in the (θ, P) system (point C.J.) and if the conditions are such that the explosive really detonates, then we can say that C_1 is an ideal detonation wave followed by a beam of rarefaction waves. As π_0^m closes in on the C.J. point, the fan of rarefaction waves narrows down and finally vanishes when π_0^m passes through the point C.J. If π_0^m passes above the C.J. point the compression waves modify in such a way that it becomes an overdetonation wave. This is explained from the fact that the compression waves cannot be added to form a shock C_2 which would follow the ideal

detonation wave: the normal component at C_1 of the down-stream velocity is sonic so that the normal component at C_2 of the upstream velocity cannot be supersonic. States 1 and 1' are thus described in the (θ, P) frame by the lowest point of intersection between π_0^m and the shock polar π_0^g , which is the image of the R-H adiabat of the detonation products, provided intersection occurs. If intersection does not occur there is no solution. Finally, at the point where the shock C_1 meets the free surface of the metal plate there arises a beam of rarefaction waves which, after crossing the plate meets the shock, weakens it and thereby increases its curvature; the state behind C_1 varies continuously and point 1 travels along an arc of π_0^g ; the curvature of C_1 vanishes when 1 coincides with the C.J. point.

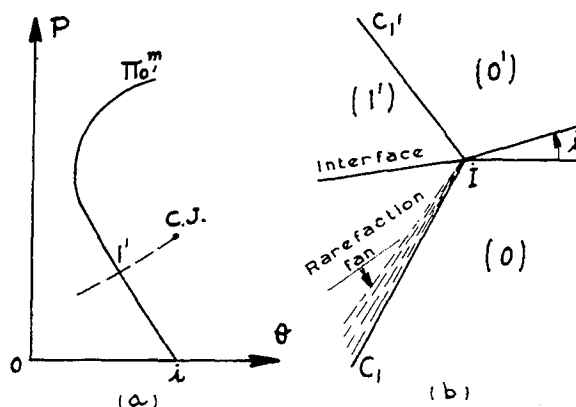


Fig. 2 - Simplified method (1st case); (a) pressure-deflection curve, (b) flow diagram

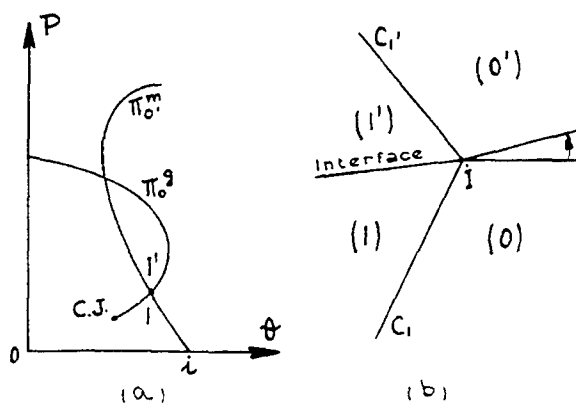


Fig. 3 - Simplified method (2nd case); (a) pressure-deflection curve, (b) flow diagram

Method of the Prestressing Shock

When impact occurs the explosive is subjected to a shock which initiates the chemical reactions more or less rapidly. The layer of explosive in contact with the metal-explosive interface reaches detonation conditions at a distance $q_0 \tau$ from the point of impact (point in Fig. 4), where τ is the induction-delay time. For a given explosive, τ is a function of the strength of the prestressing shock C_{0*} . A detonation wave C_{1*} , initiated at B, has a front whose shape depends upon the rate of reaction of the explosive when met by the shock C_{1*} . For a homogeneous explosive, the thermodynamic quantities are practically constant within the region of induction and the wave is plane. For a heterogeneous explosive, the rate of reaction varies along C_{1*} which is curved, concavity rearwards facing. This description is valid only if the horizontal component of the velocity of C_{1*} is less than q_0 everywhere. Shocks C_{1*} and C_{0*} meet in A; at this point a detonation wave develops in the intact explosive, whose characteristics can be obtained by a graphical method in the (θ, P) frame. When O^* travels along the shock polar π_0^e of the intact explosive, 1^* traces out a curve π^* which, by continuity, has its origin in the C.J. point. 1 is the intersection of π_0^e and the right hand prong of the rarefaction curve Δ (of the detonation products) originating in 1^* ; $1'$ describing the state behind the shock induced in B in the metal plate, is at the intersection of the metal shock polar π_0^m and the left-hand prong of Δ . It can be seen that this solution is possible only if π^* , which is completely unknown a priori, lies entirely within π_0^e .

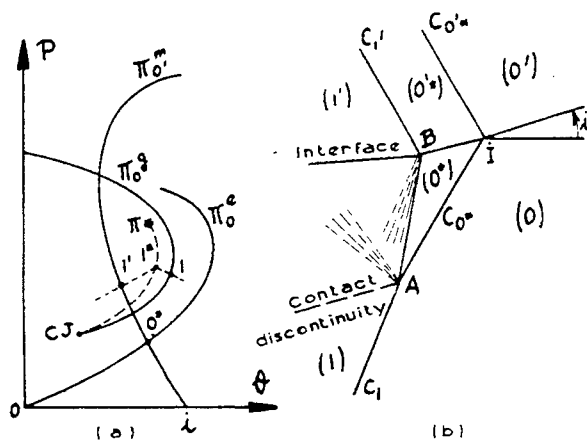


Fig. 4 - Method of prestressing shock: (a) pressure-deflection curve, (b) flow diagram

COMPARISON WITH EXPERIMENT

Figure 5 gives a schematic description of the experimental layout and the type of recording made on photographic plates. The speed of the point of impact:

$$q_0 = D_0 \frac{\sin \phi}{\sin (\phi - \psi)}$$

is measured giving us the angle of plate deflection ϕ :

$$\cot \phi = \frac{q_0 \cos \psi - D_0}{q_0 \sin \psi}$$

and $i = \phi - \psi$. The main point of the experiment is to register the shape of the wave C_1 ; i.e., we want to measure the angle α_1 which C_1 makes with the direction of q_0 in all points and in particular near the point of impact. In other words we want to estimate the curvature of C_1 which is predicted theoretically and established experimentally. In order to carry out these measurements we observe by means of a streak camera (aligned along the plane of symmetry of the apparatus), the luminosity of the air induced by the shock C_1 . The observation is made simultaneously on the face opposite the impact and on the "exit" face of the explosive block. In order to measure α_1 accurately, the exit face is cut away at an angle a approximately equal to α_1 . The reference system on the photographic plate is as follows: t the unit vector of the time axis in the direction of sweep, x the unit vector of the space coordinate towards the image of the point of impact, T the unit vector tangent to image of shock C_1 . $\gamma = (X, T)$ is the angle made between the space coordinate and the tangent to the shock image with the given orientations ($\gamma > 0$ if $\alpha_1 > a$ and $\gamma < 0$ if $\alpha_1 < a$). If v denotes the speed of sweep of the plate, and g the camera magnification, we can write:

$$\cot \alpha_1 = \cot a - \frac{q_0}{v} \times \frac{g}{\sin a} \times \tan \gamma.$$

The inclined position of the explosive block enables us to observe the side opposite the side of impact both directly and by means of a mirror. Two traces of the image of this face are registered, thereby reducing the error of measurement of q_0 . If Γ denotes the angle made between one of these traces and the space-coordinate, then:

$$q_0 = \frac{v}{g} \cot \Gamma.$$

Consider the simplified method: if π_0^m is known then the two measured quantities (α_1 at

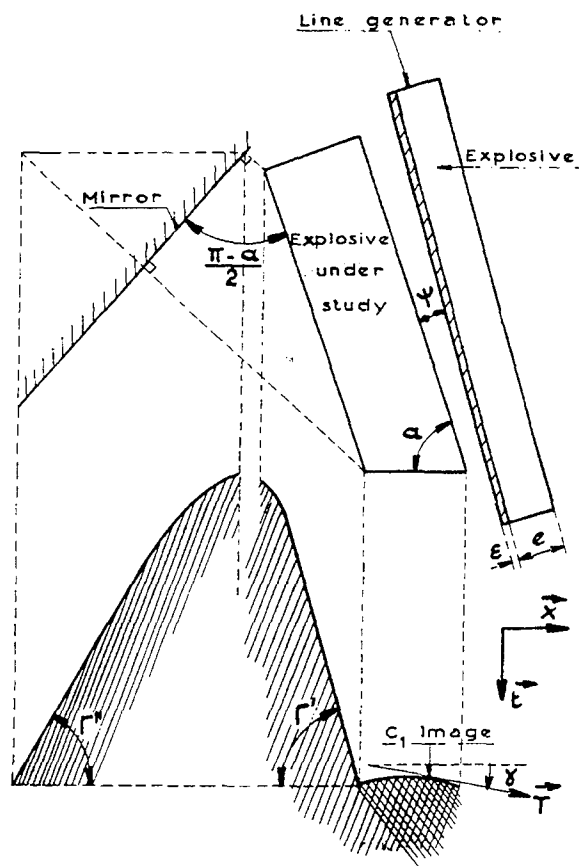


Fig. 5 - Photographic arrangement

the point of impact, and q_0) are sufficient to determine the state 1 in the neighbourhood of the point of impact whenever π_0^g and π_0^m intersect. In (θ, P) space, 1 is then at the intersection of π_0^m and Σ , giving:

$$P = \frac{\rho_0 q_0^2}{1 + \cot \alpha_1 \times \cot \theta}$$

as a function of θ . This equation is obtained by eliminating ρ_0/ρ from the shock equations and ρ_0/ρ is given by:

$$\frac{\rho}{\rho_0} = \frac{\tan \alpha_1}{\tan (\alpha_1 - \theta_1)}$$

In the experiments, copper was projected by means of an explosive of detonation speed $D_0 = 8.15 \text{ mm}/\mu\text{s}$, upon a block of sample explosive D (Ref. 2) of initial density ρ_0 which can vary from experiment to experiment. Plate 1 shows the results obtained when the "simplified method" yields a solution. The experimental point given by Σ and π_0^m , is very near π_0^g , the calculated curve (Ref. 2). Plate 2 shows the results obtained when the "simplified method" does not yield a solution; α_1 , the angle made by C_1 and q_0 in the neighbourhood of the point of impact is about 90° and this value is a deal greater than the value which is obtained when the simplified method yields a solution. Thus the overdetonation velocity is approximately equal to q_0 , i.e., in this case $9 \text{ mm}/\mu\text{s}$. In all measurements, $\hat{\alpha}$ the angle between q_0 and the plane part of shock C_1 , is very close to the theoretical value when C.J. conditions are assumed to hold behind C_1 .

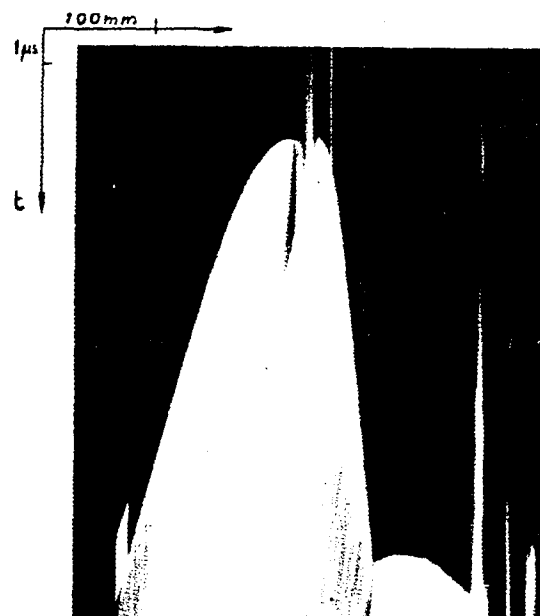
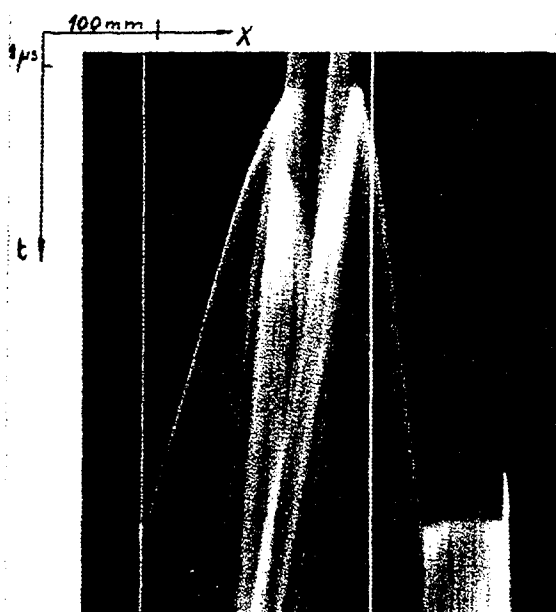
CONCLUSION

The experiment shows clearly that overdetonation occurs at impact. The simplified method seems to give a reasonable account of observation within experimental error, in so far as a solution is possible and knowing that the theoretical π_0^g is not sufficiently accurate. When this method offers no solution, experiments show that the overdetonation shock is very strong and it seems that this shock suffers a large discontinuity as we go from the determinate to the indeterminate case. Finally, no observation can be made of the prestressing shock in the photographs and this is probably due to the smallness of the induction region.

REFERENCES

1. T. Camion, Mémorial de l'Artillerie Française 1962, 2, 357.
2. J. Berger, J. Favier, and Y. Nault Annales de Physique, 13^{ème} série T, 5, 1960.

(We have used results based on chemical equilibrium - unpublished results, rather than those based on frozen equilibrium, as given here.)



$\xi(\text{mm})$	$e(\text{mm})$	ψ	α	ρ_0	$q_0(\text{mm}/\mu\text{s})$
1,5	20	2°	60°	1,61	9,2
φ	i	$\hat{\alpha}_{\text{exp.}}$	$\hat{\alpha}_{\text{theor.}}$	$\alpha_{\text{exp.}}$	$\alpha_{\text{theor.}}$
18°	16°	56°30'	57°	63°	59°

$\xi(\text{mm})$	$e(\text{mm})$	ψ	α	ρ_0	$q_0(\text{mm}/\mu\text{s})$
2	30	2°	70°	1,65	9
φ	i	$\hat{\alpha}_{\text{exp.}}$	$\hat{\alpha}_{\text{theor.}}$	$\alpha_{\text{exp.}}$	$\alpha_{\text{theor.}}$
19°	17°	62°20'	61°55'	87°30'	?

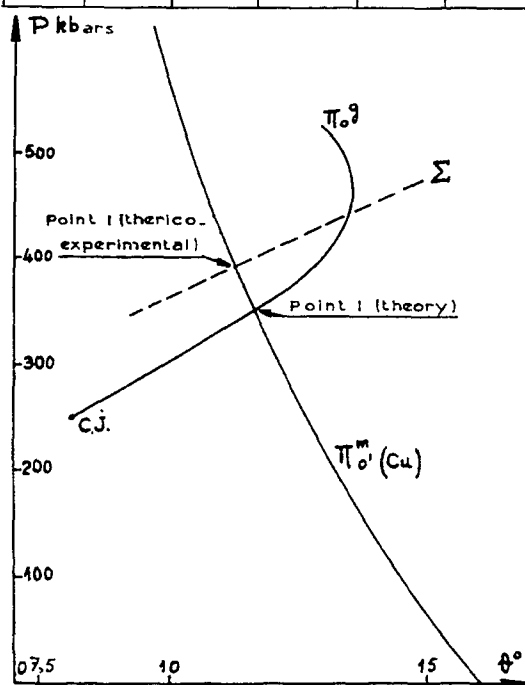


Plate 1 - Simplified method (2nd case), pressure-deflection curve

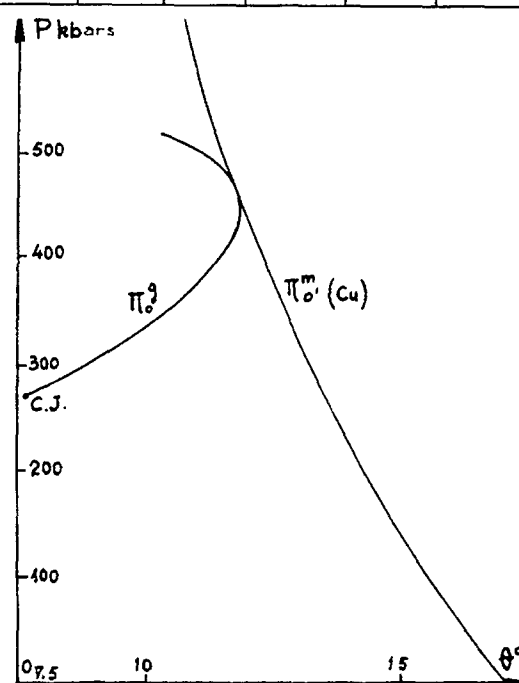


Plate 2 - Simplified method (3rd case), pressure-deflection curve

EXPERIMENTAL OBSERVATIONS OF INITIATION OF NITROMETHANE BY SHOCK INTERACTIONS AT DISCONTINUITIES

J. R. Travis
*Los Alamos Scientific Laboratory
Los Alamos, New Mexico*

ABSTRACT

Shock interactions at density discontinuities introduced into nitromethane compressed by a plane shock wave can reduce the induction time for initiation of detonation near the discontinuity. Experimental results are presented which illustrate this phenomenon and which corroborate the theoretical results presented by Mader in his paper in this symposium. The initiating efficacy of a discontinuity formed by a solid inclusion immersed in nitromethane is strongly dependent on the material used. It is also dependent on the dimensions of the object in the directions parallel and perpendicular to the front of the initiating shock when these dimensions are between a lower critical size and an upper effectively infinite size, and on the angle of incidence between the shock and the discontinuity. Data which relate the induction time to these parameters are presented.

INITIATION AT DISCONTINUITIES

Initiation of detonation in nitromethane compressed by a one-dimensional plane shock wave occurs after an induction time which is determined by the pressure of the initiating shock and the initial temperature of the nitromethane [1]. The shock wave heats the explosive and initiation takes place as a thermal explosion beginning as a detonation in the compressed explosive very near the driver interface, which is where it has been hot longest. Initiation resulting from a shock wave generated by a plane-wave booster in a typical experiment is rough; i.e., initiation is not truly plane but occurs earlier at some points than others. This roughness is attributed to pressure variation along the shock front produced by local shock interactions in the explosive and attenuator materials of the booster. Interactions deliberately introduced in the driving plate or between the initiating wave and an inclusion in the nitromethane can significantly shorten the induction time for detonation in the neighborhood of the interactions. The edges of the nitromethane container, for example, or bubbles adhering to the driving plate can cause early initiation.

The effectiveness of bubbles and shock interactions in general as initiating centers in

liquid explosives has long been recognized. Bowden and Yoffe [2] reviewed much of the pertinent research done before 1958. More recently Campbell and co-workers [1] determined the critical bubble size for prompt shock initiation and illustrated the phenomena associated with initiation of detonation by shock bubbles and small solid inclusions. Mader in his paper of this symposium shows that calculations using reactive two-dimensional hydrodynamics can reproduce initiation phenomena which occur near a void or near an aluminum pellet in nitromethane.

The experimental program described in this paper was undertaken to explore in detail how much earlier initiation occurs at discontinuities, in the hope that the mechanisms could be understood. In particular, the effects of size, shape, and shock properties of a solid inclusion on its initiation efficacy were studied for selected geometrical arrangements. Some of the experiments were designed specifically to test Mader's computations.

From the experiments, rules can be found which relate the induction time to the size and the material of the solid inclusion for a specific geometrical arrangement, but to understand and predict completely the initiation phenomena that occur near any discontinuity detailed knowledge

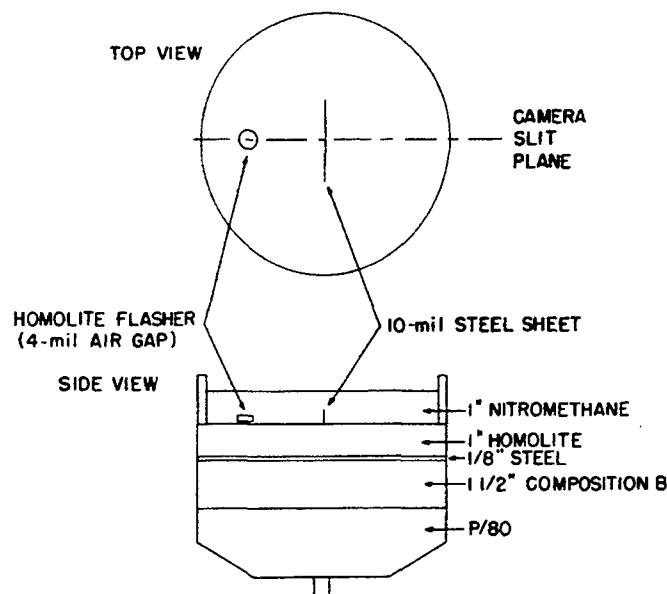


Fig. 1 - Schematic diagrams of an initiation experiment

of the complex shock interactions peculiar to each case is required. This knowledge is not available at present from either experiments or theoretical analysis.

EXPERIMENTAL DESIGN AND ANALYSIS OF THE DATA

Events of interest in the shock initiation of nitromethane at room temperature occur for shock pressures from 80 to 90 kbar. If the initiating shock is much stronger, initiation delay is unresolvable; if much weaker, detonation does not occur within the time of the experiment* even from interactions. The booster systems were designed to produce well-supported shock waves of about 85 kbar in nitromethane. Figure 1 shows a schematic diagram of a shot with a charge diameter of 20 cm. The shock wave from the booster arrives at the attenuator-nitromethane interface simultaneously within $\pm 0.03 \mu\text{sec}$ over an area 10 cm in diameter. The variation in the induction time for initiation over this area in a given shot may be as much as $\pm 0.10 \mu\text{sec}$ about the average of $1.3 \mu\text{sec}$. Thirty-centimeter diameter charges were used

in some of the experiments so that more information could be obtained in each shot.

The quality of the attenuator materials determines the smoothness of the wave. The polyester plastic, Homolite, was chosen because it was as uniform as any material tested and was not attacked by nitromethane.

Solid inclusions were either suspended in the nitromethane or glued to the driving plate along a diameter. Smear camera pictures of the detonation light were obtained by aligning the camera slit on the row of inclusions with the optic axis of the camera perpendicular to the face of the driving plate. A smear camera picture showing early initiation occurring at the edges of a flasher and a steel sheet immersed in nitromethane is reproduced in Fig. 2.

Since the induction time at a discontinuity is dependent on the pressure of the initiating shock, it is necessary to correct the measured times because of the variation in pressure found along the shock front in a given shot and because of the difficulty of reproducing boosters exactly. This was done by reducing each experimental time to a normalized induction time, τ , by dividing the induction time for detonation at the discontinuity, t_1 , by the induction time for detonation in the surrounding plane-shocked region, t_2 . Considerable inaccuracy is inherent in the determination of τ . The onset of detonation near a discontinuity appears as a point on the

*This time, determined by the shot geometry, is less than that required by rarefactions or shocks from the sides or rear of the charge to enter the region of study and is less than $8 \mu\text{sec}$ in these experiments.

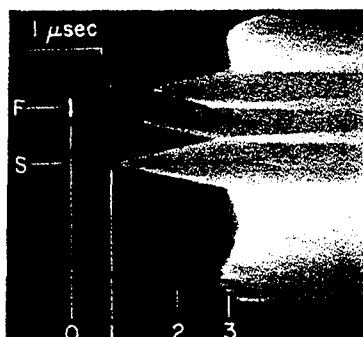


Fig. 2 - Early initiation of nitromethane at discontinuities; time increases to the right;

- F: Homolite flasher
 S: 0.25 mm steel sheet, 12 mm high
 O: Entry of shock into nitromethane, t_0 .
 1. Onset of detonation at edges of steel, t_1 .
 2. Onset of detonation along attenuator surface, t_2 .
 3. Overtake of shock wave by the detonation wave in the compressed nitromethane.

$$\tau = (t_1 - t_0) / (t_2 - t_0)$$

film, sometimes so ill-defined that it is hard to observe. Since initiation in the plane-shocked region is obscured by the detonation expanding from the discontinuity, interpolation is necessary to determine its induction time. The times, t_1 and t_2 , therefore, are often estimates rather than precision measurements, but the error is probably never more than 0.15 μsec .

Considerable care was taken in preparing and mounting the inclusions. It was particularly important that the squared-off end of each inclusion be mounted cleanly on the driving plate with no fillet of glue at the joint. Any bubbles adhering to an inclusion or to the driving plate were wiped away before the shot was fired. Despite these precautions, an occasional record showed evidence of the effect of a perturbation additional to that caused by the inclusion. A few measurements which were well outside the expected range were discarded.

Only results from experiments in which the induction time in the unperturbed plane-shocked regions was between 1 and 1.5 μsec are included in this report. There is some evidence that the nature of the effect of discontinuities changes somewhat as the induction time becomes long ($>3 \mu\text{sec}$).

Several geometrical arrangements of the solid inclusions were used, designated as sheets, slabs, rods, and corners, defined in relation to the plane of the shock front in the following way. A sheet is mounted as shown in Fig. 1 with its shortest dimension (thickness) parallel to the shock front and to the camera slit. A slab forms a step in the driving plate. Its shortest dimension (height) is perpendicular to the shock front, its dimension perpendicular to the camera slit is effectively infinite, and its dimension parallel to the camera slit is effectively infinite in the direction away from the edge of the step. A rod is a long cylinder with its axis perpendicular to the shock front. A corner is a block

of effectively infinite dimensions mounted to form one perpendicular boundary of the nitromethane.

An additional arrangement, using the rod-type inclusion, tested a combination of the effects of angle of incidence and size. Two rods of the same diameter and material were mounted differently, one in contact with the driving plate, the other suspended one-half to one millimeter above the plate. In the first case a shock wave was driven directly into the rod by the shock in the plate. In the second, the shock in the rod was generated by the shock wave in the nitromethane and a reflected wave was sent back into the nitromethane under the end of the rod. A comparison of these two cases provides a test of Mader's computations.

Materials of greatly different shock properties were used. The range in density was from 0.91 to 21.3 g/cc with a corresponding range in shock impedance ($\rho_0 u_s$, where ρ_0 is the initial density and u_s is the shock velocity) of 0.494 to 8.5 g/cm²- μsec . The density of nitromethane is 1.13 g/cc and its shock impedance is 0.508 g/cm²- μsec .

The data are presented in the form of graphs in Fig. 3 through 7. Normalized induction times are plotted against the logarithm of the thickness in Fig. 3 and 4 for sheets. τ vs height is plotted in Fig. 5 for slabs. τ vs logarithm of the diameter is plotted in Fig. 6 and 7 for rods in contact with the driving plate.

An indication of the reproducibility of the data is the mean deviation of the normalized induction time for initiation at the Homolite flasher of $\pm 5.9\%$ obtained from a set of 22 shots.

INITIATING EFFICACY OF DIFFERENT MATERIALS

For all of the materials used as inclusions in these experiments, early initiation occurs if

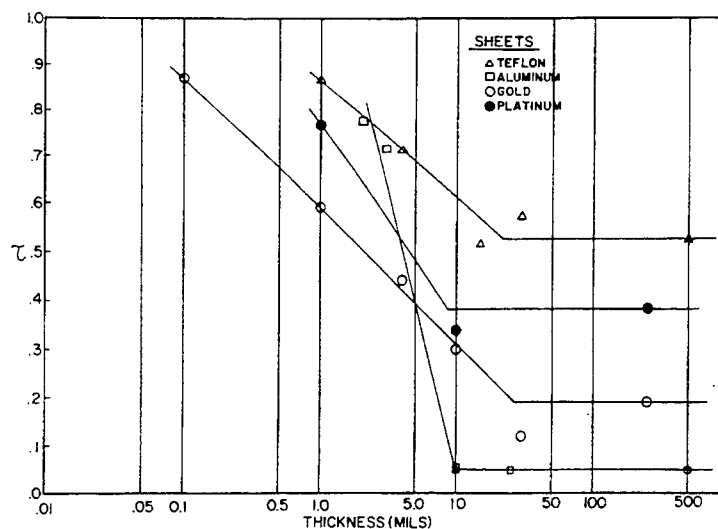


Fig. 3 - τ vs log (thickness) for sheets of Teflon, aluminum, gold, and platinum

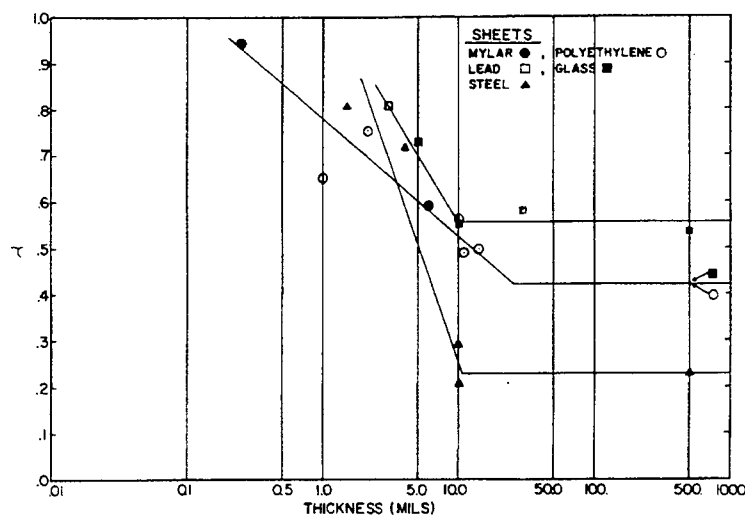


Fig. 4 - τ vs log (thickness) for sheets of lead, polyethylene, Mylar, steel, and glass

the primary* dimension of the inclusion is above a critical value, L_c , which is less than 0.1 mm for the materials and types of inclusions studied. $\tau = 1$ when the primary dimension of a discontinuity is L_c . As the primary dimension of the inclusion is increased, τ decreases until it reaches a minimum. For further increases in

size, the change in τ is dependent on the type of inclusion and the material. As can be seen in Fig. 3 to 7 the variation of τ with dimension in this transition region is very complex. For large enough dimensions, τ becomes constant and is independent of size. This is the value τ_{lim} measured in a corner experiment. Of the types of inclusions studied, a corner should be the simplest to analyze. In sheets, rods, and slabs, shocks (or rarefactions in some cases) interact within the inclusion and are reflected back into the nitromethane, but in a corner there

*The primary dimensions of sheets, slabs, and rods are thickness, height, and diameter, respectively.

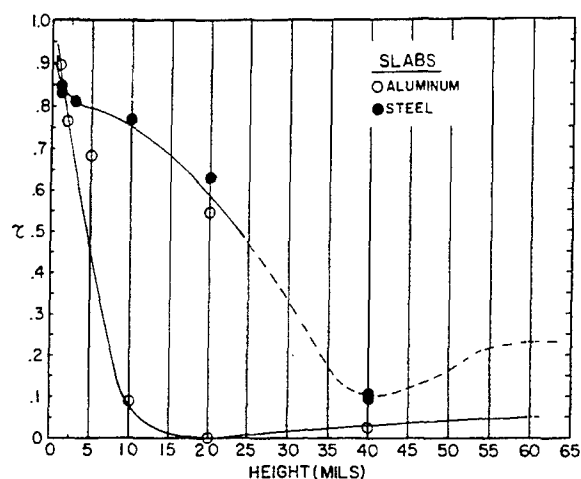


Fig. 5 - τ vs height for slabs of aluminum and steel

is only one interaction, the one at the boundary between the inclusion and the nitromethane.

Even in this case, the initiating efficacy of a material cannot be related in a simple way to any of its shock properties.

This can be seen from the results collected in Table 1. Materials are arranged in order of decreasing efficacy for corner initiation. The initial density of the material and the shock velocity and pressure of the shock wave computed for the simple plane-wave condition are included to illustrate the lack of correlation between shock parameters and initiating efficacy. The shock parameters were determined by impedance matching on the appropriate $P-u_p$ plot for the shock at the boundary between the

Homolite* and the inclusion. Some examples will illustrate the point. The shock impedance of polyethylene differs from that of nitromethane by only 3%, but when used as an inclusion, it can reduce the induction time for initiation in its neighborhood by 60%. Glass which has a shock velocity nearly that of nitromethane causes early initiation effectively. The densities of materials when arranged in order of τ_{lim} are almost randomly distributed.

Clearly, trying to relate initiating efficacy to plane-wave shock properties is an oversimplified approach. Exact treatment of the interaction at the discontinuity is needed to determine the effectiveness of a given material.

The preceding discussion considers initiating efficacy in the limit of large dimensions. Consider now the critical limit, L_c , below which no effect is resolved. Table 2 lists materials in order of decreasing efficacy determined by the critical thickness. Also included are the minimum thickness which caused early initiation and τ_{lim} . L_c is the intersection of the line fitted to the plot of τ vs logarithm of the primary dimension and the line $\tau = 1$. Since the data are not accurate nor complete enough for good curve fitting, the extrapolated values should be considered only as estimates. The order of materials determined by L_c is different from the order based on minimum τ_{lim} but again cannot be simply related to shock properties. The critical dimension, L_c , is smaller for sheets (.04 to 1.5 mils) and slabs (<1.5 mils) than for rods (3 to 7 mils).

*Or nitromethane, since the resulting values are the same within the precision of the listed values.

TABLE 1
 τ_{lim} for Different Materials

Material	Density (g/cc)	u_s^a (mm/sec)	p_a (kbar)	τ_{lim}
Aluminum	2.8	5.9	162	.05
Gold	19.2	3.6	230	.16
Stainless Steel	7.8	4.9	206	.23
Silver	10.5	4.0	210	.29
Nylon	1.15	-	-	.36
Platinum	21.4	4.0	237	.39
Polyethylene	0.91	5.4	85	.42
Glass	2.24	4.6	120	.43
Homolite	1.22	5.0	96	.46
Teflon	2.15	4.1	117	.52
Lead	11.3	3.0	199	.53

^aPressure and shock velocity in the inclusion calculated from impedance matching at the boundary between the driving plate and the inclusion.

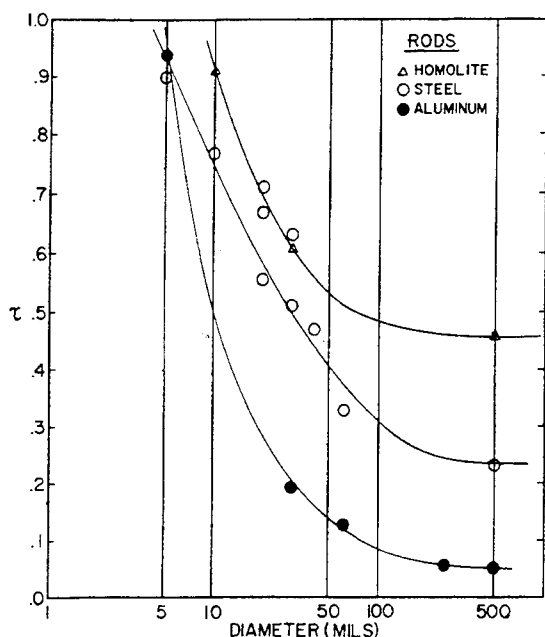


Fig. 6 - τ vs log (diameter) for rods of Homolite, steel, and aluminum

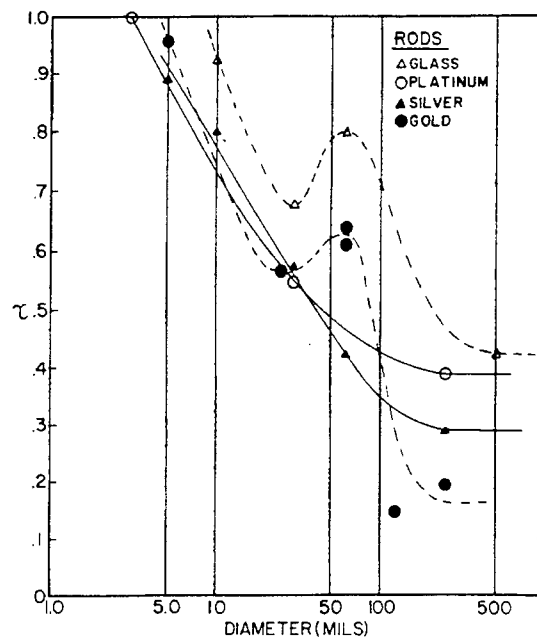


Fig. 7 - τ vs log (diameter) for rods of glass, platinum, silver, and gold

TABLE 2
Critical Thicknesses for Different
Materials from Sheet Experiments

Material	L_c^a (mils)	L_{lim}^b (mils)	τ_{lim}
Gold	0.04	0.1	.16
Mylar	-	0.25	-
Polyethylene	0.15	1.5	.42
Platinum	0.3	1	.39
Teflon	0.3	1	.52
Iron (Stainless Steel)	1.3	1.5	.23
Lead	1.2	3	.53
Aluminum	1.5	3	.05

^aObtained by graphical extrapolation; see text.

^bMinimum thickness used which caused early initiation.

EFFECT OF GEOMETRY ON τ

As was pointed out in the preceding section, the effect of geometry on τ is pronounced. The details of the dependence of τ on dimension have not been worked out, but some of the important features are illustrated by the graphs in Fig. 3 through 7. Consider sheets first. The curves in Fig. 3 and 4 are plotted showing exponential dependence on thickness from $\tau = 1$ to $\tau = \tau_{lim}$. There is some evidence that there is a dip in

the curve followed by a rise before τ_{lim} is reached when the thickness is about 10 mils, but it is not well resolved. The curves for data from slabs, Fig. 5, show broad minima in τ before τ_{lim} is reached. The curves in Fig. 7 for the data from glass and gold rods have a pronounced peak in τ occurring in a limited range in diameter (between 40 and 80 mils for gold). In all likelihood similar peaks should appear in the curves for the other rods. Perhaps experiments with rods of diameter between 40 and 100 mils will reveal additional complexities in the curves.

If its dimensions are greater than a few mils an inclusion of aluminum in any of the forms tried is the most effective initiator of all materials tested. Gold is the next most effective material, particularly when used as a sheet. A complete description of the curves is probably not useful at this time, but an intercomparison of the effectiveness of aluminum, gold, and steel will illustrate several interesting points. The relative effectiveness of these materials when used as sheets changes from the order gold, steel, and aluminum when the thickness is less than 2 mils to aluminum, gold and steel for sheets greater than about 50 mils.

As rods, aluminum is the most effective at all diameters, gold and steel are about equally

effective for diameters less than 40 mils, but gold is more effective than steel for diameters greater than 80 mils.

Only aluminum and steel were tested as slabs. The shapes of the two curves are different, but both show that a slab of a given material some tens of mils high is a better initiator than a corner.

TESTS OF MADER'S COMPUTATIONS AND EFFECT OF ANGLE OF INCIDENCE

The initial angle of incidence between the shock wave in the nitromethane and the discontinuity boundary was 0° in the experiments already discussed. Attempts with wedges to investigate the effect of oblique angles between the shock front and the boundary were unsuccessful. The toe of the wedge must be sharp or initiation occurs from the slab-type discontinuity formed there. Better wedges were required for the experiments than were available.

The effect of head-on shock interactions (90° angle of incidence) was determined for the restricted case of rod initiation. As can be seen in Table 3, the reduction of τ , found when a rod was suspended in the nitromethane, shows that a head-on shock interaction initiates nitromethane more effectively than a 0° interaction at an edge. This observation supports Mader's computations which predict the formation of an initiating hotspot below the shocked rod. He calculates that detonation becomes apparent along the boundary of an aluminum rod 0.64 mm in diameter about $0.08 \mu\text{sec}$ after the shock hits the bottom face of the rod. Experimentally an induction time of $0.12 \mu\text{sec}$ was measured for

initiation at an aluminum rod 0.75 mm in diam. Mader found that initiation would not occur if a shock of the same strength as that used in the above calculation interacted with an aluminum rod 0.04 mm in diam. This agrees with the observed critical diameter of 0.06 mm below which no initiation is expected for a rod in contact with the driving plate. Although no experiments were done with suspended aluminum rods of this small diameter, results with silver rods indicate that the effectiveness of the hotspot under the rod end becomes small as the diameter approaches the critical value.

Mader also reports initiation occurring at a void in nitromethane. His results agree well with the experimental ones reported by Campbell and co-workers [1] and referred to earlier in this paper.

DISCUSSION

No simple relationship between initiating efficacy and shock properties has been found. This is not surprising considering the complex nature of the dependence of τ on the geometry of the inclusion. Although it is not shown directly by these experiments, shock interactions appear to be the most probable cause of early initiation at a discontinuity. The agreement noted in this paper between the experimental results and Mader's calculations gives some support to this interpretation. In subsequent work Mader attempted to calculate initiation behavior at an aluminum corner [3]. Although he could not resolve details of the shock interactions or plot the progress of reaction well, his results indicated that corner shock interactions were sufficiently strong to cause initiation. He observed no jets.

TABLE 3
 τ for Rods in Contact With and Suspended Above the Driving Plate

Diameter (mils)	τ^a			
	<u>5</u>	<u>10</u>	<u>20</u>	<u>30</u>
Aluminum C ^b S ^c				0.19(7) \pm .034 0.09(6) \pm .043
Stainless Steel C S			0.56 0.54(2)	0.46(2) 0.25
Silver C S	0.88 0.87	0.80 0.74(2)		

^aThe number of experiments in parentheses, when more than 1, is given following the value of τ .

^bRod in contact with driving plate.

^cRod suspended 1/2 to 1 mm above plate.

Campbell and co-workers reported at the Second ONR Symposium [4] results from an entirely different kind of experiment with metal foils which add further support to these ideas. It was found that thin foils lining a glass tube of diameter close to the failure diameter of nitromethane prevented the development of failure waves. The effectiveness of the metals tried was correlated with the density, thickness, and shock properties of the foil and was independent of the surface quality of the foil.

Other mechanisms have been postulated of which boundary instabilities and chemical sensitization will be considered here.

The strong dependence on size of the initiating efficacy of sheets of the same material (and the same surface quality) shows that boundary instabilities or turbulence are probably not responsible for initiation. Since all of the materials used are chemically stable in nitromethane, no local sensitization is to be expected. The anomalous performance of aluminum suggested possible surface effects. One aluminum rod, 1/4 inch in diameter, was coated with a very thin, smooth layer of Apiezon grease. Early initiation was observed at the rod with the expected τ , ruling out sensitization as an important mechanism.

Although shock interactions appear to be the primary mechanism, some unaccountable results have been found. No material has been found that can be inserted as an inclusion with a minimum dimension greater than 0.1 mm which will not cause early initiation in its neighborhood. Materials with shock velocities higher and lower than the nitromethane shock velocity are equally effective. A material which has a

shock impedance close to that of nitromethane is as effective as one which has an impedance greatly different. Perhaps the most surprising result is the great effectiveness of aluminum. All of these results lead to the conclusion that if shock interactions are the primary initiating mechanism, the initiating efficacy of a particular material in a particular configuration must be determined by the specific nature of the shock interactions. The angle between the shock wave in the nitromethane and the shock in the material forming a corner must be an important parameter. The additional complication of the interaction of shocks and rarefactions within rods and sheets must be considered. Details of these shock interactions must be discovered before the initiation at discontinuities can be understood fully.

ACKNOWLEDGMENT

This work was performed under the auspices of the United States Atomic Energy Commission.

REFERENCES

1. A. W. Campbell, W. C. Davis, and J. R. Travis, *Physics of Fluids*, **4**, 498, (1961).
2. F. P. Bowden and A. D. Yoffe, *Fast Reactions in Solids*, 1958.
3. C. L. Mader, *The Two-Dimensional Hydrodynamic Hot Spot*, Volume II, Los Alamos Scientific Laboratory Report, LA-3235, 1965.
4. A. W. Campbell, M. E. Malin, and T. E. Holland, *Detonation in Homogeneous Explosives*, Second ONR Symposium on Detonation, 1955.

INITIATION OF DETONATION BY THE INTERACTION OF SHOCK WITH DENSITY DISCONTINUITIES*

Charles L. Mader
*Los Alamos Scientific Laboratory
Los Alamos, New Mexico*

ABSTRACT

The basic processes in the shock initiation of homogeneous explosives have been investigated theoretically using the model of a cylinder of nitromethane containing a void or an aluminum pellet. The interaction of a shock with the density discontinuities, the resulting formation of a hot spot, and the buildup to propagating detonation were computed using two-dimensional numerical hydrodynamics of the "PIC" type with chemical reaction and accurate equations of state. The hot spots formed at aluminum pellets exhibit failure or propagation of detonation in approximately the same manner as the one dimensional, hydrodynamic hot spots studied previously. The failure of hot spots formed at voids could be studied only in those cases in which the failure mechanism did not depend on details of the structure of the reaction zone, as this structure could not be reproduced in the calculation.

*This paper has been published in *Phys. Fluids* 8, 1811-16 (1965).

AN EQUATION OF STATE AND DERIVED SHOCK INITIATION CRITICALITY CONDITIONS FOR LIQUID EXPLOSIVES

Julius W. Enig and Francis J. Petrone
*U.S. Naval Ordnance Laboratory, White Oak
Silver Spring, Maryland*

ABSTRACT

An E, P, V equation of state based on an assumption of Walsh and Christian and experimental shock data has been derived for nitromethane and liquid TNT. From experimental temperature data along the 1 bar isobar, the temperatures, specific heats at constant volume, and "internal pressures" are calculated. Application of simple adiabatic explosion theory leads (1) to accurate predictions of the experimental explosion times for shocked homogeneous nitromethane and liquid TNT at 86 and 125 kbar, respectively, and (2) to a predicted steady-state reaction zone width of 0.0011 cm for detonation in nitromethane that is in satisfactory agreement with the widths deduced from detonation failure and electrical conductivity experiments. In addition, the problem of the initiation of explosives by the formation of hot spots by shocks is considered. By approximating the hot spot volume by the original void volume and averaging the hot spot energy density increase to give an energy density increase twice that of the shocked explosive surrounding the hot spot, a critical hot spot size is obtained that is in satisfactory agreement with the experimental critical bubble size for propagation of detonation in nitromethane.

This paper has been published in *Phys. Fluids* 9, 398 (1966).

COMMENTS

CHARLES L. MADER (Los Alamos Scientific Laboratory, Los Alamos, New Mexico): All the equations of state which have been used for the computation of Hugoniot temperatures for condensed phase materials are empirical. Evaluation of the equations of state must be made by comparison with experimental data. The temperatures and pressures of interest in shock initiation problems are so high that only dynamic experimental evidence is available. Unfortunately, the interpretation of the dynamic experimental evidence is also dependent upon other unknowns such as chemical kinetics and opacities.

Enig and Petrone have proposed an equation of state assuming that one should maximize the Riemann integral to obtain the

isentropes. It has the advantage that it is consistent with low pressure experimental data while the one used by this author is not. The Hugoniot temperatures that they obtain for nitromethane and liquid TNT are compared with the values we have used in our shock initiation calculation [1,2] in the following table. In the lower pressure region where most of the shock initiation data are available, the temperatures are similar, but at higher pressures the Enig and Petrone temperatures are lower. Comparison in this region is difficult and must be made with the assistance of complicated hydrodynamic calculations. We shall describe the results of such comparisons.

Two-dimensional calculations of bubble closure in nitromethane using Enig and Petrone's

Pressure	Enig and Petrone	Ref. 1
Nitromethane		
86	1103	1180
170	1560	2100
201.3	1662	2472
Liquid TNT		
125	1154	1132
265	1992	2409

equation of state would give temperatures around 1600°K in the ~170 kbar fluid above the void and temperatures above 2000°K in the fluid below it. Since the hot spot is formed at the shock front and the temperatures are sufficiently high that reaction is almost instantaneous ($\sim 10^{-9}$ seconds) in the time and space scale of such calculations, one would not observe failure of the hot spots formed from the interaction of an 85 kbar shock with a void using their equation of state. The two-dimensional features of the flow result in a hot spot for which the important features of propagation and failure occur at the shock front in previously unshocked nitromethane, and not behind the shock front in shocked explosive as in the one-dimensional hot spot model. Thus the one-dimensional treatment used by Enig and Petrone to compute critical hot-spot sizes is really not pertinent to the problem. Since one obtains the same behavior with both equations of state in the two-dimensional treatment, the comparison is inconclusive.

Two-dimensional calculations of the interaction of a shock with a cylinder of aluminum using the Enig and Petrone equation of state would probably yield considerably lower temperature hot spots and correspondingly poorer agreement with experimental data than using our equation of state, which results in excellent agreement with the experimental failure data [2].

The treatment of reaction zone thickness by the method of Enig and Petrone results in reaction zone thicknesses for liquid TNT and nitromethane that are essentially the same. Using our equation of state one obtains reaction zone thicknesses of liquid TNT that are several orders of magnitude larger than that of nitromethane. Almost any reasonable interpretation of the available experimental data suggests that the reaction zone thickness of liquid TNT is much larger than that of nitromethane [3].

The equation of state we have used gives Hugoniot temperatures that are in good

agreement with brightness measurements for nitromethane at 85 kbar, water at 190 kbar, and carbon tetrachloride at 170 kbar. In addition, the experimental shock initiation induction times of nitromethane and single crystal PETN are in good agreement with those calculated using the temperatures obtained from our equation of state and Arrhenius rate laws which adequately reproduce experimental adiabatic explosion times ranging from hours to milliseconds [1]. For liquid TNT both we and Enig and Petrone calculate temperatures which are too high to reproduce the experimental shock initiation induction time if Arrhenius kinetics obtained from lower temperature thermal initiation data are used [1]. Enig and Petrone use Arrhenius kinetics that will not describe the experimental thermal initiation of TNT at lower temperatures to obtain their agreement with the experimental shock initiation induction time.

The comparison of the two equations of state with the experimental evidence is not conclusive; however, for the reasons given above, we feel that the Hugoniot temperatures calculated using our equation of state are somewhat more realistic than those obtained using the Enig and Petrone equation of state. Further studies of equations of state and of the methods of comparing them with experimental data are needed.

REFERENCES

1. Phys. Fluids **6**, 375 (1963) and LA-2703.
2. Los Alamos Scientific Laboratory Reports LA-3077 and LA-3235.
3. Los Alamos Scientific Laboratory Report LA-3297.

J. W. ENIG and F. J. PETRONE (U.S. Naval Ordnance Laboratory, White Oak, Silver Spring, Maryland): We and Mader agree that more theoretical and experimental work must be done on the derivation of equations of state of liquids. Indeed the present work is an endeavor to find a more satisfactory equation of state than was previously available.

In his Comment above, Mader has compared our E,P,V and T,P,V equations of state for unreacted nitromethane and liquid TNT with the Mie-Grüneisen equations used in his calculations, and concluded that though comparison with experiment does not provide a conclusive test for the superiority of either set, his equations give better Hugoniot temperatures.

However, we prefer our equations of state because they satisfy thermodynamic consistency conditions and the observed low pressure behavior of liquids, whereas his do not. The rest of this reply discusses the specific reasons, which we do not consider valid, raised by Mader in arriving at his conclusion.

It is important to point out that any reasonably behaved E, P, V equation of state can be expected to yield in two-dimensional calculations the results observed in experiments, e.g., the void closure experiments of Venable [1]. This is because the P, u isentropes do not vary enough among different equations of state to change the qualitative behavior of the fluid flow. The point of contention is concerned with the associated T, P, V equation of state which is strongly influenced by the E, P, V equation and certain temperature input data which are necessary for its derivation.

Mader states that had our equation of state been used in the two-dimensional numerical bubble closure experiments, it would have predicted temperatures above 2000°K in the fluid below the void. This is a conjecture since the calculations were never done; the temperatures cannot be reasonably estimated without detailed calculation in this region of very complicated convergent and divergent flow. Hence his conclusion that both equations would lead to the same two-dimensional behavior (i.e., failure to find a critical bubble and hot spot size which if exceeded will lead to detonation propagation in the bulk nitromethane), a behavior which is at variance with that shown by our one-dimensional calculations, is unsupported. Interestingly, earlier computations by us using his equation of state, the Mie-Grüneisen equation, in a one-dimensional model showed that detonation did not propagate away from the reacted hot spot when the incident shock pressure in the bulk nitromethane was below 50 kbar, in approximate agreement with his two-dimensional computations.

On analyzing his two-dimensional computations [1], two important deficiencies are apparent. Assuming for the moment that his T, P, V equation of state is accurate, it is clear that the E, P, V and T, P, V equations of state are thermodynamically inconsistent for the same reason we discussed in an earlier paper [2]. This must affect the temperature values at various positions in the hot spot and, therefore, greatly affect the chemical induction times. Another point, particularly applicable to the numerical void closure experiments

where complicated shock interactions occur, is related to the "particle-in-cell" method of computation. Unfortunately, this method smears out contact discontinuities with the result that values of E and T are inaccurate in the neighborhood of the discontinuities [3]. This is clearly seen from Mader's own calculations by noting that the isotherms are computed as continuous across the contact surface (dashed line) formed by the closure of a spherical void (see Fig. 2 of Ref. 1) or cylindrical void (see p. 24 of Ref. 4) or a biconical void (see p. 46 of Ref. 4) when, in fact, T should be discontinuous. The effect of this nonphysical energy diffusion on the hot spot reaction must be investigated further.

His conjecture concerning the possible comparison of calculations using our equation of state with the experimental [5] results for the interaction of a shock with an aluminum cylinder in nitromethane has not been tested. His point that he has obtained excellent agreement with experiment is open to question on two counts. First, if he had calculated the temperatures in a manner consistent with the Mie-Grüneisen E, P, V equation, then the temperatures would have been higher than the ones he obtained by 100 or 200°K , resulting in much smaller induction times and therefore a much smaller critical diameter of the aluminum cylinder that leads to failure of detonation propagation. Therefore, his agreement with the experiments of Travis would probably vanish. Conversely, if the E, P, V equation were suitably modified to be consistent with his T, P, V equation, then it is not obvious how the hydrodynamic flow and, therefore, the critical cylinder diameter might change. A second point is that the actual experiments [5] were performed using very long aluminum cylinders so that failure to propagate detonation was due solely to lateral rarefaction waves from the sides. In Mader's computations [1], a very short cylinder (length = 0.002 cm and diameter = 0.004 cm) was used. It is easy to see that the failure to propagate detonation could be due to the rarefaction wave starting at the top face of the short cylinder and moving downward through the cylinder into the reacted hot spot at the base at the cylinder rather than due to much weaker lateral rarefaction waves.

Mader is correct in noting that the reaction zone width for liquid TNT should be much larger than that of nitromethane, while a calculation based on Eq. (9) of our paper in the Preprints [6] would yield one of essentially the same size.

The reaction zone width is too small because the temperature T_N at 265 kbar is too high. The latter results from extrapolation of the linear density versus temperature experimental data at 1 bar to temperatures far beyond the experimentally measured range. It is easy to show that this extrapolation must always lead to temperatures that are too high, and reaction zones that are too small. When additional temperature data at 1 bar become available, we will recalculate the T, P, V values for reaction zone pressures for liquid TNT.

We found that use of the Arrhenius kinetic data measured by Robertson gave slightly better results than those of Zinn and Rogers used by Mader. The differences are much smaller than those discussed above.

REFERENCES

1. C. L. Mader, *Phys. Fluids* **8**, 1811 (1965).
2. J. W. Enig and F. J. Petrone, *Phys. Fluids* **8**, 769 (1965).
3. R. Papetti and R. Bjork, submitted to the *J. of A.S.C.E.*
4. C. L. Mader, "The Two-Dimensional Hydrodynamic Hot Spot, Volume II," Los Alamos Scientific Laboratory Report No. LA-3235 (1965).
5. J. R. Travis, *Preprints of the Fourth Symposium on Detonation, Volume II*, p. C-45 (1965).
6. This specific equation does not appear in J. W. Enig and F. J. Petrone, *Phys. Fluids* **9**, 398 (1966).

R. F. CHAIKEN (Chemistry Department, University of California, Riverside, California): In the papers by Enig and Petrone (B-133) and by Mader (C-38), considerable emphasis has been placed on the agreement between calculated and experimental detonation induction times in nitromethane (NM) when the Arrhenius rate constant for the vapor decomposition of NM was extrapolated to detonation conditions. In fact, it is this agreement which presumably justifies the equation of state used in the computer calculations.

I would like to point out that this type of justification must be viewed with some caution, since it is highly doubtful that the Arrhenius form of the rate constant, determined at low pressure and temperature (e.g., ~1 atm and

~500°K), can be extrapolated reliably to shock initiation conditions (e.g., ~10⁵ atm and ~10³°K); even assuming that the rate controlling step in the decomposition reaction remains the same.

From the Eyring Absolute Rate Theory, the rate constant for unimolecular decompositions can be expressed as

$$k_r = \kappa(kT/h) \exp(-\Delta F^*/RT)$$

where κ is the transmission coefficient (~1); ΔF^* is the difference in standard free energies between the activated and initial states; and the other terms have their usual meaning.

The pressure and temperature dependence of ΔF^* is given by the thermodynamic relation

$$\Delta F^* = \Delta E^* + P\Delta V^* - T\Delta S^*$$

where the changes in molar internal energy, volume and entropy are standard state changes and refer to differences between the activated and initial states.

Combining the above equations and comparing the result with the Arrhenius form of the rate constant yields

$$k_r = (kT/h) \exp(\Delta S^*/R) \exp[-(\Delta E^* + P\Delta V^*)/RT] \\ = A \exp(-E_a/RT)$$

or

$$A = (kT/h) \exp(\Delta S^*/R)$$

$$E_a = \Delta E^* + P\Delta V^*.$$

Now for the unimolecular decompositions, ΔV^* is positive and small (2 to 3 cm³) so that at low pressure the $P\Delta V^*$ term can be neglected giving $E_a = \Delta E^*$. However, at shock pressures of ~10⁵ atm, the pressure term can contribute significantly to the free energy of activation. In this case E_a will be greater than ΔE^* . From the studies that I carried out on the kinetics of shock initiated NM (Eighth Symposium (International) on Combustion, Williams and Wilkins Co., Baltimore, 1962, p. 759), it can be estimated that the $P\Delta V^*$ term can account for a factor of ~20 in the value of the rate constant under shock initiation conditions. From this value and the expected increase in A with temperature, it can be estimated that the rate of decomposition which was used by the authors in their computer calculations may be too high by a factor of ~10. If this is so, then the excellent agreement between the calculated and experimental induction times is merely fortuitous, and might indicate that the computed shock temperatures are too low by as much as 100°K.

THE EFFECT OF WAX ON THE SHOCK SENSITIVITY OF EXPLOSIVE COMPACTS

John Eadie

*Atomic Weapons Research Establishment
Aldermaston, Berkshire, England*

ABSTRACT

The shock sensitivity of HMX/wax compacts was found to decrease as the amount of the HMX surface coated with wax increased. It is therefore suggested that the shock sensitivity of a compact depends on the surface area of the reactive explosive exposed to reaction products. The effect of particle size on the shock sensitivity of both high and low density compacts can then be explained.

INTRODUCTION

Numerous mechanisms have been suggested for the shock initiation of heterogeneous explosives. In 1949, Eyring [1] proposed that reaction was initiated at points of contact on the surface of crystals where hot spots were produced by intercrystalline friction under the compression of the shock wave. Subsequently, Taylor [2] suggested that initiation was due to heating of the interstitial gas by adiabatic compression by the shock although later work by Cachia and Whitbread [3] and Blackburn and Seely [4] discredited this mechanism. Johansson [5], moreover, in a discussion of methods of initiation of homogeneous explosives, showed that it was improbable that the explosive could reach its ignition temperature by heat transmission from compressed air. He suggested, however, that spray from the surface of cavities might be thrown into the hot compressed gas and thus be heated rapidly to a temperature sufficient to cause detonation. A similar explanation for hot spot formation in heterogeneous explosives was given by Blackburn and Seely [4] who suggested that high temperatures could be produced by explosive being broken off the surface of crystals and accelerated across open spaces by the action of the shock. Campbell [6] on the other hand suggested that hot spots were produced by local shock convergences caused by inhomogeneities in the explosive whereas Jacobs [7] favoured shock-produced micro-shear or micro-fracture at or near voids as the path by which HE was locally initiated.

On reviewing the literature on shock sensitivity, an apparent inconsistency in the effect of explosive particle size on shock sensitivity was noticed. Campbell [6] reported that compacts of fine TNT were more sensitive than those of coarse TNT of the same density and explained this by suggesting that the shock sensitivity of a compact depended on the number rather than on the volume of voids which were present. Dinegar [8] on the other hand found that the shock sensitivity of low density PETN compacts decreased with an increase in the surface area of the PETN.

The effect of explosive particle size has also been considered by Griffiths and Grocock [9] in connection with the ease of burning to detonation of solid explosives. They found that over a range of particle sizes there was close correlation between the ease of production of detonation and the air permeability of the explosive, the transition to detonation taking place more rapidly as the particle size increased. The effect reached an upper limit presumably because the energy transfer from the gaseous products to the unchanged explosive became less efficient as the surface to volume ratio of the explosive particles was reduced. They therefore suggested that detonation depended on the buildup of a very high combustion velocity by the penetration of hot reaction products into the unchanged explosive.

If a similar mechanism held for shock initiation, then the effect of particle size on the shock sensitivity of both high and low density

charges could be explained. An important difference between high and low density compacts is that the former have closed pores only and are impermeable, whereas the latter have interconnected pores and are permeable. If it is postulated therefore that the shock sensitivity of a compact depends on the area of surface exposed to reaction products then it follows that at low relative densities the shock sensitivity will be a function of permeability and will decrease as the explosive particle size decreases whereas at high relative densities it will normally be a function of the surface area of the closed pores and will increase as the explosive particle size decreases. Such a theory would therefore reconcile the work of Campbell and Dinegar.

If, however, the initiation of detonation by shock depends on a surface reaction mechanism, then it would be reasonable to expect that the shock sensitivity of a compact would be reduced by coating the surfaces of the explosive crystals with an inert barrier. It was comparatively easy to examine this point at AWRE since a method of measuring the coated surface area of waxed explosives had just been developed in connection with an investigation into the relationship between surface coverage and powder impact sensitiveness. Several HMX/wax powders of known coating were therefore available and a short investigation of the relationship between surface coating and shock sensitivity was carried out.

EXPERIMENTAL METHOD

Wax Coating Estimation

Wax coatings were estimated by a chromous chloride reduction method.

Jamison [10] found that under identical conditions RDX was 100% and HMX 96% reduced by chromous chloride solutions, the reduction being reproducible in both cases. Since the rate of reduction of a sample of RDX or HMX is a function of surface area, then the amount reduced in a specified time under standard conditions is also a function of the surface area. This should be so, even if the material is not completely reduced as is the case with HMX. The following technique was consequently adopted to measure the surface area of RDX and HMX and therefore to estimate the proportion of the explosive surface coated by wax in waxed samples.

Chromous chloride is a very strong reducing agent which must be stored and used in an

oxygen free atmosphere. The apparatus used in the present work was based on that of Stone and Beeson [11] except that the chromous chloride solution was made up in the storage flask as recommended by Lingane and Pecsok [12]. The normalities and volumes of the reagents were chosen to give reasonable rates of reaction and manageable volumes of solution. Four litres of approximately 0.35 N solution were prepared by dissolving 385 g of hydrated chromic chloride ($\text{CrCl}_3 \cdot 0.6 \text{H}_2\text{O}$) in 3.5 litres of distilled water and 500 cm^3 of concentrated hydrochloric acid. A kilogram of amalgamated zinc was then added and reduction was complete in about three days.

The chromous chloride solution was standardised by adding an excess of 0.3 N potassium dichromate and back-titrating potentiometrically against 0.3 N ferrous ammonium sulphate. A platinum wire was used as an indicator electrode and a salt bridge provided the connection to a calomel reference electrode. It was necessary to add a few grams of syrupy phosphoric acid before titrating to obtain a sharp endpoint. The normality of chromous chloride solutions was found not to change over several weeks of storage.

To reduce samples of explosive, 0.1 g of RDX or 0.8 g of HMX were added to a standard volume of chromous chloride solution and reduction was allowed to proceed under carefully controlled standard conditions for exactly ten minutes.* In this way the percentage reduction of sieve fractions of RDX and HMX was measured. The surface area of each fraction was determined by a gas permeability method and graphs of surface area against percentage reduction were prepared. The curve for HMX is reproduced in Fig. 1.

Samples of paraffin wax, beeswax, candleilla wax and polyethylene wax were also examined and no measurable reduction was detected.

A method was therefore provided of measuring the surface area of HMX in the range 0-600 cm^2/g and, since the waxes examined were not attacked by chromous chloride, it was possible to measure the uncoated surface area of waxed HMX samples. It followed that with colloid-milled HMX, which was used in all the experimental work and which had a surface area of approximately 2000 cm^2/g , coating efficiencies in the range 75-100% could be measured.

*Reaction was stopped by the rapid addition of excess potassium dichromate which was then back-titrated.

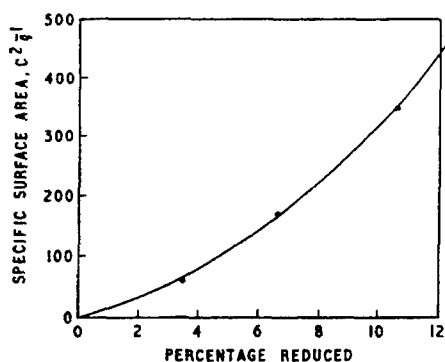


Fig. 1 - Percentage of HMX reduced vs surface area

The experimental method was comparatively quick and easy to use, the only difficulty being in the storage and use of the very readily oxidised chromous chloride solutions. Considerable care had to be taken over the stirring of the HE suspension to prevent crystals splashing up onto the sides of the flask and so being removed from the reaction. During all reductions, both of RDX and HMX, small bubbles appeared on the surfaces of the crystals and the method of stirring had to be chosen so that these bubbles did not adhere to crystal surfaces and so prevent further reduction taking place.

Shock Sensitivity Measurements

All the results quoted were obtained using a small scale gap test similar to that described by Cachia and Whitbread [3]. The experimental arrangement is shown in Fig. 2. The PETN donor pellet was initiated by low density PETN which had been fired by an exploding wire. This produced a standard shock which was attenuated to various extents by passage through a stack of brass shims which comprised the "gap." The shims were in close contact with the one-inch diameter acceptor pellet and detonation of the acceptor was assessed by the production of a sharp dent in a steel witness bar at its other end. The gap thickness was varied according to the Bruceton "up and down" procedure and the results quoted are the number of thousandths of an inch of brass shim required to obtain detonation of 50% of the samples.

RESULTS

The results of the shock sensitivity and coating measurements made on HMX/wax compositions are collected in Table 1. To examine

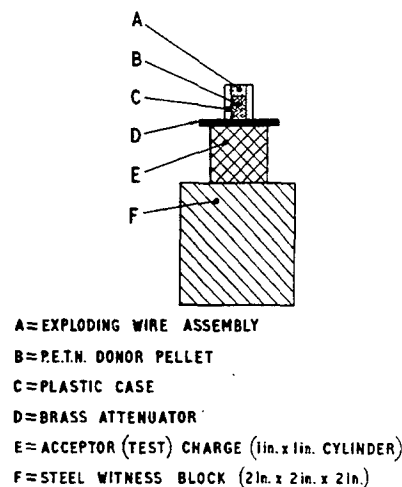


Fig. 2 - Gap test assembly

whether wax coatings affected the shock sensitivity of both high density (impermeable) and low density (permeable) compacts, a range of densities was examined and the results are grouped in density ranges in the table. It must be remembered, however, in considering these results that, because of the work done on the coated HMX crystals during pelleting, the amount of explosive surface covered with wax in a compact is almost certainly different from that of the powder on which coating measurements were made. A case in point is the mechanical mix of HMX and powdered candelilla wax in which the amount of HMX surface coated in the blended powder must be insignificant and yet in pellets there must be some HMX surface coverage because of the compaction that has taken place. No estimate has been made of this coating and it is described as "low" in Table 1.

In spite, however, of this uncertainty about the true explosive coverage, there would appear to be no doubt that coating the explosive surface with wax significantly reduces the shock sensitivity.

Most of the work was done on candelilla wax mixtures although a few tests were done with paraffin wax and, as can be seen from Table 1, these fit in with the candelilla wax results.

Further evidence that coating the surface of an explosive reduces its shock sensitivity was obtained some years ago in some hitherto unreported work [13] in which increasing amounts of beeswax were incorporated with HMX using an aqueous slurry technique. Since no method of measuring coating was available

TABLE 1
Effect of Coating on Shock Sensitivity
of 95/5 HMX/Waxes

Wax	Density (Percent of Void- less)	Coating (Percent- age Covered)	Shock Sensi- tivity (0.001-in.)
Beeswax ¹	64	low ²	184
Beeswax ¹	52	>75	94
Candelilla	66	95	65
Candelilla	76	low ²	162
Candelilla	76	60	72
Candelilla	73	82	51
Candelilla	88	low ²	144
Paraffin	86	low ³	150
Candelilla	91	70	115
Paraffin	89	86	98
Candelilla	87	89	79
Candelilla	88	92	74
Candelilla	95	low ²	107
Candelilla	95	84	91
Candelilla	95	89	73

¹Data taken from Table 2 and coatings therefore not measured. The slurry mixed composition (density = 52%) would almost certainly however, have had more than 75% of its surface coated.

²Mechanical mix.

³Aqueous slurry mix, coating too poor to be measured (i.e., below 60%).

at that time, the actual amount of HMX surface covered in these compositions is unknown, but it seems reasonable to assume that a progressively greater amount of the HMX surface was coated as the beeswax content increased. If this is so, then the results quoted in Table 2 again show clearly that the shock sensitivity is reduced significantly by covering the HMX surface with wax.

DISCUSSION

The above work shows that coating HMX crystals with wax significantly reduces their shock sensitivity and provides evidence for the shock initiation of explosives being due to a surface reaction. This idea is of course not new. For example Campbell [6] suggested that the relationship between void size and shock sensitivity indicated that a surface reaction was taking place, although he thought that it was more likely that reaction was taking place at the surface of the hot spots produced by shock convergence beyond the voids than at the voids themselves.

The point that has not been demonstrated before, however, is that the actual surface area of the explosive exposed is important. The number, surface area or volume of the voids between the explosive particles also affect the shock sensitivity of an explosive charge, but it may be postulated that they do so only insofar as they affect the exposed surface area of the explosive.

TABLE 2
Effect of Beeswax on Shock Sensitivity of HMX

Composition	Density (Percent of Voidless)	Shock Sensitivity (0.001-in.)
HMX, APD = 84 microns	64.3	199
95/5 HMX/beeswax - mechanical mix	63.8	184
99/1 HMX/beeswax - slurry mix	61.0	170
98/2 HMX/beeswax - slurry mix	53.9	137
96/4 HMX/beeswax - slurry mix	53.8	118
95/5 HMX/beeswax - slurry mix	52.0	94
90/10 HMX/beeswax - slurry mix	44.1	20

It is considered, therefore, that of possible mechanisms for the initiation of detonation by shock, a surface reaction mechanism is the most plausible since it allows a simple explanation to be given for almost all published shock sensitivity data. The actual process by which initiation takes place remains uncertain however. Spalling, spraying or jetting mechanisms [4,5,14,15] could all be important and further experimental work will be required before a complete understanding of shock initiation is obtained.

ACKNOWLEDGMENTS

The shock sensitivity data was obtained by Mr. E. S. Clinch working under the direction of Mr. W. Connick and, latterly, of Mr. M. Chick. The author would also like to thank Mr. G. P. Cachia and Mr. G. Hornby for helpful discussions on this subject.

REFERENCES

1. H. Eyring, R. E. Powell, G. H. Duffey and R. B. Parlin, *Chem. Revs.* 45, 69 (1949).
2. J. Taylor, "Detonation in Condensed Explosives," Oxford University Press, 1952, p. 173.
3. G. P. Cachia and E. G. Whitbread, *Proc. Roy. Soc. A246*, 268 (1958).
4. J. H. Blackburn and L. B. Seely, *Nature* 194, 370 (1962).
5. C. H. Johansson, *Proc. Roy. Soc. A246*, 160 (1958).
6. A. W. Campbell, W. C. Davis, J. B. Ramsay and J. R. Travis, *Phys. Fluids* 4, 511 (1961).
7. S. J. Jacobs, T. P. Liddiard, Jr. and B. E. Drimmer, Ninth Symposium on Combustion, New York, 1962.
8. R. H. Dinegar, R. H. Rochester and M. S. Millican, 145th National Meeting of American Chemical Society (Division of Fuel Chemistry) Vol. 7, No. 3, pp. 24-27 (1963).
9. N. Griffiths and J. M. Grocock, *JCS*, 1960, 4154.
10. C. C. Jamison, Picatinny Arsenal Technical Memorandum No. ACS-3-60 (1960).
11. H. W. Stone and C. Beeson, *Ind. Eng. Chem.* 8, 188 (1936).
12. J. J. Lingane and R. L. Pecsok, *Anal. Chem.* 20, 425 (1948).
13. Private Communication, W. Connick, E. S. Norton and M. C. Chick.
14. R. W. Watson and F. C. Gibson, *Nature* 204, 1297 (1964).
15. J. H. Blackburn and L. B. Seely, *Trans. Faraday Soc.* 61, 537 (1965).

DIRECT CONTACT DETONATION SENSITIVITY

Jacob Savitt
EXPLOSIFORM, INC.
San Francisco, California

and

Capt. Nicholas Leone and Carl Kyselka
Detachment 4, RTD Eglin Air Force Base
Florida

ABSTRACT

A new system for measuring the sensitivity of explosives is described. In this system explosives samples are exposed to pressure pulses which are generated by the detonation of long cylinders of cardboard confined NITROGUANIDINE in direct end contact with them. The amplitudes of these signals are varied by control of the density to which the NITROGUANIDINE is packed. The shapes and durations of these initiating waves are controlled by the system geometry. Direct contact detonation sensitivity results may be expressed in terms of the amplitudes and durations of the signals which are required for high order detonations of the samples. Results of measurements of the effects of sample size, density and confinement upon the direct contact detonation sensitivity of several common solid secondary high explosives are presented and discussed.

INTRODUCTION

The sensitivities of explosives to initiation by the detonation of other explosives are most often measured by the use of the minimum-booster sensitivity test (Ref. 1), the air-gap test (Ref. 2), or the barrier sensitivity test (Ref. 3).

In the minimum-booster sensitivity test, the sensitivity of the sample explosive is measured by systematically varying the weight of a standard explosive charge which is detonated in direct contact with the sample, and determining the minimum weight of the standard booster explosive which is required to detonate the sample.

In the air-gap or barrier sensitivity test, the sensitivity of the sample explosive is measured by systematically varying the distance between a standard detonating explosive charge and the test sample, and determining the distances across which detonation may be transmitted between them across air-gaps or through barriers (Ref. 4).

In the minimum-booster sensitivity test, it is usual for the test sample to be exposed to nearly constant amplitude shock waves of

varying, but not well controlled, shape and duration. In the gap and barrier tests, it is usual for the test sample to be exposed to variable amplitude shock waves of varying, but not controlled shape and duration.

It is the purpose of this report to describe a sensitivity test system in which the test samples can be exposed to initiating shock waves of controlled amplitudes and durations, and to present the results of some measurements of the effects of sample size, density, and confinement upon sensitivity as determined in this system.

The test system consists of a donor and an acceptor. The input pressure signal to this acceptor is provided by detonation of the donor charge. The donor is a right circular cylinder with a large length-to-diameter ratio. When the donor is detonated at one face, the detonation propagates along the axis to the other face. The acceptor charge is in direct contact with the donor at that face so that the donor output is fed directly to the sample without being attenuated by gaps or barriers. The response of the acceptor is detected by the deformation which is produced in a metal witness plate in contact with it.

If the length-diameter ratio of the donor is large enough, the detonation velocity and the detonation head are stabilized before the detonation front reaches the donor-acceptor interface. Thus, the shape and duration of the initiating shock wave in the direct contact detonation sensitivity test can be controlled by control of donor diameter, while the amplitude of this wave can be controlled by control of the detonation pressure of the donor explosive.

If NITROGUANIDINE is used for the donor, its detonation pressure may be easily controlled and varied from between about 1 to about 150 kilobars by controlling the density to which it is loaded.

CONTROL OF DETONATION PRESSURE

For stable detonations, the well known hydrodynamic relationship (Ref. 5)

$$P = \rho D u \quad (1)$$

accurately defines the detonation pressure, P , in terms of the loaded density, ρ , the detonation velocity, D , and the particle velocity, u . For solid C-H-N-O explosives,

$$u = 1/4 D \quad (2)$$

and

$$P = 1/4 \rho D^2 \quad (3)$$

Pressures calculated by means of Eq. (3) generally show good agreement (Ref. 6) with measured detonation pressures.

For NITROGUANIDINE (Ref. 5)

$$D = 0.144 + 0.402 \rho \quad (4)$$

Since NITROGUANIDINE may be loaded at densities from about 0.12 to about 1.4 gm/cc without difficulty, detonation pressures from about 1 to about 150 kilobars can be easily obtained.

EXPERIMENTAL ARRANGEMENT

The system illustrated in Fig. 1 was used to obtain the data to be presented. The donor was an 8-inch long 2-inch diameter column of NITROGUANIDINE. The NITROGUANIDINE was loaded in 1-inch long increments, into cardboard tubes into which acceptor assemblies had previously been inserted. The first increment

was loaded on top of, and compressed against, the acceptor explosive assembly.

During the course of the tests, increments weighing from 100 grains to over 700 grains were loaded. For the higher density loadings, it was necessary to support the entire system in steel loading tools to prevent distortion of the cardboard containers during loading.

A No. 8 regular blasting cap, and a 1/2-inch diameter 1/2-inch long pressed TETRYL pellet loaded at 10,000 psi was used to initiate the donor.

Acceptors were of two different types as indicated in Fig. 1. In both cases, test samples were 1.03 ± 0.02 inches long. When only wood confinement was used, test samples were prepared by first fabricating short pellets and stacking these into drilled holes in wood spools as shown. When steel and aluminum confinement was used, 1.03 ± 0.02-inch long 3/4-inch diameter tubes having 1/4-inch walls were loaded with the test explosive. These loaded metal tubes were inserted into appropriately drilled holes in the wood acceptor spools as shown.

Except for the 0.520-inch diameter charges, acceptor explosives were loaded to pressures of 32,000 psi. The 0.520 inch diameter charges were loaded at 3,400, 6,800, 10,100, 16,800, and 32,000 psi to obtain samples at various densities for the study of the effect of loading density upon sensitivity.

The entire assembly was detonated as shown in Fig. 1, with the test sample in direct contact with a 1/2-inch thick aluminum witness plate whose purpose it was to aid in classifying the response of the explosive sample in accordance with the resulting distortions.

All explosives used were obtained from normal military or commercial sources and except for the NITROGUANIDINE, which was sifted through ordinary window screening, all explosives were loaded in an untreated "as received" condition.

Pellets for testing were formed in heavy-walled, hardened steel explosives pelleting tools under appropriate pressures. Volumetric loading was used to approximately control pellet length. After compression, the formed pellets were removed from the tool for weighing and measuring. An analytical balance and a machinist's micrometer were used to determine densities of the pellets and of the other explosives samples.

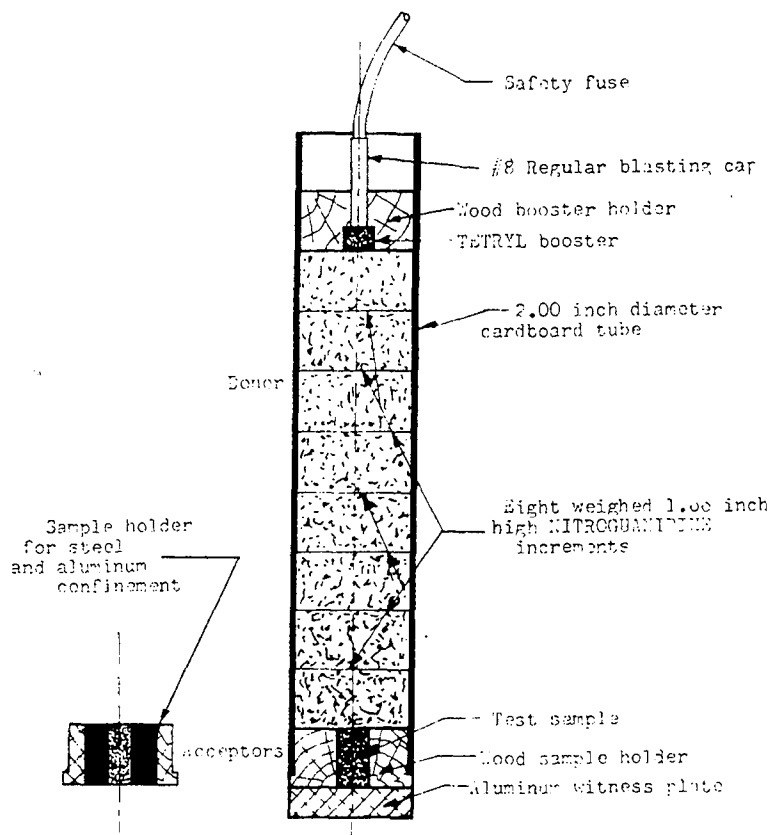


Fig. 1 - Direct contact detonation sensitivity test system

TEST PROCEDURE

A "Bruceton Type" (Ref. 7) staircase procedure with a donor density step size of 20 grains per inch long increment of NITROGUANIDINE was used to determine the donor loading density required for the 50% probability of high order detonation of the sample. Each shot was classified as a fire, X, or a misfire, O, in accordance with whether a deep crater or no crater was produced in the aluminum witness plate.

When a misfire was obtained, the next shot was made with a donor loaded with 20 additional grains of NITROGUANIDINE in each of the eight 1.00-inch long increments. When a fire was obtained, the next shot was made with a donor loaded with 20 fewer grains of NITROGUANIDINE in each of the increments. This procedure was followed for all of the tests. Usually, 30 test shots were fired for each material. In some few cases, however, only 10-shot runs were used. Table 1 contains sample "Bruceton Type" test data for TNT and TETRYL to illustrate the test procedure.

In order to minimize systematic errors associated with loading procedures, weather, and personnel, a randomized loading and firing procedure was adopted. In addition, all acceptors were prepared in advance before test firings began, but NITROGUANIDINE charges were fired on the same days that they were loaded.

TEST RESULTS

A. Loaded Density Effects

The results of measurements of the direct contact detonation sensitivity of three standard and three experimental solid explosive materials loaded under pressures varying from 3,400 to 32,000 psi are shown in Fig. 2. The acceptor explosives were 0.520 inches in diameter and confined in wood.

At the highest loading pressures, Explosive α is the least sensitive. Explosive β and TETRYL are the most sensitive of the six under these loading conditions, but significant

TABLE 1
Some Bruceton Type Direct Contact Detonation Sensitivity Test Data
(see Fig. 1)

Acceptor	Donor Loading (Grains/inch)	Observations (X is Fire, O is Misfire)
0.254-Inch Diameter Steel-Confined TNT Pressed at 32,000 psi	280 260 240 220	<div style="text-align: center;">X</div> <div style="text-align: center;">X X X X X X X X X X</div> <div style="text-align: center;">X O X X O O O O O O X O O</div> <div style="text-align: center;">O O O O O O O</div>
0.254-Inch Diameter Aluminum-Confined TETRYL Pressed at 32,000 psi	160 140 120 100	<div style="text-align: center;">X X X X X X X X X X</div> <div style="text-align: center;">X X X X X X X X X X X X</div> <div style="text-align: center;">O X X O O O O O O O O O O</div> <div style="text-align: center;">O</div>
0.520-Inch Diameter Wood-Confined TNT Pressed at 16,800 psi	320 300 280 260	<div style="text-align: center;">X</div> <div style="text-align: center;">X X O X X X X X</div> <div style="text-align: center;">O O O O X O O X X X X</div> <div style="text-align: center;">O O O O O</div>
0.520-Inch Diameter Wood-Confined TETRYL Pressed at 16,800 psi	200 180 160	<div style="text-align: center;">X X X</div> <div style="text-align: center;">X X O X X O O X X X X X X</div> <div style="text-align: center;">O O O O O O O O O O</div>

sensitivity differences between them cannot be detected. TNT, Explosive γ and TNB are intermediate in sensitivity, but sensitivity differences between them cannot be detected at the highest loading pressures. While orders of sensitivity for all of these explosives do not significantly change with loading pressure, their relative sensitivities change dramatically as pressures under which the test pellets were prepared are varied. Thus, while Explosive α is very much less sensitive than TNT when these materials are loaded at 32,000 psi, significant sensitivity differences cannot be detected between them when pellets are prepared under loading pressures of 3,400 psi.

While sensitivity differences between TNT, Explosive γ and TNB cannot be detected when these materials are loaded at 32,000 psi, pellets prepared under pressures of about 10,000 psi do exhibit differences in sensitivity; with TNB the most, and TNT the least sensitive of the three. Under most conditions it is hard to detect any sensitivity differences between TETRYL and Explosive β .

As indicated in Fig. 2, the relative sensitivities of the explosives tested clearly depend upon the pressures under which pellets were prepared. When the data presented in Fig. 2 is considered from another point of view, however (that is when we plot the donor detonation pressures required for critical initiation of the samples as a function of the density of these samples as in Fig. 3), we find, where it is

possible to compare sensitivities of these explosives at the same density, that the order of sensitivity is everywhere the same in the order: Explosive α TNT, TNB, Explosive β , TETRYL and Explosive γ ; with Explosive α least sensitive, and Explosive γ most sensitive.

When we reexamine this same data, and consider comparing the sensitivities of these explosives when they are loaded to the same percentages of their voidless densities, we find (see Fig. 4) that where they can be compared, TETRYL, rather than Explosive γ (as in Fig. 3) is the most sensitive material. The order of sensitivity of Explosive β , TNB and Explosive γ is a function of the percent of voidless density to which these materials have been loaded.

The order of sensitivity of the explosives tested, thus, clearly depends upon whether we compare samples loaded at constant loading pressures, at constant loading densities, or at constant percentages of voidless density. Furthermore, in any of these comparisons, when the generally most insensitive explosive, Explosive α is loaded at its lowest density, it is more sensitive (see Fig. 3) than TNT, TNB and Explosive γ when these are loaded at their highest densities.

B. Size Effects

The effect of sample size upon sensitivity for wood confined pellets is shown in Fig. 5.

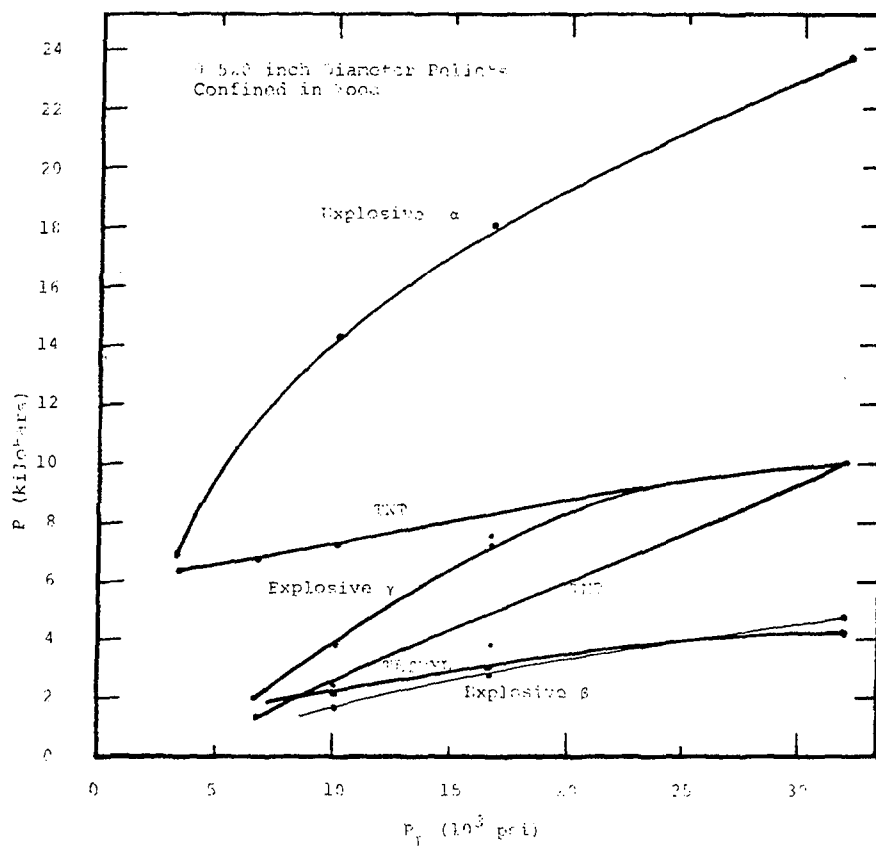


Fig. 2 - Donor detonation pressure, P , required for the 50% probability of initiation of detonation in pressed explosive pellets loaded under various pressures, P_L .

The sensitivities of 0.254-, 0.378- and 0.520-inch diameter 1-inch long wood confined pellets loaded at 32,000 psi are compared in Fig. 5.

For all of the explosives, apparent sensitivity increases with pellet size. Differences in sensitivity with size are greatest for the most insensitive explosives, and become less with increasing sensitivity. For Explosive α , the donor detonation pressure required to initiate 0.254 diameter samples is more than twice that required to initiate 0.520-inch diameter samples. For TETRYL and Explosive β , however, it is difficult to distinguish sensitivity differences 0.254- and 0.520-inch diameter samples.

Sensitivity differences between Explosive γ , TNT, and TNB cannot be detected for samples which are 0.520 inches in diameter. However, as seen in Fig. 5, differences can be distinguished more clearly as sample size is decreased. For samples which are 0.378 or smaller, the order of sensitivity is Explosive γ ,

TNT, and TNB with Explosive γ the least sensitive.

It is unsettling then, when we refer to Fig. 3 and note that when these same three explosives are all loaded at a density of 1.55 gm/cc, the order of sensitivity is TNT, TNB and Explosive γ ; with Explosive γ the most, instead of the least, sensitive of these materials.

For all of the explosives shown in Fig. 5, it appears that the apparent sensitivities of these materials loaded under pressures of 32,000 psi will not be greatly different if samples larger than 0.520 inches in diameter are used in these tests.

C. Confinement Effects

The effect of confinement upon direct contact detonation sensitivity of 0.254 inch diameter, 1-inch long columns of explosives loaded at 32,000 psi is shown in the bar graphs of

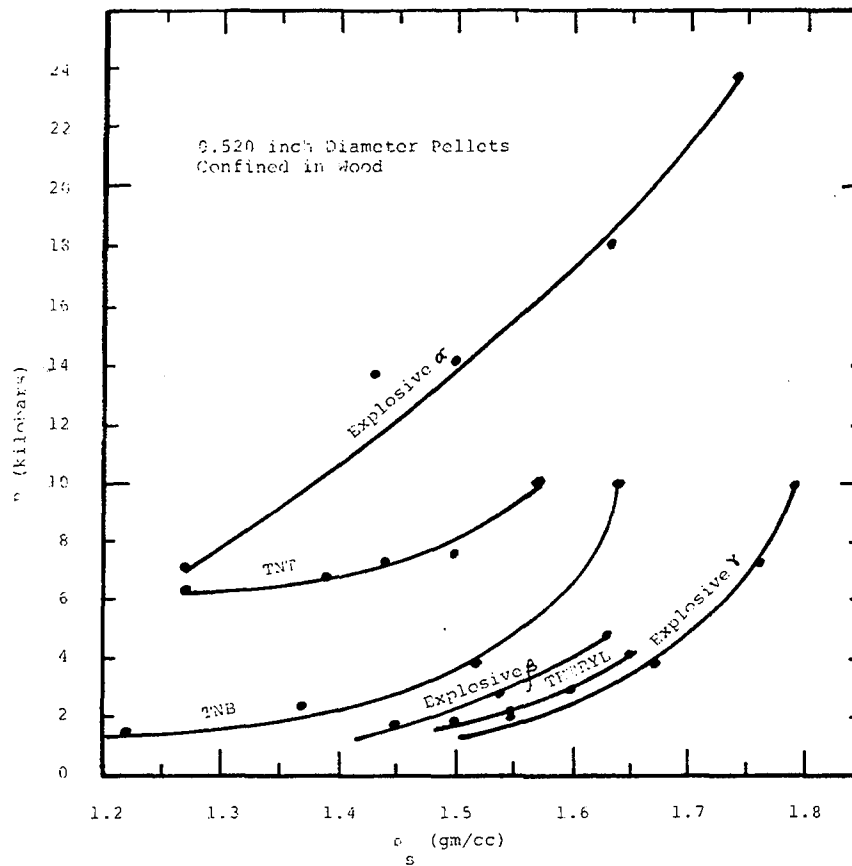


Fig. 3 - Effect of sample loading density, ρ_s , upon the donor detonation pressure, P , required for the 50% probability of initiation of detonation in pressed explosive pellets

Fig. 6. As expected, the sensitivity of all of these materials is increased when confinement is increased from wood to aluminum or steel.

Except for Explosive γ , however, the sensitivities of steel-confined explosives are not significantly greater than those of the aluminum confined materials. This is another unexpected result. In air-gap and barrier tests (Refs. 8 and 9), for example, critical gaps when acceptors are confined in brass or steel, are generally of the order of five times the gaps when aluminum is used to confine the samples.

CONCLUSIONS

The direct contact detonation explosives sensitivity test appears to be a convenient reliable and reproducible test for measuring the sensitivities of explosives at least as insensitive as TETRYL. In general, the orders of sensitivity of explosives vary as expected,

with variations of sample density, size, and confinement.

The sensitivity results which have been presented were obtained using donors of one diameter only. During these tests, therefore, the shape and duration of the initiating shock waves were held constant, while the amplitudes of these waves were varied to obtain the critical amplitudes for the initiation of the sample explosives studied. By using donors with diameters different from 2 inches (those used in these tests), and by maintaining large donor length-to-diameter ratios, the effect of duration of the initiating shock wave upon the critical pressure required to detonate the explosive samples may be studied.

The data obtained, namely the donor detonation pressures required to initiate critical detonation in the samples, may be used to calculate the amplitude and duration of the initiating shock waves entering the explosive samples which are required for their critical initiation.

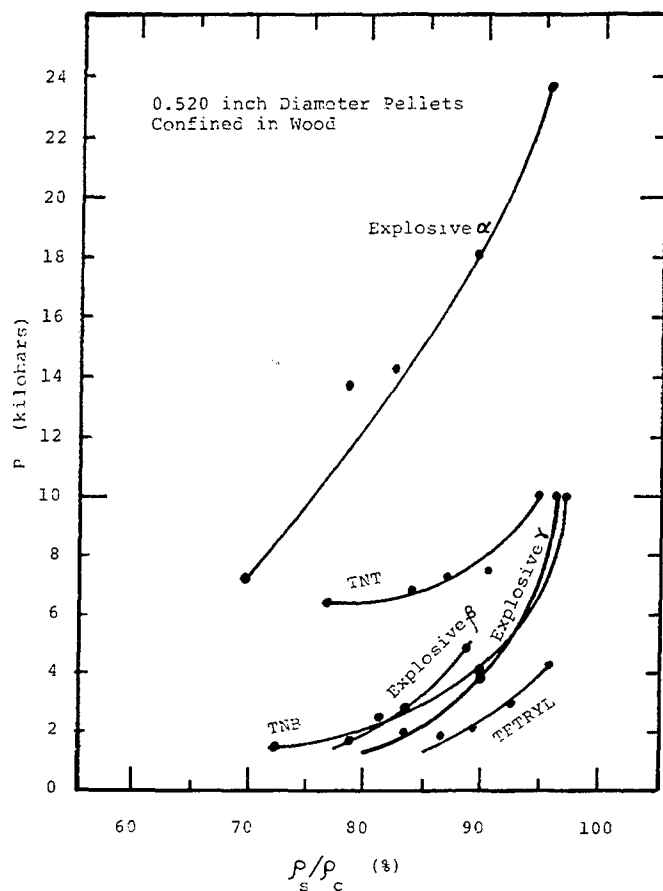
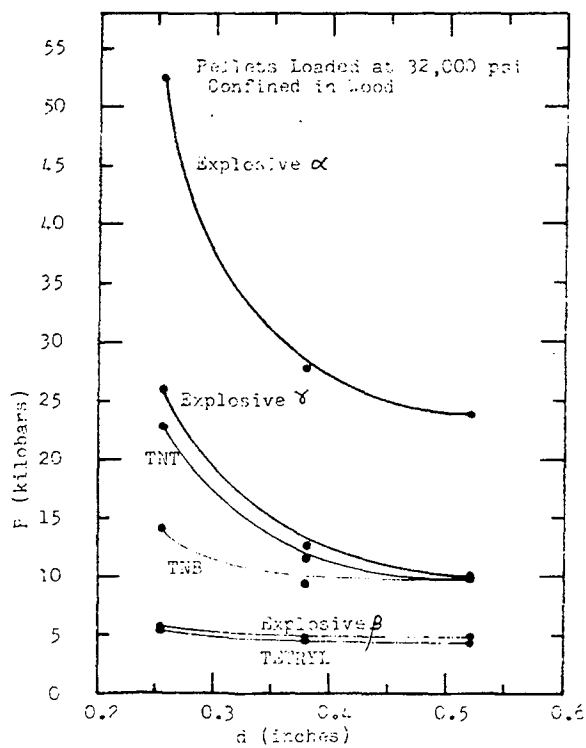


Fig. 4 - Variation of the donor detonation pressure P , required for the 50% probability of initiation of detonation in pressed explosive pellets with the fraction, ρ_s/ρ_c , of the crystal density, ρ_c , to which these pellets are compressed

Fig. 5 - Effect of sample pellet diameter, d , upon the donor detonation pressure, P , required for the 50% probability of initiation of detonation in pressed explosive pellets



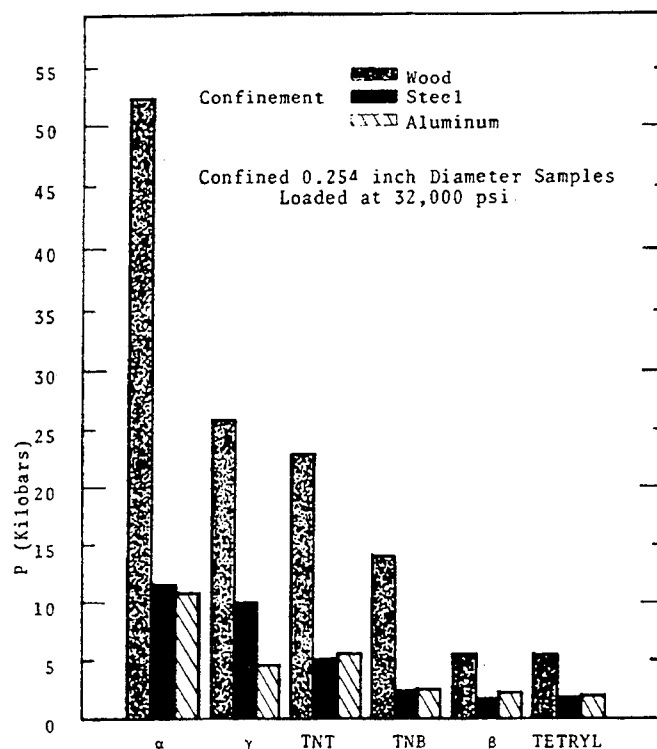


Fig. 6 - Effect of sample explosive confinement upon the donor detonation pressure, P , required for the 50% probability of initiation of detonation in the sample

Only donors of NITROGUANIDINE have thus far been used in these direct contact detonation sensitivity experiments. Other explosives can be used to the extent that their detonation pressures are continuously variable in the pressure range of interest. These may include liquid and gaseous materials as well as solids.

ACKNOWLEDGMENT

The strenuous efforts of A. Herbst and R. E. Conover, who performed most of the experimental firings, and the good natured patience of Miss Carolyn Findley who prepared this manuscript, are gratefully acknowledged.

REFERENCES

1. L. C. Smith and E. H. Eyster, "Miscellaneous Sensitivity Tests," OSRD 5746, 21 November 1945
2. R. H. Stresau and L. B. Starr, "Some Studies of Propagation of Detonation Between Small Confined Explosive Charges," NOLM 10577, 15 July 1950
3. D. Price and I. Jaffee, "Large Scale Gap Test," ARS Journal, May 1961
4. E. H. Eyster, L. C. Smith and S. R. Walton, "The Sensitivity of High Explosives to Pure Shocks," NOLM 10, 336, 14 July 1949
5. M. A. Cook, "The Science of High Explosives," Reinhold Publishing Corporation, New York (1958)
6. 2nd ONR Symposium on Detonation, Washington, D. C., February 9-11, 1955. See papers by W. E. Deal, Jr., R. E. Duff and E. E. Houston, H. D. Mallory and S. J. Jacobs, and N. Fickett and R. D. Cowan
7. "Statistical Analysis for a New Procedure in Sensitivity Experiments," Princeton University Statistical Research Group, Report No. 101.1R of the Applied Mathematics Panel, NDRC, July 1944
8. W. E. Dimmock, Jr., "A Small Scale Gap Sensitivity Test," NAVORD 2494, 2 July 1952
9. J. Savitt, "Effect of Acceptor Explosive Confinement upon Acceptor Sensitivity," NAVORD 2938, 13 November 1953

THE EFFECT OF PHYSICAL AND CHEMICAL PROPERTIES ON THE SENSITIVITY OF LIQUID EXPLOSIVES

J. E. Hay, J. Ribovich, F. H. Scott and F. C. Gibson
Explosives Research Center, Bureau of Mines
U.S. Department of the Interior
Pittsburgh, Pennsylvania

ABSTRACT

The sensitivities of a number of liquid explosive systems to both low-velocity detonation (LVD) and high-velocity detonation (HVD) have been determined by means of an instrumented modification of the card-gap test. The systems investigated include nitroglycerin-ethylene glycol dinitrate (NG-EGDN) with various diluents, experimental casting solvents for double-base propellants, nitromethane (NM) alone and in mixtures with tetranitromethane (TNM), and hydrogen peroxide-glycerol. Emphasis has been placed on the relationship between apparent sensitivity and the physico-chemical characteristics of the system and its mechanical interaction with its environment. Results indicate that, while the energy content, viscosity, and homogeneity of the system and the charge diameter and container material are very important, other fundamental factors, as yet undetermined, affect the tendency of a liquid explosive system to undergo LVD.

INTRODUCTION

The mechanism of the initiation of condensed explosives to high-velocity detonation (HVD) by strong shocks (of the order of tens of kilobars) is now generally considered to be well understood. In contrast to this, the mechanisms of deflagration-to-detonation transition, LVD, and low-to-high-velocity transition in initially homogeneous liquid explosives have been explained only in general and qualitative terms. The latter two regimes are particularly important as low-order detonations are distinguished by the relative ease with which they can be initiated as well as by their low velocity of propagation. Of particular interest from a practical standpoint is the susceptibility to LVD of liquid systems used as monopropellants or as casting solvents where the latter are used in the formulation of double-base propellants.

Several terms need to be defined. During the course of research conducted at the Explosives Research Center, it has been found that the low-velocity regime in a given explosive is not characterized by a unique set of properties analogous to C-J pressure and velocity, etc., appropriate to HVD's, but embraces a variety of modes of reaction. These have average

propagation rates in the approximate range 1-2.5 mm/ μ sec and produce pressures in the approximate range 1-10 kilobars [1]; however, among them there are seemingly important differences. The most important empirical distinction is that some LVD's have a steady propagation rate well above the sonic velocity in the explosive and produce well-defined shocks of the order of 5-10 kilobars, and other LVD's have a fluctuating propagation velocity well below the sonic velocity and produce pressures of the order of 2 kilobars or less but no clearly discernible shock wave. Also, modes of reaction have been observed in which the propagation is so irregular that the term "velocity" is inappropriate or in which propagation appears to cease, often after traversing distances greater than 4 charge diameters.

For the purposes of this paper, the term LVD will be taken to include any explosive reaction which propagates at a rate in the range from 50 percent less to 50 percent greater than the sonic velocity in the unreacted explosive and generates pressures of the order of a few kilobars—a definition which undoubtedly includes reactions which some investigators would prefer to call fast deflagrations.

The term "sensitivity" will be taken to refer to the susceptibility to the initiation of LVD by shock interactions such as occur in any real system subject to shock loading, specifically in this case to the card-gap test for liquids where a container must be used.

General Discussion

The basic problem in understanding the initiation of rapid chemical reactions by weak shocks (of the order of a few kilobars) is that the bulk temperature rise associated with such shocks—a few degrees—is far less than the temperatures required to attain the reaction rates usually associated with detonations, viz., several hundred degrees. This difficulty has been answered by the energy concentration or "hot spot" model of Bowden and coworkers [2]. When dealing with homogeneous systems, specifically liquids, a difficulty arises in that there are no obvious sources of such hot spots. Related work at the Explosives Research Center (ERC), described in a paper by Watson et al., on Detonations in Liquid Explosives—The Low-Velocity Regime and presented at this Symposium, has shown that under shock loading, the liquid cavitates and that reaction is initiated in, or at the surface of, the resulting cavities. Although the exact mechanism by which the liquid in the vicinity of these cavities attains the required temperature has not been definitely established, we believe that a plausible one may be summarized as follows:

1. Cavitation of the liquid explosive;
2. Formation of microjets in the cavities and impact of the jets on the liquid bounding the cavities;
3. Initiation of a deflagration-like reaction at the points of impact;
4. Propagation of the above sequence of events throughout the liquid.

It should be noted that each element of liquid must be subjected to two distinct stimuli, a rarefaction which cavitates the liquid and a shock which causes cavity collapse. Both of these conditions must be self-sustaining if the reaction is to continue.

Cavitation

Although cavitation of the liquid explosive appears to be a necessary condition for the initiation and propagation of an LVD, we have not

as yet been successful in attempts to measure either the cavitation threshold of the explosives used or the amplitudes of the rarefactions generated by shock loading in the experimental arrangement. Thus, it is not yet possible to state whether the cavitation threshold is a limiting factor in the sensitivity of ordinary liquid explosives or whether the threshold can be raised in some way so that it becomes a limiting factor. Moreover, it is questionable whether the rarefaction wave(s) causing the cavitation can persist indefinitely except under special conditions of confinement. The origin of the rarefaction(s) due to release or boundary reflection of the initial shock stimulus is easy to visualize but, ultimately, it must decay or be supported by the LVD. Whether the latter is possible or not depends upon the geometry and environment of the explosive rather than its intrinsic properties.

Formation and Impingement of Micro-Munro Jets

The hydrodynamics of these processes is not sufficiently well known to permit analysis of the effects of the physical properties of the liquid. In fact, although this mechanism appears to be a plausible energy-concentrating process, it is not necessary to our model of an LVD that it be the one actually operative.

Ignition of the Liquid by Jet Impact

The hot-spot ignition process is presumed to be controlled by competition between heat loss due to thermal conduction and heat generation due to chemical reaction. As the thermal diffusivities of typical liquid explosives of the CHNO class are not expected to differ widely one from another, it would be expected that the thermochemistry and kinetics of the explosive are the principal factors controlling this stage of the process.

Propagation

Apart from considerations affecting the stability of the rarefaction wave which causes cavitation, the stability of an LVD depends upon the ability of the reaction to support the compression wave which induces it by jetting or other means. The nature of the reaction occurring at and spreading from the initiation centers is presumed to be similar to high-pressure propellant burning. There is at present no satisfactory theory from which the propellant burning rate as a function of pressure can be

calculated, knowing the fundamental physical and chemical properties of the propellant. It would be expected, however, that again the most important factors would be the thermochemistry and kinetics of the combustion process.

Because of the complexity of the over-all process and a limited knowledge of the presumably important factors, the present approach has been restricted to an experimental study of the initiation and propagation of LVD's. A variety of liquid explosive systems has been studied using an instrumented gap test in an attempt to determine the effects of modification of the physical and chemical properties of the explosive on its LVD characteristics.

EXPERIMENTAL

Instrumentation

The charge configuration used in most of these studies is shown in Fig. 1; it conforms to the usual card-gap test [3] except that the length of the acceptor is generally longer and both continuous rate-measuring probes and

peak-pressure measuring transducers are employed.

The gap value which is used as a measure of sensitivity is expressed in terms of the overall gap thickness at which 50% of the trials are expected to have a "positive" result. Evidence of initiation and propagation of detonation in the explosive is provided by the records of the pressure transducer and continuous rate measuring probes; however, the extent of damage to the container and to the steel witness plate may provide additional information.

The peak pressure transducer consists of a resistive element imbedded in a polyethylene rod that is immersed in the liquid explosive to a predetermined level near the downstream end. The element is connected with a source of emf and a load resistor; the change in resistance with pressure is determined from the change in the potential drop across the load resistor and is recorded oscillographically. This device has been calibrated over a range extending from about 1 to 70 kilobars. A pressure-actuated switch, positioned approximately 1 inch ahead of the transducer, permits the use of a short-sweep time base on the oscilloscope. Typical oscillograms showing the response of the pressure transducer are illustrated in Fig. 2. A peak pressure in excess of 70 kilobars is shown for nitromethane detonating at 6330 m/sec in Fig. 2(a). A peak pressure of 7.5 kilobars was measured in nitroglycerin-ethylene glycol dinitrate (NG-EGDN) corresponding to a detonation velocity of 1940 m/sec (Fig. 2(b)). The peak pressure value represents only the amplitude of the first pulse delivered to the transducer. The device is not employed to obtain a continuous pressure profile.

A resistance-type probe for continuously determining wave front positions with respect to time was also used as a means of placing the gap-test results on a more quantitative basis. With the probe, it is possible to follow the wave movement during initiation and growth of detonation and to determine detonation velocities, approximate location of initiation, and to ascertain the direction of propagation. The probe consists essentially of a length of 3-mil diameter Nylon covered (skip wound) resistance wire (approximately 2.8 ohms/cm) inserted into a small bore aluminum tube (0.023-inch od x 0.0015-inch wall). When immersed in an explosive column, the probe functions by virtue of a change of resistance as the pressure wave collapses the tube onto the bare resistance wire. With a constant current in the circuit the emf across the probe, which is proportional to the

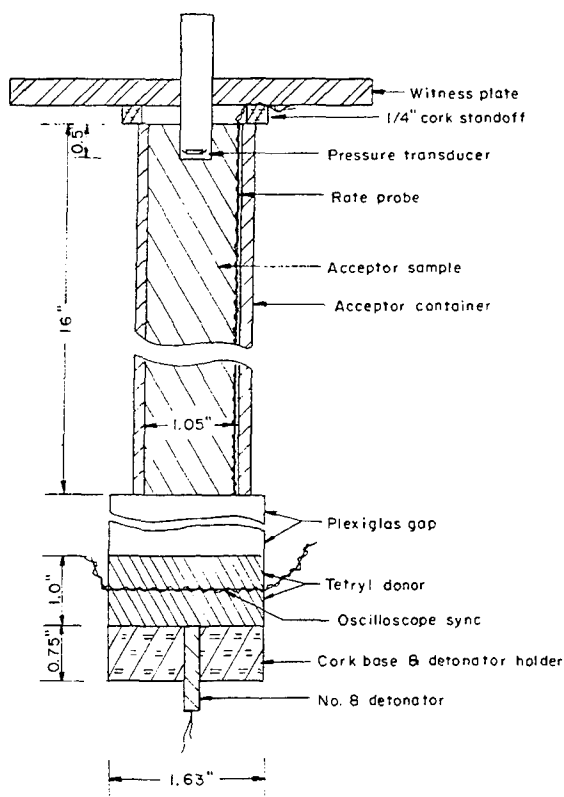
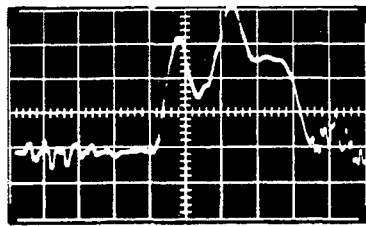


Fig. 1 - Charge configuration (dimensions are for 1-inch scale)



(a)

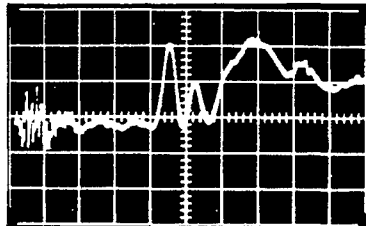
(Sweep time - 0.5 μ sec/div)Nitromethane
(6330 m/sec)

> 70 kb peak pressure

Zero gap

Polyethylene

(1" scale; 48" long)



(b)

(Sweep time - 1 μ sec/div)NG-EGDN
(1940 m/sec)

7.5 kb peak pressure

5-inch Plexiglas gap

Plexiglas

(1" scale; 16" long)

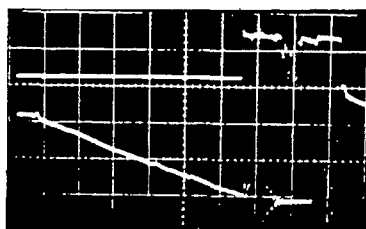
Fig. 2 - Typical oscillograms illustrating response of the instrumentation

length of undisturbed resistance wire in the probe, is recorded oscillographically; thus, velocities can be determined from the slope of the record for any instant [4].

Typical oscillograms for various types of reaction extending from high-velocity detonation to noninitiation, employing the Nylon-wound probe, are given in Figs. 3 and 4.

A detonation velocity of 6360 m/sec was measured in nitromethane contained in an aluminum container (Fig. 3(a)). A low-velocity detonation of 1980 m/sec was measured in 90 percent NG-EGDN/10 percent triacetin (TA) contained in a Plexiglas* container (Fig. 3(b)), and a low-velocity detonation of 1190 m/sec was measured in a similar mixture contained in a polyethylene container (Fig. 3(c)). A failing detonation is shown in Fig. 4(a) for 85 percent NG-EGDN/15 percent TA contained in a Plexiglas container. In this particular experiment, both the expendable pressure transducer and the velocity probe were disabled at the downstream end of the charge by precursor shock waves when the reaction wave was at about the midpoint of the container. Figure 4(b) typifies an incomplete reaction in which a 13-inch length of the container was destroyed, with the remainder, including a steel witness plate, recovered undamaged. A noninitiation (NI) result for 90 percent NG-EGDN/10 percent TA using an 8-inch gap is shown in Fig. 4(c).

*Trade names are used for information only and endorsement by the Bureau of Mines is not implied.



(a)

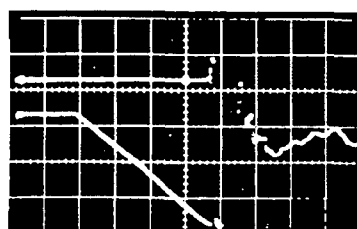
Pressure (top)

Velocity - 6360 m/sec (bottom)

Nitromethane

Zero gap

Aluminum



(b)

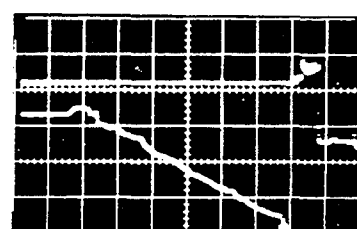
Pressure (top)

Velocity - 1980 m/sec (bottom)

90% NG-EGDN/10% TA

7-inch Plexiglas gap

Plexiglas



(c)

Pressure (top)

Velocity - 1190 m/sec (bottom)

90% NG-EGDN/10% TA

8-inch Plexiglas gap

Polyethylene

Fig. 3 - Typical oscillograms illustrating response of the instrumentation; 1-inch scale

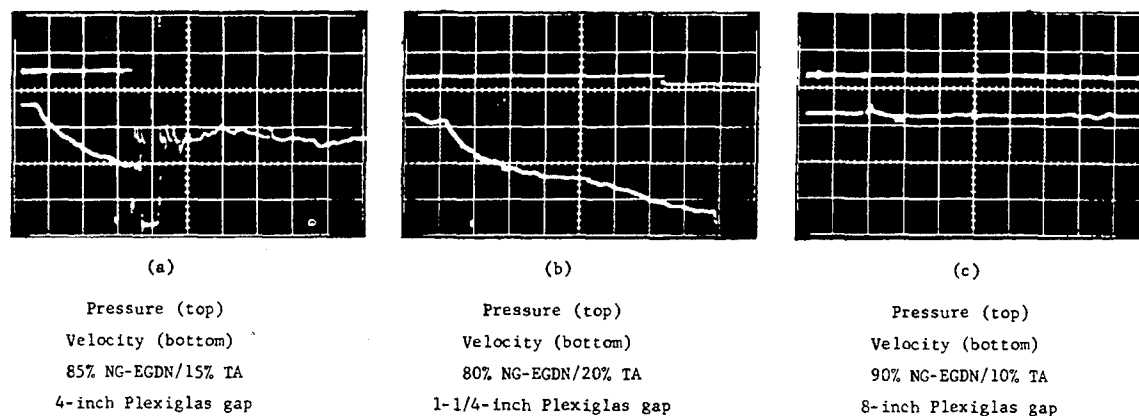


Fig. 4 - Typical oscillograms illustrating response of the instrumentation; Plexiglas container 1-inch scale

RESULTS OF SHOCK SENSITIVITY MEASUREMENTS ON VARIOUS LIQUID EXPLOSIVE SYSTEMS

Nitroglycerin-Ethylene Glycol
Dinitrate-Triacetin (NG-EGDN-TA)

Scaled test arrangements were used in these studies for scale factors of 1/4, 1/2, 1, and 2 based on a 1-inch scale as detailed in Table 1. Gap thicknesses defining the threshold between initiation of HVD's and LVD's and between initiation of LVD's and NI's, including propagation failures or incomplete reactions, were determined for the NG-EGDN-TA system. The scaled experiments were performed to study the effect of scale or "charge size" on the apparent shock sensitivity and to determine whether the incomplete reactions and NI's found at the higher TA concentrations were related to the diameter. The thresholds are shown in Fig. 5. It should be noted that incomplete reactions (propagation failures) have been included with NI's in drawing the threshold curves. The thresholds between HVD's and

LVD's and between LVD's and NI's occur at lower percentages of TA and/or shorter gap lengths as the scale employed becomes smaller. For neat NG-EGDN, the threshold between HVD and LVD occurs with approximately 1/4, 3/4, 1-3/4, and 3-1/2-inch gaps, employing 1/4, 1/2, 1, and 2-inch scales respectively. For the 1/4-inch, 1/2-inch, 1-inch, and 2-inch aluminum containers, the limiting TA concentrations for low-velocity detonations are less than 7-1/2 percent, 15 percent, 25 percent, and 35 percent respectively.

Gap thicknesses defining the threshold curves were also determined for the NG-EGDN-TA system in Plexiglas and polyethylene containers (1-inch id x 16-inch length with a 0.125-inch wall) at 25°C; results, including those obtained in aluminum tubes, are given in Fig. 6. Thresholds between HVD's and LVD's occur with approximately 1-3/4, 3-3/4, and 5-1/2-inch gaps for neat NG-EGDN in aluminum, Plexiglas and polyethylene containers, respectively. No low-velocity detonations occurred in either the 1-inch Plexiglas or polyethylene

TABLE 1
Scales Employed in Shock Sensitivity Measurements
Charge Dimensions (inches)

Scale	Donor (Tetryl Pellets)				Gap Diameter	Acceptor (16 inches long)	
	Number	Diameter	Length	Weight (grams)		Inside Diameter	Wall
1/4	1	3/8	1/4	0.78	3/8	1/4	0.035
1/2	2	3/4	1/4	6	3/4	1/2	0.065
1	2	1-5/8	1/2	50	1-5/8	1	0.13
2	2	3	1	350	3	2	0.25

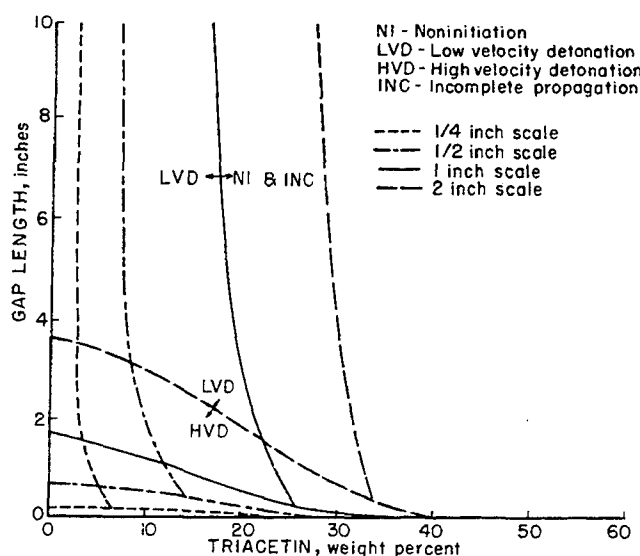


Fig. 5 - Gap sensitivity of 50-50 NG-EGDN-TA system in aluminum containers at 25°C using various scale sizes

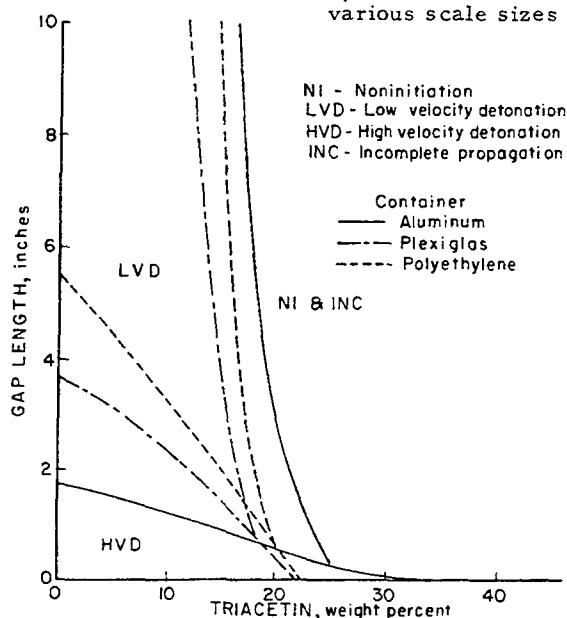


Fig. 6 - Gap sensitivity of 50-50 NG-EGDN-TA system in various containers at 25°C (1-inch scale size)

container in mixtures having 20 percent TA concentrations or greater. In the 1-inch aluminum container, no low-velocity detonation occurred in mixtures having 25 percent TA concentrations or greater.

Nitromethane

Nitromethane (NM) detonates readily at its high velocity but low-velocity detonations in this

material have, as yet, not been recognized. There is considerable interest in the possibility of an LVD regime for a number of reasons: Fundamentally, because NM is a simple nitroparaffin and thus a natural choice in a program involving comparison of explosives of different chemical structure, and because the apparent absence of this regime in an explosive of very well known properties could be an important clue to the elucidation of those properties of a liquid explosive which render it susceptible to LVD's. There is also a practical interest in the subject inasmuch as two accidental detonations of large quantities of NM have occurred under circumstances in which the initial stimulus must have been very weak compared to the shocks usually considered to be necessary to initiate HVD's (~90 kilobars).

The first trials were conducted at ambient temperature (25°C) using schedule 40 steel pipe of nominal size from 1-1/2 to 4 inches. The charge length was 16 inches in most cases except for the 4-inch diameter charges which were 72 inches long. The donor charge (either tetryl or pentolite) weight was scaled roughly as the cube of the charge diameter. Except for two doubtful cases, at a diameter of 3 inches with 0.6-inch gap with a 3-inch diameter by 2-1/2-inch long (475 g) pentolite donor, only HVD's or failures were observed. The failures actually resulted in some damage to the acceptor container but only to a degree observed even with inert liquids and attributable to hydraulic effects from the donor charge and were considered to be noninitiations (NI's). The two

doubtful cases were presumed to have been under-driven HVD's which would have failed or stabilized at the normal high velocity in a longer charge but could have been LVD's which failed to stabilize.

As the probability of achieving an LVD is believed to be greater with heavier confinement, another series of trials was run with the inside diameter fixed at 2 inches but with heavier wall tubing (0.25 inch); in this series the sample temperature was varied. In every case, the donor and attenuator were so chosen that the input shock was well below that required to initiate HVD's.

The results obtained from this series were of two types: non-initiation, as indicated by negligible damage to the acceptor container, and a very weak shock (≤ 1.5 kilobars) detected by the pressure transducer, and an explosive reaction of ambiguous nature indicated by fragmentation of the container into large pieces and, occasionally, by shock pressures of as much as 20 kilobars detected by the pressure transducer. These results have been recorded as possible low-velocity detonations in Table 2. It must be pointed out that these reactions do not possess the apparently well-defined characteristics of LVD's in NG-EGDN: the initiation delay times are long and variable (in the range of hundreds of microseconds), the pressures appear to fluctuate widely, and it has not as yet been found possible to determine the velocity of propagation

or even whether there is a regular mode of propagation. However, these reactions resemble LVD's in their qualitative characteristics.

Contrary to expectations, no appreciable temperature effect was found as may be seen from the data in Table 2. When the donor systems were calibrated, using the expendable pressure transducer, it was found that the threshold gaps derived from the data in Table 2 corresponded to shock pressures (in the NM) of about 11.5 kilobars.

NM-Tetranitromethane System

It may be speculated that the low susceptibility of NM to LVD is due to its high activation energy and low heat of explosion; these factors would be expected to increase the minimum requirements for hot-spot initiation beyond those values which can be readily attained and to reduce the burning rate in the reaction zone to a value inconsistent with stable propagation in small-scale experiments.

If this hypothesis is correct, increasing the heat of explosion and, perhaps, reducing the effective activation energy by the addition of tetranitromethane (TNM) would render the system more susceptible to LVD. TNM has an advantage over other possible oxidants in that the mixture remains a simple nitroparaffin system.

TABLE 2
Sensitivity of NM (99 Percent Grade) in 2-Inch id,
0.25-Inch Wall, 16-Inch Long Steel Tubing

Explosive	Donor			Attenuator Length (inches)	Temperature (degrees C)	Result
	Diameter (inches)	Length (inches)	Weight (grams)			
Tetryl*	3.0	2.0	360	2	90	LVD ?
Tetryl	3.0	2.0	360	2	55	LVD ?
Tetryl	3.0	2.0	360	2	20	LVD ?
Tetryl	3.0	2.0	360	3	90	LVD ?
Tetryl	3.0	2.0	360	3.5	90	NI
Tetryl	3.0	2.0	360	4.0	90	NI
Tetryl	3.0	1.0	180	2.0	90	LVD ?
Tetryl	3.0	1.0	180	2.5	90	LVD ?
Tetryl	3.0	1.0	180	3.0	90	NI
Tetryl	3.0	1.0	180	3.5	90	NI
Pentolite	2.5	1.5	200	2.0	90	LVD ?
Pentolite	2.5	1.5	200	2.0	20	LVD ? (2/2)
Tetryl*	2.0	1.0	80	1.5	90	LVD ?
Tetryl	2.0	1.0	80	1.5	20	LVD ? (2/2)
Tetryl	2.0	1.0	80	2.0	90	NI

*Pressed $\rho = 1.57 \text{ g/cm}^3$.

After it was established that this system possessed an LVD regime over a range of compositions from 5 to 50 percent TNM, at least in 1-inch id, 0.25-inch wall steel tubes, and that these could be readily initiated, particularly near the stoichiometric composition (44.5 percent TNM), the characteristics of the LVD's in the stoichiometric system were investigated for a variety of container materials. In addition, the initiation thresholds for both LVD and HVD in 1.0-inch id, 0.25-inch wall steel and Plexiglas tubes were determined as a function of the composition.

The experimental set-up was the instrumented gap test, using a 1.63-inch diameter x 1.0-inch long tetryl donor, a 1.63-inch diameter x 3.0-inch long Plexiglas attenuator, and containers of 1.0-inch id, 0.25-inch wall aluminum, lead, Plexiglas, and steel tubing. The continuous rate-measuring probe was not employed in all cases. Acceptors of various lengths from 1 to 8 inches were used with the pressure transducer to determine variations of pressure with distance from the donor system in an attempt to study the development of reaction.

No LVD's were observed with the aluminum containers; the average propagation velocity (obtained using the pressure transducers as rate stations) was found to be 7.4 mm/ μ sec. However, in two cases (with 6 and 8-inch long acceptors) pressures of the order of 5 kilobars were observed rather than the HVD pressure which is in excess of 70 kilobars. No explanation for this can be made except to assume that the HVD is decaying—an interpretation which is open to question.

With lead containers, LVD's were observed with pressures of 2 to 4 kilobars and velocities of 1.0 to 1.4 mm/ μ sec. These appeared to be decaying with increasing distance from the donor system up to about 4 inches at which point transition to HVD occurred. This behavior seems diametrically opposed to that observed in aluminum, although the apparent decay of the LVD in the early stages is consistent with both the theory and experience with other explosive systems in tubes of low acoustic velocity.

With Plexiglas containers, no LVD's were observed at all; HVD's with velocities of about 8.5 mm/ μ sec were observed up to about 4 inches from the donor system; with longer acceptors the velocity appeared to decay to about 4 mm/ μ sec. In this respect the behavior in Plexiglas resembles that of aluminum.

With steel containers, LVD's with velocities of about 2.35 mm/ μ sec were obtained; but in two cases (acceptor lengths of 6 and 8 inches)

there were indications of transition to HVD. This behavior is similar to that in lead.

In order to elucidate the above problems and to determine the effects of varying the physical and chemical parameters of the system on the susceptibility to both LVD and HVD, two series of experiments were run in 1-inch id, 0.25-inch wall, 8-inch long tubes of Plexiglas and steel. The concentration of TNM was varied from 0 to 80 percent and the attenuator length from 1 to 12 inches. These runs were instrumented with both continuous rate probes and pressure transducers. The results of these experiments are shown in Fig. 7 in which the threshold attenuator lengths for initiation of both HVD's and LVD's are shown for steel and Plexiglas containers versus mixture composition. The upper threshold for the more sensitive mixtures was not determined; additional attenuation of the donor shock obtainable by increasing the attenuator length beyond 12 inches is too small for further reduction of the input stimulus to be practical by this means.

The peculiarities of the results deserve special comment:

1. It will be noted that the maximum sensitivity to HVD or LVD, in either type of

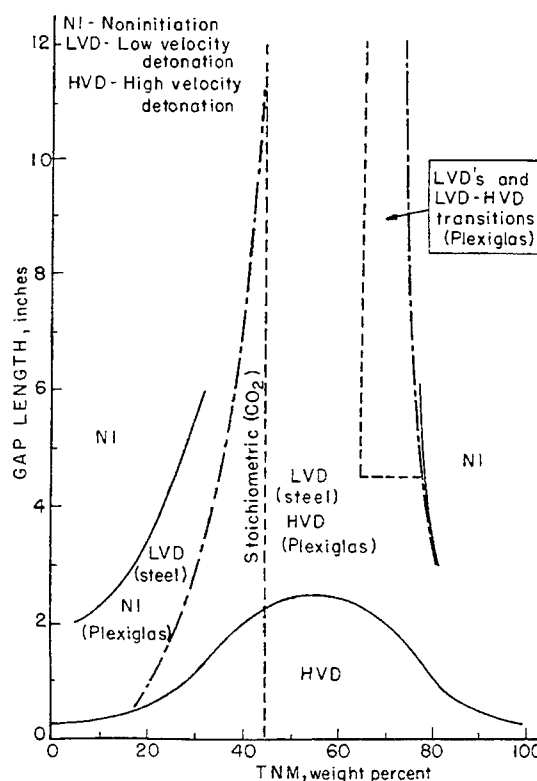


Fig. 7 - Gap sensitivity of NM-TNM system in steel and Plexiglas containers

container, is displaced toward the TNM-rich end of the composition scale relative to the stoichiometric composition of 44.5 percent TNM (oxygen-balanced to CO_2) at which the heat of explosion is a maximum. This effect is probably due in part to a lower effective activation energy of the TNM and perhaps to the higher density of TNM-rich mixtures.

2. The sensitivity curves are appreciably narrower in the case of Plexiglas tubes. This may be attributed to the fact that Plexiglas tubes rupture at very low pressures so that the pressure due to the donor stimulus and incipient reaction is relieved and thus the incipient initiation in the case of the less energetic compositions is quenched.

3. Substantial differences between both the HVD's and the LVD's are observed in the case of the two tube materials. The HVD's observed in steel have an initiation delay time of a few microseconds while those in Plexiglas, except with the shortest attenuators, are of the order of a hundred microseconds. It would appear from this that the mechanism of the HVD's in steel containers follows the classical hydrodynamic model, but that those observed in Plexiglas containers probably result from precursor activity of the same kind as that postulated for LVD's. Since the occurrence of HVD's with weak shock inputs (~ 2 kilobars) as a result of uniform hydrodynamic heating would appear to be impossible, the observation of HVD's under these conditions seems to demand the operation of a mechanism analogous to that for LVD's. This tendency toward HVD's having long initiation delay (or occasionally LVD-HVD transitions), with attenuator lengths which ordinarily result in LVD's or failures with other explosive systems, has been noted for nitrobenzene-nitric acid, trimethylolethane trinitrate (TMETN) and NG-EGDN, although the last seems to exhibit this behavior only in materials of low sonic velocity, e.g., lead and polyethylene. In these cases it is entirely conceivable that the mechanism may be qualitatively the same as that for LVD's. For example, if the cavitation-microjetting mechanism is applicable, it is conceivable that the collapse of a large cavity or group of closely spaced smaller cavities could cause sufficiently intense heating in an adequately large zone to directly initiate an HVD; alternatively, it is possible that the burning rate of the explosive is so great that transition from ignition to HVD is virtually instantaneous.

4. The location of the LVD regime in the figure shown for Plexiglas containers is particularly interesting. These reactions have been observed only at 70 percent TNM, except for one case at 60 percent. The most remarkable

feature is the existence of a regime in which LVD's are observed which subsequently transit to HVD's, a phenomenon presumably made possible by the progressively longer delay times to initiation with increasing gap length. Until the fundamental properties of this system (e.g., chemical kinetics, burning rates, factors influencing cavitation, etc.) have been determined as functions of the composition, no hypothesis can be offered; however, it is worth noting that the acoustic matching between the liquid and container walls improves with higher concentrations of TNM. This effect may allow the cavity size or density to exceed a critical value due to enhanced energy transfer from the walls.

5. A decided effect of attenuator length on the measured pressures and velocities for LVD's in steel has been detected, indicating that donor contributions have not decayed in the charge length used; hence, it is doubtful whether hydrodynamic stability of LVD has been established.

6. In general, pressures observed are much less for Plexiglas than for steel tubes; this is to be expected in view of the fact that the relatively low-tensile strength, low-density Plexiglas yields more readily, allowing lateral rarefactions to degrade the reaction pressure.

Hydrogen Peroxide - Glycerol System

This system is of interest because of its chemical structure; it is one of the few homogeneous liquid explosives whose components do not contain the NO_2 group.

Again, the experimental set-up was the gap-test arrangement described earlier; the donor was a 1.63-inch diameter x 1.0-inch long tetryl pellet ($\rho = 1.57$), the attenuator was composed of 1.63-inch diameter Plexiglas disks, and the acceptor was contained in 1.05-inch id, 0.133-inch wall, 16-inch long aluminum tubes which had been passivated. The instrumentation consisted simply of a pair of rate stations formed by twisted pairs of enameled copper wire mounted on the outer surface of the container—a technique which gives satisfactory results for HVD's but not for LVD's. The hydrogen peroxide used was 90 percent grade. The experimental results are given in Fig. 8 which shows the threshold gaps for both HVD's and LVD's as a function of mixture composition. The upper threshold for the LVD regime in the most sensitive mixtures (15-42.5 percent glycerol) was not obtained for reasons given in the preceding section. It was found in a previous investigation employing projectile impact [5,6] that these mixtures are even more sensitive

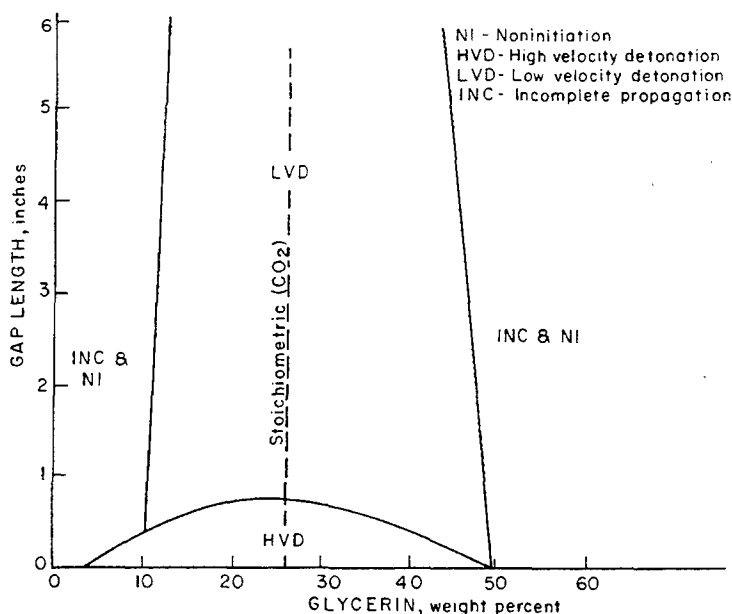


Fig. 8 - Gap sensitivity of 90 percent H_2O_2 -glycerin system in aluminum containers at 25°C

to initiation of LVD than NG-EGDN—calculated impact pressures to initiate LVD being about 2 kilobars for peroxide-glycerol as opposed to 3 kilobars for NG-EGDN. The LVD regime extends from 12.5 to 47.5 percent glycerol; heats of explosion calculated at these compositions are 739 and 753 cal/gram* respectively so that with respect to the heat of explosion the LVD "detonability limits" (under these experimental conditions) are symmetric. This suggests that the heat of explosion may be a controlling factor in determining the susceptibility of a system to LVD. This critical value of the heat of explosion should be compared with that for another system—NG-EGDN-TA; under identical environmental conditions, the highest TA concentration at which LVD's are observed is 30 percent, corresponding to a heat of explosion of 791 cal/gram.

Heat of explosion is not the only important parameter, however. Nitromethane with a heat of explosion of 1194 cal/gram barely exhibits

LVD's. Even stoichiometric NM-TNM with a heat of explosion of 1633 cal/gram is decidedly less susceptible to LVD than NG-EGDN with a heat of explosion of 1559 cal/gram. The latter in turn is less susceptible to LVD than stoichiometric peroxide-glycerin with a heat of explosion of only 1185 cal/gram. It is perhaps noteworthy that this ranking of sensitivities can be correlated with the results of thermal stability studies: nitroparaffins are usually more stable than nitrate esters which are, in turn, more stable than peroxides.

Experimental Casting Solvents for Double Base Propellants

Five experimental casting solvents, designated A through E, whose compositions are given in Table 3, were evaluated using the instrumented gap test described earlier; the samples were contained in 1.05-inch id, 0.133-inch wall, 16-inch long aluminum tubes.

Thresholds (expressed as attenuator length) for the initiation of HVD's, LVD's, and propagation failures (INC's) were obtained for each of the samples and are shown in Table 4. The correlation between oxygen balance* (O.B.) and

*The heats of explosion quoted here and elsewhere are calculated according to a variation of the usual procedure in which oxygen is consumed to form H_2O , CO , CO_2 in decreasing priority, NO , NO_2 , CH_4 , etc., are not assumed to be formed, and the Δh_f 's used were the values at 298°K , 1 atm (for H_2O the value for the gaseous state was used). The numbers quoted above are not claimed to be the correct effective values but are presented for the purpose of comparison.

*Defined by the formula $\text{O.B.} = 100 (f_{\text{O}} - 8f_{\text{H}} - 2.667 f_{\text{C}})$ where f_{O} , f_{H} , f_{C} are the weight fractions of oxygen, hydrogen and carbon respectively.

TABLE 3
Composition (Weight Percent) of Experimental Casting Solvents

Component	Sample				
	A	B	C	D	E
Nitroglycerin	70	—	—	75	80
Trimethylolethane trinitrate	—	—	80	—	—
1,2,4 butanetriol trinitrate	—	65	—	—	—
bis-2,2 dinitropropyl acetol	20	29	—	—	—
Triethylene glycol dinitrate	—	—	19	—	—
Triacetin	9	—	—	24	19
Camphor	—	5	—	—	—
Nitrodiphenylamine	1	1	1	1	1

TABLE 4
Comparison of Sensitivities of Experimental Casting Solvents and NG-EGDN-TA Mixtures

		A	B	C	D	E
Threshold Gaps (inches)	HVD/LVD	1.1	0.1 ¹	0.2	0.2	1.1
	LVD/INC	12.5 ²	—	1.4	1.5	14.0 ²
	INC/NI	—	—	5.5	5.5	—
Oxygen Balance		-24.8	-45.5	-42.3	-32.7	-25.6
Threshold Gaps for O.B. — equivalent NG-EGDN-TA (inches)	HVD/LVD	0.7	0.1 ¹	0.1 ¹	0.2 ³	0.7
	LVD/INC	6.0 ²	—	—	—	6.0 ²
	INC/NI	—	—	—	3.5	—

¹HVD/NI threshold, no LVD's or INC's observed.

²LVD/NI threshold, no INC's observed.

³HVD/INC threshold, no LVD's observed.

sensitivity may be evaluated from these data. Generally, the correlation is significant, a notable exception being sample C which resembles D in sensitivity and B in O.B. The reason for this discrepancy is not readily apparent. It is noteworthy that all samples, except B, are more sensitive at least to LVD's than NG-EGDN-TA mixtures of equivalent O.B.

Emulsified Systems

On the basis of the cavitation-microjetting-hot-spot model, it could be argued that immiscible inert liquids, dispersed in a liquid explosive system as an emulsion, might be more effective desensitizers than miscible diluents, assuming that the suspended droplets are potential cavitation nuclei, because:

1. increasing the number of opportunities for cavitation and, hence, the number of cavities produced per unit volume will result in decreased cavity size and presumably less energy concentrated at any one hot spot;

2. the presence of inhomogeneities may degrade the jet formation process;

3. the hot spots should occur at the loci of the inert droplets so that the critical phase of the initiation process occurs where the conditions for propagation are least favorable.

Accordingly, a number of experiments were conducted in which various liquids immiscible with NG-EGDN were emulsified with the latter; the samples were contained in 1.0-inch id, 0.125-inch wall, 8-inch long Plexiglas tubes.

All additives were stirred into the NG-EGDN liquid with a high-speed mixer, the mixing time being kept constant (3 minutes). The emulsified mixture was poured into the charge container and fired within 1 minute. Delay times to initiation of the order of several hundred microseconds were frequently encountered; as the instrumentation became inoperative during this time, it was difficult to determine whether the result is an HVD, LVD, or

INC. For this reason as well as a marked lack of reproducibility in the delay times, probably due to lack of control over the droplet size of the emulsions, no definitive conclusions in general were reached.

There were some surprising results, however, particularly in the experiments on H_2O additive on which a large number of tests were made so that a more meaningful analysis of the data was possible. Here, a few records indicated transitions from low to high-velocity detonations but no record showed a steady, complete LVD during the recording time of 300 μ sec. Results obtained with H_2O are illustrated in Fig. 9.

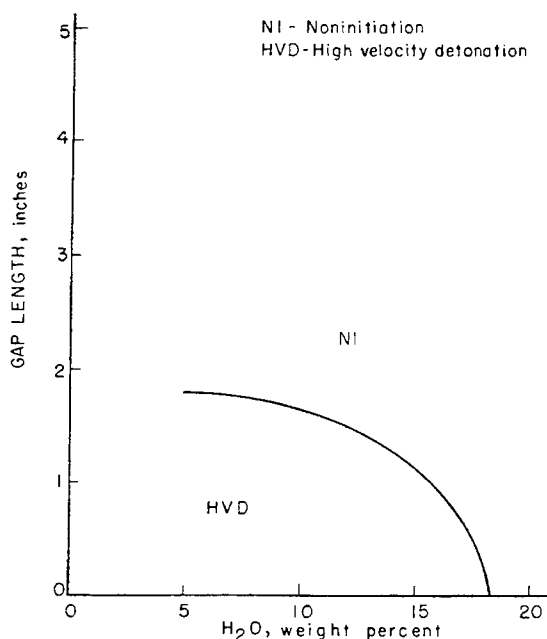


Fig. 9 - Gap sensitivity of NG-EGDN- H_2O emulsion in Plexiglas containers

NG-EGDN-Acetone System

This system was chosen for study in order to compare the effectiveness of acetone and triacetin, diluents which have different physical and chemical properties, as desensitizers. The experimental arrangement was the same as that used in the experiments with the emulsion. The experimental results are shown in Fig. 10 (with the curves for the NG-EGDN-TA system included for comparison). It will be noted that the LVD-NI threshold is drawn as a vertical line at 10 percent acetone; at this composition both LVD's and NI's occurred without correlation to the gap thickness. It is evident that acetone is a much better desensitizer to LVD's than TA.

Because the effect on the heat of explosion of equal percentages by weight of these two materials is not significantly different, this constitutes further evidence that the sensitivity of a liquid explosive to LVD is dependent on physico-chemical characteristics not usually taken into account.

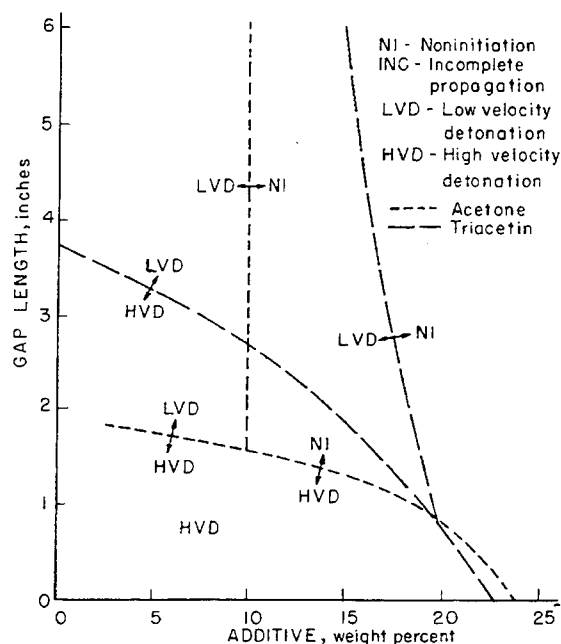


Fig. 10 - Gap sensitivity of NG-EGDN-acetone system in Plexiglas containers

NG-EGDN-TA-Polymethyl Methacrylate (PMMA) System

Since the importance of oxygen balance, viscosity, and temperature with respect to the sensitivity of a liquid explosive is frequently alluded to in the literature, this explosive system was chosen for study in an attempt to determine quantitatively the effects of these factors on the sensitivity to LVD's.

The explosive was contained in 8-inch lengths of Plexiglas tubing of 1-inch id and 1/8-inch wall thickness. Oxygen balance was controlled by the concentration of TA and PMMA, and the viscosity was controlled by the concentration of PMMA and the temperature; thus, the intrinsic effect, if any, of temperature is confounded with its effect through the viscosity. Actual viscosity measurements were not made on every sample; survey measurements were made with a falling-ball type viscosimeter. Since this system is a non-Newtonian liquid,

TABLE 5
Sensitivities (as Threshold Gap Thickness in Inches)
of NG-EGDN-TA-PMMA System

HVD-LVD Thresholds				
Oxygen Balance (percent)	Temperature	PMMA Content		
		0 percent	5 percent	10 percent
-15	3°C	1.5	1.1	1.4 ¹
-15	60°C	1.9	1.7	1.6 ¹
-22.5	3°C	0.9	1.1 ¹	0
-22.5	60°C	1.6	0.9	1.1 ¹
LVD-NI Thresholds				
-15	3°C	>6	1.6	- ²
-15	60°C	>6	>6	- ²
-22.5	3°C	4.1	- ²	0
-22.5	60°C	4.4	1.4	- ²

¹HVD-NI threshold, no LVD's observed.

²No LVD's observed.

the viscosity determined by this means has no fundamental significance and, hence, is not reported here. Thus, the concentration of viscifying agent (PMMA) rather than the actual viscosity will be referred to. In general, the apparent viscosity of the mixtures containing 10 percent PMMA was about 10 times that of the mixtures without PMMA.

Sensitivity determined as the threshold attenuator thicknesses are shown in Table 5.

The statistics of the data obtained were poor due to ambiguity caused by extreme variability of the initiation delay times and propagation rates near the threshold of principal interest (LVD-NI). One striking feature, however, is the greatly reduced incidence of LVD's in the more viscous systems relative to the less viscous systems of equivalent oxygen balance. On the basis of the cavitation - microjetting model for LVD's (see paper by Watson et al. on Detonations in Liquid Explosives - The Low-Velocity Regime presented at this Symposium), one of the parameters governing the susceptibility of a liquid explosive system to LVD should be the ease with which it responds to differential hydrodynamic stress, which is controlled by the viscosity: hence, the above results are in accord with expectations. Surprisingly, the effect of temperature on either threshold appears to be quite small.

CONCLUSIONS

A complete elucidation of the relationship between the physico-chemical properties of a liquid explosive system and conditions of its environment and its tendency to LVD has not yet been achieved. However, the present findings agree well with the model proposed for LVD and indicate the nature of the most important of these properties and of areas of further research required for a better understanding of the problem.

ACKNOWLEDGMENTS

This work was formerly supported by the Bureau of Naval Weapons, Department of the Navy, Contract IPR-19-64-8026-WEPS and, currently, by the same agency under Contract 19-65-8023-WEPS.

REFERENCES

1. Van Dolah, R. W., R. W. Watson, F. C. Gibson, C. M. Mason, and J. Ribovich. Low Velocity Detonation in Liquid Explosives. Papers of International Conference of Sensitivity and Hazards of Explosives, London, Waltham Abbey, Essex, England, October 1963.

2. Bowden, F. P. and A. D. Yoffe. Initiation and Growth of Explosion in Liquids and Solids. Cambridge at the University Press, 1952, p. 99.
3. Liquid Propellant Information Agency, The Johns Hopkins University. Card-Gap Test for Shock Sensitivity of Liquid Monopropellants, Test No. 1 in Liquid Propellant Test Methods. Silver Spring, Md., March 1960.
4. Gibson, F. C., M. L. Bowser, C. R. Summers, and F. H. Scott. An Electrical Method for the Continuous Measurement of Propagation Velocities in Explosives and Propellants. Bureau of Mines Report of Investigations 6207, 1963, 8 pp.
5. Mason, C. M., J. Ribovich, and M. L. Weiss. Sensitivity Characteristics of Liquid Explosive Systems. Bureau of Naval Weapons, Contract IPR 19-63-8029-WEPS, Progress Report No. 7, July 1 - Sept. 30, 1963.
6. Gibson, F. C., C. M. Mason, J. Ribovich, and J. E. Hay. Sensitivity Characteristics of Liquid Explosive Systems. Bureau of Naval Weapons, Contract IPR 19-64-8026-WEPS, Progress Report No. 9, Jan. 1 - Mar. 31, 1964.

RETONATION CAUSED BY THE REFLECTION OF DIVERGENT WAVES

W. R. Marlow

*Atomic Weapons Research Establishment
Aldermaston, Berkshire, England*

ABSTRACT

Initiation and retonation phenomena associated with divergent waves in 12 cm diameter 6 cm long cylindrical charges of HMX/TNT are illustrated by streak and framing camera records. A weak divergent disturbance travelling at about $2.7 \text{ mm}/\mu\text{sec}^{-1}$ is generated by a shock transmitted from a thin coaxial rod. This disturbance propagates through the charge and when it is reflected from a thick steel plate it is sufficiently strong and maintained to cause detonation in the reverse direction. When the steel is replaced by Perspex the reflected wave is too weak to cause detonation. Reflection from a composite barrier has also been studied.

INTRODUCTION

Previous shock initiation literature [1] has described phenomena in charges with nominally plane initial shocks. This paper describes an experimental investigation of phenomena resulting from weak, localised impact on a solid explosive which generates a spherically diverging shock. Impact conditions have been found which caused a low order disturbance to travel through the explosive until a barrier is reached, when the barrier composition and geometry determines whether or not detonation occurs in the reverse direction. The initiating pulse is complex and not easy to define. Conditions for the phenomena described are fairly critical and small variations can easily give rise to erratic results.

EXPERIMENTAL

The charge arrangement in use throughout the main sequence of shots is shown in Fig. 1. A standard 5.08 cms. diameter Baratol/Comp. B plane wave shaper sends a shock into the Duralumin disc shown. From this disc a steel column 0.635 cms. diameter transmits a pulse to the receptor charge, the whole being axially symmetrical. A Duralumin disc 1 mm thick and 10 cms. in diameter rests on top of the charge, underneath the steel column. This is as protection against possible spalling or hot gases. Underneath this plate is the receptor

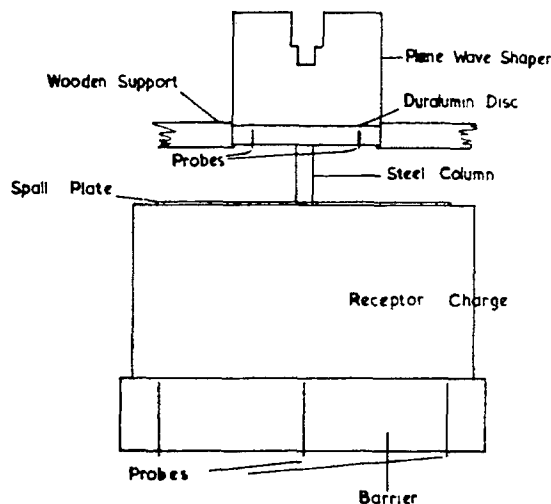


Fig. 1 - Experimental arrangement

charge of HMX/TNT 75/25 composition, 12 cms. diameter and 6 cms. deep, supported on a metal base. The assembly is fired with its axis vertical. Streak camera techniques are used together with pin probes to record transients in each experiment. Kerr cell and framing camera sequences have also been used.

Typical results are illustrated by the two framing camera sequences shown. Figure 4 illustrates the passage of the low order

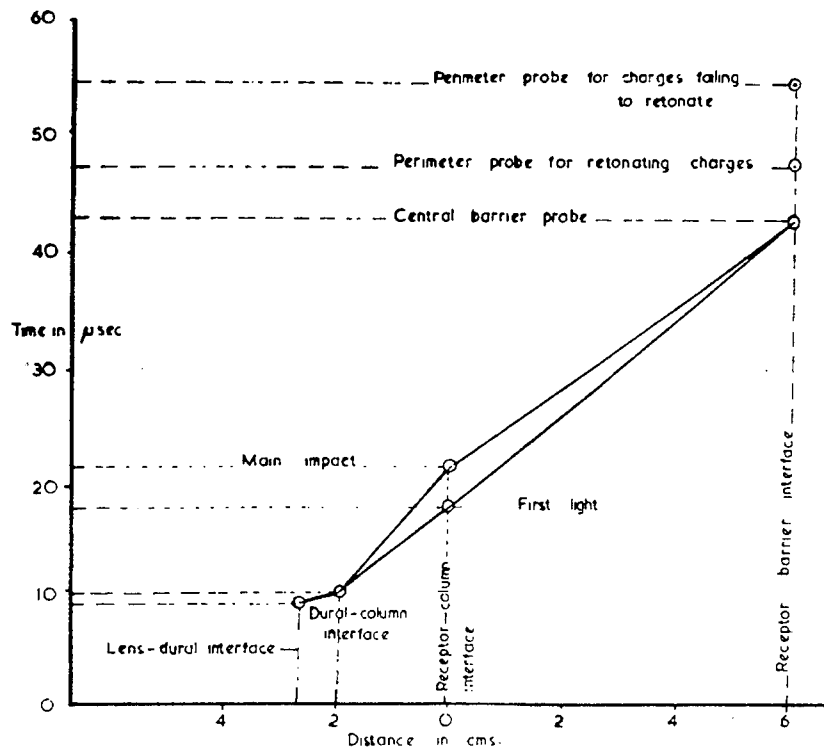


Fig. 2 - Representative times through system

disturbance through the charge to the steel barrier where it reflects as a high order detonation. As only the surface of the charge is seen this gives little direct evidence of the wave shape within the explosive. Figure 5 shows the situation when a flat is cut on the charge, parallel to its axis and 3 cms. from it. A rectangular ink grid was ruled on the charge, unit size 1 cm. by 0.5 cms. and the distortion of this grid indicates clearly the passage of the wave front. The reflectivity of the charge surface changes as the shock wave passes through. Later blurring of the grid lines is probably due to ink particles being flung off the charge. At the barrier the wave reflects as a high order detonation.

The column length is a fairly critical parameter in setting up conditions for the reported phenomena. A large number of shots were fired to establish that with a length of less than 1.5 cms. the charge always detonated immediately, and with a length greater than 2.5 cms. failure to detonate always happened, fragments of explosive being recoverable. For a 2 cm. column with the appropriate barrier under the charge retonation at this barrier was produced in 8 out of 10 shots. The other two receptor charges detonated within the body of the charge before reflection. In these rounds the barrier was of

mild steel, 12.5 cms. diameter and 2.54 cms. thick.

The initial pressure pulse which leads to retonation is not simple and depends both on the pressure of the steel column and of the Duralumin disc. Attempts to measure the pulse amplitude at the end of the steel column gave unsatisfactory results. The duralumin disc is forced down the steel column which later punches its way through the disc. The impact on the charge cover plate consists of the shock which is the precursor of the disc moving down the column followed by the impact of the disc itself. If the column is removed but the same spacing retained the charge detonates at or near the top surface. The measured impact velocity of the Duralumin disc is approximately 1.5 mm/ $\mu\text{sec.}$ corresponding to a pressure of 150 kb in the Duralumin and of about 60 kb in the receptor charge.

If the cylinder is retained but interposition of a heavy baffle prevents the disc from reaching the receptor, complete failure occurs, large fragments of the charge being recovered.

In an attempt to provide a less complex initiating pulse the 5.08 cm plane wave shaper,

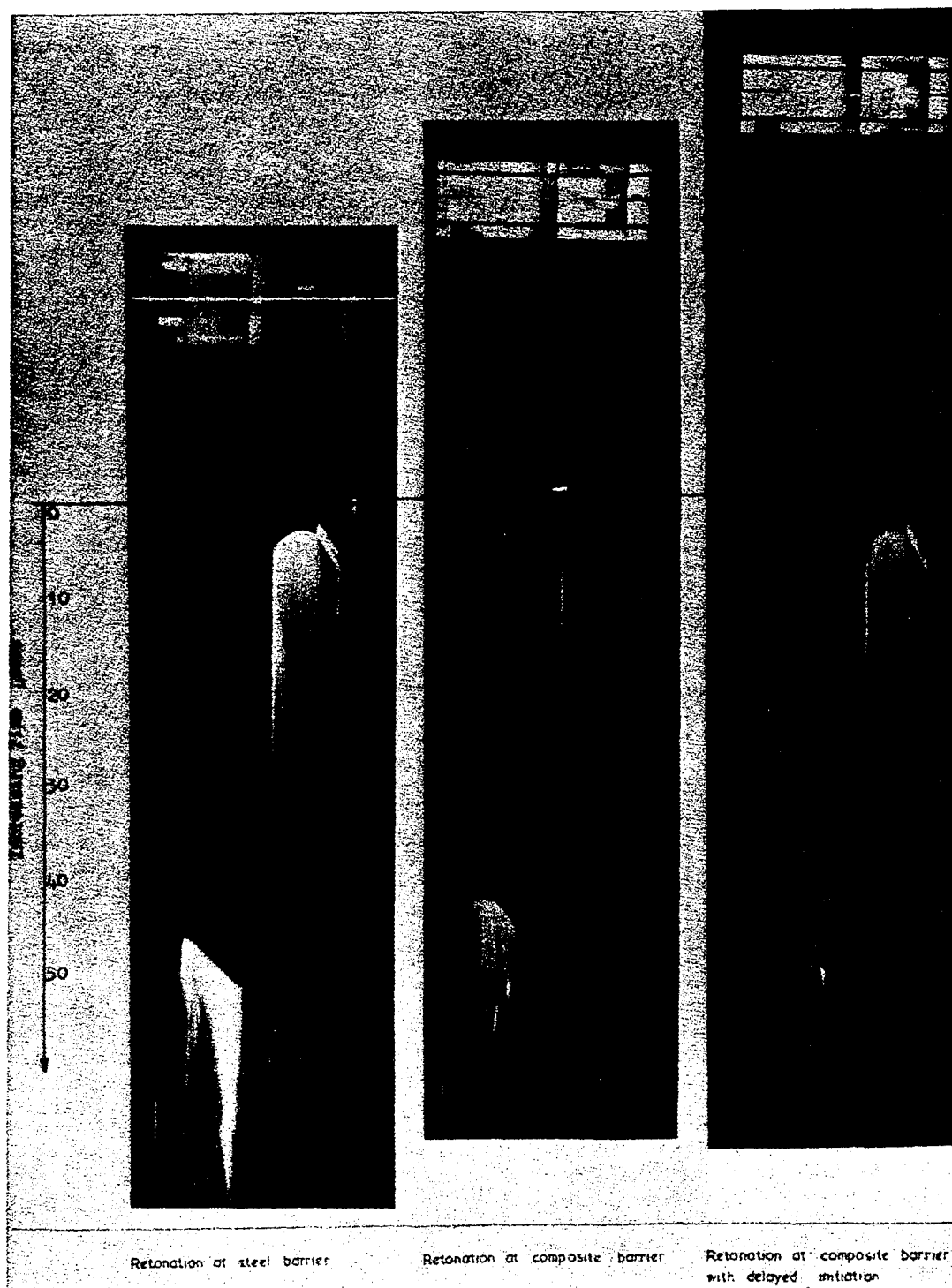


Fig. 3 - Typical streak camera records

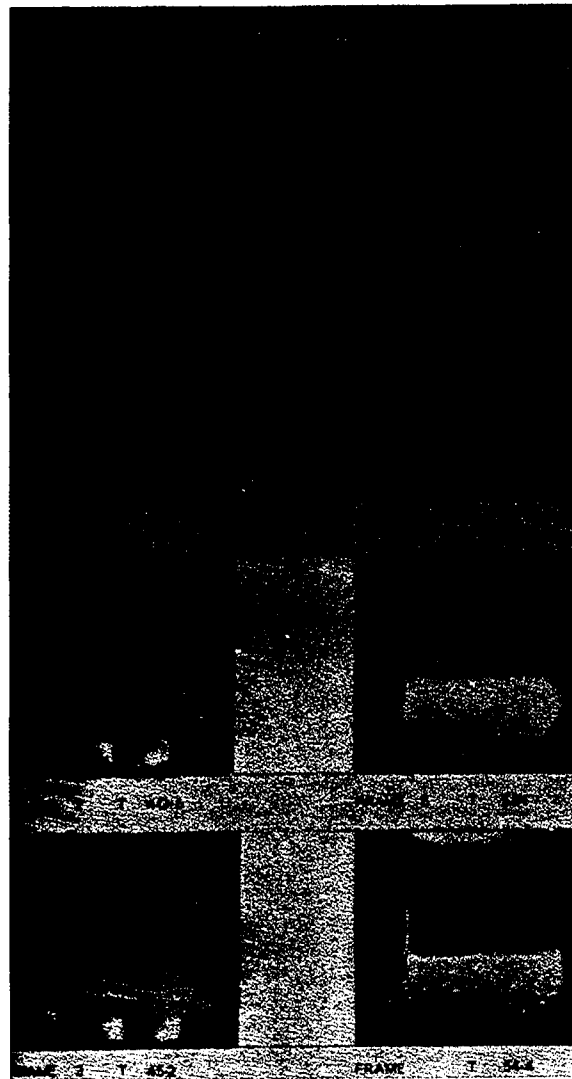


Fig. 4 - Framing camera sequence showing low order disturbance reflecting as high order detonation at a steel boundary. Time T (μsec) refers to current zero at detonator.

disc and column were replaced by a 2.54 cms. plane wave shaper, initiating a Comp. B driver charge of the same diameter, which threw a 2.54 cm. diameter, 0.635 cms. thick Duralumin disc at the receptor assembly. No column was used. With a driver charge of length 1.27 cms. or less the receptor failed to take up and pieces of explosive were recovered. When the driver was 1.59 cms. or greater the receptor detonated immediately. Of 5 such rounds fired with a driver of 1.48 cms. length 2 detonated immediately, 2 failed, and one retonated. This system was deemed too critical to work with. The disc impact velocity was measured as 2.3 mm/ μsec .

corresponding to an impact pressure of 215 kb in the disc, and approximately 82 kb in the charge.

The first group of shots was fired with a barrier of mild steel, 2.54 cms. thick and 8 out of 10 such shots retonated, the remaining two detonating spontaneously within the charge. A second group of shots was fired with a composite barrier of 0.75 cms. latex rubber next to the charge, then 8.0 mm Duralumin, and finally 2.54 cm. of steel. Of 4 such shots, 2 retonated at the charge/barrier interface and 2 retonated strongly over only half the charge

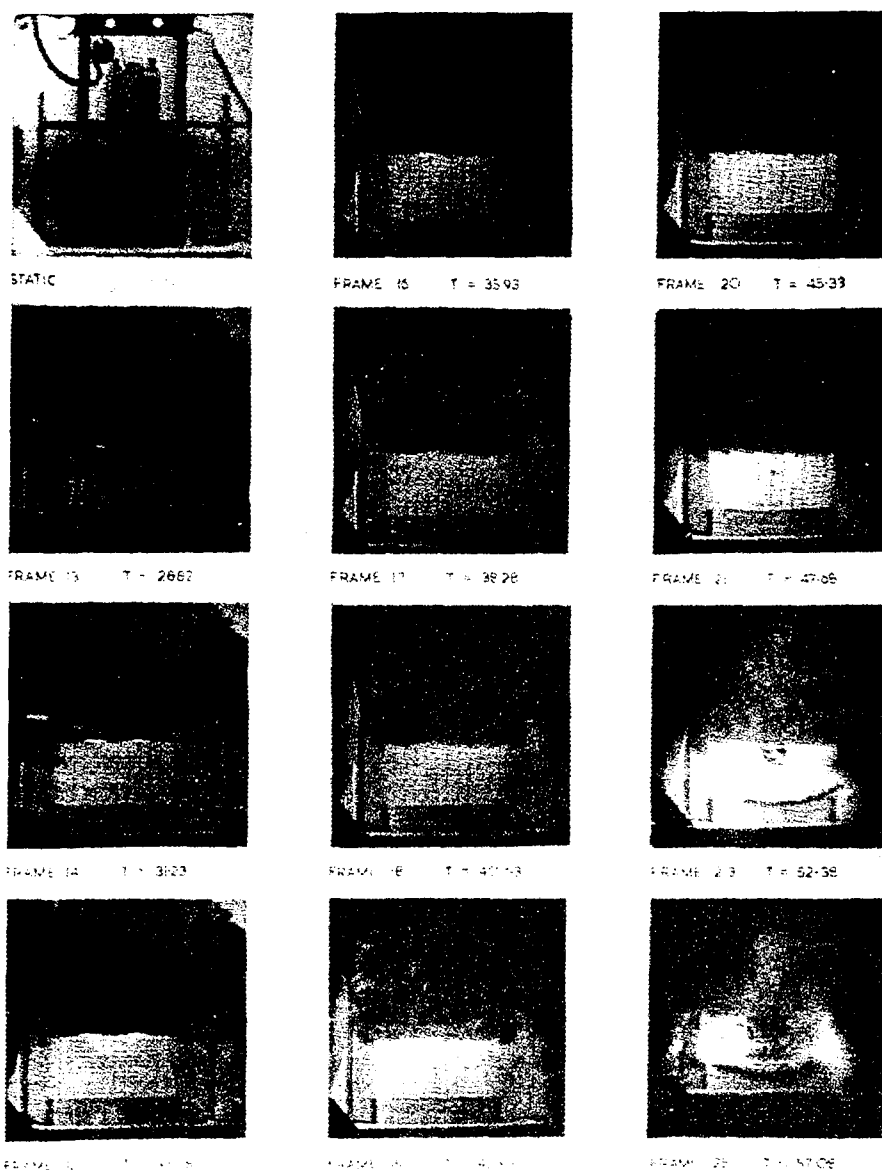


Fig. 5 - Framing camera sequence with sectioned charge showing low order disturbance reflecting as high order detonation at a steel boundary. Time T refers to current zero at detonator.

length. This is illustrated by the third streak camera photograph in Fig. 3. Repeating these shots with the steel thickness reduced to 3 mm. caused the receptor to fail but no explosive was recovered. With a barrier of 2.54 cms. of Perspex all rounds failed. Even with charges reduced to 1 cm. depth no high order reaction took place.

Because of fear of perturbing the wave within the charge no probes were placed in the explosive. Transit times throughout the charge

were derived from a series of shots made with constant initiating geometry but with the charge length varying between 1 and 6 cms. by increments of 1 cm., overall times taken from all rounds and from shots where a flat was cut on one side of the receptor. These latter were viewed with a framing camera and showed the low order disturbance travelling through the charge to the barrier and its detonation at the barrier. These results are consistent with the picture of a spherical wave with origin at the mid-point of the receptor face. Scatter from

round to round was large, but the wave velocity appears constant within any one charge, and ranged from 2.4-3.0 mm/ μ sec. with a mean at 2.7 mm/ μ sec.

DISCUSSION

Comparison of light intensities produced at the charge/perspex interface in the series fired with varying lengths of receptor suggest that the initial shock amplitude drops fairly quickly, since the light output after the second centimetre of charge is negligible. Measurements were not sufficiently sensitive to detect any difference in the shock velocity between the first part of the charge where the incident pulse could be expected to play a major part in determining shock strength, and the charge end where it is probable that the shock was maintained solely by reaction at or behind the front. In the present geometry the charges were not sufficiently large to show whether or not there was a slowly declining energy release, a quasi-stable state, or conditions that would eventually accelerate to detonation. Experiments with 5.08 cms. diameter charges and nominally plane shocks have given examples of all three possibilities [2].

Previous work by the author [1] has shown that an induced shock as low as 20 kb in the explosive, if maintained for several microseconds, will lead to detonation. If the pulse is shortened the pressure needs to be higher for detonation to follow and it has been shown that a pulse of 60 kb in the explosive, lasting for approximately one μ sec. will cause immediately detonation in 5.08 cms. diameter charges. The changed form of the initiating pulse in the main sequence of experiments described here presumably accounts for the difference in behaviour observed but it is still surprising that with the 2.54 cms. diameter initiating system

the receptor charge can either detonate immediately, show low order phenomena, or fail completely. Previous experience suggested that with a pressure of 80 kb in the explosive and a pulse length of 2 μ sec. immediate detonation would occur. Reducing the driver length by as little as one millimetre results in complete failure, increasing it by the same amount gives immediate detonation at the charge surface. The explanation may be either in the fact that here we have divergent waves and/or in the reduced area of impact of the smaller disc with rapid penetration of latest rarefactions.

The behaviour observed when the barrier composition is altered can be qualitatively explained. With a thick steel barrier the reflected disturbance is a shock of long duration and the consequence pressure and temperature rise accelerate chemical reaction to almost immediate detonation in the reverse direction. With a perspex barrier impedance considerations show that the reflected wave is a rarefaction and the pressure and temperature drop following is sufficient to quench any reaction. Composite barriers represent an intermediate state. An initial rarefaction is followed by a slow buildup of pressure due to reverberation in the barrier material, and this will build up into a shock some distance back in the explosive. The 2.54 cm. steel layer delays rarefactions from reaching the reflected front before detonation can be established, but reduction of the steel thickness to 3 mm. enables a rarefaction to quickly follow the reflected compression and quench the reaction before detonation occurs.

REFERENCES

1. Proc. Roy. Soc. A Vol. 246, 145, 1958.
2. Unpublished work.

COMPARISON BETWEEN SHOOTING AND BARRIER TESTS

N. Lundborg

Swedish Detonic Research Foundation Vinterviken
Stockholm SV, Sweden

ABSTRACT

The end velocity of an Al-barrier has been measured as a function of the length. The critical end velocity has been determined for three different explosives and compared with the critical velocity in the shooting test. The result shows that the barrier test demands a somewhat higher velocity than the shooting test for the same explosive.

INTRODUCTION

In shooting tests with coaxial impact between cylinders with plane end surfaces [1] according to Fig. 1 we get the constant impact pressure

$$p = \frac{w_e \rho_e v}{1 + w_e \rho_e / w \rho}$$

where w is the shock front velocity in the projectile and w_e in the explosive sample, ρ and ρ_e are the densities and v is the velocity of the projectile before impact. The pressure remains constant until the arrival of the first reflection-wave in the projectile. Brown and Whitbread [2] found that the length of steel projectile was insignificant down to 2 mm. This corresponds to an initiation delay of about 1 μ s. With longer projectiles the initiation occurs before the pressure begins to fall. Figure 1 shows the pressure-time-diagram when shooting an Al-projectile 15 mm in diameter and length against a TNT-sample of the same diameter and a velocity of 650 m/s.

In the barrier test (Fig. 2) the donor causes a shock wave in the barrier, which in turn gives rise to an impact pressure at the contact surface between the barrier and the explosive sample. The figure shows the pressure-time-diagram for donor and sample of pressed TNT and an Al-barrier 21 mm in diameter at the critical length, 21 mm. The pressure is not constant but falls rapidly with the time. The curve is calculated from a pressure curve according to Broberg [3].

Comparing the two tests for a number of explosives Brown and Whitbread [2] found a

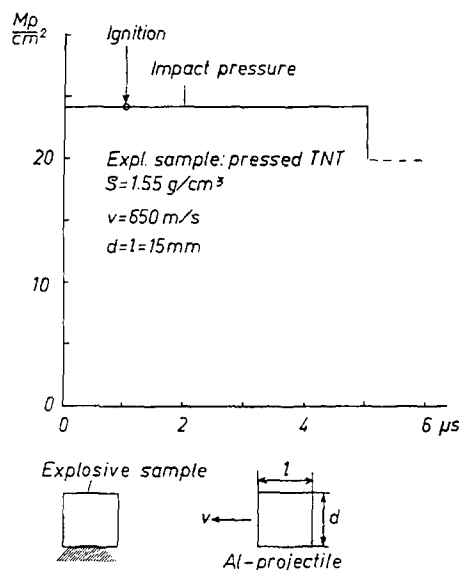


Fig. 1 - Shooting test

linear relation between the critical length of brass barriers and the critical velocity of steel projectiles, in both cases 12.7 mm in diameter (Fig. 3a). This linear relation has been confirmed here for cast TNT, pressed TNT and pressed PETN with 10% wax (Table 1, Fig. 3b). The barrier test was performed with a donor of pressed TNT and a barrier of Al at a diameter of 21 mm [4]. The critical velocities of the projectile are taken from an investigation by Eldh and others of a Swedish group [1] proposing a shooting test with projectiles of brass 15 mm in diameter and length and samples 30 mm in diameter. In Fig. 3b the values concern however 15 mm Al-projectiles.

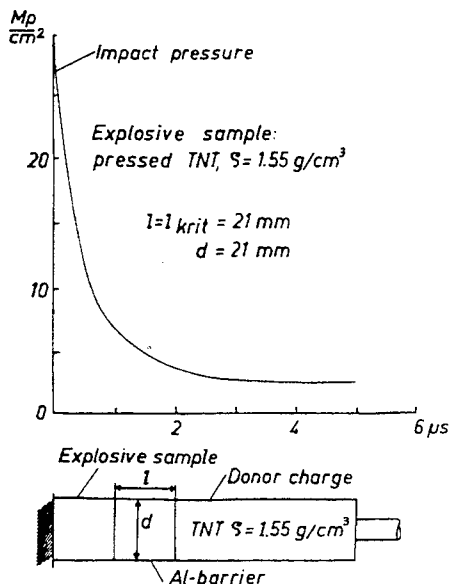


Fig. 2 - Barrier test

EXPERIMENTAL

Another way is to compare the critical projectile velocity with the end velocity of the barrier at the critical length. The latter was measured with an Al-plate 1 mm thick and 17.3 mm in diameter on the end surface of the Al-barrier (Fig. 4) and the time between two wire-contacts at a distance of 100 mm was measured. It was found that the particle velocity attenuates logarithmically with the barrier length (Table 2, Fig. 4). Extrapolation to a barrier length of 2 mm gives a velocity of 2400 m/s. Johansson and Sjölin [5] have obtained 2600-2700 m/s but then the donor was confined by a layer of clay. This causes a higher detonation velocity and therefore a higher plate velocity.

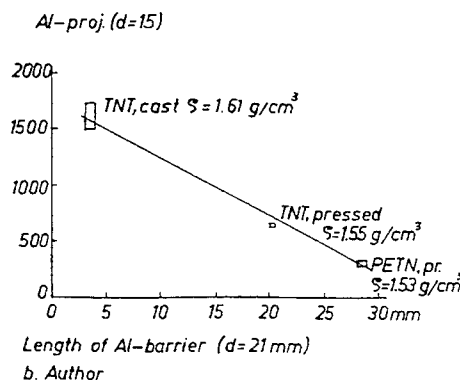
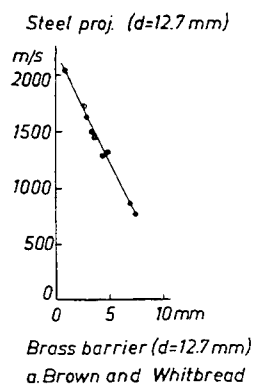


Fig. 3 - Relation between projectile velocity and barrier length

TABLE 1
Critical Length of 21 mm Al-Barrier and
Critical Velocity of 15 mm Al-Projectile
Against 25 mm Sample

Explosive	State	Density (g/cm ³)	Barrier length (mm)	Proj. velocity (m/s)
TNT	cast	1.60	3-4	1500-1720
TNT	pressed	1.54	20-21	640-650
PETN + 10% wax	pressed	1.33	28-29	290-340

Extrapolation in Fig. 4 to the barrier length zero gives 2600 m/s for the end velocity of the TNT-charge in contact with an Al-cylinder. The shock front velocity for Al is approximately 6200 m/s and by inserting 2700 kg/m³ for the density we get 217 kbars for the shock wave pressure in Al from TNT. Selberg (Report NAB 18.7.1962) has calculated 201 kbars and Broberg [3] 213-238 kbars.

Figure 5 shows the critical velocity of Al-projectiles as a function of the end velocity of Al-barriers at a critical length according to Figs. 3b and 4. The points in Fig. 5 indicate the uncertainty along the two axes. It will be noted that the required projectile velocity is somewhat lower than the barrier velocity. This may partly be due to the difference in diameter between projectile and sample in the shooting test but can also be expected from the difference in the pressure-time curves in Figs. 1 and 2.

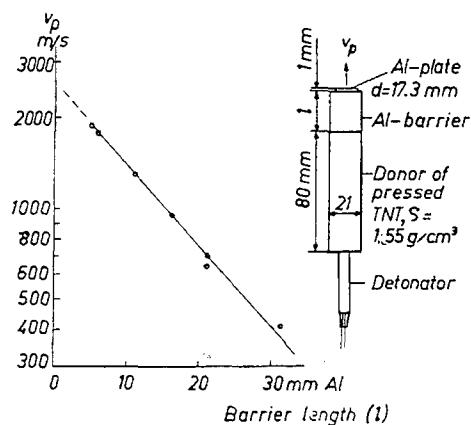


Fig. 4 - End velocity at different barrier length

TABLE 2
End Velocity of 21 mm Al-Barrier.
The Barrier Length Includes the Al-Plate
1 mm Thick.

Barrier Length (mm)	End Velocity (m/s)
5	1890
6	1820
11	1320, 1320
16	960
21	650, 700
31	410

ACKNOWLEDGMENT

The author wishes to acknowledge with thanks useful discussions with Prof. C. H. Johansson.

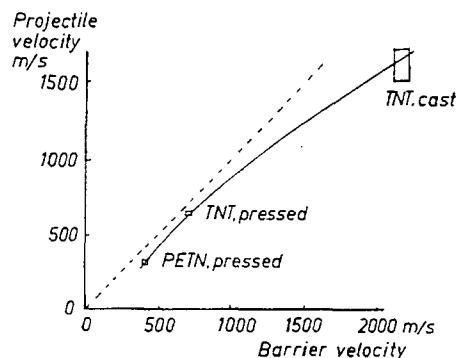


Fig. 5 - Relation between critical projectile and barrier velocity

REFERENCES

1. E. Eldh, B. Persson, B. Öhlin, C. H. Johansson, S. Ljungberg and T. Sjölin, *Explosivstoffe* **11** (1963) 97.
2. S. M. Brown and E. G. Whitbread, Coll. Int. Centre National Rech. Scient. Saint-Louis, France, 28.8-2.9.1961.
3. B. Broberg, Kungl. Fort. Förvaltningen, Stockholm. Report 109:12 (1956).
4. C. H. Johansson and T. Sjölin, *Arkiv för Fysik*, Stockholm, **24** (1963) 559.
5. C. H. Johansson and T. Sjölin, *Explosivstoffe* **9** (1961) 165.
6. M. Sultanoff, V. M. Boyle and J. Paszek, Third Symposium on Detonation ONR Symposium Reports ACR-52, 26-28.9 (1960) 520.
7. I. Jaffe, R. Beauregard and A. Amster, Third Symposium on Detonation ONR Symposium Reports ARC-52, 26-28.9 (1960) 584.
8. N. Lundborg, *Explosivstoffe* **12** (1964) 269.

THE INITIATION PROPERTIES OF BOOSTERS IN EXPLOSIVES WITH LOW SENSITIVITY*

C. H. Johansson and T. Sjölin
*Swedish Detonic Research Foundation, Vinterviken
Stockholm SV, Sweden*

ABSTRACT

The investigation has been performed with conical boosters of a high explosive with their favourable initiation capacity in relation to their weight. The critical bottom diameter and the critical weight of the boosters have been determined as a function of the cone angle for the initiation of a powder explosive of the AN-FO type and a slurry explosive of the Melvin Cook type. The propagation of the shock front in the receptor charge has been recorded for different booster diameters. When it is smaller than the critical booster diameter the detonation dies out although its shock front area at first increases.

INTRODUCTION

Progress made of recent years in shock wave initiation has applied chiefly to how a shock wave whose frontal pressure is lower than that of the detonation can develop into a stationary detonation [1-4]. When using boosters of high explosives for initiation explosives with low sensitivity, as powder explosives of the AN-FO type or TNT-AN slurries [5] a different problem applies. Shock wave pressure at the contact surface is greater than detonation pressure of the receptor charge and the detonation starts off without delay. In this case, however, there is the additional condition that the diameter of the contact surface must exceed a critical value for the detonation to continue.

EXPLOSIVES EMPLOYED

The tests have been made with boosters of "Startex," a plastic high explosive with a hydrogel containing 60% dinitroethyl-uric (DiTeU), 20% nitrates, 17.5% water, 2% hydrocarbons and 0.5% guar. DiTeU is oxygen-balanced [6,7]. The density of Startex is 1.45 g/cm³ and the detonation velocity 7100 m/s in

plexi-glass tubes with an internal diameter of 2 cm and wall thickness of 0.5 cm.

Startex has been used to initiate "Ammonit" and "Reolit." Ammonit is a powder explosive with 92% AN, 4% coal, 3% Si and 1% fuel oil. $D = 3100$ m/s at a density of 1.06 g/cm³ in iron tubes 2.5 cm in diameter. Reolit is a slurry explosive with 62.6% nitrate, 25% TNT, 12% water and 0.4% guar. The density is 1.50 g/cm³ and the detonation velocity 4900 m/s in tubes of paper-bakelit 10 cm in diameter.

THE CRITICAL DIAMETER OF THE BOOSTER [8]

When a cylindrical charge detonates the shock wave pressure is considerably greater at the end surface than along the envelope surface. A comparison of the initiation strength[†] at the end surface of cylindrical and conical boosters has shown that this is approximately the same for the same ratio between length (L) and bottom diameter (ϕ). The mutual curve for the initiation strength as a function of the ratio L/ϕ tallies with Cook's curve for the end action in an axial detonation of cylindrical charges ([5]

*Ed. Note: The first part of this paper is treated in greater detail in [8].

[†]The comparison was made with a method suggested by Johansson and Alfredsson [9]. The receptor charge is 3 cm in diameter and 5 cm in length and consists of finely ground TNT and glycol. It is packed by hand in a plastic tube on a lead cylinder immediately before the test. The glycol content when the lead cylinder is crushed to half its height is adopted as a measure of the initiation strength.

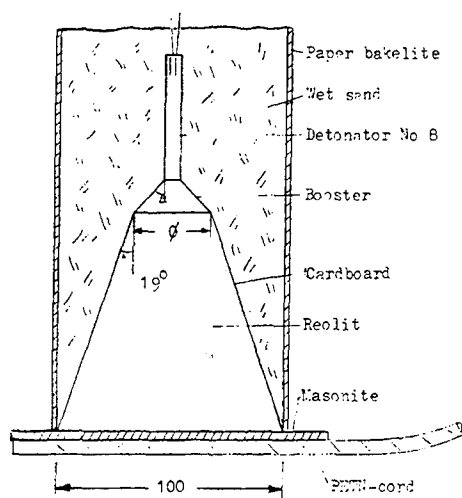


Fig. 1 - Arrangement for determining critical booster diameter

Fig. 5.5). As conical boosters are lighter in weight the continued investigation has been restricted to such.

For a direct determination of the critical diameter of Startex boosters in initiating Ammonit and Reolit an experimental arrangement as in Fig. 1 has been employed. The conical shape of the receptor charge was chosen so as to keep down the weight of the charge and the cover of wet sand so as to reduce the bang of the explosion. Some controlling tests without sand and tests with cylindrical receptors 10 cm in diameter gave approximately the same result. The critical bottom diameter of the booster was determined as a function of the cone angle (2α) between 20 and 128 degrees. Thus the shape was changed from an elongated cone, the height of which is more than double the bottom diameter, to a low conical disc the height of which is only 20% of the bottom diameter (Fig. 2). The test results are compiled in Fig. 3 for Reolit and in Fig. 4 for Ammonit.* The diagrams show that the critical booster diameter for Reolit rises approximately linearly by $\tan \alpha$ from c. 3 cm when $\tan \alpha \rightarrow 0$ (cylinder 4 cm in height) to c. 4 cm when $\tan \alpha = 2$. This implies that at small cone angles the critical weight of the booster diminishes rapidly with increasing angle and at larger angles approaches a lower limit value of c. 7 g. The result for Ammonit is similar but the critical booster diameter lies somewhat lower and the limit value for the critical

weight is c. 6 g. The continued investigation has been limited to conical boosters of Startex with a 90° cone angle and receptor charges of Reolit.

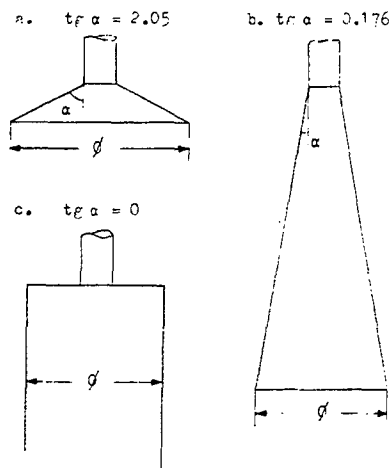


Fig. 2 - Booster shape

For determining the booster strength as a function of its bottom diameter (ϕ) at initiation of Reolit a method with receptor charges of Reolit in tubes of paper bakelite 6 cm in diameter and 40 cm in length has been used. In this the length of the tube (L) blown off is determined as a function of ϕ . The diagram in Fig. 5 shows that L to begin with rises linearly with ϕ . At approximately $\phi = 3.5$ cm the curve begins to bend upward and approaches very great values at $\phi_k = 4.5$ cm. In steel tubes 6 cm in diameter $\phi_k = 4.0$ cm was obtained.

For boosters with a cone angle of 90° and a cylindrical bottom part 0.5 cm in height the critical diameter fell from 4.5 cm to 4.0 cm, but the weight increased. At an edge height of 0.2 cm the difference in weight is negligible. The fact that low conical discs possess such a satisfactory initiation capacity and that the outer edge contributes indicates that initiation takes place even if the pressure of the booster is very brief. This is in keeping with Brown and Whitbread's results in shooting tests with varying lengths of projectiles [10].

In order to determine the critical diameter d_k for stationary detonation of Reolit in paper bakelite tubes the length of tube blasted off was determined as a function of the diameter of the charge when it was initiated across the entire end surface. According to Fig. 5 $d_k = 5.4$ cm was obtained.

*Figs. 3 and 4 reproduce measurements made by Mr. S. Alfredsson.

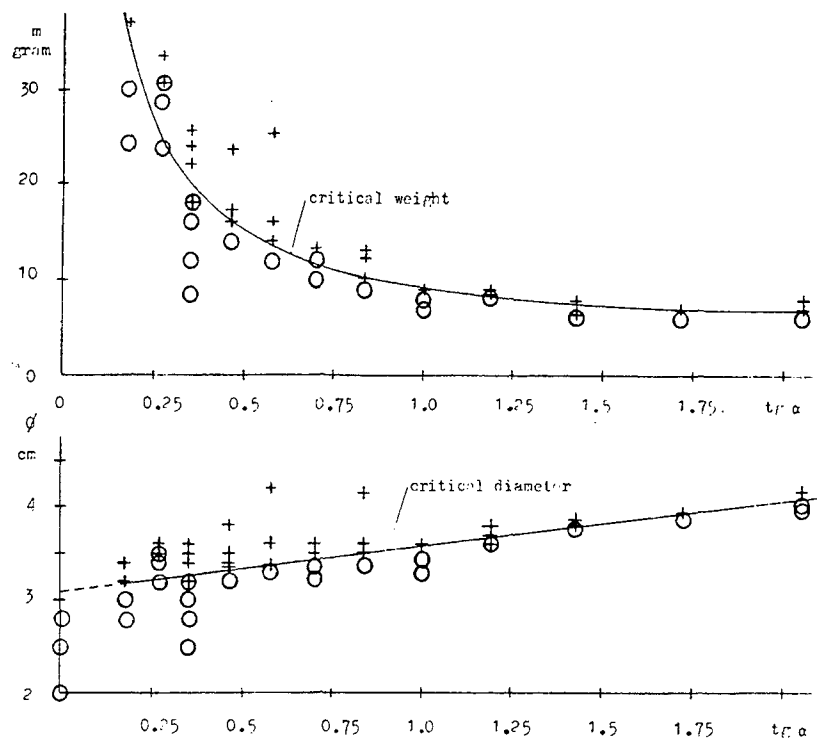


Fig. 3 - Initiation of Reolit with conical Startex booster. Rings indicate misfiring; crosses complete detonation.

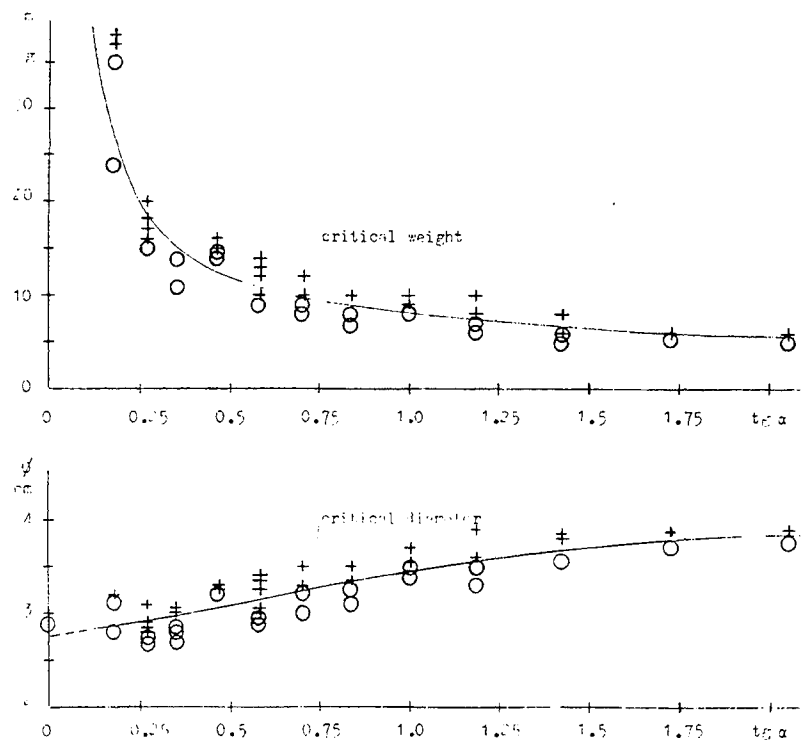


Fig. 4 - Initiation of Ammonit with conical Startex booster. Rings indicate misfiring; crosses complete detonation.

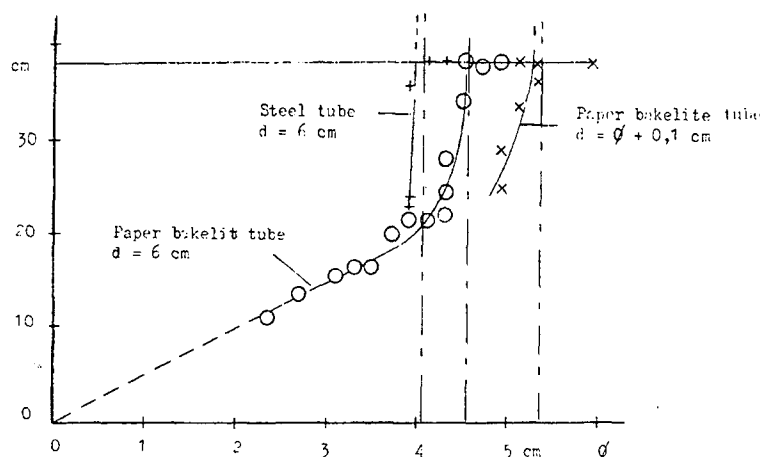


Fig. 5 - Length of Reolit charge blasted away as a function of booster diameter

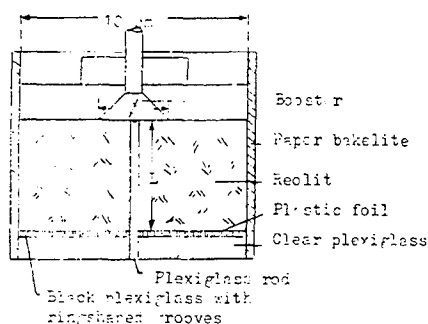


Fig. 6 - Arrangement for recording the shock wave at the end surface

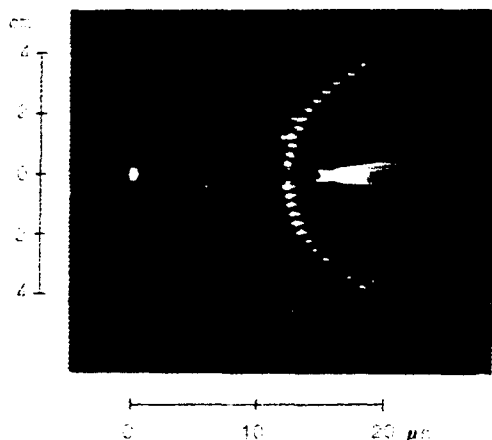


Fig. 7 - Streak camera photo according to Fig. 6. $\phi = 4.0$ cm; $L = 4.8$ cm.

PROPAGATION OF THE SHOCK WAVE IN REOLIT

In order to determine how the shock wave from the booster propagate in receptor charges of Reolit its arrival at the end surface of tube charges 10 cm in diameter and of varying lengths (L) was recorded by a streak camera. The tube was of paper bakelite with a plexi-glass bottom. The emission of light when the shock wave struck a plane plate was, as a rule, insufficient and the plate was therefore provided with circular grooves covered by a thin plastic foil. The arrangement can be seen in Fig. 6, and Fig. 7 reproduces a streak camera photo when the diameter of the booster was $\phi = 4$ cm and the length of the charge $L = 4.8$ cm. The recording for $\phi = 4$ cm and lengths of the charges up to $L = 10.8$ cm are compiled in Fig. 8. Figure 9 gives a compilation for $\phi = 4$ cm of the time for the light indications as a function of the length of the charge with radius as parameter. Figure 10a and b show for $\phi = 3$ and 4 cm instantaneous pictures of the shock front with time as parameter in the area where visible traces was obtained. Figure 10c gives a corresponding picture for $\phi = 5$ cm, but in this case a stationary detonation was obtained.

The propagation velocity of the shock front along the envelope surface of Reolit in tubes of paper bakelite has been recorded with a streak camera. The tubes were 40 cm in length and provided with holes in the wall at a distance of 3 cm. In order to obtain a visible marking of light during the passage of the front sawn-off detonators No. 4 were placed at the holes with the primary explosive turned toward the Reolit

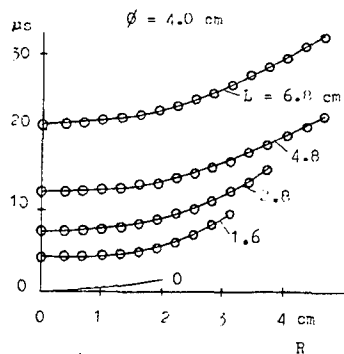


Fig. 8 - Shape of shock front in Reolit.
L distance from initiation surface.

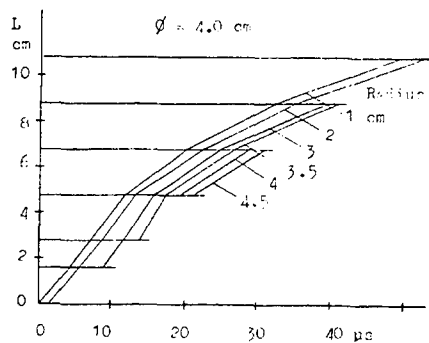


Fig. 9 - Distance-time curves for shockfront in Reolit at different radius. Charge 10 cm in diameter.

(Fig. 11). Figure 12 shows a streak camera photo with $d = 6$ cm and $\phi = 4.7$ cm. Comparative tests show that the critical booster diameter was increased by the detonators from $\phi = 4.6$ cm to 4.8 cm in tubes with 6 cm diameter. The results obtained with detonators should nevertheless give a good qualitative picture of the change of the detonation when the diameter of the booster pass the critical value.

Figure 13 shows in a distance - time diagram the propagation of the shock front for some combinations of d and ϕ . In tubes with $d = 6$ cm a booster with $\phi = 4.9$ cm gave a stationary detonation with $D = 4200$ m/s. With $\phi = 4.7$ cm the detonation propagated 25 cm with 3500 m/s and then rapidly declined. With

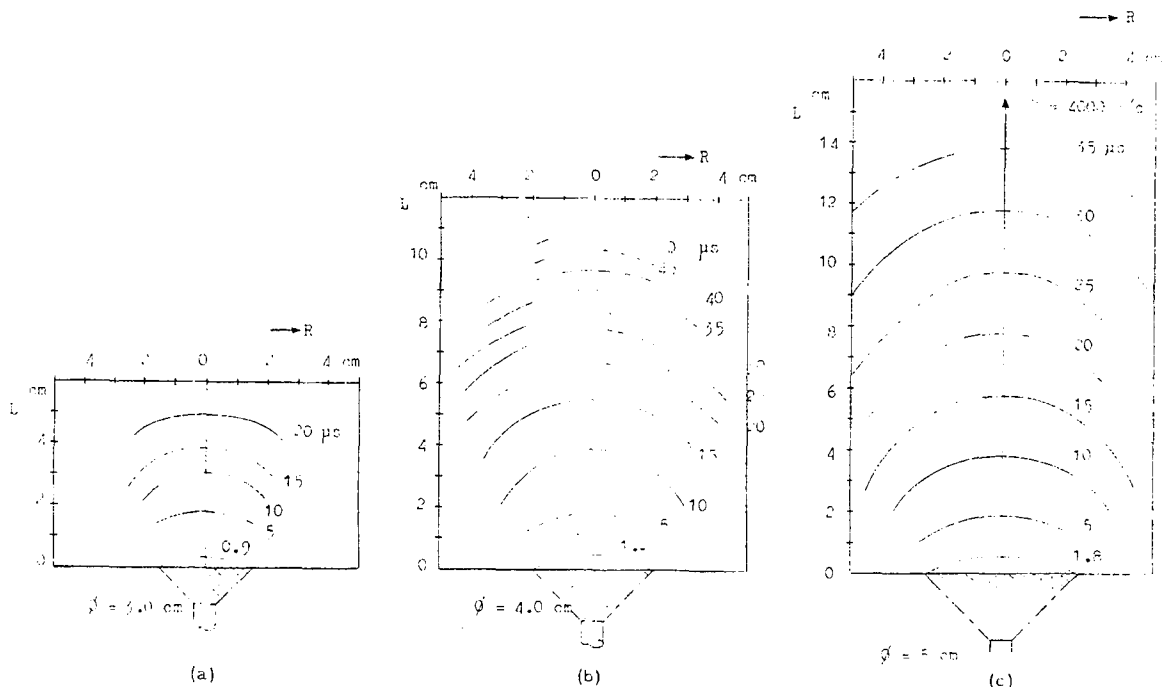


Fig. 10 - Shock fronts in Reolit charges at successive times for $\phi = 3, 4$ and 5 cm

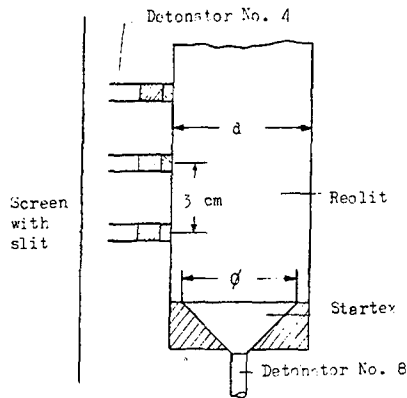


Fig. 11 - Recording of shock front velocity

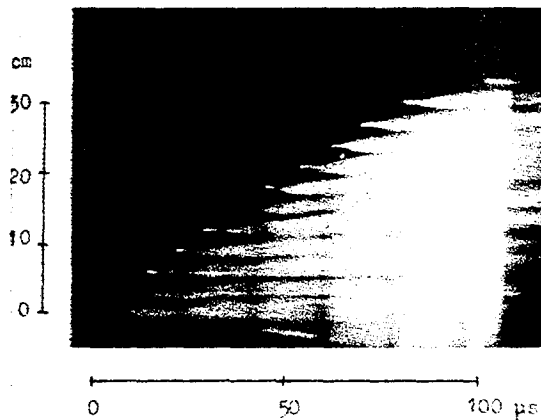


Fig. 12 - Streak camera photo according to Fig. 11. Paper bakelite tube. $d = 6.0$ cm; $\phi = 4.7$ cm.

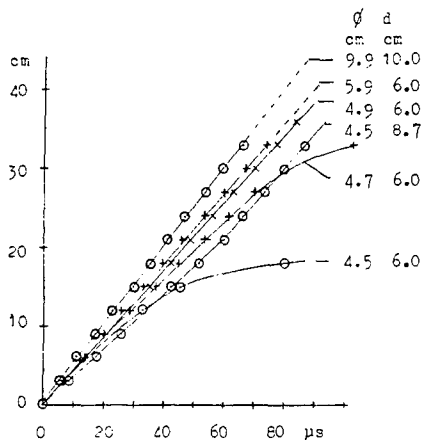


Fig. 13 - Diagrams from streak camera photos according to Fig. 11

$\phi = 4.5$ cm the velocity of the shock front began to diminish already after 6 cm and gave off no light after 18 cm. With $\phi = 4.5$ cm in a tube with a diameter of 8.7 cm complete detonation was, on the other hand, obtained with $D = 3500$ m/s for 20 cm where it rapidly was transformed into stationary detonation with $D = 4600$ m/s. In tubes with $d = 10$ cm and $\phi = 9.9$ cm $D = 4900$ m/s was obtained from the outset.

DISCUSSION

If a tube charge of large diameter (d) is initiated by a booster with an impact pressure that is greater than the detonating pressure of the receptor charge the detonation may be expected to start immediately across the entire contact surface. The development of the detonation depends on the size of the reaction energy released in the reaction zone in relation to the edge losses. If the latter predominate the frontal area will reach a maximum and then rapidly diminish. Since the relative size of the edge losses diminish with the diameter there is a critical diameter at which the booster initiates stationary detonation. This fact is clearly illustrated in Fig. 14, which shows for charges with $d = 10$ cm and $\phi = 3, 4$ and 5 cm respectively the area within which the impact front when striking the bottom plate (Fig. 6) gives rise to a visible light. If the diameter of the charge is reduced the critical diameter ϕ increases and when $d = \phi_k$ the charge has its smallest diameter for a stationary detonation.

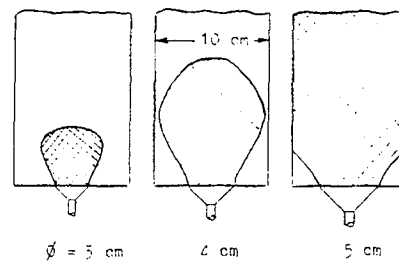


Fig. 14 - Range of visible light at bottom plate according to Fig. 6

REFERENCES

1. A. W. Campbell, W. C. Davis and J. R. Travis, *Phys. Fluids* **4** (1961) 498 and 511 (The last work with J. B. Ramsay).
2. J. M. Majowicz and S. J. Jacobs, *Bull. Am. Phys. Soc.* **5** (1958) 293.

3. S. J. Jacobs, 9 Int. Symp. Combust. Inst. 1962 Acad. Press (1963) 517.
4. C. L. Meder, Phys. Fluids 6 (1963) 375.
5. M. A. Cook, The Science of High Explosives, Reinhold Publ. Corp., New York 1958.
6. A. Wetterholm, Compt. Rend. 31 Congr. Int. Chim. Industr. Liège (1958) 226.
7. A. Wetterholm, Svensk Kemisk Tidskrift, Stockholm 76 (1964) 628.
8. C. H. Johansson, Explosivstoffe 13 (1965) 327.
9. C. H. Johansson and S. Alfredsson, Explosivstoffe 12 (1964) 200.
10. S. M. Brown and E. G. Whitbread, Coll. Int. Centre National Rech. Scient. Saint-Louis, France 1961

SIZE FACTORS IN DETONATION TRANSFER

R. H. F. Stresau
R. Stresau Laboratory, Inc.
Spooner, Wisconsin

ABSTRACT

An objective is the development of most tests which have been devised to characterize the sensitivities of explosives to initiation by other detonating charges has been the standardization of conditions to a point where the sensitivity of one explosive can be compared to those of others in terms of a single variable. For a number of quite different tests threshold conditions have been reduced to terms of critical shock pressure for initiation and agreement regarding the magnitude of this pressure has been rather good. On the other hand, inversions of ordering of sensitivities of various explosives which occur when experimental conditions are changed indicate that more than one variable can be involved.

A general principle, applicable to all initiation processes, is that initiation results when, in the nucleus of reaction, the rate at which chemical energy is liberated by the reaction exceeds that at which it is dissipated from the reaction zone. In detonation transfer, the reaction rate can be assumed to increase with shock pressure and the loss of energy can be characterized in terms of pressure drop. The rate of pressure drop is, of course, inversely related to the size of the nucleus. Assuming the "grain burning model" the reaction rate is inversely related to particle size of the acceptor explosive. It follows that the critical size of an initiating source should be directly related to the particle size of the explosive being initiated. Experimental data shows this to be the case so that it is possible, with mixtures of the same explosive and desensitizer to vary the critical pressure for threshold initiation and the critical source size independently of one another.

INTRODUCTION

Intuitive reliance on "scaling," combined with practical necessity and the general tendency for hydrodynamic phenomena to scale has resulted in the use of larger initiating components with larger charges and smaller initiating components with smaller charges. If it is implied that such scaling is necessary for reliable and complete detonation, the stability of detonation, as used, both in ordnance and research, may be questioned. In turn, doubt is possible as to the realization of the full potential of ordnance main charges and regarding the validity of conclusions based on assumptions of ideal detonation. Actually, these doubts are usually resolved by performance tests of ordnance and auxiliary

measurements of detonation parameters in conjunction with experiments. However, data regarding effects of charge dimensions upon detonation transfer are so scattered and specialized that quantitative predictions of safety or reliability in any new situation are tenuous at best.

Scaling laws are also used in most tables of distances [1,2,3] prescribed for location of magazines and manufacturing activities. Most commonly used is the simple geometric scaling law ($d/w^{1/3} = K$) where:

d = distance between charges for a given probability of detonation transfer

w = charge weight

K = constant.

This paper is based on work performed for the U.S. Naval Ordnance Laboratory Corona, California under Contract N123(62738)31089A.

This scaling law is supported by the investigations of some investigators [4]. Other investigators [5] have observed that the distance for 50 percent detonation transfer varies more nearly as $w^{2/3}$ with air gaps but approaches the cube root relationship as the density of solid barriers is increased. These relationships are empirical and necessarily based on rather limited quantities of data. It should be noted that, to the extent that tables of distance are based on experiments with quantities appreciably smaller than those to be stored or used in manufacturing, the cube root relationship assumed may result in rather hazardous conditions as quantities increase if the $2/3$ power more nearly expresses the relationship between quantities and distance for a constant probability of detonation transfer. It also should be noted that all of the scaling laws imply that the "minimum priming charge" of any explosive should be zero if the priming charge is in direct contact with the acceptor explosive.

It is believed that a more realistic and useful relationship between charge dimensions and detonation transfer probability can be derived from the fundamental conditions for the initiation of explosive reactions.

DISCUSSION

The basic condition for the initiation of any explosive reaction is the establishment of a reaction nucleus in which energy is liberated by the decomposition of the explosive at least as rapidly as it is dissipated to the surroundings [6,7,8]. Initiation systems, whether experimental or in ordnance applications, should be designed to reliably establish such reaction nuclei. Design for explosive safety should be aimed at minimizing the probability that such nuclei will be established accidentally. However, designers and those responsible for design policy sometime lose sight of these fundamentals and rely on rules of thumb based on either nebulous concepts of general sensitivity or the results of arbitrarily chosen sensitivity and output tests. In most cases the latter approach is necessitated by the lack of quantitative data regarding the various factors which combine to determine the rates of energy release and dissipation.

Wenograd's [9,10] work shows that these fundamentals can be applied quantitatively to impact sensitivity tests and illustrates the importance of details of apparatus design in determining the relative measured values of sensitivity of various explosives. It is probable that Wenograd's data and interpretive techniques would be equally successful in predicting relative

sensitivities of various explosives as measured by other impact machines, some of which significantly invert their order of sensitivities as compared with results with ERL Type 12 tools to which his analysis was applied [10]. Such predictions would have to depend, as did Wenograd's, upon the interaction of explosive characteristics with those of the test apparatus.

Although the concept with which this discussion opens is quite simple as a generality, its application to any specific situation of practical interest becomes rather difficult if account is taken of the complexities of the spatial configuration of the reaction nucleus, distribution and transport of energy, and the kinetics of reactions. The lack of much pertinent data regarding reaction kinetics, equations of state, heat transfer characteristics, etc., tends to make many mathematical analyses of explosion initiation processes academic studies whose value is mainly that of extending understanding. It is believed that a somewhat more practical application of this concept would be its use in conjunction with simplified assumptions regarding reaction and energy transport mechanism to predict general interrelationships of measurable quantities associated with threshold conditions for initiation. Such general relationships may be expected to suggest coordinate systems in which experimental data from diverse sources may be plotted to yield generalized charts of threshold firing characteristics. Such charts should make it possible to quantitatively estimate performance, safety, and reliability of explosive systems in the design stage and suggest further development of initiation theory.

A typical initiation problem is that of one high explosive charge by another, usually smaller, charge. Since most explosive train components are cylindrical, and the most frequently encountered relative position of successive elements is coaxial end to end, the typical disturbance induced in an acceptor charge is a shock wave whose frontal curvature evolves from the meniscus [11] which is characteristic of detonation of cylindrical charges to an expanding hemisphere. In Ref. 12, it was suggested that threshold conditions for the growth of detonation in such a wave might be characterized in terms of pressure versus the ratio of reaction zone length to radius of front curvature. Reference 13 describes an application of the concepts of Ref. 12 in the development of an explosive to meet specific requirement. It is believed that the design and evaluation of explosive systems and components may be made more quantitative by the application of similar concepts. However, the rationale of Ref. 12 is based upon an assumption

(implied if not stated); that the pressure-time function of an expanding shock or detonation wave is uniquely determined by its front curvature; which is valid only for special conditions.

Returning to the statement with which this discussion opens (that the basic condition for initiation is the establishment of a reaction nucleus in which energy is liberated by the reaction more rapidly than it is dissipated to the surroundings) the problem of quantitatively defining threshold conditions becomes that of relating reaction and dissipation rates to determine physical quantities. These processes may be considered in terms of any of several viewpoints. Garner [14], for example, determined the number of molecules which must decompose within a given space-time element to result in an explosion. For many initiation processes [9, 10, 15, 16] consideration in terms of temperature, heat transfer, and reaction kinetics, has yielded useful relationships which are theoretically reasonable and supported by experimental data. Although the transfer of detonation involves molecular decomposition, temperature, heat transfer, and reaction kinetics, consideration from either of these viewpoints (particularly for a granular explosive) would necessitate so many simplifying assumptions as to become a nearly meaningless academic exercise. Some of the complexities have been pointed out in Ref. 17. The characteristic mechanism of detonation transfer is that of inducing shock wave in the acceptor explosive which results in sufficient reaction to sustain itself as a detonation. This induced shock wave and the reacting explosive in its wake may be considered to be the reaction nucleus of the opening statement. It may be noted that the reaction nucleus, so defined, is moving rapidly and changing in size and shape as well as energy content. The "energy balance" of such an expanding nucleus becomes a bit ambiguous since the expansion is also dissipation. On the other hand a reaction may grow to stable detonation even though it goes through a phase in which the energy density in the expanding reaction/nucleus decreases. However, it is obvious that growth or decay is determined in part by the induced conditions.

Since, for any given medium, the shock transition is completely determinate, the strength of the shock may be expressed in terms of pressure. Assuming the "surface burning" model of the reaction of a granular high explosive, the reaction rate can be expected to vary directly with pressure. Figure 1 shows a relationship which might be anticipated on the basis of conjectures noted thereon.

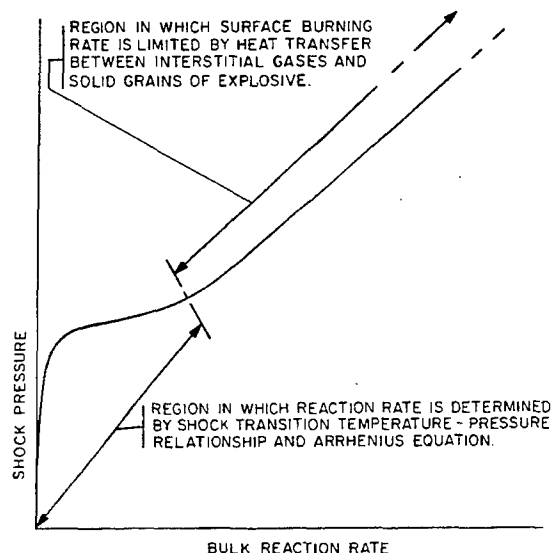


Fig. 1 - Conjectural relationship between reaction rate and shock pressure in a granular high explosive

The most important mechanism whereby energy is dissipated from the reaction nucleus in a detonation, is the movement of material from the nucleus, allowing adiabatic expansion of the material of the nucleus. In a system of coordinates which is stationary with respect to the detonation or shock front and its major axis, it becomes apparent that such expansion has both radial and rearward components. The radial rate of energy loss (per unit of nucleus volume) is inversely related to the radius and it may be expressed in terms of the reaction rate by the dimensionless quantity a_i/R where a_i is the reaction zone length for a stable detonation and R is the radius of the reaction nucleus. The rearward dissipation is the cause of the pressure decay behind the shock front. If it is assumed that the pressure decay is an exponential ($P = P_f e^{-t/\tau}$, where P is the pressure at time t , P_f is the pressure at the shock front and τ is the pressure decay time constant), the rearward dissipation can be expressed in terms of the reaction rate by the dimensionless quantity $a_i/D_i \tau$, where D_i is the propagation velocity of an ideal detonation. Since both rearward and radial dissipation are proportional to movements of material in these directions, which are perpendicular, they may be added vectorially to obtain an expression for the total dissipation, L , from the reaction nucleus:

$$L = a_i \sqrt{\frac{1}{D_i^2 \tau^2} + \frac{1}{R^2}} \quad (1)$$

Applying the statement with which this discussion opens, Fig. 1 and Eq. (1) may be combined to give Fig. 2, equating reaction rate to dissipation to give threshold conditions for the transfer of detonation. It may be noted that, with the possible exception of the reaction zone length (a_i) all of the quantities of the coordinates of Fig. 2 are relatively easily measured or calculated for at least some systems which have been or might be used to determine threshold conditions of detonation.

Existing data, unfortunately, has been obtained under rather diverse and specialized conditions so that rather little of it can be reduced to the terms of Fig. 2. However, Fig. 3 in which data from several sources have been plotted in coordinates of pressure versus the inverse of the donor charge diameter has the same general form as Fig. 2. The diversity of test procedures and conditions, which were used in obtaining the data plotted in Fig. 3, is such that it is perhaps surprising that any recognizable trend appears. Perhaps it should be dismissed as fortuitous. It is hoped that controlled and homogeneous experiments will be performed in the near future to check the validity of this general approach.

Although such factors as particle size, loading density, acceptor diameter, and confinement have not been considered in the foregoing discussion, the general framework is adaptable

to account for each of them. Assuming the "surface burning" model, the reaction zone length (a_i) should be proportional to particle size. Thus it should be possible to initiate a given explosive with a source of smaller dimensions if the particle size of the explosive is reduced. The successful developments described in Ref. 13 were based upon this prediction. In this work, it was found that RDX in particle size less than 40 microns could be initiated most of the time with a donor of 17 mils diameter while the same compound in particle size peaking at about 150 microns required charges of about 40 mil column diameter for 50 percent detonation transfer. Loading density can be expected to affect both reaction zone length and the relationship between pressure and reaction rate. Study of pertinent data should suggest modifying coefficients which can be applied to the coordinates of Fig. 2 to take account of state of aggregation factors.

Similarly, consideration of the effect of acceptor dimensions and confinement upon radial expansion should suggest modifications of the abscissa of Fig. 2 which will take these factors into account. For a given detonation pressure the rate of radial expansion due to the shock transition is inversely proportional to the shock impedance of the confining medium. Reference 18 includes data indicating that the critical gap for transfer of detonation is directly related

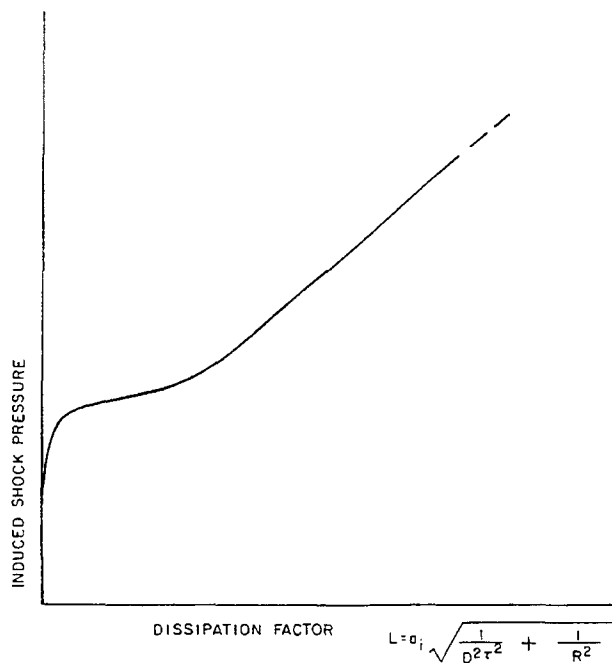


Fig. 2 - Threshold conditions for detonation transfer (from Fig. 1 and Eq. (1))

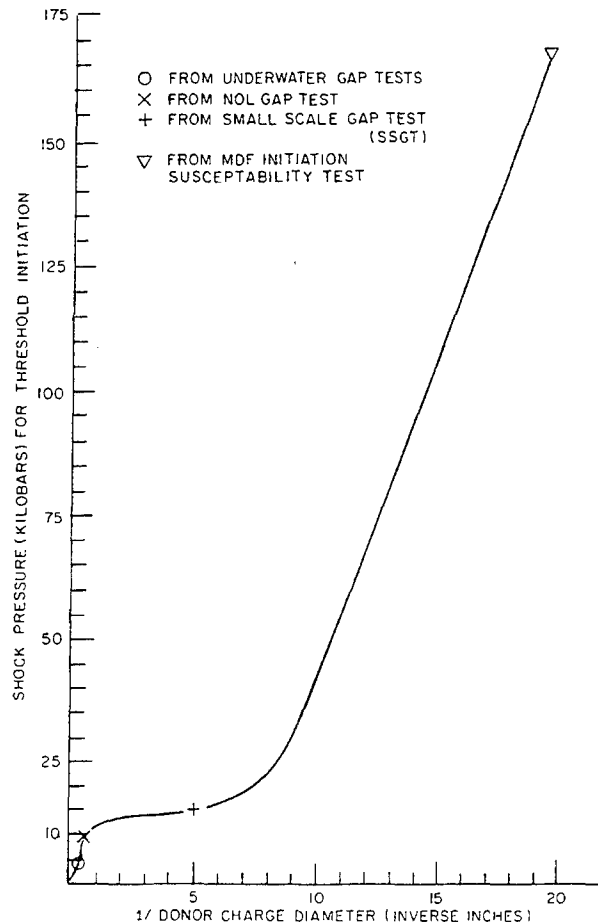


Fig. 3 - Threshold initiation pressure vs reciprocal donor charge diameter for tetryl

to the shock impedance of the donor confining medium.

The data of Ref. 18 are air gaps in which lead azide donors were used to initiate tetryl acceptors. Data are not at hand whereby the pressure induced in the acceptor can be determined from air gaps in this particular system. However, Ref. 19 includes data relating dent depths in steel witness blocks to air gaps in a similar system and Ref. 20 provides a basis for relating induced pressure to dent depth. Combining this data results in an indication that the critical pressure for initiation is approximately inversely proportional to the shock impedance of the acceptor confining media in the range of the experimental data. It is expected that further study will make it possible to account for confining media in coordinate systems similar to that of Fig. 2.

Where acceptor explosive charges are unconfined and of sizes similar to those of the donors used, it has been found [21] that the apparent sensitivity of the acceptor is inversely related to its size. This is, of course, consistent with the basic consideration that initiation depends upon the establishment of conditions such that the rate of evolution of energy due to the reaction is greater than the rate of loss to the surroundings.

Recent experiments with ammonium nitrate and ammonium nitrate/fuel oil blasting agents indicate that large charges of these materials are quite sensitive in terms of calculated pressures where the pressures result from other donor charges of the same materials. In terms of Fig. 2 this may be taken as an indication that the pressure for the double inflection of the curve is relatively low and that the apparent

insensitivity of these materials in most earlier tests is the result of the very large reaction zone length of these materials as compared with other explosives.

CONCLUSIONS

Qualitative explanations of all detonation transfer phenomena with which the writer is familiar are possible in the terms which have been discussed. Quantitative verification is inhibited by lack of data whereby most existing experimental data can be reduced to pressure and dissipation. It is hoped to perform experiments wherein these quantities can be accurately controlled or predicted.

REFERENCES

1. American Table of Distances, Pamphlet No. 2, Institute of Makers of Explosives, New York, N. Y., revised Sept. 30, 1955.
2. Ordnance Safety Manual, ORDM 7-224, May 15, 1958, pp. 17-23.
3. Blaster's Handbook, Prepared by Du Pont, Published by E. I. Du Pont De Nemours and Company (Inc.) Fourteenth Edition.
4. N. A. Tolch, Law of Similitude for Sympathetic Detonations, Aberdeen Proving Ground, BRL Report 385, 17 July 1943.
5. J. Savitt, "Investigation of Sympathetic Detonation and Evaluation of Structures for Ammunition Manufacture," Final Report, Armour Research Foundation Contract DA-11-173-ORD-416, October 20, 1955.
6. F. P. Bowden, A. D. Yoffe, "Fast Reactions of Solids" Butterworths Publication Ltd., London Academic Press, Inc., New York, 1958.
7. R. Stresau, "The Sensitivity of Explosive Initiators" JANA F Fuze Journal No. 13.
8. M. A. Cook, "The Science of High Explosives," Reinhold Publishing Corporation, New York (1958).
9. J. Wenograd, "The Correlation of the Impact Sensitivity of Organic High Explosives with Their Thermal Decomposition Rates," NavOrd Report 5730, Naval Ordnance Laboratory, White Oak, Maryland, 30 September 1957.
10. J. Wenograd, "The Behavior of Explosives at Very High Temperature," "Preprints, Third Symposium on Detonation" ONR Symposium Report ACR-52, Office of Naval Research, Department of the Navy, Vol. 1, page 60.
11. H. Eyring, R. E. Powell, G. H. Duffy, and R. B. Farlin, "The Stability of Detonation," Chem. Rev., 45, 69 (1949).
12. R. Stresau, "A Theory of the Growth of Detonation from Sources of Subcritical Dimensions," Paper 17a, Proceedings of Electric Initiator Symposium-1960, Sponsored by U. S. Naval Ordnance Laboratory White Oak, Maryland at the Franklin Institute Philadelphia, Pennsylvania, November 29 and 30, 1960.
13. R. H. Stresau, and R. L. Degner, "SPX-A Booster Explosive (Navy Definition) Which Can Be Initiated By Sources of Small Dimensions" for the U. S. Naval Ordnance Laboratory, Corona, California, Contract N123(62738)31089A, RSLR 63-7-1 Dated 13 August 1963.
14. E. E. Garner, (1938) Trans. Faraday Soc. 34, 985, 1008 as quoted by Bowden, F. F. and Yoffe, A. D. in "Initiation and Growth of Explosion in Liquids and Solids" Cambridge University Press, Cambridge, England.
15. L. D. Hampton, I. Kabik, and R. H. Stresau, "Firing Characteristics Electric Initiators Made By The Spray Metal Process" NOLM 10771, March 30, 1950.
16. H. Henkin, and R. McGill, "Rates of Decomposition of Explosives Industrial and Engineering Chemistry," Vol. 44, page 1391, June 1952.
17. R. H. Stresau, and H. S. Napadensky, "Thermal Unbalances and Initiation," Unclassified NavOrd Report 5746.
18. J. Savitt, "Effect of Acceptor Explosive Confinement Upon Acceptor Sensitivity," NAVORD Report 2938, 13 November 1953, (Confidential).
19. J. N. Ayres, "Standardization of the Small Scale Gap Test Used to Measure the Sensitivity of Explosives," NavWeps Report 7342 NOLW, 16 January 1961.

20. R. H. Stresau, and W. M. Slie, "Small Scale Plate Dent Test for Confined Charges," NavOrd 2422, NOLW, 23 April 1952.
21. E. H. Eyster, L. C. Smith, and S. R. Walton, "The Sensitivity of Big Explosives to Pure Shocks" NOLM 10336, 14 July, 1949 NOLW.

CONFINEMENT EFFECTS IN EXPLODING BRIDGEWIRE INITIATION OF DETONATION*

R. H. F. Stresau
*R. Stresau Laboratory, Inc.
Spooner, Wisconsin*

R. M. Hillyer
*U.S. Naval Ordnance Laboratory
Corona, California*

J. E. Kennedy
*IIT Research Institute
Chicago, Illinois*

ABSTRACT

The energy density in an exploding bridgewire can be many times that in the reaction zone of a detonating high explosive. Since the form of the energy is quite similar in both of the phenomena, the explosion of a bridgewire might be expected to result in immediate detonation. That it does not always is attributable to the fact that bridgewires are generally small compared with the failure dimensions of the secondary high explosives preferred for exploding bridgewire detonators. It is suggested that the limiting energy requirement for exploding bridgewire detonation is related to a minimum energy density in the region enveloped by the shock wave resulting from the bridgewire explosion as the dimensions of this region approach the "failure" diameter of the explosive. This view is supported by data found in the literature.

As has been widely observed, failure diameters can be substantially reduced by confining explosives in heavy walled tubes of materials of high shock impedance. Such confinement would be expected to similarly reduce the energy required to initiate a given explosive by means of an exploding bridgewire. However, to be effective in this respect, the confining tube must have an inside diameter which is small compared with the unconfined failure diameter of the explosive. Application of this principle has resulted in RDX loaded EBW initiators which detonate on the application of as little as 20 millijoules (threshold value), ammonium picrate loaded detonators which detonate upon the application of as little as 2 joules and TNT loaded detonators which detonate on less than ten joules. Time measurements indicate propagation rates of detonation velocity magnitudes starting with the initiating pulse. The detonators are capable of initiating larger charges of the materials with which they are loaded, so that complete explosive systems may be designed using only one insensitive explosive compound.

INTRODUCTION

The relationship between reaction rate of an explosive and the energy required to initiate detonation with an exploding bridgewire is

determined by the three-dimensional expansion of the reaction zone. Since the mechanism of this expansion is a shock wave, it can be restricted to one dimension by confining the explosive in a tube of a medium (such as steel)

*This paper is based on work performed for the U.S. Naval Ordnance Laboratory, Corona, California under Contract N123(62738)31089A and for the Directorate of Armament Development Det 4, RTD, Air Force Systems Command, Eglin Air Force Base, Florida, Contract AF08(635)3655.

of high relative shock impedance. In the experiments reported herein (and previously [1]) the use of such confining tubes, of appropriate dimensions, was found to substantially alter the relationship of exploding bridgewire energy requirements to general sensitivity making it possible to initiate booster type explosives [1] with a small fraction of the energy required for PETN detonators in current use and to initiate such insensitive materials as TNT and ammonium picrate with quite reasonable quantities of energy.

Confinement has been used to some advantage by others in the initiation of detonation by exploding bridgewires [2,3] but the considerations discussed above do not seem to have been applied. These considerations imply that, for confinement to have a substantial effect upon the energy required for exploding bridgewire initiation, the cavity in which the reaction nucleus is confined must be small enough that the intended input energy is a significant fraction of the reaction energy of the explosive which it contains. The heats of detonation of the commonly used nitro-organic explosives range from eight to fifteen hundred calories per gram. Since the loading densities ordinarily used in exploding bridgewire detonators are generally somewhat less than one gram per cubic centimeter, a thousand calories per cubic centimeter, or one calorie (four joules) per cubic millimeter is a reasonable average. Thus, if it is desired to use the two joules output of the usual exploding wire firing circuit to greater advantage (for example in the initiation of an insensitive explosive) the volume of the confining cavity should not be more than a few

cubic millimeters. If, as in the requirement which initiated this investigation [4], it is desired to effect exploding bridgewire initiation with fifty millijoules, the volume of the cavity must be a fraction of a cubic millimeter. The development of techniques for the fabrication of exploding bridgewire detonators in which the initial charge is confined in a cavity of this size and the demonstration that such detonators perform as predicted has been reported in Ref. 1. This paper reports the results of continued experiments with RDX loaded exploding bridgewire detonators which fire on input energies less than fifty millijoules and of other experiments in which TNT and ammonium picrate have been initiated by exploding bridgewires with a few joules input.

EXPERIMENTAL

The experiments discussed herein were measurements of firing characteristics of electric detonators of the general design shown in Fig. 1. Experiments included "cut and try" determinations of combinations of dimensions and loading conditions for which detonation could be initiated with available circuitry, "Bruceton" tests to determine threshold firing condition, dent tests of output, measurements of functioning times, and oscillographic observations of firing pulses.

Detonator Design

The general design of the detonators used is shown in Fig. 1. To describe the fabrication

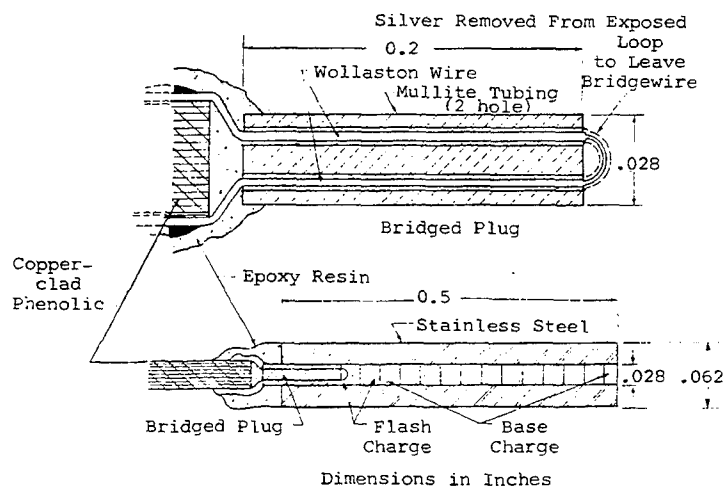


Fig. 1 - Medium energy exploding bridgewire detonator with Wollaston wire bridge

of detonators of this general design, some of the materials used must first be described.

Wollaston wire is a coaxial bimetallic material made by inserting a wire of one material (usually gold or platinum) in a tube of another (usually silver) after which the combination of tube and core is drawn through dies to a smaller size. The outer tube may be dissolved by an acid leaving the core, which may be much smaller than a wire could be drawn by any other process. High temperature double bore thermocouple insulating tubing (made of Mullite, a refractory ceramic compound of alumina and silica) is available as a catalog item in sizes down to 1/32-in. outside diameter. Since the O.D. of the ceramic tubing is the lower limit of the charge cavity diameter in the design shown in Fig. 1 and since 1/32-in. is larger than the smallest theoretically desirable for this dimension, orders were placed for the smallest double bore Mullite tubing which the supplier believed to be feasible using his current practices. Material received in various orders varied from 0.0255 to 0.0285 O.D. Stock tubing was used for larger sizes.

Stainless steel tubing was obtained to fit each size ceramic within a fraction of 1 mil. A variety of nominal wall thicknesses is available from stock.

Copper clad phenolic sheet, for use in etched circuitry, is available in a variety of thicknesses and grades of phenolic with copper coating of various weights on one or both sides. The detonator inert assemblies (Fig. 1) were fabricated in the following series of operations:

1. A "hairpin" of Wollaston wire was threaded through the two holes of a short (about 1/8 in.) length of ceramic tubing.

2. The ends of the Wollaston wire were soldered to the copper coatings of a strip of copper clad phenolic.

3. A "bead" of epoxy resin cement was applied to join the ceramic tube to the phenolic strip, and cured at an elevated temperature.

4. An ohmmeter was connected to measure the resistance between the two copper coatings of the copper clad phenolic (which is essentially that of the wire "hairpin"). The tip of the ceramic (where the curve of the hairpin is exposed) was then immersed in nitric acid. When the resistance approached the value calculated for the core diameter and desired bridge length, the tip was withdrawn from the acid, washed in distilled water and dried at an elevated temperature.

5. A stainless steel tube was slipped over the tip, the ceramic tube coated with epoxy resin cement, and the steel tube slipped down to the shoulder formed by the bead (step 3 above). The epoxy cement was cured at elevated temperature.

The higher voltages necessary for initiation of the less sensitive explosives (TNT and ammonium picrate) resulted in dielectric breakdown around the edges of the copper clad phenolic, and arcing across the loop of the bridgewire. Design variants to alleviate these difficulties are illustrated in Figs. 2 and 3. These less sensitive explosives also made the design illustrated in Fig. 4 necessary to build up the column diameter in gradual steps because the charge diameters were so much smaller than the critical diameter for initiation of semi-infinite charges of these materials.

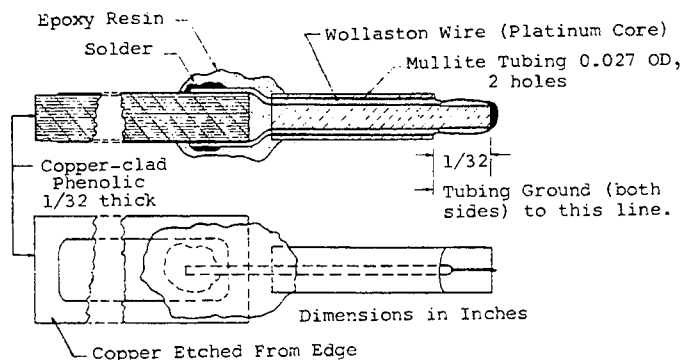


Fig. 2 - EBW plug (HV-1) modified for very high voltage

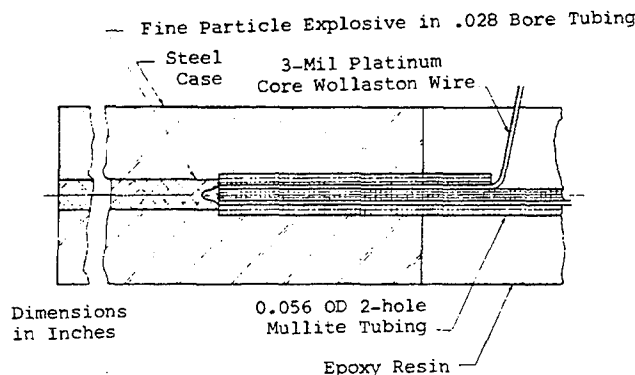


Fig. 3 - EBW detonator design for high voltage application

Explosives

Three explosives have been used in these experiments, RDX (cyclotrimethylene trinitramine), TNT (2,4,6-trinitrotoluene), and ammonium picrate. In consideration of previous experience [2,3,5-7] and the "grain burning theory" [6], which indicate that finely divided explosives are most suitable for exploding bridgewire detonators, all explosives used were of very small particle size. Most of the TNT and RDX used was reduced by dissolving in acetone and precipitating in cold water. The high water solubility of ammonium picrate prevented the use of this technique, so material which passed a 270 mesh screen (the finest at hand) was used. RDX in accordance with the specification [7], Class E (97 percent minimum through U.S. Standard Sieve No. 325) was used as received from two sources.

Detonator Loading

The loading pressures from a few to a thousand pounds per square inch, for the small diameters used, require dead loads on the ram between a few grams and a pound or two. Such pressures can be applied by holding the detonator

between thumb and forefinger, slipping it over the bottom of the ram and lifting an appropriate weight with which the ram is loaded. The explosives were loaded in this manner by increments, each increment being the quantity of explosive that would enter the mouth of the hole as the end of the detonator was pushed into a loosely stacked pile of bulk explosive. The pressed lengths of increments which result from this technique are from one-half to one times the column diameter. It was the practice to shake the first two to four increments into place around the bridgewire by tapping sideways against a hard edge before pressing for the first time. In this way, the ram never came into contact with the delicate bridgewire.

Circuitry

In EBW devices, a very high rate of energy delivery is necessary. This is because only the energy delivered prior to the time of wire burst and within one microsecond (or less) following burst can be expected to be useful since, at later times, the volume of the shock envelope grows rapidly and the energy density within it may correspondingly decrease. The design of a firing circuit for use with exploding wire

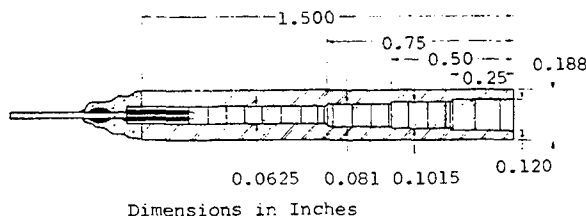


Fig. 4 - EBW detonator with stepwise increasing bore

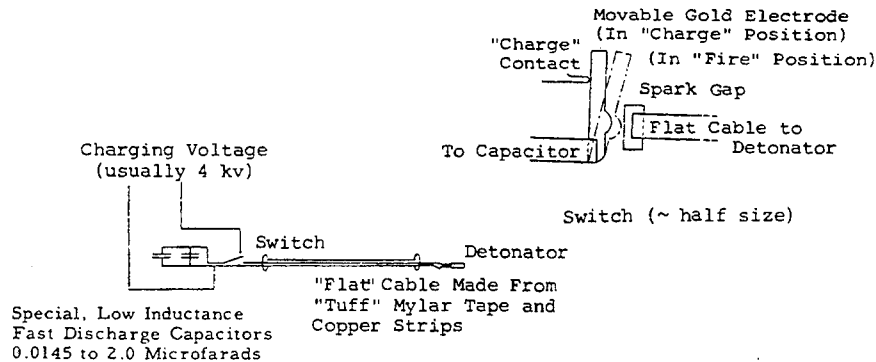


Fig. 5 - Low-voltage EBW firing circuit

phenomena has a strong effect upon the phenomena produced. To obtain short rise times, a capacitor discharge circuit is always used. Circuit inductance plays a major role in performance, limiting the rate of current rise. A circuit with very low inductance (less than one microhenry) is required to produce the rate of current rise, 10^9 amperes per second, needed for EBW applications. Separate circuits were employed for low and high voltage work. Simple condenser discharge circuits (Fig. 5), were used for the lower voltage studies (up to 5 kv). The capacitors are of special design and construction for use in high rate discharge applications, such as EBW firing circuits. The cable to the detonator is a three-layer flat cable made in the laboratory from copper sheet and Mylar tape. Every effort was made to

minimize the inductance and impedance of the cable, which are estimated to be a few hundredths of a microhenry and a few ohms, respectively. The switch used in earlier experiments is a manually operated spark-gap switch with gold electrodes designed to emulate, as nearly as possible, an extension of the flat cable. In later experiments, this switch was replaced with a coaxial switch with spherical brass electrodes (Fig. 6). This coaxial switch had dielectric of minimum thickness to minimize inductance and impedance. Results with the latter were more consistent than with the former. Condensers used in these circuits included hand stacked, flat, low impedance condensers ($0.0145 \mu f$ and $0.0454 \mu f$), specially constructed high discharge rate capacitors (1.0 and $2.0 \mu f$), and commercial glass encased tubulars.

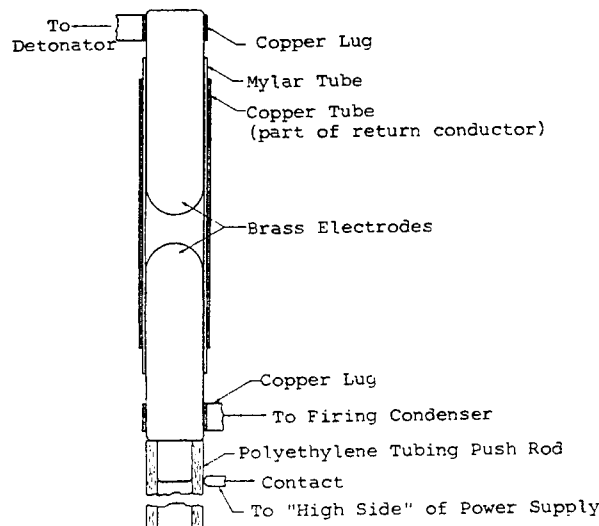


Fig. 6 - Hand operated, low impedance coaxial spark gap switch

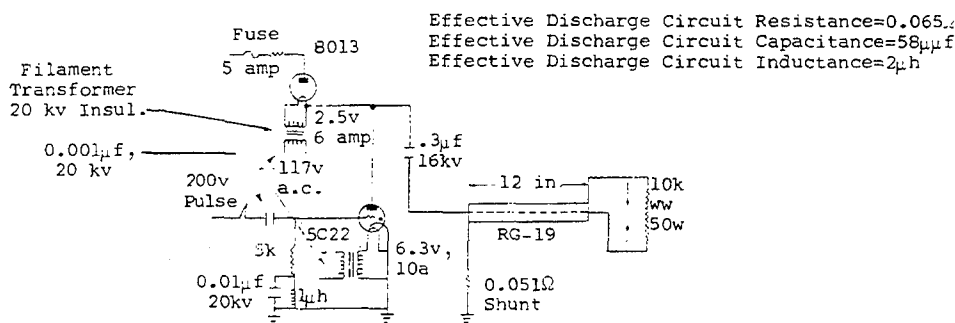


Fig. 7 - High-voltage EBW circuit

For higher voltage applications, the greater separation between leads required for insulation increased circuit inductance. A high voltage circuit (up to 16 kv) consisted of a standard 0.3 μf capacitor, a hydrogen thyratron as a high-speed switch, and coaxial cabling. Because of these components, the inductance of this circuit was much greater than that of the low voltage circuit. The components were placed and oriented so as to introduce minimal additional inductance. The circuit diagram is shown in Fig. 7. Figures 8 and 9 are oscillograms of voltage versus time for the two types of circuit.

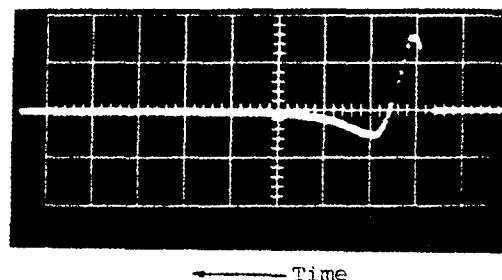


Fig. 8 - High-voltage circuit discharge characteristics. Horizontal scale: 1 μsec/division, vertical scale: 20 kv/division.

The Bruceton Procedure

The so-called "Bruceton" test procedure was used in most tests reported herein. In this procedure, the first trial of a test is performed at one of a series of pre-established conditions or "steps." If a detonation results, the next trial is performed at the adjacent step in the direction of lower input energy. If it misfires, the next trial is performed at the adjacent step in the direction of increasing energy. The test is continued in this manner, the conditions of each trial being determined by the results of the previous trial, to yield a pattern of up and down staircases on a crossed grid data sheet. Data obtained in a Bruceton test may be analyzed to obtain estimates of the mean (the condition at which 50 percent will detonate) and standard deviation of the test variable and of the errors of these estimates.

Dent Test Evaluation of Detonator Performance

A plate-dent criterion which was specifically for the evaluation of detonators and small charges (Ref. 8) was utilized to estimate reaction wave velocity as well as to simply classify

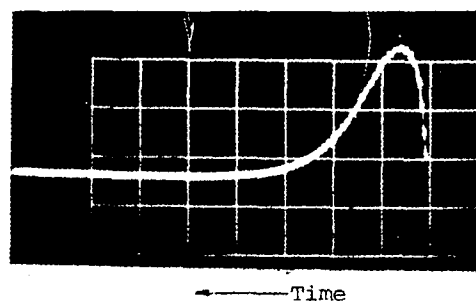


Fig. 9 - Typical voltage-time trace for EBW detonator fired with low impedance firing circuit. Horizontal scale: 0.1 μsec/division, vertical scale: not calibrated. Electrical data: voltage = 2.2 kv, capacitance = 0.0145 μf, resistance = 0.7Ω

the results of given test as detonations or deflagrations. In each trial, the detonator output was evaluated by firing the detonator against a steel block, the depth of the dent produced being the criterion of output. For long, highly-confined columns of explosive, the relationship

between propagation velocity of stable detonation and the depth of dent produced in a semi-infinite block of steel has been characterized by the equation (Ref. 8):

$$\frac{d}{R} = k \rho_c D_c D \left(1 - \frac{S}{\rho D^2} \right) \quad (1)$$

where

D = detonation velocity of the explosive,

d = depth of the dent,

k = a constant related to the properties of the witness plate,

R = charge radius,

S = proportional to the strength or hardness of the witness plate,

ρ = density of the explosive, and

ρ_c = density of the confining medium.

Figure 10 is a plot of Eq. (1) with the constants adjusted to fit experimental data for TNT with steel confinement and a steel witness plate, taken from Ref. 8. Because of the similarity of detonation velocity-density relationships of ammonium picrate and TNT, the curve for ammonium picrate should be very close to that for TNT. Note that any dent at all indicates a velocity over 3000 meters per second.

Functioning Time Measurements

Functioning times were measured by means of a vacuum-thermocouple timer, described in Ref. 9, in which a "start" signal triggers a thyatron causing a current to flow through the heater of the vacuum thermocouple and a "stop" signal triggers another thyatron which shunts the first and the thermocouple heater. The energy delivered to the heater (and hence the temperature rise thereof) is proportional to the time interval between the two signals. The voltage output of the thermocouple, which is proportional to the temperature rise and hence to the time is amplified and recorded. This instrument, calibrated periodically using the transit times of pulses through various lengths of coaxial cable has a resolution and "jitter" close to 0.01 microsecond. The "start" signal used was obtained by attenuating the firing pulse by means of a high resistance shunting potentiometer circuit and the "stop" signal was obtained from an ionization probe placed within a few mils of the output end of the detonator.

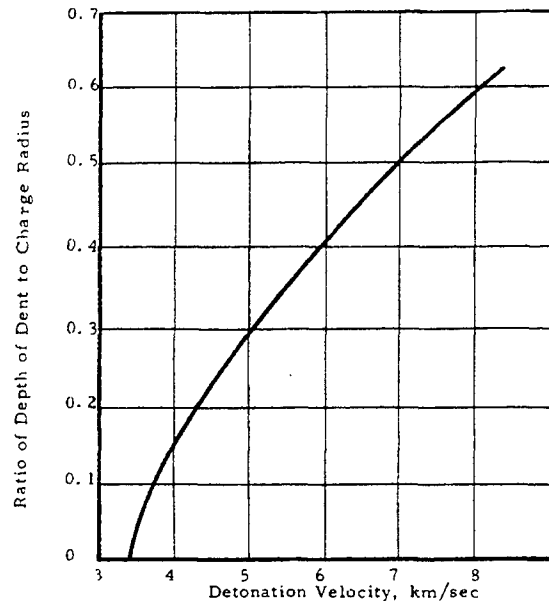


Fig. 10 - Relationship between depth of dent produced in mild steel witness plate and detonation velocity of heavily confined long column of TNT (Ref. 9)

RESULTS

From the viewpoint of their pure research aspects, all of the experiments reported herein are a continuation of those reported in Ref. 1, although some of them were under other sponsorship with different practical objectives. Where appropriate, pertinent data from Ref. 1 will be reviewed herein.

Threshold Firing Characteristics of RDX Loaded Detonators

The experiments reported in Ref. 1 established the feasibility of initiating RDX, confined in a steel tube about 1/32 in. in diameter (Fig. 1) by means of an exploding bridgewire in which less than fifty millijoules of electrical energy has been dissipated. These experiments [1] also indicated that:

1. Threshold energy requirement of such items was nearly independent of bridgewire diameter (between twenty-five and thirty millijoules) for bridgewires between 0.2 and 0.5 mil. For larger bridgewires, the threshold energy requirement seemed to be proportional to the volume of the bridgewire.

2. Threshold energy requirement varied with loading density reaching a minimum value

at an "optimum" density. The "optimum" density was different for each combination of bridgewire diameter and charge diameter. The "optimum" was apparently a direct function of the ratio of bridgewire diameter to charge diameter.

3. Threshold firing energy was proportional to the cube of the charge diameter. However, this relationship was deduced from two sets of data, one of which was obtained with a firing circuit of rather poor characteristics for the purpose and the other of which was obtained with a rather limited range of charge diameters.

4. Electrical circuit characteristics are quite critical. A circuit constructed from commercial capacitors and "standard" EBW circuit components required four times as much energy to initiate a detonator of given dimensions and loading than a laboratory constructed low inductance low impedance circuit.

Continuation of this work since that mentioned above has been largely concentrated in the refinement of fabrication techniques, firing circuits and experimental procedures. These refinements have resulted in a slight reduction in threshold firing energies and in a substantial reduction in their variability (both from lot to lot and within lots).

In the course of this effort, it was found that the gold core Wollaston wire which had been used in the experiments reported in Ref. 1 had an outside diameter so large as to seriously affect the quality of the bridged plugs (see Fig. 1). The large diameter resulted in "undercutting" of the etching below the surface of the epoxy so that the effective bridge length was substantially more than that of the exposed loop. When gold core Wollaston wire of smaller outside diameter was used, detonators with gold bridgewires 0.3 and 0.42 mil in diameter detonated on mean threshold stored energies of 21 and 19.7 millijoules respectively, which is 20 percent lower than the most sensitive detonators with platinum bridgewires. This superiority of gold over platinum, which is in agreement with observations of others [10], had not been apparent in the data reported in Ref. 1 because of the poorer quality of the inert assemblies with gold bridgewires which were used in the earlier experiments.

A series of experiments were performed to determine the effects of charge diameter upon threshold firing energy requirements. All of these tests were performed with three fabrication lots of bridged plugs with 0.4 mil

Bridgewires: Platinum, 0.4 Mil Diameter,
15 Mils Long

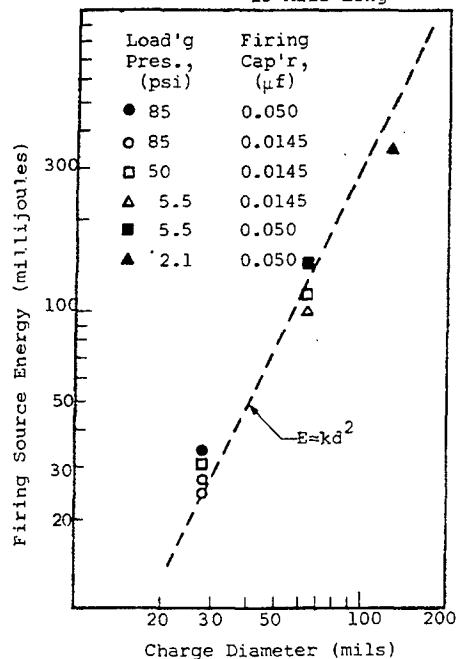


Fig. 11 - Threshold firing energies vs charge diameters for RDX loaded EBW detonators

diameter platinum bridgewires 15 mil long. Each lot was separated, by random selection, into two or three groups which were then assembled with confining tubes of 28, 64 and (in one case) 125 mil bores. Data are plotted in Fig. 11.

Functioning Times

Functioning times were measured for a rather large number of RDX loaded detonators (all of which had 0.4 mil diameter bridgewires). A substantial number of the leftover units from the fabrication development were loaded with flash charges at 40 to 50 pounds per square inch and pressures increasing to various values up to about 400 pounds per square inch at the output end. These were fired at various voltages from the 2.0 to 3.65 kilovolts (from 30 to 100 millijoules). Functioning times (for charge lengths approximately 0.7 millimeters long) ranged from about 1.9 to 3.0 microseconds. The shortest functioning time at 2.0 kilovolts was about two microseconds, but the time scatter was larger at low voltages and decreased to about 0.2 microseconds at 3.5 kilovolts. The time scatter was largest for the items loaded at the highest pressure, although the output velocities of these items, as indicated by plate dent data were very close to their ideal velocities.

Functioning time versus explosive column length is plotted for two groups of detonators in Fig. 12. The two items for which "infinite" functioning times were recorded apparently started to detonate but faded since their output ends were found, shattered up to a point but with explosive left in the last couple of millimeters.

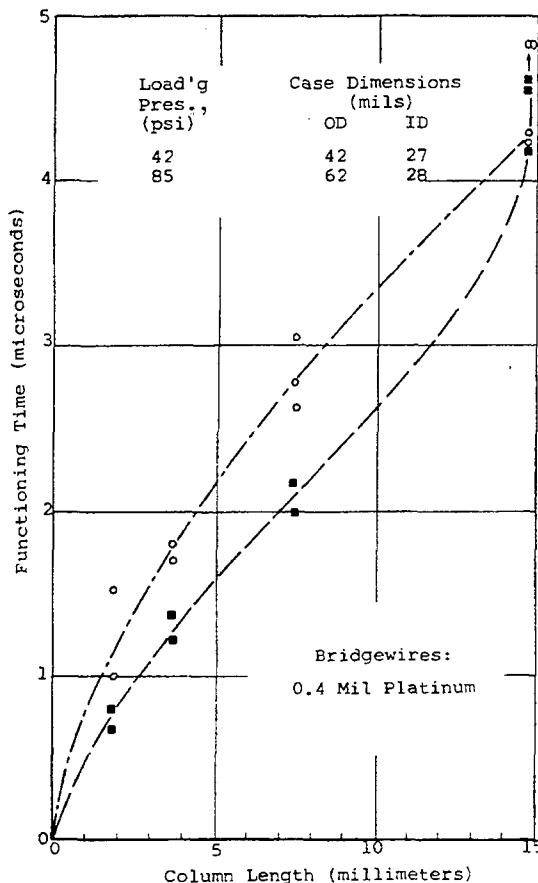


Fig. 12 - Functioning time vs column length for RDX loaded detonators

Functioning times of RDX loaded detonators with 0.4 mil diameter bridgewires 15 mil long (loaded at 50 pounds per square inch) with column diameters of 28 and 64 mil were 2.09, 2.11, and 2.13 (for 28 mil diameter) and 2.39, 2.44, and 2.48 (for the 64 mil diameter).

An ammonium picrate loaded detonator, loaded at pressures gradually increased from 100 pounds per square inch at the flash charge to 500 pounds per square inch at the output end functioned 4.7 microsecond after discharge of a 2 microfarad condenser charged to 2.6 kilovolts.

Detonation of TNT and Ammonium Picrate (General)

Most experiments with TNT and ammonium picrate were "cut and try" experiments in which dimensions and loading conditions were varied in an attempt to find combinations for which consistent detonation and maximum output could be obtained. When such combinations were determined, a few tests were made with lower input energies to obtain indications of the lower limits of input energy which would result in detonation. Other experiments demonstrated the feasibility of EBW systems, containing no explosives more sensitive than TNT or ammonium picrate, which may be used to initiate larger charges. Detonation of TNT and ammonium picrate was initiated with source energies of 2 to 15 joules in EBW detonators of designs shown in Figs. 1, 2 and 3. Initiation occurred at comparable source energy levels in both the high voltage EBW circuit (up to 11.5 kv across 0.3 μ f) and the low voltage EBW circuit (3 to 4 kv across 1 or 2 μ f). The criterion of detonation in these tests was the production of a well-defined dent in a steel witness plate. The ability of the detonation to propagate to charges of larger diameter and greater density was demonstrated for ammonium picrate.

In the discussion of results, studies carried out with the high voltage EBW circuit are described separately from those carried out with the low voltage circuit. While there was frequent communication and exchange of promising results between those conducting these concurrent studies, some aspects of the development were treated in different ways in the two efforts.

Experiments with the High-Voltage EBW Circuit

The detonator design used in this phase of the program is shown in Fig. 3. A constant low density of explosive was used along the entire column length, so the depth of dent which could be produced in a steel plate was quite shallow. Only TNT was used in experiments with high-voltage circuit.

As Fig. 10 shows, TNT and ammonium picrate must detonate at a velocity of 3000 meters per second to give any dent at all. Since this is close to the stable rates for the densities used, this calculation was considered to be justification for the use of a detectable dent as a criterion of detonation. Typical dents were about 1.1 mil, which from Fig. 10 indicates a detonation velocity of 3500 meters per second. Approximations and extrapolations in the calculations reduce the quantitative significance of

this number, but it leaves little room for doubt that the reaction was a true detonation.

Effects of Bridgewire Diameter in TNT Detonators

Table 1 summarizes the results of the experimentation conducted to determine the effect of bridgewire diameter on the energy required to achieve detonation in TNT. The bridgewire diameter was the only parameter intentionally varied. The charge diameter and loading pressure were held constant at 0.040 in. and 25 psi.

The platinum wire was used for all tests. Since the number of detonators available for testing was limited, no attempt was made to present a statistically representative value.

TABLE 1
Minimum Energy to Achieve Detonation of TNT as a Function of Bridgewire Diameter

Wire Diameter (mil)	Minimum Firing Energy (joules)
4	19.8
3	9.6
2	No detonation

Note: Maximum available firing energy was 19.8 joules.

Experiments on TNT and Ammonium Picrate with the Low-Voltage EBW Circuit

The detonator design represented an extension of that shown in Fig. 1, modified and scaled up to withstand the higher voltage. The explosive column diameter most frequently used was 1/16 in. In loading the detonator, the first few increments near the bridgewire were usually loaded at very low pressure, then the pressure was increased along the length of the column. The increased pressure in the increments near the output end of the detonator increased the density of those increments and thereby increased the depth of dent attainable in a steel witness block. In the high-voltage studies, dents about 1 mil in depth were observed following detonations. Dents up to 6 mil in depth were produced by the detonation of these charges of increased density.

Observed dents were appreciably shallower than predicted from ideal detonation velocities for the densities used. This is hardly surprising since these predictions are based on ideal detonation velocities, while diameter effects for the explosives and small diameters used must be quite appreciable. While quantitative application of Eq. (1) and Fig. 10 to nonideal and incipient detonation is dubious at best, it is encouraging to note that they imply velocities well above 3 km per sec if any dent at all is made.

Promising results were obtained with both TNT and ammonium picrate. With both, detonations were obtained at source energies of 10 to 16 joules (2 μ f at 3.2 to 4 kv). Of the two materials, ammonium picrate seems to have a broader range of conditions under which EBW initiation is attainable. In one set of tests, ammonium picrate (in 28 mil column diameter) was detonated with a stored energy of 2 joules (1 μ f at 2 kv). This apparent superiority of ammonium picrate for EBW applications may be the result of a fortuitous choice of conditions that are closer to the optimum of this material than to that of TNT. However, it should be noted that the superior results were obtained with ammonium picrate in a state of aggregation which, from all indications, is less ideal for EBW applications than that of the TNT used to get less favorable results.

Bridgewire diameter, charge diameter, and loading pressure are so interdependent in their effects that they must be discussed together. In general, greatest output resulted when the flash charge around the bridgewire was loaded at a relatively low pressure and the pressure increased gradually to a maximum at the output end. For the smallest charge diameters with bridgewires larger than 1 mil, the optimum pressures for the flash charge seemed to be over 100 psi, which was increased to 1000 psi at the output end. Either small bridgewires or larger charge diameters apparently resulted in a decrease of this optimum as mentioned in an earlier paragraph. In the larger-diameter charges (Figs. 3 and 4), the optimum loading pressure for the flash charge was apparently less than 10 psi, increased gradually to 20 to 40 psi at the output end. Results were more consistent with the larger charges than with the smaller ones. Possibly the smaller diameter (~0.028 in.) is too close to the failure diameters of TNT and ammonium picrate. If so, perhaps ammonium picrate as finely divided as was the TNT would give very interesting and useful results in the smaller diameter detonators.

Detonation Propagation into Larger Explosive Charges

Attempts were made to initiate heavily confined leads of the same explosive used in the detonators by means of some of these detonators. The lower-voltage EBW circuit was used. The leads were loaded into 13/64-in. diameter holes, centrally drilled in 1-in. by 1-in. steel cylinders. In four such trials with TNT in the 1/16-in. bore detonators, one lead produced a dent 8 mil deep; the others failed. Two such trials with ammonium picrate resulted in one failure and one 10-mil-deep dent. Such a lead, loaded with ammonium picrate at pressures gradually increasing from 15 psi at the input end to 10,000 psi at the output end, produced a dent 39 mil deep when initiated with the detonator shown in Fig. 4 loaded with ammonium picrate. A dent of 39 mil is close to the maximum depth expected from such a lead and should be ample to initiate a booster of this material. Since no TNT-loaded detonators were made in accordance with Fig. 4, the performance of such detonators is a matter of conjecture but, on the basis of the general parallelism of results with the new materials, it is expected that this, or a very similar design, would give satisfactory results with TNT.

DISCUSSION

It had been shown, in Ref. 1, that the energy required to initiate RDX by means of exploding bridgewires can be substantially reduced by the judicious use of confinement. Data given herein demonstrate the applicability of this principle to less sensitive explosives like TNT and ammonium picrate. Practical implications of these results include the possibility of eliminating PETN (which is considered by many to be undesirable because of its sensitivity and relatively poor thermal stability) from exploding bridgewire systems, that of reducing the bulk and weight of such systems, and that of developing EBW systems with very insensitive explosives, some of which are also stable at the high temperatures which are encountered in many modern weapon systems.

The data reported in Ref. 1 relating threshold energy to charge diameter seemed to indicate that the energy requirement was proportional to the cube of the charge diameter. This relationship was explained in terms of a critical energy density within the area affected by the exploding bridgewire at the time the shock wave reached the wall of the tube. The present data (Fig. 11) approach more closely a proportionality of the energy requirement to the square

of the charge diameter. A simple explanation for this might be based on the general scaling law whereby the energy necessary to produce a spherical shock wave of a given pressure is proportional to the cube of the radius, in combination with the proposition of Refs. 7 and 12 that the critical pressure for propagation of an expanding spherical detonation wave is inversely proportional to the radius. Thus

$$P = j/R$$

and

$$E = kPR^3 = jkR^2$$

where P is the critical pressure for a self-propagating spherically-expanding detonation wave, of radius R , E is the energy required to initiate a shock wave which has a pressure P at a radius R and j and k are constants. Of course, this is an oversimplified explanation, but the data at hand are hardly sufficient basis for a more rigorous approach. The results of these experiments indicate that a rather complex interaction exists between bridgewire dimensions, confinement dimensions, loading variables, and electrical parameters. Since the experiments which yielded the data given were directed toward rather limited and specific practical objectives, neither time nor funding allowed the broad research which would be necessary to satisfactorily define the variables.

The time measurements (Fig. 12) for the RDX loaded items indicate an initial propagation rate of 1.5 to 2 millimeters per microsecond, accelerating to about 5 millimeters per microsecond (which is very near the ideal detonation rate for this material). It is of interest to note that the thin cases used in one set of experiments apparently afforded sufficient confinement for initiation and growth to nearly the stable rate, but not enough to support stable detonation. A suggested failure mechanism derives from the fact that shock waves in steel propagate faster than did the detonation, particularly in its earlier phases. As a result, the expansion of the tube may have outrun the detonation, relieving the confinement.

The longer functioning times of the detonators with 64 mil charge diameters than those with 28 mil charge diameters tends to support a qualitative description which has been proposed of the mechanism whereby confinement affects threshold firing energy. As the shock (or "low order detonation"), expanding spherically from the exploded wire, impinges upon the bore of the confining tube, it is reflected to multiply the pressure and generate an annular

"Mach wave." The reflected overpressure and Mach wave cause a sudden and substantial increase in the vigor of the reaction. Based on this explanation, it is possible to calculate the propagation rate of the expanding wave from the differences in bores and functioning times. This rate turns out to be 1.45 millimeters per microsecond.

A subject of much informal discussion has been the question as to the quantitative definition of detonation as it pertains to exploding bridgewire detonators. It seems to be generally agreed that a detonation must be "supersonic." This leads to the question of the sound velocity in a loose packed powder with 40 percent to 50 percent voids or more. If it is calculated assuming the elasticity to be that of the interstitial air and the density to be the measured value, calculated sound velocities are in the range of urban speed limits. A measured value for insulating wallboard which has some similarity to these materials [12] is about 330 feet per second. Actually, the basic concept of sound is that of elastic waves and powders of low density have so little elasticity that such concepts lose much of their meaning. It is suggested that, in such media, any reaction in which a pressure-displacement wave plays an important role in propagation must be considered to be a detonation. In contrast, burning or deflagration are propagated by thermal conduction and convection. It follows that a reaction which propagates at a rate which is supersonic with respect to the interstitial air must be considered to be a detonation. In these terms, detonation, in exploding bridgewire detonators, starts with the explosion of the bridgewire. The initial velocities in excess of a millimeter per microsecond are indications that the items discussed herein are true exploding bridgewire detonators rather than "burning to detonation" devices as has been suggested.

ACKNOWLEDGMENTS

The majority of detonators used in this research were fabricated and fired by Mr. Donald D. Degner of R. Stresau Laboratory, Inc. The experiments at the IIT Research Institute were conducted principally by Mr. Ernest P. Bergmann. The contributions of these men and others among the various organizations participating in this work are gratefully acknowledged.

REFERENCES

1. R. M. Hillyer, and R. H. Stresau, "Exploding Bridgewire Initiation of RDX with Fifty Millijoules," Paper No. 5, Electric Initiator Symposium, Franklin Institute, Philadelphia, Oct. 1-2, 1963.
2. R. C. Maninger, "Initiation of PETN and RDX by Exploding Bridgewires," Paper No. 9, Electric Initiator Symposium, Franklin Institute, Philadelphia, Nov. 29-30, 1960.
3. M. T. Hedges, "Exploding Bridgewire Initiators," Paper No. 13, Electric Initiator Symposium, Franklin Institute, Philadelphia, Nov. 29-30, 1960.
4. Contract No. N123 (62738) 31089A between U.S. Navy Purchasing Office, Los Angeles (in behalf of U.S. Naval Ordnance Laboratory, Corona) and R. Stresau Laboratory dated 29 June 1962.
5. Engineering Design Handbook, Explosives Series, Explosive Trains, AMCP 706-179, March 1965.
6. H. Eyring, R. D. Powell, G. H. Duffy and R. B. Parlin, "The Stability of Detonation," Chem. Rev. 45, 69, 1949.
7. Military Specification MIL-R-00398C (Ord.) RDX.
8. W. M. Slie, and R. H. Stresau, "Small Scale Plate Dent Test of Confined Charges," NavOrd Report 2422, 23 April 1952.
9. R. H. F. Stresau, and C. Goode, "Recent Developments in the Vacuum Thermocouple Timer," NavOrd Report 2137, 29 June 1951.
10. H. S. Leopold, "Initiation of Explosives by Exploding Wires, V. Effect of Wire Material on the Initiation of PETN by Exploding Wires," NOLTR 64-146, 26 Oct. 1964.
11. R. H. Stresau, "A Theory of the Growth of Detonation from Sources of Sub-Critical Dimensions," Paper 17A, Electric Initiator Symposium, Franklin Institute, Philadelphia, Nov. 29-30, 1960.
12. H. S. Napadensky, and R. H. Stresau, "Observation and Measurement of the Behavior of Porous Materials When Rapidly Compressed," Exp. Mech. 1, 15-22, Jan. 1962.

SURFACE RATE PROCESSES AND SENSITIVITY OF HIGH EXPLOSIVES

R. F. Chaiken and F. J. Cheselske
Solid Propellant Research Operations
Aerojet-General Corporation
Sacramento, California

ABSTRACT

The nature and rate of linear surface regression of TNT, RDX, Tetryl and PETN have been studied utilizing a hot plate pyrolysis technique over surface temperatures ranging as high as 500°C. The data, when compared to similar data for benzoic acid, suggest that the primary surface rate process appears to be an endothermic melt-flow having an apparent activation energy suggestive of heat transfer and viscous flow as a rate controlling step.

These data, when used as a measure of surface heat dissipation, correlate very well with the measured values of impact sensitivity. Also, they offer an explanation for the fact that attempts to correlate impact and/or friction sensitivity with melting point alone could lead to misleading results when PETN and RDX are considered.

Notes:

- This paper has been published in J. Chem. Phys. 43, 3228-36 (1965).
- This work was supported by the Advanced Research Projects Agency under Contracts NOmr 2804(00) monitored by the Office of Naval Research and AF 49(638)-851 monitored by the Air Force Office of Scientific Research.
- R. F. Chaiken is technical consultant to Aerojet-General Corporation.
- Present address of F. J. Cheselske is: Airesearch Manufacturing Co., Division of Garrett Corp., Los Angeles, California.

LOW ORDER REACTIONS IN SHOCKED EXPLOSIVES

Neill Griffiths and V. C. Broom

*Royal Armament Research and Development Establishment
Fort Halstead, Sevenoaks, Kent, United Kingdom*

ABSTRACT

The initiation of RDX/TNT, TORPEX and MINOL in Gap-Test type of experiments has been studied and emphasis has been placed on producing events other than high order detonation. It is shown that by accentuating the loss factor in the usual energy balance equation that various degrees of reaction can be produced with the explosives examined. It is suggested that the probability of producing consistent low order reactions is associated with reaction zone length. An indication is given of the application of the model work to the disposal of high explosive filled bombs.

INTRODUCTION

An explosive/metal/explosive combination is a common occurrence in weapon systems, and during the post-war years such systems have been evaluated in considerable detail. Generally, however, the evaluation has been directed towards deriving the mechanism whereby detonation is established. A typical experimental technique which has played an important part in elucidating the mechanism by which detonation is achieved is the Gap-Test, although its prime purpose is to determine the sensitivity of explosives to shock wave initiation. Many workers [1,2,3] have described the Gap-Test, but generally they have been concerned with the probability of the test explosive detonating high order. The techniques and information available could be directed, however, towards assessing the necessary conditions for producing a low order reaction in an explosive. These thoughts are immediately applicable towards designing systems for the disposal of high explosive filled bombs. There is a current need for improved bomb disposal techniques and because of this, the possibility of producing reproducible low order reactions in high explosives is being examined in the United Kingdom.

This paper describes a number of gap-test type experiments in which the donor charge is adjusted to produce reactions other than detonation in the acceptor charge. The work is not complete, but a number of interesting points have been uncovered. The results obtained are discussed, and applied to preliminary full-scale trials.

GAP-TEST ANALOGY

In the Gap-Test, a detonator and an explosive pellet, (THE DONOR) is used to produce a shock, which traverses a metal barrier (THE GAP) and enters the explosive under test (THE ACCEPTOR). When pressure and temperature is applied to an explosive for a given time in this way, whether the explosive will detonate or not is controlled by the balance of energy gained and lost by the shock wave [4]. For the present purpose the loss factor is of great interest. The characteristics of the initiating shock are determined by the donor/gap combination, and together with the properties of the explosive acceptor will determine the rate of energy production. The geometry of the acceptor charge, together with the shock wave profile will to a large extent determine the magnitude of the energy lost.

When an explosive charge is placed on a high explosive bomb, one has in effect the same situation as exists in the gap test. The situation is illustrated in Fig. 1. If the explosive donor charge used is in the form of a thin sheet, pressure and temperature for a short period

Note:

"British Crown copyright reserved. Published with the permission of the Controller of Her Britannic Majesty's Stationery Office."

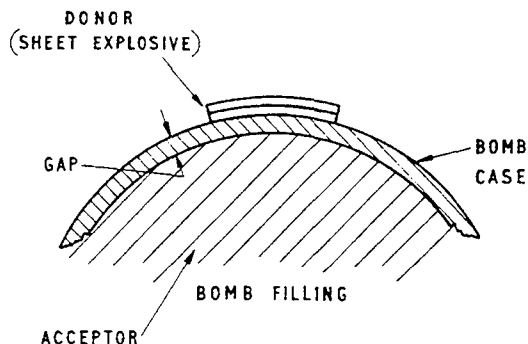


Fig. 1 - Bomb disposal gap test

will be applied to the system when it detonates. The high explosive filling starts to react and the reaction is governed by the energy balance equation. If the pressure rises in a suitable manner, the bomb case will rupture; the pressure will fall and the loss term of the energy balance equation becomes predominant and the reaction fades. It was considered, therefore, that the parameters of such a situation should be examined on a model basis, and that where possible applied to a typical high explosive filled bomb.

EXPERIMENTAL

Two experimental arrangements were used, and these are illustrated in Figs. 2 and 3. The first arrangement employs a circular donor of sheet explosive and both its diameter and thickness were varied during the course of the experiments. The sheet explosive used consists of RDX in a thermoplastic matrix and it was initiated by an A.S.A. Briska Electric Detonator. The gap used was a 6×6 in. mild steel plate and its thickness was varied from $1/8$ to $1/2$ in. Initial experiments examined the effect of the sheet explosive donor on the gap alone. Then, cylindrical acceptor charges 4 in. dia, 4 in. long were introduced; the explosives used were Minol 2, Composition B, Torpex 2B and Torpex 4B.*

A witness plate in the form of $6 \times 6 \times 1/8$ in. mild steel plate was located at the end of the acceptor charge. The order of the reaction in the acceptor charge was estimated by assessing the damage to the metal plates.

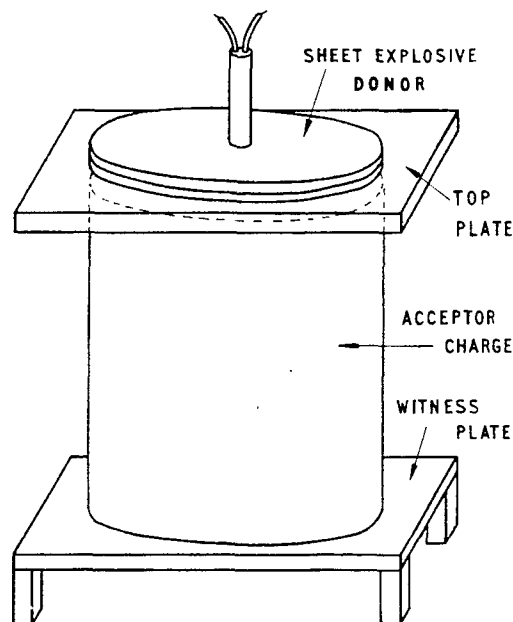


Fig. 2 - Perpendicular gap test arrangement

It was thought to be necessary to introduce curved surfaces into the experimental programme, as this was likely to be one of the conditions which would be met in bomb disposal tasks. Accordingly, the second experimental arrangement illustrated in Fig. 3 was adopted. A donor charge of sheet explosive is located on the outer surface of a cylindrical tube of mild steel of internal dia 4 in., wall thickness 0.5 in. and length 8 in.; this in effect is the gap. The explosive acceptor charge, 4 in. dia, 8 in. long, is located inside the steel tube and the types of explosives used as acceptors were as mentioned above. The circular donor charge was located midway along the length of the tube as shown in Fig. 3. In designing this experimental arrangement, attempts were made to take account of the effects of rarefaction waves, and it is likely that with the dimensions chosen, they will have little effect on the reaction zone during the critical time in which the probability of detonation occurring is being determined. The order of reaction obtained was assessed by estimating the amount of damage to the cylindrical steel tube. A number of examples are given in the illustrations and this will be discussed later. Towards the end of the experimental programme, the overpressure at various stand-off distances from the charges was measured with mechanical and piezoelectric gauges. From this data and standard pressure/distance relationships for given weights of explosive, an estimate could be made of the weight of explosive reacted.

*Aluminised NH_3NO_3 /TNT, RDX/TNT, Aluminised RDX/TNT.

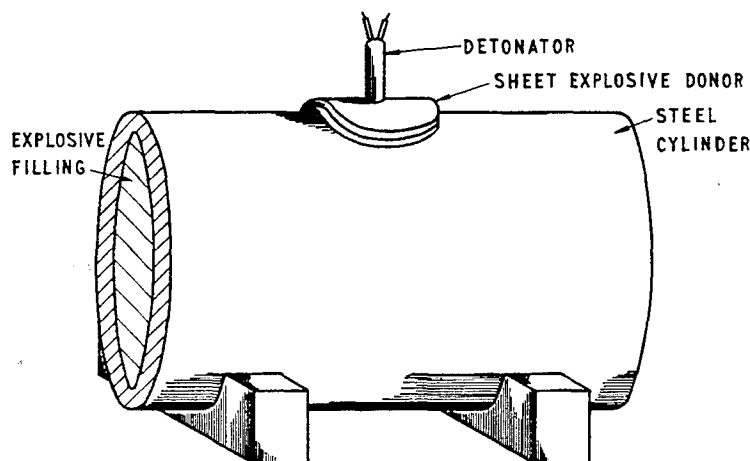


Fig. 3 - Cylindrical gap test arrangement

TABLE 1
Donor, 1/8 in. Sheet Explosive: Gap 6×6 in.
Mild Steel Plate, No Acceptor

Gap thickness (in.)	Donor dia. (in.)	Observation
1/8	1.0	Plate holed, dia. ~1 in.
1/8	2.0	Plate holed, dia. ~2 in.
1/4	1.0	Smaller hole, scab
3/8	1.0	Dent only

TABLE 2
Donor as Specified, Gap 3/8×6×6 in.
Mild Steel Plate, No Acceptor

Donor		Observation
Diameter (in.)	Thickness (in.)	
1	1/4	Deep dent, scab
1	3/8	Deep dent, scab
1	3/4	Deep dent, pinhole scab
2	1/8	Dent, large dia. scab
2	1/4	Hole, scab
2-1/2	1/8	Dent, scab
2-1/2	1/4	Hole, scab
2-1/2*	1/8	Scab only
1	1/8	

*Equivalent by weight to 2 × 1/4 in.

TABLE 3
Donor as Specified, Gap 1/2×6×6 in.
Mild Steel Plate, No Acceptor

Donor		Observation
Diameter (in.)	Thickness (in.)	
2-1/2	1/8	Dent, scab
3-1/2	1/8*	Dent, scab
2	1/4°	Dent, scab
2-1/2	1/4*	Hole, scab
2	3/8*	Hole, scab
1	1-1/2*	Dent, scab
1-1/2	5/8	Small hole, scab
1	1/8	
1-1/2	3/8°	Small hole, scab
2	1/8°	Dent, scab
1-1/2	1/8	
1	1/4	Dent, scab
2-1/2	1/8°	
1	1/4	Dent, scab
1-1/2	1/2	
1-1/2	1/2	Hole

*and ° indicate equivalent weights of donor.

RESULTS

Effect of Sheet Explosive on the Gap

With the experimental arrangement shown in Fig. 2, the effect of varying the donor and gap with no acceptor present, was first examined. The results obtained are tabulated in Tables 1, 2 and 3. As the donor charge is varied, different degrees of damage can be obtained on the gap and examples of these are shown in Figs. 4-7.



Fig. 4 - Deep dent in 1/2 in. plate

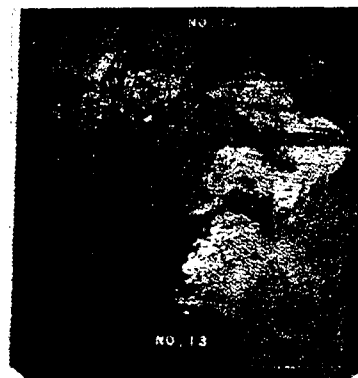


Fig. 6 - Scab only from 3/8 in. plate

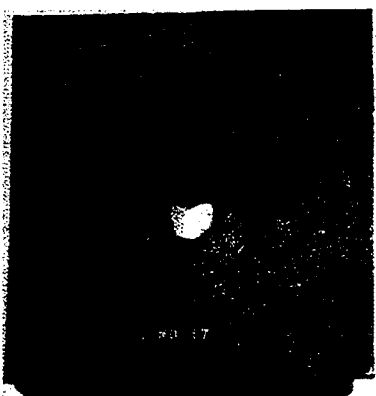


Fig. 5 - Hole and scab in 1/2 in. plate

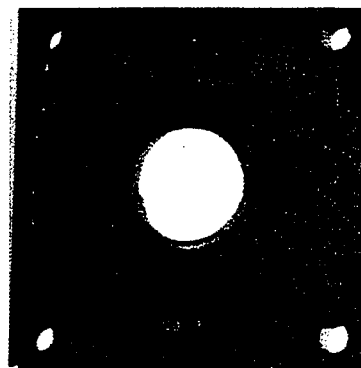


Fig. 7 - 1/8 in. plate holed

For a hole to be obtained in a plate the results suggest that the weight of donor required must be distributed in such a manner so that the ratio of diameter to thickness is within certain critical values. For example, in Table 3, where 1/2 in. plate is being examined, at a donor thickness of 3/8 in., the critical diameter is 1-1/2 in., however, increasing the diameter enables the thickness to be reduced. A limit is reached however at 1/8 in. thickness.

Effect of Acceptor Charges

The experiments were continued with acceptor charges and witness plates introduced below the gap; the order of reaction achieved by the acceptor was assessed by examining both gap and witness plates. If high order detonation occurred both plates were lost; otherwise

the bottom plate was either undistorted with the imprint of the acceptor charge on it, or badly distorted. Figures 8 and 9, illustrate these features. Using the acceptor charges already specified, the results obtained are tabulated in Table 4, the damage to the gap plate being indicated where possible.

The results show that by carefully adjusting the donor charge a variety of events, in which both the amount and the rate of reaction vary, can be produced in the acceptor charge. The incidence of fires should be noted as they can cause no little difficulty. Comparison of these results and the earlier ones indicates that the reaction in the acceptor charge is contributing towards the damage of the gap. From both the experiments with the 1/8 and 1/2 in. gap it is clear that the type of explosive charge affects the class of event obtained in the acceptor and the order of sensitiveness is Comp. B: Torpex 2: Torpex 4 and Minol 2.

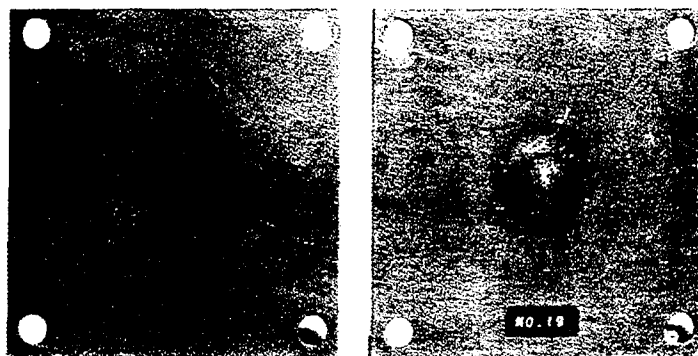


Fig. 8 - Imprint of charge on undistorted bottom plate and hinged scabbled top plate

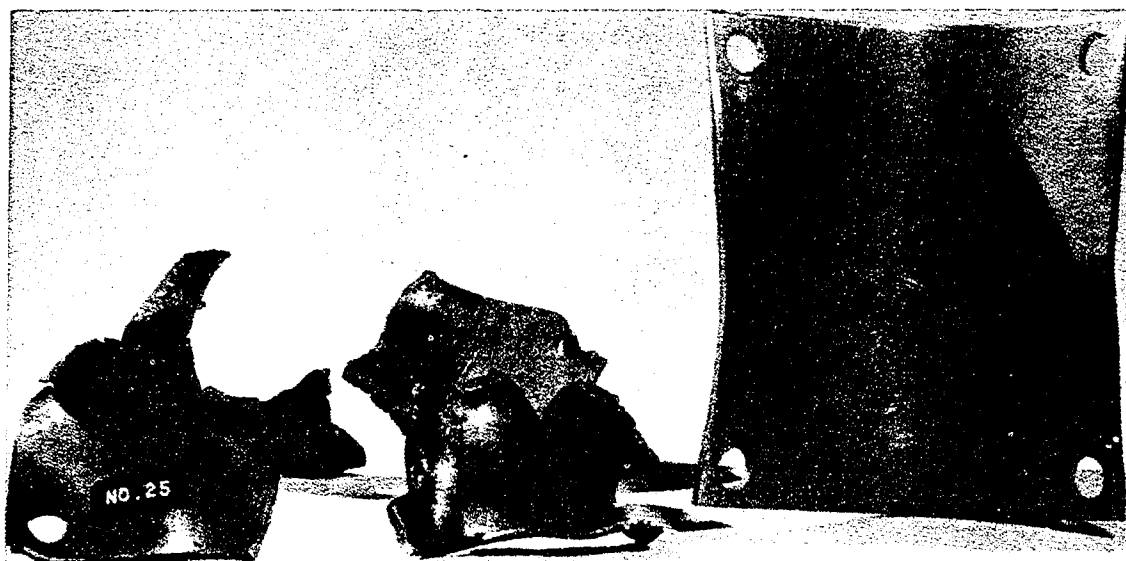


Fig. 9 - Broken top plate and distorted bottom plate

Experiments with Cylindrical Gaps

With the experimental arrangement shown in Fig. 3, the effect of varying the donor charge was examined; the main emphasis has been placed on studying the effects in Torpex 2, as this was the filling of bombs available for full scale trial. The results obtained are tabulated in Table 5. A slightly different notation has been used here to classify the event obtained; the scheme chosen is shown at the head of the columns of Table 5. It is based on the condition of the cylindrical container recovered after firing. The reproducibility of the scheme is remarkably good, although it will be noticed

that sometimes there are intermediate degrees of reaction which have a tendency to fall in one or other of the chosen classes. A typical example is shown in Fig. 10; Figs. 11-16 are typical examples of the classes of events chosen. The results of Table 5 indicate that with the experimental arrangement used, various low order reactions can be obtained in which the metal case surrounding the charge is broken to various degrees.

Reference is made in Table 5 to post ignition which occurred particularly with Torpex. The charges were necessarily fired in a cell of limited volume, with confinement of steel

TABLE 4

Donor		Acceptor	Gap Thickness (in.)	Observation (effect on gap)
Diameter (in.)	Thickness (in.)			
1	1/8	Comp. B Torpex 2 Torpex 4 Minol 2	1/8	Full detonation, both plates lost No reaction, hole No reaction, hinged scab No reaction, dent
2	1/8	Torpex 2 Torpex 4 Minol 2	1/8	Partial Detonation, broken up No reaction, holed No reaction, scab (witness plate distorted)
2-1/2	1/8	Torpex 2 Torpex 4 Minol 2	1/8	Full Detonation Partial Reaction, Fire, holed Partial Reaction, holed
2	1/4	Minol 2 Torpex 4	1/8	No reaction No reaction
2-1/2	1/4	Minol 2 Torpex 4	1/8	Complete reaction Partial reaction
2-1/2	1/8	Comp. B Torpex 2	1/2	No reaction No reaction
2	1/4	Comp. B Torpex 2	1/2	Partial Reaction, heavy dent Partial Reaction, heavy dent
2-1/2	1/4	Comp. B Torpex 2 Torpex 4	1/2	Partial Reaction, heavy dent Partial Reaction, burning, dent No reaction, partial scab
2-1/2	1/4 1/8	Torpex 2 Torpex 4 Minol 2	1/2	Complete Reaction, dent Partial Reaction, burning, hole Partial Reaction, dent

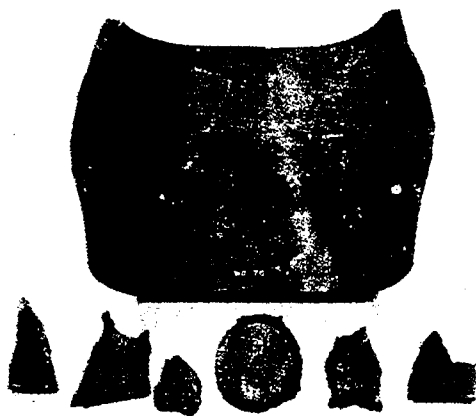


Fig. 10 - Fragments of steel tube recovered after partial reaction - intermediate case

and wood. The post ignitions which occurred might be associated with impact, friction and squashing of unreacted explosive on the walls of cells. Later, in field trials however, it was found that Torpex filled bombs started to burn vigorously some five minutes after it was shocked and was still burning some fifty minutes later!

Table 5 indicates that the order of sensitivity of the explosives tested is Comp. B: Torpex 2: Torpex 4: Minol 2, which agrees with the previous results.

Experiments With High Explosive Filled Bombs

Having demonstrated the feasibility of producing controlled amounts of reaction in

TABLE 5

Acceptor Explosive	No Reaction Case Not Holed Fig. 11	Partial Reaction Case Opened Some Post Ignition Fig. 12	Partial Reaction Case in Large Pieces Some Post Ignition Fig. 13	Partial Reaction Case in Many Pieces Fire Fig. 14	Full Reaction No Explosive Left Case in Small Pieces But No Detonation Striations Fig. 15	High Order Detonation Fig. 16
Comp. B					$2 \times 1/8$ $3 \times 1/8$	$3 \times 1/8$ $4 \times 1/8$
Torpex 2	$2 \times 1/8$ $2 \times 1/8$ $3 \times 1/8$ $3 \times 1/8$ $3-1/2 \times 1/8$	$2 \times 1/8$ $2 \times 1/8$ $2 \times 1/8$ $2-1/2 \times 1/8$ $2 \times 1/8$ $2-1/2 \times 1/8$ Tendency \rightarrow	Tendency $2 \times 1/8$ $\leftarrow 3 \times 1/8$ $2 \times 1/8$ $3 \times 1/8$	$2-1/2 \times 1/4$ $2-1/2 \times 1/4$		$3 \times 1/4$
Torpex 4	$4 \times 1/4$ $4 \times 1/4$				$3 \times 1/4$ $4 \times 1/4$	
Minol 2					$4 \times 1/4$	

Dimensions quoted are the diameter and thickness of the donor charge.
When two pieces of sheet explosive are used, the smaller diameter piece is located on top.

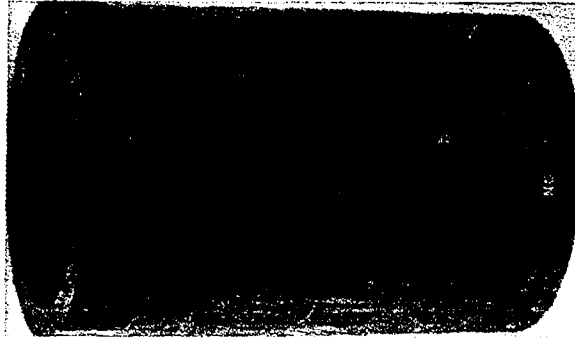


Fig. 11 - No reaction steel tube not holed

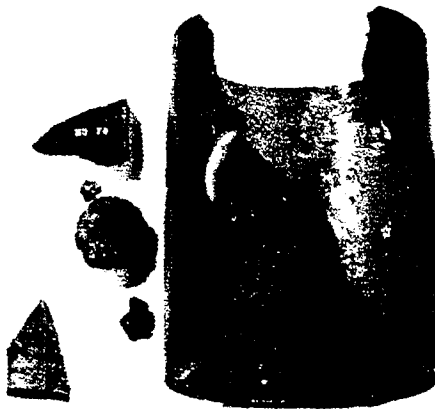


Fig. 12 - Partial reaction steel tube opened



Fig. 13 - Partial reaction steel tube in large pieces



Fig. 14 - Partial reaction steel tube in many pieces



Fig. 15 - Full reaction, no explosive left, steel tube in small pieces

explosives and reproducible damage to the metal surrounding the explosive, attempts were made to apply the technique to high explosive filled bombs. The bombs used were filled Torpex 2, were unfused and contained no exploder pellets (gaines or primers). The thickness of the bomb casing was measured accurately and sections of the bomb were radiographed. Consequently a detailed knowledge of the metal/explosive conditions was available; this together with the experimental data reported above enabled suitable donors to be chosen.

The preliminary trials showed that the following conditions could be achieved:

- (i) Bomb holed, filling broken up (see Fig. 17)
- (ii) Bomb broken apart, filling disgorged (see Fig. 18)
- (iii) Bomb burnt out (see Fig. 19)

The work is by no means complete, but it is considered that the feasibility of the method has been demonstrated. Pressure measurements taken during the course of this work suggested that less than 2% of the bomb filling was involved in the reaction.

DISCUSSION

When a solid explosive is shocked the energy can be released either rapidly or slowly, the intensity of the shock determining the rate of release. If sufficient energy is contributed



Fig. 16 - High order detonation



Fig. 17 - Bomb holed, filling broken up



Fig. 18 - Bomb broken apart, filling disgorged



Fig. 19 - Bomb burnt out

to the shock front it will accelerate and stable detonation will eventually be achieved, whereas if insufficient energy is contributed to the shock it will decay, and detonation will not ensue. Now, if a shock wave of short duration is used the rarefaction wave arrives soon after the reaction has started and the explosive is cooled and reaction may be stopped. As the pressure of the shock wave is increased there is more and more decomposition and consequently more energy is contributed towards the shock front. Whether detonation is established or not is simply dependent on the energy balance [4], i.e., whether the energy produced outweighs the losses. By varying the duration of the shock pulse it is possible to vary continuously the energy contributed to the shock front. If the pulse length is gradually increased a balance can eventually be obtained between energy lost and energy produced, and a pseudo stable detonation is set up.

During the period in which the probability of detonation is being determined - sometimes called the critical time, explosive is being consumed and gas generated. Under some conditions this can take many microseconds, and this means that the shock has traversed many millimetres of the charge length [5]. Clearly no little quantity of the charge is reacting and this is independent of the final event; thus even when detonation is not achieved, high pressures can be generated.

Now with explosives which have short reaction zone lengths, the critical time mentioned above is much shorter than for those of long reaction zone lengths. It follows, therefore, that with the former the amount of explosive consumed during the critical time will be small and the pressure developed low. It is considered unlikely, therefore, that with explosives like pressed RDX and Tetryl anything other than high order detonation could be obtained reliably. However, with explosives of long reaction zone length, variation of the shock pulse will effect significantly the critical time, with a consequent variation in the amount of explosive reacted.

In the experiments described in this paper a shock wave of very short duration has been used and aluminised explosives, which have long reaction zones, and as discussed above significant amount of reaction have been obtained and

high pressures developed. It is considered, therefore, that the processes occurring in the experiments described are compatible with current shock initiation theory.

The experimental work described has not been very sophisticated, but the basic thought behind the work was to obtain information which would be useful for a prospective bomb demolition tool. More quantitative measurements are now required, particularly on the shock wave profile and the rate of reaction in the shocked explosive.

Finally, it is worth mentioning the alternative approach to the one discussed in this paper. The use of an intense shock wave applied for a short time has been discussed - this technique requires that some of the shocked explosive must react, thereby introducing its inconsistencies into the balance for power. Alternatively, if a shock wave whose intensity is such that the explosive will never react [6] is used and applied for some time the container will eventually burst. This approach might eliminate the idiosyncrasies of the acceptor charge.

ACKNOWLEDGMENTS

The authors are pleased to acknowledge the assistance of Mr. A. May and Mr. H. B. Young, and Mr. G. P. Cachia for his valuable advice.

REFERENCES

1. Campbell, Davis & Travis, Proc. of the Third Detonation Symposium, Princeton, September 1960.
2. Cachia & Whitbread, Proc. Roy. Soc., 1958, A, 246, 268.
3. Griffiths & Grocock, J. Chem. Soc., 1960 4154.
4. Griffiths & Laidler, Comb. and Flame, Vol. 7, Dec. 1963.
5. Griffiths & Laidler, J. Chem. Soc., June, 1962, 443.
6. Marlow & Skidmore, Proc. Roy. Soc., 1958, A, 246, 285.

INITIATION OF EXPLOSIVES BY LOW VELOCITY IMPACT

Hyla S. Napadensky
IIT Research Institute
Chicago, Illinois

ABSTRACT

A sensitivity test has been devised wherein cylindrical, unconfined specimens of high explosive of the order of several pounds in weight are squeezed between an explosively driven plate and a massive anvil. At one extreme of the initiation spectrum the shock transmitted is of sufficient intensity to initiate detonation before or at the instant when the shock wave reaches the face of the anvil. At the threshold of initiation however, the time between initial movement of the plate and evidence of explosion is long enough for extensive crushing of the HE to occur. The impact velocity required for initiation has been found to be strongly dependent upon the size of the explosive specimen. Sensitivity increases rapidly as the length of the specimen is decreased. Marginal initiation is the result of a slow crushing process for short samples. As specimen length is increased, the critical impact velocity approaches a limiting upper value which is sufficient for shock initiation of the explosive.

INTRODUCTION

This impact sensitivity test was designed with the intent of simulating the loading conditions that are likely to be imposed on the explosive component of an ordnance item as a result of a severe accidental impact. In this test, unconfined cylindrical high explosive billets, of the order of several pounds in weight, are squeezed between a rapidly moving steel plate and a massive stationary steel anvil. This type of loading results in the explosive being initiated after a relatively slow crushing process, as occurs in situations of severe accidental impact such as transportation accidents or jettison from aircraft, rather than being promptly initiated by a shock process. Initiation of explosion occurs at much lower stress levels by the crushing process than by the shock process.

THE TEST METHOD

The response of explosive billets to impact loads is determined by a series of experiments using the apparatus shown schematically in Fig. 1. In each experiment, a 6-inch-diameter by 1-inch-thick steel plate is propelled by the uniform plane-wave initiation of low-density tetryl explosive in contact with the plate. It is the initiation of the tetryl almost simultaneously over

its surface that results in the plate being uniformly accelerated. This initiation is accomplished by the fragmentation of the aluminum disk, which occurs when the booster is ignited by a blasting cap. The fast-flying, hot aluminum fragments strike the tetryl explosive driver charge in a large number of places simultaneously and cause the driver explosive to detonate.

The use of tetryl powder at a density of 1 gm per cm³ permits us to project the steel plate to a maximum velocity of 1000 fps. Tetryl powder pressed to a density of 1.2 gm per cm³ enables us to achieve up to 2000 fps for the same size plate. By varying the quantity and density of explosive driver we can achieve plate velocities ranging from about 25 fps to 2000 fps.

RESULTS AND INTERPRETATION

The impact velocity of the steel plate required to initiate an explosive reaction has been found to depend upon the dimensions of the test specimen. For a fixed diameter, the required minimum impact velocity increases with increasing length, but rapidly approaches an upper limit which is sufficient for shock initiation of the explosive. This upper limit decreases with increasing diameter. A limit diameter is also

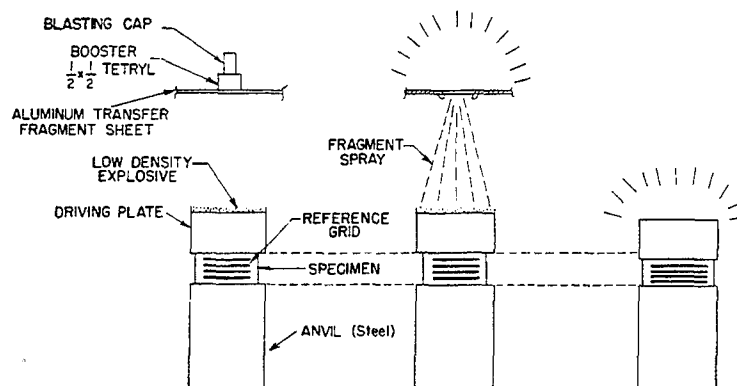


Fig. 1 - Test arrangement showing method of initiating driver explosive

reached beyond which any further increase in diameter will not lower the critical impact velocity. The limit diameter is in the neighborhood of 3-3/4 inches for 9404PBX, based on tests on 1-1/2, 2-1/2, 3-3/4 and 6-inch diameter billets. All data presented here are for 6-inch-diameter billets. For this diameter, the limit impact velocity is 440 fps for 9404PBX (Ref. [1]), 640 fps for H-6 (Ref. [2]) and 1900 fps for Tritonal (Ref. [3]).

The experimentally determined relationships between the thickness of the explosive billet and the impact velocity required for initiation of an explosion is shown in Fig. 2 for 9404PBX. In region A of Fig. 2, we see that above a certain velocity (~440 fps), the explosive always detonates high-order. For a much lower impact velocity, region D, which depends upon explosive charge length, no chemical reaction is obtained. For intermediate impact velocities, regions B and C, the explosive reaction is generally less violent than the high-order detonation of region A. Further, this graph illustrates the experimental results that, for a given diameter, as the thickness of explosive billet increases an increase in impact velocity is required to cause an explosion.

High-speed framing camera photographs showing the crushing and subsequent initiation of the explosive billets yielded information on some of the processes involved during impact.

In region A of Fig. 2 high-order detonations occur at impact velocities above 440 fps and calculated pressures of the order of 10 kilobars. The criterion of fire for a high-order detonation is that a hole is punched through the 1-inch thick mild steel witness plates placed beneath the explosive. The propagation velocity as measured on microsecond framing camera photographs

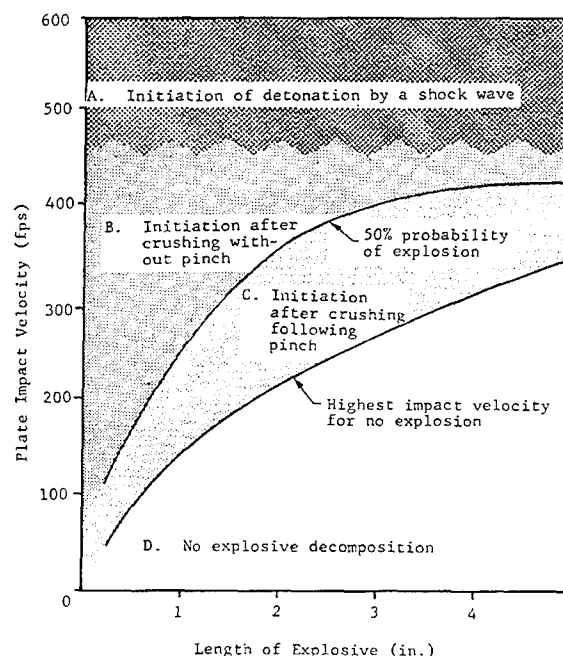


Fig. 2 - Critical impact velocity as a function of explosive length, for 6-inch diameter 9404 PBX billets impacted by 6-inch diameter by 1-inch thick steel plates

confirmed this criterion. Explosions occur during the first passage of the nonreactive stress wave through the explosive billet or immediately upon reflection of this stress pulse from the back-up anvil.

In region B, initiation of explosion occurs at impact velocities less than 440 fps and after some small amount of crushing and lateral extrusion of the explosive billet occurs. The explosion which

may be a violent deflagration or detonation of part of the explosive still trapped between the driving plate and the anvil occurs within 100 microseconds to 1 millisecond after impact. The witness plates may either show evidence of metal flow over the surface or a deep bulge is formed.

In region C, which we consider to be the initiation threshold region, explosions occur only after the majority of the explosive has been extruded beyond the original diameter and the remaining explosive is crushed to a very thin layer. This condition has been observed to occur within one to three milliseconds after impact for the plastic bonded HMX-based materials [4]. Under these loading conditions no unreacted explosive remains and the witness plate is not marred in any way.

Explosions do not occur in region D, the no-go region. Under these conditions a layer of unreacted explosive remains on the witness plate after impact.

Finally, we observe explosions occurring external to the original charge diameters and after complete crushup and extrusion of the billet. Here the explosion originates in the explosive dust which was extruded from between the colliding plates. This type of reaction can cause considerable damage and noise.

A single mechanism or several mechanisms may be responsible for initiation during crushing impact. One cannot deduce simply from the shape of the curve in Fig. 2 or from high speed photographs of the crushing process and subsequent explosion, which of several possible initiation mechanisms is dominant. The applicable mechanism may depend upon the explosive geometry, its environment and its composition (as reflected in properties as brittleness, thermal diffusivity, explosive crystal form, etc.). The relationship between impact velocity and charge size which characterizes the sensitivity to impact of one material would not be the same for another explosive composition. The curve representing this relationship for uniform impact loading of one explosive material would be shifted or changed in shape for an explosive of a different composition or for the same explosive subjected to a concentrated load. This can be seen from the curves in Fig. 3, for uniform loading, showing the relationship between explosive charge length and impact velocity required for the 50 percent probability of initiation of 9404PBX, H-6 and Tritonal.

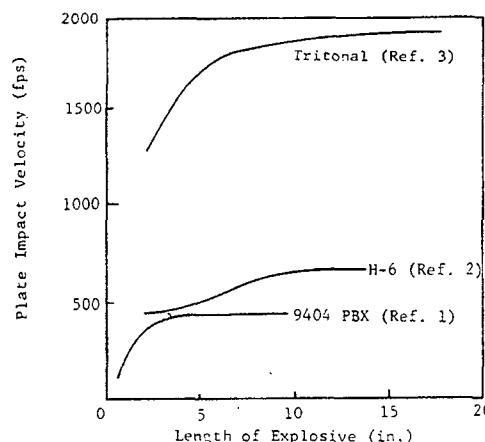


Fig. 3 - Impact velocity as a function of explosive length for 50 percent probability of reaction, various explosives

Curves of this type have been applied to assessing the likely hazards of severe accidental impact to ordnance items containing high explosives without understanding the mechanisms responsible for initiation. Successful application of this sensitivity data requires that for a given explosive thickness the same mechanism controls the explosive's response in both the laboratory tests and in the accidental impact situation (Ref. [2, 3, 5]).

REFERENCES

1. Napadensky, H. S., "Development of Methods for Predicting the Response of Explosive Material to Impact (U)," AFSWC TR 61-8, DASA 1225, March 1961 (SRD)
2. Napadensky, H. S., "The Impact Vulnerability of the MLU-10/B Aerial Land Mine," ATL-TDR-64-60, 15 Jan. 1964, AD 447 917
3. Napadensky, H. S., "The Impact Vulnerability of the Tritonal-Loaded MLU-10/B Aerial Land Mine," ITRI Report No. T6053-FR for AFSC under Contract No. AF 08(635)-3789, April 1965
4. Napadensky, H. S., "The Effects of Impact Loading on Plastic-Bonded Explosive Materials," DASA 1391, April 1963
5. Kennedy, J. E. and H. S. Napadensky, "The Vulnerability of Special Weapons to Fire and Impact, (U)," DASA 1276, Vol V, Part 2, Jan. 1964, (SRD)

ACKNOWLEDGMENT

Investigations on plastic-bonded explosives were supported by FC/DASA under Contracts

AF 29(601)-2133, DA-29-044-XZ-885 and AF 29(601)-1959. Work on H-6 and Tritonal was supported by Detachment 4, RTD, AFSC, under Contract AF 08(635)-3789.

COMMENT

J. E. KENNEDY (IIT Research Institute, Chicago, Illinois): In considering marginal initiation as in region C of Fig. 2, recent work at ITRI, Lawrence Radiation Laboratory (Ref. 1), and Brobeck Associates (Ref. 2) has led to a hypothesis that a lateral extrusion flow process may be the mechanism by which local hot spots are developed of intensity sufficient to initiate a burning or deflagration process in the high explosive specimen. Analyses assumed either that the specimen deformed as a rigid body (Ref. 2) or flowed as a viscous fluid (Ref. 3). Either assumption indicated that maximum temperature increases due to irreversible conversion of mechanical energy to heat during flow should occur along the flat interface between the explosive and the plate or the anvil, and near the outer periphery of the explosive.

To test the hypothesis experimentally, we have installed fast response surface thermocouples flush with the surface of the anvil in order to determine the trends and magnitudes of temperature increases in the explosive at the plate surface as a function of radial position under test conditions appropriate to cause marginal ignition. Thermocouples were installed below the center of the explosive specimen and at positions halfway toward the outer periphery of the specimen and slightly inside the outer periphery. We have found that the thermocouples, made by Nanmac Corporation,

have a rise time of 1 to 5 microseconds or less, which is quite adequate response for study of this millisecond-duration phenomenon.

Preliminary experimental results have indicated maximum temperature increases near the outer periphery of the samples, and little or no temperature increase at the cylindrical axis, in qualitative agreement with the extrusion analyses. The indicated maximum temperature levels were a few hundred degrees centigrade for test conditions appropriate for marginal ignition.

REFERENCES

1. L. G. Green, and G. D. Dorrough, "Further Studies on the Ignition of Explosives," Proc. of Fourth NOL-ONR Symposium on Detonation, October 12-15, 1965.
2. A. M. Weston, "Code Crash. A Study of the Impact Ignition of a Thin Wafer of Explosive Material." Lawrence Radiation Laboratory, Livermore, California, Doc. No. 4500-95-3-R28, 1966.
3. J. E. Kennedy and H. S. Napadensky, "Behavior of Explosive Systems Under Mild Impact," IIT Research Institute, Chicago, Illinois. DASA 1801, 1966.

FURTHER STUDIES ON THE IGNITION OF EXPLOSIVES*

L. G. Green and G. D. Dorough
*Lawrence Radiation Laboratory
Livermore, California*

ABSTRACT

This paper summarizes the results of an experimental investigation on the ignition of explosives by low velocity impact. The impact experiments are carried out with explosive billets approximately one pound in weight. One cast and three plastic-bonded materials are studied in three different impact geometries. Both the mechanical and chemical nature of the impact process for each geometry is explored in some detail.

In all cases, ignition appears to result simply from frictional heating of the explosive. The ultimate course of the chemical reaction after ignition (mild burning, violent burning, detonation, etc.) is strongly influenced by the impact configuration and velocity and by the nature of the explosive. Surface finish does not appear to play any significant role in either the threshold velocity for reactions or in the ultimate course of the reaction.

INTRODUCTION

Nearly all accidental impact situations involving explosives or explosive containing assemblies occur in the relative velocity range of a few ft/sec to a few hundred ft/sec. The behavior of explosives under this type of stimulus is thus of prime interest from a safety point of view.

Impacts in this low velocity range generate only very low amplitude stress waves, stress waves much too weak to shock initiate directly most explosive materials. The primary mechanism for producing chemical reaction in these situations appears to be some form of frictional heating in which the mechanical energy of the impact is deposited as heat in very limited regions of the explosive. The heated explosive then begins to decompose, producing a deflagration which continues, dies out, or builds to detonation depending on the explosive and the impact geometry.

Over the last several years this Laboratory has conducted an extensive investigation of the behavior of explosives under conditions of low velocity impact. This paper, which is in the nature of a progress report, summarizes

some of our current thoughts on the phenomenology of impact ignition.

EXPLOSIVE MATERIALS

For the purposes of this paper, we shall confine our attention to four high performance explosive formulations. Three of these are plastic bonded explosives, the other is a cast explosive. All four are high density materials with void volumes less than two percent. All four are characterized as "brittle" materials with maximum elongations to rupture being less than one-half percent at room temperature. Table 1 cites some general information on the four explosives.

IMPACT GEOMETRIES

In this paper we shall consider only three impact geometries, designated Susan Test, Type 1 Test, and Type 2 Test. We describe below in brief fashion these three geometries, and the mechanical nature of the impact process in each case.

*This work was supported by the U.S. Atomic Energy Commission.

TABLE 1
General Information on Explosives Discussed in Text

Explosive	Main Explosive Constituent	Binder Used and Wt. Percentage		Billet Fabrication	Compressive Strength at 68°F (psi)	Tensile Strength at 68°F (psi)
Composition B-3	RDX	TNT	40%	Casting and machining	~1600	~300
LX-04-1	HMX	Viton A	15%	Hot vacuum pressing and machining	~2000	~300
PBX-9011-02	HMX	Estane	10%	Hot vacuum pressing and machining		~300
PBX-9404-03	HMX	Nitrocellulose	3%	Hot vacuum pressing and machining	~1400	~100
		Chloroethyl phosphate	3%			

Susan Test

The Susan Test [1,2] is a projectile impact test used by this and other laboratories as a technique for evaluating the sensitivity of an explosive under conditions of crushing impact. Figure 1 shows the projectile used in the test. The projectile is fired from a smooth bore gun against a steel target at velocities that may range from one hundred to fifteen hundred feet per second. The chemical reactions produced by the impact are monitored photographically with Fastax cameras; air shocks generated by the reacting explosive are monitored with over-pressure gauges. Additional information is

also obtained from the physical examination of impacted projectiles.

Figure 2 shows the deformation soon after impact. The end of the aluminum nose cap has opened up, but the longitudinal section of the cap has not yet split open. Some, but not all, explosives will exhibit fire or burning at this stage of the impact. This early burning reaction is usually quite mild; the best evidence to date indicates that it starts at a fracture plane within the explosive. The mechanism is simply frictional heat generated at the fracture plane in the explosive by slippage under pressure.

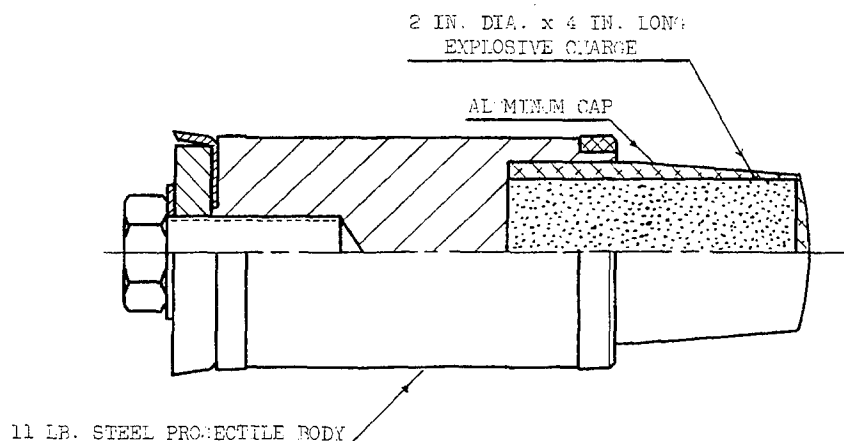


Fig. 1 - Mod I Susan projectile

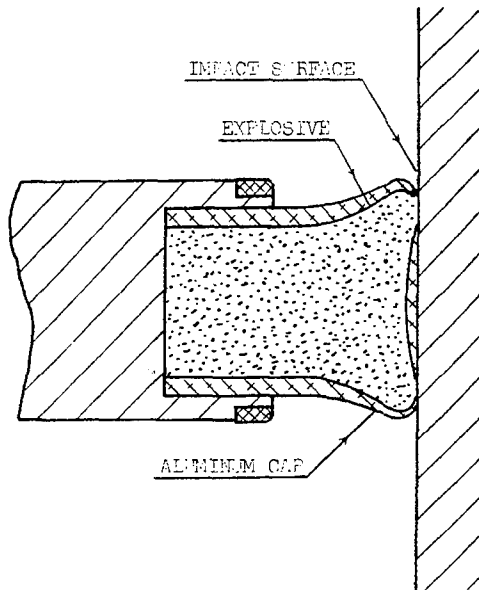


Fig. 2 - Mod I Susan projectile early deformation

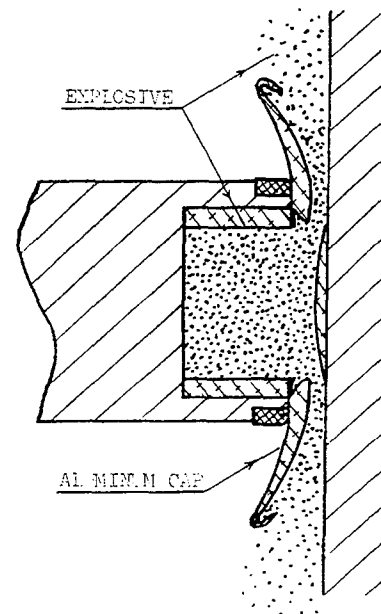


Fig. 3 - Mod I Susan projectile pinch stage

Figure 3 shows the deformation late in the impact. The aluminum cap has completely failed by longitudinal splitting, and the steel rim of the projectile body is in near contact with the target plate. We call this the pinch stage. The most violent reactions from a Susan type impact almost always occur at the pinch stage. In fact, most soft, rubbery, plastic bonded explosives and all cast explosives tested to date do not react at all in this test until the pinch stage is reached. The pinch stage is characterized mechanically by a rapid radial extrusion of explosive material from between the target plate and the incoming projectile. This rapid motion of explosive material past projectile and target surfaces which are stationary in the radial direction, under a pressure which is maintained by the forward momentum of the projectile body, represents a condition of severe frictional heating. Some thirty-odd explosive formulations have been examined in the Susan Test, and all are observed to ignite under the pinch conditions. Pinch ignition often builds to quite violent deflagrations, but detonations are only rarely (if ever) observed.

Type 1 and Type 2 Impact Tests

These two tests represent variations of an anvil-driver test first described by Napadensky, et al. [3]. As conducted by this Laboratory, the drive plate is an 8-inch diameter, 1-inch-thick

plate of mild steel; the target plate or anvil is a 10-inch-square plate of mild steel. The driver plate is attached to one end of a 4-foot-long tube; a pressure seal is fitted to the other end. This tube is inserted in the muzzle of a smooth bore rifle, and the entire tube-driver plate assembly is fired down a short range with a propellant charge appropriately sized to attain terminal driver-plate velocities in the range of 80-400 ft/sec. Impact of the driver and target surfaces is plane and parallel within a degree. In the Type 1 experiments a 2 inch diameter by 4-inch-long explosive billet (identical to the Susan Test billet) is lightly glued to the center of the driver plate (see Fig. 5); Type 2 experiments are identical in every way except that a 1-inch-thick, 4-inch-diameter disk of explosive substitutes for the long explosive cylinder of the Type 1 experiment. The main diagnostic tool used in both Type 1 and Type 2 experiments has been the high-speed camera framing at the rate of ~11,000 frames/sec. Experiments using mock explosives have also been informative in defining the mechanical nature of the impact processes in these experiments.

In the Type 1 experiments, the initial compression produced in the explosive by the impact is relieved by fracturing as the long cylinder of explosive breaks up. The fracturing process starts at the target explosive interface, and proceeds towards the driver plate. Eventually, much of the broken explosive is trapped and re-compacted between the driver and target

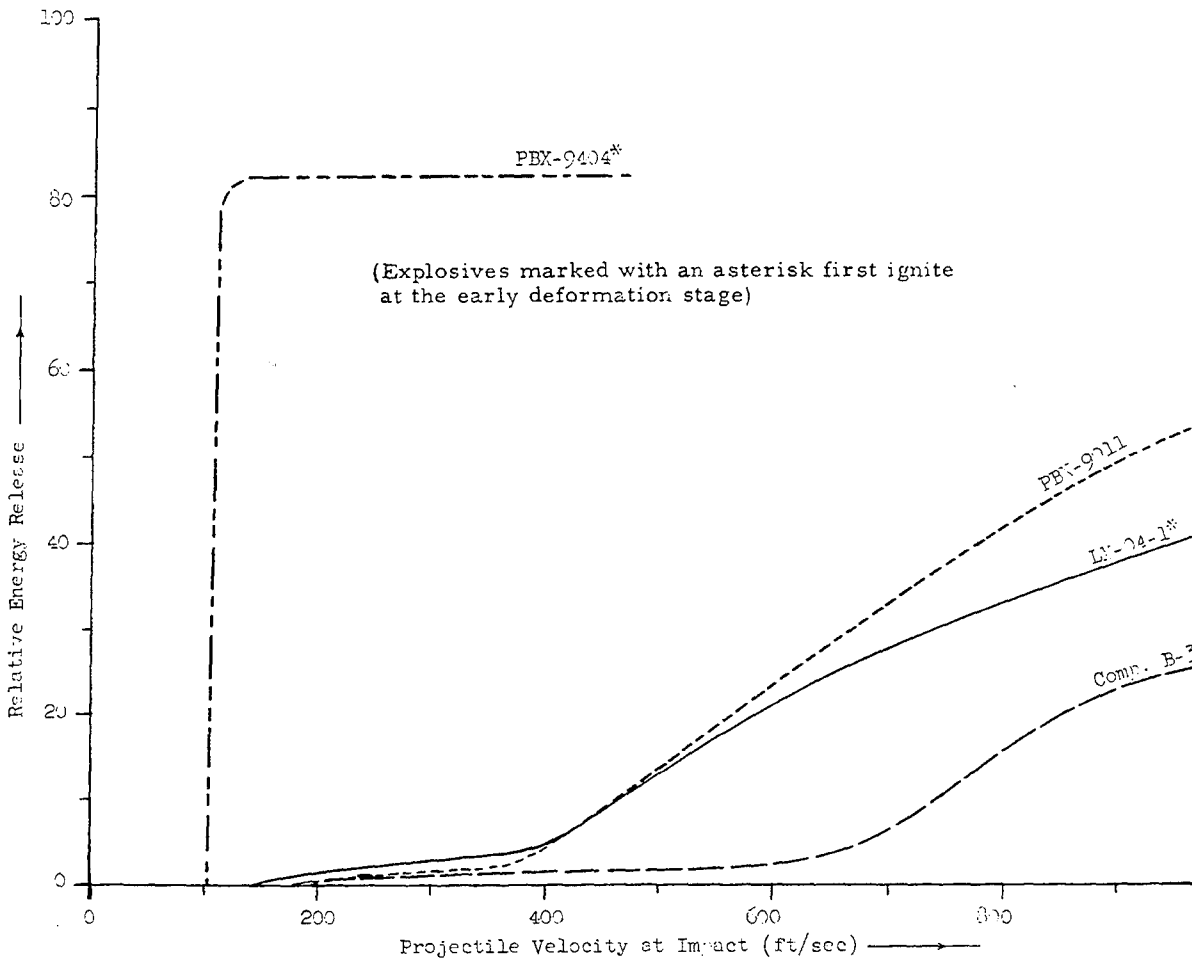


Fig. 4 - Susan test results, chemical energy released at pinch stage

plates as they near contact. Ignition in the Type 1 experiment is presumed to be by a mechanism similar to that described for pinch ignition in the Susan Test. If the ignition occurs at a time when the explosive is still in a highly divided state, the burning reaction frequently builds to a high order detonation.

In the Type 2 experiments, the disk of explosive is under compression during the entire course of the impact, and is forced to flow at quite high rates from between the driver and target plates. The situation bears a strong resemblance to the pinch stage of the Susan Test. For explosives which are essentially brittle in nature, the flow is of a granular type, and may not be well represented as a plastic or viscous flow. Film records indicate that ignition occurs at the metal-explosive interface. Detonations are rarely produced in this impact geometry.

General Comments on the Three Impact Geometries

There is a basic difference between the Type 1-Type 2 experiments and the Susan Test. The Susan Test has been designed and is conducted as a comparative test. Considerable care is expended to make sure that each Susan projectile is fabricated like other Susan projectiles, and that the conditions and geometry of impact are reasonably standard from test to test. While we know a great deal about the Susan Test and what it measures, it nevertheless is a very complicated test from the standpoint of its impact geometry. Thus, it has not been chosen for detailed studies on impact behavior per se.

The Type 1-Type 2 experiments are intended to explore the subtleties of impact behavior. The geometries are simple, hopefully

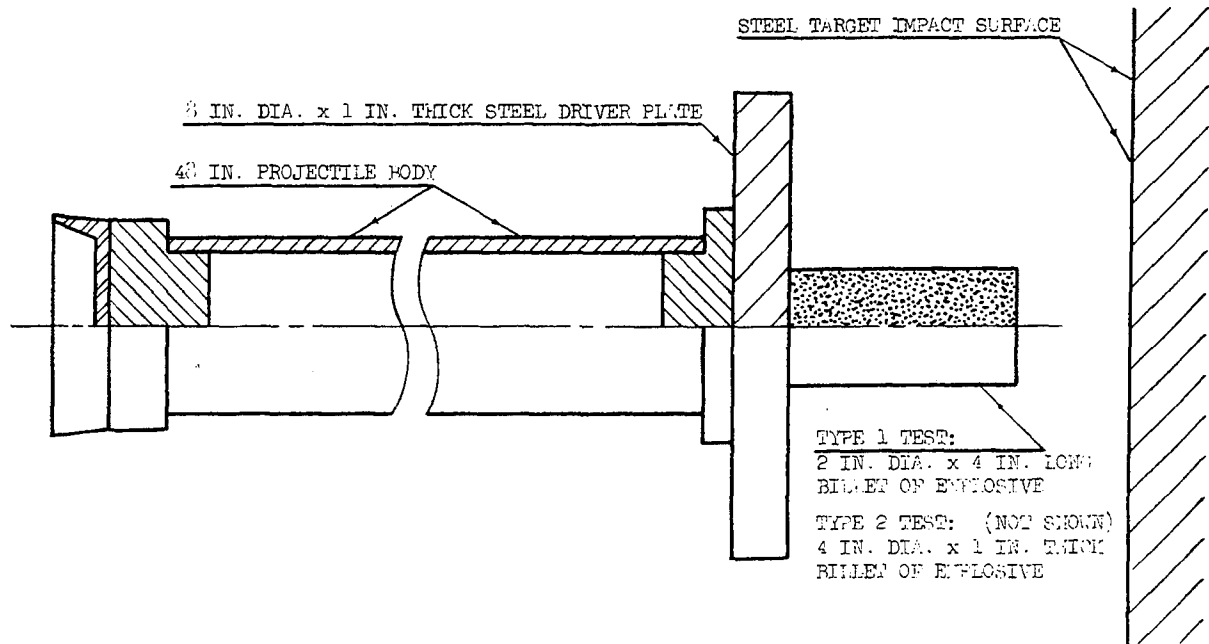


Fig. 5 - Muzzle-loaded projectile for Type 1-Type 2 tests

simple enough to be attacked in time by theoretical approaches. Unlike the Susan Test, where such things as surface finish and gluing procedures are held constant, fabrication variables are carefully changed in Type 1-Type 2 tests to note their effect, if any, on impact behavior. Briefly stated, then, the Susan Test is a quick and reliable way of obtaining a comparative assessment of an explosive's behavior under impact. The Type 1-Type 2 experiments provide a way of elaborating on that behavior, but at the cost of a considerably larger number of experiments than that required for the Susan Test.

The principal variables explored to date in Type 1-Type 2 experiments have been impact velocity and the surface finish of the metal impacting surfaces. A few other variables have also been cursorily examined.

RESULTS AND DISCUSSION

The four explosives described in Table 1 have been investigated in some detail under the three conditions of impact discussed in the preceding section. In this section we compare the behavior of the four materials.

Susan Test Results

A convenient way to display Susan Test results is to convert the overpressure transit time data for each projectile impact to an equivalent point-source detonation energy [5]. This energy, arbitrarily normalized to a scale of 0 to 100,* is then plotted against the projectile velocity. For the four explosives in question reasonably smooth curves result (see Fig. 4). These curves are reflective of the relative chemical energies liberated at the "pinch" stage of the Susan impact. Two of the explosives, PBX-9404 and LX-04-1, also show ignition at the early deformation stage, but the reactions are mild, and do not contribute measurably to the overall energy release. The mild burning in LX-04-1 usually appears to die out before pinch; PBX-9404 appears to continue burning. Both materials are reignited at the pinch stage. Neither Composition B-3 nor PBX-9011 show evidences of ignition during the early stages of deformation. The presumption is therefore made that the mechanism for doing work on the explosive during early deformation

*The procedure for doing this is described in detail in Ref. 1.

is unable to produce sufficiently high temperatures in these two materials. In the case of Composition B-3, it is believed that the frictional heating melts the TNT, thus providing both a lubricant and a heat sink to limit the temperature rise. For PBX-9011, the plastic becomes very soft with increasing temperature; the relatively low viscosity of the binder at higher temperatures thus helps limit the temperature rise. Only under the severe frictional conditions of the pinch stage, then, are these two materials ignited.

From a general safety point of view, the Susan Test results might be summarized as follows: Composition B-3 is clearly the least reactive, producing only moderate deflagrations up to 1500 ft/sec in velocity. PBX-9011 and LX-04-1 run a close second to Composition B-3 behavior at pinch, but the early ignition behavior of LX-04-1 is a warning that in other geometries trouble might develop for this material.

PBX-9404 is the poorest of the four materials, flipping from no reaction to violent deflagrations at the pinch stage over a short velocity range. This material is also easily ignited as evidenced by the early deformation ignition and the very low threshold velocity at which reactions occur.

Type 1 Test Results

The most extensive Type 1 Test results are available for LX-04-1; the data are collected in Table 2. The results indicate that there is a reasonably smooth progression of reaction intensities from dud to burning to detonation as the impact velocity is increased. The surface finishes shown in column 3 seem to play no strong role in this progression; neither does the fact the shots were conducted at three different laboratories (column 6), or that aluminum was substituted for steel in shots

TABLE 2
Type 1 Test Results on LX-04-1

Shot No.	Impact Velocity (ft/sec)	Surface Finish ^a (Target and Driver) (microinches)	Results Observed ^b	Relative Energy Release	Firing Site	Comments
125	105	16 to 32	Dud		IITRI ^c	6-in.-dia. anvil and driver
124	130	16 to 32	Burn		IITRI	6-in.-dia. anvil and driver
122	134	16 to 32	Burn		IITRI	6-in.-dia. anvil and driver
ML-45	137	125	Very mild burn	0.4	NWL ^d	
ML-43	141	16	Dud	0.0	NWL	
ML-68	153	16	Near dud	<0.1	NWL	
ML-22	173	125	Mild burn	1.7	NWL	
ML-10	176	64	Detonation	63	NWL	
K-710-28	203	64 to 125	Detonation		LRL	
ML-30	248	16	Detonation	76	NWL	
ML-29	253	125	Detonation	92	NWL	
K-710-23	255	64 to 125	Detonation		LRL	Aluminum anvil and driver
ML-34	273	16	Detonation	96	NWL	
K-710-27	283	64 to 125	Moderate burn		LRL	
ML-13	284	125	Detonation	64	NWL	
K-710-29	286	64 to 125	Moderate burn		LRL	Aluminum driver
K-710-22	291	64 to 125	Moderate burn		LRL	
ML-24	305	125	Detonation	76	NWL	
ML-31	324	16	Detonation	83	NWL	
ML-26	326	125	Detonation	78	NWL	

^aThese are measures of surface finish quality, the smaller the value, the finer the finish.

^bReactions labeled "detonation" showed extensive metal flow and fracture in the driver and target plates plus a sudden intense evolution of light in the framing camera records.

^cIllinois Institute of Technology Research Institute. (Data from Ref. 4.)

^dNaval Weapons Laboratory, Dahlgren, Virginia.

K-710-23 and K-710-29. The LRL and the NWL results on LX-04-1 do seem divergent at the higher velocities. This may be due to the much stronger projectile body used in the NWL shots.

Since solid pieces of LX-04-1 show little propensity to detonate when ignited, we interpret the detonations observed as resulting from flame propagation through the fractured and trapped explosive. There may well be a critical relation between time of ignition and the degree and state of fracture in the explosive for a detonation to occur. This conjecture is supported by the fact that LX-04-1 reverts to a burn at higher velocities in the LRL version of the test, and by the fact that PBX-9404 shows such a marked variation in response at different impact velocities (see Table 3).

As with LX-04-1, there is no strong indication that surface finish plays a significant

role in the behavior of Composition B-3, PBX-9011, or PBX-9404 (see Table 3). What is observed is a rather wide spectrum of responses between different explosives. PBX-9011 is apparently very well behaved and no detonations have been observed although more tests are needed. That PBX-9011 is quite difficult to even ignite by impact is shown by the high threshold velocity required for ignition. Composition B-3 is about as difficult to ignite as PBX-9011, but it has quite a different response. Reactions can vary from almost nothing to what seem to be detonations. These detonations with Composition B-3 always occur very late in the impact when the amount of explosive trapped between the driver plate and the target would be rather small. As a consequence, the damage to the driver plate and target is much less than when PBX-9404 detonates, which happens with a large fraction of the explosive still trapped between the driver plate and the target.

TABLE 3
Type 1 Test Results on Three Explosives Tested at NWL

Shot No.	Explosive	Impact Velocity (ft/sec)	Surface Finish ^a	Results Observed	Relative Energy Release	Comments
ML-27	Comp. B-3	227	125	Mild burn	10	
ML-19	Comp. B-3	253	16	Dud	0.0	
ML-48	Comp. B-3	253	125	Near dud	<0.1	Small puff of smoke
ML-41	Comp. B-3	255	16	Incipient detonation	34	Slight metal flow
ML-53	Comp. B-3	272	16	Moderate burn	32	
ML-54	Comp. B-3	276	125	Vigorous burn	36	
ML-51	Comp. B-3	277	16	Incipient detonation	30	Slight metal flow
ML-52	Comp. B-3	277	125	Incipient detonation	19	Slight metal flow
ML-40	Comp. B-3	277	125	Moderate burn	9	Small area of metal flow on driver plate
ML-38	Comp. B-3	278	16	Very mild burn	Low	Nearly a dud
ML-1	PBX-9011-02	188	64	Dud	0.0	
ML-3	PBX-9011-02	201	64	Dud	0.0	Possible puff of smoke
ML-4	PBX-9011-02	225	64	Near dud	<0.1	Small puff of smoke
ML-44	PBX-9011-02	235	125	Dud	0.0	Possible puff of smoke
ML-2	PBX-9011-02	264	64	Moderate burn	—	
ML-5	PBX-9011-02	310	64	Mild burn	6	
ML-17	PBX-9404-03	131	16	Dud	0.0	
ML-28	PBX-9404-03	131	125	Dud	0.0	
ML-21	PBX-9404-03	149	16	Dud	0.0	
ML-7	PBX-9404-03	156	64	Detonation	59	Extensive metal flow
ML-64	PBX-9404-03	172	125	Vigorous burn	15	
ML-63	PBX-9404-03	173	16	Mild burn	0.1	
ML-13	PBX-9404-03	250	64	Detonation	66	Extensive metal flow
ML-65	PBX-9404-03	313	16	Detonation	58	Extensive metal flow
ML-66	PBX-9404-03	315	125	Violent deflagration	73	
ML-67	PBX-9404-03	331	125	Violent deflagration	74	

^a"Surface Finish" is the specified finish of the metal target and driver plates. Random samples indicated that the actual finish was quite close to the specified finish.

TABLE 4
Type 2 Test Results on Four Explosives Tested at NWL

Shot No.	Explosive	Impact Velocity (ft/sec)	Surface Finish ^a	Results Observed	Relative Energy Release	Comments
ML-56	Comp. B-3	203	125	Moderate burn	16	Small puff of smoke Nearly a dud Extensive metal flow
ML-55	Comp. B-3	206	16	Mild burn	6	
ML-58	Comp. B-3	222	125	Near dud	<0.1	
ML-57	Comp. B-3	224	16	Moderate burn	17	
ML-39	Comp. B-3	228	16	Very mild burn	<1	
ML-46	Comp. B-3	231	125	Detonation	90	
ML-59	Comp. B-3	233	16	Mild burn	5	
ML-60	Comp. B-3	242	125	Moderate burn	9	
ML-61	Comp. B-3	281	16	Vigorous burn	41	
ML-62	Comp. B-3	283	125	Vigorous burn	30	
ML-15	Comp. B-3	292	64	Mild burn	3	Slight metal flow Small puff of smoke
ML-35	Comp. B-3	315	16	Mild burn	6	
ML-32	LX-04-1	165	16	Incipient detonation	14	
ML-36	LX-04-1	167	125	Mild burn	1	
ML-8	LX-04-1	175	64	Near dud	<0.1	
ML-11	LX-04-1	186	64	Mild burn	3	
ML-37	LX-04-1	188	125	Moderate burn	8	
K-710-31	LX-04-1	195	64 to 125	Moderate burn		
K-710-25	LX-04-1	207	64 to 125	Moderate burn		
ML-42	LX-04-1	248	125	Moderate burn	9	
ML-14	LX-04-1	252	64	Mild burn	4	Fired at LRL Fired at LRL Fired at LRL Fired at LRL
K-710-26	LX-04-1	267	64 to 125	Moderate burn		
ML-25	LX-04-1	283	16	Moderate burn	8	
K-710-24	LX-04-1	284	64 to 125	Vigorous burn		
ML-17A	PBX-9011-02	163	16	Dud	0	
ML-18	PBX-9011-02	165	125	Near dud	<0.1	
ML-9	PBX-9011-02	190	64	Mild burn	2	
ML-33	PBX-9011-02	281	16	Moderate burn	9	
ML-49	PBX-9404-03	124	125	Dud	0.0	
ML-47	PBX-9404-03	128	16	Violent deflagration	64	
ML-50	PBX-9404-03	145	16	Violent deflagration	37	Driver plate dished
ML-6	PBX-9404-03	150	64	Violent deflagration	40	Driver plate dished
ML-12	PBX-9404-03	274	64	Violent deflagration	54	Driver plate dished

^a"Surface Finish" is the specified finish of the metal target and driver plates. Random samples indicated that the actual finish was quite close to the specified finish.

Type 2 Test Results

The similarity of the mechanics of the Type 2 experiment to that of the "pinch" stage of the Susan Test would lead one to expect considerable correspondence between Type 2 data of Table 4 and the Susan Test data. This expectation is only partially fulfilled. PBX-9011 and PBX-9404 behave about as would be predicted from the Susan Test and LX-04-1 behaves almost as would be predicted from the Susan Test, but Composition B-3 behaves in a completely unexpected manner. In the Susan

Test, Composition B-3 is one of the best behaved materials ever tested. The results are very predictable and reaction levels are moderately violent (see Fig. 4) only at rather high impact velocities. The Type 2 test results on Composition B-3 bear no resemblance whatsoever to the Susan test results. Here, the Composition B-3 behaves in a capricious and unpredictable manner and has the distinction of having given the most violent reaction (a detonation) yet observed in a Type 2 test. The results are not inconsistent with the Type 1 test results. In the Type 1 test the reactions with

Composition B-3 occurred so late in the impact as to be a fair approximation of a Type 2 test.

Supplemental Investigations

Two supplemental investigations now in progress should also contribute to our understanding of these phenomena. We hope to report on them in more detail in October. One investigation [6] concerns a theoretical mechanochemical investigation of the Type 2 geometry. The theoretical model assumes a constant-volume flow of explosive with flow characteristics consistent with granular flow. Decomposition kinetics of the explosive and heat transport parameters for both explosive and metal are also included in the model. With an assumed constant coefficient of friction of 0.1 between metal and explosive, the model deposits very little energy into friction at the interface. However, because of the poor heat conductivity of the explosive, this small amount of energy leads to temperatures at the outermost radius of the explosive-metal interface which are easily high enough to ignite the explosive. Although the predicted results are of interest, the model needs considerable refinement, particularly with respect to the assumed constant coefficient of friction and with respect to the flow characteristics of the crushed explosive, before it can be said to represent the real behavior of an explosive in a Type 2 experiment.

The second investigation [7] is an experimental evaluation of the coefficients of friction of the four explosives discussed in this paper. The values are being determined as a function of surface finish, material, and temperature. First results for LX-04-1 vs steel indicate a room temperature dynamic value of the coefficient of friction of 0.6. The value is essentially invariant over a load range of 250-750 psi, sliding velocities of 0.2 to 20 in./min and surface finishes of 16 μ and 32 μ . The coefficient rises to a value of 0.8 under the same conditions for a 125 μ surface finish.

CONCLUSIONS

Some progress has been achieved in unraveling the complex phenomena which have been termed "impact sensitivity." The process by which chemical reaction is started in the explosive (ignition by friction) has been better characterized by this study. Some of the parameters external to the explosive which influence the threshold of ignition and the ultimate fate of the ignited explosive have been explored.

Among these parameters are impact configuration, velocity of impact, and surface finish of impact hardware. Parameters internal to the explosive, also of obvious importance, have received some attention.

Much remains to be learned about the behavior of explosives under impact. Our goal of the immediate future is to thoroughly explore, both theoretically and experimentally, a relatively simple impact geometry (e.g., such as that of the Type 2 test). The calculation and prediction of experimentally observed results on the basis of a theoretically sound model, if such can be achieved, would materially advance our understanding of the ignition of explosives by impact and the chemical events which follow such ignition.

ACKNOWLEDGMENTS

We acknowledge with appreciation the many helpful discussions with our colleagues, Edward James, Jr. and Richard Wasley.

The Naval Weapons Laboratory of Dahlgren, Virginia, with funds provided by the Defense Atomic Support Agency, conducted the firing of many of the tests reported herein. Douglas Gray and his group at NWL, in particular, have contributed much to the investigation.

REFERENCES

1. G. D. Dorough, L. G. Green, E. James, Jr., and D. T. Gray, "Ignition of Explosives by Low Velocity Impact," Proceedings of the International Conference on Sensitivity and Hazards of Explosives, London, October 1963.
2. G. D. Dorough, L. G. Green, and D. T. Gray, "The Susan Test for Evaluating the Impact Safety of Explosive Materials," Lawrence Radiation Laboratory Report UCRL 7394, Aug. 1965.
3. H. S. Napadensky, R. H. Stressan, and J. Savitt, "The Behavior of Explosives at Impulsively Induced High Rates of Strain," Third Symposium on Detonation, Office of Naval Research Report ACR-52, Vol. 2, pp. 420-435, 1960.
4. H. S. Napadensky, "Experimental Studies of the Effects of Impact Loading on Plastic Bonded Explosive Materials," ARF Project No. K6011, Defense Atomic Support Agency

- Report No. 1391 published by Illinois Institute of Technology Research Institute, April 1963.
5. H. L. Brode, "Point Source Explosion in Air," Rand Corporation Research Memorandum 1824, AEC, Dec. 1956 (DDC Document No. AD 133030).
 6. A. Weston, "Analytical Program on Impact Ignition of Explosives," report in preparation, Wm. Brobeck and Associates, Berkeley, California.
 7. K. Hoge, "Friction Measurements on Explosive Materials," report in preparation, Lawrence Radiation Laboratory, Livermore, California.

THE INITIATION OF BURNING IN HIGH EXPLOSIVES BY SHOCK WAVES

T. P. Liddiard, Jr.

*U.S. Naval Ordnance Laboratory, White Oak
Silver Spring, Maryland*

ABSTRACT

High-explosive samples (acceptors 50.8 mm diam \times 12.7 mm thick) submerged in water are subjected to spherical shocks. The distances between a one-pound spherical donor charge and the acceptors are adjusted to give various peak entering shock pressures in the acceptors, typically in the range of 5-25 kbar. Burning is detected by the expansion of the acceptor after being struck by the shock. Observations are made with a high-speed framing camera using diffuse reflected back-lighting. The threshold for burning in this geometry is deduced from plots of expansion velocity vs entering pressure. The reciprocal of the time for expansion to start vs pressure also is used. The results on five solid high explosives show that the threshold for burning obtained in the underwater test is roughly one-third of that obtained in the modified gap test configuration. The lower thresholds in the underwater system are attributed to the longer pulse duration, less curvature of the wave front, and the confinement offered by the water.

INTRODUCTION

This paper is concerned with an experimental study of the initiation of chemical reaction by mechanical shocks of low amplitude. A great deal is known about initiation and growth to detonation in high explosives at high shock amplitudes [1]. An interesting and equally important area for research is in the low pressure region of 1-10 kbar. Relatively less research has been done in this pressure domain. Pressures (or more exactly, stresses) that cause burning are important numbers for assessing the sensitivity of an explosive. The length of time that the stress is applied also is important in assessing the effect of stress on initiation of reaction.

Certain sensitivity tests have shown that burning can be produced in some high explosives with stresses as low as 1-5 kbar. The mechanisms causing initiation and burning are complicated by the presence of more than one externally applied stimulus. The skid test [2], for example, involves a substantial amount of rubbing over a rough slanted surface coupled with mild compression as a consequence of a low drop velocity. The Susan test [3] makes use of a blunt-nose projectile to carry the explosive sample at a measured velocity, the explosive

being subjected to crushing impact against an armor plate target. Napadensky et al [4] have carried out photographic studies in the weak-shock range in which the acceptor was crushed between a shock-driven steel plate and a steel platform. In spite of the complexities involved in these tests, they have yielded much valuable and practical information on explosive sensitivity.

In our low-pressure initiation studies we have tried to limit ourselves to experimental conditions in which such things as crushing of the explosive between metal components and rubbing over a rough surface are avoided. We wanted to see if relatively simple systems, having more easily defined parameters, could be made to yield threshold-for-burning data which could be correlated with results obtained in the tests mentioned above. The relative importance of compression, rubbing, shear and secondary impact might then be established more clearly.

One such test configuration, the modified gap test, Fig. 1, uses the same donor-gap system employed in the NOL standardized gap test [5]. In the latter test the acceptor is 36.5 mm diam, 139.7 mm long, and confined in a steel tube with a 5.6-mm wall thickness. The

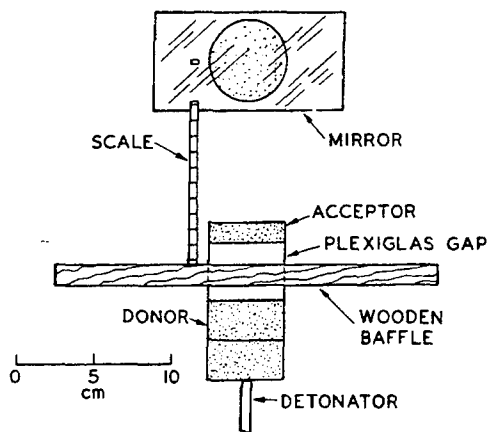


Fig. 1 - The modified gap test

acceptor in the modified gap test has been shortened to 12.7 mm, the diameter increased to 50.8 mm, and it is left unconfined. The results of the modified gap test, reported in detail in Ref. 6, show that for solid high explosives burning typically is just detected at stresses of 10-25 kbar, about one-half the stress needed to build-up to detonation. These thresholds of burning are high compared to those estimated for the skid and Susan tests. From these results, the question arises: can these thresholds be lowered significantly by applying shocks that are of longer duration and more nearly plane? In the modified gap test the pressure falls rapidly because of the action of strong rarefaction waves. In addition, the shock front entering the explosive is quite curved.

An experimental arrangement which gives a much better (more nearly 1-D) shock front and a longer, more predictable duration is one which can be carried out in a large tank of water using a spherical donor. Such configuration was first exploited by Eyster, Smith and Walton [7] to determine a few 50%-point pressures for transition to detonation. Winning [8] employed

this system with a 73-g spherical donor for photographic observations. The superiority of the underwater experiment over the usual gap-test configuration is due in part to the confinement of water which greatly reduces rarefaction effects. The underwater test is described in detail in this paper and a comparison is made between the results of this test and those obtained in the modified gap test. The latter test is reviewed briefly below.

EXPERIMENTS

The Modified Gap Test

In the modified gap test the effect of chemical reaction is detected by end-on and side-view surveillance of the acceptor, Fig. 1. Burning is directly evidenced by the break-out of gaseous products. The time for the break-out to occur is measured as a function of entering shock pressure. A plot of the data can be extrapolated to give the threshold pressure required to initiate burning. It is possible to have internal burning such that gaseous products are not visible. However, internal burning increases the surface velocity above that observed for a comparably shocked inert material. Consequently the free-surface velocity was also measured as a function of the entering shock pressure. Typically, the surface velocity-pressure curve shows an abrupt change in slope at the critical pressure for burning.

The Underwater Test

The underwater explosive system, shown in Fig. 2, is similar to the experimental arrangement used by Winning [8]. The donor charge is a 82-mm diam cast pentolite sphere weighing 475-480 g (nominally one pound). The acceptors are the same size as those used in the modified gap test. Pairs of thin, 6-mm wide polyester tapes hold the acceptors securely at their cylindrical surfaces. The tapes prevent

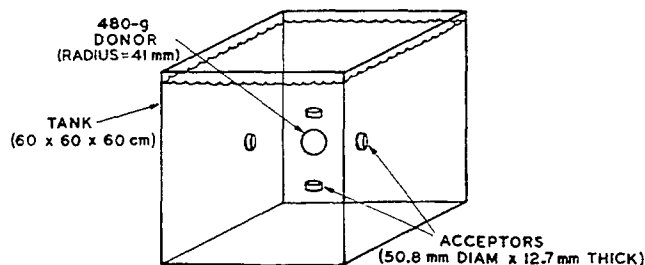


Fig. 2 - The underwater system

twisting and do not cause interference in the regions of interest. The donor charge is held in a harness of nylon thread. The axis of the detonator is located in a position normal to the plane of the acceptors. This reduces irregularities in the shock front, since the initiation of the donor is more symmetrical around the axis of the detonator. The detonator is positioned in the donor to produce very nearly simultaneous break-out of detonation from the donor. Parallel pairs of fiducial strings are stretched both horizontally and vertically across the field of view in the plane of the acceptors. The completed charge assembly, pre-mounted in a frame, is submerged in a $60 \times 60 \times 60$ -cm tank of water.

Observations are made with the Jacobs focal plane shutter framing camera [9]. Diffuse reflected backlighting is obtained by an argon flashlamp which illuminates a white cardboard in back of the tank. A photographic sequence taken from a typical record is shown in Fig. 3. The interframe time shown is $10.9 \mu\text{sec}$. (Six frames actually were obtained on the original record for very frame shown here.) To form each frame the focal plane shutter (slit) sweeps the field of view from top to bottom in $10.9 \mu\text{sec}$.

The exposure during the passage of a 0.5-mm slit is about $0.1 \mu\text{sec}$, giving, therefore, a sharp outline of the shock front. The slit motion causes time distortion. In making measurements of relatively slow-moving subjects, such as an expanding acceptor, the scanning shutter distortion can be neglected. However, necessary corrections are made for shutter displacement on measurements of fast-moving subjects, such as shock fronts, moving in the same (or opposite) direction to that of the scanning slit.

Acceptor Explosives

Five pressed explosive compositions were used in the underwater tests: TNT, 50/50 pentolite, 60/40 cyclotol, PBX 9404-03, and LX-04-1. PBX 9404-03 is a mixture of HMX, tris (β -chloroethyl) phosphate, and nitrocellulose; 94/3/3 percentages by weight. The "-03" denotes a bimodal particle distribution of HMX. LX-04-1 is a mixture of HMX and Viton A (85/15). The "-1" denotes a fine HMX particle size. The samples were prepared from the same bulk explosive batches that were used in the modified gap tests. In both tests the explosive was isostatically pressed and then machined

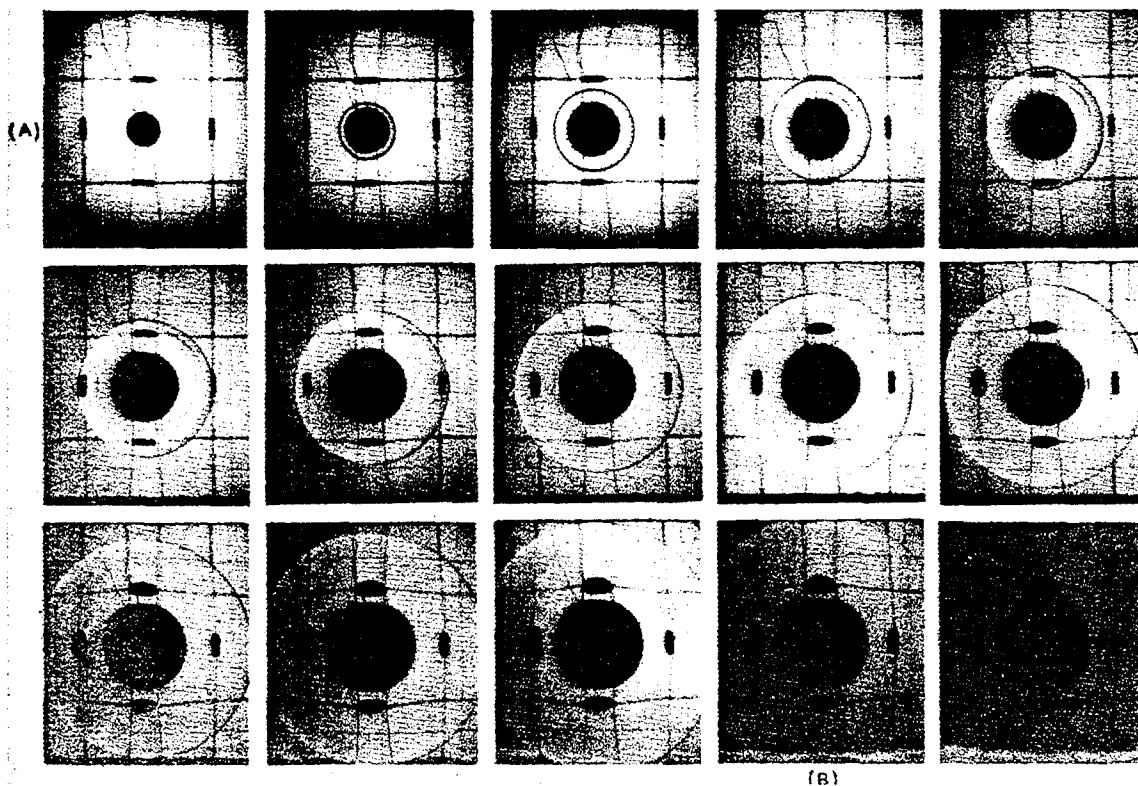


Fig. 3 - Typical record of an underwater experiment. The interframe time is $10.9 \mu\text{sec}$. The donor diameter is 82 mm. See Fig. 4 for explanatory sketches.

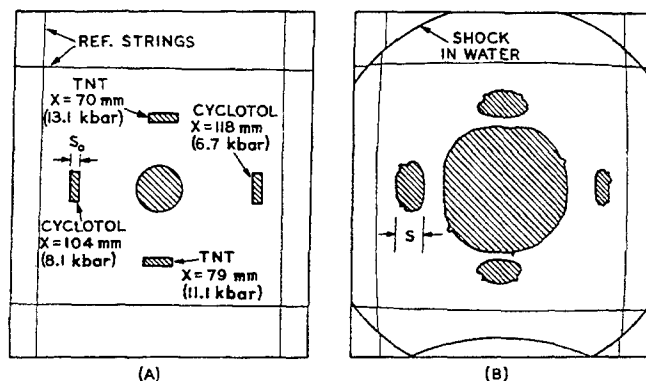


Fig. 4 - Sketches of two frames from the sequence in Fig. 3. (A) The initial arrangement of charges; (B) The frame labeled (B) in Fig. 3.

to form a disk 12.7 mm thick by 50.8 mm diam. The particle size range of the TNT, pentolite, and cyclitol was 149 to 210 μ (70-100 mesh). The PBX 9404 and LX-04-1 bulk explosives were in the form of large particles made up of aggregates of explosive and binder.

Detection of Reaction

Chemical reaction is detected by observing the expansion of the acceptor after being struck by the shock. Note the shapes of the shocked acceptors in Fig. 3. The most vigorous burning is at the surface facing the donor. Apparently no reaction is occurring around the perimeter of the opposite (initially) flat surface. The initial charge conditions for obtaining the sequence in Fig. 3 are shown in the sketch, for the frame labeled (A), in Fig. 4A. In Fig. 4B is a sketch of Frame (B) of Fig. 3. The "thickness" (axial length, S) is measured, as indicated, for each frame. Zero time is chosen as the instant the shock strikes the acceptor. Typically, at pressures near the threshold the acceptor will show no gross expansion for a relatively long time, then expansion will start suddenly. This induction time, i.e., the period for reaction to become apparent, can be as much as 35 μ sec or even more.

TREATMENT OF DATA

Thickness of Acceptor vs Time

If the thickness (S) of the shocked acceptor is plotted as a function of time (t), after being struck by the shock, such curves as shown in Fig. 5 for pressed TNT are obtained. At 7.8 kbar no gross expansion of the cylinder occurs,

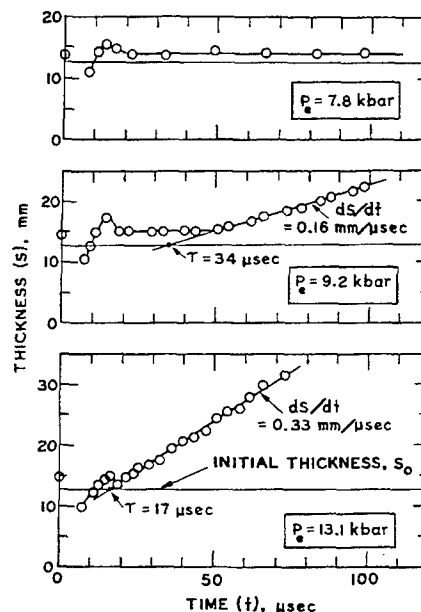


Fig. 5 - Three examples of acceptor expansion (S vs t): TNT at $P_c = 7.8, 9.2$, and 13.1 kbar. Expansion is measured as shown in Fig. 4B.

although tiny jets of material may be seen leaving the surfaces. The inflection at the start of the curve is caused by refraction of light through the shock envelope. No attempt was made to correct for this since the apparent distortion of the acceptor becomes small at about 20 μ sec after the passage of the shock. At 9.2 kbar, expansion appears to start at about 50 μ sec. Actually, the acceptor is slightly tilted so that the true start is unobserved. To obtain the actual

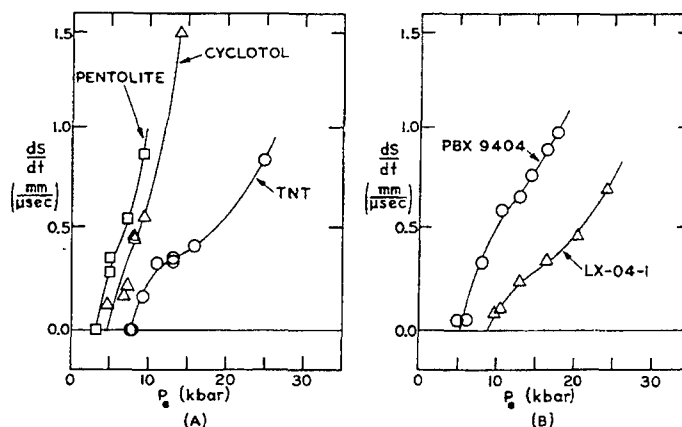


Fig. 6 - Rate of expansion (dS/dt) as a function of the entering pressure (P_e) for: (A) pentolite, 60/40 cyclotol, and TNT; (B) PBX 9404 and LX-04-1.

start time (τ) the slope (dS/dt) of 0.16 mm/μsec is extrapolated back to the line which indicates the actual thickness of the undisturbed acceptor; this occurs at 34 μsec. At 13.1 kbar the slope becomes steeper, 0.33 mm/μsec, and τ becomes shorter, 17 μsec. These results suggest that either the slope or τ might be plotted as functions of the entering pressure (P_e) to determine the threshold for burning.

Slope vs Entering Pressure

The slope (dS/dt) vs the entering pressure (P_e) data for the five high explosives are given in Table 1 along with the distance (X) from the donor surface. The data are plotted in Figs. 6A and 6B. The pentolite and TNT data include points at $dS/dt = 0$, i.e., no gross expansion was observed for 100 μsec or more. The 3.2-kbar datum point for pentolite is especially interesting since, in this case, the shock did not initiate any appreciable burning over an indefinitely long time. Proof of this was provided by the recovery of the acceptor which was relatively undamaged. No recovery was made of the TNT acceptors at 4.9, 7.8, and 7.9 kbar.

Time Taken for Reaction to Begin

Curves similar to those shown for the slopes are obtained by plotting $1/\tau$ as a function of P_e , Figs. 7A, 7B, and 7C. Although nearly the same thresholds are obtained by the latter means, there is more uncertainty in the extrapolation to the P_e -intercept. The extrapolations are indicated by the dashed lines. Although curved lines are drawn through the data points, in some cases a straight line undoubtedly fits

the data as well. However, since the S-shaped curve is apparent in the plots of PBX 9404, and LX-04-1, it is probable that there is some curvature in all the curves.

If the time for jetting to start (τ_j) is measured, the results are the same within experimental error as obtained by measuring the time for expansion to start. An exception is TNT, where jetting starts at a much lower pressure, 3 kbar for jetting and 8 kbar for expansion. The data are given in Table 1 and plotted as the shaded points in Figs. 7A, 7B, and 7C. It is not certain what role the tiny jets play in the interpretation of the results. They may indicate sites of burning at or near the surface of the acceptor facing away from the donor. On the other hand, they may be entirely mechanical in nature being caused by tiny surface imperfections or air bubbles adhering to the surface. Most likely, though, they are a combination of both.

Pressure and Stress Determinations

The peak stress (P_e) entering an acceptor is changed by altering its distance (X) from the spherical donor, where X is the distance from the surface of the donor to the donor-facing surface of the acceptor. Since the peak pressure-distance relation scales with charge radius, the distance from a spherical charge is commonly expressed in terms of charge radii, R/r_o , where R is the radial distance from the center of the charge and r_o is the charge radius. The peak pressure in water (P_w), at a given value of X (or R/r_o) is obtained from the corresponding instantaneous shock velocity (U_w). The latter is determined by differentiating along

TABLE 1

Rate of Expansion (dS/dt), Time for Expansion to Start (τ), and Time for Jetting to Start (τ_j) for Various Peak Stresses (P_e) Entering the Acceptor. P_w is the Corresponding Pressure in the Water. X is the Distance Between Donor and Acceptor Surfaces. R/r_o is the Radial Distance from the Center of the Donor to the Surface of the Acceptor.

Explosive (Pressed)	X (mm)	R/r_o *	P_w (kbar)	P_e (kbar)	dS/dt (mm/ μ sec)	τ (μ sec)	τ_j (μ sec)
A. Pentolite ($\rho_o = 1.66$ g/cm ³)	170	5.15	2.2	3.2	0.00	∞	-
	140	4.42	3.3	5.0	0.35	24	16
	140	4.42	3.3	5.0	0.28	22	18
	113	3.74	4.6	7.2	0.54	10	-
	94	3.29	6.0	9.2	0.86	6	-
B. 60/40 Cyclotol ($\rho_o = 1.695$ g/cm ³)	144	4.51	3.1	4.8	0.13	35	30
	118	3.88	4.3	6.7	0.17	21	18
	113	3.74	4.6	7.2	0.22	20	17
	104	3.54	5.2	8.1	0.46	14	14
	104	3.54	5.2	8.1	0.45	15	18
	94	3.29	6.0	9.3	0.55	10	-
	70	2.71	9.1	13.9	~1.5	-	-
C. TNT ($\rho_o = 1.61$ g/cm ³)	139	4.39	3.3	4.9	-	>100	33
	102	3.49	5.3	7.8	-	>100	18
	101	3.46	5.4	7.9	-	>100	16
	91	3.22	6.3	9.2	0.16	34	15
	79	2.93	7.7	11.1	0.32	21	13
	70	2.71	9.1	13.1	0.35	16	13
	70	2.71	9.1	13.1	0.33	17	-
	61	2.49	11.1	15.9	0.41	12	10
	44	2.08	17.3	24.7	0.83	-	-
D. PBX 9404-03 ($\rho_o = 1.84$ g/cm ³)	146	4.56	3.0	4.8	0.05	22	23
	128	4.12	3.8	6.0	0.05	-	33
	107	3.61	5.0	8.0	0.33	17	16
	97	3.37	5.7	9.0	-	21	-
	88	3.15	6.6	10.5	0.59	14	-
	76	2.86	8.2	12.8	0.65	8	-
	70	2.71	9.1	14.2	0.76	8	-
	64	2.56	10.4	16.2	0.89	6	-
	60	2.46	11.4	17.6	0.97	6	-
E. LX-04-1 ($\rho_o = 1.86$ g/cm ³)	94	3.30	6.0	9.6	-	-	26
	94	3.30	6.0	9.6	0.08	-	30
	88	3.15	6.6	10.5	0.10	20	27
	76	2.86	8.1	12.7	0.24	17	14
	64	2.56	10.4	16.2	0.34	15	-
	54	2.32	13.2	20.2	0.46	8	-
	48	2.17	15.5	24.1	0.69	7	-

*The radial distance, R , to the acceptor is obtained by adding the donor radius, $r_o = 41$ mm, to X .

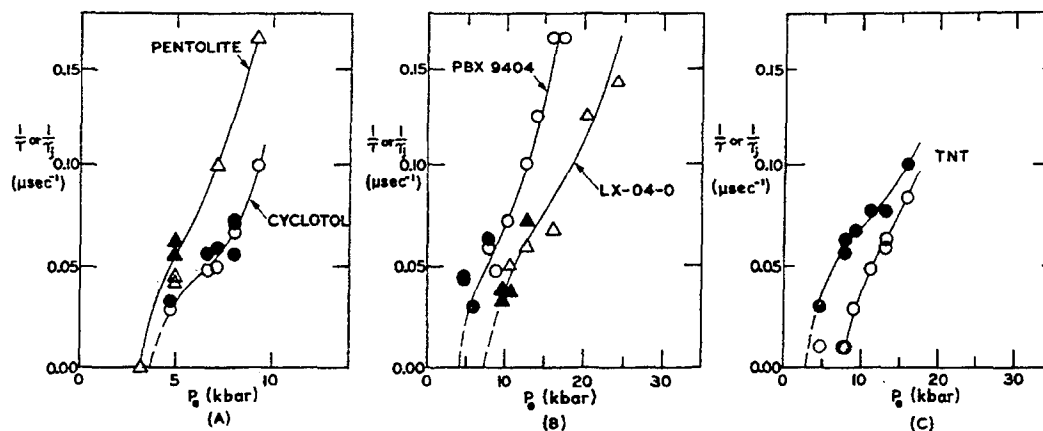


Fig. 7 - Reciprocals of times for expansion (τ) and jetting (τ_j) to start as functions of entering pressure (P_e): (A) pentolite and cyclotol, (B) PBX 9404 and LX-04-1, and (C) TNT. Clear circles and triangles are for τ ; shaded ones are for τ_j .

an X-time curve drawn from data obtained from framing camera sequences, such as the one in Fig. 3. The shock pressure in the water (P_w) for various experimental values of X (or R/r_o) are given in Table 1. The calibration will be refined as more data are available on the 480-g pentolite system. Experimental P_w vs R/r_o data also are available for 1.8-kg pentolite charges [10], these being derived from smear-camera traces. At the time of this writing, the results of recent hydrodynamic calculations on spherical shocks in water, based on the experimental data of Ref. 10, became available [11]. However, the calibration given here is adequate (within 5%) for the purpose of determining the threshold of burning down to $P_w = 5$ kbar. Under 5 kbar the experimental curve for the 480-g donors falls below the experimental and calculated 1.8-kg curves. For example, using either one of the latter curves, the threshold of burning for pentolite would be about 4 kbar, instead of the 3.2-kbar value given here.

The conversion from the pressure in water to the transmitted stress in the acceptor is depicted by the P vs u curves in Fig. 8. The method of conversion is described in Ref. 12. In making the pressure calculation the relation, $P = \rho_o u U$, is used (ρ_o = initial density). The corresponding value for the particle velocity (u) is obtained from published Rankine-Hugoniot (P -volume) data for water [13-15], which had been fitted to a seventh power polynomial [16]. The derived values of P_e are included in Table 1.

The P - u (unreactive) curves shown for two explosives were derived from U - u linear relations experimentally obtained for TNT ($U = 2.39$

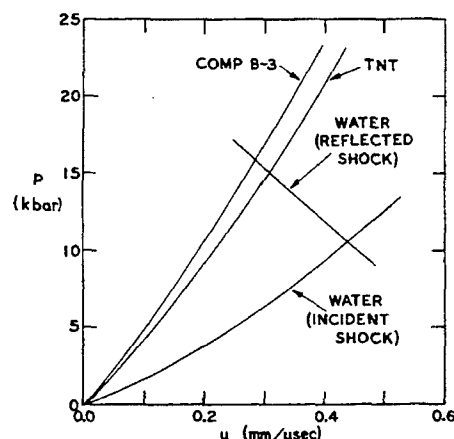


Fig. 8 - Pressure-particle velocity curves for water and unreactive composition B-3 and TNT

+ 2.05 u , mm/ μ sec) and Composition B-3 ($U = 2.71 + 1.86u$) [17,18]. In making calculations of P_e , Comp. B-3 and 60/40 cyclotol are considered to be equivalent. In addition, pentolite, PBX-9404, and LX-04-1 are considered to have the same U - u relation as Comp. B-3, but their individual densities are used in calculating the stresses.

RESULTS AND DISCUSSION

Threshold of Burning

The thresholds for burning (P_b) in Table 2 are taken from the slope vs P_e curves of Figs.

TABLE 2
Comparison of Pressure, P_b , at Which Burning is Just Detectable
in the Underwater and Modified Gap Tests

Explosive	Loading Density (g/cm ³)	P_b Underwater (kbar)	P_b Mod. Gap (kbar)
Pentolite	1.67	3	10
60/40 Cyclotol	1.70	4	13
PBX 9404-03	1.83	5	16
TNT	1.62	8	23
LX-04-1	1.86	9	23

6A and 6B for the five explosives. The results from the $1/\tau$ (and $1/\tau_j$) vs P_e curves lend support to the slope- P_e results, but the threshold values are not as firmly established from the delay in times. Also in Table 2 a comparison is made with values of P_b obtained by the modified gap test. This comparison shows that in the underwater experiments P_b is about one-third of that obtained in the modified gap test.

The Threshold for Detonation

Winning [8] reports that detonation occurs in cast pentolite at 3.5 charge radii from a 73-g donor; $P_e = 8.0$ kbar by our calibration. His acceptors (roughly 17-mm diam \times 80-mm long) were much longer than those used in the experiments reported here. Detonation, then, should certainly occur at the same scaled distance, R/r_o , in our experiments, if the charges were made comparably longer. In addition, one would expect pressed pentolite to detonate at a somewhat lower stress than cast pentolite. As yet we have not attempted to pinpoint any thresholds for detonation in the underwater experiments. This, though, has been done for 12.7-mm thick acceptors in the modified gap experiments. We are extending our studies to include the determination of the threshold for detonation using considerably longer acceptors. Some data on longer TNT acceptors has been obtained with the modified gap test, but none so far have been gotten using the underwater system.

Effect of Pressure Pulse Shape

The results of the underwater experiments show that the peak pressure at which detectable burning starts is greatly affected by the shape of the pressure pulse, i.e., the rate of pressure decay after shock impact. The time for the

shock pressure to decay to 50% of its peak value is estimated to be about one microsecond in the modified gap test [19]. For the underwater system, hydrodynamic calculations have shown that the decay time to 50% of peak is an order of magnitude longer [11]. The confinement offered by the water drastically reduces the rarefaction rate relative to that encountered when air is the surrounding medium. In addition, the spherical shock wave in water more closely approaches a 1-D situation that does the shock wave in the polymethyl methacrylate (Plexiglas or lucite) cylinder used in the modified gap test.

SUMMARY

Photographic studies were made of high explosives subjected to low amplitude shock. Two types of experiments are discussed, the modified gap and underwater systems.

Methods of analysis are presented whereby the threshold stresses for burning of solid high explosives are deduced. The thresholds are greatly dependent on the system geometry.

A comparison is made of the results obtained with the two shock-producing systems on five pressed explosives. The underwater threshold values are roughly one-third of those obtained in the modified gap experiments.

The underwater experiments show thresholds for burning which are comparable in magnitude to those obtained in the Susan and similar tests. Thus, it appears that compression by a 3 or 4 kbar shock is, of itself, a sufficient external stimulus to start chemical reaction in an inhomogeneous solid explosive such as pentolite. Burning probably can be produced at even lower shock levels if the pressure were held longer and the wave front made flatter.

ACKNOWLEDGMENT

The author is indebted to Dr. S. J. Jacobs for the many helpful suggestions he has made during the investigation and for his constructive criticism during the writing of this paper. The painstaking way in which James Schneider carried out the experiments is greatly appreciated. The plastic bonded explosives, PBX 9404-03 and LX-04-1, were acquired through the courtesy of G. Dorough, UCLRL, Livermore, Calif. The excellent job of preparing the charges by members of the Chemical Engineering Division of NOL is acknowledged.

REFERENCES

1. S. J. Jacobs, T. P. Liddiard, Jr., and B. E. Drimmer, "The Shock-to-Detonation Transition in Solid Explosives," 9th Symposium on Combustion, Academic Press, N.Y. (1963) p. 517-526. (A fairly complete bibliography of earlier work is given on p. 526.)
2. A. Popolato, "Experimental Techniques Used at LASL to Evaluate Sensitivity of High Explosives," Int'l Conf. on Sensitivity and Hazards of Explosives, London, 1-3 Oct 1963. Explosives Research and Development Laboratory, Waltham Abbey, Essex, England. (Reference mentions that the test was suggested by G. P. Cachia and first performed at AWRE.)
3. G. D. Dorough, L. G. Green, E. James, Jr., and D. T. Gray, "Ignition of Explosives by Low Velocity Impact" *ibid.*
4. H. S. Napadensky, R. H. Stresau, and J. Savitt, "The Behavior of Explosives at Impulsively Induced High Rates of Strain," 3rd Symp. on Detonation, Princeton Univ., 26-28 Sep 1960. ONR Symp. Rpt. ACR-52, Vol. 2, p. 420-435.
5. I. Jaffe, R. Beauregard, and A. Amster, "Determination of Shock Pressure Required to Initiate Detonation of an Acceptor in the Shock Sensitivity Test," *ARS Jour.* 32, 22-25 (1962).
6. T. P. Liddiard, Jr. and S. J. Jacobs, "Initiation of Reaction in Explosives by Shocks," *NOLTR* 64-53 (1965).
7. E. H. Eyster, L. C. Smith, and S. R. Walton, "The Sensitivity of High Explosives to Pure Shocks," *NOLM* 10336 (1949).
8. C. H. Winning, "The Underwater Shock-Wave Initiation of Cast Pentolite," *Proc. Roy. Soc.* 246, 288-296 (1958).
9. S. J. Jacobs, J. D. McLanahan, E. C. Whitman, "A High-Speed Focal Plane Shutter Framing Camera," *J. SMPTE* 72, No. 12, 923 (1963).
10. N. L. Coleburn and B. E. Drimmer, "Spherical Shock Waves in Water," *APS Bull., Ser. II. Vol. 7*, p. 20 (Jan 24, 1962) and private communication.
11. W. A. Walker and H. M. Sternberg, "Underwater Detonation of a Spherical Pentolite Charge," this Symposium.
12. J. M. Walsh, M. H. Rice, R. G. McQueen, and F. L. Yarger, "Shock-Wave Compressions of Twenty-Seven Metals. Equations of State of Metals," *Phys. Rev.* 108, 196 (1957).
13. M. H. Rice and J. M. Walsh, *J. Chem. Phys.* 26, 824 (1957).
14. P. W. Bridgman, *J. Chem. Phys.* 3, 597 (1935).
15. W. T. Holser and G. C. Kennedy, *Am. J. Science* 256, 744 (1958).
16. N. L. Coleburn, "Chapman-Jouguet Pressures of Several Pure and Mixed Explosives," *NOLTR* 64-58 (1964).
17. T. P. Liddiard, Jr., "The Unreacted Shock Hugoniot for TNT and Composition B-3," Int'l Conf. on Sens. and Hazards of Explosives; see Ref. 2.
18. N. L. Coleburn, T. P. Liddiard, Jr., "Hugoniot Equations of State of Several Unreacted Explosives" *J. Chem. Phys.* 44, 1929 (1966).
19. I. Jaffe, J. Toscano, D. Price, "Behavior of Plexiglas under Shock Loading by a Tetryl Donor," *NOLTR* 64-66 (1964).

MECHANICAL AND DETONATION PROPERTIES OF RUBBER BONDED SHEET EXPLOSIVES

Werner Kegler and Rudi Schall
*Deutsch-Französisches Forschungsinstitut
St. Louis, France*

ABSTRACT

Different methods for the manufacture of flexible sheet explosives containing PETN as the explosive component bonded with 10-20% rubber are described. The mechanical characteristics of these compositions (tensile strength, elongation at break, flexibility) are also given. At a density of 1.4 g/cm^3 , the detonation rate is 7000 m/s which is almost independent of the sheet thickness and decreases only slightly near the critical thickness which may be as low as 1 mm, where the detonation fails. By introducing porosities, much lower detonation velocities can be obtained. The detonation velocity decreases drastically when the sheet explosive is stretched. This reduction in velocity is induced by a decrease in density which is typical for rubbers containing fillers. This effect may be used for continuous control of the detonation rate.

Kerr-cell photographs taken of detonating sheets with one-dimensional elongation (up to 130%) show anisotropy in the detonation rate which increases with the applied tension. The detonation rate along the axis under tension becomes appreciably higher than in the normal direction. This anisotropy effect is independent of the direction in which the sheet was rolled.

INTRODUCTION

Flexible sheet explosives have been used extensively in the last decade, especially for explosive forming, welding and cladding. Most of the commercially available sheet explosives are plastic bonded. This paper describes efforts made to obtain natural rubber-bonded sheet explosives with special qualities for numerous applications. The use of rubber as a binder for explosives has been proposed earlier [1,2] but details about the properties of these explosives are lacking.

Vulcanized India rubber was the binder for all the compositions of the present investigation. PETN was used as the explosive component since it was most easily incorporated into the rubber network, but RDX and HMX were also tried because of their ability to withstand higher temperatures.

MANUFACTURE AND MECHANICAL PROPERTIES

Three methods of manufacture have been detailed; each differing by the original form in which the rubber was applied.

The first method is a casting procedure which uses a 60% rubber in water latex emulsion. Latex, explosive, vulcanizer (like sulfur and zinc oxide), and anti-aging additives are mixed to a homogeneous composition in a planetary mixer. This mixture is then poured on a plate of plaster of Paris which absorbs most of the water content within one or two days and aids in drying and shaping the composition. Final drying and vulcanization at 60°C combined with pressurizing under a calender terminates the procedure. Rubber contents between 15% and 20% are typical by this method which allows hollow explosive bodies to be made from plaster matrices by procedures well known in the rubber industry. In this case, the rubber content should be increased to about 25%.

A second method starts with natural, raw rubber. It is then necessary to use a convenient solvent (like benzene or heptane) in order to obtain a free flowing composition. The water wet explosive and the vulcanizer are incorporated in this solution, which is kneaded until a homogeneous plastic product is obtained. This is formed into sheets in a calender and dried to a water content of about 7% at a temperature of

40°C. The sheets are then compressed on a calender by a standard procedure and completely dried. Using this procedure a flexible product is obtained. Explosive contents of 85% to 90% are obtained by this method.

The final method studied uses a depolymerized rubber, which is a crude India rubber which has been made into a highly viscous form by chemical and physical treatment. This viscous rubber allows solvent-free processing in the same manner as the manufacture of double base powders. Here, too, the binder is mixed with wet explosive in a masticator. During mixing most of the water is separated from the explosive. Most of the remaining water is squeezed out by passing the explosive through rollers heated to 40°C. With a water content of 1% the final product can be shaped into plates or ribbons by means of a calender. Vulcanization at 80°C and a final pressing on a calender gives the product rubber-like mechanical properties.

Table 1 compares the advantages and disadvantages of sheet explosives made by the above procedures.

Mechanical properties of these sheet explosives are listed in Table 2, where the tensile strength, elongation at break and the number of flexures at 90° or 180° which the sheet can withstand before tearing, are listed. Values depend to some extent on the rubber content.

DETONATION PROPERTIES

Sensitivity

Sheets can be initiated by a No. 8 detonator placed either normal or parallel to the sheet surface. The drop weight impact machine indicates that these rubber-bonded explosives are considerably less sensitive to weak shocks than the pure explosive. Sheets can be cut with scissors or torn without any risk of explosion. Bullet tests run with 7.9 mm military bullets fired into sheets at a 10 m distance always gave negative results when the explosive was fixed to a wooden board; when fixed on a steel plate, no detonations or explosions were obtained, although in some cases the explosive slowly burned because of ignition at heated locii. Where burning occurred, there was a delay in the onset of burning after the bullet hit the explosive. This burning phenomenon depended only slightly on the rubber content and did not vary too much when RDX or HMX was substituted for the PETN. The impact hammer sensitivity diminished as the rubber content increased and HMX and RDX containing explosives were less sensitive. Results of sensitivity tests are listed in Table 3. Drop weight impact tests were accomplished following the BAM* procedure. A positive mark in the bullet test means that deflagration occurred.

*German Federal Institute for Materials Testing.

TABLE 1
Comparison of Manufacture Procedures

Procedure	Advantages	Shortcomings
casting method with latex	simplicity, low cost apparatus, manufacture of hollow explosive samples	sheet dimensions less accurate, unconvenient for underwater use, thickness >8 mm difficult, medium mechanical properties, rubber content $\geq 15\%$
natural rubber with solvent	low dimension tolerances, excellent mechanical properties, rubber content as low as 10%, detonates down to .6 mm thickness, convenient for underwater use	working with solvents, sheets thicker than 10 mm difficult to be manufactured, slow drying procedure
solvent free depolymerized rubber	low tolerances, no limitations in sheet dimensions, manufacture by rolling and extrusions, convenient for underwater use, fast procedure	mechanical properties intermediate between the 2 other methods, rubber content $\geq 15\%$

TABLE 2
Mechanical Properties

Procedure	Tensile strength (kg/cm ²)	Elongation at break (%)	Flexibility (numbers of 180° flexures before break)
casting (20% rubber)	4 - 5	150 - 180	>50
natural rubber			
10%	8 - 10	100 - 150	>50
15%	15 - 18	250 - 350	>50
15% depolymerized rubber			
Δ = 1.3 - 1.4	3 - 4	200 - 250	>50
Δ = 1.1 - 1.2	2 - 3	150 - 200	extremely soft and resistant to flexures

TABLE 3
Sensitivity

	Rubber content (%)	Bullet test		Drop weight test (mkg)
		on wood	on steel	
PETN	10	20 x -	15 x - 5 x +	0.65
	15	10 x -	10 x -	0.65
	20	10 x -	8 x - 2 x +	0.75
RDX	10	20 x -	14 x - 6 x +	0.7 - 0.8
	15	10 x -	5 x - 5 x +	2.0
	20	10 x -	11 x - 1 x +	2.25
HMX	10	20 x -	15 x - 5 x +	0.7 - 0.8
	15	10 x -	10 x -	1.2
	20	10 x -	8 x - 2 x +	1.2

Detonation Rates

Densities of sheets obtained by following the above described procedures were nearly identical and were in the order of 1.4 g/cm³. The detonation rate at this density was about 7000 m/s and varied only slightly with sheet thickness. Figure 1 shows the thickness effect of a PETN containing sheet with 15% rubber. The plot of the detonation rate versus the inverse thickness shows that the rate decreases linearly from the ideal rate, $D_i = 7040$ m/s to $D = 6800$ m/s, at 1 mm thickness. The curve

then drops drastically at the failure thickness which is somewhat less than 0.8 mm.

At present, the most extensive application for sheet explosives is in explosive welding. Experimentally it has been found that not only the explosive thickness but also the detonation rate has to be adapted to each particular welding problem. One reason for this is that only a jet-forming collision of the metal partners guarantees clean welding surfaces. For this to occur, the junction point must travel at subsonic speed. This means that the detonation rate

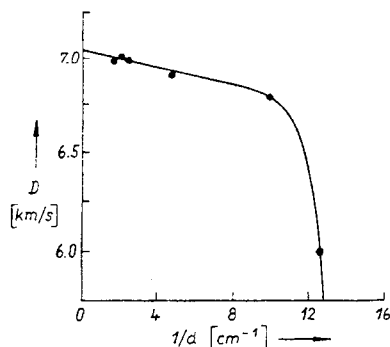


Fig. 1 - Detonation rate of PETN sheets ($\Delta = 1.4$, 15% natural rubber) as a function of inverse thickness d

should not appreciably exceed the sonic speed in the metal since the distance between the welding partners and the angle between them must be kept small.

Figure 2 shows flash radiographs of a jetless collision produced with a sheet of $D = 7000$ m/s and a jet forming condition with a sheet of lower rate. In the latter case, the initial angle between the plates is unrealistically great in order to better visualize the material ejected at the junction.

The lower detonation rates necessary for welding applications have to be obtained without an increase in the failure thickness and without loss of homogeneity. This means that the effect should be obtained by lowered densities rather than in lower specific energies of the explosive.

In order to decrease the sheet density in a homogeneous manner, two methods were found to be practicable. The first was an extensive calendering which created very small voids in the sheet. The second procedure used to obtain

fine porosities in the explosive involved the addition of water-soluble salts to the composition and the subsequent dissolution of these salts from the vulcanized product. Curves 1 - 3 of Fig. 3 show the range of detonation rates which can be obtained by these techniques. Rates as low as 4500 m/s can be obtained at a density of 0.9 g/cm^3 . Failure thickness of these low density sheets was less than 1 mm. Their tensile strength is much lower than that of the compact sheets; nevertheless they exhibit good flexibility properties.

Detonation of Stretched Sheets

Rubber-bonded explosives offer an opportunity to study detonation phenomena in explosives under strong mechanical tension. From hydrodynamic theory one could expect the tension to result in an increase in detonation rate, as the reaction releases the mechanical energy at the same time as the chemical energy. This effect, however, is small as the mechanical energy is quite negligible compared to the chemical potential. It is—as a matter of fact—completely masked by other predominately greater effects.

Experiments conducted with stretched explosive sheets show to the contrary that detonation rates decrease drastically with applied stress. This is due primarily to the decreased density filled rubbery materials exhibit when elongated. This volume increase by stretching is known as the Schippel-effect. It depends on the grain size of the filler, coarser fillers giving a greater effect.

When a ribbon is one-dimensionally stretched, neither density nor stress are uniform across the ribbon width. Immersing the sheet into water and observing the volume increase when stress is applied gives only mean values. Experimental results of this kind are plotted in Fig. 4. They refer to a ribbon

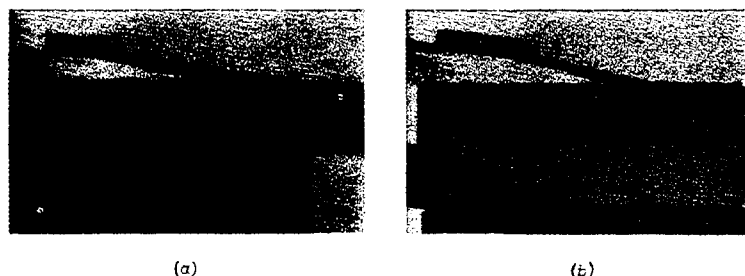


Fig. 2 - (a) Jetless and (b) jet-forming welding obtained with sheets of different rate (a) 7000 m/s, (b) 5700 m/s

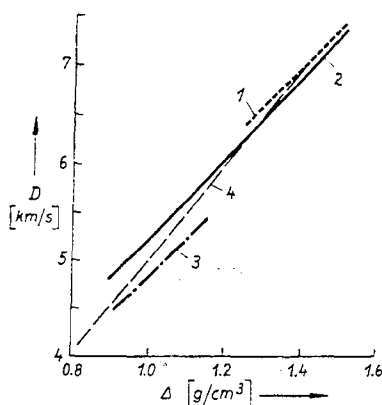


Fig. 3 - Density effect of stretched and unstretched explosives: curves 1-3 refer to unstressed sheets; 1 = 15% natural rubber, 2 = 15% depolymerized rubber, 3 = 20% depolymerized rubber. Curve 4 refers to a stretched 15% rubber containing explosive of 1.4 g/cm^3 initial density.

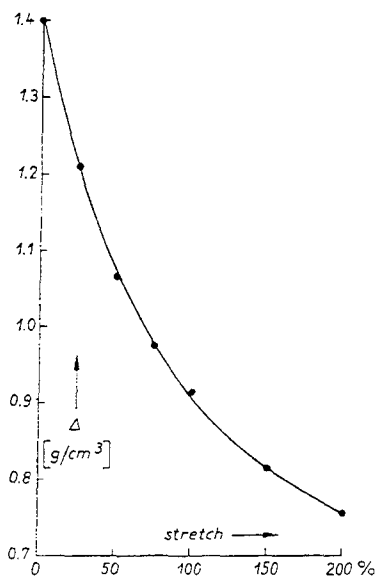


Fig. 4 - Density decrease by linear stress

containing 15% rubber and PETN of 20μ mean particle size. This figure shows that the volume is nearly doubled when the sheet is stretched by 200%. It is obvious that this effect can be used to vary the detonation rate continuously in a well-controlled manner.

The deontation rate of one-dimensionally stretched ribbons were measured by a pin technique. The results are plotted in Fig. 5. The rate drops down from 7000 m/s for the unstretched explosive to 4100 m/s at 150% stretch. When the data of Fig. 4 and 5 are combined, curve 4 of Fig. 3 is obtained. The difference in slope (4.9 m/s/mg/cm^3) compared to the value for unstretched explosives (4.0 m/s/mg/cm^3) means, that the decrease of detonation rate by stress is not a pure density effect.

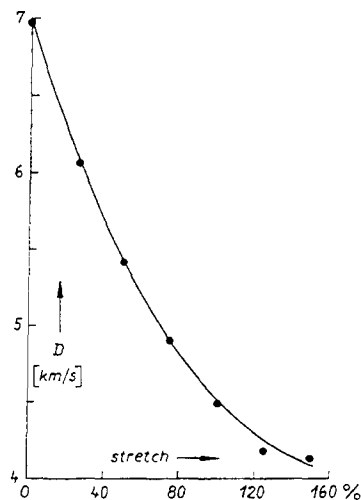


Fig. 5 - Detonation rate versus stretch

Kerr-cell photographs were taken from unstretched (Fig. 6) and one-dimensionally stretched (Fig. 7 and 8) sheets. In these experiments (Fig. 7 and 8) the distortion of a given explosive area induced by the stress is illustrated by a square grid which was coated with carbon black on the undeformed sheet.

From a series of photographs taken of 80% and 130% stretched sheets - Fig. 7 and 8 give particular phases from these series - a certain anisotropy in detonation rate is demonstrated; the rate parallel to the axis under tension being higher than the axis normal to the tension. This anisotropy increases when higher stresses are applied, as this is the case for the difference in density effect between stretched and unstretched explosives.

The anisotropic phenomena has nothing to do with the direction in which the sheet was

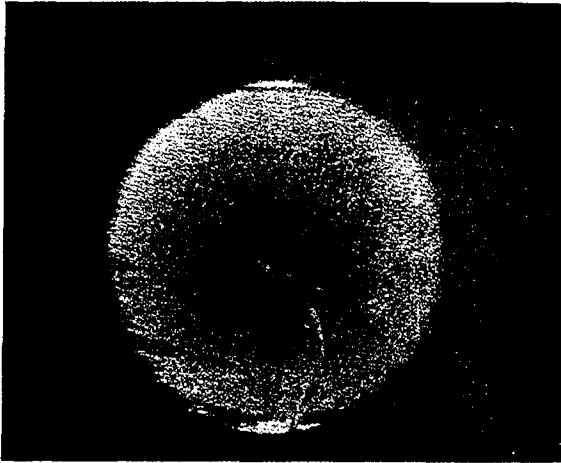


Fig. 6 - Kerr-cell photograph of an unstressed sheet showing circular detonation propagation

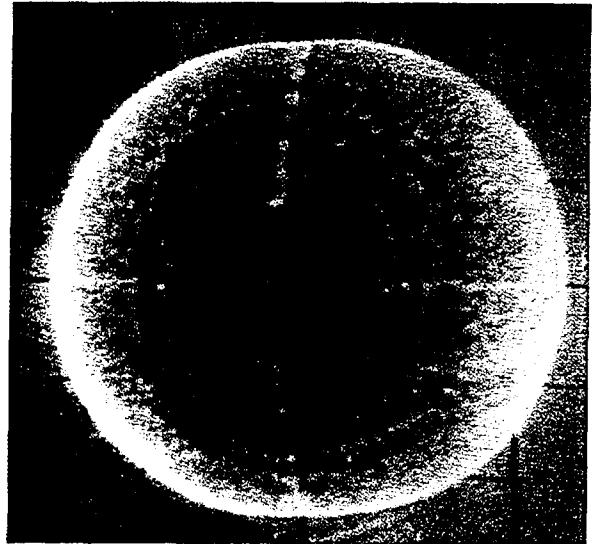


Fig. 8 - Distinct anisotropy at 130% stretch

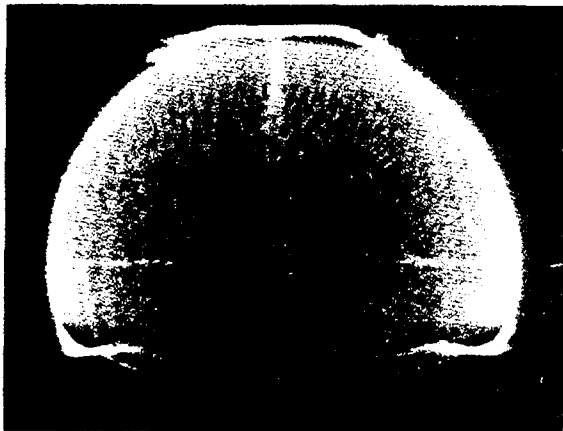


Fig. 7 - At 80% stretch a slight anisotropy becomes visible

rolled. The same effect is observed when tension is applied parallel to or normal to the rolling direction.

At this time, there is no definite explanation for the anisotropy effect which is a new example of the influence of strength properties in hydrodynamically controlled phenomena. It is believed that this phenomenon is caused by an anisotropy in the reaction rate induced by the stratification of the stretched rubber network.

REFERENCES

1. British Patent No. 534616, 2 March 1941.
2. U.S. Patent 2999793 and 2992087 Du Pont de Nemours and Co.

EXPLICIT SOLUTIONS FOR UNSTEADY SHOCK PROPAGATION IN CHEMICALLY REACTING MEDIA

G. K. Adams and M. Cowperthwaite
*Explosives Research and Development Establishment
Waltham Abbey, Essex, England*

ABSTRACT

We consider the one-dimensional flow problem of a piston moving into a fluid medium capable of releasing heat energy by chemical reaction. The piston is assumed to be instantaneously accelerated so that a shock forms at the piston face, and to continue to move along a path defined by an arbitrary function of time. If we restrict the material flow between the piston and the preceding shock front to that where the particle velocity is a linear function of position, and the velocity gradient is an arbitrary function of time, the differential equations of motion can be integrated to give the density, pressure and particle velocity fields. The shock and particle paths are obtained by using the Hugoniot conditions which must hold at the shock front. It is convenient to assume an ideal polytropic fluid and a strong shock, whereupon the integral equation for the shock path takes a simple form and can be solved in terms of explicit functions of time for some classes of the arbitrary functions defined by the piston path and velocity gradient.

The space-time distribution of the rate of pressure change due to chemical reaction at constant volume, consistent with the solutions of the equations of motion, is found by substituting these solutions into the energy equation. Thus we obtain explicit solutions to the reactive, non-steady, shock problem in terms of the initial and rear boundary conditions, the thermodynamic properties of the medium and the chemical reaction rate. The space-time distribution of the latter is of course determined by the assumption as to the form of the velocity gradient function and will not necessarily correspond to that demanded by any chemical kinetic relations between the rate and the state variables. The solutions may, however, be of use in understanding the general problem and of value in setting limits to the behaviour of systems where the reaction rate is arbitrarily specified.

INTRODUCTION

The course of development of a shock wave which initiates heat release by chemical reaction is an important problem in the initiation of detonation. A number of investigators have obtained solutions by the step-by-step numerical integration of the partial differential equations governing the flow behind the shock using particular forms of the chemical reaction rate function and equations of state. One of the present authors has suggested that useful information on the initial phase of the solution can be obtained by making approximations to the reaction rate function and to the flow behind the

shock which enable the shock parameters to be obtained by integration of an ordinary differential equation. Pack and Warner [2] have obtained the same type of solution by the application of Whitham's approximation which assumes that the differential relationship between pressure and particle velocity valid along the positive characteristic holds approximately along the shock path.

The validity of these approximate methods of solution can be checked only by comparison with the results of exact calculations and, for this purpose, it would be useful to have exact analytic solutions for simple formulations of

Note: Present address of M. Cowperthwaite: Stanford Research Institute, Menlo Park, California.

the heat release function, even if these were not representative of those demanded by the laws of chemical kinetics.

The first problem which we examined was the growth of a plane shock generated by a constant velocity piston moving into a material where heat was generated behind the front at a constant rate per unit volume. Since it appeared that a possible solution was an accelerating step shock uniform in pressure, we determined the condition for this solution by equating the time rates of change of pressure along a particle path and along the shock path. The assumptions made were that the material obeyed a polytropic equation of state with a constant isentropic index and that the conditions across the shock front obeyed the strong shock approximation.

Since the assumptions of a zero pressure gradient and a constant velocity piston boundary determine the particle velocity field, it was easy to show that a necessary condition for the equality of the rates of change of pressure with a constant volumetric heat release rate, is that the isentropic index has a value of two.

We then found that if we chose any form for the particle velocity gradient which enabled the velocity, density and pressure fields to be determined by integration of the equations of motion, subject to the boundary conditions imposed by the piston and the shock front, the heat release distribution function could be found from the energy conservation equation. In this paper we describe a general method for solving such one-dimensional reactive shock problems and illustrate it by application to some specific cases where the solutions can be written explicitly.

THE EQUATIONS FOR ONE-DIMENSIONAL UNSTEADY MOTION OF A PERFECT FLUID

The time variation of density, ρ , particle velocity, u , and pressure, p , along particle paths are given by the equations of conservation of mass, momentum and energy [4]:

$$\frac{D\rho}{Dt} = -\rho \left[\frac{\partial u}{\partial r} + (n-1) \frac{u}{r} \right] \quad (1)$$

$$\frac{Du}{Dt} = -\frac{1}{\rho} \frac{\partial p}{\partial r} \quad (2)$$

and

$$\frac{Dp}{Dt} = \left(\frac{\partial p}{\partial \lambda} \right)_{e,p} \frac{D\lambda}{Dt} - p \left(\frac{\partial \ln p}{\partial \ln \rho} \right)_{s,\lambda} \frac{D\rho}{Dt} \quad (3)$$

where s , e and λ denote the specific entropy, specific internal energy and extent of reaction respectively; $n = 1, 2$ or 3 for plane, cylindrically symmetric and spherically symmetric flows.

For a polytropic equation of state $p = (\gamma - 1)\rho e$ with γ constant, $(\partial \ln p / \partial \ln \rho)_s$ is equal to γ .

BOUNDARY CONDITIONS

We shall assume that the rear boundary is specified by the motion of a piston which starts to move at $t = 0$ from a position $r = r_0$ along a path

$$r_p = r_0 F(t)/F(0). \quad (4)$$

The piston velocity is obtained by differentiation as

$$u_p = r_0 F'(t)/F(0). \quad (4a)$$

The form of the arbitrary function $F(t)$ is assumed to be such that a shock wave is generated from the piston face at $t = 0$ and that no subsequent discontinuities form between this and the piston.

The boundary condition at the shock moving in the same direction as the fluid is given by the jump conditions:

$$\left. \begin{aligned} \rho_o(U - u_o) &= \rho_s(U - u_s) \\ p_s - p_o &= \rho_o(U - u_o)(u_s - u_o) \\ p_s + p_o &= \frac{2\rho_o \rho_s (e_s - e_o)}{\rho_s - \rho_o} \end{aligned} \right\} \quad (5)$$

For a polytropic equation of state and $p_s \gg p_o$, these become:

$$\left. \begin{aligned} U &= \frac{\gamma+1}{2} u_s - \frac{\gamma-1}{2} u_o \\ p_s &= \frac{\gamma-1}{2} (u_s - u_o)^2 \rho_s \\ \rho_s &= \frac{\gamma+1}{\gamma-1} \end{aligned} \right\} \quad (5a)$$

and

$$\frac{\rho_s}{\rho_o} = \frac{\gamma+1}{\gamma-1}$$

The suffixes s and o denote quantities just behind and just ahead of the shock discontinuity.

THE MOTION BETWEEN THE REAR BOUNDARY AND THE SHOCK FRONT

We shall assume that the particle velocity gradient is a function of time only and can be written in terms of an arbitrary function $f(t)$ as

$$\frac{\partial u}{\partial r} = \frac{f'(t)}{f(t)} \quad (6)$$

a function which is continuous and finite between the piston and the shock.

The velocity field can be obtained by integration of (6) with the boundary conditions (4) and (4a).

$$u = u_p + (r - r_p) f'(t)/f(t). \quad (7)$$

The particle paths are given by integration of the equation

$$\frac{dr}{dt} = u(r, t) \quad (8)$$

from the shock boundary. If η is the space coordinate of the particle when traversed by the shock at $t = \tau$, its subsequent path is given by

$$r = r_p(t) + [\eta - r_p(\tau)] f(t)/f(\tau). \quad (9)$$

If we assume that the strong shock approximation is valid Eq. (5a) then the shock path can be obtained from the equation

$$\frac{dr_s}{dt} = U = \frac{\gamma+1}{2} u_s - \frac{\gamma-1}{2} u_o \quad (10)$$

or

$$\frac{dr_s}{dt} = \frac{\gamma+1}{2} [u_p + (r_s - r_p) f'(t)/f(t)] - \frac{\gamma-1}{2} u_o.$$

This can be integrated to give

$$r_s = r_p + \frac{\gamma-1}{2} [f(t)]^{\frac{\gamma+1}{2}} \int_0^t (u_p - u_o) [f(t)]^{-\frac{\gamma+1}{2}} dt. \quad (11)$$

The parameter η (r_s at $t = \tau$) can therefore be expressed as a function of τ ; it will be convenient to use τ, t as the independent variables in place of r, t . The value of τ is constant along any one particle path and related with r through Eq. (9).

The density field is obtained by integrating the mass conservation Eq. (1), expressed in the equivalent form:

$$\frac{\partial \ln \rho r^{n-1}}{\partial t_\tau} = - \frac{\partial u}{\partial r_t}. \quad (1a)$$

We obtain:

$$\frac{\rho(\tau, t)}{\rho(t = \tau)} = \frac{f(\tau)}{f(t)} \left(\frac{\eta}{r} \right)^{n-1} \quad (12)$$

where η/r is expressible as a function of τ and t through Eqs. (9) and (11). The density at the shock front, $\rho(t = \tau)$ or ρ_s , is constant in the strong shock approximation and determined by the last of Eqs. (5a).

From the momentum Eq. (2), we have

$$\frac{\partial p}{\partial \tau_t} = \frac{\partial p}{\partial r_t} \frac{\partial r}{\partial \tau_t} = -\rho \frac{\partial u}{\partial \tau_t} \frac{\partial r}{\partial \tau_t}. \quad (13)$$

From (7) and (9)

$$u = u_p + [\eta - r_p(\tau)] f'(t)/f(\tau) \quad (14)$$

and

$$\frac{\partial u}{\partial \tau_t} = u'_p + [\eta - r_p(\tau)] f''(t)/f(\tau). \quad (14)$$

From (9),

$$\frac{\partial r}{\partial \tau_t} = [\eta' - r'_p(\tau)] \frac{f(t)}{f(\tau)} - [\eta - r_p(\tau)] \frac{f(t) f'(\tau)}{[f(\tau)]^2}.$$

Substituting

$$[\eta - r_p(\tau)] f'(\tau)/f(\tau) = u_s(\tau) - u_p(\tau)$$

and

$$\eta' = U(\tau), \quad r'_p(\tau) = u_p(\tau)$$

we have

$$\frac{\partial r}{\partial \tau_t} = [U(\tau) - u_s(\tau)] f(t)/f(\tau). \quad (16)$$

Combining (12), (13), (15) and (16) we obtain

$$\begin{aligned} \frac{\partial p}{\partial \tau_t} = & -\rho_s \left(\frac{n}{r} \right)^{n-1} \left[u'_p(t) + (\eta - r_p(\tau)) \frac{f''(t)}{f(\tau)} \right] \\ & \times [U(\tau) - u_s(\tau)]. \end{aligned} \quad (17)$$

Since all the variables are known function of τ and/or t we can integrate this equation from the shock front boundary to determine the pressure field

$$p(\tau, t) = p_s(t) + \int_t^\tau \frac{\partial p}{\partial \tau_t} d\tau. \quad (18)$$

The shock pressure p_s can be found from the Hugoniot relations and the particle velocity at the shock front. The latter is obtained by inserting the value of r_s determined by Eq. (11) into the equation for the velocity field (7).

THE RATE OF PRESSURE CHANGE DUE TO CHEMICAL REACTION

Combining the mass and energy conservation Eqs. (1) and (3) we obtain

$$\frac{\partial p}{\partial t_\tau} = \dot{p} - \gamma p \left[\frac{\partial u}{\partial r} + (n-1) \frac{u}{r} \right] \quad (19)$$

where \dot{p} stands for

$$\left(\frac{\partial p}{\partial \lambda} \right)_{e, \rho} \frac{d\lambda}{dt},$$

the time rate of pressure change due to chemical reaction at constant volume, and

$$\gamma = \left(\frac{\partial \ln p}{\partial \ln \rho} \right)_{s, \lambda}$$

is the polytropic index, assumed to be constant. If we substitute $\partial u / \partial r = f' / f$ and $u = dr / dt$ we may write Eq. (19) in the form

$$\dot{p} = (f r^{n-1})^{-\gamma} \partial [p f^\gamma r^{(n-1)\gamma}] / \partial t_\tau. \quad (20)$$

Since r and the pressure field p are functions of τ and t the reaction term will, in general, be determinable in terms of functions of these variables. We may choose some function $f(t)$ which gives a desired behaviour of the pressure in the shock wave and determine the function $\dot{p}(\tau, t)$ which generates this wave. Alternatively, we may find the set of functions which satisfy a given restriction on the form of $p(\tau, t)$ or $\dot{p}(\tau, t)$. One such restriction is that \dot{p} should be independent of τ .

SOLUTIONS WHEN \dot{p} IS A FUNCTION OF TIME ONLY

Rear Boundary is a Plane Piston Moving
with Constant Velocity ($n = 1$, $u_p = 0$)

With these conditions, Eq. (17) reduces to

$$\frac{\partial p}{\partial \tau} = -\rho_s (U - u_s) (\eta - r_p(\tau)) f''(t) / f(\tau). \quad (21)$$

On integration, this gives an equation of the form

$$p = p_s(t) + f''(t) [g(\tau) - g(t)]. \quad (22)$$

Putting $n = 1$ into Eq. (20) gives

$$\dot{p} = f^{-\gamma} \partial p f^\gamma / \partial t.$$

Substituting for p from (22) we see that for the term containing $g(\tau)$ to vanish, $d(f^\gamma f'') / dt$ must equal zero. Equivalently,

$$f^\gamma f'' = c_1, \quad (23)$$

an arbitrary constant. Integrating this equation, we obtain

$$[f']^2 = [f'(0)]^2 + 2c_1(1 - f^{1-\gamma}) / (\gamma - 1) \quad (24)$$

and

$$t = \int_1^f \{ [f'(0)]^2 + 2c_1(1 - f^{1-\gamma}) / (\gamma - 1) \}^{-1/2} df. \quad (25)$$

Since $f'(0) = f(0)(\partial u / \partial r)_0$, we have been able to set $f(0)$ equal to unity without loss of generality. The value of $f'(0)$ will then be determined by the characteristic time scale of the problem, that is, by the value of $\dot{p}(0) / p(0)$. The value of the arbitrary constant c_1 determines the pressure gradient. We observe from Eq. (21) that the gradient is positive for c_1 less than zero and negative for $c_1 > 0$. When the constant is put equal to zero the solution corresponds to the reactive step shock with no pressure gradient between the piston and the shock front.

The Step Shock Solution in Plane Flow

A piston moving at constant velocity into a nonreactive medium gives rise to a step shock of constant strength. Although we may guess that an accelerating step shock (in pressure) could be produced if the generation of pressure by chemical reaction is uniformly distributed between the piston and the front (\dot{p} independent of τ), this will depend upon whether the time rate of change of pressure along the shock front boundary can be made equal to the rate of change along a particle path. Since the relation between pressure and particle velocity at the shock front depends upon the value of γ through the Hugoniot relations, we might expect this equality to depend upon the value of γ .

If we assign a value to c_1 we can determine $f(t)$. Thus, from Eqs. (24) and (25) with $c_1 = 0$, we have

$$f'(t) = f'(0) \quad \text{and} \quad f(t) = t f'(0) + 1.$$

The shock path can then be determined from Eq. (11). Putting $u_0 = 0$, i.e., assuming the case of a piston moving into a stationary medium and substituting $dt = df/f' = df/f'(0)$, we obtain the shock path as

$$r_s - r_p = \frac{\gamma-1}{2} \frac{u_p}{f'(0)} f^{\frac{\gamma+1}{2}} \int_1^f \frac{f^{\frac{\gamma+1}{2}}}{f} df \quad (11a)$$

or

$$r_s - r_p = u_p (f^{(\gamma+1)/2} - 1) / f'(0). \quad (11b)$$

Substituting for $r_s - r_p$ and f' in the equation for the particle velocity along the shock path,

$$u_s = u_p + (r_s - r_p) f' / f \quad (7a)$$

we obtain

$$u_s = u_p f^{(\gamma-1)/2} = u_p (tf'(0) + 1)^{(\gamma-1)/2}. \quad (26)$$

Since, for a strong shock, the pressure varies as the square of the particle velocity at the shock and, since the condition $c_1 = 0$ corresponds to zero pressure gradient behind the shock, we find that

$$p(t) = p_s(t) = p(0) f^{\gamma-1} = p(0) (tf'(0) + 1)^{\gamma-1}. \quad (27)$$

From Eq. (20) with n put equal to unity, the required function for \dot{p} is given by

$$\begin{aligned} \dot{p}(t) &= p(0) f^{-\gamma} df^{2\gamma-1}/dt \\ &= p(0)(2\gamma-1) f^{\gamma-2} f' \\ &= p(0)(2\gamma-1) f'(0) (tf'(0) + 1)^{\gamma-2}. \end{aligned} \quad (28)$$

The constant of integration $f'(0)$ is obtained by putting $t = 0$ in Eq. (28) to obtain

$$f'(0) = \dot{p}(0) / (2\gamma-1) p(0). \quad (29)$$

It is therefore determined by the value of γ and of the initial reaction time constant $p(0)/\dot{p}(0)$.

Since the pressure behind the shock and the reaction term are both functions of time only, we may write the function \dot{p} in terms of pressure only

$$\frac{\dot{p}}{p(0)} = \left(\frac{p}{p(0)} \right)^{(\gamma-2)/(\gamma-1)}. \quad (30)$$

Therefore a step shock in pressure is produced by a plane, constant velocity, piston

moving into a reactive medium only if the rate of change of pressure, due to chemical reaction at constant volume, is proportional to the pressure raised to the power of $(\gamma-2)/(\gamma-1)$. The case of a constant value of \dot{p} and $\gamma=2$ is a special case of this condition.

If we assume that the change in pressure by reaction is due to the heat released by the reaction, then for an ideal gas law, $\dot{p} = (\gamma-1) \rho \dot{q}$ where \dot{q} is the rate of heat release per unit mass. From (12) the density varies as

$$(r/\eta)^{1-n} f(\tau)/f(t)$$

or in this case, as $(\tau f'(0) + 1) / (t f'(0) + 1)$. The condition which must be imposed upon \dot{q} therefore becomes

$$\frac{\dot{q}}{q(0)} = \left(\frac{p}{p(0)} \right)^{(\gamma-2)/(\gamma-1)} \frac{(t f'(0) + 1)}{(\tau f'(0) + 1)}$$

which, in the initial progress of the shock when $\tau f'(0) < t f'(0) \ll 1$, approximates to:

$$\frac{\dot{q}}{q(0)} = \left(\frac{p}{p(0)} \right)^{(\gamma-2)/(\gamma-1)} [1 + f'(0)(t - \tau)]. \quad (31)$$

Thus the rate of heat release per unit mass is proportional to a fractional power of the pressure in the wave (dependent upon the value assigned to γ) and increases with time along a particle path.

If the rate does not increase along particle paths as demanded by Eq. (31), but is constant or decreasing, we may expect that the pressure will increase less rapidly along particle paths than along the shock path and that the wave will develop a positive pressure gradient, the pressure being highest at the shock front. The rate of growth must depend on the rate at which work is done on the system by the piston against the rear boundary pressure and the rate at which heat is being added by reaction in the region between the piston and the shock front. Since, if the rate of heat release is constant or decreasing along particle paths both must be lower than in the step shock case, the shock must accelerate more slowly.

It is not immediately clear what happens to the form of the shock if \dot{q} varies with some power of pressure which is not identical with $(\gamma-2)/(\gamma-1)$. Since, even in cases where it is possible to assume that the heat release is proportional to some power of pressure, it is unlikely that the exponent will be related in this way to the isentropic index, this question is of considerable interest. Since p is a function of $tf'(0) + 1$ the condition for the step shock solution can be written in a different form as:

$$\dot{q}/\dot{q}(0) = p/[p(0)(\tau f'(0) + 1)] \quad (32)$$

Thus \dot{q} for the step shock is proportional to the first power of the pressure if it also decreases with increase in the time at which particles are traversed by the shock and is independent of time along particle paths as in (32). This would correspond with a medium in which the heat release rate for successive particle elements has been arranged to decrease with increasing distance, say by progressive dilution. If such an artifice produces a step shock with an amplification rate defined by Eq. (27) we may deduce that a medium in which the rate of heat release is directly proportional to pressure but is independent of the initial particle position, must give rise to a wave which grows more rapidly and has a positive pressure gradient behind the front.

These conclusions depend of course upon the assumption of plane flow and constant piston velocity. We shall indicate the form of the reactive shock solutions which can be obtained under other conditions. Generally, one obtains functions for the heat release distribution which are too unwieldy to be simply related to the pressure in the shock wave and the time along particle paths. The interest of the step shock solution lies in the fact that it results from a heat release rate which is, in the region of the shock front, proportional to a simple power of the shock pressure. In an earlier paper [1], one of us has suggested that the growth of a shock wave to detonation in granular solid explosives may be consistent with a heat release rate proportional to a power of the shock pressure of the order of unity.

The rate of change of the pressure with the position of the shock front, in the spherically symmetric case, was obtained [1] by replacing the velocity gradient term in the energy equation along the shock path by the quotient of the particle velocity at the shock front and the distance of the shock front from the origin. This reduced the partial differential equation for the rate of change of shock pressure to an ordinary differential equation for p_s as a function of r_s .

We may now examine the validity of this type of approximation for plane flow and constant piston velocity. The equation for the rate of change of pressure along the shock path (Eq. (3) of Ref. 1) is, under strong shock conditions, given by (for $n = 1$)

$$\frac{3}{2} \frac{dp_s}{dt} + \frac{\gamma+1}{2} p_s \frac{\partial u}{\partial r_t} = \dot{p} \quad (33)$$

Now, since

$$\frac{\partial u}{\partial t_\tau} = -\frac{1}{\rho} \frac{\partial p}{\partial r_t}$$

must vanish along the piston path where $\tau = 0$, and

$$\frac{dp_s}{dt} = \frac{\partial p}{\partial t_\tau} + (U-u) \frac{\partial p}{\partial r_t},$$

the initial value of $\partial u/\partial r_t$ is determined by setting $dp_s/dt = \partial p/\partial t_\tau$ in Eq. (33) and eliminating it by using the equation for the particle path

$$\frac{\partial p}{\partial t_\tau} + \gamma p \frac{\partial u}{\partial r_t} = \dot{p}.$$

The initial value of $\partial u/\partial r_t$ for any function \dot{p} is then $\dot{p}(0)/[p(0)(2\gamma-1)]$. A suitable approximation for $\partial u/\partial r_t$ which gives the correct initial value as $r_s \rightarrow 0$ and $u_s \rightarrow u_p$ is

$$\partial u/\partial r_t = u_s/[r_s + u_p p(0)(2\gamma-1)/\dot{p}(0)] \quad (34)$$

Substituting this into Eq. (33) and using $dt = dr_s/U$ and $u_s = 2U/(\gamma+1)$ we obtain an ordinary differential equation in $P = p_s/p(0)$ and

$$R = r_s + u_p p(0)(2\gamma-1)/\dot{p}(0):$$

$$\frac{3}{2} \frac{dP}{dR} = \frac{2\dot{p}P^{-1/2}}{(\gamma+1)u_p p(0)} - \frac{P}{R} \quad (35)$$

If $\dot{p} = \dot{p}(0) P^m$ in the vicinity of the shock front, this equation can be reduced to the Bernoulli equation and integrated to give the variation of shock pressure with distance as in Ref. 1.

The exact solution for $\dot{p}/\dot{p}(0) = P^{(\gamma-2)/(\gamma-1)}$ is now known from Eqs. (11b) and (27) to be:

$$P = \left[\frac{r_s + u_p f'(0)}{u_p f'(0)} \right]^{2(\gamma-1)/\gamma+1} \quad (36)$$

where $f'(0) = \dot{p}(0)/p(0)(2\gamma-1)$. It can be verified by substitution that this is a solution to Eq. (35) when $m = (\gamma-2)/(\gamma-1)$.

The substitution of $\partial u/\partial r_t$ by

$$u_s \left[r_s + u_p \left/ \left(\frac{\partial u}{\partial r_t} \right)_0 \right. \right]$$

is therefore exact when $m = (\gamma-2)/(\gamma-1)$ and will be least in error when m is not very different from this value. Since Eq. (35) has been constructed to give the correct initial value of $\partial u/\partial r_t$ for any value of m , it should be a good approximation for the initial development of the wave when $r_s < u_p p(0)(2\gamma-1)/\dot{p}(0)$. We have

not so far found a way of obtaining a simple quantitative measure of the rate of increase of error as m is varied on either side of $(\gamma-2)/(\gamma-1)$.

Solutions where $p = \phi(t, \tau)$ but $\dot{p} = \theta(t)$

These solutions where the pressure behind the shock is a function of the particle path (i.e., a pressure gradient exists behind the shock front) even though the reaction term depends only on the time, can be examined by choosing non-zero values of the constant c_1 in Eqs. (23), (24). We shall illustrate this by setting

$$c_1 = -[f'(0)]^2 (\gamma-1)/2. \quad (37)$$

If c_1 is less than this value, f is not a monotonic increasing function of t and the velocity gradient will pass through zero at some finite time.

When c_1 is determined by Eq. (37) the required solutions of $f''f^\gamma = c_1$ are

$$f' = f'(0) f^{(1-\gamma)/2} \quad (38)$$

and

$$f^{(\gamma+1)/2} = (\gamma+1) t f'(0)/2 + 1. \quad (39)$$

The equation for the shock path can then be integrated to obtain

$$r_s - r_p = \frac{\gamma-1}{2} \frac{u_p}{f'(0)} f^{(\gamma+1)/2} \ln f. \quad (40)$$

The particle velocity at the shock front is then given by

$$u_s = u_p \left(1 + \frac{\gamma-1}{2} \ln f\right). \quad (41)$$

Using these relations in the equation for the pressure gradient and setting $n = 1$ and $u_p' = 0$ we obtain the differential equation for the plane, constant velocity, piston case:

$$\left(\frac{\partial p}{\partial f}\right)_t = p(0) \frac{(\gamma-1)^2}{4} [f(t)]^{-\gamma} \times f^{\gamma-1} \ln f \left(1 + \frac{\gamma-1}{2} \ln f\right). \quad (42)$$

Integrating this from the shock front, $p = p_s$, $f = f(t)$ to a particle path, p , $f(\tau)$ we obtain

$$p/p(0) = p_s/p(0) + \frac{(\gamma-1)^2}{4\gamma} \left\{ \left[\frac{f(\tau)}{f(t)} \right]^\gamma \times H(\tau) - H(t) \right\} \quad (43)$$

where

$$H = \frac{\gamma-1}{2} (\ln f)^2 + \frac{1}{\gamma} \ln f - \frac{1}{\gamma^2} \quad (44)$$

and

$$p_s/p(0) = \left(1 + \frac{\gamma-1}{2} \ln f(t)\right)^2. \quad (45)$$

The required heat release distribution is calculated from

$$\dot{p} = f^{-\gamma} \frac{\partial f^\gamma p}{\partial t_\tau}$$

as

$$\dot{p}/p(0) f'(0) = f^{-\frac{\gamma+1}{2}} \left(1 + \frac{\gamma-1}{2} \ln f\right) \times \left(2\gamma-1 + \frac{\gamma^2-1}{4} \ln f\right). \quad (46)$$

There is in this case no simple relationship between the heat release term, the pressure and the independent variables. This is the case with the majority of the reactive shock solutions which result from the assumption that the particle velocity gradient is a function of time only. This assumption cannot therefore be used to determine the quantitative effect of changing a single parameter in the reaction term such as the pressure exponent, or of varying only the value of the isentropic exponent in the equation of state. Such problems are now seen to require a more general assumption as to the form of the velocity gradient function.

The solutions for problems with spherical or cylindrical symmetry are in general too algebraically complex to be useful, but under one rear boundary condition they assume a particularly simple form.

Rear Boundary is a Plane, Cylindrical or Spherical Piston with $F(t) = f(t)$

A piston starting at $t = 0$, $r = \eta_0$ moves along a path $r_p = \eta_0 f(t)$ with a velocity given by

$$u_p = \eta_0 f'(t). \quad (47)$$

The piston path therefore obeys the same function of time as other particle paths in the region between it and the shock front. If the medium ahead of the latter is at rest, the equation for the shock path,

$$r_s = r_p + \frac{\gamma-1}{2} f^{\frac{\gamma+1}{2}} \int_0^t u_p f^{-\frac{\gamma+1}{2}} dt$$

reduces to

$$r_s = \eta_0 f^{(\gamma+1)/2}. \quad (48)$$

The particle paths, Eq. (9), becomes

$$r = \eta f(t)/f(\tau) \quad (49)$$

and the particle velocity, Eq. (7), becomes

$$\begin{aligned} u &= r f'(t)/f(t) = \eta f'(t)/f(\tau) \\ &= \eta_0 [f(\tau)]^{(\gamma-1)/2} f'(t). \end{aligned} \quad (50)$$

At the shock front, $t = \tau$,

$$u_s = \eta_0 [f(t)]^{(\gamma-1)/2} f'(t) \quad (51)$$

and

$$p_s/p(0) = [f(t)]^{\gamma-1} [f'(t)]^2 / [f'(0)]^2. \quad (52)$$

The variation of pressure behind the shock front is found, as before, from Eq. (17) which becomes

$$\frac{\partial p}{\partial \tau} = -\rho_s \frac{\gamma-1}{2} \eta_0^2 [f(t)]^{1-n} f''(t) [f(\tau)]^{\gamma+n-2} f'(\tau). \quad (53)$$

Since $\eta_0 = u_p(0)/f'(0)$ and

$$\rho_s \frac{\gamma-1}{2} [u_p(0)]^2 = p(0),$$

integrating Eq. (53) gives

$$p = p_s \frac{p(0)}{[f'(0)]^2} [f(t)]^{1-n} f''(t) \int_{f(t)}^{f(\tau)} f^{\gamma+n-2} df \quad (54)$$

or

$$\begin{aligned} p &= \frac{p(0)}{[f'(0)]^2} \left\{ [f(t)]^{\gamma-1} [f'(t)] \right. \\ &\quad \left. - \frac{[f(t)]^\gamma f''(t)}{\gamma+n-1} \left[\frac{f(\tau)^{\gamma+n-1}}{f(t)} - 1 \right] \right\}. \end{aligned} \quad (55)$$

Assuming some relation between f'' and f which can be integrated to give f'' as an explicit function of f , we can now obtain the pressure field in terms of the shock front coordinate, r_s , and the Lagrangian coordinate η , by the substitutions

$$\begin{aligned} \text{and} \quad r_s &= \eta_0 f(t)^{(\gamma+1)/2} \\ \eta &= \eta_0 [f(\tau)]^{(\gamma+1)/2}. \end{aligned}$$

One such relationship is the equation

$$f'' f^{n(\gamma-1)+1} = c_1 \quad (56)$$

which is shown to be the condition that \dot{p} is not a function of τ . The equation for the reaction term simplifies to

$$\dot{p} = f^{-n\gamma} \frac{\partial p f^{n\gamma}}{\partial t} \quad (57)$$

obtained by substituting (49) in (20).

The combination of (55) and (57) gives Eq. (56) on the condition for the term in $f(\tau)$ to vanish.

The solution of (56) is analogous to that of (23) obtained previously, the exponent $k = n(\gamma-1)+1$ replacing γ .

If we write $1 + 2c_1/(k-1)[f'(0)]^2 = c_2$ so that c_2 is an arbitrary, dimensionless number then

$$[f'/f'(0)]^2 = c_2 + (1-c_2) f^{1-k} \quad (58)$$

and the general solution for this case becomes

$$\begin{aligned} \frac{p}{p(0)} &= \left(\frac{r_s}{\eta_0} \right)^{\frac{2(\gamma-1)}{\gamma+1}} \left[c_2 + (1-c_2) \left(\frac{r_s}{\eta_0} \right)^{\frac{2(1-k)}{\gamma+1}} \right] \\ &\quad + \left(\frac{r_s}{\eta_0} \right)^{\frac{2(\gamma-k)}{\gamma+1}} \frac{(1-c_2)(k-1)}{2(\gamma+n-1)} \left[\left(\frac{r_s}{\eta_0} \right)^{\frac{2(\gamma+n-1)}{\gamma+1}} - 1 \right] \end{aligned} \quad (59)$$

and

$$\begin{aligned} \frac{\dot{p}}{p(0)f'(0)} &= \left(\frac{r_s}{\eta_0} \right)^{\frac{2(\gamma-2)}{\gamma+1}} \left[c_2 + (1-c_2) \left(\frac{r_s}{\eta_0} \right)^{\frac{2(1-k)}{\gamma+1}} \right]^{1/2} \\ &\quad \times \left[c_2(\gamma(n+1)-1) + (1-c_2) \frac{(2-n)\gamma+3n-2}{2} \left(\frac{r_s}{\eta_0} \right)^{\frac{2(1-k)}{\gamma+1}} \right] \end{aligned} \quad (60)$$

Two consequences of our initial assumption regarding the piston path are that (a) it is simply related to the shock path

$$\frac{r_p}{\eta_0} = \left(\frac{r_s}{\eta_0} \right)^{2/(\gamma+1)} \quad (61)$$

and (b) that the initial piston velocity and position cannot be chosen independently since they are related by the equation

$$u_p(0) = \eta_0 f'(0) \quad (62)$$

where

$$f'(0) = 2\dot{p}(0)/p(0) [\gamma(2+n(3c_2-1)) - \{2+3n(c_2-1)\}] \quad (63)$$

The solutions (59) and (60) have certain interesting properties. If c_2 is put equal to unity we obtain step shock solutions with constant piston speeds. The difference between the step shock solutions for diverging flow and for linear flow is that the former are obtained for only one value of the initial condition defined by putting $c_2 = 1$ in Eqs. (62) and (63)

$$\frac{u_p}{\eta_0} = \frac{\dot{p}(0)}{[(n+1)\gamma-1] p(0)}$$

The general step shock solution requires a particular value of the initial divergence in terms of γ and the initial reaction rate. In the plane case the form of the solutions must be independent of the initial coordinate of the piston and a step shock can be obtained for all values of u_p and $\dot{p}(0)/p(0)$.

The derived function $\dot{p}/\dot{p}(0)$ is independent of n and is still given by

$$\dot{p}/\dot{p}(0) = [p/p(0)]^{(\gamma-2)/(\gamma-1)}$$

However, the heat release per unit mass, $\dot{q}/\dot{q}(0) = \rho_s \dot{p}/\rho \dot{p}(0)$, is dependent on n since $\rho/\rho_s = [f(\tau)/f(t)]^n$ and the function $f(t)$ is given by

$$f(t) = \frac{\dot{p}(0)t}{p(0)[(n+1)\gamma-1]} + 1$$

For $n = 2$ or 3 , when $c_2 < 1$, the shock has a positive pressure gradient at the rear and it initially diminishes in strength. If

$$1 > c_2 > \frac{n-1}{n},$$

it passes through a minimum pressure at a radius given by

$$\frac{1}{n-1} \left(\frac{r_s}{\eta_0} \right)^{\frac{2n(\gamma-1)}{\gamma+1}} = \frac{1-c_2}{c_2} \quad (64)$$

If, however, $(n-1)/n > c_2 > 0$, $\gamma > 1$, the shock decays asymptotically to zero pressure. The effect of varying c_2 is to vary both the time dependence of \dot{p} and of the piston speed. The variation of the shock pressure with time and position is a combination of these two factors.

For plane flow, when $n = 1$, the shock pressure is continuously increasing provided that $c_2 > 0$. If $c_2 = 0$ and $n = 1$ we find the curious situation of a shock moving with constant speed and shock front pressure but with continuously decreasing piston speed and heat release rate behind it. At the shock front the finite reaction rate is exactly compensated by the rarefaction wave due to the deceleration of the piston.

For spherical flow, $n = 3$, and $c_2 = 0$ we obtain the solutions:

$$\frac{p}{p(0)} = \left(\frac{r_s}{\eta_0} \right)^{\frac{4(1-\gamma)}{\gamma+1}} \left\{ 1 + \frac{3(\gamma+1)}{2(\gamma+2)} \left[\left(\frac{\eta}{r_s} \right)^{\frac{2(\gamma+2)}{\gamma+1}} - 1 \right] \right\} \quad (65)$$

$$\frac{\dot{p}}{p(0)} = \left(\frac{r_s}{\eta_0} \right)^{\frac{5-7\gamma}{\gamma+1}} \quad (66)$$

The shock path is given by:

$$\frac{r_s}{\eta_0} = \left(\frac{3\gamma-1}{7-\gamma} \frac{\dot{p}(0)}{p(0)} t + 1 \right)^{\frac{\gamma+1}{3\gamma-1}}; \quad (67)$$

the particle paths by

$$r/\eta = (r_s/\eta)^{2/(\gamma+1)}; \quad (68)$$

and the density distribution by

$$\rho/\rho_s = (\eta/r_s)^{6/(\gamma+1)}. \quad (69)$$

Since the initial conditions are determined by (62) and (63) as

$$u_p(0)/\eta_0 = 2\dot{p}(0)/p(0)(7-\gamma) \quad (70)$$

we observe that for finite values of u_p/η_0 the reaction rate, $\dot{p}(0)/p(0)$, must vanish as $\gamma \rightarrow 7$. For $\gamma = 7$ the solution is identical with the Primakof similarity solution [3] for a shock generated in an inert medium by a point source explosion.

We see that this similarity solution is a special case of the general solution, Eq. (55), for the condition $\partial u/\partial r = u/r$ with $\gamma = 7$ and the restriction that \dot{p} is independent of position.

If the variation of \dot{p} along the shock front is a given function of the shock pressure or position, the use of the relation $\partial u/\partial r = u/r$ as in Ref. 1, or some similar assumption, to determine the shock pressure/distance relationship

implies a particular $\dot{p}(r, t)$ distribution behind the shock front. This distribution can be determined as an explicit function of r and t by the method described in this paper.

Although we have used the Hugoniot relations appropriate to a strong shock in an ideal polytropic fluid, it is possible to extend the solutions to other cases.

Crown Copyright. Published with the permission of the Controller, Her Britannic Majesty's Stationery Office.

REFERENCES

1. G. K. Adams, Ninth Symposium on Combustion, Academic Press, 1963, p. 545.
2. D. C. Pack and F. J. Warner, Tenth Symposium on Combustion, Cambridge, England, August 1964.
3. R. Courant and K. O. Friedrichs, Supersonic Flow and Shock Waves, p. 424, Interscience, 1948.
4. J. G. Kirkwood and W. W. Wood, J. Chem. Phys., 22, 1915, 1954.

Invited Paper
SUMMARY PAPER ON INITIATION, IGNITION AND
GROWTH OF REACTION

G. P. Cachia
Atomic Weapons Research Establishment
Aldermaston, Berkshire, England

When I was invited to present a summary paper with this title, it was suggested that I might survey the advances made during the symposium and indicate profitable areas for future work.

An obvious way to do this was to group together those papers dealing with similar topics and I studied them with this intention. I found papers dealing with initiation and ignition, by heat, impact, shock and exploding wires. The explosives studied were homogeneous and heterogeneous, high density and low density, solid and liquid. In fact, I had nearly as many topics as papers. I then attempted to identify the common target for all the workers in the field and it seemed clear that in either the short or long term the study of the initiation of detonation must be directed to the design of improved explosive systems, both from the aspects of functional efficiency and resistance to accidental initiation and ignition.

With this in mind, I grouped the papers according to their approach to the common goal and it is in the following four groups that I shall discuss them -

1. Studies of the Processes of Initiation
2. Initiation Theories and Calculations
3. Experimental Determination of Initiation Characteristics
4. The Technology of the Initiation of Explosives

The division is somewhat arbitrary and some papers make appreciable contributions to more than one group, nevertheless it is of assistance in summarising the presented work.

I have selected what I consider to be the important features from each group of papers

and since most of these have good introductions reviewing the prior state of knowledge I have not reviewed past work in this summary.

STUDIES OF THE PROCESSES
OF INITIATION

Detailed knowledge of the mechanisms of ignition and initiation is desirable on general grounds but its application to explosive systems is important, since once it is known how a process occurs it is often relatively easy to reduce its occurrence if it is undesirable, or to vary and control the process if it is relevant to normal explosive functioning.

I have taken the following seven papers in this first group -

"Surface Rate Processes and Sensitivity of High Explosives," by Chaiken and Cheselske

"Further Studies on the Ignition of Explosives," by Green and Dorough

"Initiation of Explosives by Low Velocity Impact," by Napadensky

"The Effect of Physical and Chemical Properties on the Sensitivity of Liquid Explosives," by Hay, Ribovich, Scott, and Gibson

"The Initiation of Burning in High Explosives by Shock Waves," by Liddiard

"Experimental Observations of Initiation of Nitromethane by Shock Interactions at Discontinuities," by Travis

"The Effect of Interstitial Gas on the Shock Sensitivity of Low Density Explosive Compacts," by Chick

Chaiken and Cheselske have studied the physical factors which control the heating of explosive

from an adjacent high temperature source and found that the temperature to which an explosive is raised in any particular situation depends upon its ability to dissipate heat either by conduction or by fluid flow. This melt and flow model provides a basis for explaining the perplexing differences in impact sensitivities between explosives with similar chemical decomposition characteristics. When the work is extended to include chemical factors I think we shall be able to make a much sounder approach to developing explosives with low impact sensitivities.

The two papers by Green and Dorrough, and Napadensky deal with initiation by impact at velocities below 1000 feet per second. These velocities are relevant to many accident situations and the observed reactions varied from detonation to mild burning. The experiments were designed to permit crushing and lateral motion of the explosive since this is normally possible. The mechanisms are complex but factors which were shown to be important are ignition by friction at the various interfaces and the subsequent burning to detonation. This latter process is strongly affected by the fracture properties of the explosive.

Hay and others report a systematic investigation into the chemical and physical factors affecting the phenomenon of low velocity detonation in liquid explosives. Their model includes a precursor shock which leads to cavitation in the explosive. The subsequent collapse of the cavities produce hot spots and localised reaction. The pressure wave produced by this reaction then propagates the sequence of events. This model is very convincing but the factors which govern the processes are not yet all identified. Liquid explosives are used in many applications and I am sure that this work will make a substantial contribution to their safety.

The paper by Liddiard describes the ignition of explosives by shock, a process not previously studied in detail. He finds that threshold pressures are lower than those required to initiate detonation but in general a longer duration is necessary.

Chick has tested the theory that the high shock sensitivity of low density explosive compacts is due to the presence of interstitial gas. He found that in fact the gas hinders initiation, possibly by its cooling properties or by lessening convection. He thus concludes that the high shock sensitivity is due to geometrical effects. He also found that by raising the interstitial gas pressure he can make fine powder compacts more shock sensitive than those made from coarse

powders. He suggests that coarse powders are normally more sensitive because of their greater gas permeability and that this is reduced by increasing the interstitial gas pressure. This is an important point because it allocates a decisive role to surface reactions in the shock initiation of low density explosives. Another feature of this work is the clear indication that shock initiation can proceed either by a continuous intensification of the entering shock or via an intermediate burning phase which may last tens of microseconds.

The last paper in the group is the interesting experimental investigation by Travis into the effect of density discontinuities in shocked nitromethane. He concluded that the initiations he observed were due to shock interactions and with sustained shocks of 85 kbars he found that any discontinuity with a minimum dimension greater than 0.1 mm leads to initiation. To avoid shock interactions it would be necessary for a discontinuity to have not only the same shock impedance as the explosive at the relevant pressure but also the same shock velocity. It would be an interesting test of Travis's conclusion if such a material could be found and its effect examined on the shock initiation of nitromethane.

The work covered by this first group of papers represents a considerable advance in our knowledge of the mechanisms of initiation of explosives by a variety of stimuli. A feature which emerges clearly is that in many circumstances ignition is brought about in explosive systems by stimuli which are below the threshold for the initiation of detonation. The subsequent history of such ignitions depends upon the nature of the explosive and the geometry of the system but the transition to detonation can occur. Thus, from the safety viewpoint, the results are bound to lead to improvements in explosive compositions.

Additionally, these studies of the processes of shock initiation of detonation have provided better models for future theoretical work and a sounder basis for controlling and varying the shock initiation properties of explosives to meet their functional requirements. From the work reported it would also seem probable that for many initiation conditions the sequence of events is shock-ignition-shock-initiation. The second shock is generated by the burning reaction and may be produced soon after the initial shock or much later. If shock initiation can be brought about either with or without an intermediate burning phase this might explain why shock initiation is sometimes observed as a smooth acceleration of the shock front and in other cases as an abrupt change to detonation. Consolidation and extension of these studies of initiation processes will surely continue to be rewarding.

INITIATION THEORIES AND CALCULATIONS

This approach to the subject is attractive because in general, calculations are cheaper and quicker than experiments, although establishment of sound theories is of course tightly bound to confirmatory experiments. The usefulness of such theories depends upon their reliable application to the actual problems posed. Calculations applied to the relatively simple system of a homogeneous explosive initiated by a plane sustained shock have been quite successful and consideration has also been given to the effect of the introduction of various simple inhomogeneities. There are five papers in this second group.

"Initiation of Detonation by the Interaction of Shocks with Density Discontinuities," by Mader

"An Equation of State and Derived Shock Initiation Criticality Conditions for Liquid Explosives," by Enig and Petrone

"Explicit Solutions for Unsteady Shock Propagation in Chemically Reacting Media," by Adams and Cowperthwaite

"Size Factors in Detonation Transfer," by Stresau

"Oblique Impact of a Layer of Explosive by a Metal Plate," by David, Fauquignon, Bernier, and Potau

The paper by Mader extends his earlier work and he investigates the formation of a hot spot in nitromethane due to a discontinuity. The subsequent decomposition of the hot spot is also followed and his results are consistent with the experiments of Travis but he has been unable to study failures to propagate where these are due to rarefactions penetrating the reaction zone.

Enig and Petrone have used experimental shock data to derive equations of state for nitromethane and liquid TNT. They have used these equations of state to predict explosion times for nitromethane and TNT and the reaction zone width and critical hot spot size for nitromethane. These calculated values are in satisfactory agreement with experiment.

Adams and Cowperthwaite have attempted to apply analytical solutions to shock initiation problems. These solutions can be obtained with economy of computer time compared with numerical solutions but the model used appears unlikely to apply to normal explosive systems and confirmatory experiments would be encouraging.

Stresau discusses the concept that initiation occurs when energy is liberated at least as rapidly as it is dissipated. To apply this concept he suggests that the lack of basic data limits the use of mathematical analyses and considers that attention should be concentrated on interrelating the experimentally determinable variables associated with initiation.

David and others have studied theoretically the initiation of an explosive charge by the oblique impact of a metal plate. The theory shows that with certain conditions an overdriven detonation must occur. Experiments have shown the existence of an overdriven detonation.

In considering the advances made by this second group of papers, it seems that although steady progress is being maintained in explaining, in terms of chemical and physical data, the initiation of explosives which are homogeneous or contain single defects, the extension to heterogeneous explosives is remote. Stresau points to the lack of data but even if this were rectified, an exact mathematical definition of the microstructure of a solid explosive is clearly impossible. The value of this type of work in improving our general understanding of initiation processes, is clear, but I consider that useful calculations of initiation problems with heterogeneous explosives must be based on experimental data from initiation experiments. This point is taken further in discussing the next group of papers.

THE EXPERIMENTAL DETERMINATION OF INITIATION CHARACTERISTICS

If we appreciate the difficulties of solving initiation problems using basic chemical and physical data, the experimental approaches become more significant. However, the number of different explosives and the variety of geometries in which they are used, preclude the amassing of comprehensive experimental data. Faced with this situation we can either limit our experiments to the actual systems in which we are interested at any one time or we can attempt to find relationships which will enable initiation properties to be calculated from relatively few experiments. There are six papers in this third group.

"The Initiation Properties of Boosters in Explosives with Low Density," by Johansson and Sjölin

"Comparison between Shooting and Barrier Test," by Lundborg

"Direct Contact Detonation Sensitivity," by Savitt, Leone and Kyselka

"Shock Initiation of Low-Density Pressings of Ammonium Perchlorate," by Evans, Reese, Seely, Lee

"Initiation of a Solid Explosive by a Short-Duration Shock," by Gittings

"Retonation Caused by the Reflection of Divergent Waves," by Marlow

The paper by Johansson and Sjölin described experiments closely related to practical systems, where they examined the initiation of mining explosives with different booster configurations.

Lundborg, and Savitt and co-workers deal with the gap test. This test is easy to carry out but the initiating shock pulses are not so easily defined. On the other hand projectile impact tests require more experimental effort but the shock pulse parameters are more readily determined. Lundborg has compared results from the two tests with three explosives. He found that threshold peak pressures were somewhat higher for the gap tests. Savitt suggests that by placing a donor charge of nitroguanidine and the acceptor charge in direct contact and determining the donor density required to initiate 50% of the receptors the pulse length and shape are kept constant and that the peak pressure is the only variable.

Evans and co-workers described extensive experiments to survey the initiation properties of a typical insensitive explosive, ammonium perchlorate.

Gittings has used short duration shock pulses to study the initiation of PBX 9404. The pulses were produced by impacting thin films of aluminum on to the explosive. In the last paper Marlow reported observations of retonation brought about by the reflection of a divergent shock wave in an explosive.

The use of the gap test is the simplest way of describing the shock initiation characteristics of an explosive. It is surprisingly successful in many cases but its limitations are clear to anyone who has been asked to predict initiation delays solely on the basis of a gap test value. The next approach must surely be to obtain accurate shock initiation data for a number of explosives, starting with rectangular initiating shock waves relevant to impacting plates and extending the study to exponentially decaying waves which approximate to those generated by explosive donor charges. The work of Gittings with thin shock pulses and Evans and workers in their comprehensive study of the initiation properties of

ammonium perchlorate, are useful additions to the necessary data. The paper by Ramsay and Popolato earlier in this Symposium (pg. 233) is also relevant, in this case dealing with sustained shocks.

THE TECHNOLOGY OF THE INITIATION OF EXPLOSIVES

Returning to our stated goal of designing better explosive systems, some improvements are the result of the application of new knowledge but many others are due to ingenuity, inspiration and perseverance and might be correctly classified as inventions. I have taken three papers to represent this group.

"The Effect of Wax on the Shock Sensitivity of Explosive Compacts," by Eadie

"Confinement Effects in Exploding Bridge Wire Initiation of Detonation," by Stresau, Hiller and Kennedy

"Low Order Reactions in Shocked Explosives," by Griffiths and Broom

Eadie has shown that with the HMX/Wax system, the shock sensitivity decreases as the wax coverage of the HMX crystals increases even if the composition is kept constant. This result is not only important in connection with the control of the shock sensitivity of explosive formulations but also gives support to the surface burning theory. Eadie suggests that apparently conflicting evidence on the effect of particle size on the shock sensitivity of explosive charges can be reconciled by considering the additional effects due to charge permeability.

Stresau and co-workers described bursting bridge wire initiating systems using insensitive secondary explosives. The feature of these detonators is their moderate electrical energy requirements i.e. 2 joules for ammonium picrate and 10 joules for TNT and this is achieved by appreciable confinement in the vicinity of the bridge wire. Such detonators should make an important contribution to safety in many applications.

The final paper by Griffiths and Broom reports an attempt to utilise the energy released when an explosive receives a shock which is below the threshold for the initiation of detonation. This application is likely to be most successful with explosives with long reaction zones.

I have now completed the review of the work dealing with ignition, initiation and growth of reaction in explosives and have made some

suggestions for future work. I believe that good progress can only be maintained by continuing via a number of approaches and I feel that I cannot do better than conclude by quoting Sir Cyril Hinshelwood who said:

"If we wish to plan research we can only do so by assembling a community of people with varied and mutually complementary talents, operating with strategic flexibility, and in an atmosphere of curiosity in which members know and understand what the others are talking about."

COMMENTS

G. K. ADAMS (Explosives Research and Development Establishment, Essex, England): I must dispel the impression that the analysis presented in the paper by Dr. Cowperthwaite and myself depends upon any assumptions as to the mechanism of chemical energy release. The physical model represented is just that implied by the use of the continuum conservation equations and the neglect of diffusional transport terms, a model which is common to most of the numerical studies. In an earlier paper* I suggested that for a grain burning mechanism the energy release rate would be a weak function of pressure rather than, as in the homogeneous reaction case, a strong function of temperature. I then developed an approximate relation between the degree of pressure dependence of the reaction rate and the initial behaviour of the reactive shock.

The analytic method presented in this paper enables one to check the range of usefulness of such approximations. We have been primarily concerned to examine the consequences of a pressure dependent reaction process but could equally well have discussed the temperature dependence required to give certain forms of shock behaviour. The solutions obtained are exact but restricted by the form of the particle velocity field which, in the examples given, has been chosen to allow the solutions to be expressed in closed form. It is possible to develop less restrictive solutions by adding additional terms to the equation for the particle velocity gradient. One of the advantages of an analytic treatment is that the energy release rate distribution required by an observed shock behaviour can be very simply calculated. Although this distribution does not tell us anything directly about the mechanism of the initiation process it enables us to test the plausibility of any assumed mechanism.

*G. K. Adams, Ninth Symposium on Combustion, p. 545, Academic Press, 1963.

HYDRODYNAMIC COMPUTATION METHODS

Chairman: J. Berger

*Commissariat à l'Energie Atomique,
France*

THE USE OF ONE- AND TWO-DIMENSIONAL HYDRODYNAMIC MACHINE CALCULATIONS IN HIGH EXPLOSIVE RESEARCH

Mark L. Wilkins
*Lawrence Radiation Laboratory
Livermore, California*

ABSTRACT

Hydrodynamic calculations in conjunction with experiments provide an effective method for obtaining otherwise inaccessible information on high explosives. The credibility of the calculational program (code) is established by comparison with the steady state solutions for certain detonation problems obtained by the method of characteristics.

The machine calculation is then applied to specific problems in one- and two-dimensions to explain some of the difficulties an experimenter would encounter in attempting to measure the pressure at a detonation front.

INTRODUCTION

The ability to obtain a complete hydrodynamic solution to a given problem allows the experimenter to investigate areas of high explosive research that would otherwise be inaccessible; for example, the low pressure equation of state work using exploding cylinders that is reported in [1]. In addition, with a complete solution to a given problem available, the experimenter is better able to pose and to interpret simple experiments. Disagreement between the calculations and experiment is an indication that the physical model is not adequate.

Finite difference equations using the Von Neumann Q method [2,3] afford the technique to solve the partial differential equations of hydrodynamics in one- and two-space dimensions and time.

CHECKS ON THE NUMERICAL TECHNIQUE

In order to use a hydrodynamic code in a quantitative manner it is first necessary to establish the confidence level of the numerical technique. For geometries in one-space variable and time, the method of characteristics provides a closed form solution for a Chapman-Jouguet detonation. It is then very readily shown that the numerical technique can reproduce the

results to any desired accuracy [4]. For two-space variables and time a closed form solution for a detonation is not mathematically possible; however, the steady state solution for a detonation in two-space variables can be obtained by the method of characteristics and a numerical integration scheme. A fairly critical test of a code to calculate effects due to edge rarefactions is to compare a time-dependent code calculation with the solution by the method of characteristics.

A calculation was made of a detonation in plane geometry with a two-dimensional time-dependent hydrodynamic code, HEMP [3]. A steady state condition was noted by examining the parameters at a fixed distance behind the detonation front and observing that they did not change with time. In a two-dimensional steady state detonation, the rarefactions from the lateral edges extend into the fluid up to the detonation front itself. The time-dependent calculation showed that the steady state condition was approached from the outside to the inside of the fluid. Figure 1 shows a steady state detonation, as calculated by the method of characteristics [5], compared to a time-dependent calculation where the detonation has proceeded a distance equal to four times the original high explosive thickness. At a fixed distance behind the front, parameters were compared after a length of burn of three and four thickness units. They were also compared to parameters calculated by the method of characteristics. The

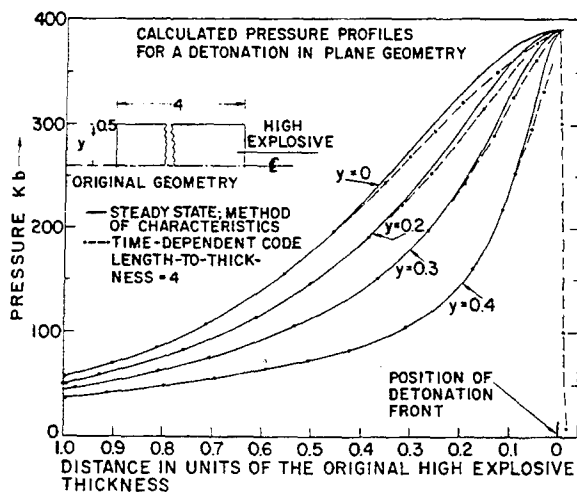


Fig. 1. Approach to steady state conditions for a time dependent calculation. The outside profiles reach a steady state before the profile along the axis.

agreement was to the fourth decimal place. These comparisons show that not only does the time-dependent code reach a steady state condition but it reaches the correct steady state condition. It can be seen from the figure that the time-dependent calculation has not yet reached a steady state for positions close to the front.

The calculations used Chapman-Jouguet (CJ) theory and a gamma law equation of state for the detonation product gases ($\gamma = 2.6536$, $P_{CJ} = 0.39$ mb, detonation velocity = 0.88 cm/ μ S, $\rho^0 = 1.84$ gm/cc). The numerical results for the profiles shown in Fig. 1 by the method of characteristics are given in [5].

Figure 2a shows a code calculation of an exploding copper cylinder as is used in conjunction with experiment to determine the equation of state at low pressures for the detonation product gases of an explosive [1]. The explosive

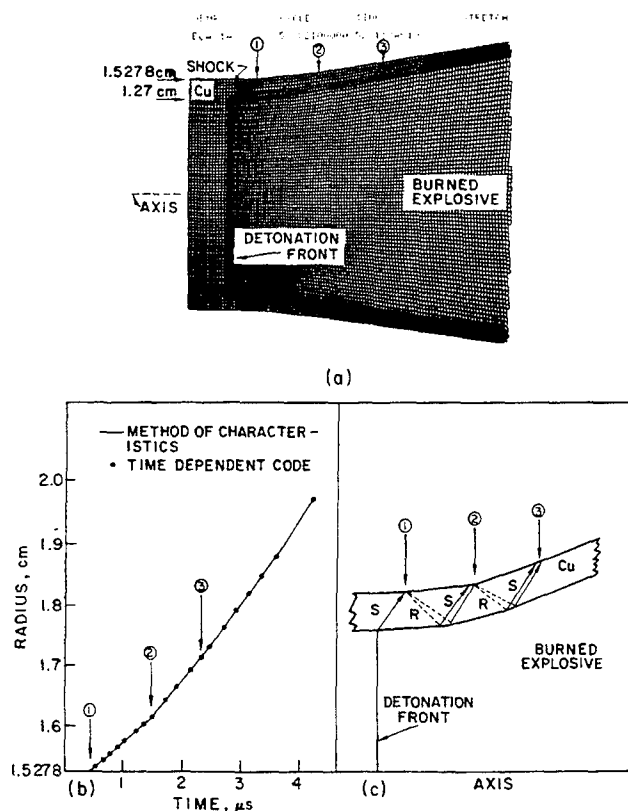


Fig. 2. (a) HEMP calculation of an explosive charge detonated inside a copper cylinder; (b) profile of the outside surface at a fixed position on the axis; (c) schematic view showing the shocks, S, and rarefactions R

used in this calculation was LX-04-1; the equation of state is given in [6]. The calculation was allowed to proceed in time until a steady state condition was reached as noted by comparing parameters at a fixed distance behind the front for different lengths of run and noting that they did not change. This calculation was compared with the same problem done by Dr. N. E. Hoskin, AWRE, Aldermaston, England, who used the method of characteristics and included the shocks and rarefactions in the copper cylinder. The two calculations agreed, on the average, to better than 10^{-2} μ sec for comparisons of the arrival times of the outside of the copper cylinder at a given radius. The numerical results are given in Table 1.

TABLE 1
Numerical Values for the Graph
Shown in Fig. 2b

Radius (mm) $R^0 = 15.278$	Time (μ sec) Method of Characteristics	Time (μ sec) HEMP Code
15.283	0.455	0.352
0.342	0.525	0.527
0.460	0.667	0.662
0.561	0.793	0.772
0.655	0.913	0.897
0.765	1.054	1.042
0.914	0.254	0.227
16.008	0.380	0.347
0.151	0.502	0.503
0.256	0.589	0.602
0.416	0.723	0.737
0.527	0.818	0.825
0.631	0.910	0.909
0.812	2.075	2.068
0.925	0.182	0.171
17.045	0.295	0.279
0.154	0.388	0.376
0.286	0.482	0.488
0.436	0.590	0.610
0.591	0.705	0.729
0.742	0.821	0.836
0.888	0.936	0.940
18.033	3.054	3.049
0.171	0.169	0.156
0.293	0.268	0.252
0.428	0.361	0.360
0.569	0.455	0.471
0.773	0.598	0.620
18.926	3.707	3.728
19.695	4.269	4.271

Figure 2b shows the radius-versus-time history at a fixed position on the axis of the outside surface of the copper cylinder as would be seen by a slit camera [1].

Figure 2c is a schematic view showing the origin of the breaks in the cylinder, called out by 1, 2, and 3. A time-dependent calculation was also made with one-fourth the number of zones used for the calculation shown here, and the agreement was again to 10^{-2} μ sec. These checks serve to establish that the numerical techniques used to solve the partial differential equation of hydrodynamics are sufficiently accurate such that the hydrodynamic code can be used with confidence for the analysis of hydrodynamic experiments.

APPLICATION TO DETONATION PRESSURE EXPERIMENTS

One of the main reasons for developing hydrodynamic codes is to be able to calculate the flow due to rarefactions. Calculations involving shocks and shock interactions can be made in a rather straightforward manner; it is the effect of rarefactions that cannot be readily calculated. It is the nature of hydrodynamics that rarefactions always overtake shocks. This effect can make experiments with high explosives very difficult to interpret. For example, consider the experimental problem of measuring a pressure at the detonation front after the detonation has reached a steady state. A convenient geometry would be to place a thin plate of metal at the end of an explosive charge that had a length-to-diameter ratio of about four and then to measure the initial front surface velocity for two thicknesses of the plate. In principle, the particle velocity at the high explosive metal interface can be determined by extrapolation from front surface velocity measurement for two thicknesses of metal; it is assumed that the relation between the front surface velocity and the particle velocity is known. With this information and the acoustic approximation [7] the pressure at the detonation front can be determined. Some of the difficulties associated with this technique are discussed in the following paragraphs.

Figure 3 shows a calculation of a shock induced in an aluminum disc by a charge of explosive that had an original length-to-diameter ratio of four. For the cylindrical geometry used in this calculation a steady state condition was reached a little after three diameters of explosive burn. (For the plane geometry discussed earlier a steady state for positions just behind the front had not yet been attained after four lengths of explosive burn.) The pressure profiles in the explosive before striking the disc are shown in Fig. 4a.

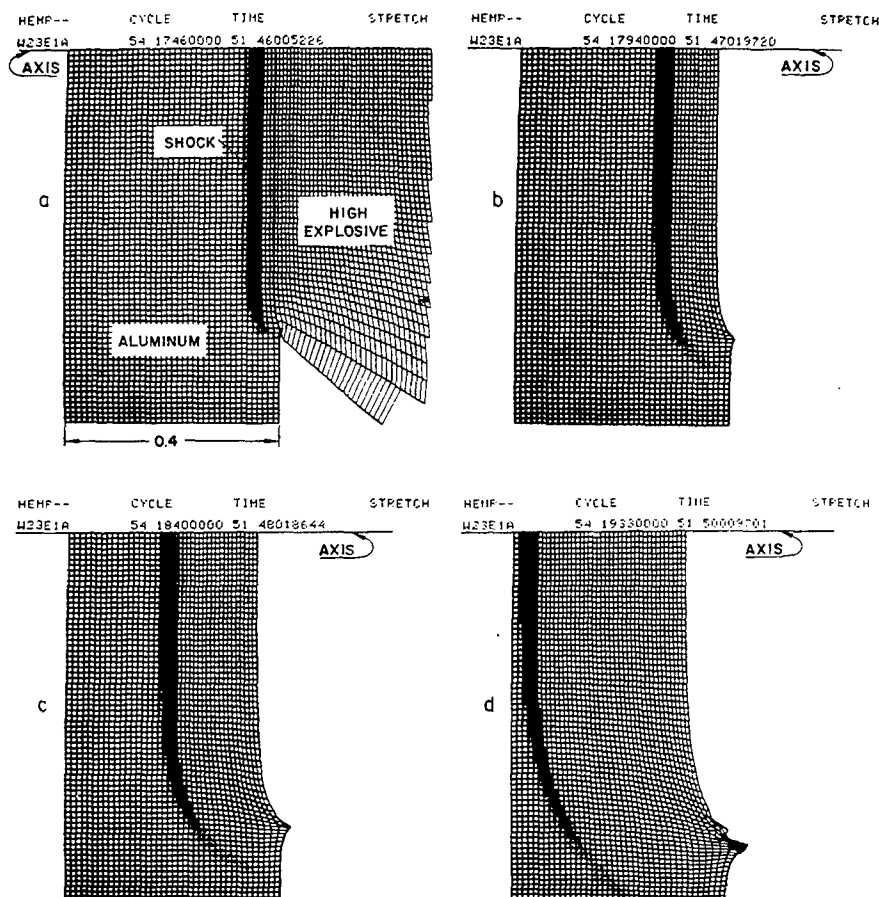


Fig. 3. HEMP calculation of a cylindrical explosive charge, length to diameter 4, in contact with an aluminum disc. For clarity the explosive is shown only for the first frame.

Figures 4b and 4c show the pressure profiles in the aluminum disc at three different times. It is noted that the peak pressure attenuates rapidly and that the pressure profiles steepen as the shock progresses into the disc. In one-space dimension the profiles would tend to become flatter rather than steeper as the shock wave progressed. The significance of these calculations is that the pressure wave attenuates very rapidly as it traverses the aluminum, due to the two-dimensional rarefactions present. The rapid drop in pressure will cause a tension wave to develop when the pressure wave reaches the free surface. The tension wave will greatly complicate the measurement of a front surface velocity by a distance-time technique since the material will decelerate during the measurement and, no doubt, will spall. Erroneous detonation pressures can be inferred from measurements if the experimenter is not fully aware of the severe effects of rarefactions.

In Fig. 4 it is seen that distance scales with respect to the charge diameter. The pressure profile t_3 in Fig. 4 will become t_1 across the same physical plate thickness if the charge diameter is made larger. There will be two effects on a front surface velocity measurement. First, the velocity corresponding to profile t_1 will be greater than that due to profile t_3 because the pressure attenuation is less. Second, there is a much smaller pressure gradient across the fixed dimension plate for the profile t_1 . Therefore, for the same base time measurement the effect of tensions will be less for profile t_1 than for profile t_3 .

If the detonation pressure is to be measured in this particular geometry, all the dimensions should be scaled by a factor that will allow sufficient time for the front surface velocity measurement to be made for a metal witness plate whose thickness is a small fraction of the high explosive diameter. However,

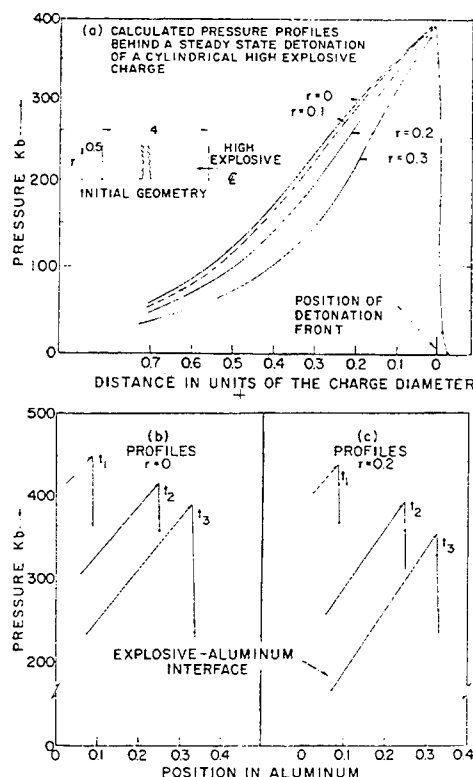


Fig. 4. Top: steady state detonation calculated with a time dependent hydrodynamic code. Bottom: pressure profiles along the axis, $r = 0$, and off the axis, $r = 0.2$, in an aluminum disc placed on the end of the charge above. See Fig. 3.

the plate thickness must not be chosen so small that the effects of the reaction zone are still present.

Code calculations allow the experimenter to obtain "behind the scene" information and to better choose the parameters used for a specific experiment. A more suitable geometry for making detonation pressure measurements is to design a one-dimensional experiment, but even here the effects of rarefactions are very pronounced.

Figure 5 shows the results of a plane one-dimensional calculation for a geometry that could be used to determine a detonation pressure experimentally. An aluminum witness plate has been placed on one end of a unit length of high explosive. A gamma law equation of state was used for the detonation product gases ($\gamma = 2.6536$, $P_{CJ} = 0.39$ mb). The figures show the progress of the pressure wave and the material velocity as the shock traverses the

aluminum. It can be seen that the peak transmitted pressure in the aluminum decays rapidly. This decay is due solely to the one-dimensional rarefaction behind the original detonation front. The physics model used here does not include a reaction zone in the explosive. The pressure wave in the aluminum would have additional structure if the reaction zone were included.

In Fig. 6 the pressure at the shock front is plotted as a function of the shock distance in the aluminum plate. A similar plot of the particle velocities would show the same shape. It is the particle velocity at essentially zero thickness that is required to determine a detonation pressure by the acoustic approximation [7]. This velocity can be determined experimentally by measuring the front surface velocity for two thicknesses of metal and then extrapolating to find the material velocity at the high explosive metal interface. The usual assumption is that the particle velocity is one-half the free surface velocity where the free surface velocity is obtained by a distance time experiment. With reference again to Fig. 6 it is seen that a linear extrapolation should not be attempted unless the experiment has been performed with the ratio of plate thickness to charge length less than about 0.1. If the two velocity measurements are made with ratios greater than this, the inferred detonation pressure will be too low since this curve is really not linear.

ACOUSTIC APPROXIMATION

As is well known, the acoustic approximation assumption is that the detonation products Hugoniot has a slope equal to $-\rho^0 D$ at the metal Hugoniot point in the P - U plane. Chapman-Jouguet theory states that the slope of the Hugoniot is also equal to $-\rho^0 D$ in the P - U plane at the detonation front. Therefore, for measurements made near the detonation pressure, where the effect of any curvature in the detonation products Hugoniot is small, the acoustic approximation is very nearly exact for a Chapman-Jouguet detonation.

At this point it is interesting to try out the acoustic approximation. For the problem shown in Fig. 5 the code calculation gives, $P = 0.450$ mb and $U = 0.204$ cm/ μ sec for the values of the pressure and the particle velocity in the metal at the explosive interface. The detonation velocity and the initial density of the explosive are, respectively, $D = 0.88$ cm/ μ s and $\rho^0 = 1.84$ gm/cc.

Substitution into the acoustic approximation, $P_d = 1/2 [P + \rho^0 D U]$, will give the detonation

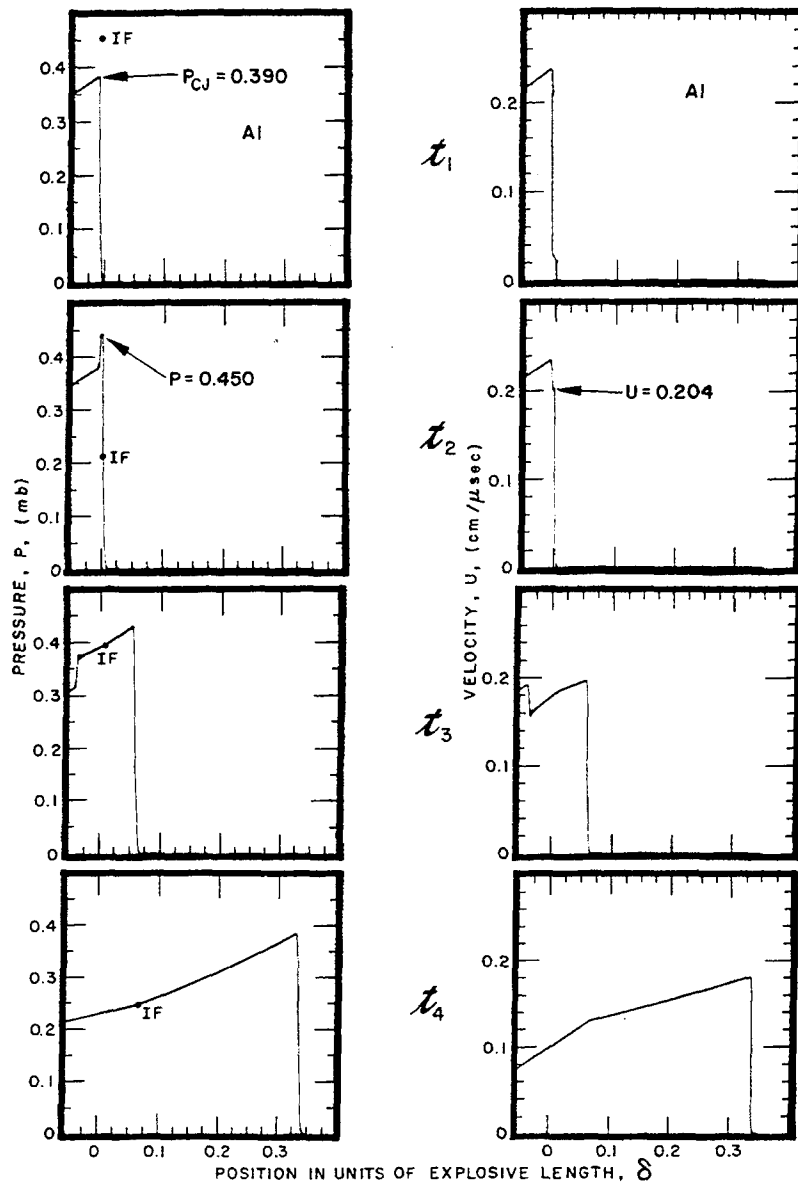


Fig. 5. Explosive in contact with an aluminum plate. IF = interface between explosive and aluminum. t_1 = pressure and material velocity profiles just before explosive strikes plate. t_2 = pressure and velocity just after explosive strikes plate. t_3 = shocks in explosive and plate. t_4 = pressure and velocity at a late time.

pressure P_d . The result of the substitution is: $P_d = 0.390$ mb, which is, in fact, the Chapman-Jouguet detonation pressure that was used in the calculation. This calculation provides a further check on the codes.

THE EFFECT OF TENSIONS

Usually the particle velocity in the metal witness plate is obtained by a measurement of the time required for the metal front surface to

traverse a given distance. The code calculations show that the front surface velocity is decelerated by a tension wave that originates when the shock wave reaches the front surface. A different average velocity will be recorded if the base distance of the measurement is changed [9]. The hydrodynamic codes can be used to monitor the magnitude of the tension and the extent of its effect on the front surface velocity as a guide to the experimentalist.

When the calculation just described is repeated with magnesium as a witness plate

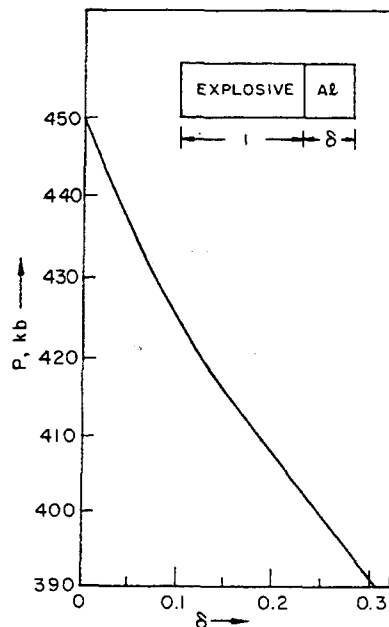


Fig. 6. Peak pressure, P , vs position, δ , (units of explosive length) for the shock wave traversing the aluminum plate of Fig. 5

instead of aluminum, the rate of decay for the pressure pulse is less. Consequently, the tension at the front surface is less for any given ratio of plate thickness to charge length. The use of magnesium as a witness plate allows a ratio of plate thickness to charge length a little greater than the 0.1 for aluminum since the decay curve corresponding to Fig. 6 is not as rapid. Also, for measurements made in this ratio, there are no tension waves present for a reasonable time. The hydrodynamic reason for these effects is that the magnesium has a lower shock impedance than has this particular explosive, and a more flat-top wave is transmitted into the magnesium than is transmitted into the higher-impedance material, aluminum.

APPLICATION TO REACTION ZONE THICKNESS MEASUREMENTS

The reaction zone pressure and velocity distribution span a fixed distance in space. Therefore, scaling the explosive dimensions will have no effect on the reaction zone pressure profile, but will, of course, change the pressure profiles over fixed distances for the flow behind the detonation pressure. The very difficult problem of obtaining the correct reaction zone thickness by experimental front

surface measurements on plates of varying thicknesses without the aid of a hydrodynamic code is discussed in the following paragraphs.

Figure 7 shows the calculated attenuation of the pressure in an aluminum plate in contact with a plausible reaction zone pressure profile. The other hydrodynamic parameters of the profile were chosen consistent with the Von Neumann detonation model. It is seen that the peak pressure decays at a decreasing rate as the pulse traverses the plate. Front surface velocity measurements for plates a few reaction zones in thickness will show a sharp drop in velocity due to the early rapid pressure decay. For measurements made on plates of increasing thicknesses the velocities will fall off slower because the rate of pressure decay is less. It is apparent from Fig. 7 that measurements made on a discrete number of plate thicknesses would show a break in velocity-versus-thickness curve. This break in the curve might erroneously be interpreted as the end of the reaction zone. There will be another break in the velocity curve that corresponds to the Chapman-Jouguet state. However, the slow fade out of the pulse will make this state difficult to determine and could very well lead to an assumed Chapman-Jouguet pressure that is too high.

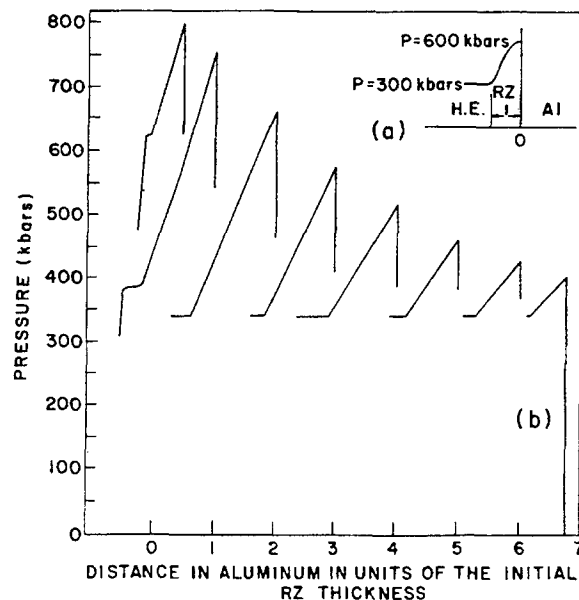


Fig. 7. Calculated pressure profiles in an aluminum plate induced by the reaction zone of an explosive. (a) Initial profile of the reaction zone, RZ, corresponding to a detonation pressure of 300 kb and a spike twice this value. (b) Pressure profiles in the aluminum at successive times. The peak pressure decays rapidly at first and then at a slower rate as the profiles tend to flatten.

The experimental problem is further complicated by tensions and possible spall. Thin plates have sharp pressure profiles that will cause large tensions. For thicker plates the profiles flatten out and the induced tension when they arrive at a front surface will be less.

A recent paper by A. N. Dremin [8] states for the same reasons as above that the properties of witness plates used in front surface velocity measurements result in a reaction zone that is too thin and in apparent breaks in the explosive pressure profile.

Interference of the reaction zone with a Chapman-Jouguet pressure determination can be avoided by choosing a plate thickness that is thought to be too large to show the effect of the pressure spike. A hydrodynamic code calculation can then be made where the detonation pressure is adjusted until the calculation matches the experimental measurement on the witness plate [6].

CONCLUSION

It has been shown that hydrodynamic codes are capable of accurately solving the equations of hydrodynamics. They, therefore, offer the means to perform calculations in conjunction with experiments and use an iterative technique to obtain otherwise inaccessible data [1]. In addition, they serve an important role in setting up and interpreting experiments in high explosive research.

REFERENCES

1. J. W. Kury et al., "Metal Acceleration by Chemical Explosives," this symposium.
2. J. Von Neumann and R. D. Richtmyer (1950), *J. Appl. Phys.* 21, 232.
3. M. L. Wilkins, "Methods in Computational Physics," Vol. 3, Academic Press Inc., N.Y., 1964, pp. 211-263.
4. "Les Ondes de Detonation," pp. 165-175 (Pro. Collog. held at Gif-sur-Yvette, France, Aug. 28-Sept. 2, 1961), Editions du Centre National de la Recherche Scientifique, Paris.
5. G. T. Richards, UCRL 14228, 1965, Lawrence Radiation Laboratory.
6. M. L. Wilkins, B. Squier, and B. Halperin, UCRL 7797, 1964, Lawrence Radiation Lab.
7. R. E. Duff and E. Houston, 1955, *J. of Chem. Phys.*, Vol. 23, No. 7, July 1955.
8. A. N. Dremin and K. K. Shvedov, *Zhurnal Prikladnoi Mekhaniki i Tekhnicheskoi Fiziki* No. 2, 1964, pp. 154-159.
9. B. D. Lambourn and J. H. Harley, "The Calculation of the Hydrodynamic Behaviour of Plane One-Dimensional Explosive/Metal Systems," this symposium.

CALCULATION OF UNSTEADY 2-D FLOWS BY VARIOUS NUMERICAL METHODS

A. Vidart, P. Béatrix, Y. Chevalier and H. Bouchon
*Commissariat à l'Energie Atomique
France*

ABSTRACT

Four numerical methods are studied and developed for the treatment of unsteady one or two dimensional flows. The state which is studied is the solid state in the range of pressures obtained by shock waves.

In a first part, the principle of the methods and the equations used are exposed in the following cases:

1. Use of finite differences schemes with pseudo-viscosity in Lagrangian coordinates.
2. Use of "Particle In Cell" method modified in the way of evaluating the accelerations.
3. Use of "Particle and Gradient" method with a moving grid.
4. Use of the Generalized Integral method (Eulerian coordinates).

In a second part two applications are developed:

1. A sphere in copper, stricken by a converging shock wave (one dimension in space) treated with the first and the last of the four methods exposed.
2. The evolution of a metallic projectile looking like a plate-charge, thrown according to a law of velocity in terms of the inverse of the radius of the charge (two dimensions in space), and computed with the three first methods exposed.

The analysis of the results shows that many difficulties are still present in the use of the methods.

INTRODUCTION

The treatment of the propagation of shocks and of unsteady flows, in two dimensions of space, has been generally approached for many years, by the way of finite differences schemes in Lagrangian coordinates with pseudo-viscosity.

One may have seen, later on, appear the methods based on particles with a fixed grid, as the "Particle In Cell" method proposed by the mathematicians of Los Alamos. We have tried here two other methods, one with particles and "cells of gradient" where the grid may be moved with a uniform velocity and the other, in a mixed Eulerian-Lagrangian system of coordinates,

named the method of the generalized integral which has been developed by the Professors Lattes and Lions. We have also used the two classical methods signaled above, trying to improve "the Particle In Cell" method in the case of solids.

We shall precise, at first, the principles of the four numerical methods and present, after that, some applications allowing a comparison between these treatments.

STUDIES OF THE NUMERICAL METHODS

All these methods introduce finite-differences schemes or integral forms on an interval

of time Δt . We shall not be concerned with the mathematical foundation of these different solutions but just expose some of the basic principles of each.

Finite Differences Scheme in Lagrangian Coordinates

This scheme is directly issued from the finite difference scheme proposed by Richtmyer in one dimension of space and has been exposed in two papers from W. B. Goad and M. L. Wilkins [1,2]. The shocks are treated with a pseudo-viscosity proportional to the square of the variation of the volume of the cell with respect to the time.

"Particle In Cell" Method

This method has been described by M. Evans and F. H. Harlow in papers published in 1957 and 1959 [3,4]. We used it in the case of flows in solid state. A pseudoviscosity proportional to the divergence of the velocity vector in the cell, has been added for the treatment of shocks. To try to improve the repartition of the particles in the cells when you have large distortions in the flow, we modified the formulas giving the acceleration in phase I: the equations of the equilibrium, applied to the center of a cell, conduct to the following expressions in two dimensional plane geometry:

$$\ddot{X}_{(i)(j)} = \frac{1}{\rho_{(i)(j)}} \frac{P_{(i-1)(j)} - P_{(i+1)(j)}}{\Delta x}$$

$$\ddot{Y}_{(i)(j)} = \frac{1}{\rho_{(i)(j)}} \frac{P_{(i)(j-1)} - P_{(i)(j+1)}}{\Delta y}$$

These accelerations for the center of the cell $(i)(j)$ depend only on the values of the pressure in the cells $(i-1)(j)$ and $(i+1)(j)$ or $(i)(j-1)$ and $(i)(j+1)$.

To obtain a more general contribution of all the cells surrounding the cell $(i)(j)$ we used the integral definition of the gradient:

$$\text{grad } f(M) = \lim_{Q \rightarrow 0} \frac{1}{Q} \int_C f(P) \mathbf{n} ds$$

and we applied also

$$\rho \frac{d\mathbf{V}}{dt} = - \text{grad } p$$

at each of the four vertexes of the cell that is to say, at the points:

$$A = \left(i - \frac{1}{2}\right) \left(j - \frac{1}{2}\right) \quad B = \left(i + \frac{1}{2}\right) \left(j - \frac{1}{2}\right)$$

$$C = \left(i + \frac{1}{2}\right) \left(j + \frac{1}{2}\right) \quad D = \left(i - \frac{1}{2}\right) \left(j + \frac{1}{2}\right)$$

The acceleration of the center of the cell becomes then:

$$\ddot{X}_{(i)(j)} = \frac{1}{4} (\ddot{X}_A + \ddot{X}_B + \ddot{X}_C + \ddot{X}_D)$$

and the same for $\ddot{Y}_{(i)(j)}$.

For example, the explicit equation for $\ddot{X}_{(i)(j)}$ is:

$$\ddot{X}_{(i)(j)} = \frac{1}{2\Delta x} \times \left\{ \frac{[p_{(i-1)(j-1)} - p_{(i)(j-1)}] + [p_{(i-1)(j)} - p_{(i)(j)}]}{\rho_{(i-1)(j-1)} + \rho_{(i)(j-1)} + \rho_{(i)(j)} + \rho_{(i-1)(j)}} + \frac{[p_{(i)(j-1)} - p_{(i+1)(j-1)}] + [p_{(i)(j)} - p_{(i+1)(j)}]}{\rho_{(i)(j-1)} + \rho_{(i+1)(j-1)} + \rho_{(i)(j)} + \rho_{(i+1)(j)}} + \frac{[p_{(i)(j)} - p_{(i+1)(j)}] + [p_{(i)(j+1)} - p_{(i+1)(j+1)}]}{\rho_{(i)(j)} + \rho_{(i+1)(j)} + \rho_{(i)(j+1)} + \rho_{(i+1)(j+1)}} + \frac{[p_{(i-1)(j)} - p_{(i)(j)}] + [p_{(i-1)(j+1)} - p_{(i)(j+1)}]}{\rho_{(i-1)(j)} + \rho_{(i)(j)} + \rho_{(i-1)(j+1)} + \rho_{(i)(j+1)}} \right\}$$

The equation of state for the solid was of the Mie Gruneisen form with a development in

$$\left(\frac{\rho}{\rho_0} - 1\right)$$

until the term of second order to compute the isentropic part.

"Particle and Gradient" Method (Pique-Peg)

This method has been developed in our laboratory in order to obtain a tool well adapted to large distortions for which the Lagrangian techniques appear to be inconvenient.

The mechanical equations for a perfect fluid are easily handled when written as follows:

$$\frac{du}{dt} + \frac{1}{\rho} \frac{\partial p}{\partial x} = 0 \quad \frac{dv}{dt} + \frac{1}{\rho} \frac{\partial p}{\partial y} = 0$$

$$\frac{dp}{dt} + \rho \text{div } \mathbf{V} = 0 \quad \frac{dp}{dt} = a^2 \frac{d\rho}{dt}$$

$$\frac{dx}{dt} = u \quad \frac{dy}{dt} = 0.$$

(a = a local sound velocity.)

The method consists in following the motion of a number of material "particles" (or "molecules") which are supposed to represent the actual continuous flow. A pressure, a density and a velocity (two components) are attached to each one. The grid devised for the PIC method is employed in order to locate the different particles and in the search of neighbours. Moreover, at each time the grid cells are given values of the four mechanical variables (p, ρ, u, v) by simply averaging over the inner molecules.

The particles are moved independently with the help of finite difference equations:

$$[\Delta x]_n^{n+1} = u_n \Delta t \quad [\Delta u]_n^{n+1} = \left(-\frac{1}{\rho} \frac{\partial p}{\partial x} \right)_n \Delta t, \text{ etc.}$$

The gradients are computed by the general and useful method proposed by Kolsky. Let us suppose a convex polygonal contour (C) surrounding an area (S) and approximately centered in A_0 ; we may write for an arbitrary function Q :

$$\left[\frac{\partial Q}{\partial x} \right]_{A_0} = \frac{1}{S} \int_C q dy$$

$$\left[\frac{\partial Q}{\partial y} \right]_{A_0} = -\frac{1}{S} \int_C q dx$$

or using the known values of Q at the vertexes of the polygonal line B_1, B_2, \dots, B_ϕ :

$$\left[\frac{\partial Q}{\partial x} \right]_{A_0} = \frac{\sum_{i=1}^{\phi} (Q_i y_{i+1} - Q_{i+1} y_i)}{\sum_{i=1}^{\phi} (x_i y_{i+1} - x_{i+1} y_i)}$$

$$\left[\frac{\partial Q}{\partial y} \right]_{A_0} = -\frac{\sum_{i=1}^{\phi} (Q_i x_{i+1} - Q_{i+1} x_i)}{\sum_{i=1}^{\phi} (x_i y_{i+1} - x_{i+1} y_i)}$$

The contour is drawn through the grid cells surrounding the one in which A_0 happens to be and it links fictitious particles (to which the cell values of the mechanical variables are assigned) located at the barycenter of the inner molecules of each square.

The grid is allowed to move by uniform translation so that we may control its velocity

with respect to the molecules and consequently adjust the inherent pseudoviscosity.

Various modifications or tentatives improvements to this method have been tested:

(a) We tried to treat differently the particles belonging to a particular cell according to their position inside the square. In particular we used two circuits instead of a single one for the gradient computation and averaged the results. (First modified version.)

(b) We endeavoured to smooth slightly and at each time step, the field of the mechanical variables. This is equivalent to the addition of pseudo-viscosity and seems to be extremely efficient. (Second modified version.)

Shocks may be dealt with the addition of pseudoviscosity; as regards free surfaces and interfaces it is convenient to use bicharacteristics for the grid of the PIC method permits one to interpolate the mechanical variables in any point with respect to the neighbouring particles.

Method of the Generalized Integral

Such a name is given to an implicit and probably new method to integrate the hydrodynamic equations.

This method is based on the coupled use of Lagrangian and Eulerian coordinates and on the transformation from one system into the other.

Equations of the Problem — In Eulerian coordinates, it is the classical system of equations in a geometry with cylindrical symmetry; that is to say (coordinates r, z).

$$\frac{\partial u}{\partial t} + u \frac{\partial u}{\partial r} + v \frac{\partial u}{\partial z} + \frac{1}{\rho} \frac{\partial p}{\partial r} = 0$$

$$\frac{\partial v}{\partial t} + u \frac{\partial v}{\partial r} + v \frac{\partial v}{\partial z} + \frac{1}{\rho} \frac{\partial p}{\partial z} = 0$$

$$\frac{\partial p}{\partial t} + u \frac{\partial p}{\partial r} + v \frac{\partial p}{\partial z} + \rho \left(\frac{\partial u}{\partial r} + \frac{u}{r} + \frac{\partial v}{\partial z} \right) = 0$$

$$\frac{\partial E}{\partial t} + u \frac{\partial E}{\partial r} + v \frac{\partial E}{\partial z} + \frac{p}{\rho} \left(\frac{\partial u}{\partial r} + \frac{u}{r} + \frac{\partial v}{\partial z} \right) = 0.$$

In Lagrangian coordinates, you obtain:

$$\frac{du}{dt} + \frac{1}{\rho} \frac{\partial p}{\partial r} = 0 \quad (2)$$

$$\frac{dv}{dt} + \frac{1}{\rho} \frac{\partial p}{\partial z} = 0 \quad (\text{Cont.})$$

$$\begin{aligned} \frac{d\rho}{dt} + \rho \operatorname{div} \mathbf{V} &= 0 \\ \frac{dE}{dt} + \frac{p}{\rho} \operatorname{div} \mathbf{V} &= 0. \end{aligned} \quad (2)$$

\mathbf{V} is the velocity vector and

$$\operatorname{div} \mathbf{V} = \frac{\partial u}{\partial r} + \frac{u}{r} + \frac{\partial v}{\partial z};$$

the pseudoviscosity is given by

$$q = G(\rho, \operatorname{div} \mathbf{V}).$$

These last equations are used for the numerical integration of the system.

Integration of the System — Exact integral relations.

The equations have the following shape:

$$\frac{df}{dt} = -g(M, t).$$

They are expressed for the point M at the time t . By an explicit calculus* using especially the transformation between Eulerian and Lagrangian coordinates, it is possible to write, supposing that g is continuous, what is precisely the reason for the introduction of the pseudoviscosity q , needed to obtain the uniqueness of the solution:

$$f(M, t_0 + \Delta t) = f(M^*, t_0) + \int_{t_0}^t g(m(\tau), \tau) d\tau$$

where $m(\tau)$ represents the intermediate position occupied at the instant τ by the particle which occupied the positions M^* and M , respectively, at t_0 and $t_0 + \Delta t$.

Applying this result to the Eqs. (2), we obtain:

$$\begin{aligned} u(M, t_0 + \Delta t) &= u(M^*, t_0) - \int_{t_0}^{t_0 + \Delta t} \frac{1}{\rho} \frac{\partial(p+q)}{\partial r} d\tau \\ v(M, t_0 + \Delta t) &= v(M^*, t_0) - \int_{t_0}^{t_0 + \Delta t} \frac{1}{\rho} \frac{\partial(p+q)}{\partial z} d\tau \\ \rho(M, t_0 + \Delta t) &= \rho(M^*, t_0) - \int_{t_0}^{t_0 + \Delta t} \rho \operatorname{div} \mathbf{V} d\tau \end{aligned} \quad (3)$$

(Cont.)

$$E(M, t_0 + \Delta t) = E(M^*, t_0) - \int_{t_0}^{t_0 + \Delta t} \left[\frac{p+q}{\rho} \operatorname{div} \mathbf{V} \right] d\tau. \quad (3)$$

It is therefore necessary to make a connection between any point M at the time $t_0 + \Delta t$, and the corresponding point M^* at the time t_0 . For that, starting from the equation

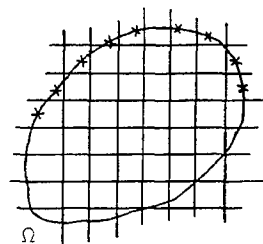
$$\frac{dm(t)}{dt} = \mathbf{V}(m(t), t)$$

we obtain by integration by parts between t_0 and $t_0 + \Delta t$:

$$M(t_0 + \Delta t) - M^*(t_0) = \Delta t \mathbf{V}(M(t_0 + \Delta t), t_0 + \Delta t) - \int_{t_0}^t (\tau - t_0) \frac{\partial \mathbf{V}(m(\tau), \tau)}{\partial \tau} d\tau. \quad (4)$$

This equation, as the other ones, is implicit. To integrate numerically the system, it is now necessary to estimate the integrals which appear in the second members of the Eqs. (3) and (4).

Discrete Formulas and Principle of the Iterative Algorithm — Some points are given along the frontier at the instant t_0 . The motion



of these points between t_0 and $t_0 + \Delta t$ is first computed and this gives the frontier at the instant $t_0 + \Delta t$ and the area Ω at the same time. In Ω we choose points placed at the nodes of a mesh, where we want to compute the hydrodynamics variables.

At each of these points M , a position M^* is connected. In M^* , an evaluation by interpolation of the quantities $f(M^*, t_0)$ is made. For a first iteration, one can be satisfied with the evaluation $\Delta t g(M^*, t_0)$ of the integral in the first part of the equations. Like that a first approximation of the quantities such as $f(M, t_0 + \Delta t)$ is easy to get. Later on, in the iterations, one can estimate the integrals such as:

$$\int_{t_0}^t g[m(\tau), \tau] d\tau$$

*Paper to be published by Pr Lattes and Pr Lions.

by mean of

$$\frac{\Delta t}{2} [g(M, t_c + \Delta t) + g(M^*, t_0)] .$$

The procedure is repeated up to the convergence.

Characteristics Points of this Method —
The method, which has been described briefly, presents the following advantages:

- It is very general; it may be applied to any geometry, plane, cylindrical or spherical with one, two or three dimensions in space.
- It can work with a variable step in time.
- The problem of doing a new mesh does not exist, for this operation is done implicitly by the choice of the points where you want to execute the computing part.
- The mesh, defined at the time t , can be absolutely the one you want and be independent of the initial mesh at t_0 .
- The boundary conditions can be very diversified.

NUMERICAL APPLICATIONS

Two applications have been chosen:

Comparison between the generalized integral method and the method with Lagrangian coordinates (one dimension of space).

This example deals with a metallic sphere of copper with an outside radius of one hundred millimeters. The equation of state of the copper was taken in a PACK EVANS and JAMES form, the initial density was 8.92 T/m^3 .* The outside surface of the sphere was submitted to a law of pressure having the following characteristics:

$$p = \begin{cases} \frac{1}{2} \frac{p_{\max}}{1 - \cos \pi(t/t_{\max})} & \text{for } 0 \leq t \leq t_{\max} \\ p_{\max} \left[1 - \frac{p_{\max}}{\tau} (t - t_{\max}) \right] & \text{for } t_{\max} \leq t \\ & \text{and } t \leq t_{\max} + \frac{\tau}{p_{\max}} \\ 0 & \text{for } t \geq t_{\max} + \frac{\tau}{p_{\max}} \end{cases}$$

*One ton = 1000 kilograms.

with

$$p_{\max} = 400 \text{ Kbar}$$

$$t_{\max} = 50 \times 10^{-8} \text{ s}$$

$$\tau = 500.$$

The steps of space and of time were of 1 mm and $2 \times 10^{-8} \text{ s}$ for the Lagrangian method and 2 mm and $1 \times 10^{-8} \text{ s}$ for the generalized integral method.

The graphs 1, 2 and 3 show us the results obtained respectively for:

- the position of the maximum of density versus time (graph 1),
- the position of the free surface versus time (graph 2),
- the curves of density versus the radius at two different times (graph 3).

The generalized integral method give us results whose general aspect is correct but the velocity of propagation of the shock is lower than the one in the Lagrangian method.

This difference is probably due to the way of taking in account the boundary conditions and in fact this point is very sensitive in this method.

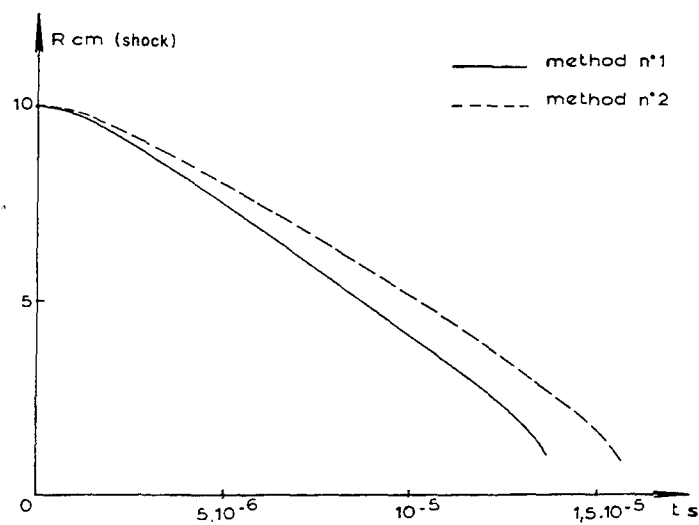
A systematic study is on hand at the present time. Some bidimensional results in a spherical geometry are also expected and will be published later on.

Evolution of a Projectile Looking Like a Plate Charge

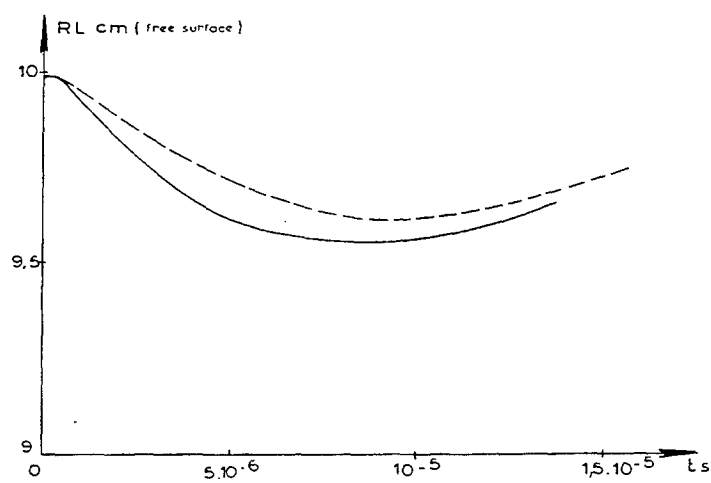
This example allows the comparison between the method in Lagrangian coordinates (method 1), the modified "particles in cell" (method 2) and the "particles and gradient" (method 3). The geometry is cylindrical with two dimensions of space.

The characteristics of the pellet are:

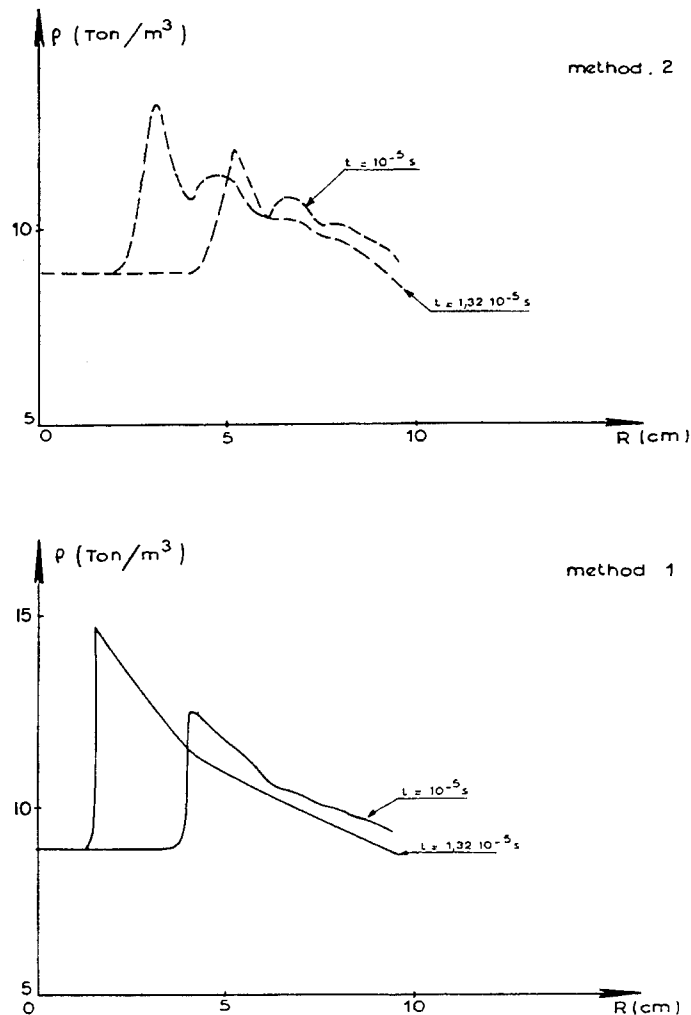
- geometrical shape: portion of sphere obtained by the rotation along the axis of the area limited by two concentric circles, a radius and the axis, the angle between the axis and the radius being 40° ;
- dimensions: the radius of the two circles are $R_0 = 143 \text{ mm}$, and $R_1 = 126.14 \text{ mm}$;



Graph 1



Graph 2



Graph 3

- the weight of the projectile is four kilograms;
- the modula of the initial velocities of the different points of the projectile are given by a law in terms of the inverse of the radius; the initial angle between the velocity vector and the axis is given in each point by another relation in terms of the distance from the point to the axis.

Graph 4 is a picture of the projectile at time zero. The velocity of the center of gravity is about 1700 m/s.

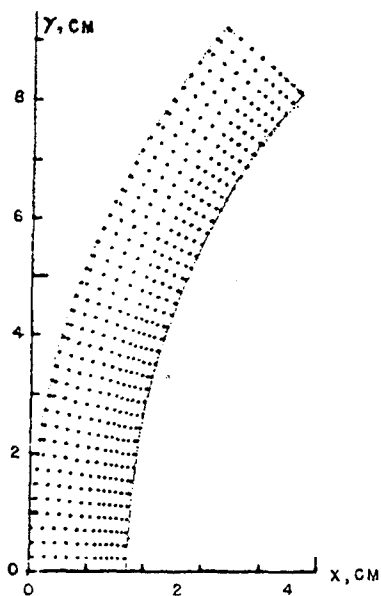
The shapes of the projectile given by the different methods are represented on the 5 through 10 at the time $T = 70 \times 10^{-6} \text{ s}$.

Graph 5 is a comparison between the PIC method and the Lagrangian method.

The graphs 6 through 10 give a comparison between Lagrangian method and the different versions of Pique-Peg method, that we have described before.

Although the PIC method results are not good fits to the Lagrangian results, we can say that the second modified version of Pique-Peg method, with a velocity of the grid of 1600 m/s, gives a pretty good agreement.

In Lagrangian method, we have made a complete calculation with the explosive behind the pellet. Therefore, a law of velocity is not necessary.



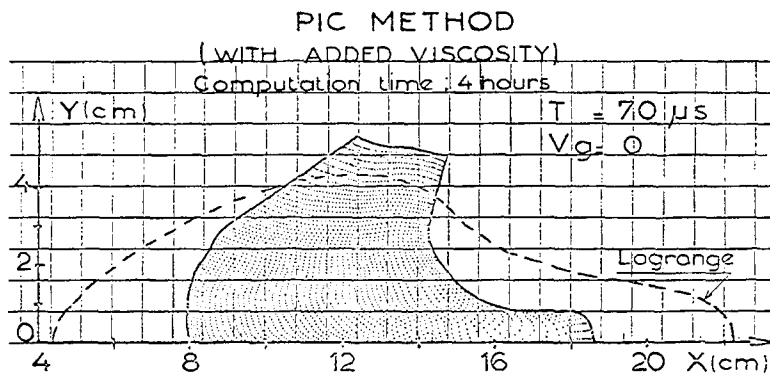
Graph 4

The explosive was initiated spherically on all its outside surface. It was possible then to compare the shape of the actual projectile, obtained by flash X rays, radiographs and the shape given by the computer.

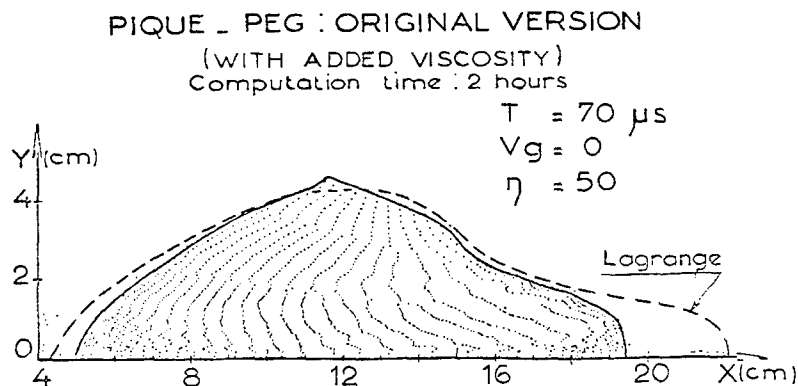
Graphs 11 and 12 show this comparison. The agreement is quite good, especially for the front part of the projectile. On graph 12, the rear of the pellet in the computed version is late; we suppose it is due to the fact that after 40×10^{-6} s, we stopped to compute the explosive and the effect of the burned gas was not completely achieved.

In conclusion, this study confirms that it is possible to get very good quantitative results with Lagrangian methods when the distortion allows you to use it.

The methods with particles are always quite good in qualitative results and we are trying to get good quantitative results with the Pique-Peg method.



Graph 5

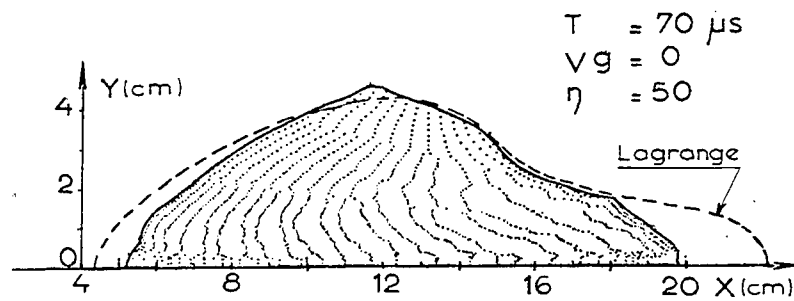


Graph 6

PIQUE - PEG : FIRST MODIFIED VERSION

(WITH ADDED VISCOSITY)

Computation time : 2 hours 30 minutes

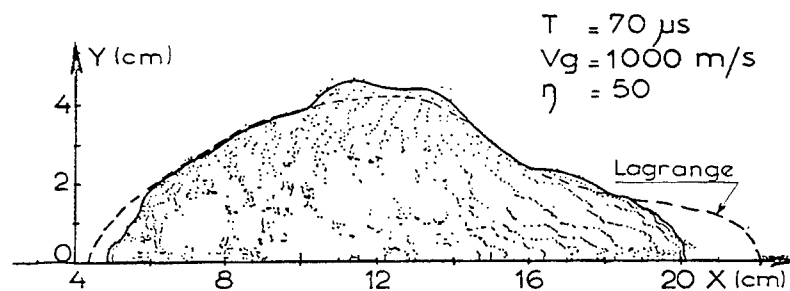


Graph 7

PIQUE - PEG : FIRST MODIFIED VERSION

(WITH ADDED VISCOSITY)

Computation time: 2 hours 30 minutes

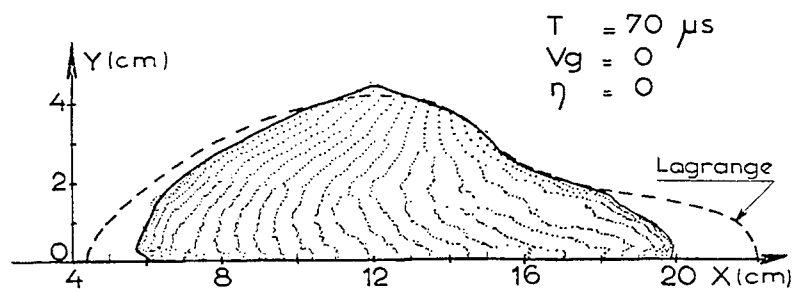


Graph 8

PIQUE - PEG : SECOND MODIFIED VERSION

(NO ADDED VISCOSITY)

Computation time : 2 hours 30 minutes



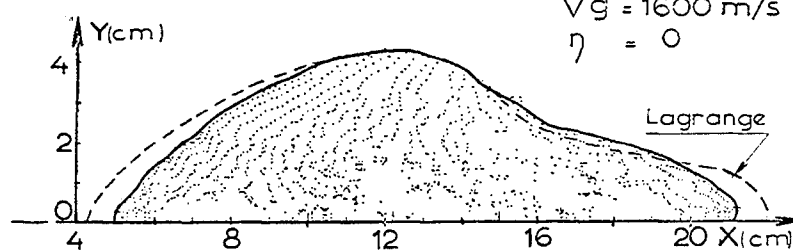
Graph 9

PIQUE - PEG: SECOND MODIFIED VERSION

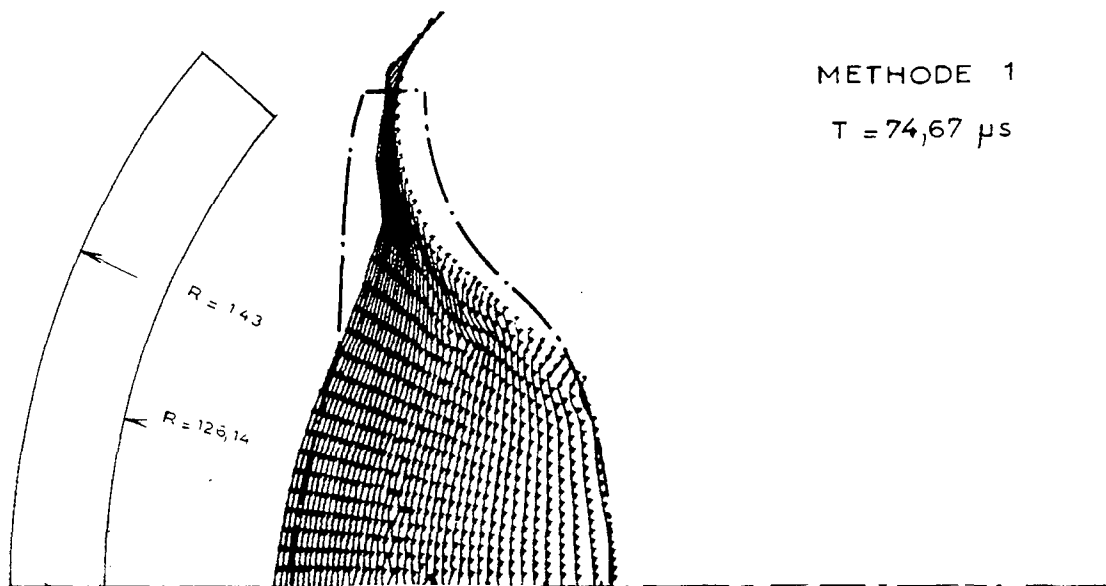
(NO ADDED VISCOSITY)

Computation time : 2 hours 30 minutes

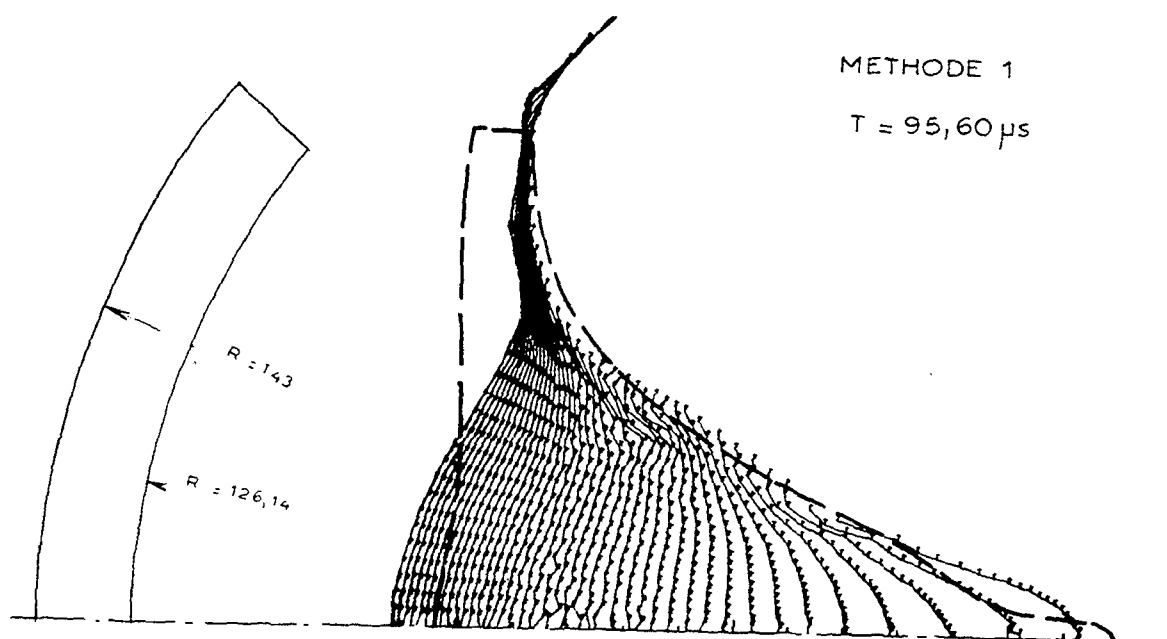
$$\begin{aligned} T &= 70 \mu s \\ Vg &= 1600 \text{ m/s} \\ \eta &= 0 \end{aligned}$$



Graph 10



Graph 11



Graph 12

REFERENCES

1. W. B. Goad, LAMS Report 2365, November 1960.
2. M. L. Wilkins, UCRL Report 7322, April 1963.
3. M. W. Evans and F. H. Harlow, LAMS Report 2139, November 1957.
4. F. H. Harlow, LAMS Report 2301, September 1959.

THE CALCULATION OF THE HYDRODYNAMIC BEHAVIOUR OF PLANE ONE DIMENSIONAL EXPLOSIVE/METAL SYSTEMS

B. D. Lambourn and J. E. Hartley
*Atomic Weapons Research Establishment
Aldermaston, Berkshire, England*

ABSTRACT

An outline is given of the code NIP which uses the method of characteristics to compute the motion of a plane compressible plate driven by a plane detonation wave at normal incidence. The virtue of the method is that it computes the fine structure of the motion unaffected by the computational "smears" and oscillations inherent in mesh methods. It is demonstrated how such calculations can provide guidance in the accurate determination of Chapman-Jouguet states. In addition NIP has been used in conjunction with precise free surface motion experiments to investigate spall phenomena in stainless steel plates.

1. INTRODUCTION

At the 3rd O.N.R. Symposium on Detonation, Aziz, Hurwitz and Sternberg [1] presented results of calculations on the motion of a rigid piston driven by a detonation wave at normal incidence. The charge and piston are considered to be semi-infinite so that the problem is one-dimensional (Fig. 1). In this paper the calculations are extended to the case where the piston is compressible, the emphasis now being on its early motion rather than the ultimate energy extracted from the explosive. The compressible material may be gas, liquid or solid, but after being traversed by the initial shock it is assumed to behave like a perfect fluid. For simplicity it will be referred to as a plate.

There are two principal ways of calculating one dimensional unsteady flows; these are the method of characteristics and mesh methods. In the method of characteristics, e.g., Refs. 2-5, the partial differential equations of motion are transformed to the total differential sound wave relations for compressible flow, which in turn are put into difference form for the purpose of the integration. In mesh methods, e.g., Refs. 6 and 7, the partial differential equations are themselves put into difference form and a viscous term is either directly or implicitly added to the pressure to smear out shocks.

Each method has its advantages and disadvantages. Characteristics are generally more accurate than mesh methods. For example, in

characteristics, discontinuities across shocks are preserved, and so are discontinuities in derivatives at the boundaries of rarefactions and compressions. Mesh methods smear out all these discontinuities. Interactions of waves with interfaces are treated correctly by characteristics and poorly by mesh methods. For example, after a smeared out shock traverses an interface, spurious oscillations appear in profiles behind reflected and transmitted waves, the entropies in the meshes adjacent to the interface are left incorrect [7], and rarefactions reflected from the interface are centred incorrectly [8]. On the other hand the methods of characteristics are much less flexible than mesh methods. The introduction of gas ahead of a plate or the steepening of a compression into a shock may require major changes to a characteristic program and only relatively minor changes to a mesh program. In general it may be said that mesh methods are used where greater flexibility is required and characteristics are used to give greater accuracy in particular situations.

Apart from blast wave calculations in which both characteristics and mesh methods have been used, little has been reported on the motion of plane compressible materials driven by normally incident detonation waves. Drummond [9] calculated the decay of initial shock strength by characteristics but did not take the calculation as far as the interaction with a free surface. Wilkins [10] has used mesh methods to calculate the spalling of uranium plates.

In this paper we briefly outline a characteristic program called NIP and compare its results firstly with a mesh program written by Pearson of A.W.R.E., and secondly with experimental determinations of free surface motion. NIP was first written about seven years ago. At that time experimental methods could barely resolve the arrival of the plate reverberations at the free surface. More recently accurate optical techniques such as the method developed by Eden and Wright [11] have not only clearly shown the plate reverberations, but have also demonstrated experimentally the decay of instantaneous free surface velocity between the arrival of the shock and the first plate reverberation. Although mesh methods show these phenomena, the smearing of waves and the spurious oscillations already referred to, often make it difficult to follow waves and to predict phenomena associated with specific waves. These difficulties are not present in a characteristic program, so NIP has been revived to aid the interpretation of experiments.

Section 2 of this paper briefly outlines NIP; Section 3 compares its results with the rigid piston theory and with a mesh method code; Section 4 compares NIP with experimental free surface trajectories. Finally, Section 5 shows how NIP can provide guidance in the analysis of experiments to determine Chapman-Jouguet states of explosives and conditions for spall in plates.

2. THE CHARACTERISTIC PROGRAM

The "Normal Initiation Program" (NIP) calculates by the method of characteristics, the one dimensional motion of a plane compressible plate driven by a normally incident detonation wave from an explosive charge of finite length. The plane of initiation of the explosive is taken to be unconstrained (Fig. 1) and detonation is assumed to take up immediately at the Chapman-Jouguet (C-J) state. The detonation wave in the charge is therefore followed by a rarefaction, the Taylor wave. When the detonation wave reaches the plate a shock is transmitted and is followed immediately by a rarefaction which progressively reduces the strength of the shock. Each particle of the plate is therefore shocked to a different entropy. Since heat conduction and viscous effects are neglected, and since in most cases there are no further shocks transmitted into the plate, each particle retains the entropy it is given initially by the shock. Drummond [9] has simplified his calculations on the transmission of a shock into a metal by assuming that the whole plate is at constant entropy. He justifies this on the

grounds that entropy change is of third order in shock strength and that shock strength is small in a metal. NIP does not make this approximation, and so it can also calculate the motion of very compressible materials in which entropy variations are not negligible.

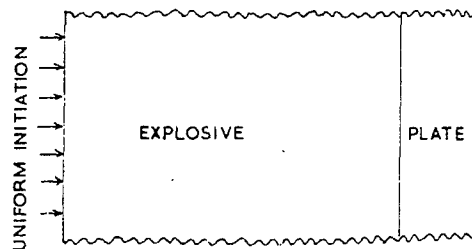


Fig. 1 - The 1D geometry calculated by NIP

In summarising NIP it is convenient to give a description of the physical behaviour of the plate before outlining the method of calculation used. These methods are similar to those described by Glennie [4] and Hoskin [5]. A more detailed account of the calculational features of NIP is being prepared [12].

The Physical Behaviour of the Plate

When the detonation wave meets the explosive-plate interface, a shock is transmitted into the plate and a shock or rarefaction is reflected into the detonation products (Fig. 2). Following the detonation wave is the Taylor wave, a rarefaction centred on the back surface of the explosive. This is transmitted into the plate as a rarefaction following the shock. When the shock reaches the free surface of the plate, the free surface starts moving and a rarefaction is reflected and propagates back through the plate to the interface. As the rarefaction is dispersive, its width increases. It is reflected off the interface as a compression, and the interface is accelerated to approximately the same velocity as the free surface. When the compression reaches the free surface a second rarefaction wave is generated and this process of compression and rarefaction continues throughout the flight of the plate.

Equations of State

The equation of state used for the detonation products is of perfect gas form, with specific internal energy e given as a function of pressure p and specific volume v by

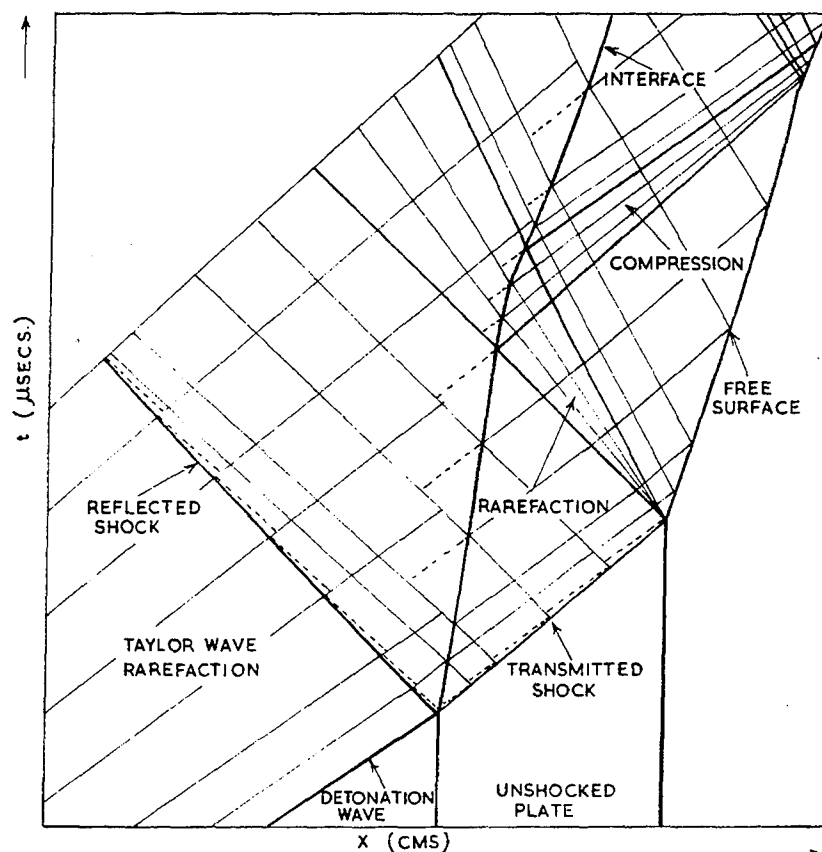


Fig. 2 - Network of characteristics (reflected shock)

$$e = \frac{pv}{\gamma - 1} \quad (1)$$

where γ is the adiabatic exponent. For the compressible plate material, a modified Tait equation of state [13] is used

$$e = \frac{(p + na)v - nav_0}{n - 1} \quad (2)$$

when n and a are constants. This is very convenient since Eq. (1) is a special case of (2) with $n = \gamma$, $a = 0$.

The adiabatic relation for the Tait equation of state can, for later application, be written

$$(p + a)v^n = Ae^{n(n-1)Z} \quad (3)$$

where Z is some function of entropy and A is a constant. The velocity of sound c is then given by

$$c^2 = n(p + a)v. \quad (4)$$

It can be shown that with suitable choice of constants n and a , Eq. (3) can be a very good

approximation to adiabats for metals calculated from more complicated equations of state over a wide range of pressures. These constants also give a good fit to the Hugoniot curve over the limited range of pressures that are likely to be encountered in NIP calculations.

The Hugoniot relation for a Tait like equation is

$$\frac{v}{v_0} = \frac{(n-1)(p+a) + (n+1)(p_0+a)}{(n+1)(p+a) + (n-1)(p_0+a)} \quad (5)$$

where p_0 , v_0 are pressure and specific volume ahead of the shock. Particle velocity u and shock velocity w can then be determined from the mechanical shock wave relations and are

$$u = u_0 \pm \sqrt{\frac{2(p-p_0)^2 v_0}{(n+1)(p+a) + (n-1)(p_0+a)}} \quad (6)$$

$$w = u_0 \pm \sqrt{\frac{v_0}{2} [(n+1)(p+a) + (n-1)(p_0+a)]} \quad (7)$$

where the + and - signs refer to forward and backward facing shocks respectively and u_0 is the particle velocity ahead of the shock.

Characteristics

The characteristics of one dimensional unsteady flow in the Eulerian plane are from Courant and Friedrichs [2].

$$dp + \rho c du = 0 \quad \text{on} \quad \frac{dx}{dt} = u + c \quad (8)$$

$$dp - \rho c du = 0 \quad \text{on} \quad \frac{dx}{dt} = u - c \quad (9)$$

$$dS = \begin{cases} \delta S \text{ across shocks} \\ 0 \text{ elsewhere} \end{cases} \quad \text{on} \quad \frac{dx}{dt} = u \quad (10)$$

where ρ is density, and S is entropy. Equation (8) represents a differential relation along the curve in (x, t) space whose trajectory is given by $dx/dt = u + c$. This is called a positive characteristic. Similarly (9) represents a negative characteristic. Equation (10) states that entropy is conserved on a particle path except across shocks. Equations (8), (9), and (10) represent differential relations along three directions through every point in the $x-t$ plane. Because each particle in the plate has a different entropy, it is convenient to consider also the characteristics in the Lagrangian plane. Here the differential relations along the characteristics are the same, but the trajectories of the characteristics are given by

$$\frac{d\ell}{dt} = \pm \frac{\rho c}{\rho_0} \quad (11)$$

and the particle path by

$$d\ell = 0 \quad (12)$$

where ℓ is the initial coordinate of a particle, and $\rho_0 = 1/v_0$ is the initial density of the plate. For the special case of the Tait and perfect gas equations of state, Rudinger [3] has shown by differentiating (3) and (4), that the differential equations along the characteristics can be written in the form

$$du + \frac{2}{n-1} dc = cdZ \quad \text{on} \quad \frac{dx}{dt} = u + c \quad (13)$$

$$du - \frac{2}{n-1} dc = -cdZ \quad \text{on} \quad \frac{dx}{dt} = u - c \quad (14)$$

$$dZ = \begin{cases} \delta Z \text{ across shocks} \\ 0 \text{ elsewhere} \end{cases} \quad \text{on} \quad \frac{dx}{dt} = u \quad (15)$$

which are more convenient for calculational purposes than (8), (9) and (10).

For the purposes of the numerical integration it is necessary to write the differential Eqs. (13) to (15) in finite difference form. To second order accuracy the trapezium rule is used, so that for example (13) becomes for two adjacent points 1, 2 on a positive characteristic

$$u_2 - u_1 + \frac{2}{n-1} (c_2 - c_1) = \frac{1}{2} (c_1 + c_2) (Z_2 - Z_1) \quad (16)$$

and the characteristic trajectory is

$$x_2 - x_1 = \frac{1}{2} (u_1 + c_1 + u_2 + c_2) (t_2 - t_1) \quad (17)$$

in Eulerian coordinates and

$$\ell_2 - \ell_1 = \frac{v_0}{2} (c_1/v_1 + c_2/v_2) (t_2 - t_1) \quad (18)$$

in Lagrangian coordinates.

The solution is built up in the plate by constructing a network of characteristics. In fact successive negative characteristics are constructed at constant intervals along the shock. The parameters are evaluated at the intersection of these negative characteristics with positive characteristics starting from the interface. The network can be understood by reference to Fig. 2 which shows a typical mesh when a shock is reflected into the detonation products. When the plate shock interacts with the free surface a rarefaction is reflected, which is represented by a fan of negative characteristics centred on the interaction point. After this, new negative characteristics are created in the plate every time a positive characteristic runs into the free surface.

In the explosive the solution is built up along positive characteristics starting at equally spaced points along the reflected shock or leading characteristic of the reflected rarefaction. Parameters are evaluated at the intersection of these characteristics with negative characteristics starting at the interface. A new positive characteristic is constructed in the explosive only when it is needed to continue the solution in the plate; i.e., after the previous positive characteristic has run into the interface. In this way only the minimum amount of computing is done in the explosive.

There are two places at which trouble can arise in the characteristic mesh. Firstly a compression moving forward in the plate is represented by a converging set of characteristics. If the plate is thick enough the compression

can steepen into a shock which is signified by a positive characteristic running into its neighbour. The solution becomes meaningless if two like characteristics cross. Hence to avoid the computational difficulty of forming a shock, the slower of the two characteristics is discarded, since the faster one carries the information of higher pressures. In a similar way when there is a rarefaction reflected into the detonation products, a shock builds up on the tail of the rarefaction (the second shock of blast calculations). Again when this happens in NIP the slower of the two crossing characteristics is thrown away.

The Principal Cycles

The NIP program is divided into cycles some of which are repeated many times. Each cycle involves the calculation of the parameters at an ordinary point, a shock point, an interface point or a free surface point. In outlining these cycles it is convenient to label the points of the characteristic mesh by letters A, B, ..., and to use these letters as subscripts for parameters at the points. There are always two points at the interface and on the reflected shock.

The Initial Cycle

The initial strengths of the transmitted shock and reflected wave are found by solving the equations across the waves such that pressure and particle velocity are equated across the interface. This gives the values of parameters at points A, B in Fig. 3a. However, as conditions do not remain constant along any of the unknown boundaries in the problem, some special method is needed for starting the solution away from the interaction point. This is accomplished by solving the characteristic relations between the four points D, E, F and G; where D is on the transmitted shock, E and F are at the interface such that DE is a negative characteristic, and G on the head of the reflected wave (taken to be a shock in Fig. 3a) such that GF is a positive characteristic. To completely define D and G it is necessary to interpolate points R and S on the interface such that RD and SG are characteristics. An iterative process is used to solve the equations, involving the guessing of four parameters p_D , u_E , t_G and w_G . For a reflected rarefaction the problem is similar but G is replaced by a set of points across the fan of negative characteristics.

The Ordinary Point

Figure 3b shows the situation for an ordinary point where the solution is known at points

A, B, D and is required at E. Again iteration is required and this time Z_E is guessed where Z is the function of entropy defined by (3). The characteristic relations along AE and DE written in difference form as in (16) are now used to find u_E and c_E , and the characteristic trajectories written like (17) give x_E and t_E . The two characteristic relations in Lagrangian coordinates (18) now give two estimates* of t_E , and their mean is taken as the required value of t_E . Each particle of the explosive and plate has an initial coordinate l and is given some particular value of entropy Z by the initial reflected wave and transmitted shock. Hence in the neighbourhood of the mesh ABDE there is a unique $Z(l)$ relation, which in NIP is taken to be a quadratic through the known points A, B, D. Substituting into this quadratic the value t_E obtained above, a new estimate of Z_E is found. The iteration is repeated until the value of t_E changes by less than some prescribed proportional error.

The Shock Point

For a shock point in the plate (Fig. 3c), the solution is known at A and D on a negative characteristic, and is required at B on the shock. The iteration begins by guessing pressure p_B at B. The other conditions at B are then calculated from the shock wave relations, and t_B is found from

$$t_B = t_A + 2\delta x_p / (w_A + w_B).$$

A point E is now interpolated on AD such that EB is a positive characteristic, and p_B is adjusted until the characteristic relation along EB is satisfied. For a reflected shock point a slightly different procedure is needed because conditions ahead of the shock are varying, fortunately according to the known Taylor Wave solution.

The Interface Point

In this case (Fig. 3d) the solution is known at A, B and F in the plate and at G, J and K in the explosive. The iteration begins by guessing

*Only one of the two differential equations for the characteristic trajectories AE, DE in Lagrangian coordinates is independent of the differential trajectories in Eulerian coordinates. However, in difference form the two Lagrangian trajectories give different values of t_E because of the finite size of the mesh. The difference between the two estimates is used as a measure of the accuracy of integration.

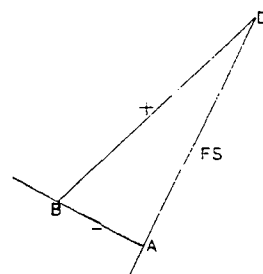
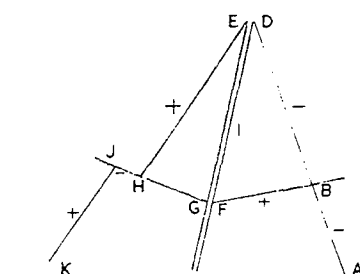
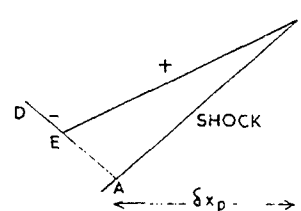
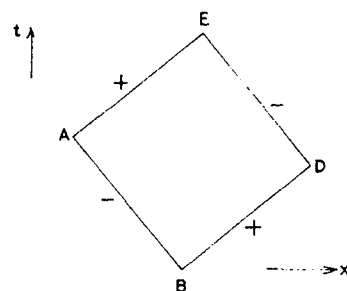
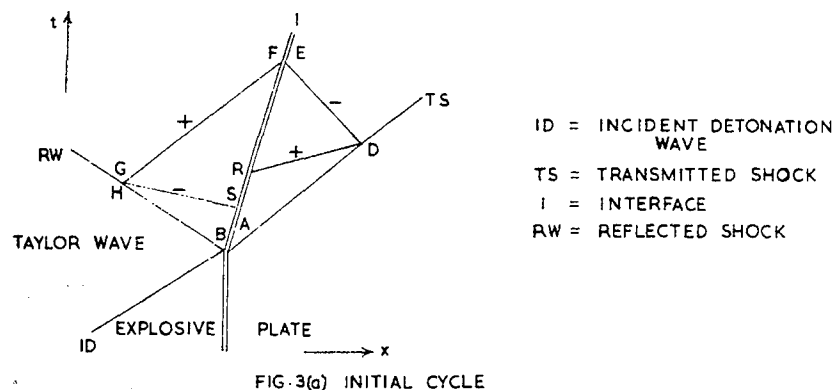


Fig. 3 - NIP cycles

p_D , from which velocity of sound c_D can be found since the particles at the interface expand adiabatically. Then u_D is determined from the characteristic relation along BD and the coordinates of D are found from the trajectory of BD and the interface FD. Finally a point H is interpolated on GJ such that HE is a positive characteristic and p_D is adjusted until the characteristic relation on HE is satisfied.

The Free Surface Point

Since pressure on the free surface AD (Fig. 3e) is zero the calculation of a new free surface

point D needs no iteration. For then $Z_D = Z_A$, so that the characteristic relation BD immediately gives u_D . Then the coordinates of D follow from the intersection of the characteristic trajectory BD given by (17) and the free surface trajectory

$$x_D = x_A + \frac{1}{2} (u_A + u_D) (t_D - t_A).$$

3. COMPARISON OF NIP WITH OTHER CALCULATIONS

Drummond [9] made the approximation that because the shock transmitted into a metal is

weak, the metal can be taken to be isentropic. As a consequence the rarefaction behind the shock wave is a simple wave, so that conditions along a positive characteristic in the plate should be constant until the characteristic meets the rarefaction reflected from the free surface.

In NIP the approximation of a weak shock has not been made. From calculations on various metals with quite thick plates it appears that pressure and other quantities only change by 0.3% or less along positive characteristics, so that the approximation is reasonably valid. For a shock into air the particle velocity only changes by 0.6% along a positive characteristic when the shock has travelled four explosive thicknesses, but because of the fairly large entropy change, pressure and density change by considerably more than this.

In the remainder of this section we consider a typical geometry of a 0.2 in. stainless steel plate driven by a 2 in. Comp B charge. Figure 4

is an $x-t$ trajectory of the steel plate showing the various rarefactions and compressions reverberating in the plate, and the regions of negative pressure which always exist in the triangle formed by the free surface, the rarefaction and the compression. The tensions arise from the interaction of the initial Taylor wave transmitted into the plate and every rarefaction reflected from the free surface, and are only cancelled by the compression travelling forward in the plate. With no dissipative mechanism in NIP, the amplitude of the reverberations diminishes very slowly. For example in the geometry under consideration, the maximum tension in the first reverberation is 94 kbars, and the pressure difference across the compression is 183 kbars. After eight reverberations, the peak tension calculated has only dropped to 78 kbars and the pressure difference across the compression is 87 kbars.

This very slow decay of reverberations is also illustrated by Fig. 5 where the full line is the calculated velocity of the explosive-metal

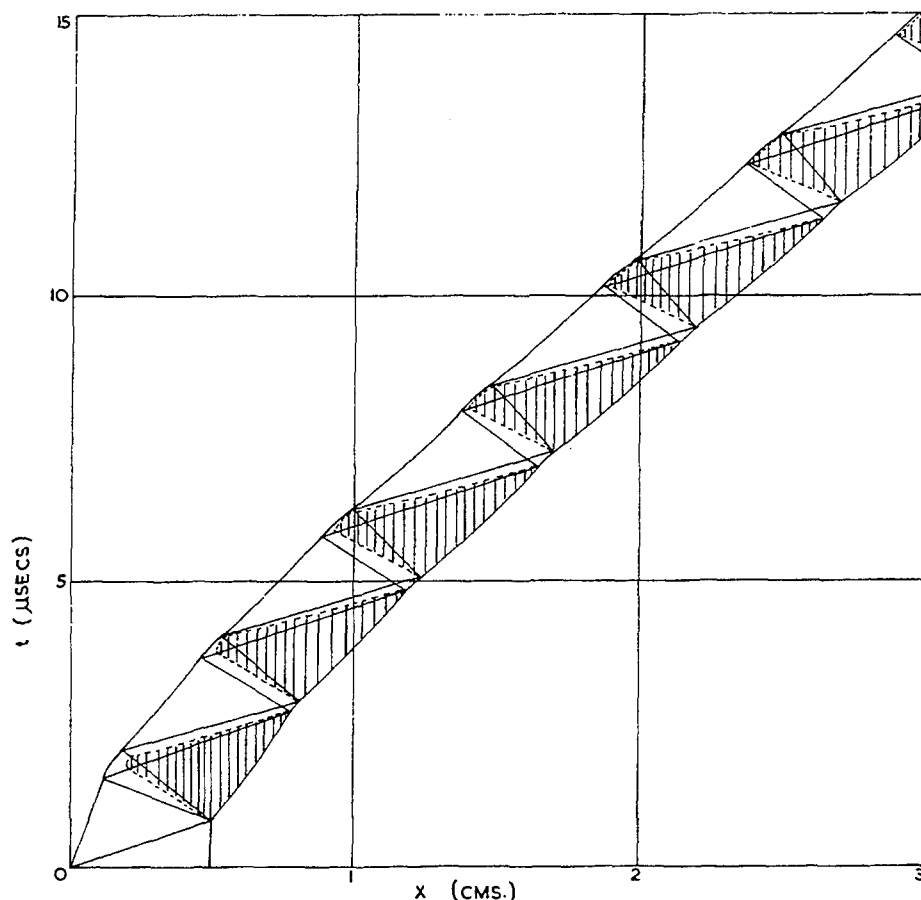


Fig. 4 - Plate trajectory showing regions of negative pressure (shaded) (2 in. Comp. B, 0.2 in. stainless steel)

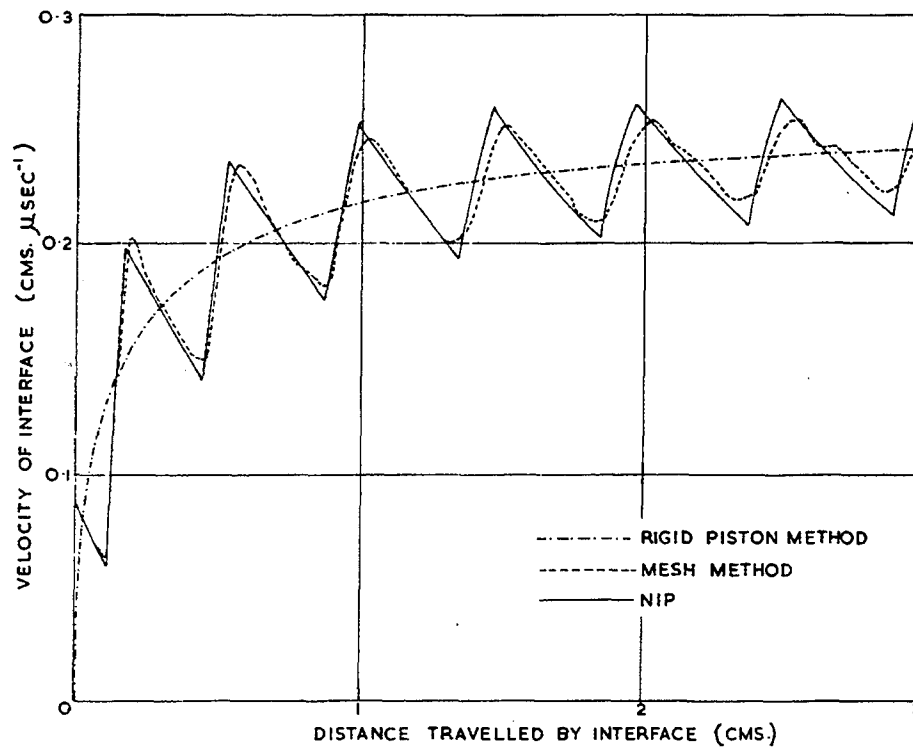


Fig. 5 - Calculated velocity of explosive-plate interface (2 in. Comp. B, 0.2 in. stainless steel)

interface. It will be seen that the interface spends most of its time decelerating, though the deceleration is smaller than the rapid bursts of acceleration. Also plotted in Fig. 5 are the velocity according to the rigid piston theory and the velocity calculated by Pearson's mesh method code.

The rigid piston theory is clearly a very good estimate of the average motion of the interface. This is confirmed by calculating from NIP and rigid piston theory the energy delivered to the plate as a function of time. The difference in final energy is very small and arises in the first few reverberations of the plate. NIP shows that in the geometry under consideration the plate receives 40% of its final energy in the first reverberation and 80% by the end of the third reverberation.

Returning to Fig. 5 and the comparison of the $u-x$ curves calculated by characteristics and the mesh method code, two points emerge:

1. It was suggested by Fyfe et al. [8] that in a mesh method code the rarefaction reflected from the free surface is too spread out and overshoots compared with characteristic calculations.

This is confirmed by the first acceleration period of the interface.

2. The reverberations of velocity decay more rapidly in the mesh calculation. Presumably this is because the viscous dissipative forces are still acting during the passage forward of every compression wave and are progressively increasing the entropy of the plate.

4. COMPARISON OF NIP WITH EXPERIMENT

In choosing geometries for which experimental results can be compared with NIP calculations, it is necessary to consider some of the differences between NIP and experiment. Firstly NIP assumes that the charge-plate system is one dimensional whereas all experiments are at least two dimensional. However, the central regions of a cylindrical charge may be regarded as one dimensional until they are progressively engulfed by side rarefactions. Secondly NIP assumes that the charge is initiated uniformly over its free surface, whereas in experiments the charge is usually initiated by an explosive lens. This lens has the effect of

producing an incomplete Taylor wave to follow the detonation wave in the main charge. Thirdly NIP cannot yet calculate the motion of a plate which spalls.

It follows that the comparisons that can validly be made between NIP (or any other one dimensional non-spalling code) and experiment are restricted to the early motion of the central region of a plate which is thin enough not to spall.

Variation of Free Surface Velocity in a Single Experiment

NIP predicts that for a plate that does not spall, the instantaneous free surface velocity will first decay and then be rapidly accelerated by the arrival of the first compression wave. This is confirmed by Fig. 6 which compares the results of an experiment carried out on stainless steel by the accurate optical method described by Eden and Wright [11], with a NIP calculation. Similar agreement in behaviour between NIP and experiment have been obtained for thinner steel plates and thin titanium plates.

Variation of Free Surface Velocity with Plate Thickness

The most extensive set of results relating free surface velocity with plate thickness has

been given by Deal [14]. For each plate thickness, Deal measured the flight time over a short but unspecified flight distance and hence obtained a mean free surface velocity. Deal's results for aluminium are plotted in Fig. 7 together with the calculations by NIP of the variation of initial instantaneous velocity and mean velocity over the first decay period. It is seen that these two NIP curves straddle all but the results for very thin plates. A more detailed comparison between NIP calculations and Deal's results could be carried out if the precise values of flight distances were known.

5. APPLICATIONS OF NIP TO ANALYSIS OF EXPERIMENTS

Determination of Chapman-Jouguet Pressure

Chapman-Jouguet conditions are often determined by measuring free surface velocity for several different plate thickness and extrapolating back to zero thickness. This extrapolated free surface velocity can then be related through the known equation of state of the plate to a $p-u$ point on the reflected shock or adiabat for the detonation products, from which in turn the C-J point is derived [14].

From Fig. 7 it is clear that a wide range of mean velocities can be obtained for any plate thickness, depending on the flight distance

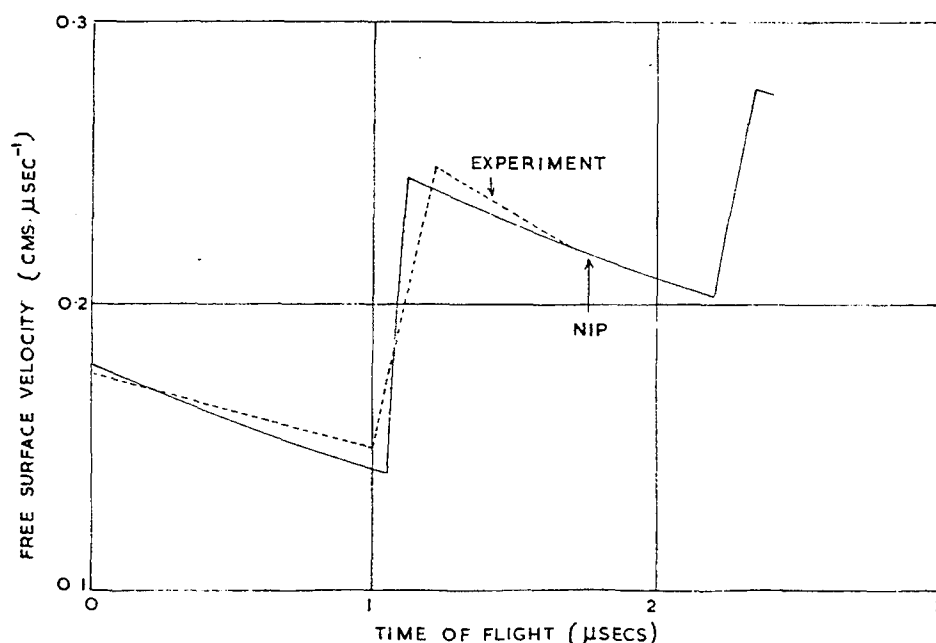


Fig. 6 - Comparison of NIP with experimental free surface velocity (1.9 in. Comp. B, 0.11 in. stainless steel)

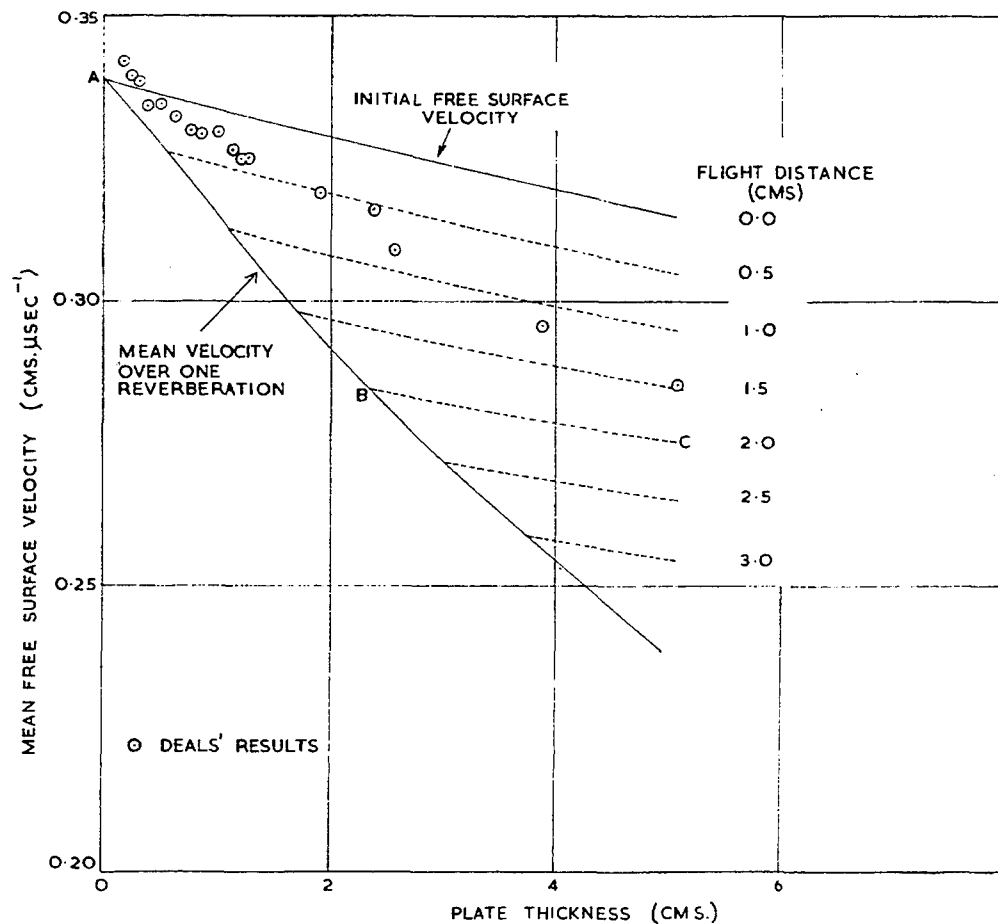


Fig. 7 - Comparison of NIP with Deals' results for aluminum

chosen. Clearly if a large number of different thicknesses are used with say flight distance proportional to plate thickness, then an extrapolation of experimental velocities to zero thicknesses should give a valid result. If only a few measurements are made with no particular attention to the choice of flight distance, it is convenient to use a code like NIP to extrapolate back to instantaneous initial velocity for zero plate thickness. The magnitude of the corrections for different flight distances can be seen from Fig. 7 in which the dashed curves represent mean velocity over the constant flight distances specified.

Clearly if flight distance is not proportional to plate thickness many different shapes can be obtained for the decay of velocity. For example, a steep decay followed by a slower decay is given by choosing flight distances equal to reverberation distances for thin plates, and constant for thicker plates (curve ABC in Fig. 7). In addition the inception of spalling at some

plate thickness can reduce the apparent rate of decay. Finally the effect of the finite diameter of the charge and the presence of a plane wave lens will at some stage alter the rate of decay of free surface velocity with plate thickness.

Analysis of Spalling Phenomena

Negative pressures occur in plates due to the interaction of the rarefaction reflected from the free surface and the Taylor wave transmitted through to the plate. For a given plate the negative pressure builds up in the tail of the rarefaction until it is released by the compression coming forward. As the thickness of the plate is increased, more of the Taylor wave is transmitted into the plate and hence a larger tension is developed. Table 1 gives the peak tensions calculated by NIP for stainless steel plates in contact with Comp B. For any given thickness ratio r , the value of peak tension depends on the precise form of equation of state

TABLE 1
Variation of Peak Tension (T_{max})
with Ratio (r) of Plate Thickness
to Charge Thickness

r	T_{max} (kb)
0.05	55
0.10	94
0.15	122
0.20	142

used, but the NIP values are not thought to be too much in error. For a given plate thickness peak tension increases with the impedance of the plate material. Simple ideas suggest that the plate will spall when the tension reaches some critical value. Hence there is a critical plate thickness such that all thicker plates will spall.

Eden and Wright [11] have used their accurate optical technique to measure the free surface trajectory for a range of stainless steel plate thicknesses with a flight distance chosen to cover about one and a half plate reverberations. For thin plates they obtain a trajectory which has a free surface velocity like Fig. 6, with a decay followed by a rapid acceleration on

the arrival of the compression wave. The value of the initial velocity, the magnitude of the slow deceleration, the time of arrival and magnitude of the plate reverberation and the magnitude of the subsequent deceleration are all in good agreement with theory. Figure 8 compares the experimental free surface velocity with calculation for a thicker plate which spalls. The experiment shows an initial velocity lower than that predicted by NIP, a very small deceleration, and a delayed arrival of the plate reverberation. As the plate thickness is increased through the critical thickness for spalling, the apparent initial free surface velocity falls more rapidly than predicted by NIP and the deceleration decreases. For slightly thicker plates the plate reverberation begins to be delayed compared with NIP. Hence by comparing NIP with experimental results for a range of plate thicknesses, it has been deduced that the critical tension for spalling of stainless steel is about 65 kb corresponding to a critical ratio of plate to explosive thickness of 0.06.

At present NIP cannot calculate the motion of a plate after spalling. However, because it gives smooth pressure profiles, it is convenient to first use NIP to determine the thickness of the spall and then to use a mesh method code to actually calculate the subsequent motion of the

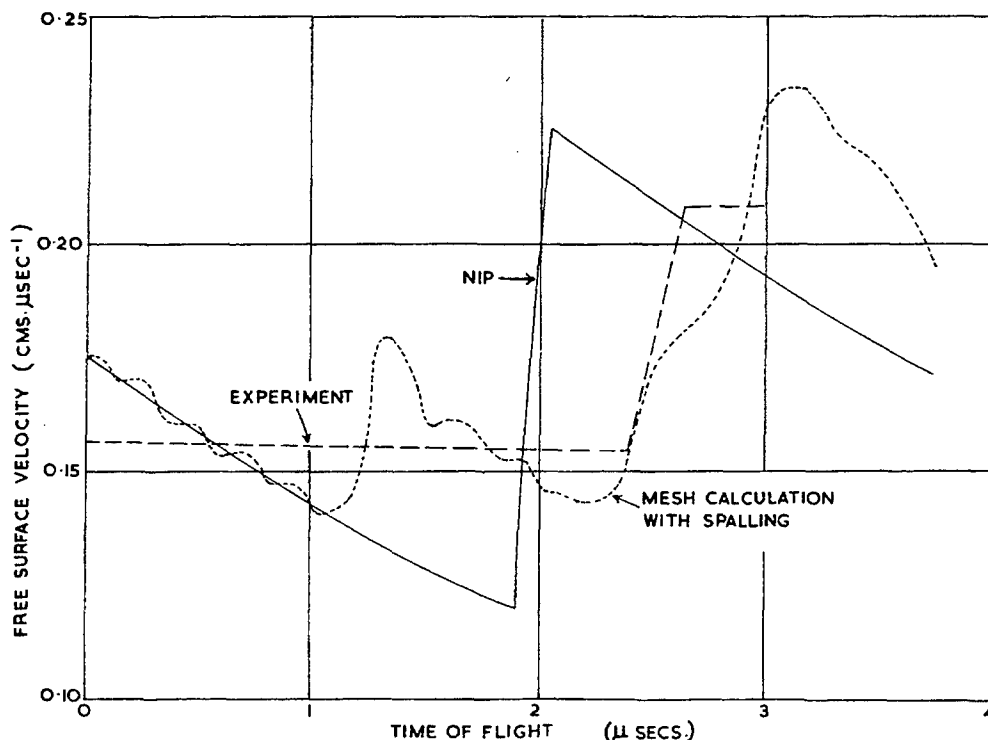


Fig. 8 - Comparison of experiment with theory in case where plate spalls (2.0 in. Comp. B, 0.2 in. stainless steel)

two parts of the plate. If the mesh code is used itself to determine the spall thickness it produces untrustworthy values because of spurious small oscillations in the pressure profiles calculated by the code.

For the geometry illustrated in Fig. 8 (2 in. Comp. B., 0.2 in. stainless steel), a NIP calculation was used to find the spall thickness corresponding to the point which first developed a tension of 65 kb. The mesh code was then used to calculate the motion of the spall and its

parent. The resulting free surface velocity curve is given in Fig. 8, and Fig. 9 in the corresponding wave diagram showing the various spall and parent reverberations. It is seen that the arrival of the main plate reverberation at the free surface is delayed because it first has to close the gap between parent and spall. The mesh calculation gives this time in reasonable agreement with experiment. The approximately constant free surface velocity observed in a plate which spalls is clearly the average velocity of the spall reverberations.

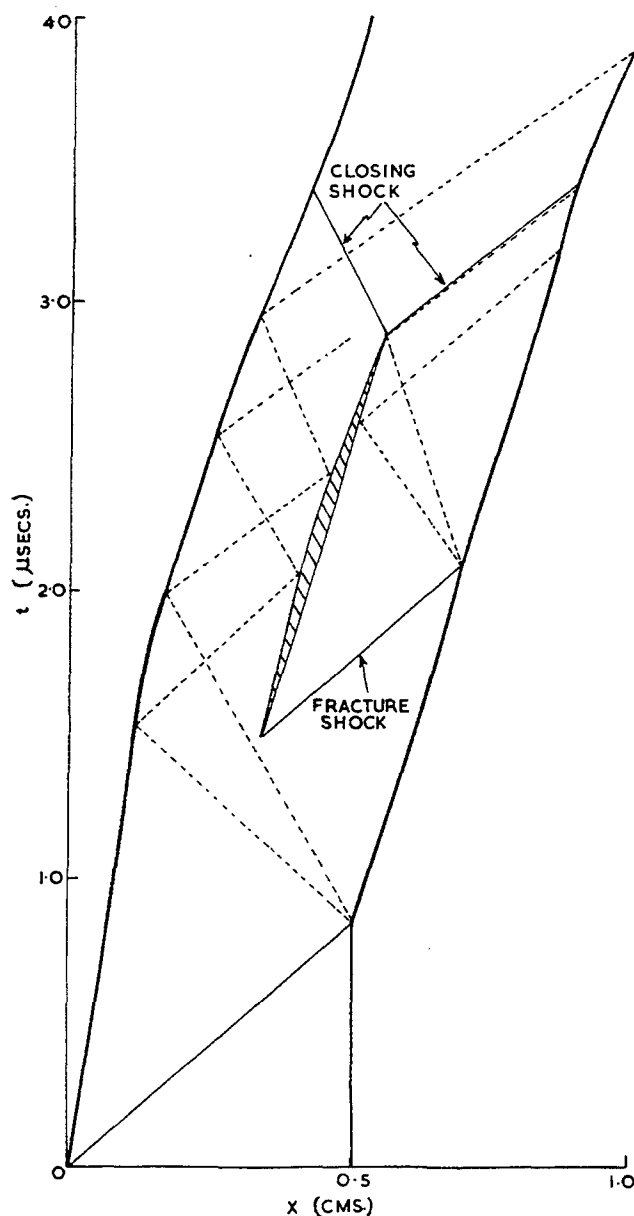


Fig. 9 - Wave diagram for stainless steel that spalled (2 in. Comp. B, 0.2 in. stainless steel)

The transition from non-spalling to a spalling behaviour is not sharply defined by the optical experiments so far discussed. Hence the figure of 65 kb for fracture strength of stainless steel must be regarded as preliminary. A more precise value would be obtained if the actual spall thickness could be determined. This would be available if the optical method could resolve the reverberations of the spall. In fact Eden and Wright have now been able to resolve the arrival of the fracture shock at the free surface, though the magnitude of the shock is smaller than expected.

Another method of determining spall thickness is by radiographing a plate in flight. This has been done for a 0.5 in. stainless steel plate driven by a 3 in. Comp. B charge, and the radiograph is shown in Fig. 10. There appears to be a normal fracture surface at a position corresponding to a calculated tension of 53 kb. The difference between the spalling tensions given by the radiograph and the optical method may be due to the cumulative uncertainties in both methods or it may be significant. For example, one possible interpretation is that since the optical experiments were done with 2 in. thick Comp. B charges, and the radiograph experiment with a 3 in. charge, the different critical tensions could imply that fracture strength is time or rate dependent.

of these breaking fronts with the velocities of the fracture shocks. These are generated at the fracture point to relieve the tension and also move in both directions in the plate. The initial velocities of these shocks may easily be determined from the calculated conditions at the point that spalls. The forward moving breaking front is not especially interesting since it travels at roughly particle velocity and therefore the peak tension is relieved immediately by the forward moving fracture shock. However, the calculations show that the initial velocity of the backward moving breaking front is greater than the initial velocity of the backward moving fracture shock. This suggests that until the breaking front is reversed by the main plate reverberation, every particle will experience the spalling tension for a small time interval before it is recompressed by the backward moving fracture shock. If this is so, a section through a spalled plate in flight from the free surface backwards should show a solid spall, a void, a region of broken up material and a solid rear part of the plate. To some extent this is confirmed by the radiograph in Fig. 10.

These illustrations of calculations by NIP have shown some of the advantages of its greater accuracy compared with an equivalent mesh code. However, it is somewhat restricted in the range of calculations it can carry out, and



Fig. 10 - Radiograph for spalled stainless steel plate in flight (3 in. Comp. B, 0.5 in. stainless steel)

Although NIP has not yet been adapted to calculate the motion of a plate which spalls, it does demonstrate one important feature of spalling phenomena: the trajectories of the breaking fronts. These are the boundaries of regions in x, t space which experience the fracture criterion. If this criterion is taken to be a critical tension, then the breaking fronts are the boundaries of the contour of this tension radiating from the fracture point. NIP calculations show that this contour commences on the tail of the rarefaction reflected from the free surface and propagates in both directions in the plate (Fig. 11). It is interesting to compare the velocities

also it uses equations of state which are too simple. Nevertheless it is proving useful at AWRE in helping to analyse experiments both for determining C-J states and spalling phenomena.

ACKNOWLEDGMENT

The authors are indebted to Mr. P. G. Parish who planned much of the first version of the NIP program.

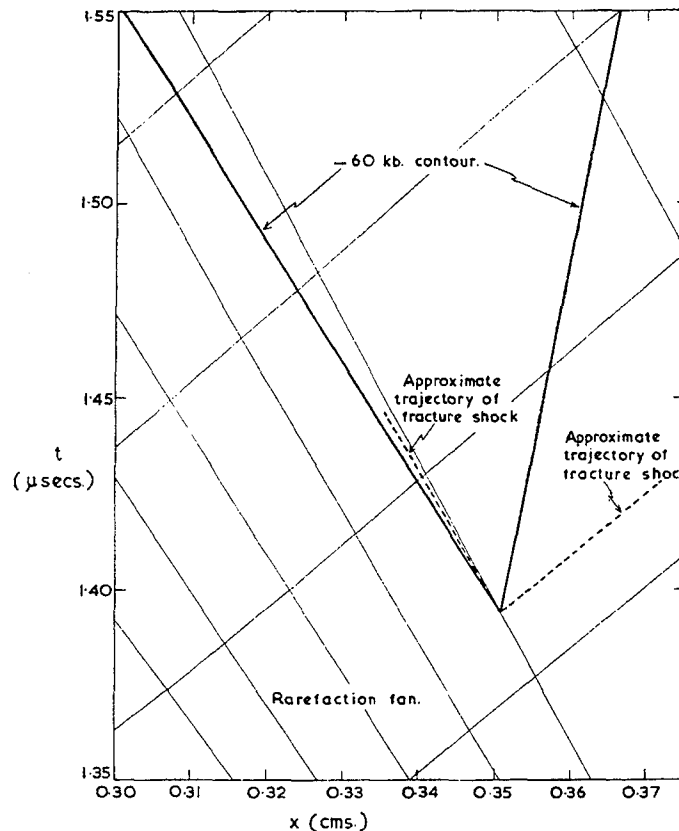


Fig. 11 - Characteristic mesh in region where 60 kb tension is developed (2.0 in. Comp. B, 0.2 in. stainless steel)

REFERENCES

1. A. K. Aziz, H. Hurwitz and H. M. Sternberg, "Energy Transfer to a Rigid Piston under Detonation Loading," 3rd ONR Symposium on Detonation, 205-225 (1960).
2. R. Courant and K. O. Friedrichs, "Supersonic Flow and Shock Waves," Interscience (1948).
3. G. Rudinger, "Wave Diagrams for Non-Steady Flow in Ducts," Van Nostrand (1955).
4. A. E. Glennie, "Solution by Characteristics of the Equations of One Dimensional Unsteady Flow," Chapter 26 of "Numerical Solution of Ordinary and Partial Differential Equations," edited by L. Fox, Pergamon Press (1962).
5. N. E. Hoskin, "Solution by Characteristics of the Equations of One-Dimensional Unsteady Flow," Methods in Computational Physics, Vol. 3, 265-293, Academic Press (1964).
6. R. D. Richtmyer, "Difference Methods for Initial Value Problems," Interscience Tracts in Pure and Applied Mathematics, Number 4, Interscience (1957).
7. N. E. Hoskin and B. W. Pearson, "Finite Difference Methods for One-Dimensional Unsteady Flow," Chapter 27 of "Numerical Solution of Ordinary and Partial Differential Equations," edited by L. Fox, Pergamon Press (1962).
8. I. M. Fyfe, R. C. Eng and D. M. Young, "On the Numerical Solution of the Hydrodynamic Equations," SIAM Review 3 (4), 298-308 (Oct. 1961).
9. W. E. Drummond, "Explosively Induced Shock Waves, I. Plane Shock Waves," J. Appl. Phys. 28 (12), 1437-1441 (Dec. 1957).
10. M. L. Wilkins, "Calculation of Spall Based on a One Dimensional Model," International Symposium, "Les Ondes de Detonation," CNRS, 459-468 (1961).

11. G. Eden and P. W. Wright, "A Technique for the Precise Measurement of the Motion of a Plane Free Surface," Paper in 4th ONR Symposium.
12. B. D. Lambourn and J. E. Hartley, "The Normal Initiation Program," AWRE Report to be published.
13. R. H. Cole, "Underwater Explosions," Princeton University Press (1948).
14. W. E. Deal, "Measurement of the Reflected Shock Hugoniot and Isentrope for Explosive Reaction Products," Phys. Fluids 1 (6), 523-527 (Nov.-Dec. 1958).

EXPERIMENTAL METHODS

*Chairman: L. Lundberg
Försvarets Forskningsanstalt, Sweden*

A METHOD FOR THE STUDY OF PROPERTIES OF SOLID EXPLOSIVES AND OTHER SOLID (INCLUDING POROUS) MATERIALS WHEN SUBJECTED TO SHOCK WAVES

W. L. Murray and J. Plant
*Ministry of Power, Safety in Mines Research Establishment
Buxton, England*

SUMMARY

This paper describes a method for determining simultaneously the pressure and density in shock waves in solid (including porous) materials. The shock is produced in a cylinder of the material using the usual solid barrier technique that is used for determining the sensitivity of explosives to shock initiation. The velocity of the shock is determined by using schlieren photography to detect its time of arrival at small holes bored in the material and the particle velocity is found from the velocity of the shock wave produced in the air at the free end of the material. Then, applying the equations for conservation of mass and momentum across a shock, both the pressure and density behind the shock front in the material at the free end may be calculated. Subsidiary experiments that were carried out to examine the validity of the assumptions made for the interfaces between the barrier and the material and between the material and the air are described and the results discussed. The method has been used to investigate the critical shock pressures required to initiate detonation in two coal mining explosives.

1. INTRODUCTION

The arrangement that has been used is a modification of the "card-gap" method in which two explosives are placed coaxially but separated by a solid barrier. In the present work an attempt has been made to determine the pressure behind the shock when it enters the receptor. Since it is not practicable to measure the pressure directly it is necessary to measure other parameters of shock wave propagation from which the pressure may be calculated.

The relation between the variables in a plane steady shock disturbance travelling into a stationary medium is given by the equation for conservation of momentum:

$$P_{1c} - P_{0c} = \rho_{0c} U_c u_c \quad (1)$$

where P_{1c} is the pressure immediately behind the shock front, P_{0c} the pressure in the undisturbed medium in front of the shock (usually atmospheric), ρ_{0c} the density of the undisturbed medium, U_c the velocity of the shock front and u_c the particle velocity behind the front. If the

equation of state of the material, $P_{1c} = f(\rho_{1c})$ say, is known ρ_{1c} being the density behind the shock front, and ρ_{0c} is known, then by measuring only one of the two quantities U_c or u_c and using the equation for the conservation of mass:

$$\rho_{0c} U_c = \rho_{1c} (U_c - u_c) \quad (2)$$

it is possible to calculate the remaining two variables in Eq. (1). However, if the equation of state is not known then in order to calculate P_{1c} it is necessary to measure both U_c and u_c , assuming that P_{0c} and ρ_{0c} are known.

Cook, Pack and McEwan (1960) have determined the critical shock pressures for initiation in certain military explosives. Fauquignon (1960) has made use of the momentum equation to determine the shock pressure in a receptor cartridge just before the transition to a detonation wave occurs. In both of these methods it was necessary to carry out subsidiary experiments to determine certain properties of the experimental system. Cook, Pack and McEwan used an aquarium method to determine the intensity of the shock wave set up in the barrier by the donor explosive and Fauquignon used a

predetermined equation of state for the products of detonation of the receptor explosive.

In an attempt to evaluate the critical pressures required to initiate detonation in coal-mining explosives about which no previous knowledge has been gained, a method has been used which involves the use of only three assumptions. They are (1) that the interface between the explosive and air may be treated as a free surface so far as the explosive is concerned, (2) that the explosive can be regarded as inert until detonation takes place, and (3) that air can be regarded as a perfect gas with $\gamma = 1.4$; the last assumption produces less than 1% difference from the Hugoniot curve for air for shock speeds up to Mach 5.

The values of the parameters U_c and u_c at the end of the receptor cartridge, immediately before the shock wave was reflected at the receptor air interface, have been measured for different lengths of receptor when detonation did not occur; the barrier was of such a thickness as to give a 50% chance of detonation being reestablished in the receptor. The velocity of the shock front in the receptor was determined by using schlieren photography and a streak camera of writing speed $0.3 \text{ mm}/\mu\text{sec}$ to detect its time of arrival at small holes bored through the receptor. The particle velocity was calculated from the speed of the shock wave transmitted into the air at the end of the receptor.

The initial particle velocity, u_g , of the air behind the transmitted shock is related to the initial wave velocity, U_g (in the air), by the well-known equation

$$u_g = \frac{2}{\gamma_g + 1} \left[U_g - \frac{a_0^2}{U_g} \right] \quad (3)$$

where γ_g is the ratio of the specific heats for air and a_0 the velocity of sound in still air.

If it is assumed that the receptor-air interface is effectively a free surface so far as the explosive is concerned, then u_g will be twice the particle velocity, u_c , at the end of the explosive at the instant the incident shock in the explosive begins to be reflected as a rarefaction wave. By combining Eqs. (1) and (3) the pressure in the receptor is given by

$$P_{1c} - P_{0c} = \frac{\rho_{0c} U_c}{(\gamma_g + 1) U_g} \left[U_g^2 - a_0^2 \right] \quad (4)$$

where c denotes the receptor and g denotes the air, or gas, at the end of the receptor. By using receptor cartridges of different lengths, the pressure at the end of the receptor can be

plotted against its length; and by extrapolating to zero length, the pressure behind the shock front in the receptor at the interface between the barrier and receptor can be determined.

The instantaneous density of the material behind a shock front can be calculated from the conservation of mass Eq. (2), so that a graph of pressure against density can be obtained and an equation of state formulated.

2. RESULTS

2.1 Coal-Mining Explosives

Figures 1 and 2 show the results obtained for two coal-mining explosives (mixtures of nitroglycerine, ammonium nitrate, cellulose and inerts including sodium chloride and barium sulphate) one a powder of loading density 0.80 gms/cc (N.G. Powder A), the other a gelatine of density 1.59 gms/cc (N.G. Gelatine C). Mild steel was used as the barrier material.

The straight lines relating pressure to the length of the receptor in Fig. 1 have been derived numerically on the bold assumption that the pressure attenuates linearly with respect to length.

The relation between pressure and density behind the shock fronts in the two explosives is shown in Fig. 2. Owing to the spread in the results, again a simple linear relationship between these two parameters has been assumed and equations of the following form have been derived by the method of least squares:

$$P_{1c} = 1.3700\rho_{1c} - 1.0633 \text{ kbars} \quad (5)$$

for the powder, with a critical shock pressure for initiation of $0.47 \pm 0.11 \text{ kbars}$ and,

$$P_{1c} = 1.4821\rho_{1c} - 2.3203 \text{ kbars} \quad (6)$$

for the gelatine, with a critical shock pressure of $0.79 \pm 0.17 \text{ kbars}$. The spread in the results may be explained by the fact that mining explosives are difficult subjects for exact experiments because of their heterogeneous composition and irregular physical texture; this produces an inevitable variation in the results especially when more than one batch has to be used. Their properties are also affected by aging.

A less obvious cause of probable error lies in the equation relating the pressure to the measurable quantities U_c and U_g . Since P_{1c} is a function of U_c and U_g then

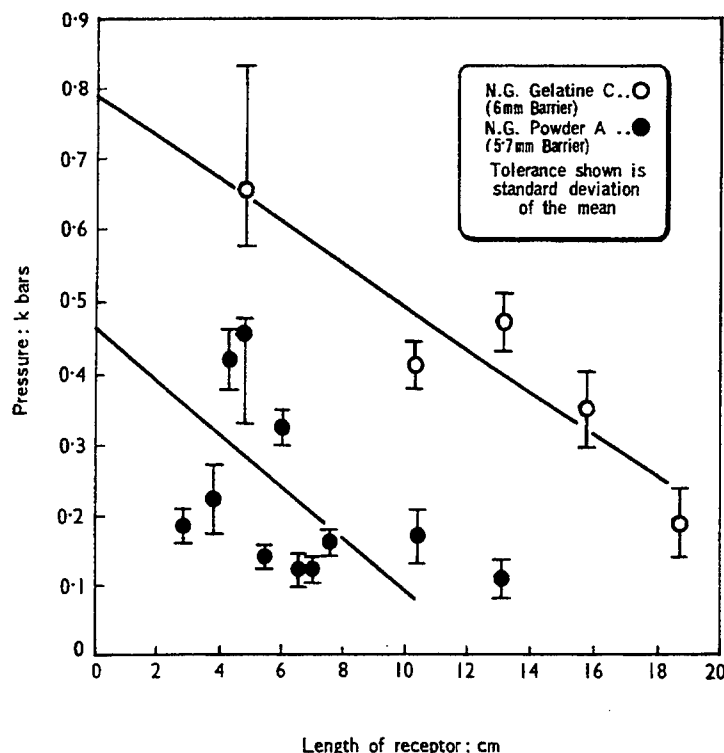


Fig. 1 - Relationship between the pressure at the free end of the receptor and the length of the receptor

$$\delta P_{1c} = \left(\frac{\partial P_{1c}}{\partial U_c} \right)_{U_g} \delta U_c + \left(\frac{\partial P_{1c}}{\partial U_g} \right)_{U_c} \delta U_g$$

which leads to

$$\frac{\delta P_{1c}}{P_{1c}} = \frac{\delta U_c}{U_c} + \frac{\delta U_g}{U_g} \left[\frac{U_g^2 + a_0^2}{U_g^2 - a_0^2} \right] \quad (7)$$

where δ is the expected error in the quantity concerned. From this equation it can be seen that when U_g is only slightly greater than the speed of sound in the gas at the end of the receptor, as is the case with mining explosives, the second of these error factors is large.

2.2 Solids Other than Mining Explosives

The method is useful for the determination of shock wave parameters for any solid material. The free-surface assumption, the validity of which will be discussed later, introduces more error when an examination is being made of a discontinuous medium, such as a granular explosive, than when a homogeneous material such as a plastic is being studied.

Table 1 shows the results obtained with receptors of a more homogeneous nature; lead, perspex and wood (pine, along the grain). Much higher shock velocities may be produced in these nonreacting materials together with much higher shock velocities in the air at the end of the receptors. These factors make for greater accuracy, as also does the fact that a better junction can be obtained between the barrier and the receptor. Table 2 shows a result with a blasting gelignite explosive. This material, like the materials shown in Table 1, is more homogeneous than normal mining explosives and will therefore yield more accurate results.

3. VALIDITY OF THE ASSUMPTIONS

3.1 Validity of the Extrapolation to Zero Length

The extrapolation to zero length is only valid if any sharp pressure gradients, such as might be present in the detonation reaction zone of the donor, are completely attenuated in the metal barrier. The attenuation of the shock as it travels down the receptor will be governed by the rate at which the pressure exerted by the

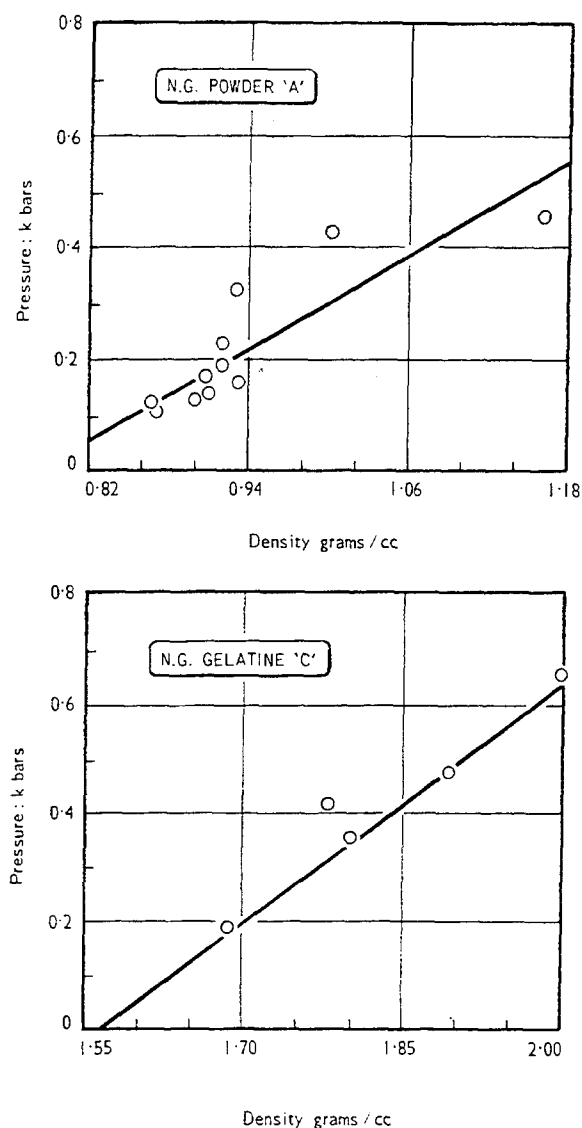


Fig. 2 - Dynamic pressure-density curves for the two explosives

donor on the barrier decreases and, if the detonation reaction zone is thin, this will in turn be controlled in the main by the expansion of the products of detonation behind the Chapman-Jouguet plane. This expansion has been discussed in a one-dimensional treatment by Taylor (1950) and in a two-dimensional treatment by Hill and Pack (1947).

One method of determining whether there are sharp pressure gradients after the pulse has passed through the barrier is to measure the movement of the free surface of the barrier in the absence of a receptor material. This can be done by using a "pin-contact" method in which two long, fine, brass pins are mounted perpendicular to the plate, in such a way that the tip of one is very close to the plate and the other is at a known distance away. The pins form part of an electric circuit, and contact between the tips of the pins and the barrier produces pulses that can be detected by a micro-second counter. Figure 3 shows the results obtained with the two explosives that were used as donors in obtaining the results shown in Fig. 1. The relevance of the other results shown in this figure will be discussed in Section 3.2. It must be emphasized that the measurements of the velocity of the free surface of the barrier, shown in Fig. 3, were obtained with only two pins and the graph of distance against time was based on several experiments carried out with the pins at each of several distances from the boundary. There is no indication from these results that there are sudden changes in the velocity of the free surface of the barrier.

3.2 Validity of the Free-Surface Assumption at a Receptor-Air Interface

It has been assumed that because the density of air is much lower and its compressibility

TABLE 1
Shock Parameters of Various Materials

Donor: Low Density, N.G. Powder A (0.8 gms/cc, 3.65 cm diameter, and 15 cm length)

Barrier: Mild steel

Receptor	U_c (m/sec)	U_g (m/sec)	P_{1c} (kbars)	Initial Density, (gms/cc)	Density, Behind Shock (gms/cc)
Lead	1780	370	3.28	11.37	11.47
Perspex	2930	410	1.63	1.20	1.22
Pine	3560	440	1.20	0.50	0.51

The result for lead gives a compressibility factor of $2.70 \times 10^{-6} \text{ atm}^{-1}$ compared with $2.077 \times 10^{-6} \text{ atm}^{-1}$ obtained by Bridgman (1923) for static compression at 11,600 atm pressure and 30°C.

TABLE 2
 Shock Parameters of Blasting Gelignite

Donor and Receptor: Blasting Gelignite (60% N.G., Cellulose and KNO_3)
 Receptors of length 2.8 cm and diameter 4.4 cm
 Donors of length 10 cm and diameter 4.4 cm

Barrier: Mild Steel, 0.8 cms thick

U_c (m/sec)	U_g (m/sec)	P_{1c} (kbars)	Initial Density, (gms/cc)	Density, Behind Shock (gms/cc)
850	460	1.05	1.5	1.65

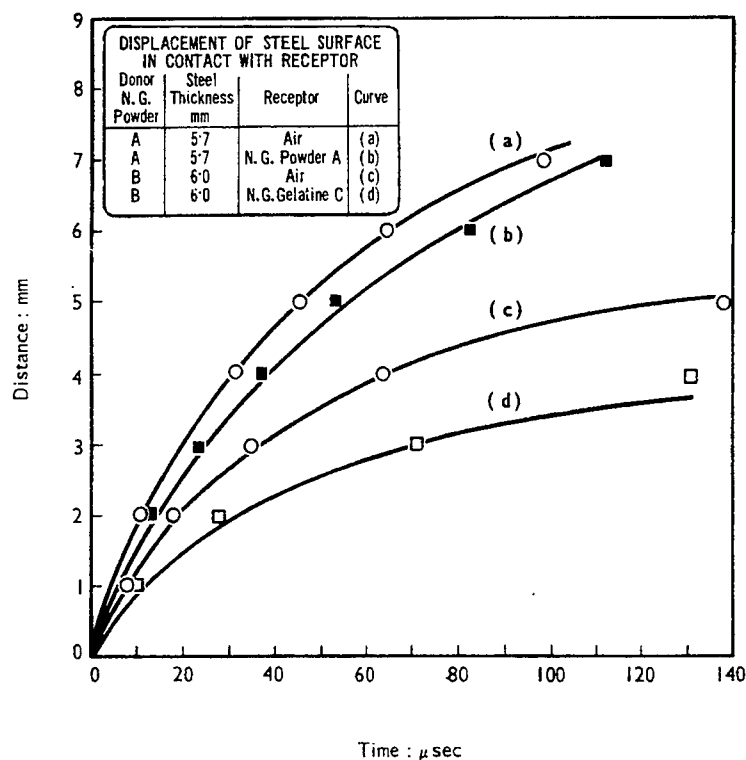


Fig. 3 - Displacement of steel when in contact with a detonated cartridge of explosive

much higher than that of the explosive or other solid receptor material, the shock front in the receptor will be reflected at the receptor/air interface in the same way as at a free-surface.

At metal to air or liquid to air boundaries this assumption is valid; the former condition has been discussed in detail (Walsh and Christian, 1955), but the match of discontinuous materials to air needs further consideration. This question is particularly important with the N.G.

Powder A, which has a bulk density of only 0.8 gms/cc. An estimate of the density of its solid components leads to the conclusion that about 50 percent of the volume of this explosive is occupied by air.

Confirmation of the correctness of the free surface assumption and indeed a verification of the overall reliability of the order of the derived pressures in the receptor at the barrier-receptor boundary, may be obtained by using the

pin-contact method to measure directly the velocity of the barrier-receptor interface. The pins are now mounted inside the receptor charge, but are again used to measure the movement of the receptor side of the plate surface.

The results obtained are shown in Fig. 3. Considering the first millimetre from the plate, the mean barrier-receptor interface velocity is 175 m/sec for N.G. Powder A receptor and 100 m/sec for N.G. Gelatine C receptor. Since a typical shock speed would, according to previous measurements, be about 450 m/sec and its loading density is 0.8 gms/cc, application of Eq. (1) gives the mean pressure behind the shock over the first millimetre as 0.63 kbars. Similarly with a typical shock speed of 550 m/sec for N.G. gelatine C and loading density of 1.59 gms/cc, the mean pressure over the first millimetre of the receptor would be 0.87 kbars. These values compare with 0.47 ± 0.11 kbars and 0.79 ± 0.17 kbars respectively, obtained by the previous method (see Fig. 1).

4. THE MATHEMATICAL TREATMENT OF THE ATTENUATION OF A SHOCK WAVE PRODUCED IN A METAL BARRIER IN CONTACT WITH A DETONATING EXPLOSIVE

The work described so far has been concerned only with the value of quantities immediately behind the shock front. Whilst this is adequate if one is merely trying to establish the relationship between pressure and density, it may not be sufficient when describing the initiation of detonation in explosives by shocks, for then the shape of a shock pulse is important. In mining explosives of the type that have been considered in this paper, if detonation does occur it takes place close to the surface of the steel barrier, i.e., within a millimetre or so. However, in certain high explosives there is evidence that an incident shock may travel a considerable distance into an explosive before detonation begins. In such cases, the shape of the shock pulse is obviously of importance. The shape of the pulse entering the receptor from the solid barrier will now therefore be considered from a theoretical standpoint; it is necessary to make certain assumptions in order to reduce the arithmetical work involved to manageable proportions. (See Cachia and Whitbread, 1958, Eichelberger and Sultanoff, 1958, Cook and others, 1958, and Marlow and Skidmore, 1958.)

4.1 Detonation Wave in the Donor

It is assumed (i) that the cartridge is perfectly confined in the lateral directions; (ii) that the reaction zone is sufficiently thin and uniform for its effects to be neglected; (iii) that if the explosive is detonated at its free end, a plane stable detonation wave will be established immediately; (iv) that the detonation products behave as a perfect gas with $\gamma = 3$.

As the detonation wave travels down the cartridge an adiabatic expansion wave is formed in the burned gases behind it; the form of this expansion wave has been discussed by Taylor (1950).

The conditions at the Chapman-Jouguet (C.-J.) plane are governed by the equations for conservation of Mass, Momentum and Energy and the Chapman-Jouguet Condition. If D is the detonation velocity and u_1 and a_1 are the particle velocity and velocity of sound, respectively, at the C.-J. plane, then from these equations and the equations of state for a perfect gas it can be shown that

$$u_1 \approx \frac{D}{\gamma + 1} \quad (8)$$

$$a_1 \approx \frac{\gamma D}{\gamma + 1} \quad (9)$$

and

$$P_1 \approx \frac{\rho_0 D^2}{\gamma + 1} \quad (10)$$

where γ is the ratio of specific heats, P_1 is the pressure at the C.-J. plane, and ρ_0 the density in the undecomposed explosive.

Thus, if ρ_0 , D and γ are known, P_1 can be calculated.

4.2 Expansion Wave Behind the Detonation Front at the Time of Impact

The expansion wave behind the detonation front will be centred at the initiation point. The head of the wave is the Chapman-Jouguet plane travelling with velocity

$$D = u_1 + a_1 \quad (11)$$

and the tail moves out into the surrounding media. It will suffice to describe the expansion in the form of the equation:

$$\frac{x}{t} = D + \frac{\gamma + 1}{2} (u_r - u_1) \quad (12)$$

where x is the distance from the point of initiation parallel to the axis of the donor, t is the time after initiation and subscript r refers to the rarefaction zone behind the C.-J. plane.

u_r may therefore be calculated in the region behind the C.-J. plane at the instant at which the whole of the cartridge had detonated (since then $t = t_d$ where $t_d = L/D$, L being the length of the cartridge).

Also, the distribution of P_r and a_r may be calculated from the isentropic relationships

$$u_r = u_1 - \frac{2a_1}{\gamma - 1} \left\{ 1 - \left(\frac{P_r}{P_1} \right)^{\frac{\gamma - 1}{2\gamma}} \right\} \quad (13)$$

and

$$a_r = a_1 \left(\frac{P_r}{P_1} \right)^{\frac{\gamma - 1}{2\gamma}} \quad (14)$$

(see Courant and Friedrichs, 1948, p. 92).

4.3 Initial Conditions at the Explosive Barrier Interface

Let the time of impact be now taken as zero time. At this instant a shock wave will be set up in the barrier and a shock wave will also be reflected back into the products of detonation.

The conditions across the interface, or boundary, are:

(a) Pressure is continuous, $P_{2m} = P_{2r}$

(b) Particle velocity is continuous, $u_{2m} = u_{2r}$

The conservation Eqs. (1) and (2) will apply across the shock front in the barrier together with an equation of state for the barrier material, $\rho_m = \phi(P_m)$ say.

Rearrangement of the conservation equations gives

$$u_{2m}^2 = (P_{2m}) \left[\frac{1}{\rho_{0m}} - \frac{1}{\rho_{2m}} \right] \quad (15)$$

since $P_2 \gg P_0$, ρ_{2m} is the density of the metal behind the shock, ρ_{0m} , the normal density.

The reflected shock will also obey the conservation equations but with the initial Chapman-Jouguet particle velocity and pressure superposed. The equation for the reflected shock then becomes

$$u_{2r} = u_1 - a_1 \sqrt{\frac{2}{\gamma}} \left[\frac{P_{2r} - P_1}{[P_1 \{ (\gamma + 1) P_{2r} + (\gamma - 1) P_1 \}]^{1/2}} \right] \quad (16)$$

(see Courant and Friedrichs, 1948, p. 148).

Since the particle velocity and the pressure are continuous across the boundary, simultaneous solution of Eqs. 15 and 16 gives the conditions at the instant when the shock wave first enters the barrier.

4.4 Subsequent Motion of the Contact Surface

In order to estimate subsequent movement of the contact surface, or interface, four assumptions are made:

(i) The relationship between the particle velocity and the pressure in the metal at the contact surface is always given by the shock wave Eq. 15. This assumption is justified because the small compressibility of metals means that the entropy change across a shock front is negligible at these pressures, which in turn means that all changes are reversible and that states reached by adiabatic compression are identical with states reached by shock compression (Chandrasekhar (1943) and Drummond (1957)).

(ii) Since the ratio $(P_{2r} - P_1/P_1)$ for the reflected shock in the detonation gases of mining safety explosives is only about 1.5 even when steel barriers are used, the entropy change across this front can be neglected and the front can be regarded as a simple compression wave. The region containing the products, therefore, remains isentropic throughout. (Courant and Friedrichs, 1948, p. 156.)

(iii) The ratio of the specific heats for the products is constant and equal to 3 (Berry and Holt (1954), Stanyukovich (1960) and Deal (1958)).

Since the characteristic directions for flow in the region are $u_r \pm a_r$ along which the Riemann invariants $u_r \pm 2a_r/(\gamma - 1)$ are constant, the value $\gamma = 3$ makes the slopes and invariants equal. The characteristics are therefore a

family of straight lines throughout the products region even after interaction with other disturbances.

(iv) Over small intervals of time the displacement of the contact surface with respect to time may be represented by a polynomial in which third and higher order of time may be neglected. It will thus obey a parabolic equation of the form

$$x = At - Bt^2 \quad (17)$$

so that

$$u = A - 2Bt \quad (18)$$

where u is the velocity of the contact surface and A and B are constants.

Since the movement of the contact surface represents an actual particle path, the entropy in the immediate vicinity on either side the contact surface will be constant; therefore,

$$a_a = a_{2r} \left(\frac{P_a}{P_{2r}} \right)^{\frac{\gamma-1}{2\gamma}} = a_{2r} \left(\frac{P_a}{P_{2r}} \right)^{1/3} \quad (19)$$

along the product gases side of the contact surface in the x, t plane. The procedure for fixing a point in the (x, t) plane (Fig. 4) for a contact surface is therefore as follows:

(i) Take a small time interval t of say $0.05L/D$

(ii) Determine a value of x (x_a , say) from Eq. (17) by using an estimated value of B .

(iii) Determine a value of u_a from Eq. (18).

(iv) Determine a corresponding pressure P_a for a shock with a particle flow of velocity equal to the calculated value of u_a from Eq. (15).

(v) From Eq. (19) determine the value of the speed of sound for the product gases where P_{2r} and a_{2r} are the values of pressure and sound speed behind the shock reflected from the contact surface at zero time.

(vi) The sum of the values found for u_a and a_a will then be equal to the Riemann invariant at the point x_a in the (x, t) plane. This value of $(u_a + a_a)$ must be equal to the Riemann invariant at the point where a straight line of the same slope through x_a intercepts the line OX . The x -coordinate of the intercept is $x_a - (u_a + a_a)0.05L/D$ and the value of $(u_a + a_a)$ at this point can be calculated from Eqs. (12)-(14).

(vii) If the two values of $(u_a + a_a)$ do not agree another value of B has to be chosen until agreement to the required accuracy is obtained.

In order to obtain further points on the contact surface, the procedure is repeated with the origin of coordinates moved to the previously determined point.

Table 3 shows the results obtained assuming that the explosive detonates at 1850 m/sec and that the bulk density ρ_0 is 0.8 gms/cc; the length of the cartridge was taken to be 15 cms.

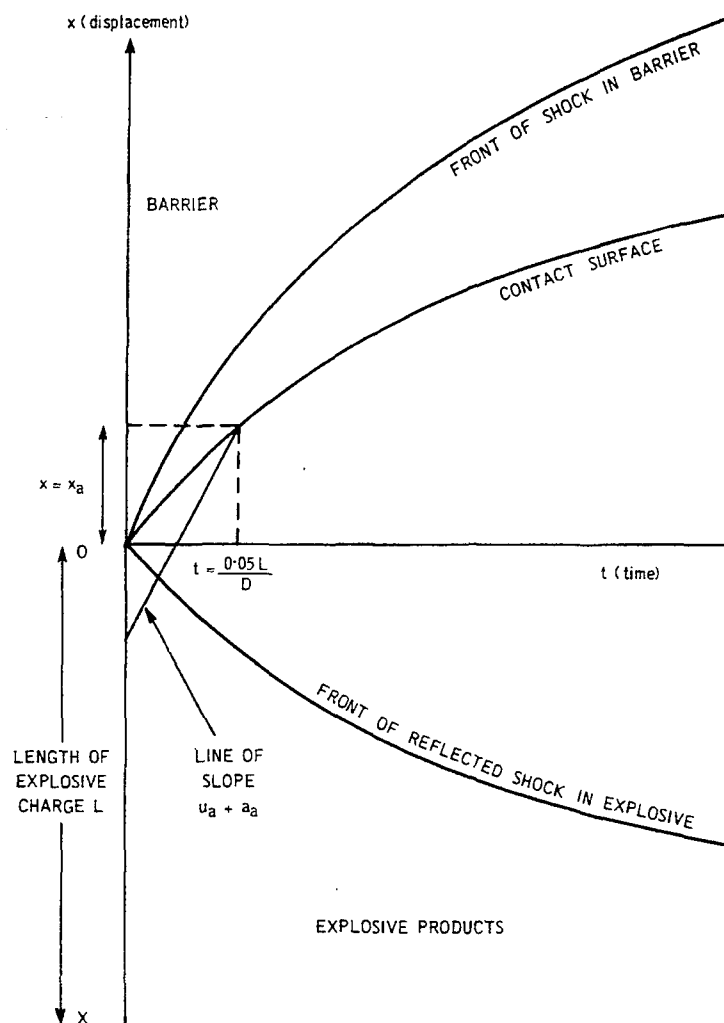
The equation of state taken for steel was that used by Pack, Evans and James (1948):

$$P_{2m} = K \left[\exp M \left[1 - \left(\frac{\rho_{0m}}{\rho_{2m}} \right)^{1/3} \right] - 1 \right] \left(\frac{\rho_{2m}}{\rho_{0m}} \right)^{2/3} \quad (20)$$

where ρ_{0m} is 7.8 gm/cc, K is 1201.6 kbars and M is 4.203.

The results of these calculations may be compared with the measurement of free surface velocity made using the pin-contact method and given in Fig. 3. The calculations show that the explosive N.G. Powder A, should give to the free interface of a steel barrier of thickness 6 mm an initial velocity of about 100 m/sec; however, the results shown in Fig. 3 show that the initial free surface velocity in these conditions was approximately 200 m/sec. It is at first sight surprising that the experimental value is greater than the calculated value, because it has been assumed in the calculations that the donor explosive was perfectly confined in the lateral direction. The difference in the results may be due to the fact that in the theoretical approach no account was taken of the effects of the detonation reaction zone; in a mining explosive this zone may be of the order of 1 cm in length and the pressure at the detonation front may be twice its value at the C.-J. plane. The transient effect of this zone, therefore, may not be completely attenuated at the time the shock front arrives at the free surface of a barrier 6 mm thick. In military explosives the effect would be far less serious since the reaction zone is very much smaller and may be as short as one tenth of a millimetre [Duff and Houston (1955)].

There are disadvantages in using steel as a barrier therefore. In order to reduce the particle velocity of the barrier at the interface with the receptor to the critical level at which detonation is produced, a barrier material which has similar acoustic impedance to the products of detonation of the donor, would be more desirable. The critical thickness of such



Values of u , a , and P along OX , that is in the explosive at time $t = 0$, are obtained from equations 12, 13 and 14

Fig. 4 - Conditions in the displacement-time plane

TABLE 3

Time After Impact Microseconds	Displacement of Contact Surface (mms)	Contact Surface Velocity (m/sec)	Pressure (kbars)
0	0	43.0	15.2
4.05	0.156	35.5	13.0
8.1	0.291	30.9	11.3
12.16	0.409	27.4	10.0
16.22	0.513	24.2	8.9
20.27	0.606	21.4	7.9
24.32	0.688	19.1	7.0
28.38	0.760	17.2	6.3
32.43	0.826	15.5	5.7
36.49	0.886	14.0	5.1
40.54	0.940	12.6	4.6
44.59	0.989	11.4	4.2
48.65	1.033	10.3	3.8
52.70	1.073	9.5	3.5
56.76	1.110	8.7	3.2
60.81	1.144	8.1	3.0
64.86	1.176	7.4	2.7
68.92	1.204	6.8	2.5
72.97	1.231	6.2	2.3
77.03	1.235	5.8	2.16
81.08	1.278	5.4	2.0

a barrier would be much greater (the thickness of a perspex barrier with which there is a 50% chance of detonation, has been found to be 25.6 mms) and consequently the attenuation of the transient disturbance produced in the barrier by the reaction zone would be greater. The particle velocity at the interface between the barrier and the receptor would be controlled by the general expansion of the products therefore and not by the reaction zone: the shape of the pressure pulse could be made square by increasing the length and confinement of the donor.

ACKNOWLEDGMENTS

The authors wish to thank the members of the Explosives Research Section, all of whom contributed to this work, especially Mr. L. P. Barbero. The text and illustrations of this paper are British Crown Copyright, reproduced with the permission of the Controller of Her Britannic Majesty's Stationary Office.

REFERENCES

- F. J. Berry and M. Holt (1954), Proc. Roy. Soc. A, 224, 236-251, 1954
- P. W. Bridgman (1923), Proc. Amer. Acad. Arts and Sciences 58, 166, 1923
- S. Chandrasekhar (1943), On the Decay of Plane Shock Waves, Aberdeen Proving Ground, Ballistics Research Laboratory, Report No. 423, Nov. 8, 1943
- M. A. Cook, D. H. Pack, and W. S. McEwan (1960), Trans. Faraday Soc. 56, Pt. 7, 1028-1038, July 1960
- M. A. Cook (1958), The Science of High Explosive, Reinhold Pub. Corp., 84-88, 1958
- R. Courant and K. C. Friedrichs (1948), Supersonic Flow and Shock Waves, Interscience Publishers, Inc., New York, 1948
- W. E. Deal (1958), Physics of Fluids, 1, 6, 523, 1958
- W. E. Drummond (1957), Interaction of Non-uniform Shock Waves, Brit. J. Appl. Phys., 28, 1, 76, 1957
- C. Fauquignon (1960), C. R. Acad. Sci. (Paris), 4, 7, 1960, 251, (1), 38-40

- R. Hill and D. C. Pack (1947), Proc. Roy. Soc. A., 191, p. 524, 1947
- D. C. Pack, W. M. Evans, and H. J. James (1948), Proc. Phys. Soc., 60, No. 337, p. 1, 1948
- K. P. Stanyukovich (1960), Unsteady Motion of Continuous Media, Pergamon Press, p. 357, 1960
- G. I. Taylor (1950), Proc. Roy. Soc. A., 200, p. 235, 1950
- J. M. Walsh and R. H. Christian (1955), Phys. Rev., 97, 1544, 1955
- G. P. Cachia and E. G. Whitbread, R. J. Eichelberger and M. Sultanoff, M. A. Cook, D. H. Pack, and W. A. Gey, W. R. Marlow and I. C. Skidmore, Proc. Roy. Soc. A., 246, No. 1245, July 1958

EXPERIMENTAL METHOD FOR ANALYSIS OF THE STRUCTURE OF A SHOCK WAVE IN A SOLID

C. Peyre, J. Pujol, and J. Thouvenin
*Commissariat à l'Energie Atomique
Paris, France*

ABSTRACT

The experimental device which we present permits us to observe the number of shock waves which traverse a solid in a given experiment, and to measure their velocities and pressures. The principle of the device consists in making the shock waves reach the free surface of the solid in an oblique manner in such a way as to record with the aid of a streak camera successive displacements of the image of a fixed luminous source. The fundamental character of the shock phenomenon, i.e., its discontinuous aspect, can be observed directly on the film. The apparatus design may have several slightly different variations, depending on whether the material studied remains or does not remain reflective under the effect of the shock. This device is used to observe elastic precursors in weak shocks, to analyze changes of state, and in a general way to investigate the causes of shock-wave doubling. The transition of iron at 135 kilobars is shown as an example.

1. INTRODUCTION — DIFFERENT SHOCK WAVE STRUCTURES IN A SOLID

The simplest structure of a shock wave which propagates in a solid at rest is one for which there is a jump in pressure quasi instantaneously which brings the pressure in the solid from atmospheric pressure to some tens or hundreds kilobars. The wave is then represented by a vertical front followed by a profile which in general decreases according to the influence of rarefaction waves which propagate from the rear of the shock generating system. This wave remains stable, that is to say unique in a certain pressure range. We know, however, of two structures which are more complex for the shock wave (Ref. 1):

a. The pressure of the incident shock is sufficiently weak that the shock wave has a velocity which is less than the velocity of the longitudinal elastic waves in the solid. In this case an elastic wave of limited pressure precedes the shock wave. This phenomenon was observed notably by Fowles [2] with oblique shocks in aluminum.

b. The solid may undergo as a result of a sufficiently high pressure, a crystalline transformation. If the pressure is above the threshold

where the transition appears, but is nonetheless not too high, the shock separates into two waves; the first brings the solid to a pressure which is equal to the transition pressure; the second brings it to the final pressure. It can be shown in fact (Ref. 1), that the velocity of the first wave is necessarily greater than that of the second. This effect of doubling of shock waves associated with a crystalline transition was evidenced experimentally by several authors (Ref. 3-4) in the case of iron and of bismuth.

We have sought to observe directly the structure of a shock wave in all of the cases described above, by an optical method suggested by a procedure which was described by Fowles [2], but applied to normal shocks. The method permits one to (a) emphasize the appearance of several waves, thus to signal the existence of a crystalline transition in the solid which is being studied, or to observe the conditions of formation of an elastic precursor, and (b) to measure the velocity and pressure of these waves.

2. PRINCIPLE OF THE EXPERIMENTAL METHOD

A plane shock wave generated by an explosive cartridge is propagated in a metallic base plate (Fig. 1). On this base there is placed a

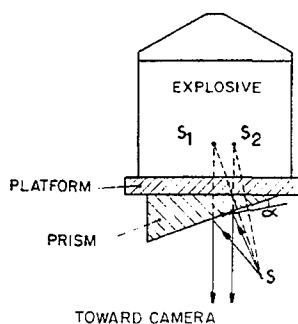


Fig. 1 - Diagram of the principle

prism of the solid to be studied. The free surface of the prism is polished and it reflects at S_1 the virtual image of a luminous source, S . During the passage of the shock wave, the free surface which is reached obliquely, undergoes a rotation, α , and the image of S is displaced to S_2 . If the shock wave has a complex structure it will produce successive rotations of the free surface, hence, positions S'_2, S''_2, \dots , of the image of S , which we record as a function of time with a streak camera. The measurements of the displacement $S_1S_2, S_1S'_2, \dots$, permit us to go back to the rotations α, α', \dots , and from these rotations to the pressures of the successive shock waves.

The essential attribute of the method is that the fundamental character of the shock phenomenon, its property of being discontinuous, is made measurable and clearly evident by the discontinuous displacement of an image, and not by the change of slope of a continuous plot of the path (x, t) .

The photographs which will be presented below reproduce approximately the shape of the pressure wave which passes through the solid.

2.1 Free Surface Rotation Produced by an Oblique Shock

Let D be the velocity of the shock wave at the time it arrives at a point A of the free surface (Fig. 2) forming an angle β with the latter. The velocity discontinuity propagated by the shock wave in the solid has an amplitude u .

The shock wave is reflected at A into rarefaction waves, which communicate to the material a supplementary velocity which is usually designated by σ , and has a value which differs by a very small amount from u (Ref. 1). We assume that the vector σ forms an angle equal

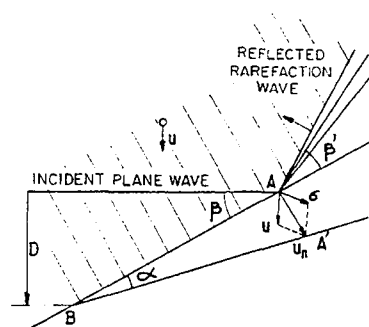


Fig. 2 - Rotation of the free surface

to β with the normal at A to the free surface. The resultant velocity of point A is therefore a vector u_n , which is normal to the free surface, and has amplitude

$$u_n = u \cos \beta + \sigma \cos \beta \approx 2u \cos \beta.$$

From this we obtain the angle of rotation, α , of the free surface

$$\tan \alpha = \frac{u_n}{D} \sin \beta = \frac{u}{D} \sin 2\beta. \quad (1)$$

2.2 Measurement of the Rotation Angle α

The luminous source, S , (Fig. 3) is actually a slit, which is placed normal to the plane of the figure, at a distance $SH = d$ from the free surface (M) of the prism. The image of this slit given by (M) is viewed at S_1 by the objective lens of the camera, to which the observation slit is perpendicular to the luminous slit S .

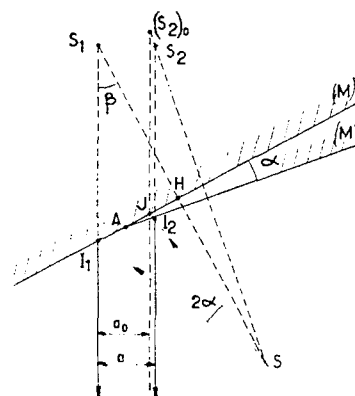


Fig. 3 - Measuring the angle α

At the time the shock wave arrives at A, the free surface already reached by the shock has rotated by an angle α , and is located at the position (M'). There is recorded on the film of the camera, therefore, two images of S. The first, S_1 reflected by (M) seen through I_1 ; the other S_2 reflected by (M') seen through I_2 .

The two reflected rays being parallel to each other (observer at infinity), the incident rays SI_1 and SI_2 subtend an angle 2α whatever the position of A is on (M). The second image of S appears, therefore, at the time the shock wave arrives at a point J defined by:

$$(SI_1, SJ) = 2\alpha.$$

This image appears at $(S_2)_0$, and the separation as viewed by the camera has the value

$$a_0 = S_1J \sin 2\alpha = SJ \sin 2\alpha,$$

or

$$a_0 = d \frac{\sin 2\alpha}{\cos (\beta - 2\alpha)}. \quad (2)$$

While the shock wave progresses from J toward I_1 the image S_2 has a slight displacement toward the right, but in the arrangement utilized above, a simple calculation shows that this displacement is always smaller than 5% of the value a_0 .

Finally, by the time the wave arrives at I_1 , the image S_1 disappears.

A more detailed analysis of the optical properties of the apparatus show that in order to make precise measurements of α one must close the diaphragm of the objective lens of the camera as much as possible and place the camera at a distance which is several times the focal length from the subject.

If it is known that the rotation, α , will be small, for example, of the order of several minutes, we increased the distance, d , which separates the prism and the flash, in such a fashion as to obtain a displacement a_0 which is measurable. Conversely, if it is known that α is large, we bring the flash nearer.

2.3 The Experimental Setup

The luminous source S consists of several parallel slits engraved in a plate of black Plexiglas and placed at the extremity of an argon flash (Fig. 4). The use of several slits enables one to measure the velocity, D , of the shock

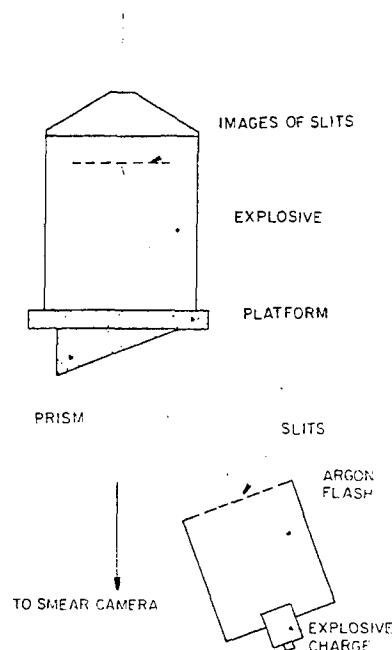


Fig. 4 - Experimental arrangement

wave by means of the time intervals which separate the appearances of the images S_2 .

The metallic prism has an apex angle of $\beta = 20^\circ$. Two versions were utilized:

a. First, the plate which separates the explosive and the prism is made of a metal having known shock characteristics (for example copper and aluminum). The prism is made of the metal to be studied. This version is convenient for the study of elastic waves, and for studies whenever the material is easily polished.

b. Second, if the metal studied cannot be polished, or if it loses its polish under the effect of the shock, it is used to form the base plate. We then utilize for the prism a metal which is easily polished (copper, aluminum), having known shock characteristics.

The eventual doubling of the shock wave in the metal which is being studied is transmitted to the metal of the prism in the form of two successive shocks; but in this case the second shock has a tendency to overtake the first shock, since the metal of which the prism is made does not exhibit a crystalline transition. In order to observe this doubling, despite the overtaking, it

suffices that the retardation suffered by the second shock with regard to the first shock in the metal of the base plate be sufficient not to be annulled during its passage over the prism; we thus choose a thick base and a thin prism.

3. ANALYSIS OF ELASTIC PRECURSORS

We have sought to observe these in two cases: Armco iron and quartz. The experimental apparatus is utilized in its first version: aluminum or copper base, and a prism made up of iron or quartz.

3.1 Armco Iron

We choose the explosive in such a way as to produce a shock pressure of 120 kilobars in aluminum and 170 kilobars in the iron prism. A record is presented on Photo No. 1; we observe a first displacement of the sources, of feeble amplitude, which is due to the elastic wave which precedes the shock wave; then, at the end of an interval of time which increases with the thickness traversed the disappearance of these images due to the arrival of the shock wave. This produces a rotation of larger amplitude of the free surface of the prism, and will be analyzed later.

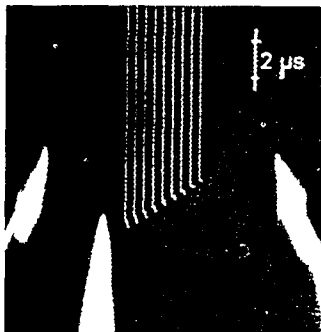


Photo No. 1 - Elastic wave in iron

This record permits us to measure the velocity of the elastic wave and the velocity of the shock wave. Table 1 gives the values measured in the course of four experiments.

The record permits us to measure likewise the material velocity u behind the elastic wave, by means of formula (1), the velocity D being already measured. Table 2 gives results which

TABLE 1
Velocity of Waves in Armco Iron

Test No.	D, elastic (mm/ μ sec)	D, shock (mm/ μ sec)
1	6.15	5.27
2	6.35	5.06
3	5.98	5.29
4	6.09	4.78

TABLE 2
Progress of an Elastic Wave in Armco Iron

Thickness of Iron Traversed, mm	u (mm/ μ sec)	p (kilobars)
3.7	0.0234	11.1
5.5	0.0228	10.8
7.4	0.0210	9.9
9.2	0.0216	10.2
11.0	0.0210	9.9
12.8	0.0198	9.4
14.6	0.0174	8.2
16.5	0.0162	7.6
18.3	0.0162	7.6

were obtained in the course of a single experiment, in which D was found to be 6.00 mm/ μ microsec.

It appears that the pressure associated with the elastic wave decreases as it passes through the iron, a phenomenon which is similar to the weakening of sound waves in a solid. The presence of the shock wave behind the elastic wave cannot influence this weakening, since this shock wave has a lower velocity.

3.2 Quartz

Elastic pressure waves of large magnitude were observed in quartz by Wackerle [5].

We also find the same order of magnitude in our experiments. Photo No. 2 shows a record obtained with a quartz prism having an axis parallel to the direction of the shock: we observe the large displacement due to the elastic wave, followed by one due to the shock wave. Table 3 and Graph No. 1 give the results of these measurements which are in good accord with those of Wackerle.

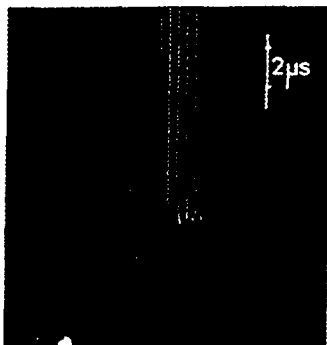
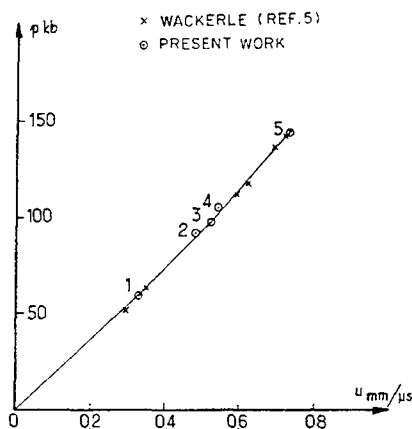


Photo No. 2 - Elastic wave in quartz

TABLE 3
Elastic Wave in Quartz

Test No.	D (mm/μsec)	u (mm/μsec)	p (kilobars)
1	6.87	0.33	60
2	7.30	0.48	93
3	7.15	0.52	99
4	7.35	0.54	106
5	7.49	0.73	145



Graph 1 - $p(u)$ for the elastic wave in quartz

4. ANALYSIS OF SHOCK WAVES

We present, in succession, the case of a simple shock wave in duraluminum AU4G, the case of a shock wave with doubling in Armco

iron, and the case of a simple shock wave followed by reflection of waves on the interfaces of a composite base plate.

4.1 Shock Waves in Duraluminum AU4G

The base plate and the prism are made up of the same metal, duraluminum AU4G. We induce varied shock pressures.

In the case where the shock pressure is sufficiently weak, for example 120 kilobars, we observe (Photo No. 3) an elastic precursor which precedes the shock wave by a small amount. The pressure of the elastic wave is of order 8 kilobars, and its velocity is of order 6.6 mm/microsec. The displacement due to the arrival of the shock wave is clearly visible, and permits us to make precise measurements. These are shown in Table 4.

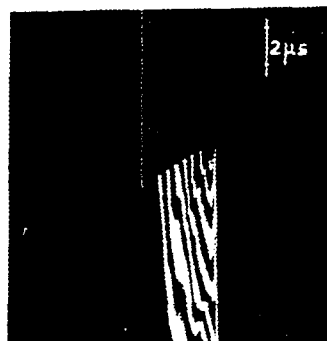


Photo No. 3 - Shock wave in duraluminum AU4G

TABLE 4
Shock Waves in AU4G Aluminum

Test No.	α	D (mm/μsec)	u (mm/μsec)	p (kilobars)
1	2°50'	6.09	0.455	78
2	4°0'	6.44	0.700	125

In the case of more intense shocks having velocities which are of order 7.5 mm/microsec and pressures of 350 kilobars, we note that the elastic precursor is not formed. The elastic wave appears only if the shock velocity is smaller than 6.6 mm/microsec, associated with a shock pressure which is smaller than 160 kilobars.

4.2 Shock Waves in Armco Iron

The observation of the transition of iron at 135 kilobars, described by the authors cited in Refs. 3-4, have been made using the two versions of the method described in 2.3.

Photo No. 4 illustrates a record obtained with the aid of an iron prism placed on a base plate made up of AU4G. The successive displacement of the image of the sources due to the elastic wave and to the two shock waves are clearly visible. We note also, by means of the observation of slopes of various hooks, that the velocities of these three waves appear in a decreasing order. Table 5 gives the values measured for the first shock wave.

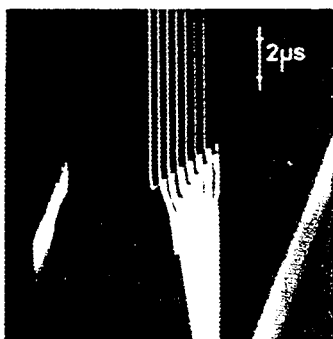


Photo No. 4 - Shock wave in Armco iron

TABLE 5
First Shock Wave in Iron

Test No.	D (mm/μsec)	u (mm/μsec)	p (kilobars)	ρ_0/ρ
1	5.27	0.346	145	0.934
2	5.06	0.342	136	0.933
3	5.29	0.327	136	0.938
4	4.78	0.332	125	0.931

These results are in good accord with the transition point data for iron given in Ref. 4:

$$p = 136 \text{ kilobars,}$$

$$u = 0.340 \text{ mm/microsec,}$$

$$D = 5.08 \text{ mm/microsec,}$$

$$\rho_0/\rho = 0.933.$$

The record of Photo No. 4 gives direct evidence of the doubling of the shock wave related to a crystalline transition.

Photo No. 5 relates to an assembly of the second version: the iron is placed directly on the explosive, and the measurements were made on a copper prism placed on the iron base. We observe again two successive waves, but this time the second wave has a higher velocity than the first; this proves that:

a. The shock wave has in reality doubled in iron.

b. A double shock wave is not stable in a metal having no transition, such as copper.

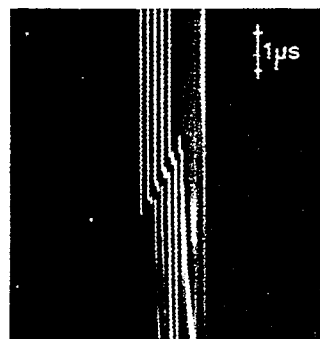


Photo No. 5 - Shock wave in Armco iron

The shock parameters of copper which were measured for the first wave are $p = 135$ kilobars and $u = 0.330$ mm/microsec.

The shock polars (p - u relations) corresponding to copper and to iron are thus coincident below the transition point of Armco iron.

4.3 Shock Waves Followed by Compression Waves

If the base is made of successive and different materials, the rarefaction waves which emanate from the free surface will undergo reflections as they traverse the various interfaces. In the experiment presented here, the base consists, from the side of the explosive, of 15 mm of copper, 5 mm of Plexiglas, and 5 mm of duraluminum AU4G; on the base is placed a prism of AU4G. At the time the shock wave arrives at the interface of the Plexiglas - AU4G, it creates in the Plexiglas a pressure which is greater than the pressure brought

about by the incident wave, as a consequence of the reflection on the AU4G. Later, at the time rarefaction waves which issue from the free surface of the prism again meet the interface, Plexiglas - AU4G, they are reflected in compression waves: this train of compression waves goes again forward, and causes a progressive increase in the material velocity of the AU4G, bringing about a second rotation of its free surface.

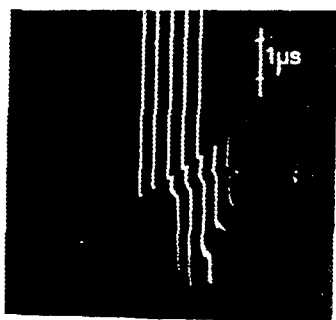


Photo No. 6 - Shock wave following a compression wave

This is what is shown in the record of Photo No. 6, in which we observe: the elastic precursor (the shock wave in AU4G has here a pressure of about 120 kilobars), the incident shock wave which produces a sharp displacement of the source image, and the arrival of the compression waves which progressively displace the images towards the right. A second train of compression waves is again observed later.

This apparatus thus permits one to distinguish between shock waves and compression waves which are spaced in time.

REFERENCES

1. Rice, McQueen and Walsh, Solid State Physics, Vol. 6, p. 1, Academic Press Inc., 1958
2. G. R. Fowles, J. Appl. Phys., 32, 1475 (1961)
3. Minshall, J. Appl. Phys. 26, 463 (1955)
4. Bancroft, Peterson and Minshall, J. Appl. Phys. 27, 291 (1956)
5. J. Wackerle, J. Appl. Phys. 33, 922 (1962).

A TECHNIQUE FOR THE PRECISE MEASUREMENT OF THE MOTION OF A PLANE FREE SURFACE

G. Eden and P. W. Wright
*Atomic Weapons Research Establishment
Aldermaston, Berkshire, England*

ABSTRACT

A streak camera technique is described for the accurate measurement of the motion of a plane free surface, based on the extinction of total internal reflection from a transparent block inclined at a small angle to the surface. The method is considered to be more universally applicable than methods based on extinction of reflectivity of a shocked surface or those utilizing gas shock luminosity. The first application of the method is to the measurement of the free surface motion of a plate driven by a normally incident detonation wave. The technique is sufficiently sensitive to detect reverberations of a coherent plate, which are seen as rapid accelerations of the plate surface, separated by deceleration phases due to the Taylor wave associated with the finite length of the detonating charge. Such measurements, used in conjunction with precise calculations can be used to infer spalling criteria of plates. The second application is to the detection of precursor waves, such as occur in a system where the direction of detonation is tangential to a plate which has a bulk sound velocity (minimum shock velocity) greater than the detonation velocity of the explosive; for example, Baratol/aluminium and Comp. B/beryllium. The method is also applied to the measurement of the precursor disturbance in normally shocked glass.

INTRODUCTION

In order to obtain information on the detononic properties of explosives or the behaviour of shocked materials (e.g., equation of state and spallation criteria), it is often necessary to measure accurately the motion of an explosively driven plate and to relate this observed motion via hydrodynamic theory to the quantities to be derived.

Studies of the detailed motion of plates moving under the influence of shocks, have, at AWRE, led to a reappraisal of known methods and to further work on optical methods using high speed rotating mirror streak cameras.

Existing optical methods examined included:

(a) Observation of the luminosity due to shock compression of a gas in contact with a plate or in a gap closed by the plate, e.g., argon-gap method [Walsh and Christian (1955)].

(b) Observation of the motion of an image reflected in the mirror surface of the plate,

e.g., knife-edge, and optical lever techniques [Craig and Davies (1961), Marsh and McQueen (1960) and Fowles (1961)].

(c) "Shuttering" methods which depend on the sharp reduction in specular reflectivity from some surfaces when shocked with or without glass or transparent plastic backing [Doran (1962)].

The methods are collectively described and reviewed in the literature by Doran (1962) and Duvall and Fowles (1963).

All of the above methods have been found to have some limitations regarding the material being studied and shock strength, e.g., Method (a) requires that the shock be sufficiently intense for the argon to flash and is affected by the finite duration of glow of the gas [Plauson and Mallory (1964)]. Method (b) requires that the surface of the plate remains a coherent plane reflector, whilst Method (c) depends on a rather obscure mechanism which is reasonably expected to be shock strength dependent.

This present paper describes a method which depends on the simple physical principle of total "internal" reflection which is not dependent on plate material or shock strength but only on the optical proximity of two surfaces.

PRINCIPLE

Total reflection of light can take place at the boundary between a solid transparent medium and a vacuum or gas, provided that the angles of incidence within the solid are greater than a certain critical value. When an object moving in the vacuum or gas comes into optical contact with the surface of the solid, total reflection ceases. This may be observed statically and the effect does not require destruction or alteration of the reflecting surface.

EXPERIMENTAL METHOD

Light from an extended source was reflected "within" a transparent prism at one of its flat surfaces as in Fig. 1. The flat plate under examination was placed "in contact" with the reflecting surface of the prism. These two mechanically flat surfaces may be clamped together at a fair pressure without coming into optical contact at more than a few points. A rotating mirror streak camera was placed to collect the light after reflection, as Fig. 2, and the image of the reflecting surface was focused on its slit. When a shock arrived at the surface of the plate, the plate moved into optical contact with the prism and the light intensity received at the camera decreased from that due to specular reflection at the prism-air interface, to that of diffuse reflection from the plate surface. This change in intensity was found to be sufficient to give a well defined time vs distance trace on the camera film, representing the shape of the shock front arriving at the free surface of the plate.

In order to allow flexibility of viewing angle θ , in Fig. 1, the section of the transparent prism may be cut so that for all values of θ between 0° and 90° , total "internal" reflection at the base must occur. This condition holds if the symmetrical base angle ψ is $2 \sin^{-1} (1/n)$, where n is the refractive index of the prism material. For glass and Perspex prisms this angle is sufficiently near 90° for square section prisms to be used.

Further motion of plate surfaces was resolved by tilting the block through a precisely known angle, as in Fig. 3, so that each point on the reflecting surface represented a known flight

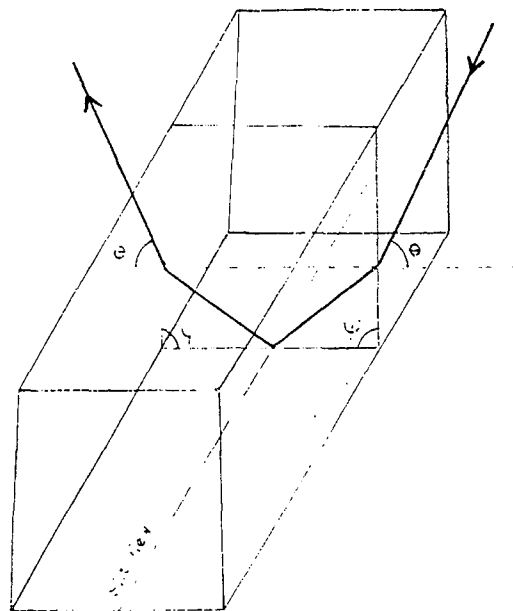


Fig. 1 - Light path in transparent block

distance. In order to monitor the "start-time" of the plate, a block flush with the plate surface was placed on each side of the tilted block. Ink-filled grooves A and B in Fig. 3, provided calibration marks of known flight distance on the resulting camera trace.

The magnitude of the angle between plate and prism is limited by the following considerations:

- (a) The velocity of the line of contact between them, along either surface, should not be less than the velocity of the disturbance produced in the material of the plate or prism,
- (b) The angle should not be great enough to allow a jet of material to form at the line of contact [Walsh, et al. (1953)].

Great care and cleanliness was necessary in assembling the plate and prism since the time taken for a plate, moving at say $1/2 \text{ mm}/\mu\text{sec}$, to cross a spurious gap of 0.001 inch due to dust or edge burrs on a prism is $0.05 \mu\text{sec}$. This interval could be easily resolved with the camera used, a Barr and Stroud S4 which had an image sweep speed of $20 \text{ mm}/\mu\text{sec}$ on the film.

Plate materials used have included liquid and solid metals (the latter mainly having a fine

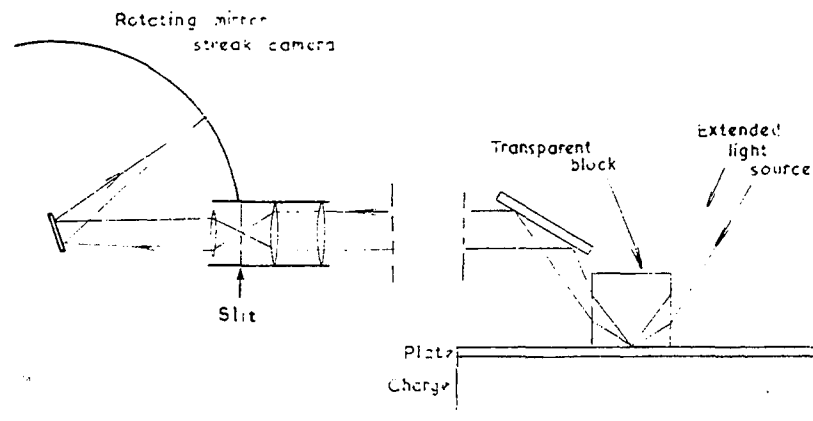


Fig. 2 - Experimental arrangement

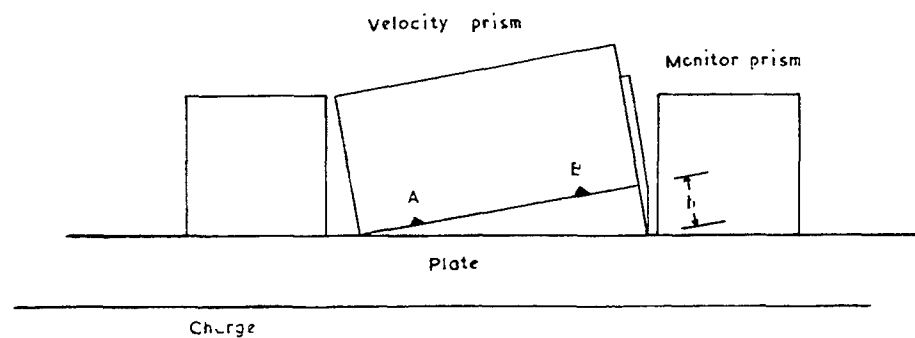


Fig. 3 - Plate velocity measurement

mat finish for maximum change in light intensity when they entered the 'view' of the slit), glass, plastics (opaque and transparent), undetonated and detonating explosive.

It is desirable, when studying relatively long flight distances, to use the method in vacuo, to avoid perturbation of plate motion and movement of the prism by a reverberating gas shock. However, in the type of experiments studied with flights ranging from 0.25 mm to 7.5 mm, evacuated systems were found to be unnecessary.

Examples of the streak camera records obtained are shown in Figs. 4 and 5, the central region showing the flight of the surface, the shock arrival being shown on either side. With knowledge of camera sweep speed, magnification of image and angle of inclination of the transparent block, the distance (x)-time (t) trajectory of the free surface may be plotted. Due to the finite length of charge, a rarefaction follows the initial shock in the plate causing a

deceleration of the free surface after its initial shock-induced velocity. The concomitant tensile pressure developed in the plate can be considerable and it will cause fracture (spalling) when it exceeds the dynamic tensile strength of the plate material. The deceleration and reverberation of the plate is clearly seen in the streak camera record (Fig. 4). Polynomials of various powers were fitted statistically to the deceleration phases of the $x-t$ trajectory of the plate but it was found that the experimental accuracy did not warrant considering polynomials of higher power than quadratic. This, of course, implies a linear variation of free surface velocity with time (e.g., Figs. 6, 7, and 8). The corresponding theoretical treatment [Lambourn and Hartley (1965)] predicted that the velocity variation during decelerations was, in fact, quite close to being linear.

In each complete deceleration phase, more than one hundred x, t readings were normally taken in punched card form, for analysing and plotting by computer code.

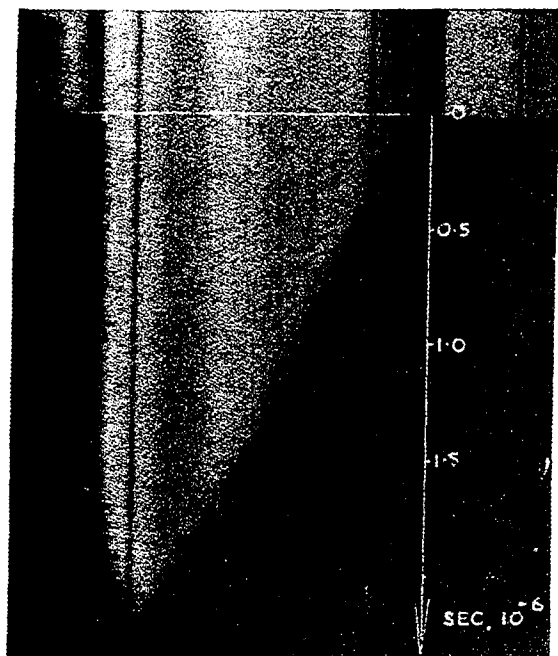


Fig. 4 - Typical result

The analysis of film records gave an average reading error of $\pm 1/2\%$. The instrumental error, depending for example on accuracy of prism angle, planarity of surfaces, etc., is estimated at 2% to 3% in the experiments so far conducted. As a mutual check, carefully metrologised pin contactor rounds have shown comparable or greater reading errors with absolute velocity values not significantly different from the streak camera results.

A minor contribution to the experimental error concerns the optical resolution of the position of the line of contact between a perfectly flat plate and a perfectly flat prism base, inclined to each other at some angle. When light is totally reflected, the electromagnetic field across the prism-air boundary is continuous, and its amplitude in air drops exponentially with distance of penetration; but it is effectively contained within a distance of the order of a wavelength of light. Hence the plate intercepts an increasing proportion of the reflected light intensity as it approaches the prism base, and in a streak camera experiment, this affects the resolution of both position and time of contact. It may be shown that the resulting thickness of increasing density of the edge of a trace recorded on grainless film via optics of perfect resolution is of the order of 7×10^{-5} cm for typical plate motion experiments. This is very small compared with the reading accuracy,

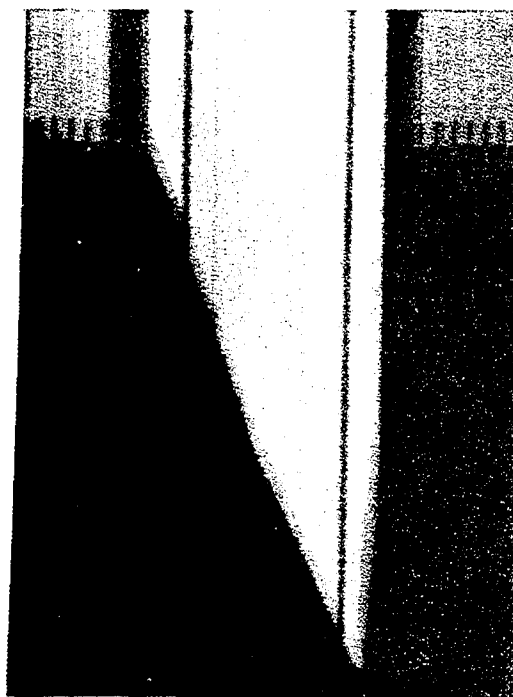


Fig. 5 - Typical trace using two slits

camera resolution, etc., but the thickness of the edge of the trace could become appreciable if both the plate velocity and angle of inclination of the prism are very small.

APPLICATIONS

A. Free Surface Motion Studies

1. Nonspalling, H. E./Plate Systems

Studies of the motions of plane plates driven by detonated H. E. charges can give information on the detonic properties of the H. E. and/or the behaviour of the plate material under transient stresses. Defining H as the ratio of charge to plate thickness then for low values of H considerable tensions can develop in the plate. These result from the following rarefactions and in some cases theory predicts tensions in excess of 100 kilobars. When the tensions exceed the tensile strength of the plate, fracture will occur. This phenomenon is known as "spalling" or "scabbing."

For most materials the normal (static) tensile strength does not exceed 5~10 kb. However, it has been shown that at high rates of strain the dynamic tensile strength of some materials is increased several-fold [Taylor and Whiffin (1948), Skidmore (1965)].

In particular, steel exhibits this behaviour. For the majority of experiments an 18/8 Stainless Steel (E. N. 58B) was used as the plate. This type of steel was chosen since in some of the attenuated systems studied (but not reported here) the amplitude of the first shock in the plate ranged from 100~200 kilobars. In these situations the polymorphic transition occurring at 130 kilobars in low carbon steel would have confused the interpretation of results [Bancroft et al. (1956), Skidmore (1965)]. For the 18/8 Stainless steel used the amount of transition was negligible [Fowler, et al. (1961)].

Another metal which we have found to have a relatively high dynamic tensile strength is titanium.

With these materials in systems, for example with $H > 20$ and a charge length of 2 inches, the plates remain coherent despite negative pressures (tensile stresses) of up to approximately 60 kilobars in steel and approximately 40 kilobars in titanium. The motion of the plate free surface should then follow the trajectory predicted by (nonspalling) theory: i.e., an almost instantaneous rise to an initial value of free surface velocity followed by a steady deceleration until the arrival of a second pressure pulse originating from reflection at the plate rear surface of the centred rarefaction from the front surface. In Fig. 6 are given the free surface velocity vs time plots derived from the results of two identical shots. Each shot consisted basically of a 3-inch cylinder of Comp. B, 5-inch diameter, initiated by a 5-inch diameter Comp. B/Baratol plane wave lens and driving a titanium disc, where the value of H was 21.4. An example of a streak record obtained from a titanium plate is shown in Fig. 5,

where two parallel slits in the camera gave two traces on the film. By using fine slits 0.001 inch in width it is possible to only partially expose the film on the first trace and thus the second trace can be superposed [Doran (1963)]. In this case, the side prisms for monitoring plate start time, were grooved to improve contact with the plate and to improve resolution of the time datum trace for each slit.

Also in Fig. 6 is shown the variation of free surface velocity with time as predicted by theory. This theoretical plot was obtained by the N.I.P. computer code [Lambourn and Hartley (1965)]. N.I.P. is a one-dimensional characteristic computation using a polytropic equation of state for the detonation products and a Tait equation of state for the plate.

It is seen that the agreement between the experiments, and between the experiments and theory, is quite good in this nonspalling situation, although there is increasing evidence that the compression wave arrives earlier than N.I.P. predicts for some plate materials and this slight defect may result from the simple equation of state used [Lambourn and Hartley (1965)].

In Fig. 7 is shown the results for a Comp. B/Steel nonspalling system with $H = 15.6$, and a charge length of one inch.

The deceleration of the free surface, from the initial shock induced velocity to the arrival of the subsequent pressure pulse, is $0.65 \text{ mm}/\mu\text{sec}/\mu\text{sec}$ as given by theory and confirmed by experiment. While this appears to be a small value, which is, in any case, difficult to detect, it is salutary to note that in everyday terms

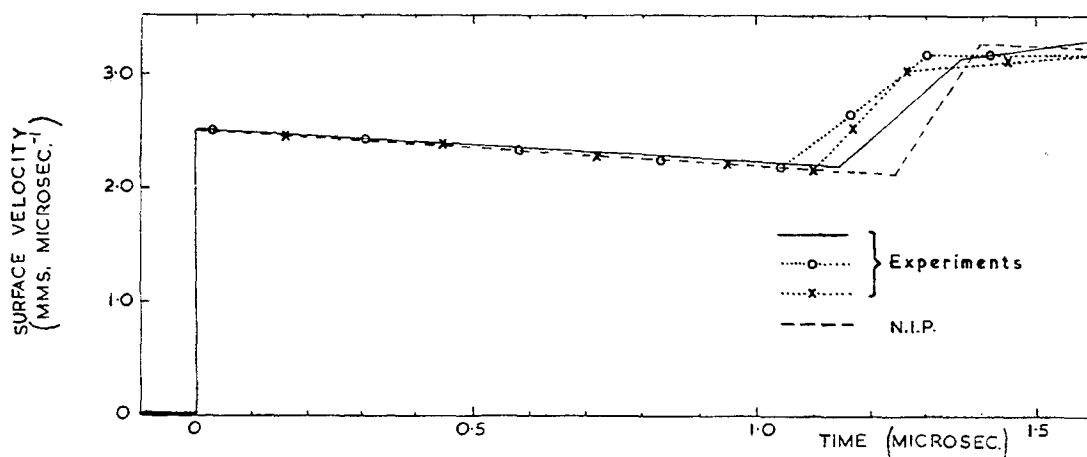


Fig. 6 - Titanium driven by Comp. B. Non-spalling, $H = 21.4$ (0.14 ins. titanium, 3.0 Comp. B)

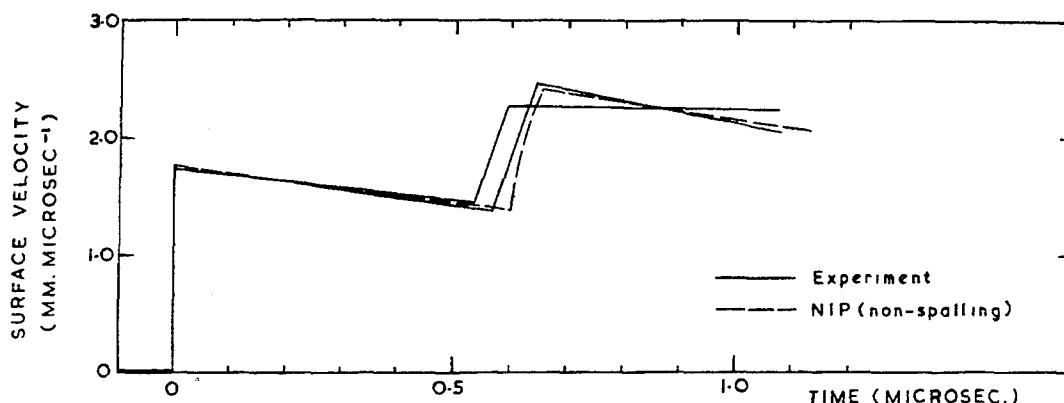


Fig. 7 - Stainless steel driven by Comp. B. Non-spalling, $H = 15.6$ (0.064 ins. steel, 1.0 Comp. B)

this deceleration is equivalent to approximately sixty-five million "g"!

A rough estimate can be made of the maximum negative pressure associated with this deceleration by assuming the pressure is localized at a predetermined plane in the body of the plate and decelerates the material between that plane and the free surface, e.g., if the plane were located 1-1/4 mms from the free surface of the steel plate then a negative (tensile) pressure of 64 kilobars would be necessary to decelerate the intervening material by 0.65 mm/ μ sec/ μ sec.

The location of the plane of maximum negative pressure can be experimentally estimated from subsidiary (recovery) experiments on similar systems which just spall.

Nonspalling theory (N.I.P.) gives a maximum negative pressure of 67.5 kilobars during the first reverberation of the steel plate in this particular system.

Similarly the results of the nonspalling Comp. B/Titanium system shown in Fig. 6 give a mean deceleration of 0.28 mm/ μ sec/ μ sec which corresponds to a maximum negative pressure of 35 kilobars. The theoretical (N.I.P.) value for this system is 36 kilobars.

The surprising agreement between the values of maximum negative pressure obtained from experiment via the crude approximation and those given by the N.I.P. computation is due to the fact that the increase in negative pressure is very nearly linear with respect to distance from the free surface.

2. Spalling, H. E./Plate Systems

A series of experiments were undertaken with Comp. B/Steel systems having values of H ranging from 25 to 5. It was observed that agreement with the (nonspalling) N.I.P. run ceased at $H = 16$ to 17. It is concluded therefore that spalling occurs at this value. Comparison with the N.I.P. computations for the various values of H , indicates that spalling occurred when the maximum tensile pressure in the plate reached about 66 kilobars.

The result for $H = 10$ is shown in Fig. 8 where it is seen that the major acceleration at 2.5 μ secs, occurs appreciably later than is theoretically predicted for a coherent plate. In this case, the sudden increase in free surface velocity is due to shock originating from the collision of the parent with the spall, reaching the free surface. The theoretical treatment of this spalling and catch-up situation is dealt with by Lambourn and Hartley (1965).

The free surface initially decelerates. The magnitude of this deceleration should correspond to the tensions developed in the plate, up to a limit controlled by the ultimate dynamic tensile strength of the plate. This deceleration phase should be terminated by an acceleration due to the arrival at the free surface of a shock, of magnitude approximately equal to the fracture stress, originating from the fracture plane. Subsequent reverberations of the spall should continue until the parent, which is still being accelerated by detonation products, rejoins the spall, sending a further shock to the free surface.

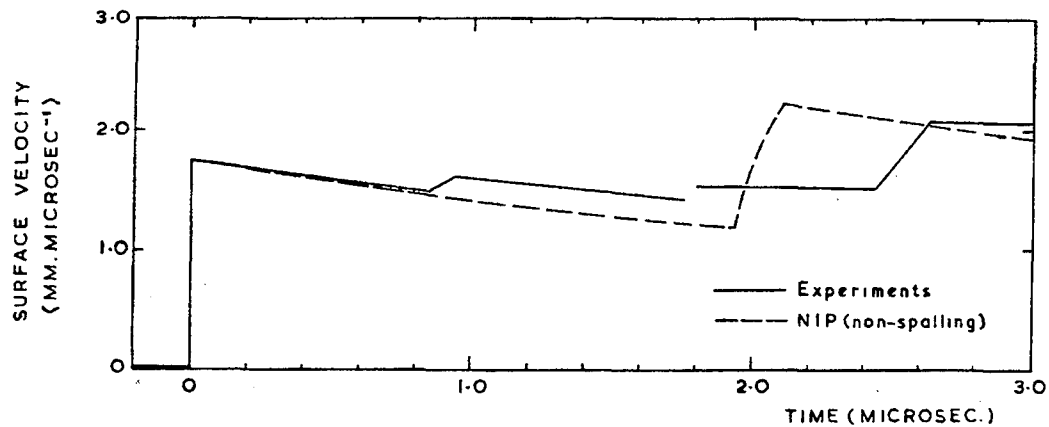


Fig. 8 - Stainless steel driven by Comp. B. Spalling, $H = 10$ (0.2 ins. steel, 2.0 ins. Comp. B)

By observing and analysing shorter flights of spalling systems, this type of spall reverberation has been detected. For example, in Fig. 8, a short flight experiment showed the first two accelerations (at 0 and 0.9 μsec) and decelerations of the spall, while a longer flight showed the major acceleration due to parent catch-up (at about 2.5 μsec). The spall acceleration was however appreciably less than would have been produced by the expected 60~65 kb shock.

B. Detection of Precursor Shock and Elastic Waves

A detonation wave moving tangentially along an explosive/inert boundary produces a shock wave in the inert. The velocity of the shock cannot be less than the bulk sound velocity in the inert, hence an unstable condition arises in a system where this bulk sound velocity is greater than the detonation velocity of the explosive. In this case a precursor disturbance moves progressively further ahead of the detonation front. Two such systems, Baratol/aluminium and Comp. B/beryllium, have been examined using the total reflection method.

Figure 9 shows diagrammatically the Baratol/aluminium system, and the type of results obtained are shown in Figs. 10 and 11. The disturbance in the aluminium is shown to advance beyond the detonation wave, as the length (L) of aluminium in contact with the Baratol is increased, and to cause an increased detonation velocity along the boundary.

Measurement of initial shock and particle velocities in the aluminium when $L = 2.0$ inches resulted in an estimated shock pressure of 53 ± 5 kilobars, the shock velocity being slightly

greater than the bulk sound velocity. The detonation velocity in Baratol adjacent to the aluminium can be up to 5% greater than the normal plane wave value and is produced by precompression of the undetonated explosive by the precursor shock and possibly the additional confinement provided by shocked aluminium. Evidence of the precompression may be seen on enlargements of the records in Fig. 11 which show the aluminium expanding and compressing the Baratol before detonation takes place.

The Comp. B/beryllium system showed similar effects.

An example of detection and measurement by the total reflection method of the precursor disturbance in glass is shown in Fig. 12. Here a plane shock wave, of amplitude 180 kilobars, was passed into 1/4-inch thickness of soda glass. Shock transit time and free surface velocity were measured, using the shock shuttering of light reflected from an aluminium mirror surface at the H. E./glass interface [Duvall and Fowles (1963), Doran (1963)], and by the total reflection method at the glass free surface. The initial low velocity is caused by the precursor wave of approximately 56 kilobars amplitude. It is interesting to note that a limitation of the mirror method became apparent when it was used on the glass free surface in the above system. This is exemplified in Fig. 13 in which both the mirror and total reflection methods were used to detect the arrival of the precursor wave at the free surface of the glass. It may be seen that the mirror method does not respond to the precursor shock. Nevertheless, it is known that the mirror method may be used on other materials at considerably lower pressures than 50 kilobars.

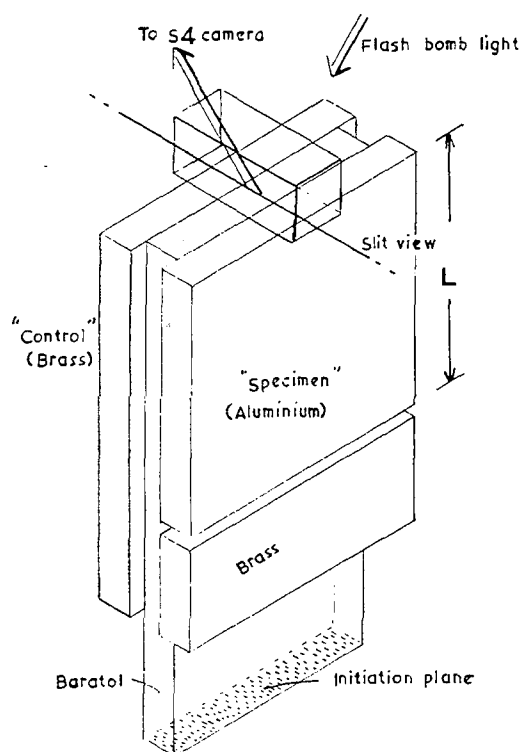
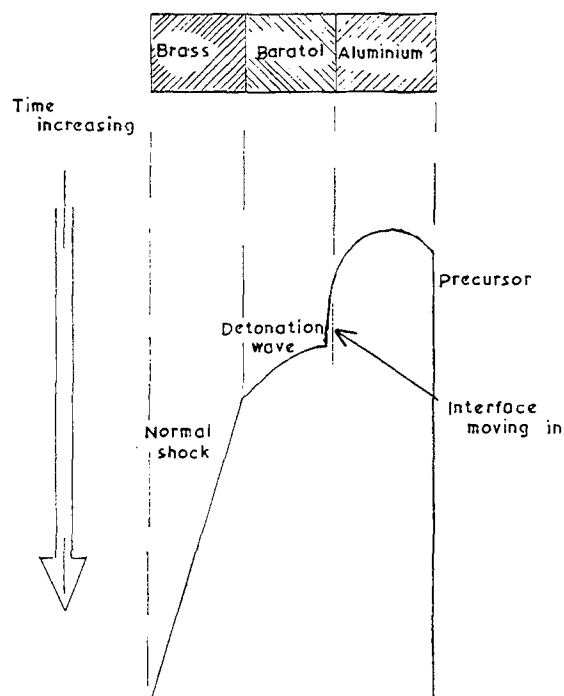


Fig. 9 - Experimental arrangement, precursor detection

Fig. 10 - Interpretation of photographic results



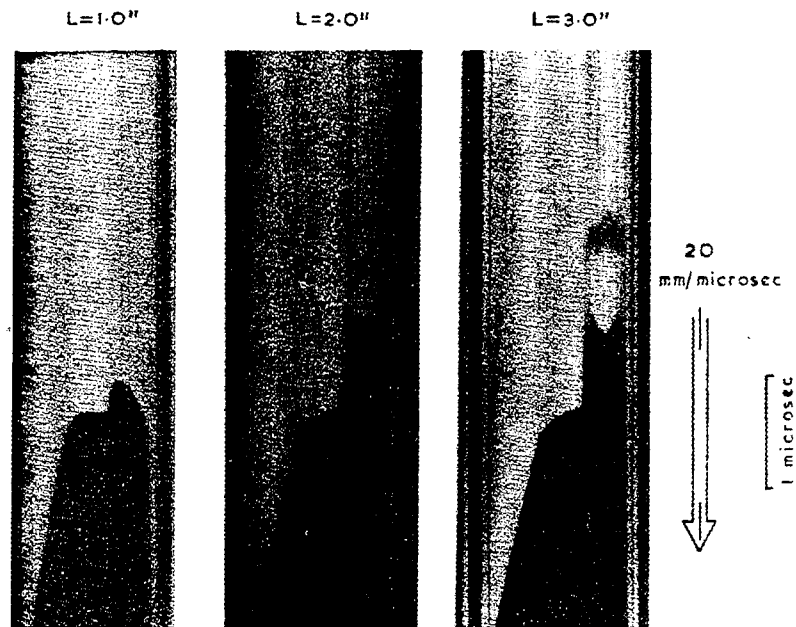


Fig. 11 - Streak camera results showing aluminium shock advancing as 'L' increases

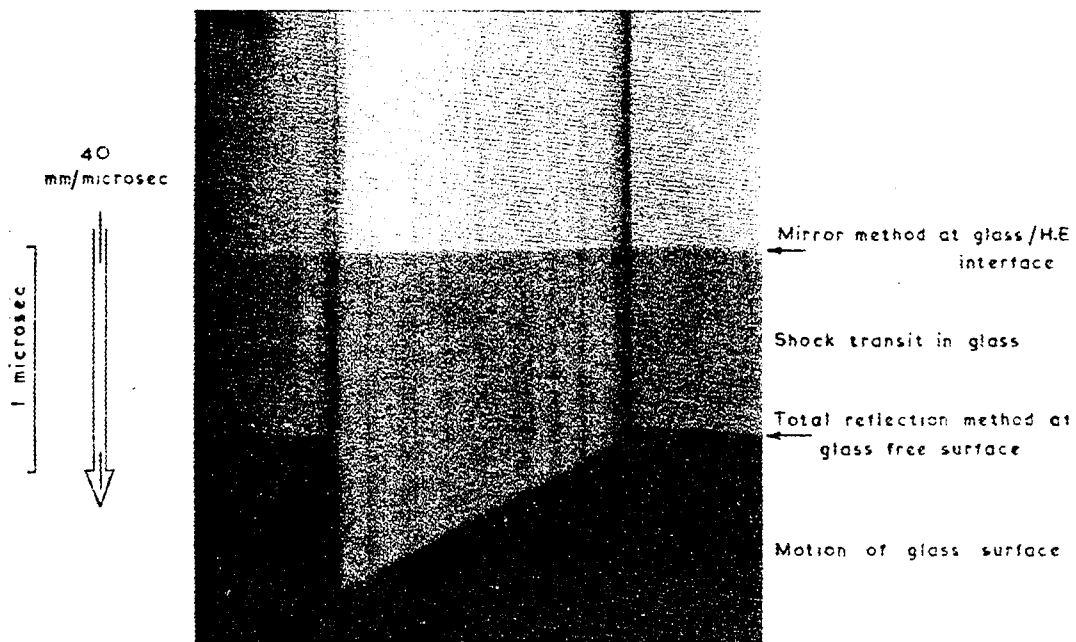


Fig. 12 - Precursor shock in glass

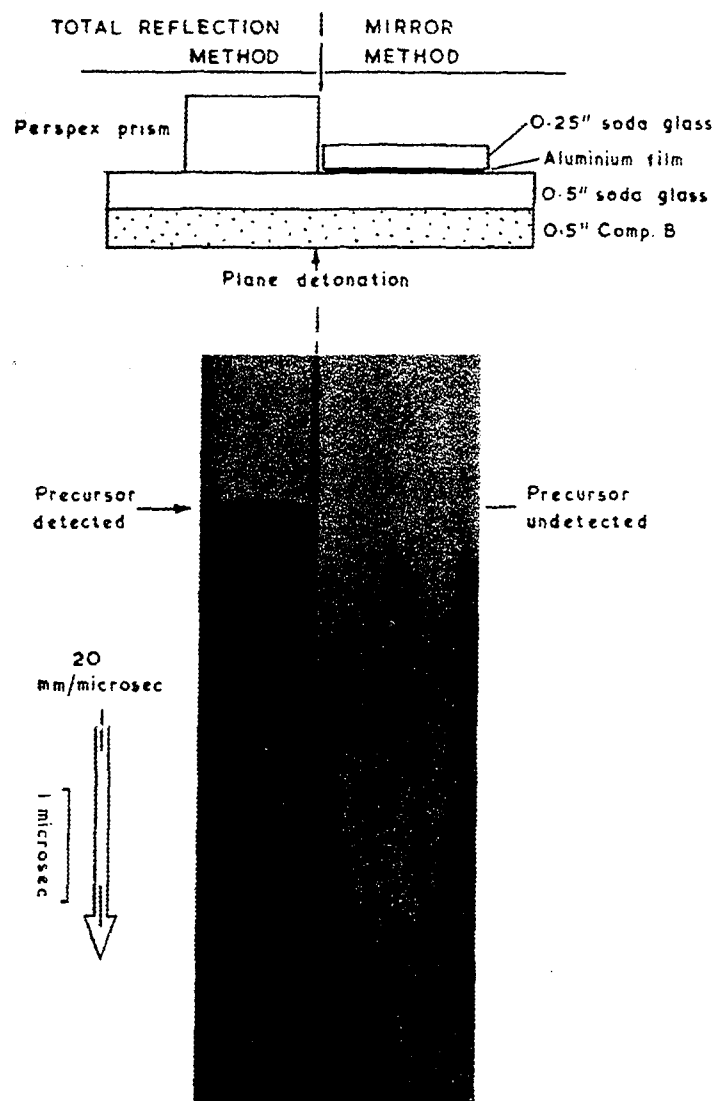


Fig. 13 - Detection of precursor arrival in glass

ACKNOWLEDGMENTS

The authors wish to thank Messrs. C. P. M. Smith and K. I. Read for some of the results quoted in this paper, and to thank Mr. F. Irons for his painstaking reading of films.

REFERENCES

- D. Bancroft, E. L. Peterson, and E. J. Minshall, *Journ. Appl. Phys.* **27**, 291 (1956)
- W. C. Davis and B. G. Craig, *Rev. Sci. Inst.*, **32**, 579 (1961)
- D. G. Doran, "Measurement of Shock Pressure in Solids" in "High Pressure Measurement," ed. A. A. Giardini and E. C. Lloyd, Butterworths (Washington) (1963)
- G. E. Duvall and G. R. Fowles, "Shock Waves" in "High Pressure Physics & Chemistry," Vol. 2, ed. R. S. Bradley, Academic Press (London and New York) (1963)
- C. M. Fowler, F. S. Minshall, and E. G. Zukas, "Hugoniot Curves for Iron Alloy," in "Response of Metals to High Velocity Deformation," ed. P. G. Shewmon and V. F. Zackay, Interscience (New York) (1961)

- B. D. Lambourn and J. E. Hartley paper, "The Calculation of the Hydrodynamic Behaviour of Plane One Dimensional Explosive/Metal System," 4th O.N.R. Symposium on Detonation (1965)
- S. P. Marsh and R. G. McQueen, Bull. Amer. Phys. Soc. II (5), 506 (1960)
- R. A. Plauson and H. D. Mallory, Journ. Appl. Phys. 35, 3 (Part 1), 502-507 (1964)
- I. C. Skidmore, Applied Materials Research 4, 131 (1965)
- G. I. Taylor and A. C. Whiffin, Proc. Roy. Soc. A. 194, 289 (1948)
- J. M. Walsh and R. H. Christian, Phys. Rev. 97, 1544 (1955)
- J. M. Walsh, R. G. Shreffler, and F. G. Willig, Journ. Appl. Phys. 24, 349 (1953)

A MICROWAVE TECHNIQUE FOR STUDYING DETONATION PHENOMENA

Edgar G. Johnson
Rohm and Haas Company
Redstone Arsenal Research Division
Huntsville, Alabama

ABSTRACT

A microwave technique has been developed for studying shock phenomena in condensed phases. The microwave energy reflected by the shock front has been used to determine velocities of both reactive (detonation) and nonreactive shocks.

This technique used standard microwave components and an expendable, dielectric rod waveguide as a transmission line to the sample under study. The oscillogram of the output of a crystal detector is a continuous displacement-time trace of the shock front as it moves through the sample. The trace can be interpreted in terms of microwave interferometry, in that the detected signal goes through a maximum and a minimum for each displacement of the shock front by a half wavelength, or as the Doppler shift in frequency produced by the velocity of the approaching shock front.

This technique has been applied to the problem of determining the growth to detonation near the 50% card gap value of 1-inch diameter charges of Composition C-4 explosive and of 2-inch diameter charges of ammonium perchlorate confined in glass. Simultaneous microwave and streak-camera measurements of the detonation of 2-inch diameter charges of pentolite have been made.

INTRODUCTION

A technique of microwave interferometry has been developed for studying shock phenomena in condensed phases. This technique is applicable to many explosives and other materials of interest in solid propellant research because they have relatively low losses at microwave frequencies. It can be used with both reactive (detonation) and nonreactive shocks. The technique yields an oscillogram that is a continuous displacement time trace of the shock front as it moves through the sample.

The use of microwaves in detonation studies has been previously reported by Cook, Doran and Morris [1], who used a horn antenna and a lens to focus the microwave energy into the end of a cylindrical charge. This method was limited by multiple modes of propagation in the charge. Another investigation, reported by Cawsey, Farrands, and Thomas [2], used a charge confined in a metal waveguide of a

diameter small enough (0.152 inches at 34.5 Gc/sec) that only one mode of propagation was possible.

EXPERIMENTAL

Standard microwave equipment has been used at frequencies between 10 and 33 Gc/sec which correspond to a free space wavelength of from 3 to about 1 cm. A schematic diagram of the instrumentation used is shown in Fig. 1.

The klystron generated the microwave energy, the attenuator was used to adjust the power level, and the frequency meter was used to determine the microwave frequency. The directional coupler was used to separate the transmitted from the reflected energy and was oriented in the transmission line to pass the reflected energy. The crystal detector was used to monitor the reflected energy passed by the directional coupler and converted the

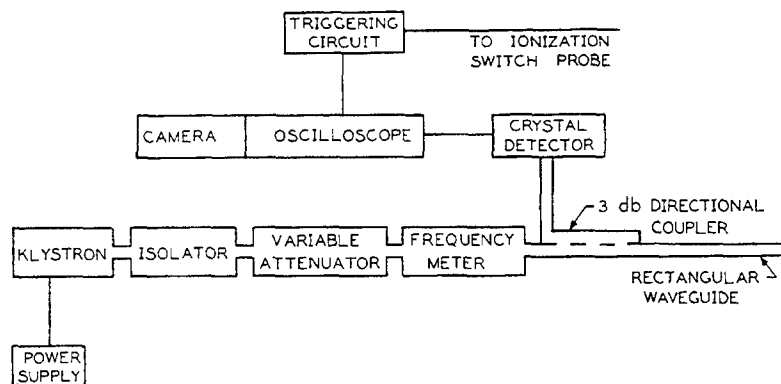


Fig. 1 - Schematic diagram of the instrumentation

reflected microwave energy to a voltage. An oscilloscope and a camera were used to record the output voltage of the crystal detector.

The oscilloscope was usually triggered from an ionization switch probe by the detonation. A dielectric rod waveguide (3) was used as a transmission line between the instrumentation and the sample. The dielectric rod waveguide was expendable and acted as a mode selector to launch a pure mode of transmission in the sample. A schematic diagram of the experimental setup is shown in Fig. 2. The standard rectangular waveguide from the instrumentation shown in Fig. 1 was converted to circular waveguide by a transition. A polystyrene rod, tapered to a point to reduce reflections, was inserted a short distance into the circular waveguide. The polystyrene rod was then tapered to a smaller diameter rod to reduce losses in transmission and then expanded to the diameter of the sample.

The voltage developed in the crystal detector can be considered as the sum of two reflected microwave signals. One is the sum of all fixed reflections in the transmission line and is of constant phase. The other is the reflection from the shock front and goes through a 2π phase shift for each displacement of the front by a half wavelength of the microwaves. Thus the voltage from the crystal detector goes through a maximum and minimum for each displacement of the shock front by a half wavelength.

In terms of the Doppler effect, the frequency of the voltage from the crystal detector can be considered as the Doppler shift in frequency f_d given by

$$f_d = \frac{2vf}{c'}$$

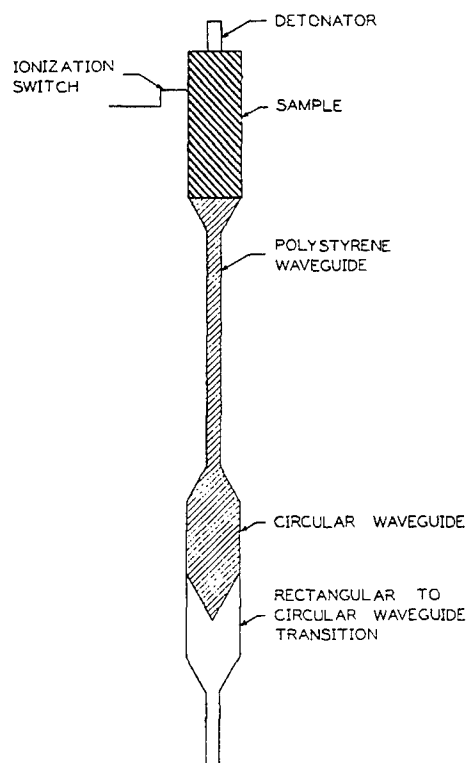


Fig. 2 - Schematic diagram of the experimental setup

where v is the velocity of the reflecting shock front, f is the microwave frequency and c' is the velocity of propagation of the microwaves in the medium through which the shock travels.

The wavelength of the microwaves in the sample was usually determined by observing the number of peaks in the voltage from the crystal detector as the shock front traversed a sample of known length. When multiple modes of

propagation were present in the sample, the voltage from the crystal detector appeared modulated because the modes had different wavelengths.

GROWTH TO DETONATION IN AMMONIUM PERCHLORATE

The explosive used in this investigation was 68μ median particle size ammonium perchlorate. The charges were hand packed to a density of 1.31 gm/cm^3 in 2-inch O. D. glass tubes having a wall thickness of 0.08 inches. The donor charge was two (50/50) pentolite pellets 2 inches in diameter and 1 inch long. The acceptor charge was 8 inches long. The card gaps were made of 2-inch disks of Plexiglas®.*

X-band microwave equipment was used and measurements were made at a frequency of 9.903 Gc/sec. The charge was initiated by J-2 electric blasting cap [4]. The oscilloscope was triggered when the detonation front in the donor charge reached the ionization switch probe, which had been placed between the two pentolite charges. The oscilloscope recorded the displacement of the detonation front in the last inch of the donor charge, the displacement of the shock wave in the Plexiglas gap, and the growth of the detonation in the acceptor charge.

The microwave wavelength was determined in the charge of explosive by observing the number of wavelengths traversed by a detonation front as it moved through a charge of known length. Using acceptors of measured length and no gap between the donor and the acceptor, the number of wavelengths traversed were counted on the oscilloscope trace. The location of the interface between the donor and the acceptor was not apparent from the oscilloscope trace. The location of this interface was determined by measuring from streak camera photographs the time required for the detonation front in pentolite to travel through the last inch of the donor charge. A wavelength of 16.6 mm at 9.930 Gc/sec was determined from two shots.

A photograph of an oscilloscope trace is shown in Fig. 3 for a gap of 1.596 inches of Plexiglas. An oscilloscope with a raster sweep was used to obtain a longer time base. The sweep starts in the lower left hand corner and sweeps back and forth across the face of the tube. A timing signal with $5 \mu\text{sec}$ time marks was first recorded on the film. The beginning and the end of the signal from the acceptor

charge are marked by arrows on the trace.

Figure 4 is the displacement-time curves for 3 charges. The interface between the donor and the acceptor or the Plexiglas and the acceptor was used as a reference point and displacements were measured from it. Curve 1 of Fig. 4 shows an initial reaction moving at less than the steady state detonation velocity. Curve 3, with no gap shows an initial velocity much greater than the detonation velocity. Figure 5 shows the velocity-distance curves for 4 charges with increasing gap thickness, from no gap to a gap of 1.808 inches which failed to detonate (a large amount of ammonium perchlorate was found in the detonation bay after the shot was fired). The velocities were determined by taking the average velocity of the detonation between peaks of the recorded signal.

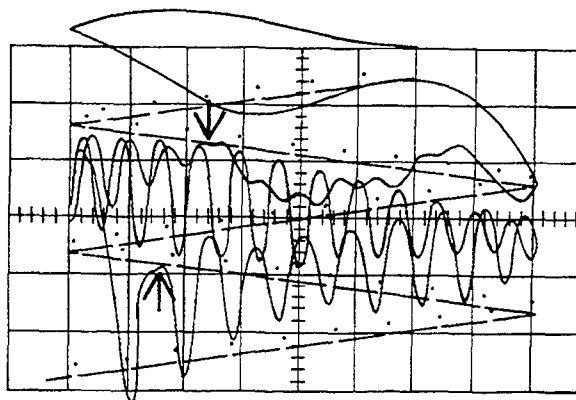


Fig. 3 - Oscillogram of growth to detonation in ammonium perchlorate

GROWTH TO DETONATION IN COMPOSITION C-4*

The explosive used in this investigation was Composition C-4. The charges were hand packed to a density of 1.59 gm/cm^3 in cardboard tubes having a wall thickness of 0.01 inches. The donor charge was 1 inch in diameter and 3 inches long. The acceptor charge was 1 inch in diameter and 4 inches long. The card-gaps were made up of 1-inch disks of Plexiglas having a total thickness of approximately 0.8 inches. K-band microwave equipment was used and measurements were made at a frequency of 24 Gc/sec. The charge was initiated by a No. 8 electrical blasting cap. The oscilloscope was triggered when the detonation front in the donor

*Trademark for thermoplastic poly(methyl methacrylate)-type polymers, Rohm and Haas Company, Philadelphia, Pennsylvania.

*This section has been submitted to the AIAA Journal for publication.

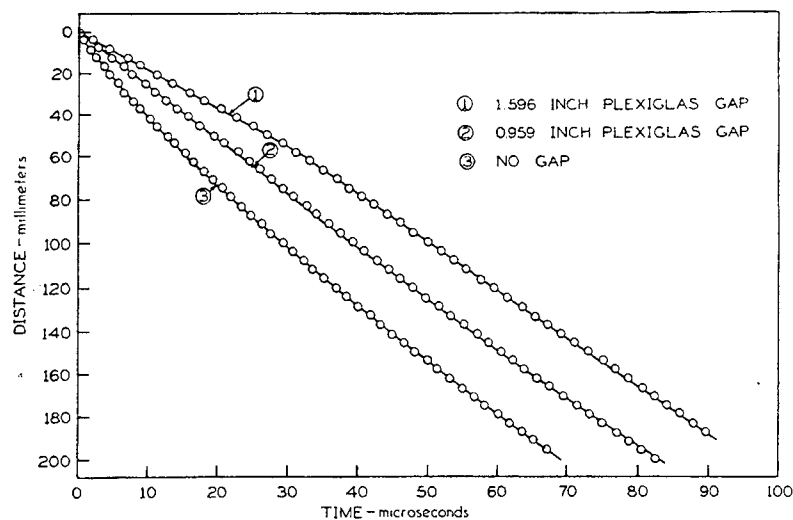


Fig. 4 - Displacement-time curves of growth to detonation in ammonium perchlorate

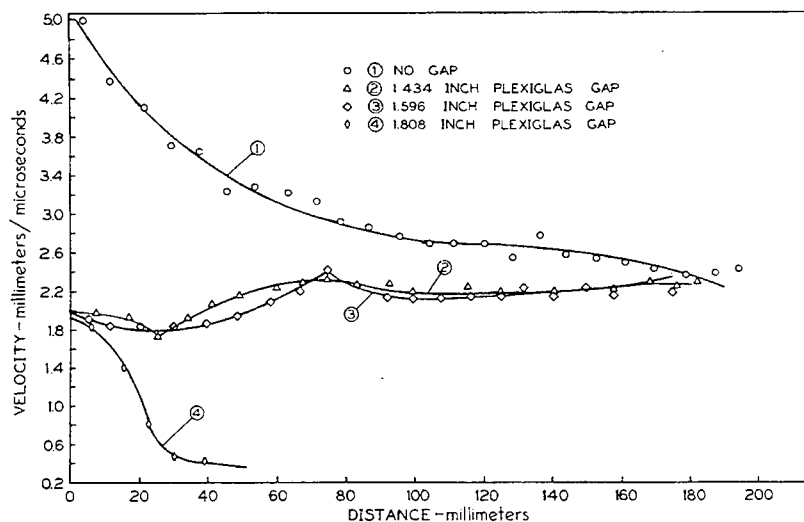


Fig. 5 - Velocity-distance curves of growth to detonation in ammonium perchlorate

charge reached the ionization switch probe, which had been placed 1 inch from the base of the charge. The oscilloscope recorded the displacement of the detonation front in the last inch of the donor charge, the displacement of the shock wave in the Plexiglas gap, and the growth of detonation in the acceptor charge.

The microwave wavelength was determined in the charge of explosive by observing the number of wavelengths traversed by a detonation front as it moved through a charge of known

length. Using acceptors of measured length and a thin sheet of aluminum foil between the donor and the acceptor, the number of wavelengths traversed was counted on the oscilloscope trace. A wavelength of $7.08^{+0.04}_{-0.08}$ mm at 24 Gc/sec was determined from three such shots. For 1-inch diameter rods of Plexiglas having a dielectric constant [5] of 2.65, a wavelength of 7.88 mm was calculated [6] for the dominant hybrid mode at 24 Gc/sec.

A photograph of a typical oscilloscope trace having a sweep rate of $5 \mu\text{sec}/\text{cm}$, is shown in Fig. 6. The trace is divided into three parts (a) the last inch of the donor charge, (b) the Plexiglas gap, and (c) the acceptor charge. From the oscilloscope trace, the time at which the detonation front reached the base of the donor and the acceptor charge is easily determined. However, the time at which the shock reached the end of the Plexiglas and entered the acceptor charge is not apparent. The progress of the shock wave through the Plexiglas gap could not be determined accurately because the shock front was partially transparent to the microwaves. The fracture front, moving at a lower velocity behind the shock front, produced a large reflection. The reflections from the shock and fracture fronts were superimposed to complicate the trace. This same complication was observed in the acceptor charge of the shots that failed to reach detonation. The front in the C-4 seemed to be partially transparent and other reflections complicated the trace. This complication was not observed in shots that reached detonation since the front in an acceptor charge that reached detonation was a reactive front and reflected more energy.

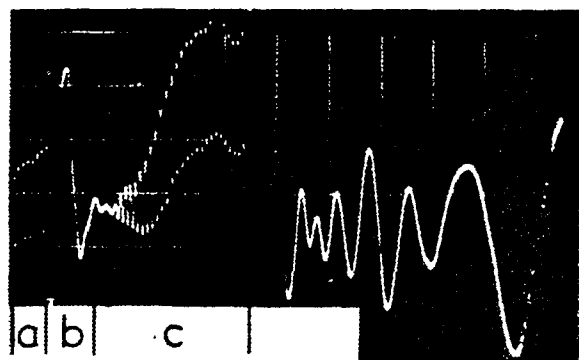


Fig. 6 - Oscillogram of growth to detonation in composition C-4

The location of the interface between the Plexiglas and the acceptor was determined by measuring from streak camera photographs [7] the time required for a shockwave from a 1-inch diameter charge of Composition C-4 to travel through 0.80 inches of Plexiglas; this was $4.8 \mu\text{sec}$. The position of the interface between the Plexiglas and the acceptor, determined by the above method, was checked by accounting for the number of wavelengths that would be present from an acceptor of known length. In all

cases this check was within the accuracy of the determination of the wavelength.

Figure 7 is the displacement-time curve reduced from the oscilloscope trace shown in Fig. 5. The interface between the Plexiglas and the acceptor was arbitrarily taken as a reference point and displacements were measured from it. Figure 8 shows the displacement-time curves of the growth to detonation at other gap thicknesses near the 50% card gap. Table 1 shows data taken from 10 shots. The first and last shots were well below and above the 50% card gap value while the remaining shots were near the 50% card gap value. The velocities reported in Table 1 were determined graphically as the slopes of smooth curves through the data points. The accuracy of the data obtained in the Plexiglas gap was not good enough to show any real differences between shock wave velocities that reached detonation and those that failed to reach detonation.

DETONATION OF PENTOLITE

The explosive used in this investigation was (50/50) Pentolite. The charge consisted of six 2-inch diameter by 1-inch long pentolite pellets of average density $1.555 \text{ gm}/\text{cm}^3$. K-band microwave equipment was used and measurements were made at a frequency of 20 Gc/sec. The charge was initiated by a J-2 electric blasting cap [8]. The oscilloscope was triggered by an ionization switch probe on top of the charge beside the blasting cap or from a signal from the streak camera 15 to 20 μsec before the initiation of detonation.

The microwave wavelength was determined by observing the number of wavelengths traversed by the detonation front as it moved through the 6-inch charge. A wavelength of $4.56^{+0.06}_{-0.10} \text{ mm}$ at 20.000 Gc/sec was determined from 4 shots. A photograph of an oscilloscope trace is shown in Fig. 9. A timing signal with $1 \mu\text{sec}$ time marks was first recorded on the film. The oscilloscope was triggered by an ionization switch on top of the charge and was delayed about a microsecond from the initiation of the detonation. Figure 10 shows the simultaneous microwave interferometry and streak camera determination of the displacement-time curves of a shot. The detonation velocity, determined by a least squares fit of the microwave interferometry data to a straight line, is $7.36 \text{ mm}/\mu\text{sec}$. The detonation velocity determined by the slope of the streak camera photograph for the last 4 inches of the charge is $7.43 \text{ mm}/\mu\text{sec}$. Table 2 shows the values of detonation velocity

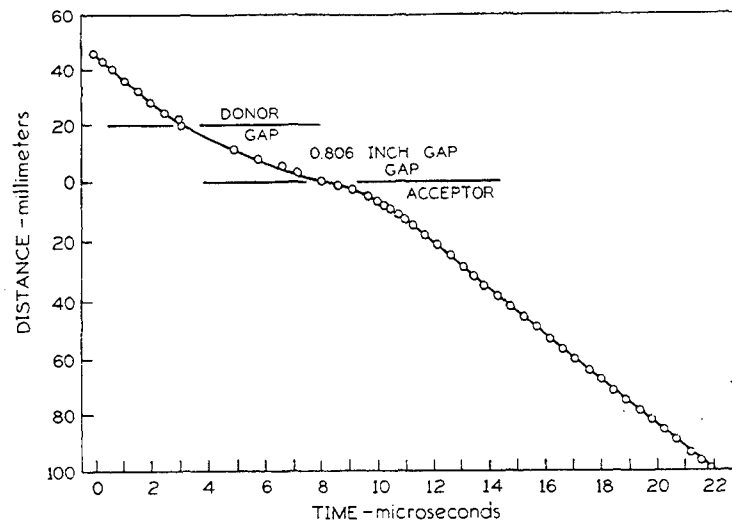


Fig. 7 - Displacement-time curve from the oscillogram in Fig. 6

TABLE 1
Summary of Results

Plexiglas gap (inches)	Time to Detonation (μ sec)	Distance to Detonation (mm)	Final Velocity in Plexiglas (mm/ μ sec)	Initial Velocity in Acceptor (mm/ μ sec)
0.734	<0.4	<4.0	a	a
0.789	1.6	10.0	a	a
0.798	2.5	8.8	3.8	3.4
0.803	1.6	5.7	a	3.5
0.806	1.8	6.0	3.8	3.3
0.808	Failed to Detonate		3.8	3.8
0.812	4.4	15.0	3.9	3.5
0.820	Failed to Detonate		3.9	4.0
0.833	Failed to Detonate		3.9	4.0
1.003	Failed to Detonate		3.3	3.3

^aVelocities could not be determined.

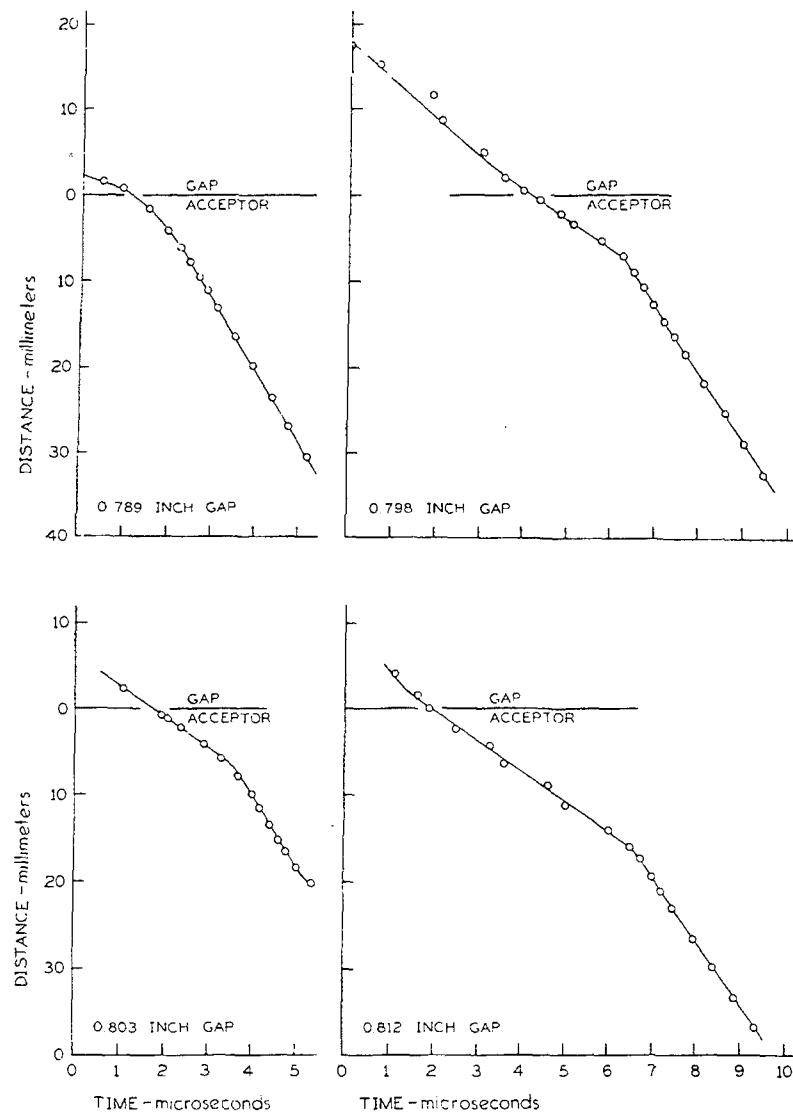


Fig. 8 - Growth to detonation for several gap thicknesses

Fig. 9 - Oscillogram of detonation in pentolite

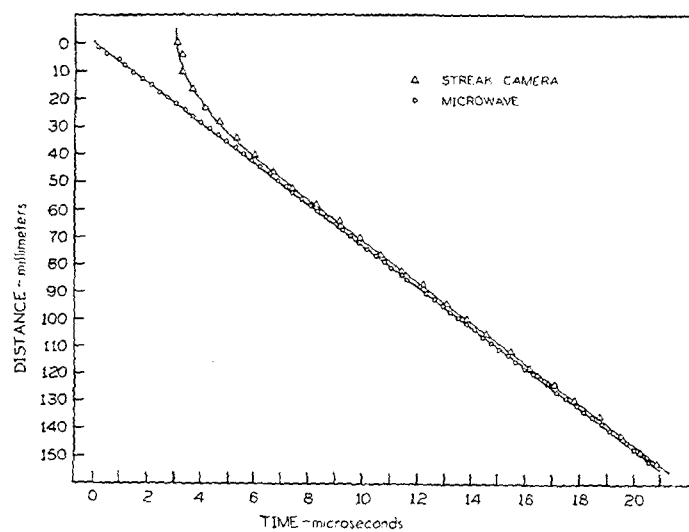
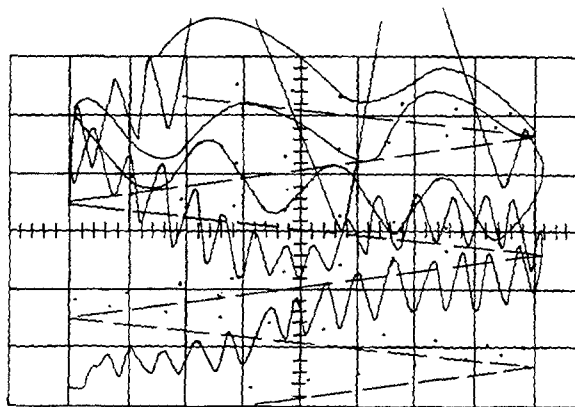


Fig. 10 - Displacement-time curves of detonation in pentolite

TABLE 2
Detonation Velocity of Pentolite

Microwave Interferometry (mm/ μ sec)	Streak Camera (mm/ μ sec)
7.30	7.08
7.32	7.25
7.32	7.43
7.32	7.57
7.34	7.67
7.36	Average 7.40
Average 7.33	

determined by the above methods from six shots with microwave interferometry and from 5 shots with the streak camera. The average velocity determined by microwave interferometry is 7.33 and by the streak camera is 7.40 mm/ μ sec. Considering the possible error in determining the wavelength of the microwaves in the charge, the average value determined by microwave interferometry would be $7.33^{+0.10}_{-0.15}$ mm/ μ sec. A previously determined value [9] for a density of 1.549 gm/cm³ is 7.27 mm/ μ sec.

Figure 11 shows the velocity-distance curves for 4 shots determined by microwave interferometry. The velocities were determined by taking the average velocity of detonation between

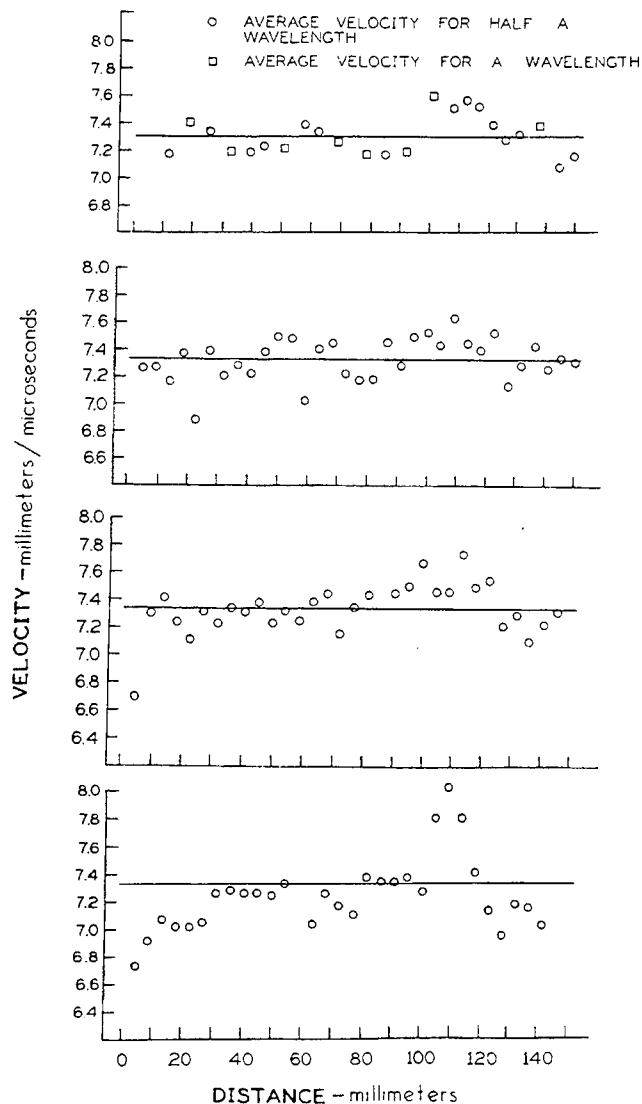


Fig. 11 - Velocity-distance curves of detonation in pentolite

peaks of the recorded signal. The variation of the velocity from a constant value toward the end of each charge is almost surely due to a small amount of the microwave energy propagating in a second mode and can be observed in Fig. 9 by the decrease in amplitude and a change in level of the recorded signal.

CONCLUSION

Microwave interferometry has been used to observe the growth to detonation of Composition C-4. The results confirm the information on growth to detonation of high explosives obtained from streak camera photographs of wedge shaped charges covered with a thin reflecting film [10]. The microwave interferometry technique has been used to observe the growth to detonation of a porous, low density charge of ammonium perchlorate. The results have confirmed a detonation where the usual witness plate technique was doubtful. This technique has been able to give detonation velocities of comparable accuracy with streak camera photographs, and certainly relates information from the interior of the charge and not just information from the lateral surface as usually obtained from streak camera photographs.

The instrumentation set up and data reduction are relatively simple and easily performed. The only expendables involved are the film for the oscilloscope camera and the polystyrene rod waveguide. This method should be most useful in studying accelerating and decelerating shock fronts. The accuracy of the technique can be improved by using longer samples to determine the microwave wavelength since this determination is the largest source of error in the technique.

The problem of launching a pure mode is not completely solved for large samples (diameter and length). A pure mode could not be launched in a 2-inch diameter by 6-inch long charge at 24 Gc/sec. No attempts have been made to launch a pure mode in cylindrical samples larger than 2 inches in diameter. A pure mode has been launched into samples (under 4 inches long) with 4-inch square cross section. A small diameter polystyrene rod waveguide was simply placed against the base of the sample, which was then treated as an infinite dielectric medium.

ACKNOWLEDGMENTS

I wish to thank Dr. H. M. Shuey for suggesting this problem and for his continued

encouragement, Mr. J. E. DeMore for his advice and assistance with the instrumentation, and Dr. K. F. Ockert and Dr. T. H. Pratt for their advice and assistance in performing these experiments.

This research was supported by the Advanced Research Projects Agency, under Contract DA-01-021 ORD-11909(Z).

REFERENCES

1. M. A. Cook, R. L. Doran, and G. J. Morris, "Measurement of Detonation Velocity by Doppler Effects at Three-Centimeter Wavelength," *J. Appl. Phys.*, **26**, 426-428 (1955)
2. G. F. Cawsey, J. L. Farrands, and S. Thomas, "Observations of Detonation in Solid Explosive by Microwave Interferometry," *Proc. Roy. Soc. (London)* **248**, Series A, 499-521 (1958)
3. C. H. Chandler, "An Investigation of Dielectric Rod as Wave Guide," *J. Appl. Phys.*, **20**, 1188-1192 (1949)
4. Hercules Powder Company, Wilmington, Delaware
5. *Techniques of Microwave Measurements*, Edited by Carol G. Montgomery (McGraw-Hill Book Company, Inc., New York, 1947) 1st ed., Chap. 10, p. 666
6. W. M. Elsasser, "Attenuation in a Dielectric Circular Rod," *J. Appl. Phys.* **20**, 1193-1196 (1949)
7. Unpublished data obtained by Dr. T. H. Pratt at Rohm and Haas Company, Huntsville, Alabama
8. Hercules Powder Company, Wilmington, Delaware
9. Leo S. Wise, "Study Fundamental Properties of High Explosives," Technical Report No. 1466, Picatinny Arsenal, 3 January 1945
10. A. W. Campbell, W. C. Davis, J. B. Ransay, and J. R. Travis, "Shock Initiation of Solid Explosives," *Phys. Fluids*, **4**, 511-521 (1961)

COMMENT

C. FAUQUIGNON (Commissariat a l'Energie Atomique, France): A similar use of microwaves (70 GHz in frequency) in time resolved interferometry has been developed in our laboratory (Ref. 1).

Figure 1 shows the experimental set-up beyond the wave guide, i.e., in free space propagation. An elliptic mirror is used to focus the beam on the charge, and a double plane reflection and a Teflon window protect the antenna from the explosion. More than five pounds of

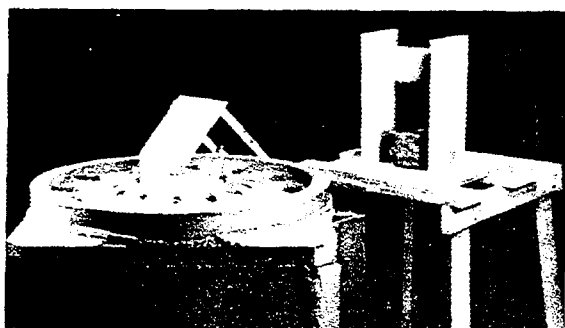


Figure 1

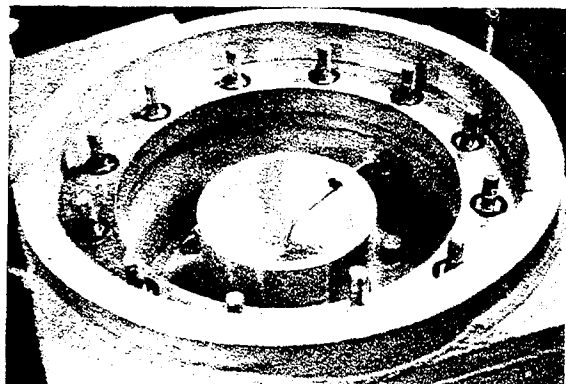


Figure 2

explosive can be fired under such conditions.

Figure 2 shows a more detailed view of the horn and the antenna.

The second point I want to discuss concerns the possibilities of this technique. As it has been pointed out by Mr. Johnson, an interesting feature of this method is to give information on what happens inside the charge. Moreover, it is possible by observing a change in amplitude of the reflected energy to detect the passage of a shock or a detonation wave from one material to another. Figure 3 illustrates this possibility in showing the transmission of detonation from a low velocity (low density) explosive (on the left) to a high velocity (high density) explosive (on the right) — the ionization in the first explosive is much larger than in the second one and, hence, the reflectivity is better.

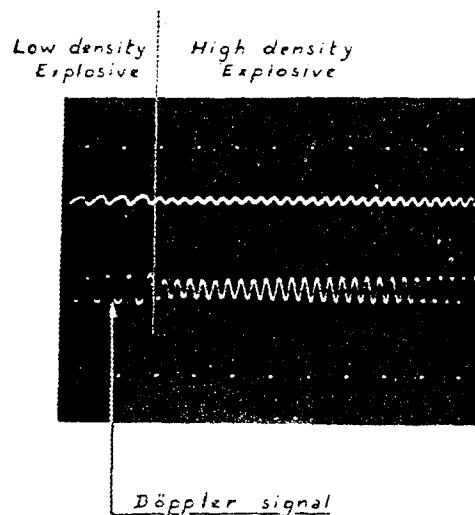


Figure 3

REFERENCE

1. G. Garcin, Annales de Physique, Paris No. 7-8, 1964

ON ELECTRICAL CONDUCTIVITY IN DETONATION PRODUCTS

Bernard Hayes
*Los Alamos Scientific Laboratory
Los Alamos, New Mexico*

ABSTRACT

The purpose of this paper is threefold: to discuss electronic techniques appropriate to high-resolution electrical conductivity measurements in the detonation products of condensed explosives; to present evidence to show that if the detonation products contain free carbon, that carbon is the main conductor of electricity; and to demonstrate the usefulness of the measurement technique to explore reaction-zone structure.

INTRODUCTION

Until recently, electrical conductivity measurements in the detonation products of high explosives have been made with electronic systems having a least resolved time of a few tenths of a microsecond [1,2]. Improved time resolution, which increases the rate at which information can be recorded, requires an increase in the frequency bandwidth of all components used in the measuring system. This paper reports on conductivity experiments utilizing modern traveling wave oscilloscopes along with dynamic conductivity cells to improve time resolution from a few tenths of a microsecond to a few tenths of a nanosecond—three orders of magnitude. In terms of frequency, the bandwidth has been increased from a few megacycles to over a thousand megacycles. As a consequence of this increase in resolution, electrical conductivity measurements have taken on increased significance by revealing information which was previously unavailable.

Thus, instead of obtaining a single value for the conductivity of detonation products, a conductivity-time profile with subnanosecond time resolution can be generated. These profiles, in which micron distances behind detonation fronts are being resolved, reveal that, while explosive products become conductive very quickly after the passage of the front, relatively large differences occur in the times required for different explosives to reach peak conductivity. Also, each explosive presents a different profile as well as different value for the peak conductivity.

The value of the peak conductivity is strongly correlated with the amount of solid carbon present in the detonation products. So much so that the data suggest the principal mechanism for electrical conduction in detonation products is a continuous network of solid carbon. That is to say, in detonation products containing free carbon, the phenomenon of charge conduction can be attributed to the conduction electrons available in the carbon, and the bulk conductivity is governed primarily by the fractional carbon density. On the other hand, explosives with little or no free carbon in their products have relatively low conductivities, and the charge carriers are probably ions produced by high temperature.

Finally, it is believed that the high time resolution offered by the technique affords the best hope for resolving reaction zones in liquid explosives. However, of those studied only liquid TNT has yielded informative data.

THEORY AND ASSUMPTIONS

The basis for determining electrical conductivity in detonating high explosives is the proper use of a suitable conductivity cell. The cell employed herein to obtain profile data consisted of a long cylindrical tube with a small hemispherically shaped probe mounted on one end and with a plane-wave initiation system on the other end. The tube serves as the explosive container as well as the common return for the probe current. This arrangement is particularly good for liquid explosives and with proper probe fitting may be used with solids. Measurements

are made in times that are less than the time required for a detonation wave to traverse a probe radius. For this situation the hydrodynamic disturbance is negligible and the electrical boundary conditions are well known.

In this connection, Mader [3] has computed the interaction of a nitromethane detonation wave with an aluminum probe using his two-dimensional hydrodynamic code. His results are shown in Fig. 1. The change in probe radius is linear with time and in this case results in a reduction in probe length of 16% when the wave front just covers the hemisphere. The products under the probe can be thought of as being doubly shocked: the first shock causes the nitromethane to detonate, the second shock arises from the interaction of the detonation wave with the probe. The temperature rise in the products as a result of the second shock is quite small, about 200 degrees in this case. The shock velocity in the products is about half the detonation velocity, and therefore the reflected shock does not expand to an important extent compared to the electric sensing distance of about ten probe radii. For dense probe materials such as steel, changes in probe radius are even less pronounced. The effect of radius changes can be taken into account when distances behind the detonation front are required; however, for convenience in plotting, time rather than distance will be used.

The electric current stream lines emerging from a hemispherical probe as it is being engulfed by a detonation wave constitute the electric boundary value problem. The exact solution to this problem for a homogeneous isotropic medium can be obtained by solving Laplace's equation in toroidal coordinates [4,5]. Omitting the details of the derivation, the solution for the normalized conductance under a hemispherical probe as a function of time after a detonation front first contacts the probe (horizontal line 1 in Fig. 1) can be written

$$\frac{g(t)}{4a\sigma} = \frac{\pi(2 - Dt/a)\sqrt{Dt/a}}{2 \cos^{-1}(Dt/a - 1)}$$

$$\int_0^{\infty} \frac{\sqrt{\cosh \omega + 1} d\omega}{(\cosh \omega + 1 - Dt/a) \cosh [\pi\omega/2 \cos^{-1}(Dt/a - 1)]}$$

(1)

where g is the conductance and σ is the conductivity of the material under the probe; a is the probe radius, D is the detonation velocity, and t is the time; ω is a parameter to account for the continuous spectrum of separation constants which naturally occur in the solution of the

Laplace equation. The integral can be easily evaluated for $t = 0$ and $Dt = a$. Between these two limits it is necessary to resort to numerical integration methods for a solution.

A simple approximation for the normalized conductance is [2]

$$g(t)/4a\sigma = \cos^{-1}(1 - Dt/a). \quad (2)$$

This expression matches the exact expression at the probe tip and for a hemispherical section, has the same general shape but results in a value of conductance at position 2 in Fig. 1 which is low by 5.6%. As it turns out, changes in probe shape due to the interaction of the detonation wave with the probe favor results which lie between these two limits. Furthermore, beyond position 2 in Fig. 1 the results become less and less accurate as the probe shape deviates from a true hemisphere.

The experimental record consists of an oscilloscope trace of voltage vs time, the voltage being the probe voltage as it penetrates the detonation products. The initial voltage on the probe is supplied by a transmission line of impedance Z . The reason for using a transmission line as the electrical energy source is that no ordinary power supply, such as a battery or a condenser, has the necessary high-frequency response required for this application. Also, as we shall see, the cable impedance serves as a conductance multiplier.

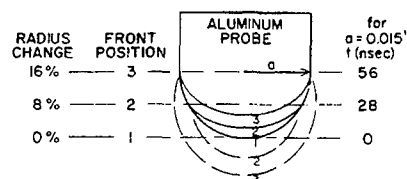
The waveform to be recorded is carried on a separate cable of impedance R to the recording oscilloscope. Both the feed line and the receiving line are connected to the probe with very short leads to preserve high-frequency response. A useful guide to charge radius, probe length, and lead dress, in this respect, is that no dimension should exceed a quarter wavelength of the upper bandwidth frequency. Otherwise the bandwidth will be reduced. Decreased bandwidth is most harmful at the instant of contact between probe and detonation wave, when voltage gradients are greatest.

Treating the source transmission line, supplied by a voltage V , as a series impedance Z shunted by both the fixed receiving line impedance R and the variable conductance of the cell, the cell conductance as a function of the measured voltage-time waveform $f(t)$ at the oscilloscope is

$$g(t) = (1/Z + 1/R)(V/f(t) - 1), \quad (3)$$

where V is the initial voltage on the probe. The actual value of the voltage is not important since

Fig. 1 - Hemispherical probe shape changes (curved lines numbered 1, 2, 3) and shock wave position (curved dashed lines 2 and 3) for corresponding nitromethane detonation front (horizontal dashed lines 1, 2, and 3) advancing over an aluminum probe. The percentage change in radius is shown on the left for a detonation advance of $a/2$ and a .



only voltage ratios are required, and these can be obtained from the shot record. In general, the waveform $f(t)$ is a monotonically decreasing function similar to the record of nitromethane shot shown in Fig. 2. From measurements made on the shot record the instantaneous conductance as a function of time, $g(t)$, can be computed using Eq. (3), and if the conductivity of the products were constant the value of the conductivity could be obtained directly from Eqs. (1) or (2). However, since the conductivity may not be constant a different approach is required.

To this end, the detonation products are imagined to consist of a large number of thin layers stacked one on top of the other. A layer thickness will depend on the time resolution employed, and in this connection it is convenient to use microns per nanosecond as the velocity dimension. The layer thickness is then written

$$\Delta x = (D - u_p) \Delta t. \quad (4)$$

For nitromethane with $D \approx 6.4$, $u_p \approx 2.0$, and a resolution time of 0.25 nanoseconds, the approximate layer thickness, Δx , is 1.1 microns.

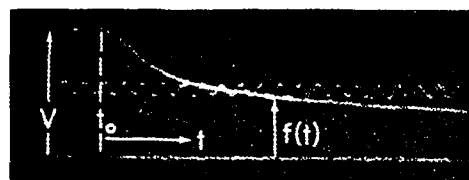
As each layer of products contacts the probe, conductance which is characteristic of the conductivity of the layer is added to the electrical circuit. Consequently, the shape of the electric waveform reflects the changes in conductivity as they take place. By accounting for the conductance of each layer as it moves up the probe an estimate of the conductivity of the n th layer can be made from the residual conductance up to that layer. To rephrase this mathematically,

$$\sigma_n = \left[0.25 g_n - \sum_{j=1}^{n-1} \sigma_j (S_{n+1-j} - S_{n-j}) \right] / S_1. \quad (5)$$

where σ_n is the conductivity of the n th layer, g_n is the conductance of the n th layer, and the summation accounts for preceding layers which have moved up the probe. Each layer with a conductivity σ_j is assigned a new value of conductance in accordance with the requirements of Eqs. (1) or (2) to approximate closely the electrical boundary conditions with S being the geometric factor. Equation (5) is somewhat in error because it does not take into account refraction of the electric streamlines at the boundary between layers when conductivity changes are large. In the neighborhood of large conductivity gradients (except the jump at the front of the detonation wave) changes are averaged over too great a distance, which is to say the gradient is reduced. Thus, the analysis will produce a value of conductivity for each layer which is somewhat higher than the actual value should be. Nevertheless, the qualitative profile will reasonably approximate the true profile, showing changes in conductivity without generating spurious steps. Equation (5) is valid, however, for regions of constant conductivity which sometimes exist well behind a detonation front. Because of the difficulty in handling the geometric factor S , Eq. (5) was coded in Version III Fortran to accommodate Eqs. (1) and (2). Typical results for nitromethane are shown in Fig. 3, where the lower curve is the result of using the geometric factor from Eq. (1) and while the upper curve results from Eq. (2).

In situations where it is not convenient to use hemispherical probes a flat-bottomed probe

Fig. 2 - A nitromethane shot record. The timing wave is a 2000 megacycle sine wave ($t = 1/f$). The probe radius for this shot was 3.0 ± 0.3 mils; and $Z = 33$ ohms and $R = 125$ ohms.



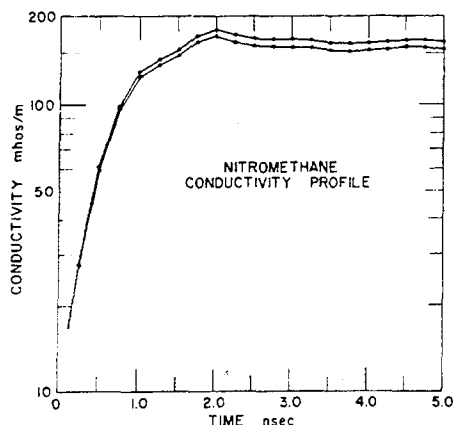


Fig. 3 - Typical conductivity profiles of nitromethane near the detonation front. The lower curve makes use of Eq. (1) while the upper curve makes use of Eq. (2).

can be employed to obtain a good estimate of the detonation products' bulk conductivity [6]. For this case the normalized conductance is

$$g/4a\rho = 1. \quad (6)$$

where a is the radius of the wire or rod contacting the explosive. This configuration is particularly useful when comparisons of different explosives in the same geometry are desired or when a parameter such as density is the only variable. Again, good time resolution is required as equation (6) does not hold if the conducting products have covered any appreciable length of the probe.

Typical shot records for two different PETN densities are shown in Fig. 4. Divergent or tilted detonation waves affect the electric waveform causing the discontinuity to be somewhat rounded so that conductance measurements (using Eq. 3) in the 7 to 15 nanosecond time interval are averaged to obtain an estimate of the conductivity from Eq. (6).

Alternatively, conductance plots alone furnish interesting comparison data such as those shown in Fig. 5 for PETN with different initial densities. It is apparent from this plot (which should not be construed as a profile) that as the initial density of the explosive decreases the conductance decreases, implying that the conductivity also decreases.

The geometry for this series of shots was quite simple. It consisted of a small brass cylinder with a 5/16-in.-diameter hole 0.2-in.-deep for the explosive. The booster was an SE-1 detonator with a 40-mil-thick 9404 pellet driving a 15-mil-thick brass shim which formed the bottom of the acceptor charge. The probe was the center wire of the coaxial line from the recording oscilloscope, and the source line in this case was a 93-ohm coaxial cable. The geometry in this situation is marginal for obtaining a good value of conductivity, because the detonation wave is divergent and the ratio of charge diameter to probe diameter is also marginal: 12.4 to 1. As a general rule charge

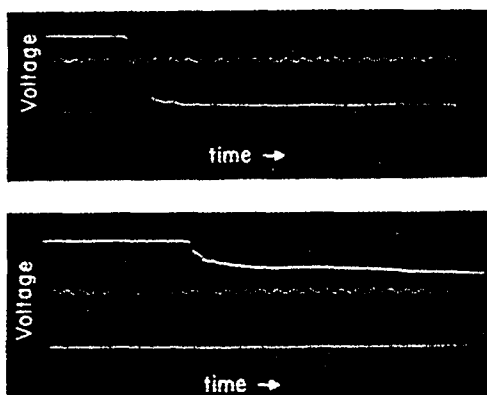
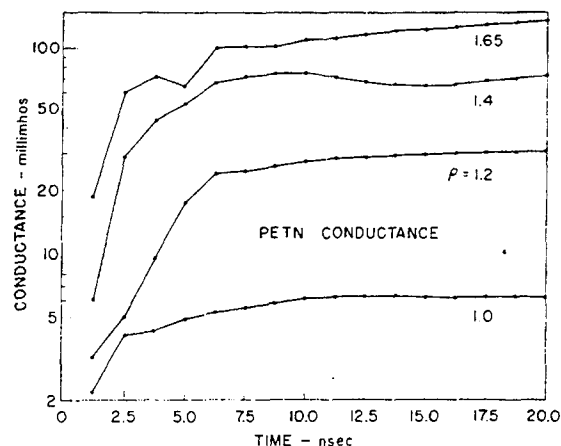


Fig. 4 - Conductance waveforms using flat probes. The timing trace is a 400 Mc/sec sine wave.

Fig. 5 - Electrical conductance measurements in PETN products for different initial densities. See text for shot geometry configuration.



diameter to probe diameter should exceed a 25 to 1 ratio.

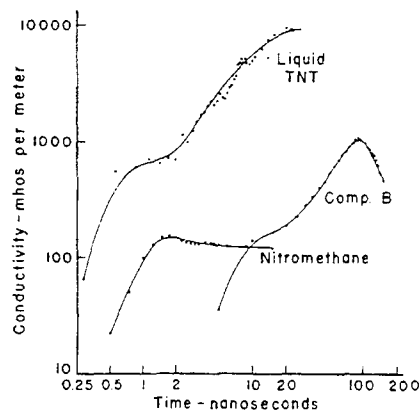
RESULTS

Conductivity profiles for nitromethane, Composition B, and liquid TNT have been obtained, and the results are shown in the log-log plot of Fig. 6. The onset of conductivity is seen to be quite rapid in the nitromethane and the liquid TNT relative to the Composition B. The time to the first inflection in both liquid TNT and Composition B is thought to be connected with reaction-zone thickness, although further experimental evidence appears warranted before a final judgement can be made. In the case of nitromethane there has been no indication of an inflection, which tends to confirm the hypothesis that the reaction zone is too thin to be resolved. The conductivity peak evidenced in all three explosives has been attributed to carbon precipitation which takes place near the end of chemical reaction.

Conductivity profiles of PETN have not been generated as yet because of the difficulty in making small hemispherical holes in this material. However, since the profile is thought to be similar to nitromethane (very thin reaction zone, fast-rising, flat-topped conductivity profile) bulk conductivity measurements have been made. The best estimate of PETN conductivity is 60 mhos per meter for an initial density of 1.699 g/cc, a charge diameter of 1.625 in., a charge length of 1 in., and a flat-bottomed probe of 30 mils — see Fig. 4a for a typical shot record.

The maximum values of the conductivities for the above four explosives were plotted against carbon content as shown in Fig. 7. The values of the carbon content were computed by Mader using the BKW equation of state [7]. Because of the uncertainties in the form of the equation of state used to calculate the solid carbon content, the numbers may not be accurate, but their relative values should be quite reliable. The correlation is excellent, and it is

Fig. 6 - Conductivity profiles for nitromethane, Composition B, and liquid TNT. The inflection on the front of Composition B and liquid TNT curves are thought to be associated with the ends of the reaction zones in these materials and the peaks with carbon precipitation.



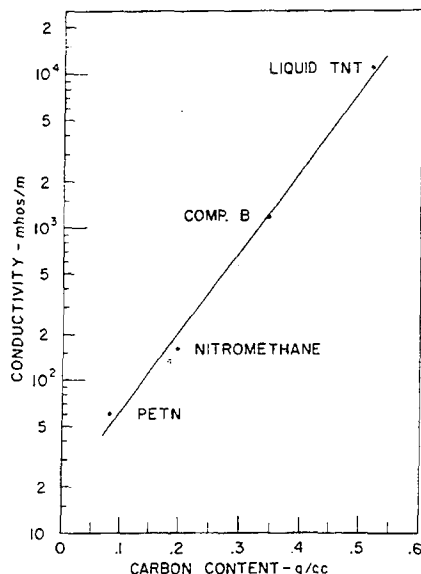


Fig. 7 - Correlation of electrical conductivity with the solid carbon content in the detonation products of various explosives

believed that in these explosives electricity is conducted in a network of solid carbon.

As further evidence of the validity of the carbon hypothesis, the bulk conductivity of PETN as a function of initial density can be estimated from the data of Fig. 5. The computed values are somewhat high compared to the best estimate for high-density PETN (probably due to marginal geometry), but since firing conditions and geometry were identical in all cases the relative conductivities should be quite satisfactory. Figure 8 is a plot of the results along with a few physical properties of PETN obtained from Mader-type calculations.

The most revealing feature in connection with Fig. 8 is that all parameters except temperature increase with increasing density. At low density the temperature is high, there is no solid carbon present (the carbon combines with oxygen to form carbon monoxide), and yet the conductivity is low relative to the high-density material. The point is that thermal ionization is not as effective as solid carbon in enhancing electrical conduction. In fact, at low density the conductivity is only a little more than an order of magnitude higher than that of detonation products from a gas mixture of acetylene and oxygen [8]. Furthermore, while references are not available it is known that the conductivity of tetranitromethane and nitroglycerine are also quite low and that these materials also have carbon-free products.

SUMMARY

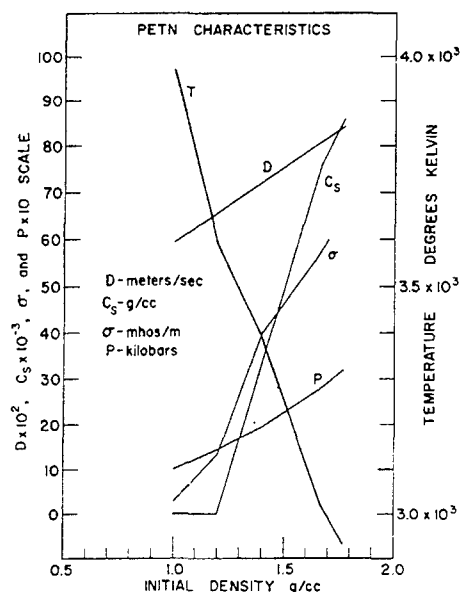
To conclude, this investigation has shown that the electrical conductivity of detonation products for different explosives ranges from 1 to 10^4 mhos per meter. A strong correlation between the value of the peak conductivity and the calculated carbon content in the detonation products was noted. That is, in explosion products containing free carbon the conductivity is primarily determined by the fractional solid carbon density in the products. This suggests that a network of solid carbon forms and is the dominating conductor. In detonation products which do not contain free carbon the electrical conductivity is low and probably conduction is primarily by ions which are present because of the high temperature of the products.

The technique described here, yielding two to three orders of magnitude improvement in time resolution over conventional conductivity methods, constitutes a new diagnostic tool for probing into detonation products. The full benefits of the technique have not been fully assessed as yet, but further experiments to elucidate reaction-zone structure are being considered.

ACKNOWLEDGMENT

The author wishes to thank C. L. Mader for carrying out the probe interaction computations,

Fig. 8 - PETN properties as a function of initial density. Illustrating the inverse relationship between temperature and conductivity.



B. G. Craig for his assistance in shot preparation, and W. C. Davis for his assistance in the preparation of this paper. This work was performed under the auspices of the United States Atomic Energy Commission.

REFERENCES

1. R. L. Jameson, S. J. Lukasik and J. Pernick, "Electrical Resistivity Measurements in Detonating Composition B and Pentolite," *J. Appl. Phys.* **35**, 714 (1964)
2. B. Hayes, "Electrical Measurements in Reaction Zones of High Explosives," Tenth Symposium (International) on Combustion at Cambridge, England, August, 1964
3. C. L. Mader, private communication
4. H. Bateman, *Partial Differential Equations of Mathematical Physics* (Dover Publications, N. Y., 1944), 1st Am. ed., pp. 461, 472
5. E. Weber, *Electromagnetic Fields* (John Wiley and Sons, Inc., N. Y., 1950), p. 68
6. F. L. Jones, *The Physics of Electrical Contacts* (Clarendon Press, Oxford, 1957), Chapter 2
7. C. L. Mader, "Detonation Properties of Condensed Explosives Computed Using the Becker-Kistiakowsky-Wilson Equation of State," Los Alamos Scientific Laboratory Report LA-2100 (1963)
8. S. Basu and J. A. Fay, "Ionization in Detonation Waves," Seventh Symposium (International) on Combustion at London and Oxford, England, 1958

A TECHNIQUE FOR DETAILED TIME-RESOLVED RADIATION MEASUREMENTS IN THE REACTION ZONE OF CONDENSED EXPLOSIVES

Per-Anders Persson,* Bertil Andersson, Sven-Olof Ståhl
Research Institute of National Defense (Försvarets Forskningsanstalt)
Stockholm 80, Sweden

ABSTRACT

A fast photomultiplier and high speed oscilloscope is used to record the intensity of light emitted from within the reaction zone in some condensed explosives. The light from a thin translucent disc of explosive in contact with the end surface of a cylindrical charge of the same explosive is recorded while the detonation wave travels across the thickness of the disc. A very thin layer of opaque material is used to screen off the light from the main charge. The time-resolution of the recording system is better than 2 millimicrosec. The sensitivity of the photomultiplier is sufficiently high for temperature measurements to be made without loss in time-resolution. Preliminary experiments with Comp. B and nitromethane are described.

INTRODUCTION

There has always been a shortage of direct experimental information on the processes occurring in that zone of a detonating explosive where the chemical decomposition actually takes place. After the recent pressure profile measurements of Duff and Houston [1], Berg and Persson [2] and Craigh [3] it now seems clear that the steady detonation wave in high-density RDX-TNT explosives consists of a shock front followed by a zone of rapidly decreasing pressure. The shock front pressure is perhaps double the Chapman-Jouguet pressure which indicates that very little decomposition has occurred in the shock front itself. It has not been shown that the decomposition reaction is always completed within the zone of rapidly decreasing pressure. On the contrary the results of Craigh [3] of pressure-measurements in steady detonation in stick charges rather support the idea that some reaction takes place in a rather larger zone of more slowly decreasing pressure following the first zone.

It seems likely that the reaction is triggered by the temperature rise associated with

the shock compression. The pressure and temperature profile in the reaction zone is presumably determined by the rate of reaction at each stage of the complicated chain of reactions involved in the decomposition of the explosive. The equilibrium profile would then be the result of a delicate balance everywhere in the reaction zone between energy released by reaction and energy lost by expansion. In addition, the reaction rate would be governed by the local temperature, which is in turn a function of pressure as required by the equation of state of the explosive at its various stages of decomposition.

Temperature, in this picture, plays a central role in the process. A knowledge of the temperature at various points within the reaction zone is necessary for any sort of quantitative treatment of the process. It is the purpose of this paper to present a simple technique which might make possible actual measurements of temperature within the reaction zone. The results of some light intensity measurements on reacting RDX/TNT and nitromethane are given, mainly to illustrate the potentialities of the technique. The conclusions drawn from the rather small material are of necessity tentative.

*Present address of Mr. Persson: Swedish Detonic Research Foundation, Vinterviken, Stockholm SV, Sweden.

OPTICAL AND PHOTOMULTIPLIER SYSTEM

The central feature of the technique is the use of a fast photomultiplier and high-speed single sweep oscilloscope for recording the light emitted from the reaction zone of the explosive. Figure 1 is a schematic drawing of the arrangement. An objective lens system images the explosive specimen (which is usually mounted on the end surface of a cylindrical charge of as nearly as possible the same explosive) on to the photo-cathode surface of the multiplier. A pin-hole diaphragm placed close to the cathode prevents all light except that originating from a small central area* of the specimen charge from reaching the cathode surface. In this way, the lens and photomultiplier, mounted together on an optical bench, can be used in much the same manner as an internal slit streak camera. Figure 2 shows this arrangement.

In the experiments to be described, a 56 AVP multiplier was used, giving a rise-time of about 2 millimicrosec. The multiplier was connected to a Tektronix 519 single sweep distributed deflection oscilloscope with rise-time

about 0.3 millimicrosec and a top sweep speed of 5000 mm/ μ s. The multiplier and coaxial cable were impedance matched to the 125 Ω input impedance of the oscilloscope. Light intensity versus photomultiplier voltage calibration was made using the light from a 7 millimicrosec duration discharge flash from a simple mercury-wetted switch together with the calibrated lens aperture. At the accelerating voltages used, the recorded voltage was proportional to light intensity over the full range of the oscilloscope.

The time resolution of the whole system is determined by the photomultiplier jitter and is better than 2 millimicrosec.

The sensitivity limit of the whole system is perhaps best given by comparison with an 8 mm/ μ s streak camera of overall aperture f:7.5. Light phenomena which are just barely recorded by the camera using tri-X film and forced development give a 5 volt output signal at 1800 V multiplier voltage and the objective lens stopped down to f:32. Records can thus be made of phenomena about 400 times less intense than this, simply by increasing the objective lens aperture and the multiplier voltage.

The triggering mode is by signal. This has certain disadvantages, as light originating from early stages of the main charge detonation has

*Diameter: 0.85 mm in 60/40 RDX/TNT experiments; 1.25 mm in nitromethane experiments.

Fig. 1 - Optical system for recording the light from a small area of specimen charge mounted on the end surface of high explosive charge

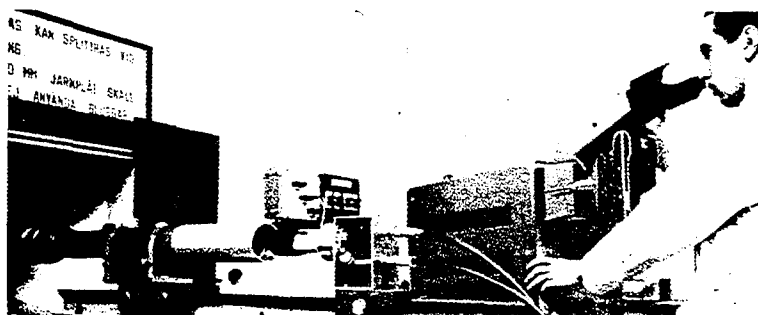
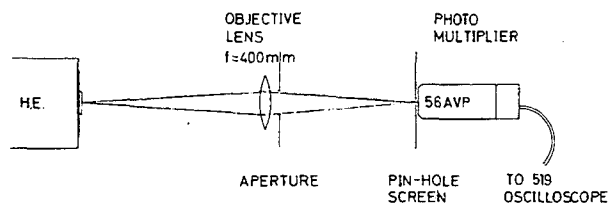


Fig. 2 - Objective lens and photomultiplier mounted together on optical bench. Photomultiplier unit pulled back to show 56 AVP tube normally enclosed in tubular cover at left.

to be excluded. A useful addition, which is at present under consideration, would be an electronic gating system allowing the sweep to be triggered only during a predetermined short time interval synchronised with the detonator pulse.

LIGHT EMISSION FROM REACTION IN NONPOROUS 60/40 RDX/TNT

Experimental

The original purpose of these experiments was to send a pressure pulse similar to that in a steady detonation through a wafer of explosive thinner than the reaction zone thickness and to study the light emission or temperature in the wafer as a function of wave amplitude and time. By making the wafer thin and placing it in contact with the end surface of a stick of explosive, the pressure in the explosive wafer would run through the steady wave pressure profile in the stick.

In later experiments, the wafer was made thicker so that the whole reaction zone or a greater part of it could be contained within it. The amplitude and duration of the pressure pulse were varied by varying the stick diameter. Another way of altering the pressure pulse was to insert a slice of inert material between the two charges.

Figure 3 shows the schematic arrangement. Glass and 60/40 RDX/TNT were chosen because of the nearly perfect shock impedance match between these two materials in the pressure region 200-400 kbar [2]. The explosive, having an RDX grain size $<10 \mu$, was vacuum melted in 20 mg batches and vibrated to get rid of air inclusions. A drop of the melted explosive was then placed on a preheated 1 mm thick clean glass plate about 7 mm square and was covered by a thin (0.1 mm) clean glass plate. The assembly was lightly pressed to give the required wafer thickness, which could be chosen between the limits 50 and 500 μ .

The explosive could be undercooled to below room temperature, and a slight mechanical deformation at the edge of the charge was usually needed to set off crystallization, which then proceeded very slowly across the width of the wafer.

The wafers made in this way showed no air inclusions under microscopic examination.

Normally, the explosive adhered to the glass surface, and any lack of contact was shown up by the interference patterns produced in the gap. If required, the 0.1 mm glass plate could be removed, exposing a smooth explosive surface.

The end surface of the main charge was ground flat on carborundum paper and then sprayed with a thin coat of black paint to fill in any small pores. A second coat was then applied and the explosive wafer with or without its 0.1 mm glass cover was pressed into the wet paint. After drying, the enclosed paint layer was found to have a thickness of 10-20 μ .

Observations

The following observations were made in the experiments with 60/40 RDX/TNT explosive wafers:

1. The light emission starts, within a measuring error of ± 3 millimicrosec, immediately when the wave front reaches the explosive (Fig. 4).

2. The light intensity increases almost linearly from zero intensity up to a certain level, where it suddenly becomes constant or decreases slightly to a roughly constant level. Little or no overshoot of the type seen in the nitromethane experiments is found. If the wafer is thick, the break in the curve occurs at a point about 25 millimicrosec after the wave entered the wafer, in which time a detonation wave would move nearly 0.20 mm (Fig. 5). If the wafer is

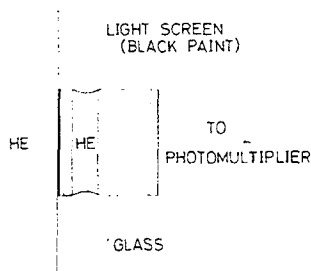


Fig. 3 - Schematic drawing of specimen 60/40 RDX/TNT charge between two glass plates mounted on end of stick charge. In most of the later experiments, the thin glass plate was removed.

Fig. 4 - Experimental arrangement and oscilloscope record showing the light emission from wafer charge to start at the moment wave front reaches the glass-explosive interface. Marker light flashes from 15 μ thick air gaps on either side of wafer charge assembly (1st and 4th peaks from the left) indicate position of wave front. The time between 1st peak and the start of the following light phenomenon due to the wafer charge (0.025 μ sec) is equal to the time for the shock wave to travel across the glass thickness. The strong light 0.2 μ sec after the second air gap light flash is due to air compressed by the free surface of the lower glass (thickness 1 mm).

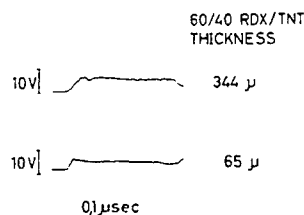
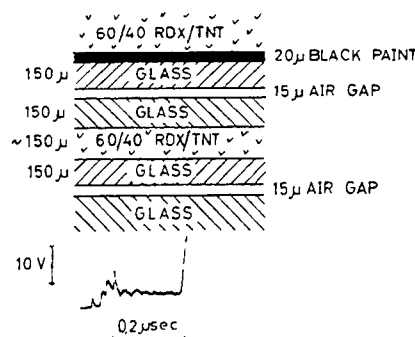


Fig. 5 - Records of light emission from wafer charges of thickness 344 μ and 65 μ thick, separated from the 75 mm diameter stick charge by 20 μ paint layer. Trace starts at left.

thinner than 0.20 mm, the break occurs at an earlier time, although often appreciably later than the moment a detonation wave would have reached the opposite side of the wafer (Fig. 5).

3. In spite of the great care taken to prepare the wafer charges to a uniform high quality, the light emission showed a great variability between charges. In particular, known air inclusions and crystal defects were found to give rise to high amplitude light signals. Similar high amplitude signals occurred from time to time in apparently perfect wafers, possibly due to defects (air inclusions) in the stick charge.

4. Changes were made in the input pressure profile by varying the stick charge diameter between 20 and 75 mm at a constant length to thickness ratio of 5, and also by varying the thickness of glass between the two charges (0 to 0.25 mm). Any small effect of these changes was hidden by the charge-to-charge variations in emission.

The observations suggest either of the following mechanisms:

1. With the thin barriers used, varying from an 0.02 mm thick paint layer to an 0.25 mm thick layer of glass, reaction proceeds in the wafer charge in very much the same way as in the stationary detonation. No shock-to-detonation transition other than that constituting the normal reaction zone is present. The

reaction products transmit light sufficiently well for the emission from a zone about 0.20 mm thick to be recorded.

2. An alternative possibility could be that the reaction products are highly absorbent. The emission would then come from a layer perhaps 5 or 10 μ thick near the front. The increase in light intensity could only be explained by assuming that the reaction and front temperature increase to a steady state over 0.20 mm travel, i.e., some sort of shock-to-detonation transition.

Against this latter hypothesis speaks the absence of any evidence of cooling after the front has reached the thick glass plate. The temperature in a wafer layer a few microns thick would be appreciably affected by thermal conduction into the glass.

With the former hypothesis on the other hand, it is not clear why the break in the light intensity curve is so sudden. The sudden break could perhaps indicate a sharp increase in absorption (free carbon?) at some stage in the reaction or a sharp decrease in temperature or the development of a sharp temperature peak.

LIGHT EMISSION FROM NITROMETHANE REACTION

Experimental

The purpose of the nitromethane experiments was to find out whether anything of the

reaction zone structure in this explosive could be resolved. Previous experiments have shown the zone to be extremely thin [4], although the critical diameter and wave front curvature data do not support this.

The experiments were made by introducing thin barriers (0.025-0.5 mm thick) of carbon black filled polyethylene in the way of a steady detonation in a cylindrical nitromethane charge enclosed in a thin-walled tufnol tube. Polyethylene has a slightly lower shock impedance than nitromethane. The light emitted from the explosive behind the polyethylene foil was transmitted to the photomultiplier through a glass window (Fig. 6).

Observations

Three observations were made:

1. The results were highly regular, with very little variation from shot to shot, in striking contrast to the 60/40 RDX/TNT experiments.

2. With nitromethane, in contrast to 60/40 RDX/TNT, the light emission does not start when the wave front reaches the explosive. This is seen from the experiment in Fig. 7,

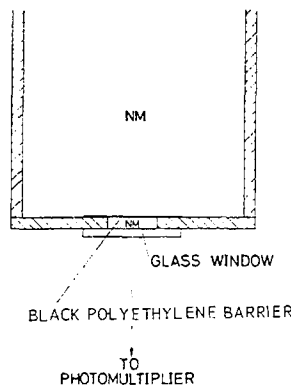


Fig. 6 - Experimental arrangement used in the nitromethane experiments

Fig. 7 - Experimental arrangement and oscilloscope record showing (left) the two intense light flashes from the 75 μ air gaps and (right) the start of light emission from nitromethane in receptor charge. First reaction light appears about 0.075 μ sec after shock front reaches receptor charge.

where the time of arrival of the wave front at the polyethylene-explosive interface can be determined with the help of the light flashes from air-gaps introduced between the polyethylene and glass plates. Instead, the well-known shock-to-detonation transition phenomenon is seen to occur even with the thinnest barrier tried so far, 25 μ polyethylene. The phenomenon shows the features previously seen in shock initiation of nitromethane [5], i.e., a nonluminous or very weakly luminous primary shock, followed by a high pressure steady detonation in the preshocked explosive. Because of the low temperature in this detonation, it is less luminous than the normal steady state detonation. When the high pressure detonation catches up with the shock front, an overdriven high temperature nonsteady detonation results, which quickly decays into a normal steady detonation (Fig. 8).

3. Varying the input pressure by varying the charge diameter between 22 and 57 mm ($l/d = 5$) made little difference to the behaviour. The small charges (lower pressure) gave ca 5% higher peak amplitude and ca 20% longer high pressure detonation plateaus than the large ones (Fig. 9).

The observations are in agreement with the assumption that the nitromethane reaction

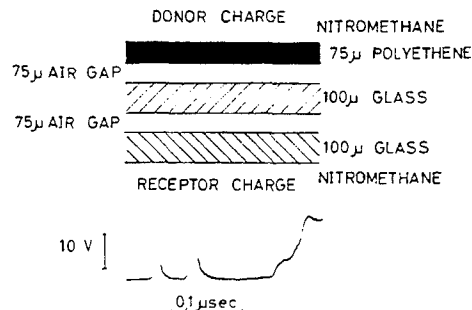


Fig. 8 - Records of light emission from shock-to-detonation transition in nitromethane at different polyethylene barrier thicknesses. Note two-stage increase in intensity and overshoot after second increase.

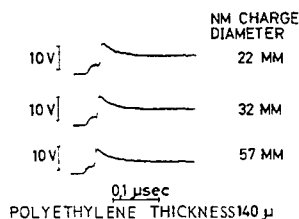
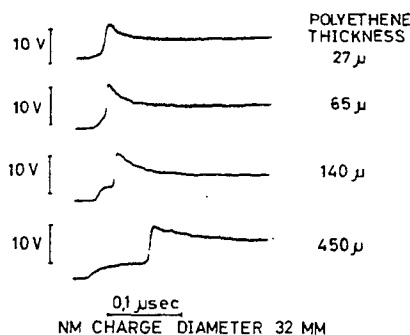


Fig. 9 - Records of shock-to-detonation transition in nitromethane at different charge diameters. Note longer plateau and higher over-shoot amplitude at small charge diameter.

zone has a very sharp pressure peak near the front. The peak would seem to be attenuated while the wave travels through a thickness of $25\ \mu$ polyethylene. The peak can then be estimated to be less than $10\ \mu$ thick, which means that an appreciable part of the decomposition is completed in less than 2 millimicrosec. This could be the reason why small wall surface irregularities give rise to "streamers" of apparently incompletely detonated explosive.

It is not proposed that the whole reaction takes place within this peak — on the contrary, well established data on wave front curvature and charge diameter effects indicate that the Chapman-Jouguet plane is roughly as far behind the front in nitromethane as in RDX/TNT mixtures.

CONCLUSIONS

1. The photomultiplier technique has been shown to be a useful tool in detonation and particularly reaction zone investigations. The method has a development potential, it is simple, and it is in addition very much cheaper (even including the cost of the high speed oscilloscope) than an f:7.5 and 8 mm/ μ sec streak camera system, which it beats by a factor of 400 in light sensitivity and a factor of 2 or 3 in time resolution.

2. Nitromethane shows the detonation-to-shock and shock-to-detonation transition characteristic of a homogeneous explosive even with barriers as thin as $25\ \mu$. The reaction zone has a peak of probably less than $10\ \mu$ thickness.

3. Nonporous 60/40 RDX/TNT is less sensitive to disturbance by thin barriers than nitromethane. A $250\ \mu$ thick barrier may cause a disturbance in the reaction, but there is no delay and very little overshoot of the type usually associated with homogeneous explosives.

REFERENCES

1. R. E. Duff and E. Houston, J. Chem. Phys. **23**, 1268 (1955)
2. U. Berg and P. A. Persson, ERDE Int Conference on Sensitivity and Hazards of Explosives, London, 1963
3. B. G. Craigh, 10th Int Symposium on Combustion, Cambridge, England, 1964
4. B. Hayes, 10th Int Symposium on Combustion, Cambridge, England, 1964
5. A. W. Campbell, W. C. Davis, and J. R. Travis, Phys. Fluids **4**, 498 (1961)

COMMENT

H. J. Mueller (Basic Research Laboratory, U. S. Army Engineer Research and Development Laboratories, Fort Belvoir, Virginia): I should like to mention that I am using a similar photomultiplier-oscilloscope arrangement successfully for studying the kinetics of the induction period of thermally initiated azides.

G. D. Singer and I have shown in a recent paper* that the intensity of the chemiluminescence which is emitted during the thermal decomposition of azides is proportional to the reaction rate. The light emission is considered to be due to excited nitrogen and lies essentially in the ultraviolet. There is, however, an emission band in the visible at $560\text{ m}\mu$. In this wavelength range the azide crystals are translucent and, thus, the $560\text{ m}\mu$ emission is very

suitable for kinetic studies. However, unlike the detonation proper, which is a highly luminous event, the transient reaction during the induction period is nearly dark and the chemiluminescence is invisible to the naked eye. Nevertheless, it is possible to achieve sufficient sensitivity of the photomultiplier by sacrificing some of the theoretically possible time resolution, and oscilloscope traces were obtained which can be quantitatively evaluated. As an example, Fig. 1 shows the luminescence vs time trace of exploding silver azide ($\sim 2\text{ mg}$). A red-blind EMR photomultiplier was used in connection with a Tektronix 585 scope. The sensitivity of the scope was 0.2 v/cm , the sweep speed amounted to 10 m sec/cm . Quantitative evaluation of such traces showed, for instance, that during the induction period the reaction rate increases exponentially with time, indicating an autocatalytic reaction.

*Nature 207, 1073 (1965)

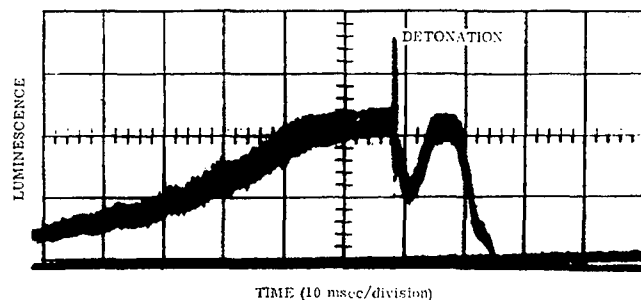


Fig. 1 - Delayed detonation of AgN_3

ELECTRICAL TRANSDUCER STUDIES OF INITIATION OF LIQUID EXPLOSIVES

J. R. Travis
*Los Alamos Scientific Laboratory
Los Alamos, New Mexico*

ABSTRACT

Electrical signals are generated by initiation processes occurring in dielectric liquid explosives. A transducer utilizing this effect has been developed. Comparison of the results obtained with the transducer and with a smear camera shows that the transducer can measure the time of events occurring during the initiation process with high precision. The transducer technique is particularly useful in the study of those explosives in which, because of their low luminosity, the entire initiation process cannot be observed with a smear camera. Differences in the initiation behavior of nitromethane, solutions of TNT in nitromethane, molten DINA, and molten TNT are described.

INTRODUCTION

The following thermal explosion model for one-dimensional shock initiation of liquid explosives [1,2] adequately incorporates most of the experimental observations. A plane shock wave entering a liquid explosive compresses and heats it. After an induction time during which chemical reaction is occurring, detonation in the heated, compressed explosive begins near the interface where the explosive has been hot longest. This detonation travels as a supersonic wave through the compressed explosive, overtakes the initial shock wave, and overdrives a detonation in the unshocked nitromethane. This overdriven detonation decays to a steady-state detonation in a few microseconds.

These events can be photographed with a high-speed rotating-mirror smear camera. In an experiment of the kind shown schematically in Fig. 1, a smear camera is aligned so that its slit subtends a diameter of the charge and its optic axis is congruent with the charge axis. As initiation takes place, the camera records light successively from the flasher when the shock wave enters the nitromethane, from the detonation in the compressed explosive, from the strong interaction between this detonation wave and the overtaken shock wave, and finally from the steady-state detonation in the unshocked nitromethane. In some explosives, for example nitromethane, light from the supersonic detonation, although weaker than the light from

steady-state detonation, is readily photographed. In others such as Dithenite 13,* molten TNT, and some solutions of TNT in nitromethane, light from the supersonic detonation has never been detected. In all other respects the initiation behavior of these explosives is the same as that of nitromethane. No explanation for the lack of luminosity of the supersonic wave in these explosives has yet been confirmed.

The presence or absence of luminosity from the supersonic detonation in solutions of TNT in nitromethane is dependent on the TNT concentration. For a solution containing 30% by weight of TNT† no light is observed. For solutions containing less than 20% TNT, light is observed, but it occurs later in the time scale of the initiation process than it does in pure nitromethane. Optical experiments with reflected light have shown that an opaque layer forms in shock-compressed TNT/nitromethane (30/70) shortly before it detonates. Nothing more is known about this layer, whether it is related to the nonluminosity or, if it is, how it can totally obscure the light from the detonation in the shock-compressed TNT/nitromethane (30/70).‡

*Nitric acid and nitrobenzene in the mole ratio 5 to 1, plus 13 wt % water.

†Hereafter designated TNT/nitromethane (30/70).

‡This problem is discussed more fully by Travis and coworkers [3].

Since optical techniques could not be used to study events occurring within the opaque layer, a new technique was needed if this problem were to be studied more thoroughly. Interest in this problem led to an investigation of other techniques and ultimately to the discovery of the charge generation phenomena associated with initiation processes.

The experimental device used to study the charge generation phenomena is a transducer in the form of an uncharged parallel-plate capacitor which has explosive as a dielectric. One plate is connected to the signal input terminal of an oscilloscope. The other plate, at ground potential, acts as part of the attenuator in the boosting system. When the shock wave in the grounded attenuator plate hits the explosive a voltage appears across the capacitor and a pulse is displayed on the oscilloscope.

The output of an explosive-filled transducer changes with time as the shock wave proceeds through it. The first experimental problem was to correlate the events already described which occur during initiation with the observed changes in the transducer signal. This has been done successfully for the explosives nitromethane, TNT/nitromethane, molten TNT and molten DINA (dinitroxyethyl-nitramine). Now that this correlation has been established, experiments can be performed in which the transducer results can be combined with results from optical and other electronic techniques to study some of the remaining unsolved problems in the initiation of explosives.

THE EXPLOSIVE-FILLED TRANSDUCER

Studies of the charge generation by shocks in inert dielectrics have been reported by Eichberger and Hauver [4] and Harris [5] in recent publications. They have considered the effect to be due to mechanical polarization produced at the shock front. The current generated by a polarization transducer is a function of the nature of the dielectric material, increases monotonically with pressure until saturation occurs, is inversely proportional to the electrode separation, and is directly proportional to the effective area of the electrodes.

A schematic diagram of an explosive-filled transducer mounted in a charge assembly is illustrated in Fig. 1. The transducer was designed to meet conflicting requirements: (1) The diameter needs to be small so that the initiation phenomena occurring in the region near the probe can be photographed with a smear camera; (2) The spacing between the probe and the

ground plate needs to be great enough to allow sufficient time for coverage of the initiation phenomena; (3) The diameter must be large enough and the spacing small enough to give an adequate signal strength. Transducers with spacings of 5 and 6 mm and probe diameters of 7.5 and 12 mm have proven satisfactory, giving signals of a few tenths to a few hundredths of a volt across a 93 Ω RG-71/U signal cable.

Two oscilloscopes were used to record the waveform of the current in the transducer circuit which consisted of a small capacitance shunted by the small resistance of the signal cable. One of the oscilloscopes, a Tektronix 581, was set with a sweep speed of 0.1 or 0.2 $\mu\text{sec}/\text{cm}$ for optimum resolution of the events of interest. The other, a Tektronix 545, was used for long time coverage.

The design of the booster system was determined by the electrode spacing and was adjusted for each test explosive so that initiation would occur in less than one microsecond.

The output pulse from a polarization transducer has a characteristic shape for a given material. The pulse from Plexiglas, for example, rises sharply in the positive direction when the shock hits the Plexiglas, then rises slowly until the shock nears the signal probe at which time it rises rapidly to a height several times its initial height. The pulse from water starts with a large positive spike which decays rapidly before building up again as the shock wave approaches the probe. The output signal from liquid explosives is very different. A sample oscilloscope trace showing initiation polarization is reproduced in Fig. 2. The first short positive signal signifies the entry of the shock wave into the nitromethane. This is followed by a second positive pulse which occurs at the time the super-velocity detonation starts in the compressed explosive. A sharp negative signal occurs a short time later when the supervelocity detonation overtakes the shock wave. Correlation between the three parts of the signal and the initiation events has been demonstrated by comparing the transducer signal with the smear camera picture taken at the same time in many experiments. A smear camera picture reproduced below the transducer signal in Fig. 2 shows this correlation.

EXPERIMENTAL RESULTS

A. Relative Times of Occurrence of Initiation Events

Initiation polarization has been observed in four liquid explosives: nitromethane, molten

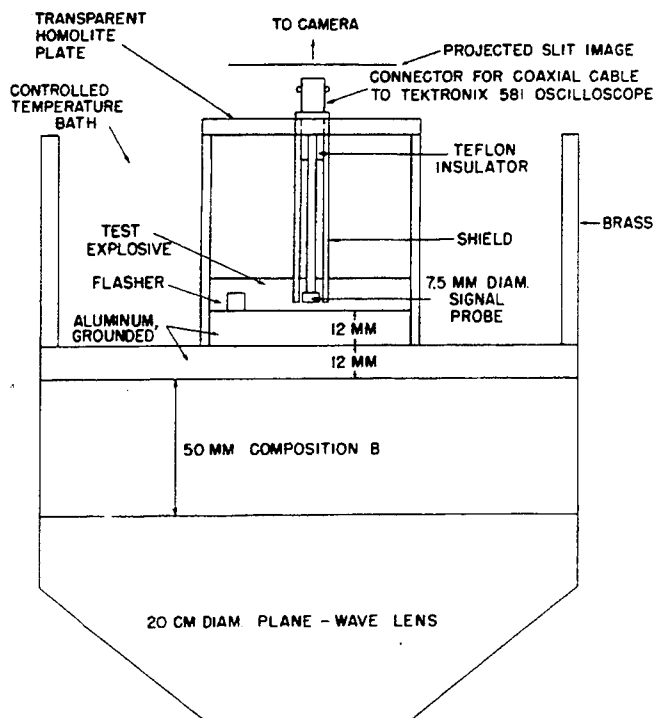


Fig. 1 - Schematic diagram of transducer mounted in a charge assembly. The probe shield is electrically connected to the grounded attenuator plate, to the wall of the explosive container, and to the ground lead of the signal cable.

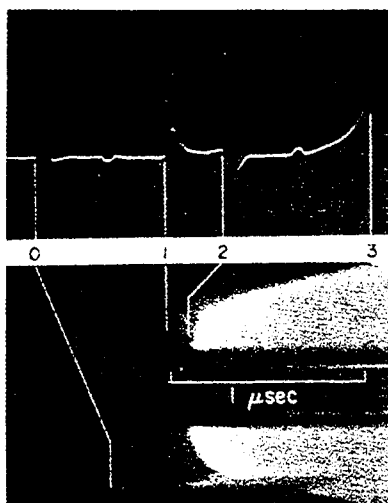


Fig. 2 - Transducer and smear camera records of initiation phenomena in nitromethane

DINA, TNT/nitromethane (30/70), and molten TNT. The qualitative appearance of the transducer signals obtained from the first three is the same as that shown in Fig. 2: two positive pulses followed by a negative one. But only the first positive pulse and the negative pulse are seen from molten TNT. Just as in the optical record no signal is detected from the detonation in the shock-compressed molten TNT, although the transducer does give a signal for TNT/NM (30/70) and the optical record does not.

The times of occurrence of the initiation events measured by both the transducer and optical techniques are given in Table 1. τ , the induction time, is the time from the entry of the shock wave to the time of the onset of detonation in the compressed explosive. The time, t , is the time from the entry of the shock wave to the time at which the detonation in the compressed explosive overtakes the shock wave. There is no doubt that the two techniques are detecting the same events.

TABLE 1
Comparison of Transducer and Camera Data

Explosive	Shot	Transducer			Smear Camera		
		τ	t (μ sec)	τ/t	τ	t (μ sec)	τ/t
Nitromethane	B5209	.114	.176	.648			
	B6086	.172	.246	.698	.174	.252	.690
	B6088	.213	.323	.660	.227	.328	.692
	B5203	.230	.332	.693			
	B5201	.325	.472	.667			
	B6093	.345	.500	.690	.340	.484	.703
	B5217	.424	.620	.684			
			Avg.	.677		Avg.	.695
Molten DINA	B6087	.160	.208	.769	.134	.171	.784
	B6089	.233	.305	.764	.265	.337	.787
Molten TNT	B6092	--	.122	--	--	.098	--
	B6091	--	.278	--	--	.296	--
TNT/Nitromethane ^a	(8/92) B5220	.438	.632	.693	.563	.632	.888
	(15/85) B5219	.820	--	--	1.11	1.15	.965
	(30/70) B5211	.198	.286	.693	b	--	1.0

^aCamera data taken on replicate shots -- adjusted for comparison with the transducer results.

^bNo light detected.

Another experimental fact that demonstrates the validity of the interpretation is the constancy of the ratio τ/t . This ratio is dependent only on the values of the velocity of the detonation wave in the compressed explosive and the shock and particle velocities of the initiating shock, which are all almost constant for the small range of shock pressures (85-90 kbar) used in these experiments.* τ/t as reported by Campbell and coworkers [1] is equal to 0.672 for nitromethane. The average value obtained from seven transducer measurements was 0.677 with a mean deviation of ± 0.016 .

The values of τ/t given in Table 1 for solutions of TNT in nitromethane are the same within experimental error as the value of τ/t for pure nitromethane. Therefore, the initiation events occur at the same relative times in the TNT solutions as in pure nitromethane. However, the optical technique shows that light from the detonation in the compressed TNT/nitromethane starts relatively later or is not seen at all. The conclusion from this is that detonation starts at the interface at the proper time in TNT/nitromethane, but must emerge from the growing dark layer before it can be

observed. Apparently, when the TNT concentration is 30%, the entire volume of shock-compressed explosive has become opaque before the supersonic detonation overtakes the shock wave.

In a few experiments with molten DINA, no light from the supersonic detonation was detected, but in others, including those listed in Table 1, light from this wave was unmistakably observed, although the same camera exposure was used. The results obtained with the transducer agree fairly well with the camera results of Table 1. τ/t for DINA is greater than for nitromethane, which indicates that the wave velocities are quite different in the two explosives.

The agreement between the transducer and camera results for molten TNT is likewise good. Only the entry of the initial shock wave and the overtake of the shock by the detonation in the compressed explosive are observed. The onset of detonation in the compressed explosive is not detected by either method. Except for the absence of a signal either from the transducer or the optical method, the experimental evidence agrees with the initiation model. The size of the change in t as the initial pressure is changed, the intensity of the photographed light at its onset relative to that from steady-state detonation,

*A complete analysis is given in Ref. 1.

and the sensitivity to the presence of solid inclusions or bubbles all confirm the proposition that molten TNT initiates in the manner described in the introduction.

Several polycrystalline solid explosives (Composition B, for one) were tested in the transducer with disappointing results. A positive pulse was observed when the shock entered the explosive, but the succeeding parts of the signal were not reproducible and, therefore, not interpretable.

B. Measurement of the Initiating Shock Pressure

Another capability of the polarization transducer, besides precision time measurement, is measurement of the pressure of the initiating shock wave. In Table 2 are given the heights of pulses from the three steps in the initiation process for the four explosives. With a few exceptions, the pulse height decreases monotonically with increasing τ ; that is with decreasing pressure. τ is a very sensitive indicator of the initiating pressure. In nitromethane, the range of pressures is less than 5 kbar for the range in τ of 0.1 to 0.45 μsec .

Before the pulse-height measurement can be used as a measure of pressure, it must be

calibrated by determining the pressure in the shock wave in nitromethane and the pulse height in the same experiment. Although this has not been done, it can be.

The ratios of the pulse heights of the different events have different values for each of the four explosives tested. In nitromethane, the pulse generated when detonation starts has about the same amplitude as the shock pulse, but in DINA it is only slightly more than half as high. The pulse generated when the supersonic detonation overtakes the shock wave is very large in DINA, but has an amplitude only slightly larger than the first pulse in nitromethane and molten TNT. The shapes, heights, and signs of the pulses must be related to the molecular properties of the explosive and to the changing state of the explosive in the initiation process, but the details of the mechanism that generates the electric charge must be better understood before an interpretation can be made.

ADVANTAGES AND LIMITATIONS OF THE TRANSDUCER TECHNIQUE

In the preceding section, measurements were presented which showed that initiation events can be identified and studied with an electrical transducer. The transducer technique has advantages over optical techniques for

TABLE 2
Transducer Pulse Height Data

Explosive	Shot	τ (μsec)	Pulse Height ^a (volts)		
			Shock	Detonation	Overdrive
Nitromethane	B5207	(.093) ^b	--	.042	>.05 negative
	B5209	.114	.042	.044	>.05 negative
	B6086	.172	.032	.032	-.044
	B5203	.230	.027	.033	>.046 negative
	B5201	.325	.018	.020	-.023
	B6093	.345	.022	.020	-.034
	B5217	.424	.021	.018	-.025
Molten DINA	B6087	.160	.186	.082	off scale negative
	B6089	.256	.146	.054	-.224
Molten TNT	B6092	.122	.084	c	-.058
	B6091	.278	.078	c	-.072
TNT/Nitromethane	(30/70) B5211	.198	.008	.004	-.007
	(8/92) B5220	.438	.019	.011	-.024

^aNormalized to the B6000 series by $V = 41 V_{\text{meas}} (s/AZ)$ where V_{meas} is the voltage measured across a cable of impedance $Z(\Omega)$, s is the spacing (in.), and A is the electrode area (in.²).

^bCalculated from a measurement of $t - \tau$.

^cNo signal.

some kinds of experiments. First, the time of the shock entry is measured on the same axis as are the later events. To do this with optical techniques requires great experimental complexity — the addition of an external light reflected from the driving plate, for example. Second, the precision of time measurement is very great (≈ 1 nanosecond resolution). It is limited by the rise time of the signal, which is determined by the planarity of the wave. As a result, very short induction times can be measured accurately. Third, the pressure of the initiating shock wave can be measured directly once the calibration has been made for each explosive to be studied.

Some of the limitations of the use of the transducer should be mentioned. Since only an insulating material shows the effect, conducting explosives, such as those containing nitric acid, cannot be studied. The rise time and height of an output pulse is influenced by the quality of the shock or detonation wave. For precision measurements the waves must be planar and parallel to the electrodes. The length of the induction zone that can be studied is limited by the minimum detectable signal, because the signal amplitude decreases as the transducer is made longer.

CONCLUSIONS

Unusual electrical phenomena have been found which occur as part of the initiation process in liquid explosives. Their study has already shed some light on initiation behavior, but the mechanism by which the observed electrical signals are produced is not really known. Polarization by mechanical orientation or deformation of the molecules within the thickness of the shock or detonation front is postulated as the primary mechanism.* The following hypothetical model is proposed to explain the electrical phenomena observed during the course of initiation of detonation in nitromethane.

As the initial shock wave enters the liquid explosive it polarizes the molecules in a thin layer near the interface. As a result an induced charge appears on the plates of the transducer. As the shock proceeds through the nitromethane it continues to polarize a thin layer of molecules, but the polarization behind the front relaxes rapidly. No additional charge is induced on the plates, so the output pulse drops to zero. When detonation starts at the attenuator

interface, it repolarizes a thin layer of molecules near the attenuator in the compressed explosive. This newly-polarized layer induces additional charge on the plates giving rise to the second observed pulse. Chemical reaction taking place immediately behind the detonation front in the compressed explosive destroys the polarization, but the reaction products form a conductive path between the detonation front and the grounded attenuator plate. The output pulse drops quickly to a value determined by the electrical properties of the reaction products. Charge continues to flow in the external circuit because the electrode spacing is being reduced (and thereby the electric field strength is increased) by the increasing layer of conducting reaction products. When the detonation in the compressed explosive overtakes the initial shock wave, the signal drops sharply in the negative direction. This must indicate that the amount of polarization between the electrodes has been reduced suddenly. Charge flows in the opposite direction and a negative signal appears across the shunt resistance. This suggests that the polarization produced by the overdriven detonation (and subsequently by the steady-state detonation) in the unshocked nitromethane, although still having the same sign, is less intense than the polarization produced by the initial shock wave. A possible inference to be drawn from this is that decomposition (with little polarization) occurring at the higher pressure of the detonation wave is a more rapid process than the polarizing deformation caused by the initiating shock. As the detonation wave nears the probe the pulse rises rapidly because of the rapidly increasing field strength resulting from the decreasing effective electrode spacing.

It is recognized that there are many causes for the appearance of charge in detonating systems. The proposed model has in no way been proved, nor does it explain all the observed facts, but is put forth only as an aid in planning additional experimental and theoretical programs.

ACKNOWLEDGMENT

This work was performed under the auspices of the United States Atomic Energy Commission.

REFERENCES

1. A. W. Campbell, W. C. Davis, and J. R. Travis, *Phys. Fluids*, **4**, 498 (1961)

*Proposed by Eichelberger and Hauver [4] and Harris [5] for inert dielectrics.

2. A. Maček, Chem. Rev., 62, 41 (1962)
3. J. R. Travis, A. W. Campbell, W. C. Davis, and J. B. Ramsay, Les Ondes de Détonation (Centre National de la Recherche Scientifique, Paris, 1962), p. 45
4. R. J. Eichelberger and G. E. Hauver, Les Ondes de Détonation (Centre National de la Recherche Scientifique, Paris, 1962) p. 363
5. P. Harris, J. Appl. Phys., 36, 739 (1965)

ELECTRICAL PROBE TECHNIQUE FOR MEASUREMENT OF DETONATION AND DEFLAGRATION VELOCITIES

Locha D. Pitts
Link Ordnance Division, General Precision, Inc.
Sunnyvale, California

ABSTRACT

Probe techniques and instrumentation have been developed for electrical measurement of instantaneous detonation and deflagration velocities of pressed PETN and pyrotechnic mixes, respectively, in confining test cylinders of 0.100-inch I.D. and 1.25-inch length. These techniques are refinements of existing techniques for detonation velocity measurements which permit measurement at the lower pressures normally produced in deflagration and in detonation-to-deflagration transitions.

The probe consists of a length of resistance wire sandwiched between two strips of insulating material. A constant current is forced through the probe, which is laid adjacent to the wall of the metallic test cylinder. Detonation or deflagration front pressure forces the resistance wire through the insulation, and a decreasing voltage inversely proportional to the distance of the front from the initiated end is read out on an oscilloscope. Excellent results have been obtained for detonation velocities in various densities of PETN and deflagration velocities in such pyrotechnic mixes as RDX-aluminum, potassium perchlorate-aluminum, and copper oxide-magnesium. Transitions from detonation to deflagration have also been observed.

Several electrical techniques for detonation velocity measurement are discussed and evaluated. The probe assembly is explained and the choice of probe materials is discussed. The instrumentation setup is presented, as well as a schematic for the small, but precise, 200-milliamperere solid state current generator built for this study.

INTRODUCTION

Electrical probes and instrumentation have been developed and used to measure detonation velocity in pressed PETN, and deflagration velocities in pyrotechnic mixes, including RDX-aluminum, potassium perchlorate-aluminum, and copper oxide-magnesium. These mixes were in direct contact with the initiating PETN inside brass test bodies of 0.100-inch I.D., 0.750-inch O.D. and 1.25-inch length. The wall resistance wire probes permit continuous measurement of reaction front velocity through the detonation-to-deflagration transition.

Electrical probe techniques for measurement of reaction front velocities in PETN and three pyrotechnic mixes will be discussed in the following categories.

- (1) possible measurement techniques
- (2) characteristics of the selected wall resistance wire probe
- (3) shot preparation
- (4) instrumentation
- (5) calibration of wall resistance wire probes.

POSSIBLE MEASUREMENT TECHNIQUES

Detonation and deflagration front velocities may be determined by measuring the velocity of some electrical phenomena (light output or conductivity) associated with the reaction front or

by measuring the time rate of change of the electrical parameters (capacitance or resistance) of some electrical element directly affected by the reaction front.

Velocity of the luminous front may be measured by means of a framing camera, a streaking camera, or a photovoltaic device. Framing camera and streaking camera records [1] can be extremely revealing about front contours but have the disadvantages of requiring expensive equipment and complex setups, and not being usable on opaquely confined explosives and pyrotechnics. Also, in the case of the framing camera, only incremental velocities are obtained. Use of a photocell and light probes at intervals on the test body has the disadvantages of giving only incremental velocities, and disturbing the explosive confinement.

Ionization front velocity measurements using the Doppler effect at microwave frequencies [2] appear to produce good results in detonation, but there is no evidence in the literature that equivalent results could be expected in deflagration where ionization front conductivity is presumably much lower than in detonation. Also to be considered are the expensive equipment and complicated setup required.

The resistance probe, a type of which was selected for Link's experiments, produces some small disturbance of the explosive geometry, but requires no complex instrumentation, is easy to assemble, and delivers a continuous record of instantaneous velocities in detonation, deflagration, and the transition between the two.

Resistance probes commonly function by continuous shorting by the reaction front of a resistance wire carrying a constant current. Front velocity may then be computed from Eq. 1:

$$v = \frac{1}{ir} \frac{dV}{dt} \quad (1)$$

where

v = instantaneous velocity (mm/ μ sec)

i = constant current (amperes)

r = resistivity of resistance wire (ohms/mm)

dV/dt = slope of voltage vs. time curve on oscilloscope trace (volts/ μ sec)

The resistance probe described by Amster in his very helpful article [3] utilizes the

ionization front and the metallic confinement for the return path for current through a bare resistance wire buried in cast explosives. Our experiments with a bare #30 copper wire down the center of a standard brass test body loaded with pressed PETN showed significant fluctuations in ionization front resistance and excessive spuriously generated emf's. Thus, when resistance wire was used down the center of a PETN column pressed in a standard test body,* the result was an unreadable trace, rather than the straight slope which should have been observed had not the above problems been present.

The resistance probe described by Bowser [4] utilizes resistance wire coiled around an insulated copper conductor. The resistance wire is progressively shorted to the copper conductor as the reaction front destroys the thin insulation. This probe has the advantages of being useful in different geometries and having the proven pressure sensitivity necessary for measurements at the relatively low pressures experienced in deflagration. This probe configuration was rejected principally because of the difficulty inherent in its manufacture and because of the problems associated in pressing explosives around such a probe.

The probes adopted for our experiments were modifications of the resistance probes described by Bowser and Amster. They consisted of resistance wire laid down the confinement wall parallel to the long axis of the test body, and thus normal to the reaction front. The wire was insulated from the wall by a thin strip of mylar tape or transformer paper or by enamel insulation deposited on the wire. In most cases another thin strip of mylar tape was placed over the wire, separating the wire from the explosive. Pressure from the reaction front forced a continuous shorting of the wire through the insulation to the wall. Figure 1 shows the trace produced by the shock wave in the acceptor of a Thru-Bulkhead geometry test body where failure to transfer occurred. Since hot gases cannot pass the bulkhead, and temperature gradients cannot pass through in a few microseconds, this shot offers proof that the mechanism of probe closure is not ionization or heat, but is certainly pressure.

This technique provides simple probe assembly, simple explosive loading techniques, high reliability, good pressure sensitivity even in deflagration, and accurate results.

*A special ram with a 0.010-inch diameter hole down the center was manufactured for these experiments. The center hole was produced by the spark erosion technique.

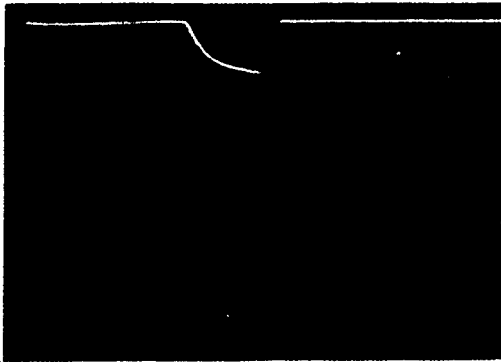


Fig. 1 - Acceptor shock wave trace, TBI body geometry

Horiz: 2 μ sec/cm
 Vert: 5 V/cm
 Thru Bulkhead Geometry (detonation failed to transfer)
 Donor: PETN (1.7 gm/cm)
 Acceptor: PETN (1.0 gm/cm)
 Probe: 0.5-mil Moleculoy probe

The effect of the wire on burning rate, as mentioned by Amster [5], is minimized by using this type of probe, since the wire is initially insulated from the pyrotechnic mix and is coupled to the cold wall at the reaction front. It should also be noted that our experiments utilized pyrotechnic mixes with velocities in the range from 0.5 to 3.0 mm/ μ sec, much too rapid for heat transfer down the probe wire to have any significant effect on burning rate.

SELECTED PROBES

Three wall probe configurations have been found useful for detonation-to-deflagration velocity experiments. They are: (1) a sandwich probe consisting of 1-mil diameter bare Nichrome wire sandwiched between an upper layer of 0.25-mil thick mylar tape and a lower layer of 0.25-mil thick mylar tape or 0.2-mil thick NDC coil paper, (2) 1.2-mil enamel insulated Nichrome wire covered by a layer of 0.25-mil thick mylar tape, and (3) a 0.5-mil enamel insulated Moleculoy wire without tape covering.

Most experiments were performed using the sandwich probe, since its sensitivity in deflagration was more reproducible than the covered 1.2-mil insulated Nichrome wire probe. However, when particularly low deflagration pressures were encountered, the 0.5-mil Moleculoy probe was developed, and showed the greatest pressure sensitivity of all the probes tested. Nevertheless, for most purposes, the

sandwich probe is preferable for its relatively good assembly and loading characteristics. The constant slope of Fig. 2 illustrates the typical operation of the sandwich resistance wire wall probe in a test body loaded with PETN at a constant density.

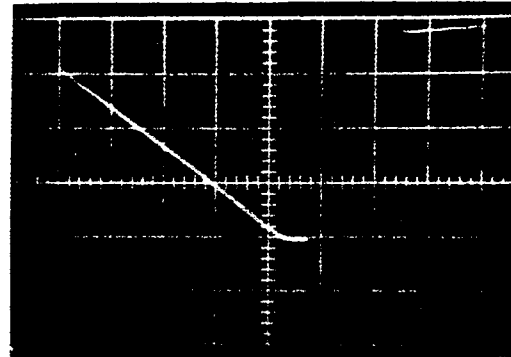


Fig. 2 - Typical trace of sandwich resistance wire wall probe

Horiz: 1 μ sec/cm
 Vert: 2 V/cm (3 μ sec delay)
 Load: PETN (constant density)
 Probe: 1-mil Nichrome sandwich probe

In general, it was found that wire diameter should be 1.5 mils or less. Larger wire tended to give slower response, be less pressure sensitive, and take longer to break its final contact. Smaller wire appeared to have a desirable knife-edge effect, slicing through the insulation. However, smaller wire does have the disadvantage of being difficult to handle because of its weakness in tension and its lack of stiffness. It was found that even the 0.5-mil wire could be used successfully under proper conditions.

The other consideration in choosing wire size is that the wire should give a drop of 1 to 10 volts across its entire length when some selected constant current between 1 and 200 milliamperes is forced through it. This range of current is easily generated from a 30-volt power supply and a solid state current generator such as used in these experiments. If the total voltage change is under 1 volt, line interference, firing pulses, and trigger circuit pulses may cause considerable distortion of the oscilloscope trace.

Mylar tape, UCC and NDC coil paper,* and regular enamel wire coating all proved

*Obtained from Peter J. Schweitzer Div. of Kimberly Clark Corporation.

satisfactory as insulation between the resistance wire and the confining metal wall. The most important factor in choosing the insulation is that insulation thickness should be as thin as possible so that the wire has only a short distance to travel to the wall and so that the insulation can be broken more easily by deflagration pressures. The insulation, however, does have to be able to withstand loading pressures. Mylar tape, which has a greater tensile strength and less tendency to tear in cutting than coil paper, is easier to load and cut. However, the transformer paper gave better results at the low deflagration pressures.

For all probes except the 0.5-mil insulated Moleculoy wire, it was found to be very important to include a layer of mylar tape over the resistance wire. This appeared to serve the function of holding the resistance wire and lower layer of insulation in place during probe insertion and loading so that no kinking occurred. The thickness of tape did not appear to influence results greatly, but thinner tape was preferred since it produced less alteration in the geometry of the explosive. It should be noted, however, that the most sensitive probe developed, the 0.5-mil insulated Moleculoy wire, functioned best without any covering layer of insulation.

Pressure sensitivity is very important at low deflagration pressures, especially in the transition region between detonation and deflagration where pressures are particularly low at the wall. The principal methods of achieving this sensitivity are: (1) use of 1.2-mil wire or smaller, (2) use of a thin (0.5-mil or less) insulator between wire and wall, and (3) proper probe tension, apparently just enough to assure that the probe lies straight.

It was noted early in the program that the probes often showed an open or no resistance change for a period of a few microseconds right at the interface between the PETN and the pyrotechnic mix. After this phenomenon was observed repeatedly, it was interpreted as being due to the reaction near the interface occurring only in the core of the pyrotechnic mix, with some finite time (on the order of a few microseconds) being required for the complete reaction to take place at the wall. Once the complete cross sectional area was reacting, the core reaction zone could drag the wall reaction along. Though the mix might not be completely reacting at the wall, some sort of pressure gradient, non-zero at the wall, appeared to be present since some shots showed continuous velocity measurements through the transition region. If the assumption about transition region pressures being greater near the center of the pyrotechnic

mix is correct, further experiments should show that good oscilloscope traces are more easily attained at diameters smaller than the 0.100 inches used for the present study and less easily attained at diameters greater than 0.100 inches. It was also observed that the opens of the probe during transition were more likely to occur when PETN density was 1.2 gm/cm^3 than when it was 1.0 for the same pyrotechnic mix at the same density. For instance, in a series of 12 shots in stainless steel test bodies using pyrotechnic mixes, all six shots containing PETN at 1.2 gm/cm^3 showed discontinuities at the PETN-pyrotechnic interface lasting at least 1 microsecond, while the six shots containing PETN at 1.0 gm/cm^3 showed interface discontinuities in only three shots and no discontinuity lasted any longer than one microsecond.

SHOT PREPARATION

Shot preparation procedure included the following basic steps:

- (1) probe installation in the test body
- (2) pressing of weighed increments of PETN and pyrotechnic mix into the test body
- (3) installation of ion probe trigger wire on PETN MDF detonating cord
- (4) attachment of detonating cord to input of test body
- (5) attachment of test body assembly to a 3" by 8" board
- (6) soldering of ground wires and probe wires to terminals attached to board
- (7) connection of #6 electric blasting cap to input end of detonating cord just prior to firing.

In assembly of sandwich probes, first the 1/16-inch wide strip of mylar tape or coil paper was inserted in the test body. Then the resistance wire was added and finally the covering strip of 1/16-inch wide mylar tape. The whole assembly was secured by scotch tape covering each end of the test body. The 0.5-mil Moleculoy probe was simply inserted and taped down on each end.

The PETN and pyrotechnic charges were loaded in increments, commonly of 0.100-inch lengths. The higher density end, requiring greater pressing pressures, was pressed first.

Pressing was done to a stop on a hydraulic press. The ram used had been flattened on one side to permit passage by the probe. Care in pressing and frequent ohmmeter checks were required to assure that the probe did not short to the test body, particularly at the lip of the hole.

The ionization trigger probe consists of a #37 insulated copper wire taped into a notch 1 inch from the output end of a 3-inch length of 10 grain PETN MDF detonating cord. The detonating cord is inserted in a 0.75-inch O.D. slice of doweling which is then taped to the input end of the test body (See Fig. 3).

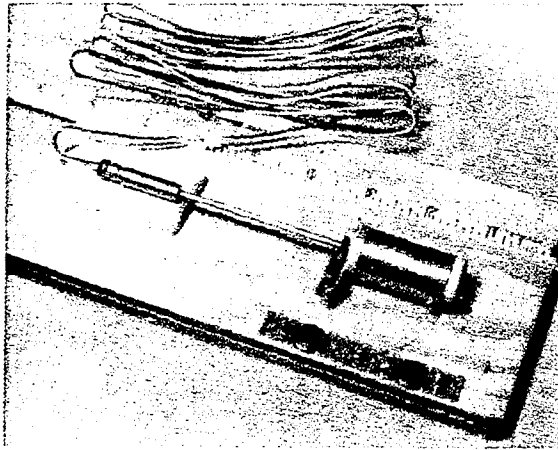


Fig. 3 - Standard brass test body ready for firing

The output end of the test body was covered by another slice of 0.75-inch diameter doweling. The wall probe wire was brought along the side of the doweling and soldered to a drive screw on the flat outer surface of the doweling. A copper wire soldered to the same drive screw was connected to a terminal on the terminal board tacked to the 3" by 8" board on which the whole assembly rested. Grounds were provided through copper wires connected to an alligator clip fastened to the lead case of the detonating cord and connected to a drive screw inserted in a hole near the output end of the test body. The ionization trigger probe was connected to the third terminal of the terminal board.

Though some experiments were made in the Thru Bulkhead Initiator (TBI) geometry with single-section units, the final series of TBI shots was made with two section TBI's consisting of a B1113 mild steel donor, including bulkhead, and a brass acceptor. Bulkhead thicknesses

of 75, 90, and 105 mils were used. The two-section construction considerably simplified probe installation, since the wall probe was not inserted in a blind hole but could be pulled completely through the acceptor hole and cut off on the bulkhead side when the shot was assembled. TBI preparation procedure was similar to that for the standard straight-through test bodies except that the two sections were held in place by a special steel fixture.

INSTRUMENTATION

Instrumentation used in the experiments consisted of a 200-ma solid state current generator and an RC pulse network. Additionally, a Hewlett-Packard 30 volt, Model 721A power supply, a Tektronix C19 oscilloscope camera, and a Tektronix 555 oscilloscope with two L plug-in amplifiers were used. Figure 4 illustrates a typical instrumentation setup for a firing. The constant current generator, whose schematic is presented in Fig. 5, uses an NPN silicon power transistor rather than large vacuum tubes such as in the current generators described in Refs. 3 and 4. Advantages of the solid state generator include:

- (1) higher reliability
- (2) a small package which is easier to move and setup and can be placed in the firing chamber if properly protected
- (3) no deterioration of electrical characteristics with time
- (4) simpler construction
- (5) no high voltages present in explosive environment.

Generally transistors, as can be seen from their characteristic curves, maintain a constant collector current when base bias is held constant. In the current generator of Fig. 5 the 6.8-volt zener diode Z_1 maintains the constant base drive. R_1 serves to keep Z_1 conducting. R_2 is used to adjust the output current to an exact value. R_2 should be larger than 100 ohms if currents under 50 milliamperes are desired. Most experiments in this study were performed with 100-milliamperere currents except for the 0.5-mil Moleculoy probe shots for which 20 milliamperes were used. These currents were chosen to produce sufficient voltage drop across the resistance probe to override any low-level noise. Otherwise, different current levels seemed to have no effect on probe performance. The transistor used, a 2N1072, is a special power transistor no longer manufactured, but

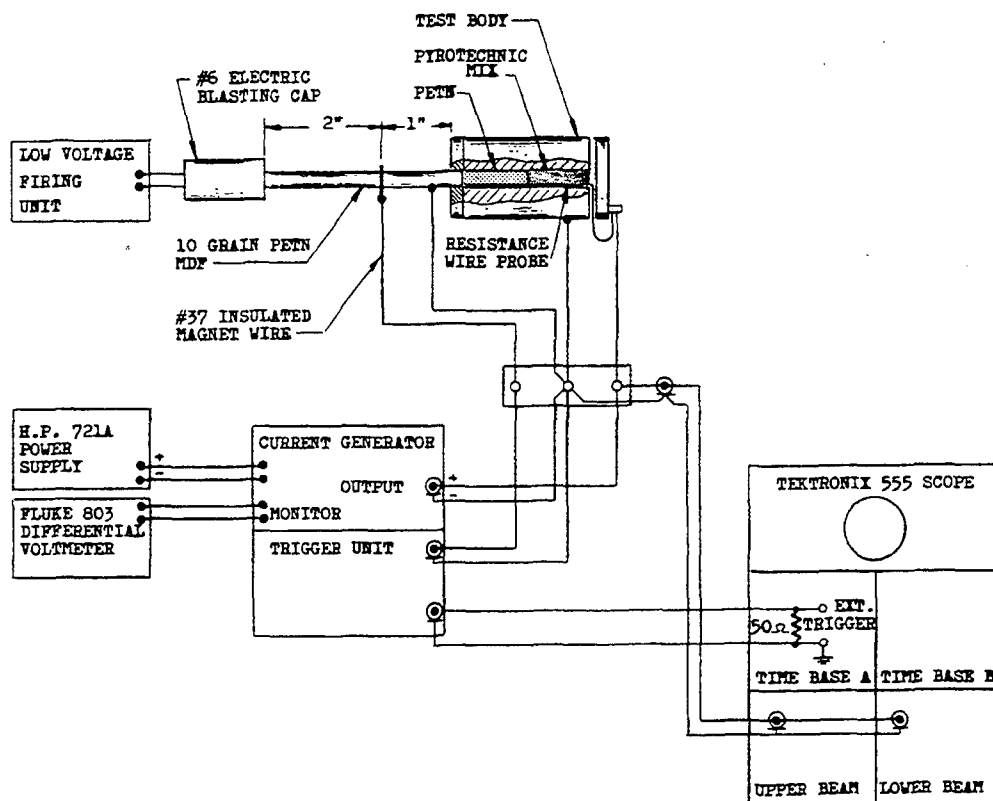


Fig. 4 - Test instrumentation

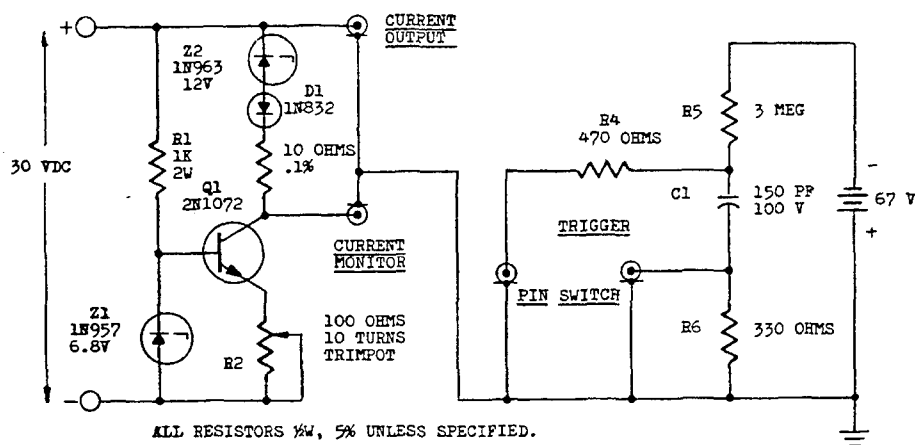


Fig. 5 - Constant current generator and trigger circuit

such transistors as the 2N2781 and 2N3327 have adequate power handling capability and frequency response for this application.

A 10-ohm, 0.1% precision resistor (R_3) was employed in series with the output as a current monitor. Output current was then determined from the voltage across this resistor as read out on a John Fluke differential voltmeter, Model 803. Regulation into loads from 0 to 100 ohms was 0.1% and short-term drift was less than 0.3% after stabilization. Most error was thus due to the Tektronix 555 oscilloscope, explosive loading error, and test body machining tolerance. However, calibration shots showed total system accuracy to be consistently below 4%.

Zener diode Z_2 across the output serves to keep the transistor Q_1 turned on prior to a firing and limits the voltage drop when initial probe shorting occurs. Diode D_1 in series with Z_2 is a microwave diode forward biased to decrease the effect of the 1000-pf zener region capacitance of Z_2 during initial probe shorting [6]. In some cases Z_2 was replaced by two zener diodes to further decrease the capacitance effect.

Cables and leads were chosen to approach a critically damped system, so that the velocity slopes had no ringing and initial fall time was as fast as possible. Flat lead, #28 stranded wire, and lossy line from a Tektronix 10:1 attenuator probe were eventually used to provide a satisfactory system. It is also important to use a fast response power supply such as the Hewlett-Packard Model 721A. The oscilloscope capacitance of 20 pf per channel has a negligible effect. The natural response of the current generator was in excess of 10 MC, which was quite satisfactory.

It was found desirable to get reliable external scope triggering from an ionization probe closure on the detonating cord approximately 4 microseconds before the cord detonation reached the input of the test body. This permitted use of the lower beam of the Tektronix 555 delay oscilloscope in the delayed mode at a faster sweep speed than for the upper beam. The RC trigger circuit was designed to work from probe closure, provide a fast rising and fast decaying (0.1-microsecond fall time) pulse, radiate minimum electromagnetic energy to the signal channel, suppress spurious trigger pulses for 500 microseconds after the initial pulse, and allow insensitive oscilloscope trigger level setting to prevent spurious noise from accidentally triggering the oscilloscope.

During this study various methods of obtaining trigger contact closure to the grounded lead sheath of the detonating cord were tried, including #37 insulated magnet wire laid across a notch in the detonating cord, the same type magnet wire wrapped around unnotched detonating cord, and 3-mil thick copper strip laid over a notch in the cord. All these methods performed satisfactorily. The ionization jet and the shock wave at the surface of the lead sheath are both strong enough to assure low resistance contact between the lead sheath and the wire or strip. The most important part of such a triggering system appears to be an appropriately designed pulse-forming trigger network to provide the trigger pulse for the oscilloscope.

CALIBRATION

A calibration curve for PETN density vs. velocity was obtained from a series of shots fired in standard test bodies and employing pin pairs, a capacitor discharge circuit, and a Tektronix 555 oscilloscope. Figure 6 shows the experimental points from these data plotted on the same graph with a curve (Solid Line) plotted from an accepted equation relating PETN velocity and density (Ref. 1). A series of calibration shots for the 1-mil Nichrome sandwich probe was fired with test bodies being loaded to 0.625 inches with one density of PETN and loaded with another density of PETN for the remaining 0.625 inches. Approximate densities of 0.8, 1.0, and 1.2 gm/cm³ were used. A typical trace appears in Fig. 7. Densities were calculated from test body weight before and after loading and from known test body diameters. Velocities were taken from Fig. 6. Correlations appear in Table 1 and Table 2.

Table 2 indicates that correlation was better than 4% in some 90% of the cases. Later experiments showed even better correlation for both the sandwich probe and the 0.5-mil Moleculoy probe.

Figures 8 through 10 show typical traces obtained from test bodies loaded for 0.625 inches with PETN and for the remaining 0.625 inches with the individual pyrotechnic mixes. These shots were obtained with the 1-mil Nichrome sandwich probe.

Figure 11 through 13 are oscilloscope traces obtained from shots of test bodies loaded for 0.500 inches with PETN and for the remaining 0.750 inches with the three individual pyrotechnic mixes. The 0.5-mil insulated Moleculoy wire probe was employed in these shots.

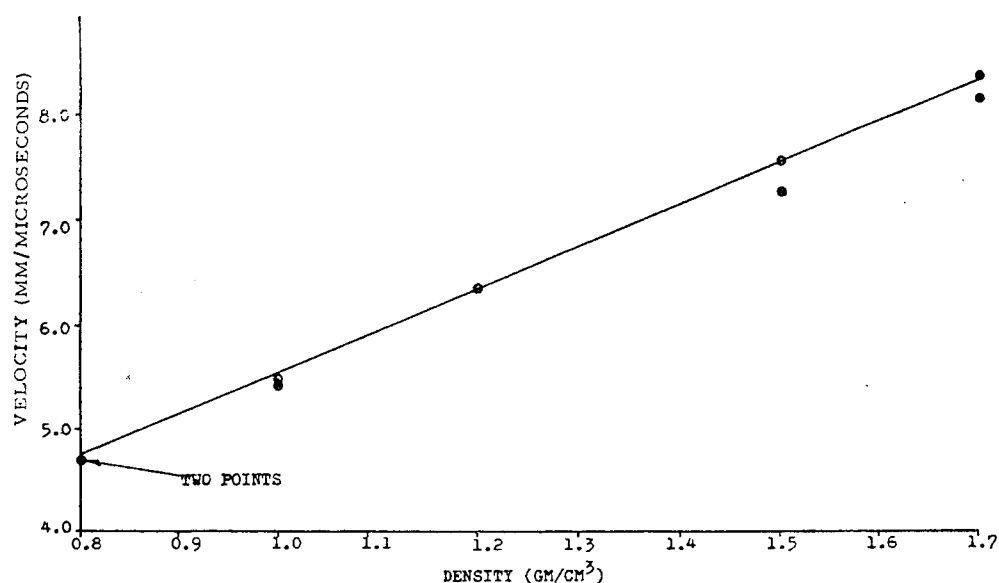


Fig. 6 - Plot of density vs detonation velocity for 325 mesh PETN

TABLE 1

Shot No.	Velocity 1 (density)	Velocity 1 (probe)	Velocity 2 (density)	Velocity 2 (probe)
1	5.8	6.0	5.5	5.6
2	6.3	6.3	5.6	5.9
3	6.3	6.3	5.6	5.7
5	5.6	5.7	4.7	4.9
6	6.2	6.3	4.7	4.8
7	6.3	6.4	-	-
9	6.3	6.1	4.7	4.9

All velocities are in mm/sec.

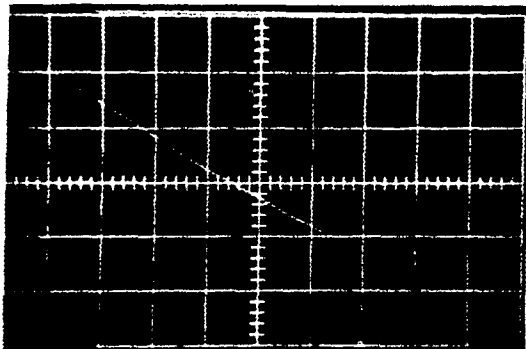


Fig. 7 - Sandwich probe record of two-density PETN

Horiz: 1 $\mu\text{sec}/\text{cm}$ (3 μsec delay)
 Vert: 2 V/cm
 Load: 0.625" PETN (1.2 gm/cm³)
 0.625" PETN (0.8 gm/cm³)
 Probe: 1-mil Nichrome sandwich probe

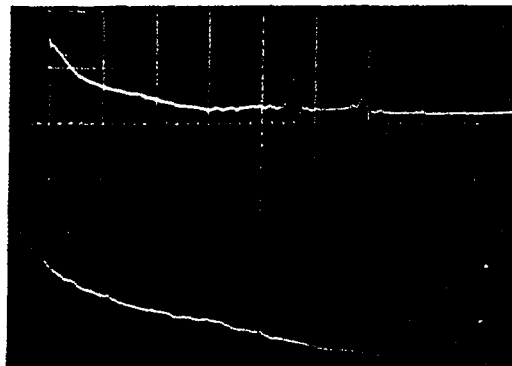


Fig. 9 - Sandwich probe record of KClO₄-Al deflagration velocity

Horiz: Upper: 5 $\mu\text{sec}/\text{cm}$
 Lower: 2 $\mu\text{sec}/\text{cm}$ (5 μsec delay)
 Vert: Upper: 5 V/cm
 Lower: 2 V/cm
 Load: 0.625" PETN (1.0 gm/cm³)
 0.625" 60% KClO₄-40% Al (1.5 gm/cm³)
 Probe: 1-mil Nichrome sandwich probe

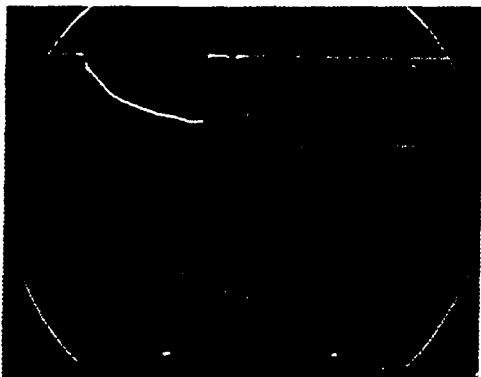


Fig. 8 - Sandwich probe record of RDX-Al deflagration velocity

Horiz: Upper: 5 $\mu\text{sec}/\text{cm}$
 Lower: 2 $\mu\text{sec}/\text{cm}$ (2 μsec delay)
 Vert: Upper: 5 V/cm
 Lower: 2 V/cm
 Load: 0.625" PETN (1.0 gm/cm³)
 0.625" 25% RDX-75% Al (1.0 gm/cm³)
 Probe: 1-mil Nichrome sandwich probe

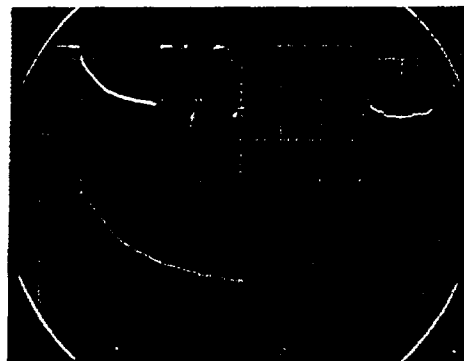


Fig. 10 - Sandwich probe record of CuO-Mg deflagration velocity

Horiz: Upper: 5 $\mu\text{sec}/\text{cm}$
 Lower: 2 $\mu\text{sec}/\text{cm}$ (3 μsec delay)
 Vert: Upper: 5 V/cm
 Lower: 2 V/cm
 Load: 0.625" PETN (1.0 gm/cm³)
 0.625" CuO-Mg (1.5 gm/cm³)
 Probe: 1-mil Nichrome sandwich probe

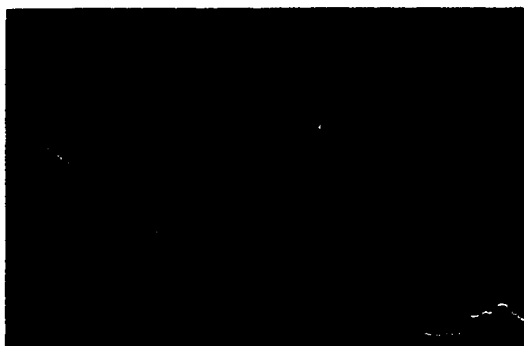


Fig. 11 - Moleculoy probe record of RDX-Al deflagration velocity

Horiz: Upper: $5 \mu\text{sec/cm}$
 Lower: $1 \mu\text{sec/cm}$ ($4 \mu\text{sec}$ delay)
 Vert: Upper: 5 V/cm
 Lower: 2 V/cm
 Load: $0.500''$ PETN (1.0 gm/cm^3)
 $0.750''$ 50% RDX-50% Al (1.0 gm/cm^3)
 Probe: 0.5-mil insulated Moleculoy wire

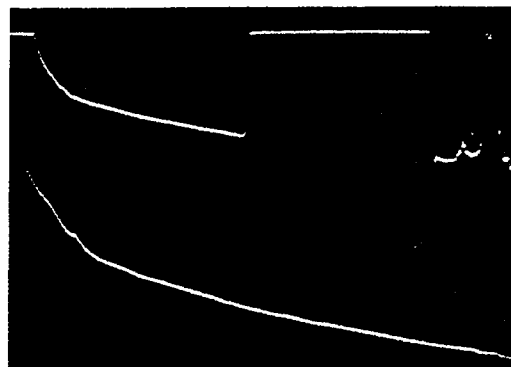


Fig. 13 - Moleculoy probe record of CuO-Mg deflagration velocity

Horiz: Upper: $5 \mu\text{sec/cm}$
 Lower: $2 \mu\text{sec/cm}$ ($3 \mu\text{sec}$ delay)
 Vert: Upper: 5 V/cm
 Lower: 2 V/cm
 Load: $0.500''$ PETN (1.0 gm/cm^3)
 $0.750''$ CuO-Mg (1.7 gm/cm^3)
 Probe: 0.5-mil insulated Moleculoy wire

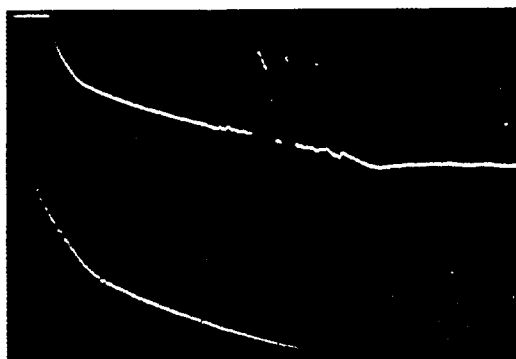


Fig. 12 - Moleculoy probe record of KClO_4 -Al deflagration velocity

Horiz: Upper: $5 \mu\text{sec/cm}$
 Lower: $2 \mu\text{sec/cm}$ ($3 \mu\text{sec}$ delay)
 Vert: Upper: 5 V/cm
 Lower: 2 V/cm
 Load: $0.500''$ PETN (1.0 gm/cm^3)
 $0.750''$ 60% KClO_4 -40% Al (1.2 gm/cm^3)
 Probe: 0.5-mil insulated Moleculoy wire

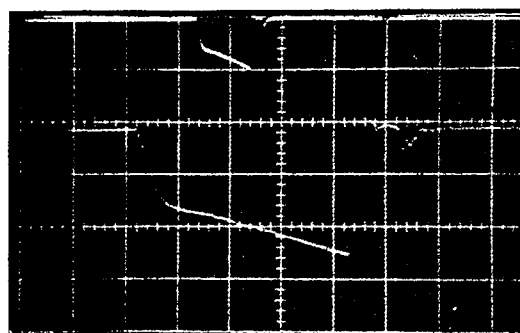


Fig. 14 - Acceptor shock wave trace, TBI body geometry

Horiz: Upper: $2 \mu\text{sec/cm}$
 Lower: $0.5 \mu\text{sec/cm}$ ($5 \mu\text{sec}$ delay)
 Vert: Upper: 5 V/cm
 Lower: 2 V/cm
 Simulated TBI geometry (90-mil bulkhead; detonation transferred)
 Load: Donor: PETN (1.65 gm/cm^3)
 Acceptor: PETN (1.25 gm/cm^3)
 Probe: 1-mil Nichrome sandwich probe

TABLE 2

Deviation (mm/ μ sec)	Number of Shots
0	2
.10	6
.20	4
.30	1

Figure 14 shows a trace obtained from a 1-mil Nichrome sandwich probe in the acceptor of a two-section TBI configuration.

ACKNOWLEDGMENT

The author wishes to express his appreciation for the advice and suggestions offered by Dr. D. E. Davenport and John N. Gardner. He also wishes to acknowledge the shot preparation performed by L. W. Gillis.

These electrical probe experiments were performed in conjunction with metallographic experiments to obtain data for Detonation-to-Deflagration Studies carried on under NASA/Huntsville Contract No. NAS 8-11472.

REFERENCES

1. Melvin A. Cook, The Science of High Explosives, Reinhold Publishing Corp.
2. Melvin A. Cook, Ray L. Doran, and Glen J. Morris, "Measurement of Detonation Velocity by Doppler Effect at Three-Centimeter Wavelength," Journal of Applied Physics, Vol. 26, No. 4, April 1955.
3. A. B. Amster, P. A. Kendall, L. J. Veillette, and B. Harrell, The Review of Scientific Instruments, Vol. 31, No. 2, February 1960.
4. Frank C. Gibson, Merle L. Bowser, Chas. M. Mason, "Method for the Study of Deflagration to Detonation Transition," The Review of Scientific Instruments, Vol. 30, No. 10, October 1959, American Institute of Physics.
5. A. B. Amster, The Review of Scientific Instruments, Vol. 31, No. 2, (Letter to the Editor), February 1960.
6. Sabri, Hussein, "High-Frequency Zener Limiters," EEE, May 1965.

ANOMALOUS THERMOELECTRIC EFFECT IN THE SHOCK REGIME AND APPLICATION TO A SHOCK PRESSURE TRANSDUCER

Jean Crosnier

*Direction des Etudes et fabrication d'Armement
Gramat, Lot, France*

and

Jean Jacquesson and Andre Migault

*Faculte des Sciences de Poitiers
Poitiers, Vienne, France*

ABSTRACT

The experimental study of the electrical response of thermocouples made with different metals, when put into shock loaded metallic samples, has shown:

1. That in respect to several physical aspects they behave like static thermocouples.
2. That the response seems to increase with pressure up to 1600 kilobars at least and is of such large magnitude that any classical interpretation appears impossible.

This effect has been used to detect and measure shock pressure in metallic targets (provided that certain requirements are filled).

This effect could be attributed to the formation of an electronic hot gas, the temperature of which would be quite a bit higher than that of the crystal lattice. This explanation seems to be the most reliable.

It may also be noticed that, according to work performed by Rodionov, the Debye temperature of the lattice becomes very large at very high pressures. Nevertheless, his theory would explain the experimental results only in a particular pressure gap.

INTRODUCTION

When a shock wave crosses the junction surface of two metals of different natures, there appears between the uncompressed extremities of the metals a difference in potential, the magnitude of which being dependent on the amplitude of the shock wave and the nature of the metals in contact.

This effect, noticed in 1959 [1], then in 1962 [2,3] and in 1964 [4] had been initially found during the investigation of a thermal electric detector for the recording of temperature at the front of a shock. In effect, the adiabatic compression of the metal in the shock gives rise simultaneously to an increase in temperature. If the wave traverses the interface of metals having adequate thermoelectric powers, one must expect the instantaneous appearance of a voltage in which the time variation can be translated into the temperature and consequently

to the pressure at the interface. The choice of metals for study, couples constantan/iron (C.T.E./iron) and constantan/copper (C.T.E./copper), was determined by the fact that their shock impedances are very close, thus avoiding wave reflections at the interface. Ilyukhin and Kologrivov [3] used the couple nickel/copper.* The voltage fronts obtained are of an amplitude well above those that would allow prediction either on the basis of thermodynamic evaluations

*By convention we will name second, in the designations of thermocouples which follow, the metal constituting the most important mass of the metallic samples submitted to the shock. This mass, which is tied to the shielding of the transmission cables, also constitutes the reference voltage in relation to which one measures the voltage of the couple. In practice this metal will be nearly always copper but sometimes iron.

in the shock front or on the basis of the normal thermoelectric powers of the metals used. For this reason it has seemed interesting to study the principal characters of the phenomena, a study which has led to its utilization as a pressure transducer. The first results of the study are given here. They tend to disclose the effective nature of the voltage observed, its amplitude as a function of the pressure, and finally the service it can render as a pressure transducer for shocks. The couple most studied is the couple constantan/copper (C.T.E./copper). The constantan is a cupro-nickel with about 43.5% of nickel with addition of manganese (less than 1.5%). Some results concerning other couples are given as preliminary tentative investigations. The basic experimental configuration used is given by Fig. 1.

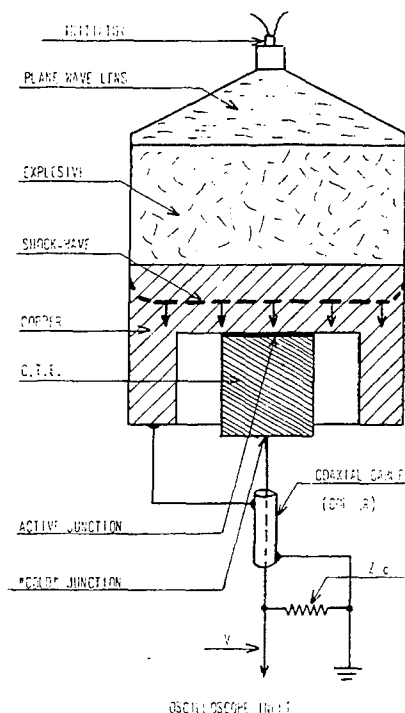


Fig. 1 - Basic thermocouple configuration

THERMOELECTRIC CHARACTER OF THE PHENOMENON

It seems at the outset that all comparisons between the normal thermoelectric effect and the effect noticed under shock should necessitate the adoption, as the accessible parameter, of the local dynamic pressure as a substitute for the notion of temperature in the classical

Seebeck effect. The notion of the warm junction is thus replaced by one of a junction under pressure. This method being adopted, without really prejudicing the true nature of the phenomena, one can nevertheless disclose a certain number of analogies between the last effect and the ordinary thermoelectric effect. Certain of the common characters have been made the object of experimental verification which we will expose below.

Heterogenous Metallic Circuit

One obtains a signal differentiated from the background noise and of a definite polarity only on the condition of making a bi or multi-metallic chain. A junction copper-copper, for example, will not give any definite signal.

Voltage Generator

The junctions studied behave as voltage sources of internal resistance of the order of a fraction of an ohm (and not as current sources). This fact has been verified in two ways; first, by a variation of the external load resistance and second, by variation of the surface of the active junctions.

In the first case eight identical junctions but with different loads (7.5, 25, 50 and 100 ohms) have been submitted simultaneously to the same shock (see Fig. 2). In the second case, eight junctions, identical except their active surfaces were varied from 3 to 75mm², have been equally submitted simultaneously to the same shock (see Fig. 4).

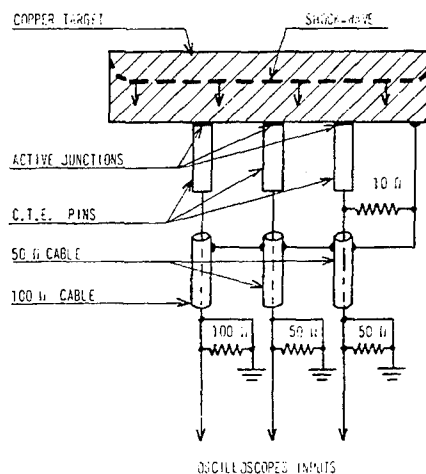


Fig. 2 - Junctions with different loads (schematic configuration). Equivalent loads: 7.5 to 100 ohm.

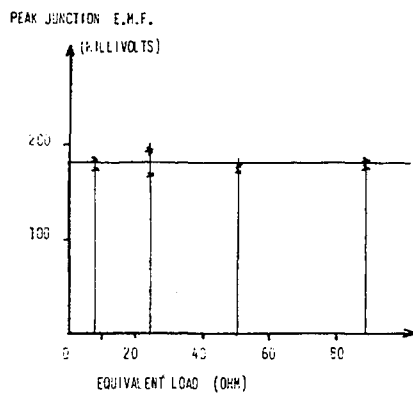


Fig. 3 - C.T.E./Cu junctions peak emf vs equivalent ohmic load. (At the same shot.) Peak emf does not depend on the ohmic load of the couple.

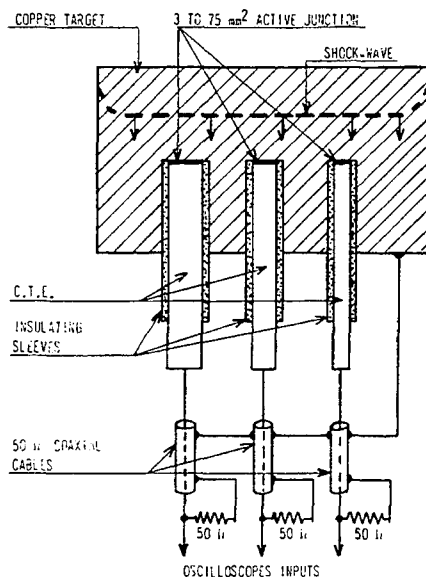


Fig. 4 - Junctions with different active areas

In the two cases the voltages given by the eight captors have been identical within about 10%. One will find, for example, the results of an experiment of the first type in Fig. 3.

Parallel Association

One knows that if several thermoelectric junctions connected in parallel are submitted to different temperatures, the potential at a

point can be calculated by Kirchhoff's laws applied to the electric network so formed. The junctions are then considered as sources of voltage. A simple configuration is the one of Fig. 5a. A common conductor ASB of constantan (C.T.E.) is in contact at A and B with a massive copper conductor. In a static system, the point S is maintained at the reference temperature, junctions A and B have two different temperatures.

One connects a copper wire at S and one measures the voltage V_S between the wire and the copper block. One has then:

$$V_S = \frac{R_B V_A + R_A V_B}{R_A + R_B}$$

where

V_A = thermoelectric potential of the couple AS

V_B = thermoelectric potential of the couple BS

R_A, R_B = resistances of the circuits AS and BS.

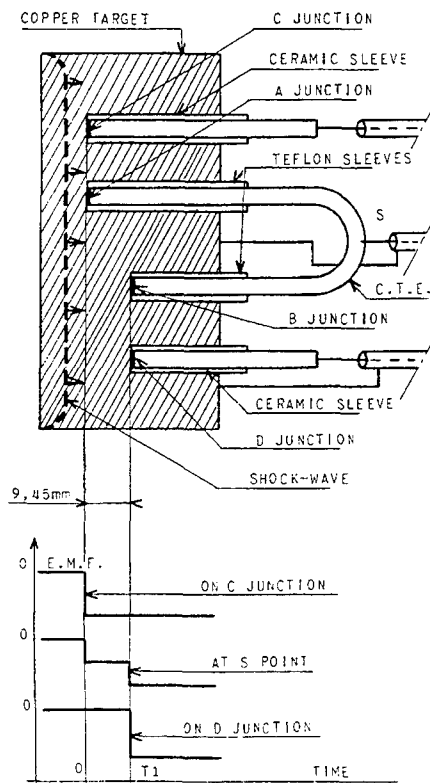


Fig. 5 - (a) Upper - target with shunt connected junctions (b) Lower - expected waveforms on C and D junctions and at S point

This configuration has been reproduced on a target, Fig. 5a. The notion of temperature being replaced by the one of instantaneous pressure, the junctions A and B are displaced along the axis of propagation of the shock in a manner that the junction A is hit first, time $t = 0$. After a time t_1 necessary for the shock to travel to B, the two junctions, A and B, give about the same emf V (the experimental conditions are such that the shock pressure does not diminish too much at A during the time t_1).

For t less than t_1 , the junction A, the only one compressed, gives an emf V . The voltage received at S will be therefore, because of the symmetry of the setup, nearly $V/2$. For $t = t_1$ the junction B compressed becomes active, and the voltage recorded rises suddenly to the value V . The expected signal is represented in Fig. 5b. The results obtained experimentally at 400 and 1100 kilobars confirm satisfactorily the theoretical scheme. The oscillograms of Fig. 6 illustrate an experiment of this type. The junctions C and D belong to pins encased in a ceramic isolating material, while the conductor ASB has been isolated by teflon. This difference of materials can explain why the junctions C and D give more complex signals and with steeper decay than the junctions A and B.

The application of these results shows that if a junction is not attacked simultaneously at all of its points by the shock, the rise time of the observed signal is at least equal to the sweep time of the junction by the shock front.

Series Association

We have tried to verify the law of thermoelectric metallic chains with the aid of the configuration of Fig. 7. The plane shock waves encountered successively a junction of copper-nickel, and a junction nickel/C.T.E. Experiments have been made at 400 and 1100 kilobars.

Measurements made elsewhere have shown that the junction nickel/copper gives at these pressures, a voltage of about half of that of couple C.T.E./copper. If one transposes from temperature to instantaneous pressure, the series law permits one to predict in these conditions a rise in voltage at two times. The experiment confirms this application of the law. (See oscillogram, Fig. 8.)

The same law permits the prediction that any superposition of metals will give a zero voltage each time that the wave traverses a sample of the same metal as the first traversed (under the reservation that the pressure stays

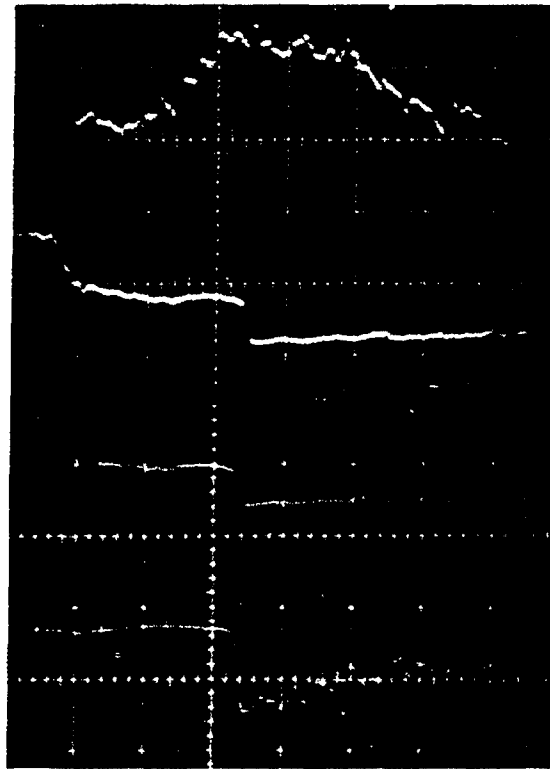


Fig. 6 - Experimental records on Fig. 5(a) configuration. From upper to lower trace:
Waveform - on C junction
- at S point
- at S point
- on D junction

On all traces: horizontal $0.5 \mu s/div.$, vertical $0.1 V/cm$, Pressure: 1160 kilobars.

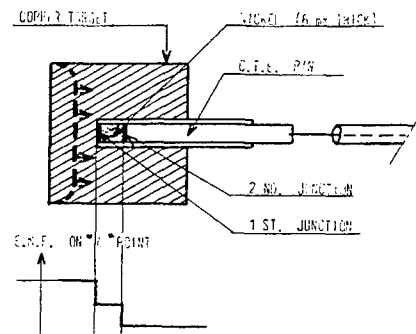


Fig. 7 - Series connected junctions, Cu, Ni, C.T.E. (upper), and expected output waveform (lower)

about constant during a time greater than the time of propagation of the shock across the successive metal layers).

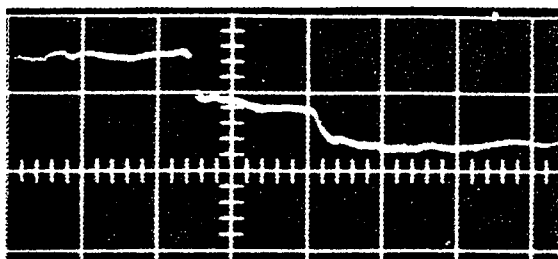


Fig. 8 - Experimental record on Fig. 7 configuration, horizontal $0.5 \mu\text{s}/\text{div.}$, vertical $100 \text{ mV}/\text{div.}$ Pressure: 1160 kilobars on the 1st junction.

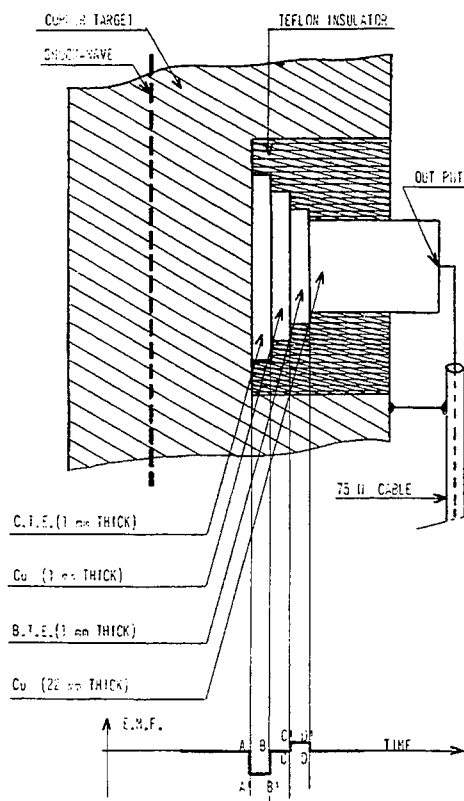


Fig. 9 - Multiple series connected metals (upper part) and expected waveform (lower part)

A very suggestive experiment has been done on a stack of thin metallic plates of the following metals (in the order of the shock passage) copper-constantan-copper-chromel.

Figure 9 describes the setup used and the shape of the expected waveform AA'B'BCC'D'D

(account taken of the results obtained elsewhere from the couple constantan/copper and chromel/copper).

The oscillogram obtained is given in Fig. 10. One sees that it reproduces rather faithfully the expected theoretical form. The droop observed on the section AA'B'B can be explained by a decrease of the pressure at the first junction when the shock reaches the second. The near equality (in voltage) of the segments AA'BB' on the oscillogram confirms this explanation.

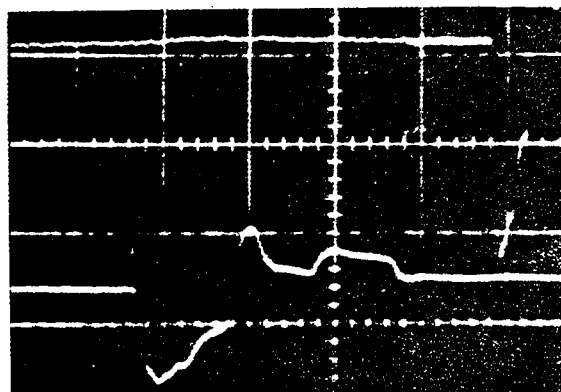


Fig. 10 - Experimental record with Fig. 9 configuration. Upper trace horizontal $0.5 \mu\text{s}/\text{div.}$, vertical $20 \text{ mV}/\text{div.}$ Lower trace horizontal $0.2 \mu\text{s}/\text{div.}$, vertical $50 \text{ mV}/\text{div.}$ Pressure: 180 kilobars on the 1st junction.

Polarity of the Junctions

A certain number of metals have been tried two by two. We have found the following metals negative with reference to the copper: aluminum, constantan, and nickel, and with reference to iron: constantan, nickel. On the other hand the alloy B.T.E. (chromel) has been found positive with reference to iron.

These results agree with usual thermoelectric polarities, with the assumption that the junction under shock pressure is considered as the hot one.

PECULIAR FEATURES OF THE PHENOMENON

The study by the analogies which we carried out has lead us to establish, nevertheless, certain definite characteristics of the phenomenon; a voltage-pressure relation; an abnormal amplitude of the signals; and the time of response of the junctions.

Voltage-Pressure Relation

A systematic study has been made on the couple constantan/copper. The very close impedance of the two metals permits adoption for the pressure at the junction that exists in copper: the error thus made is less than 2% between 200 and 1200 kilobars.

The voltage considered is the peak voltage obtained upon passage of the shock front across the junction. The junctions were placed on the back side of the target of copper so as to allow a simultaneous measurement of the pressure from the measurement of the free surface velocity.

Depending on the pressure desired, the shock wave was obtained either by direct contact, explosive on metal, or by means of a shock-driver, generally of copper, of variable thickness. The explosive was lit by a plane wave generator. The region of pressures explored extended as high as 1600 kilobars approximately. The results obtained are reproduced in Fig. 13. Taking account of the spread of the experimental points ($\pm 10\%$) the average curve can be a straight line.

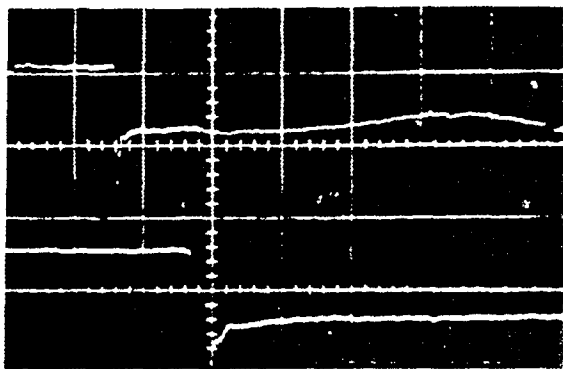


Fig. 11 - Typical record from C.T.E./Cu junction on free surface. Upper beam horizontal $1 \mu\text{s}/\text{div.}$, vertical $20 \text{ mV}/\text{div.}$ Lower beam horizontal $0.2 \mu\text{s}/\text{div.}$, vertical $20 \text{ mV}/\text{div.}$ Lower beam $2.6 \mu\text{s}$ delayed on upper beam. Pressure: 180 kilobars.

Abnormal Amplitude

One can estimate the thermal electric voltages which would appear from static compression at the pressures and temperatures prevailing in the shock wave. The calculation has been made and these results are indicated in Table 1.

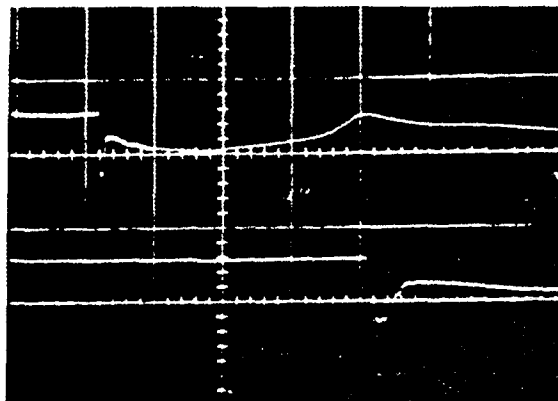


Fig. 12 - Typical record from a C.T.E. pin (Teflon insulator). Upper beam horizontal $1 \mu\text{s}/\text{div.}$, vertical $50 \text{ mV}/\text{div.}$ Lower beam horizontal $0.2 \mu\text{s}/\text{div.}$, vertical $50 \text{ mV}/\text{div.}$ Lower beam $1.8 \mu\text{s}$ delayed on upper beam. Pressure: 180 kilobars.

We have taken into consideration the influence of the pressure on the thermal electric power, but the corrections, after Bundy [5], are only known up to 70 kb. In spite of this, we have listed, on Table 1, the effect of this correction. The reference temperature has been taken at 20°C and the temperature in the shock wave is that given by R. G. McQueen and F. D. Marsh [6].

The dynamic voltages are clearly higher than those expected on the basis of the static thermoelectric properties of the couple copper/constantan. Ilyukhin and Kologrivov [3] have arrived at the same conclusion of the couple copper/nickel.

It is seen that the correction estimated from the static effect has the opposite sense to the effect observed here. The observed voltages are higher in absolute value than those expected without correction.

Inertia of the Phenomenon

If the phenomenon takes place at the interface of the two metals, as the collection of results obtained leads one to think, its response time must be extremely small and should allow for the internal exploration of the shock wave. It seems that we have not yet effectively attained the time of rise of the phenomenon itself. Two opposing effects intervene:

1. The curvature of the shock wave which is never ideally plane. The junction as a result is not hit simultaneously on all points. One can

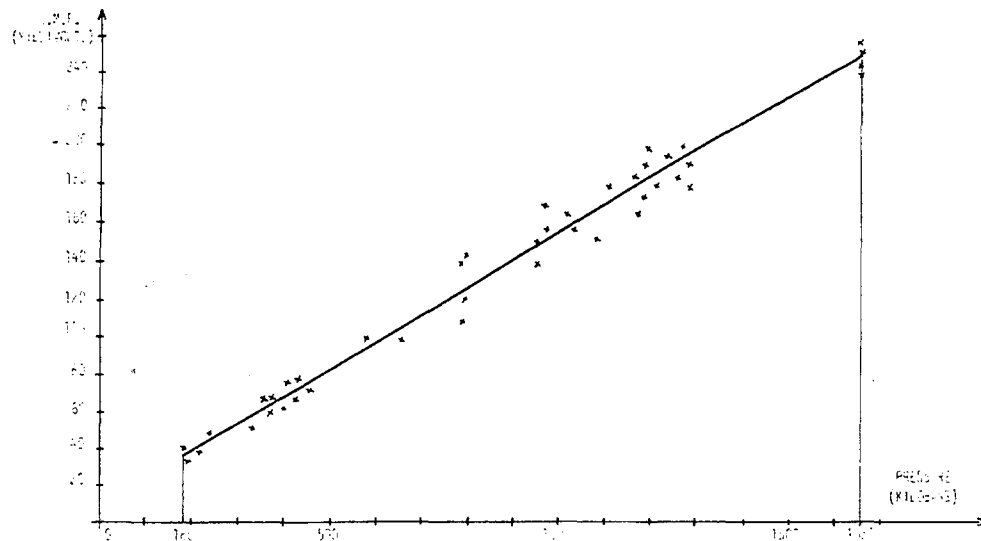


Fig. 13 - Experimental curve. C.T.E./Cu junction E.M.E. vs shock-pressure. Experimental dispersion: $\pm 10\%$.

TABLE 1
Comparative emf Obtained by Static (Thermoelectric) and Dynamic Loading of C.T.E./Cu Junction at the Same Temperature
(The Static Pressure Correction is Roughly Extrapolated from Bundy's Results)

Pressure (Kilobars)	100	200	300	400	500
Calculated Temperature	63°C	121°C	201°C	311°C	446°C
Static Thermocouple emf (Millivolts Ref: 20 °C)	2	4.4	8.5	14.8	22.7
Pressure Correction (Millivolts 0.25 mV/100 Kb/100 °C)	-0.12	-0.5	-1.8	-3	-5.3
Resultant emf (Millivolts)	1.88	3.9	6.7	11.8	17.4
Dynamic emf (Millivolts)	30	45	60	73	87

reduce the consequences of this fault by diminishing the surface of the junction.

2. The difficulties which arise on the use of junctions of small surface area from the fact that lateral rarefactions develop in contact with isolating material of low acoustic impedance.

By making compromises, and by special study of the form of the junctions, we have been able to record some rise times of 25 to 30 nanoseconds. It does not seem that we have attained the limit of the phenomenon itself (see oscillograms Figs. 11 and 12).

Trials on Different Metals

We have already indicated the correct polarity of the signals obtained with the different metallic couples. The voltages obtained at different pressures are reported in Table 2. The indicated pressures are the pressures incident, that is to say the pressures in the target metal, (copper or iron). One will equally find complementary results concerning the couples B.T.E./copper, zinc/copper and bismuth/copper, which call for the following remarks:

The couple B.T.E./copper gives a voltage nearly zero at 1100 kb in spite of a notable static

TABLE 2
Experimental emf from Different Metals (Millivolts)

Incident Pressure (Kilobars)		100	130	150	180	360	400	1160
Tested Metal	Reference Metal							
Constantan	Copper	-30		-36	-43		-73	-180
Aluminum	Copper			-10				
Nickel	Copper						-35	-90
Bismuth	Copper				+11		-100	-170
Chromel (B.T.E.)	Copper				+10			0
Zinc	Copper							-90
Constantan	Iron	-35	-50			-500		
Chromel (B.T.E.)	Iron		+20					

thermoelectric power. It gives a small positive voltage at 180 kb.

The couple zinc/copper for which the static thermoelectric power is extremely small, gives by contrast a notable negative voltage at 1100 kb.

For the couple bismuth/copper (negative static thermoelectric power) one obtains a negative signal and very weak for 100 kb, positive and weak for 180 kb, and again negative but with a strong amplitude at 1160 kb.

This behavior is not too astonishing if one considers the numerous phase changes exhibited by bismuth, and, for this reason the result is not in contradiction with a thermoelectric origin.

The results found on the couple nickel/copper coincide with those obtained by Ilyukhin and Kologrivov.

POSSIBLE THEORETICAL APPROACHES

Being given the analogy of the phenomenon with the Seebeck effect one can think of studying it in the framework of the theory of transport phenomena.

Application of Transport Theory

If one "expands" the gage submitted to shock, as represented in Fig. 1, one obtains the metallic chain of Fig. 14. We will call x the thickness of the copper traversed by the shock before the wave front reaches the interface of the constantan/copper situated at D' . The shock develops from the instant $t = 0$ at O towards

the left and the right in Fig. 14 with the speeds D_i which depends on the medium.

At an instant, t , the thermodynamic state behind the shock front is determined by the knowledge of one of the three variables P (pressure), T (temperature), v (specific volume). Experimentally, one measures the voltage $V_b - V_a$ between a and b ends of the chain.

At this instant, the shock is at C and D and there exists in the medium between these points a temperature gradient: $\partial T / \partial x$ and an electron thermodynamic potential gradient: $\partial W_F / \partial x$ where W_F is the Fermi level of the electron gas. At zero current, we know that there exists in all points of the metal a "fictitious" field given by classical theory [7].

$$E_x = S \partial T / \partial x + (1/e) (\partial W_F / \partial x)$$

where S is the thermal electric power of the metal and e the negative charge of the electron.

Following Ziman [7], the effective electric field observed is:

$$E'_x = E_x - \frac{1}{e} \frac{\partial W_F}{\partial x}$$

The difference of measured potential is equal, therefore, to:

$$V_B - V_A = \int_A^B E'_x dx$$

The gradient of temperature is zero between A and C and between D and B . Two cases must be considered according to whether or not the wave reaches the interface D' copper/constantan, that is to say, has passed or not passed the points D' and C' .

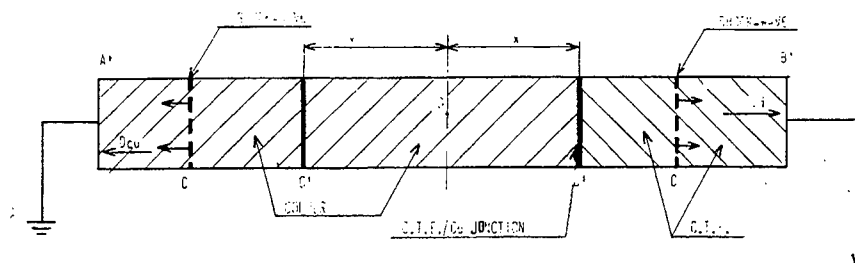


Fig. 14 - Developed metallic chain

If the wave has not reached C' and D', ($V_B - V_A$) is 0 by symmetry. If the wave has gone beyond C' and D' the difference of potential reduces to:

$$V_B - V_A = \int_{C'}^C S \left(\frac{\partial T}{\partial x} \right)_{cu} dx - \int_{D'}^D S \left(\frac{\partial T}{\partial x} \right)_{C.T.E.} dx.$$

If one supposes that the position of the wave is such that the pressure maximum is at D' (therefore equally at C') the preceding expression must give the value of the voltage at the observed crest on the recorded waveforms.

This expression describes an effect purely thermoelectric. The numerical exploitation of this expression involves the calculation of S as a function of pressure. In effect S is given [7] by:

$$S = (\pi^2 K^2 T / 3e) (\partial \log \sigma / \partial W)_{W=F}$$

where σ is the electric conductivity of the metal and K the Boltzman constant. S depends, therefore, in a very sensitive way on the deformation of the Fermi surface under pressure.

The static study for the voltage ($V_B - V_A$) is expressed in fact in Table 1 for the couple copper/constantan. One has seen that the voltages obtained under shock are very high, by comparison, and the difference is in an inverse sense to the correction that would come from the predicted static correction.

One should note that, for iron, the compression under shock tends to increase the resistivity [8] while a static compression diminishes it [9]. We are therefore lead to conclude: (1) Either the thermoelectric effect is modified and amplified by the dynamic effect of the shock or its anisotropy, or (2) The local effect of

temperature is higher than that calculated on the basis of thermodynamic equilibrium, or (3) The effect entering into play is of a different nature than the thermoelectrical effect.

Electronic Temperature

The temperature deduced by a thermoelectric measurement is rigorously that of the electronic gas. The weak inertia of this gas as compared to that of the crystalline lattice can allow it to acquire, under a shock, an activation energy corresponding to an electronic temperature very high relative to that of the lattice as given by the results of McQueen and Marsh [6].

Therefore with a Maxwell gas, weakly ionized, in an electric field E constant within the time of electronic relaxation τ , one can calculate the difference of the temperatures $T_e - T_r$ of the electrons and of the lattice:

$$T_e - T_r = 1/3 e^2 E^2 \tau^2 M / K m$$

where e and m are charge and mass of the electron; M is the mass of the ions of the lattice.

Utilizing the experimental results on the basis of this interpretation one can evaluate the electric field E. At 150 kb for example, for a junction constantan/copper, one can translate into temperature with the usual tables the emf of 35 millivolts measured. One obtains: $t_E = 660^\circ$. The thermodynamic temperature being taken as that of the lattice is known [5] and is equal to 160°C , whence the value of the field: $E = 9 \times 10^4$ volt/meter.

One will note that this field is around 10^5 times weaker than that of the coulomb attraction between two neighboring atoms of copper. One can see the origin of such a field in the abrupt setting in motion of the ions at the sites

of the lattice under the influence of the shock wave. Such a process would be particularly capable of explaining a voltage peak often observed at the arrival of the shock at the interface.

"Phonon-Drag" Effect

According to Rodionov [10,11] the thermoelectric effect due to the "phonon drag" [7] may become important under high pressures, taking account of an increase of the Debye temperature. Although the Debye temperature does, in fact, increase with pressure the shock conditions are such that the temperature of the lattice remains well above that of the Debye θ in spite of the influence of the pressure. It seems, therefore, that one cannot make use of this phenomena to interpret our results; however, we felt it necessary to take note of this argument.

Deformation of the Fermi Surface

A knowledge of the Fermi surface is essential to the study of transport properties in metals. One has seen its role in the expression for the thermal electric power. Under static pressures J. J. Dugdal and J. N. Mundy [12] made use of the deformation of the surface to try to interpret the variation of thermoelectric power. In a compression by a shock wave one can separate two effects of pressure on the Fermi surface; the one of static character through the intermediary of the variation of the crystalline parameter (local anisotropic variation) which modifies the Brillouin zones and the energy bands of the metal; the other of dynamic character through the intermediary of electrons having energies near those of the Fermi level w_F , being activated in the shock by interaction with the ions of the lattice.

UTILIZATION AS A TRANSDUCER

Utilization of this effect to make a pressure transducer for shock measurement is particularly attractive for the following reasons.

1. The zone of measure can be as small as one desires since it can be reduced in thickness to the theoretical zero thickness of the junction.

2. The transducer can be an intimate part of the material submitted to the shock if the metal to be studied is of suitable nature.

3. The structure of the transducer is particularly simple and, subject to the restriction of using an isolating material adopted in acoustic impedance to the metal in the couple, this transducer would produce a minimum perturbation upon the phenomena being studied.

4. The problems of electric insulation are always very difficult to resolve in the case of very strong shocks. Without misjudging that there is a research problem with regard to insulation, one can note that in the present case its solution is facilitated by the simplicity of the structure of the junctions and especially by the fact that it requires only a very mediocre insulator under shock-pressure because the internal electrical impedance of the junction is so low.

Construction of a Transducer

The development of transducers has, at present, been based solely on the use of the couple constantan/copper. Teflon has been the insulating material most often used; but its low acoustic impedance allows it to be distorted more easily than the junction metals under the influence of the shock wave. The junction, for this reason, considerably spreads while the shock wave progresses in the target, and one cannot obtain the profile of the shock wave behind the front; most often the electrical signal appears as a plateau. Better results have been obtained with ceramics of dense metal oxides; unfortunately, these latter are much more difficult to fabricate. A model of a coaxial transducer is shown in Fig. 15.

Recording of Double Shocks

The response of junctions on a shock front has been studied in adequate detail, as one has seen previously. On the other hand, the form of the signal behind the rise front seems to be much more sensitive to the technology of the transducers. In order to test different types of transducers, we have used the setup shown in Fig. 16. The "shock driver" of 24 ST aluminum is projected at a higher velocity than the "shock driver" of copper. The first induces, therefore, in the copper target, a first shock relatively weak (around 400 kb). The second arrives a fraction of a microsecond later and induces a much more intense shock (of the order of 800 kb). At two and five mm from the point of impact of the target the two shock fronts are clearly separated. At 10 mm from the point of impact of the target the second shock, which

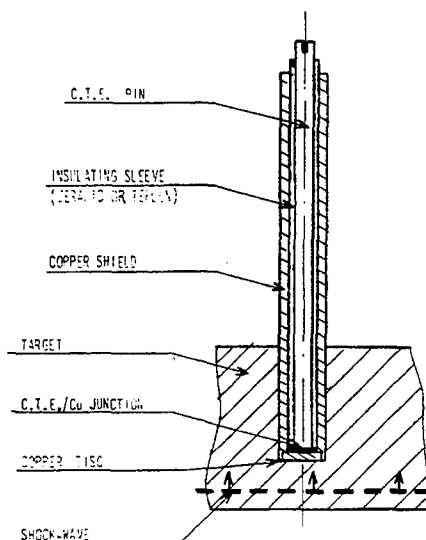


Fig. 15 - Typical coaxial C.T.E./Cu transducer

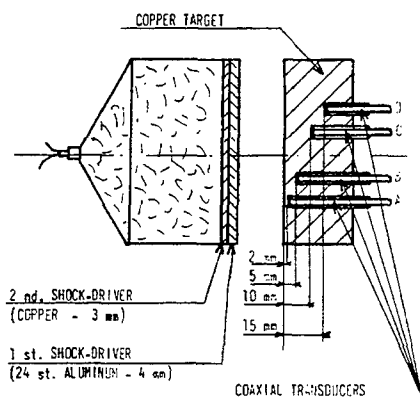


Fig. 16 - Double shock-driver configuration

moves more quickly than the first, has partially overtaken it. At 15 mm it has totally overtaken the first shock and one only distinguishes a single shock. (All distances are given in Lagrange coordinates.) The transducers are insulated with the aid of a ceramic of high density. The oscillograms obtained are shown in Fig. 17. One will note that the amplitude of the second rise front is much weaker than the amplitude of the first, even though they should be approximately equal. This can be attributed to a partial deterioration of the insulating properties of the ceramic due to the first shock.



Fig. 17 - Experimental records on Fig. 16 configuration. From upper to lower trace:

- A transducer--distance - 2mm
- B transducer--distance - 5mm
- C transducer--distance - 10mm
- D transducer--distance - 15mm

For all traces, horizontal $0.5 \mu\text{s}/\text{div.}$, vertical $100 \text{ mV}/\text{div.}$ Pressures: 400 and 800 kilobars.

CONCLUSION

These preliminary results concerning the bi-metal junctions submitted to shock waves seem promising. The remaining work to be carried out from the points of view of theory, experiment, and technology is considerable. But aside from the possibility, already very interesting in itself, of perfecting a sensor of shock pressure, this phenomenon seems able to be useful for more fundamental research on the physics of shocked solids. It should permit, for cross-checking of theoretical studies and experimental results, acquisition of valuable information about the alteration of Fermi surfaces and Brillouin zones in metallic crystals subjected to strong shock waves.

Besides, one may hope, by improving junctions technology, to get some knowledge of the intimate structure of the shock-front itself from detailed studies on the rise front of the electrical waveforms.

REFERENCES

1. J. Jacquesson, Analyse des contraintes. Bulletin du G.A.M.A.C. - IV,4,33 - 1959.
2. J. Jacquesson, Colloque international sur les ondes de détonation. Edit. C.N.R.S. Paris - 1962 - p. 415.
3. U. S. Ilyukhin and V. N. Kologrivov, Zhur. Fiz. n°5 - Sept.-Oct. 1962.
4. E. P. Palmer and G. H. Turner, J. Appl. Phys. - 35 - 3055 (1964).
5. F. P. Bundy, J. Appl. Phys. - 32 - 483 (1961).
6. R. G. McQueen and S. P. Marsh, J. Appl. Phys. - 31 - 1253 (1960).
7. Ziman, Electrons and Phonons. Oxford - 1963.
8. P. J. A. Fuller and J. N. Price, Nature - 193 - 262 (1962).
9. A. S. Balchan and H. G. Drickamer, Proc. Scient, Instruments - 32 - 308 (1961).
10. Rodionov, Zhur. teckn. Fiz. - 26 - 375 (1956).
11. Rodionov, Trud. Inst. Fiz. Metal. - 20 - 273 (1958).
12. J. J. Dugdal and J. N. Mundy, Phil. Mag. - 6 - 1463 (1961).

PHERMEX APPLICATIONS TO STUDIES OF DETONATION WAVES AND SHOCK WAVES

Douglas Venable and T. J. Boyd, Jr.
*Los Alamos Scientific Laboratory, University of California
Los Alamos, New Mexico*

ABSTRACT

A 20-MeV, high intensity, high current, flash radiographic machine, PHERMEX, has been built to complement other hydrodynamics facilities of the Los Alamos Scientific Laboratory. In many experimental situations, observations of hydrodynamic phenomena may be obtained by means of techniques unique to flash radiography. This device is used primarily to implement studies in areas related to detonation and shock waves, jet formation and the interaction of jets with matter, spalling and cratering. In certain simple geometries, shock wave and rarefaction wave velocities, particle velocities, and time variation of both edge positions and mass density distributions can be obtained. This facility and the choice of its design parameters are discussed. Radiographs illustrating typical experiments are included. Results of several experiments, germane to this symposium are presented; these include measurements of the Hugoniot pressure at zero particle velocity, and the particle velocity and sound speed behind a detonation wave in solid explosives.

INTRODUCTION

For many years flash radiography has provided and continues to provide an elegant technique for observing high-speed hydrodynamic phenomena [1-18] associated with shock and detonation waves. Although many other methods are used to acquire information relative to these same phenomena, flash radiography is one of very few schemes that offers direct observations. Until recently only modest flash radiographic facilities existed. Commercially available equipment, as well as the state of the art, still impose rather severe constraints upon both techniques and apparatus. When utilizing conventional flash radiographic equipment, the choice of object size may be dictated not by what is optimum hydrodynamically, but rather overwhelmingly by the penetration capability of available radiation flux consistent with blast protection. Often this choice is not consistent with acquiring the most precise information.

Precision radiography requires accurate resolution of edges and discontinuities as well as accurate resolution of mass density distributions. Precision is degraded by many things but especially by scattered radiation. In this

sense scattered radiation, which increases with object thickness, can serve to establish a practical upper limit of object thickness which can be radiographed usefully. Results of both theoretical and experimental studies at Los Alamos [19] clearly demonstrated that precision determination of mass distributions in very thick sections, even greater than ten mean-free-paths thick, is not only physically feasible with adequate flux but also practical with a variety of object configurations provided careful control is exercised over alignment, penumbra effects, geometric symmetry, scattered radiation, detector latitude [20], calibration techniques, and the host of other problems which are ever present. This study also demonstrated the feasibility of constructing an electron accelerator capable of performing tasks of interest to the Los Alamos Scientific Laboratory. Indeed, such a device was considered practical as early as 1952 utilizing techniques and commercially available apparatus which existed then. However, this project formally began with the initiation of detailed design and construction in 1957 at which time both techniques and equipment had matured vastly, resulting in a far superior flash radiographic facility than could have been constructed in 1952.

PHERMEX is capable of performing precision flash radiography in objects about four mean-free-paths thick when using conventional film techniques and about ten mean-free-paths when using electronic detectors.

Although there has been significant advancement in the production of intense sources of x-rays, almost insignificant progress has been achieved in the techniques of precise data acquisition in this field. The great increase of useful radiation flux has only made the application of photographic processes, i.e., film blackening techniques, somewhat less unpalatable.

PHERMEX CHARACTERISTICS

In flash radiographic studies of explosives and explosive-driven systems there are two significantly important aspects. One of these is the precise location of edges as well as hydrodynamic discontinuities; the other is the statistically significant measurement of areal distributions of mass density. Areal density is defined here as the integral of the mass density taken over the rectilinear path followed by the primary radiation traversing the object. It is this function which radiography is so well suited to determine. These two aspects are not mutually exclusive; both demand high radiation intensity, considerable total flux and a small but finite size radiation source. Therefore the choice of optimum x-ray machine characteristics needed for a given class of problems requires consideration of radiation production efficiency, absorption statistics, detector efficiency and latitude, total flux, as well as radiation intensity, and the spatial distribution of the useful portion of the radiation field. A detailed study of these parameters was made with respect to experiments of general interest to this laboratory [21]. It was demonstrated that for many experiments an acceptable radiation flux was equivalent to that generated by 5 to 10 μC of 20-MeV electrons providing they were delivered to a 3-mm diameter tungsten target for 0.2 to 0.1 μsec or less.

When this project formally started, the most attractive device for this service was the standing wave linear accelerator [22-24]. This same situation is still true today. The PHERMEX accelerator system consists of three cylindrical copper-lined cavities operating at 50 Mc/sec in the TM_{010} mode. Physically each cavity is about 4.6 meters in diameter and about 2.6 meters long. Each contributes about 7 MeV to the injected electrons. Although the present ejected current is about 70 A, averaged over 0.1- or 0.2- μsec pulses, only a fraction of these

electrons are useful in that one-fourth to one-third have momenta components which, upon striking a tungsten target, can produce radiation within a useful spectral range and spatial distribution.

Finally the electron beam is focused upon a 3-mm diameter aperture in a thick beryllium collimator. After emerging from this collimator, the beam passes through a 0.5-mm thick beryllium window and falls on a 1-mm thick tungsten target. Target currents greater than 20 A at about 20 MeV now provide fluxes of about 10 roentgen per 0.2- μsec pulse or 5 roentgen per 0.1- μsec pulse measured on-axis at 1 meter from the target. Because of the nature of this accelerator, a 0.2- μsec pulse of gamma rays consists of 10 sub-bursts, each about 6-nsec long. The average dose rate during a pulse is 50 r/ μsec . Considering a bremsstrahlung production efficiency in the tungsten target of say 42 percent, gamma radiation is produced at an average rate of about 170 MW for 0.2 μsec whereas the on-axis intensity at 1 meter is several megawatts per square centimeter.

PHERMEX is illustrated by the line drawing in Fig. 1. Here the course of the electron beam can be traced from the thermionic cathode in the electron gun to the radiation generating target. The physical layout of the PHERMEX complex was dictated primarily by its reinforced concrete housing which provides necessary protection from blast and shrapnel. Indeed, this is one reason why the ejected electrons are piped about 10 meters to the target located outside of the blast-proof bunker.

The present capability of PHERMEX has been expressed in terms of its beam energy, radiation flux output, pulse length, and spot size. It should be mentioned in passing that a program aimed at virtually doubling the radiation intensity and increasing the beam energy to about 25 MeV is nearing completion. This should greatly enhance the radiographic capability of the machine.

ARRANGEMENTS AND PROCEDURES FOR EXPLOSIVE EXPERIMENTS

Figure 2 represents schematically a radiographic geometry used for many of the explosive experiments reviewed below. Target protection is also shown in this illustration. Data are recorded on photographic film which must be protected from blast damage. The photograph in Fig. 3 is an illustration of the type of blast-proof cassette that is used most often. The

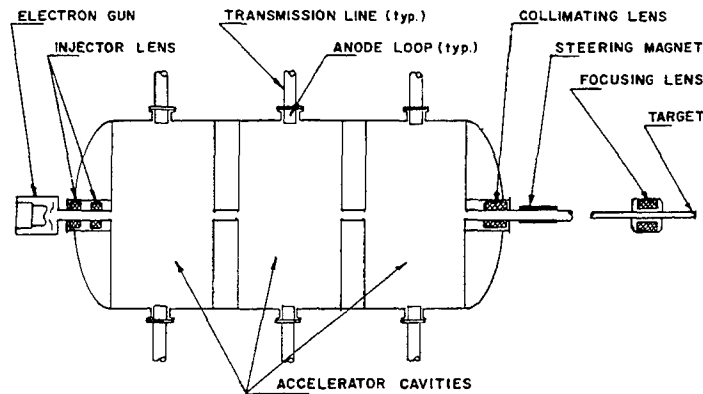


Fig. 1 - Schematic diagram of PHERMEX

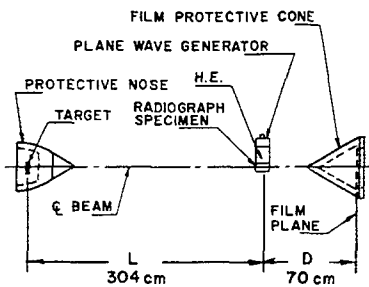


Fig. 2 - Experimental geometry

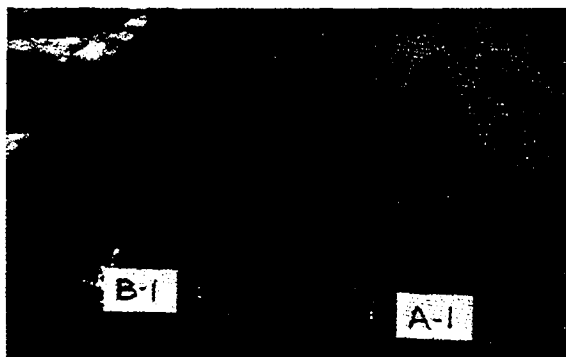


Fig. 3 - Blast proof cassettes. Typical damage is shown

hollow aluminum cone is capable of protecting a 35.5-cm diameter film from the ravages of about 20 kg of high explosive located with the film plane as close as 70 cm from the charge center. Experience has demonstrated that film can be protected even less expensively by using thick plates of duraluminum; indeed other

workers have found this method satisfactory for their specific applications. However, scattered radiation which reaches the film from such an array effects a significant loss of radiographic resolution. As a result of this attendant degradation of information the conical aluminum cassettes, developed at Los Alamos, are preferred.

Because of the extreme latitude of the transmitted radiation intensity that is encountered in some experiments, several film-screen combinations may be used in one cassette. For example, with the typical geometry shown in Fig. 2, useful film blackening has been realized for x-ray flux transmission ranging from 10^{-3} to almost unity. Typical film-screen combinations could include three films: one Kodak KK film intensified with two 1-mm thick lead screens, one Kodak KK film intensified by one 1-mm thick lead screen, and one Kodak AA film intensified with two 1-mm thick lead screens. In those experiments having adequate flux, wherein transmission is bound within a small range of latitude, one type KK film with lead screens is often adequate. Where greater sensitivity is required, type F films, intensified by tungstate screens, are used.

Although high-speed electronic detectors, about 10^3 times more sensitive than the fastest film-screen combination, have been developed for special radiographic experiments, these involve only standard electronic techniques, hence they will not be discussed. In general, mass distribution measurements are obtained from film by means of existing well known photometric techniques supported by appropriate film calibration. In spite of the fact that recent radiation detection schemes, such as thermoluminescent devices, have extended detector latitude by several orders of magnitude, the best known

method of measuring radiation flux for flash radiographic applications is still conventional industrial photometry.

TYPICAL EXPERIMENTS

Among the experiments that are reported below there are several that pertain to measurements of the Chapman-Jouguet particle velocity and sound speed and one that is concerned with an examination of the polytropic equation of state for reaction products of condensed explosives. Other experiments are discussed to indicate the scope of parameters that can be investigated by flash radiographic techniques.

By embedding a series of foils at precisely known initial positions in an explosive to be studied and allowing the detonation wave to sweep by these foils, a flash radiograph, appropriately timed, permits a study of foil displacement as a function of time. This displacement can in turn be related to the particle velocity behind the front by the theory being examined. The quality of fit of these data thus provides the means of testing the applicability of the theoretical model. One model is in rather good agreement with experiment. Such a model assumes plane wave motion, that mass and momentum are conserved, and that the Chapman-Jouguet condition is satisfied. A polytropic equation of state, $P = K\rho^\gamma$, is assumed to describe the adiabatic relation at any point behind the front [25]. The K and γ are taken to be constant throughout the region of interest. Analysis of this model leads to a linear relationship between the instantaneous position of each foil as normalized to the position of the detonation front and the particle velocity at the foil position as normalized to the Chapman-Jouguet particle velocity.

Figure 4 illustrates such an experiment. A 10-cm cube of Composition B was initiated by a plane wave generator. Eight foils of 2.5×10^{-3} cm thick tantalum were embedded in the HE. Another was placed on the surface and the assembly was then capped with two 0.635-cm thick slabs of Lucite, with the tenth foil sandwiched between them to serve as a position fiducial. When the detonation wave had proceeded to a point roughly midway between the eighth and ninth foils, the radiograph was taken. The resultant data are shown in Fig. 5. Circles represent experimental points — one for each of the eight foils acted upon by the detonation. The solid line is derived from the polytropic equation of state [25]. The dashed line is of interest inasmuch as it originates from use of the Becker-Kistiakowsky-Wilson equation of state in a one-dimensional hydrodynamic calculation [26].

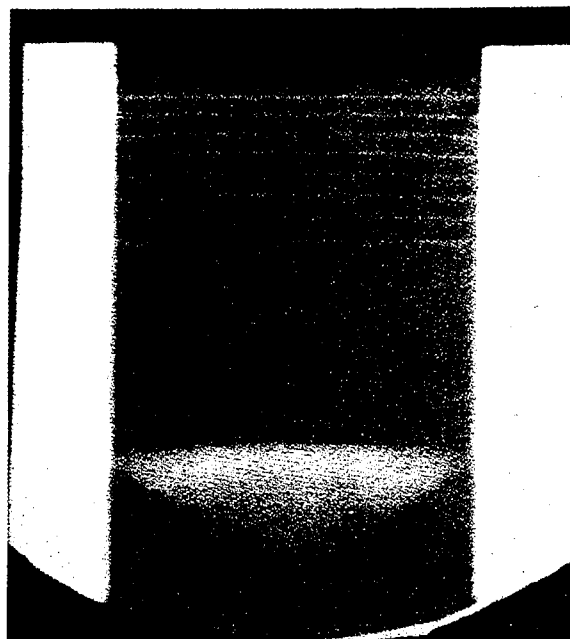


Fig. 4 - Dynamic radiograph of foils embedded in high explosive

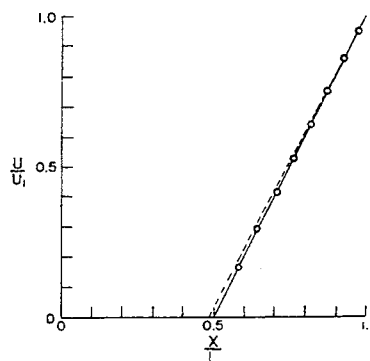


Fig. 5 - Foil experiment data

These data can also be used to determine that value of the C-J particle velocity which satisfies the assumed model. A weighted average of the velocity data gives a value for the C-J particle velocity of $0.208 \text{ cm}/\mu\text{sec}$. No error is assignable until an error analysis of the overall experiment has been performed.

The foregoing discussion of the hydrodynamic model of a detonation wave leads naturally into the second experiment in which the sound speed behind a plane detonation wave was determined. When a detonation wave strikes a

free-surface of explosive, a rarefaction wave is born and immediately proceeds into the explosive reaction products. With a sufficiently high degree of reproducibility of explosive systems, the progress of such a rarefaction wave can be followed by means of radiographs of successive shots. A radiograph of such a rarefaction wave is seen in Fig. 6. This was formed when a plane detonation wave in Composition B impinged normally upon a planar free-surface. Here the free-surface expanded into a vacuum to eliminate the complications of shock waves in air.

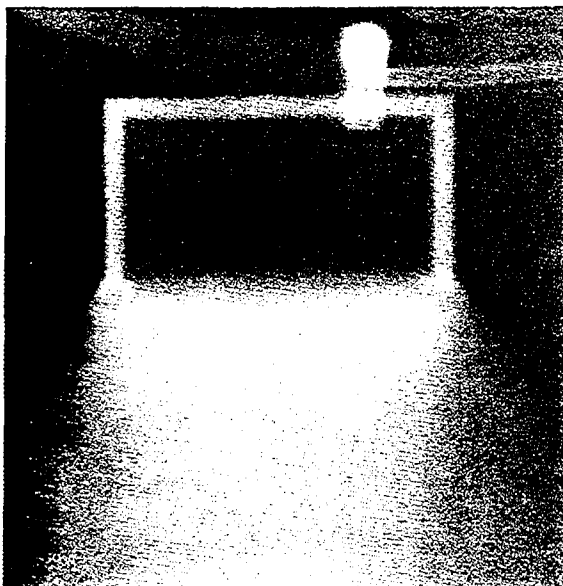


Fig. 6 - Radiograph of rarefaction wave

The slope of the space-time history of this wave, taken at the instant the detonation wave struck the free-surface, provides a measure of the rarefaction wave velocity, u_r . With an independent measure of the Chapman-Jouguet particle velocity, u_1 , the sound speed is simply $c_1 = u_1 + u_r$, when accounting for the relative direction of the rarefaction wave and the particle flow.

This work is still in progress and, as yet, there is insufficient evidence to establish the ultimate precision with which the Chapman-Jouguet sound speed can be determined by this technique. So far, preliminary data, without an error estimate, show a sound speed value of about 0.578 cm/ μ sec in Composition B.

A third experiment was performed to determine the zero-particle-velocity Hugoniot pressure [27]. This involved observing the speed of the reflected shock waves U_2 which arise from the normal collision of two identical plane detonation waves of speed D . The ratio of the pressure behind the shock wave, P_2 , to the C-J pressure, P_1 , is given by the equations of conservation of mass and momentum

$$\frac{P_2}{P_1} = \Pi_{21} = \frac{D + U_2}{D - U_1} \quad (1)$$

If D and u_1 are already known then a measure of U_2 provides the missing piece of information. Equation (1) can be further modified if one invokes the Chapman-Jouguet hypothesis and assumes a constant gamma polytropic equation of state for the detonation reaction products. Thus

$$\Pi_{21} = \frac{\gamma_1 + 1}{\gamma_1} \left(1 + \frac{U_2}{D} \right) \quad (2)$$

Using the value of $\gamma_1 = 2.767 \pm 0.035$ given by Deal [28] for Composition B and the measured values of U_2 and D of 0.575 cm/ μ sec and 0.795 cm/ μ sec respectively, the pressure ratio is 2.345. The error in the ratio U_2/D is about 1%. The data from which U_2 was determined are shown in Fig. 7 in a space-time plot, and a typical radiograph of reflected shock waves in Composition B may be seen in Fig. 8.

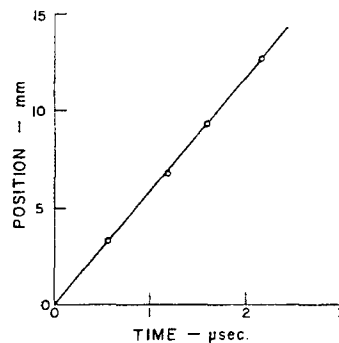


Fig. 7 - X-T plot of reflected shock wave

A bit more information might be inferred from these same values of U_2 and D . If one uses the equations of conservation of mass, momentum, and energy, assumes a constant gamma polytropic equation of state for the gases, and invokes the Chapman-Jouguet

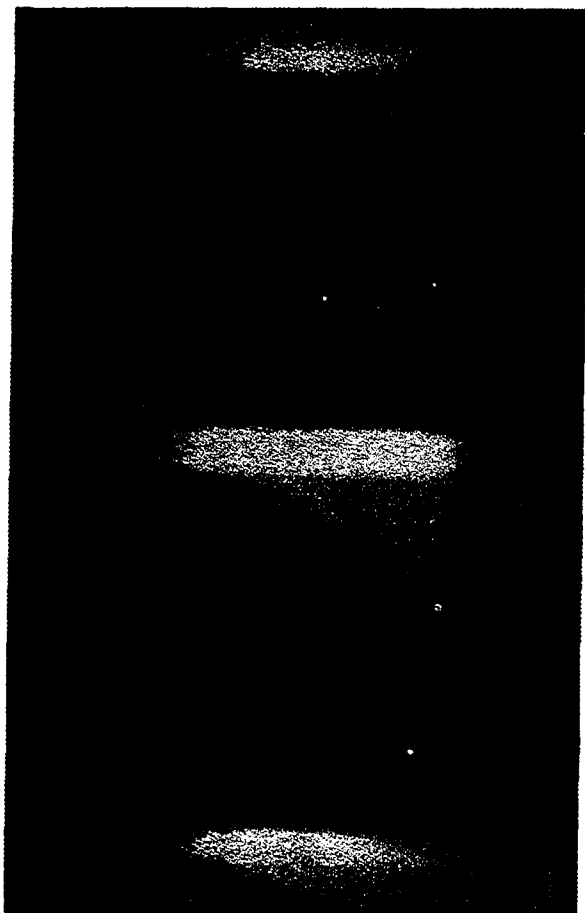


Fig. 8 - Reflected shock waves arising from two colliding detonation waves

hypothesis, then the velocity ratio, U_2/D , can be described by a function of gamma only. Indeed, if γ_1 and γ_2 represent respectively the gas ahead of and the gas behind the reflected shock, the pressure ratio across the reflected shock can be expressed as

$$\Pi_{21} = \frac{A}{2} \left[1 + \sqrt{1 - 2A^2 \left(\frac{\gamma_2 - 1}{\gamma_1} \right) \left(\frac{\gamma_1 + 1}{\gamma_1 - 1} \right)} \right] \quad (3)$$

where

$$A = \frac{2\gamma_1 + \gamma_2 + 1}{2\gamma_1} + \frac{\gamma_2 - 1}{\gamma_1 - 1}$$

Thus

$$\frac{U_2}{D} = \frac{\gamma_1 \Pi_{21}}{\gamma_1 + 1} - 1 \quad (4)$$

Equation (3) obviously implies a double gamma Hugoniot equation. However, if a single polytropic equation were to be used with $\gamma_1 = \gamma_2 = \gamma$, then the experimentally measured ratio of U_2/D implies $\gamma_2 = 2.514 \pm 0.045$ for the gases behind reflected shock. On the other hand, if $\gamma_1 = 2.769$ as reported in Ref. [28] then $\gamma_2 = 2.692$ from Eq. (4). Furthermore, the pressure ratio as given by Eq. (2) remains unchanged since the gamma in that equation is always γ_1 .

This experiment may appear to question the validity of the constant gamma polytropic equation of state for the reaction products of solid explosives. However, inconsistency of data, small aplanarities of the detonation waves and even deviation from the Chapman-Jouguet hypothesis [29] could provide comparable results. Much more extensive work is needed to uniquely clarify some of these issues.

Figures 9 and 10 illustrate the development of a Munroe jet which is formed in a flat-bottomed rectangular cross section groove in Composition B. The first of these radiographs indicates an early state in the growth process. The second shows the equilibrium form of the jet. Over a rather wide range of parameters the transient shape of this jet scales with the ratio of detonation wave excursion from the groove bottom to the width of the groove.

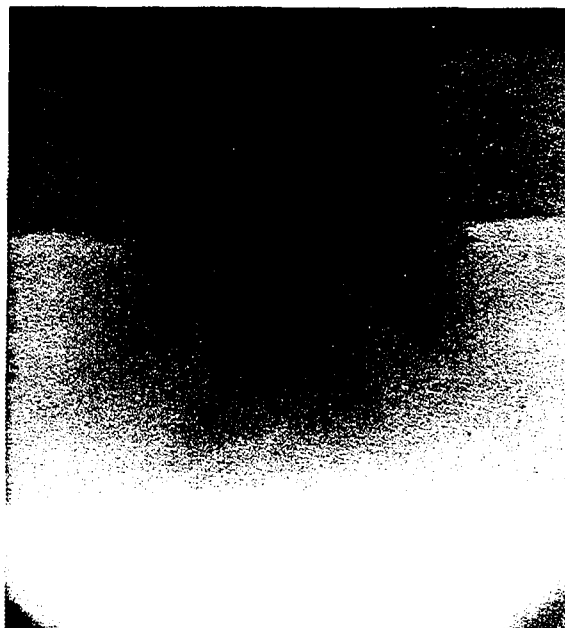


Fig. 9 - Formation of a Munroe jet



Fig. 10 - Equilibrium shape of a Munroe jet

The radiograph of Fig. 11 is that of an explosive-driven thin aluminum plate colliding obliquely with a thicker plate of the same material. This radiograph shows the collision process, the shock wave generated in the thicker aluminum, a reflected shock wave in the high explosive gas products, and rarefaction waves in both the aluminum and the HE gases. The store of information in these kinds of experiments is obvious.

Several 25-mm thick aluminum plates were driven by 10-cm cubes of Composition B. The trajectories of the back surface, the transmitted shock, the reflected shock, and the front surface were determined radiographically from a sequence of shots. The unadjusted raw data, plotted in Fig. 12, illustrate these trajectories

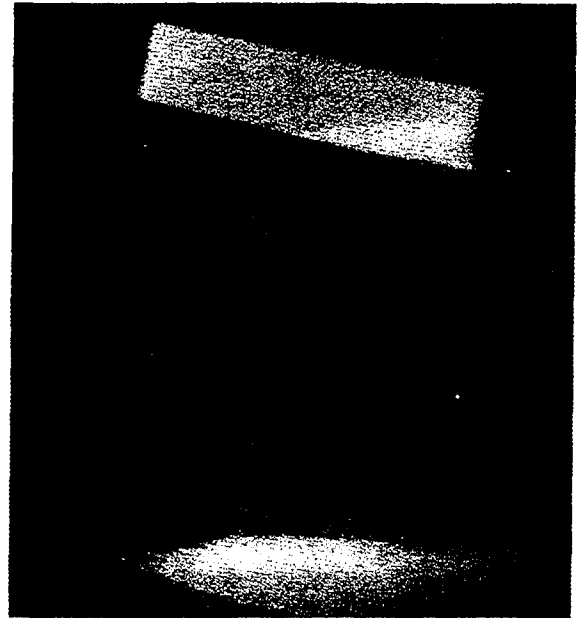


Fig. 11 - Oblique collision of a flying plate with a stationary plate

in space and time. The solid lines were computed by means of codes developed at the Los Alamos Scientific Laboratory [26]. The radiograph of Fig. 13 represents this type of experiment. A series of experiments like these, using suitable target materials can provide directly Hugoniot and isentrope data on the reaction products in a way that is independent of measurements of free-surface velocities of plates.

Figure 14 is typical of spalling experiments. In this case a 25-mm thick plate of

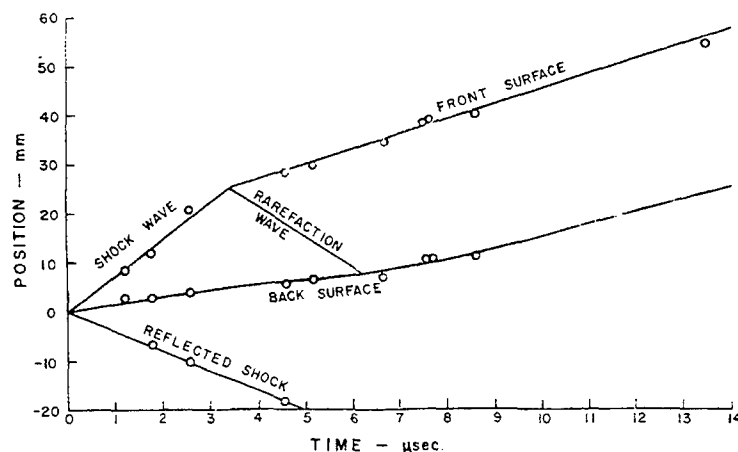


Fig. 12 - Trajectories of various discontinuities in explosive driven plate experiments

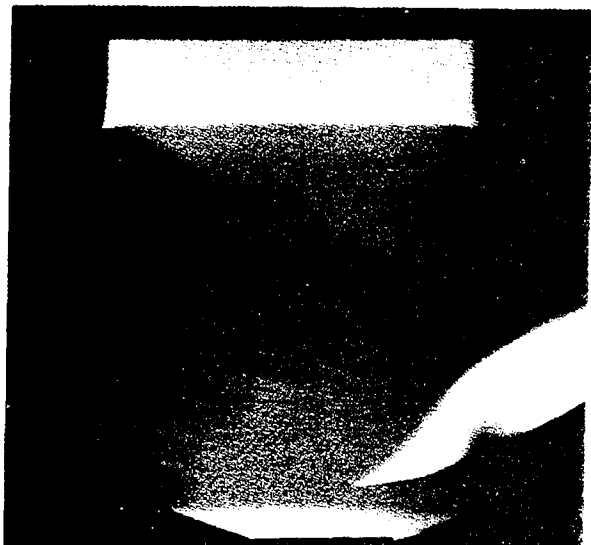


Fig. 13 - Radiograph of explosive driven aluminum plate showing shock wave in metal and shock wave in detonation products

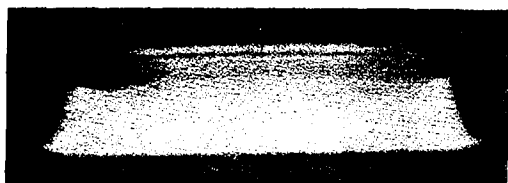


Fig. 14 - Spalling in nickel plate

nickel was driven by Composition B. Dynamic tensile strengths of a number of metals have been determined for a variety of pressure gradients and stress rates. Since this work is still incomplete no results will be reported here.

The last example of PHERMEX experiments presented here is illustrated in the radiograph of Fig. 15, where two aluminum jets have collided at right angles and appear to be vaporizing. This is representative of studies now under way to investigate the formation of jets, especially metallic jets arising from known surface perturbations. Unlike the more common Munroe jets which are formed by explosive-driven metal lined cavities, these kinds of jets seem to possess many of the characteristics of the gaseous Munroe jets discussed earlier in that their origin lies in the collision of the expanding free-surfaces provided the free-surface collision occurs before spalling.



Fig. 15 - Colliding aluminum jets

DISCUSSION

PHERMEX can be employed in multiple experiment flash radiography to obtain time histories of various hydrodynamic phenomena. It is possible to locate edges as in normal skiagraphy, to measure the velocity of shock waves, rarefaction waves, contact surfaces, and to measure particle velocity behind shocks, detonations, and rarefactions. Mass density distributions can be obtained. A time sequence of such distributions provides a means of determining velocity gradients, hence viscosity as well as the time variation of mass density gradients. Accurate measurements of these hydrodynamic variables provide Hugoniot and isentrope information for extreme states of matter.

ACKNOWLEDGMENTS

PHERMEX was designed and built by members of Group GMX-11 of the Los Alamos Scientific Laboratory. It is a tribute to these same people that they quickly adapted themselves to the tasks of applying flash radiography to explosives experiments. Furthermore, the authors wish to thank Drs. W. C. Davis, W. E. Deal, Wildon Fickett, and C. L. Mader for their contributions to our experimental work through their discussions and criticisms and especially C. L. Mader for performing many relevant calculations.

This work was performed under the auspices of the U.S. Atomic Energy Commission.

NOTES AND REFERENCES

1. V. A. Zukerman, *Compt. Rend. (Doklady)* 40, 267 (1943)
2. David Hawkins, *Manhattan District History; Project Y, The Los Alamos Project; Vol. I*, Los Alamos Scientific Laboratory, Report LAMS-2532, 1946 and 1947
3. L. E. Simon, *German Research in World War II*, John Wiley and Sons, 1947
4. J. C. Clark, *Phys. Rev.* 72, 741 (A) (1947); *J. Appl. Phys.* 20, 363 (1949); *Am. Soc. Test. Mat. Special Technical Publication* No. 96 (1950)
5. W. Schaaffs and F. Trendelenburg, *Z. Naturforsch.* 4a, 463 (1949) and 5a, 132 (1950); *Z. Physik* 137, 200 (1954) and 142, 642 (1955)
6. R. Schall, *Z. Angew. Phys.* 2, 83 and 252 (1950); 4, 291 (1952); *Z. Naturforsch.* 8a, 676 (1953)
7. G. Thomer, *Z. Angew. Phys.* 5, 217 (1953)
8. W. Schaaffs and K. H. Herrmann, *Z. Angew. Phys.* 6, 23 (1954)
9. R. Schall and G. Thomer, *Z. Physik* 142, 632 (1955)
10. W. Schaaffs, *Z. Physik* 142, 642 (1955)
11. V. A. Zukerman and M. A. Manakov, *Soviet Phys. - Tech. Phys.* 2, 353 (1957)
12. R. Schall, *Explosivstoffe* 6, 120 (1958)
13. W. N. Hess, M. D. Martin, G. C. McFarland, W. A. Rutz, and J. A. Welch, *Rev. Sci. Instr.* 30, 794 (1959)
14. F. J. Grundhauser, W. P. Dyke, and S. D. Bennett, *J. Soc. Motion Picture Television Engrs. (USA)* 70, 435 (1961)
15. L. V. Al'tshuler and A. P. Petrunin, *Soviet Phys. - Tech. Phys.* 6, 516 (1961)
16. R. Schall and G. Thomer, *Flash Radiographic Measurement of the Shock Compressibility of Magnesium Alloy, Lucite, and Polyethylene*, Air Force Special Weapons Center, Report AFSWC-TOR-62-134 (October 1962)
17. A. S. Balchan, *J. Appl. Phys.* 34, 241 (1963)
18. A. S. Balchan and G. R. Cowan, *Rev. Sci. Instr.* 35, 937 (1964)
19. Most of this work, performed at the Los Alamos Scientific Laboratory by Leo. F. Perry, Glenn E. Seay, and Douglas Venable, was completed in 1952
20. N. C. Miller and J. D. Steely, AECU-2721 (Oct. 1953), U.S. Government Printing Office, Washington, D.C.
21. Douglas Venable, *A Pulsed High Energy Radiographic Machine Emitting X-Rays: I. The Radiation Problem*, Los Alamos Scientific Laboratory, Report LA-3130 (1964)
22. V. J. Tolok, L. I. Bolotin, V. V. Chechkin, N. I. Nazarov, and N. A. Khizhnyak, *At. Energ. (USSR)* 11, 41 (1961)
23. Douglas Venable, *Rev. Sci. Instr.* 33, 456 (1962)
24. T. J. Boyd, B. T. Rogers, F. R. Tesche, and Douglas Venable. This paper has been submitted for publication in one of the technical journals
25. G. I. Taylor, *Proc. Roy. Soc. (London)* A200, 235 (1950)
26. C. L. Mader, *STRETCH SIN: A Code for Computing One-Dimensional Reactive Hydrodynamic Problems*, Los Alamos Scientific Laboratory, Report TID-18571 (1963)
27. T. J. Boyd, Jr. and Douglas Venable, *Bull. Am. Phys. Soc. II*, 10, 275 (1965)
28. W. E. Deal, *Phys. Fluids* 1, 523 (1958)
29. W. C. Davis, B. G. Craig, and J. B. Ramsay, *Failure of the Chapman-Jouguet Theory for Liquid and Solid Explosives*, Fourth Symposium on Detonation (1965)

LIST OF ATTENDEES

M. T. Abegg
Advanced Development Division
Sandia Corporation
P. O. Box 5800
Albuquerque, New Mexico 87115

James E. Ablard
Naval Ordnance Laboratory
White Oak
Silver Spring, Maryland 20910

Gordon K. Adams
Explosives R&D Establishment
Waltham Abbey
Essex, England

I. B. Akst
Pantex Plant, Mason & Hanger
Silas Mason Co., Inc.
P. O. Box 647
Amarillo, Texas

J. W. S. Allan
Atomic Weapons Research Est.
Bldg. H12
Aldermaston, Berkshire, England

Robert C. Allen
McCormick-Selph Associates
Hollister Airport
Hollister, California

John M. Allred
Martin Co.
P.O. Box 5837
Orlando, Florida

Adolph B. Amster
Stanford Research Institute
Menlo Park, California 94025

W. Hoyt Andersen
Shock Hydrodynamics, Inc.
15010 Ventura Blvd.
Sherman Oaks, California 91403

G. D. Anderson
Stanford Research Institute
Menlo Park, California 94025

Roger W. Anderson
Ensign-Bickford Co.
Simsbury, Connecticut

Thomas O. Anderson
Naval Ordnance Laboratory
White Oak
Silver Spring, Md. 20910

Douglas D. Antrobus
Field Emission Corp.
1753 Rockville Pike
Rockville, Maryland

C. J. Aronson
Naval Ordnance Laboratory
White Oak
Silver Spring, Maryland 20910

James L. Austing
IIT Research Institute
10 West 35th Street
Chicago, Illinois 60616

Theodore D. Austin
Naval Propellant Plant
Indian Head, Md. 20640

W. H. Avery
Applied Physics Laboratory
8621 Georgia Avenue
Silver Spring, Maryland

James N. Ayres
Naval Ordnance Laboratory
White Oak
Silver Spring, Maryland 20910

Marvin E. Backman
Research Dept.
U.S. Naval Ordnance Test Station
China Lake, California 93557

Robert A. Bailey
Engineer R&D Laboratory
Ft. Belvoir, Virginia 22060

Anthony S. Balchan
E. I. duPont deNemours & Co., Inc.
Eastern Laboratory
P. O. Box B
Gibbstown, New Jersey 08027

Robert H. Barlett
University of California
Lawrence Radiation Laboratory
Livermore, California

Philip Barnhard, IV
E. I. duPont deNemours & Co.
Eastern Laboratory
Gibbstown, New Jersey 08027

C. M. Bean
Atomic Weapons Research Est.
Aldermaston, Berkshire,
England

P. Beatrice
Commissariat a l'Energie
Atomique
B.P. N°7
Sevran (93), France

Charles W. Beckett
National Bureau of Standards
Washington, D. C. 20234

Louis J. Belliveau
Naval Ordnance Systems Command
Navy Department
Washington, D. C. 20360

William B. Benedick
Sandia Corp.
Sandia Base
Albuquerque, N. M. 87115

Jean Berger
Commissariat a l'Energie
Atomique
B. P. N°7
Sevran (93), France

Jean C. Bergon
Centre d'Etudes de Gramat
Gramat (Lot), France

N. E. Berkholtz
Military Products Group
Honeywell, Inc.
600 2nd Street North
Hopkins, Minnesota 55343

H. Bernier
Commissariat a l'Energie
Atomique
B. P. N°7
Sevran (93), France

Eugene R. Bissell
Lawrence Radiation Lab.
P. O. Box 808
Livermore, California

David F. Bleil
Naval Ordnance Laboratory
White Oak
Silver Spring, Md. 20910

Carl Boyars
U.S. Naval Ordnance Lab.
White Oak
Silver Spring, Md. 20910

M. H. Boyer
Philco Corporation
Ford Road
Newport Beach, California

Vincent M. Boyle
Ballistic Research Labs.
Aberdeen Proving Ground
Maryland 21005

Cyril J. Breza
E. I. duPont deNemours & Co., Inc.
Eastern Laboratory
P. O. Box B
Gibbstown, New Jersey 08027

Stuart R. Brinkley
Combustion & Explosives Res., Inc.
1007 Oliver Building
Pittsburgh, Pa. 15222

William P. Brooks
Sandia Corp.
Sandia Base
Albuquerque, N. M. 87115

Charles R. Brown
Applied Physics Lab.
JHU
8621 Georgia Ave.
Silver Spring, Md.

W. G. Brownlee
Defence Research Board
Canadian Armament R&D Est.
P. O. Box 1427
Quebec, P. Q., Canada

Frank B. Burdick
Explosive Technology, Inc.
P. O. Box KK
Fairfield, California

Marvin W. Burnham
Falcon R&D Company
1441 Ogden Street
Denver, Colorado 80218

Bernard Burke
Naval Ordnance Lab.
White Oak
Silver Spring, Md.

B. M. Butcher
Sandia Corporation
Sandia Base
Albuquerque, N. M. 87115

G. P. Cachia
Atomic Weapons Research Est.
Aldermaston, Berkshire
England

R. F. Chaiken
344 E. Hurst Avenue
Covina, California

Roger Cheret
Commissariat a l'Energie
Atomique
B. P. N°7
Sevran (93), France

Yves Chevalier
Commissariat à l'Energie
Atomique
B. P. N°7
Sevran (93), France

A. R. Clairmont
Naval Ordnance Lab.
White Oak
Silver Spring, Md. 20910

Eric N. Clark
Picatinny Arsenal
Dover, New Jersey 07801

Nathaniel L. Coleburn
Naval Ordnance Lab.
White Oak
Silver Spring, Md. 20910

Joseph G. Connor, Jr.
Naval Ordnance Lab.
White Oak
Silver Spring, Md. 20910

Robert L. Conger
U.S. Naval Ordnance Lab.
Corona, Calif. 91720

W. C. Connick
Via: Desmond Dousley
Australian Embassy
2001 Connecticut Ave., N.W.
Washington, D. C.

David L. Coursen
E. I. duPont de Nemours & Co., Inc.
Eastern Laboratory
P. O. Box B
Gibbstown, N. J. 08027

George R. Cowan
E. I. duPont de Nemours & Co., Inc.
Eastern Laboratory
P. O. Box B
Gibbstown, N. J. 08027

Michael Cowperthwaite
Stanford Research Institute
Menlo Park, Calif. 94025

Fred W. Cox, Jr.
Reynolds Experiment Lab.
Atlas Chemical Industries
Tamaqua, Pa. 18252

B. C. Craig
Los Alamos Scientific Lab.
P. O. Box 1663
Los Alamos, N. M. 87544

Jean Crosnier
Direction des Etudes et
Fabrication d'Armements
Centre d'Etudes de Gramat
Gramat (Lot), France

Charles B. Dale
Naval Propellant Plant
Indian Head, Md. 20640

Everett W. Dalrymple
Explosives Lab. F.R.L.
Picatinny Arsenal
Dover, New Jersey

Glenn H. Damon
Bureau of Mines
Dept. of Interior
Washington, D. C.

Jere Dando
Engineer R&D Lab.
Fort Belvoir, Va. 22060

James A. Dare
Operations & Admin.
Defense Atomic Support Agency
Washington, D. C. 20301

D. E. Davenport
General Precision, Inc.
Link Ordnance Division
670 Arques Avenue
Sunnyvale, Calif. 94086

Francis W. Davies
Boeing Aircraft Corp.
Seattle, Washington

Harvey Lee Davis
The Martin Co.
Sand Lake Road
Orlando, Florida

William C. Davis
Los Alamos Scientific Lab.
P. O. Box 1663
Los Alamos, N. M. 87544

William E. Deal
Los Alamos Scientific Lab.
P. O. Box 1663
Los Alamos, N. M. 87544

Peter J. Deas
DRDS
British Embassy
3100 Massachusetts Ave.
Washington, D. C. 20008

Allan B. Dietemann
Naval Ordnance Lab.
White Oak
Silver Spring, Md. 20910

Charles F. Dieter, Jr.
Naval Ordnance Systems Command
Navy Department
Washington, D. C. 20360

Robert H. Dinagar
Los Alamos Scientific Lab.
Los Alamos, N. M.

Vern T. Dinsdale
Thiokol Chemical Corp.
P. O. Box 524
Brigham City, Utah

Gus D. Dorough
Lawrence Radiation Lab.
P. O. Box 808
Livermore, Calif. 94551

Bernard E. Drimmer
Naval Ordnance Systems Command
Navy Department
Washington, D. C. 20360

Hiram E. Driscoll
Hercules Powder Co.
Port Ewen, N. Y. 12466

Brian Dunne
General Dynamics Corp.
General Atomic Division
P. O. Box 608
San Diego, California

George E. Duvall
Department of Physics
Washington State University
Pullman, Washington 99163

Russell Duff
Lawrence Radiation Lab.
P. O. Box 808
Livermore, Calif. 94551

Cyrus G. Dunkle
Applied Physics Lab.
8621 Georgia Avenue
Silver Spring, Md. 20910

John Eadie
Defence Standards Lab.
Melbourne
Victoria, Australia

Robert J. Eichelberger
Ballistic Research Labs.
Aberdeen Proving Ground
Maryland 21005

Clyde W. Eilo
Hercules Powder Co.
Kenvil, New Jersey

Julius W. Enig
Naval Ordnance Lab.
White Oak
Silver Spring, Md. 20910

John O. Erkman
Stanford Research Institute
Menlo Park, Calif. 94025

Gerald R. Eskelund
Liquid Rocket Propulsion Lab.
Picatinny Arsenal
Dover, New Jersey 07801

Harold W. Euker
Harvey Aluminum, Inc.
19200 South Western Ave.
Torrance, Calif.

Majorie W. Evans
Stanford Research Institute
Menlo Park, Calif. 94025

Robert W. Evans
Denver Research Institute
University of Denver
University Park
Denver 10, Colorado 80210

Claude Fauquignon
Commissariat à l'Energie
Atomique
B. P. N°7
Sevran, France

John N. Fedenia
Naval Ordnance Lab.
White Oak
Silver Spring, Md. 20910

William S. Filler
Naval Ordnance Lab.
White Oak
Silver Spring, Md. 20910

M. Finger
Lawrence Radiation Lab.
P. O. Box 808
Livermore, Calif. 94551

David Finlayson
Naval Weapons Lab.
Dahlgren, Va.

Elbert Fisher
Honeywell, Inc.
Systems & Research Div.
2345 Walnut St.
St. Paul, Minnesota

Robert F. Flagg
Institute for Aerospace Studies
University of Toronto
Toronto, Ontario, Canada

Rebecca W. Fleming
Bermite Powder Co.
22116 Soledad Canyon Rd.
Saugus, California

Charles Fossé
Centre de Recherches pour
l'Industrie des produits
Explosifs
Val du Bois (Sterrebeek)
Brabant, Belgium

Harold C. Foust
U.S. Naval Propellant Plant
Indian Head, Md.

Robert E. Franz
Ballistic Research Labs.
Aberdeen Proving Ground
Maryland 21005

H. M. Freiwald
Bundesminister der Verteidigung
53 Bonn
Ermekeilstafe, W. Germany

Morton H. Friedman
Applied Physics Lab.
8621 Georgia Avenue
Silver Spring, Md. 20910

P. J. A. Fuller
Atomic Weapons Research Est.
Foulness, Southend-on-Sea
Essex, England

Albert G. Funk
870 West 26th So.
Salt Lake City, Utah 84119

Carbs E. Garcia
New Mexico Tech R&D
Socorro, New Mexico

Benjamin A Gay
Atlas Chemical Industries, Inc.
Valley Forge Industrial Park
Valley Forge, Pa. 19481

Frank C. Gibson
Explosives Research Center
Bureau of Mines
4800 Forbes Avenue
Pittsburgh, Pa. 15213

Henry Giclas
New Mexico Tech R&DD
Socorro, New Mexico

John H. Giese
Ballistic Research Labs.
Aberdeen Proving Ground
Maryland 21005

Bryan E. Giesler
RPMX, AFRPL
Edwards AFB, Calif.

Elisabeth F. Gittings
Los Alamos Scientific Lab.
P. O. Box 1663
Los Alamos, N. M. 87544

Donald J. Glover
Naval Ordnance Lab.
White Oak
Silver Spring, Md. 20910

Charles Godfrey
Physics International Co.
2700 Merced
San Leandro, Calif.

John Goertner
Naval Ordnance Lab.
White Oak
Silver Spring, Md. 20910

Donald P. Graham
Hercules Powder Co.
Port Ewen, N. Y. 12466

Robert A. Graham
Sandia Corporation
Sandia Base
Albuquerque, N. M. 87115

Gordon A. Greene
U.S. Naval Ordnance Test
Station
China Lake, Calif. 93557

LeRoy G. Green
Lawrence Radiation Lab.
P. O. Box 808
Livermore, Calif. 94551

Chester Grelecki
Thiokol Chemical Corp.
Reaction Motors Division
Denville, N. J. 07834

Neill Griffiths
El Branch
Royal Armament R&D Est.
Ft. Halstead, Sevenoaks
Kent, England

Harold J. Gryting
U.S. Naval Ordnance Test
Station
China Lake, Calif. 93557

Laurence D. Hampton
Naval Ordnance Lab.
White Oak
Silver Spring, Md. 20910

Richard Hanson
Office of Naval Research
Room 0410
Department of the Navy
Washington, D. C. 20360

Jere G. Harlan
Sandia Corporation
P. O. Box 5800
Albuquerque, N. M. 87115

Robert O. Harper
General Electric Co.
P. O. Box 2500
Daytona Beach, Florida

Paul Harris
Naval Ordnance Lab.
White Oak
Silver Spring, Md. 20910

Stewart Hart
Physics Dept.
Aberdeen University
Aberdeen, Great Britain

Gregory K. Hartmann
Naval Ordnance Lab.
White Oak
Silver Spring, Md. 20910

Z. V. Harvalik
Engineer R&D Lab.
Ft. Belvoir, Va. 22060

George E. Hauver
Terminal Ballistics Lab.
Ballistic Research Labs.
Aberdeen Proving Ground
Maryland 21005

J. Edmund Hay
Explosives Research Center
Bureau of Mines
4800 Forbes Avenue
Pittsburgh, Pa. 15213

Bernard Hayes
Los Alamos Scientific Lab.
P. O. Box 1663
Los Alamos, N. M. 87544

Dennis Hayes
Sandia Corp.
P. O. Box 5800
Albuquerque, N. M. 87115

Albert Hawkins
Ballistic Research Labs.
Aberdeen Proving Ground
Maryland 21005

Robert Heinemann
Picatinny Arsenal
Dover, N. J. 07801

Franz-Josef Heinen
Naval Propellant Plant
Indian Head, Md. 20640

Harry Heller
Naval Ordnance Lab.
White Oak
Silver Spring, Md. 20910

Joseph A. Herickes
Atlantic Research Corp.
Shirley Hwy & Edsall Rd.
Alexandria, Va.

Walter Herrmann
Sandia Corporation
Sandia Base
Albuquerque, N. M. 87115

Joseph Herschkowitz
Feltman Research Lab.
Picatinny Arsenal
Dover, N. J. 07801

John A. Hicks
Explosives R&D Est.
Waltham Abbey
Essex, England

F. K. Hill
Applied Physics Lab.
The Johns Hopkins University
8621 Georgia Avenue
Silver Spring, Md.

R. Lenton Hill
DET 4, RTD (ATWR)
Eglin AFB, Florida 32542

Robert M. Hillyer
U.S. Naval Ordnance Lab.
Corona, Calif. 91720

Victor L. Hirschy
DAD, RTD,
Eglin AFB, Florida

Lee S. Holloway
Ballistic Research Labs.
Aberdeen Proving Ground
Maryland 21005

Douglas C. Hornig,
Naval Ordnance Lab.
White Oak
Silver Spring, Md. 20910

H. C. Hornig
Lawrence Radiation Lab.
P. O. Box 808
Livermore, Calif. 94551

Nicholas E. Hoskin
Atomic Weapons Research Est.
Aldermaston, Berkshire
England

James H. Hosman, Jr.
McDonnell Aircraft Corp.
P. O. Box 516
St. Louis, Mo.

Richard C. Hu
Naval Ordnance Lab.
White Oak
Silver Spring, Md. 20910

Harold Hurwitz
Naval Ordnance Lab.
White Oak
Silver Spring, Md. 20910

Robert J. Irvine
758 Channing Avenue
Palo Alto, Calif. 94301

O. R. Irwin
Aerojet-General Corp.
Downey, Calif.

Bernard L. Iwanciw
United Technology Center
P. O. Box 358
Sunnyvale, Calif. 94088

Sigmund J. Jacobs
Naval Ordnance Lab.
White Oak
Silver Spring, Md. 20910

Irving Jaffe
Naval Ordnance Lab.
White Oak
Silver Spring, Md. 20910

Edward James, Jr.
Lawrence Radiation Lab.
P. O. Box 808
Livermore, Calif. 94551

Robert L. Jameson
Ballistic Research Labs.
Aberdeen Proving Ground
Maryland 21005

Daniel J. Janzen
Field Emission Corp.
1753 Rockville Pike
Rockville, Md.

Lawrence S. Jessie
Picatinny Arsenal
Dover, New Jersey 07801

Wayne E. Jewsbury
The Northrop-Carolina
Box 3049
Asheville, N. C. 28802

C. F. Johnson
Naval Weapons Laboratory
Dahlgren, Virginia

Edgar G. Johnson
Rohm and Haas Company
Redstone Arsenal Research Div.
Huntsville, Alabama 35807

Theodore B. Johnson
Remington Arms Co., Inc.
939 Barnum Avenue
Bridgeport, Connecticut

Suzanne Joigneau
Commissariat a l'Energie
Atomique
B. P. 511
Paris XV, France

Arfon H. Jones
General Motors Defense
Research Lab.
Box T
Santa Barbara, Calif.

Clyde Jones
Unidynamics
P. O. Box 2990
Phoenix, Arizona 85002

Norman M. Junk
Atlas Chemical Industries
P. O. Box 271
Tamaqua, Pa. 18252

Irving Kabik
Naval Ordnance Lab.
White Oak
Silver Spring, Md. 20910

Ahmed D. Kafadar
Ordnance Engrg. Ass. Inc.
1030 E. North Avenue
Des Plaines, Illinois 60016

F. W. Kasdorf
Naval Weapons Lab.
Dahlgren, Va.

J. V. Richard Kaufman
Chief Scientist
U.S. Army Munitions Command
Dover, New Jersey

Werner Keger
Institute Franco-Allemand de
Recherches de Saint-Louis
12, rue de l'Industrie
Saint Louis (Haut-Rhin)
France

Bennett W. Kelley
Military Products Group
Honeywell, Inc.
600 2nd Street North
Hopkins, Minnesota 55343

M. D. Kemp
USAERDL Basic Research
Ft. Belvoir, Va

Paul Kendall
Naval Ordnance Lab.
White Oak
Silver Spring, Md. 20910

James E. Kennedy
IIT Research Institute
10 West 35th Street
Chicago, Illinois 60616

Jean Kieffer
Laboratoire des Hautes
Pressions
C.N.R.S. - Bellevue (S&O)
1 Place Aristide Briand
France

E. Eugene Kilmer
Naval Ordnance Lab
White Oak
Silver Spring, Md. 20910

Martin W. Kordas, Jr.
Remington Arms Co., Inc.
939 Barnum Avenue
Bridgeport, Connecticut

John W. Kury
Lawrence Radiation Lab.
P. O. Box 808
Livermore, Calif. 94551

Carl Kyselka
RTD Weapons Division
Eglin AFB, Florida 32542

Brian D. Lambourn
Bldg. H12
Atomic Weapons Research Est.
Aldermaston, Berkshire
England

W. D. Lanning
Technical Operations, Inc.
Burlington, Mass.

Thomas E. Larson
Los Alamos Scientific Lab.
P. O. Box 1663
Los Alamos, N. M. 87544

Robert W. Lawrence
Hercules Powder Co.
910 Market Street
Wilmington, Del. 19899

Edward L. Lee
Lawrence Radiation Lab.
P. O. Box 808
Livermore, Calif. 94551

Nicholas L. Leone
Det. 4, RTD (ATWR)
Eglin AFB, Florida 32542

Howard S. Leopold
Naval Ordnance Laboratory
White Oak
Silver Spring, Md 20910

William B. Leslie
Sandia Corp.
P. O. Box 5800
Albuquerque, N. M. 87115

Bernard Lewis
Combustion & Explosives
Research, Inc.
1007 Oliver Building
Pittsburgh, Pa. 15222

Thomas P. Liddiard, Jr.
Naval Ordnance Lab.
White Oak
Silver Spring, Md. 20910

Paul Lieberman
IIT Research Institute
10 West 35th Street
Chicago, Ill. 60616

Jackson K. Lightfoot
Hi-Shear Corporation
2600 West 247th Street
Torrance, Calif. 90509

Stanhope K. Ligon
Foreign Tech. Div. (TDETC)
Wright-Patterson AFB,
Ohio 45433

C. D. Lind
U.S. Naval Ordnance Test
Station
China Lake, Calif. 93557

David T. Liu
Lockheed Research
Dept. 52-20
Palo Alto, Calif.

Elwyn E. Lockwood
Rocketdyne, D/991-368, Z-11
6633 Canoga Avenue
Canoga Park, Calif.

Lennart P. Lundberg
Forsvarets Forskningsanstalt
Avdelning 2
Stockholm 80, Sweden

Jacques Lutfalla
Commissariat a l'Energie
Atomique
B. P. 511
Paris XV, France

Morton Lutzky
Naval Ordnance Lab.
White Oak
Silver Spring, Md. 20910

Duncan P. MacDougall
Los Alamos Scientific Lab.
P. O. Box 1663
Los Alamos, N. M. 87544

Andrej Maček
Atlantic Research Corp.
Alexandria, Va.

Charles L. Mader
Los Alamos Scientific Lab.
P. O. Box 1663
Los Alamos, N. M. 87544

Michael Maes
520 S. Portland St.
Seattle, Washington

A. H. Makomaski
National Research Council
of Canada
Gas Dynamics Laboratory
Division of Mechanical Engr.
National Research Council
Ottawa 2, Ontario, Canada

Walter H. Mandelco
General Atomic Division
General Dynamics Corp.
P. O. Box 608
San Diego, Calif. 92112

Orin W. Marks
Research Center
Hercules Powder Co.
Wilmington, Delaware

Patrick J. Martin
Chemical Propulsion Information
Agency
The Johns Hopkins University
Applied Physics Laboratory
8621 Georgia Avenue
Silver Spring, Md.

C. Masaitis
Ballistic Research Labs.
Aberdeen Proving Ground
Maryland 21005

D. W. Mayer
Applied Physics Dept.
Franklin Institute
20th & Benjamin Franklin Pkwy
Philadelphia, Pa. 19103

William McBride
U.S. Naval Weapons Station
Yorktown, Va.

Russell L. McCally
Applied Physics Laboratory
8621 Georgia Avenue
Silver Spring, Md.

Leonard W. McCleary
Dept. 81-74 Bldg 153
Lockheed Missile & Space Co.
Sunnyvale, Calif.

William E. McQuiston
U.S. Naval Propellant Plant
Indian Head, Md.

Giordano Melani
Ballistic Research Labs.
Aberdeen Proving Ground
Maryland 21005

Vincent J. Menichelli
Naval Ordnance Laboratory
White Oak
Silver Spring, Md. 20910

George E. Metcalf
Boeing Aircraft Co.
Seattle, Washington

Carroll C. Misener
Naval Ordnance Laboratory
White Oak
Silver Spring, Md. 20910

Chi-Hung Mok
EBL, Bldg 120
Aberdeen Proving Ground
Maryland 21005

J. M. Moniod
Commissariat a l'Energie
Atomique
B. P. 511
Paris XV, France

Louis J. Montesi
Naval Ordnance Laboratory
White Oak
Silver Spring, Md. 20910

James F. Moulton, Jr.
Defense Atomic Support Agency
The Pentagon
Washington, D. C.

D. A. Moyant
Atlas Chemical Industries, Inc.
Valley Forge Industrial Park
Valley Forge, Pa. 19481

Herbert J. Mueller
Engineer R&D Labs.
Ft. Belvoir, Va. 22060

D. E. Munson
Sandia Corporation
Sandia Base
Albuquerque, N. M. 87115

Maurice F. Murphy
Naval Ordnance Laboratory
White Oak
Silver Spring, Md. 20910

Mas Nakano
General Precision, Inc.
670 Arques Avenue
Sunnyvale, Calif.

Hyla S. Napadensky
IIT Research Institute
10 West 35th Street
Chicago, Illinois 60616

A. Nordio
Picatinny Arsenal
Dover, New Jersey 07801

C. H. Noren
E. I. duPont de Nemours & Co.
Potomac River Dev. Lab.
P. O. Box 761
Martinsburg, West Va.

Floyd A. Odell
Field Emission Corp.
1753 Rockville Pike
Rockville, Maryland

John T. Oleksy
Naval Ordnance Lab.
White Oak
Silver Spring, Md. 20910

M. K. Oprecht
Northrop-Carolina
Box 3049
Asheville, N. C. 28802

D. L. Ornellas
Lawrence Radiation Lab.
P. O. Box 808
Livermore, Calif. 94551

M. R. Osborne
Defence Standards Labs.
P. O. Box 50
Ascot Vale Victoria
Australia

O. B. Osmondson
Naval Weapons Lab.
Dahlgren, Virginia

D. C. Pack
Univ. of Strathclyde
Glasgow, Scotland

Mary L. Pandow
Rohm and Haas Co.
Redstone Arsenal Res. Div.
Huntsville, Alabama 35807

John B. Panowski
Los Alamos Scientific Lab.
P. O. Box 1663
Los Alamos, N. M. 87544

Robert A. Papetti
Aero-Astronautics Dept.
The Rand Corporation
1700 Main Street
Santa Monica, Calif. 90406

Daniel K. Parks
Falcon R&D Co.
1441 Ogden Street
Denver, Colorado 80218

Dale S. Partridge
Prod. Devl.-Blasting Mats.
Spencer Chemical Division
Gulf Oil Corporation
Dwight Building
Kansas City, Missouri 64105

D. John Pastine
Naval Ordnance Lab.
White Oak
Silver Spring, Md. 20910

John J. Paszek
Ballistic Res. Labs.
Aberdeen Proving Ground
Aberdeen, Maryland 21005

James B. Patton
Mail No. T0533
Martin Company
P. O. Box 179
Denver, Colorado 80201

James C. Pearson
Feltman Res. Labs.
Picatinny Arsenal
Dover, N. J. 07801

Russel G. Perkins
Armed Ser. Explosives
Safety Bd.
Nassif Building
Washington, D. C. 20315

Per-Anders Persson
Swedish Detonic Res. Found.
Vinterviken
Stockholm SV, Sweden

Joseph Petes
Naval Ordnance Lab.
White Oak
Silver Spring, Md. 20910

Francis J. Petrone
Naval Ordnance Lab.
White Oak
Silver Spring, Md. 20910

Vasil Philipchuk
USNWL Code TE-2
Dahlgren, Virginia 22448

Dante Piacesi, Jr.
Naval Ordnance Lab.
White Oak
Silver Spring, Md. 20910

Sylvester C. Piccoli
Harvey Aluminum, Inc.
5273 Burton Street
Philadelphia, Pa. 19124

R. S. Pickford
Douglas Aircraft Co. Inc.
2121 Campus Drive
Newport Beach, Calif. 92663

Donald Pitt
3M
2301 Hudson Road
St. Paul, Minnesota 55119

J. F. Pittman
Naval Ordnance Lab.
White Oak
Silver Spring, Md. 20910

Locha D. Pitts
Link Ordnance Division
General Precision, Inc.
670 Arques Avenue
Sunnyvale, Calif. 94086

John Plant
Safety in Mines Res. Est.
Field Laboratories
Harper Hill
Buxton, Derbyshire
England

A. Popolato
Los Alamos Scientific Lab.
P. O. Box 1663
Los Alamos, N. M. 87544

L. A. Potteiger
Naval Weapons Lab.
Dahlgren, Virginia

Thomas H. Pratt
Rohm and Haas Co.
Redstone Arsenal Res. Div.
Huntsville, Alabama 35807

Z. Pressman
Stanford Research Institute
Menlo Park, Calif. 94025

Donna Price
Naval Ordnance Lab.
White Oak
Silver Spring, Md. 20910

J. H. Price
Atomic Weapons Res. Est.
Foulness, Southend-on-Sea
Essex, England

James Price
Naval Weapons Lab.
Dahlgren, Virginia

James F. Proctor
Naval Ordnance Lab.
White Oak
Silver Spring, Md. 20910

H. H. Radke
Aerospace Corp.
P. O. Box 1308
San Bernardino, Calif.

John B. Ramsay
Los Alamos Scientific Lab.
P. O. Box 1663
Los Alamos, N. M. 87544

Carl W. Randall
Naval Ordnance Lab.
White Oak
Silver Spring, Md. 20910

Armand Rauch
Commissariat a l'Energie Atomique
B. P. N°7
Sevran (93)
France

R. F. Reinking
Atlas Chemical Industries, Inc.
Valley Forge Industrial Park
Valley Forge, Pa. 19481

J. R. Rempel
Stanford Res. Institute
Menlo Park, Calif. 94025

N. O. Rhoton
Pantex Plant, Mason & Hanger
Silas Mason Co., Inc.
P. O. Box 647
Amarillo, Texas

Robert H. Richardson
Hercules Powder Co.
Cumberland, Md.

J. K. Rigdon
Pantex Plant
Silas Mason Co. Inc.
P. O. Box 647
Amarillo, Texas

Glenn L. Roark
Chief, Armament Branch BBGO
Douglas Aircraft Co.
3000 Ocean Park Blvd.
Santa Monica, Calif. 90406

G. R. Roberson
Naval Ordnance Lab.
White Oak
Silver Spring, Md. 20910

Ralph Roberts
Office of Naval Research
Room 0410 Main Navy
Washington, D.C. 20360

M. F. Rose
Naval Weapons Lab.
Dahlgren, Virginia

William Rose
Unidynamics
P. O. Box 2990
Phoenix, Arizona 85002

Alvin H. Rosen
Naval Ordnance Lab.
White Oak
Silver Spring, Md. 20910

Jerome M. Rosen
Naval Ordnance Lab.
White Oak
Silver Spring, Md. 20910

Hyman Rosenwasser
Engineer R&D Labs.
Ft. Belvoir, Virginia 22060

Leslie A. Roslund
Naval Ordnance Lab.
White Oak
Silver Spring, Md. 20910

Julius Roth
Stanford Res. Institute
Menlo Park, Calif. 94025

Klaus G. Rucker
E. I. duPont deNemours & Co., Inc.
Eastern Laboratory
P. O. Box B
Gibbstown, N. J. 08027

Leonard Rudlin
Naval Ordnance Lab.
White Oak
Silver Spring, Md. 20910

Norman L. Rumpff
Head, Explosives & Pyrotechnics Div.
Code 454
U. S. Naval Ordnance Test Station
China Lake, California

Bernard G. Ryle
AMP Inc.
Harrisburg, Pennsylvania

Lippe D. Sadwin
Naval Ordnance Lab.
White Oak
Silver Spring, Maryland 20910

J. Martin Sandler
E. I. duPont deNemours & Co., Inc.
Eastern Laboratory
P. O. Box B
Gibbstown, N. J. 08027

Joseph M. Santiago, Jr.
Ballistic Res. Labs.
Aberdeen Proving Ground, Md. 21005

Jacob Savitt
Explosiform Lab.
1001 Skyline Blvd.
San Francisco, Calif. 94132

Rudi Schall
NATO Headquarters
Div. of Sci. Affairs
Porte Dauphine
Paris 16^e, France

Morry L. Schimmel
McDonnell Aircraft Corp.
Box 516
St. Louis, Missouri 63166

Garry L. Schott
Los Alamos Scientific Lab.
P. O. Box 1663
Los Alamos, N. M. 87544

H. S. Schuld
Sandia Corp.
P. O. Box 5800
Albuquerque, N. M. 87115

Calvin L. Scott
Naval Ordnance Lab.
White Oak
Silver Spring, Md. 20910

L. B. Seely
Stanford Res. Institute
Menlo Park, Calif. 94025

Arnold E. Seigel
Naval Ordnance Lab.
White Oak
Silver Spring, Md. 20910

Robert W. Selden
Lawrence Radiation Lab.
P. O. Box 808
Livermore, Calif. 94551

Henry M. Shuey
Rohm and Haas Co.
Redstone Arsenal Res. Div.
Huntsville, Alabama 35807

Ronald G. Shuttleworth
Scientific Attache
South African Embassy
3051 Massachusetts Ave. N. W.
Washington, D. C. 20010

John C. Silva
Naval Ordnance Lab.
White Oak
Silver Spring, Md. 20910

D. A. Silva
Naval Weapons Lab.
Dahlgren, Virginia

James E. Sinclair
Naval Postgraduate School
Monterey, Calif. 93940

G. D. Singer
Basic Res. Lab.
Engineer R&D Lab.
Ft. Belvoir, Va. 22060

T. E. Slylhouse
Chemicals Lab.
1710 Bld.
The Dow Chemical Co.
Midland, Michigan

Allan H. Smith
Dept 62-22
Lockheed Missiles & Space Co.
P. O. Box 504
Sunnyvale, California

Arthur C. Smith
Physics Department
The Rand Corporation
1700 Main Street
Santa Monica, Calif. 90406

Louis C. Smith
Los Alamos Scientific Lab.
P. O. Box 1663
Los Alamos, N. M. 87544

S. Smith
Naval Weapons Lab.
Dahlgren, Virginia

William M. Smith
Contract R&D
Ensign-Bickford Co.
660 Hopmeadow Street
Simsbury, Conn. 06070

William H. Snyder
Denver Res. Institute
University of Denver
Denver, Colorado 80210

A. D. Solem
Systems Analysis Staff
U. S. Naval Ordnance Lab.
White Oak, Silver Spring, Md.

Max Solow
U. S. Navy Marine Engng. Lab.
Annapolis, Maryland 21402

W. G. Soper
Naval Weapons Lab.
Dahlgren, Virginia

Leland E. Starr
Naval Ordnance Lab.
White Oak
Silver Spring, Md. 20910

Ronald F. Stauder
Applied Physics Lab.
8621 Georgia Ave.
Silver Spring, Md. 20910

T. S. Sterling
Defence Res. Board
Canadian Armament R&D Est.
P. O. Box 1427
Quebec, P. Q.
Canada

Hyman M. Sternberg
Naval Ordnance Lab.
White Oak
Silver Spring, Md. 20910

Fred Strange
Lawrence Radiation Lab.
P. O. Box 808
Livermore, Calif. 94551

Roger A. Strehlow
Aeronautical & Astronautical
Engr. Dept.
University of Illinois
Urbana, Illinois

Richard H. F. Stresau
R. Stresau Lab., Inc.
Star Route
Spooner, Wis. 54801

Wilhelm Struck
Ernst Mach Inst.
7858 Weil am Rhein
Hauptstr. 188
Germany

Howard Sugiuchi
Waterways Experiment Station
Jackson, Mississippi

Morton Sultanoff
Ballistic Res. Labs.
Aberdeen Proving Ground
Maryland 21005

J. C. Talley
Naval Weapons Lab.
Dahlgren, Virginia

Boyd C. Taylor
Ballistic Res. Labs.
Attn: AMXBR-TD
Aberdeen Proving Ground
Maryland 21005

John W. Taylor
School of Applied Science
Leeds University
Leeds 2, England

Stanley M. Taylor, Jr.
Ballistic Res. Labs.
Aberdeen Proving Ground
Maryland 21005

Eugene A. Tkatchenko
Shock Hydrodynamics Inc.
15010 Ventura Blvd.
Sherman Oaks, Calif.

Martin D. Torrey
Technical Operations, Inc.
Burlington, Massachusetts

John P. Toscano
Naval Ordnance Laboratory
White Oak
Silver Spring, Md. 20910

J. R. Travis
Los Alamos Scientific Lab.
P. O. Box 1663
Los Alamos, N. M. 87544

Donald H. Tsai
National Bureau of Standards
Washington, D. C. 20234

Robert W. VanDolah
Explosives Res. Center
Bureau of Mines
4800 Forbes Avenue
Pittsburgh, Pa. 15213

Andrew Van Tuyl
Naval Ordnance Lab.
White Oak
Silver Spring, Md. 20910

Douglas Venable
Los Alamos Scientific Lab.
P. O. Box 1663
Los Alamos, N. M. 87544

Alain Vidart
Commissariat a l'Energie Atomique
B. P. N°7
Sevran (93)
France

Richard Vitali
USA Ballistic Res. Labs.
Aberdeen Proving Ground
Maryland 21005

Gunther VonElbe
Atlantic Research Corp.
Alexandria, Virginia

Jerry Wackerle
Los Alamos Scientific Lab.
P. O. Box 1663
Los Alamos, N. M. 87544

William A. Walker
Naval Ordnance Lab.
White Oak
Silver Spring, Md. 20910

F. J. Warner
University of Strathclyde
Glasgow C. 1
Scotland

Richard J. Wasley
Lawrence Radiation Lab.
P. O. Box 808
Livermore, Calif. 94551

Richard W. Watson
Explosives Res. Center
Bureau of Mines
4800 Forbes Avenue
Pittsburgh, Pa. 15213

Franz Wecken
Institut Franco-Allemand de
Recherches de Saint-Louis
12, rue de l'Industrie
Saint-Louis (Haut-Rhin)
France

Clarence E. Weinland
U. S. Naval Ordnance Test Sta.
China Lake, California

L. F. Welanetz
Applied Physics Lab.
The Johns Hopkins Univ.
8621 Georgia Avenue
Silver Spring, Maryland

Joseph Wenograd
United Aircraft Res. Lab.
E. Hartford, Connecticut

Alex Wenzel
General Motors Defense Res. Lab.
Box T
Santa Barbara, California

E. G. Whitbread
Explosives R&D Est.
Waltham Abbey
Essex, England

James H. Whitley
AMP Inc.
Harrisburg, Pa.

John C. Whitson
Code 45412
U. S. Naval Ordnance Test Sta.
China Lake, California 93557

Mark L. Wilkins
Lawrence Radiation Lab.
P. O. Box 808
Livermore, Calif. 94551

Earl M. Wintermoyer
Directorate of Armament Dev.
(ATWR)
Eglin AFB, Florida

W. N. Wishard
Naval Weapons Lab.
Dahlgren, Virginia

John Wisotski
Denver Res. Institute
University of Denver
Denver, Colorado 80210

N. R. Zabel
General Precision, Inc.
670 Arques Avenue
Sunnyvale, California

Dino Zei
Capitano A. N.
Marina Militare Italiana
Ministero Difesa
Marina (Marinarmi), Roma

Louis Zernow
Shock Hydrodynamics, Inc.
15010 Ventura Blvd.
Sherman Oaks, Calif. 91403

Martin Zimmer
Code RRCC
Naval Propellant Plant
Indian Head, Md. 20640

Csaba K. Zoltani
Ballistic Res. Lab. - IBL
Aberdeen Proving Ground
Maryland 21005

AUTHOR INDEX

(C) indicates comments.

- Adams, G. K., 502, 516 (C)
Allan, J. W. S., 14, 52
Amster, Adolph B., 126
Andersson, Bertil, 602
Andersen, W. H., 13 (C), 205
Anderson, G. D. 213
Argous, J. P., 135
Bailey, W. A., 14
Béatrix, P., 527
Berger, J., 238 (C)
Bernier, H., 381
Bouchon, H., 527
Boyd, T. J., Jr., 639
Boyle, V. M., 241
Broom, V. C., 462
Butcher, B. M., 295
Cachia, G. P., 84 (C), 512
Cameron, I. G. 305
Carpenter, J. H., 167
Chaiken, R. F., 398 (C), 461
Chéret, R., 78, 201 (C)
Cheselske, F. J., 461
Chevalier, Y., 527
Chick, Michael C., 349
Coleburn, N. L., 240
Cowperthwaite, M., 372 (C), 502
Craig, B. G., 84
Crosnier, Jean, 627
David, F., 381
Davis, W. C., 84
Deal, W. E., 321
Deffet, Louis, 156
Dorough, G. D., 477
Duff, Russell E., 198
Dunkle, G. G., 13 (C)
Duvall, George E., 248
Eadie, John, 399
Eden, G., 573
Elliott, L. A., 316
Enig, Julius W., 395
Erkman, John O., 277
Evans, Marjorie W., 359
Fahrenbruch, A. L., 213
Fauquignon, C., 39, 381, 594 (C)
Finger, M., 3
Fossé, C., 156
Fowles, G. R., 213
Fuller, P. J. A., 290
Gardner, S. D., 154, 154 (C)
Gibson, F. C., 117, 412
Gittings, Elisabeth, F., 373
Gordon, William E., 179
Graham, R. A., 222, 257 (C)
Green, LeRoy, G., 86, 477
Griffiths, Neill, 462
Gunn, S. R., 167
Halpin, W. J., 222
Hart, S., 47
Hartley, J. E., 538
Hay, J. F., 412
Hayes, Bernard, 595
Hershkowitz, Joseph, 168, 201 (C)
Hillyer, R. M., 449
Horie, Y., 248
Hornig, H. C., 3
Hoskin, N. E., 14
Jacquesson, Jean, 627
James, Edward, Jr., 86
Jameson, R. L., 241
Johansson, C. H., 435
Johnson, Edgar, G., 584
Joigneau, S., 152 (C), 154
Junk, Norman M., 92
Kegler, Werner, 496
Kennedy, J. E., 449, 476 (C)
Kury, J. W., 3
Kyselka, Carl, 404
Lambourn, B. D., 52, 142, 152 (C), 538
Lee, E. L. 3, 359
Leone, Nicholas, Capt., 404
Lethaby, J. W., 14
Liddiard, T. P., Jr., 214, 230 (C), 240, 487
Lundborg, N., 176, 432
Mader, Charles L., 394
Marlow, W. R., 426
McDonnel, J. L., 3
McEachern, D. M., Jr., 126
Migault, Andre, 627
Mueller, H. J., 608 (C)
Munson, D. E., 229 (C), 295
Murray, W. L., 555
Napadensky, Hyla S., 473
O'Brien, Joseph F., 239
Ockert, K. F., 96, 102
Ornellas, D. L., 3, 167

- Pandow, Mary L., 96, 102
Pearson, James C., 289
Persson, Per-Anders, 602
Petrone, Francis J., 395
Peyre, C., 135, 566
Piacesi, D., 153
Pike, H. H. M., 305
Pitts, Locha D., 616
Plant, J., 555
Popolato, A., 233
Potau, J., 381
Pratt, T. H., 102
Pressman, Z., 126
Price, J. H., 290
Prouteau, M., 39
Pujol, J., 566

Ramsay, J. B., 84, 233, 344 (C)
Rauch, Q., 154 (C)
Reese, B. O., 359
Rempel, John R., 266
Ribovich, J., 412
Roth, J., 358 (C)

Sadwin, Lippe, D., 92
Savitt, Jacob, 404
Schall, Rudi, 496
Schmidt, David N., 266
Schott, Garry L., 67

Scott, F. H., 412
Seely, L. B., 359
Shuey, H. M., 96
Singer, G. D., 608 (C)
Sjölin, T., 435
Skidmore, I. C., 14, 47
Ståhl, Sven-Olof, 602
Sternberg, H. M., 27, 153
Strange, F. M., 3
Stresau, R. H. F., 442, 449
Sultanoff, M., 241
Summers, C. R., 117

Thouvenin, J., 135, 258, 566
Travis, J. R., 386, 609

Van Dolah, R. W., 117
Venable, Douglas, 639
Verdés, G., 39
Vidart, A., 527

Wackerle, J., 154, 154 (C)
Walker, W. A., 27
Warner, F. J., 84 (C)
Wasley, Richard J., 239
Watson, R. W., 117
Wecken, Franz, 107
Wilkins, M. L., 3, 519
Wright, P. W., 142, 573